ROCK PHYSICS AND GEOFLUID DETECTION

EDITED BY: Jing Ba, José M. Carcione, Erik H. Saenger, Beatriz Quintal, Liyun Fu, Ludmila Adam and Ravi Sharma

PUBLISHED IN: Frontiers in Earth Science

frontiers Research Topics

frontiers

Frontiers eBook Copyright Statement

The copyright in the text of individual articles in this eBook is the property of their respective authors or their respective institutions or funders. The copyright in graphics and images within each article may be subject to copyright of other parties. In both cases this is subject to a license granted to Frontiers.

The compilation of articles constituting this eBook is the property of Frontiers.

Each article within this eBook, and the eBook itself, are published under the most recent version of the Creative Commons CC-BY licence. The version current at the date of publication of this eBook is CC-BY 4.0. If the CC-BY licence is updated, the licence granted by Frontiers is automatically updated to the new version.

When exercising any right under the CC-BY licence, Frontiers must be attributed as the original publisher of the article or eBook, as applicable.

Authors have the responsibility of ensuring that any graphics or other materials which are the property of others may be included in the CC-BY licence, but this should be checked before relying on the CC-BY licence to reproduce those materials. Any copyright notices relating to those materials must be complied with.

Copyright and source acknowledgement notices may not be removed and must be displayed in any copy, derivative work or partial copy which includes the elements in question.

All copyright, and all rights therein, are protected by national and international copyright laws. The above represents a summary only. For further information please read Frontiers' Conditions for Website Use and Copyright Statement, and the applicable CC-BY licence.

ISSN 1664-8714
ISBN 978-2-88971-562-6
DOI 10.3389/978-2-88971-562-6

About Frontiers

Frontiers is more than just an open-access publisher of scholarly articles: it is a pioneering approach to the world of academia, radically improving the way scholarly research is managed. The grand vision of Frontiers is a world where all people have an equal opportunity to seek, share and generate knowledge. Frontiers provides immediate and permanent online open access to all its publications, but this alone is not enough to realize our grand goals.

Frontiers Journal Series

The Frontiers Journal Series is a multi-tier and interdisciplinary set of open-access, online journals, promising a paradigm shift from the current review, selection and dissemination processes in academic publishing. All Frontiers journals are driven by researchers for researchers; therefore, they constitute a service to the scholarly community. At the same time, the Frontiers Journal Series operates on a revolutionary invention, the tiered publishing system, initially addressing specific communities of scholars, and gradually climbing up to broader public understanding, thus serving the interests of the lay society, too.

Dedication to Quality

Each Frontiers article is a landmark of the highest quality, thanks to genuinely collaborative interactions between authors and review editors, who include some of the world's best academicians. Research must be certified by peers before entering a stream of knowledge that may eventually reach the public - and shape society; therefore, Frontiers only applies the most rigorous and unbiased reviews.
Frontiers revolutionizes research publishing by freely delivering the most outstanding research, evaluated with no bias from both the academic and social point of view. By applying the most advanced information technologies, Frontiers is catapulting scholarly publishing into a new generation.

What are Frontiers Research Topics?

Frontiers Research Topics are very popular trademarks of the Frontiers Journals Series: they are collections of at least ten articles, all centered on a particular subject. With their unique mix of varied contributions from Original Research to Review Articles, Frontiers Research Topics unify the most influential researchers, the latest key findings and historical advances in a hot research area! Find out more on how to host your own Frontiers Research Topic or contribute to one as an author by contacting the Frontiers Editorial Office: frontiersin.org/about/contact

ROCK PHYSICS AND GEOFLUID DETECTION

Topic Editors:
Jing Ba, Hohai University, China
José M. Carcione, Istituto Nazionale di Oceanografia e di Geofisica Sperimentale (Italy), Italy
Erik H. Saenger, Bochum University of Applied Sciences, Germany
Beatriz Quintal, University of Lausanne, Switzerland
Liyun Fu, China University of Petroleum (Huadong), China
Ludmila Adam, The University of Auckland, New Zealand
Ravi Sharma, Indian Institute of Technology Roorkee, India

Citation: Ba, J., Carcione, J. M., Saenger, E. H., Quintal, B., Fu, L., Adam, L., Sharma, R., eds. (2021). Rock Physics and Geofluid Detection. Lausanne: Frontiers Media SA. doi: 10.3389/978-2-88971-562-6

Table of Contents

frontiers in Earth Science

EDITORIAL
published: 10 September 2021
doi: 10.3389/feart.2021.752172

Editorial: Rock Physics and Geofluid Detection

Jing Ba[1,2]*, *Zhijian Fang*[2], *José M. Carcione*[2,3], *Li-Yun Fu*[4] *and Qiang Guo*[2,5]

[1]State Key Laboratory of Shale Oil and Gas Enrichment Mechanisms and Effective Development, Beijing, China, [2]School of Earth Sciences and Engineering, Hohai University, Nanjing, China, [3]National Institute of Oceanography and Applied Geophysics (OGS), Trieste, Italy, [4]School of Geosciences, China University of Petroleum (East China), Qingdao, China, [5]College of Information Engineering, China Jiliang University, Hangzhou, China

Keywords: rock physics, geofluid detection, theories, experiments, geophysical exploration

Editorial on the Research Topic

Rock Physics and Geofluid Detection

Rock physics is the discipline that allows the characterization of the properties of rocks mainly based on theoretical and experimental non-destructive methods. The effect of pore fluids is of interest due to its applicability to the hydrocarbon industry. The methods involve wave propagation and low-frequency tests on field samples and seismic and electromagnetic experiments and models under varying conditions of saturation and pore pressure. This requires the establishment of constitutive relations with particular attention to the interaction between the mineral components and the saturating fluids. The relations can be of elastic, electromagnetic, or diffusive (flow) nature. Geophysical methods aim to obtain information about fluid type, porosity, permeability, mineralogy, and the presence of cracks and fractures. In this sense, experiments, mathematical theories, and numerical algorithms are essential for a quantitative characterization of subsurface geological structures, *in-situ* conditions, and for the detection of geofluids. Rock physics is applied in different fields, such as geology, geophysics, petrophysics, mining and resource exploration, hydrology and natural hazards.

This research topic, "*Rock Physics and Geofluid Detection*," contains high-quality original research contributions regarding novel methodologies and applications to characterize the physical behavior of rocks aiming at geofluid detection. The purpose is to solve the pivotal problems related to theories/methods and prospective technologies from different areas which can be helpful for improving the developments of accurate exploration methods. The twenty-five papers collected mainly cover the following four subtopics.

NOVEL ROCK-PHYSICS EXPERIMENTS, THEORETICAL APPROACHES, AND NUMERICAL MODELING

The twelve papers collected in this subtopic mainly include laboratory measurements of rock properties, wave propagation theories, and numerical modeling.

Deng et al. conducted a detailed petrological and geochemical analysis, and microstructure observation of the shale samples of the Wufeng-Longmaxi Formation in southeastern Sichuan Basin, and tested their acoustic and geochemical behaviors. This integrated study provides important insight into the reservoir parameters that control the dynamic and static elastic behaviors of shale.

By studying the propagation of waves in porous media with a specific structure in saturating immiscible fluids, Xiong et al. established a wave equation system with a relatively simple structure.

OPEN ACCESS

Edited by:
Mourad Bezzeghoud, Universidade de Évora, Portugal

Reviewed by:
Giovanni Martinelli, National Institute of Geophysics and Volcanology, Italy

***Correspondence:**
Jing Ba
jingba@188.com

Received: *02 August 2021*
Accepted: *24 August 2021*
Published: *10 September 2021*

Citation:
Ba J, Fang Z, Carcione JM, Fu L-Y and Guo Q (2021) Editorial: Rock Physics and Geofluid Detection. Front. Earth Sci. 9:752172. doi: 10.3389/feart.2021.752172

This study improves the stability of the Tuncay-Corapcioglu model based on the volume average method.

Fu et al. studied the effect of the crack surface roughness on the elastic stiffness of dry and saturated rocks. Rough surfaces cause stress concentration around the cracks, reducing the elastic modulus of the rock.

Ikeda et al. proposed a method to predict the spatial distribution of the elastic properties in multi-mineral rocks, based on digital rock physics. It uses the homogenization theory and overcomes the monomineralic limitation. The method is applied to a carbonate sample, composed of dolomite and calcite.

Tisato et al. measured seismic wave attenuation and dynamic Young's modulus of dry and partially-saturated Berea sandstone within the range of 1–100 Hz and 0–20 MPa confining pressure. The data was compared with those predicted by phenomenological models of ultrasonic elastic properties and wave-induced-fluid flow. The analysis shows that the attenuation is strongly dependent on pressure. This result can help interpreting near-surface geophysical data and improve subsurface imaging.

In order to study the effect of nanopore distribution on the pressure sensitivity of P-wave velocity in dry rocks, Raj et al. used a set of 23 samples of a vertical core collected from the Mississippian-age mixed carbonate-siliciclastic Meramec formation. The analysis shows that the velocity-pressure relation depends on the distribution of pore shape and size.

Cao et al. considered the elastic interaction between cracks to investigate the effective elasticities in complex fractured media. They compared the analytical solution without stress interaction and the numerical result with interaction. The results show that regardless of the spatial distribution of the cracks, their size determines the dominant type of interaction, significantly affecting the effective properties.

Ma et al. studied the fluid sensitivity to petrophysical properties based on experimental data by using fluid indicators and crossplots, which can discriminate well between gas and liquids (i.e., water and oil). Siltstone and dolomite can be identified according to the distribution of the data (the area specifically).

Based on modeled low-frequency longitudinal forced oscillations, Mikhaltsevitch et al. studied the effect of the strain gauge location on the measurements, the creep effect related to the rock mineralogy, and the dispersion/attenuation in a liquid-saturated rock sample caused by the existence of an external pore fluid volume (dead volume). The results are independent of the location of the strain gauges, the low-frequency moduli are noticeably reduced with time, and the relaxation frequency is independent of the dead volume.

Spikes and Sen analyzed the inherent dependence and correlation among the input parameters of a petrophysical model by using a Bayesian framework. This method takes into account the fluid type and saturation, mineralogy, pressure, and critical porosity. When applied to well data, the results show that there is a similar correlation between pressure and critical porosity in dry and clean sands.

Charoensawan et al. modeled the P-wave velocity in Alpine fault rocks with and without microfractures. The results reveal the influence of the crack orientation and shape. Anisotropy, clearly observed in the shear zone of the mylonite Alpine fault, is caused by different minerals and structural features and becomes more complex due to the presence of cracks.

Cheng et al. performed ultrasonic measurements on 15 tight gas sandstone samples of the Xujiahe formation in western Sichuan under different confining pressures. By analyzing log and seismic data, a 3-D rock-physics template was established. The estimated stiff porosity and crack porosity are consistent with data from two wells.

HIGH-PRECISION INVERSION OF STRATA PROPERTIES FROM GEOPHYSICAL DATA

The three papers collected in this subtopic deal with stability-enhanced, high-resolution and rock-physics-model-based linear and nonlinear inversion schemes applied to geophysical data.

Yu et al. proposed a model to describe the elastic properties of mud-rich source rocks, filled with kerogen at different maturity stages. The model provides a theoretical basis for seismic forward modeling and inversion and allows the characterization of this type of unconventional resource.

Jin et al. obtained the velocity dispersion and attenuation caused by fluid squirt flow in tight-gas sandstones with a complex pore space. Frequency-dependent AVO and inversion of a P-wave dispersion attribute are studied as a function of gas saturation. Higher saturation implies lower P-wave velocity and stronger attenuation. The inversion of synthetic data shows that the attribute is an effective indicator of saturation.

Avseth and Lehocki proposed a new integrated workflow for generating AVO feasibility maps/cubes by using data from the Barents Sea. This method can quickly extrapolate away from the expected rock physics characteristics of well control along the selected horizon, which is constrained by seismic velocity information, geological input and rock physics properties. This workflow allows faster, seamless, and geologically consistent direct hydrocarbon identification to reduce prospecting risks in the areas with complex geological and tectonic impacts.

GEOFLUID DETECTION WORKFLOWS AND APPLICATIONS WITH CASE STUDIES

The four papers collected in this subtopic include new techniques, methods, and workflows for detecting geofluids and the verification by comparing theories and real data.

Vesnaver et al. developed a new method for imaging seismic attenuation in a seismic survey acquired at the Gulf of Trieste (Italy). The method combines the macroscopic model obtained by seismic tomography with the microscopic model obtained by seismic attributes of instantaneous frequency, leading to a high-resolution image of Q.

Zhou et al. developed a rock-physics template based on a double double-porosity theory, which could effectively identify

fluids in ultra-deep reservoirs. The template is applied to fault-controlled karst reservoirs in the Tarim Basin (China), revealing ultra-deep oil and gas resources with diverse pore-crack systems, low permeability, and complex spatial distributions of oil and water.

Balcewicz et al. combined a high-resolution image from X-ray tomography, transmission optical microscope and scanning electron microscope with attributes such as geological diagenesis, mineral composition, microstructure and porosity to obtain the best spatial segmentation image of a Ruhr sandstone. The image histogram is compared with a numerical simulation, providing a workflow to describe the microstructural characteristics of the sandstone.

Alabbad et al. proposed a deterministic seismic interpretation method, based on rock physics to discriminate pore fluids and quantify the porosity and mineralogy from seismic impedance. The method was applied to carbonate and clastic oil fields. The pore fluid plays a role in the evolution of porosity.

LABORATORY AND FIELD MODELS AND APPLICATIONS

The six papers collected in this subtopic use rock physics by combining field and experimental data, to predict reservoir properties.

Dvorkin et al. analyzed wireline data from Wolfcamp and Woodford gas shales and showed that porosity and mineralogy control the elastic properties. A model is established based on digital images to estimate these properties from small irregular rock fragments.

Huang et al. proposed a model of seismic anisotropy to perform forward modeling. The model can be used to characterize the anisotropic properties of a Precambrian carbonate with fractured vuggy pores and caves.

Xu et al. combined discrete element models with discrete fracture networks. The method provides a simple approach with a high computation efficiency to achieve a realistic and detailed description of a fracture system.

Guo et al. established three models to describe the complex pore space of tight-gas sandstone reservoirs. One model assumes a single pore aspect ratio, another considers hard and soft pores, and third model is based on the mean and variance aspect ratios to represent a statistical distribution. The accuracy of the models is verified by numerical simulations.

Gas hydrate is a new energy resource with great potential, widely distributed in permafrost and seabed sediments. Rock physics is useful to study wave dissipation with increasing hydrate concentration at different frequencies. Two relevant papers are:

Wang et al. considered two different rock-physics models to analyze gas-hydrate bearing sediments based on the Biot-Rayleigh double-porosity theory. The theoretical results agree with the experimental data. In particular, at sonic frequencies one of the models predicts high attenuation due to wave-induced local fluid flow. Moreover, the analysis reveals that attenuation increases up to a given hydrate concentration and then decreases.

Guo et al. introduced a critical hydrate saturation indicator to describe the type of pore filling and the presence of grain cementation. This indicator is implemented in a petrophysical model to compute the P-wave velocity dispersion and attenuation caused by squirt flow. When the gas-hydrate saturation is less than the critical one, the velocity slightly increases with increasing saturation, while the velocity increases significantly in the presence of cementation.

In summary, the research topic covers a wide range of methodologies and approaches which provide fundamental insights into geofluid detection. These works are useful to show how to integrate different disciplines, which facilitate the improvement of accurate exploration methods based on rock physics.

AUTHOR CONTRIBUTIONS

All authors listed have made a substantial, direct, and intellectual contribution to the work and approved it for publication.

ACKNOWLEDGMENTS

We thank all authors for their valuable contributions to this research topic, the reviewers who shared their precious time to improve the manuscripts, the members of the Frontiers Team and Editor in Chief for their help at different stages of preparing this collection of papers.

Conflict of Interest: The authors declare that the research was conducted in the absence of any commercial or financial relationships that could be construed as a potential conflict of interest.

Publisher's Note: All claims expressed in this article are solely those of the authors and do not necessarily represent those of their affiliated organizations, or those of the publisher, the editors and the reviewers. Any product that may be evaluated in this article, or claim that may be made by its manufacturer, is not guaranteed or endorsed by the publisher.

Copyright © 2021 Ba, Fang, Carcione, Fu and Guo. This is an open-access article distributed under the terms of the Creative Commons Attribution License (CC BY). The use, distribution or reproduction in other forums is permitted, provided the original author(s) and the copyright owner(s) are credited and that the original publication in this journal is cited, in accordance with accepted academic practice. No use, distribution or reproduction is permitted which does not comply with these terms.

frontiers in Earth Science

ORGINAL RESEARCH
published: 14 January 2021
doi: 10.3389/feart.2020.613716

Velocity-Porosity-Mineralogy Model for Unconventional Shale and Its Applications to Digital Rock Physics

Jack Dvorkin[1]*, *Joel Walls*[2] *and Gabriela Davalos*[2]

[1]College of Petroleum Engineering and Geosciences, King Fahd University of Petroleum and Minerals, Dhahran, Saudi Arabia, [2]Halliburton, Houston, TX, United States

By examining wireline data from Woodford and Wolfcamp gas shale, we find that the primary controls on the elastic-wave velocity are the total porosity, kerogen content, and mineralogy. At a fixed porosity, both V_p and V_s strongly depend on the clay content, as well as on the kerogen content. Both velocities are also strong functions of the sum of the above two components. Even better discrimination of the elastic properties at a fixed porosity is attained if we use the elastic-wave velocity of the solid matrix (including kerogen) of rock as the third variable. This finding, fairly obvious in retrospect, helps combine all mineralogical factors into only two variables, V_p and V_s of the solid phase. The constant-cement rock physics model, whose mathematical form is the modified lower Hashin-Shtrikman elastic bound, accurately describes the data. The inputs to this model include the elastic moduli and density of the solid component (minerals plus kerogen), those of the formation fluid, the differential pressure, and the critical porosity and coordination number (the average number of grain-to-grain contacts at the critical porosity). We show how this rock physics model can be used to predict the elastic properties from digital images of core, as well as 2D scanning electron microscope images of very small rock fragments.

Keywords: rock physic model, unconventional shale gas, elastic properties, fluid effect, digital rock analysis

OPEN ACCESS

Edited by:
Jing Ba,
Hohai University, China

Reviewed by:
Zhiqi Guo,
Jilin University, China
Thomas Finkbeiner,
King Abdullah University of Science and Technology, Saudi Arabia
Luanxiao Zhao,
Tongji University, China

***Correspondence:**
Jack Dvorkin
jackdvorkin007@gmail.com

Specialty section:
This article was submitted to Solid Earth Geophysics, a section of the journal Frontiers in Earth Science

Received: *03 October 2020*
Accepted: *25 November 2020*
Published: *14 January 2021*

Citation:
Dvorkin J, Walls J and Davalos G (2021) Velocity-Porosity-Mineralogy Model for Unconventional Shale and Its Applications to Digital Rock Physics. Front. Earth Sci. 8:613716. doi: 10.3389/feart.2020.613716

INTRODUCTION

Relations between the elastic properties of unconventional rocks and their volumetric properties, namely porosity, mineralogy, and kerogen content, are important in guiding reservoir development based on seismic data. Examples of interpreting seismic-scale impedances and density, product of simultaneous impedance inversion, for porosity, mineralogy, and water saturation are presented for conventional gas- and oil-bearing reservoirs by Arevalo-Lopez and Dvorkin (2016), Wollner et al. (2017), Arevalo-Lopez and Dvorkin (2017). Such interpretation based on a rock physics model (RPM) is also possible in shale and other unconventional resource rocks.

Relations of elastic properties of unconventional sediments to their volumetric properties can also be used is a reverse mode. Specifically, porosity, mineralogy, and kerogen content that are assessed using rock material, such as drill cuttings, from deviated and horizontal wells, where direct logging measurements are complicated or virtually impossible, can be related to the elastic moduli of the formation. Nowadays, this volumetric information contained in drill cuttings is readily quantified from their 3D or even 2D digital SEM images (e.g., Al Jallad et al., 2019). Where these dynamic elastic properties can be connected to the static elastic constants, among them Young's modulus and Poisson's ratio (e.g., Sone and Zoback, 2013; Hamza et al., 2015; Meléndez-Martínez and Schmitt,

2016; Elkatatny et al., 2018; He et al., 2019), they can be immediately used in hydraulic fracture prediction and modeling. The same principle applies to formations designated for CO_2 sequestration and waste disposal.

Theoretical rock physics analysis based on laboratory or wireline data is key to developing a relevant and general enough RPM. The USA domestic shale revolution has given impetus to such rock physics developments, some of them endeavoring to introduce no less than the general rock physics of all organic shales (e.g., Vernik and Milovac, 2011; Khadeeva and Vernik, 2014; Yenugu and Vernik, 2015; Vernik et al., 2018).

At the same time, serious and careful laboratory studies have addressed the effects of mineralogy and microstructure of unconventional shale on its elastic and other properties (e.g., Prasad et al., 2009; Beloborodov et al., 2019). Shale anisotropy is also a prolific topic, giving rise to a host of observations of limited generality (e.g., Vernik and Landis, 1996) and theoretical models requiring a large number of inputs (e.g., Sayers, 2013; Sayers et al., 2015; Sayers and Dasgupta, 2019). A model by Vernik and Kachanov (2010) is another example of an elaborate anisotropic theory requiring a number of essentially unknown inputs, such as pore shape factors, pore orientations, and crack density as a function of stress.

The latest installment into this branch of geosciences is by Sayers et al. (2019), where a careful and mathematically involved analysis of anisotropic parameters is conducted using wireline data from the Wolfcamp formation. This paper shows good agreement between model prediction and wireline log data in the Wolfcamp when reasonable assumptions are made about the elastic properties of kerogen and clay. The authors demonstrate that robust, local wireline petrophysical and elastic rock properties data are essential for calibrating a RPM. Once again, the theory pertaining to deriving anisotropic elastic constants, although elaborate, is not substantiated by data simply because anisotropic *in-situ* measurements are extremely rare.

Here we aim at establishing a data-driven, physics-based, and "as simple as possible but not simpler" theoretical RPM based on wireline data in two vertical wells, one in Woodford and the other in Wolfcamp shale. The input data include the bulk density, resistivity-derived water saturation, and the P- and S-wave velocity. Detailed mineralogy and kerogen content in the wells under examination are produced using advanced well log interpretation techniques. The data available come from a vertical well. Hence, we are not able to assess the elastic anisotropy of this shale and limit this discussion to the elastic properties of the formation only measured in the vertical ("33") direction.

Based on these data, we conduct rock physics diagnostics, the technique aimed at establishing a theoretical RPM. We find that the constant-cement model, which has the mathematical form of the modified lower Hashin-Shtrikman elastic bound, accurately describes the data. At fixed porosity, the elastic-wave velocity appears to be a unique function of the elastic properties of the solid matrix that includes the minerals and kerogen. These elastic properties, in turn, strongly depend on the volumetric fractions of the softest solids, clay and kerogen.

We present applications of this RPM in the context of digital rock physics (DRP), where we compute the elastic properties as a function of porosity, mineralogy, and kerogen content obtained from digital images of core, as well as 2D SEM images of small rock fragments.

WIRELINE DATA

The wireline data and interpreted curves for the Woodford well are shown in **Figure 1**. The mineralogy in Woodford is dominated by clay (illite) and quartz with small amounts of dolomite. The kerogen content is between 10 and 20% by volume and is essentially constant 15% in the main reservoir. The total porosity varies between 5 and 8%. The Wolfcamp well (**Figure 2**) is dominated by quartz, clay (illite), calcite, and dolomite, with kerogen content between 5 and 10% and the total porosity smaller than in Woodford, varying between 4 and 8%.

In both wells, all mineral fractions, including kerogen, are volumetric and normalized to add up to 100%. The mineralogy, as well as the kerogen content were estimated using existing well log interpretation methods (e.g., Zhao et al., 2016).

Both wells contained high-salinity brine and wet gas. The densities and bulk moduli of these pore-fluid components were computed using the Batzle and Wang (1992) equations. The inputs to these equations are: the pore pressure 51 and 45 MPa in Woodford and Wolfcamp, respectively; temperature 95 and 84 C; and salinity 250,000 and 100,000 ppm. The gas gravity in both wells was estimated to vary between 0.7 and 0.9. Using either of these two bounds did not noticeably affect the total porosity computations or fluid substitution (see below) results. This is why in the following quantitative analysis we assumed gas gravity 0.8. The resulting densities and bulk moduli of the brine and gas are listed in **Table 1**.

The total porosity ϕ along the intervals was computed using the mass-balance equation

$$\phi = \frac{(\rho_s - \rho_b)}{(\rho_s - \rho_f)}, \tag{1}$$

where ρ_s and ρ_f are the densities of the solid phase and pore fluid, respectively, and ρ_b is the bulk density.

The density of the pore fluid was computed from those of brine and gas (ρ_w and ρ_g, respectively) and water saturation S_w as

$$\rho_f = S_w\rho_w + (1 - S_w)\rho_g. \tag{2}$$

The density of the solid phase was computed as the arithmetic average of those of the solid components (**Table 1**) weighted by the respective volume fractions. The elastic properties, namely the bulk and shear moduli of the solid phase, were computed as Hill (1952) average using the elemental elastic constants also listed in **Table 1**.

The values for the elastic moduli of pure kerogen available in literature span fairly wide ranges, which is fairly typical for some minerals, especially clays (see Mavko et al., 2020). For example, Mavko et al. (2020) suggest 2.9 and 2.7 GPa for the bulk and shear moduli of kerogen, respectively. Vernik et al. (2018) quote 3.9 and 3.8 GPa for the same moduli of nano-porous kerogen. This means that the respective moduli of pure non-porous kerogen can be

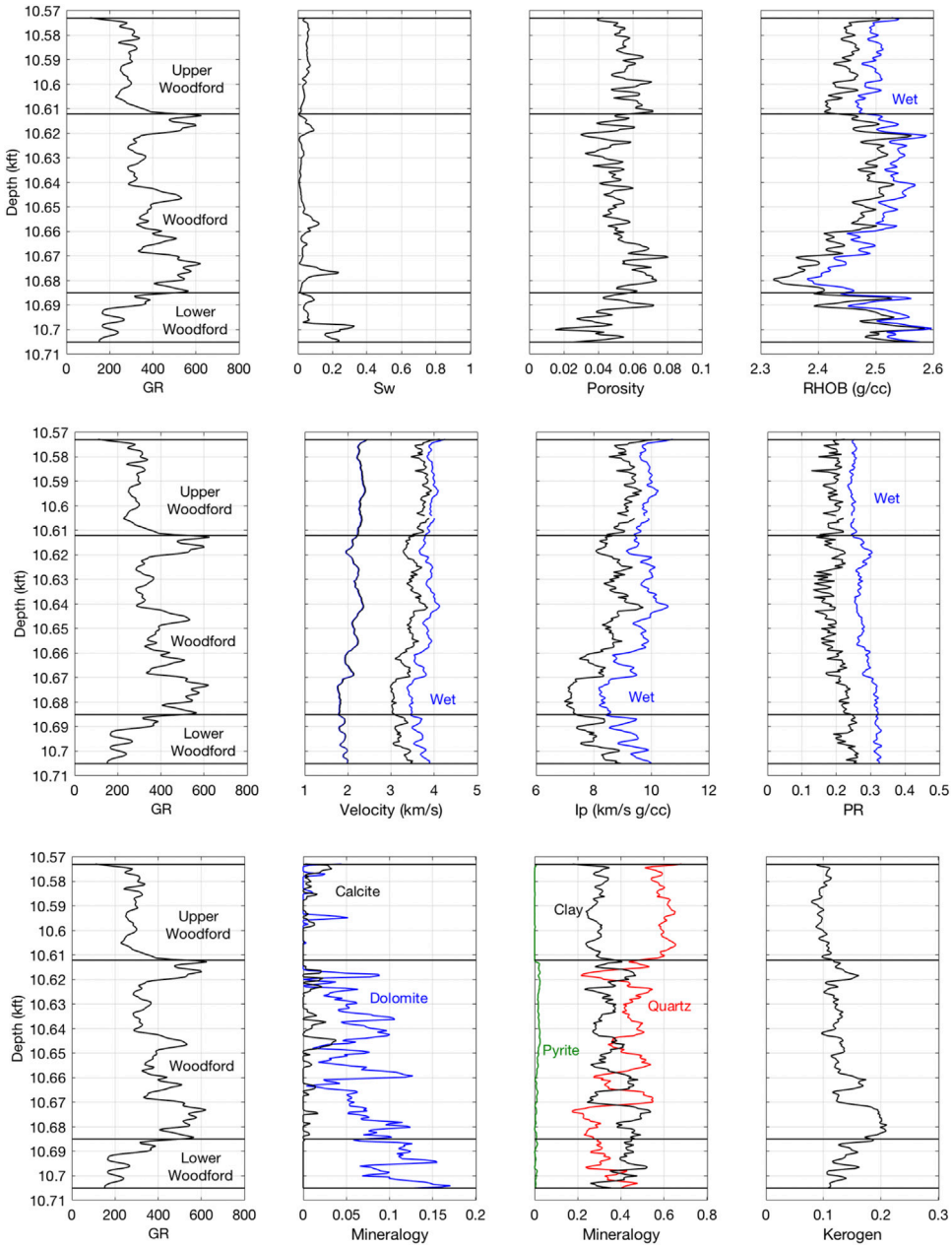

FIGURE 1 | Woodford well. Top: GR; water saturation; the total porosity; and bulk density. Middle: GR; V_p and V_s; P-wave impedance; and Poisson's ratio. The *in-situ* data are shown in black, while the variables for 100% water saturated conditions are shown in blue. Bottom: GR; dolomite (blue) and calcite (black) volume fractions; quartz (red), clay (black), and pyrite (green) volume fractions; and kerogen content.

higher. Sayers et al. (2015) use 5.5 and 3.2 GPa, respectively. Much smaller values, 1.8 and 0.4 GPa, respectively, are reported by Wolf (2010) based on laboratory measurements in a large pure bitumen sample at 60 C.

Khatibi et al. (2018) obtained Young's modulus as high as 16 MPa based on Raman spectroscopy analysis. With Poisson's ratio assumed 0.14 (Mavko et al., 2020), this value translates into 7.4 GPa for bulk modulus and 7.0 GPa for shear modulus. Yan and Han (2013) list the bulk modulus as high as 5 GPa with the shear modulus about half of this value. Kashinath et al. (2020) provide approximately 20 and 8 GPa, respectively, for the bulk and shear moduli of kerogen based on atomistic models and for 1.3 g/cc density.

Generally, the elastic properties of organic matter depend on its maturity (e.g., Zhao et al., 2016; Suwannasri et al., 2019). The values listed in **Table 1** were selected to provide a best fit to the wireline data in the two wells under examination, as well as in a number of other wells not discussed here. These values fall within

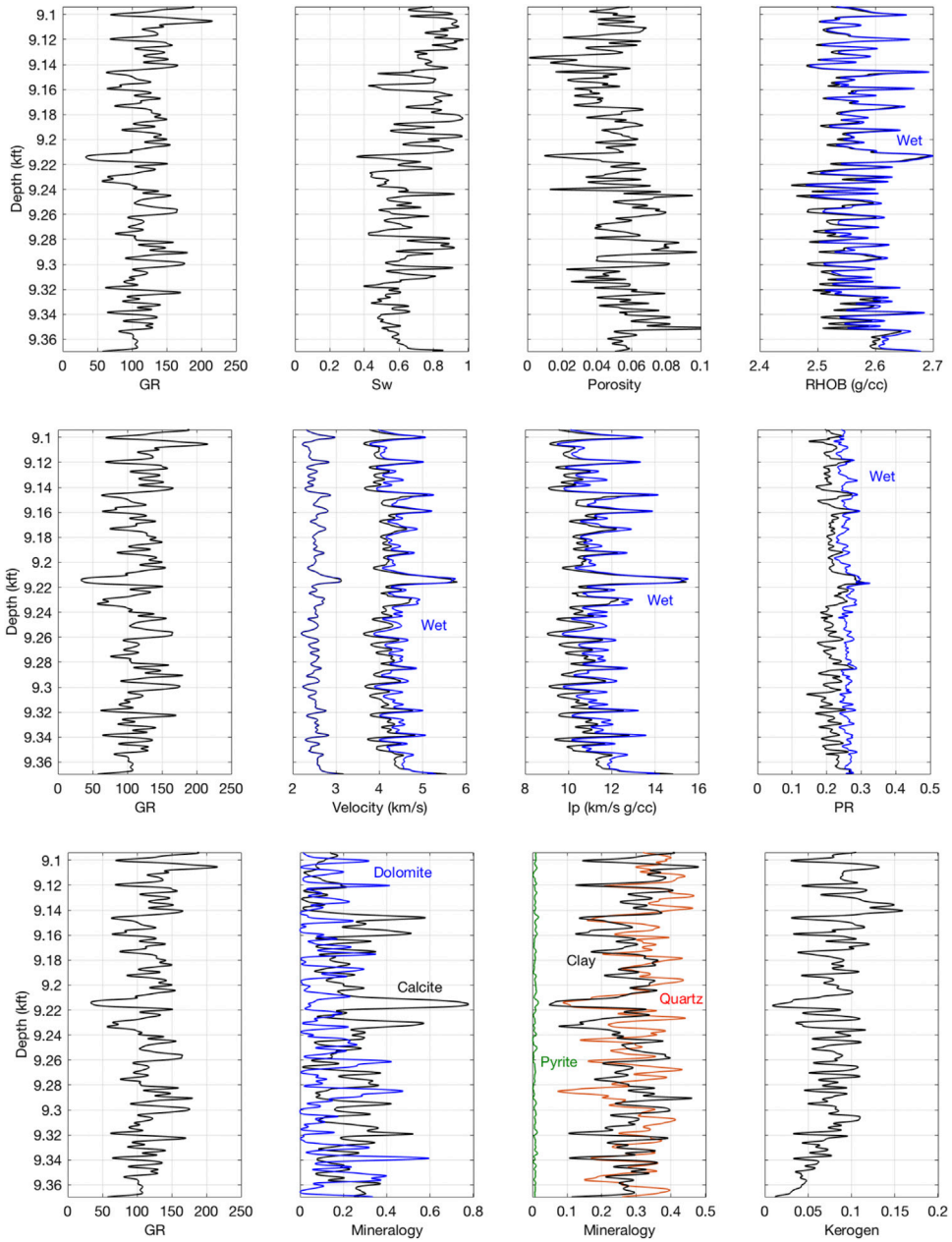

FIGURE 2 | Same as **Figure 1** but for the Wolfcamp well.

the permissible range of these elastic moduli and can certainly be used in future analyses.

FLUID SUBSTITUTION

In order to conduct rock physics diagnostics, i.e., find the RPM, we first need to bring the entire interval under examination to the so-called common fluid denominator by using theoretical fluid substitution to compute the elastic properties and density at 100% formation water saturation. This step helps us remove one variable, the pore fluid, from the diagnostics process.

We conducted fluid substitution using two different methods: (a) Gassmann (1951) method using the bulk modulus K computed from ρ_b, V_p, and V_s as

$$K = \rho_b\left(V_p^2 - \frac{4}{3}V_s^2\right) \tag{3}$$

and the V_p -only method (Mavko et al., 1995) using the compressional modulus M:

TABLE 1 | Fluid and solid component properties used in computations (the latter are from Mavko et al., 2020, except for the elastic moduli of kerogen).

Component	Density (g/cc)	Bulk Modulus (GPa)	Shear Modulus (GPa)
Brine Woodford	1.1629	3.7388	0
Brine Wolfcamp	1.0573	3.1146	0
Gas Woodford	0.3191	0.1811	0
Gas Wolfcamp	0.3111	0.1606	0
Dolomite	2.87	94.9	45.0
Calcite	2.71	76.8	32.0
Quartz	2.65	36.6	45.0
Clay (Illite)	2.85	21.0	9.0
Pyrite	4.93	147.4	132.5
Kerogen	1.30	7.0	2.2

$$M = \rho_b V_p^2. \tag{4}$$

Gassmann's (1951) equations read

$$K_{Sat} = K_s \frac{\phi K_{Dry} - (1+\phi) K_f K_{Dry} / K_s + K_f}{(1-\phi) K_f + \phi K_s - K_f K_{Dry} / K_s}; \quad G_{Sat} = G_{Dry}, \tag{5}$$

where K_{Sat} is the bulk modulus in fluid-saturated rock; K_{Dry} is the dry-rock bulk modulus; K_s is the bulk modulus of the solid phase; K_f is that of the pore fluid; and ϕ is the total porosity. The shear modulus G is fluid-independent.

The V_p only method uses the same functional form, but with the bulk modulus replaced by the compressional modulus:

$$M_{Sat} \approx M_s \frac{\phi M_{Dry} - (1+\phi) K_f M_{Dry} / M_s + K_f}{(1-\phi) K_f + \phi M_s - K_f M_{Dry} / M_s}, \quad G_{Sat} = G_{Dry}. \tag{6}$$

Both methods gave almost identical results for V_p at 100% water saturation. The resulting 100% wet-rock properties are shown in **Figures 1**, **2** as blue curves.

Both aforementioned fluid substitution methods assume zero-frequency (static) deformation of rock. In other words, the minute pore pressure oscillations induced by a passing wave have to be able to equilibrate across a rock volume during the oscillation period. Such equilibration often does not occur in the laboratory where the frequency of the signal is on the order of MHz. It may not occur even at the relative low wireline sonic and dipole frequencies on the order of 1–10 kHz if the pore fluid has high viscosity, such as heavy oil. Because the pore fluid phases in the case under examination are low-viscosity brine and gas, we can assume that the fluid substitution methods employed are applicable.

ROCK PHYSICS DIAGNOSTICS

We start with the Woodford well. Let us cross-plot the 100%-wet-rock V_p and V_s versus porosity (**Figure 3A**). The result is quite discouraging. At a fixed porosity value, V_p may vary by more than 1,000 m/s, while the V_s scatter is about 750 m/s.

This picture changes if we color-code these datapoints by a third variable. **Figures 3B,C** show plots of V_p and V_s versus porosity color-coded by clay and kerogen contents, respectively. Both variables provide strong discrimination of the velocity at fixed porosity. Using the sum of the clay and kerogen (the softest components of the solid matrix) contents also provides strong velocity discrimination (**Figure 3D**).

Since clay and kerogen are the softest components of the solid phase, it is not surprising that color-coding V_p and V_s by the respective velocities (V_{ps} and V_{ss}) computed in the solid phase (all minerals plus kerogen) also provides powerful discrimination of these velocities at fixed porosity (**Figure 4**). These velocities are computed from the bulk (K_s) and shear (G_s) moduli and the density (ρ_s) of the solid phase (the minerals plus kerogen) as

$$V_{ps} = \sqrt{\frac{K_s + (4/3)G_s}{\rho_s}}; \quad V_{ss} = \sqrt{\frac{G_s}{\rho_s}}, \tag{7}$$

where ρ_s is the weighted arithmetic average of the elemental densities listed in **Table 1**

$$\rho_s = \sum_{i=1}^{N} f_i \rho_i, \tag{8}$$

where f_i is the volume fraction of the ith mineral component in the solid matrix; ρ_i is its density; and N is the number of the solid-matrix components.

K_s and G_s are computed as Hill (1952) average using the elemental elastic moduli listed in **Table 1**:

$$K_s = \frac{K_V + K_R}{2}, \quad G_s = \frac{G_V + G_R}{2}, \tag{9}$$

with

$$K_V = \sum_{i=1}^{N} f_i K_i; \quad G_V = \sum_{i=1}^{N} f_i G_i; \quad K_R^{-1} = \sum_{i=1}^{N} f_i K_i^{-1}; \quad G_R^{-1} = \sum_{i=1}^{N} f_i G_i^{-1}, \tag{10}$$

where K_i and G_i are the bulk and shear moduli of the ith component, respectively.

We can conclude now that the elastic-wave velocities in Woodford uniquely depend on the total porosity and mineralogy, the latter represented by the elastic moduli of the solid phase.

This somewhat anticipated and obvious, in retrospect, result is still novel in the rock physics field. The traditional and commonly used approach is to relate the elastic properties to the clay or kerogen or feldspar content examining these mineralogies as separate inputs. Here we mathematically combine these mineralogies in only two self-similar variables, V_p and V_s in the solid matrix, that serve as discriminators for V_p and V_s, respectively, in the porous rock itself. Such self-similarity in rock physics transforms was first described by Gal et al. (1998) and Dvorkin (2007), where one of such variables was a linear combination of porosity and clay content. It is akin to the classic self-similarity in mechanics where, e.g., fluid flow characteristics can be related to a single variable, Reynolds

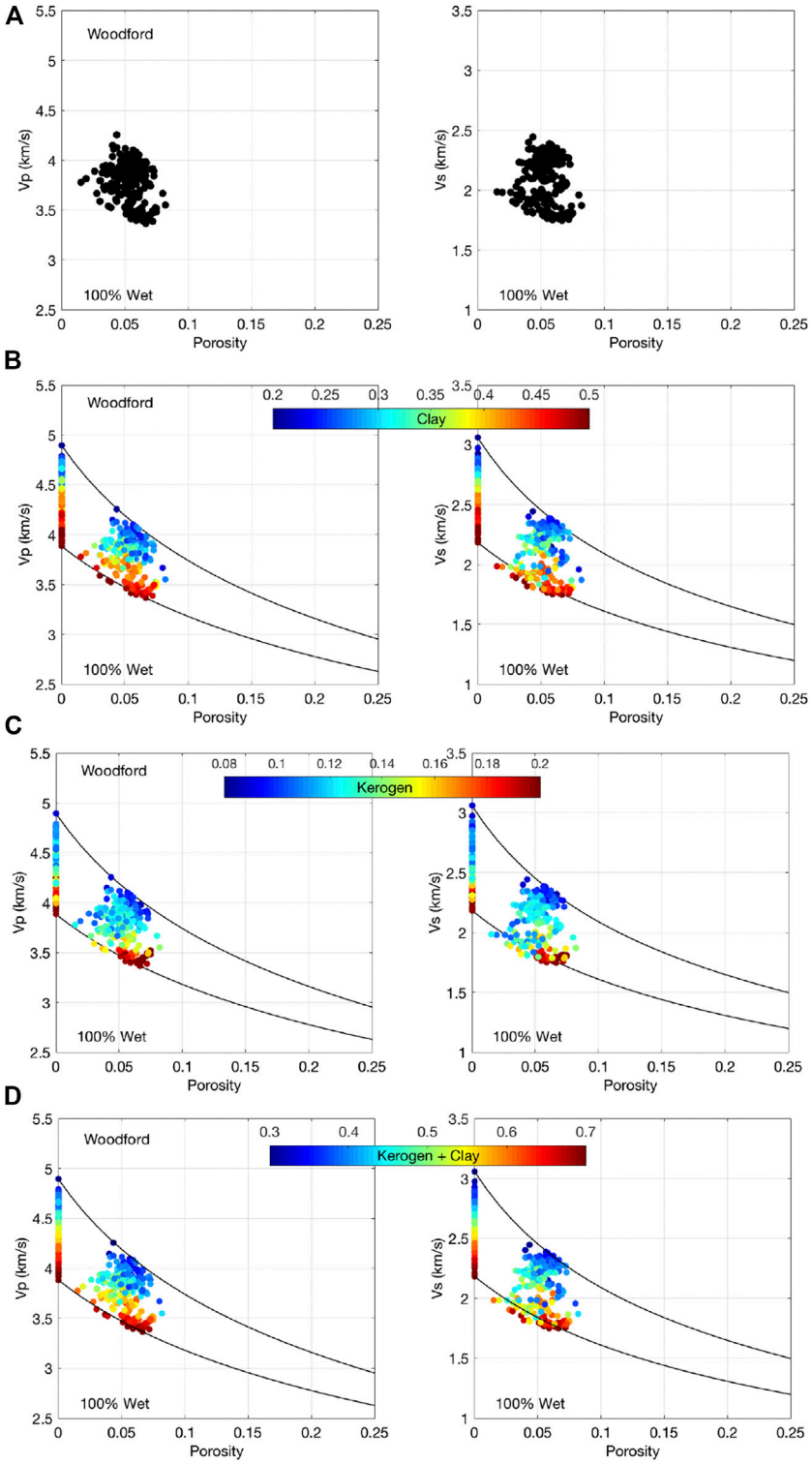

FIGURE 3 | Woodford well. **(A)** 100%-wet-rock V_p **(left)** and V_s **(right)** versus porosity. **(B)** Same as "**(A)**" but color-coded by the clay content. Colored symbols at zero porosity are for V_p **(left)** and V_s **(right)** in the solid phase and are color-coded by the same third variables. Upper solid black line is computed from the constant-cement model starting from the stiffest zero-porosity data point. Lower solid black line is computed from the same model starting from the least stiff zero-porosity data point. **(C)** Same as "**(B)**" but color-coded by kerogen content. **(D)** Same as "**(B)**" but the color is the sum of the clay and kerogen contents.

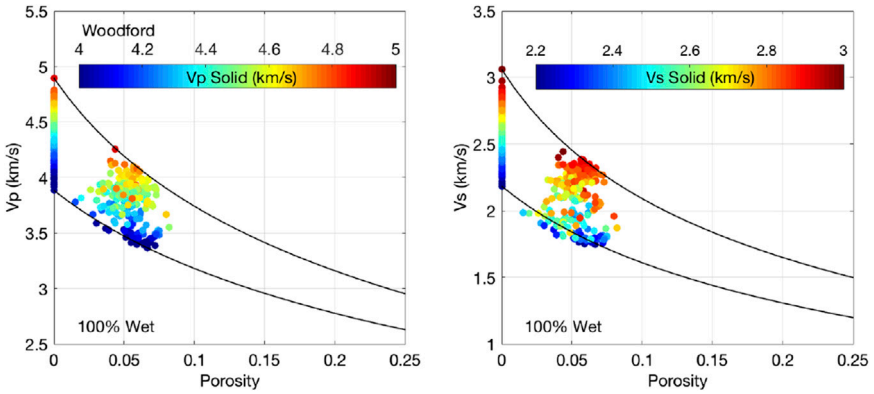

FIGURE 4 | Woodford well. Same as **Figure 3** but the color is V_p in the solid phase **(left)** and V_s in the solid phase **(right)**.

TABLE 2 | Constant-cement model parameters.

Formation	P_{Diff} (MPa)	ϕ_c	C	f	ρ_w (g/cc)	K_w (GPa)
Woodford	25.75	0.40	12	1.0	1.1629	3.7388
Wolfcamp	29.37	0.40	22	0.6	1.0573	3.1146

P_{Diff}, *differential pressure;* ϕ_c, *critical porosity;* C, *coordination number;* f, *shear stiffness reduction factor;* ρ_w, *mean density of brine;* K_w, *mean bulk modulus of brine.*

number, instead of separately to the viscosity, velocity of flow, and size of the orifice.

In order to theoretically match these data, we select the constant-cement model that has the mathematical form of modified lower Hashin-Shtrikman bound described in, e.g., Dvorkin et al. (2014) and expressed by the following equations:

$$K_{Dry} = \left[\frac{\phi/\phi_c}{K_{HM}+\frac{4}{3}G_{HM}} + \frac{1-\phi/\phi_c}{K+\frac{4}{3}G_{HM}}\right]^{-1} - \frac{4}{3}G_{HM};$$

$$G_{Dry} = \left[\frac{\phi/\phi_c}{G_{HM}+z_{HM}} + \frac{1-\phi/\phi_c}{G+z_{HM}}\right]^{-1} - z_{HM};$$

$$z_{HM} = \frac{G_{HM}}{6}\left(\frac{9K_{HM}+8G_{HM}}{K_{HM}+2G_{HM}}\right), \tag{11}$$

where K_{Dry} and G_{Dry} are the dry-rock bulk and shear moduli, respectively; ϕ_c is the critical porosity (about 0.40), and

$$K_{HM} = \left[\frac{n^2(1-\phi_c)^2 G_s^2}{18\pi^2(1-\nu_s)^2}P\right]^{\frac{1}{3}};$$

$$G_{HM} = \frac{2+3/f-\nu(1+3/f)}{5(2-\nu)}\left[\frac{3n^2(1-\phi_c)^2 G^2}{2\pi^2(1-\nu)^2}P\right]^{\frac{1}{3}}, \tag{12}$$

where n is the coordination number (the average number of contacts per grain, usually greater or equal 5); G_s and ν_s are the effective shear modulus and Poisson's ratio of the mineral phase, respectively; P is the differential stress; and f is the shear stiffness reduction factor (usually greater or equal 1).

The inputs required by this model are the differential stress (overburden minus pore pressure); critical porosity; coordination number (the average number of contacts per grain at critical porosity); and the shear stiffness reduction factor. The parameters we chose for the case under examination are listed in **Table 2**. The densities and elastic moduli of the solid phase and pore fluid are required as well.

This model, as well as its counterparts, the soft-sand and stiff-sand transforms, although originally developed for sandstones, have all proven to be fairly universal and work for other rock types, such as shales (Dvorkin et al., 2002) and carbonates (Dvorkin and Alabbad, 2019). Let us remind that the essence of these models is in the mathematical form of the curves connecting the high- to zero-porosity endpoints in the velocity-porosity space. The zero-porosity endpoint is the velocity of the mineral matrix. The high-porosity (or critical-porosity) endpoint can be computed from a contact theory, such as expressed by **Eq. 12**, or simply determined based on the data.

We compute velocity versus porosity curves according to this model for 100% water saturation case and a) using the minimum density and the bulk and shear moduli of the solid phase in the interval under examination and b) the maximum values of these inputs. In other words, the a) model curve starts from the softest zero-porosity data point, while the b) curve starts from the stiffest zero-porosity data point. The resulting curves almost perfectly envelop the data (**Figures 3**, **4**).

Notice that color gradation in velocity data shown in **Figures 3**, **4** is practically the same as that in the solid-phase velocity data displayed at zero-porosity. This fact illustrates our finding that the solid-phase elastic properties act as robust discriminators of the porous shale elastic properties at fixed porosity and that these properties are unique functions of the total porosity, and mineralogy and kerogen content.

The next step is to apply this model in the entire interval using the depth-dependent inputs and the *in-situ* fluid properties. The results are shown in **Figure 5**. The match between the model predictions and wireline data is fairly accurate except for Lower Woodford where the predicted velocities are higher than measured. We could certainly adjust the model in this interval to better match the data, but the difference is likely caused by over-pressure in this interval for which we have no information.

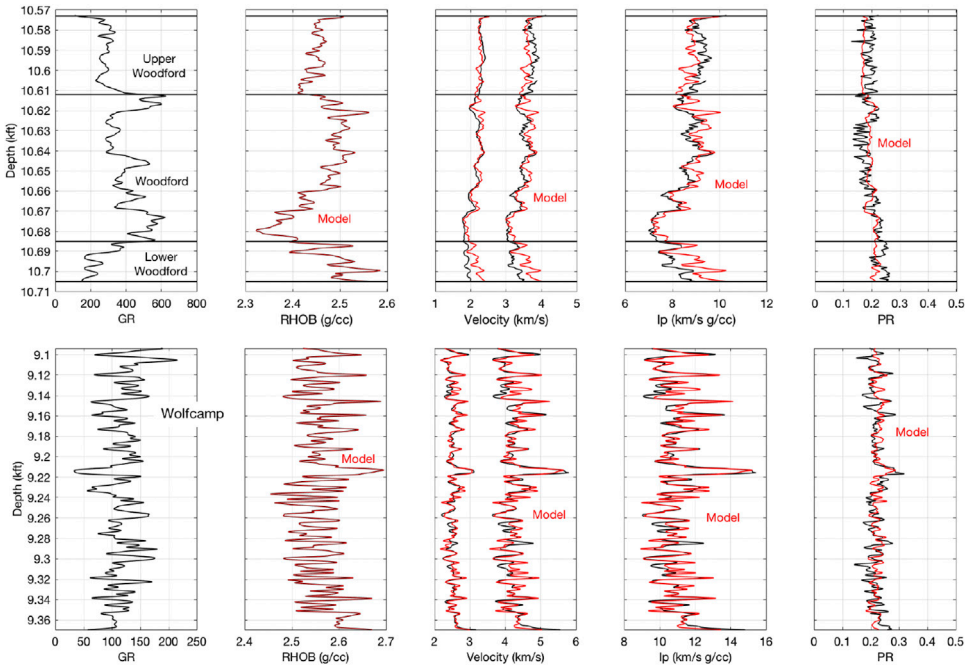

FIGURE 5 | Top. Woodford well. GR, bulk density, V_p and V_s, P-wave impedance, and Poisson's ratio versus depth at *in-situ* conditions. Black is for recorded data, while red is for constant cement model predictions. Bottom. Same but for Wolfcamp well.

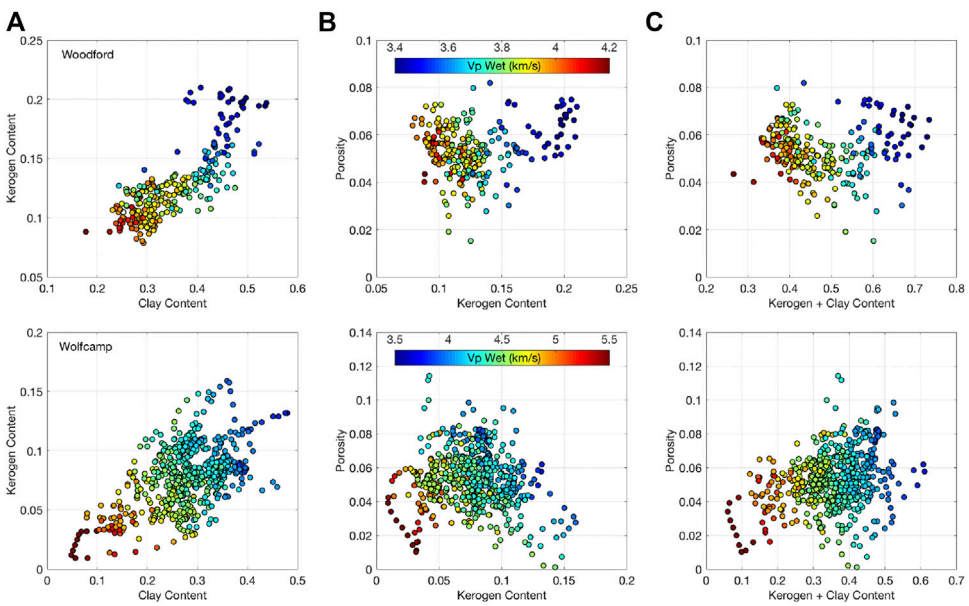

FIGURE 6 | Top. Woodford well. **(A)** Kerogen versus clay content. **(B)** Porosity versus kerogen content. **(C)** Porosity versus the sum of clay and kerogen contents. The datapoints are color-coded by V_p adjusted for 100%-wet-rock conditions. Bottom. The same but for the Wolfcamp well.

Let us finally make several useful cross-plots using Woodford data. The cross-plot in **Figure 6A** (top) indicates that there is (albeit not very sharp) connection between the clay and kerogen contents: both increase in accord. Plotting the total porosity versus kerogen content (**Figure 6B**, top) and the sum of clay and kerogen contents (**Figure 6C**, top) produces a curious V-shaped pattern with maximum porosity practically the same at the lowest and highest contents and minimum porosity at

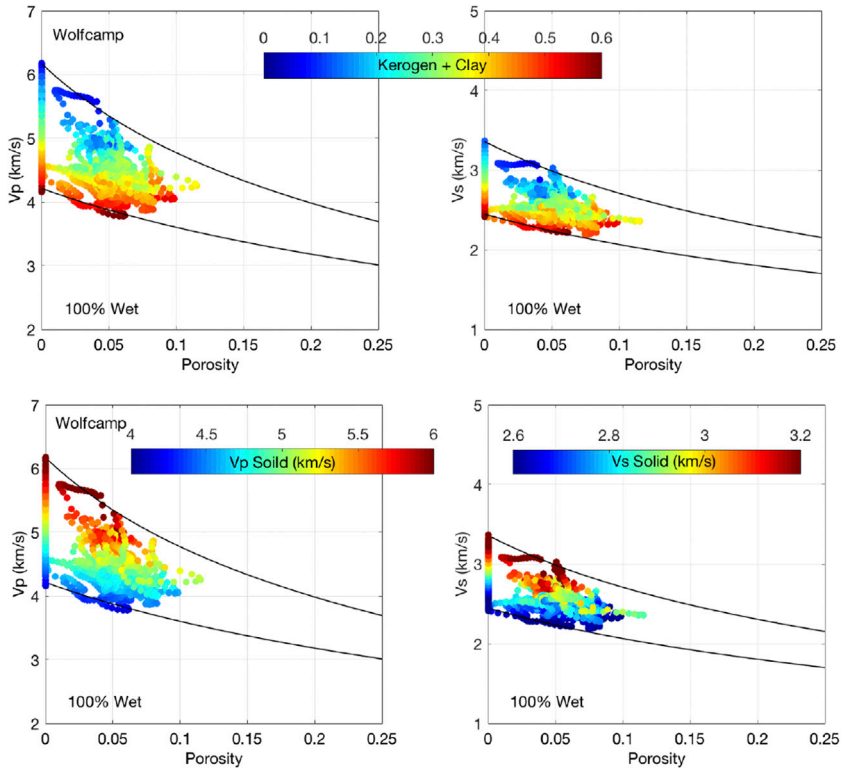

FIGURE 7 | Wolfcamp well. Top. Display is the same as in **Figure 3D**. Bottom. Display is the same as in **Figure 4**.

approximately 0.13 kerogen content and 0.50 clay plus kerogen content. This pattern arguably points out to how porosity is partitioned among the components of the solid phase.

The positive correlation between the clay and kerogen contents observed in this figure is fairly common in the continental US deposits (e.g., Sone and Zoback, 2013).

Figure 7, top and bottom, is for the Wolfcamp well with the displays same as in **Figures 3**, **4**, respectively. Data quality in this well is worse than in the Woodford well, which is clear from the "lacy" character of the cross-plots in these figures. Such configurations are characteristic of the petrophysicist's attempts to shift and smooth the original curves. Yet, the patterns similar to those observed in the Woodford emerge here as well. Once again, it appears that the elastic properties of this shale are also unique functions of the total porosity, and mineralogy and kerogen content.

The same RPM is applicable in Wolfcamp shale, but with some parameter adjustments. Perhaps because the calcite and dolomite contents in Wolfcamp are higher than in Woodford (**Figure 2**), this rock appears stiffer and requires an increase in the coordination number to 22. Also, the shear stiffness reduction factor f in this case is 0.6.

Having this factor less than 1.0 is unphysical in the context of the original constant-cement model, where the critical porosity endpoint elastic moduli come from the Hertz-Mindlin contact theory (Mindlin, 1949). However, if we remember that this factor is only an adjustment parameter for the high-porosity end member in the modified lower Hashin-Shtrikman bound, using $f = 0.6$ is permissible. The reason behind this selection is to honor the fact that the apparent Poisson's ratio measured in the vertical direction is quite small in this well (about or even less than 0.2). Let us emphasize again that the essence of this model is not the selection of the critical porosity endpoint, but rather the functional form of the curves connecting this endpoint with the zero-porosity (pure-mineral) endpoint.

The model predictions are compared to measured data for this well in **Figure 5** (bottom). As in Woodford, we observe an accurate match. **Figure 6** (bottom) is the same as **Figure 6** (top), but now for the Wolfcamp well. Because of the poorer quality of this wireline data, it is difficult to make any meaningful conclusions here.

APPLICATION TO DIGITAL ROCK PHYSICS

High resolution petrophysical properties can be determined from dual energy computed tomography (CT) imaging on core material extracted from a well (Walls et al., 2016). Dual-energy CT-scanning for evaluating reservoir rocks involves scanning the same location within the rock twice, using a different X-ray energy each time. One image intensity is proportional to the bulk density, while the other is proportional to the atomic number. These two inputs are combined with spectral gamma ray readings to obtain high-

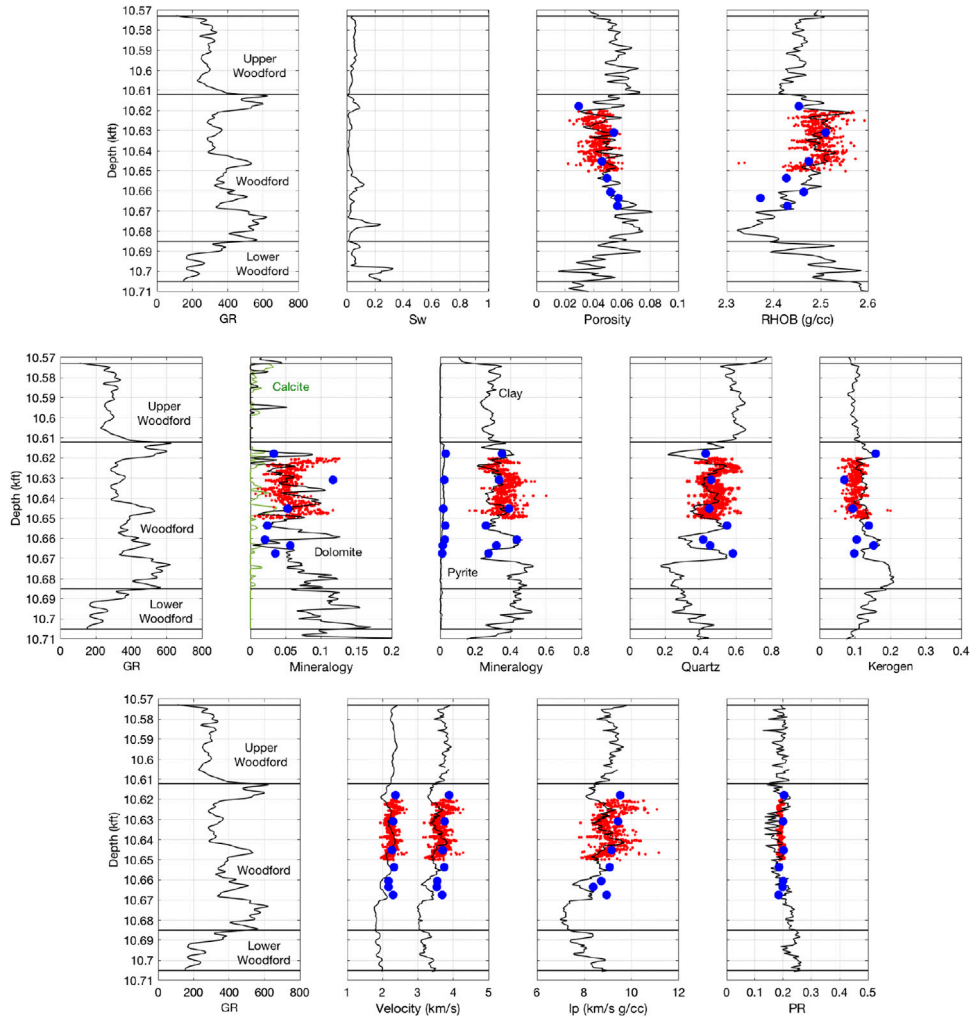

FIGURE 8 | Woodford well. The display is the same as in **Figure 1**. Red symbols are for the whole core dual energy outputs (the bulk density and the dolomite, clay, quartz, and kerogen contents), as well as for the resulting model-based computed properties (the total porosity, V_p, V_s, I_p, and Poisson's ratio). Blue symbols are for the 2D SEM outputs.

resolution bulk density and mineralogy data along the core. The output includes the total porosity (computed from the mass balance equation), as well as the volume fractions of kerogen, carbonate, silica and clay. Usually these 3D volumetric data are averaged across the sample for each cross-section, however nothing prevents utilizing these results in the entire volume, voxel by voxel, given adequate dynamic memory handling. Now, by applying the RPM derived here from wireline data to petrophysical results from such core CT scanning, we can obtain high-resolution profiles of the dynamic elastic properties along the core.

For this purpose we assumed that the carbonate is pure dolomite, silica is quartz, and clay is illite. The constant-cement model established for the Woodford well was implemented with the abovementioned CT outputs. The results are shown in **Figure 8**, where the elastic properties thus computed, as well as the dual energy outputs, are compared with the wireline data.

The high-resolution density, mineralogy, and mass-balance-computed total porosity closely match those inferred from the wireline data. As a result, the elastic-wave velocities, P-wave impedance, and Poisson's ratio are also close to the values measured in the well. Such high-resolution elastic property profiles are essential in highly laminated thinly layered unconventional formations.

Another digital rock methodology is based on 2D SEM images of rock material (**Figure 9**), such as drill cuttings recovered from deviated or horizontal wells. Image analysis combined with X-ray fluorescence (XRF) data yields the total porosity, as well as the kerogen, pyrite, silica, carbonate, and clay contents. By applying a RPM to these outputs, we can estimate the elastic properties in deviated or horizontal wells where wireline measurements and core extraction are difficult and risky, if not impossible.

These rock-physics-based elastic property results are also plotted in **Figure 8**. The velocities thus computed slightly overestimate V_p and V_s measured in the well, likely due to the

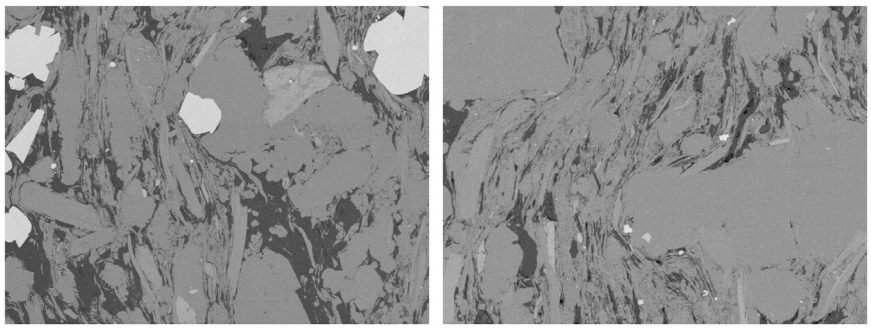

FIGURE 9 | Examples of 2D SEM images from Woodford. Pyrite appears bright-white, dolomite is light-gray, quartz and clay (the latter appearing as fibrous features) are darker-gray, organic matter is dark-gray, and the pores inside the organic matter are black.

difference in the scale of the measurement. Still, these results confirm the robustness of the methodology where DRP is combined with traditional rock physics to estimate the elastic properties where no other rock material but drill cuttings are available.

As could be expected, both aforementioned DRP methods provide the inputs that are close to the wireline data but are not exactly the same. This situation is typical when comparing laboratory to wireline data in conventional rock physics analysis. Even such basic properties as porosity, density, and the elastic-wave velocities show discrepancies. Among the reasons for these differences are the conditions of the measurements, as well as the devices used. Still, in the case under examination, these inputs match reasonably well hence providing a close match between the elastic properties measured in the well and computed using DRP.

DISCUSSION

DRP has rapidly evolved during the last decade. Many publications have reported reliable estimates of the absolute and relative permeability, as well as electrical properties, based on microimages of natural rock (e.g., Arns et al., 2005; Dvorkin et al., 2011; Andra et al., 2012). Yet, correctly computing the elastic properties from microimages has remained elusive. The main reason is that these properties strongly depend on microscopic elastic defects, such as hairline cracks or grain contacts, which are impossible to resolve within a reasonably large field of view.

Still, some authors report DRP-based plausible values for the elastic moduli. These results are based on ad-hoc alteration of material properties (Knackstedt et al., 2009), special image processing (Dvorkin et al., 2011), or an application of an inclusion effective-medium theory to digital images (Karimpouli et al., 2018). The latter approach is arguably questionable since it has to include an ad-hoc element since the finest elastic cracks most responsible for the elastic properties cannot be adequately imaged.

The approach used here is somewhat different. We combine two types of data, physical measurements (wireline) and digital (images). The first type provides us with a robust site-specific rock physics transform between the volumetric and elastic properties, which is then applied to the second type to estimate these elastic properties from image-based volumetrics. This approach appears to be quite powerful as it can be applied to images of drill cuttings in wells where other types of measurements are hardly attainable.

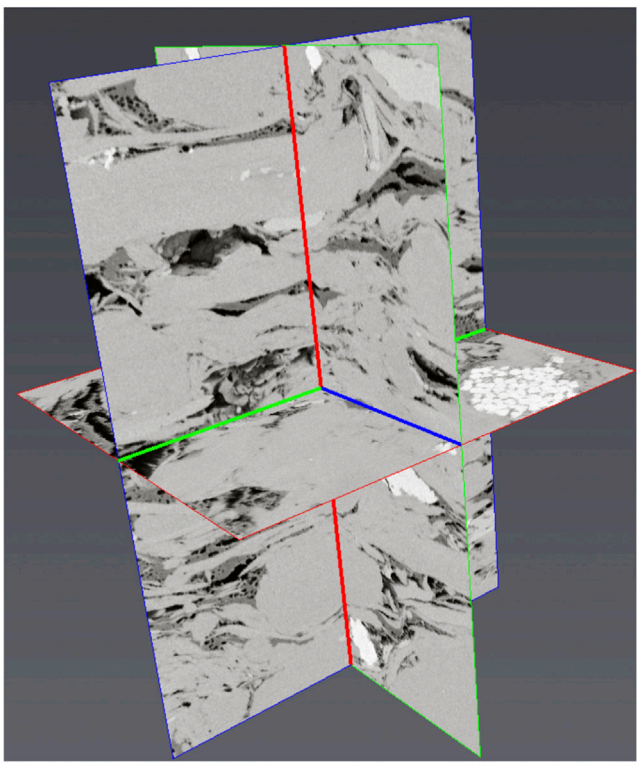

FIGURE 10 | A 3D focused ion beam-scanning electron microscope (FIB/SEM) image of unconventional shale from Woodford. The color-to-mineralogy correspondence is the same as in **Figure 9**.

In this study, we only used two wells. Nevertheless, this RPM appears to be general as it also works in other wells in the US and Middle East. We could not publish these data due to

confidentiality restrictions. What is very important is that a fairly simple and ubiquitous RPM helped us quantify the velocity-porosity-mineralogy behavior in a sediment whose microstructure is prohibitively complex (**Figure 10**) for any implicit modeling involving elaborate effective-medium theories.

It may be tempting to try to determine the parameters of this model from micro-images of shale. However, it is arguably impossible since the inputs, such as the coordination number, are assigned to the critical-porosity end-member, while here we are dealing with low-porosity rocks. Once again, the essence of this RPM is the connection between the two endpoints rather than the specific properties at these endpoints.

We only used data from vertical wells. In other words, the information available only pertains to the "33" direction in generally anisotropic shales. Here we did not attempt to estimate the anisotropic elastic coefficients simply because the input information for such evaluation is not available. Moreover, such information is almost never available in the field since high-quality wireline data usually come from vertical wells. The workflow used here is self-consistent in the sense that the RPM pertains to the properties along the same direction as the measurements were made. Should the elastic properties in other directions be required, they can be estimated from the "33" properties using the existing studies of anisotropy in shales (e.g., Hornby et al., 1994; Sayers and Dasgupta, 2019).

The main result of this work is establishing a simple RPM that relates the volumetric properties of rock to its elastic properties. This model requires such additional inputs as the elastic moduli and densities of the mineral components and kerogen, as well as those of the brine and gas. The latter were computed using the fluid properties provided by the operator of the field. The former were assigned commonly used values tabulated in existing literature.

Let us emphasize again that the elastic properties of organic shale reservoirs depend on many and often hardly controllable geological factors (e.g., Bandyopadhyay, 2009; Suwannasri, et al., 2018; Zhao et al., 2018). We show here that in spite of this complexity, a simple RPM can be used to describe wireline data.

Perhaps the most uncertain input is the properties of the kerogen as discussed above. These were selected to ensure the best fit between the data and model-derived elastic properties. Hence, if these properties are consistently employed in any application of this model, be it seismic-based reservoir interpretation or DRP, no uncertainty propagation into the predictions is expected.

The workflow offered here uses a number of assumptions, such as attributing all clay mineralogy to illite. All these assumptions were based on concrete field and laboratory data. Most importantly, they allowed us to generate a meaningful RPM and successfully apply it to digital rock physics inputs.

An important issue to be aware of when using a RPM in interpretation is the spatial scale of investigation. The scale of wireline data is on the order of ft, while that of the digital rock physics input is on the order of mm. In spite of this difference, it has been shown (e.g., Dvorkin et al., 2011) that RPM (transforms) are often approximately scale independent and, hence, while established at one spatial scale can be used at another.

The quality of the controlled-experiment data is key to establishing meaningful rock physics trends. The concept of data quality depends on the purpose of the experiment. For example, the log interpreter attempts to process the acoustic waveforms and/or bulk density readings to achieve the accuracy best possible, often forgetting to cross-plot velocity versus density to ensure that the cross-plot is physically meaningful. The rock physics data quality criterion is somewhat different. Here we pay special attention to cross-plots, their theoretical meaning, and their agreement with appropriate effective-medium theories. In other words, if the data allow for establishing a meaningful relation between different rock attributes, the data quality is deemed satisfactory. The Wolfcamp case study discussed here is an example of such approach. In spite of the less-than-perfect data quality, these wireline measurements can still be used to generate a meaningful cross-correlation and exploit it is a predictive fashion.

CONCLUSION

Wireline data from Woodford and Wolfcamp gas shale indicate that two unique controls of the elastic properties are the total porosity and mineralogy, the latter's effect combined in the elastic-wave velocities of the mineral phase plus kerogen. A theoretical RPM that accurately relates the elastic-wave velocities to the volumetric properties of rock has been established based on this finding. A powerful application of this model is in using digital rock physics to estimate the elastic properties of rock from its small irregular fragments, such as drill cuttings.

DATA AVAILABILITY STATEMENT

The data analyzed in this study is subject to the following licenses/restrictions: confidential. Requests to access these datasets should be directed to jackdvorkin007@gmail.com.

AUTHOR CONTRIBUTIONS

All authors contributed to the article and approved the submitted version.

FUNDING

This work was supported by King Fahd University of Petroleum and Minerals and Halliburton.

ACKNOWLEDGMENTS

We thank Marjory Matic for carefully editing this manuscript. We also thank Halliburton for permission to publish this material.

REFERENCES

Al Jallad, O., Koronfol, S., and Grader, A. (2019). *Robust characterization methods of cuttings derived from siliciclastic reservoir and seal rocks - a case study from New Zealand, Conference paper SPE-196616-MS, SPE Reservoir Characterization and Simulation Conference and Exhibition*. Abu Dhabi, UAE: SPE.

Andra, H., Combaret, N., Dvorkin, J., Glatt, E., Han, J., Kabel, M., et al. (2012). *Digital rock physics benchmarks — Part II: computing effective properties, computers and geosciences*. Amsterdam: Elsevier, 1–11.

Arevalo-Lopez, H. S., and Dvorkin, J. (2016). Porosity, mineralogy, and pore fluid from simultaneous impedance inversion. *TLE* 35, 423–429. doi:10.1190/tle35050423.1

Arevalo-Lopez, H. S., and Dvorkin, J. P. (2017). Simultaneous impedance inversion and interpretation for an offshore turbiditic reservoir. *Interpretation* 5, SL9–SL23. doi:10.1190/int-2016-0192.1

Arns, C. H., Bauget, F., Ghous, A., Sakellariou, A., Senden, T. J., Sheppard, A. P., et al. (2005). Digital core laboratory: petrophysical analysis from 3D imaging of reservoir core fragments. *Petrophysics* 46, 260–277. doi:10.2118/0504-0066-jpt

Bandyopadhyay, K. (2009). Seismic anisotropy: geological causes and its implications to reservoir geophysics. PhD thesis. Stanford (CA): Stanford University.

Batzle, M., and Wang, Z. (1992). Seismic properties of pore fluids. *Geophysics* 57, 1396–1408. doi:10.1190/1.1443207

Beloborodov, R., Pervukhina, M., Josh, M., Clennel, M. B., and Hauser, J. (2019). Assessing shale mineral composition: from lab to seismic scale. *TLE* 38, 385–391. doi:10.1190/tle38050385.1

Dvorkin, J., and Alabbad, A. (2019). Velocity-porosity-mineralogy trends in chalk and consolidated carbonate rocks. *Geophys. J. Int*. 219, 662–671. doi:10.1093/gji/ggz304

Dvorkin, J., Derzhi, N., Diaz, E., and Fang, Q. (2011). Relevance of computational rock physics. *Geophysics* 76, E141–E153. doi:10.1190/geo2010-0352.1

Dvorkin, J., Gutierrez, M., and Grana, D. (2014). *Seismic reflections of rock properties*. New York, NY: Cambridge University Press.

Dvorkin, J., Gutierrez, M., and Nur, A. (2002). On the universality of diagenetic trends. *Lead. Edge* 21, 40–43. doi:10.1306/61eee624-173e-11d7-8645000102c1865d

Dvorkin, J. (2007). Self-similarity in rock physics. *TLE* 26, 946–950. doi:10.1190/1.2775996

Elkatatny, S., Mahmoud, M., Mohamed, I., and Abdulraheem, A. (2018). Development of a new correlation to determine the static Young's modulus. *J. Pet. Explor. Prod. Technol.* 8, 17–30. doi:10.1007/s13202-017-0316-4

Gal, D., Dvorkin, J., and Nur, A. (1998). A physical model for porosity reduction in sandstones. *Geophysics* 63, 454–459. doi:10.1190/1.1444346

Gassmann, F. (1951). Elasticity of porous media: Uber die elastizitat poroser medien. *Vierteljahrsschrift Naturforschenden Gesselschaft* 96, 1–23.

Hamza, F., Chen, C., Gu, M., Quirein, J., Martysevich, V., and Matzar, L. (2015). Characterization of anisotropic elastic moduli and stress for unconventional reservoirs using laboratory static and dynamic geomechanical data. *SPE/CSUR Unconv. Resour. Conf*, 1–17. doi:10.2118/175907-ms

He, J., Ling, K., Wu, X., Pei, P., and Pu, H. (2019). Static and dynamic elastic moduli of Bakken formation. *Int. Pet. Technol. Conf*, 1–13. doi:10.2523/19416-ms

Hill, R. (1952). The elastic behavior of crystalline aggregate. *Proc. Phys. Soc. Sect. A* 65, 349–354. doi:10.1088/0370-1298/65/5/307

Hornby, B. E., Schwartz, L. M., and Hudson, J. A. (1994). Anisotropic effective-medium modeling of the elastic properties of shales. *Geophysics* 59, 1570–1583. doi:10.1016/0148-9062(95)93233-f

Karimpouli, S., Tahmasebi, P., and Saenger, E. H. (2018). Estimating 3D elastic moduli of rock from 2D thin-section images using differential effective medium theory. *Geophysics* 83, MR211–MR219. doi:10.1190/geo2017-0504.1

Kashinath, A., Szulczewski, M., and Dogru, A. H. (2020). Modeling the effect of maturity on the elastic moduli of kerogen using atomistic simulations. *Energy Fuels* 34, 1278–1385. doi:10.1021/acs.energyfuels.9b03221.s001

Khadeeva, Y., and Vernik, L. (2014). Rock physics model for unconventional shales. *TLE* 33, 318–322. doi:10.1190/segam2013-0986.1

Khatibi, S., Ostadhassan, M., Tuschel, D., Gentzis, T., Bubach, B., and Carvajal-Ortiz, H. (2018). Raman spectroscopy to study thermal maturity and elastic modulus of kerogen. *Int. J. Coal Geol*. 185, 103–118. doi:10.1016/j.coal.2017.11.008

Knackstedt, M. A., Latham, S., Madadi, M., Sheppard, A., Varslot, T., and Arns, C. (2009). Digital rock physics: 3D imaging of core material and correlations to acoustic and flow properties, The Leading Edge, *Geophysics* 28, 28–33.

Mavko, G., Chan, C., and Mukerji, T. (1995). Fluid substitution: estimating changes in V_p without knowing V_s. *Geophysics* 60, 1750–1755. doi:10.1190/1.1443908

Mavko, G., Mukerji, T., and Dvorkin, J. (2020). *Rock physics handbook*. 3rd Edition. New York, NY: Cambridge University Press.

Meléndez-Martínez, J., and Schmitt, D. R. (2016). A comparative study of the anisotropic dynamic and static elastic moduli of unconventional reservoir shales: implication for geomechanical investigations. *Geophysics* 81, D245–D261. doi:10.1190/geo2015-0427.1

Mindlin, R. D. (1949). Compliance of elastic bodies in contact. *J. Appl. Mech*. 16, 259–268.

Prasad, M., Pal-Bathija, A., Johmston, M., Rydzy, M., and Batzle, M. (2009). Rock physics of the unconventional. *Lead. Edge* 28, 34–38.

Sayers, C. M., and Dasgupta, S. (2019). A predictive anisotropic rock-physics model for estimating elastic rock properties of unconventional shale reservoirs. *Lead. Edge* 38, 358–365. doi:10.1190/tle38050358.1

Sayers, C. M., Dasgupta, S., Koesoemadinata, A., and Shoemaker, M. (2019). Rock physics of the Wolfcamp formation, Delaware basin. *SEG Tech. Program Expanded Abstr. 2017* 84, 358–365. doi:10.1190/segam2017-17402408.1

Sayers, C. M., Fisher, K., and Walsh, J. J. (2015). Sensitivity of P- and S-impedance to the presence of kerogen in the Eagle ford shale. *Lead. Edge* 34, 1482–1486. doi:10.1190/tle34121482.1

Sayers, C. M. (2013). The effect of kerogen on elastic anisotropy of organic-rich shales. *Geophysics* 78, D65–D74. doi:10.1190/geo2012-0309.1

Sone, H., and Zoback, M. D. (2013). Mechanical properties of shale-gas reservoir rocks — Part 1: static and dynamic elastic properties and anisotropy. *Geophysics* 78, D381–D392. doi:10.1190/geo2013-0050.1

Suwannasri, K., Vanorio, T., and Clark, A. (2019). Data-driven elastic modeling of organic-rich marl during maturation. *SEG Tech. Program Expanded Abstr. 2018*. doi:10.1190/segam2018-2995177.1 85, MR11–MR23.

Suwannasri, K., Vanorio, T., and Clark, A. (2018). Monitoring the changes in the microstructure, and the elastic and transport properties of Eagle Ford marl during maturation. *Geophysics* 83, MR263–MR281. doi:10.1190/geo2017-0797.1

Vernik, L., Castagna, J., and Omovie, J. (2018). S-wave velocity prediction in unconventional shale reservoirs. *Geophysics* 83, MR35–MR45. doi:10.1190/geo2017-0349.1

Vernik, L., and Kachanov, M. (2010). Modeling elastic properties of siliciclastic rocks. *Geophysics* 75, E171–E172. doi:10.1190/1.3494031

Vernik, L., and Landis, C. (1996). Elastic anisotropy of source rocks: implications for hydrocarbon generation and primary migration. *Am. Assoc. Pet. Geol. Bull*. 80, 531–544. doi:10.1306/64ed8836-1724-11d7-8645000102c1865d

Vernik, L., and Milovac, J. (2011). Rock physics of organic shales. *Lead. Edge* 30, 318–322. doi:10.1190/1.3567263

Walls, J., Morcote, A., Hintzman, T., and Everts, M. (2016). "Comparative core analysis from a Wolfcamp formation well: a case study," in International symposium of the society of core analysts, Snow Mass, CO, August 21–26, 2016 (SCA), 1–6.

Wolf, K. (2010). Laboratory measurements and reservoir monitoring of bitumen sand reservoirs. PhD thesis. Stanford (CA): Stanford University.

Wollner, U., Arevalo-Lopez, H. S., and Dvorkin, J. (2017). Seismic-scale petrophysical interpretation and gas volume estimation from simultaneous impedance inversion. *TLE* 36, 910–915. doi:10.1190/tle36110910.1

Yan, F., and Han, D.-H. (2013). *Measurement of elastic properties of kerogen, SEG-2013-1319*. Houston: SEG Annual Meeting, 1–4. Expanded Abstract, 2013.

Yenugu, M., and Vernik, L. (2015). Constraining seismic rock-property logs in organic shale reservoirs. *Lead. Edge* 34, 1326–1331. doi:10.1190/tle34111326.1

Zhao, L., Qin, X., Han, D., Geng, J., Yang, Z., and Cao, H. (2016). Rock-Physics modeling for the elastic properties of organic shale at different maturity stages. *Geophysics* 81, D527–D541. doi:10.1190/geo2015-0713.1

Zhao, L., Qin, X., Zhang, J., Liu, X., Han, D., Geng, J., et al. (2018). An effective reservoir parameter for seismic characterization of organic shale reservoir. *Surv. Geophys.* 39, 509–541. doi:10.1007/s10712-017-9456-9

Zhao, P., Zhuang, W., Sun, Z., Wang, Z., Lao, X., Mao, Z., et al. (2016). Methods for estimating petrophysical parameters from well logs in tight oil reservoirs: a case study. *J. Geophys. Eng.* 13, 78–85. doi:10.1088/1742-2132/13/1/78

Conflict of Interest: The authors JW and GD were employed by the company Halliburton.

The remaining author declares that the research was conducted in the absence of any commercial or financial relationships that could be construed as a potential conflict of interest.

Copyright © 2021 Dvorkin, Walls and Davalos. This is an open-access article distributed under the terms of the Creative Commons Attribution License (CC BY). The use, distribution or reproduction in other forums is permitted, provided the original author(s) and the copyright owner(s) are credited and that the original publication in this journal is cited, in accordance with accepted academic practice. No use, distribution or reproduction is permitted which does not comply with these terms.

frontiers in Earth Science

ORIGINAL RESEARCH
published: 05 February 2021
doi: 10.3389/feart.2020.620276

Rock Physics Based Interpretation of Seismically Derived Elastic Volumes

Abrar Alabbad[1], *Jack Dvorkin*[2]*, *Yazeed Altowairqi*[1] *and Zhou F. Duan*[1]

[1]Saudi Aramco, Dhahran, Saudi Arabia, [2]King Fahd University of Petroleum and Minerals, Dhahran, Saudi Arabia

A rock physics based seismic interpretation workflow has been developed to extract volumetric rock properties from seismically derived P- and S-wave impedances, I_p and I_s. This workflow was first tested on a classic rock physics velocity-porosity model. Next, it was applied to two case studies: a carbonate and a clastic oil field. In each case study, we established rock physics models that accurately relate elastic properties to the rock's volumetric properties, mainly the total porosity, clay content, and pore fluid. To resolve all three volumetric properties from only two inputs, I_p and I_s, a site-specific geology driven relation between the pore fluid and porosity was derived as a hydrocarbon identifier. In order to apply this method at the seismic spatial scale, we created a coarse-scale elastic and volumetric variables by using mathematical upscaling at the wells. By using I_p and I_s thus upscaled, we arrived at the accurate interpretation of the upscaled porosity, mineralogy, and water saturation both at the wells and in a simulated vertical impedance section generated by interpolation between the wells.

Keywords: interpretation, rock physics, impedance, porosity, seismic

OPEN ACCESS

Edited by:
Jing Ba,
Hohai University, China

Reviewed by:
Aldo Vesnaver,
National Institute of Oceanography and Applied Geophysics, Italy
Chenghao Cao,
Nanjing Tech University, China

***Correspondence:**
Jack Dvorkin
jackdvorkin007@gmail.com

Specialty section:
This article was submitted to Solid Earth Geophysics, a section of the journal Frontiers in Earth Science

Received: *22 October 2020*
Accepted: *22 December 2020*
Published: *05 February 2021*

Citation:
Alabbad A, Dvorkin J, Altowairqi Y and Duan ZF (2021) Rock Physics Based Interpretation of Seismically Derived Elastic Volumes. Front. Earth Sci. 8:620276. doi: 10.3389/feart.2020.620276

INTRODUCTION

Most rock physics models are designed to arrive at the elastic properties of porous rocks from their petrophysical properties, such as the total porosity, mineralogy, organic matter content in unconventional reservoirs, and pore fluid saturation and individual fluid phase properties. Such current models are based on various effective medium theories taking into account the pore-space geometry, degree of cementation, as well as such conditions as the differential pressure and water saturation. These models (or transforms) usually predict the elastic P- and S-wave impedances (I_p and I_s, respectively), as well as the bulk density (ρ_b), from the aforementioned petrophysical and environmental inputs. These transforms are often used in the forward-modeling mode to generate the elastic properties and the resulting synthetic seismograms for geologically plausible what-if scenarios for varying inputs, among them porosity, lithology, and saturation. Can these models be used in an inverse mode to generate the seismic-scale petrophysical variables from seismically derived impedances and density?

The seemingly unresolvable issue of such interpretation is the so-called "rock physics bottleneck," meaning that the few elastic properties depend on a larger number of volumetric and environmental inputs, such as porosity, mineralogy, water saturation, differential stress, and rock-frame texture (e.g., cemented vs. friable sediments). Hence, the interpretation is impossible in a strictly mathematical sense. Yet, by carefully analyzing controlled-experiment data, especially those from wireline measurements, and putting this analysis into the geological context, one can resolve even a single elastic input for more than one volumetric variable. For example, Dvorkin and Alkhater (2004) found, by plotting I_p vs. porosity (ϕ) from wireline data in an unconsolidated-sand offshore reservoir, that two very distinct I_p–ϕ trends emerge, one for the gas and the other for the liquid (oil and water)

leg. This finding helped obtain volumes of the pore fluid and porosity from only one variable, the seismically derived acoustic impedance.

This concept of adding a site-specific equation to the rock physics model was further developed by Arevalo-Lopez and Dvorkin (2016) and Arevalo-Lopez and Dvorkin (2017) where simultaneous impedance inversion was performed to quantify porosity, mineralogy, and pore fluid in a siliciclastic turbidite oil reservoir offshore northwest Australia. Specifically, the I_p/I_s ratio was utilized as a hydrocarbon identifier for oil-saturated rock where this ratio was small. Once the pore fluid was thus identified, a theoretical rock physics model was used to estimate the porosity and clay content from the two inputs, I_p and I_s, in a binary-mineral environment, a quartz/clay system.

Of course, the high-quality simultaneous impedance inversion results can be interpreted in a strictly mathematical fashion. Wollner et al. (2017) used all three seismic-scale variables, I_p, I_s, and ρ_b, to arrive at the total porosity, clay content, and water saturation. The main contribution of that work was to translate the well-scale rock physics model into the seismic scale. Specifically, it was found that unlike at the wellbore scale, the relation between the effective bulk modulus of the gas/brine system and S_w at the seismic scale was according to the "patchy" rather than "uniform" saturation scheme.

Here we revisit this interpretation concept and give two examples thereof where a mathematical rock physics model was supplemented with a geology-based pore-fluid discrimination thus allowing for quantifying the porosity, mineralogy, and the pore fluid from only one (I_p) or two (I_p and I_s) inputs.

As mentioned above, there are at least two issues to be addressed during such interpretation. One is the issue of the spatial scale. Indeed, a rock physics model is usually derived from the laboratory or wireline data where the spatial resolution is on the order of a ft. The question is whether these transforms are usable at the seismic scale of tens or hundreds of ft. The other issue is related to the fact that the number of petrophysical inputs is often larger than just the two (I_p and I_s) and at the most three (I_p, I_s, and ρ_b) variables provided by the simultaneous impedance inversion. How can two (or three) equations be resolved for more than two (or three) unknowns?

To test the concept, we first employed the arguably simplest rock physics model, the Raymer et al. (1980) transform that relates V_p to porosity, pore fluid properties, and mineralogy. We assumed a binary quartz/clay mineralogy and fixed fluid properties. By creating an objective function that minimizes the difference between the measured and assumed I_p and I_s as a function of porosity and clay content, we successfully interpreted these two elastic variables for the petrophysical variables in question.

Next, we used wireline data from an offshore oil chalk reservoir to, once again, interpret the measured impedances for the desired petrophysical properties, porosity and water saturation. In this formation, there is a fairly robust relation between the porosity and water saturation. Specifically, due to diagenetic processes, the high-porosity rock contains oil, while the low-porosity rock is essentially 100% water saturated. Prior to interpretation, we established that the velocity-porosity model for this formation is the stiff-rock model (the modified upper Hashin-Shtrikman bound). By using this model in reverse within the objective function, as well as the abovementioned relation between porosity and the pore fluid, we accurately predicted the porosity and saturation from I_p and I_s both at the well and also using the spatially upscaled impedances to address this interpretation method at the seismic scale.

In the second case study, we used wireline data from an onshore clastic reservoir with oil. We had to interpret I_p and I_s for three variables, the total porosity, clay content, and water saturation. As in the first case study, the rock physics diagnostics indicated that the velocity-porosity model was the stiff-rock model, now applied to the quartz/clay mineralogy. The additional equation required to resolve the two elastic inputs for the three unknowns was very similar to that used in the first case study. It appeared that although the two oil fields under examination are located thousands of miles apart and in very different depositional environments, the diagenetically-driven relations between the porosity and pore fluid are qualitatively the same. The low-porosity intervals were predominantly water-saturated, while the higher-porosity intervals contained oil. By using the respective porosity-saturation threshold, we accurately interpreted the measured impedances for the desired three variables at the well and also at the seismic scale using mathematically upscaled elastic and volumetric properties.

The new methods and examples introduced here show how to combine mathematical rock physics models with geology-driven quantitative relations to interpret seismically-derived impedance volumes for volumetric reservoir attributes.

Proof of Concept

Arguably, the simplest rock physics model is the Raymer et al. (1980) transform relating the mineralogy and pore-fluid properties to V_p and V_s as:

$$\begin{aligned} V_p &= V_{ps}(1-\phi)^2 + V_{pf}\phi; \\ V_s &= V_{ss}(1-\phi)^2\sqrt{(1-\phi)\rho_s/\rho_b} \end{aligned} \tag{1}$$

where V_{ps} and V_{ss} are the P- and S-wave velocities in the mineral matrix, respectively; V_{pf} is the P-wave velocity in the pore fluid; ϕ is the total porosity; and ρ_s and ρ_b are the density of the mineral matrix and the bulk density, respectively. The second line in **Eq. 1** is due to Dvorkin (2008). The P- and S-wave impedances (I_p and I_s) are simply

$$I_p = \rho_b V_p; \quad I_s = \rho_b V_s, \tag{2}$$

Assume for simplicity that the mineralogy is binary (quartz/clay). The densities of quartz and clay are both assumed 2.65 g/cc. The bulk moduli of quartz and clay are 36.6 and 21 GPa, respectively, while their shear moduli are 45 and 7 GPa, respectively. Let us next generate three forward modeling scenarios for varying porosity, clay content (C), and water saturation (S_w). The inputs to these three scenarios are listed in **Table 1**. Also, assume that the immiscible pore-fluid phases are gas and

TABLE 1 | Inputs (porosity ϕ, clay content C, and water saturation S_w) for forward modeling scenarios using the Raymer et al. (1980) model and the computed P- and S-wave impedances (I_p and I_s, respectively).

Scenario #	ϕ	C	S_w	I_p (km/s g/cc)	I_s (km/s g/cc)	ϕ Interpreted	C Interpreted
1	0.252	0.271	0.10	6.11	3.58	0.250	0.280
2	0.153	0.020	0.90	10.50	6.65	0.150	0.030
3	0.050	0.133	1.00	12.80	8.11	0.040	0.170

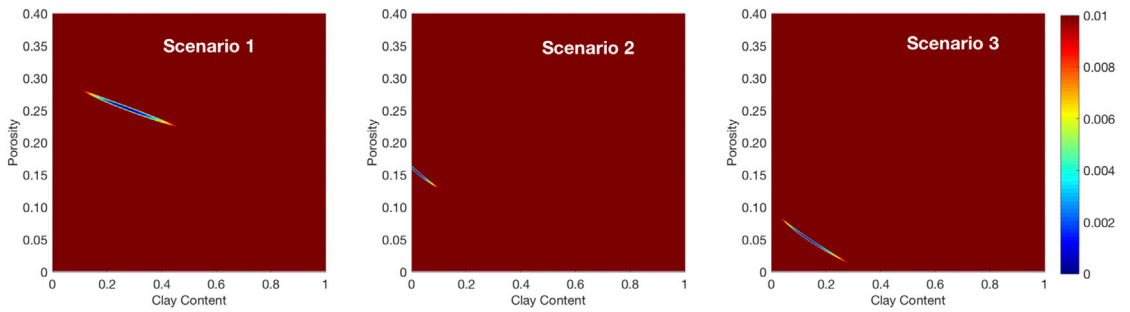

FIGURE 1 | The objective function as given by **Eq. 3** plotted inside the porosity (vertical axis) and clay content (horizontal axis) mesh with the minima shown in color (blue) on the solid-color background.

brine whose densities are 1.05 and 0.24 g/cc, respectively, while their bulk moduli are 3.09 and 0.11 GPa, respectively.

Because the P- and S-wave impedance volumes are usually the product of simultaneous impedance inversion, our goal is to arrive at the volumetric inputs listed in **Table 1** using these impedances. Specifically, first we forward-model these impedances I_p and I_s using **Eqs. 1**, **2** and the inputs from the aforementioned three scenarios. These forward modeling results are also listed in **Table 1**.

Our next goal is to arrive at these volumetric inputs now using these I_p and I_s as inputs and, once again, **Eqs. 1**, **2**. Needless to say that we cannot derive more than two unknowns from two inputs. Hence, we select these two unknowns as ϕ and C and assume that S_w and the resulting bulk modulus and density of the pore fluid are known. Next we cycle through a matrix of as yet unknown ϕ and C and generate an objective function

$$F_o = \left(I_p - I_{p0}\right)^2 + (I_s - I_{s0})^2, \tag{3}$$

where I_{p0} and I_{s0} are now the known input impedances from forward modeling (**Table 1**).

We find the minimum of this function and select ϕ and C associated with this minimum as our interpretation results. We have found that in this example, the objective function has only one global minimum (**Figure 1**) thus rendering interpretation unique. Earlier studies (Arevalo-Lopez and Dvorkin, 2016, 2017; and; Wollner et al., 2017) also point at uniqueness of such interpretation. This is also the case in the following two case studies.

These interpretation results for the aforementioned three scenarios are also listed in **Table 1**. As we can see, they are very close to the volumetric inputs. The small mismatch is caused by the coarseness of the lookup table for the variable I_p and I_s. A much more accurate match can be attained if the search grid in this table is fine enough.

The location of the minimum of the objective function for these three scenarios is shown in **Figure 1**, which illustrates that using the two impedances as an input for interpretation produces distinctive extrema.

Case Study A: Carbonate Oil Field

Porosity and hydrocarbon saturation are two important parameters for resource assessment. In this case study, we investigate the applicability of our rock physics based seismic interpretation workflow to quantifying porosity and pore fluid from measured elastic properties. Wireline data of two wells within oil-bearing off-shore chalk deposits with high-to-medium porosity were used in this exercise. The mineralogy is practically 100% calcite. The goal is to interpret the elastic impedances for the desired petrophysical properties, namely porosity and water saturation. The rock physics analysis of the wireline data used here is given by Dvorkin and Alabbad (2019). Here we use these data to illustrate our interpretation strategy.

Sensitivity to Pore Fluid. Traditional approach to discriminating the pore fluid from seismic data is based on the difference in the AVO response at the reservoir depending on whether the reservoir contains water or hydrocarbon. This difference is, in turn, governed by the V_p/V_s ratio (or Poisson's ratio) that is low in gas-saturated rock and relatively high in 100% wet rock. This difference affects the slope of the AVO curve, also known as the gradient.

However, in some cases, the effect of the pore fluid on the elastic properties is weak. This may happen where the difference between the compressibility and density of the hydrocarbon and brine is small (as in oil vs. water case) and/or where the rock frame is stiff, even at high porosity (as in some carbonates). An

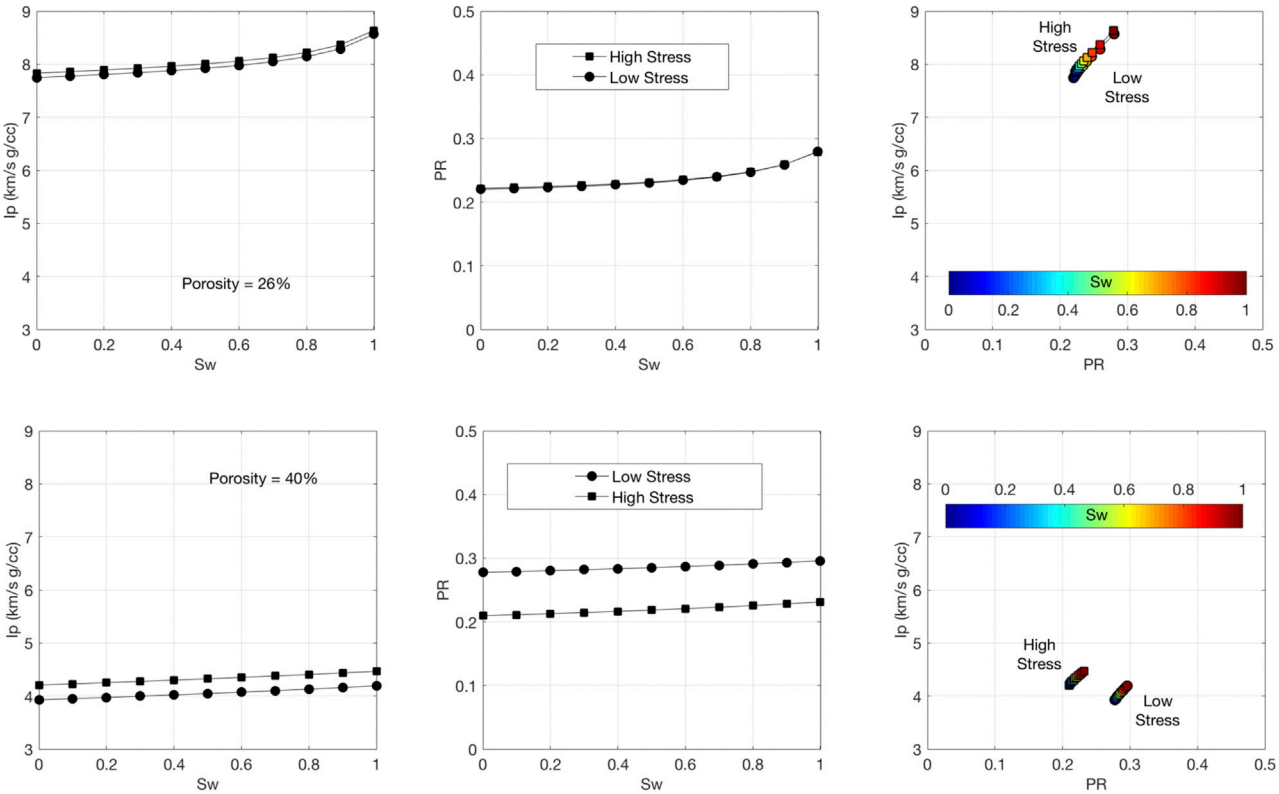

FIGURE 2 | I_p (left) and ν (center) vs. S_w as computed from the dry-rock data using fluid substitution. Circles are for the low-stress data, while squares are for the high-stress data. Top: Sample with porosity 26%. Bottom: Sample with porosity 40%. The third frame in each row shows I_p vs. ν cross-plots color-coded by S_w.

TABLE 2 | The elastic moduli and densities of the rock components.

Component	Bulk modulus (GPa)	Shear modulus (GPa)	Density (g/cc)
Calcite A	68.21	29.51	2.71
Calcite B	56.66	21.25	2.71
Clay	21.00	7.00	2.65
Brine	2.63	0.00	1.00
Oil	0.40	0.00	0.65

example of such a situation is shown in **Figure 2** based on the laboratory measurements of V_p and V_s in dry rock vs. hydrostatic confining stress. These measurements were carried out on several samples extracted from the wells under examination. As stated earlier, the mineralogy is essentially 100% calcite.

We selected two samples, one with porosity (ϕ) 26% and the other with porosity 40%. Fluid substitution was conducted using Gassmann's (1951) equation assuming the bulk modulus of the mineral phase 62.44 GPa, the average between the two values for pure calcite as described in Dvorkin and Alabbad (2019) and listed in **Table 2**. The properties of the brine and oil are also listed in **Table 2**. The bulk modulus of the pore fluid for S_w varying between zero and 100% was computed as the harmonic average of those of brine and oil, while the density was computed as the arithmetic average of the respective densities. The velocity measurements were conducted in the hydrostatic confining stress range between 7 and 40 MPa. For this example, we selected the data obtained at the lowest and highest stresses.

The results for the sensitivity of I_p and Poisson's ratio (ν) to S_w are shown in **Figure 2**. As we can see, this sensitivity is very weak, no matter whether the sample has high or low porosity.

Fluid substitution performed on wireline data from the same field (**Figure 3**) also shows very weak sensitivity of the elastic properties to water saturation (Dvorkin and Alabbad, 2019) even in the intervals with relatively high porosity. This conclusion is reconfirmed by the cross-plots also shown in **Figure 3**. Indeed, even at the highest porosity, the difference between the *in-situ* I_p and that computed for 100% water saturation is significantly smaller than the vertical variations of this variable, which will make it difficult to elucidate the pore-fluid effect in seismic data. The respective variations in Poisson's ratio are also relatively small.

Pore Fluid Discrimination. The above plots indicate low sensitivity of both the impedance and Poisson's ratio to the pore fluid. Does this mean that in this situation we cannot interpret seismically derived impedances for pore fluid? Yes, if we solely rely on mathematical fluid substitution as the primary means of pore fluid identification. No, if we look deeper into interrelations among various rock attributes.

By plotting the impedance vs. porosity (**Figure 4**), we observe that in this case, the low-porosity intervals contain practically

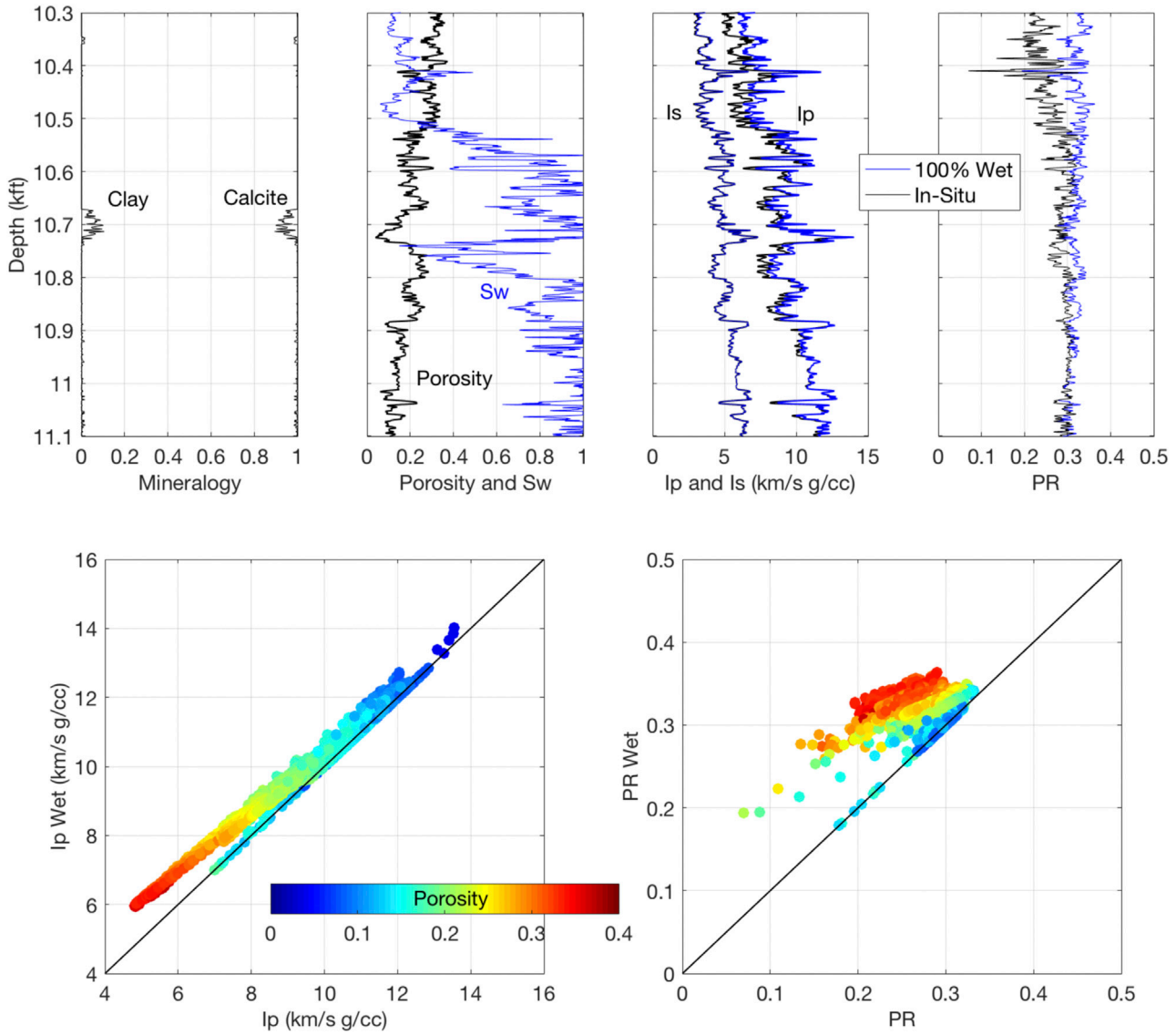

FIGURE 3 | Top: Depth plots for one of the wells from the field under examination. From left to right: Mineralogy; the total porosity and water saturation; P- and S-wave impedances; and Poisson's ratio. In the last two frames, black curves are for measured properties, while blue curves are for these properties at 100% water saturation computed using Gassmann's (1951) fluid substitution. Bottom: Cross-plots of the *in-situ* vs. 100% wet P-wave impedance (left) and Poisson's ratio (right) color-coded by the total porosity and using the data shown in top row.

100% water, while high-porosity intervals contain sizable volumes of oil. Respectively, rock with oil has relatively low impedance, while rock with water has higher impedance. It appears that the porosity determines the pore fluid. In fact, the effect is the opposite: the pore fluid has influenced the porosity evolution. Where oil entered the porous chalk, the diagenesis was halted. At the same time, where brine remained dominant, diagenesis and porosity reduction continued (Dvorkin and Alabbad, 2019).

Based on **Figure 4**, we can propose now that the rock contains oil where the total porosity exceeds approximately 20% and it is 100% wet in the lower-porosity intervals. The respective I_p cutoff is about 8 km/s g/cc.

Rock Physics Modeling. Dvorkin and Alabbad (2019) show that the stiff-sand model (e.g., Dvorkin et al., 2014) accurately describes the wireline data in the carbonate oil field under examination. This model has the mathematical form of the modified upper Hashin-Shtrikman bound. The inputs specific to this case study are: 30 MPa differential pressure; 0.40 critical porosity; and 6 coordination number. The fairly tight impedance-porosity cross-plots (**Figure 4**) were accurately bounded by this model curves using two different pure-calcite end-member properties as listed in **Table 2**.

Figure 5 compares the model-based computed elastic properties to those measured *in situ*. The former were computed using the following inputs: mineralogy (calcite and

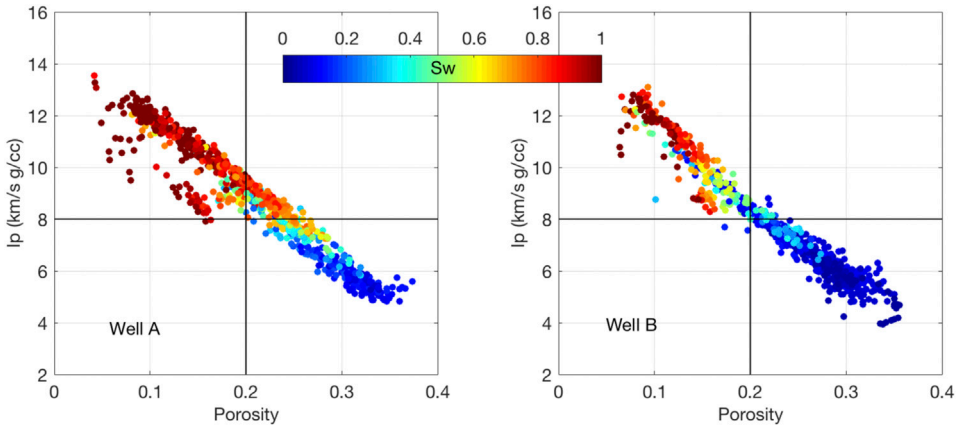

FIGURE 4 | Cross-plots of I_p as measured vs. porosity color-coded by water saturation for Wells A and B.

clay); the total porosity; and water saturation. The effective elastic moduli of the mineral matrix were obtained as Hill's (1952) average of those of calcite and clay, while its density was the arithmetic average of the respective densities. The densities and bulk moduli of the two fluid phases, oil and brine, were computed from pore pressure, temperature, salinity, oil API gravity, and gas-to-oil ratio using Batzle and Wang (1992) equations. The effective bulk modulus of the immiscible oil/brine system was the harmonic average of the components, while the density was the arithmetic average. All these inputs are listed in **Table 2**.

The modeled elastic property curves using the Calcite A and B inputs tightly bound the wireline data at *in-situ* conditions for both wells under examination. An example for Well A is shown in **Figure 5**.

Interpretation at Well A. Figure 3 indicates that the sensitivity of the elastic properties to the pore fluid (or water saturation) is weak. At the same time, both the P- and S-wave impedances show a strong dependence on porosity. Hence, our interpretation strategy in this case study is to interpret the impedances for the total porosity and then use the porosity-saturation cutoff shown in **Figure 4** to predict the pore fluid.

With this goal in mind, let us explore the sensitivity of porosity interpretation to the assumed pore fluid and the elastic properties of the calcite (Calcite A vs. B). Specifically, we use the same interpretation method as described in the previous section and conduct it along the well at each depth station. We examine four variants: 1) $S_w = 0.20$ and Calcite A; 2) $S_w = 1.00$ and Calcite A; 3) $S_w = 0.20$ and Calcite B; and 4) $S_w = 1.00$ and Calcite B. Also, we implement this interpretation workflow based only on the measured I_p, as well as based on both I_p and I_s. The interpretation results shown in **Figure 6** indicate that the interpreted porosity only weakly depends on these variants.

Based on the observed weak sensitivity of porosity interpretation to the model inputs, we will simply use single values for the bulk and shear moduli of pure calcite as the means of the respective moduli of Calcite A and B. Namely, these bulk and shear moduli are 66.44 and 25.38 GPa, respectively.

Seismic-Scale Interpretation. In order to show how our interpretation method works at the seismic scale, we first use the Backus (1962) averaging to upscale the elastic curves in both wells. The example using Well A is shown in **Figure 7**, where we also show the arithmetically upscaled porosity, bulk density, and water saturation curves.

This upscaling is conducted using a running window of approximately 1/8 of the wavelength (about 50 ft or 15 m) assuming 40 Hz frequency. During interpretation, we had to assign the effective bulk modulus and density of the brine/oil system. To do this, we used the cutoffs shown in **Figure 4** by assuming $S_w = 1.00$ for porosity smaller 0.20 and $S_w = 0.20$ for porosity greater than or equal 0.20.

The interpreted porosity and water saturation curves for both wells are shown in **Figure 7**. The interpreted porosity closely follows the upscaled porosity curves in both wells. The interpreted S_w appears blocky simply because of the porosity-saturation cutoff we have chosen. This interpretation clearly identifies oil-saturated zones in Well B. At the same time, it appears overly optimistic in Well A, where it shows high oil saturation in the lower part of the reservoir. Of course, we could have had a more precise reservoir delineation in this well if we have chosen a different porosity cutoff. This may be a strategy for providing upper and lower reserve estimates during field interpretation. Here, for the purpose of simplicity, we will use the originally selected cutoff.

In order to illustrate the application of our methodology to an impedance inversion section, we generate a pseudo-section for the upscaled I_p between Well A and the upper portion of Well B (**Figure 7**, bottom) using linear interpolation along the offset. These pseudo-seismic sections were produced using the Backus-upscaled P- and S-wave impedances from the two wells. First, we matched the lengths of the data vectors from both wells by simple linear interpolation. Then, a 2D linear interpolation was performed on a monotonic and plaid matrix with the length of the well along the *Y*-axis (depth or time) and the distance between the two wells along the *X*-axis (offset). In this example, the distance between the wells was assigned to be 100 pixels.

The resulting 2D P- and S-wave impedances are then used as an input to the seismic interpretation workflow. Let us emphasize that these are not real seismic sections but rather pseudo-sections

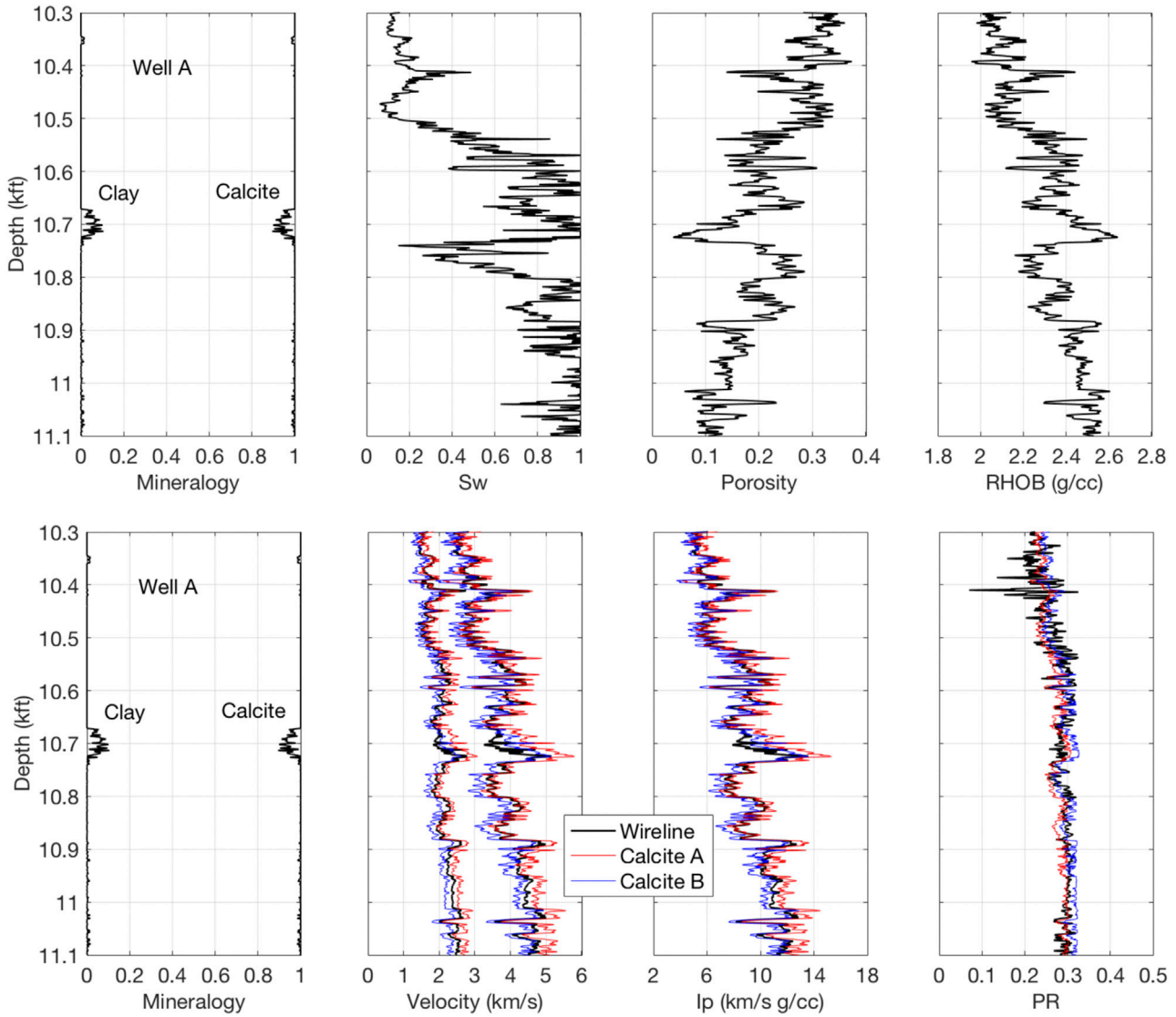

FIGURE 5 | Wireline curves at *in-situ* conditions for Well A (top) with the stiff-sand model curves (bottom) shown in the velocity, impedance, and Poisson's ratio frames using the Calcite A (red) and Calcite B (blue) inputs.

generated for purely visual purpose to show how the proposed interpretation might look in a real seismic world.

Next, we apply the same interpretation routine as used to generate the porosity and S_w profiles. As before, we only use I_p as the input, as well as the average calcite elastic moduli and density. The results shown in **Figure 7** (last two rows) indicate that indeed our interpretation method provides reasonable porosity and water saturation estimates.

Case Study B: Clastic Oil Field

The oil-bearing clastic reservoir under examination is composed of predominantly quartz low-to-medium porosity rock. The mineralogy is binary, quartz/clay. The oil has low gas-to-oil ratio and fairly low (about 20) API gravity. The rock physics diagnostics of wireline data from this field was conducted by Dvorkin (2019). The elastic moduli and densities of the minerals and fluid phases used are listed in **Table 3**.

In the present case study, we will use two wells out of four described in Dvorkin (2019). The respective wireline data are shown in **Figure 8**.

Only the P-wave velocity data were available in this study. The rock physics model determined based on these data (Dvorkin, 2019) is the stiff-rock model (the modified upper Hashin-Shtrikman bound), similar to the model used in the first case study. The model parameters are as follows: the differential pressure 50 MPa; coordination number 12; and critical porosity 0.40.

The total porosity was computed from the measured bulk density, water saturation, and mineralogy using the mass-balance equation. The clay content was model-predicted from the

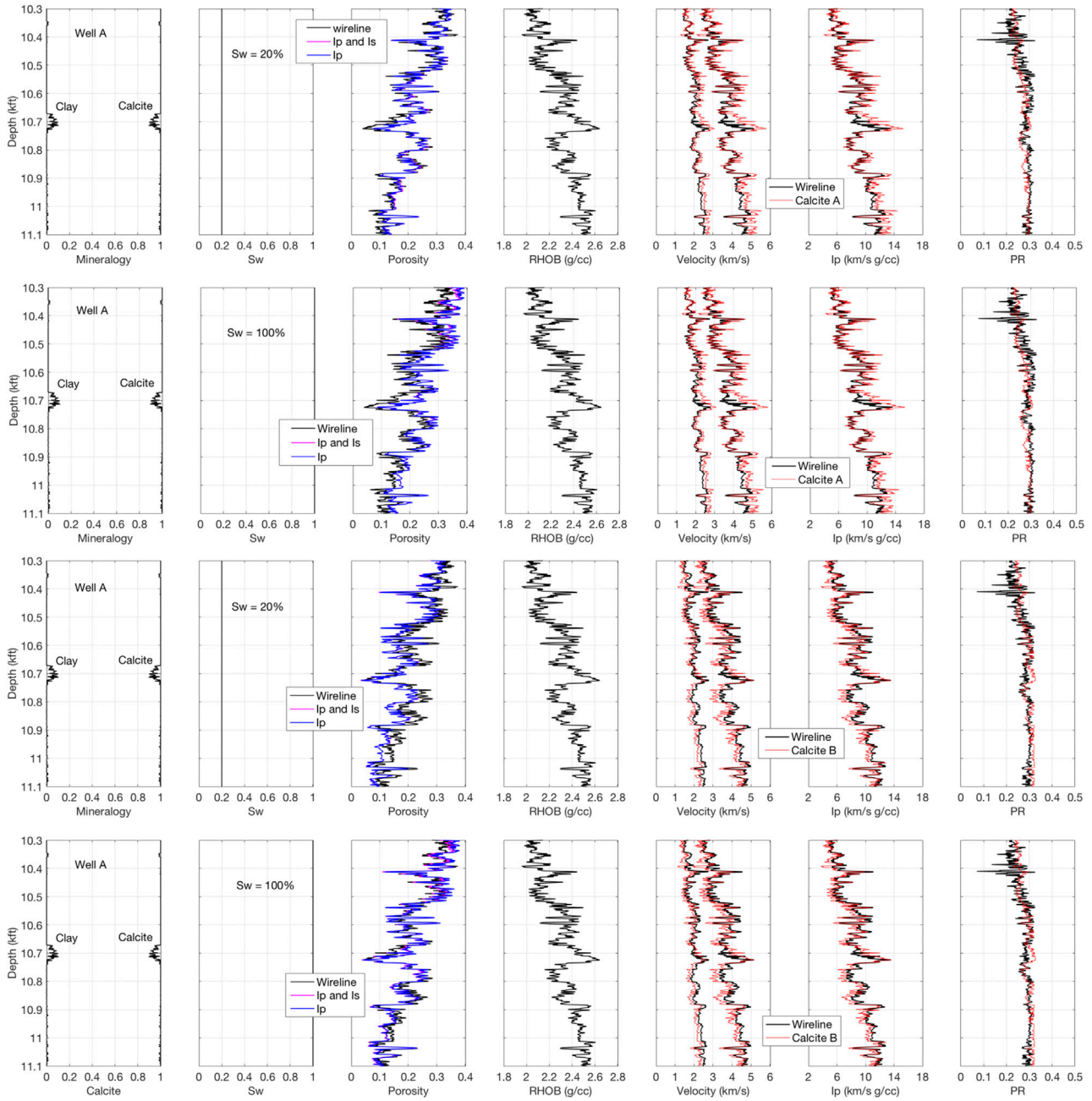

FIGURE 6 | Interpretation for porosity using the four variants as described in the text and also using only I_p and I_p and I_s together. From top to bottom: Variants 1, 2, 3, and 4. The interpreted porosity curves are shown in color and described in the legends. Red curves in the elastic property frames are from the stiff-sand model using the respective inputs.

measured V_p and the total porosity using the stiff-rock model in reverse as described in Dvorkin et al. (2014). Finally, V_s was predicted from the mineralogy, porosity, and pore fluid, once again, using the same rock physics model.

Next, we assume that the measured V_p, bulk density, and predicted V_s are the inputs to the interpretation workflow, compute the respective I_p and I_s, and interpret these elastic properties for the total porosity, clay content, and water saturation. As in the previous case study, we only have two inputs (I_p and I_s) and require three outputs.

The missing equation is very similar to that used in the first case study. Dvorkin (2019) shows that in this clastic reservoir we face diagenesis-driven pore fluid discrimination. Namely, the intervals with oil have porosity higher that approximately 15%, while the 100%-wet intervals have porosity below 15%. We utilize this finding by assuming that $S_w = 0.20$ for $\phi > 0.15$ and

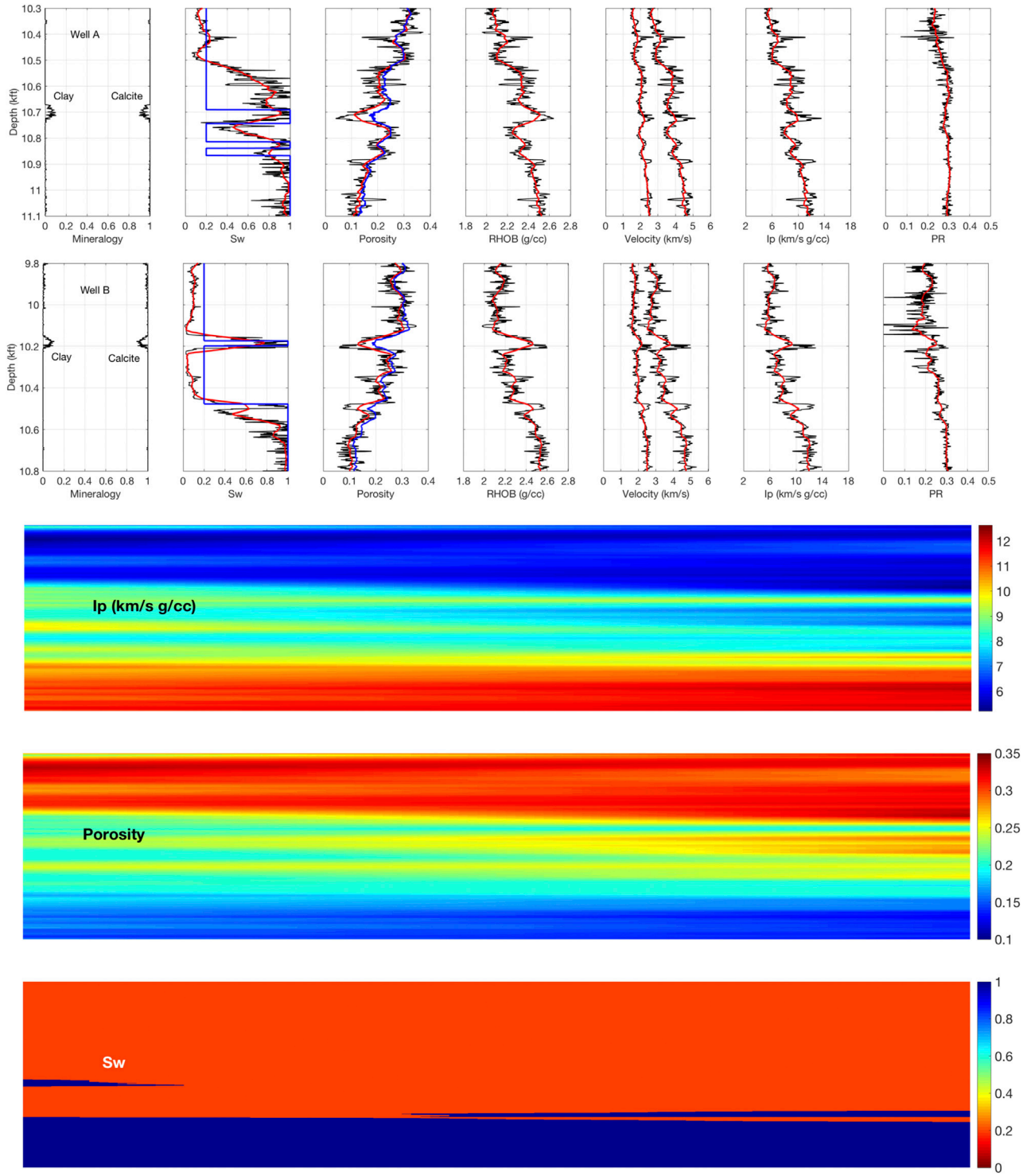

FIGURE 7 | Top two rows: Upscaled curves in Well A and B (red) and interpretation for porosity and water saturation (blue). Bottom three rows: I_p pseudo-section **(top)** and the interpreted porosity **(middle)** and water saturation **(bottom)** sections between Well A **(left)** and B **(right)**.

S_w = 1.00 for smaller porosity. The ensuing interpretation results at both wells are shown in **Figure 9**. We observe accurate match between the measured and interpreted variables.

Next, after validating the interpretation workflow at the wireline scale, we test it at the seismic scale by applying it to the Backus-upscaled elastic properties, same as described in the

TABLE 3 | Densities and elastic moduli of the minerals and pore-fluid phases used in rock physics modeling.

Mineral/ Fluid	Density (g/cc)	Bulk modulus (GPa)	Shear modulus (GPa)
Quartz	2.65	36.60	45.00
Clay	2.65	21.00	7.00
Brine	0.96	2.42	0.00
Oil	0.85	1.13	0.00

previous case study. Once again, the interpretation results accurately match the arithmetically-upscaled porosity, clay content, and water saturation, except for minor S_w misinterpretation intervals (**Figure 10**). Finally, to illustrate the application of our interpretation method to a seismic section, we generate a pseudo-section of I_p and I_s between the two wells with the interpretation results also shown in **Figure 10**.

DISCUSSION

The field of impedance inversion is very extensive and extremely mathematically involved (e.g., Russell, 1999; Mallick, 2001; Mallick, 2007; and; Lau et al., 2002). The challenge here is to derive *absolute* elastic properties from seismic waveforms that depend on the *relative* elastic property contrast in the subsurface. Still, even where accurate impedance volumes are produced, they hardly provide the information needed for exploration and development. Arguably, the ultimate product of such inversion should be an interpretation for porosity, saturation, and lithology.

This is why such interpretation is now considered one of the new frontiers in exploration. Previous attempts include the already quoted work by Arevalo-Lopez and Dvorkin (2016) and Arevalo-Lopez and Dvorkin (2017) and Wollner et al. (2017). Souvannavong et al. (2013) present a petro-elastic concept of such inversion for an offshore carbonate field.

Here we revisit the concept of deterministic rock-physics based interpretation of seismically-derived elastic properties and show how geology-based information can be incorporated into this workflow. The two new case studies presented here illustrate this concept. The novelty is the combination of the rock physics diagnostics methodology, spatial upscaling of the ensuing rock physics transforms, and geology-based fluid-porosity-impedance discrimination. Finding such relationships between different rock petrophysical properties is key to extracting rock properties from its impedance response. Essential also is the optimization method using an objective function. This workflow chart is shown in **Figure A1**.

In both cases, the theoretical stiff-rock model (the modified upper Hashin-Shtrikman bound) appears to accurately quantify the data. This model, as any other rock physics model, requires a number of assumptions, including the elastic properties of the mineral components. In the case studies under examination, these inputs were assigned commonly-used and well documented values.

Another important assumption is the absence of velocity-frequency dependence in the wireline and seismic frequency ranges. Such dependence (dispersion) is well documented when comparing laboratory data acquired at about 1 MHz

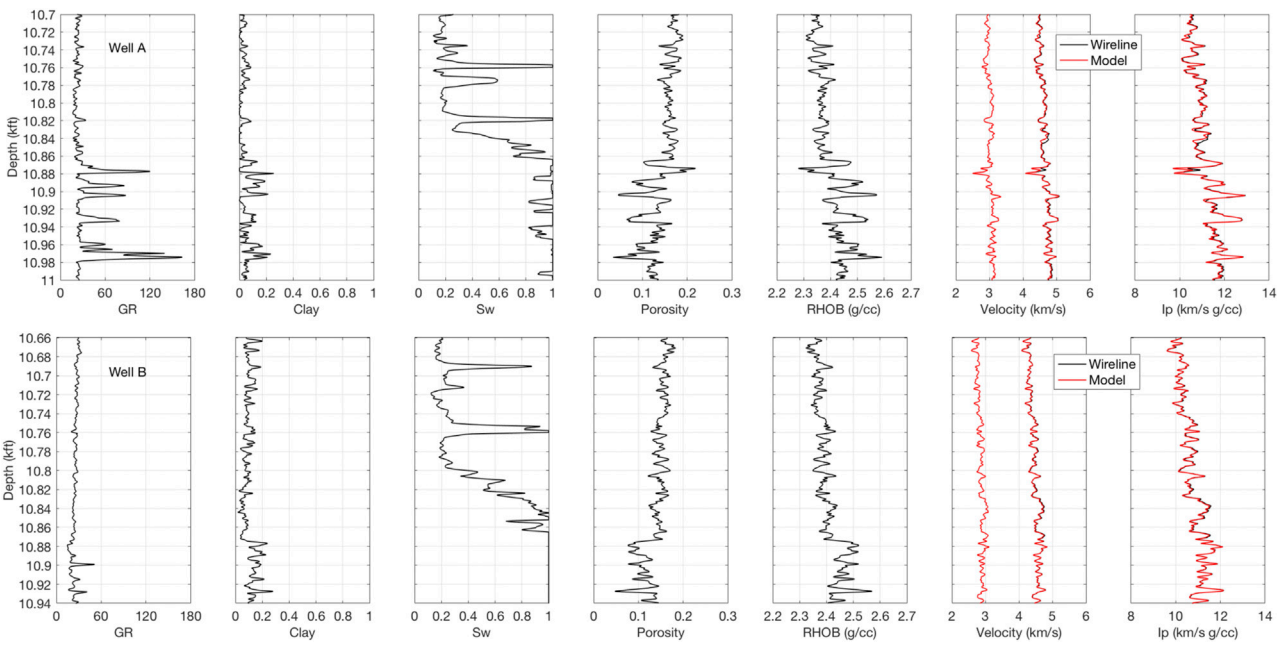

FIGURE 8 | Wireline data for Well A **(top)** and Well B **(bottom)**. From left to right: GR; clay content; water saturation; the total porosity; bulk density; V_p and V_s; and the P-wave impedance. Black curves are for measured properties, while red curves are for model-predicted.

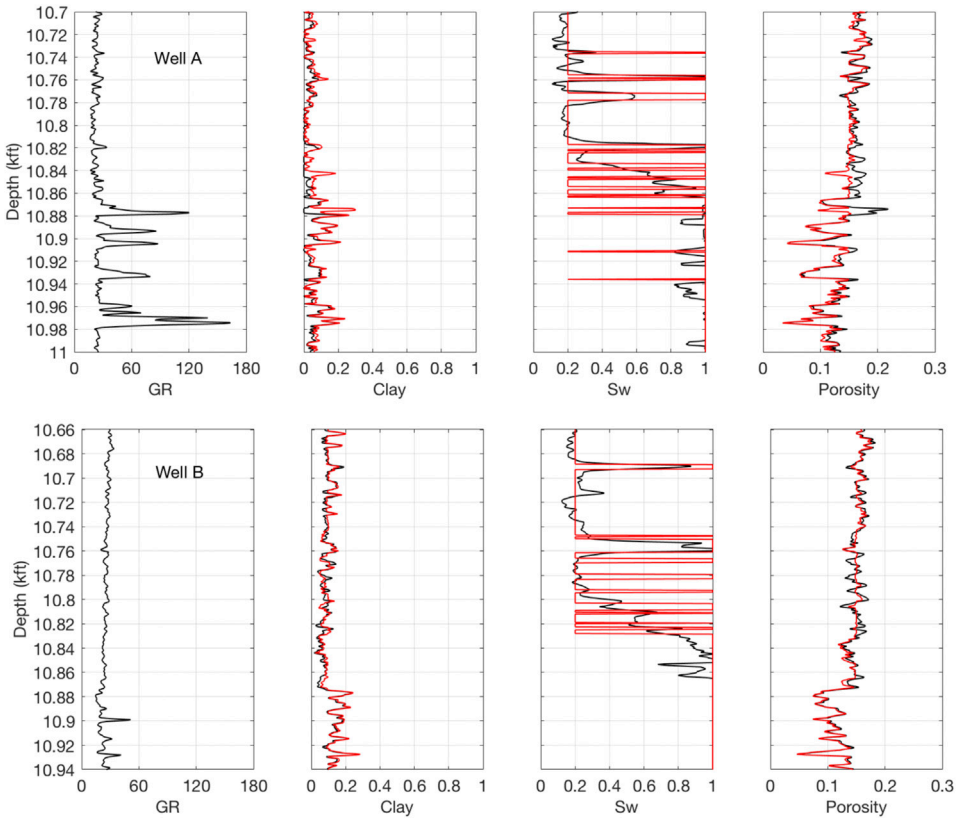

FIGURE 9 | Interpretation results **(red)** for Well A (top) and Well B **(bottom)**. The measured variables are shown in black.

frequency with low-frequency measurements (see, e.g., Mavko et al., 2020). It also becomes apparent when comparing ultrasonic velocity measurements of liquid-saturated porous materials with the results of Gassmann's (1951) fluid substitution on the same dry samples. Such dispersion can occur even at wireline and seismic frequencies where the pore fluid has very high viscosity, such as heavy oil. In the cases we examine here, the pore fluid components are water and conventional oil. This is why we feel it is reasonable to neglect velocity-frequency dependence and use the low-frequency fluid substitution methods.

Such fluid substitution as employed here assumes that the effective bulk modulus of the brine/hydrocarbon system is the harmonic average of the elemental bulk moduli. In other words, we use the concept of "uniform" fluid distribution in the pore space as opposed to "patchy" distribution. The latter may occur during oil recovery due to uneven displacement of the fluid phases in real time (e.g., Dvorkin and Nur, 1998; Monachesi et al., 2020). However, it is reasonable to assume that in exploration studies, under the condition of geologically long-term fluid equilibrium, fluid distribution is uniform (e.g., Arevalo-Lopez and Dvorkin, 2017).

An important development introduced here is the application of the rock physics models at the seismic scale required in order to ensure that the interpretation workflow proposed can be used with real seismic data. To facilitate this application, we generated synthetic seismic-scale impedance inversion data for the P- and S-wave impedances by using the standard Backus (1962) elastic upscaling. The upscaling running window was selected as appropriate for the seismic frequency range. Such upscaling was conducted at each well and then synthetic impedance sections were generated by simple deterministic interpolation between the wells. Because here to prove the concept we deal with synthetic seismic data, no uncertainty needs to be taken into consideration.

At the same time, impedance inversion of real seismic data often carries a significant element of uncertainty as it requires adjusting many inversion parameters and, as a result, is often subjective (e.g., Russell, 1999; Mallick, 2007). The best way of reducing this uncertainty is to ensure an accurate match of the seismically-derived impedances and density at the wells. The interpretation method offered here carries additional controls on inversion uncertainty as it translates the elastic properties into porosity, mineralogy, and water saturation, the quantities whose reasonableness can be ascertained from the geological and sedimentological viewpoint.

There are several factors that contribute to the efficiency and accuracy of this workflow. First, it is building a robust rock physics model that captures the relationship between rock's elastic and volumetric properties. Second, it is the sensitivity of the model to small changes in the volumetric

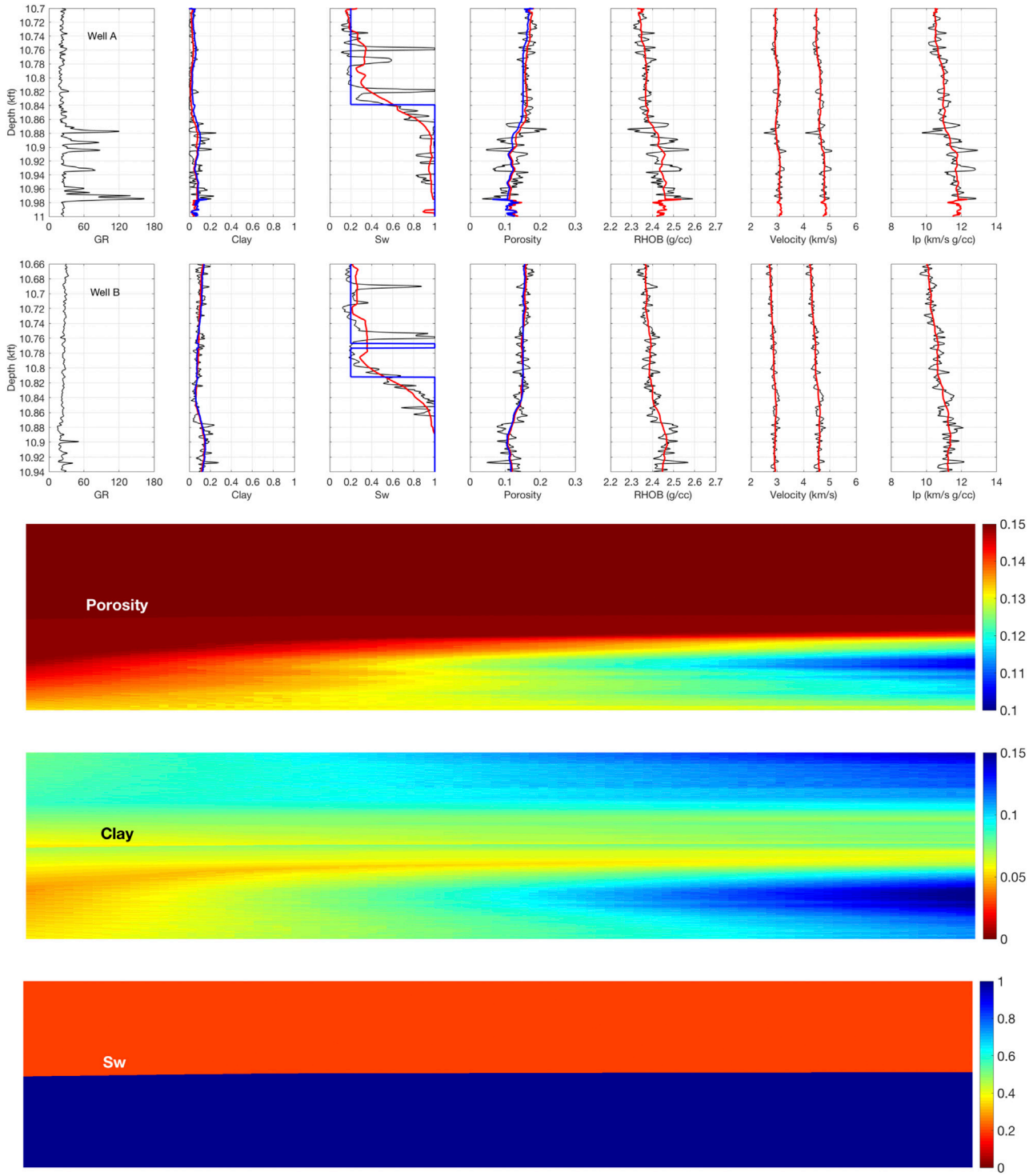

FIGURE 10 | Top: Interpretation results at the seismic scale (blue) for Well A and B. The upscaled variables are shown in red, while the wireline-scale variables are shown in black. **Bottom:** Interpreted porosity **(top)**, clay content **(middle)**, and water saturation **(bottom)** sections between Well B **(left)** and A **(right)**. The inputs used were the interpolated upscaled I_p and I_s.

variables. It is desirable to have a finer mesh, however, it comes with a computational cost which also needs to be accounted for.

Finally, the physics-based deterministic approach discussed here opens ways for a data-driven stochastic analysis and probabilistic interpretation.

CONCLUSION

The deterministic seismic interpretation method presented here depends on combining mathematical rock physics models with a site-specific geology-based pore-fluid discrimination to quantifying the total porosity, mineralogy, and the pore fluid from one (I_p) or two (I_p and I_s) inputs. The pore fluid in these two case studies played a role in the evolution of porosity, which helped supplement the mathematical rock physics models with an additional geology-driven equation and, by so doing, enhance the interpretation ability. This method is applicable at the seismic-scale where the impedance is less sensitive to fine-scale changes in the reservoir.

DATA AVAILABILITY STATEMENT

The datasets presented in this article are not readily available due to data confidentiality. Requests to access the datasets should be directed to jackdvorkin007@gmail.com.

AUTHOR CONTRIBUTIONS

AA–computing and writing JD–supervision and writing YA–comments ZD–comments

FUNDING

This work was supported by Saudi Aramco and the College of Petroleum Engineering and Geosciences of King Fahd University of Petroleum and Minerals.

ACKNOWLEDGMENTS

We thank Tapan Mukerji for helping create the impedance pseudo-sections. We also thank Marjory Matic for editorial comments.

REFERENCES

Arévalo-López, H. S., and Dvorkin, J. P. (2016). Porosity, mineralogy, and pore fluid from simultaneous impedance inversion. *Lead. Edge* 35, 423–429. doi:10.1190/tle35050423.1

Arévalo-López, H. S., and Dvorkin, J. P. (2017). Simultaneous impedance inversion and interpretation for an offshore turbiditic reservoir. *Interpretation* 5, SL9–SL23. doi:10.1190/int-2016-0192.1

Backus, G. E. (1962). Long-wave elastic anisotropy produced by horizontal layering. *J. Geophys. Res.* 67, 4427–4440. doi:10.1029/jz067i011p04427

Batzle, M., and Wang, Z. (1992). Seismic properties of pore fluids. *Geophysics* 57, 1396–1408. doi:10.1190/1.1443207

Dvorkin, J., and Alabbad, A. (2019). Velocity-porosity-mineralogy trends in chalk and consolidated carbonate rocks. *Geophys. J. Int.* 219, 662–671. doi:10.1093/gji/ggz304

Dvorkin, J. (2019). Diagenesis-driven pore fluid discrimination. *Lead. Edge* 38, 40–43. doi:10.1190/tle38050366.1

Dvorkin, J., Gutierrez, M., and Grana, D. (2014). Seismic reflections of rock properties. Cambridge University Press.

Dvorkin, J., and Alkhater, A. (2004). Pore fluid and porosity mapping from seismic. *First Break*. 22, 53–57.

Dvorkin, J., and Nur, A. (1998). Acoustic signatures of patchy saturation. *Int. J. Solid Struct.* 35, 4803–4810. doi:10.1016/s0020-7683(98)00095-x

Dvorkin, J. P. (2008). Yet another vs equation. *Geophysics* 73, E35–E39. þdoi:10.1190/1.2820604

Gassmann, F. (1951). Uber die elastizitat poroser medien. *Viertel. Naturforsch. Ges. Zürich* 96, 1–23.þ

Hill, R. (1952). The elastic behavior of crystalline aggregate. *Proc. Physic. Soc.* A65, 349–354.

Lau, A., Gonzalez, A., Mallick, S., and Gillespie, D. (2002). Waveform gather inversion and attribute-guided interpolation: a two-step approach to log prediction. *Lead. Edge* 21, 1024–1027. doi:10.1190/1.1518440

Mallick, S. (2007). Amplitude-variation-with-offset, elastic-impedence, and wave-equation synthetics - a modeling study. *Geophysics* 72, C1–C7. doi:10.1190/1.2387108

Mallick, S. (2001). AVO and elastic impedance. *Lead. Edge* 20, 1094–1104. doi:10.1190/1.1487239

Mavko, G., Mukerji, T., and Dvorkin, J. (2020). *Rock physics handbook*. 3rd Edn. Cambridge, UK: Cambridge University Press, 396.

Monachesi, L. B., Wollner, U., and Dvorkin, J. P. (2020). Effective pore fluid bulk modulus at patchy saturation: an analytic study. *JGR Solid Earth* 125, 1–12. doi:10.1029/2019jb018267

Raymer, L. L., Hunt, E. R., and Gardner, J. S. (1980). "An improved sonic transit time-to-porosity transform," in SPWLA 21st annual logging symposium, society of petrophysicists and well-log analysts, Lafayette, Louisiana, July 08, 1980 (Lafayette, LA: þSociety of Petrophysicists and Well Log Analysts), 1–13.

Russell, B. (1999). Comparison of poststack inversion methods. *SEG Tech. Program Expand. Abst.* 10, 1–4. doi:10.1190/1.1888870

Souvannavong, V., Allo, F., Coleou, T., Colnard, O., Machecler, I., Dillon, L., et al. (2013). "Petrophysical seismic inversion over an offshore carbonate field," in International petroleum technology conference, Rio de Janeiro, Brazil, August 15–18 2013 Beijing, China: European Association of Geoscientists and Engineers, 1–5.

Wollner, U., Arevalo-Lopez, H., and Dvorkin, J. (2017). Seismic-scale petrophysical interpretation and gas-volume estimation from simultaneous impedance inversion. *Lead. Edge* 36, 910–915. doi:10.1190/tle36110910.1

Conflict of Interest: Authors AA, YA, and ZD were employed by the company Saudi Aramco.

The remaining author declares that the research was conducted in the absence of any commercial or financial relationships that could be construed as a potential conflict of interest.

Copyright © 2021 Alabbad, Dvorkin, Altowairqi and Duan. This is an open-access article distributed under the terms of the Creative Commons Attribution License (CC BY). The use, distribution or reproduction in other forums is permitted, provided the original author(s) and the copyright owner(s) are credited and that the original publication in this journal is cited, in accordance with accepted academic practice. No use, distribution or reproduction is permitted which does not comply with these terms.

APPENDIX: WORKFLOW CHART.

Figure A1 shows a flowchart of the interpretation method discussed in this work.

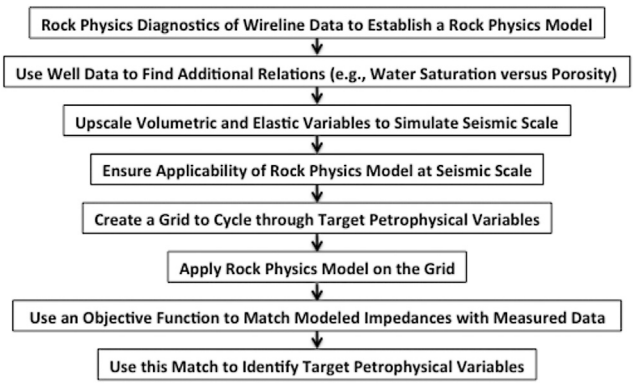

FIGURE A1 | Interpretation flowchart.

frontiers in Earth Science

ORIGINAL RESEARCH
published: 18 February 2021
doi: 10.3389/feart.2021.628544

Low-Frequency Elastic Properties of a Polymineralic Carbonate: Laboratory Measurement and Digital Rock Physics

Ken Ikeda[1], Shankar Subramaniyan[2], Beatriz Quintal[3], Eric James Goldfarb[1], Erik H. Saenger[4,5,6] and Nicola Tisato[1]*

[1]Jackson School of Geosciences, The University of Texas at Austin, Austin, TX, United States, [2]Department of Earth Sciences, ETH Zurich, Zurich, Switzerland, [3]Institute of Earth Sciences, University of Lausanne, Lausanne, Switzerland, [4]Department of Civil and Environmental Engineering, Bochum University of Applied Sciences, Bochum, Germany, [5]Fraunhofer IEG, Institution for Energy Infrastructures and Geothermal Systems, Bochum, Germany, [6]Ruhr Universität Bochum, Institute of Geology, Mineralogy and Geophysics, Bochum, Germany

We demonstrate that the static elastic properties of a carbonate sample, comprised of dolomite and calcite, could be accurately predicted by Digital Rock Physics (DRP), a non-invasive testing method for simulating laboratory measurements. We present a state-of-the-art algorithm that uses X-ray Computed Tomography (CT) imagery to compute the elastic properties of a lacustrine rudstone sample. The high-resolution CT-images provide a digital sample that is used for analyzing microstructures and performing quasi-static compression numerical simulations. Here, we present the modified Segmentation-Less method withOut Targets method: a combination of segmentation-based and segmentation-less DRP. This new method assigns the spatial distribution of elastic properties of the sample based on homogenization theory and overcomes the monomineralic limitation of the previous work, allowing the algorithm to be used on polymineralic rocks. The method starts by partitioning CT-images of the sample into smaller sub-images, each of which contains only two phases: a mineral (calcite or dolomite) and air. Then, each sub-image is converted into elastic property arrays. Finally, the elastic property arrays from the sub-images are combined and fed into a finite element algorithm to compute the effective elastic properties of the sample. We compared the numerical results to the laboratory measurements of low-frequency elastic properties. We find that the Young's moduli of both the dry and the fully saturated sample fall within 10% of the laboratory measurements. Our analysis also shows that segmentation-based DRP should be used cautiously to compute elastic properties of carbonate rocks similar to our sample.

Keywords: Digital Rock Physics (DRP), carbonate, X-ray computed tomograghy, low-frequency measurement, numerical simulation, finite element analysis

OPEN ACCESS

Edited by:
Pier Paolo Bruno,
University of Naples Federico II, Italy

Reviewed by:
Guo Tao,
Khalifa University, United Arab Emirates
Mohamed JOUINI,
Khalifa University, United Arab Emirates

****Correspondence:***
Ken Ikeda
ikeda.ken@utexas.edu

Specialty section:
This article was submitted to Solid Earth Geophysics, a section of the journal Frontiers in Earth Science

Received: *12 November 2020*
Accepted: *18 January 2021*
Published: *18 February 2021*

Citation:
Ikeda K, Subramaniyan S, Quintal B, Goldfarb EJ, Saenger EH and Tisato N (2021) Low-Frequency Elastic Properties of a Polymineralic Carbonate: Laboratory Measurement and Digital Rock Physics. Front. Earth Sci. 9:628544. doi: 10.3389/feart.2021.628544

INTRODUCTION

Digital Rock Physics (DRP) applied to carbonates is an important and quickly evolving research topic (e.g., Amabeoku et al., 2013; Saenger et al., 2016; AlJallad et al., 2020; Han et al., 2020), especially regarding the prediction of elastic moduli of polymineralic carbonate rocks. In general, the most common methods in DRP are based on segmentation, which tend to strongly overpredict the

elastic moduli of such rocks. It has been suggested that such inaccuracy is due to the inability of segmentation in resolving micro-features, such as pores, grain contacts, and cracks (e.g., Madonna et al., 2012; Andrä et al., 2013a). Carbonate rocks can contain a significant amount of micropores that cannot be resolved by CT imaging (Saenger et al., 2016). In carbonates, pores can lie between mineral grains or particles (interparticle and intercrystal pores), within particles (intraparticle pores), or within mineral grains due to, for instance, dissolution processes (moldic pores). Pores can be smaller than 1 μm (Scholle and Ulmer-Scholle, 2003), which is below the spatial resolution of a typical CT-scanner (Iassonov et al., 2009). One could scan samples at nanometric resolutions, capturing only millimetric volumes that, however, might not be a Representative Elementary Volume (REV) for the studied lithology (Saenger et al., 2016).

Several methods have been proposed to extract sub-resolution features - especially microporosity - from CT-images with a resolution around 10 microns. Sok et al. (2010) introduced the multiscale analysis technique where images of a sample at different resolutions were combined. They scanned a carbonate rock sample at ~1 micron resolution and recognized three phases in the CT-images: solid grains, resolvable pore spaces, and micropores. The porosity calculated from resolvable pore spaces yielded 11% porosity, whereas the porosity of the sample, measured with the Mercury Injection Capillary Pressure (MICP) technique, was 36%. Therefore, they assumed that approximately 25% of the total pore volume was in micropores. A multiscale analysis estimated the microporosity by stochastically mapping micropores with Scanning Electron Microscopy (SEM). Micro-CT and SEM images were taken at the same locations and registered: the average porosities of the SEM image were paired with the average X-ray attenuation of CT-images. Pairs of average porosities and average X-ray attenuation were used to create an X-ray attenuation-to-porosity calibration curve. Such a multiscale analysis technique estimated a sample porosity of 35%, which agreed with the MICP result. Lin et al. (2016) tackled the sub-resolution porosity problem in the acquisition process. They performed a differential measurement of X-ray attenuation by comparing CT-images of dry and brine saturated samples. Lin et al. (2016) concluded that the sub-resolution porosity contributed to up to 10% of the total porosity of the sample. Other authors have proposed methods to incorporate sub-resolution information from CT data. Such approaches rely on the local variation of X-ray attenuation to estimate effective rock properties such as density and porosity (e.g., Taud et al., 2005; Dunsmuir et al., 2006; Gupta et al., 2018).

To estimate the effect of sub-resolution features on elastic properties, several methods have been proposed. Tisato and Spikes (2016) introduced a DRP technique that does not require segmentation. Their method relies on homogenization theory, where the spatial distribution of elastic properties is the interpolation between the elastic properties of the materials composing the rock. The interpolation function depends on the chosen effective medium theory (EMT). As a result, each voxel is assigned a specific elastic modulus that depends on the X-ray attenuation. The method was tested on a Berea Sandstone, yielding results that agreed with laboratory measurements. Ikeda et al. (2020) furthered the study of Tisato and Spikes (2016) by introducing the Segmentation-Less method withOut Targets (SLOT) that do not require calibration targets - often referred to as phantoms in the CT community.

Saenger et al. (2016) proposed a method called "*two-phase wave propagation simulations*" to obtain porosity dependent P and S-wave velocities of sedimentary rocks. They created several CT derived digital rock models by varying the segmentation threshold of the CT number used to separate the solid phase (calcite) from the pore phase (vacuum). As a consequence, each model had a different porosity. Each model underwent numerical simulations where the results were used to obtain effective P-wave and S-wave velocities. The variation of P and S-wave velocities with porosity were used to create velocity bounds for the lithology. Sun et al. (2017) performed a multiscale analysis on carbonate CT-images to predict elastic properties. Some estimated physical properties agreed with the laboratory measurements except for the P-wave and the S-wave velocities. Nonetheless, both methods approaches have not been used on carbonate samples containing both dolomite and calcite.

Here, we propose a modified segmentation-less method (modified-SLOT), which is based on the SLOT algorithm whose main limitation is that it can be applied only on monomineralic rocks. The present work relaxes such a limitation, allowing the estimation of elastic properties of polymineralic rocks from CT-images. Numerical simulation results are compared to low-frequency sub-resonance laboratory measurements and segmentation-based DRP. The proposed methodology, modified-SLOT, estimates static Young's modulus of a polymineralic carbonate sample within 10% of laboratory measurements.

MATERIALS AND METHODS

Description of the Physical Sample

Our sample was collected from the pre-salt Barra Velha formation of the Santos Basin in Brazil (Gomes et al., 2020). The formation contains massive to cross stratified units. The sample is a lacustrine carbonate formed in the early stages of the Atlantic ocean rifting and was cored from a facies of reworked carbonate shrubs and spherulites. Spherulites are spherical to sub-spherical allochems, that in the Barra Velha formation are commonly dolomitized with secondary porosity. Shrubs are aggregated fibrous to coarse bladed calcite crystals (Wright & Barnett, 2015; Chafetz et al., 2018).

The original sample was a cylinder of size 25.4 cm in diameter and ~100 mm in length. A cylindrical plug of size 25.4 mm in diameter and 62.4 mm in length was obtained from the original sample. Such a sample is called sample A, and it was used for the measurement of Young's modulus and attenuation at frequencies in the range 1–100 Hz (**Figure 1A**). The porosity of the sample A is $\phi_{lab} = 15.5\%$. The remaining sample was cored to obtain a small cylinder of size 8 mm in diameter and few mm in length - sample B (**Figure 1B**). We used X-ray micro-computed tomography

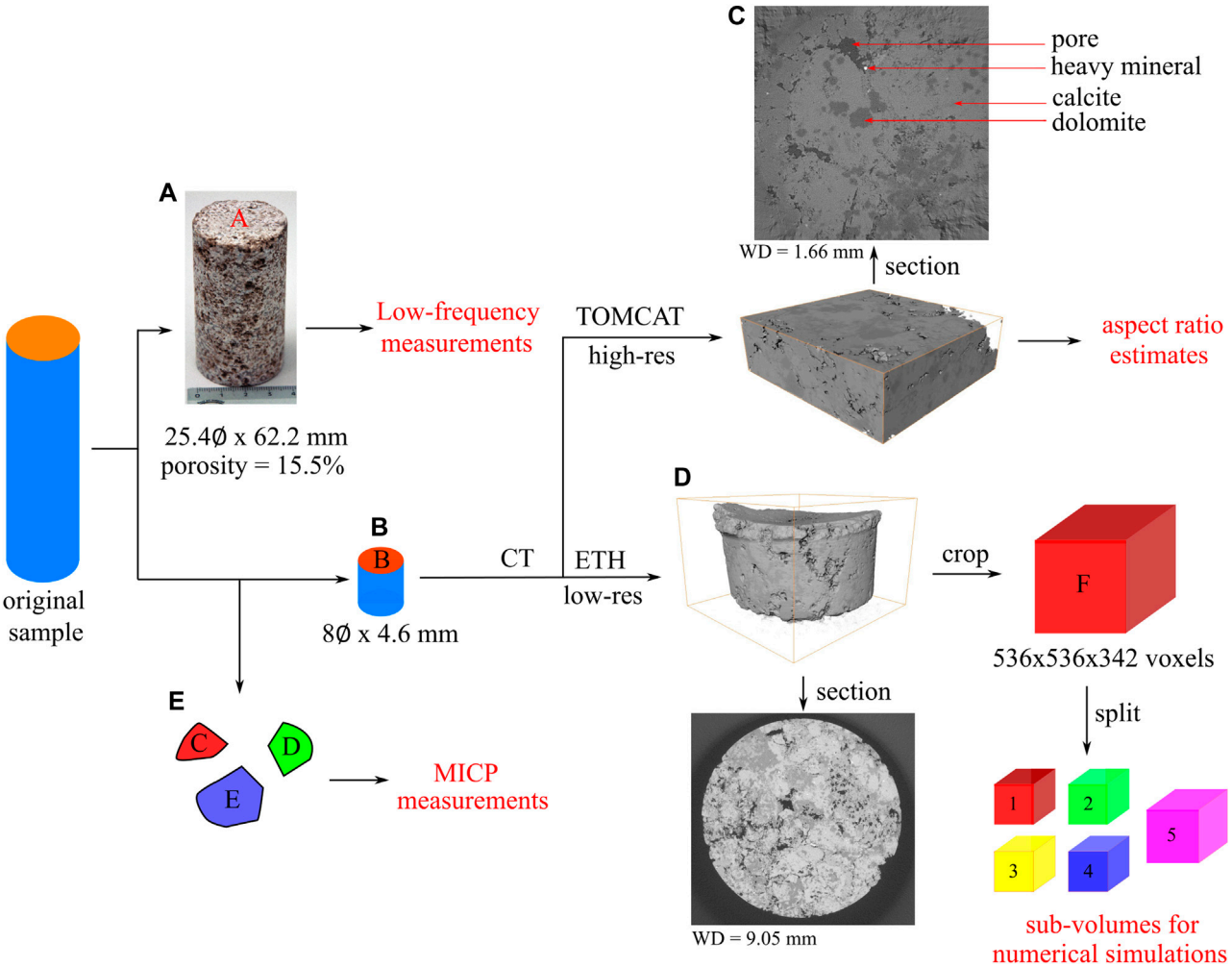

FIGURE 1 | Sample descriptions and workflow of the process. The original sample was cut into sample **(A)** for the low-frequency measurement. The remaining part of the sample was used for CT-scan (sample **B**) and MICP measurement (sample **C–E**). Sample **(B)** was scanned at two facilities: TOMCAT and ETH. The TOMCAT scan provided high-resolution images in which we use for estimating aspect ratio of pore spaces. The ETH scan, whose resolution was lower, covered more area of the sample and was used for numerical simulations. The ruler in the sample **(A)** figure is in centimeters and WD represents the width of the image.

(micro-CT) to obtain a 3D digital model of one of the 8 mm core plugs (**Figures 1C,D**). The remainder of the original sample comprised three samples with no regular shape that were used for mercury injection capillary pressure tests (MICP), namely sample C, sample D, and sample E (**Figure 1E**).

MICP analyses were performed at the claylab of the Swiss Federal Institute of Technology Zurich (ETH Zürich, Switzerland) by means of a Pascal 140 + 440 instrument from POROTEC (Hofheim am Taunus, Germany). The MICP porosities for samples C, D, and E are 14.99%, 17.65%, and 14.39%, respectively; and the average of such measurements is 15.7%, which is 0.2% higher than ϕ_{lab}. **Figure 1** provides a synoptic panel reporting the samples and the tests performed. The MICP test (**Figure 2**) also indicates that some pores have a radius below 50 μm (~6%). Most of the pore throats lie in the range 10^3–10^4 μm (**Figure 2**). Note that MICP only measures the connected porosity of the sample.

Description of the CT-Dataset

We collected 3D images of sample B by means of X-ray micro-computed tomography (ETH dataset) and synchrotron X-ray tomography (TOMCAT dataset). The ETH dataset was obtained at the Swiss Federal Institute of Technology Zurich (ETH Zürich, Switzerland) using a phoenix v|tome|x 240 X-ray scanner (GE Sensing & Inspection Technologies GmbH, Germany). The X-ray tube voltage and current were 150 kV and 65 μA, respectively. We used a 0.5 mm copper filter to minimize beam hardening. Images were taken every 0.2° for an entire revolution. The final reconstructed 3D volume had a voxel size of 9.88 microns and a cross-section of 916 × 869 pixels. The spatial distribution of X-ray attenuation was scaled and stored as an array of 16-bit integers, known as CT-numbers (Ketcham and Carlson, 2001). CT-number is a proxy for the density of the material irradiated by the X-rays (Mull, 1984). **Figures 1C,D** show an arbitrary cross-section from the micro-CT data. The resolution of our scan was

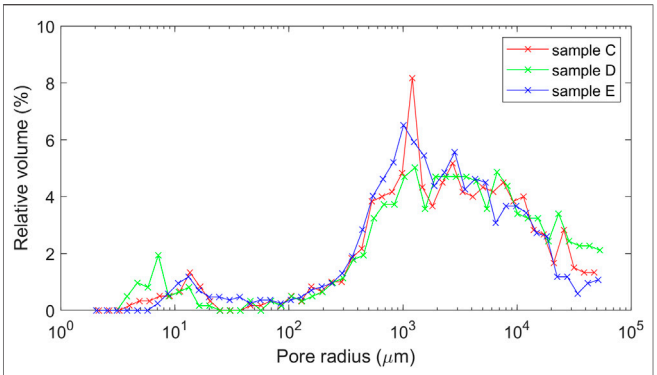

FIGURE 2 | MICP data for the carbonate sample investigated. Here, we show the result obtained from one of the core plugs.

not high enough to resolve all the features within the sample, such as small pores and microcracks. Only the bigger pores were resolved, appearing as a dark color in the micro-CT images. The ETH dataset was then used to compute the elastic properties of the sample. In particular, we extracted a sub-volume of size 536 × 536 × 342 voxels from such a dataset (sample F). This volume was the largest artifact-free rectangular volume that could be extracted from the dataset. The CT-images of the sub-volume were processed and visualized with Fiji (Schindelin et al., 2012). We applied a local mean filter with the smoothing factor of 3 and the automatic standard deviation to denoize the CT-images. Then, we applied the statistical region merging to group similar voxels (Buades et al., 2005, p.; Nock and Nielsen, 2004). Due to the limitation of computational resources, we performed the numerical simulations of five cascaded sub-volumes extracted from sample F (**Figures 1**, **3**). The location of each sub-volume is listed in **Table 1**. The first four sub-volumes are 300 × 300 × 300 voxels in size. The fifth sub-volume, on the other hand, is 350 × 350 × 300 voxels in size. The fifth sub-volume was intentionally chosen, such that its porosity was 15.44% i.e., only 0.06% from $\varnothing_{lab}$.

On the other hand, the synchrotron TOMCAT dataset was obtained at the X-ray Tomographic Microscopy and Coherent rAdiology experimenTs beamline of the Swiss Light Source (SLS; Paul Scherrer Institute, Villigen, Switzerland). The beam energy was 26 keV with 500 ms exposure time. The final reconstructed 3D volume yielded a volume with a section of 2560 × 2560 pixels with a voxel size of 0.65 microns/voxel. Such a scan covers 0.1% of sample B, and its elastic properties might not represent the elastic properties of the lithology under study. However, we assume that the microporosity of the TOMCAT dataset properly represents

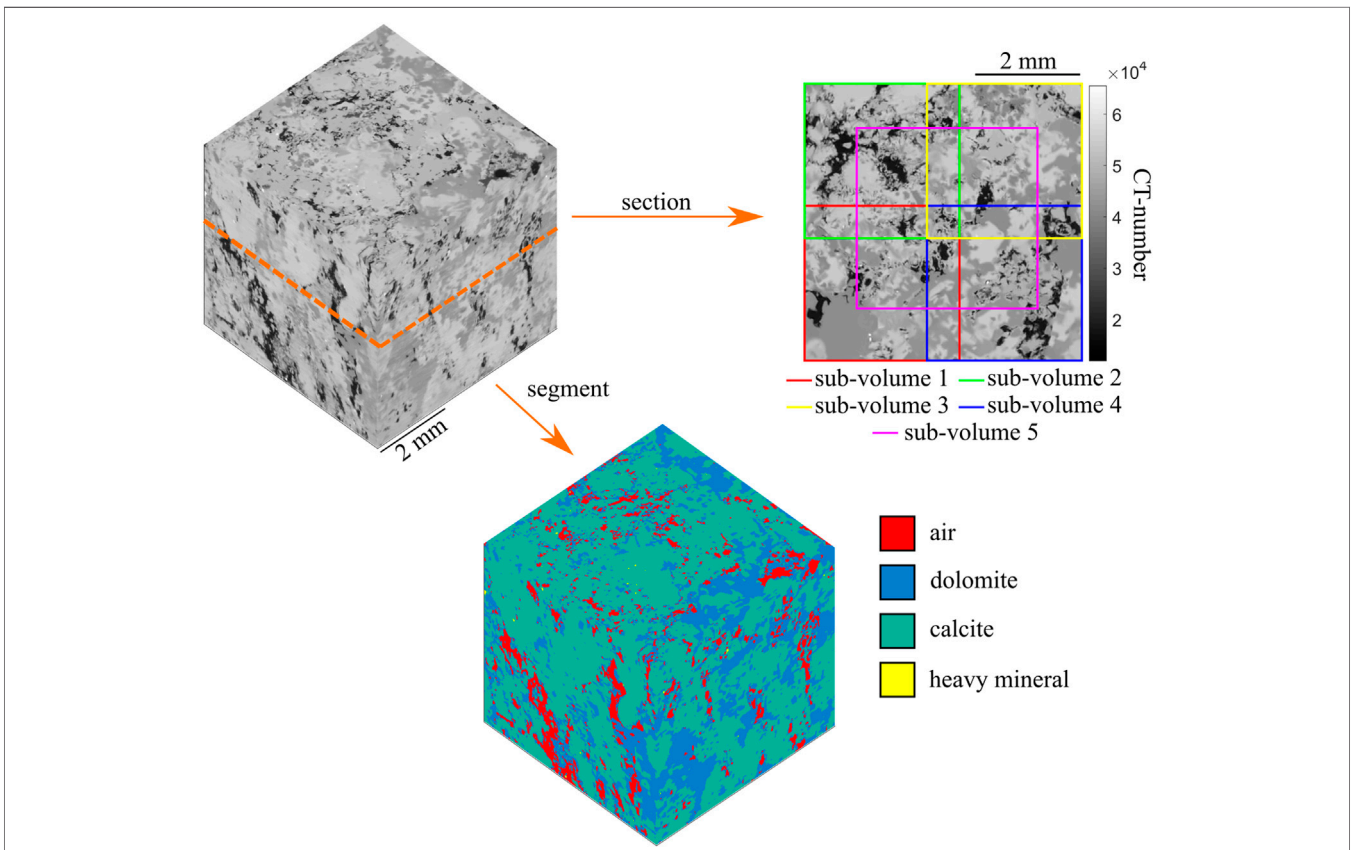

FIGURE 3 | A CT-volume of the sample with the interpreted mineral compositions. The CT-volume has been segmented into four phases: air, dolomite, calcite, and heavy mineral. The section of the CT-volume shows the location where sub-volumes have been extracted for the numerical simulations.

TABLE 1 | Numerical simulation results from the modified-SLOT.

Sub-volume number	Extracted location	ϕ	Aspect ratio = 0.4		Aspect ratio = 0.5	
			E_{dry} (GPa)	E_{sat} (GPa)	E_{dry} (GPa)	E_{sat} (GPa)
1	(1:300, 1:300, 1:300)	0.1583	25.5	27.3	26.1	29.4
2	(237:536, 1:300, 1:300)	0.1669	22.6	25.0	25.1	27.0
3	(1:300, 237:536, 1:300)	0.1571	25.3	27.6	26.8	30.0
4	(237:536, 237:536, 1:300)	0.1427	28.2	30.5	29.2	31.5
5	(101:450, 101:450, 1:300)	0.1544	25.6	27.9	26.9	30.5

TABLE 2 | Properties of the carbonate sample and aluminum standard.

Sample	Permeability (mD)	Porosity (%)	Length (mm)	Diameter (mm)
Carbonate	45	15.5	62.4	25.4
Aluminum standard	0	0	59.9	25.4

the microporosity of sample B. Thus, we use such a dataset to estimate the aspect ratio of the micropores.

According to the CT-images, four distinct shades of gray (i.e., CT-numbers clusters) are observed in the CT-images: 1) black, 2) light-gray, 3) dark-gray, and 4) white (**Figure 3**). Such shades are interpreted to represent 1) air, 2) dolomite, 3) calcite, and 4) a heavy mineral, based on the X-ray attenuation characterization of each material and the petrophysical analyses on the core sample. At our scanning conditions, dolomite attenuates X-rays less than calcite and therefore bears a darker shade (i.e., lower CT-numbers) than calcite (see **Supplementary Information**) (Chantler et al., 2005; Wang et al., 2013). A first-order analysis of the CT-images shows that the volumetric fractions of voxels classified as air ($f_{\mathrm{air}}^{\mathrm{seg}}$), calcite ($f_{\mathrm{cal}}^{\mathrm{seg}}$), dolomite ($f_{\mathrm{dol}}^{\mathrm{seg}}$), and heavy minerals ($f_{\mathrm{heavy}}^{\mathrm{seg}}$) are 8.65%, 69.17%, 22.13%, and 0.05%, respectively.

As $f_{\mathrm{air}}^{\mathrm{seg}}$ is 8.65% and ϕ_{lab} is 15.5%, we concluded that our sample comprises 6.85% of sub-resolution porosity. Such a mismatch suggests that 6.85% of the porosity cannot be resolved with the ETH dataset. Thus, $f_{\mathrm{cal}}^{\mathrm{seg}}$, $f_{\mathrm{dol}}^{\mathrm{seg}}$, and $f_{\mathrm{heavy}}^{\mathrm{seg}}$, indeed, represent the volume fractions of the minerals plus the sub-resolution porosity, while the actual volume fractions of the minerals are denoted as V_{cal}, V_{dol}, and V_{heavy} for calcite, dolomite, and heavy mineral, respectively. We neglected the sub-resolution pore spaces in the heavy mineral fraction (i.e., $f_{\mathrm{heavy}}^{\mathrm{seg}} = V_{\mathrm{heavy}}$), because such a phase represents a very tiny portion of the total volume, and minerals such as sulfides and oxides are likely to have limited porosity (<1%) (Baumgartner et al., 2019).

Methods

Laboratory Measurements of Low-Frequency Young's Modulus

To measure Young's modulus and attenuation of seismic waves for sample A, we used the Seismic Wave Attenuation Module (SWAM, Madonna and Tisato, 2013). The SWAM uses the forced oscillation method to measure such properties. The measurements were performed at seismic frequencies (1–100 Hz). **Table 2** lists the physical properties of the carbonate sample and the aluminum standard that were used as a reference in the laboratory measurements. The SWAM has a piezo actuator to produce a sinusoidal vertical stress, while a couple of Linear Variable Differential Transformers (LVDTs) measures the bulk shortenings of the rock sample and the aluminum standard. Shortenings are recorded by an oscilloscope after amplification (**Figure 4**). As aluminum is nearly elastic, its shortening can be considered to be in phase with the applied stress. The amplitude ratio and the phase shift between the shortening across the rock sample and across the aluminum standard allowed calculating the sample Young's modulus and attenuation, respectively.

The SWAM was placed in a Paterson pressure rig (Paterson and Olgaard, 2000), which employed argon gas as a confining medium. To avoid flow of pore fluid across the curved side of the sample, and to prevent argon from seeping into the sample, a 0.1 mm thick copper jacket was used as a sealing (**Figure 5A**). The aluminum standard was enclosed in a 0.75 mm thick heat-shrinkable fluorinated ethylene propylene (FEP) tube (**Figure 5B**). The SWAM was connected to a syringe pump using pipes of 1 mm internal diameter to saturate the sample. Over time, there was a tiny leak of argon into the sample (0.01–0.05 MPa/h, as per the pump reading). The pore pressure system was kept open to the atmosphere so that the gas could escape through the pore fluid pipes. Therefore, during measurements, pore pressure was equal to atmospheric pressure (Subramaniyan et al., 2015).

Laboratory measurements were conducted at 5 MPa confining pressure, 20°C temperature, and two fluid saturation conditions: dry and 100% water-saturated. The sample was oven-dried before performing the measurements in dry conditions. Once such a measurement was completed, a water volume corresponding to the desired saturation level (100%) was introduced into the sample. To ensure full saturation, the sample was flushed with a volume of water more than ten times the sample pore volume. While flushing the pressure gradient across the sample was kept at ~2 MPa. After each saturation step, the pore fluid valves were left open, thereby the pore pressure equilibrated to the atmospheric pressure.

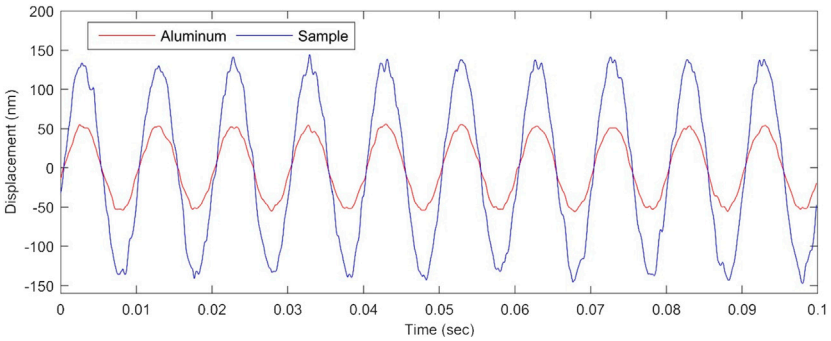

FIGURE 4 | Displacement signals of the sample and aluminum standard at 100 Hz.

Each series of measurements resulted in 20 data points across the frequency range of 1–100 Hz. By looping five times over the frequency range, we obtained five repetitions of the measurement and the corresponding precision error. Such an error and those corresponding to sample length and LVDTs calibration were propagated into the results of Young's modulus. The strain across the sample was 2×10^{-6}, hence similar to the strain caused by seismic waves measured in exploration geophysics (Mavko et al., 2020).

Digital Rock Physics on CT-Images

In our study, we simulated the static compression of the digital sample to calculate the effective elastic properties of the sample. The numerical solver employed in this study was elas3D (Garboczi, 1998). Details about the numerical solver will be explained in the next section. Elas3D numerically solves the elastic deformation of the digital sample using the Finite Element method on a cubic mesh. The first step of DRP is to estimate the bulk and shear modulus for each voxel as input parameters for the solver. We considered two methods to define the elastic tensor at each element: a segmentation-based method and a newly developed segmentation-less method. Elements were defined at each voxel in the CT-images, and we assumed that our sample was isotropic.

Segmentation-Less DRP

In our segmentation-less method we consider a voxel being a mixture of two different materials e.g., a mineral (e.g., calcite or dolomite) and air; and we assume that the elastic tensor of the voxel is a weighted average of the elastic properties of the two materials. Two segmentation-less procedures are briefly summarized as follows, and a complete description of such methods can be found in Ikeda et al. (2020).

The Segmentation-Less wIth Targets (SLIT) uses the densities and CT-numbers of reference materials–targets–to calibrate the CT dataset and obtain a density map of the CT imagery. On the other hand, if targets are not scanned along with the sample, the Segmentation-Less withOut Targets (SLOT) could be used. SLOT assumes that extreme CT-numbers within the CT-dataset represent pristine materials to create a CT-number-to-density calibration. The algorithm iteratively optimizes the calibration curve to minimize the difference between ϕ_{lab} and ϕ_{CT}, which is the porosity of the CT-imagery dataset - this step is called optimization process. The calibration creates a density model that is then converted to a porosity model. Both the methods use a negative-linear-proportional relationship. For example, to convert the density model to the porosity model, we apply:

$$\phi(\mathbf{X}) = \begin{cases} \dfrac{\rho_0 - \rho(\mathbf{X})}{\rho_0 - \rho_{\text{air}}} & \rho(\mathbf{X}) < \rho_0 \\ 0 & \rho(\mathbf{X}) \geq \rho_0 \end{cases} \quad (1)$$

where $\phi(\mathbf{X})$ is the porosity at loation $\mathbf{X}$ in the CT-imagery, $\rho(\mathbf{X})$ is the density at location $\mathbf{X}$, and ρ_{air} is the density of the pore-filled fluid (in our case, this is air and $\rho_0 \gg \rho_{\text{air}} \sim 0$), and ρ_0 is the cut-off porosity of the solid phase. These two methods are currently limited to monomineralic rocks because in such rocks ρ_0 is the density of the solid phase i.e., the methods cannot define the proper value for ρ_0 if the rock comprises two or more minerals. The present work overcomes such a limitation.

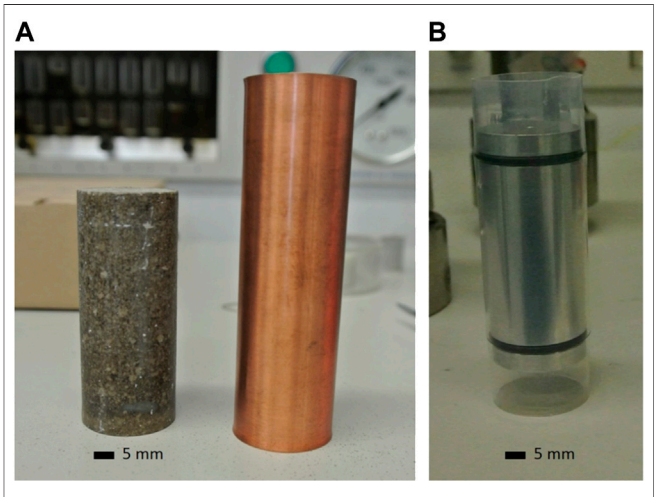

FIGURE 5 | Jacketing **(A)** Copper jacket, used for the carbonate **(B)** Shrink tube, used for the aluminum standard.

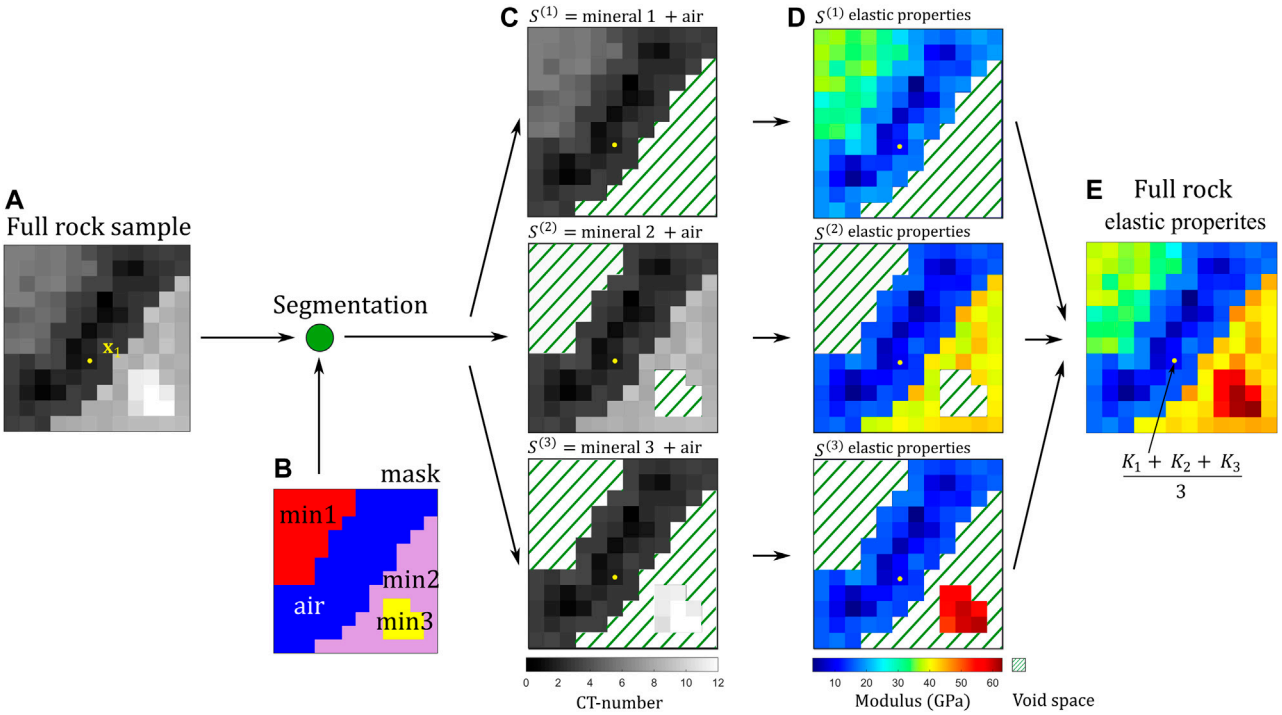

FIGURE 6 | The diagram of the modified-SLOT. Here, we show an example of a two-dimensional section of a rock sample consisting of three mineral phases **(A)**. In the CT-volume, the domain is discretized on a uniform grid depending on the resolution of the scan. The first step of the modified-SLOT is to partition the domain into small subdomains ($S^{(1)}$, $S^{(2)}$, and $S^{(3)}$) using the segmentation mask **(B)**. Each subdomain consists of two phases: a mineral phase and the air phase **(C)**. Next, since the subdomains are monomineralic, we apply the SLOT to each subdomain, transforming the CT-volumes in the elastic properties volumes **(D)**. Finally, we combine each subdomain, getting back the full volume elastic properties volume. In the figure, $\mathbf{x}_1$ is located in the air phase. The elastic properties at $\mathbf{x}_1$ in the full volume is the average of the elastic properties from each subdomain (i.e., $(K_1 + K_2 + K_3)/3$) **(E)**.

After we obtain the porosity model, we convert the porosity model to the elastic properties model using an Effective Medium Theory (EMT). In this study, we use the modified-Differential Effective model (modified-DEM) as our choice of EMT (Norris et al., 1985; Mukerji et al., 1995; Mavko et al., 2020). DEM solves a set of differential equations to evaluate the effective elastic properties of a composite medium comprising a solid and inclusions. The solution to DEM depends on the shape of the inclusions. The modified-DEM assumes a critical porosity. To estimate the low-frequency elastic properties of the dry sample, we considered inclusion that are air-filled. On the other hand, to compute the low-frequency elastic modulus of the saturated sample, we avoided using water-filled inclusions, as such would have provided the high-frequency or undrained limit of the moduli (Mavko et al., 2020). Instead, to obtain the drained limit of the elastic moduli we created the elastic property models of the saturated sample by applying Gassmann fluid substitution to each voxel of the dry sample.

Modified-SLOT

CT-Imagery Partitioning.

The modified-SLOT consists of three steps: 1) partitioning, 2) SLOT, and 3) recombination. With the partitioning, the modified-SLOT subdivides a polymineralic rock into smaller monomineralic subdomains. Each subdomain contains only two phases: pore space and one of the minerals making up the rock.

Let us consider a CT-volume of a rock sample that comprises three mineral phases and an air phase (**Figure 6A**). By segmenting the sample CT-images, we obtain a mask that contains the spatial distribution of each phase (**Figure 6B**). With a polymineralic rock with three minerals, the sample is partitioned into three subdomains: 1) mineral 1 and air ($S^{(1)}$), 2) mineral 2 and air ($S^{(2)}$), and 3) mineral 3 and air ($S^{(3)}$). Notice that voxels, which are classified as the air phase, are repeatedly counted in all subdomains. Since each subdomain is monomineralic, the original SLOT method is applied directly to each subdomain. We use SLOT to transform subdomain CT-images into subdomain elastic properties maps. Nonetheless, such a step requires the knowledge of the porosity of each subdomain (e.g., $\phi^{(1)}$, $\phi^{(2)}$, and $\phi^{(3)}$). One can approximate the porosity of each subdomain from the laboratory-measured density of the sample, the laboratory-measured porosity of the sample (MICP data), and the CT-imagery. In fact, in the next section, we show that the exact sub-resolution porosity in each subdomain could be computed in a special case when a sample only comprises of two minerals.

The last step of the modified-SLOT is to recombine all subdomains elastic property maps, obtaining an elastic

properties model of the full sample. The processes to recombine minerals and pores are different. For minerals, the elastic properties of the voxels in the subdomain and in the recombined volume are the same. For pores, the elastic properties in the recombined volume are computed as the arithmetic average of the voxel elastic properties in all the subdomains. For example, in a polymineralic rock with three minerals, a voxel that is located at $\mathbf{x}_1$ is classified as air (i.e., pore space) (**Figures 6A,B**). The partitioning step copies this voxel into three subdomains (**Figure 6C**). The SLOT algorithm will assign to such a voxel a slightly different elastic modulus in each subdomain (K_1, K_2, and K_3) (**Figure 6D**). K_1, K_2, and K_3 values are slightly different from one another due to the different parameters used by the SLOT in each subdomain. When the voxel is recombined to the full sample elastic properties model, the modulus of $\mathbf{x}_1$ will be $(K_1 + K_2 + K_3)/3$ (**Figure 6E**).

Estimating Sub-Resolution Pore Space in Each Subdomain

When the rock sample contains only two-minerals, the sub-resolution porosity in each subdomain ($\boldsymbol{f}_{\mathbf{pore1}}$ and $\boldsymbol{f}_{\mathbf{pore2}}$) can be computed from the measured porosity (ϕ_{lab}), the density of the sample (ρ_{lab}), and the segmented CT-images.

The segmentation described in the previous section provides approximations for 1) the volume fraction of mineral 1 ($f_1^{\text{seg}} - \boldsymbol{f}_{\mathbf{pore1}}$), 2) the volume fraction of mineral 2 ($f_2^{\text{seg}} - \boldsymbol{f}_{\mathbf{pore2}}$), and 3) the volume fraction of air ($f_{\text{air}}^{\text{seg}}$). f_1^{seg} and f_2^{seg} comprises $S^{(1)}$ and $S^{(2)}$, respectively, and unknown amounts of sub-resolution pore space that here we call f_{pore1} and f_{pore2} - i.e., the unknown volume fractions of sub-resolution pore space in f_1^{seg} and f_2^{seg}, respectively. Thus, the density of the CT-imagery is:

$$\rho_{\text{CT}} = \rho_1\left(f_1^{\text{seg}} - \boldsymbol{f}_{\mathbf{pore1}}\right) + \rho_2\left(f_2^{\text{seg}} - \boldsymbol{f}_{\mathbf{pore2}}\right) + \rho_{air}\left(f_{\text{air}}^{\text{seg}} + \boldsymbol{f}_{\mathbf{pore1}} + \boldsymbol{f}_{\mathbf{pore2}}\right) \tag{2}$$

where ρ_1, ρ_2, and ρ_{air} are the densities of the mineral comprised of $S^{(1)}$, $S^{(2)}$, and air, respectively. Moreover, the estimated porosity from the CT-volume is:

$$\phi_{\text{CT}} = \boldsymbol{f}_{\mathbf{pore1}} + \boldsymbol{f}_{\mathbf{pore2}} + f_{\text{air}}^{\text{seg}} \tag{3}$$

If we assume that the CT-volume is a representative sample, the density obtained from **Eq. 2** and the porosity obtained from **Eq. 3** are equivalent to ρ_{lab} and ϕ_{lab}, respectively. Solving the system of two equations yields f_{pore1} and f_{pore2}. Thus, the porosity of the two subdomains are:

$$\phi_{\text{lab}}^{(1)} = \frac{f_{\text{air}}^{\text{seg}} + \boldsymbol{f}_{\mathbf{pore1}}}{f_{\text{air}}^{\text{seg}} + f_1^{\text{seg}}}$$
$$\phi_{\text{lab}}^{(2)} = \frac{f_{\text{air}}^{\text{seg}} + \boldsymbol{f}_{\mathbf{pore2}}}{f_{\text{air}}^{\text{seg}} + f_2^{\text{seg}}} \tag{4}$$

Remember that the total porosity of the sample, ϕ_{lab}, is defined as the ratio of the void space over the total volume of the sample. On the other hand, $\phi_{\text{lab}}^{(1)}$ and $\phi_{\text{lab}}^{(2)}$, are the ratio of the void space over the subdomain volumes, which are smaller than the total volume of the sample. Therefore, the values of $\phi_{\text{lab}}^{(1)}$ and $\phi_{\text{lab}}^{(2)}$ are greater than ϕ_{CT} and ϕ_{lab}.

Evaluating Effective Elastic Properties of the Sample

We used Elas3D to estimate the elastic properties of sample B. "Elas3D" is a numerical code written in Fortran 77 by the National Institute of Standards and Technology (Garboczi, 1998). Such a code uses finite element methods to solve the linear elastic equation on a discrete domain with a cubic mesh. The code solves the equation:

$$-\nabla \cdot \sigma = f \tag{5}$$

where $\boldsymbol{\sigma}$ is the stress tensor, $\mathbf{f}$ is the body force, and $\nabla\cdot$ is the divergence operator. **Equation 5** is subjected to the prescribed strain boundary condition:

$$\epsilon = \epsilon_0 \tag{6}$$

where ϵ_0 is the prescribed strain tensor at the domain boundary. In this study, we apply a strain boundary condition of ϵ_0 = [1.0, 1.0, 1.0, 0.5, 0.5, 0.5] to the sample (Voigt's notation). Note that solving **Eq. 5** and **Eq. 6** is equivalent to the energy minimization problem:

$$\min_{\boldsymbol{\sigma}} \int_{\Omega} \frac{1}{2}\mathbf{C} : \epsilon \tag{7}$$

where $\mathbf{C}$ is the elastic properties tensor and : denotes the inner tensor product (dot product). The elas3D code is implemented with a periodic boundary condition. Given the elastic properties of a material at each voxel and the prescribed strain magnitude at the boundaries, the code numerically solves **Eqs 5–7** for the stress tensor at each element with the conjugate gradient algorithm. Then, effective elastic properties are calculated with the average stress and the average strain. Using Voigt's notation, let $\boldsymbol{\sigma}_i(x,y,z)$ and $\epsilon_i(x,y,z)$ denote the ith component of the stress and the strain tensor at (x,y,z), respectively. Assuming that the sample is isotropic, the effective Bulk modulus K_{eff}, and the effective shear modulus G_{eff}, of the sample are:

$$K_{eff} = \frac{\sum \boldsymbol{\sigma}_1 + \sum \boldsymbol{\sigma}_2 + \sum \boldsymbol{\sigma}_3}{3\left(\sum \epsilon_1 + \sum \epsilon_2 + \sum \epsilon_3\right)}$$
$$G_{eff} = \frac{1}{3}\left(\frac{\sum \boldsymbol{\sigma}_4}{2\sum \epsilon_4} + \frac{\sum \boldsymbol{\sigma}_5}{2\sum \epsilon_5} + \frac{\sum \boldsymbol{\sigma}_6}{2\sum \epsilon_6}\right) \tag{8}$$

where Σ denoted the sum over the entire domain. The effective Young's modulus is computed as:

$$E_{eff} = \frac{9K_{eff}G_{eff}}{3K_{eff} + G_{eff}} \tag{9}$$

Segmentation-Based DRP

We also created and tested a segmented model to compare a segmentation-based DRP approach to our proposed technique. In the segmentation-based DRP, voxels are categorized based on the CT-number. The voxels are then assigned with the elastic properties of the pristine material. For example, a voxel that had

TABLE 3 | Elastic properties of minerals and air.

Phase	Bulk modulus (GPa)	Shear modulus (GPa)	References
Air	1.0×10^{-4}	0	International Standard Atmosphere (ISA)
Calcite	65	32	Carmichael (1989)
Dolomite	95	45	Carmichael (1989)
Water	2.2	0	Carmichael (1989)
Heavy mineral[a]	147	132	Carmichael (1989)

[a]*The bulk and the shear modulus of the heavy mineral phase are assumed to be equal to that of pyrite.*

been identified as the calcite would have the bulk modulus of 65 GPa and shear modulus of 32 GPa (**Table 3**). Each voxel is associated with only one material. To create our segmented model, we use the simple-threshold method, where a cut-off CT-number is defined to separate different phases. Here, the cut-off CT-number is chosen so that the digital sample porosity equals $\varnothing_{\mathrm{lab}}$.

Parameters and Assumptions

To compute the sub-resolution porosity, we assumed that the sample contains only two mineral phases: dolomite and calcite. Voxels that were classified as heavy minerals were grouped alongside calcite. To verify that such an approximation did not significantly affect the final effective modulus of the sample, we compared the Young's moduli of two samples calculated through the Voigt-Reuss-Hill average (Hill, 1963). The first sample comprised 8.65% pore space, 69.17% calcite, 22.13% dolomite, and 0.05% heavy mineral (i.e., the volumetric fractions estimated via segmentation). The second sample comprised of 8.65% pore space, 69.22% calcite, and 22.13% dolomite. We then assumed that the heavy mineral was pyrite (one of the most rigid and stiff heavy minerals) with bulk and shear modulus of 147 GPa and 132 GPa, respectively. The absolute difference between the two estimated Young's moduli was 0.2% (i.e., 41.5 vs. 41.4 GPa), suggesting that a sample comprising only dolomite and calcite was a good proxy for our sample.

The pore aspect ratio of the sub-resolution porosity, that was an input parameter for the modified-DEM, was estimated from the TOMCAT dataset using AVIZO 9.0 (Avizo, 2019) with the following workflow. First, pore space was segmented from the images with the AVIZO thresholding tool. Then, we applied the watershed algorithm (*Separate Object* command in AVIZO) to label each pore. We then computed the aspect ratio of each pore with the *Label Analysis* tool. Finally, the weighted harmonic average of the aspect ratios of all the pores was computed. Such an estimate yielded a pore aspect ratio of 0.47. Nonetheless, to account for uncertainties, we computed the elastic properties of sample B for aspect ratio end-members of 0.4 and 0.5. Note that the higher the aspect ratio, the higher the effective elastic properties.

To convert CT-numbers to density, we used a linear calibration. Such a procedure is described in detail in the **Supplementary Information**. In the density-to-porosity conversion, the cut-off densities (ρ_0) for the two subdomains ($S_{\mathrm{dol}}^{(1)}$ and $S_{\mathrm{cal}}^{(2)}$) were the density of dolomite (2870 kg/m^3) and calcite (2710 kg/m^3), respectively. The elastic properties used in the modified-DEM are given in **Table 3**. We assumed a critical porosity for both subdomains of 0.40, which is a typical value for carbonate rocks (Nur et al., 1998; Fournier et al., 2018).

RESULTS

Laboratory Results

Attenuation curves (**Figure 7**) reveal that for both cases, dry and full saturation (100%), attenuation ranges between 0 and 0.03 and increases with increasing frequency. Young's modulus patterns show dispersion in each case in agreement with a non-zero attenuation. At 5 MPa confining pressure and frequencies between 1 and 5 Hz, the average Young's modulus are 23.8 ± 0.1 GPa and 29.4 ± 0.1 GPa for the dry and 100% water-saturated case, respectively. It can also be observed that the saturated sample presents an increased values of the Young's modulus as predicted by the Gassmann theory (Gassmann, 1951).

DRP Results

Modified-SLOT on the Sample

According to the segmented CT-volume, the super-resolution porosity is 8.65%. The segmented volumes fraction of the first mineral (dolomite) and the second mineral (calcite) are $f_1^{\mathrm{seg}} = 0.2213$ and $f_2^{\mathrm{seg}} = 0.6922$, respectively. We substitute ρ_{lab} and ϕ_{lab} into **Eqs 2–4** and perform the optimization process, this gives the porosity volumes of the two subdomains equal to $\phi_{\mathrm{CT}}^{(1)} = 0.294$ and $\phi_{\mathrm{CT}}^{(2)} = 0.192$, respectively (**Figure 8**). Recombination yields a porosity for the entire sample $\phi_{\mathrm{CT}} = 0.1535$, which is 0.97% lower than ϕ_{lab}. The five sub-volumes extracted from sample F have porosities ranging between 0.1427 and 0.1669 (**Table 3**).

Young's Modulus from Numerical Simulations

The five sub-volume Young's moduli that were computed from the modified-SLOT range between 22.6 and 29.2 GPa and from 25.1 to 31.5 GPa for aspect ratio of 0.4 and 0.5, respectively (**Table 1**). On average, the predicted Young's modulus is 26.1 ± 1.7 GPa and 28.7 ± 1.9 GPa for the dry case and the water-saturated case, respectively. The fifth sub-volume, which has the closest porosity to the laboratory-measured porosity, yields Young's modulus of 25.6 GPa and 26.9 GPa for aspect ratio of 0.4 and 0.5 scenarios, respectively. The results suggest that, in the worst-case scenario, the calculated Young's modulus of the sample computed with aspect ratio of 0.5 would give 13% higher than the laboratory-measured Young's modulus. We

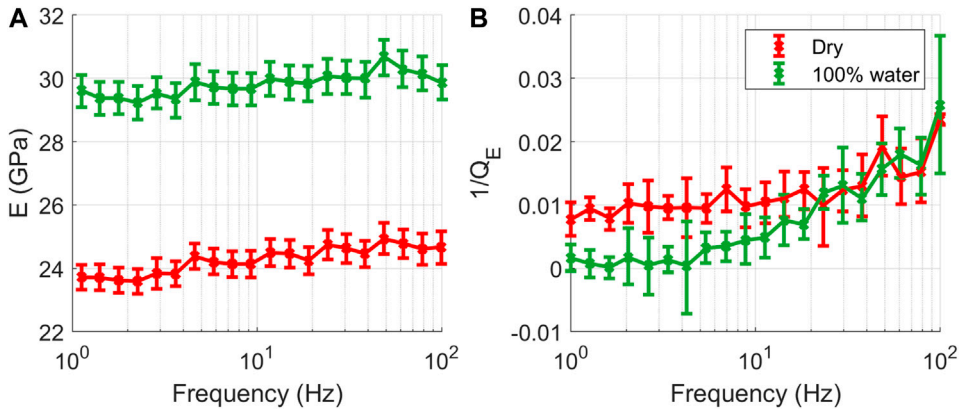

FIGURE 7 | Laboratory measurements of Young's modulus (E) and attenuation ($1/Q_E$) for the carbonate under dry conditions and full saturation (100%) with water (1 cP) at confining pressures of 5 MPa.

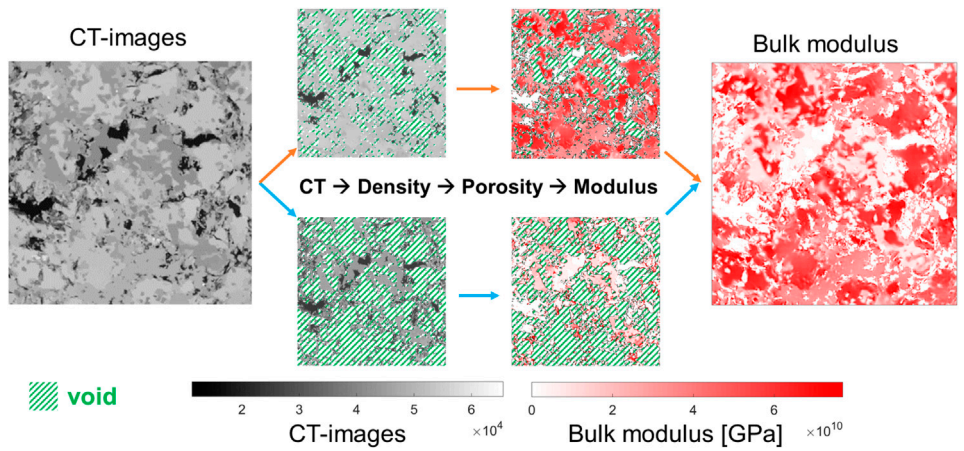

FIGURE 8 | A schematic diagram of the modified-SLOT on the sample. The sample is partitioned into two subdomains. The dolomite subdomain ($S_{dol}^{(1)}$) is shown in the bottom row and the calcite subdomain ($S_{cal}^{(2)}$) is shown in the top row. Notice that the air phases in both samples are the same.

observe a similar trend in the 100% water-saturated case. On the fifth sub-volume with the simulation aspect ratio of 0.5, Young's modulus obtained from modified-SLOT is 30.5 GPa, which is 4.1% higher than the laboratory measurement at 1 Hz. Instead, Young's modulus predicted from the segmentation-based DRP overpredicts the laboratory-measured Young's modulus by 180% and 140% for the dry and the water-saturated case, respectively. **Table 1** and **Figure 9** summarize the numerical simulation results from the modified-SLOT.

DISCUSSION

Microporosity Estimation

Roughly 40% of the porosity of our sample is not detectable from the ETH-dataset. The amount of sub-resolution porosity agrees with the literature on similar lithologies (e.g., Sok et al., 2010; Lin et al., 2016) and the MICP test. The distribution of sub-resolution porosity cannot be estimated using the segmentation-based DRP on CT-images. As such, we suggest that the segmentation-less DRP is a more suitable technique. Note that the aspect ratio of pores could be estimated from the MICP data and the CT-images. Future research should focus on improving the estimate of pore aspect ratios.

Static Young's Modulus Estimation

The static Young's modulus that is computed from the numerical simulations is a proxy for the zero-frequency limit of the laboratory measured Young's modulus measured in the laboratory. Nonetheless, the overprediction of the modulus might come from the type of boundary conditions that we used in the simulation. Here, the numerical code prescribes strain boundary conditions. The strain boundary condition gives the upper bound of the effective modulus if the size of the sample is not representative (Ostoja-Starzewski, 1999). On the other hand, the stress boundary condition gives the lower

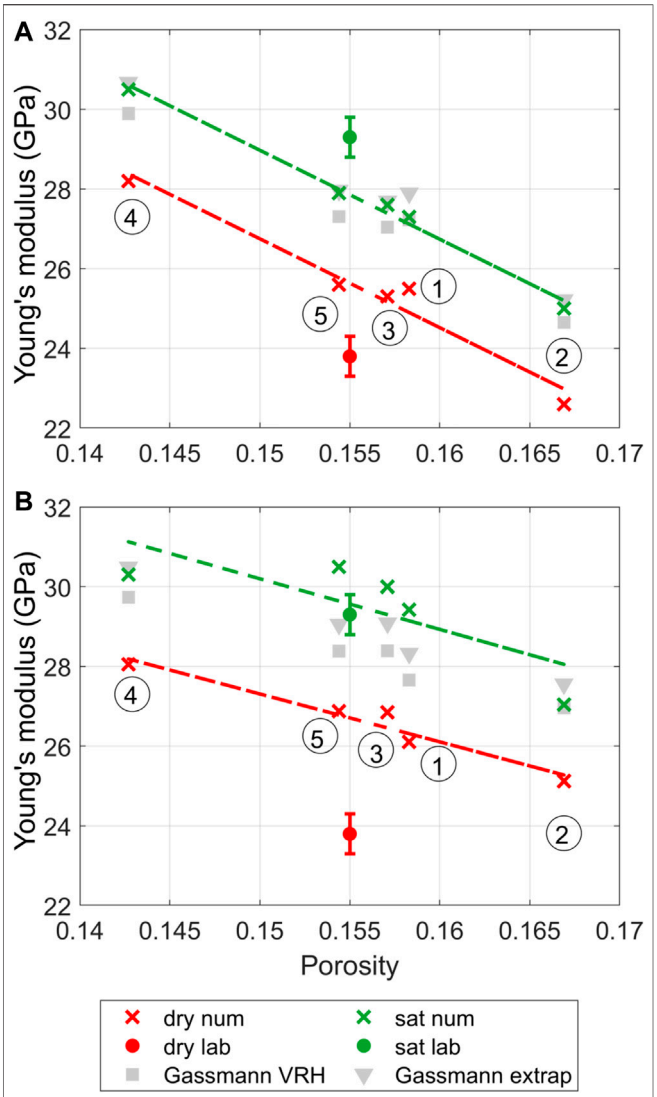

FIGURE 9 | The comparison between the laboratory-measured and the numerical simulated Young's modulus. Here, we show the result from two scenario: simulation with aspect ratio of 0.4 **(A)** and aspect ratio if 0.5 **(B)**. The dry case and the 100% water-saturated case are represented in red and green, respectively. Five numerical simulations on sub-volumes are shown with the cross symbol, and the sub-volume numbers are labeled next to the cross symbol. We fit the first-order polynomial through the numerical simulation results, observing a decreasing trend between the Young's modulus and the porosity. The gray triangle and square symbols represent the estimated Young's modulus using Gassmann's equation. The mineral modulus is approximated with the linear extrapolation of the sub-volume modulus (triangle symbols) and the Voight-Reuss-Hill average (square symbols).

bound under the same condition. Hence, the numerical predicted modulus might give the upper limit of the Young's modulus instead of the actual modulus of the sample that was measured by applying stress boundary conditions.

The static Young's moduli that we obtained from the modified-SLOT are more precise than those from the segmentation-based DRP. We speculate that such an improvement is due to the material-mixing strategy, creating a more realistic and flexible model (Tisato and Spikes, 2016). In addition, the improvement is also from the ability of the modified-SLOT to account for the effect of microporosity on the elastic properties.

In the segmentation-based DRP, the predicted Young's modulus overestimates the laboratory-measured result by 180% even though the porosity of the model matches ϕ_{lab}. This observation suggests that the spatial distribution of the pore space does affect the effective Young's modulus of the sample. Note that the simple threshold-based segmentation method has been shown to be ineffective for computing elastic properties of carbonate rocks (e.g., Madonna et al., 2012; Andrä et al., 2013b; Saenger et al., 2016; Sun et al., 2017). Therefore, we also conclude that the threshold-based segmentation is not a suitable technique for rocks with complex mineralogy and pore structures.

The successful result using modified-SLOT implies that we could have used the same strategy with the SLIT if we had physical targets scanned along with the sample. Such a method could have spared the measurement of porosity from the laboratory. In the worst-case scenario where the simulations are performed with aspect ratio of 0.5, the average error in Young's modulus computed from the modified-SLOT is 9.9%, which implies an error on the extensional wave velocity of 4.8%. An error of ~5% on wave velocities is similar to that yielded by the SLOT method that was applied on a Berea sandstone sample (Ikeda et al., 2020). We know the precision but not the accuracy of our laboratory measurements. Nevertheless, we can assume that accuracy for our laboratory measurements is around ±7%, which is similar to the uncertainty of the modified-SLOT.

Young's Modulus Prediction from Effective Medium Theories

The effective Young's modulus of the rock could also be estimated using theoretical models. We compare the effective Young's modulus of the fifth sub-volume obtained from the numerical simulation and EMTs, applied to the entire sample. The composition of the fifth sub-volume, estimated from the modified-SLOT, is 20.7% dolomite, 63.8% calcite, and 15.4% air. Dolomite has 0.35% of sub-resolution pore space, and calcite has 7.20% of sub-resolution pore space. Overall the sample has 7.85% super-resolution pore space. We consider the dry case and three EMTs to estimate Young's modulus of the sample: 1) Voigt-Reuss-Hill average (Hill, 1963), 2) average Hashin-Shtrikman bounds (Hashin and Shtrikman, 1963), and 3) modified-DEM. The latter provides a comparison between the modified-SLOT, where the modified-DEM is applied to each voxel, and the modified-DEM applied on the entire sample. Unfortunately, the modified-DEM is only applicable to a rock with two minerals. Thus, we estimate the Young's modulus of the sample using the modified-DEM with a mixture material strategy as follow. First, we define two new phases: the porous dolomite phase and the porous calcite phase. The modulus of the porous dolomite phase, M_{dol}, is computed by mixing dolomite with penny shaped inclusions whose aspect ratio is 0.4. The volume

fraction of the inclusions is 0.35%. Similarly, the modulus of the porous calcite phase, M_{cal}, is computed by mixing calcite to penny shaped pores having aspect ratio 0.4 and volume fraction 7.20%. These inclusion volume fractions are equal to the missing porosity in each subdomain. Then, the mixed moduli are computed from the modified-DEM where the critical porosity is 0.40. Next, the modulus of the sample -i.e., the mixture of the porous calcite and dolomite - is obtained from the Voigt-Reuss-Hill average.

The Young's modulus of the sample computed from Voigt-Reuss-Hill average, average Hashin-Shtrikman bounds, and modified-DEM are 38.4 GPa, 33.9 GPa, and 30.5 GPa, respectively. Such estimates are approximately 44% higher than the laboratory-measured Young's modulus. EMTs overestimate elastic properties because they do not incorporate the spatial distribution of phases and the geometry of grains and pores.

Gassmann Fluid Substitution on DRP

The Young's modulus of the 100% water-saturated sample from the numerical simulation mostly agrees with Gassmann fluid substitution. **Figure 9** shows a comparison between all the numerical simulations (green dots) and the algebraically estimated Young's modulus (gray dots). We also show the results on both simulation scenarios: aspect ratio of 0.4 and 0.5 (**Figures 9A,B**). The algebraically estimated Young's modulus is computed by directly applying Gassmann's fluid substitution to the dry bulk and shear modulus, porosity, mineral fraction, and mineral modulus (usually refer as K_0) of each sub-volume. The mineral modulus is estimated in two ways. The first method approximates the mineral modulus by computing the Voigt-Reuss- Hill average of the mineral constituents (square symbol in **Figure 9**). The second method finds K_0 by linearly extrapolating the dry bulk modulus of the sample at zero porosity. Both methods yield similar results except for sample sub-volume 1, 3, and 5 in the aspect ratio of 0.5 simulations (**Figure 9B**).

The fluid substituted Young's modulus computed from the modified-SLOT underestimates the laboratory measurement. The results from the laboratory measurement suggest a 23% increase in Young's modulus when the sample is fully saturated. On the other hand, Gassman predicts that the average increment in Young's modulus should be 9.7%. A similar modulus mismatch between the Gassmann prediction and the laboratory measurement for carbonate samples has been reported in the literature (e.g., Marion and Jizba, 1997; Wang, 1997; Røgen et al., 2005). These discrepancies imply that the Gassmann fluid substitution does not provide accurate results for this type of rock. We hypothesize that some reasons could be:

- During the saturation process in the laboratory, chemical interaction between pore fluid and rock frame altered the elastic properties of the rock (e.g., Assefa et al., 2003; Baechle et al., 2005);
- Compliant pore spaces (aspect ratio of ~0.4–0.5) in the sample might introduce anisotropic behaviors (Adam et al., 2006); hence, the isotropic Gassman substitution equation might not be valid; and,
- As previously mentioned, the laboratory measurement of Young's modulus has an error ~7%.

Another source of uncertainty is related to the boundary conditions. The laboratory experiment was performed under drained conditions. The numerical simulation, on the other hand, is performed under undrained condition and the modulus computed under the undrained condition is expected to be higher than that in the drained condition. Therefore, further investigation is needed for a more suitable model to simulate the elastic properties of rocks at drained water-saturated conditions.

Size of the Sample in the Numerical Simulation

We would like to emphasize that due to limitations on computational resources, the numerical simulations are performed on sub-volumes smaller than the core used in laboratory measurements. We assume that the numerical simulation on the small sample is still a proxy for the laboratory-sized sample. We consider the lithology understudy to have a low heterogeneity degree. Such an assumption is partially supported by the fact that sample C, D and E have similar measured porosity.

Nevertheless, the size of REVs depends on the heterogeneity level of the lithology. Rozenbaum and Roscoat (2014) studied REVs of CT-images of carbonate samples. They found that a sub-volume of size ~3 mm^3 is considered to be a representative size for calculating the porosity of limestone. Araújo et al. (2018), on the other hand, suggested that sub-volumes of size ~10 mm^3 could be used to compute porosities effectively. Nonetheless, the physical properties of the sub-volumes still depend on the location where the sub-volumes are extracted. Therefore, we cannot certainly conclude that the subsamples used in the numerical simulations are REVs for the sample. Nonetheless, the purpose of this manuscript is to demonstrate the possibility of using the segmentation-less DRP on polymineralic samples and achieve an improvement over the segmentation-based DRP. Future study is required to simulate the numerical tests on a larger rock sample. Such additional tests will be more efficiently performed on shared memory cluster systems and a parallelized version of elas3D using, for instance, OpenMPI (Bohn and Garboczi, 2003).

The Effect of Phase Segmentation

The modified-SLOT uses a segmentation algorithm to separate different phases. In our study, we used a simple threshold-based algorithm. Nevertheless, other algorithms could be chosen, introducing uncertainty in the final results as different segmentation algorithms could potentially lead to different rock models (e.g., Andrä et al., 2013a). Here, we consider the uncertainty related to the threshold-based segmentation method in segmenting the air phase. We suppose that an x fraction of dolomite voxels, due to the segmentation threshold, is classified as air. We can write:

$$f_{air}^{seg,\ new} = f_{air}^{seg} + (1-x)f_1^{seg},\ f_1^{seg,\ new} = (1-x)f_1^{seg} \tag{10}$$

The porosity of the segmentation-based model will increase by x. On the other hand, the porosity of the model created from the modified-SLOT, will increase only by a fraction of x. For example, if $x = 0.05$, solving **Eqs 2–5** gives $\phi_{lab}^{(1),\ new} = 0.298$ and $\phi_{lab}^{(2),\ new} = 0.197$, which are ~0.3% and ~2% greater than the porosities obtained in the original model. Then, when we apply the SLOT optimization process, the effective porosity of sample F is estimated to be 0.159, which is 1.3% higher than the original estimated porosity. Using different thresholds, we obsevere an increase in porosity of 0% (no change) and 2.6% when $x = 0.01$ and $x = 0.1$, respectively. Such limited analysis suggests that the modified-SLOT is less sensitive to the threshold level compared to the segmentation-based DRP. Future investigation is needed to study how the segmentation algorithm and parameters affect the final result: elastic properties of materials. And, we need to investigate the effect of the segment threshold on the other phases.

Possible Applications

Segmentation-less DRP allows capturing sub-resolution features without having to scan a sample at nanometric resolutions (i.e., segmentation-based DRP). The low-resolution scan (microns) covers a larger portion of the sample, which are likely to be REVs of formations (e.g., Lai et al., 2017; Hertel et al., 2018). Hence, such a scan could be used to compute properties of samples, served as a first-order approximation for further analysis.

Since the modified-SLOT relaxes the monomineralic assumption of the current segmentation-less DRP workflows, numerical simulations could be performed on a wide variety of rocks such as limestone and lithic sandstone. The EMT needs to be adjusted according to the sample lithology (e.g., grain packing model for clastic rocks). Incorporating EMTs to DRP also allows us to combine theoretical rock physics templates with digital rock physics simulations, giving the possibilities of investigating the impact of different rock physics models on rocks' properties. Note that the procedure could also be used to compute petrophysical properties other than elastic properties. For example, we can use the Hashin-Shtrikman bounds of electrical conductivity with modified-SLOT to create a conductivity model (Hashin and Shtrikman, 1963; Waff, 1974; Brovelli and Cassiani, 2010). Further studies are needed to test the validity of the concept.

CONCLUSION

We have introduced the modified-SLOT, a new digital rock physics technique, to evaluate the elastic properties of polymineralic rocks. The modified-SLOT combines segmentation-based DRP to reconstruct the spatial distribution of mineral phases, and segmentation-less DRP to account for the effect of sub-resolution features. Segmentation partitions a polymineralic rock sample into smaller subsamples that are monomineralic. Then, segmentation-less converts CT-images into density, porosity, and elastic property arrays. DRP results were compared to low-frequency measurements of Young's modulus on a polymineralic carbonate sample. The modified-SLOT provides a more accurate prediction of Young's modulus over the segmentation-based DRP. Such an improvement is because the modified-SLOT can capture the effect of microporosity on the sample elastic properties. Thus, modified-SLOT provides more realistic models for numerical simulations. Nonetheless, the modified-SLOT still inherits the segmentation-based DRP uncertainties in choosing segmentation algorithms. Future works need to be focused on assessing the uncertainties arising from the choice of segmentation algorithms. Although the modified-SLOT needs the information about the porosity of the samples, the success of modified-SLOT implies that a similar technique could be used when phantoms are presented in the scan (i.e., SLIT). Hence, the modified-SLOT and modified-SLIT could be used as a first-order proxy for predicting petrophysical properties of samples, cores, or cuttings, assisting geoscientists in creating fast and accurate subsurface models using X-ray CT technology.

DATA AVAILABILITY STATEMENT

The datasets presented in this article are not readily available because CT-scan data are proprietary. All the other data are sharable. Requests to access the datasets should be directed to Ken Ikeda, ikeda.ken@utexas.edu

AUTHOR CONTRIBUTIONS

The laboratory experiment was performed by SS, BQ, and ES. Digital Rock Physics and data analysis were performed by KI, EG, and NT. The preparation of the manuscript, including figures and tables were led by KI, under the supervision of NT. SS, BQ, ES, and EG assisted in the preparation process.

FUNDING

The first-author of the manuscript, KI, was funded by the EDGER Forum, The University of Texas at Austin. The AVIZO program and computer resources were supported by NSF grant EAR-1762458 to the University of Texas High-Resolution X-ray Computed Tomography Facility.

ACKNOWLEDGMENTS

We would like to thank Michael Plötze for performing X-ray computed tomography of the sample and the MICP measurement at the claylab of ETH Zürich, Switzerland. Access to AVIZO and computer resources, used to run AVIZO, were supported by NSF grant EAR-1762458 to the University of Texas High-Resolution X-ray Computed Tomography Facility. We would also want to thank the editor and the reviewers for suggestions on the manuscript. The datasets presented in this article are not readily available because CT-scan data are proprietary. All the other data are sharable. Requests to

access the datasets should be directed to the corresponded author. Code for the SLOT is available at https://github.com/ikedatu72/SegmentaionLessW-OTarget. The information on the numerical simulation solver is available at https://github.com/ikedatu72/elas3D-python.

SUPPLEMENTARY MATERIAL

The Supplementary Material for this article can be found online at: https://www.frontiersin.org/articles/10.3389/feart.2021.628544/full#supplementary-material.

REFERENCES

Adam, L., Batzle, M., and Brevik, I. (2006). Gassmann's fluid substitution and shear modulus variability in carbonates at laboratory seismic and ultrasonic frequencies. *Geophysics.* 71 (6), F173–F183. doi:10.1190/1.2358494

AlJallad, O., Dernaika, M., Koronfol, S., Naseer Uddin, Y., and Mishra, P. (2020). "Evaluation of complex carbonates from pore-scale to core-scale," in International petroleum technology conference, January 13–15, 2020, Dhahran, Kingdom of Saudi Arabia.

Amabeoku, M. O., Al-Ghamdi, T. M., Mu, Y., Ingrain, R., and Toelke, J. (2013). *Evaluation and application of digital rock physics (DRP) for special core analysis in carbonate formations.*

Andrä, H., Combaret, N., Dvorkin, J., Glatt, E., Han, J., Kabel, M., et al. (2013a). Digital rock physics benchmarks—part I: imaging and segmentation. *Comput. Geosci.* 50, 25–32. doi:10.1016/j.cageo.2012.09.005

Andrä, H., Combaret, N., Dvorkin, J., Glatt, E., Han, J., Kabel, M., et al. (2013b). Digital rock physics benchmarks—part II: computing effective properties. *Comput. Geosci.* 50, 33–43. doi:10.1016/j.cageo.2012.09.008

Araújo, O., Sharma, K., Machado, A., Ferreira, C. G., Straka, R., Tavares, F., et al. (2018). Representative elementary volume in limestone sample. *J. Instrum.* 13, C10003. doi:10.1088/1748-0221/13/10/C10003

Assefa, S., McCann, C., and Sothcott, J. (2003). Velocities of compressional and shear waves in limestones. *Geophys. Prospect.* 51 (1), 1–13. doi:10.1046/j.1365-2478.2003.00349.x

Avizo (2019). [Computer software]. Thermo fisher scientific. Available at: https://www.thermofisher.com/ (Version 9). (Accessed December 1, 2020)

Baechle, G. T., Weger, R. J., Eberli, G. P., Massaferro, J. L., and Sun, Y.-F. (2005). Changes of shear moduli in carbonate rocks: implications for Gassmann applicability. *Lead. Edge.* 24 (5), 507–510. doi:10.1190/1.1926808

Baumgartner, R. J., Kranendonk, M. J. V., Wacey, D., Fiorentini, M. L., Saunders, M., Caruso, S., et al. (2019). Nano–porous pyrite and organic matter in 3.5-billion-year-old stromatolites record primordial life. *Geology.* 47 (11), 1039–1043. doi:10.1130/G46365.1

Bohn, R. B., and Garboczi, E. J. (2003). NIST Interagency/Internal Report (NISTIR) – 6997. User manual for finite element and finite difference programs: a parallel version of NISTIR 6269 and NISTIR 6997. Available at: https://www.nist.gov/publications/user-manual-finite-element-and-finite-difference-programs-parallel-version-nistir-6269 (Accessed December 25, 2020).

Brovelli, A., and Cassiani, G. (2010). A combination of the Hashin-Shtrikman bounds aimed at modelling electrical conductivity and permittivity of variably saturated porous media. *Geophys. J. Int.* 180 (1), 225–237. doi:10.1111/j.1365-246X.2009.04415.x

Buades, A., Coll, B., and Morel, J.-M. (2005). "A non-local algorithm for image denoising," in IEEE computer society conference on computer vision and pattern recognition (CVPR'05) Vol. 2, 60–65.

Carmichael, R. S. (1989). *Practical handbook of physical properties of rocks and minerals*. Boca Raton, Fla: CRC Press.

Chafetz, H., Barth, J., Cook, M., Guo, X., and Zhou, J. (2018). Origins of carbonate spherulites: implications for Brazilian Aptian pre-salt reservoir. *Sediment. Geol.* 365, 21–33. doi:10.1016/j.sedgeo.2017.12.024

Chantler, C. T., Olsen, K., Dragoset, R. A., Chang, J., Kishore, A. R., Kotochigova, S. A., et al. (2005). X-Ray form factor, attenuation and scattering tables. National Institute of Standards and Technology. Available at: http://physics.nist.gov/ffast, Version 2.1. (Accessed November 15, 2020)

Dunsmuir, J. H., Bennett, S., Fareria, L., Mingino, A., and Sansone, M. (2006). X-ray microtomographic imaging and analysis for basic research. *Powder Diffr.* 21 (2), 125–131. doi:10.1154/1.2204956

Fournier, F., Pellerin, M., Villeneuve, Q., Teillet, T., Hong, F., Poli, E., et al. (2018). The equivalent pore aspect ratio as a tool for pore type prediction in carbonate reservoirs. *AAPG Bull.* 102 (7), 1343–1377. doi:10.1306/10181717058

Garboczi, E. J. (1998). NIST interagency/internal report (NISTIR) – 6269. Finite element and finite difference programs for computing the linear electric and elastic properties of digital images of random materials | NIST. Available at: https://www.nist.gov/publications/finite-element-and-finite-difference-programs-computing-linear-electric-and-elastic (Accessed November 15, 2020).

Gassmann, F. (1951). *Über die Elastizität poröser Medien. Viertel. Naturforsch. Ges. Zürich*, 1–23.

Gomes, J. P., Bunevich, R. B., Tedeschi, L. R., Tucker, M. E., and Whitaker, F. F. (2020). Facies classification and patterns of lacustrine carbonate deposition of the Barra Velha Formation, Santos Basin, Brazilian Pre-salt. *Mar. Petrol. Geol.* 113, 104176. doi:10.1016/j.marpetgeo.2019.104176

Gupta, L. P., Tanikawa, W., Hamada, Y., Hirose, T., Ahagon, N., Sugihara, T., et al. (2018). Examination of gas hydrate-bearing deep ocean sediments by X-ray Computed Tomography and verification of physical property measurements of sediments. *Marine Pet. Geol.* 108, 239–248. doi:10.1016/j.marpetgeo.2018.05.033

Han, J., Han, S., Kang, D. H., Kim, Y., Lee, J., and Lee, Y. (2020). Application of digital rock physics using X-ray CT for study on alteration of macropore properties by CO2 EOR in a carbonate oil reservoir. *J. Petrol. Sci. Eng.* 189, 107009. doi:10.1016/j.petrol.2020.107009

Hashin, Z., and Shtrikman, S. (1963). A variational approach to the theory of the elastic behaviour of multiphase materials. *J. Mech. Phys. Solid.* 11 (2), 127–140. doi:10.1016/0022-5096(63)90060-7

Hertel, S. A., Rydzy, M., Anger, B., Berg, S., Appel, M., and de Jong, H. (2018). "Upscaling of digital rock porosities by correlation with whole core CT Scan Histograms," in SPWLA 59th annual logging symposium.

Hill, R. (1963). Elastic properties of reinforced solids: some theoretical principles. *J. Mech. Phys. Solid.* 11 (5), 357–372. doi:10.1016/0022-5096(63)90036-X

Iassonov, P., Gebrenegus, T., and Tuller, M. (2009). Segmentation of X-ray computed tomography images of porous materials: a crucial step for characterization and quantitative analysis of pore structures. *Water Resour. Res.* 45 (9), W09415. doi:10.1029/2009WR008087

Ikeda, K., Goldfarb, E., and Tisato, N. (2020). Calculating effective elastic properties of Berea Sandstone using the segmentation-less method without targets. *J. Geophys. Res.: Solid Earth* 125, e2019JB018680. doi:10.1029/2019JB018680

Ketcham, R., and Carlson, W. D. (2001). Acquisition, optimization and interpretation of X-ray computed tomographic imagery: applications to the geosciences. *Comput. Geosci.* 27, 381–400. doi:10.1016/S0098-3004(00)00116-3

Lai, J., Wang, G., Fan, Z., Chen, J., Qin, Z., Xiao, C., et al. (2017). Three-dimensional quantitative fracture analysis of tight gas sandstones using industrial computed tomography. *Sci. Rep.* 7, 1825. doi:10.1038/s41598-017-01996-7

Lin, Q., Al-Khulaifi, Y., Blunt, M. J., and Bijeljic, B. (2016). Quantification of sub-resolution porosity in carbonate rocks by applying high-salinity contrast brine using X-ray microtomography differential imaging. *Adv. Water Resour.* 96, 306–322. doi:10.1016/j.advwatres.2016.08.002

Madonna, C., and Tisato, N. (2013). A new Seismic Wave Attenuation Module to experimentally measure low-frequency attenuation in extensional mode: a seismic wave attenuation module to measure low-frequency attenuation. *Geophys. Prospect.* 61 (2), 302–314. doi:10.1111/1365-2478.12015

Madonna, C., Almqvist, B. S. G., and Saenger, E. H. (2012). Digital rock physics: numerical prediction of pressure-dependent ultrasonic velocities using micro-CT imaging. *Geophys. J. Int.* 189 (3), 1475–1482. doi:10.1111/j.1365-246X.2012.05437.x

Marion, D., and Jizba, D. (1997). "5. Acoustic properties of carbonate rocks: use in quantitative interpretation of sonic and seismic measurements," in *Carbonate seismology*. (Tulsa, OK: Society of Exploration Geophysicists), Vol. 1, 75–94.

Mavko, G., Mukerji, T., and Dvorkin, J. (2020). *The rock physics handbook*. 3rd Edn. Cambridge: Cambridge University Press.

Mukerji, T., Berryman, J., Mavko, G., and Berge, P. (1995). Differential effective medium modeling of rock elastic moduli with critical porosity constraints. *Geophys. Res. Lett.* 22 (5), 555–558. doi:10.1029/95GL00164

Mull, R. T. (1984). Mass estimates by computed tomography: physical density from CT numbers. *AJR Am. J. Roentgenol.* 143 (5), 1101–1104. doi:10.2214/ajr.143.5.1101

Nock, R., and Nielsen, F. (2004). Statistical region merging. *IEEE Trans. Pattern Anal. Mach. Intell.* 26 (11), 1452–1458. doi:10.1109/TPAMI.2004.110

Norris, A. N., Callegari, A. J., and Sheng, P. (1985). A generalized differential effective medium theory. *J. Mech. Phys. Solid.* 33 (6), 525–543. doi:10.1016/0022-5096(85)90001-8

Nur, A., Mavko, G., Dvorkin, J., and Galmudi, D. (1998). Critical porosity: a key to relating physical properties to porosity in rocks. *Lead. Edge.* 17 (3), 357–362. doi:10.1190/1.1437977

Ostoja-Starzewski, M. (1999). Scale effects in materials with random distributions of needles and cracks. *Mech. Mater.* 31 (12), 883–893. doi:10.1016/S0167-6636(99)00039-3

Paterson, M. S., and Olgaard, D. L. (2000). Rock deformation tests to large shear strains in torsion. *J. Struct. Geol.* 22, 1341–1358. doi:10.1016/S0191-8141(00)00042-0

Røgen, B., Fabricius, I. L., Japsen, P., Høier, C., Mavko, G., and Pedersen, J. M. (2005). Ultrasonic velocities of North Sea chalk samples: influence of porosity, fluid content and texture. *Geophys. Prospect.* 53 (4), 481–496. doi:10.1111/j.1365-2478.2005.00485.x

Rozenbaum, O., and du Roscoat, S. R. (2014). Representative elementary volume assessment of three-dimensional x-ray microtomography images of heterogeneous materials: application to limestones. *Phys. Rev. E – Stat. Nonlinear Soft Matter Phys.* 89, 053304. doi:10.1103/PhysRevE.89.053304

Saenger, E. H., Vialle, S., Lebedev, M., Uribe, D., Osorno, M., Duda, M., et al. (2016). Digital carbonate rock physics. *Solid Earth* 7 (4), 1185–1197. doi:10.5194/se-7-1185-2016

Schindelin, J., Arganda-Carreras, I., Frise, E., Kaynig, V., Longair, M., Pietzsch, T., et al. (2012). Fiji: an open-source platform for biological-image analysis. *Nat. Methods.* 9 (7), 676–682. doi:10.1038/nmeth.2019

Scholle, P. A., and Ulmer-Scholle, D. S. (2003). *A color guide to the petrography of carbonate rocks: grains, textures, porosity, diagenesis*. Tulsa, OK: American Association of Petroleum Geologists.

Sok, R., Varslot, T., Ghous, A., Latham, S., Sheppard, A., and Knackstedt, M. (2010). Pore scale characterization of carbonates at multiple scales: integration of micro-CT, BSEM, and FIBSEM. *Petrophysics*, 51 (6), 379–387.

Subramaniyan, S., Quintal, B., Madonna, C., and Saenger, E. H. (2015). Laboratory-based seismic attenuation in Fontainebleau sandstone: evidence of squirt flow: attenuation in Fontainebleau Sandstone. *J. Geophys. Res.: Solid Earth* 120 (11), 7526–7535. doi:10.1002/2015JB012290

Sun, H., Di, D., Tao, G., Vega, S., Li, K., Liu, L., et al. (2017). "Carbonate rocks: a case Study of rock properties evaluation using multi-scale digital images," in Abu Dhabi international petroleum exhibition and conference, November 13–16, 2017, Abu Dhabi, UAE.

Taud, H., Martinez-Angeles, R., Parrot, J. F., and Hernandez-Escobedo, L. (2005). Porosity estimation method by X-ray computed tomography. *J. Petrol. Sci. Eng.* 47 (3), 209–217. doi:10.1016/j.petrol.2005.03.009

Tisato, N., and Spikes, K. (2016). "Computation of effective elastic properties from digital images without segmentation," in *SEG technical program expanded abstracts 2016.* (Tulsa, OK: Society of Exploration Geophysicists), Vol. 1, 3256–3260.

Waff, H. S. (1974). Theoretical considerations of electrical conductivity in a partially molten mantle and implications for geothermometry. *J. Geophys. Res.* 79 (26), 4003–4010. doi:10.1029/JB079i026p04003

Wang, Z. (1997). "3. Seismic properties of carbonate rocks," in *Carbonate seismology*. (Tulsa, OK: Society of Exploration Geophysicists), Vol. 1, 29–52.

Wang, Y., Yang, Y., Xiao, T., Liu, K., Clennell, B., Zhang, G., et al. (2013). Synchrotron-based data-constrained modeling analysis of microscopic mineral distributions in limestone. *Int. J. Geosci.* 4 (2), 344–351. doi:10.4236/ijg.2013.42032

Wright, V. P., and Barnett, A. J. (2015). An abiotic model for the development of textures in some South Atlantic early Cretaceous lacustrine carbonates. *Geol. Soc., London, Spec. Publ.* 418 (1), 209–219. doi:10.1144/SP418.3

Conflict of Interest: The authors declare that the research was conducted in the absence of any commercial or financial relationships that could be construed as a potential conflict of interest.

Copyright © 2021 Ikeda, Subramaniyan, Quintal, Goldfarb, Saenger and Tisato. This is an open-access article distributed under the terms of the Creative Commons Attribution License (CC BY). The use, distribution or reproduction in other forums is permitted, provided the original author(s) and the copyright owner(s) are credited and that the original publication in this journal is cited, in accordance with accepted academic practice. No use, distribution or reproduction is permitted which does not comply with these terms.

frontiers in Earth Science

ORIGINAL RESEARCH
published: 08 March 2021
doi: 10.3389/feart.2021.618909

Wave Equations of Porous Media Saturated With Two Immiscible Fluids Based on the Volume Averaging Method

Fansheng Xiong[1,2], *Jiawei Liu*[3,4,5]*, *Zhenwei Guo*[3,4,5] *and Jianxin Liu*[3,4,5]

[1]*Institute of Applied Physics and Computational Mathematics, Beijing, China,* [2]*Zhou Pei-Yuan Center for Applied Mathematics, Tsinghua University, Beijing, China,* [3]*School of Geosciences and Info-Physics, Central South University, Changsha, China,* [4]*Hunan Key Laboratory of Nonferrous Resources and Geological Hazard Exploration, Changsha, China,* [5]*Key Laboratory of Metallogenic Prediction of Nonferrous Metals and Geological Environment Monitoring (Central South University), Ministry of Education, Changsha, China*

OPEN ACCESS

Edited by:
Jing Ba,
Hohai University, China

Reviewed by:
Liyun Fu,
China University of Petroleum (Huadong), China
Jixin Deng,
Chengdu University of Technology, China

***Correspondence:**
Jiawei Liu
jw-liu@csu.edu.cn

Specialty section:
This article was submitted to Solid Earth Geophysics, a section of the journal Frontiers in Earth Science

Received: *19 October 2020*
Accepted: *18 January 2021*
Published: *08 March 2021*

Citation:
Xiong F, Liu J, Guo Z and Liu J (2021) Wave Equations of Porous Media Saturated With Two Immiscible Fluids Based on the Volume Averaging Method. Front. Earth Sci. 9:618909. doi: 10.3389/feart.2021.618909

Simulating and predicting wave propagation in porous media saturated with two fluids is an important issue in geophysical exploration studies. In this work, wave propagation in porous media with specified structures saturated with two immiscible fluids was studied, and the main objective was to establish a wave equation system with a relatively simple structure. The wave equations derived by Tuncay and Corapcioglu were analyzed first. It was found that the coefficient matrix of the equations tends to be singular due to the inclusion of a small parameter that characterizes the effect of capillary stiffening. Therefore, the previously established model consisting of three governing equations may be unstable under natural conditions. An improved model based on Tuncay and Corapcioglu's work was proposed to ensure the nonsingularity of the coefficient matrix. By introducing an assumption in which one fluid was completely wrapped by the other, the governing equation of the wrapped fluid was degenerated. In this way, the coefficient matrix of wave equations became nonsingular. The dispersion and attenuation prediction resulting from the new model was compared with that of the original model. Numerical examples show that although the improved model consists of only two governing equations, it can obtain a result similar to that of the original model for the case of a porous medium containing gas and water, which simplifies the complexity of the calculations. However, in a porous medium with oil and water, the predictions of dispersion and attenuation produced by the original model obviously deviate from the normal trend. In contrast, the results of the improved model exhibit the correct trend with a smooth curve. This phenomenon shows the stability of the improved model and it could be used to describe wave propagation dispersions and attenuations of porous media containing two immiscible fluids in practical cases.

Keywords: volume averaging method, porous media, two fluids, wave equations, dispersion and attenuation

1 INTRODUCTION

Wave propagation in partially saturated porous media is of interest in the research areas of geophysics, petroleum engineering and underground science. For instance, partial saturation of two or more fluid components usually occurs in complex unconventional reservoirs (Santos et al., 2019).

There are plenty of works related to this issue. Some scholars have studied modulus calculations for composite materials. White (1975) established the first bulk modulus expression that considered dissipation mechanisms on a mesoscopic scale, which is also known as the patch saturation model. A model of concentric spheres with periodic distribution was formulated to simulate the heterogeneity of fluids in porous media. Then, based on the quasi-static Biot theory (Biot, 1956; Biot, 1962), Johnson (2001) proposed a dynamic frequency-dependent bulk modulus to calculate the dispersion and attenuation relations of patches with arbitrary geometries. The bifurcation function of the bulk modulus under different limit conditions was considered. Subsequently, Tserkovnyak and Johnson (2003) improved this model by considering the effect of membrane surface tensions between two fluids in pore space. Thereafter, a patch saturation model with a random distribution was proposed by Müller and Gurevich (2015).

In the work of wave equations, there are two main modeling methods: the mixture theory and volume averaging theory. It is assumed in the mixture theory that the pore media is homogeneously distributed on a macroscopic level and it is therefore not necessary to describe the pore structure (Tuncay and Corapcioglu, 1997). There is a vast body of work operating under the mixture theory, and only a few of them are listed here. In early studies, Brutsaert and Luthin (1964) extended Biot's theory (Biot, 1956; Biot, 1962) to a case with two fluids, and three kinds of compressional waves were predicted. Based on the principle of analytical mechanics, Berryman (1986), Berryman (1988) first established the kinetic and potential energy functions of a porous medium containing two fluids. Then, wave equations for partially saturated media based on separating fluid were established to analyze the dissipation caused by the interactions between fluids and solids. The model inadequately considered the influence of the interaction between the two fluids on the seismic wave energy (Sun et al., 2015). According to the fluid separation theory (Berryman, 1986; Berryman, 1988), as mentioned above, Santos et al. (1990a), Santos et al. (1990b), Santos et al. (2004) derived wave equations for porous media with two fluids. The capillary pressure function was introduced, and the idealized test method was used to determine the elastic coefficients. However, some parameters of the model may have had no practical physical meaning due to the use of the idealization test (Sun et al., 2015). Lo et al. (2005), Lo et al. (2007), Lo et al. (2015) further studied the model proposed by Berryman (1986), Berryman (1988) and added an inertial coupling term in the equations. Ba et al. (2016) studied the effect of rock matrix stiffening caused by clay squirt flow on wave dispersion. Moreover, Ba et al. (2017) proposed a double double-porosity model to describe wave propagation in anelasticity rock. Such a model takes into account both the heterogeneity of rock fabric and that of fluid distribution.

Another important way to derive wave equations is the volume averaging method, which benefits from the proof and development of the volume averaging theorem (Anderson and Jackson, 1967; Slattery, 1967). It does not require the assumption of a uniform spatial distribution of pores. The variables have clear physical meanings, and there is no need to consider fluid distribution shapes on a microscopic level with this technique. In this way, motion equations and the constitutive relations can be obtained by taking the average of the corresponding microscopic equations. A theorem for the volume averaging of a gradient is employed during the derivation process.

De la Cruz and Spanos (1983), De la Cruz and Spanos (1985) used the volume averaging method to derive wave equations for porous media saturated with one fluid. It was demonstrated by numerical examples that the results obtained from their final equations are almost the same as those of Biot's theory within a certain frequency range for the case of a given fluid with a relatively low viscosity. The volume averaging method was also used in the modeling of the so-called double-porosity dual-permeability model developed by Pride and Berryman (2003a), Pride and Berryman (2003b). They used this method to define the physical quantities in a heterogeneous porous media. A representative work of wave equations considering two fluids is a model developed by Tuncay and Corapcioglu (1995), Tuncay and Corapcioglu (1996), Tuncay and Corapcioglu (1997). They applied this method to explore wave propagation in poroelastic media saturated by two immiscible fluids. The capillary effect was considered, and they proposed a new way to express the relation of volume variation to determine the coefficients of the constitutive relations. Alternatively, one can use the two-space method proposed by Burridge and Keller (1981). They started from the microscopic, linearized elasticity equations for the solid phase and the Navier-Stokes equations for the fluid component. The asymptotic expansion technique was used. Although the derivation process was complicated, the final equations they obtained were equivalent to Biot's equations when the viscosity of the fluid was low. In principle, the final expressions derived by the volume averaging method are equivalent to those of the two-space method (Tuncay and Corapcioglu, 1997).

Comparing the two mainstream methods, the former assumes a porous medium with a homogeneous structure, regardless of the geometric details. The specific geometric structure of the pore space is considered by the latter. Based on this difference, we think the volume averaging method is a more general modeling method since it is convenient to obtain a physical model in line with the real world.

This study aims to establish numerical stable wave equations for porous media containing two fluids using the volume averaging method, and the manuscript is organized as follows. In **Section 2**, the model describing wave propagation in porous media saturated with two immiscible fluids developed by Tuncay and Corapcioglu is analyzed. It is found that the coefficient matrix of the equations tends to be singular due to the small parameter that characterizes the capillary stiffening effect. Then, wave equations for porous media saturated with an effective fluid are proposed as an improved model based on their study. Two numerical examples related to dispersion and attenuation are given in **Section 4**. From the results, the improved model can obtain similar results as the original model in the case of porous media containing gas and water. However, for the case of oil and

water, the curve calculated by the original model is unstable; one can obtain smooth solutions using the improved model.

2 METHOD

2.1 The Analysis of Tuncay and Corapcioglu's Model

Considering a porous medium containing two immiscible fluids, Tuncay and Corapcioglu (1997) started from a microscopic momentum balance equation between the solid and the two fluids, respectively. Only the low-frequency case was considered in their study. The corresponding macroscopic equations were obtained by the volume averaging method. Meanwhile, they obtained the macroscopic constitutive relation in a novel way (Tuncay and Corapcioglu, 1997). The final wave equations are obtained by combining the macroscopic momentum balance equation and the constitutive relation, which can be written as follows (Tuncay and Corapcioglu, 1997):

$$\begin{aligned}
\langle\rho_s\rangle\ddot{\mathbf{u}}^s &= \nabla\left(a'_{11}\nabla\cdot\mathbf{u}^s + a_{12}\nabla\cdot\mathbf{u}^{f1} + a_{13}\nabla\cdot\mathbf{u}^{f2}\right) + \nabla\cdot\left(G\nabla\mathbf{u}^s\right) + C_1\left(\dot{\mathbf{u}}^{f1} - \dot{\mathbf{u}}^s\right) + C_2\left(\dot{\mathbf{u}}^{f2} - \dot{\mathbf{u}}\right),\\
\langle\rho_{f1}\rangle\ddot{\mathbf{u}}^{f1} &= \nabla\left(a_{21}\nabla\cdot\mathbf{u}^s + a_{22}\nabla\cdot\mathbf{u}^{f1} + a_{23}\nabla\cdot\mathbf{u}^{f2}\right) - C_1\left(\dot{\mathbf{u}}^{f1} - \dot{\mathbf{u}}^s\right),\\
\langle\rho_{f2}\rangle\ddot{\mathbf{u}}^{f2} &= \nabla\left(a_{31}\nabla\cdot\mathbf{u}^s + a_{32}\nabla\cdot\mathbf{u}^{f1} + a_{33}\nabla\cdot\mathbf{u}^{f2}\right) - C_2\left(\dot{\mathbf{u}}^{f2} - \dot{\mathbf{u}}^s\right),
\end{aligned} \tag{1}$$

Where $\mathbf{u}^s$ is the solid displacement and $\mathbf{u}^{f1}$ and $\mathbf{u}^{f2}$ are the two fluid displacements. Note ϕ is the porosity and S_1 and S_2 are the saturations of the two fluids in which $S_1 + S_2 = 1$ and $\phi = \phi_1 + \phi_2$, where $\phi_1 = S_1\phi$ and $\phi_2 = S_2\phi$. ρ_s, ρ_{f1} and ρ_{f2} are the mass densities of the solid and the two fluids, respectively. The averaged densities are denotes as $\langle\rho_s\rangle = (1-\phi)\rho_s$, $\langle\rho_{f1}\rangle = \phi_1\rho_{f1}$ and $\langle\rho_{f2}\rangle = \phi_2\rho_{f2}$. C_1 and C_2 are two dissipation coefficients expressed as $C_1 = \eta\phi_1^2/\kappa_1$ and $C_2 = \eta\phi_2^2/\kappa_2$, where η denotes the fluid viscosity; and κ_1 and κ_2 are the relative permeabilities of the two fluids in pore space, respectively. Note that t represents the time, and the dot above the physical quantity indicates the derivative of time. In addition, the elastic constants are expressed as follows (Tuncay and Corapcioglu, 1997):

$$\begin{aligned}
a_{11}A_3 &= K_s\left[A_1(1-\phi)\left(K_{f1}A_2S_1 + K_{f1}K_{f2} + K_{f2}A_2S_2\right) + K_sK_b\phi\left(K_{f1}S_2 + K_{f2}S_1 + A_2\right)\right],\\
a_{12}A_3 &= K_sK_{f1}A_1S_1\phi\left(A_2 + K_{f2}\right),\\
a_{13}A_3 &= K_sK_{f2}A_1S_2\phi\left(A_2 + K_{f1}\right),\\
a_{21} &= a_{12}\\
a_{22}A_3 &= K_{f1}S_1\phi\left[K_s^2\phi\left(K_{f2}S_1 + A_2\right) + K_{f2}A_2A_1S_2\right],\\
a_{23}A_3 &= -K_{f1}K_{f2}S_1S_2\phi\left(-K_s^2\phi + A_2A_1\right),\\
a_{31} &= a_{13},\\
a_{32} &= a_{23},\\
a_{33}A_3 &= K_{f2}S_2\phi\left[K_s^2\phi\left(K_{f1}S_2 + A_2\right) + K_{f1}A_2A_1S_1\right]
\end{aligned} \tag{2}$$

A_1, A_2, and A_3 are expressed as follows:

$$\begin{aligned}
A_1 &= (1-\phi)K_s - K_b\\
A_2 &= \frac{\mathrm{d}p_{\mathrm{cap}}}{\mathrm{d}S_1}S_1(1-S_1) = \frac{\beta}{100}\left[(1-S_1)^{-n/(n-1)} - 1\right]^{(1-n)/n}(1-S_1)^{-(2n-1)/(n-1)}\\
A_3 &= A_1\left(K_{f1}A_2S_1 + K_{f1}K_{f2} + K_{f2}A_2S_2\right) + K_s^2\phi\left(K_{f1}S_2 + A_2 + K_{f2}S_1\right)
\end{aligned} \tag{3}$$

Where K_s, $K_{f\,1}$ and $K_{f\,2}$ are the bulk moduli of the solid matrix material and two fluids, respectively; K_b and G are the drained bulk modulus and shear modulus of the solid skeleton, respectively. Note $a_{11}^* = a_{11} + G/3$. β and n are two fitting parameters needed to calculate the capillary force p_{cap} (Van Genuchten, 1980; Tuncay and Corapcioglu, 1997; Lo et al., 2005).

Equation 1 contains three governing equations, which is the major difference between the wave equations of porous media saturated with two fluids and that of one fluid. It is obvious that the structure of the second equation is the same as that of the third equation, but the coefficients in front of each term differ.

It is worth noting that an important contribution of this model was that the effect of the capillary force was considered through the elastic constant A_2, which is generally a positive real number. As seen in **Eq. 2**, A_2 interacts with elastic parameters, such as K_{f1}, and characterizes the strengthening effect of the capillary force on the elastic parameters. However, as will be shown in **Section 3**, the magnitude of A_2, as calculated by **Eq. 3**, is much smaller than that of K_{f1} and K_{f2}, especially in the case of a porous medium saturated with two liquids. Different works (Tserkovnyak and Johnson, 2003; Pride et al., 2004; Kobayashi and Mavko, 2016) have studied this issue. For example, Kobayashi and Mavko (2016) showed that the effect of capillary forces on the P-wave velocity was not significant by testing a set of experimental samples. Thus, it seems that the strengthening effect of the capillary force on elastic parameters can be ignored in most cases since A_2 has a small value compared with the related parameters and can be neglected.

Once the relations of $A_2 \ll K_{f1}$, $A_2 \ll K_{f2}$ and $A_2 \ll K_s$ are identified, one can represent the relationship between the elastic coefficients of the second and third governing equations as follows:

$$\frac{a_{21}}{a_{31}} = \frac{a_{22}}{a_{32}} = \frac{a_{23}}{a_{33}} = \frac{S_1}{S_2} \tag{4}$$

Equation 4 shows that the three elastic coefficients of the second governing equation are proportional to that of the third equation. In other words, the matrix composed of these nine coefficients tends to be singular. This may cause the instability of the solutions of **Eq. 1** since the determinant of the matrix will appear in the Christoffel equation of the compressional waves (Tuncay and Corapcioglu, 1997).

In this work, numerical examples are given to illustrate this phenomenon, and the corresponding mathematical proof of instability needs to be studied further. Generally, it is necessary to consider the influence of capillary forces in the study of wave propagation in porous media containing two fluids, which depends on the characteristics of the two fluids and the conditions. Therefore, the influence mechanisms of capillary forces on wave propagation need to be further studied, for example, to establish a new calculation method.

2.2 The Effective Fluid Model

The above analysis shows that this potential issue can be eliminated by combining the latter two governing equations. Hence, one solution is to reduce the number of equations from three to two by equivalent reduction of Tuncay and Corapcioglu's model. First, we review the derivation of the

constitutive relation for a porous medium with two immiscible fluids. Three relations were provided as follows (Tuncay and Corapcioglu, 1997):

1) The definition of the capillary force is as follows:

$$p_{cap} = p_{cap}(S_1) = \frac{\mathrm{d}p_{cap}}{\mathrm{d}S_1}\delta S_1 \tag{5}$$

Where δS_1 represents the disturbance to S_1.

2) The bulk deformation of the solid phase, which can be expressed as follows:

$$\nabla\cdot\overline{\mathbf{u}}^s = -(1-\phi)\frac{\left(\overline{p}_s - S_1\overline{p}_{f1} - (1-S_1)\overline{p}_{f2}\right)}{K_b} - \frac{S_1\overline{p}_{f1} + (1-S_1)\overline{p}_{f2}}{K_s} \tag{6}$$

Where $\overline{p}_s$, $\overline{p}_{f1}$ and $\overline{p}_{f2}$ are the pressures exerted on the solid and two fluids, respectively. The bar above each quantity indicates that it is obtained by averaging the volume of the microscopic quantity.

3) The volume variation relations of the representative element volume (REV) are calculated as follows:

$$-\alpha_j\overline{P}_j = \frac{1}{3}tr\left(\alpha_j\overline{\tau}_j\right) = K_j\left(\alpha_j\nabla\cdot\overline{\mathbf{u}}^j + \Delta\alpha_j\right) \tag{7}$$

Where $j = s, f1$ and $f2$ represents the relations for the solid and two fluids, respectively; α_j is the volume fraction; $\overline{P}_j$ is the effective stress of each phase; $\overline{\tau}_j$ is the stress tensor; K_j is the bulk modulus; and $\overline{u}^j$ is the macroscopic displacement of each phase.

The expressions of the solid and fluid pressure can be solved according to **Eqs. 5–7**. The constitutive equation is obtained, and the expressions of the elastic coefficients are also determined at the same time (Tuncay and Corapcioglu, 1996; Tuncay and Corapcioglu, 1997).

Then, an attempt to transform the two fluids into an equivalent fluid in a reasonable way is made. Based on the results of Pride et al. (2004), a special case is considered in which one fluid phase (noted as fluid 2) is completely wrapped by the other phase (noted as fluid 1). Specifically, fluid 2 has no contact the solid skeleton. This means that there is no interaction between fluid 2 and the solid phase, while fluid 1 is in contact with both fluid 2 and the solid skeleton, which resembles the model constructed by White (1975). The discontinuous interface of fluid pressure still exists, and therefore, capillary forces still exist. Compared with the conventional effective fluid model, the main advantage of this effective method is that it retains the nonuniform fluid pressure distribution in space; as a result, the wave equation contains two independent fluid pressures.

Furthermore, the wrapped fluid (fluid 2) is assumed to have no contact with the boundary of the REV selected by the volume averaging method. Thus, the deformation of fluid 2 does not affect the whole unit, and one can obtain $\nabla\cdot\overline{u}^{f2} = 0$. In this way, **Eq. 7** with $j = f2$, which represents the pressure of fluid 2, can be solved and expressed in terms of the related quantities. The resultant equation system can be listed as follows:

$$\begin{bmatrix} \frac{K_{f2}}{\phi} & \frac{\mathrm{d}p_{cap}}{\mathrm{d}S_1}+\frac{K_{f2}}{S_2} & 0 & -1 \\ \frac{(1-\phi)S_2K_{f2}}{\phi K_b}-\frac{S_2K_{f2}}{\phi K_s} & \frac{(1-\phi)K_{f2}}{K_b}-\frac{K_{f2}}{K_s} & -\frac{1-\phi}{K_b} & \frac{(1-\phi)S_1}{K_b}-\frac{S_1}{K_s} \\ -\frac{1}{1-\phi} & 0 & -\frac{1}{K_s} & 0 \\ \frac{1}{\phi} & -\frac{1}{S_1} & 0 & -\frac{1}{K_{f1}} \end{bmatrix} \begin{bmatrix} \delta(1-\phi) \\ \delta S_1 \\ \overline{P}_s \\ \overline{P}_{f1} \end{bmatrix} = \begin{bmatrix} 0 \\ \nabla\cdot\overline{\mathbf{u}}^s \\ \nabla\cdot\overline{\mathbf{u}}^s \\ \nabla\cdot\overline{\mathbf{u}}^{f1} \end{bmatrix} \tag{8}$$

The expressions of $\overline{P}_s$ and $\overline{P}_{f1}$ in terms of $\nabla\cdot\overline{u}^s$ and $\nabla\cdot\overline{u}^{f1}$ can be obtained by solving **Eq. 8**. Then, similar to Tuncay and Corapcioglu's definition (1997), one can obtain the following:

$$\begin{aligned} -(1-\phi)\overline{P}_s &= \tilde{a}_{11}\nabla\cdot\overline{\mathbf{u}}^s + \tilde{a}_{12}\nabla\cdot\overline{\mathbf{u}}^{f1} \\ -\phi S_1\overline{P}_{f1} &= \tilde{a}_{21}\nabla\cdot\overline{\mathbf{u}}^s + \tilde{a}_{22}\nabla\cdot\overline{\mathbf{u}}^{f1} \end{aligned} \tag{9}$$

The new elastic coefficients are denoted as $\tilde{a}_{ij}(i,j=1,2)$ with the following expressions:

$$\begin{aligned} \tilde{a}_{11}A_3 &= K_s\left[A_1(1-\phi)\left(K_{f1}A_2S_1 + K_{f1}K_{f2} + K_{f2}A_2S_2\right) + K_sK_b\phi\left(K_{f1}S_2 + K_{f2}S_1 + A_2\right)\right] \\ \tilde{a}_{12}A_3 &= K_sK_{f1}A_1S_1\phi\left(A_2 + K_{f2}\right) \\ \tilde{a}_{21} &= \tilde{a}_{12} \\ \tilde{a}_{22}A_3 &= K_{f1}S_1\phi\left[\phi K_s^2\left(K_{f2}S_1 + A_2\right) + K_{f2}A_2A_1S_2\right] \end{aligned} \tag{10}$$

where A_1, A_2 and A_3 are the same as **Eq. 3**.

Then, the constitutive relation of the effective fluid model is obtained as follows:

$$\begin{cases} \langle\boldsymbol{\sigma}\rangle = \left(\tilde{a}_{11}\nabla\cdot\overline{\mathbf{u}}^s + \tilde{a}_{12}\nabla\cdot\overline{\mathbf{u}}^f\right)\mathbf{I} + G\left(\nabla\overline{\mathbf{u}} + (\nabla\overline{\mathbf{u}})^{\mathrm{T}} - \frac{2}{3}(\nabla\cdot\overline{\mathbf{u}})\mathbf{I}\right) \\ \langle\mathbf{s}\rangle = \left(\tilde{a}_{21}\nabla\cdot\overline{\mathbf{u}}^s + \tilde{a}_{22}\nabla\cdot\overline{\mathbf{u}}^f\right)\mathbf{I} \end{cases} \tag{11}$$

where $\langle\boldsymbol{\sigma}\rangle$ and $\langle\mathbf{s}\rangle$ are the stress tensors of the solid and the effective fluid, respectively, and $\mathbf{I}$ is the unit tensor.

Note that in **Eq. 11**, $\overline{u}^f$ rather than $\overline{u}^{f1}$ is used to denote the displacement of the effective fluid. Here, the effective fluid means that only fluid 1 is needed when the interaction between solid and fluid is considered, while the parameters of fluid 2 are needed for the calculation of the coefficients in the constitutive relation.

It is easy to verify that the elastic constants $\tilde{a}_{ij}(i,j=1,2)$ in the constitutive relation of the effective fluid model are equal to those of **Eq. 2**. In the following text, the elastic constants are uniformly noted as $a_{ij}(i,j=1,2)$ for convenience.

Analogous to previous studies (De la Cruz and Spanos, 1985; Tuncay and Corapcioglu, 1997), the momentum conservation equation of a porous medium with an effective fluid can be expressed as follows:

$$\begin{cases} \langle\rho_s\rangle\ddot{\overline{\mathbf{u}}}^s = \nabla\cdot\langle\boldsymbol{\sigma}\rangle + \frac{\eta\phi^2}{\kappa}\left(\dot{\overline{\mathbf{u}}}^f - \dot{\overline{\mathbf{u}}}^s\right) \\ \langle\rho_f\rangle\ddot{\overline{\mathbf{u}}}^f = \nabla\cdot\langle\mathbf{s}\rangle + \frac{\eta\phi^2}{\kappa}\left(\dot{\overline{\mathbf{u}}}^f - \dot{\overline{\mathbf{u}}}^s\right) \end{cases} \tag{12}$$

where $\langle \rho_f \rangle = S_1 \langle \rho_{f2} \rangle + S_2 \langle \rho_{f2} \rangle$; $\eta = \eta_1 (\eta_2/\eta_1)^{S_1}$; and κ is the intrinsic permeability of the effective fluids.

The bars over $\overline{u}^s$ and $\overline{u}^f$ can be left out for simplicity. After combining **Eqs. 11**, **12**, the final wave equations of porous media saturated with effective fluid are obtained as follows

$$\begin{cases} \langle \rho_s \rangle \ddot{\mathbf{u}}^s = \nabla \left[a^*_{11} \nabla \cdot \mathbf{u}^s + a_{12} \nabla \cdot \mathbf{u}^f \right] + \nabla \cdot (G \nabla \mathbf{u}^s) + C\left(\dot{\mathbf{u}}^f - \dot{\mathbf{u}}^s\right) \\ \langle \rho_f \rangle \ddot{\mathbf{u}}^f = \nabla \left(a_{21} \nabla \cdot \mathbf{u}^s + a_{22} \nabla \cdot \mathbf{u}^f \right) - C\left(\dot{\mathbf{u}}^f - \dot{\mathbf{u}}^s\right) \end{cases} \tag{13}$$

where $C = \eta\phi^2/\kappa$.

Compared with **Eq. 1**, the proposed model **Eq. 13** is simpler in form since it includes only two governing equations. It is also easier to solve such equations. Although this model looks like that of the wave equations for a porous medium saturated with a single fluid, the expressions of the elastic coefficients are determined by two fluids. In addition, it is also similar to but different from Biot's equations (Biot, 1956; Biot, 1962) since there are no inertial terms of acceleration between the solid and fluid phases. Therefore, a relatively simple and stable wave equation structure is established, and a more complicated mechanism of wave propagation dissipation needs to be further proposed.

3 NUMERICAL EXAMPLES

Two sets of rock parameters are selected to verify the effectiveness and reliability of the improved model. The rock samples saturated with gas-water and oil-water are case 1 and case 2, respectively. Combined with the principle of plane wave analysis (Carcione, 2007), **Eqs. 1**, **13** are applied to calculate the attenuation and dispersion curves in these two cases. The detailed Christoffel equations for the compression and shear waves are given in the Appendix.

3.1 Porous Media Containing Gas and Water

A sample of Massillon sandstone (Tuncay and Corapcioglu, 1996) saturated with gas and water is selected for calculation. Here, fluid 1 is water and fluid 2 is air. The water saturation is denoted as S_w. The experimental parameters are shown in **Table 1**. Four water saturations (S_w = 0.1, 0.5, 0.8, and 0.9) are chosen for comparison. Under the parameters of **Table 1**, the value of A_2 according to **Eq. 3** is 326.56, which is two orders of magnitude smaller than K_{f2} and much smaller than K_s and K_{f1}. Therefore, the strengthening effect of the capillary forces on the elastic parameters is not significant and can be ignored reasonably.

The dispersion curves of the two compression waves (fast and slow P-wave) and the shear wave (S-wave) are shown in **Figure 1**. For the dispersion curve of the fast P-wave, both sets of wave equations produce similar results at different S_w values, as shown in **Figures 1A,B**. They both have close limits for high (>10^6 Hz) and low frequency (<10^4 Hz) range. Although each curve varies smoothly and presents an 'S' shape as a whole, it can be seen that the velocity curves resulting from the new model hold that in the intermediate frequency range; the greater the water saturation is, the lower the velocity. In contrast, there is no such consistency in the original model, and different characteristics occur in the intermediate-high frequency range. From previous work (Liu et al., 2015), it is known that the magnitude of velocity decreases with larger S_w values in the low-frequency band, and the variations in velocity increase as S_w increases. In addition, the velocity predictions of the fast P-wave by the Biot-Gassmann-Wood (BGW) model are 1,145.04 m/s, 1,150.34 m/s, 1,168.18 m/s, and 1,193.72 m/s, corresponding to the four saturations. They are basically consistent with the corresponding low-frequency limit values with different S_w values predicted by the two models. The predictions by the Biot-Gassmann-Hill (BGH) model are 1933.24 m/s, 1769.30 m/s, 1,461.24 m/s, and 1,239.29 m/s, corresponding to the four saturations, which are larger than the results predicted by the two models. This shows that the two models can obtain the velocities that are covered by two bounds; however, they still need to be improved further by introducing other physical mechanisms, such as local fluid flow.

For the dispersion curve of the slow P-wave, as shown in **Figures 1C,D**, one can see that the value of each curve is very small in the low-frequency band (<10^4 Hz) and then increases as the frequency increases, finally converging to a constant value in the high-frequency band. From **Figure 1C**, the higher the water saturation is, the larger the velocity will be, but they converge to the same value with increasing frequency. The results do not converge to the same value, as shown in **Figure 1D**. Different from the fast P-wave, the dispersion curves of the slow P-wave obtained by the two sets of equations are quite different compared with **Figures 1A,B**. This is because the number of governing equations is different, which leads to different mechanisms when slow P-wave propagation occurs in a porous medium. As we know that slow P-waves are not an elastic wave but rather a type of dissipative wave, its dispersion pattern differs from that of a fast P-wave. It should be noted that there is another type of slow P-wave for the solution of **Eq. 1**, while there is only one type of slow P-wave for **Eq. 8**, so the second type of slow P-wave is not shown here.

TABLE 1 | Parameters of Massillon sandstone containing air and water (Tuncay and Corapcioglu, 1996).

Parameter and unit	Symbol	Value
Bulk modulus of solid matrix, GPa	K_b	1.02
Bulk modulus of solid grain, GPa	K_s	35
Shear modulus of solid skeleton, GPa	G	1.44
Density of solid skeleton, kg/m^3	ρ_s	2,650
Density of water, kg/m^3	ρ_{f1}	997
Density of air, kg/m^3	ρ_{f2}	1.10
Bulk modulus of water, GPa	K_{f1}	2.25
Bulk modulus of air, MPa	K_{f2}	0.145
Viscosity of water, Pa·s	η_1	1×10^{-3}
Viscosity of air, Pa·s	η_2	1.8×10^{-5}
Porosity	φ	0.23
Intrinsic permeability, m^2	κ	9×10^{-13}
Fitting parameter	β	0.025
Fitting parameter	n	10

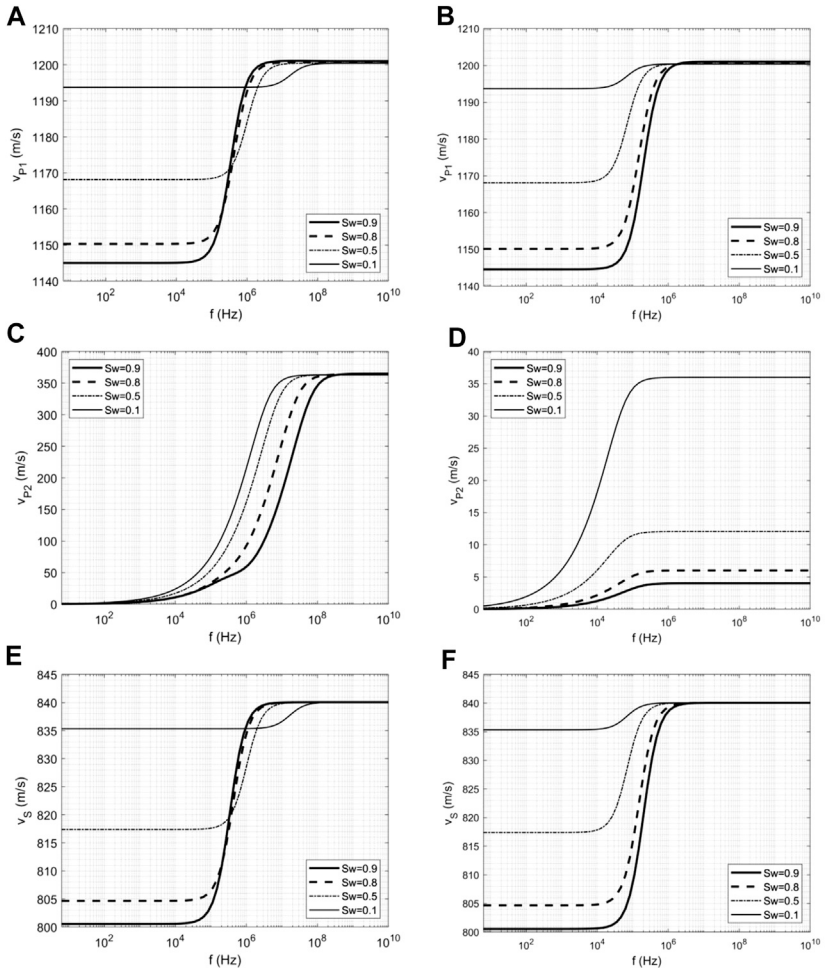

FIGURE 1 | The dispersion curve of seismic wave propagation in porous media containing gas and water: **(A,C,E)** are the dispersion curves of the fast P-wave, the slow P-wave and the S-wave corresponding to four saturations calculated by **Eq. 1**, respectively; **(B,D,F)** are those of dispersion curves by the improved model proposed in this work.

For the dispersion curve of the S-wave, as shown in **Figures 1E,F**, the results obtained by the two models are basically the same. The trend of the results is similar to that of the fast P-wave but with a lower magnitude.

According to the results of the fast P-wave and the S-wave under the sample condition, the results produced by the improved and original models are similar, especially within the frequency range of the seismic waves. This indicates that the original model developed by Tuncay and Corapcioglu can be replaced by the improved model proposed in this paper, and the improved model is simple in form and easier to solve. The velocity of the fast P-wave and S-wave vs. the water saturation were also calculated in their study (Tuncay and Corapcioglu, 1996), and the results matched well with the experimental data. We note that the predicted results of the improved model also match the experimental data well under the sample since one can obtain similar results as that of the original model.

The attenuation curves are shown in **Figure 2**. The attenuation curves of the fast P-wave and the S-wave resemble a downward parabola, and the maximum value is obtained at the frequency at which the velocity varies fastest in the corresponding dispersion curve. The attenuation curve of the fast P-wave is basically the same as that of the S-wave. In fact, the variation law of each attenuation curve can be roughly obtained from the dispersion curve. The two models have different trends in the low- and high-frequency bands. The frequency of the maximum attenuation is low for high S_w values according to the original model, while for the new model, the opposite is true. As mentioned above, the velocity variations produced by the original model are irregular. Therefore, it can be considered that the results of the new model are more realistic.

Slow P-waves are usually a type of diffusion wave with a strong attenuation, whose attenuation curve is different from other wave types. It can be seen from **Figures 2C,D** that for each S_w, the attenuation curve presents a horizontal line at low frequencies ($<10^4$ Hz). Then, this value gradually decreases linearly, and there is a smooth transition between the two lines. It should be noted from **Figure 2C** that the variation of the attenuation value for $S_w = 0.9$ is

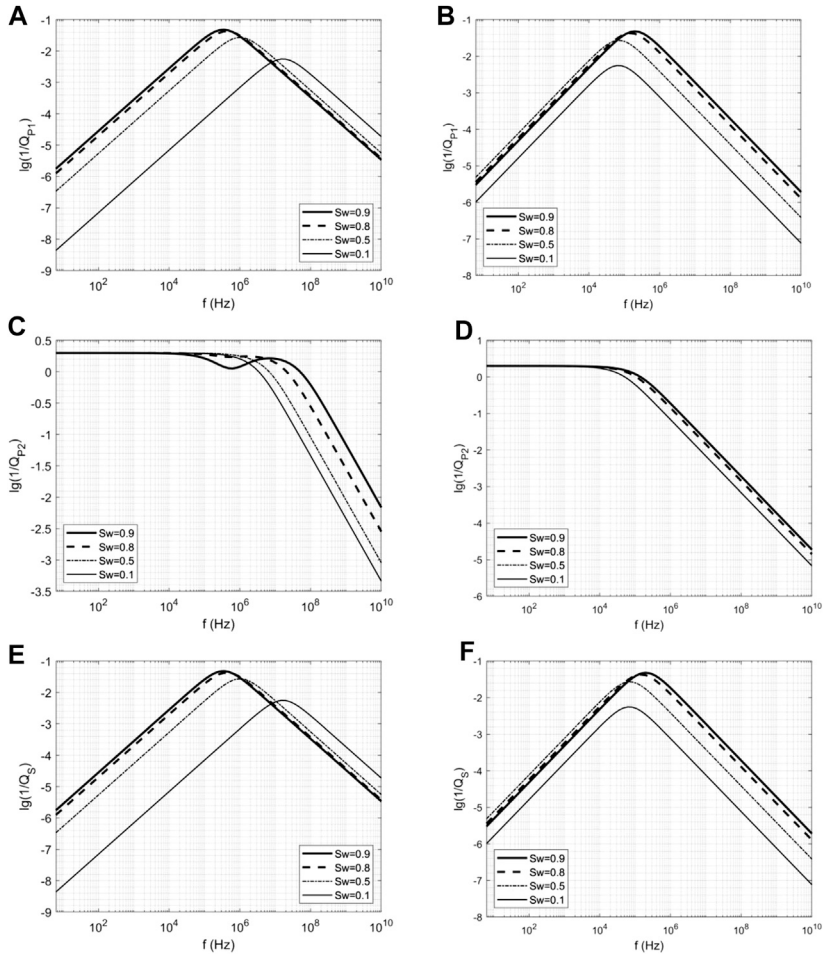

FIGURE 2 | The attenuation curve of seismic wave propagation in the porous media containing gas and water: **(A,C,E)** are the attenuation curves of the fast P-wave, the slow P-wave and the S-wave corresponding to four saturations calculated by **Eq. 1**, respectively; **(B,D,F)** are those of results by the improved model proposed in this work.

not a horizontal line like that of others in the intermediate frequency band (10^5–10^7 Hz). Correspondingly, it can be seen from **Figure 1C** that the dispersion curve at S_w = 0.9 does not resemble the other curves since a convex shape appears in the curve, which is believed to be caused by the instability of the model. The instability of the model makes the solution unstable with variable parameters such as frequency.

In this example, the attenuation curves obtained by the two models are smooth overall, which is consistent with the results of some traditional models (Biot, 1956; Biot, 1962; Santos et al., 1990a; Santos et al., 1990b; Pride and Berryman, 2003a; Pride and Berryman, 2003b).

3.2 Porous Media Containing Oil and Water

The differences in the physical properties of oil and water are less notable than that of gas and water. To further verify the applicability of the established model, a rock sample containing oil and water is taken from a Columbian sandy loam unit (Johnson, 2001; Lo et al., 2005). The rock parameters are shown in **Table 2**. In this example, the magnitude of the intermediate parameter A_2 is 10.488, which is much smaller than that of the former case. Therefore, it is more reasonable to ignore the strengthening effect of capillary forces on elastic parameters for porous media containing two liquids according to **Eq. 3**.

The results of the dispersion curves are shown in **Figure 3**. It shows the dispersion curves of the fast P-wave calculated by the two models. It can be seen that the curves corresponding to different saturations no longer have an 'S' shape when using the model developed by Tuncay and Corapcioglu. The value remains constant within the low- and middle-frequency ranges ($<10^6$ Hz) at various water saturations, while the curves are convex at approximately 10^7 Hz and then decrease gradually. This trend is somewhat surprising and differs from that of case 1. As shown in **Figure 3B**, the curves obtained by the improved model remain 'S' shaped, similar to that in the case of gas and water. In this case, the model is more unstable due to the smaller A_2 value. Therefore, the mathematical solution of the unstable model can no longer.

TABLE 2 | Parameters of Columbia loam containing oil and water (Johnson, 2001; Lo et al., 2005).

Parameter and unit	Symbol	Value
Bulk modulus of solid matrix, GPa	K_b	2.637
Bulk modulus of solid grain, GPa	K_s	35
Shear modulus of solid skeleton, GPa	G	1.74
Density of solid skeleton, kg/m^3	ρ_s	2,650
Density of water, kg/m^3	ρ_{f1}	997
Density of air, kg/m^3	ρ_{f2}	762
Bulk modulus of water, GPa	K_{f1}	2.25
Bulk modulus of air, GPa	K_{f2}	0.57
Viscosity of water, Pa·s	η_1	1×10^{-3}
Viscosity of air, Pa·s	η_2	1.44×10^{-3}
Porosity	φ	0.284
Intrinsic permeability, m^2	κ	1.0×10^{-13}
Fitting parameter	β	2.39
Fitting parameter	n	2.037

Represent the physical phenomenon correctly. It is difficult to obtain the velocity variation range of the results using the original model, and it is difficult to compare these results with those of the BGW and BGH models. In addition, the magnitude of the fast P-wave velocity in the former case is obviously lower than that resulting from the oil-water case as the physical properties of gas and oil are quite different, and the compressibility of oil is closer to that of water.

For the slow P-wave, as shown in **Figures 3C,D**, the trend of these results is similar to that of the previous example. However, it seems that the curve related to $S_w = 0.5$ in **Figure 3C** is not smooth enough. Note that the second type of slow P-wave in **Eq. 1** is not listed here.

Figures 3E,F show that the velocities of the S-waves corresponding to different saturations obtained by the two models are roughly the same. Differing from the fast P-wave,

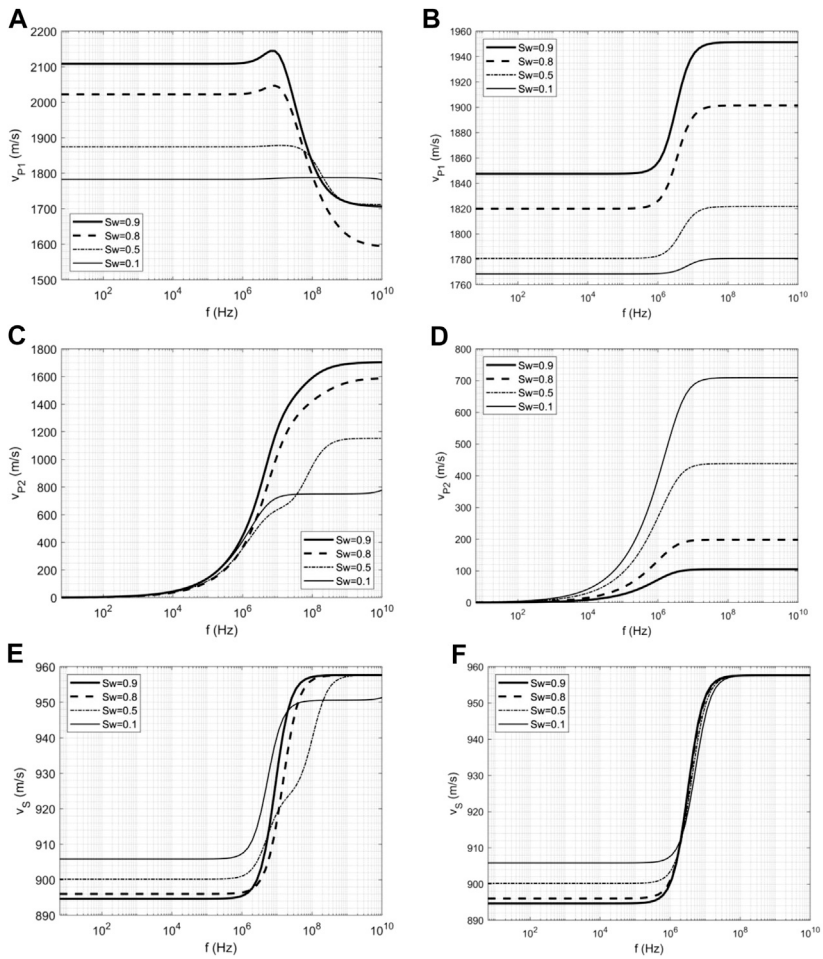

FIGURE 3 | The dispersion curve of seismic wave propagation in a porous media containing oil and water. **(A, C, E)** are the dispersion curves of the fast P-wave, theslow P-wave and the S-wave corresponding to four saturations calculated by **Eq. 1**, respectively; **(B, D, F)** are those of dispersion curves by the improved model proposed in this work.

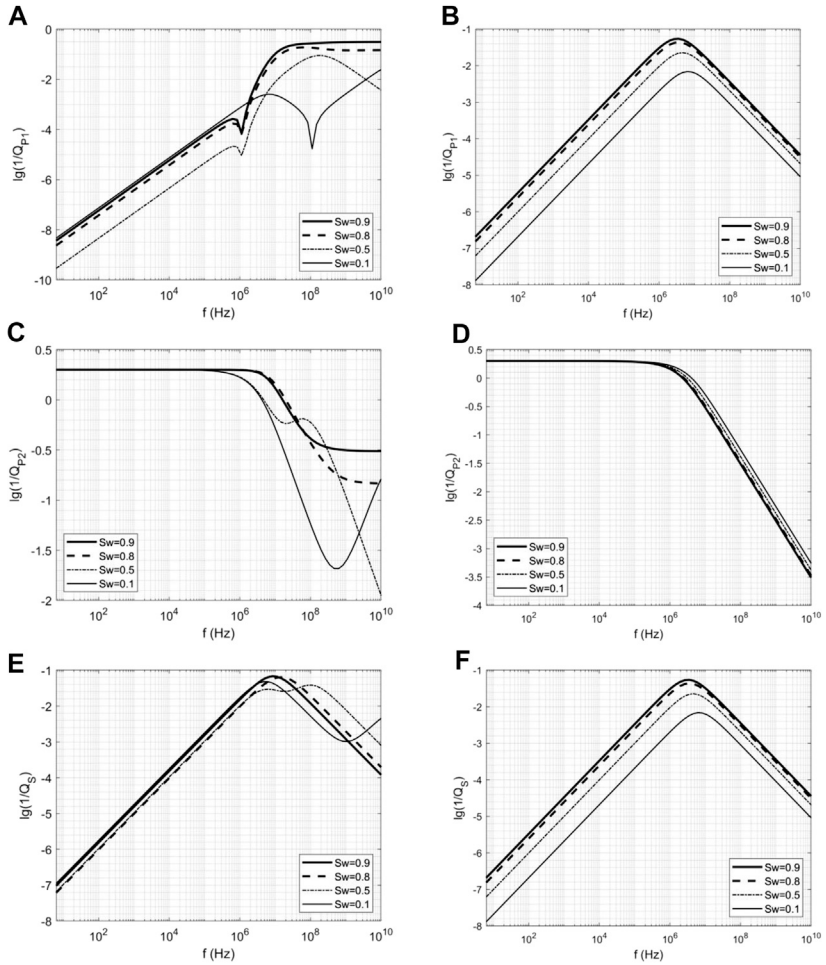

FIGURE 4 | The attenuation curve of seismic wave propagation in a porous medium containing oil and water. **(A, C, E)** are the attenuation curves of the fast P-wave, the slow P-wave and the S-wave corresponding to four saturations calculated by **Eq. 1**, respectively; **(B, D, F)** are those of results by the improved model proposed in this work.

the dispersion curves of the S-wave obtained by the two models are smooth. The corresponding curves are basically the same, but it can be seen from **Figure 3F** that the value tends to the same eventually while that is not the case in **Figure 3E**. This shows that the predictions output by the new model are close to those of the original model if its solutions are relatively stable.

The attenuation curve results are shown in **Figure 4**. It shows that the shape of the attenuation curve of the fast P-wave is very strange, which indicates that the model is unstable when predicting the attenuation of a porous medium containing oil and water. A smooth curve can still be obtained by the improved model, which suggests a stable solution. The attenuation value decreases with larger S_w values. **Figure 4C** shows that the value of the attenuation curve is unstable in the high-frequency band. The attenuation curve of the S-wave is relatively stable, which can also be seen from the dispersion curve. These results indicate that the original model may have deficiencies when predicting the attenuation of oil and water.

4 CONCLUSION

Theoretical analysis showed that the model developed by Tuncay and Corapcioglu based on the volume averaging method may be unstable since the structure of the wave equations may be problematic. In this work, an effective fluid model of wave propagation is proposed based on their study. The dispersion and attenuation curves calculated by the former are not smooth enough in the case of a porous medium saturated with oil and water. In contrast, the effective fluid model can obtain smooth dispersion and attenuation curves, which are consistent with the results of classical models. The stability of the two models from a mathematical perspective as well as the corresponding numerical simulations need to be further studied. In addition, the improved model alone may not be enough to describe the mechanisms of wave attenuation and dissipation. It is still worth noting that wave equations with a simple and stable structure is found by introducing an effective fluid.

Future studies will focus on three points. Firstly, wave equations that consider more interaction mechanisms between the two fluids need to be developed. Secondly, it is necessary to compare the theoretical calculation results with more experimental data to verify the validity of the new model. Finally, the effect of the geometric structure of porous media on wave propagation should be studied. For example, a porous medium with porous space consisting of interconnected microtubes can be selected as the REV, and the permeability and elastic constants of such a network can be calculated (Xiong et al., 2020). Alternatively, one can consider cracked porous media with penny-shaped inclusions (Zhang et al., 2019) as the REV. Then, it is possible to obtain wave equations that connect the microscopic details of a porous medium with macroscopic wave propagation by the volume averaging method.

DATA AVAILABILITY STATEMENT

The raw data supporting the conclusions of this article will be made available by the authors, without undue reservation.

AUTHOR CONTRIBUTIONS

FX completed the conceptualization, investigation, methodology, data curation, formal analysis, writing–original draft, writing–review & editing in the manuscript. JL completed the Idea generation, methodology, data curation, writing–original draft, writing–review & editing in this manuscript. ZG completed the funding acquisition, data curation, formal analysis, writing–review & editing, supervision in this manuscript. JL completed the funding acquisition, formal analysis, writing–review & editing, supervision in this manuscript.

FUNDING

This research is supported by the Natural Science Foundation of China (NSFC) (42074169; 41804073) and the Project of Innovation-driven Plan in Central South University (2020CX0012); The research also funded by Open Research Fund Program of Key Laboratory of Metallogenic Prediction of Nonferrous Metals and Geological Environment Monitoring (Central South University), Ministry of Education (Grant: 2020YSJS08).

REFERENCES

Anderson, T. B., and Jackson, R. (1967). A fluid mechanical description of fluidized beds. *Ind. Eng. Chem. Fund.* 6 (4), 527. doi:10.1021/i160024a007

Ba, J., Zhao, J., Carcione, J. M., and Huang, X. (2016). Compressional wave dispersion due to rock matrix stiffening by clay squirt flow. *Geophys. Res. Lett.* 43, 6186–6195. doi:10.1002/2016GL069312

Ba, J., Xu, W., Fu, L.-Y., Carcione, J. M., and Zhang, L. (2017). Rock anelasticity due to patchy saturation and fabric heterogeneity: a double double-porosity model of wave propagation. *J. Geophys. Res. Sol. Ea.* 122, 1949–1976. doi:10.1002/2016JB013882

Berryman, J. G. (1986). Effective media approximation for elastic constants of porous solids with microscopic heterogeneity. *J. Appl. Phys.* 59 (4), 1136–1140. doi:10.1063/1.336550

Berryman, J. G. (1988). Seismic-wave attenuation in fluid-saturated porous-media. *Pure Appl. Geophys.* 128, 423–432. doi:10.1007/978-3-0348-7722-0_21

Biot, M. A. (1956). Theory of propagation of elastic waves in a fluid-saturated porous solid .1. low-frequency range. *J. Acoust. Soc. Am.* 28 (2), 168–178. doi:10.1121/1.1908239

Biot, M. A. (1962). Mechanics of deformation and acoustic propagation in porous media. *J. Appl. Phys.* 33 (4), 1482–1498. doi:10.1063/1.1728759

Brutsaert, W., and Luthin, J. N. (1964). The velocity of sound in soils near the surface as a function of the moisture content. *J. Geophys. Res.* 69 (4), 643–652. doi:10.1029/JZ069i004p00643

Burridge, R., and Keller, J. B. (1981). Poroelasticity equations derived from microstructure. *J. Acoust. Soc. Am.* 70 (4), 1140–1146. doi:10.1121/1.386945

Carcione, J. M. (2007). *Wave fields in real media: wave propagation in anisotropic, anelastic, porous and electromagnetic media [M]*: Sgonico, Trieste, Italy: Elsevier.

De la Cruz, V., and Spanos, T. J. T. (1983). Mobilization of oil ganglia. *Aiche. J.* 29 (5), 854–858. doi:10.1002/aic.690290522

De la Cruz, V., and Spanos, T. J. T. (1985). Seismic wave propagation in a porous medium. *Geophysics* 50 (10), 1556–1565. doi:10.1190/1.1441846

Johnson, D. L. (2001). Theory of frequency dependent acoustics in patchy-saturated porous media. *J. Acoust. Soc. Am.* 110 (2), 682–694. doi:10.1121/1.1381021

Kobayashi, Y., and Mavko, G. (2016). Variation in P-wave modulus with frequency and water saturation: extension of dynamic-equivalent-media approach. *Geophysics* 81 (5), D479–D494. doi:10.1190/GEO2015-0045.1

Liu, J., Sun, W., and Ba, J. (2015). P-wave velocity prediction in porous medium with liquid-pocket patchy saturation. *Appl. Math. Mech. Engl.* 36 (11), 1427–1440. doi:10.1007/s10483-015-1993-7

Lo, W.-C., Sposito, G., and Majer, E. (2005). Wave propagation through elastic porous media containing two immiscible fluids. *Water Resour.* 41, W02025. doi:10.1029/2004WR003162

Lo, W.-C., Sposito, G., and Majer, E. (2007). Low-frequency dilatational wave propagation through unsaturated porous media containing two immiscible fluids. *Transp. Porous. Med.* 68, 91–105. doi:10.1007/s11242-006-9059-2

Lo, W.-C., Chao, L. Y., and Lee, J. W. (2015). Effect of viscous cross coupling between two immiscible fluids on elastic wave propagation and attenuation in unsaturated porous media, *Adv. Water Resour.* 83, 207–222. doi:10.1016/j.advwatres.2015.06.002

Müller, T. M., and Gurevich, B. (2015). Wave-induced fluid flow in random porous media: attenuation and dispersion of elastic waves. *J. Acoust. Soc. Am.* 117 (5), 2732–2741. doi:10.1121/1.1894792

Pride, S. R., and Berryman, J. G. (2003a). Linear dynamics of double-porosity dual-permeability materials. I. Governing equations and acoustic attenuation. *Phys. Rev. E Stat. Nonlin. Soft Matter Phys.* 68, 036603. doi:10.1103/PhysRevE.68.036603

Pride, S. R., and Berryman, J. G. (2003b). Linear dynamics of double-porosity dual-permeability materials. II. Fluid transport equations. *Phys. Rev. E Stat. Nonlin. Soft Matter Phys.* 68, 036604. doi:10.1103/PhysRevE.68.036604

Pride, S. R., Berryman, J. G., and Harris, J. M. (2004). Seismic attenuation due to wave-induced flow. *J. Geophys. Res. Sol. Ea.* 109 (B1), B01201. doi:10.1029/2003JB002639

Santos, J. E., Corbero, J. M., and Douglas, J. (1990a). Static and dynamic behavior of a porous solid saturated by a two-phase fluid. *J. Acoust. Soc. Am.* 87, 1428–1438. doi:10.1121/1.399439

Santos, J. E., Douglas, J., Corbero, J., and Lovera, O. M. (1990b). A model for wave-propagation in a porous-media saturated by a two-phase fluid. *J. Acoust. Soc. Am.* 87, 1439–1448. doi:10.1121/1.399440

Santos, J. E., Ravazzoli, C. L., Gauzellino, P. M., Carcione, J. M., and Cavallini, F. (2004). Simulation of waves in poro-viscoelastic rocks saturated by immiscible fluids. Numerical evidence of a second slow wave, *J. Comput. Acoust.* 12 (1), 1–21. doi:10.1142/S0218396X04002195

Santos, J. E., Savioli, G. B., Carcione, J. M., and Ba, J. (2019). Effect of capillarity and relative permeability on Q anisotropy of hydrocarbon source rocks. *Geophys. J. Int.* 218 (2), 1199–1209. doi:10.1093/gji/ggz217

Slattery, J. C. (1967). Flow of viscoelastic fluids through porous media. *Aiche. J.* 13 (6), 1066. doi:10.1021/i160023a012

Sun, W., Liu, J., Ba, J., and Cao, H. (2015). Theoretical models of elastic wave dispersion in porous media. *Prog. Geophys* 30 (2), 0586–0600. [in Chinese]. doi:10.6038/pg20150100

Tserkovnyak, Y., and Johnson, D. L. (2003). Capillary forces in the acoustics of patchy-saturated porous media: *J. Acoust. Soc. Am.* 114, 2596–2606. doi:10.1121/1.1621009

Tuncay, K., and Corapcioglu, M. Y. (1995). Effective stress principle for saturated fractured porous media. *Water Resour. Res.* 31 (12), 3103–3106. doi:10.1029/95WR02764

Tuncay, K., and Corapcioglu, M. Y. (1996). Body waves in poroelastic media saturated by two immiscible fluids. *J. Geophys. Res. Sol. Ea.* 101 (B11), 25149–25159. doi:10.1029/96JB02297

Tuncay, K., and Corapcioglu, M. Y. (1997). Wave propagation in poroelastic media saturated by two fluids. *J. Appl. Mech. T. ASME.* 64 (2), 313–320. doi:10.1115/1.2787309

Van Genuchten, M. T. (1980). A closed-form equation for predicting the hydraulic conductivity of unsaturated soils 1. *Soil sci. soc. Am. J.* 44 (5), 892–898. doi:10.2136/sssaj1980.03615995004400050002x

White, J. E. (1975). Computed seismic speeds and attenuation in rocks with partial gas saturation. *Geophysics* 40 (2), 224–232. doi:10.1190/1.1440520

Xiong, F., Sun, W., Ba, J., and Carcione, J. M. (2020). Effects of fluid rheology and pore connectivity on rock permeability based on a network model, *J. Geophys. Res. Sol. Ea.* 125 (3), e2019JB018857. doi:10.1029/2019JB018857

Zhang, L., Ba, J., Carcione, J. M., and Sun, W. (2019). Modeling wave propagation in cracked porous media with penny-shaped inclusions. *Geophysics* 84 (4), 1–11. doi:10.1190/GEO2018-0487.1

Conflict of Interest: The authors declare that the research was conducted in the absence of any commercial or financial relationships that could be construed as a potential conflict of interest.

Copyright © 2021 Xiong, Liu, Guo and Liu. This is an open-access article distributed under the terms of the Creative Commons Attribution License (CC BY). The use, distribution or reproduction in other forums is permitted, provided the original author(s) and the copyright owner(s) are credited and that the original publication in this journal is cited, in accordance with accepted academic practice. No use, distribution or reproduction is permitted which does not comply with these terms.

APPENDIX

The plane wave analysis method (Carcione, 2007) is used to solve **Eq. 1** to obtain the dispersion and attenuation results in Tuncay and Corapcioglu, 1996; Tuncay and Corapcioglu, 1997. Note k_P and k_S are the complex wavenumber of the compressional waves and shear wave, respectively. The Christoffel equation for compressional waves is as follows:

The coefficients of Eq. A1 are given as

$$Z_1 X_P^3 + Z_2 X_P^2 + Z_3 X_P^3 + Z_4 = 0 \tag{A1}$$

$$Z_1 = \frac{C_1 C_2\left(\langle\rho_s\rangle + \langle\rho_{f1}\rangle + \langle\rho_{f2}\rangle\right) - \langle\rho_s\rangle\langle\rho_{f1}\rangle\langle\rho_{f2}\rangle\omega^2}{\omega^2} - \sqrt{-1}\ \frac{C_2\langle\rho_{f1}\rangle\left(\langle\rho_s\rangle + \langle\rho_{f2}\rangle\right) + C_1\langle\rho_{f2}\rangle\left(\langle\rho_s\rangle + \langle\rho_{f1}\rangle\right)}{\omega} \tag{A2}$$

$$Z_2 = -\frac{a'_{11}\left(C_1 C_2 - \langle\rho_{f1}\rangle\langle\rho_{f2}\rangle\omega^2\right) + 2C_1 C_2\left(a_{12} + a_{13} + a_{23}\right) + a_{22}\left(C_1 C_2 - \langle\rho_s\rangle\langle\rho_{f2}\rangle\omega^2\right) + a_{33}\left(C_1 C_2 - \langle\rho_s\rangle\langle\rho_{f1}\rangle\omega^2\right)}{\omega^2} +$$
$$\sqrt{-1}\ \frac{a'_{11}\left(C_2\langle\rho_{f1}\rangle + C_1\langle\rho_{f2}\rangle\right) + 2a_{12}C_1\langle\rho_{f2}\rangle + 2a_{13}C_2\langle\rho_{f1}\rangle + a_{22}\left(C_2\left(\langle\rho_s\rangle + \langle\rho_{f2}\rangle\right) + C_1\langle\rho_{f2}\rangle\right) + a_{33}\left(C_2\langle\rho_{f1}\rangle + C_1\left(\langle\rho_s\rangle + \langle\rho_{f1}\rangle\right)\right)}{\omega} \tag{A3}$$

$$Z_3 = -\frac{a'_{11}\left(a_{22}\langle\rho_{f2}\rangle + a_{33}\langle\rho_{f1}\rangle\right) - a_{12}^2\langle\rho_{f2}\rangle - a_{13}^2\langle\rho_{f1}\rangle + \langle\rho_s\rangle\left(a_{22}a_{33} - a_{23}^2\right)}{\omega^2}$$
$$- \sqrt{-1}\ \frac{a'_{11}\left(a_{22}C_2 + a_{33}C_1\right) - a_{12}^2 C_2 - 2a_{12}\left(a_{23}C_2 - a_{33}C_1\right) - a_{13}^2 C_1 + 2a_{13}\left(a_{22}C_2 - a_{23}C_1\right) + \left(C_1 + C_2\right)\left(a_{22}a_{33} - a_{23}^2\right)}{\omega} \tag{A4}$$

$$Z_4 = a'_{11}\left(a_{22}a_{33} - a_{23}^2\right) - a_{12}^2 a_{33} + a_{13}\left(2a_{12}a_{23} - a_{13}a_{22}\right) \tag{A5}$$

where $X_P = \omega^2/k_P^2$ and $a'_{11} = a_{11} + \frac{4}{3}G$. The meaning of each symbol is the same as above.

The Christoffel equation for the shear wave is

$$X_S^2\left(Y_1 X_S + Y_2\right) = 0 \tag{A6}$$

The coefficients of Eq. A6 are given as

$$Y_1 = \frac{C_1 C_2\left(\langle\rho_s\rangle + \langle\rho_{f1}\rangle + \langle\rho_{f2}\rangle\right) - \langle\rho_s\rangle\langle\rho_{f1}\rangle\langle\rho_{f2}\rangle\omega^2}{\omega^2} - \sqrt{-1}\ \frac{C_2\langle\rho_{f1}\rangle\left(\langle\rho_s + \langle\rho_{f2}\rangle\right) + C_1\langle\rho_{f2}\rangle\left(\langle\rho_s\rangle + \langle\rho_{f1}\rangle\right)}{\omega} \tag{A7}$$

$$Y_2 = -\frac{G\left(C_1 C_2 - \langle\rho_{f1}\rangle\langle\rho_{f2}\rangle\omega^2\right)}{\omega^2} + \sqrt{-1}\ \frac{G\left(C_2\langle\rho_{f1}\rangle + C_1\langle\rho_{f2}\rangle\right)}{\omega} \tag{A8}$$

where $X_S = \omega^2/k_S^2$.

The Christoffel equation of the improved model is also given here, they are

$$\tilde{Z}_1 X_P^2 + \tilde{Z}_2 X_P + \tilde{Z}_3 = 0 \tag{A9}$$

$$\tilde{Y}_1 X_S + \tilde{Y}_2 = 0 \tag{A10}$$

with

$$\tilde{Z}_1 = \left(\langle\rho_s\rangle + \frac{\sqrt{-1}C}{\omega}\right)\left(\langle\rho_f\rangle + \frac{\sqrt{-1}C}{\omega}\right) + \frac{C^2}{\omega^2} \tag{A11}$$

$$\tilde{Z}_2 = -a'_{11}\langle\rho_f\rangle - a_{22}\langle\rho_s\rangle - \frac{\sqrt{-1}C\left(a'_{11} + a_{12} + a_{21} + a_{22}\right)}{\omega} \tag{A12}$$

$$\tilde{Z}_3 = a'_{11}a_{22} - a_{12}a_{21} \tag{A13}$$

and

$$\tilde{Y}_1 = \langle\rho_s\rangle\langle\rho_f\rangle - \frac{\sqrt{-1}C}{\omega}\left(\langle\rho_s\rangle + \langle\rho_f\rangle\right) \tag{A14}$$

$$\tilde{Y}_2 = -\left(\frac{\sqrt{-1}C}{\omega} - \langle\rho_f\rangle\right)G \tag{A15}$$

The velocity and inverse quality factor of seismic waves are calculated as follows (Carcione, 2007):

$$v_P = \left[\mathrm{Re}\left(1/\sqrt{X_P}\right)\right]^{-1},\ \ v_S = \left[\mathrm{Re}\left(1/\sqrt{X_S}\right)\right]^{-1}, \tag{A16}$$

$$Q_P^{-1} = \frac{2\mathrm{Im}\left(v_P\right)}{\mathrm{Re}\left(v_P\right)},\ \ Q_S^{-1} = \frac{2\mathrm{Im}\left(v_S\right)}{\mathrm{Re}\left(v_S\right)}. \tag{A17}$$

frontiers in Earth Science

ORIGINAL RESEARCH
published: 11 March 2021
doi: 10.3389/feart.2021.654205

A Laboratory Forced-Oscillation Apparatus for Measurements of Elastic and Anelastic Properties of Rocks at Seismic Frequencies

Vassily Mikhaltsevitch[1], Maxim Lebedev[1], Rafael Chavez[2], Euripedes A. Vargas Jr.[2] and Guilherme F. Vasquez[3]*

[1] Exploration Geophysics, Curtin University, Perth, WA, Australia, [2] Department of Civil Engineering, Pontifical Catholic University of Rio de Janeiro, Rio de Janeiro, Brazil, [3] Rock Seismic Profile Integration, Petrobras, Rio de Janeiro, Brazil

OPEN ACCESS

Edited by:
Erik H. Saenger, Bochum University of Applied Sciences, Germany

Reviewed by:
Samuel Chapman, École Normale Supérieure, France
Jerome Fortin, UMR 8538 Laboratoire de Géologie de l'Ecole Normale Supérieure (LG-ENS), France

***Correspondence:**
Vassily Mikhaltsevitch
V.Mikhaltsevitch@cuerin.edu.au;
V.Mikhaltsevitch@curtin.edu.au

Specialty section:
This article was submitted to Solid Earth Geophysics, a section of the journal Frontiers in Earth Science

Received: *15 January 2021*
Accepted: *22 February 2021*
Published: *11 March 2021*

Citation:
Mikhaltsevitch V, Lebedev M, Chavez R, Vargas EA Jr and Vasquez GF (2021) A Laboratory Forced-Oscillation Apparatus for Measurements of Elastic and Anelastic Properties of Rocks at Seismic Frequencies. Front. Earth Sci. 9:654205. doi: 10.3389/feart.2021.654205

In presented paper, we describe the technical and physical aspects of the application of a low-frequency (LF) apparatus based on a longitudinal type of forced oscillations. In particular, we investigate the influence of the strain gauge position on a tested sample on measurement results, we also examine the creep effect associated with the mineralogy of rocks, as well as the dispersion and attenuation in a liquid-saturated rock sample caused by the presence of the volume of pore fluid exterior to the sample (dead volume). The effect of the position of the strain gauges is investigated using a cylindrical acrylic sample and two pairs of strain gauges fixed in the middle and at one of the sample ends under a uniaxial pressure of 15 MPa. The obtained results demonstrate that elastic and anelastic parameters of the tested sample are independent from the location of the strain gauges. The impact of the creep phenomenon on elastic moduli was studied using three room-dry samples of Savonnieres limestone, Berea sandstone and Eagle Ford shale. The measurements were conducted for 120 h at a frequency of 2 Hz under a uniaxial pressure of 10 MPa and demonstrated that the LF moduli of all rocks were noticeably reduced with time. The effect of dead volume was investigated at seismic frequencies using limestone saturated with n-decane. It was found that the Young's and bulk moduli exhibit strong dispersion at frequencies above 10 Hz if the dead volume is close to or greater than the pore volume of the sample. We also found that the characteristic frequency of dispersion corresponding to the attenuation peak is independent of the size of the dead volume and determined only by the physical parameters of the sample and pore fluid. We present also the results of the Young's modulus and attenuation measurements conducted at seismic frequencies on vertical and horizontal shale samples saturated with water. It was shown that the relationship between the extensional attenuation and the Young's modulus dispersion observed in the samples saturated at a relative humidity of 97.5% is consistent with the Kramers–Kronig relation.

Keywords: forced-oscillation, apparatus, elastic, attenuation, rock physics

INTRODUCTION

In the past decades, a variety of forced-oscillation (FO) methods have been employed to measure the mechanical properties of rocks, in which dissipated energy is characterized by a phase lag between stress and strain. The upper frequency of the FO methods, generally covering the frequency range from 10^{-5} to 100 Hz, is limited by spurious acoustic resonances in the tested sample or in the mechanical parts of the instrument (D'Anna and Benoit, 1990; Lakes, 2004).

The first FO measurements of the intrinsic attenuation and elastic parameters of rocks were performed by Bruckshaw and Mahanta (1961); Peselnick and Outerbridge (1961), and Usher (1962). Bruckshaw, Mahanta and Usher developed à forced vibration method where the Young's modulus of a specimen is estimated by measuring the magnitude of vibration for an exciting sinusoidal force at a frequency much less than the resonant frequency of the measurement system, and the attenuation is determined as the phase shift (loss angle) between the specimen vibrations and the applied force. Peselnick and Outerbridge (1961) designed a torsion pendulum, where a tested specimen is submitted to a harmonic torque at frequencies of 1 to 10 Hz, that enables measurements of attenuation and shear moduli of coherent rocks. Bruckshaw and Mahanta (1961) observed an increase of 2% in the Young's modulus of various dry rocks at frequencies between 40 and 120 Hz. A similar result for dry sedimentary and igneous rocks was obtained by Usher (1962) at the frequency range from 2 to 40 Hz. Usher also observed a decrease in the Young's modulus of the rocks containing moisture, accompanied by a large increase in attenuation with frequency. Peselnick and Outerbridge (1961) combined attenuation data for dry Solnhofen limestone obtained using the torsional pendulum (4–10 Hz) and a bar resonance setting (10 kHz) with the results of the ultrasonic attenuation measurements (10 MHz) of Peselnick and Zietz (1959) conducted on the same sample. They found that the shear internal friction in the dry limestone increases fivefold with an increase of frequency from 4 to 10 MHz, while the shear modulus remains constant.

In all first FO experiments the amplitude of strains in rocks was not controlled. Later in a number of studies (Gordon and Davis, 1968; Mavko, 1979; Winkler et al., 1979), it has been reported that frictional attenuation in rocks depends on strain amplitude but it becomes strain-independent for amplitudes $<10^{-6}$, which more adequately represent seismic-wave strains in real fields. Therefore, to meet the reservoir conditions, laboratory measurements should be performed with strains below 10^{-6}.

Another requirement, which should be taken into account when constructing an FO device, is related to the boundary conditions. As was shown by Dunn (1986) and White (1986) in their analysis of the experiments carried out by Spencer (1981), the attenuation in a fluid-saturated rock sample with open boundaries can stem from radial fluid flow due to the pressure difference between the central and peripheral parts of the sample (the Biot–Gardner effect). Hence, to avoid the distortion of the attenuation associated with intrinsic absorption mechanisms by the Biot–Gardner effect, the boundaries of the tested samples have to be closed with the membrane impenetrable for fluids and sealed by the confining pressure which has to be higher than the pore pressure in the sample.

The low-frequency (LF) laboratory tests that have been considerably developed in recent decades, utilize a stress-strain relationship and differ by the type of the forced oscillations applied to a specimen under investigation: torsional (Jackson and Paterson, 1987; Paffenholz and Burkhardt, 1989; Nakagawa, 2013; Saltiel et al., 2017), longitudinal (Spencer, 1981; Paffenholz and Burkhardt, 1989; Batzle et al., 2006; Takei et al., 2011), and volumetric (Adelinet et al., 2010). However, the devices based on torsional types of oscillations are not capable to measure the complete set of elastic properties of rocks.

The FO laboratory apparatuses, which are capable of measuring the complete set of elastic moduli, such as Young's, bulk and shear moduli, and also satisfy the strain-amplitude and boundary conditions, were designed by Spencer et al. (1994); Batzle et al. (2006), Mikhaltsevitch et al. (2014); Pimienta et al. (2015), Szewczyk et al. (2016); Sun et al. (2018), and Borgomano et al. (2020).

In the devices proposed by Spencer et al. (1994); Batzle et al. (2006) and Sun et al. (2018) the hydrostatic confining pressure is exerted by pressurized nitrogen gas. An axial periodical dynamic force is applied to the sample by an electromechanical shaker at a frequency of 0.2–155 Hz (Spencer et al., 1994), 5 Hz–2 kHz (Batzle et al., 2006), or 1 Hz–2 kHz (Sun et al., 2018). Since the shaker is unable to operate under high load, the entire device, including the jacketed rock sample with two strain gauges (Batzle et al., 2006) or capacitive displacement transducers (Spencer et al., 1994) to measure axial and radial strains, is mounted inside a gas pressure vessel. This design creates significant limitations on the dimensions of mechanical assembly of the device. The insufficient mass of the mechanical assembly is a source of spurious resonances (Batzle et al., 2006; Sun et al., 2019).

Another FO laboratory apparatus with the longitudinal type of the forced oscillations and hydraulic oil as a confining-pressure medium was built at the Department of Exploration Geophysics of Curtin University and at the Department of Civil Engineering of Pontifical Catholic University of Rio de Janeiro (Mikhaltsevitch et al., 2014). The apparatus operates at seismic frequencies and measures Poisson ratio and Young modulus by comparing the strains in a rock and in a standard with well-known parameters. The dynamic strains generated in the rock by a piezoelectric actuator do not exceed 10^{-6}. The extensional attenuation is measured as a phase lag between the phases of the applied stress and strain in the sample.

The setups reported by Pimienta et al. (2015) and Szewczyk et al. (2016) are conceptually similar in design to the devices presented by Spencer et al. (1994) and Batzle et al. (2006). A few modifications in the instrument proposed by Pimienta et al. (2015) and Szewczyk et al. (2016) include the replacement of the medium for confining pressure by hydraulic oil and using a piezoelectric actuator instead of an electromechanical shaker. The setup described by Pimienta et al. (2015) is built on the basis of the apparatus presented earlier by Adelinet et al. (2010) and allows to measure bulk modulus using oscillations of the confining pressure at teleseismic frequencies (0.01–0.1 Hz). An upgraded version of this setup reported by

Borgomano et al. (2020) is able to measure the complex bulk modulus up to 1 Hz, and Young's modulus and Poisson ratio up to 1 kHz at temperatures of 20–100°C.

The widespread use of LF measurements of elastic and inelastic properties of rocks based on the FO method in laboratory research has led to the need to summarize the special features of such measurements. Due to certain differences in the utilized techniques underlying various LF apparatuses based on different aspects of the general FO method, and also in medium used to create confining pressure, such generalizations, apparently, should be carried out for each technique separately. In this paper, we describe the technical and physical peculiarities of the application of a LF apparatus based on a longitudinal type of forced oscillations and using a liquid (hydraulic oil) to create confining pressure. In particular, we investigate the influence of the position of the strain gauges on the measurement results, the creep effect associated with the mineralogy of the sample, as well as the dispersion and attenuation in a liquid-saturated sample caused by the presence of the so-called dead volume, i.e., the volume formed by the parts of the fluid line adjoined to both ends of the sample. The effect of the position of the strain gauges was investigated on a 15 cm length cylindrical acrylic sample using two pairs of strain gauges fixed in the middle and at 2 cm from one of the sample ends under an axial pressure of 15 MPa. The impact of the creep phenomenon on elastic moduli was studied using three sedimentary rocks represented by three room-dry samples of Savonnieres limestone, Berea sandstone and Eagle Ford shale. The LF measurements were conducted for 120 h at frequencies of 0.1–120 Hz under a uniaxial pressure of 10 MPa and demonstrated that the moduli of all rocks were reduced with time, upon that the largest reduction was observed in Eagle Ford shale, where the bulk and shear moduli were decreased by 12 and 8%, correspondingly. Furthermore, we present the results of the measurements of the transversely isotropic Young's moduli and extensional attenuation obtained for two Wellington shale samples as a function of water saturation at frequencies between 0.1 and 100 Hz. The samples were cored along vertical and horizontal directions with respect to the formation bedding and saturated with water at four values of relative humidity ranging from 12 to 97.5%. Peaks of attenuation were found for both samples at relative humidity of 97.5% Hz. Our analysis demonstrates the applicability of the Kramers–Kronig relations for the quantitative analysis of the relationship between the extensional attenuation and the transversely isotropic Young's moduli of Wellington shale.

EXPERIMENTAL FORCED-OSCILLATION SETUP

The mechanical assembly of the experimental setup is presented in **Figure 1**. The assembly comprises the frame formed by two steel platforms, four poles connecting and supporting the platforms, and a column of units located in the center of the frame (the total mass of the frame is 650 kg). The column is formed by hydraulic and piezoelectric actuators, a Hoek's triaxial cell, an aluminum standard, a rock sample mounted inside an elastomer sleeve and placed in a Hoek's cell and two plugs with passages for pore fluid (**Figure 1**). The Hoek's cell and the hydraulic actuator are connected with two manual hydraulic pumps, which provide lateral and longitudinal static forces applied to the sample. The dynamic stress applied to the rock sample by the

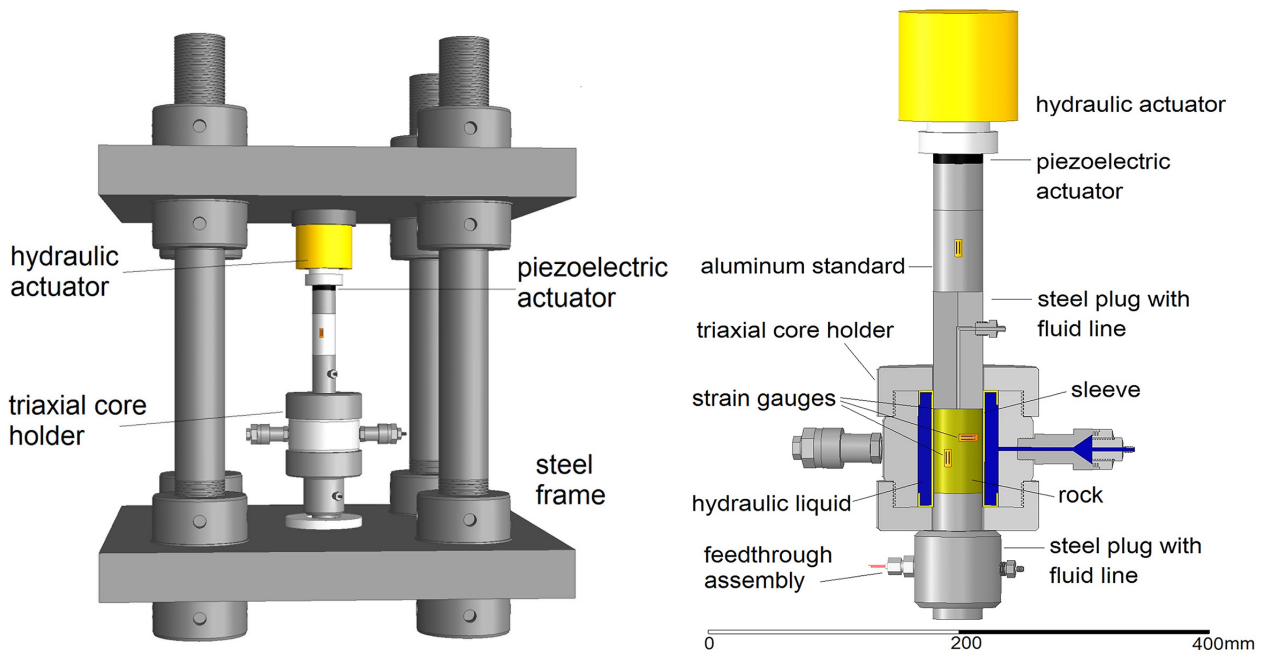

FIGURE 1 | The seismic frequency laboratory rig.

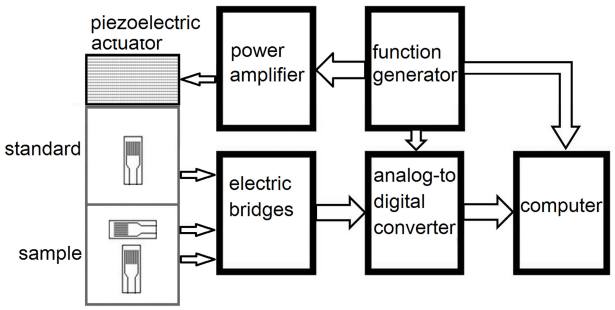

FIGURE 2 | The electrical schematics of the seismic frequency laboratory apparatus.

piezoelectric actuator and strains in the rock are controlled by three semiconductor strain gauges (type KSP-6-350-E4, Kyowa Ltd). One gauge attached to the aluminum standard is oriented in the axial direction and the other two, attached to the sample, are orientated to measure radial and axial strains. All strain gauges are connected with electric bridges (BCM-1 Wheatstone Bridge, Omega Engineering) via a feedthrough assembly.

The electrical schematic of the apparatus is presented in **Figure 2**. The periodic voltage of a generator is converted by the piezoelectric actuator into mechanical stress, which induces displacements in the standard and the rock. The displacements modulate the resistance of the strain gauges. The electric bridges transform the modulated resistance into electric signals, which are digitized by an analog to-digital converter (model 100, InstruNet, Omega Engineering) and then averaged and processed in a data acquisition computer. The extensional attenuation is found as the phase delay between the dynamic stress and the strain in the rock.

METHOD AND OPERATION

Measurements are performed using the stress-strain technique developed by Spencer (1981); Paffenholz and Burkhardt (1989), and Batzle et al. (2006). Our approach is outlined below in more detail.

The Young's modulus E of the rock sample is obtained as

$$E = -E_{st}\frac{\varepsilon_{st}}{\varepsilon_{ax}}, \tag{1}$$

where ε_{st} and ε_{ax} are the axial strains measured on the standard and rock sample, correspondingly, E_{st} is the known Young's modulus of the standard.

The Poisson ratio ν is found using the relation

$$\nu = -\frac{\varepsilon_{rad}}{\varepsilon_{ax}}, \tag{2}$$

where ε_{rad} is the radial strain in the rock. For isotropic rocks, the bulk K and shear μ moduli of the sample can be found as

$$K = \frac{E}{3(1-2\nu)}, \quad \mu = \frac{E}{2(1+\nu)}, \tag{3}$$

P- and S-velocities are given by

$$V_P = \sqrt{\frac{(K+4\mu/3}{\rho}}, \quad V_S = \sqrt{\frac{\mu}{\rho}}, \tag{4}$$

where ρ is the rock density.

To derive the relationship for the extensional attenuation Q_E^{-1} related to internal frictions in the rock, let us consider the viscoelastic material with the complex Young's modulus E equal to

$$E = \frac{\sigma}{\varepsilon} = E_0(\cos\phi + i\sin\phi), \tag{5}$$

where E_0 is the absolute value of the Young's modulus, ϕ is the phase angle between the stress applied to the sample and the strains in the sample (loss angle), σ is the applied stress. Assuming that the loss angle in aluminum is negligible, the Eq. 5 can be rewritten as

$$E = \frac{E_{st}\varepsilon_{st}}{\varepsilon} = E_0(\cos\phi + i\sin\phi), \tag{6}$$

where $E_0 = E_{st}\varepsilon_{st}/\varepsilon_0$, $\varepsilon = \varepsilon_0\exp(-i\phi)$ is the complex amplitude of the strain in the rock, ε_{st} and ε_0 are the absolute values of the axial strain amplitudes in the standard and rock sample, respectively.

Thus, the extensional attenuation Q_E^{-1} can be presented as

$$Q_E^{-1} = \frac{Im(E)}{Re(E)} = -\frac{Im(\varepsilon)}{Re(\varepsilon)} = \tan\phi. \tag{7}$$

The phase angle ϕ can be found as the phase difference between the strains in the aluminum standard and in the sample.

The uncertainty of the phase measurements in our experiments is ± 0.003 rad.

EFFECT OF THE STRAIN GAUGE POSITION ON MEASUREMENTS

In a FO laboratory apparatus, a sample to be measured, which is usually cylindrical, is placed between metal plugs under high static pressure. Presumably, due to the cohesion between the sample and plug ends under applied pressure, the measured specimen can be deformed non-uniformly along its axis, resulting in a "barrel" geometry (**Figure 3**). In this study, we investigate the "barrel shape" effect using a cylindrical viscoelastic sample of a 15 cm length (acrylic material ASTM-D-5436, Spartech Townsend). To enhance the effect, the ends of the sample were glued to the adjacent metal plugs and only axial pressure was applied in this experiment. The measurement tests were carried out at a uniaxial pressure of 15 MPa. Two pairs of semiconductor strain gauges were attached to the sample, one of which was glued in the middle of the sample, and the other at a distance of two centimeters from one of the ends, and one strain gauge was glued on the standard. The strain gauges of each pair attached to the sample are orientated to measure axial and radial strains.

The results of the direct measurements of the Young's modulus and Poisson ratio are presented in **Figure 4**. The

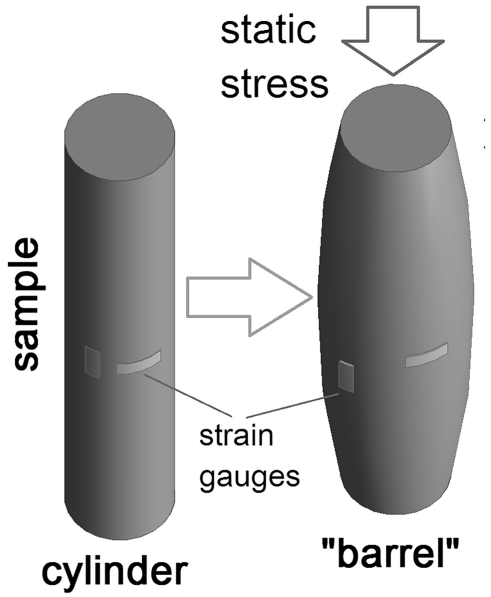

FIGURE 3 | The "barrel" effect under uniaxial static pressure.

bulk and shear moduli calculated using Eq. 3 and the value of extensional attenuation Q_E^{-1} derived from the phase difference between the strains in the sample and the standard in accordance with Eq. 7 are shown in **Figure 5**. The error bars for the moduli estimates were computed in accordance with the uncertainty analysis procedure elaborated for LF stress-strain measurements in Adam et al. (2009).

As can be seen from **Figures 4**, **5**, the results of the measurements are not affected by the position of the strain gauges.

Therefore, we can conclude that the location of the strain gauges on the sample does not affect the results of the LF experiment. Also note that the results of the attenuation measurements demonstrate that the extensional attenuation is also independent of the position of the strain gauges.

The results of our study demonstrate that elastic and anelastic parameters of a cylindrical solid sample made of a relatively soft material such as acrylic are independent of the location of the strain gauges on the sample. However, it should be noted that, as shown by Sun et al. (2020), in the case of fluid-saturated rock samples, the measurement results can be dependent on the position of the strain gauges due to local squirt flow.

CREEP EFFECT IN LOW-FREQUENCY EXPERIMENTS

The time-delayed deformation under constant stress, or the creep effect, is one of the most fundamental properties of sedimentary rocks. The creep effect, which originates from viscoelastic properties of the solid framework of a rock, has been extensively studied in recent decades [see, e.g., Lexcellent (2018)]. A significant portion of the experimental techniques developed for the laboratory study of the creep effect is focused on the static and quasi-static aspects of the viscoelastic behavior of a rock (Brantut et al., 2013). However, the influence of the creep effect on the results of LF laboratory measurements of elastic moduli of rocks has not been pursued in detail in rock physics research. As was noted by Takei et al. (2011), the LF methods are sensitive to the contact conditions between a tested rock and surrounding metal plugs, which to a considerable degree depend on the creep properties of the rock. Takei et al. (2011) found that nearly perfect contact for plastic materials can be achieved after a plastic sample experiences a few days of creep under a stress to minimize dislocations. It can be also noted that taking into account the creep effect is important for comparing the results of LF measurements with the results of ultrasonic tests. The latter usually last no longer than a few hours, while LF experiments take in general several days, and therefore creep drifts can have a significant effect on the difference in the measured values of the elastic properties of rocks. Since the LF techniques become common practices in many rock physics laboratories (Subramaniyan et al., 2014; Ògúnsànmì et al., 2020), the influence of the creep effect on the results of the LF measurements becomes an important object of research.

In this section, we present the results of our experimental study conducted on three sedimentary rocks, Savonnieres limestone, Berea sandstone and Eagle Ford shale, at a seismic frequency of 2 Hz, which demonstrate that viscous deformation of the solid framework noticeably affects the dynamic elastic moduli of rocks measured at a relatively low (10 MPa) constant uniaxial pressure.

Creep Experiment

Our experiments were performed using the uniaxial version of the FO apparatus at strain amplitudes of 10^{-8}–10^{-7}. The measurements were carried out for 120 h on three room-dry sedimentary rocks, which are represented by Savonnieres limestone, Berea sandstone and Eagle Ford shale, at a frequency of 2 Hz under a constant uniaxial pressure of 10 MPa. The physical characteristics of the specimens used in our measurements are summarized in **Table 1**.

Results of Creep Measurements

The time dependences of the dynamic elastic moduli obtained at 2 Hz using the FO method for three specimens are presented in **Figures 6–8**. We found that the changes in elastic moduli obtained after 120 h of the experiment were as follows: Eagle Ford shale–9% (Young), 12% (bulk) and 8% (shear); Savonnieres limestone–5% (Young), 10% (bulk) and 4% (shear); Berea sandstone–3% (Young), 5% (bulk), and 2.5% (shear). The observed decrease in the Poisson ratio was 1% in Eagle Ford shale, and 6% in Savonnieres limestone and Beria sandstone. Our results also show that for all tested rocks the change in both bulk and shear moduli measured 24–30 h after commencing the experiments does not exceed 2%.

The time dependences of the extensional attenuation and P- and S-wave velocities are presented in **Figure 9**. As can be seen

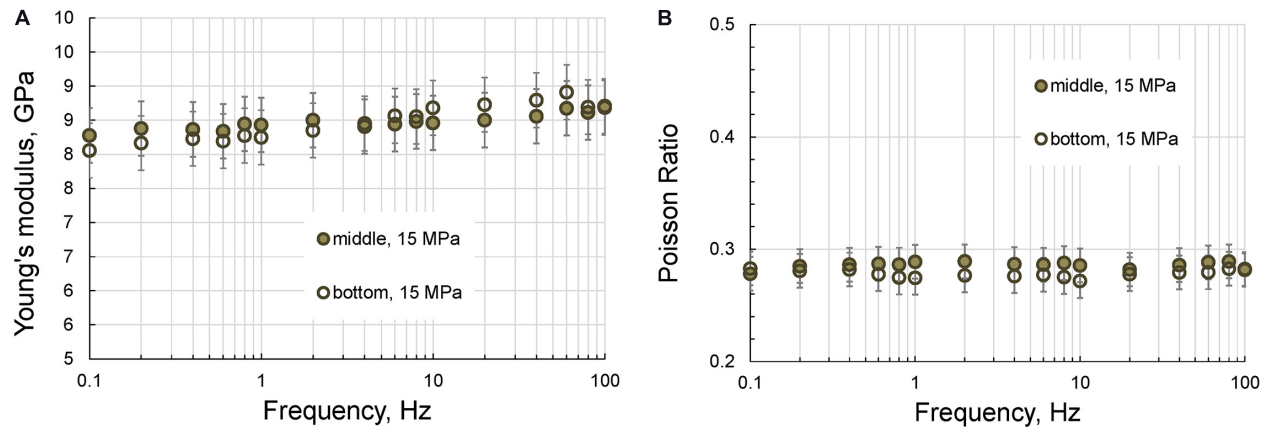

FIGURE 4 | The frequency dependences of the Young's modulus **(A)** and Poisson ratio **(B)** of the acrylic sample measured at a uniaxial of 15 MPa.

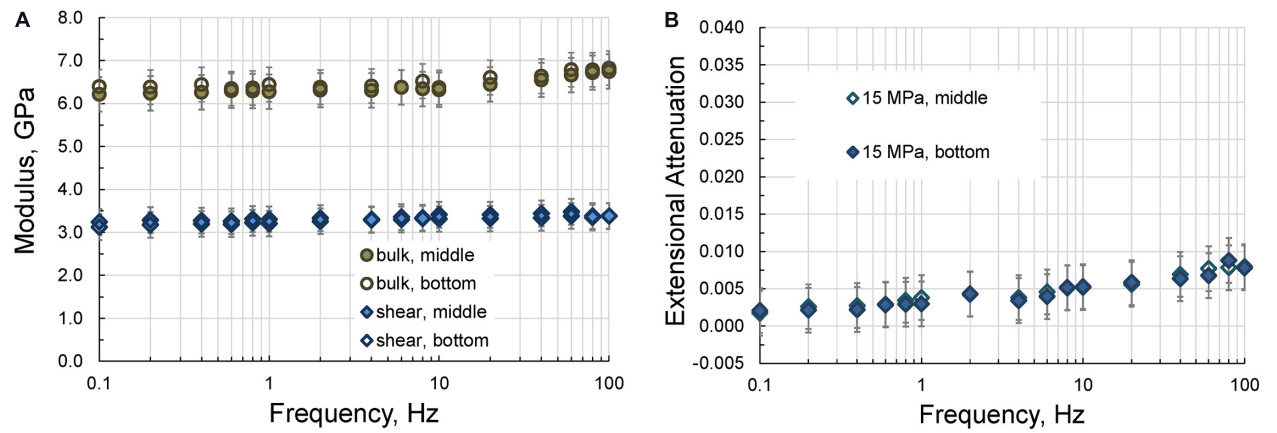

FIGURE 5 | The frequency dependences of the bulk and shear moduli **(A)** and the extensional attenuation **(B)** measured on the 15-cm acrylic sample in the middle and at a distance of 2 cm from the lower end of the sample at a uniaxial pressure of 15 MPa.

from **Figure 9B**, the dispersion of the S-wave velocity is less than the dispersion of the P-wave velocity for all rocks. Thus, the decrease of the P- and S-velocities is, correspondingly, 5 and 4% in Eagle Ford shale, 4 and 2% in Savonnieres limestone, and 2 and 1% in Berea sandstone.

Our study of the influence of the creep on the dynamic elastic moduli of three room-dry sedimentary rocks (Savonnieres limestone, Berea sandstone, and Eagle Ford shale), which was carried out at a seismic frequency of 2 Hz under a constant uniaxial pressure of 10 MPa, demonstrates that the creep effect can have a significant impact on the values of the measured moduli that should be taken into consideration, in particular, when comparing the results of ultrasonic and LF measurements.

TABLE 1 | Physical characteristics of the specimens.

Sample	Savonnieres limestone	Berea sandstone	Eagle Ford shale
Porosity, %	29.0	19.0	8.5
Permeability, mD	14.3	130	$<10^{-3}$
Density, kg/m^2	1895	2308	2210
Length, mm	76	61	70
Diameter, mm	38	39	38

THE EFFECT OF THE BOUNDARY CONDITIONS IN THE FORCED-OSCILLATION DEVICES ON LOW FREQUENCY MEASUREMENTS

The dispersion of moduli and attenuation observed in the LF experiments based on the FO method are often crucially depend on the boundary conditions of the tested rock sample, whether the sample surface is properly sealed (Dunn, 1986; White, 1986) or surrounded by rigid pore-fluid containers connected with the pore space of the rock, so-called "dead" fluid volumes (Cheng, 2016). As a rule, these dead volumes are represented by the segments of the fluid line located between the sample ends

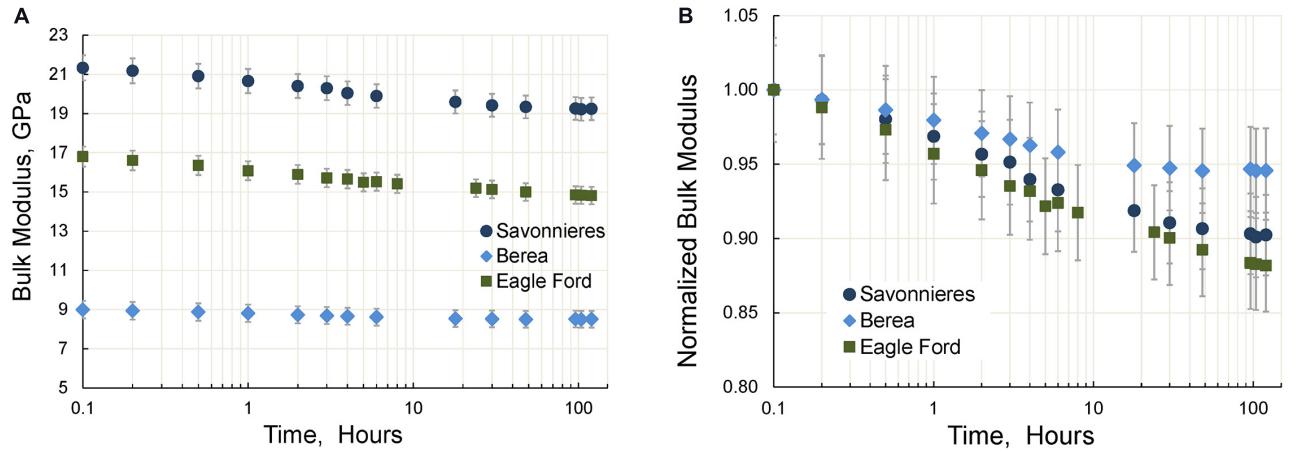

FIGURE 6 | The dependencies of the Young's modulus **(A)** and Poisson ratio **(B)** on time measured for three rock samples. The measurements are conducted at a uniaxial pressure of 10 MPa.

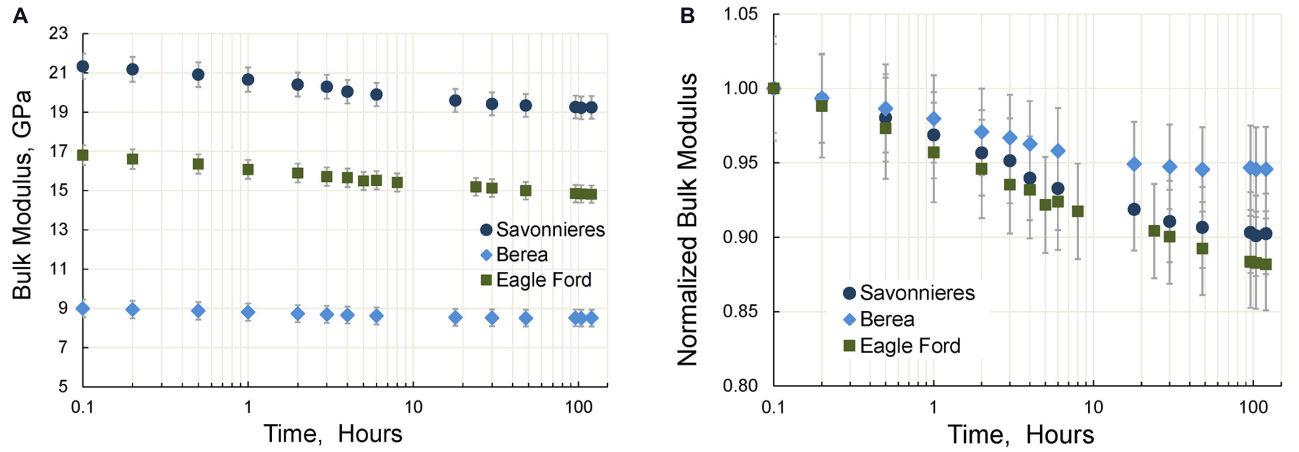

FIGURE 7 | The time dependencies of the bulk **(A)** and normalized bulk **(B)** moduli of three tested samples. The measurements are conducted at a uniaxial pressure of 10 MPa.

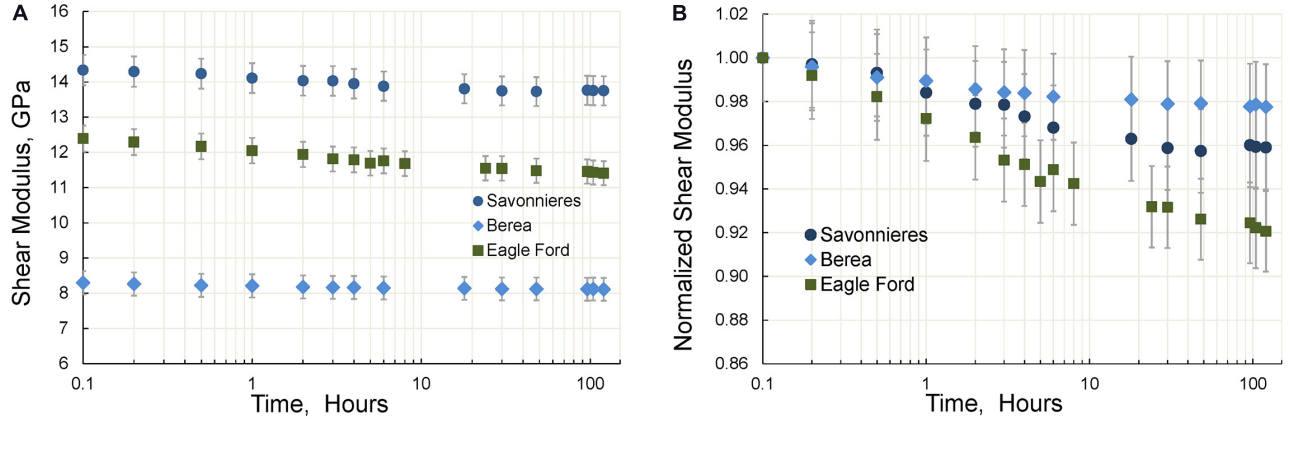

FIGURE 8 | The time dependencies of the shear **(A)** and normalized shear **(B)** moduli of three tested samples. The measurements are conducted at a uniaxial pressure of 10 MPa.

and the nearby valves. Dunn (1986) and White (1986) showed that open boundary conditions cause radial fluid flow due to the pressure difference between the center and the surface of the tested sample, which results in the observed dispersion of moduli and the attenuation (Dunn, 1986). Using the results of the experiments carried out on water- and glycerol-saturated Fontainebleau and Berea sandstones with a dead volume of 6.6 ml at frequencies of 0.004–0.4 Hz (Pimienta et al., 2015), Pimienta et al. (2016) demonstrated that the dead volume can also be accountable for the flow of the pore fluid even under conditions of à fully saturated rock and a closed pore-fluid line, and, as a consequence, for the observed attenuation and bulk modulus dispersion.

The purpose of this study is to quantify the dead volume effect in a seismic frequency range of 0.1–120 Hz. We estimate the impact of the size of the dead volume on the frequency dependences of the elastic moduli.

Experiments With Dead Volume

In this study, the LF experiments were carried out on a Savonnieres limestone sample at a differential pressure of 7 MPa. The physical parameters of the dry sample are as follows: the density is 1920 kg/m^3, porosity and permeability are 29% and 14.3 mD, correspondingly. The diameter of the sample is 38 mm, the length is 71 mm, and the pore space is 23 ml.

In our FO apparatus, the storage capacity of the pore fluid can be varied from 2 to 270 ml. We used this capacity as a variable dead volume to estimate the impact of the dead volume on the measured elastic moduli of the sample. The pore fluid used in our experiments was n-decane. The parameters of n-decane at 20°C are as follows: the density is 730 kg/m^3, viscosity is 0.92 mPas, the bulk modulus is equal to 1.15 GPa (Prak et al., 2017).

Here we present the frequency dependences of the elastic moduli measured with dead volumes equal to 2, 30, and 100 ml at a pore pressure of 3 MPa, as well as with the open fluid line, in the frequency range of 0.1–120 Hz. The confining pressure was 10 MPa in the experiments with the dead volumes and 7 MPa when the fluid line was open.

Results of Experiments With Dead Volume

The frequency dependences of the Young's modulus and Poisson ratio measured with three dead volumes and with the open fluid line are given in **Figure 10**.

The frequency dependences of the extensional attenuation, bulk and shear moduli obtained in accordance with Eq. 3 for the open line are presented in **Figure 11**. The dependencies of the bulk moduli demonstrate strong dispersion at frequencies above 20 Hz when the dead volume is close to the pore volume of the sample or exceeds it. Our measurements show that the size of the dead volume does not affect the characteristic frequency of the Young's/bulk modulus dispersion associated with the attenuation peak, but completely determines the magnitude of this dispersion. As can be seen in **Figure 11B**, the dispersion of the shear modulus is negligible at all dead volumes.

Analysis of the Experiments With Dead Volume

To estimate the characteristic frequency of the dispersion in a fluid-saturated homogeneous and isotropic porous rock caused by the presence of the dead volume V_D, we consider the change in the volumetric strain ε_V in response to the change in the confining p_c and fluid p_f pressures. According to Cheng (2016), ε_V, p_c, and p_f are connected by the following constitutive equation of poroelasticity

$$-p_c = K_d \varepsilon_V - n p_f, \tag{8}$$

where K_d is the drained bulk modulus, n is the pore pressure coefficient.

Pimienta et al. (2016) developed a poroelastic model for LF experiments with dead volume by solving the one-dimensional diffusion equation. Based on this model, they obtained the following expression for the pore fluid pressure p_f in a fully saturated specimen connected to a dead volume container in response to the applied harmonic stress $p_c = \Delta p_0 e^{i\omega t}$ with an amplitude of Δp_0 :

$$p_f(z,\omega) = B\Delta p_0 e^{i\omega t}\left(1 - \frac{\cosh\left(a\left(\frac{L}{2} - z\right)\right)}{c\cdot\sinh\left(a\frac{L}{2}\right) + \cosh\left(a\frac{L}{2}\right)}\right), \tag{9}$$

where B is the Skempton coefficient, L is the length of a rock sample, z is the distance from one of the sample ends, $a = (1+i)\sqrt{\omega/2D}$ with $D = k/(S_s\eta)$ being the fluid pressure diffusivity, $S_s = n/(B\cdot K_d)$, k is the rock permeability, η is the fluid viscosity, $c = (1-i)\frac{AS_s}{S}\sqrt{\omega/2D}$, A is the cross-sectional area of the rock sample, $S = V_D/K_f$, K_f is the bulk modulus of fluid, $\omega = 2\pi f$, f is the frequency of the harmonic stress applied to the rock.

After substituting Eq. 9 into Eq. 8, we find the volumetric strain ε_V in the sample subjected to the harmonic stress p_c :

$$\varepsilon_V(z,\omega) = \frac{B\Delta p_0}{K_d}\left(\left(n - \frac{1}{B}\right) - n\frac{\cosh\left(a\left(\frac{L}{2} - z\right)\right)}{c\cdot\sinh\left(a\frac{L}{2}\right) + \cosh\left(a\frac{L}{2}\right)}\right)e^{i\omega t}. \tag{10}$$

The local effective bulk modulus $K^e(z,\omega)$ of the combined fluid-saturated sample–dead volume system can be found as

$$K^e(z,\omega) = -\frac{p_c}{\varepsilon_V(z,\omega)}. \tag{11}$$

Since, as demonstrated by our experiments, the characteristic frequency of dispersion does not depend on the size of the dead volume, let us consider only the case with the open fluid line, i.e., when $V_d \to \infty$ and $c \to 0$:

$$\begin{aligned}\varepsilon_V(z,\omega) &= \varepsilon_{AV}(z,\omega)e^{i\omega t}\\ &= \frac{B\Delta p_0}{K_d}\left(\left(n - \frac{1}{B}\right) - n\frac{\cosh\left(a\left(\frac{L}{2} - z\right)\right)}{\cosh\left(a\frac{L}{2}\right)}\right)e^{i\omega t}\\ &= (\varepsilon_V^0 + \varepsilon_{VD})e^{i\omega t},\end{aligned} \tag{12}$$

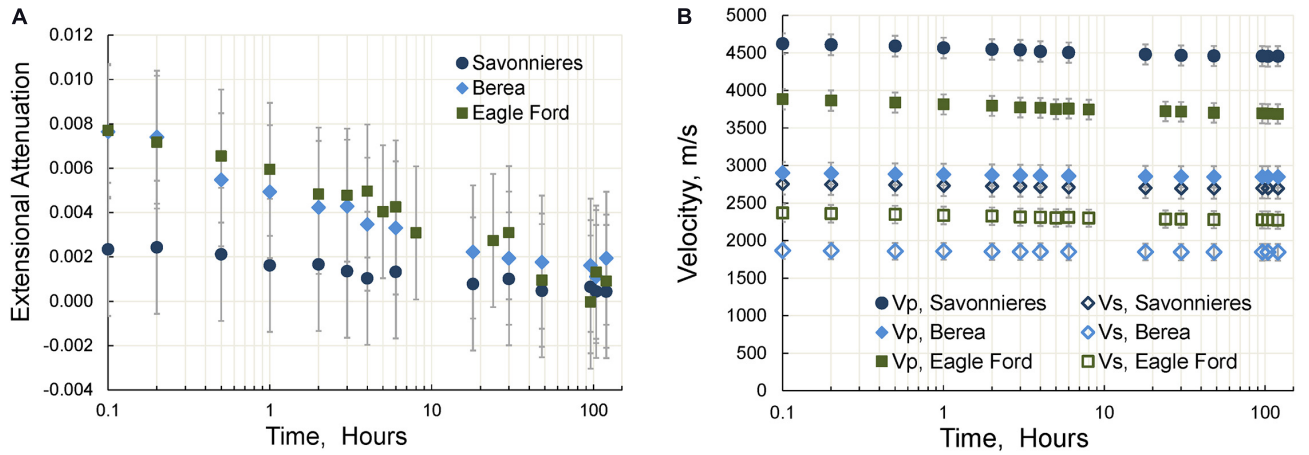

FIGURE 9 | The dependencies of the extensional attenuation **(A)** and P-wave and S-wave velocities **(B)** on time. The measurements are carried out at a uniaxial pressure of 10 MPa.

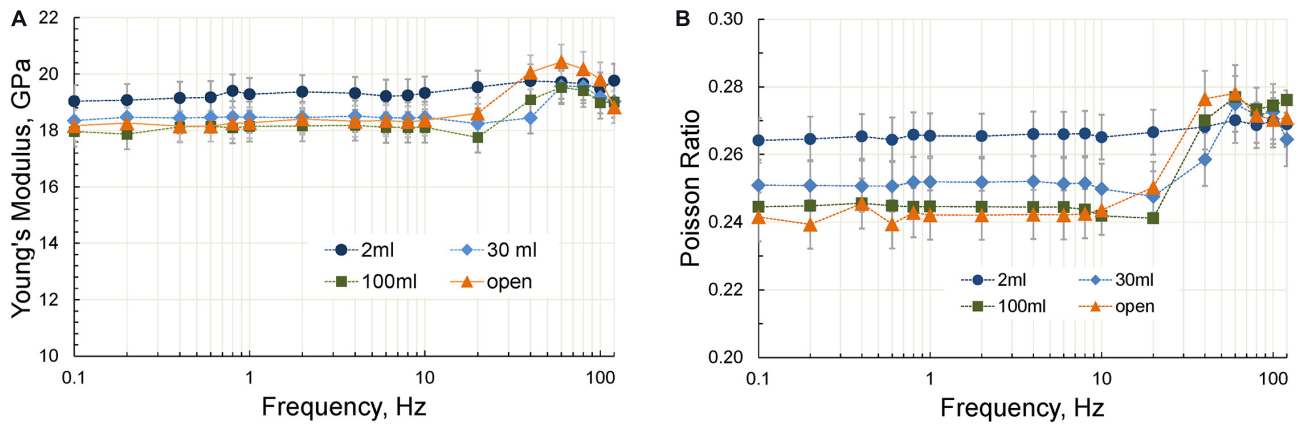

FIGURE 10 | The frequency dependences of the Young's modulus **(A)** and Poisson ratio **(B)** measured at dead volumes of 2, 30, and 100 ml, as well as with the open fluid line. All measurements are performed at a differential pressure of 7 MPa.

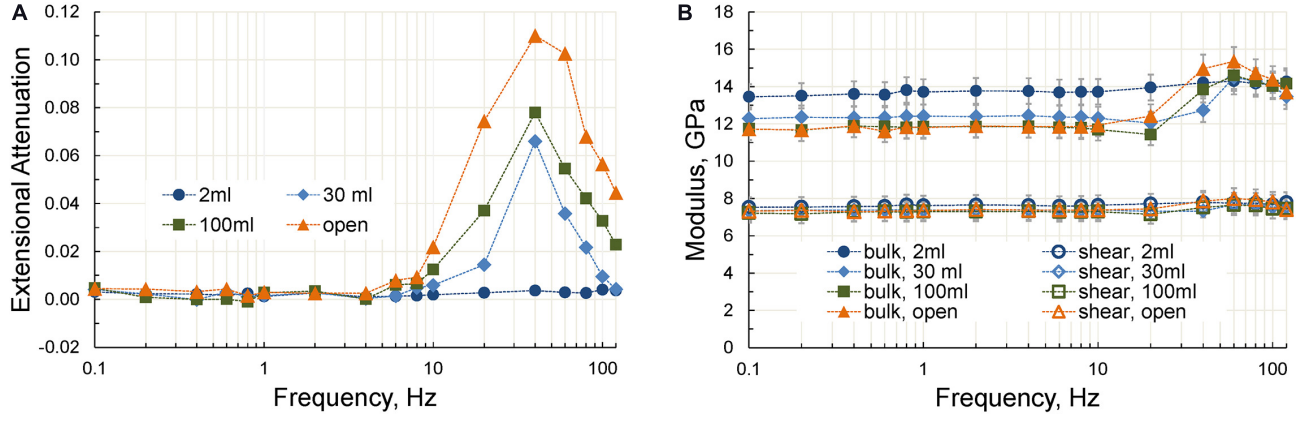

FIGURE 11 | The frequency dependences of the extensional attenuation **(A)** and the bulk and shear moduli **(B)** obtained for dead volumes of 2, 30, and 100 ml and for the open fluid line. The measurements are carried out at a differential pressure of 7 MPa.

where $\varepsilon_{AV}(z,\omega)$ is the volumetric strain amplitude, ε_V^0 corresponds to the strain amplitude in the undrained regime

$$\varepsilon_V^0 = \frac{\Delta p_0}{K_d}(nB-1), \tag{13}$$

ε_{VD} is the strain amplitude associated with pressure diffusion

$$\varepsilon_{VD} = \varepsilon_{VD}^0 \frac{\cosh\left(a\left(\frac{L}{2}-z\right)\right)}{\cosh\left(a\frac{L}{2}\right)}, \tag{14}$$

where $\varepsilon_{VD}^0 = -\frac{nB\Delta p_0}{K_d}$.

The attenuation Q_K^{-1} corresponding to the effective bulk modulus K^e is

$$Q_K^{-1} = \frac{Im(K^e(z,\omega))}{Re(K^e(z,\omega))} = -\frac{Im(\varepsilon_V(z,\omega))}{Re(\varepsilon_V(z,\omega))} = -\frac{Im(\varepsilon_{DV})}{\varepsilon_V^0 + Re(\varepsilon_{DV})}. \tag{15}$$

As follows from Eqs 12, 14, $Im(\varepsilon_V) = Im(\varepsilon_{DV}) = 0$ at both ends of the sample $z = 0$ and $z = L$, and, as a consequence, the bulk attenuation is also equal to 0 at both sample ends.

The amplitude of the bulk strain at the location of the strain gauges, in the middle of the sample, is

$$\varepsilon_{AV}(L/2) = \varepsilon_V^0 + \varepsilon_{VD}^0 \frac{1}{\cosh(aL/2)}. \tag{16}$$

As follows from Eq. 16, $\varepsilon(L/2) \to \varepsilon_0 + \varepsilon_D^0$ at $\omega \to 0$ and $\varepsilon(L/2) \to \varepsilon_0$ at $\omega \to \infty$. In accordance with Eqs 11, 16, the ratio of the undrained bulk modulus K_u and the local drained modulus K_d^e measured at $z = L/2$ and $\omega \to 0$ can be expressed as

$$\frac{K_u}{K_d^e} = \frac{\varepsilon_V^0 + \varepsilon_{VD}^0}{\varepsilon_V^0} = 1 + \frac{\varepsilon_{VD}^0}{\varepsilon_V^0}. \tag{17}$$

If we consider the results of our measurements for bulk moduli presented in **Figure 11B** and assume that the bulk modulus measured at a dead volume of 2 ml is a good approximation for the undrained bulk modulus K_u, we obtain

$$\left|Re(\varepsilon_{VD}^0)\right| \ll \varepsilon_V^0. \tag{18}$$

Therefore, the attenuation Q_K^{-1} can be estimated as

$$Q_K^{-1} = -\frac{Im(\varepsilon_{DV})}{\varepsilon_V^0 + Re(\varepsilon_{DV})} \approx -\frac{Im(\varepsilon_{DV})}{\varepsilon_V^0} = -\frac{\varepsilon_{VD}^0}{\varepsilon_V^0} Im\left(\frac{1}{\cosh(aL/2)}\right)$$
$$= -\frac{\varepsilon_{VD}^0}{\varepsilon_V^0} Im\left(\frac{1}{\cosh((1+i)L\sqrt{\omega/2D}/2)}\right). \tag{19}$$

The analysis of the function $-1/\cosh((1+i)x)$ with real variable $x = L\sqrt{\omega/2D}/2$ shows that the maximum of its imaginary part is reached at

$$L\sqrt{\omega/2D} = 2.16. \tag{20}$$

With good accuracy, Eq. 20 can be approximated as follows:

$$L\sqrt{\omega/2D} = 2\pi/3. \tag{21}$$

Thus, the characteristic frequency of the dispersion f_C corresponding to the attenuation peak is

$$f_C = \frac{4}{9}\frac{\pi D}{L^2}. \tag{22}$$

As was demonstrated by Chandler and Johnson (1981), if the drained bulk and shear moduli of a rock are much larger than the bulk moduli of fluid K_f, the diffusivity D is

$$D = \kappa K_f/\eta\phi. \tag{23}$$

In this case, Eq. 22 can be rewritten as

$$f_C = \frac{4}{9}\frac{\pi\kappa K_f}{\eta\phi L^2}. \tag{24}$$

Substituting the n-decane viscosity η = 0.92 mPas (Prak et al., 2017) and parameters of the sample into Eq. 24, we obtain

$$f_C \approx 20 \text{ Hz}. \tag{25}$$

As can be seen in **Figure 11A**, the analytical solution given by Eq. 24 underestimates the frequency of the attenuation peak observed in the experiment. This can be explained by using the one-dimensional approach in our calculations, which takes into account only the fluid movements along the axis of a sample and neglects the movements orthogonal to the axis. However, the found analytical solution is a reasonably good estimate for the characteristic frequency of the dispersion and attenuation observed in the experiment. The advantage of this solution, besides its simplicity, is that it is based only on the physical parameters of the sample and fluid.

Let us note, that the frequency of the attenuation peak in the case of the open fluid line can also be considered as the cut-off frequency associated with the transition between drained and undrained regimes. As follows from dimensional analysis of diffusion process, this frequency is proportional to the diffusion coefficient D and inversely proportional to a squared characteristic length l (Cleary, 1978):

$$f_D = \frac{D}{l^2}. \tag{26}$$

Combining Eqs 23, 26, we obtained (David et al., 2013):

$$f_D = \frac{\kappa K_f}{\eta\phi l^2}. \tag{27}$$

For axial diffusion, l is equal to half the length of the sample L, which yields

$$f_D = 4\frac{\kappa K_f}{\eta\phi L^2}. \tag{28}$$

After substituting the parameters of n-decane and the sample, we obtain the estimate of the frequency of the attenuation associated with diffusion along the saturated sample

$$f_D = 57 \text{ Hz}, \tag{29}$$

which is higher than the frequency of the attenuation peak obtained in the experiment.

Therefore, Eqs 24, 28 can be considered as the lower and upper bounds for the observed frequency of the attenuation peak f_{exp}

$$f_C < f_{exp} < f_D. \quad (30)$$

The important finding of our experiments with dead volume, carried out in the seismic frequency band on Savonnieres limestone saturated with n-decane, lies in the fact that the characteristic frequency of dispersion does not depend on the size of the dead volume and is completely determined by the parameters of a tested sample and saturating fluid.

APPLICATION OF THE KRAMERS–KRONIG RELATION TO THE MEASUREMENTS ON WELLINGTON SHALE AT SEISMIC FREQUENCIES

As was pointed out in Mikhaltsevitch et al. (2016b), one of the main issues encountered when using an FO apparatus is the intrinsic spurious resonances occurring in the mechanical parts of the apparatus, which can significantly affect the signals obtained from a tested specimen (Adam et al., 2009; Sun et al., 2019; Li et al., 2020). This issue can be resolved by using a diagnostic tool, such as the Kramers–Kronig relation, which can verify the quality of the measurement results and control the signal distortions stemming from the external interference or intrinsic spurious resonances.

Mikhaltsevitch et al. (2016b); Chapman et al. (2019), and Sun et al. (2020) demonstrated that the Kramers–Kronig relation in the form found by Mikhaltsevitch et al. (2016b) can be used for verification of the laboratory measurements carried out on solid isotropic specimens at low frequencies. Here we illustrate the applicability of the Kramers–Kronig relation to validate the experimental data obtained for the transversely isotropic (TI) medium represented by Wellington shale. It is shown that the relationship between the measured TI Young's moduli and extensional attenuation can be validated using the Kramers–Kronig relation.

In this study, we present the results of the measurements of the TI Young's moduli and extensional attenuation obtained for two smectite-bearing Wellington shale samples drilled at 0° (V-sample) and 90° (H-sample) angles with respect to the bedding plane and saturated with water at relative humidity (RH) of 12, 44, 72, and 97.5%. To avoid a laceration of strain gauges due to the high compressibility of the shale, the laboratory tests were carried out at a relatively low confining pressure of 6 MPa.

Description of Wellington Shale Samples

The Wellington shale samples used in this study are described previously in Mikhaltsevitch et al. (2018). The helium gas permeability and porosity of both samples were estimated at <1 μD and 9%, correspondingly. The XRD analysis of the samples shows that the mineralogy of the shale is as follows: smectite–6%, illite-smectite–19%, kaolinite–9%, quartz–22%, calcite–31%, mica–5%, dolomite–3%, and albite–2%. The shale samples were saturated in desiccators with salt solutions providing RH of 12, 44, 72, and 97.5%. The time of saturation at each HR was 7 weeks. The length of the V- and H-samples is 71 mm and 65 mm, correspondingly, the diameter of both samples is 38 mm, the density is ∼2500 kg/m^3 at 44% RH. The TI Young's moduli and extensional attenuation are evaluated in accordance with expressions (1) and (7), correspondingly.

Results of the Measurements on Wellington Shale

The dependences of the TI Young's moduli and attenuation on the frequency of stress oscillations obtained at frequencies of 0.1–100 Hz for RH of 12, 44, 72, and 97.5% are shown in **Figures 12**, **13**, respectively. The noticeable Young's modulus dispersion and attenuation were observed only at saturation corresponding to 97.5% RH. The peaks of attenuation were found at frequencies 2 and 6 Hz for the V- and H-samples, respectively (**Figure 13**). An estimate of the characteristic frequency f_C

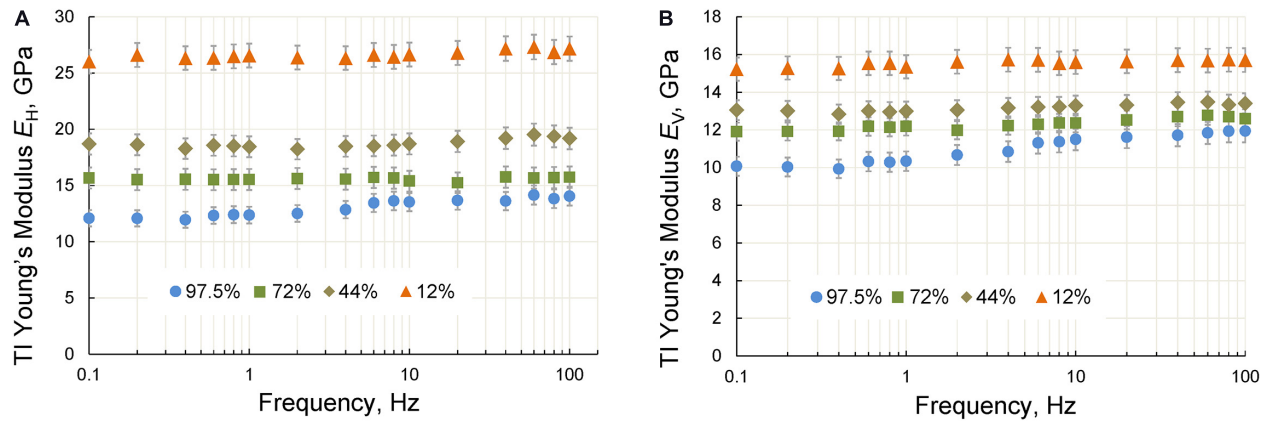

FIGURE 12 | The TI Young's moduli measured on the horizontal **(A)** and vertical **(B)** shale samples saturated at relative humidity of 12, 44, 72, and 97% under a confining pressure of 6 MPa.

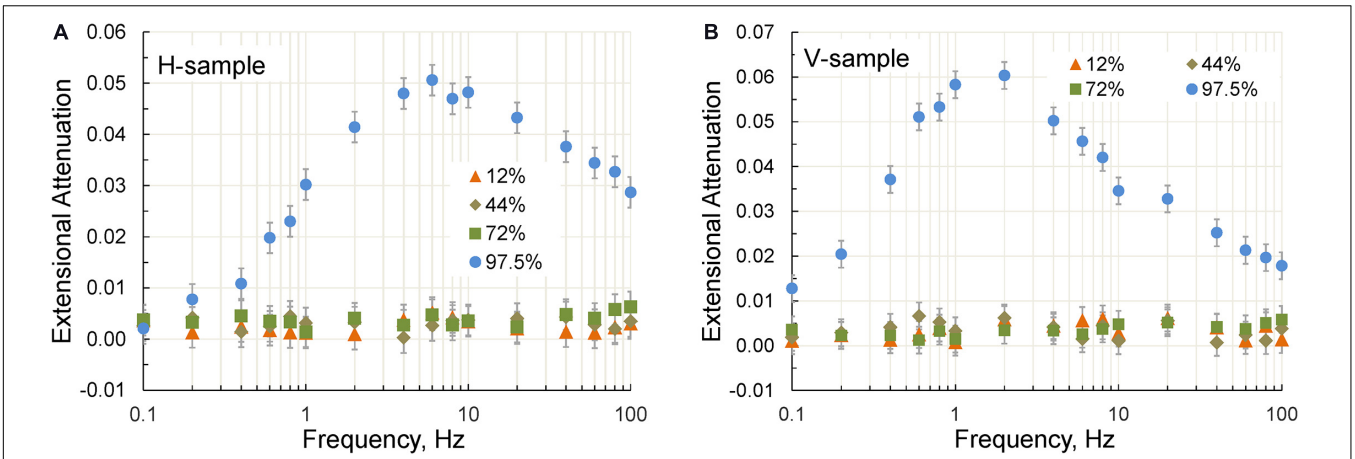

FIGURE 13 | The extensional attenuation measured on the horizontal **(A)** and vertical **(B)** samples at a confining pressure of 6 MPa and relative humidity of 12, 44, 72, and 97.5%.

corresponding to a peak of attenuation is given by the following expression (Dutta and Seriff, 1979)

$$f_C = \frac{1}{\pi}\frac{kK_w}{\phi\eta_w h^2}, \tag{31}$$

where K_w is the bulk modulus of water, ϕ is the rock porosity, η_w is the water viscosity, k is permeability of the sample, and h is the characteristic size of the water patches in the sample.

Based on Eq. 31, the difference in the peak frequencies observed in the V- and H-samples can be explained by the anisotropy of the permeability of Wellington shale.

Inasmuch as the measurements of Young's modulus and attenuation were performed synchronously and independently in the frequency range covering most of the attenuation peaks, we can verify the consistency of the experimental data with the causality principle presented by the Kramers–Kronig relations, as described in detail by Mikhaltsevitch et al. (2016b). The Kramers–Kronig relation linking the extensional attenuation Q_E^{-1} with the Young's modulus E measured at a frequency f and at some reference frequency f_0 can be expressed as

$$E(f) = E(f_0) + 1.47E(f_0)\int_{\lg(f_0)}^{\lg(f)} Q_E^{-1}\, d\lg(f'). \tag{32}$$

The Young's moduli computed from the attenuation data are presented in **Figure 14**. Good agreement between the measured and computed Young's moduli indicates that the measurements are consistent with the causality principle and confirms the physical nature of the observed attenuation and Young's modulus dispersion. Let us note that the obtained results are qualitatively similar to those previously reported for Mancos shale (Mikhaltsevitch et al., 2016a).

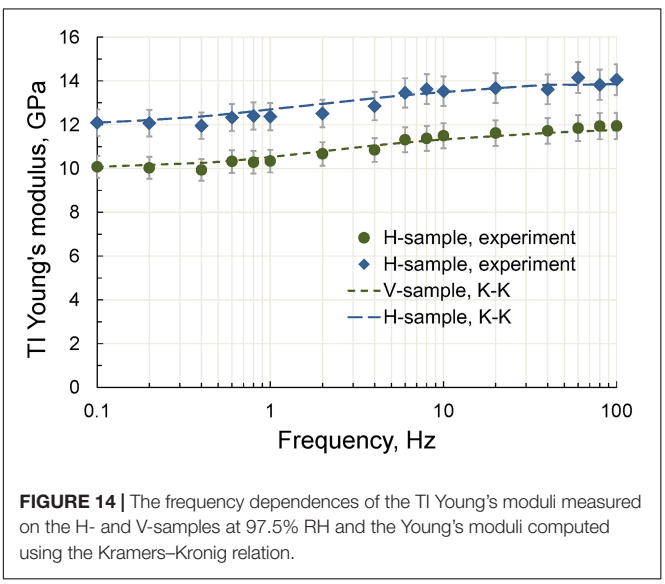

FIGURE 14 | The frequency dependences of the TI Young's moduli measured on the H- and V-samples at 97.5% RH and the Young's moduli computed using the Kramers–Kronig relation.

CONCLUSION

In this paper, we give a detailed description of the technical characteristics and main features of operation of a LF apparatus based on a longitudinal type of forced oscillations, and also present the results of our study of some physical aspects associated with the application of the FO method to the measurements of elastic and anelastic properties of rocks. Specifically, we investigated the effect of the strain gauge position on a solid specimen under test on the measurements, we also studied the effect of creep on the elastic moduli of three different rock specimens, as well as the elastic modulus dispersion and attenuation in liquid-saturated sandstone associated with the presence of a dead fluid volume, i.e., the volume of fluid located outside the rock, but connected with its pore space.

The influence of the strain gauge position on the elastic moduli and attenuation measurements was studied using a cylindrical acrylic sample with a length of 15 cm and two pairs of strain gauges glued in the center of the sample and at a distance of 2 cm from the lower end of the sample under a uniaxial

pressure of 15 MPa. The results of our tests show that elastic and anelastic parameters of the acrylic sample are independent from the location of the strain gauges on the sample. The effect of creep on the LF moduli was studied on three dry samples of Savonnieres limestone, Berea sandstone and Eagle Ford shale. The tests were carried out for 120 h at a frequency of 2 Hz under a uniaxial pressure of 10 MPa. It was shown that the moduli of all rocks decrease with time. The largest decrease was found in Eagle Ford shale, where the bulk and shear moduli decreased by 12 and 8%, correspondingly, and the lowest decrease was observed in Berea sandstone, where the reduction of the bulk and shear moduli were 5 and 2.5%.

We also present the results of the laboratory tests conducted at seismic frequencies on an n-decane saturated limestone sample with the dead volume gradually changed from 2 to 100 ml, as well as with the open pore-fluid line. It was shown that the Young's and bulk moduli exhibit strong dispersion accompanied by attenuation at frequencies exceeding 10 Hz, if the dead volume is comparable to or exceeds the pore volume of the sample. Using a one-dimensional poroelastic model, we found that the characteristic frequency of dispersion is determined only by the parameters of the rock sample and saturating fluid.

Furthermore, we demonstrate of the applicability of the Kramers–Kronig relation for verification of the TI Young's modulus and extensional attenuation measurements on shale. The TI Young's moduli and attenuation were measured on two Wellington shale samples, vertical and horizontal, saturated with water at four values of relative humidity in the range from 12 to 97.5%. It was shown that the relationship between the extensional attenuation and the TI Young's modulus dispersion observed in the shale samples saturated at a relative humidity of 97.5% is consistent with the Kramers–Kronig relation.

DATA AVAILABILITY STATEMENT

The datasets presented in this study can be found in online repositories. The names of the repository/repositories and accession number(s) can be found below: http://doi.org/10.5281/zenodo.4442082.

AUTHOR CONTRIBUTIONS

VM: experimental work, results analysis, and manuscript writing. ML: scientific advice, experimental suggestion, and manuscript review. RC: experimental work, calculations, and manuscript writing. EV: manuscript review and scientific advice. GV: manuscript review and experimental suggestion. All authors contributed to the article and approved the submitted version.

REFERENCES

Adam, L., Batzle, M., Lewallen, K. T., and van Wijk, K. (2009). Seismic wave attenuation in carbonates. *J. Geophys. Res.* 114:B06208. doi: 10.1029/2008JB005890

Adelinet, M., Fortin, J., Gueguen, Y., Schubnel, A., and Geoffroy, L. (2010). Frequency and fluid effects on elastic properties of basalt. experimental investigations. *Geophys. Res. Lett.* 37:L02303. doi: 10.1029/2009GL041660

Batzle, M. L., Han, D.-H., and Hofmann, R. (2006). Fluid mobility and frequency-dependent seismic velocity - direct measurements. *Geophysics* 71, N1–N9. doi: 10.1190/1.2159053

Borgomano, J. V. M., Gallagher, A., Sun, C., and Fortin, J. (2020). An apparatus to measure elastic dispersion and attenuation using hydrostatic- and axial-stress oscillations under undrained conditions. *Rev. Sci. Instrum.* 91:034502. doi: 10.1063/1.5136329

Brantut, N., Heap, M. J., Meredith, P. G., and Baud, P. (2013). Time-dependent cracking and brittle creep in crustal rocks: a review. *J. Struct. Geol.* 52, 17–43. doi: 10.1016/j.jsg.2013.03.007

Bruckshaw, J. M., and Mahanta, P. C. (1961). The variation of the elastic constants of rocks with frequency. *Geophys. Prospect.* 9, 65–76. doi: 10.1111/j.1365-2478.1961.tb01690.x

Chapman, S., Borgomano, J. V. M., Yin, H., Fortin, J., and Quintal, B. (2019). Forced oscillation measurements of seismic wave attenuation and stiffness moduli dispersion in glycerine-saturated Berea sandstone. *Geophys. Prospect.* 67, 956–968. doi: 10.1111/1365-2478.12710

Chandler, R. N., and Johnson, D. L. (1981). The equivalence of quasistatic flow in fluid saturated porous media and Biot's slow wave in the limit of zero frequency. *J. Appl. Phys.* 52, 3391–3395. doi: 10.1063/1.329164

Cheng, A. H.-D. (2016). *Poroelasticity*. Switzerland: Springer. doi: 10.1007/978-3-319-25202-5

Cleary, M. P. (1978). Elastic and dynamic response regimes of fluid-impregnated solids with diverse microstructures. *Int. J. Solids Struct.* 14, 795–819. doi: 10.1016/0020-7683(78)90072-0

D'Anna, G., and Benoit, W. (1990). Apparatus for dynamic and static measurements of mechanical properties of solids and of fluxlattice in typeII superconductors at low frequency (10^{-5}–10 Hz) and temperature (4.7–500 K). *Rev. Sci. Instrum.* 61, 3821–3826. doi: 10.1063/1.1141507

David, E. C., Fortin, J., Schubnel, A., Guéguen, Y., and Zimmerman, R. W. (2013). Laboratory measurements of low- and high-frequency elastic moduli in Fontainebleau sandstone. *Geophysic* 78, D369–D379. doi: 10.1190/geo2013-0070.1

Dunn, K.-J. (1986). Acoustic attenuation in fluid-saturated porous cylinders at low frequencies. *J. Acoust. Soc. Am.* 79, 1709–1721. doi: 10.1121/1.393232

Dutta, N. C., and Seriff, A. J. (1979). On White's model of attenuation in rocks with partial gas saturation. *Geophysics* 44, 1806–1812. doi: 10.1190/1.1440940

Gordon, R. B., and Davis, L. A. (1968). Velocity and attenuation of seismic waves in imperfectly elastic rock. *J. Geophys. Res.* 73, 3917–3935.

Jackson, I., and Paterson, M. S. (1987). Shear modulus and internal friction of calcite rocks at seismic frequencies: pressure, frequency and grain size dependence. *Phys. Earth Planet. Inter.* 45, 349–367.

Lakes, R. S. (2004). Viscoelastic measurement techniques. *Rev. Sci. Instrum.* 75, 797–810. doi: 10.1063/1.1651639

Lexcellent, C. (2018). *Linear and Non-Linear Mechanical Behavior of Solid Materials*. Cham: Springer. doi: 10.1007/978-3-319-55609-3

Li, H., Lin, J., Gao, J., He, Y., Han, D., and Zhao, L. (2020). Precision analysis of forced-oscillation device: numerical modelling and experimental investigations. *J. Geophys. Eng.* 17, 980–992. doi: 10.1093/jge/gxaa057

Mavko, G. (1979). Frictional attenuation: an inherent amplitude dependence. *J. Geophys. Res. Solid Earth* 84, 4769–4776. doi: 10.1029/JB084iB09p04769

Mikhaltsevitch, V., Lebedev, M., and Gurevich, B. (2014). A laboratory study of low-frequency wave dispersion and attenuation in water-saturated sandstones. *Lead. Edge* 33, 616–622. doi: 10.1190/tle33060616.1

Mikhaltsevitch, V., Lebedev, M., and Gurevich, B. (2016a). "A laboratory study of the elastic anisotropy in the Mancos shale at seismic frequencies," in *Paper Presented at the SEG International Exposition and 87th Annual Meeting*, (Dallas, TX), doi: 10.1190/segam2016-13850199.1

Mikhaltsevitch, V., Lebedev, M., and Gurevich, B. (2016b). Validation of the laboratory measurements at seismic frequencies using the Kramers-Kronig relationship. *Geophys. Res. Lett.* 43, 4986–4991. doi: 10.1002/2016GL069269

Mikhaltsevitch, V., Lebedev, M., and Gurevich, B. (2018). "The effect of water saturation on the elastic properties of the Wellington shale at seismic

frequencies," in *Proceedings of the 80th EAGE Conference and Exhibition*, Vol. 2018, (Copenhagen), 1–5. doi: 10.3997/2214-4609.201801546

Nakagawa, S. (2013). "Low-frequency (<100 Hz) dynamic fracture compliance measurement in the laboratory," in *Paper Presented at 47th U.S. Rock Mechanics/Geomechanics Symposium*, (San Francisco, CL).

Ògúnsànmì, A., Jackson, I., Borgomano, J. V. M., Fortin, J., Sidi, H., Gerhardt, A., et al. (2020). Elastic properties of a reservoir sandstone: a broadband inter-laboratory benchmarking exercise. *Geophys. Prospect.* 69, 404–418. doi: 10.1111/1365-2478.13048

Paffenholz, J., and Burkhardt, H. (1989). Absorption and modulus measurements in the seismic frequency and strain range on partially saturated sedimentary rocks. *J. Geophys. Res.* 94, 9493–9507. doi: 10.1029/JB094iB07p09493

Peselnick, L., and Outerbridge, W. F. (1961). Internal friction in shear and shear modulus of Solenhofen limestone over a frequency range of 10^7 cycles per second. *J. Geophys. Res.* 66, 581–588. doi: 10.1029/JZ066i002p00581

Peselnick, L., and Zietz, I. (1959). Internal friction of fine-grained limestones at ultrasonic frequencies. *Geophysics* 24, 285–296. doi: 10.1190/1.1438583

Pimienta, L., Fortin, J., and Gueguen, Y. (2015). Experimental study of Young's modulus dispersion and attenuation in fully saturated sandstones. *Geophysics* 80, L57–L72. doi: 10.1190/geo2014-0532.1

Pimienta, L., Borgomano, J. V. M., Fortin, J., and Gueguen, Y. (2016). Modelling the drained/undrained transition: effect of the measuring method and the boundary conditions. *Geophys. Prospect.* 64, 1098–1111.

Prak, D. J. L., Lee, B. G., Cowart, J. S., and Trulove, P. C. (2017). Density, viscosity, speed of sound, bulk modulus, surface tension, and flash point of binary mixtures of butylbenzene + linear alkanes (n-decane, n-dodecane, n-tetradecane, n-hexadecane, or n-heptadecane) at 0.1 MPa. *J. Chem. Eng. Data* 62, 169–187. doi: 10.1021/acs.jced.6b00542

Saltiel, S., Selvadurai, P. A., Bonner, B. P., Glaser, S. D., and Ajo-Franklin, J. B. (2017). Experimental development of low-frequency shear modulus and attenuation measurements in mated rock fractures: shear mechanics due to asperity contact area changes with normal stress. *Geophysics* 82, M19–M36. doi: 10.1190/geo2016-0199.1

Spencer, J. W. (1981). Stress relaxation at low frequencies in fluid-saturated rocks: attenuation and modulus dispersion. *J. Geophys. Res.* 86, 1803–1812. doi: 10.1029/JB086iB03p01803

Spencer, J. W., Cates, M. E., and Thompson, D. D. (1994). Frame moduli of unconsolidated sands and sandstones. *Geophysics* 59, 1352–1361. doi: 10.1190/1.1443694

Subramaniyan, S., Quintal, B., Tisato, N., Saenger, E. H., and Madonna, C. (2014). An overview of laboratory apparatuses to measure seismic attenuation in reservoir rocks. *Geophys. Prospect.* 62, 1211–1223. doi: 10.1111/1365-2478.12171

Sun, C., Tang, G. Y., Fortin, J., Borgomano, J. V. M., and Wang, S. (2020). Dispersion and attenuation of elastic wave velocities: impact of microstructure heterogeneity and local measurements. *J. Geophys. Res. Solid Earth* 125:e2020JB020132. doi: 10.1029/2020jb020132

Sun, C., Tang, G., Zhao, J., Zhao, L., Long, T., Li, M., et al. (2019). Three-dimensional numerical modelling of the drained/undrained transition for frequency-dependent elastic moduli and attenuation. *Geophys. J. Int.* 219, 27–38. doi: 10.1093/gji/ggz284

Sun, C., Tang, G., Zhao, J., Zhao, L., and Wang, S. (2018). An enhanced broad-frequency-band apparatus for dynamic measurement of elastic moduli and Poisson's ratio of rock samples. *Rev. Sci. Instrum.* 89:064503. doi: 10.1063/1.5018152

Szewczyk, D., Bauer, A., and Holt, R. M. (2016). A new laboratory apparatus for the measurement of seismic dispersion under deviatoric stress conditions. *Geophys. Prospect.* 64, 789–798. doi: 10.1111/1365-2478.12425

Takei, Y., Fujisawa, K., and McCarthy, C. (2011). Experimental study of attenuation and dispersion over a broad frequency range: 1. the apparatus. *J. Geophys. Res.* 116:B09204. doi: 10.1029/2011JB008384

Usher, M. J. (1962). Elastic behaviour of rocks at low frequencies. *Geophys. Prospect.* 10, 119–127. doi: 10.1111/j.1365-2478.1962.tb02002.x

White, J. E. (1986). Biot-Gardner theory of extensional waves in porous rods. *Geophysics* 51, 742–745. doi: 10.1190/1.1442126

Winkler, K., Nur, A., and Gladwin, M. (1979). Friction and seismic attenuation in rocks. *Nature* 277, 528–531. doi: 10.1038/277528a0

Conflict of Interest: The authors declare that the research was conducted in the absence of any commercial or financial relationships that could be construed as a potential conflict of interest.

Copyright © 2021 Mikhaltsevitch, Lebedev, Chavez, Vargas and Vasquez. This is an open-access article distributed under the terms of the Creative Commons Attribution License (CC BY). The use, distribution or reproduction in other forums is permitted, provided the original author(s) and the copyright owner(s) are credited and that the original publication in this journal is cited, in accordance with accepted academic practice. No use, distribution or reproduction is permitted which does not comply with these terms.

frontiers in Earth Science

METHODS
published: 15 March 2021
doi: 10.3389/feart.2021.642363

3D Subsurface Modeling of Multi-Scenario Rock Property and AVO Feasibility Cubes—An Integrated Workflow

Per Avseth[1]* *and Ivan Lehocki*[1,2]

[1] Dig Science, Oslo, Norway, [2] Lehocki GeoSpace, Oslo, Norway

A novel inter-disciplinary methodology for the generation of rock property and AVO feasibility maps or cubes to be used in subsurface characterization and prospect de-risking is presented. We demonstrate the workflow for 1D, 2D and 3D cases on data from the North Sea and the Barents Sea, offshore Norway. The methodology enables rapid extrapolation of expected rock physics properties away from well control along selected horizons, constrained by seismic velocity information, geological inputs (basin modeling, seismic stratigraphy and facies maps) and rock physics depth trend analysis. In this way, the expected rock physics properties of a reservoir sandstone (saturated with any pore fluid) can be predicted at any given location between or away from existing wells while honoring rock's burial and thermal history at this same location. The workflow should allow for more rapid, seamless and geologically consistent subsurface mapping and de-risking of prospects in areas with complex geology and tectonic influence. The AVO feasibility results can furthermore be utilized to generate non-stationary training data for AVO classification.

Keywords: rock physics, subsurface characterization, AVO modeling, exploration, basin analysis/modeling

OPEN ACCESS

Edited by:
Jing Ba,
Hohai University, China

Reviewed by:
José M. Carcione,
National Institute of Oceanography and Experimental Geophysics (OGS), Italy
Da Shuai,
China University of Petroleum, China

***Correspondence:**
Per Avseth
per.avseth@digsciene.no;
per.aage.avseth@gmail.com

Specialty section:
This article was submitted to Solid Earth Geophysics, a section of the journal Frontiers in Earth Science

Received: *15 December 2020*
Accepted: *23 February 2021*
Published: *15 March 2021*

Citation:
Avseth P and Lehocki I (2021) 3D Subsurface Modeling of Multi-Scenario Rock Property and AVO Feasibility Cubes—An Integrated Workflow. Front. Earth Sci. 9:642363. doi: 10.3389/feart.2021.642363

INTRODUCTION

One of the key tasks within the field of geoscience is to obtain a better understanding of the subsurface using remote sensing techniques and/or selected modeling tools. Various geophysical data and observables are acquired to characterize or map the subsurface. In particular, seismic data have been utilized in great abundance for both petroleum exploitation and aquifer characterization (e.g., Mukerji et al., 2001; Rimstad et al., 2010; Liu and Grana, 2020). However, these data are often expensive to acquire, and the seismic data need to be converted to geological properties via rock physics relations. In this study, we propose a methodology to create a 3D subsurface feasibility model for rock properties constrained by local geology (e.g., available interpreted seismic stratigraphic horizons). This modeling can give valuable information before new or additional seismic data are acquired to decide whether certain types of data will be beneficial or not at a given depth (for instance, pre-stack data are only useful if we expect to see AVO signatures in a given area/target level). Furthermore, the feasibility modeling can constrain the pre-processing, imaging and inversion of seismic data. Finally, they can be used to help guide the quantitative seismic interpretation.

Another aspect that we would like to focus on in this study is that future oil and gas exploration will likely focus on increasingly more subtle stratigraphic and/or combination traps located down-flank or up-dip from drilled/explored structures (e.g., Biswal et al., 2012; Dolson et al., 2019). Quantitative seismic interpretation (Avseth et al., 2005) will be essential in hunting for new prospects away from existing wells. A key challenge will be to do facies and fluid classification/prediction from seismic data away from existing well control, especially in areas characterized by complex tectonic history. Rock physics combined with stratigraphic interpretation and basin modeling can improve the understanding of expected seismic signatures and create augmented elastic training data for AVO classification using machine learning methods (e.g., AlKawai et al., 2018; Qadrouh et al., 2019).

This study presents an innovative and seamless workflow where rock physics combined with burial history is used to create AVO feasibility maps away from well control. The methodology is a culmination of several studies conducted in the past few years. Avseth and Lehocki (2016) showed how to combine rock physics and diagenetic modeling to predict expected AVO signatures for a given burial history (1D), and Gatemann and Avseth (2016) and Johansen (2016) showed how this method could be combined with seismic velocities to obtain calibrated net-erosion (exhumation) maps, where net-erosion is the difference between maximum burial and present-day burial depth. Avseth et al. (2020a,b) demonstrated a new workflow where rock physics combined with burial history, the latter determined from net erosion maps, was used to create AVO feasibility maps/cubes away from well control (i.e., in 2D and 3D). First, combined rock physics and compactional modeling are integrated with seismic velocities and basin modeling to create regional uplift and maximum burial maps for selected horizons/intervals. Next, geologically consistent AVO feasibility maps/cubes are created from these maximum burials and net erosion maps, while also honoring key uncertainties (rock texture, mineralogy, heterogeneity, anisotropy, temperature, etc.). This is possible because the uplift and maximum burial maps constrain the modeling of sand and shale depth trends at any given location. These depth trends are then used to estimate the expected AVO signatures for shale-sand interfaces at any given depth. The feasibility maps/cubes can be used directly during prospect maturation and de-risking. Furthermore, they can be used as a fundament to create augmented, non-stationary training data for AVO classification and seismic reservoir prediction in areas with poor well control (c.f. Lehocki et al., 2020).

In this paper, the focus is on how we go from 1D combined rock physics and burial modeling to 2D and 3D feasibility maps/cubes that can be created in real-time for multiple scenarios, where we honor variability and uncertainties in key geological parameters, including grain size, clay content, temperature history, etc. We provide an overview of the suggested workflow and demonstrate the potential of this methodology in selected areas of the Barents Sea, where the geology is complex due to spatially varying burial and uplift history. Finally, we suggest some best practices to validate the methodology and assess the uncertainties in the AVO feasibility maps.

GEOLOGICALLY CONSISTENT ROCK-PHYSICS MODELING

One of the most common methodologies in rock physics is investigating the relationships between seismic velocities and rock texture (i.e., porosity, clay, cement, grain size, etc.). The goal is either to interpret observed data in terms of geological factors, like clay content, rock texture, pressure or pore fluid saturations, or to be able to extrapolate from the data observations to predict certain "what-if" scenarios.

Figure 1 shows some useful rock physics models for high porosity sands and sandstones (sst) (Dvorkin and Nur, 1996; Avseth et al., 2000, 2005) used to quantify geologic trends and rock texture in the velocity vs. porosity domain. The models in **Figure 1** (black lines) are based on contact theory combined with modified Hashin-Shtrikman (see also Mavko et al., 2020). A steep trend in this crossplot will indicate a diagenetic trend, as quartz cement at grain contacts will significantly stiffen the rock frame, even though porosity will not reduce much. This trend can be modeled using the Dvorkin-Nur contact cement model (Dvorkin and Nur, 1996). As cement is filling macro-porosity, the model can be extrapolated to lower porosities using modified upper Hashin-Shtrikman bound. The friable sand model is a combination of Hertz-Mindlin contact theory at high porosity end member and modified lower-bound Hashin-Shtrikman for decreasing porosities. The constant cement model is a combination of the contact cement model to a certain cement volume, and a lower-bound Hashin-Shtrikman. This is a useful model for a cemented sandstone reservoir at a given burial depth,

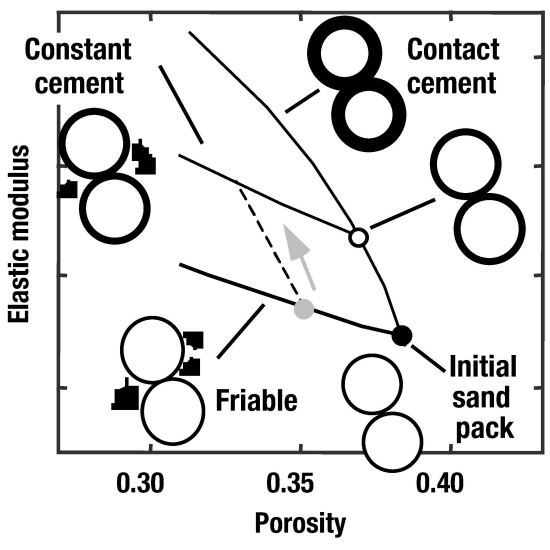

FIGURE 1 | Rock physics diagnostic models used in this study, applicable for high porosity, poorly to moderately consolidated sandstones (Avseth et al., 2000).

assuming cement volume is more or less constant. In contrast, porosity at a given depth will vary as a function of depositional porosity. The model equations used in this study are found in Avseth et al. (2005) or Mavko et al. (2020).

For unconsolidated sediments, mechanical compaction is handled via empirical relationships between porosity and burial depth (e.g., Athy, 1930; Magara, 1980). The rate of porosity decrease for sands and shales is more rapid at shallow depths and slows at greater depths of burial. The porosity as a function of burial depth can be expressed with the following exponential function:

$$\phi(z) = \phi_0 \cdot \exp(-kz) \tag{1}$$

where ϕ is the porosity at burial depth z, ϕ_0 is the depositional porosity (i.e., critical porosity) at the sea-floor ($z = 0$), and k is a compactional coefficient [m^{-1}]. Both the depositional porosity and the constant k will vary depending on lithology and clay content. Equation 1 can be modified to include clay content in sandstones (see Ramm and Bjørlykke, 1994). Alternatively, it can be expressed in terms of effective stress instead of burial depth (e.g., Lander and Walderhaug, 1999). We assume hydrostatic pressure and normal compaction for both sands and shales, yet overpressure or underpressure may be included in the modeling. At any given depth, the porosity can be used as a "critical porosity" input for the Hertz-Mindlin contact theory, according to Eq. 1. Sorting variation in sands can then be modeled using the friable sand model. Note that effective stress indirectly controls the rock physics properties via porosity changes in the mechanical compaction domain, c.f., Eq. 1, and at the same time affects the velocities via Hertz-Mindlin contact theory (i.e., pure pressure effect at grain contacts and porosity effect).

Quartz cementation will typically start at temperatures around 70 °C, which generally corresponds to a burial depth of around 2 km. Avseth and Lehocki (2016) and Lehocki and Avseth (2021) showed how the Walderhaug diagenetic model (Walderhaug, 1996) could be combined with the rock physics models above to predict seismic properties as a function of chemical diagenesis for quartz-rich sandstones. Temperature and time are the key parameters controlling the cement volume (fraction), according to the Walderhaug cement model:

$$\begin{aligned} &V_{cem_i} \\ &= V_{cem_{(i-1)}} + \left(\phi_{0cc} - V_{cem_{(i-1)}}\right) \frac{MA_{(i-1)}a}{bc_i\rho_{ma}\phi_{0cc}\ln(10)} \\ &\cdot \left(10^{b(c_i t_i + d_i)} - 10^{b(c_i t_{(i-1)} + d_i)}\right) \end{aligned} \tag{2}$$

where

- V_{cem_i}, $V_{cem_{(i-1)}}$ [–]: cumulative quartz cement volume fraction precipitated from $t = 0$ s to $t = t_i$, and from $t = 0$ s to $t = t_{(i-1)}$, respectively,
- ϕ_{0cc} [–]: porosity at the start of cementation,
- M [g/mol]: molar mass; the value used for quartz is $M_{qz} = 60.09$ g/mol,
- $A_{(i-1)}$ [cm^2]: cumulative quartz surface area at $t = t_{(i-1)}$,
- ρ_{ma} [g/cm^3]: (quartz) matrix density,
- a, b: constant with a = $1.98 \cdot 10^{-22}$ mol/(cm^2s) and $b = 0.022$ 1/C,
- c_i [°C/s]: heating rate of the i-th segment, estimated from burial/thermal history curves for different stratigraphic intervals,
- d_i [°C]: initial temperature of the i-th segment of the burial/thermal history curve under scope.

Figure 2 (Lehocki and Avseth, 2021) shows examples of various scenarios for a given burial history, where the sand grain size, sorting and coating are the varied parameters. The initial quartz surface area can be expressed as the cumulative surface area of spheres with a diameter of D:

$$A_0 = \frac{6fV}{D}(1 - coat) \tag{3}$$

where

- f [–]— a fraction of detrital quartz
- V [cm^3]—a unit volume of the sandstone
- D [cm]—a diameter (size) of the idealized sand sphere (grain)
- $coat$ [–]—a fraction of coated quartz grains

Then, the quartz surface area, A, when V_{cem} volume fraction of quartz cement has precipitated, is calculated as:

$$A = A_0\left(1 - \frac{V_{cem}}{\phi_{0cc}}\right) \tag{4}$$

Equation 4 mathematically expresses that the change in quartz surface area caused by precipitation of quartz cement is proportional to the porosity loss caused by quartz precipitation.

In particular, we see that grain size is an important parameter that will affect the cement volume, as it directly affects the specific surface area available for quartz overgrowths. Smaller grain size will have a larger specific surface area than larger grains (e.g., Carman, 1938; Salem and Chilingarian, 1999). Hence, fine-grained sandstones tend to be more cemented than medium- and coarse-grained sandstones for the same burial history. Clay coating will reduce the specific surface area available for nucleation of quartz cementation, commonly associated with authigenic illite and chlorite coatings (Shelukhina et al., 2021).

1D AVO MODELING CONSTRAINED BY BURIAL HISTORY AT WELL LOCATIONS

The one-dimensional modeling of rock physics properties of sandstones and shales as a function of burial depth in continuously subsiding basins was first presented by Helset et al. (2004), and further developed by Avseth and Dræge (2011); Dræge et al. (2014), and Avseth and Lehocki (2016). An example is shown in **Figure 3**. Based on burial and temperature history (subplot 1), the Walderhaug (1996) model is used to predict quartz cement volume (subplot 2). This quartz volume will affect the porosity depth trends of the sandstones (subplot 3). Using the Hertz-Mindlin contact theory for the mechanical compaction

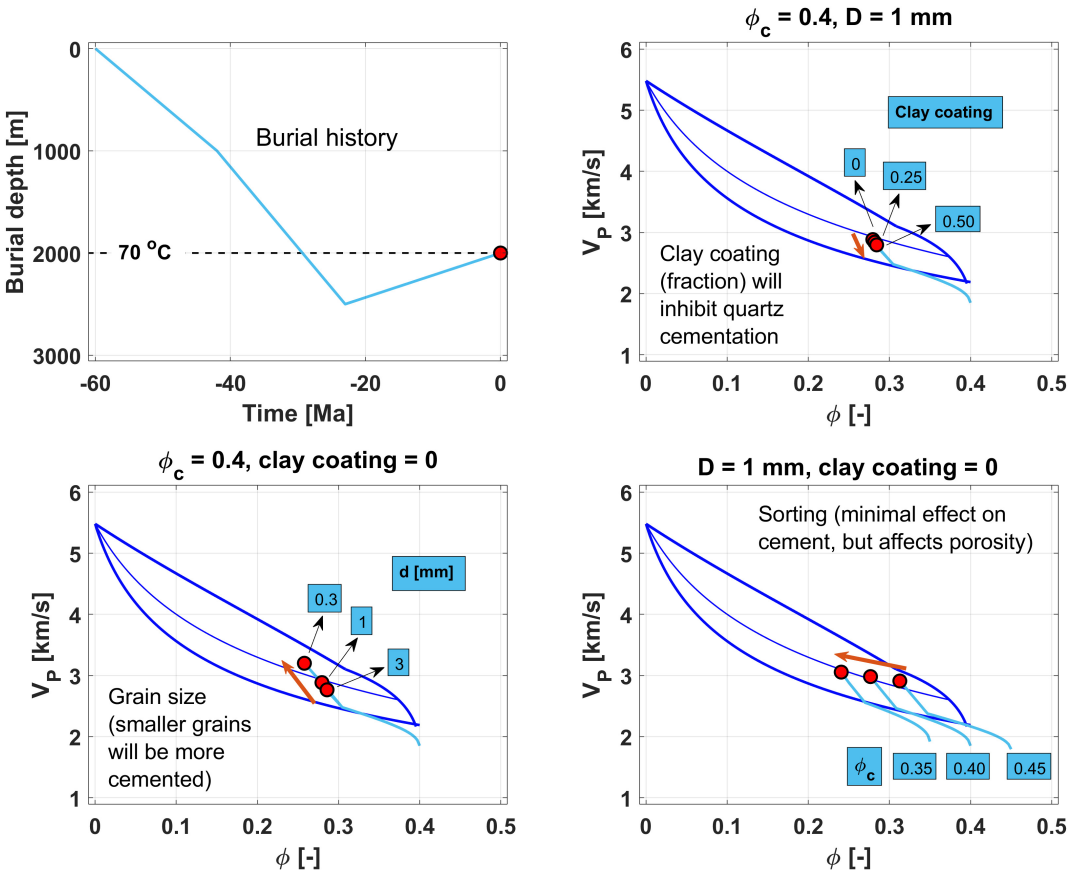

FIGURE 2 | Combined burial (mechanical and chemical compaction) and rock physics modeling using contact theory. The end-points in red represent the present-day properties, whereas the light blue curves show the rock physics properties as a function of geological time. The modeled rock represents a Tertiary age sandstone deposited 60 Ma ago that reached the chemical compaction domain (>70°C) around 30 Ma ago, then maximum burial around 25 Ma ago before the rock was exposed to tectonic uplift (which would also erode a significant part of the overburden) and is presently buried at 2 km beneath the sedimentary surface. The various subplots show the combined burial and rock physics modeling sensitivity to various input geological parameters, comprising clay coating, grain size (D), and sorting (via varying critical porosity).

domain and the Dvorkin-Nur contact cement model combined with modified upper bound Hashin-Shtrikman for the chemical compaction domain, the corresponding rock physics properties can be modeled corresponding to the burial, packing and quartz cement growth. The resulting acoustic impedances and V_P/V_S ratios are shown in subplots 4 and 5, respectively, including different fluid scenarios (gas, oil, and brine-filled sandstones). A crossplot of V_P/V_S vs. acoustic impedance for the modeled depth range is shown in subplot 6. The burial history can also be used to constrain the modeling of shale depth trends, either using inclusion based models (c.f. Dræge et al., 2006; Avseth et al., 2008; Carcione and Avseth, 2015) or calibrated contact theory (c.f., Avseth et al., 2003; Avseth and Lehocki, 2016), where the transition from smectite-rich to illite-rich shales is particularly important to honor. As we will show below, shale trends can also easily be modeled with empirical models, given that several wells are available. Shales constitute most of the subsurface in the first few kilometers depth, so even with a few wells, there should be empirical data available to constrain shale trends. Having established both sandstone and shale depth trends, one can create expected AVO signatures of a reservoir sandstone capped by a shale at any given depth (subplot 7 in **Figure 3**). In the example shown in **Figure 3**, there is a gradual change from a class 2–3 to class 1–2p (see Castagna and Swan, 1997) for hydrocarbon-filled sandstones when burial depth increases and reservoir rock becomes more consolidated.

Figure 4 shows another synthetic example, where the burial history includes an uplift episode. Note that the maximum burial happens around 35 Ma ago, at ca. 2.1 km below the sea-floor. The dashed horizontal line in all five upper subplots indicates the 70°C thermocline where we assume that quartz cementation commences. The cementation happens both during subsidence and exhumation as long as the temperatures are higher than ca. 70°C (Bjørlykke, 2015). Hence, porosity decreases, and cement volume increases both during subsidence and uplift below the dashed line. The rock physics properties change drastically due to the cementation effect. Moreover, fluid sensitivities decrease. In this example, we assess uncertainties in input parameters during the AVO modeling of today's rock physics properties (by adding 5% error to modeled elastic parameters both for reservoir

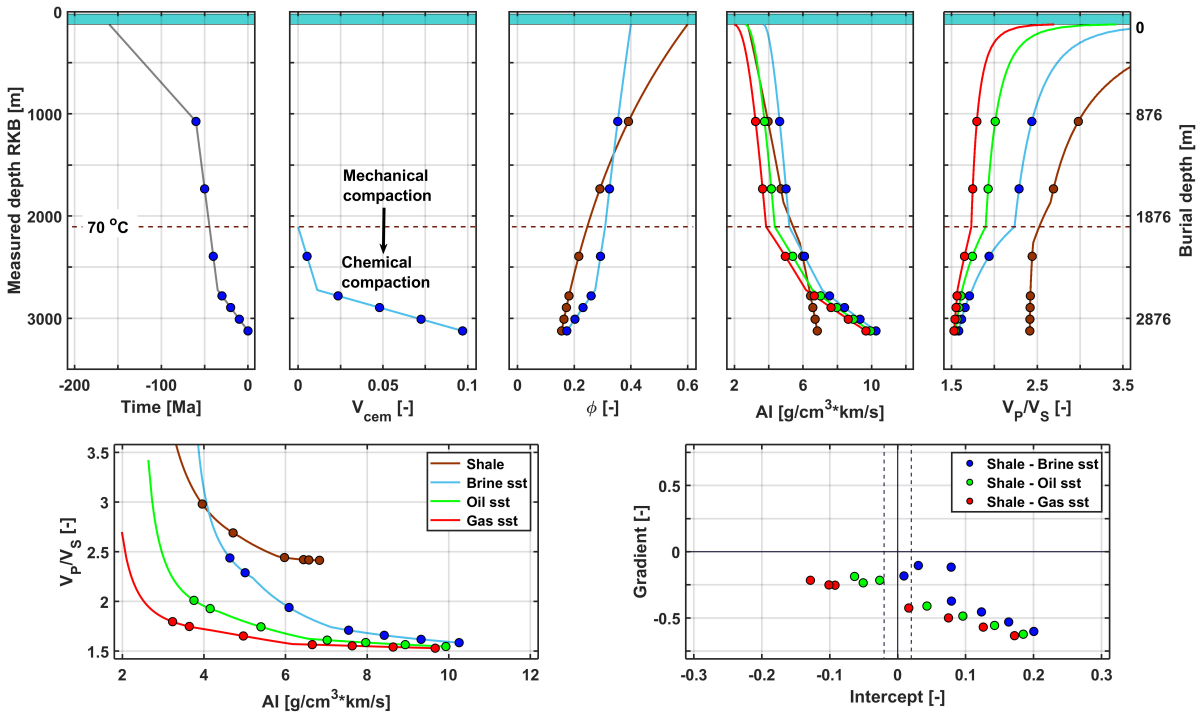

FIGURE 3 | Combined burial and rock physics modeling for a Jurassic sandstone with continuous subsidence. Note the drastic change in rock-physics, and seismic properties as the burial goes from mechanical to chemical compaction domain (>ca. 70°C).

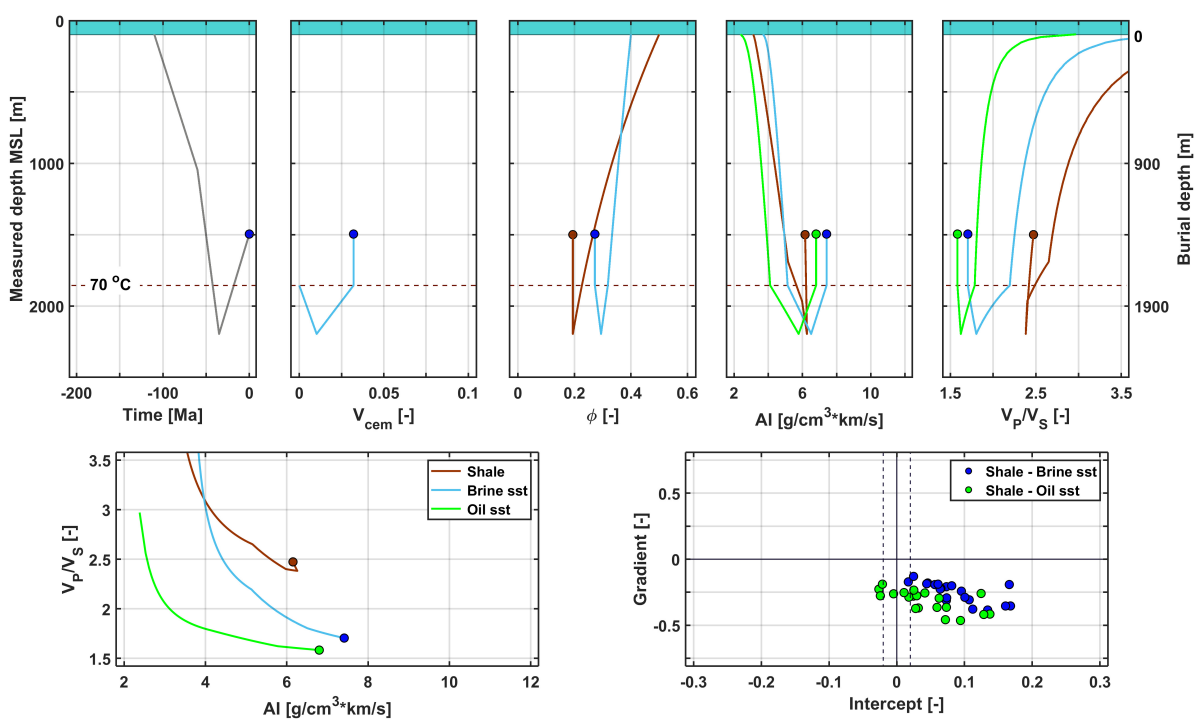

FIGURE 4 | Combined burial and rock physics modeling for a Cretaceous sandstone with Cenozoic tectonic uplift. Note the drastic change in rock physics, and seismic properties as the burial goes from mechanical to chemical compaction domain (>ca. 70°C indicated by the dashed horizontal line).

sandstone and cap-rock shale; see Avseth et al. (2003) for the established methodology of depth-dependent AVO scatter-plots). However, for the modeled scenario, we still expect quite a good separation between oil-saturated and brine saturated sandstones, still with significant overlaps in the intercept-gradient subplot.

Figure 5 shows a real data example of 1D AVO feasibility modeling performed at a well (15/5-5) in the Glitne Field, North Sea (see Avseth et al., 2001, for more background information about this field example). The temperature gradient in this well is estimated to be 34.4^{o}C/km, and the average grain size in the target zone is 0.2–0.3 mm (fine-to-medium-grained sandstone), and clay content is around 10–15%. The rock physics modeling at the Top Heimdal Fm (upper) fits with observed well log data, and we expect AVO class 2p-2 for brine-saturated sandstones and class 2–3 for oil-saturated sandstones. The top reservoir is located just beneath the onset of chemical compaction, and the burial history is quite simple with continuous subsidence since the deposition of the Tertiary age turbidite sandstones. We also model the expected AVO signature at the slightly deeper Top Ty Fm (lower). Here we expect a slightly stiffer (i.e., more cemented) sandstone with AVO class 1 for brine-saturated sandstones and class 2p for oil-saturated sandstones. This real-data example illustrates how important control the burial history has on the expected AVO signatures (c.f. Avseth et al., 2008).

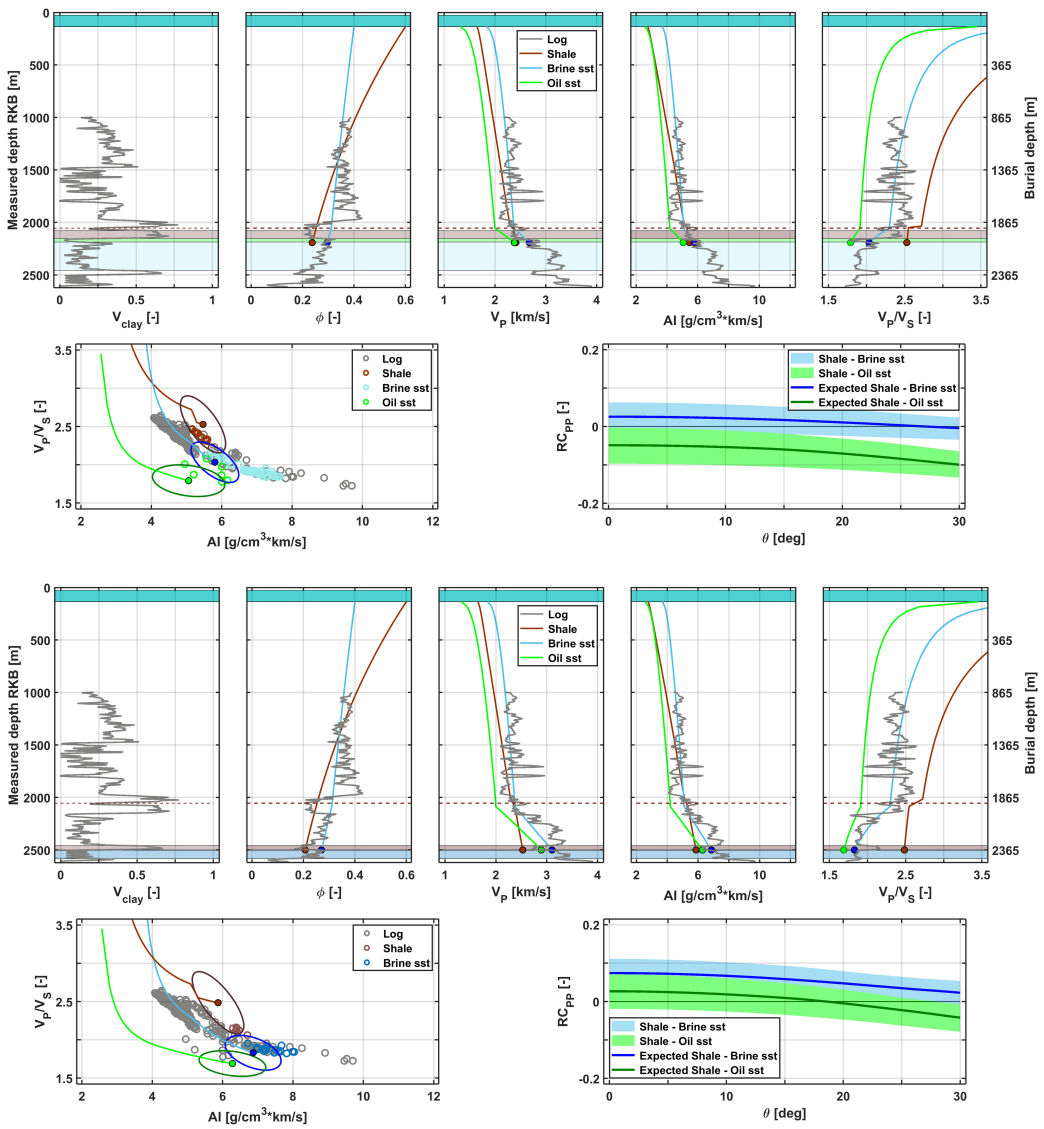

FIGURE 5 | Combined burial and rock physics modeling for Paleocene sandstones in Well 15/5-5 in the Glitne Field, North Sea. Note the change in elastic properties as we go from mechanical to chemical compaction at around 2,000 m burial depth (indicated by dashed brown horizontal line). The expected AVO signatures change drastically as we go from the Top Heimdal Fm horizon **(upper)** to the slightly deeper Top Ty Fm horizon **(lower)**. The expected oil response for the Ty Formation is similar to the expected brine response of the Heimdal Formation. This shows the importance of burial history as a key constraint in AVO analysis.

2D AVO FEASIBILITY MODELING (BARENTS SEA DEMONSTRATION)

Deriving Burial History and Net Erosion From Seismic Velocities

The same approach, as described above, can be used to model expected AVO signatures along a given seismic horizon. The burial history can be derived from seismic velocities where a normal compaction curve is defined for an area, and the deviation from this reference trend at a given location will provide information about maximum burial (e.g., Hjelstuen et al., 1996; Japsen, 1999; Baig et al., 2016). This exercise can be done on well log data and/or on seismic velocity data. Additional geological information (basin modeling, stratigraphic analysis, vitrinite reflectance, etc.) can guide the calibration of velocities into maximum burial and net erosion or exhumation maps (e.g., Gatemann and Avseth, 2016). From a given horizon (or a defined interval around this horizon), one can then derive a net exhumation map from seismic velocity data (e.g., interval velocities, tomography, or FWI P-wave velocities), which will be input to the burial constrained AVO modeling at any location of this horizon (**Figure 6**). Here, we demonstrate this workflow on a data set from the Barents Sea.

Temperature gradients vary both spatially and with time. Temperature gradient maps can be used directly as input in the modeling (Avseth et al., 2020b), or we can select constant temperature gradients during the modeling of feasibility maps. Then, via several plausible scenarios, we can test different temperature gradients. The modeling of the feasibility maps is performed in the same way as for the 1D modeling done at a well location in the previous section. In this way, we are extrapolating the AVO modeling away from well locations in agreement with the geological variation estimated from the seismic velocities via the net erosion and maximum burial maps.

Burial-Constrained Modeling of Sandstone Properties

Next, forward modeling of the expected rock physics properties and associated AVO responses for selected scenarios is performed, given the input burial history (**Figure 7**). The methodology introduced by Avseth and Lehocki (2016) for combined compaction and rock physics modeling in 1D (outlined in the previous section) is extended to perform 2D modeling of rock physics properties and associated AVO feasibility maps constrained by the net erosion map shown in **Figure 6**. In this way, the expected rock physics properties of a sandstone (saturated with any pore fluid) can be predicted at any given location of a 2D map while honoring the rock's burial (and thermal) history at this very location. Each curve in any of the subplots of **Figure 7**, indicated by orange points representing both maximum burial and present-day depth, corresponds to a given X-Y location in the net-erosion map shown in **Figure 6**.

Empirical Shale Trends

Before we can conduct the AVO modeling at any given depth, we also need to establish shale depth trends. The rock physics modeling of shale depth trends is a challenging task. Several rock physics models have been used to model shale depth trends (e.g., Avseth et al., 2003, 2008; Dræge et al., 2006; Carcione and Avseth, 2015). However, the complexity of shale texture and the lack of knowledge related to chemical diagenesis in shales make it particularly challenging to create predictive models for shales using physical models. As shown in **Figure 3**, we see that the shale depth trends can be modeled heuristically using calibrated contact theory (see also Avseth et al., 2005). However, physical models for shales tend to work well in the mechanical compaction domain, but not very well for the chemical compaction domain, due to complex cementation processes in shales. The illitization of marine smectite-rich shales happens around the same burial depth and temperature as quartz cementation of sandstones (i.e., 60–80°C). Carcione and Avseth (2015) showed how to account for the transition from smectite-rich to illite-rich shales in the rock physics modeling of clay-rich organic-rich shales using a kinetic equation. However, this chemical diagenesis also produces micro-crystalline quartz as a by-product, in addition to extra water that is released into the pore-space. The water may cause overpressure and reduced velocities. On the contrary, the micro-crystalline quartz will likely

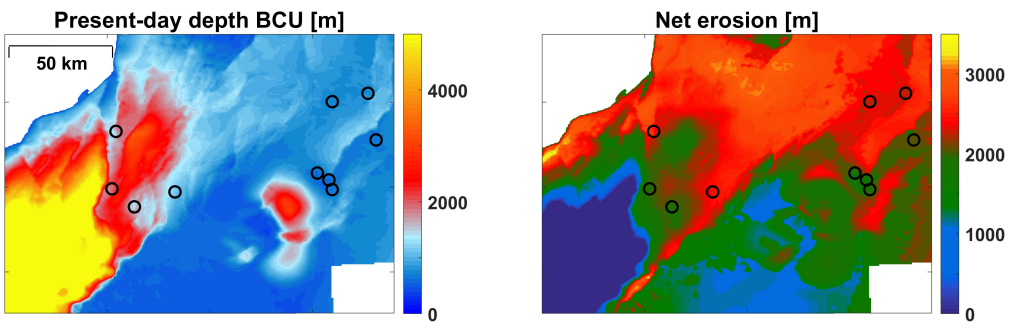

FIGURE 6 | Left: Present-day Base Cretaceous Unconformity (BCU) horizon (which is close to the Top Stø Fm sandstone horizon) in the selected area in the southern Barents Sea (offshore Norway), and selected well locations used in the calibration study (black circles). **Right:** Estimated net erosion map derived from seismic velocities relative to a normal compaction trend (Adapted from Avseth et al., 2020b).

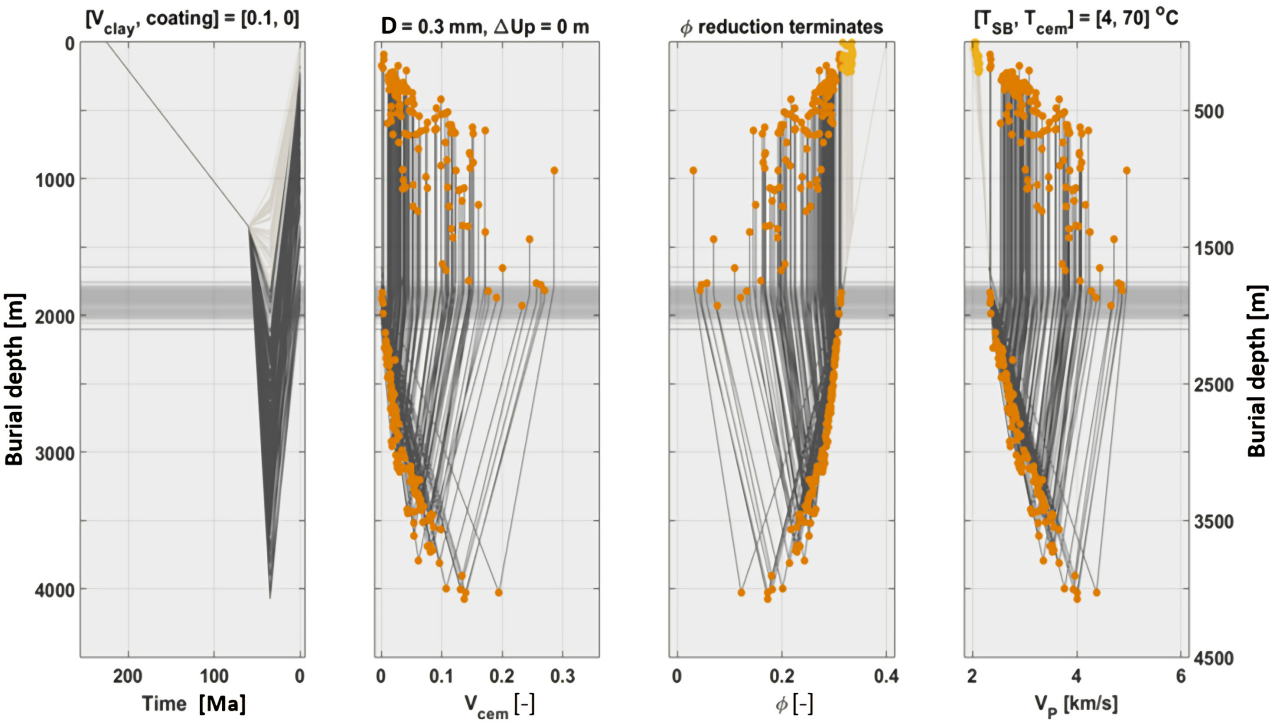

FIGURE 7 | Combined burial and rock physics modeling for clean sandstone of a Jurassic sandstone with varying burial history at different locations of the map shown in **Figure 6**. Walderhaug model predicts the cement volume (subplot 2) for a given burial/temperature history (subplot 1), and the porosities are updated accordingly (subplot 3). Eventually, the seismic velocities are predicted using rock physics models (subplot 4). Note that the lighter burial history curves seen in subplot 1 are those that do not enter the cementation window (i.e., the T = 70 °C lower limit), not even at the time of their maximum burial. The corresponding end-points in porosity and V_P subplots are marked by lighter orange color to discern them from the (majority of darker) orange points that have been at least slightly cemented. Note also that since the T_{grad} varies from point-to-point, the depth of cementation onset can change from one X–Y point to another: this transition from a mechanical compaction domain to a chemical compaction domain for each curve is seen as a horizontal (gray) line in each subplot.

stiffen the rock frame and lithify the shale into a mudrock and cause a significant increase in velocity and a drop in V_P/V_S (Thyberg et al., 2009).

As of today, there is no good holistic rock physics model to mimic all these complex geologic processes. Hence, we select to estimate empirical regression models for the shales from the well log data. **Figure 8** shows the resulting empirical trends for separate key shale intervals and a regression model for all key shale intervals lumped together. We have plotted well log data corrected for uplift, according to the analysis above (i.e., against the maximum burial). We have also superimposed well-known regression models for Norwegian shelf shales published in the literature, including the model by Hjelstuen et al. (1996) and Japsen (1999). The green circles are average values from well log data (from the wells indicated in the map in **Figure 6**) for the various shale intervals. We test out both power-law regressions (of the form $y = a \cdot x^b + c$) and linear regression models ($y = a \cdot x + b$). The power law seems to better describe the data in the Fuglen Fm. However, the two data points in the 2,300–2,500 m interval represent two wells where the Fuglen Fm is very silty, likely due to the early transgression availability of near-shore silty particles. Hence, we find it is better to describe the compaction trends in shales using the linear trends, even though the local fit to more silty shales is poorer. Care should be taken using a power-law, as this one can give large errors outside the observation span (particularly when doing extrapolation to more shallow depth). The empirical shale trends in **Figure 8** are essential as inputs for the AVO modeling constrained by burial history.

Elastic Property Feasibility Maps

From the burial-constrained rock physics modeling, we create forward-modeled maps of elastic properties for the Fuglen Fm cap-rock shale and the Stø Fm reservoir sandstones (**Figure 9**). We test out various scenarios and the sensitivity of important input parameters. **Figure 9** shows a scenario where the dominating grain size of sandstones is 0.3 mm (i.e., medium grain size), the pore-filling clay content is 0.1, the temperature gradient is 38°C/km, and the pore fluid is oil. Note the significant imprint of geologic structures and tectonics. This is geologic information brought into the modeling from the seismic velocity data and stratigraphic interpretations. The area in the west has the largest maximum burial, which explains the very high acoustic impedance values (>10 g/cm^3·km/s). This is an area where we expect very low seismic fluid sensitivity. Eastward, the maximum burial is lower, and in some areas the rocks have not even been cemented (T < ca. 70°C at maximum burial). Here, the impedance values are significantly

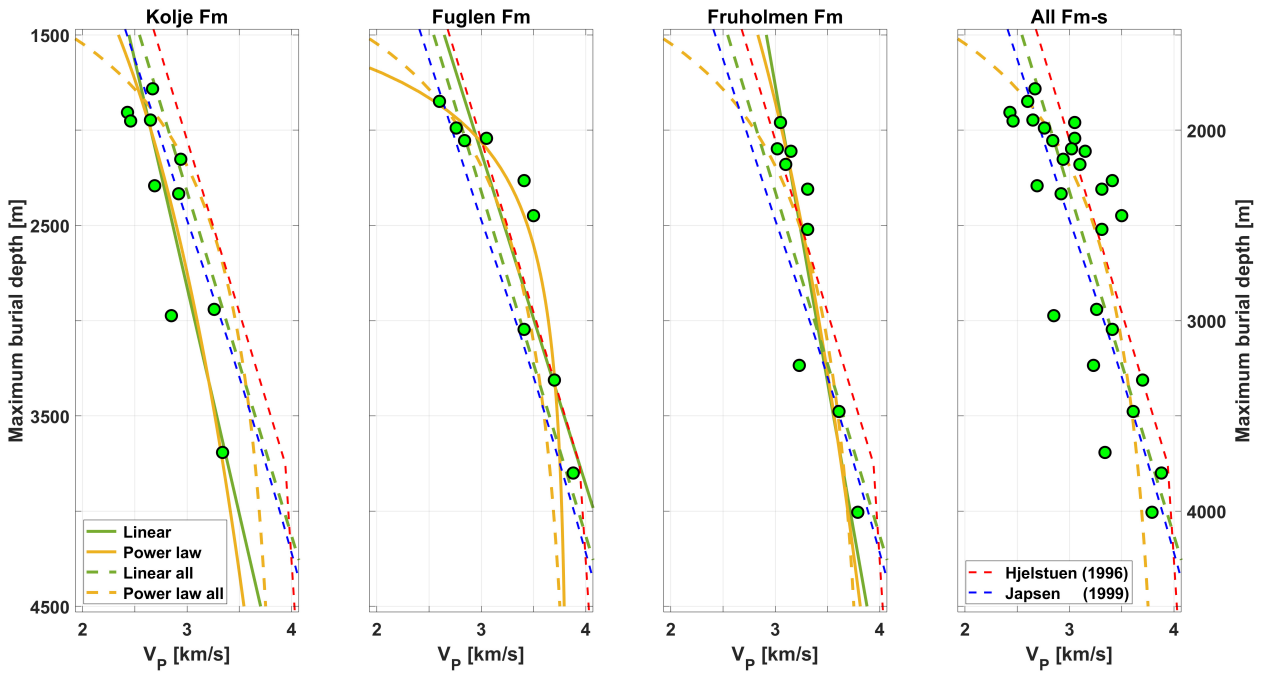

FIGURE 8 | Empirical shale trends. Models for separate shale intervals are shown from **left to right**, comprising Kolje, Fuglen, and Fruholmen Fm-s. Regression lines are also made for all shale intervals together (rightmost subplot). Published trends by Hjelstuen et al. (1996) and Japsen (1999) are superimposed.

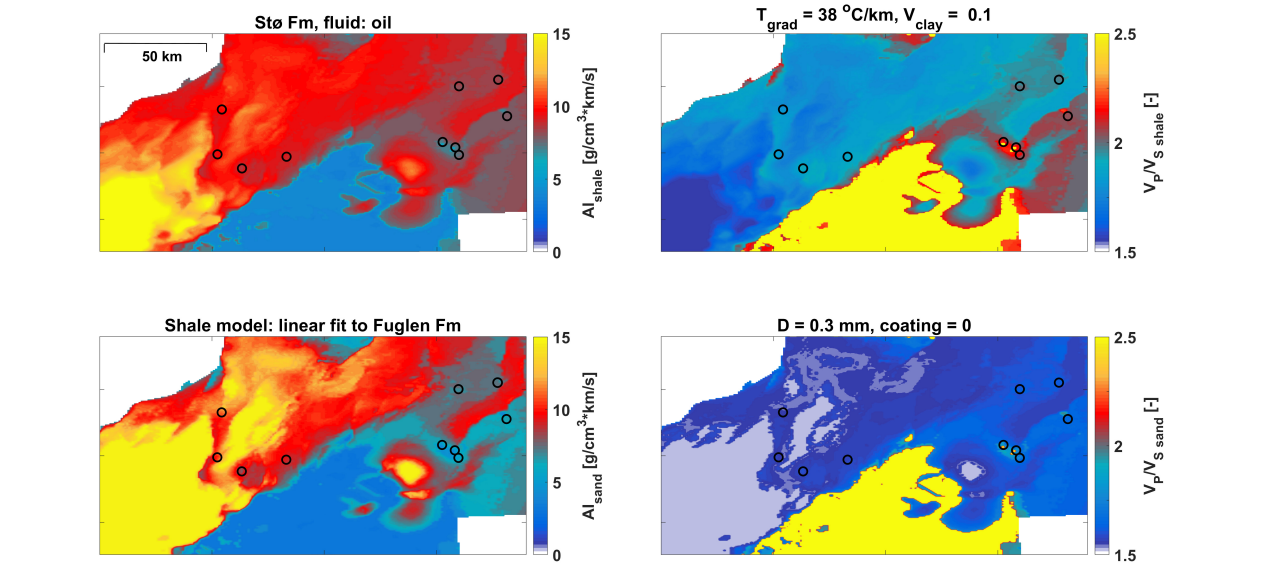

FIGURE 9 | Elastic property feasibility maps for a given geological scenario. **Upper:** Expected acoustic impedance and V_P/V_S of cap-rock Fuglen Fm shale; **Lower:** Expected acoustic impedance and V_P/V_S for brine-filled reservoir sandstone of Stø Fm. Note that these maps are modeled values for shales and sandstones constrained by the burial maps (i.e., net erosion) in **Figure 6**, which are again derived from the seismic velocity data.

lower (<10 g/cm^3·km/s), and we would expect better seismic detectability of oil.

AVO Feasibility Maps

Next, we create the AVO feasibility maps (**Figure 10**) from the elastic property maps, using full Zoeppritz modeling (Zoeppritz, 1919). Here we show the expected AVO classes for various pore fluid scenarios. Oil-filled Stø Fm will predominantly show AVO class 1 in the western area, similar to what we expect for water-filled and gas-filled sandstones. We see a larger variability in expected AVO classes in the eastern part, but predominantly we expect AVO class 3 for oil and gas.

Hence, there is a much better ability to seismically discriminate hydrocarbons from brine in the eastern part. Avseth et al. (2020a) also demonstrated how AVO feasibility maps could be generated for a given prospect, and showed how AVO classes could change with pore fluid depending on the input temperature gradient. In this way, they demonstrated the power of the proposed workflow to perform AVO de-risking of prospects away from well control.

3D AVO FEASIBILITY CUBES (BARENTS SEA DEMONSTRATION)

Finally, we perform a full 3D modeling of rock physics properties and associated AVO feasibility cubes. We extrapolate between 2D maps using compaction/depth trends honoring the burial history at any given location. In this way, we can forecast the expected rock physics properties of a given rock, sandstone or shale, at any given location of a 3D cube, while honoring the burial (and thermal) history of the rock at this same location. By combining the elastic properties of sandstone and shale cubes, we can generate the so-called AVO feasibility cubes (in 3D) that predict the expected AVO response for a given pore fluid at any location in the cube.

Figure 11 shows a 3D AVO feasibility cube and associated rock properties, and we focus on a Tertiary age target interval, the Intra Torsk Fm sandstones of Paleocene/Eocene age, in a selected area in the Barents Sea. These sands are located in a deep-marine setting. As **Figure 11** shows, we expect no quartz cementation in these sands toward the top of the formation, based on our modeling. This is because the sands have never reached a depth where temperatures are large enough (greater than ca. 70°C) to form quartz cement. However, we need to honor the mechanical compaction with porosity reduction and increasing effective stress with depth. The shale depth trends used for the AVO feasibilities in the Torsk Fm interval, are

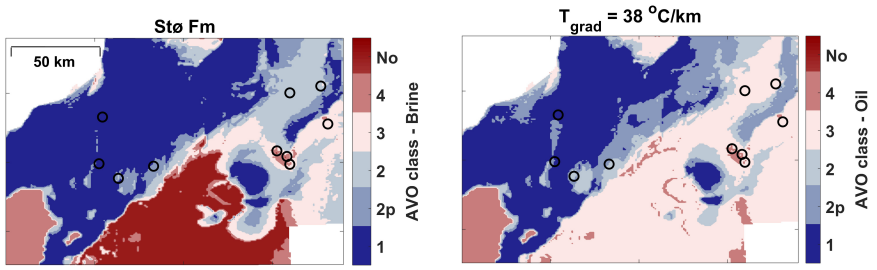

FIGURE 10 | AVO feasibility maps, including AVO classes for brine saturated sandstones **(left)** and oil-saturated sandstones **(right)**. Regional AVO feasibility maps that show significant geologic imprint on the expected AVO classes of different fluid scenarios.

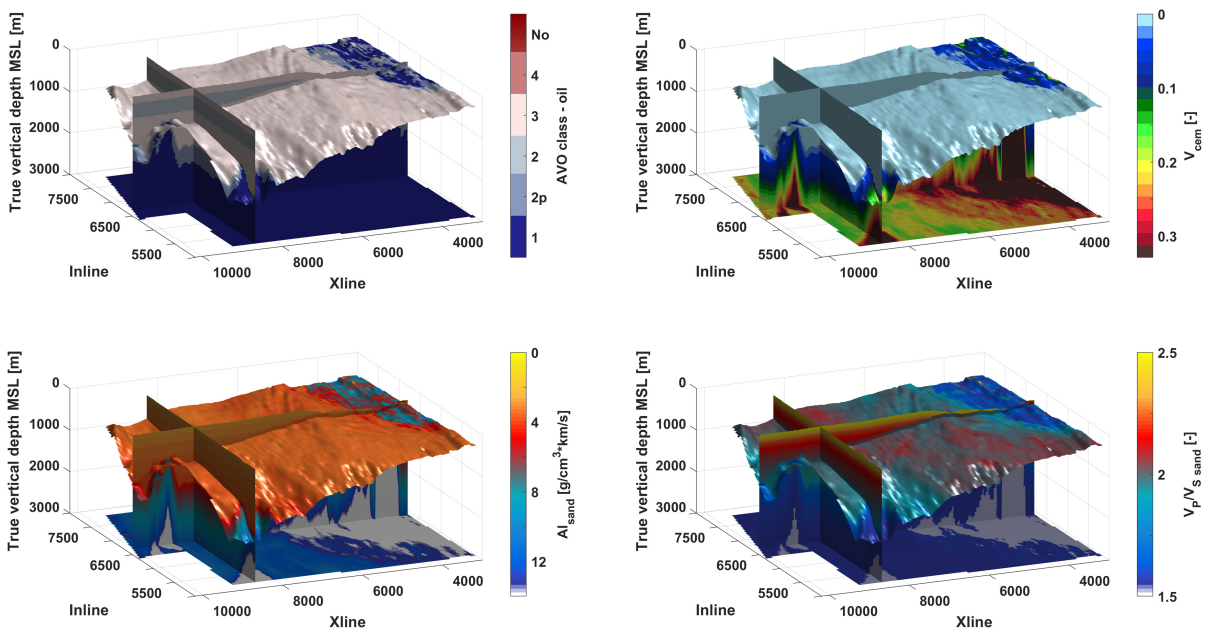

FIGURE 11 | Rock property and AVO feasibility cubes in a selected area of the Barents Sea. Oil-filled Tertiary sands show mostly class 3 AVO response in the area, and cement volume is 0, as the sands are not buried deep enough to be cemented (figure adapted from Avseth et al., 2020a).

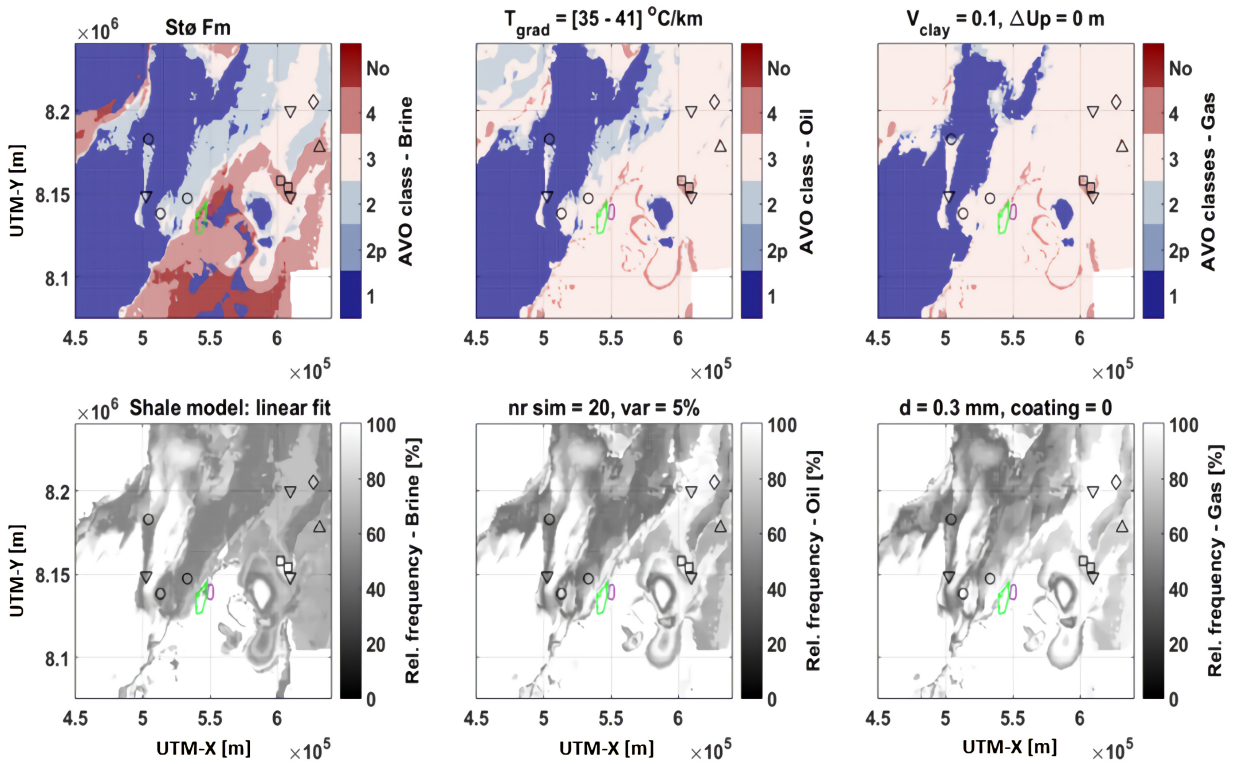

FIGURE 12 | Uncertainty assessment of AVO feasibility maps testing a range of constant temperature gradients. The white areas in the three lower subplots indicate where AVO classes do not change (i.e., low uncertainty). In contrast, the gray areas indicate where AVO classes will change within this temperature range (i.e., higher uncertainty).

empirical trends derived from intra Torsk shales in nearby wells. We see that mainly AVO class 3 is expected for oil-filled Torsk Fm sands, whereas brine sands (not shown here) will give a class 1.

VALIDATION AND UNCERTAINTY ASSESSMENT OF AVO FEASIBILITIES

The resulting AVO feasibility maps/cubes should be validated against real data observations, if available. The water-saturated signatures are often well constrained by the fact that most of the subsurface is indeed water-filled. The observed brine-filled AVO response in a down-flank area of a prospective structure, where one knows there must be water-filled sandstones, should match the modeled AVO brine response for this location. Furthermore, blind-well validations of expected rock properties and AVO signatures should be conducted if there are several wells inside the area of interest. If there is a mismatch with the observed (pre-stack seismic or well log) data, the AVO feasibility modeling input must be updated. In a scenario-based modeling, geological parameters like facies, grain size, temperature gradient, clay content, etc., can be edited. This exercise should be done in integrated teams with input from domain experts covering a range of different geological constraints (basin modeling, sedimentology, geochemistry). Note that the AVO feasibility maps could also highlight the poor quality or insufficient pre-conditioning of the seismic data.

Regardless of any validation, there are uncertainties associated with the AVO feasibility maps related to both geological variability and modeling bias/ambiguities (i.e., input parameters and model assumptions). The key geological uncertainties include uncertainties in burial history and net erosion from seismic velocities, both associated with the choice of shale reference trend and the seismic interval velocities. However, this information is better than no information and linear interpolation between wells. Furthermore, we can test uncertainties in uplift and how they will affect the AVO feasibility maps. Another key geological uncertainty is associated with the assumed sandstone texture for different intervals, including grain size, clay volume, sorting, and clay coating. Temperature gradients and their variation in space and time can also significantly impact the AVO feasibility maps/cubes. This variation can be associated with distances to the basement craton. It could also be related to tectonic uplift processes and the timing of uplift. One of the best ways to mitigate temperature-gradient-related uncertainties is to perform a probabilistic tectonic heat flow modeling (Van Wees et al., 2009).

In the 2D AVO feasibility map generated above, we focused on a scenario with a spatially constant temperature gradient of 38°C/km. **Figure 12** shows a test where we simulate AVO

feasibility maps for several cases where we vary the temperature gradient. Then, we test how this will affect the AVO classification for different fluid scenarios. Interestingly, we see that the classes stay constant regardless of temperature gradient in some parts of the map, but will change in other parts.

It should also be mentioned that we have used default values for brine, oil and gas in this study. These may indeed vary spatially and with burial depth (fluid pressure effect that will change with burial depth is accounted for already). Variability in salinity, oil API/GOR and gas gravity represents uncertainties that could be handled via scenarios or sensitivity studies, but in this study, we consider the variability of these properties to be second-order compared to other geological uncertainties.

CONCLUSION

We have demonstrated a new integrated workflow for generating AVO feasibility maps/cubes with data from the Barents Sea. The methodology enables rapid extrapolation of expected rock physics properties away from well control, along selected horizons, constrained by seismic velocity information, geological inputs (basin modeling, seismic stratigraphy and facies maps) and rock physics depth trend analysis. The workflow should allow for more rapid, seamless and geologically consistent DHI de-risking of prospects in areas with complex geology and tectonic influence. The AVO feasibility maps can furthermore be utilized to generate non-stationary training data for AVO classification.

DATA AVAILABILITY STATEMENT

The data analyzed in this study is subject to the following licenses/restrictions: Confidential seismic velocity data have been used to generate maps/cubes. Well log data used in this study are released through Norwegian Petroleum Directorate, but permission requires membership of their Diskos database. Requests to access these datasets should be directed to www.npd.no/en/diskos.

AUTHOR CONTRIBUTIONS

PA did concept and rock physics. IL did coding and implementation. Both authors have contributed equally.

ACKNOWLEDGMENTS

We thank Spirit Energy and partners of license PL962 on the Norwegian Continental Shelf for data and financial support for this study.

REFERENCES

AlKawai, AlKawi, W., Mukerji, T., Scheirer, A. H., and Graham, S. A. (2018). Combining seismic reservoir characterization workflows with basin modeling in the deepwater Gulf of Mexico Mississippi Canyon area. *AAPG Bull.* 102, 629–652. doi: 10.1306/0504171620517153

Athy, L. (1930). Density, porosity, and compaction of sedimentary rocks. *AAPG Bull.* 14, 1–24. doi: 10.1306/3D93289E-16B1-11D7-8645000102C1865D

Avseth, P., and Dræge, A. (2011). Memory of rocks – how burial history controls present-day seismic properties. example from troll east, North Sea. *Paper Presented at the 2011 SEG Annual Meeting: SEG Extended Abstract*, San Antonio, TX. doi: 10.1190/1.3627620

Avseth, P., Dræge, A., van Wijngaarden, A.-J., Johansen, T. A., and Jørstad, A. (2008). Shale rock physics and implications for AVO analysis: a North Sea demonstration. *Lead. Edge* 27, 788–797. doi: 10.1190/1.2944164

Avseth, P., Dvorkin, J., Mavko, G., and Rykkje, J. (2000). Rock physics diagnostic of North Sea sands: link between microstructure and seismic properties. *Geophys. Res. Lett.* 27, 2761–2764. doi: 10.1029/1999GL008468

Avseth, P., and Lehocki, I. (2016). Combining burial history and rock-physics modeling to constrain AVO analysis during exploration. *Lead. Edge* 35, 528–534. doi: 10.1190/tle35060528.1

Avseth, P., Lehocki, I., Feuilleaubois, L., Hansen, T. N., Angard, K., and Reiser, C. (2020a). Exploration workflow for real-time modelling of rock property and AVO feasibilities in areas with complex burial history – a Barents Sea demonstration. *First Break* 38, 51–56. doi: 10.3997/1365-2397.fb2020065

Avseth, P., Lehocki, I., Hansen, T., Angard, K., Schjeldrup, S., and Shelavina, E. (2020b). "A new integrated workflow to generate AVO feasibility maps for prospect de-risking," in *Proceedings of the 82nd EAGE Annual Conference & Exhibition. EAGE Extended Abstract*, Vol. 2020 (Houten: European Association of Geoscientists & Engineers), 1–5. doi: 10.3997/2214-4609.202010498

Avseth, P., Mukerji, T., Jørstad, A., Mavko, G., and Veggeland, T. (2001). Seismic reservoir mapping from 3-D AVO in a North Sea turbidite system. *Geophysics* 66, 1157–1176. doi: 10.1190/1.1487063

Avseth, P., Mukerji, T., and Mavko, G. (2005). *Quantitative Seismic Interpretation – Applying Rock Physics Tools to Reduce Interpretation Risk*. Cambridge: Cambridge University Press. doi: 10.1017/CBO9780511600074

Avseth, P., van Wijngaarden, A.-J., and Flesche, H. (2003). AVO classification of lithology and pore fluids constrained by rock physics depth trends. *Lead. Edge* 22, 1004–1011. doi: 10.1190/1.1623641

Baig, I., Faleide, J. I., Jahren, J., and Mondol, N. H. (2016). Cenozoic exhumation on the southwestern Barents Shelf: estimates and uncertainties constrained from compaction and thermal maturity analyses. *Mar. Pet. Geol.* 73, 105–130. doi: 10.1016/j.marpetgeo.2016.02.024

Biswal, S. K., Vachak, H. S., Rawat, D. S., Bhagat, S., Bharsakale, A., and Tandon, A. K. (2012). "Deliberate search for stratigraphic traps within Oligocene sediments of Central Graben in the Western Offshore Basin, India," in *Proceedings of the 9th Biennial International Conference and Exposition of Petroleum Geophysics, Hyderabad 2012*, Hyderabad, 275.

Bjørlykke, K. (2015). *Petroleum Geoscience: From Sedimentary Environments to Rock Physics*. Berlin: Springer.

Carcione, J., and Avseth, P. (2015). Rock-physics templates for clay-rich source rocks. *Geophysics* 80, D481–D500. doi: 10.1190/geo2014-0510.1

Carman, P. C. (1938). The determination of the specific surface of powders. I. *J. Soc. Chem. Indus.* 57, 225–234. doi: 10.1190/1.1437626

Castagna, J. P., and Swan, H. W. (1997). Principles of AVO crossplotting. *Lead. Edge* 16, 337–344. doi: 10.1190/1.1437626

Dolson, J. C., Merrill, R., and Sternbach, C. (2019). Advances in stratigraphic trap exploration. *GeoExPro Mag.* 16, 74–76.

Dræge, A., Duffaut, K., Wiik, T., and Hokstad, K. (2014). Linking rock physics and basin history — Filling gaps between wells in frontier basins. *Lead. Edge* 33, 240–246. doi: 10.1190/tle33030240.1

Dræge, A., Jakobsen, M., and Johansen, T. (2006). Rock physics modelling of shale diagenesis. *Pet. Geosci.* 12, 49–57. doi: 10.1144/1354-079305-665

Dvorkin, J., and Nur, A. (1996). Elasticity of high−porosity sandstones: theory for two North Sea data sets. *Geophysics* 61, 1363–1370. doi: 10.1190/1.1444059

Gatemann, H., and Avseth, P. (2016). Net uplift estimation using both sandstone modeling and shale trends, on the Horda Platform area in the Norwegian North Sea. *Paper Presented at the 2016 SEG International Exposition and*

Annual Meeting: SEG Extended Abstract, Dallas, TX. doi: 10.1190/segam2016-13865497.1

Helset, H. M., Matthews, J. C., Avseth, P., and van Wijngaarden, A.-J. (2004). "Combined diagenetic and rock physics modelling for improved control on seismic depth trends," in *Proceedings of the 66th Conference and Ex-hibition: EAGE Extended Abstract* (Houten: EAGE).

Hjelstuen, B. O., Elverhøi, A., Faleide, J. I., Solheim, A., Riis, F., Elverhoi, A., et al. (eds) (1996). "Cenozoic erosion and sediment yield in the drainage area of the Storfjorden Fan," in *Impact of Glaciations on Basin Evolution: Data and Models from the Norwegian Margin and Adjacent Areas. Global Planet. Change*, Vol. 12 (Amsterdam: Elsevier), 95–117. doi: 10.1016/0921-8181(95)00014-3

Japsen, P. (1999). Overpressured Cenozoic shale mapped from velocity anomalies relative to a baseline for marine shale. North Sea. *Pet. Geosci.* 5, 321–336. doi: 10.1144/petgeo.5.4.321

Johansen, N. (2016). *Regional Net Erosion Estimations and Implications for Seismic AVO Signatures in the Western Barents Sea*. Master thesis, NTNU, Trondheim.

Lander, R., and Walderhaug, O. (1999). Predicting porosity through simulating sandstone compaction and quartz. *AAPG Bull.* 83, 433–449.

Lehocki, I., and Avseth, P. (2021). From cradle to grave: how burial history controls the rock-physics properties of quartzose sandstones. *Geophys. Prospect.* 69, 629–649. doi: 10.1111/1365-2478.13039

Lehocki, I., Avseth, P., and Mondol, N. (2020). Seismic methods for fluid discrimination in areas with complex geologic history – A case example from the Barents Sea. *Interpretation* 8, SA35–SA47. doi: 10.1190/INT-2019-0057.1

Liu, M., and Grana, D. (2020). Petrophysical characterization of deep saline aquifers for CO2 storage using ensemble smoother and deep convolutional autoencoder. *Adv. Water Resour.* 142:103634. doi: 10.1016/j.advwatres.2020.103634

Magara, K. (1980). Comparison of porosity-depth relationships of shales and sandstone. *J. Pet. Geol.* 3, 175–185. doi: 10.1111/j.1747-5457.1980.tb00981.x

Mavko, G., Mukerji, T., and Dvorkin, J. (2020). *The Rock Physics Handbook*, 3rd Edn. Cambridge: Cambridge University Press. doi: 10.1017/9781108333016

Mukerji, T., Jørstad, A., Avseth, P., Mavko, G., and Granli, J. R. (2001). Mapping lithofacies and pore−fluid probabilities in a North Sea reservoir: seismic inversions and statistical rock physics. *Geophysics* 66, 988–1001. doi: 10.1190/1.1487078

Qadrouh, A. N., Carcione, J. M., Alajmi, M., and Alyousif, M. M. (2019). A tutorial on machine learning with geophysical applications. *Boll. Geofis. Teor. Appl.* 60, 375–402.

Ramm, M., and Bjørlykke, K. (1994). Porosity/depth trends in reservoir sandstones: assessing the quantitative effects of varying pore-pressure, temperature history and mineralogy. Norwegian Shelf data. *Clay Mineral.* 29, 475–490. doi: 10.1180/claymin.1994.029.4.07

Rimstad, K., Avseth, P., and Omre, H. (2010). Bayesian lithology/fluid prediction constrained by spatial couplings and rock physics depth trends. *Lead. Edge* 29, 584–589. doi: 10.1190/1.3422457

Salem, H. S., and Chilingarian, G. V. (1999). Determination of specific surface area and mean grain size from well-log data and their influence on the physical behavior of offshore reservoirs. *J. Pet. Sci. Eng.* 22, 241–252. doi: 10.1016/S0920-4105(98)00084-9

Shelukhina, O., El-Ghali, M. A. K., Abbasi, I. A., Hersi, O. S., Farfour, M., Ali, A., et al. (2021). Origin and control of grain-coating clays on the development of quartz overgrowths: example from the lower Paleozoic Barik Formation sandstones, Huqf region, Oman. *Arab. J. Geosci.* 14:210. doi: 10.1007/s12517-021-06541-5

Thyberg, B., Jahren, J., Winje, T., Bjørlykke, K., and Faleide, J. I. (2009). From mud to shale: rock stiffening by micro-quartz cementation. *First Break* 27, 53–59. doi: 10.3997/1365-2397.2009003

Van Wees, J. D., van Bergen, F., David, P., Nepveu, M., Beekman, F., Cloetingh, S., et al. (2009). Probabilistic tectonic heat flow modeling for basin maturation: assessment method and applications. *Mar. Pet. Geol.* 26, 536–551. doi: 10.1016/j.marpetgeo.2009.01.020

Walderhaug, O. (1996). Kinetic modeling of quartz cementation and porosity loss in deeply buried sandstone reservoirs. *AAPG Bull.* 80, 731–745. doi: 10.1306/64ED88A4-1724-11D7-8645000102C1865D

Zoeppritz, K. (1919). Nachrichten von der Königlichen Gesellschaft der Wissenschaften zu Göttingen, Mathematisch-physikalische Klasse, (Gottingen: Eng: Royal Society of Sciences), 66–84.

Conflict of Interest: The authors declare that the research was conducted in the absence of any commercial or financial relationships that could be construed as a potential conflict of interest.

Copyright © 2021 Avseth and Lehocki. This is an open-access article distributed under the terms of the Creative Commons Attribution License (CC BY). The use, distribution or reproduction in other forums is permitted, provided the original author(s) and the copyright owner(s) are credited and that the original publication in this journal is cited, in accordance with accepted academic practice. No use, distribution or reproduction is permitted which does not comply with these terms.

frontiers in Earth Science

ORIGINAL RESEARCH
published: 15 March 2021
doi: 10.3389/feart.2021.640698

Bayesian Analysis to Determine Relative Significance of Inputs of a Rock-Physics Model

Kyle T. Spikes[1]* *and Mrinal K. Sen*[1,2]

[1]Department of Geological Sciences, Jackson School of Geosciences, The University of Texas at Austin, Austin, TX, United States, [2]Insitute for Geophysics, Jackson School of Geosciences, The University of Texas at Austin, Austin, TX, United States

Rock-physics models relate rock properties to elastic properties through non-unique relationships and often in the presence of seismic data that contain significant noise. A set of inputs define the rock-physics model, and any errors in that model map directly into uncertainty in target seismic-scale amplitudes, velocities, or inverted impedances. An important aspect of using rock-physics models in this manner is to determine and understand the significance of the inputs into a rock-physics model under consideration. Such analysis enables the design of prior distributions that are informative within a reservoir-characterization formulation. We use the framework of Bayesian analysis to find internal dependencies and correlations among the inputs. This process requires the assignments of prior distributions, and calculation of the likelihood function, whose product is the posterior distribution. The data are well-log data that come from a hydrocarbon-bearing set of sands from the Gulf of Mexico. The rock-physics model selected is the soft-sand model, which is applicable to the data from the reservoir sands. Results from the Bayesian algorithm are multivariate histograms that demonstrate the most frequent values of the inputs given the data. Four analyses are applied to different subsets of the reservoir sands, and each reveals some correlations among certain model inputs. This quantitative approach points out the significance of a singular or joint set of rock-physics model parameters.

Keywords: rock physics, bayesian analyses, model sensitivity, elastic properties, fluid effect

OPEN ACCESS

Edited by:
Beatriz Quintal,
University of Lausanne, Switzerland

Reviewed by:
Priyank Jaiswal,
Oklahoma State University, United States
Jack Petrovich Dvorkin,
Stanford University, United States

***Correspondence:**
Kyle T. Spikes
kyle.spikes@jsg.utexas.edu

Specialty section:
This article was submitted to Solid Earth Geophysics, a section of the journal Frontiers in Earth Science

Received: *11 December 2020*
Accepted: *02 February 2021*
Published: *15 March 2021*

Citation:
Spikes KT and Sen MK (2021) Bayesian Analysis to Determine Relative Significance of Inputs of a Rock-Physics Model. Front. Earth Sci. 9:640698. doi: 10.3389/feart.2021.640698

INTRODUCTION

The application of a rock-physics model to a relevant data set has a number of uses. An appropriate model based on geologic context can provide an aid in the interpretation of depositional and diagenetic history of a formation or sequence of formations of interest. Another use is to understand what seismic velocities to expect from in scenarios both represented and not represented in a relevant data set. In either case, inputs into rock-physics models can be treated as qualitative nearly arbitrary values that satisfy a fit to data. That fit could be deemed successful from a visual standpoint, or a quantitative comparison with the data could be used to determine a successful fit. This process, however, potentially could exclude any unknown correlations among inputs, where some physical connection could be used to determine more confidently the values of the inputs. Our work here identifies the most significant sets of model inputs as well as significant correlations among them. We do this by quantitatively fitting an established rock-physics model to appropriate well-log data using a Bayesian analysis process. In the

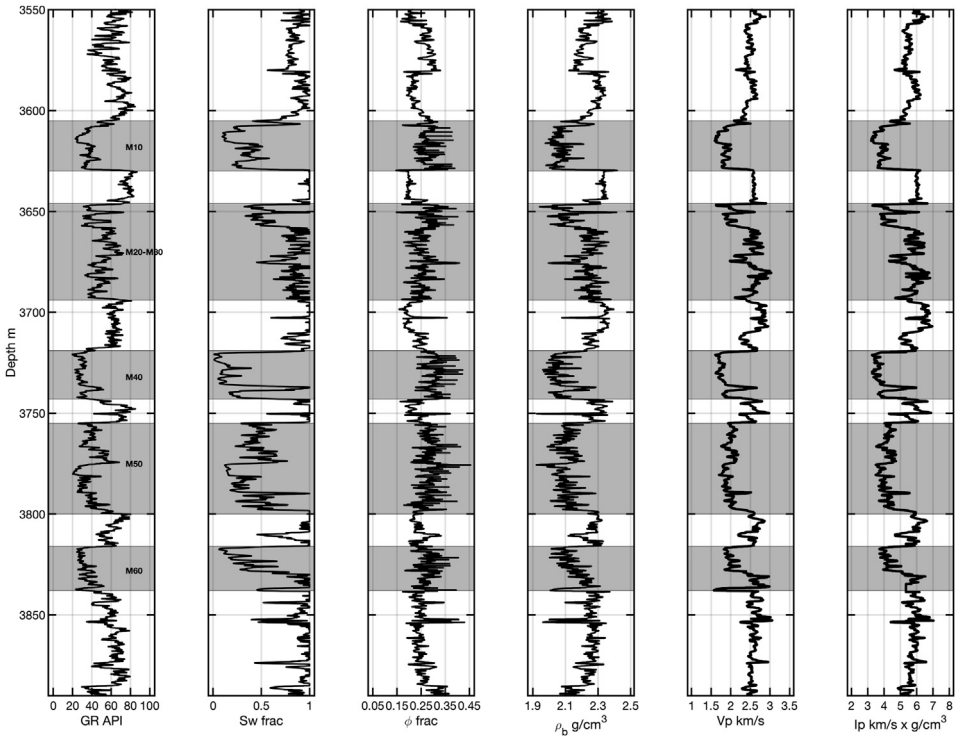

FIGURE 1 | Log data from the Gulf of Mexico data set. Included are **(A)** gamma ray, **(B)** water saturation, **(C)** porosity, **(D)** density, **(E)** P-wave velocity, and **(F)** P-impedance. In gray are the M10-M60 sands, also labeled in **(A)**. The sands have lower impedances than the shales and tend to separate cleanly in that domain.

context of seismic reservoir characterization, this type of statistical analysis is important because it provides information to define realistic prior distributions in the rock-physics part of a reservoir-characterization workflow.

Bayesian approaches are commonly used to infer rock or elastic properties from geophysical observations such as Bosch et al. (2010), Ulvmoen and Omre (2010), Ulvmoen et al. (2010), Nawaz and Curtis (2017), Grana (2018). The goal of these works is to obtain subsurface distributions of rock properties of interest. The work here determines the sensitivity of model parameters for a model fit to a data set. The work in this paper uses one model and well-log data from the Gulf of Mexico. Our work is unique and important because it directly interrogates the rock-physics model to determine the significance and any internal dependencies and/or correlations of the inputs. Many other models and relevant data could be treated in this way, so the results are not necessarily useful for application to other models. However, the results for an individual model are applicable to other data sets where the inputs can be considered from most to least significant.

MATERIALS AND METHODS

Data and Rock-Physics Model

We use a data set from a clastic reservoir in the Gulf of Mexico with water depth about 1300 m. Selected well logs (**Figure 1**) from one well included gamma ray (GR), water saturation (S_w), porosity (ϕ), density (ρ_b), P-wave velocity (V_P), and the calculated P-impedance (I_P). The stratigraphic sequence consists of alternating sands and shales with P-impedances being higher in shales than in the unconsolidated sands. The hydrocarbon-bearing sands are named M10–M60, labeled in **Figure 1A**. These sands are Tertiary age, and they resulted from deep water sand deposition. Hydrocarbon traps resulted from salt movement and growth faults (Contreras, 2006).

The model selected for this analysis work is the soft-sand model (Dvorkin and Nur, 1996). It has been used with this data set in other publications (e.g., Xie and Spikes,2021). The model is a combination of Hertz-Mindlin (1949) contact theory and modified Hashin-Strikman forms. The Hertz-Mindlin (1949) theory expresses the effective bulk (K_{HM}) and shear moduli (μ_{HM}) for an identical set of spherical grains in the dry condition for a specific hydrostatic pressure (P),

$$K_{\mathrm{HM}} = \left[\frac{C_n^2(1-\phi_c)^2\mu^2}{18\pi^2(1-\nu)^2}P\right]^{\frac{1}{3}} \tag{1}$$

and

$$\mu_{\mathrm{HM}} = \frac{5-4\nu}{5(2-\nu)}\left[\frac{3C_n^2(1-\phi_c)^2\mu^2}{2\pi^2(1-\nu)^2}P\right]^{\frac{1}{3}}. \tag{2}$$

The terms in **Eqs. 1**,**2** are the Lamé parameters (μ and ν) of the effective homogeneous mineral, the coordination number (C_n),

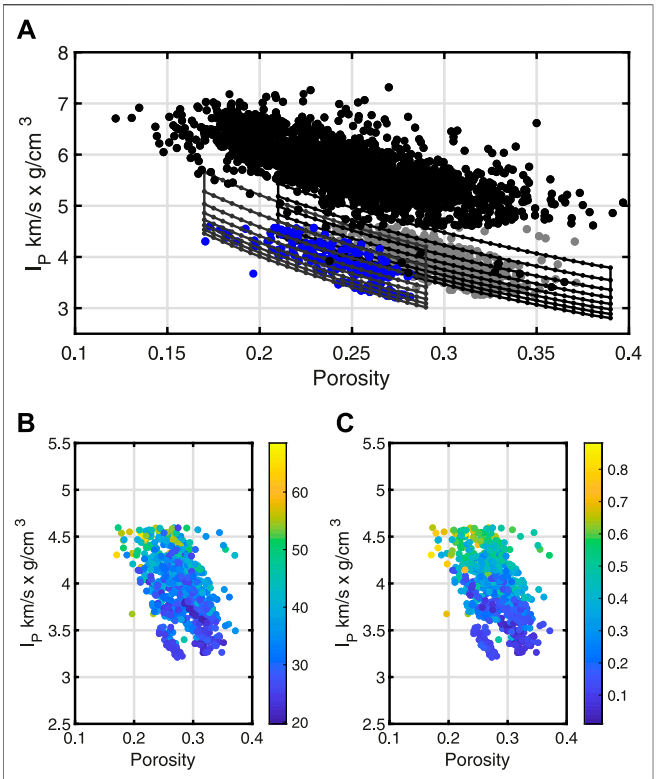

FIGURE 2 | Cross plots of P-impedance as a function of porosity. In **(A)**, the black points correspond to shale, gray to oil sands, and blue to gas sands. A series of model lines from the soft sand model are plotted in black for the oil sands and dark gray for the gas sands. The variation in the model lines correspond to porosity in the horizontal direction and water saturation in the vertical. Plots with shading contain only the oil and gas sands color coded by gamma ray **(B)** and water saturation **(C)**.

and the critical porosity (ϕ_c). The soft sand model represents a modified Hashin and Strikman (1963) lower bound for porosities from zero to ϕ_c. Additional equations are necessary to determine the elastic moduli at ϕ_c. Gassmann (1951) fluid substitution translates the moduli to the saturated condition. In this work, we deal with four fitting parameters: S_w, mineralogy, P, and ϕ_c. Variations in S_w control the effective fluid bulk modulus (computed using the Reuss average) and the fluid density. Mineralogy is limited to quartz and clay (C) content, where C = (1–the fraction of quartz). Preliminary work demonstrated that the contributions of C_n and shear stiffness reduction (SSR) were not significant when fitting this model to laboratory data, so they are held constant here.

Figure 2A contains cross plots of I_P as a function of ϕ for the shales (black points), oil sands (gray points), and gas sands (blue points). Overlain on the sand points are rock-physics model lines from the soft sand model. Those models for both the sand types vary as a function of ϕ and S_w while the other inputs are constant. **Tables 1**,**2** contains the values for the inputs and respective moduli and densities. **Figures 2B**,**C** are also plots of I_P as a function of ϕ but only for the two sands. The color code in

TABLE 1 | Rock physics model input values.

	ϕ	S_w	P (MPa)	ϕ_c	C_n	SSR
Gas sand	0.17–0.29	0.2–1.00	20	0.36	5	3
Oil sand	0.21–0.39	0.2–1.00	20	0.38	5	4

TABLE 2 | Elastic moduli and densities used in the rock-physics models [modified from Mavko et al. (2009)].

	Gas	Oil	Brine	Clay	Quartz
K (GPa)	0.37	0.8	3	16.8	36
μ (GPa)	–	–	–	5.60	45
ρ (g/cc)	0.15	0.60	1.05	2.58	2.65

Figure 2B is GR, and in **Figure 2C** it is S_w, both of which show variation in this domain.

The models plotted in **Figure 2A** are repeated in **Figure 3A** without the shale data for clarity. Plots in **Figures 2B–D** are the same data, but the models have been perturbed relative to those in **Figure 3A**. In **Figure 3B**, C changed from 20 to 30%. In **Figure 3C**, C was changed back to the original, P was reduced from 20 to 15 MPa. Last, the pressure change was removed, and ϕ_c was changed from 0.36 to 0.35. For simplicity these perturbations were the same for both the gas and oil-sand models. In all four cases, the models qualitatively fit the data, but these fits do not give an indication of which inputs are more significant to change. The Bayesian approach provides a way to assess the significance of the model parameters.

Bayesian Analysis

The Bayesian approach includes a quantitative match of model to data. Within it we must compute a prior, $p(\mathbf{m})$, and likelihood function, l $(\mathbf{d}|\mathbf{m})$ (i.e., Ulrych et al., 2001; Tarantola, 2005; Sen 2006). The prior (**Eq. 3**),

$$p(\mathbf{m}) \propto exp\left[\left(\mathbf{m} - \mathbf{m}_{prior}\right)^T \mathbf{C}_M^{-1}\left(\mathbf{m} - \mathbf{m}_{prior}\right)\right], \quad (3)$$

is proportional to the exponential that contains differences between the model $\mathbf{m}$ and $\mathbf{m}_{prior}$, which is a second and more informed model. Inputs to the rock physics model populate vectors of $\mathbf{m}$ and $\mathbf{m}_{prior}$. The differences are scaled by the inverse of the covariance matrix of the prior model, $\mathbf{C}_M$.

Next, we define the objective function $[E(\mathbf{m})]$,

$$E(\mathbf{m}) = \left(\mathbf{d} - g(\mathbf{m})\right)^T \mathbf{C}_D^{-1}\left(\mathbf{d} - g(\mathbf{m})\right), \quad (4)$$

where $g(\mathbf{m})$ is the rock-physics model that calculates simulated values based on the model values in $\mathbf{m}$, $\mathbf{d}$ is the real data vector, and the data covariance matrix is represented by $\mathbf{C}_D$. The likelihood function (**Eq. 5**) is then proportional to the negative exponent of the objective function

$$l(\mathbf{d}|\mathbf{m}) \propto \exp\left(-E(\mathbf{m})\right). \quad (5)$$

Last the posterior distribution $(\sigma(\mathbf{m}|\mathbf{d}))$ is proportional to the product of the prior and the likelihood (**Eq. 6**)

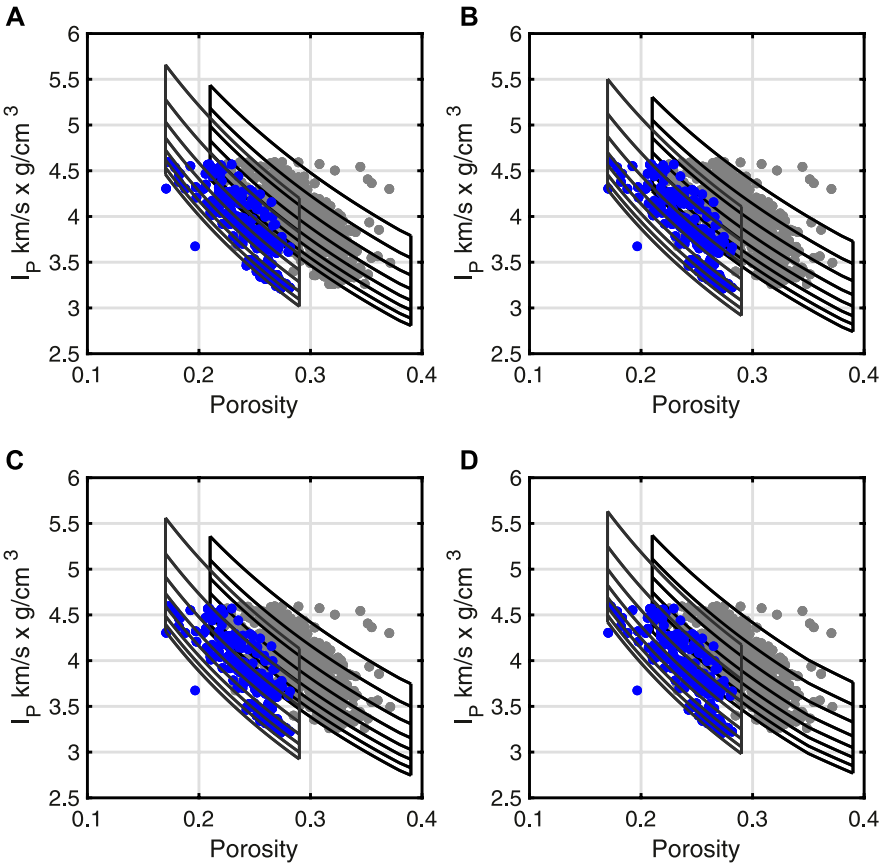

FIGURE 3 | The four plots contain perturbed versions of the rock physics models in **Figure 2**. The oil sands are in gray points and gas sands in blue. The models in **(A)** are the same as those in **Figure 2A**. The composition was altered slightly in **(B)** relative to **(A)**. In **(C, D)** the pressure and critical porosity, respectively, were changed relative to the models in **(A)**. All four sets of models match the data from a qualitative perspective.

$$\sigma(\mathbf{m}|\mathbf{d}) \propto l(\mathbf{d}|\mathbf{m})p(\mathbf{m}). \quad (6)$$

The number of model parameters is four, which is small enough to allow for a tractable analytical solution. No sampling methods are required. We analyze posterior multivariate histograms, so a normalizing factor to obtain probabilities is not needed.

Data Selection

Data input into the analysis is a subset of the oil or gas sands. The selection of the subset is a two-step process. First, one of the rock-physics model lines shown in **Figure 2A** or **Figure 3A** is used as a reference. The reference is required because the computed models must be relatively close to the data used in the Bayesian framework. If the data and model are significantly far apart, then the objective function in **Eq. 4** has large values, and so the likelihood function (**Eq. 5**) will have exceedingly small values. Second, data are selected that occur within a certain percent of both I_P and ϕ from that reference model. Some scatter in the data is necessary as to not overfit the models to the data. **Figure 4A** shows two subsets (black points) on which we perform the analysis separately. The reference models had S_w values of 0.4 for the lower set and 0.8 for the upper set. For both, the percent away from the reference was 2%, which resulted in 216 data points for the lower set and 155 for the upper set. Similarly, for the gas sands, two reference models were used with S_w values of 0.4 and 0.8 (**Figure 4B**). The percent away from the reference was 1%. The numbers of points were, respectively, 127 and 75. We conduct the analyses on these four subsets of data and call them analysis 1, 2, 3, and 4. Analyses 1 and 2 correspond to the lower and upper subsets, respectively, for the oil sands. Likewise, analyses 3 and 4 refer to the lower and upper subsets, respectively, for the gas sands.

RESULTS

The first set of results comes from analysis 1, for one subset of the oil sands. The model priors are user provided based on some knowledge of the data. The models $\mathbf{m}$ and $\mathbf{m}_{prior}$ were normal distributions of size 200 × 4, so 200 values of each of the four inputs. Mean values for $\mathbf{m}_{prior}$ were [S_w, C, P, ϕ_c] = [0.4, 0.2, 20, 0.38] and covariance matrix

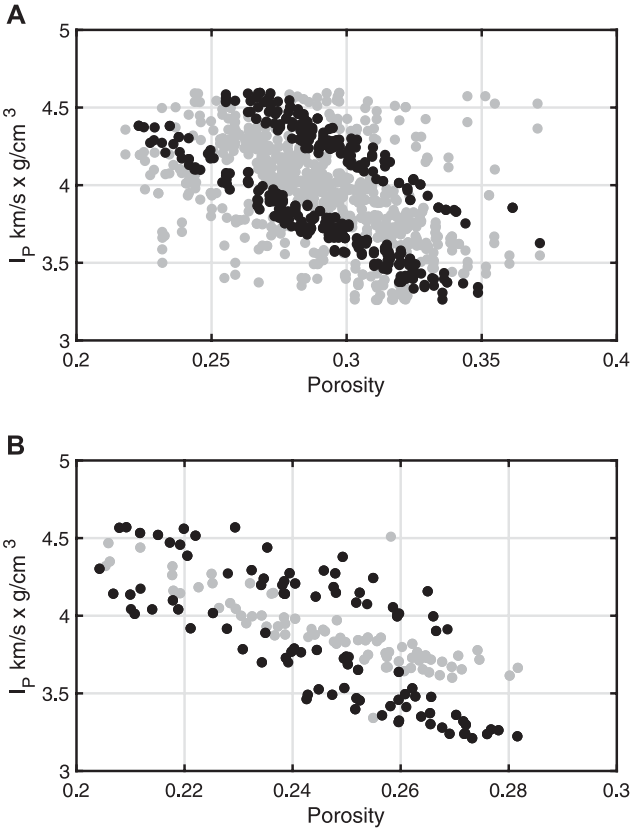

FIGURE 4 | (A) Portions of the oil sand data (black points) used in analyses one and two. The lower set corresponds (216 points) to analysis one and the upper (155 points) to analysis two. For the gas sand data **(B)**, the lower set of black points (127 points) corresponds to analysis three and the upper (75 points) to analysis four.

$$\begin{bmatrix} 0.0020 & 0 & 0 & 0 \\ 0 & 0.0010 & 0 & 0 \\ 0 & 0 & 0.1000 & 0 \\ 0 & 0 & 0 & 0.019 \end{bmatrix}$$

The mean of **m** was slightly different, and the covariance matrix for it had slightly larger values on the diagonal. All combinations of the priors were computed, so 200^4 models with no sampling. The data to model comparison (**Eq. 4**) used I_P. The posterior is four dimensional with size $200 \times 200 \times 200 \times 200 \times$, which is not possible to display nor visualize. Instead, we sum over two given dimensions to compute bivariate histograms, both priors and posterior, which are easy visualize. Each bivariate histogram is a joint histogram of the two variables. Thus, a combination of two values of two variables has a frequency for that pair of values together. Prior bivariate histograms for pairs of $C - S_w$, $P - S_w$, and $\phi_c - S_w$ are in **Figures 5A–C**. **Figures 5D–F** contain their accompanying bivariate posterior histograms. The priors have smooth appearances with relatively small frequencies. The posteriors show much different appearances among themselves. In **Figure 5D**, many pairs of C and S_w have relatively large frequencies, whereas in **Figures 5E, F**, a wide range S_w values are present for narrow ranges of P and ϕ_c, respectively. Priors for pairs of P–C, $\phi_c - C$, and $\phi_c - P$ are in **Figures 5G–I**, respectively, with their corresponding posteriors in **Figures 5J–L**. The priors are relatively smooth and have wide ranges of possible pairs. Posteriors in **Figures 5J, K** display a wide range of C values for narrow ranges of P and ϕ_c. The plot in **Figure 5L**, however, shows isolated pairs of ϕ_c and P.

Figure 6 contains the bivariate priors and posterior histograms for analysis 2, the second oil sand analysis. The procedure for analysis 2 was the same as analysis 1. The only differences were the mean of $\mathbf{m}_{prior}$, which was $[S_w, C, P, \phi_c] = [0.6, 0.2, 20, 0.38]$, and the covariance matrix, which was

$$\begin{bmatrix} 0.0030 & 0 & 0 & 0 \\ 0 & 0.0010 & 0 & 0 \\ 0 & 0 & 0.1000 & 0 \\ 0 & 0 & 0 & 0.019 \end{bmatrix}$$

Similar updates were made for **m**. The layout of **Figure 6** is the same as **Figure 5**. All six priors are relatively smooth. Four of the six posteriors (**Figures 6E,F,J,K**) have wide ranges of one parameter with a narrow range of the other. **Figure 6D** indicates many possible pairs, but the posterior in **Figure 6L**, like **Figure 5L**, shows isolated, joint values of ϕ_c and P.

Results from analyses 3 and 4 are plotted in **Figures 7**, **8**, respectively. The same analysis procedure was repeated again. The means and covariance matrices of the models in analysis 3 were the same as in analysis 1. The difference is that the effective fluid bulk modulus and density is a function of the gas-brine mixture rather the oil-brine mixture. In **Figure 7**, the posterior histograms resemble the counterparts in **Figures 5**, **6** although with different peak frequency values. Most notably, the histogram in **Figure 7F** again shows an isolated joint pair of ϕ_c and P. Last, in analysis 4, the mean for $\mathbf{m}_{prior}$ was $[S_w, C, P, \phi_c] = [0.72, 0.2, 20, 0.38]$ and covariance matrix

$$\begin{bmatrix} 0.0036 & 0 & 0 & 0 \\ 0 & 0.0010 & 0 & 0 \\ 0 & 0 & 0.1000 & 0 \\ 0 & 0 & 0 & 0.019 \end{bmatrix}.$$

The bivariate histograms in **Figure 8** also resemble their counterparts in **Figures 5–7**. **Figure 8L** displays an isolated pair of ϕ_c and P.

DISCUSSION

The Bayesian analysis method allowed us to determine quantitatively the most and least significant model inputs. Importantly, it revealed correlations between parameters that are not obvious. In all four analyses, the posterior of pressure and critical porosity indicated isolated pairs. Each analysis had a different set of values. If another prior is used, the result would change in terms of the value of pressure and critical porosity, but an isolated set occurs. This correlation is not intuitive, but it indicates that these two parameters are the most significant. Posterior histograms that contain saturation or clay content is more intuitive. More specifically, it is

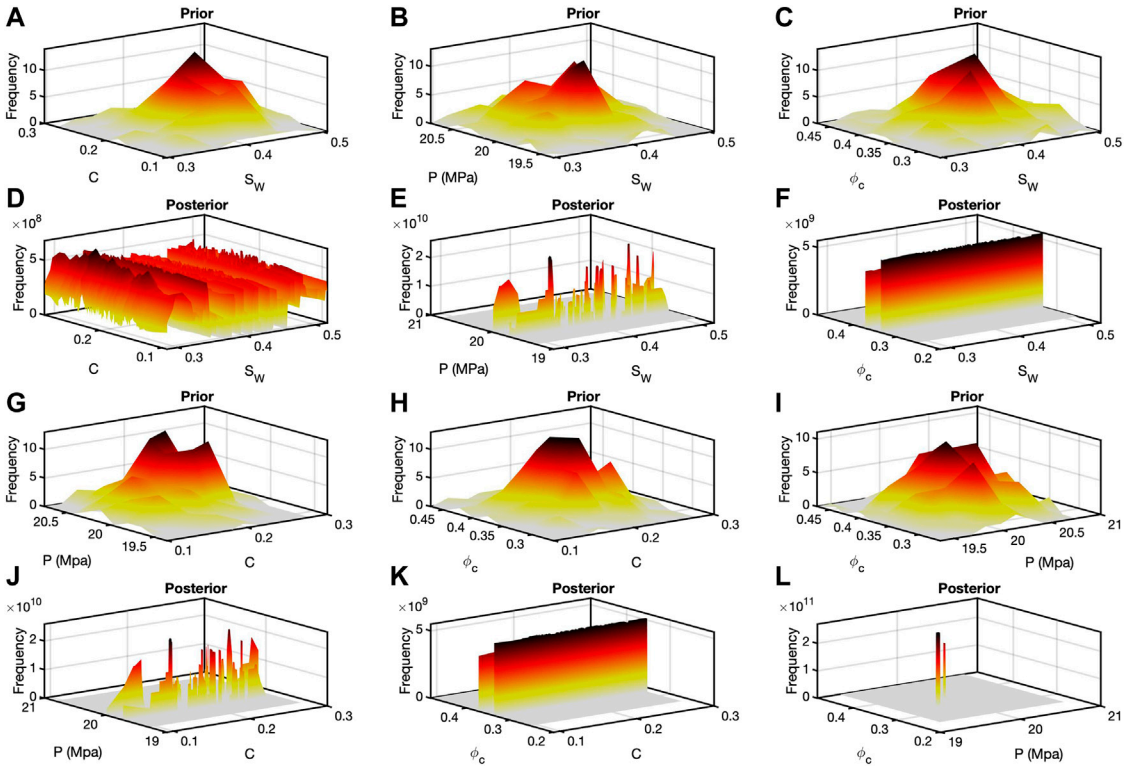

FIGURE 5 | Bivariate histograms for analysis one. Plots **(A–C)** are the bivariate prior histograms for $C - S_w$, P-S_w, and $\phi_c - S_w$, respectively. Plots **(D–F)** contain the posterior histograms corresponding to the priors in **(A–C)**. Priors for P-C, $\phi_c - C$, and $\phi_c - P$ are in **(G–I)** with their corresponding posteriors in **(J–L)**. When many pairs in a posterior occur together, such as in **(D)** ($C - S_w$) that indicates relative insensitivity to those two variables. Counter to that is **(L)** where isolated pairs of ϕ_c and P occur together in even larger numbers.

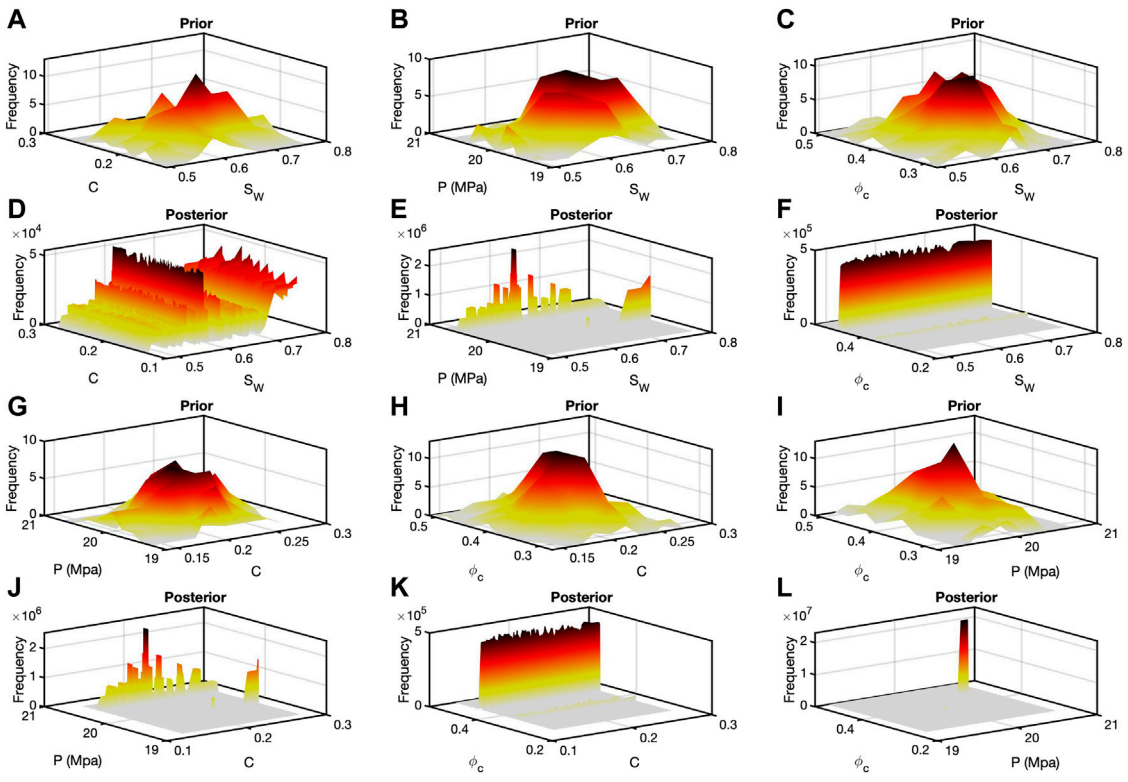

FIGURE 6 | Bivariate histograms for analysis two. The juxtaposition is the same as in **Figure 5**. The prior model differed between analysis one and two, but the bivariate posterior histograms show patterns similar to those in **Figure 5**.

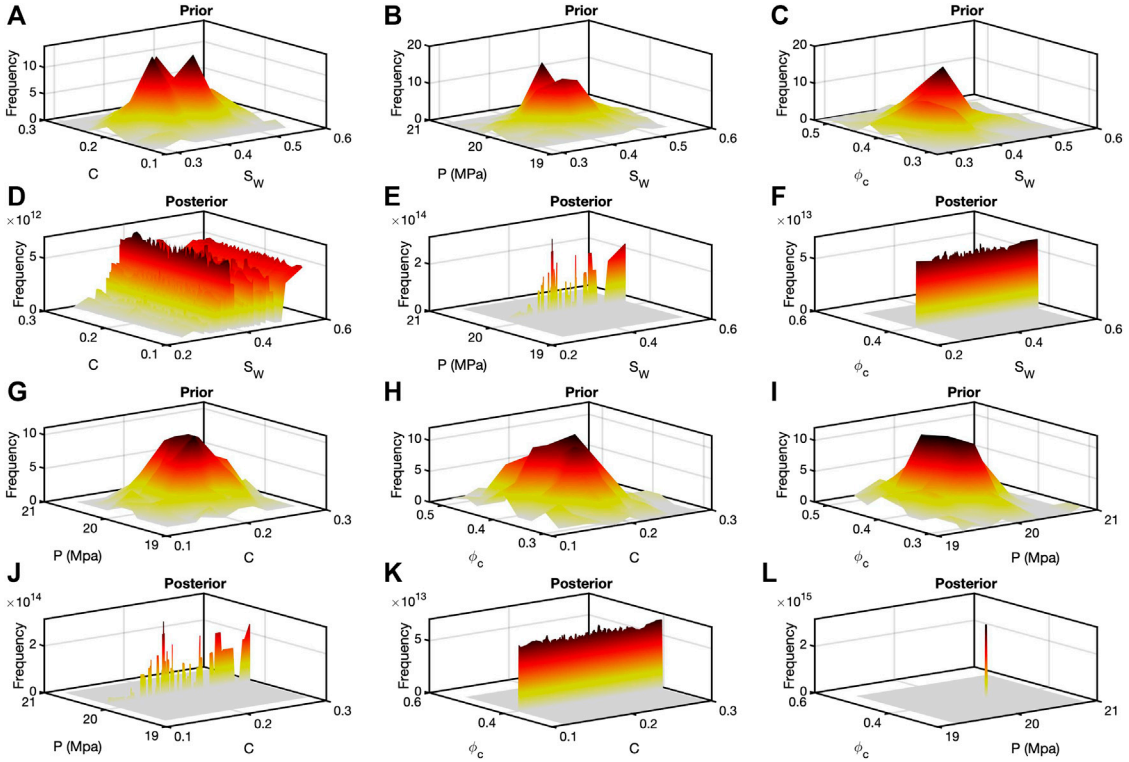

FIGURE 7 | Results from anallysis three for gas sands displayed again as bivariate prior and posterior histograms. The layout is identical to **Figure 5**. The prior was different from inversions one and two including different fluid properties of gas relative to oil. However, the posterior histograms, in particular **(D)** and **(L)**, resemble their counterparts in **Figures 5, 6**.

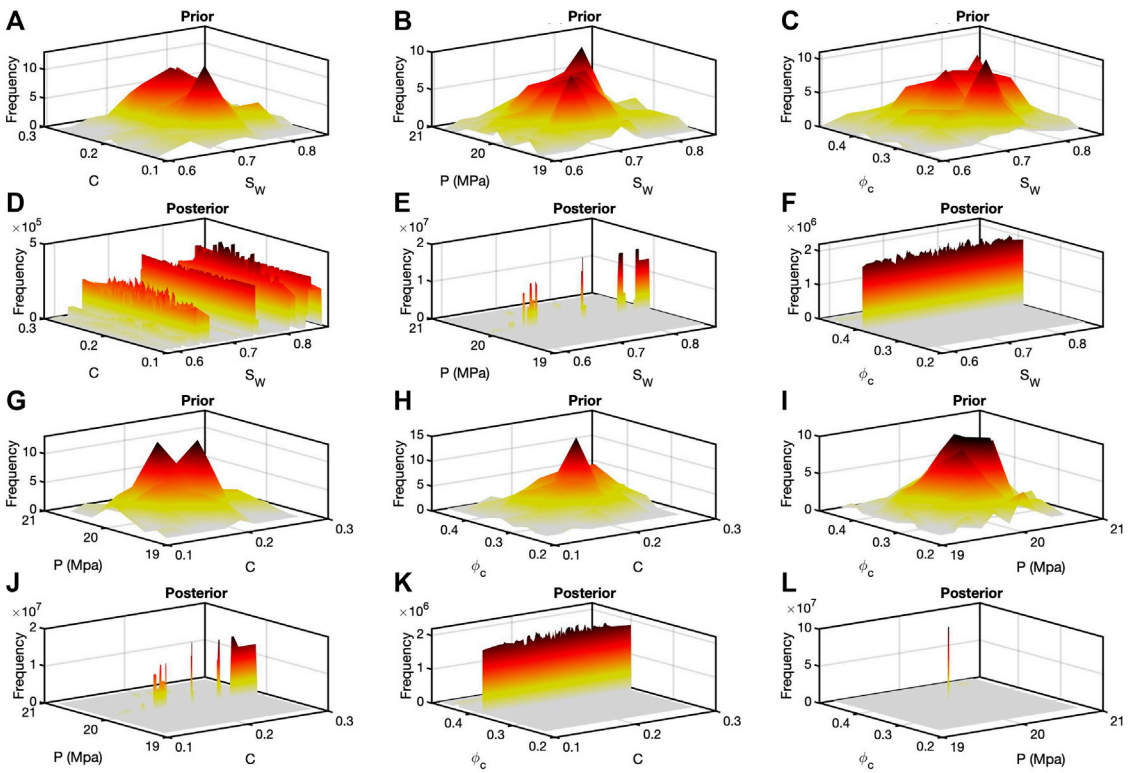

FIGURE 8 | Analysis four, for gas sands, resulted in similar bivariate histograms compared with those in **Figure 7**. However, the frequencies are considerably lower. This is the result of the prior model not being as close to the data as they were in the other inversions. Nonetheless, the patterns repeated themselves among the different posteriors.

understandable that a small change in either might not change the velocity very much. When one or the other is paired with pressure or critical porosity, the result is a relatively broad range of with a narrow selection of pressure or critical porosity. When applying this method to well data, we considered, fluid types and saturations, and mineralogy along with pressure and critical porosity. Preliminary work indicated similar correlations between pressure and critical porosity on dry, clean sands. The extension to include fluids and composition indicates similar patterns and correlations that were not expected.

This study demonstrates a way to determine the significance of inputs into one rock-physics model. The significance becomes evident of any singular or joint set of rock-physics model parameters. In an application to reservoir characterization, the most significant terms should be set first, and the others can be more loosely defined. If this model was deemed appropriate on a different data set, then in a deterministic application, the most significant inputs should be selected first and jointly. The other inputs would then provide more subtle fine tuning. This approach would limit the number of variables to consider within the requisite sensitivity study for that data set. If this model was used in a statistical seismic inversion, a user could set narrow limits on the priors for the most significant parameters and wider ranges for the lesser ones. The effect of this would be to reduce the size of the model parameter space to explore. This was work done on one model one data set, and the results are relevant specific to this model and applicable to other data sets. Knowledge about this one particular model might be useful for similar types of models, given an appropriate data set, but not likely for other types of models.

DATA AVAILABILITY STATEMENT

The data analyzed in this study is subject to the following licenses/restrictions: Data release contract does not allow of public dissemination of the data used. Requests to access these datasets should be directed to KS, kyle.spikes@jsg.utexas.edu.

AUTHOR CONTRIBUTIONS

KS wrote the codes, the manuscript, and generated the figures MS provided initial motivation for the work, edited the manuscripts, and critiqued the results.

REFERENCES

Bosch, M., Mukerji, T., and Gonzalez, E. (2010). Seismic inversion for reservoir properties combining statistical rock physics and geostatistics: a review. *Geophysics* 75 (5), 75A165–75A176. doi:10.1190/1.3478209

Contreras, A. J. (2006). Spatial delineation, fluid-lithology characterization, and petrophysical odeling of deepwater Gulf of Mexico reservoirs through joint AVA deterministic and stochastic inversion of 3D partially-stacked seismic amplitude data and well logs. *Doctoral dissertation*. Austin, (TX): The University of Texas at Austin.

Dvorkin, J., and Nur, A. (1996). Elasticity of high-porosity sandstones: theory for two North Sea data sets. *Geophysics* 61, 1363–1370. doi:10.1190/1.1444059

Gassmann, F. (1951). Uber die elastizitat poroser medien. *Vier. der Natur.* 96, 1–23.

Grana, D. (2018). Joint facies and reservoir properties inversion. *Geophysics* 83 (3), M15–M24. doi:10.1190/geo2017-0670.1

Hashin, Z., and Shtrikman, S. (1963). A variational approach to the theory of the elastic behavior of multiphase materials. *J. Mech. Phys. Solids* 11, 127–140. doi:10.1016/0022-5096(3)90060-7

Mavko, G., Mukerji, T., and Dvorkin, J. (2009). *The rock physics handbook*. Cambridge, United Kingdom: Cambridge University Press, 254.

Mindlin, R. D. (1949). Compliance of elastic bodies in contact. *ASME J. Appl. Mech.* 16, 259–268.

Nawaz, M. A., and Curtis, A. (2017). Bayesian inversion of seismic attributes for geological facies using a hidden Markov model. *Geophys. J. Int.* 208, 1184–1200. doi:10.1093/gji/ggw411

Sen, M. K. (2006). *Seismic inversion*. Richardson, TX: Society of Petroleum Engineers, 120.

Tarantola, A. (2005). *Inverse problem theory and methods for model parameter estimation*. Paris, France: Society for Industrial and Applied Mathematics, 352.

Ulrych, T. J., Sacchi, M. D., and Woodbury, A. (2001). A Bayes tour of inversion: a tutorial. *Geophysics* 66 (1), 55–69. doi:10.1190/1.1444923

Ulvmoen, M., Omre, H., and Buland, A. (2010). Improved resolution in bayesian lithology/fluid inversion from prestack seismic data and well observations: part 2—real case study. *Geophysics* 75 (2), B73–B82. doi:10.1190/1.3335332

Ulvmoen, M., and Omre, H. (2010). Improved resolution in bayesian lithology/fluid inversion from prestack seismic data and well observations: part1—methodology. *Geophys.* 75 (2), R21–R35. doi:10.1190/1.3294570

Xie, W., and Spikes, K. T. (2021). Reservoir facies design and modeling using probabilistic rock-physics templates. *Geophysics* 86 (1), 1–12. doi:10.1190/geo2020-0044.1

Conflict of Interest: The authors declare that the research was conducted in the absence of any commercial or financial relationships that could be construed as a potential conflict of interest.

Copyright © 2021 Spikes and Sen. This is an open-access article distributed under the terms of the Creative Commons Attribution License (CC BY). The use, distribution or reproduction in other forums is permitted, provided the original author(s) and the copyright owner(s) are credited and that the original publication in this journal is cited, in accordance with accepted academic practice. No use, distribution or reproduction is permitted which does not comply with these terms.

frontiers in Earth Science

ORIGINAL RESEARCH
published: 18 March 2021
doi: 10.3389/feart.2021.617831

Depositional and Diagenetic Controls on Macroscopic Acoustic and Geomechanical Behaviors in Wufeng-Longmaxi Formation Shale

Jixin Deng[1,2,3]*, *Chongyi Wang*[1,2]*, *Qun Zhao*[4], *Wei Guo*[4], *Genyang Tang*[3] and *Jianguo Zhao*[3]

[1]State Key Laboratory of Oil and Gas Reservoir Geology and Exploitation, Chengdu University of Technology, Chengdu, China, [2]Lab of Geophysics, School of Geophysics, Chengdu University of Technology, Chengdu, China, [3]State Key Laboratory of Petroleum Resources and Prospecting, China University of Petroleum, Beijing, China, [4]Petrochina Research Institute of Petroleum Exploration and Development, Beijing, China

This integrated study provides significant insight into parameters controlling the dynamic and static elastic behaviors of shale. Acoustic and geomechanical behaviors measurement from laboratory have been coupled with detailed petrographic and geochemical analyses, and microtexture observations on shale samples from the Wufeng–Longmaxi Formation of the southeast Sichuan Basin. The major achievement is the establishment of the link between depositional environment and the subsequent microtexture development, which exerts a critical influence on the elastic properties of the shale samples. Microtexture and compositional variation between upper and lower sections of the Wufeng–Longmaxi Formation show that the former undergoes normal mechanical and chemical compaction to form clay supported matrices with apparent heterogonous mechanical interfaces between rigid clasts and the aligned clay fabric. Samples from lower sections exhibited a microcrystalline quartz-supported matrix with a homogeneous mechanical interface arising from syn-depositional reprecipitation of biogenic quartz cement. This type of microtexture transition exerts primary control on elastic behavior of the shale samples. A clear "V" shaped trend observed from acoustic velocities and static Young's moduli document contrasting roles played by microtexture, porosity and organic matter in determining elastic properties. Samples with a quartz-supported matrix exhibit elastic deformation and splitting failure modes. The increment of the continuous biogenic quartz cemented medium with limited mechanic interface. By contrast, samples showing a predominantly clay-supported matrix exhibited more signs of plastic deformation reflecting heterogeneous mechanical interfaces at grain boundaries.

Keywords: microtexture properties, acoustic properties, geomechanical behaviors, longmaxi shale, diagenetic processes

OPEN ACCESS

Edited by:
Erik H. Saenger, Bochum University of Applied Sciences, Germany

Reviewed by:
Ya-juan Xue, Chengdu University of Information Technology, China
Luis Gago-Duport, University of Vigo, Spain

***Correspondence:**
Jixin Deng
dengjixin@cdut.cn
Chongyi Wang
cdlgrockphysics@gmail.com

Specialty section:
This article was submitted to Earth and Planetary Materials, a section of the journal Frontiers in Earth Science

Received: *03 November 2020*
Accepted: *11 February 2021*
Published: *18 March 2021*

Citation:
Deng J, Wang C, Zhao Q, Guo W, Tang G and Zhao J (2021) Depositional and Diagenetic Controls on Macroscopic Acoustic and Geomechanical Behaviors in Wufeng-Longmaxi Formation Shale. Front. Earth Sci. 9:617831. doi: 10.3389/feart.2021.617831

INTRODUCTION

Horizontal drilling and hydraulic fracturing technologies have greatly increased oil and gas production in North America and East Asia (Curtis, 2002; Jia et al., 2012; McGlade et al., 2013). The Jiaoshiba, Zhaotong and Changning shale gas fields for example represent productive and profitable concerns in China (Jia et al., 2012; Ma et al., 2012; Jin et al., 2016). Among known shale

basins however, productivity of wells varies considerably due to micro- and macro-scale heterogeneity of the reservoir rock (Ross et al., 2008; Breyer et al., 2012; Milliken et al., 2012). These conditions require geophysical prediction of "sweet-spots" using seismic methods. Total organic content (TOC), porosity, mineralogy and geomechanical parameters are all used as criteria for identifying sweet spots. Together, these indicate reservoir storage capacity as well as response to drilling and hydrofracturing (Sondergeld et al., 2000; Rickman et al., 2008). A better understanding of correlation between seismic parameters and causal mechanisms can help improve sweet-spot identification from seismic datasets.

Experimental studies have shown that shale seismic properties depend on the interplay of TOC, porosity, rock composition, ambient conditions and rock fabric. This range of factors makes it difficult to isolate the effects of variation in a single parameter on seismic response (Vernik and Liu, 1997; Sone and Zoback, 2013). Shales can also exhibit significant acoustic and mechanical anisotropy due to alignment and distribution of clay minerals (Hornby et al., 1994; Johnston and Christensen, 1995; Deng et al., 2009) and organic matter (Vernik and Nur, 1992; Vernik and Liu, 1997; Sondergeld et al., 2000; Vanorio et al., 2008; Vernik and Milovac, 2011; Sone and Zoback, 2013). Studies have demonstrated that maturity and the orientation of principal stress can significantly influence velocity anisotropy (Dewhurst et al., 2011). Theoretical models can be used to estimate the influence of varying TOC content, fluid saturation and pore pressure on seismic parameters (Sayers, 1994; Vernik and Landis, 1996; Johansen et al., 2004; Carcione and Avseth, 2015). But those theoretical relationships still have substantial limitation because of the composition, texture and diagenesis complexity of shales (Ross et al., 2008; Breyer et al., 2012; Milliken et al., 2012). However, the exact roles of composition, porosity and texture in relation with the seismic properties of shales are not fully understood. Systematical rock physics experiments are thus prerequisite to building a robust relationship for seismic-to-rock property transforms for mapping "sweet-spots" of shale reservoir. Fully capturing this complexity experimentally is still severe lack in the existing literature, partly due to the significant efforts required in core handling and preservation (Dewhurst et al., 1998; Horsrud et al., 1998; Dewhurst and Siggins, 2006).

Rock deformation in the subsurface, including that which occurs during hydraulic fracturing and fluid injection, depends rock geomechanical properties and *in-situ* stress fields. Empirical research on the geomechanical behaviors of shales from different reservoirs has demonstrated that static elastic moduli, strength and deformation of these materials depend on the applied pressure (Niandou et al., 1997; Islam, 2013; Rybacki et al., 2015), temperature (Masri et al., 2014; Rybacki et al., 2015) and rock composition (Rybacki et al., 2015; Dong et al., 2017). There is still a severe lack of mechanical understanding on how geomechancal behaviors are controlled by rock properties, including composition and rock texture, and to what extend geomechancal properties can be inferred from seismic parameters. More directly, the relationships between reservoir quality, seismic and geomechanical rock properties and depositional environment and burial history, at scales relevant to exploration and production, are prerequisite to character "sweet-spots".

This paper describes a detailed rock physics study combined with microstructural analysis and diagenetic interpretation of core material from the Late Ordovician - Early Silurian Wufeng–Longmaxi black shale of the southeast Sichuan Basin. We investigated the seismic, geomechanical, geochemical, petrophysical and microstructural properties of about 82 core samples. The objectives were 1) to identify relationships between velocity and rock composition and between TOC content and porosity, 2) to interpret observed velocity anisotropy, 3) to examine mechanical behavior and failure mode, 4) to determine static Young's moduli and any mineral content dependence and 5) to evaluate the brittleness index. An integrated study of this sort provides significant insight into key factors controlling the acoustic and geomechanical behaviors of the Wufeng–Longmaxi Formation shale, especially depositional and diagenetic controls on its macroscopic seismic and geomechanical properties (Hereafter, the Wufeng-Longmaxi Formation shale is referred to simply as the Longmaxi Formation for the sake of brevity.)

GEOLOGICAL SETTING

The Longmaxi Formation samples selected consist of core material obtained from five adjacent wells located in the Changning shale gas field along the southern edge of the Sichuan Basin (**Figure 1**), a region of Longmaxi Formation shale that is notably for its high TOC content and abundant graptolite fossils, including Glyptograptus, Parakidograptus, Cystograptus, Demirastrites (Chen et al., 2000; Chen et al., 2010). Since the Sinian Period, this large Paleozoic-Mesozoic basin experienced several major tectonic events conferring a complex stratigraphy and rhombic configuration on the basin (Guo et al., 1996). Structurally, the Changning area is located along a southerly flank of the Sichuan Fold Belt referred to as the Hubei-Huan-Guizhou fold belt. As shown in **Figure 1B**, the study area contains a wide and gentle anticline confined by several northwest trending faults. This structure exposes Jurassic strata in axial areas and Triassic strata in the fold's limbs. The Longmaxi Formation shale occurs in core material as consistent and relatively undeformed layers. Outer regions of the anticline limbs exhibit greater dip angle and show effects of bounding faults (**Figure 1B**). From Late Ordovician to Early Silurian, global transgression (Su et al., 2007) along with uplift of the Sichuan Basin margin caused by the Duyun tectonic event formed a low-energy, anoxic shelf environment hosting uniform deposition of several organic-rich shale horizons (Longmaxi Formation).

Depositional indicators in the Longmaxi Formation suggest both deep and shallow water shelf settings. The lower member of the Longmaxi Formation consists mainly of thick, black, siliceous shale, calcareous-siliceous mixed shale and micritic shale with abundant fossils, including graptolites, sponge spicules, siliceous radiolarians and other planktonic algae. This assemblage indicates the deep water conditions and low sedimentation rates (Chen et al., 2016; Han et al., 2016). The upper member

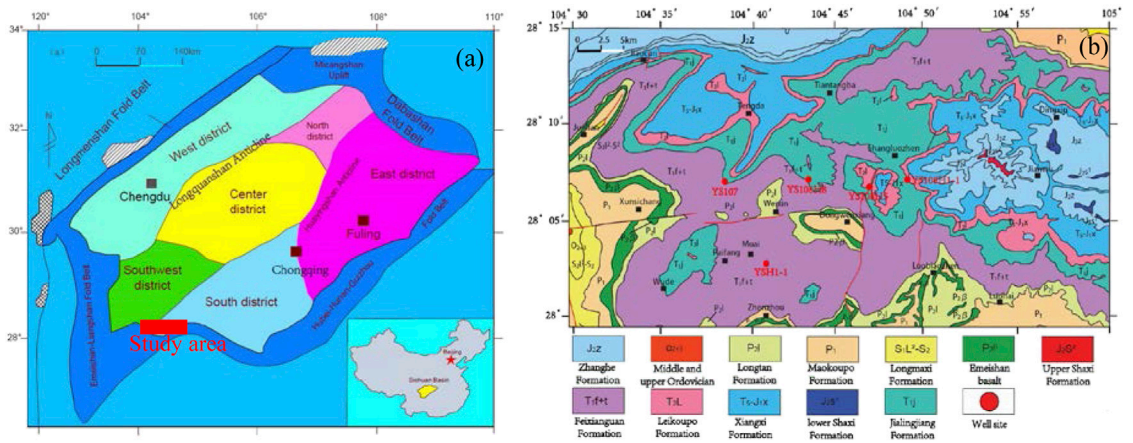

FIGURE 1 | (A) Location and paleogeographic map of the study area in south Sichuan Basin, and the structural subdivisions include the east district, the south district, the north district, the central district the (modified from Chen et al. (2016), Hao et al. (2008)). **(B)** Geological map of study area, showing sample sites.

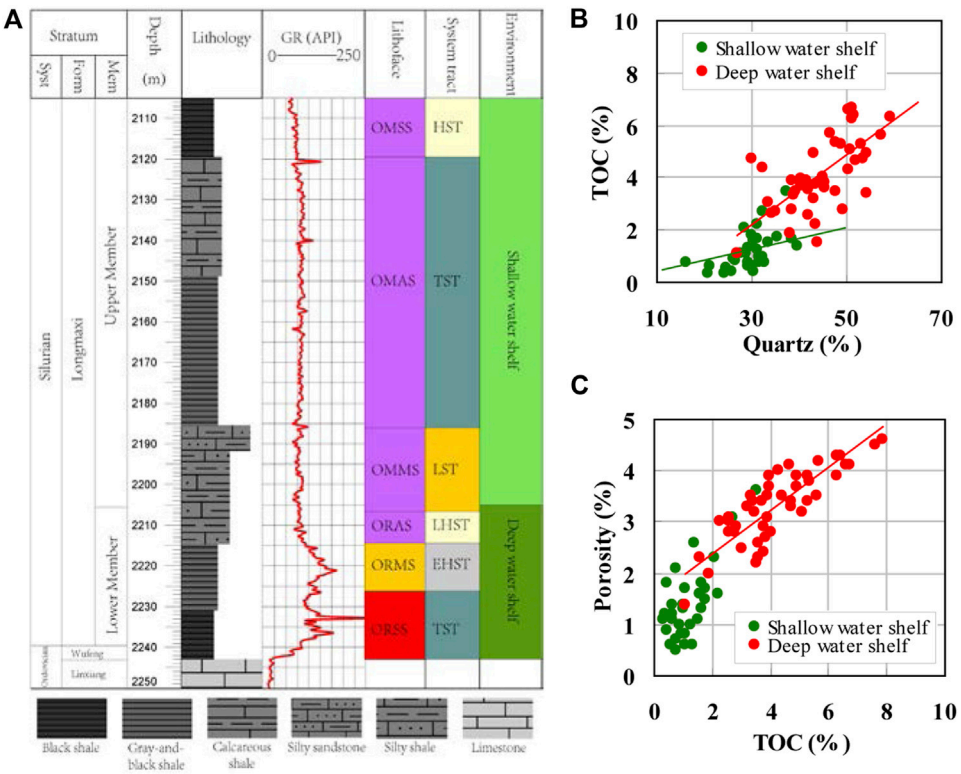

FIGURE 2 | (A) Sequence stratigraphic framework of Wufeng-Longmaxi Formation shale. ORSS: Organic-rich siliceous shale; ORMS: Organic-rich mixed shale; ORAS: Organic-lean argillaceous shale; OMSS: Organic-moderate siliceous shale; OMMS: Organic-moderate mixed shale; OMAS: Organic-moderate argillaceous shale. TST:transgressive systems tract; EHST: early highstand systems tract; LHST: late highstand systems tract (LHST); LST: low stand system tract; HST: highstand systems tract. **(B)** Relationship of TOC content and quartz content. **(C)** Relationship of TOC content and porosity. Data are sorted by sedimentary circumstance.

consists of argillaceous, laminated shale, argillaceous-calcareous mixed laminated shale and wavy bedded shale with a more depauperate fossil assemblage indicative of intermediate to shallow depositional conditions (Chen et al., 2016; Han et al., 2016). The Lower Member is equivalent to a third-order sequence, which is composed of a transgressive systems tract (TST), early highstand systems tract (EHST) and late highstand systems tract (LHST) (Chen et al., 2015; Wang et al., 2015) (**Figure 2A**). The Upper Member are combined to be a third-order sequence, which consists of a low stand system tract (LST),

a transgressive systems tract (TST) and highstand systems tract (HST) (Chen et al., 2015; Wang et al., 2015) (**Figure 2A**). Lithofacies associations indicating deep water shelf deposition are interpreted as probable reservoir rocks whereas lithofacies indicating semi-deep to shallow shelf deposition are interpreted as probable cap rock. Together, these form a seal reservoir-cap rock association (**Figure 2A**).

SAMPLING AND ANALYTICAL TECHNIQUES

Samples

A suite of 82 samples was selected for analysis from cores collected from five shale gas wells. Samples represent volumetrically dominant lithofacies of the Longmaxi Formation shale (**Figure 2**). Visible irregularities, such as fractured surfaces, were avoided in sampling to minimize sources of uncertainty in analyses of subsamples. Each sample showed some degree of subtle variation in texture and composition given the relatively thin scale of bedding and lamination relative to the sampling horizon. Two cylindrical samples ('plugs') were extracted from the full core (approximately 10 cm in diameter), one in a direction parallel to bedding and the other in a direction perpendicular to bedding. Each plug was about 25.4 mm (1 inch) in diameter and between 30 and 50 mm long. Cores were also systematically subsampled for compositional, pore structure and microstructural analysis. Inhibitive potassium-rich fluids (light mineral oil) were deployed as cooling fluid during drilling to lessen reactions between water and clay minerals (Steiger, 1982). Dry conditions in this report refer to ambient conditions for ultrasonic velocity measurements which assume no free water in pore space. Subparallel to bedding microfractures form as consequence of stress release after coring or from the expulsion of hydrocarbons. These microfractures will influence velocity and anisotropy of the rock, especially at low confining pressures (Sayers and Munster, 1991; Vernik and Liu 1997).

Geochemical Analysis

Exact mineral compositions of the 82 samples were determined through powder XRD (X-ray diffraction) analysis and pyrolysis. This procedure analyzed crushed sample powders (grain sizes less than 48 μm) using a PANalytical (Empyrean) X-ray diffractometer. Whole rock geochemical analyses were conducted on 37 samples using inductively coupled plasma-mass spectrometry (ICP-MS). These analytical methods yield data for 13 major oxides and 10 trace elements. Analytical results were calibrated with laboratory internal standards. Total organic content (TOC) was also measured for samples using standard high-temperature pyrolyzation methods and A Leco carbon/sulfur analyzer.

Petrography

Focused Ion Beam scanning electron microscopy (FIB-SEM), scanning electron microscopy (SEM), and conventional optical microscopy were used to image and interpret predominant microtextural character of samples, especially in terms of microcrystalline quartz. Ar-ion polished thin sections of typical shale samples were examined using FIB-SEM (FEI Helios 650) with a backscattered electron (BSE) detector adapted for imaging microtexture at 4 nm pixel resolution. Samples were prepared with an Ar-ion thin section polisher operated at 5 kV and 100 μA over a 10 h preparation period. The polished surface was then plasma coated with a 10 nm thick gold film to enhance conductivity. Thin sections were imaged using conventional SEM (JEOL JSM-5500LV) along with cathodoluminescent (CL) techniques commonly used on sandstones to interpret chemical compaction and diagenetic history (Götze et al., 2001; Thyberg and Jahren, 2011). Shale samples are seldom subjected to CL imaging due to the method's low resolution relative to clay grain size (Götze et al., 2001; Thyberg and Jahren, 2011). This study used SEM and CL imaging to differentiate extrabasinal quartz and diagenetic quartz, especially biogenic quartz cement, which provided important clues concerning the Longmaxi Formation's depositional and diagenetic history.

Ultrasonic Measurements

Ultrasonic transmission techniques were used to measure seismic velocity in dry samples. Measurements were conducted for various confining pressures at nominal center frequencies of 800 kHz for the P-wave transducer and 350 kHz for the S-wave transducer. Experiments began within a pressure cell at room temperature and confining pressures of 2 MPa, which ran up to 80 MPa in increments of 5 MPa. For each pressure interval, the first break of the transmitted pulse was selected from a 20 min period during which the sample strain fell below 2×10^{-4}. This technique gave velocity measurement precisions of about ±1% for the compressional wave and about ±2% for shear waves. Deviations in pressure were less than 0.3%. According to wave polarization and propagation directions with respect to bedding plane of core plugs, this method allowed measurement of six velocities. These include $V_{P\text{-}0^\circ}$, $V_{SH\text{-}0^\circ}$and $V_{SV\text{-}0^\circ}$for vertically propagating waves and $V_{P\text{-}90^\circ}$, $V_{SV\text{-}90^\circ}$and $V_{SH\text{-}90^\circ}$for horizontally propagating waves, where the subscript P represents the compressional wave, subscript S represents the shear wave, subscript SV indicates the polarization perpendicular to bedding and subscript SH indicates polarization parallel to bedding. These velocity measurements only allow for calculation of anisotropic parameters ε and γ. Total porosity was measured using a method based on the Boyle-Mariotte Law.

Mechanical Properties Measurements

Uniaxial compression experiments were performed on 26 samples using a servo-hydraulically controlled deformation apparatus (MTS). In this test, LVDTS wrapped around the samples monitored axial and lateral strain at constant deformation rates of 10^{-3} mm/s before abrupt failure at 0.1 mm/min after failure. These points correspond to an axial strain rate of less than $1 \times 10^{-5}s^{-1}$. The slope of stress-strain curves then provided estimates for a secant Young's modulus,E_S. The measurement error in stress and strain was less than 4%, a value which gave corresponding uncertainties in Young's moduli

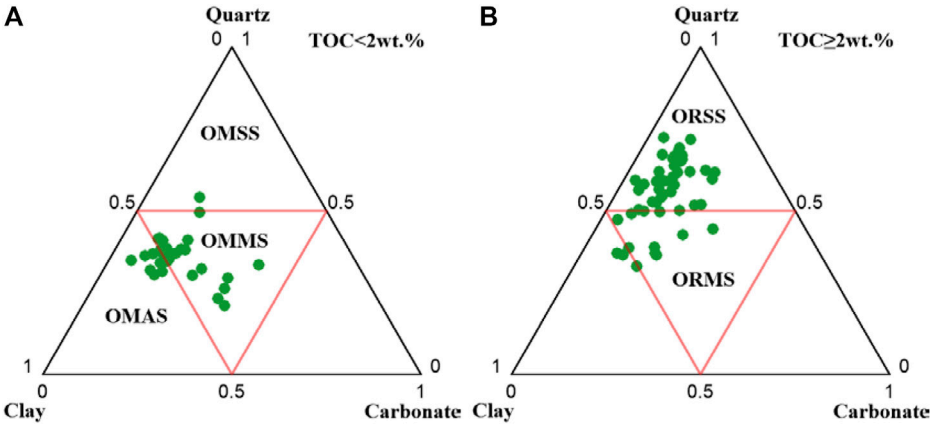

FIGURE 3 | Lithofacies classification based on TOC content and ternary diagram of mineralogy of shale samples. **(A)** Ternary diagram for samples with TOC≥2%. **(B)** Ternary diagram for samples with TOC<2%. ORSS: Organic-rich siliceous shale; ORMS: Organic-rich mixed shale; OMMS: Organic-moderate mixed shale; OMAS: Organic-moderate argillaceous shale.

of about 20%. These tests were only performed on bedding-normal samples to lessen the influence of sample bedding and lamination on estimates of brittle failure properties.

RESULTS

Lithofacies

Shale lithofacies were interpreted based on petrology and sedimentary environment. The Longmaxi Formation samples included six dominant lithofacies subdivided into organic-rich siliceous shale lithofacies (TOC≥2%) and organic-moderate shale lithofacies group (TOC<2%). Organic-rich siliceous shale lithofacies occur in lower parts of the Longmaxi Formation and consist primarily of organic-rich siliceous shale, organic-rich mixed shale and little organic-rich argillaceous shale (**Figure 3A**). Silicates (quartz, K-feldspar and Na-rich plagioclase) are the most abundant minerals found in samples of those lithofacies. Silicate fraction ranges from 38.7 to 67.6 wt% with an average of 52.9 wt%. This lithofacies contained relatively low abundances of total clay minerals (clay-sized minerals; reported as illite-semctite), measured at 30.5 wt%. Samples also exhibited low carbonate (calcite and dolomite) content ranging from 5.7 to 29.3 wt% with an average of 12.3 wt% (**Figure 3A**). TOC ranged from 2.0% to 7.87% with an average of 4.19%. The high TOC lithofacies group is interpreted to have formed in a deep water shelf environment with high paleoproductivity of planskton under anoxic condition. Fossil assemblages include radiolarians, sponge spicules and graptolites. Core material of this lithofacies exhibits thin, well-developed, black to black and gray bedding.

The organic-moderate shale lithofacies group occurs primarily in the upper part of the Longmaxi Formation and consists mainly of organic-moderate mixed shale, organic-moderate argillaceous shale and little organic-moderate siliceous shale (**Figure 3B**). The dominant mineral components found in this lithofacies are clay and silicates (38.8 wt% and 38.7 wt%, respectively). Average carbonate content ranges from 14% to 41% with an average of 19.6 wt% (**Figure 3B**). Trace minerals detected by XRD include pyrite, anhydrite and chlorite. This lithofacies is distinguished by its higher relative clay and carbonate content compared to the organic-rich lithofacies, which exhibits higher quartz content. The TOC content of the organic-moderate lithofacies ranges from 0.35% to 1.73% with an average of 1.02%. The organic-moderate shale lithofacies is interpreted to have formed in a shallow water shelf environment under dysoxic condition. The millimeter to centimeter scale silty belts in this lithofacies indicate higher energy conditions of shallow water environments. Thin sections and core samples of the organic-moderate lithofacies contain only a few graptolites. Subangular to rounded clasts of quartz, feldspar and pyrite exist in a matrix of elongated, aligned illite minerals.

For entire data set, TOC content, porosity do not display significant correlation with quartz or clay content, or any major element (**Figures 2B,C**). When samples are sorted by their depositional environment, we observe positive relation between TOC content, quartz content and their porosity for shale samples from deep water shelf (**Figures 2B,C**), consistent with the location of porosity within organic matter. However, shale samples from shallow water shelf display few significant correlations between TOC content, quartz content and their porosity (**Figures 2B,C**).

Pore Structure and Microtexture

Pores large enough to be detected by SEM (>4 nm) occur primarily within organic matter that fills intergranular space. Organic matter pores are usually elliptical or bubble-like with average diameter ranging from a few nanometers to a few hundred nanometers (**Figure 4A**). SEM images show intergranular pores as well developed and primarily localized between particles of quartz, feldspar, clay and organic matter (**Figures 4B,C**). As a conjunction result of preservation of primary pores and diagenetic alteration, intergranular pores between rigid particles, such as quartz, calcite and feldspar,

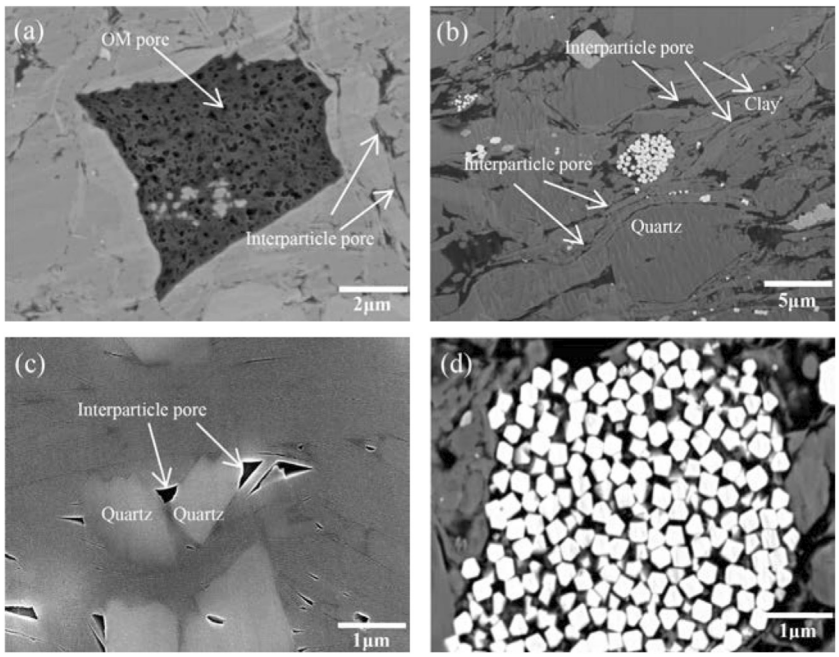

FIGURE 4 | Examples of pore type observed on BES. **(A)** organic-matter pores (OM pore) and interparticle pores (Sample C37; TOC: 5.1%; Porosity: 3.2%; 2452 m). **(B)** interparticle pores with the shape of elongated ellipsoid between aligned clay (Sample C15; TOC: 2.74%; Porosity: 2.8%; 2162 m). **(C)** interparticle pores with triangular shape between rigid quartz grains (Sample C31; TOC: 3.5%; Porosity: 2.2%; 2375 m). **(D)** intracrystalline pores within pyrite framboids (Sample C21; TOC: 2.7%; Porosity: 3.1%; 2288 m).

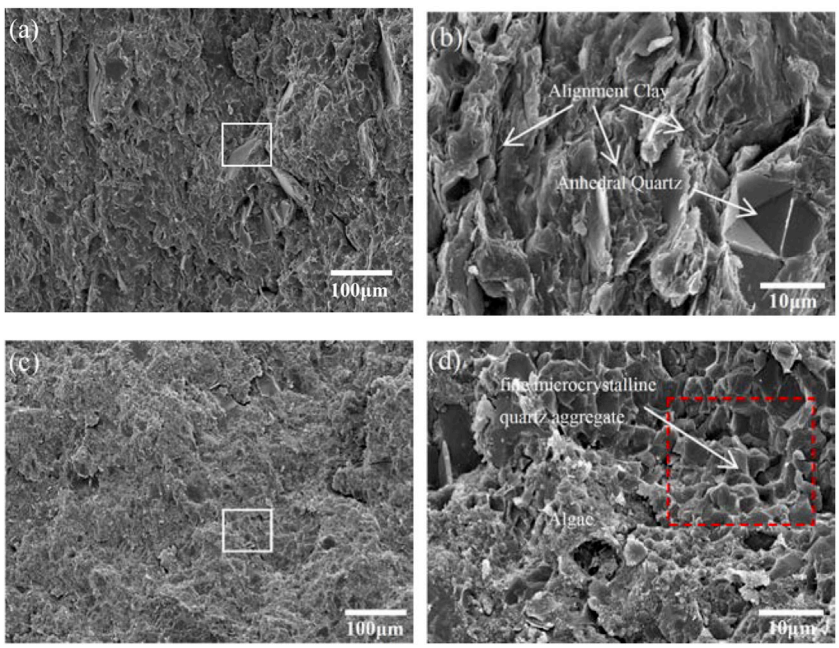

FIGURE 5 | Examples of microtextures observed on SEM. White rectangles are the magnification areas. **(A)** and **(B)** Very coarse microcrystalline quartz with surrounded alignment clay (Sample C7; TOC: 1.65%; Porosity: 1.8%; shallow water shelf). **(C)** and **(D)** Compact fine microcrystalline quartz (Sample C51; TOC: 5.68%; Porosity: 4.2%; deep water shelf).

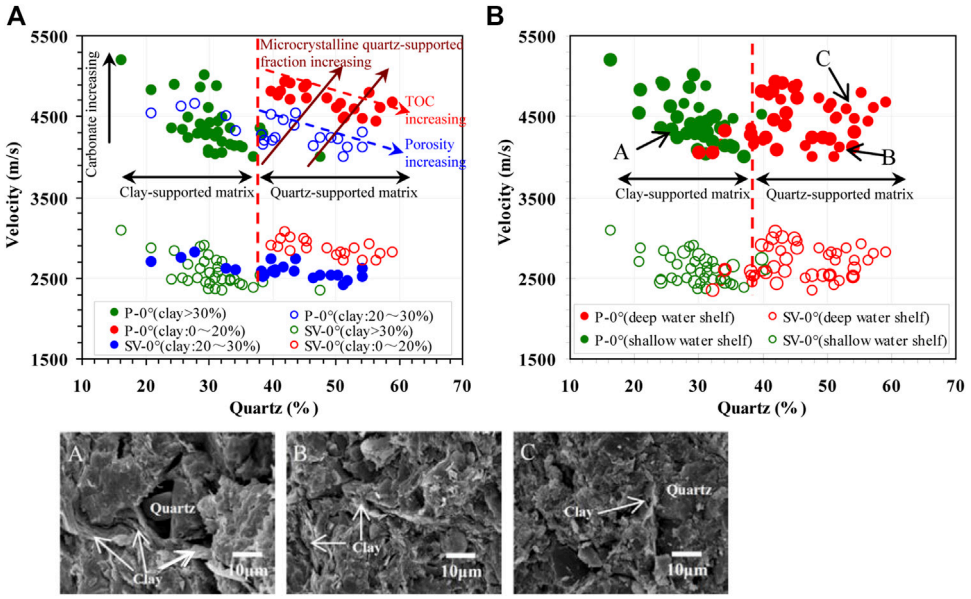

FIGURE 6 | Effect of microtexture variations on velocity of shale samples. **(A)** and **(B)** Velocity variations with quartz content, where data are sorted by clay content and sedimentary circumstance, respectively **(A)** SEM photomicrographs of clay as load-bearing grains (Sample C24; Clay: 43.7%; Quartz: 26%; TOC: 0.92%) **(B)** SEM photomicrographs of clay and quartz jointly as load-bearing grains (Sample C52; Clay: 32.4%; Quartz: 51.2%; TOC: 6.26%) **(C)** SEM photomicrographs of quartz as load-bearing grains (Sample C33; Clay: 17.5%; Quartz: 55.3%; TOC: 4.7%).

appear primarily as triangular or polygonal features with well-defined edges (**Figure 4C**). Pores between clay platelets or adjacent to rigid particles appear as elongated ellipsoids (**Figure 4C**). Interparticle pores are relatively large in size with average diameter ranging from dozens of nanometers to a few microns. Samples contain a minor component of simple intracrystalline pores (**Figure 4D**), which are primarily localized within pyrite framboids and dissolution particles having an average diameter of less than 400 nm.

SEM images exhibit two kinds of microtextures in shale samples (**Figure 5**). For sample from upper Longmaxi Formation shale, very coarse microcrystalline quartz (crystal size above 10 μm) surrounded by the aligned clay mineral constitutes the main morphology (**Figures 5A,B**). Contacts of anhedral quartz crystals are mostly punctic coalescent (particles partially welded to each other). Samples from the lower Longmaxi Formation exhibit variable proportions of compact, fine microcrystalline quartz (clast size less than 4 μm). Microcrystalline quartz consists of fully coalescent anhedral particles with distinct contacts (**Figures 5C,D**). Most of these samples exhibit a nonporous crystal mosaic microtexture similar to that described in Moshier (1989).

Velocity Versus Quartz Content

We analyzed how seismic elastic properties varied with shale composition, including organic matter content and porosity. **Figure 6A** shows bedding normal velocity ($V_{P\text{-}0}$, $V_{SV\text{-}0°}$) as function of quartz content at 30 MPa confining pressure (see **Table 1**). Velocity plotted versus quartz abundance exhibited a "V" shaped pattern shown in **Figure 6A**. Samples with quartz content of approximately less than 38% showed a subtle velocity decrease with increasing quartz content but samples with quartz content in excess of 38% showed a positive correlation between velocity and quartz content. We interpret the V-shape as recording the transition in load bearing structure from rigid quartz and carbonate grains isolated within ductile clay of the clay-supported matrix in samples with quartz content less than 38% to multiple generations of authigenic quartz surrounded by ductile clay in the quartz-supported matrix of samples with quartz content exceeding 38%. Clay-supported samples show elastic properties primarily reflecting the elasticity of clay minerals. Increasing quartz content did not change the dominant load-bearing phase but increasing grain content did enhance preservation of intergranular pores in compaction resulting in the subtle velocity decrease as function of quartz content. Carbonate components in clay-supported samples represent an important diagenetic phase that obscures variation trends due to their high velocity. Velocity increases with increasing carbonate content (black arrow) and thus contributes to the increasing slope of the velocity-quartz content trend. Relatively rigid microcrystalline quartz replaces clay as the load-bearing phase in quartz supported samples, but this substitution occurs on a continuum. Velocities therefore show a general positive correlation with quartz content with a piece-wize pattern according to clay content. Samples with quartz content above 38% fall into three groups of 0–20% clay, 20–30% clay and >30% clay. The load-bearing grains and clay fraction parameters are similar within each group (**Figure 6A**). The gradual increase in quartz-supported fraction for each group (**Figures 6A–C**) correlates with increases in bedding normal

TABLE 1 | Database of mineral content and rock physical properties of sales sample at 30 MPa confining pressure.

Samples	Density g/cm^3	Porosity (%)	Major mineral content			TOC (%)	Acoustic properties						E_s (GPa)	Depth (m)	Deposition environment
			Quartz (%)	Clay (%)	Carbonate (%)		V_{P-0° (m/s)	V_{SV-0° (m/s)	V_{P-90° (m/s)	V_{SV-90° (m/s)	E	γ			
C1	2.69	0.5	16.3	32.3	29.2	0.74	5194	3090	6233	3604	0.22	0.18	45.6	2394.4	Shallow
C2	2.62	2.3	28.3	43.3	14.3	2.10	4293	2498	4895	2826	0.15	0.14	26.4	2361	Shallow
C3	2.63	1.6	31.1	44.8	9.6	2.20	4040	2360	4746	2793	0.19	0.20		2358.7	Shallow
C4	2.61	2.0	38.1	44.0	9.2	1.90	4350	2532	5073	2931	0.18	0.17		2369.6	Deep
C5	2.66	0.7	29.3	33.4	14.4	0.77	5007	2899	6174	3644	0.26	0.29	35.9	2346.9	Shallow
C6	2.67	0.8	28.7	41.2	13.0	1.10	4862	2878	6111	3501	0.29	0.24		2351.9	Shallow
C7	2.64	1.8	31.0	44.1	9.1	1.65	4250	2489	5029	2987	0.2	0.22	26.3	2483	Shallow
C8	2.63	1.7	35.4	41.4	9.8	1.73	4120	2412	5107	2950	0.27	0.25	25.9	2488.5	Shallow
C9	2.61	0.9	30.3	40.6	10.3	0.45	4420	2564	5626	3138	0.31	0.25	31.8	2472.9	Shallow
C10	2.60	1.3	38.5	45.1	9.1	1.66	4280	2440	4930	2811	0.16	0.16		2492.7	Shallow
C11	2.60	1.1	33.5	41.9	11.8	1.53	4350	2478	5328		0.25			2486.8	Shallow
C12	2.67	1.1	21.0	37.9	31.4	0.64	4817	2867	6017	3535	0.28	0.26		2386.8	Shallow
C13	2.62	1.3	31.4	40.0	11.6	1.00	4440	2565	5546	3204	0.28	0.28		2481.1	Shallow
C14	2.63	1.5	29.9	45.6	12.3	1.79	4080	2362	4758	2815	0.18	0.21	27.4	2387.2	Shallow
C15	2.62	2.8	35.0	38.6	16.7	2.74	4134	2434	4640	2688	0.13	0.11	25.5	2162.3	Deep
C16	2.61	2.5	33.5	39.3	17.6	3.03	4156	2462	4590	2719	0.11	0.11	25.3	2179.1	Deep
C17	2.6	3.3	43.2	31.3	12.6	3.19	4134	2481	4566	2807	0.11	0.14		2176.1	Deep
C18	2.54	3.8	47.7	32.9	9.8	5.37	4000	2340	4418	2709	0.11	0.17		2181.5	Deep
C19	2.68	0.6	28.8	39.7	12.8	1.10	4400	2620	5568	3359	0.3	0.32		2198	Shallow
C20	2.65	1.6	30.3	45.7	7.4	1.60	4280	2433	5040	2758	0.19	0.14	26.3	2274.1	Shallow
C21	2.61	3.1	32.2	38.4	17.7	2.70	4190	2473	4645	2740	0.11	0.11	26.4	2288.7	Shallow
C22	2.66	0.7	31.4	42.3	11.8	0.77	4300	2630	5564	3346	0.34	0.31	31.3	2304.3	Shallow
C23	2.62	1.2	24.2	42.3	9.5	0.35	4200	2476	5489	3312	0.35	0.39	26.9	2173.7	Shallow
C24	2.67	0.8	26.0	43.7	13.1	0.92	4340	2489	5603	3253	0.33	0.35	27.7	2160	Shallow
C25	2.65	1.4	32.2	37.3	14.8	0.99	4480	2696	5523	3367	0.26	0.28		2167.2	Shallow
C26	2.67	1	26.7	45.1	4.6	0.86	4240	2468	5541	3318	0.35	0.4		2184.6	Shallow
C27	2.64	1.4	26.8	39.4	11.8	1.10	4492	2660	5502	3279	0.25	0.26	30.4	2192.1	Deep
C28	2.60	3.6	37.2	38.0	3.6	3.50	3990	2383	4549	2759	0.15	0.17	24.7	2207.6	Shallow
C29	2.66	0.6	29.4	36.7	13.3	1.30	4370	2700	5499	3203	0.29	0.2	29.2	2215.9	Shallow
C30	2.69	0.6	24.7	45.0	11.6	0.58	4886	2831	6295	3536	0.33	0.28		2406.5	Shallow
C31	2.56	2.2	39.3	13.8	10.3	3.50	4800	2894	5080	3090	0.06	0.07		2375.6	Deep
C32	2.57	2.6	45.5	18.6	9.5	3.60	4890	2951	5175	3206	0.06	0.09		2382.2	Deep
C33	2.57	3.3	53.3	17.5	9.3	4.70	4791	2914	5160	3165	0.08	0.09		2391.4	Deep
C34	2.59	3.9	53.1	17.9	9.9	5.29	4582	2875	5184	3015	0.14	0.05		2388.9	Deep
C35	2.54	4.3	51.5	17.9	9.7	6.40	4485	2799	5034	2989	0.13	0.07	34.5	2198	Deep
C36	2.56	3.5	57.2	17.4	8.2	5.60	4604	2802	5043	3120	0.1	0.12		2201.5	Deep
C37	2.57	3.2	50.8	18.8	7.5	5.10	4657	2820	5101	3037	0.1	0.08	35.6	2452.1	Deep
C38	2.57	3.4	48.8	19.2	8.5	5.30	4724	2865	5044	3190	0.07	0.12		1613	Deep
C39	2.55	4.1	51.3	18.3	7.5	6.70	4463	2707	4889	3086	0.1	0.15	31.7	1614.7	Deep
C40	2.55	3.9	59.1	19.5	8.9	6.30	4672	2814	4900	3108	0.05	0.11		1626.6	Deep
C41	2.56	2.9	40.9	25.3	9.5	3.80	4760	2885	5171	3160	0.09	0.10		1627.5	Deep
C42	2.56	3.7	42.9	20.7	10.4	4.90	4700	2838	5062	3083	0.08	0.09	35.9	2326.4	Deep
C43	2.54	4.6	56.4	18.4	3.2	7.87	4433	2710	4774	2969	0.08	0.1		2223.7	Deep
C44	2.53	4.5	54.4	17.4	9.5	7.60	4469	2712	4730	2996	0.06	0.11	34.8	2229.7	Deep
C45	2.57	41	50.2	19.8	4.8	6.60	4600	2782	4911	3022	0.07	0.09		2231.2	Deep
C46	2.54	3.5	38.6	31.6	6.5	3.90	4142	2521	4723	2874	0.15	0.15		2232.5	Deep
C47	2.63	1.8	25.7	33.3	20.5	0.42	4630	2741	5556	3401	0.22	0.27		2137.6	Shallow
C48	2.68	1.1	20.9	30.9	27.7	0.34	4531	2696	5323	3302	0.19	0.25	38.1	2374.7	Shallow
C49	2.57	3.5	38.8	34.4	5.7	3.32	4206	2531	4721	2863	0.13	0.14		2391.2	Deep
C50	2.53	3.4	40.2	32.3	8.2	3.69	4200	2580	4706	2873	0.13	0.12		2382.4	Deep
C51	2.53	4.2	46.6	31.6	4.6	5.68	4137	2494	4456	2800	0.08	0.13	35.7	2191.4	Deep
C52	2.52	4.3	51.2	32.4	2.6	6.26	4003	2406	4493	2722	0.13	0.14		2204.9	Deep
C53	2.52	4.1	52.0	28.4	7.9	4.65	4110	2461	4407	2762	0.07	0.13		2219.2	Deep
C54	2.62	2.1	32.7	32.8	14.2	0.76	4496	2614	5433	3201	0.23	0.25		2449.5	Shallow
C55	2.58	3.1	34.2	26.8	19.2	2.61	4316	2599	4728	2871	0.10	0.11		2458.1	Deep
C56	2.55	3.9	40.5	24.7	15.6	3.95	4230	2595	4595	2843	0.09	0.1		2475.1	Deep
C57	2.56	4.0	50.5	27.2	12.9	4.30	4209	2527	4611	2791	0.10	0.11		2510.4	Deep
C58	2.55	3.9	54.2	33.5	5.7	4.90	4120	2517	4556	2803	0.11	0.12		2491.5	Deep
C59	2.67	1.2	30.1	37.3	35.1	0.64	4608	2775	6009	3532	0.35	0.31		0	Shallow
C60	2.56	1.4	29.1	43.5	23.5	0.64	4260	2440	5223	2973	0.25	0.24		0	Shallow
C61	2.64	1.7	27.8	21.9	33.6	1.10	4648	2817	5259	3137	0.14	0.12		0	Shallow

(Continued on following page)

TABLE 1 | (*Continued*) Database of mineral content and rock physical properties of sales sample at 30 MPa confining pressure.

Samples	Density g/cm^3	Porosity (%)	Major mineral content			TOC (%)	Acoustic properties						E_s (GPa)	Depth (m)	Deposition environment
			Quartz (%)	Clay (%)	Carbonate (%)		$V_{P\text{-}0^\circ}$ (m/s)	$V_{SV\text{-}0^\circ}$ (m/s)	$V_{P\text{-}90^\circ}$ (m/s)	$V_{SV\text{-}90^\circ}$ (m/s)	E	γ			
C62	2.65	1.0	31.2	40.7	9.9	1.24	4870	2712	5553	3068	0.15	0.14		0	Shallow
C63	2.59	2.6	39.8	27.1	13.4	1.40	4520	2730	5074	3160	0.13	0.17		0	Shallow
C64	2.54	3.5	32.2	41.2	9.8	4.40	4045	2345	4468	2694	0.11	0.16		0	Deep
C65	2.56	3.4	30.1	43.5	7.6	4.70	4050	2267	4462	2605	0.11	0.16		0	Deep
C66	2.56	3.1	41.5	11.8	16.2	3.90	4800	2990	5089	3136	0.06	0.05		0	Deep
C67	2.56	2.7	45.5	12.7	14.8	3.82	4728	2860	5048	3159	0.07	0.11		0	Deep
C68	2.57	2.3	42.0	10.4	15.6	3.57	4930	3073	5148	3164	0.05	0.03		0	Deep
C69	2.58	2.8	45.0	10.5	7.3	4.01	4854	2992	5044	3138	0.04	0.05		0	Deep
C70	2.58	2.4	43.5	21.1	5.6	3.76	4912	3006	5245	3265	0.07	0.09		0	Deep
C71	2.55	3.2	47.7	27.6	9.2	3.44	4230	2522	4693	2831	0.12	0.13		0	Deep
C72	2.56	3.0	43.5	29.3	10.1	2.25	4379	2588	4837	2905	0.11	0.13		0	Deep
C73	2.58	2.3	43.8	25.4	11.7	1.56	4540	2730	5104	3087	0.13	0.14	33.1	0	Deep
C74	2.58	2.8	38.3	21.1	26.6	2.76	4260	2586	4719	2856	0.11	0.11	37.8	0	Deep
C75	2.59	2.9	49.4	29.3	11.3	2.81	4236	2535	4679	2823	0.11	0.12		0	Deep
C76	2.57	2.8	41.9	21.3	7.8	2.56	4450	2637	4793	2913	0.08	0.11		0	Deep
C77	2.54	3.4	54.4	26.8	11.2	3.42	4310	2611	4765	2836	0.11	0.09		0	Deep
C78	2.56	4.0	50.5	22.7	10.5	4.30	4209	2527	4611	2791	0.10	0.11		0	Deep
C80	2.55	3.9	54.2	28.5	8.6	4.90	4120	2517	4556	2803	0.11	0.12		0	Deep
C81	2.58	3.0	34.2	15.8	15.9	2.61	4316	2599	4806	2917	0.12	0.13		0	Deep
C81	2.55	3.7	40.5	20.2	17.6	3.95	4230	2566	4516	2811	0.07	0.10		0	Deep

velocity. Velocity decreases with quartz content within each group reflecting the influence of TOC and porosity on the velocity. These latter parameters increase with increasing quartz content, especially in the case of authigenic quartz, which can provide a rigid framework that prevents compaction if formed early enough (see discussion below). Data also indicate that rock microtexture (load-bearing grains) is the most significant factor in determining velocity variation in the Longmaxi Formation, whereas porosity and TOC exert secondary influence. Compared with **Figure 6B**, where data are sorted by sedimentary circumstance, we observe that microtexture related acoustic velocity variations are in good agreement with the strong control of sedimentary circumstance on velocity. Here, we can speculate that the microtexture evolution of shale samples, to a larger extent, reflects the difference of sedimentary circumstance. In other words, strong control of rock microtexture on acoustic velocity also indicates the influence of sedimentary circumstance on velocity.

Velocity Anisotropy

All shale samples are assumed to have transverse isotropic (TI) symmetry, with symmetry axis normal to the lamination or bedding plane. Five independent elastic constants C_{11}, C_{33}, C_{44}, C_{66} and C_{13} are therefore needed to fully describe shale elastic properties. These can be obtained experimentally from measured velocity and density. Following Thomsen (1986), two important anisotropy parameters are defined as:

$$\varepsilon = \frac{C_{11} - C_{33}}{2C_{33}} = \frac{V_{P-90^0}^2 - V_{P-0^0}^2}{2V_{P-0^0}^2} \quad (1)$$

$$\gamma = \frac{C_{66} - C_{44}}{2C_{44}} = \frac{V_{SH-90^0}^2 - V_{SV-0^0}^2}{2V_{SV-0^0}^2} \quad (2)$$

In general, four basic textures are responsible for the seismic anisotropy of shales: 1) alignment of mineral grains (mainly platy clay particles) at micron scale, 2) alignment of lenticular kerogen or thin kerogen layers, 3) alignment of microfractures and 4) micro-lamination with different elastic properties. **Figure 7** shows the anisotropy parameter ε as function of kerogen content at an effective pressure of 30 MPa. The figure also shows a modified Backus model for a two-layer illite/kerogen composite (Vernik and Nur, 1992) that demonstrates the theoretical effects of TOC on seismic anisotropy. The plot includes a subset of data corresponding to typical mature and immature Bakken shale samples (Vernik and Liu, 1997) for comparison. Comparing the results for Bakken shale and Longmaxi shales helps elucidate the impact of organic matter distribution on anisotropy. For the Longmaxi samples, the compressional wave anisotropy parameter ε shows only a weak negative correlation with kerogen content. The Bakken shale samples show a positive correlation for the same two parameters indicating that kerogen influence on velocity anisotropy depends on texture, diagenetic history and associated alignment of clay particles. Given the post-mature character of the Longmaxi samples and the location of its organic matter (primarily in pores as observed from SEM images), organic matter does not likely play a load-bearing role in the Longmaxi. By contrast, mature samples of the Bakken shale contain organic matter distributed in bedding parallel deposits that form a laminated lenticular texture and play a clear structural role **Table 2**. Thus, it is rational to speculate that anisotropy caused by the alignment of lenticular kerogen is not remarkable

TABLE 2 | Whole rock major element analyses of shale samples.

Samples	Major elements (%)													Zr (ppm)	Al/(Fe + Al + Mn)	Si/Al	Deposition environment
	$Si0_2$	Al_20_3	Na_20	Mg0	P_20_5	K_20	Ca0	$Ti0_2$	Mn0	$Si0_2$	Al_20_3	Fe_20_3	Fe0				
C3	44.75	18.03	0.57	1.22	0.07	4.15	5.71	0.69	0.03	9.52	2.77	1.22	0.07	49.8	0.53	0.49	Shallow
C4	54.29	16.82	0.51	1.56	0.08	2.85	5.34	0.61	0.04	8.97	2.59	1.56	0.08	109.2	0.52	0.56	Shallow
C6	41.37	16.49	0.48	0.82	0.06	3.13	7.23	0.59	0.02	8.85	2.66	0.82	0.06	66.6	0.52	0.49	Shallow
C8	50.77	16.52	0.33	1.69	0.05	2.95	5.94	0.62	0.04	7.21	2.16	1.69	0.05	104.7	0.57	0.56	Shallow
C10	54.18	17.43	0.36	1.25	0.07	3.21	5.23	0.61	0.03	6.89	1.89	1.25	0.07	96.6	0.6	0.57	Shallow
C11	48.35	17.08	0.29	1.39	0.07	2.71	7.15	0.64	0.04	7.27	1.55	1.39	0.07	64.5	0.61	0.55	Shallow
C13	45.71	16.02	0.17	1.43	0.06	3.35	6.56	0.62	0.03	7.91	1.82	1.43	0.06	70.1	0.57	0.54	Shallow
C16	48.26	16.14	0.42	1.04	0.08	2.25	10.53	0.62	0.06	8.59	2.35	1.04	0.08	113.2	0.53	0.54	Shallow
C17	58.22	13.29	0.51	1.59	0.09	2.67	7.03	0.58	0.05	5.15	1.66	1.59	0.09	98.9	0.59	0.65	Deep
C18	67.92	13.28	0.38	1.64	0.07	2.16	6.28	0.51	0.06	4.48	1.29	1.64	0.07	73.30	0.63	0.7	Deep
C19	43.54	15.71	0.37	1.02	0.04	3.55	7.04	0.57	0.04	7.88	2.14	1.02	0.04	42.3	0.55	0.52	Shallow
C20	45.26	17.58	0.46	1.38	0.05	2.73	4.89	0.67	0.03	8.12	2.23	1.38	0.05	102.6	0.56	0.51	Shallow
C25	45.92	14.2	0.44	0.99	0.06	3.58	8.07	0.52	0.02	8.26	2.35	0.99	0.06	86.2	0.50	0.55	Shallow
C27	42.45	15.85	0.52	1.67	0.05	3.39	6.56	0.59	0.02	8.71	2.16	1.67	0.05	62.3	0.53	0.51	Shallow
C28	54.45	15.33	0.29	2.18	0.08	2.56	2.08	0.51	0.06	6.54	1.75	2.18	0.08	116.2	0.59	0.6	Shallow
C29	45.56	15.07	0.37	1.12	0.05	2.38	7.33	0.58	0.08	6.83	2.10	1.12	0.05	76.7	0.56	0.55	Shallow
C31	56.57	6.42	0.54	0.98	0.09	1.79	6.43	0.26	0.05	5.73	0.92	0.98	0.09	116.2	0.45	0.74	Shallow
C32	62.91	8.05	0.32	1.56	0.08	2.11	5.32	0.44	0.06	3.88	1.05	1.56	0.08	92.1	0.55	0.76	Deep
C33	72.68	7.14	0.88	1.45	0.1	2.66	6.15	0.32	0.04	3.59	0.95	1.45	0.10	67.7	0.55	0.80	Deep
C35	68.77	7.62	0.55	1.37	0.12	2.81	5.34	0.37	0.09	4.32	0.62	1.37	0.12	90.3	0.56	0.78	Deep
C36	79.83	7.48	0.57	1.82	0.12	0.87	2.65	0.42	0.08	1.32	0.39	1.82	0.12	40.6	0.76	0.85	Deep
C37	72.25	7.82	0.49	1.86	0.09	1.88	4.88	0.34	0.12	2.43	0.51	1.86	0.09	68.9	0.67	0.81	Deep
C38	66.46	9.26	0.42	1.73	0.08	1.51	5.51	0.56	0.1	2.94	0.29	1.73	0.08	81.4	0.71	0.78	Deep
C39	70.23	7.23	0.61	1.67	0.13	2.23	4.92	0.33	0.08	3.28	0.37	1.67	0.13	96.5	0.63	0.81	Deep
C40	77.86	7.91	0.59	1.81	0.1	1.83	4.84	0.35	0.07	2.74	0.62	1.81	0.1	39.2	0.65	0.82	Deep
C43	76.68	7.62	0.38	1.91	0.16	0.96	2.54	0.36	0.07	2.48	0.66	1.91	0.16	80.3	0.65	0.82	Deep
C44	74.38	7.11	0.34	1.17	0.14	2.36	5.39	0.31	0.16	3.03	0.39	1.17	0.14	52.9	0.63	0.82	Deep
C45	69.31	9.16	0.29	2.08	0.1	1.87	2.57	0.38	0.13	2.77	0.37	2.08	0.10	105.1	0.71	0.79	Deep
C46	55.25	12.95	0.26	1.74	0.11	3.32	4.36	0.52	0.09	3.86	1.16	1.74	0.11	114.7	0.66	0.67	Deep
C47	39.24	13.29	0.21	0.65	0.06	4.05	11.31	0.53	0.06	7.28	2.11	0.65	0.06	51.4	0.52	0.53	Shallow
C49	53.16	14.24	0.36	1.16	0.07	2.22	3.64	0.54	0.06	5.46	1.58	1.16	0.07	120.9	0.6	0.62	Deep
C51	62.81	12.74	0.28	2.06	0.09	1.98	2.84	0.48	0.11	4.27	1.23	2.06	0.09	108.6	0.63	0.69	Deep
C52	71.87	12.86	0.27	1.94	0.1	2.06	1.82	0.49	0.12	3.69	1.16	1.94	0.10	76.5	0.66	0.73	Deep
C53	70.92	11.55	0.33	2.01	0.09	2.11	4.68	0.43	0.09	4.15	1.73	2.01	0.09	106.1	0.58	0.73	Deep
C54	48.78	13.76	0.31	1.73	0.08	2.35	7.73	0.52	0.09	6.83	1.66	1.73	0.08	91.1	0.56	0.59	Shallow
C57	68.14	11.72	0.29	0.88	0.13	1.61	7.26	0.45	0.1	5.29	2.21	0.88	0.13	85.1	0.52	0.70	Deep
C58	70.42	10.41	0.29	0.62	0.16	1.25	3.45	0.49	0.05	2.88	1.05	0.62	0.16	76.6	0.65	0.76	Deep

for Longmaxi Formation shale, except for samples with strong preferred orientation of clay minerals from the upper part of the Longmaxi Formation, where bed-parallel kerogen lenses along elongated pore within clay platelets can be observed.

In addition to organic matter distribution, the alignment of platy clay particles can also cause velocity anisotropy. **Figure 8** plots the two major anisotropy parameters ε andγas function of clay content at an effective pressure of 30 MPa. The data clearly show increasing ε and γ values with increasing clay content but with considerable variation in ε and γ values. This scatter does not apparently reflect variation in kerogen content as samples with relatively high ε andγ values give low TOC values. Organic matter distribution in pores also limits its influence on velocity anisotropy. Data plotted according to depositional environment showed a revealing trend. For a given clay content, shale samples from deep water shelf environments exhibit lower velocity anisotropy values relative to samples from shallow water shelf environments. These properties imply that alignment of platy clay particles is still primarily account for the velocity anisotropy of post-mature Longmaxi Formation shale. But it is also reasonable to speculate, at least, that for Longmaxi Formation shale in different dispositional environment, compaction and associated alignment of clay particles is very different. Relatively weak compaction and alignment of clay particles is observed in the shale samples from deep water shelf circumstance, consistently with lower velocity anisotropy in the samples. Note that shale samples from deep water circumstance are characterized by quartz-supported framework, which will enhance effectively the preservation of intergranular pores in compaction; moreover, weaken the alignment of clay particles by intervening them from compactional rearrangement.

Mechanical Behavior at Ambient Conditions

Figure 9A shows the measured stress-strain curves during triaxial compression at a confining pressure of 30 MPa: this

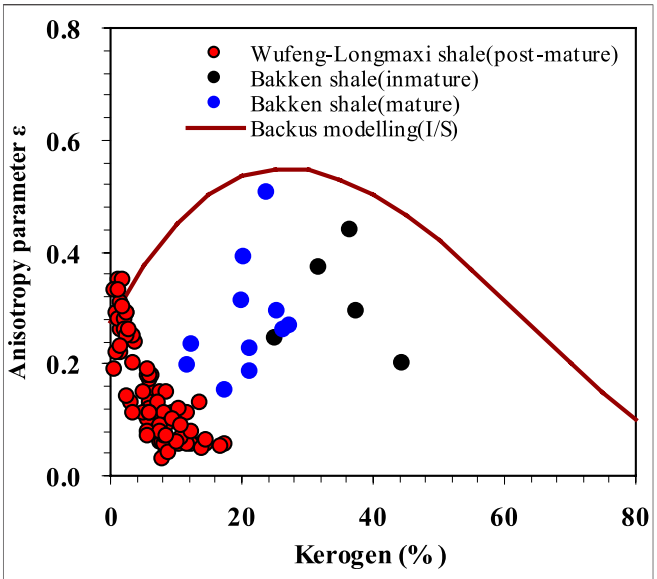

FIGURE 7 | Anisotropy parameter ε versus kerogen content for Wufeng-Longmaxi Formation shales and some mature and immature shales from Bakken shales displayed on the background of the modified Backus model for two-layer illite/kerogen composite (Vernik and Nur, 1992).

figure clearly illustrates the deformation behavior of Longmaxi shale in different dispositional environment. Note that the shape of stress-strain curves occur in two typical forms, namely, elastic deformation and elastic-plastic deformation. For representative samples C35, C42, and C55 from siliceous shale and calcareous-siliceous mixed shale of deep water shelf circumstance, the measured stress-strain curves show typically elastic deformation with either limited or none inelastic deformation until abrupt failure and small stress drops in the post-failure regime (occurrence at axial stresses up to about 110 MPa); the compressive strength almost coincide with the yield stress, as a results, the point of yield stress is often difficult to identify. For representative samples C1, C14, and C28 from argillaceous laminae shale of shallow water shelf circumstance, the measured stress-strain curves is characterized by typically elastic-plastic deformation, and the curve consists a linear segment of elastic deformation stage and a continuous non-linear plastic yield deformation stage until failure, and a relatively large stress drops in the post-failure regime can be observed. **Figures 10B–G** show sample failure modes described above. In accordance with this transition in the shape of curves, samples C35 and C55 showed brittle fracture with typical splitting failure. Samples C14 and C28 developed a single shear crack, indicating the ductile nature of rock samples. Samples C1 and C41 showed conjugate shear cracks indicating semibrittle deformation (transitional between brittle and plastic deformation). The observed differences are likely attributed not only to composition, porosity, water content, but also on the structure and texture.

Figure 10 shows SEM images of representative samples after failure. For samples C14 and C28, microfractures developed mostly between grains having apparent stiffness differences (e.g., boundary between quartz and clay). These represent a heterogonous mechanical interface (**Figures 11A,B**). Microfractures gradually connect and join to form a larger shear fracture. Given this simple failure mode, quartz grains do not show brittle cracks from failure under triaxial compression. Samples C35 and C55 showed microfractures within quartz grains or compact microcrystalline quartz aggregates (**Figures 11C,D**). **Figure 11D** for example shows a "Y" shaped crack within a quartz grain. The crack has not been infilled by other minerals demonstrating its opening during fracturing. These "Y" shaped cracks could connect to form a complex network resulting in the final splitting failure mode.

Effect of Shale Composition on Static Young's Modulus

To determine the effect of shale composition on the static elastic properties, we tested the relationship between the static Young's

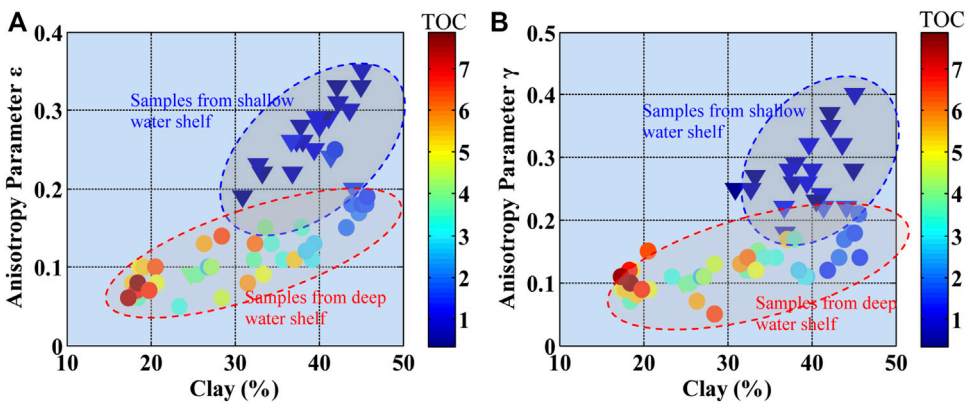

FIGURE 8 | Anisotropy parameters ε **(A)** and γ **(B)** as function of clay content of shale samples. Data points are sorted by clay content and sedimentary circumstance and TOC content (color bar).

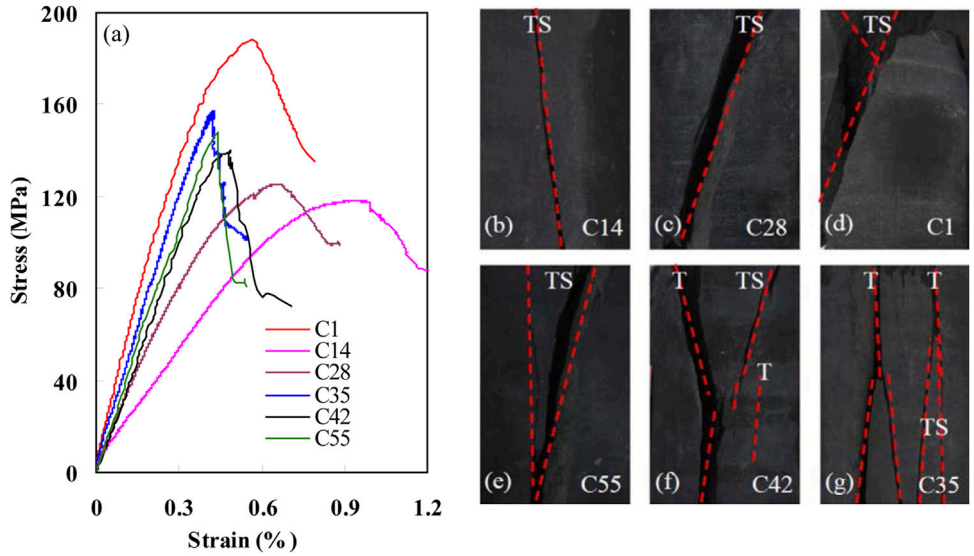

FIGURE 9 | Typical stress-strain curves of the shale samples **(A)** and fracture patterns **(B–G)** (T represents tensile crack and tensile shear crack in the figure).

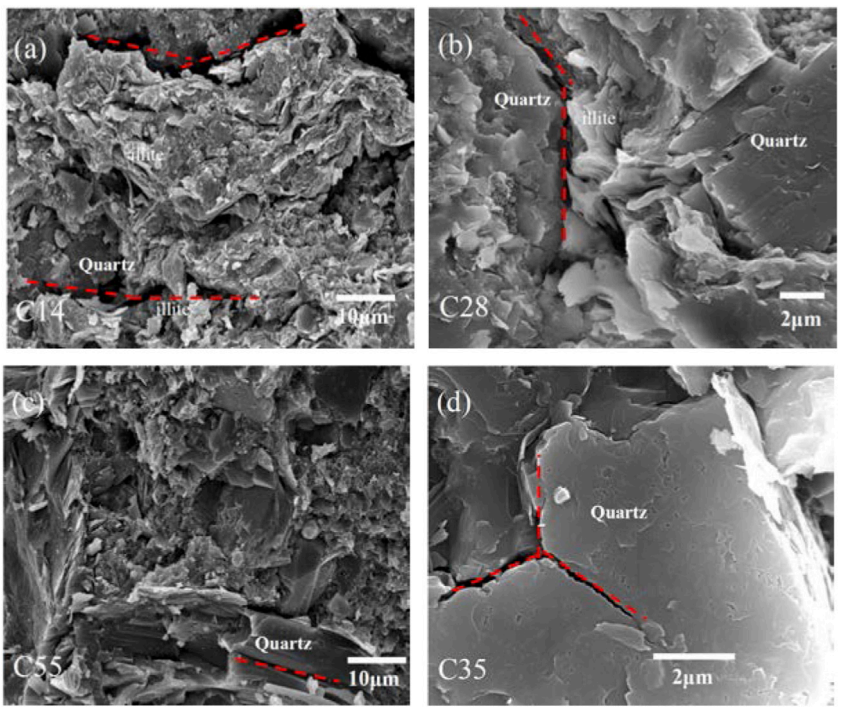

FIGURE 10 | Microscopic crack characteristics of the typical shale samples after fracturing. **(A)** Microscopic crack characteristics of sample C14. **(B)** Microscopic crack characteristics of sample C28. **(C)** Microscopic crack characteristics of sample C35. **(D)** Microscopic crack characteristics of sample C55.

modulus and the predominant mineral content, including quartz, clay, carbonate and TOC (**Figure 11**). Static Young's modulus and microtexture showed a similar "V" shaped relationship as that observed between velocity and microtexture. Static Young's modulus correlated positively with quartz content for samples with quartz content >38%. Samples with quartz content <38% showed a negative correlation between static Young's modulus and quartz content (**Figure 11A**). These correlations may arise from the macroscopic effects of clay-versus quartz-supported matrices as captured by variation in quartz content. The carbonate, as the important cementation components, has an important effect on static Yong's modulus because of their high

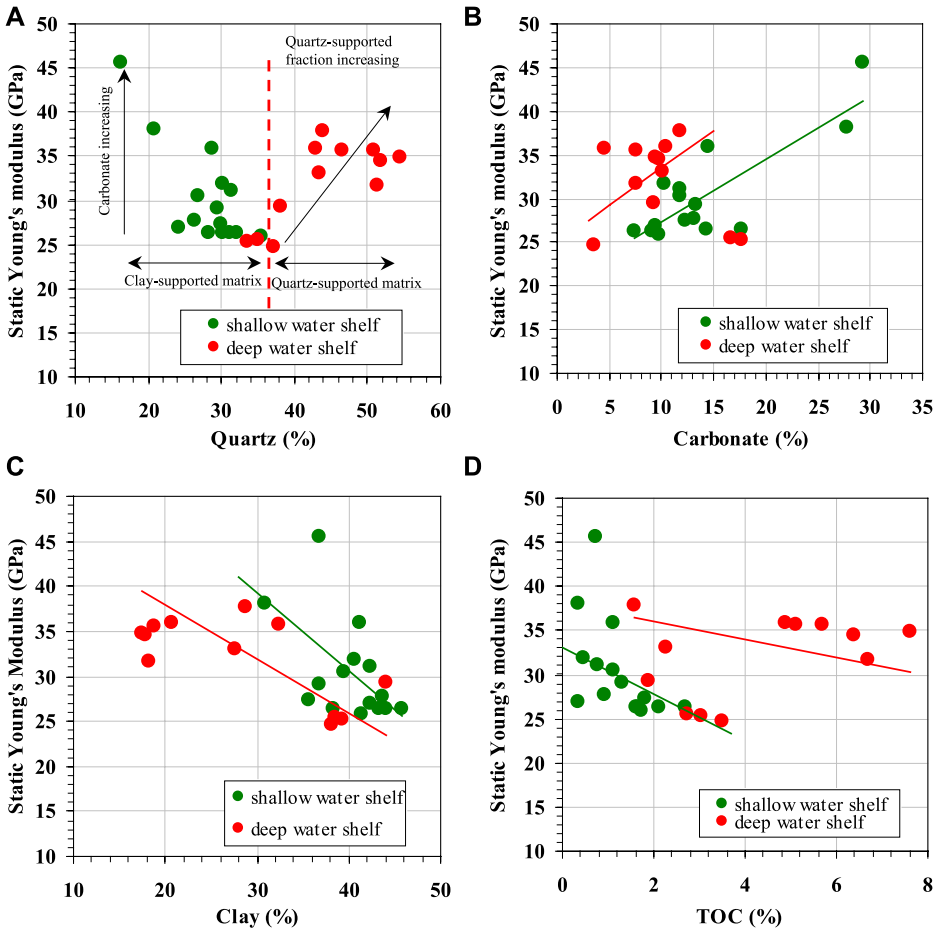

FIGURE 11 | Crossplot of static Young's modulus with major mineral composition. **(A)** Crossplot between static Young's modulus and quartz content. **(B)** Crossplot between static Young's modulus and carbonate content. **(C)** Crossplot between static Young's modulus and carbonate content. **(D)** Crossplot between static Young's modulus and TOC content.

elastic modulus, resulting in the increment of static Yong's modulus with increasing carbonate content (**Figures 11A,B**); however, we can only observe a very weak positive relationship between them, under the condition that data are discriminated by the sedimentary circumstance, indicating that the effect of carbonate on static Yong's modulus is offset by the microtexture variation. Clay minerals and TOC are usually interpreted as ductile materials due to the higher moduli of quartz and carbonates (Pickett, 1963; Mondol et al., 2008). Clay and TOC contents can thus significantly alter the elastic properties of shale (Han et al., 1986; Jarvie et al., 2007; Ahmadov, 2011; Vernik and Milovac, 2011; Eliyahu, 2015; Labani and Rezaee, 2015). Actually, static Yong's modulus does not show a clear, systematic dependence on clay or TOC content. Only when data are displayed by sedimentary circumstance, we observe a very weak negative correlation between static Yong's modulus and clay or TOC content in shale samples (**Figures 11C,D**). These weaker correlations still confirm that microtexture of shale samples (rather than mineral composition) exerts the strongest influence on static elastic properties of the Longmaxi Formation.

DISCUSSION

Quartz Cementation

Although all the samples analyzed derive from the same formation, the upper and lower members of the Longmaxi Formation (shallow water and deep water shelf environments, respectively) show systematic differences in their elastic behavior. These differences help constrain the interpretation of depositional and diagenetic factors from the mechanical properties of shale.

Comparison of sample grain assemblage textures demonstrates the importance of micro-scale quartz crystals in the matrix, which form cement within the illitized clay matrix (**Figures 5A,B**) or occur as matrix-localized microcrystalline quartz (load-bearing grains) (**Figures 5C,D**). The SEM-CL images collected show clear differences between the extrabasinal and intrabasinal character of the quartz particles. **Figures 12A,B** show typical CL spectra for samples from the upper part of the Longmaxi Formation. Two major different categories of luminescence emission bands can be observed

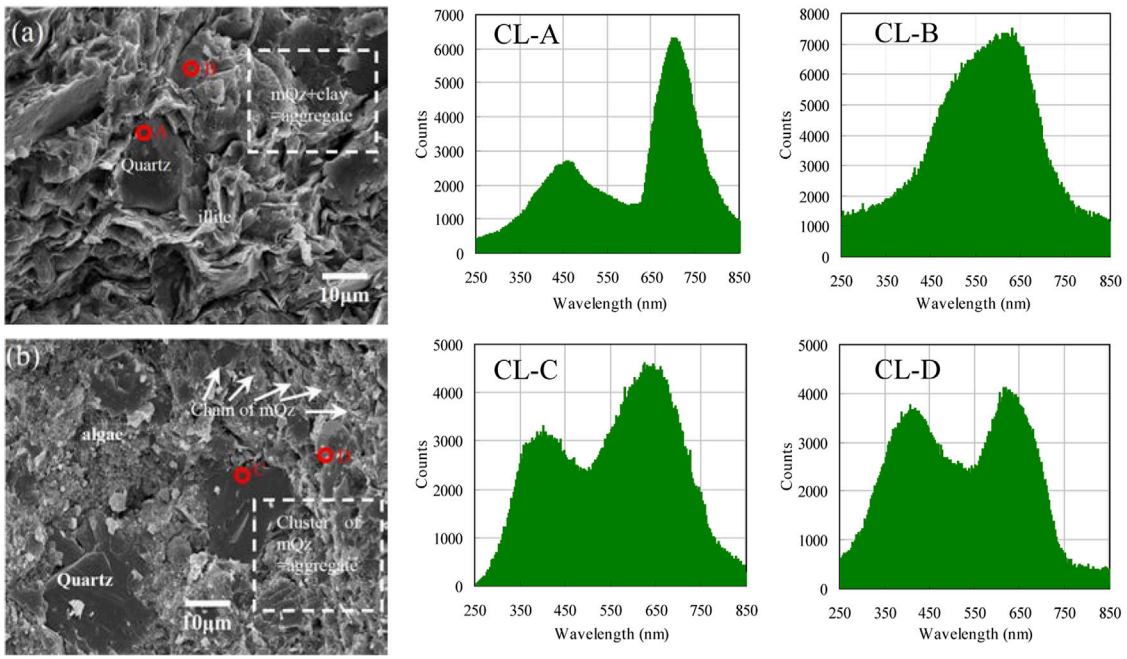

FIGURE 12 | Typical characteristics of quartz in shale samples. **(A)** SEM photomicrographs of shale sample C8 from the upper part of the Wufeng-Longmaxi Formation shale (mQz: microcrystalline quartz). Discrete microcrystalline quartz embedded in the fine-grained illitized smectitic clay matrix. **(B)** SEM photomicrographs of shale sample C39 from the lower part of the Wufeng-Longmaxi Formation shale. Microcrystalline quartz formed coalescent aggregates. CL-A corresponding CL spectrum of extrabasinal quartz. CL-B corresponding CL spectrum of authigenic quartz sourced from smectite to illite reaction. CL-C and CL-D corresponding CL spectrum of biogenic quartz.

during the monochromatic CL analysis. Silt-sized angular quartz display a characteristic CL-spectrum of two broad symmetric "bell-shaped" with major luminescence peaks close to 680 ~ 720 nm and relatively weak secondary peaks close to 430 ~ 470nm, and these quartz can be identified as extrabasinal detrital quartz (Peltonen et al., 2009; Thyberg and Jahren, 2011). The micro-sized quartz, occurred mainly within the illitized clay matrix as discrete grains, small clusters, display a characteristic CL-spectrum of "bell-shaped" with peaks close to 590 ~ 620nm, and they can be identified as authigenic quartz, soured from smectite to illite reaction (Götze et al., 2001; Thyberg and Jahren, 2011).

Typical results of the CL response for samples from lower part of Longmaxi Formation are shown in **Figures 12C,D**. We can observed that silt-sized irregular quartz and relatively large aggregates of microcrystalline quartz, display almost similar CL-spectrum with two symmetric "bell-shaped" with luminescence peaks close to 390 ~ 430 nm and 580 ~ 620 nm. Such quartz grains are often been considered as biogenic origin, re-crystallized locally during progressive burial from a biogenic precursor like radiolarians and sponge spiculus, and the weak peak close to 390 ~ 430 nm is commonly interpreted as being remnants of CL-properties of opal-A/opal-CT inheritance from biogenic precursor material to the re-crystallized microcrystalline quartz and finally to the macro-quartz during progressive diagenesis (Williams et al., 1985; Thyberg and Jahren, 2011). Comparing of the results of CL-spectrum, it can be seen that the derivation of microcrystalline quartz in the two shale units are very different. Very coarse microcrystalline quartz within clay matrix in samples from upper part is mainly soured from smectite to illite reaction, whilst compact fine microcrystalline quartz in samples from lower part is mainly biogenic origin.

In addition, biogenic quartz is characterized by high concentration of SiO_2, P_2O_5 and Fe_2O_3, and relatively low concentration of TiO_2, Al_2O_3, FeO and MgO (Wedepohl, 1971). Samples from the lower Longmaxi Formation have low TiO_2 and Al_2O_3 content and do not show correlations between SiO_2 and TiO_2 or Al_2O_3 contents. This indicates only limited extrabasinal input to overall SiO_2 content. By contrast, samples from the upper Longmaxi Formation exhibit high TiO_2 and Al_2O_3 contents and a strong positive correlation between SiO_2 and TiO_2 indicating the presence of extrabasinal quartz. The Al/(Fe + Al + Mn) index is widely used to interpret silica precipitation in sedimentary rocks (Yamamoto, 1987). Hydrothermal silica gives Al/(Fe + Al + Mn) values of around 0.01 whereas biogenic silica gives Al/(Fe + Al + Mn) values greater than 0.6. Samples from the lower Longmaxi Formation give Al/(Fe + Al + Mn) values greater 0.6 indicating a biogenic origin. Samples from the upper Longmaxi Formation give Al/(Fe + Al + Mn) values below 0.59 suggesting an extrabasinal origin. Samples from the lower Longmaxi Formation also primarily plot above the illite Si/Al line (Rowe et al., 2008) further indicating a biogenic origin (**Figure 13A**).

Wright et al. (2010) suggested that extrabasinal and biogenic silica can be differentiated on the basis of quartz (representatives of total quartz) and Zr content. Zirconium concentration is

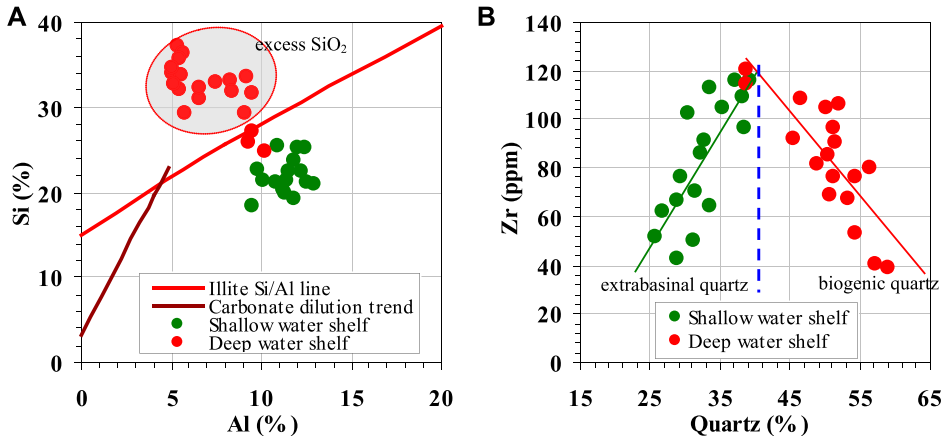

FIGURE 13 | (A) Crossplot of Si and Al of Wufeng-Longmaxi Formation shale on the background of illite Si/Al line and carbonate dilution line (Rowe et al., 2008). Excess SiO_2 indicates the biogenic quartz. **(B)** Crossplot of SiO_2 versus Zr. Bioenic quartz is distinguished from extrabasinal quartz by the slope. Data points are sorted by sedimentary circumstance.

closely related to the heavy mineral zircon, which can serve as a proxy for silt-sized material of extrabasinal origin. A negative correlation between quartz and Zr content indicates that silica is primarily biogenic in origin while a positive correlation indicates extrabasinal input. Samples from the upper Longmaxi Formation show a positive correlation between quartz and Zr content, whereas samples from the lower Longmaxi Formation exhibit a negative correlation between quartz and Zr content (**Figure 13B**). These trends affirm that the 38% quartz content threshold effectively differentiates between extrabasinal and biogenic quartz contributions. Proxies described above indicate extrabasinal quartz contribution in samples from the upper Longmaxi Formation and a major biogenic quartz contribution for samples from the lower Longmaxi Formation. This model is also consistent with our SEM–CL work and geochemical analysis.

Influence of Diagenesis and Microtexture on Macroscopic Seismic Elastic and Geomechanical Behaviors

Most important factors controlling elastic properties of reservoir rock at great burial depth are the primary sediment composition, sedimentary environment and subsequent diagenetic processes. The mechanical and chemical compaction of sediment during diagenesis drives the rock towards higher mechanical and chemical stability. Effective stress from overburden at temperatures below 70–80°C causes mechanical compaction, which includes the reorientation, shifting and ductile deformation of clay particles. These processes diminish porosity and create an aligned clay fabric. At greater depth (higher temperature) compaction in shales is mostly chemical and cementation resulting from mineral reactions, e.g. transformation of smectite to illite, will dramatically increase the rock strength, in company with the further reduction of porosity and permeability, which will in most cases effectively shut down the mechanical compaction. Therefore, mechanical compaction and chemical compaction are commonly considered as two sequential processes controlling the elastic properties of shales during burial. Actually, the stratigraphic difference in depth between the two part of Wufeng-Longmaxi Formation shales cannot explain the major difference in the macroscopic seismic elastic and geomechanical behaviors, as the maximum effective stresses and temperatures the two formations have undergone during burial and uplift must have been practically the same.

The upper part of the Longmaxi Formation is interpreted to represent a relatively shallow water dysoxic to anoxic shelf environment with minor fluctuations in depositional conditions. Correspondingly, the primary composition of shale samples from this part contains not only a prominent fraction of clay minerals but also a significant component of silt-size extrabasinal debris. Primary grain assemblage gradually mixed with organic materials formed by the decadent of algae (mainly blue algae) and other plankton (Wang et al., 2014). Lower primary productivity associated with reducing conditions contributes to lower organic matter content. In the following mechanical compaction process during burial, platy clay particles in the primary composition of shale samples were re-oriented and re-arranged under overburden to reach the maximal mechanical stability with the fabric of preferred orientation of clay minerals normal to the overburden, where silt-sized extrabasinal debris is surrounded by a matrix containing abundant alignment clay-size clay minerals. However, such stable clay fabric remains unchanged during the subsequent burial history. Hence, it is reasonable to speculate that velocity anisotropy and its magnitude are basically determined in the mechanical compaction process. Intermediate burial depths of 2.0–3.5 km correspond to temperature ranges of 80–100°C where smectite becomes unstable and transforms into mixed-layer illite-smectite (Nadeau et al., 1985; Yau et al., 1987; Nadeau et al., 2002). This reaction releases excess silica which precipitates as authigenic micro-scale quartz within the illitized clay matrix as discrete grains or small clusters of grains (**Figures 5B**, **12A**).

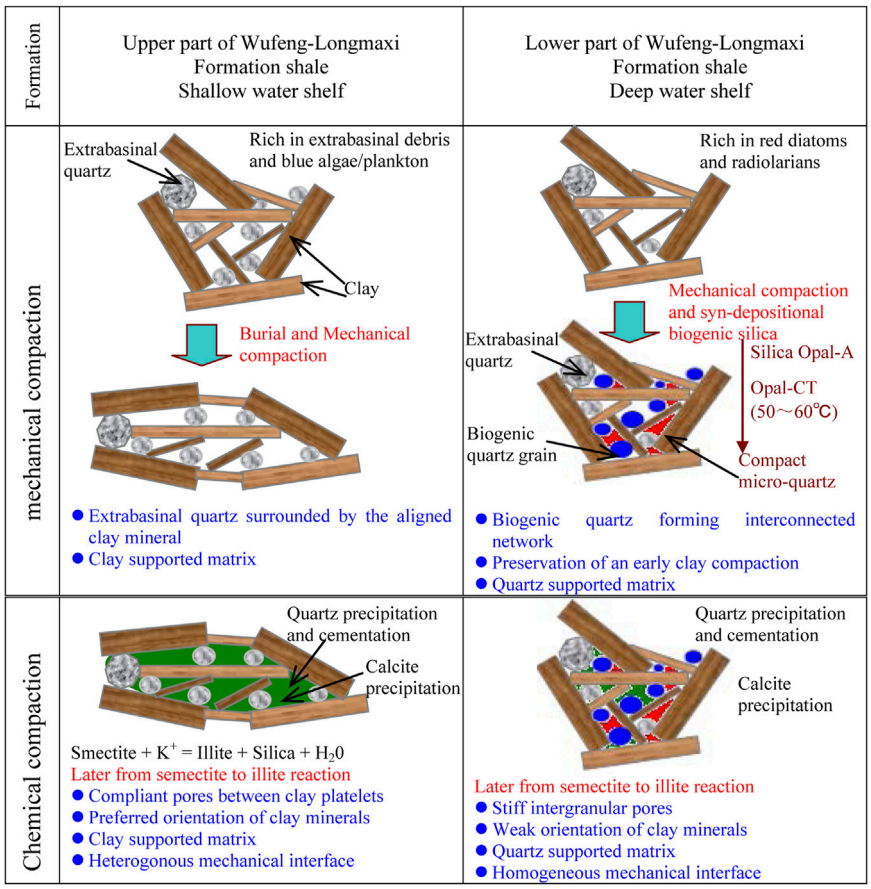

FIGURE 14 | Conceptual model summarizing the depositional and diagenetic processes of the Wufeng-Longmaxi Formation shale.

Precipitation of illite and quartz will cause a sharp increase in matrix rigidity and prevent mechanical compaction. Thus, for the upper part of the Longmaxi Formation shales, it is rational to speculate that mechanical compaction and chemical compaction are two sequential processes in controlling elastic properties. Carbonate cement in samples from upper part of Longmaxi Formation is another critical component with respect to burial diagenesis. Relatively moderate amounts of carbonate cement in samples can results in high velocity and mechanical strength at shallow depth.

The lower part of the Longmaxi Formation shales are interpreted to represent deep-water shelf sediments deposited under anoxic conditions, where the primary composition of shale samples are also assumed to mainly contain detrital quartz and clay grains. High primary productivity and reducing conditions caused biogenetic silica to dissolve and reprecipitate as microcrystalline quartz coating on detrital quartz and clay grains, after biogenetic silica reacts to form opal-A and micro-quartz at about 60 ~ 80°C (Williams et al., 1985). Precipitation of amorphous silica from pore-water solutions can only occur at shallow depths, and super-saturation of silica limits or prevents later quartz cement precipitation from smectite to illite reactions, which demonstrate that biogenetic quartz have an early diagenetic origin. The euhedral shape of the microcrystalline quartz, as well as their growth on detrital quartz grains into the pore space seen via SEM (**Figures 5D**, **12B** , isconsistent with early *in situ* precipitation in a non-compacted sediment rather than having been transported. Biogenic silica cement around primary grain assemblages during diagenetic transformation from opal-A to compact microcrystalline quartz forms a rigid, load bearing framework of interconnected quartz grains. As indicated by the CL-spectra, authigenic microcrystalline quartz cementation from the silica released by the smectite to illite reaction can also be identified, which can be considered as the primary results of chemical compaction. In a summary, microtexture and compositional reorganization of Longmaxi Formation Shale was apparently affected by the syn-depositional chemical transformation of the primary mineral assemblage. The interpretation of the depositional and diagenetic evolution of the two shale units is summarized in a simplified conceptual model in **Figure 14**.

The salient differences in microtexture and diagenetic evolution between the upper and lower Longmaxi Formation shales can be used to interpret contrasting acoustic and geomechanical properties as measured in the laboratory. Samples from the upper and lower parts of the Longmaxi

Formation specifically differed in terms of brittleness, seismic velocity anisotropy, deformation and failure modes, relations between static Young's modulus versus composition, their seismic velocity versus quartz content relationships and seismic velocity versus porosity (TOC content) relationships.

Samples from the upper Longmaxi Formation contain extrabasinal detrital and authigenic quartz surrounded by a load bearing clay matrix. The seismic elastic and geomechanical properties for these samples reflect the elastic response of their clay matrices (**Figure 5B**). For samples from lower part of Longmaxi Formation Shales, early biogenetic quartz forms the interlocking and continuous quartz cement, and biogenetic quartz will take the role as load bearing grains; therefore, the seismic elastic and geomechanical properties of the shale samples is mainly controlled by the elastic response of quartz aggregates (**Figure 5D**). Plots of seismic velocity according to clay- and quartz-supported matrix show a "V" shaped trend (**Figure 6**). It is reasonable to hypothesize, at least, that the quartz-supported fraction in the specimens will increase with the biogenetic quartz content. Similar observations are reported on the laboratory measurement for unconsolidated sand/shale mixtures (Yin, 1992) and on the Horn River Formation Group shale (Dong et al., 2017). Additional, the relationship between static Young's modulus and quartz content also indicates variation in load-bearing grains of shale samples. These trends indicate that quartz primarily has an extrabasinal origin in samples with quartz content <38%, whereas it is predominantly biogenic in origin in samples with quartz content >38%.

Contrasting diagenetic histories also influence porosity in shales. Because of the more rigid behavior of quartz-supported rock framework compared with the relatively more ductile behavior of clay-supported matrix, the existing of early biogenetic quartz in samples from lower part of Longmaxi Formation Shales is more favorable for the preservation of the primary intergranular pores in compaction. Intergranular spaces between rigid quartz particles exhibit primarily triangular or polygonal shapes (**Figures 4A,C**). Their high aspect ratio confers rigid behavior. Therefore, the velocity of these specimens is often insensitive to the porosity. Samples from the upper Longmaxi Formation contain few intergranular pores due to extreme compaction and cementation. Intergranular pores persist between clay platelets or around edges of detrital quartz (**Figure 4B**). Their elongate, ellipsoid shapes are often aligned parallel to bedding. This type of porosity is associated with considerable velocity variation. Secondary pores, including intraparticle pores within framboids and other unstable phases (e.g., feldspar, clay and calcite) also impose considerable uncertainty in velocity interpretation.

Velocity anisotropy variation in shales primarily arises from alignment of clay particles established during mechanical and chemical compaction. The preferred orientation of clay minerals, described by the orientation distribution function, depends primarily on the degree of mechanical compaction (Aplin et al., 2006; DayStirrat et al., 2008). Samples from the lower Longmaxi Formation show greater rigidity due to early diagenetic cementation of biogenic quartz, which limited mechanical compaction. Hence, it is likely that early biogenetic quartz cementation may indeed contribute to a lowering of the velocity anisotropy by the preservation of a very early clay compaction state in these shale samples; similar observations were reported on the anhydrite-cemented lithologies of the Bongabinni Formation Shale studied by Piane et al., (2015). Samples from the upper Longmaxi Formation show extreme mechanical compaction and pervasive grain-scale clay alignment. These factors contribute to the stronger velocity anisotropy values observed for samples of the lower Longmaxi Formation. The influence of chemical compaction on the velocity anisotropy is very complex, and some counteracting effects on shale anisotropy are documented in both experiments and rock physics modeling results. Illitization of semectite has been suggested as critical diagenetic process to achieve a significant illite preferred orientation (Charpentier et al., 2003; DayStirrat et al., 2008). The precipitation of pore-filling micro-quartz from illitization of semectite may form stronger vertical binding between the clay particles resulting in the reduction of velocity anisotropy (Avseth et al., 2010). Clearly, the strong clay alignment observed in the samples from upper part of the Longmaxi Formation Shales suggests the possible contribution of the semectite-illitization transformation to the overall velocity anisotropy.

Considering the larger strain amplitude (10^{-2}–10^{-3}) of static measurements, geomechanical behaviors of individual shale samples appear to be mostly affected by the elastic response of grain-to-grain contacts as a consequence of the distributed stress concentration in the zone of relatively heterogeneous components. Stress-strain curves from samples from the upper Longmaxi Formation showed an apparent plastic yield deformation stage prior to failure with ductile properties. This indicates a clay-supported matrix with apparent mechanical interface between stiff extrabasinal quartz embedded in clay. Deformation occurred as microfractures between those interfaces at the microscale. Samples from the lower part of the Longmaxi Formation showed elastic deformation indicating a more brittle quartz-supported framework with limited mechanical interfaces. Deformation occurred as microfractures within contiguous micritic quartz. Previous studies suggest that water content, bedding orientation and deformational parameters such as pressure, temperature and strain rate influence shale stress-strain behavior (see for example Rybacki et al., 2015). This study focused primarily on the influence of diagenetic and microstructural factors on macroscopic seismic elastic and geomechanical behaviors.

CONCLUSION

This research performed laboratory measurements of acoustic and geomechanical properties along with detailed petrographic, geochemical analysis of 82 high-maturity shales from core samples of the Longmaxi Formation in the southeast Sichuan Basin, China. Interpretation of the data revealed how depositional history can influence acoustic and geomechanical properties.

The major achievement is the establishment of the link between depositional environment and the subsequent microtexture development, which finally exerts a critical influence on the reservoir quality and the physical properties of the shales. Specifically, we have shown that microtexture and compositional reorganization of Longmaxi Formation shale was affected by the syn-depositional chemical reactivity of the primary grain assemblage, notable the biogenic quartz grains. The lower part of the Longmaxi Formation formed in a deep water shelf environment where early cementation by biogenic quartz formed interlocking, contiguous quartz cement with limited mechanical interfaces. This biogenetic quartz cement thus assumed the role of a load bearing framework which effectively decreased subsequent mechanical compaction during burial. A very early clay fabrics and primary intergranular pores were effectively preserved. The upper part of the Longmaxi Formation formed in a shallow water shelf environment. Absent initial diagenetic cementation, clay minerals experienced normal compaction to form elongated ellipsoidal pores and a pervasively aligned clay fabric with apparent mechanic interface that played a load-bearing role. SEM-CL images, Si-Al relationships and trace element parameters such as Zr and Ti support the interpretation of a clay-supported framework for these samples.

The microstructural differences between the upper and lower Longmaxi shales exert a primary influence on their macroscopic acoustic and geomechanical behaviors. A "V" shaped trend in seismic velocities and static Young's modulus plotted as function of quartz content for example clearly differentiates the elastic response of clay-supported and quartz-supported samples. The influence of porosity and TOC content on velocity is undeniable but velocity variation could be seen as a more direct result of the evolution of microstructure such as the load-bearing. Alignment of platy clay particles is the dominant factor in causing velocity anisotropy observed in Longmaxi Formation samples. Indeed, apparent velocity anisotropy discrepancy could be observed as a reflection of the different compaction during burial. Microtexture also exerts a strong influence on the deformation mode. Samples with quartz-supported matrix (from reprecipitation of biogenic quartz cement) exhibit typical elastic deformation and splitting failure modes. By contrast, samples with clay-supported microtexture show more plastic deformation caused by a heterogeneous medium with a mechanical interface between stiff minerals and the more ductile clay matrix. Overall, these results provide insights for the role of depositional and diagenetic controls on the microtexture and resulting rock properties of Wufeng-Longmaxi Formation Shales that could be applied positively to practical seismic-based "sweet-spots" prospecting of gas shale reservoir.

DATA AVAILABILITY STATEMENT

The original contributions presented in the study are included in the article/Supplementary Material, further inquiries can be directed to the corresponding author.

AUTHOR CONTRIBUTIONS

All authors listed have made a substantial, direct, and intellectual contribution to the work and approved it for publication.

ACKNOWLEDGMENTS

This work is sponsored by the Nation Natural Science Foundation of China Research (41774136, 41374135); the National Science and Technology Major Project (2017X05035004–004). We think Zhonghua Xu for providing the technical support on SEM-CL. The data used for building **Figures 2**,**3**,**6**–**9**,**12** are given in Table S1 in the supporting information, those for **Figure 13** are given in S2, and relevant imaging may be obtained by contacting the corresponding author (dengjixin@cdut.cn).

REFERENCES

Ahmadov, R. S. (2011). Microtextural, elastic and transport properties of source rocks. Ph.D. dissertation. California: Stanford University.

Aplin, A. C., Matenaar, I. F., Mccarty, D. K., and van der Pluijm, B. A. (2006). Influence of mechanical compaction and clay mineral diagenesis on the microfabric and pore-scale properties of deep-water gulf of Mexico mudstones. *Clays Clay Miner.* 54 (4), 500–514. doi:10.1346/ccmn.2006.0540411

Avseth, P., Mukerji, T., Mavko, G., and Dvorkin, J. (2010). Rock-physics diagnostics of depositional texture, diagenetic alterations, and reservoir heterogeneity in high porosity siliciclastic sediments and rocks—a review of selected models and suggested work flows. *Geophysics* 75, 31–147. doi:10.1190/1.3483770

Breyer, J. A., Bunting, P. J., Monroe, R. M., and Steed, M. B. (2012). "Lithologic stratigraphic variation in a continuous shale-gas reservoir: the barnett shale (mississippian), fort worth basin, Texas," in *Shale reservoirs: giant resources for the 21st century*. Editor J. A. Breyer (AAPG Memoir), 97, 368–381.

Carcione, J. M., and Avseth, P. (2015). Rock-physics templates for clay-rich source rocks. *GEOPHYSICS* 80 (5), D481–D500. doi:10.1190/geo2014-0510.1

Charpentier, D., Worden, R. H., Dillon, C. G., and Aplin, A. C. (2003). Fabric development and the smectite to illite transition in gulf ofmexico mudstones: an image analysis approach. *J. Geochemical Exploration* 78–79 (3), 459–463. doi:10.1016/s0375-6742(03)00073-6

Chen, L., Jiang, Z., Liu, K., Wang, P., Ji, W., Gao, F., et al. (2016). Effect of lithofacies on gas storage capacity of marine and continental shales in the Sichuan Basin, China. *J. Nat. Gas Sci. Eng.* 36, 773–785. doi:10.1016/j.jngse.2016.11.024

Chen, L., Lu, Y., Jiang, S., Li, J., Guo, T., and Luo, C. (2015). Heterogeneity of the lower silurian Longmaxi marine shale in the southeast Sichuan Basin of China. *Mar. Pet. Geology.* 65, 232–246. doi:10.1016/j.marpetgeo.2015.04.003

Chen, X., Fan, J., Melchin, M. J., and Mitchell, C. E. (2010). Hirnantian (latest ordovician) graptolites from the upper yangtze region, China. *Palaeontology* 48 (2), 235–280. doi:10.1111/j.1475-4983.2005.00453.x

Chen, X., Rong, J. S., Mitchell, C. E., Harper, D. A. T., Zhan, R. B., Zhang, Y. D., et al. (2000). Late Ordovician to earliest Silurian graptolite and brachiopod biozonation from the Yangtze region,South China, with a global correlation. *Geol. Mag.* 137 (6), 623–650. doi:10.1017/S0016756800004702

Curtis, J. B. (2002). Fractured shale-gas systems. *AAPG Bull.* 86 (9), 1921–1938. doi:10.1306/61EEDDBE-173E-11D7-8645000102C1865D

Day-Stirrat, R. J., Aplin, A. C., Środoń, J., and van der Pluijm, B. A. (2008). Diagenetic reorientation of phyllosilicate minerals in paleogene mudstones of the podhale basin, southern Poland. *Clays Clay Miner.* 56 (1), 100–111. doi:10.1346/ccmn.2008.0560109

Deng, J., Wang, S., and Han, D.-H. (2009). The velocity and attenuation anisotropy of shale at ultrasonic frequency. *J. Geophys. Eng.* 6 (3), 269–278. doi:10.1088/1742-2132/6/3/006

Dewhurst, D. N., Aplin, A. C., Sarda, J.-P., and Yang, Y. (1998). Compaction-driven evolution of porosity and permeability in natural mudstones: an experimental study. *J. Geophys. Res.* 103 (B1), 651–661. doi:10.1029/97jb02540

Dewhurst, D. N., and Siggins, A. F. (2006). Impact of fabric, microcracks and stress field on shale anisotropy. *Geophys. J. Int.* 165 (1), 135–148. doi:10.1111/j.1365-246x.2006.02834.x

Dewhurst, D. N., Siggins, A. F., Sarout, J., Raven, M. D., and Nordgårdbolås, H. M. (2011). Geomechanical and ultrasonic characterization of a norwegian sea shale. *Geophysics* 76 (76), WA101–WA111. doi:10.1190/1.3569599

Dong, T., Harris, N. B., Ayranci, K., and Yang, S. (2017). The impact of rock composition on geomechanical properties of a shale formation: middle and Upper Devonian Horn River Group shale, Northeast British Columbia, Canada. *Bulletin* 101 (2), 177–204. doi:10.1306/07251615199

Eliyahu, M., Emmanuel, S., Day-Stirrat, R. J., and Macaulay, C. I. (2015). Mechanical properties of organic matter in shales mapped at the nanometer scale. *Mar. Pet. Geology.* 59 (59), 294–304. doi:10.1016/j.marpetgeo.2014.09.007

Götze, J., Plötze, M., and Habermann, D. (2001). Origin, spectral characteristics and practical applications of the cathodoluminescence (CL) of quartz – a review. *Mineralogy Petrology* 71 (3–4), 225–250. doi:10.1007/s007100170040

Guo, Z., Deng, K., and Han, Y. (1996). *The forming and evolution of Sichuan Basin*. Beijing: Geological Publishing House.

Han, C., Jiang, Z., Han, M., Wu, M., and Lin, W. (2016). The lithofacies and reservoir characteristics of the upper ordovician and lower silurian black shale in the southern sichuan basin and its periphery, China. *Mar. Pet. Geology.* 75, 181–191. doi:10.1016/j.marpetgeo.2016.04.014

Han, D. h., Nur, A., and Morgan, D. (1986). Effects of porosity and clay content on wave velocities in sandstones. *Geophysics* 51 (11), 2093–2107. doi:10.1190/1.1442062

Hao, F., Guo, T., Zhu, Y., Cai, X., Zou, H., and Li, P. (2008). Evidence for multiple stages of oil cracking and thermochemical sulfate reduction in the Puguang Gas Field, Sichuan basin, China. *AAPG Bulletin* 92 (5), 611–637. doi:10.1306/01210807090

Hornby, B. E., Schwartz, L. M., and Hudson, J. A. (1994). Anisotropic effective-medium modeling of the elastic properties of shales. *Geophysics* 59 (10), 1570–1583. doi:10.1190/1.1443546

Horsrud, P., SØnstebØ, E. F., and BØe, R. (1998). Mechanical and petrophysical properties of North Sea shales. *Int. J. Rock Mech. Mining Sci.* 35 (8), 1009–1020. doi:10.1016/s0148-9062(98)00162-4

Islam, M. A., and Skalle, P. (2013). An experimental investigation of shale mechanical properties through drained and undrained test mechanisms. *Rock Mech. Rock Eng.* 46 (6), 1391–1413. doi:10.1007/s00603-013-0377-8

Jarvie, D. M., Hill, R. J., Ruble, T. E., and Pollastro, R. M. (2007). Unconventional shale-gas systems: the Mississippian Barnett Shale of north-central Texas as one model for thermogenic shale-gas assessment. *Bulletin* 91 (4), 475–499. doi:10.1306/12190606068

Jia, C., Zheng, M., and Zhang, Y. (2012). Unconventional hydrocarbon resources in China and the prospect of exploration and development. *Pet. Exploration Development* 39 (2), 139–146. doi:10.1016/s1876-3804(12)60026-3

Jin, Z., Hu, Z., Gao, B., et al. (2016). Controlling factors on the enrichment and high productivity of shale gas in the Wufeng-Longmaxi Formations, southeastern Sichuan Basin. *Earth Sci. Front.* 23 (1), 1–10. doi:10.13745/j.esf.2016.01.001

Johansen, T. A., Ruud, B. D., and Jakobsen, M. (2004). Effect of grain scale alignment on seismic anisotropy and reflectivity of shales. *Geophys. Prospecting* 52, 133–149. doi:10.1046/j.1365-2478.2003.00405.x

Johnston, J. E., and Christensen, N. I. (1995). Seismic anisotropy of shales. *J. Geophys. Res.* 100 (B4), 5991–6003. doi:10.1029/95jb00031

Labani, M. M., and Rezaee, R. (2015). The importance of geochemical parameters and shale composition on rock mechanical properties of gas shale reservoirs: a case study from the Kockatea Shale and Carynginia Formation from the Perth Basin, Western Australia. *Rock Mech. Rock Eng.* 48 (3), 1249–1257. doi:10.1007/s00603-014-0617-6

Ma, Y., Feng, J., Mu, Z., Zhao, P., Bao, S., and Wang, F. (2012). The potential and exploring progress of unconventional hydrocarbon resources in sinopec. *Eng. Sci.* 14 (6), 22–30. doi:10.3969/j.issn.1009-1742.2012.06.004

Masri, M., Sibai, M., Shao, J. F., and Mainguy, M. (2014). Experimental investigation of the effect of temperature on the mechanical behavior of tournemire shale. *Int. J. Rock Mech. Mining Sci.* 70 (9), 185–191. doi:10.1016/j.ijrmms.2014.05.007

McGlade, C., Speirs, J., and Sorrell, S. (2013). Unconventional gas - a review of regional and global resource estimates. *Energy* 55, 571–584. doi:10.1016/j.energy.2013.01.048

Milliken, K. L., Esch, W. L., Reed, R. M., and Zhang, T. (2012). Grain assemblages and strong diagenetic overprinting in siliceous mudrocks, barnett shale (mississippian), fort worth basin, Texas. *Bulletin* 96 (8), 1553–1578. doi:10.1306/12011111129

Mondol, N. H., Jahren, J., Bjørlykke, K., and Brevik, I. (2008). Elastic properties of clay minerals. *The Leading Edge* 27 (6), 758–770. doi:10.1190/1.2944161

Moshier, S. O. (1989). Microporosity in micritic limestones: a review. *Sediment. Geology.* 63 (3), 191–213. doi:10.1016/0037-0738(89)90132-2

Nadeau, P. H., Peacor, D. R., Yan, J., and Hillier, S. (2002). I–S precipitation in pore space as the cause of geopressuring in Mesozoic mudstones, Egersund Basin, *Norwegian continental shelf. Am. Mineral.* 87 (11–12), 1580–1589. doi:10.2138/am-2002-11-1208

Nadeau, P. H., Wilson, M. J., Mchardy, W. J., and Tait, J. M. (1985). The conversion of smectite to illite during diagenesis: evidence from some illitic clays from bentonites and sandstones. *Mineral. Mag.* 49 (352), 393–400. doi:10.1180/minmag.1985.049.352.10

Niandou, H., Shao, J. F., Henry, J. P., and Fourmaintraux, D. (1997). Laboratory investigation of the mechanical behaviour of Tournemire shale. *Int. J. Rock Mech. Mining Sci.* 34 (1), 3–16. doi:10.1016/s1365-1609(97)80029-9

Peltonen, C., Marcussen, Ø., Bjørlykke, K., and Jahren, J. (2009). Clay mineral diagenesis and quartz cementation in mudstones: the effects of smectite to illite reaction on rock properties. *Mar. Pet. Geology.* 26 (6), 887–898. doi:10.1016/j.marpetgeo.2008.01.021

Piane, C., Almqvist, B. S. G., Macrae, C., Torpy, A., Mory, A. J., and Dewhurst, D. (2015). Texture and diagenesis of ordovician shale from the canning basin, western Australia: implications for elastic anisotropy and geomechanical properties. *Mar. Pet. Geology.* 59, 56–71. doi:10.1016/j.marpetgeo.2014.07.017

Pickett, G. R. (1963). Acoustic character logs and their applications in formation evaluation. *J. Pet. Tech.* 15 (6), 659–667. doi:10.2118/452-pa

Rickman, R., Mullen, M., and Erik Petrel, E., (2008). "A practical use of shale petrophysics for stimulation design optimization:All shale plays are not clones ofthe barnett shale," in SPE Annual Technical Conference and Exhibition, Denver, Colorado, September 21, 2008.

Ross, D. J. K., Bustin, R. M., and Bustin, R. (2008). Characterizing the shale gas resource potential of Devonian-Mississippian strata in the Western Canada sedimentary basin: application of an integrated formation evaluation. *Bulletin* 92 (1), 87–125. doi:10.1306/09040707048

Rowe, H. D., Loucks, R. G., Ruppel, S. C., and Rimmer, S. M. (2008). Mississippian barnett formation, fort worth basin, Texas: bulk geochemical inferences and Mo-TOC constraints on the severity of hydrographic restriction. *Chem. Geology.* 257 (1–2), 16–25. doi:10.1016/j.chemgeo.2008.08.006

Rybacki, E., Reinicke, A., Meier, T., Makasi, M., and Dresen, G. (2015). What controls the mechanical properties of shale rocks? - Part I: strength and Young's modulus. *J. Pet. Sci. Eng.* 135, 702–722. doi:10.1016/j.petrol.2015.10.028

Sayers, C. M. (1994). The elastic anisotrophy of shales. *J. Geophys. Res.* 99 (B1), 767–774. doi:10.1029/93jb02579

Sayers, C. M., and van Munster, J. G. (1991). Microcrack-induced seismic anisotropy of sedimentary rocks. *J. Geophys. Res.* 96 (B10), 16529–16533. doi:10.1029/91jb01232

Sondergeld, C. H., Rai, C. S., Margesson, R. W., and Whidden, K. (2000). *Ultrasonic measurement of anisotropy on the kimmeridge shale*. New York: SEG.

Sone, H., and Zoback, M. D. (2013). Mechanical properties of shale-gas reservoir rocks - Part 1: static and dynamic elastic properties and anisotropy. *Geophysics* 78 (5), D381–D392. doi:10.1190/geo2013-0050.1

Steiger, R. P. (1982). Fundamentals and use of potassium/polymer drilling fluids to minimize drilling and completion problems associated with hydratable clays. *J. Pet. Tech.* 34 (8), 1661–1670. doi:10.2118/10100-pa

Su, W. B., Li, Z. M., Ettensohn, F. R., Johnson, M. E., Huff, D., Wang, W., et al. (2007). Distribution of black shale in the wufeng-longmaxi formations (ordovician- silurian), south China: major controlling factors and implications. *Earth Sci.* 32 (6), 819–827.

Thomsen, L. (1986). Weak elastic anisotropy. *Geophysics* 51 (10), 1954–1966. doi:10.1190/1.1442051

Thyberg, B., and Jahren, J. (2011). Quartz cementation in mudstones: sheet-like quartz cement from clay mineral reactions during burial. *Pet. Geosci.* 17 (1), 53–63. doi:10.1144/1354-079310-028

Vanorio, T., Mukerji, T., and Mavko, G. (2008). Emerging methodologies to characterize the rock physics properties of organic-rich shales. *The Leading Edge* 27 (6), 780–787. doi:10.1190/1.2944163

Vernik, L., and Landis, C. (1996). Elastic anisotropy of source rocks: implications for hydrocarbon generation and primary migration. *AAPG Bull.* 80, 531–544. doi:10.1190/1.1444461

Vernik, L., and Liu, X. (1997). Velocity anisotropy in shales: a petrophysical study. *Geophysics* 62 (2), 521–532. doi:10.1190/1.1444162

Vernik, L., and Milovac, J. (2011). Rock physics of organic shales. *The Leading Edge* 30 (3), 314–323. doi:10.1190/1.3567263

Vernik, L., and Nur, A. (1992). Ultrasonic velocity and anisotropy of hydrocarbon source rocks. *Geophysics* 57 (5), 727–735. doi:10.1190/1.1443286

Wang, S., Zou, N., Dong, H., Wang, M., Huang, L., and Guo, J. (2014). Biogenic silica of organic-rich shale in Sichuan Basin and its significance for shale gas. *Acta Scientiarum Naturalium Universitatis Pekinensis* 50 (3), 476–486. doi:10.13209/j.0479-8023.2014.079

Wang, T., Yang, K., Xiong, L., et al. (2015). Shale sequence stratigraphy of Wufeng-Longmaxi Formation in Southern Sichuan and their control on reservior. *Acta Petrolei Sinica* 36 (8), 915–925.

Wedepohl, K. H. (1971). Environmental influences on the chemical composition of shales and clays. *Phys. Chem. Earth* 8, 307–333. doi:10.1016/0079-1946(71)90020-6

Williams, L. A., Parks, G. A., and Crerar, D. A. (1985). Silica diagenesis, I. Solubility controls. *J. Sediment. Petrology* 55 (3), 301–311. doi:10.1306/212F86AC-2B24-11D7-8648000102C1865D

Wright, A. M., Spain, D., and Ratcliffe, K. T. (20102010). "Application of inorganic whole rock geochemistry to shale resource plays," in *Canadian unconventional resources and international petroleum conference* (Calgary, Canada: SPE-137946-MS), 18. doi:10.2118/137946-MS

Yamamoto, K. (1987). Geochemical characteristics and depositional environments of cherts and associated rocks in the franciscan and shimanto terranes. *Sediment. Geology.* 52 (1), 65–108doi:10.1016/0037-0738(87)90017-0

Yau, Y. C., Peacor, D. R., and McDowell, S. D. (1987). Smectite-to-illite reactions in Salton Sea shales: a transmission and analytical electron microscopy study. *J. Sediment. Petrology* 57 (2), 335–342. doi:10.1306/212F8B20-2B24-11D7-8648000102C1865D

Yin, H. (1992). *Acoustic velocity and attenuation of rocks: isotropy, intrinsic anisotropy, and stress-induced anisotropy*. Ph. D. dissertation. California: Standford University.

Conflict of Interest: QZ and WG are employed by the company Petrochina.

The remaining authors declare that the research was conducted in the absence of any commercial or financial relationships that could be construed as a potential conflict of interest.

Copyright © 2021 Deng, Wang, Zhao, Guo, Tang and Zhao. This is an open-access article distributed under the terms of the Creative Commons Attribution License (CC BY). The use, distribution or reproduction in other forums is permitted, provided the original author(s) and the copyright owner(s) are credited and that the original publication in this journal is cited, in accordance with accepted academic practice. No use, distribution or reproduction is permitted which does not comply with these terms.

frontiers in Earth Science

ORIGINAL RESEARCH
published: 18 March 2021
doi: 10.3389/feart.2021.641606

Rock Physics Model and Seismic Dispersion and Attenuation in Gas Hydrate-Bearing Sediments

Zhiqi Guo[1], Xueying Wang[1], Jian Jiao[1] and Haifeng Chen[2]*

[1] College of Geo-Exploration Science and Technology, Jilin University, Changchun, China, [2] BGP Inc., CNPC, Zhuozhou, China

A rock physics model was established to calculate the P-wave velocity dispersion and attenuation caused by the squirt flow of fluids in gas hydrate-bearing sediments. The critical hydrate saturation parameter was introduced to describe different ways of hydrate concentration, including the mode of pore filling and the co-existence mode of pore filling and particle cementation. Rock physical modeling results indicate that the P-wave velocity is insensitive to the increase in gas hydrate saturation for the mode of pore filling, while it increases rapidly with increasing gas hydrate saturation for the co-existence mode of pore filling and particle cementation. Meanwhile, seismic modeling results show that both the PP and mode-converted PS reflections are insensitive to the gas hydrate saturation that is lower than the critical value, while they tend to change obviously for the hydrate saturation that is higher than the critical value. These can be interpreted that only when gas hydrate begins to be part of solid matrix at high gas hydrate saturation, it represents observable impact on elastic properties of the gas hydrate-bearing sediments. Synthetic seismograms are calculated for a 2D heterogeneous model where the gas hydrate saturation varies vertically and layer thickness of the gas hydrate-bearing sediment varies laterally. Modeling results show that larger thickness of the gas hydrate-bearing layer generally corresponds to stronger reflection amplitudes from the bottom simulating reflector.

Keywords: rock physics, critical gas hydrate saturation, dispersion and attenuation, seismic response, gas hydrate

OPEN ACCESS

Edited by:
Jing Ba,
Hohai University, China

Reviewed by:
Weitao Sun,
Tsinghua University, China
Jiajia Zhangjia,
China University of Petroleum (Huadong), China

****Correspondence:***
Jian Jiao
43798102@qq.com

Specialty section:
This article was submitted to Solid Earth Geophysics, a section of the journal Frontiers in Earth Science

Received: *14 December 2020*
Accepted: *01 March 2021*
Published: *18 March 2021*

Citation:
Guo Z, Wang X, Jiao J and Chen H (2021) Rock Physics Model and Seismic Dispersion and Attenuation in Gas Hydrate-Bearing Sediments. Front. Earth Sci. 9:641606. doi: 10.3389/feart.2021.641606

INTRODUCTION

Elastic behaviors of gas hydrate-bearing sediments can be modeled using various rock physics methods by considering different ways of concentration for the gas hydrate in sediments. Lee et al. (1996) used the weight equation to estimate the amount of gas hydrate from seismic velocities where the gas hydrate exists as pore filling. Based on the modified Biot-Gassmann theory, Lee (2002a; 2002b) calculated the Biot coefficient and predicted elastic velocities for unconsolidated and consolidated sediments with or without gas hydrate concentration using real well data. Helgerud et al. (1999) used the Hertz-Mindlin theory to model the effect of gas hydrate on sediment elastic modulus by considering two scenarios where the hydrate modifies the pore fluid elastic properties without affecting the frame, and the hydrate modifies the elasticity of the frame when it becomes a component of the solid phase. Ecker (2001) considered three modes of aggregation for gas hydrate in reservoirs, including pore filling, particle contact and cementation, and proposed

corresponding methods of calculating elastic modulus of the hydrate-bearing sediments for the three cases. Gei and Carcione (2003) proposed a Biot-type three-phase theory that considers the existence of two solids and fluid mixture, and calculate the wave velocities and quality factors of gas hydrate-bearing sediments as a function of pore pressure, temperature, frequency, and partial saturation. Since wave-induced flow of the pore fluid is one major cause of elastic wave attenuation in heterogeneous porous media, Toms et al. (2006) and Muller et al. (2010) reviewed various models that describe different mechanisms of seismic wave attenuation and dispersion resulting from wave-induced flow in porous rocks. Sun et al. (2014) compared P-wave attenuation models of wave-induced flow and pointed out that wave-induced oscillatory fluid flow in the vicinity of inclusions embedded in porous rocks is one of the main causes for P-wave dispersion and attenuation at seismic frequencies. Zhang et al. (2016) employed the BISQ model to analyzed the velocity dispersion and attenuation of the marine unconsolidated hydrate-bearing sediments, and found that the velocity and attenuation increase with the increasing amount of gas hydrate, while porosity and clay content show little impact on the attenuation.

Many efforts had also been made on seismic characterization of gas hydrate-bearing sediments. By using rock-physics-based synthetic seismic models, Ecker et al. (1998) interpreted amplitude variation with offset (AVO) data from a bottom simulating reflector (BSR). They found that only when the hydrate depositing in the pore space is located away from grain contacts and does not affect the stiffness of the sediment frame, the modeling can qualitatively reproduce the observed AVO response. Thus, the sediment above the BSR was inferred as uncemented and mechanically weak. Song (2002) analyzed the AVO characteristics of the BSR and investigated the combined impacts of hydrate saturation and free gas saturation on seismic reflection coefficients. Marc-André et al. (2007) showed the applicability of the nonlinear Bayesian AVO inversion for seismic responses from the BSR to estimate marine gas hydrate and free-gas concentrations. Based on synthetic seismogram modeling of the BSR, Petersen et al. (2007) presented a detailed workflow of using seismic amplitude variation with offset (AVO) to quantify the amount of hydrate and free gas in the sediment, and showed the importance of multi-frequency and shear wave data for determining hydrate reservoir properties. Zhang et al. (2015) conducted AVO inversion of parameter consistency for the BSR in predicting gas hydrate in sediments and obtained the vertical and lateral features as well as saturation of gas hydrate.

In this study, we proposed a rock physical modeling method using poroelastic theories to quantify the P-wave velocity dispersion and attenuation of gas hydrate-bearing formations. The critical gas hydrate saturation parameter was introduced in the model to describe different ways of gas hydrate concentration in sediments. Elastic behaviors and dispersion and attenuation were predicted and analyzed using rock physic modeling. Then, the propagator matrix method was used to model seismic PP and mode-converted PS reflections from the gas hydrate-bearing sediments for varying gas hydrate saturation. Finally, seismic responses are modeled and analyzed for a heterogeneous model of the gas hydrate-bearing sediment where the gas hydrate saturation varies vertically and the layer thickness varies laterally.

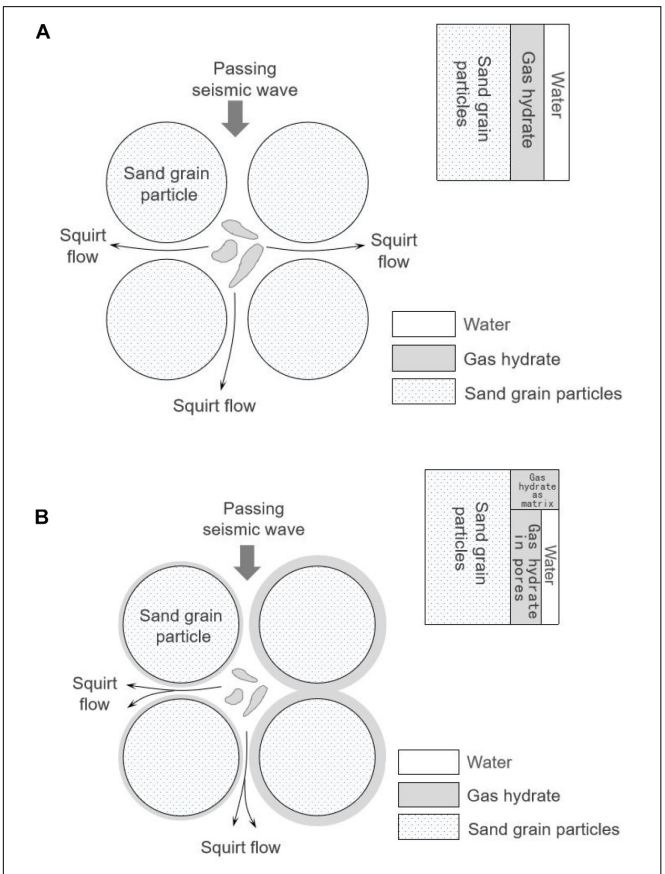

FIGURE 1 | Schematics of the gas hydrate concentration in different ways. **(A)** Pore filling and **(B)** the co-existence of pore filling and particle cementation.

ROCK PHYSICS MODEL FOR GAS HYDRATE-BEARING SEDIMENTS

Gas Hydrate Concentration and Critical Saturation

The core observations made by Berge et al. (1999) showed that when the gas hydrate saturation exceeds a certain critical value, gas hydrate starts to cement around the sandstone particles. Corresponding laboratory core measurements indicated that when the gas hydrate saturation is greater than a certain critical value (i.e., 0.35), the acoustic velocity of the gas hydrate-bearing sandstone increases significantly with increasing gas hydrate saturation. While for the gas hydrate saturation less than this critical value, the acoustic velocity of the sandstone is not sensitive to changes in the hydrate saturation. The laboratory measurements made by Yun et al. (2005) also show that for high gas hydrate saturation, the shear modulus of the gas hydrate-bearing sandstone increases significantly. Therefore, it

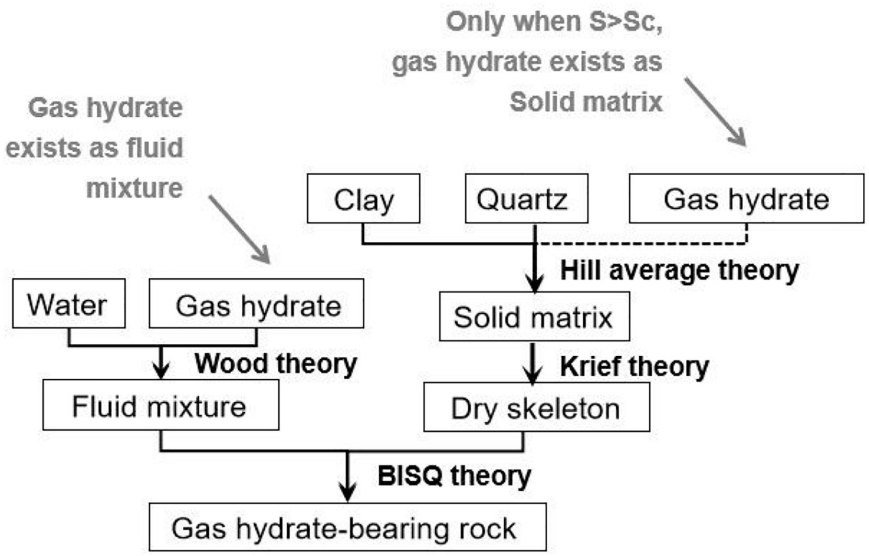

FIGURE 2 | Workflow of the rock physics modeling for a gas hydrate-bearing rock.

is inferred that the variation in the gas hydrate saturation affects depositional modes of the hydrate in sediments, and thus represents significant impact on elastic behaviors of the gas hydrate-bearing rocks.

In this study, we introduced the critical hydrate saturation parameter Sc in the rock physics model to describe various patterns of gas hydrate concentration. **Figure 1A** shows the case when the gas hydrate saturation S is less than the critical hydrate saturation Sc (S < Sc), where the hydrate exists only as pore filling. **Figure 1B** shows the case for S ≥ Sc, where the gas hydrate begins to attach to the solid mineral particles, becoming a part of the solid skeleton. At this time, the gas hydrate exists both as pore filling and particle cementation. Priest et al. (2006) showed that when existing as solid skeleton, the gas hydrate will have impact on porosity and permeability and can lead to squirt flow of the pore fluids, which in turn causes P-wave velocity dispersion and attenuation.

Rock Physic Model for Gas Hydrate-Bearing Sediments

Figure 2 shows the rock physical modeling workflow corresponding to **Figure 1**. The critical gas hydrate saturation parameter Sc was introduced into the modeling process in order to describe different concentration patterns of hydrate depositing in sediments. When S < Sc, the gas hydrates only exist as pore filling that is mixed with brine. Wood's theory (Wood, 1955) is used to calculate the properties of the fluid mixture. When S ≥ Sc, the gas hydrate saturation of the fluid mixture remains unchanged, and the gas hydrate begins to attach to the mineral particles. At this time, the concentration mode of the gas hydrate represents as the co-existence of pore filling and cementation. The elastic properties of the solid matrix are calculated using the Hill average theory (Hill, 1952) and the elastic modulus of the hydrate-bearing rock skeleton are calculated using the Krief's theory (Krief et al., 1990). Finally, frequency-dependent P-wave velocity Vp and the attenuation factor 1/Qp caused by the squirt flow of pore fluids in the gas hydrate-bearing sandstone are calculated by the BISQ theory.

TABLE 1 | Properties used in rock physical modeling.

	Density (Kg/m^3)	Bulk modulus (GPa)	Shear modulus (GPa)
Quartz	2620	36	45
Clay	2580	20.9	6.85
Gas hydrate	920	5.6	2.4
Water	1040	2.5	0

TABLE 2 | Parameters used in the BISQ theory.

Parameter	Value
Gas hydrate critical saturation Sc	0.35
Porosity φ_0	0.3
Permeability k_0(m^2)	100×10^{-15}
Viscosity of the fluid η(Pa*S)	0.03
Squirt flow length R(mm)	3

Rock Physics Theories

Based on the research of Qadrouh et al. (2015), elastic modulus of the solid skeleton of the gas hydrate-bearing sediments are calculated by the Krief model (Krief et al., 1990), where the bulk modulus K_{dry} and shear modulus G_{dry} of the solid skeleton are expressed as follows:

$$K_{dry} = K_s (1-\varphi)^{\frac{A}{(1-\varphi)}}, \quad (1)$$

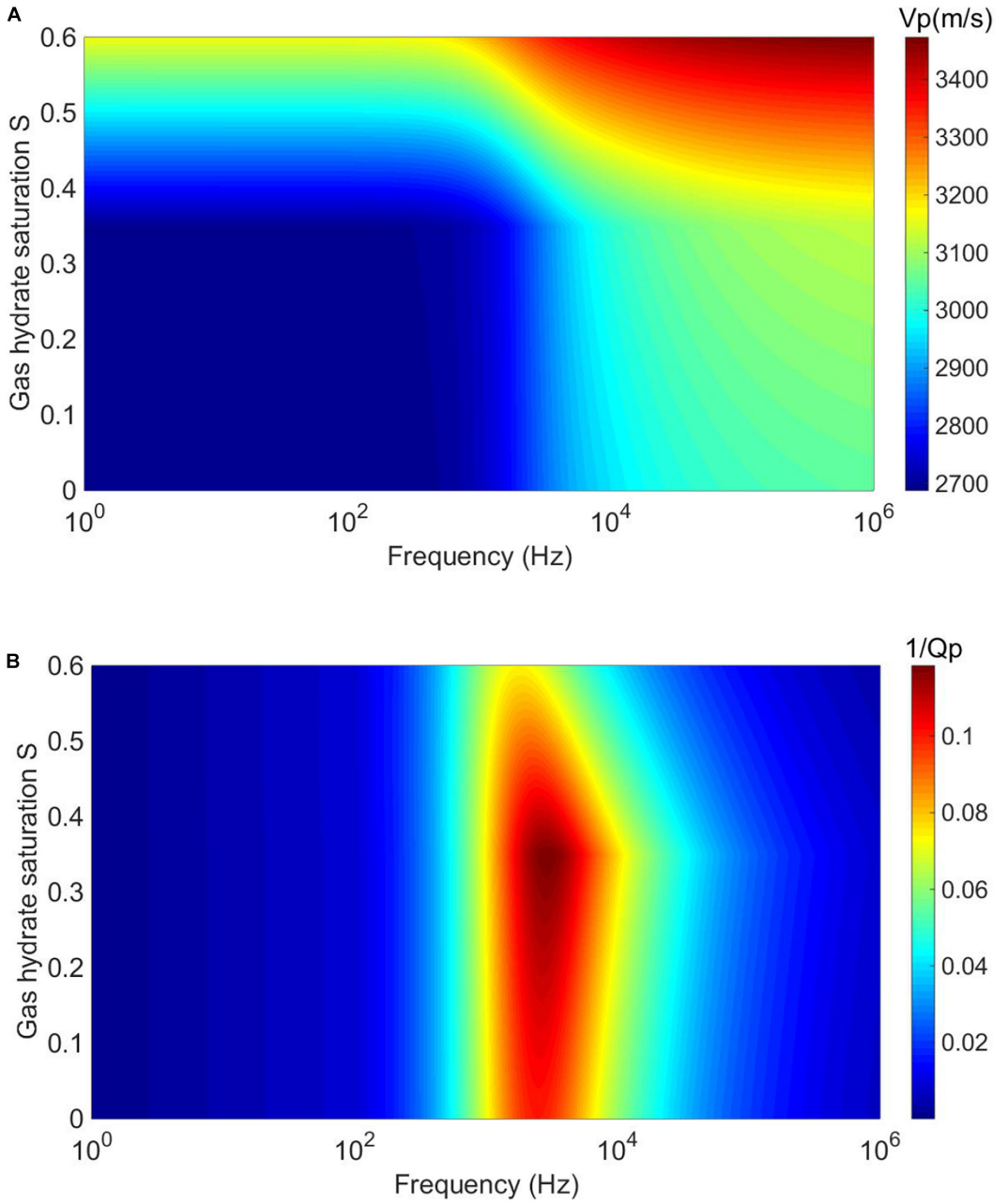

FIGURE 3 | (A) P-wave velocity Vp and **(B)** attenuation factor 1/Qp vary with gas hydrate saturation and frequency.

$$G_{dry} = K_{dry}\frac{G_s}{K_s}, \tag{2}$$

where the empirical parameter A is set to 3 to describe the case of unconsolidated sediment; φ is the porosity; G_s and K_s are the bulk modulus and shear modulus of the rock matrix, which are calculated using the Hill average theory (Hill, 1952):

$$K_s = \frac{1}{2}\left[\sum_{i=1}^{m} f_i K_i + \left(\sum_{i=1}^{m} f_i / K_i\right)^{-1}\right], \tag{3}$$

$$G_s = \frac{1}{2}\left[\sum_{i=1}^{m} f_i G_i + \left(\sum_{i=1}^{m} f_i / G_i\right)^{-1}\right], \tag{4}$$

where m is the number of solid components; f_i is the volume fraction of the i-th component; and K_i and G_i are the bulk modulus and shear modulus of the i-th component. In addition, the density of the solid matrix is calculated by averaging volume density of each individual component.

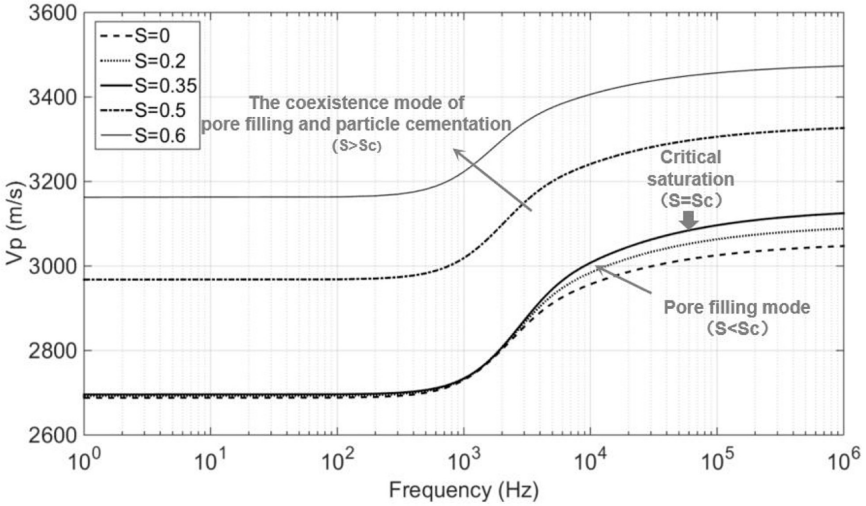

FIGURE 4 | The P-wave velocity Vp dispersion of various gas hydrate saturations.

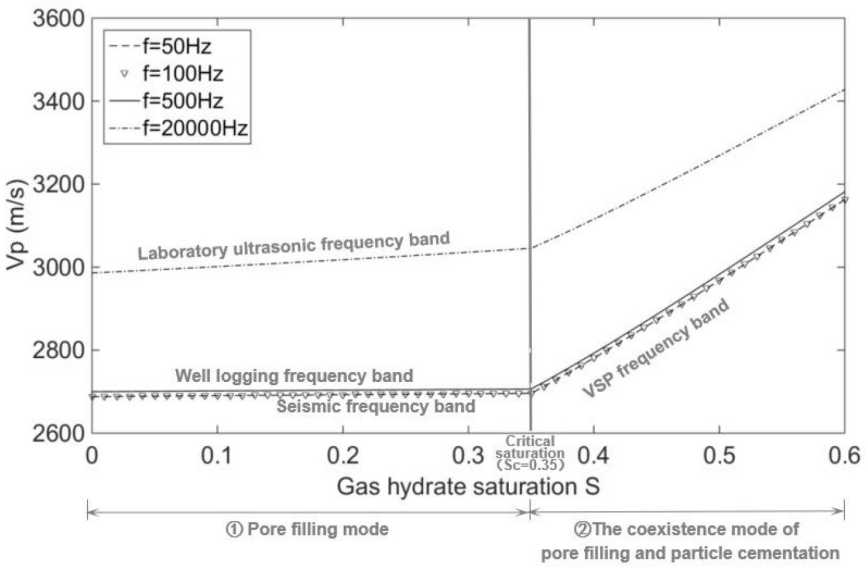

FIGURE 5 | Variations of the P-wave velocity Vp with gas hydrate saturation S for different frequencies.

The bulk moduli of the fluid mixture composed of gas hydrate and brine is calculated using the Wood's theory (Wood, 1955):

$$K_f = \left[S_1 / K_h + (1 - S_1) / K_w\right]^{-1}, \quad (5)$$

where K_h is the bulk modulus of hydrate; K_w is the bulk modulus of brine; S_1 is the saturation of hydrate as pore filling. When the hydrate represents both as the pore filling and particle cementation, $S_1 = S_c$.

For the pore filling mode, the gas hydrate saturation only affects elastic properties of the fluid mixture. For the model of hydrate co-existing as pore filling and particle cementation, the hydrate that is attached to solid particles reduces the porosity and permeability of the rock skeleton, and thus has the impact on squirt flow of pore fluids. The BISQ theory proposed by Dvorkin and Nur (1993) is used to calculate the velocity dispersion and attenuation of the gas hydrate-bearing reservoir. P-wave velocity V_p, attenuation coefficient α, and inverse quality factor Q^{-1} are expressed as follows:

$$V_p = \frac{1}{Re\left(\sqrt{Y}\right)}, \quad \alpha = \omega Im\left(\sqrt{Y}\right), \quad Q^{-1} = 2\alpha\frac{V_p}{\omega}, \quad (6)$$

where

$$Y = -\frac{B}{2A} - \sqrt{\left(\frac{B}{2A}\right)^2 - \frac{C}{A}}, \quad (7)$$

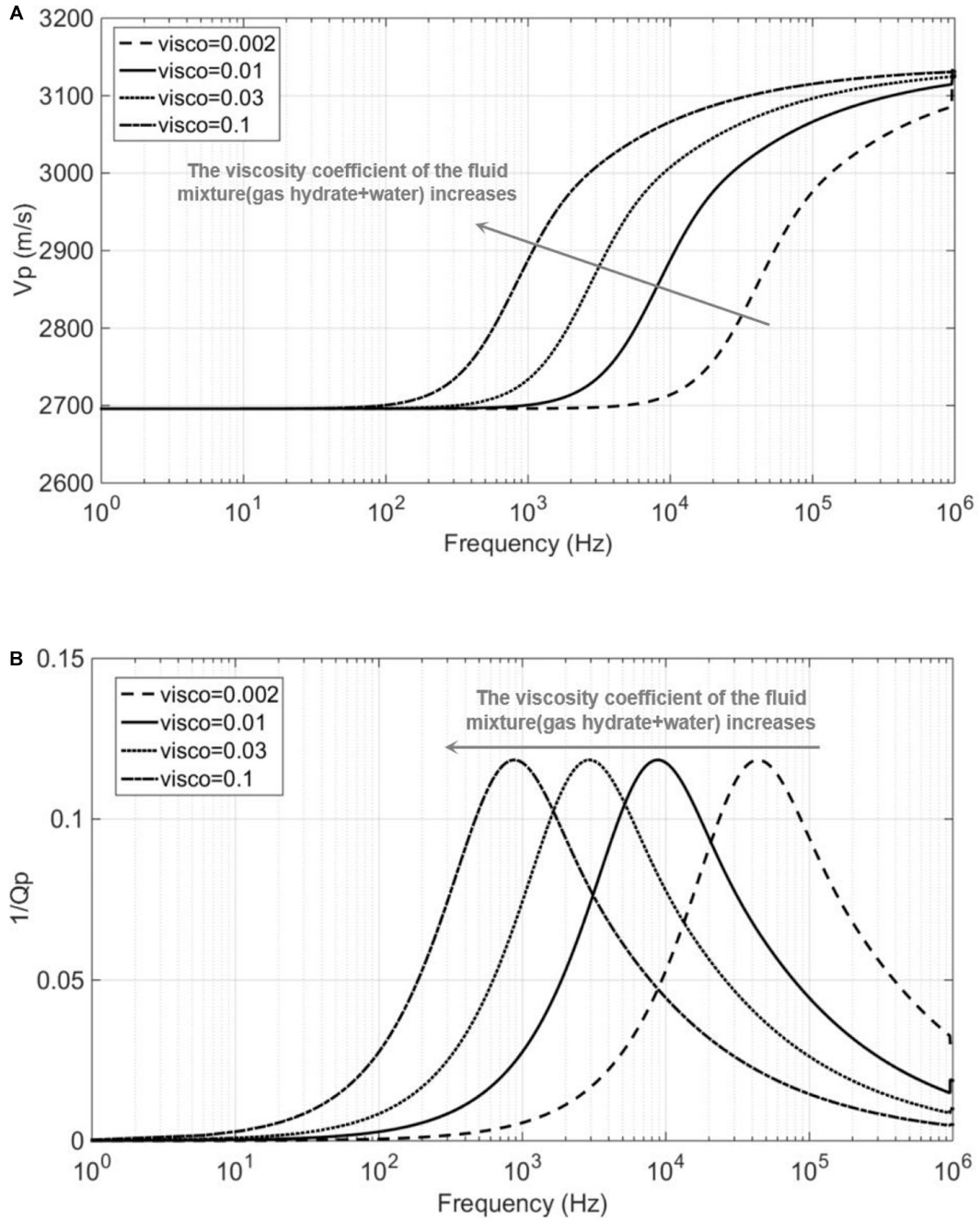

FIGURE 6 | (A) P-wave velocity Vp dispersion and **(B)** attenuation factor 1/Qp for various viscosity coefficients of the fluid mixture.

$$A = \frac{\varphi F_{sq} M}{\rho_2^2},$$

$$C = \frac{\rho_1}{\rho_2} + \left(1 + \frac{\rho_1}{\rho_2}\right)\left(\frac{\rho_a}{\rho_2} + i\frac{\omega_c}{\omega}\right), \quad F_{sq} = F\left[1 - \frac{2J_1(\lambda R)}{\lambda R J_0(\lambda R)}\right], \tag{9}$$

$$B = F\frac{F_{sq}\left(2a - \varphi - \varphi\frac{\rho_1}{\rho_2}\right) - \left(M + F_{sq}\frac{a^2}{\varphi}\right)\left(1 + \frac{\rho_a}{\rho_2} + i\frac{\omega_c}{\omega}\right)}{\rho_2}, \tag{8}$$

$$\lambda = \sqrt{\frac{\rho_f \omega^2}{F}\left(\frac{\varphi + \frac{\rho_a}{\rho_f}}{\varphi} + i\frac{\omega_c}{\omega}\right)},$$

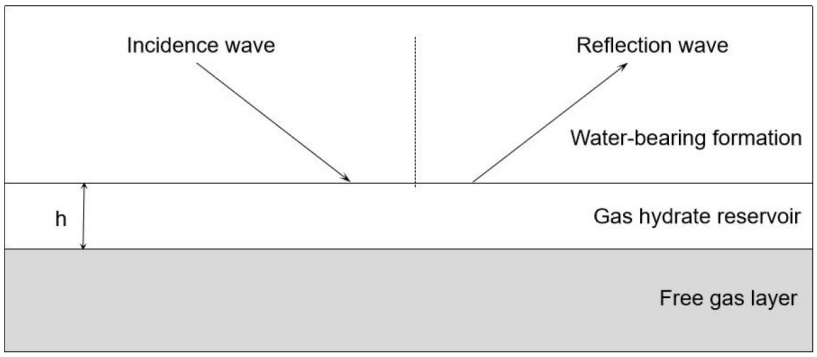

FIGURE 7 | Geological models of a gas hydrate-bearing sediment.

TABLE 3 | Parameters used in the patchy saturation model.

	Density (Kg/m^3)	Bulk modulus (GPa)	Saturation	Viscosity coefficient (Pa*s)
Gas	110	0.04	0.8	1×10^{-5}
Water	1040	2.5	0.2	0.0018

$$F^{-1} = \frac{1}{K_f} + \frac{1}{\varphi K}(a - \varphi), \quad a = 1 - \frac{K_{dry}}{K}, \tag{10}$$

and

$$M = K_{dry} + \frac{4}{3}G_{dry}, \quad \rho_1 = (1 - \varphi)\rho_s, \quad \rho_2 = \varphi\rho_f, \quad \omega_c = \frac{\eta\varphi}{k\rho_f}, \tag{11}$$

where K_{dry} and G_{dry} are the bulk and shear moduli of dry rock; φ is the porosity; ρ_s and ρ_f are the densities of the solid and fluid phases, respectively; ρ_a is the additional density of the inertial coupling between the solid and fluid phases; R is the squirt flow length; K is the bulk modulus of the solid phase; K_f is the bulk modulus of the fluid phase; η is the viscosity of the fluid; k is the permeability.

In rock physics modeling, it is considered that for the co-existence mode of hydrate both as pore filling and particle cementation, the cementation reduces the porosity of the formation by $\varphi = \varphi_0[1 - (S - S_c)]$, where S is the total saturation of the gas hydrate in the sandstone, and φ_0 is the porosity of the gas hydrate-bearing sandstone when the hydrate has not attached to the solid minerals yet. According to the Kozeny–Carman theory used by Santos et al. (1992), the permeability k of the gas hydrate formation varies with porosity φ and φ_0:

$$\frac{k(1 - \varphi)^2}{\varphi^2} = \frac{k_0(1 - \varphi_0)^2}{\varphi_0^2}. \tag{12}$$

ROCK PHYSICAL MODELING

Based on the rock physics model in **Figures 2**, **3** show the calculated P-wave velocity Vp and attenuation factor 1/Qp vary with gas hydrate saturation and frequency. Properties used for rock physical modeling are given in **Tables 1**, **2**. The volume contents of quartz and clay were assumed to be 0.8 and 0.2, respectively.

As shown in **Figure 3**, the Vp increases with increasing gas hydrate saturation at all frequencies. However, as the concentration pattern of the hydrate changes (below and above Sc = 0.35), the P-wave velocity Vp dispersion and the attenuation factor 1/Qp vary correspondingly.

Figure 4 shows the dispersion curves of P-wave velocity Vp under different gas hydrate saturations that are extracted from **Figure 3A**. For the cases of gas hydrate saturations S of 0 and 0.2, that is, less than the assumed critical saturation Sc = 0.35, when the frequency is less than about 10^3 Hz, the Vp is not sensitive to the existence of the gas hydrate that exists as pore filling. When the frequency is higher than about 10^3 Hz, the Vp increases with increasing gas hydrate saturation. For the cases of gas hydrate saturations S of 0.5 and 0.6, that is, greater than critical saturation Sc = 0.35, the Vp significantly increases with increasing gas hydrate saturation.

According to **Figure 3A**, the variation in Vp with gas hydrate saturation S at different frequencies is extracted and shown in **Figure 5**. At the laboratory ultrasonic frequencies, the Vp is higher than those at low frequencies. Meanwhile, there are two trends of Vp with increasing S. For the pore filling mode (S < Sc), the Vp is not sensitive to the change in S; and for the co-existence mode of pore filling and particle cementation (S ≥ Sc), the Vp increases significantly with increasing S.

It reveals that when the gas hydrate exists as a mixture of pore fluids, it has a weak impact on elastic properties of the rock. Only when the gas hydrate exists as a part of the solid matrix, will it have a significant impact on the elastic properties of the rock. Moreover, for the same gas hydrate saturation, the P-wave velocity at high frequency (such as ultrasonic waves) is higher than that at low frequency. According to Toms et al. (2006) and Muller et al. (2010), the pore fluid pressure may be higher at high frequency compared with that at low frequency, and the unrelaxed state of pore fluid causes the high velocity at high frequency.

In addition, Dvorkin and Nur (1993) and Dvorkin et al. (1994) showed that the frequency at which the velocity dispersion

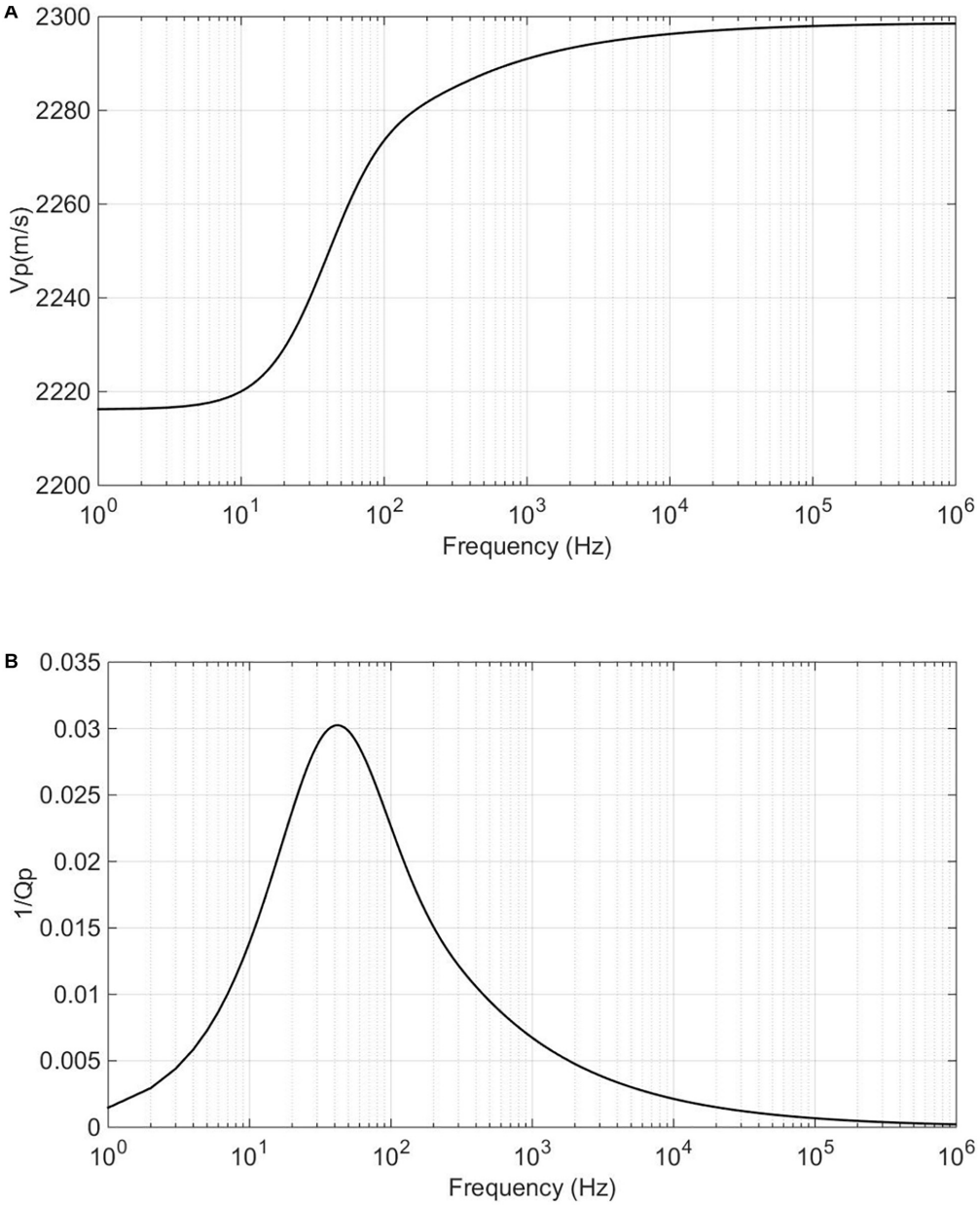

FIGURE 8 | (A) The P-wave velocity Vp dispersion and **(B)** attenuation factor 1/Qp for a free gas layer.

and attenuation occurs can be affected by the viscosity of the fluids involved in the fluid squirt flow. Therefore, the viscosity coefficient of the mixture of gas hydrate and water may play as an important role in determining poroelastic behaviors of gas hydrate-bearing sediments. However, due to the lack of laboratory data, it is difficult to determine the viscosity coefficient of the mixture of gas hydrate and brine. Thus, we assume a set of values for the viscosity coefficient (e.g., 0.002, 0.01, 0.03, and 0.1) in order to investigate its influences on P-wave velocity dispersion and attenuation. As shown in **Figure 6A**, for increasing viscosity coefficient, the frequency where the P-wave velocity dispersion occurs tends to move to the low frequency, and the attenuation peak moves to the low frequency correspondingly as shown in **Figure 6B**.

SEISMIC RESPONSE OF GAS HYDRATE-BEARING SEDIMENTS

Geological Model

Figure 7 shows a geological model of a gas hydrate-bearing layer, which overlies above a layer containing free gas, and is overlaid by a brine-saturated layer. The P-wave velocity

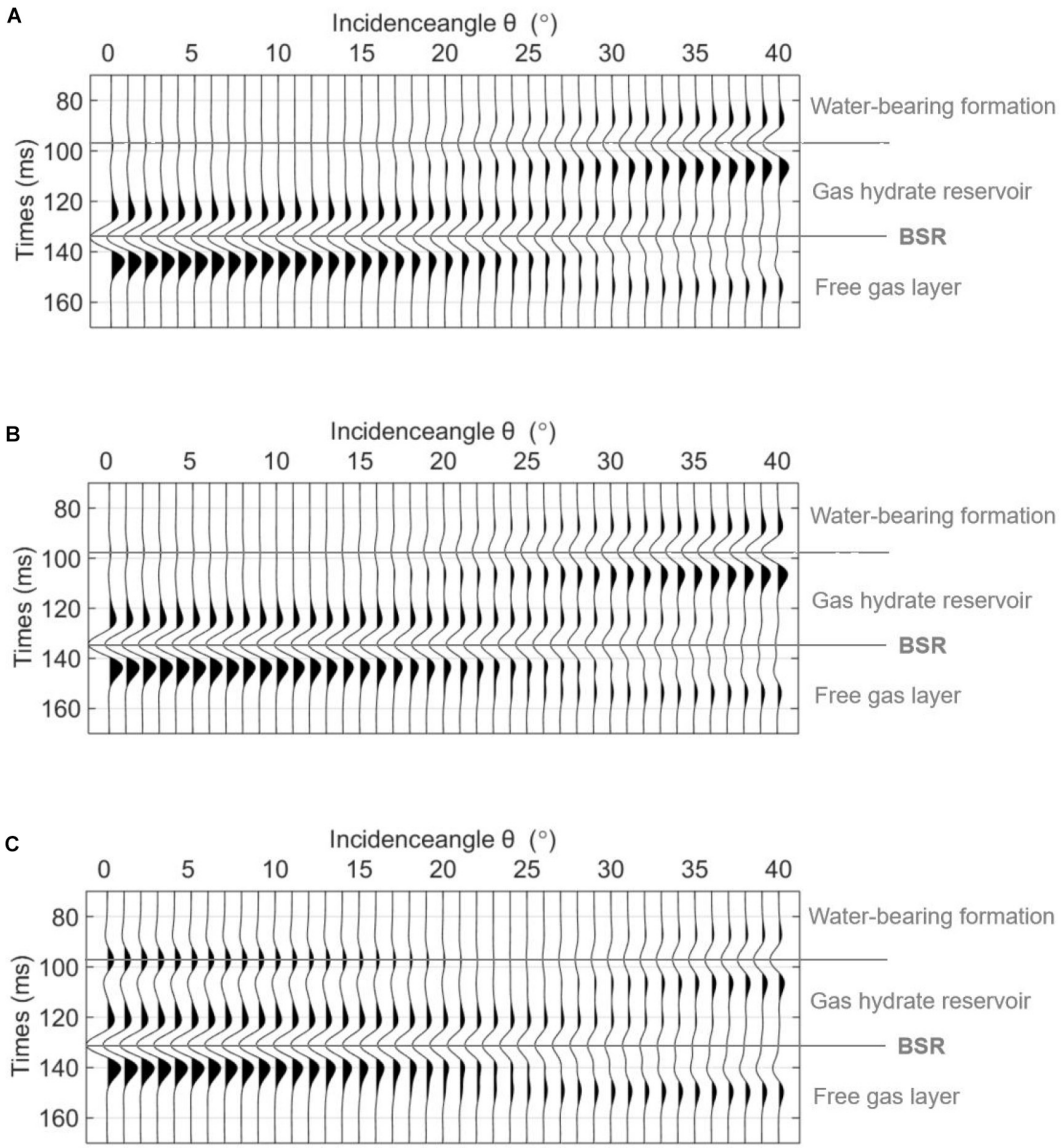

FIGURE 9 | The PP AVO responses for different hydrate saturations S. **(A)** S = 0.2, **(B)** S = 0.35, and **(C)** S = 0.5.

dispersion and attenuation of the gas hydrate-bearing layer are shown in **Figure 3**.

The P-wave velocity of the brine-bearing formation was 2628 m/s, and the density was 2140 kg/m^3. The velocity dispersion and attenuation of the free gas layer are calculated using the patchy saturation theory (White, 1975), where the bulk modulus and shear modulus of the rock matrix are calculated using the Hill average theory (Hill, 1952). Properties used in modeling are shown in **Table 1**. The elastic modulus of the solid skeleton are calculated using the Krief model (Krief et al., 1990). Porosity and permeability are given in **Table 2**. Fluid properties used in the model are given in **Table 3**. Calculation results of the P-wave velocity dispersion and attenuation of the free gas layer are shown in **Figure 8**.

Seismic Modeling for a Gas Hydrate-Bearing Reservoir

Seismic responses for the model in **Figure 7** are calculated by integrating the built rock physics model and the propagator matrix method.

In the propagator matrix theory, the reflection and transmission coefficient vector $r=[R_{PP},R_{PS},T_{PP},T_{PS}]^T$ for the P-wave incidence is given by (Carcione, 2001):

$$r = -\left[A_1 - \left(\prod_{\alpha=1}^{N} B_\alpha\right) A_2\right]^{-1} i_p, \tag{13}$$

where A_1 and A_2 are the propagator matrices related to the elastic parameters of the upper and lower media; $B_\alpha =$

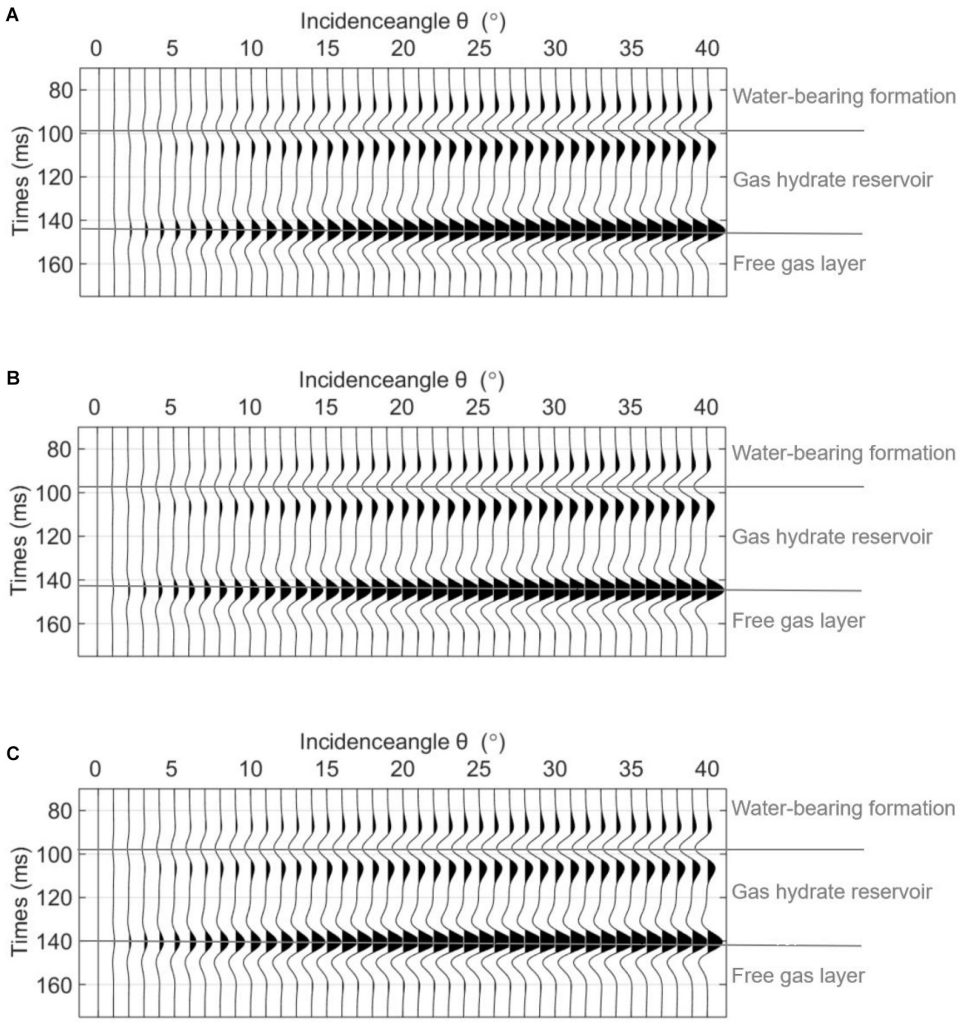

FIGURE 10 | The mode-converted PS AVO for different hydrate saturations S. **(A)** S = 0.2, **(B)** S = 0.35, and **(C)** S = 0.5.

$T(0)\,T^{-1}\left(h_\alpha\right)(\alpha = 1, \ldots, N)$ is the propagator matrix of the intermediate layer with an N layer structure; h_α is the thickness of each layer; and for a single-layered medium, $N = 1$. i_p is the P-wave incident vector, which is related to the physical parameters of the incident medium. **Appendix A** shows details of the propagator matrix theory.

The frequency-dependent reflection coefficient R_f of the PP wave (that is, R_{pp}) was calculated using the propagator matrix theory. It is multiplied by the seismic wavelet W_f in the frequency domain to obtain the corresponding amplitude spectrum U_f:

$$U_f = W_f \times R_f. \tag{14}$$

By implementing the inverse Fourier transform to U_f, the waveform U of reflection wave in the time domain is obtained:

$$U(t) = \frac{1}{2\pi}\int_{-\infty}^{\infty} U(f)\exp\left[-ift\right]df, \tag{15}$$

where f is the angular frequency; i is an imaginary unit; t is time.

In **Figure 7**, the thickness of the gas hydrate reservoir is set as 50 m, and the dominant frequency of the Ricker wavelet is set as 40 Hz. The P-wave velocity dispersion and attenuation of the gas hydrate reservoir and the free gas are shown in **Figures 3**, **8**, respectively.

Figure 9 shows the seismic AVO responses of the PP reflections for gas hydrate saturations of 0.2, 0.35, and 0.5. Among them, and the second type of AVO response is observed at the top interface of the gas hydrate reservoir. The interface between the gas hydrate reservoir and the free gas layer has a negative reflection amplitude, known as the BSR. As shown in **Figure 9**, a higher gas hydrate saturation corresponds to a higher BSR amplitude.

Figure 10 shows the mode-converted PS reflections for gas hydrate saturations of 0.2, 0.35, and 0.5. The interface between the gas hydrate-bearing reservoir and the free gas layer generates a mode-converted PS wave that has a positive phase of amplitude.

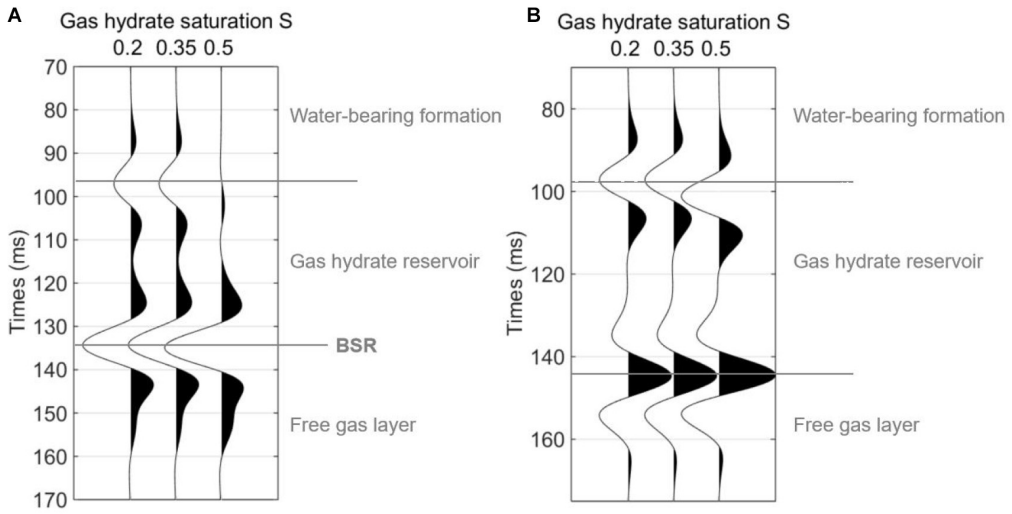

FIGURE 11 | Post-stacked seismograms corresponding to **Figures 9**, **10**. **(A)** PP reflections **(B)** mode-converted PS reflections.

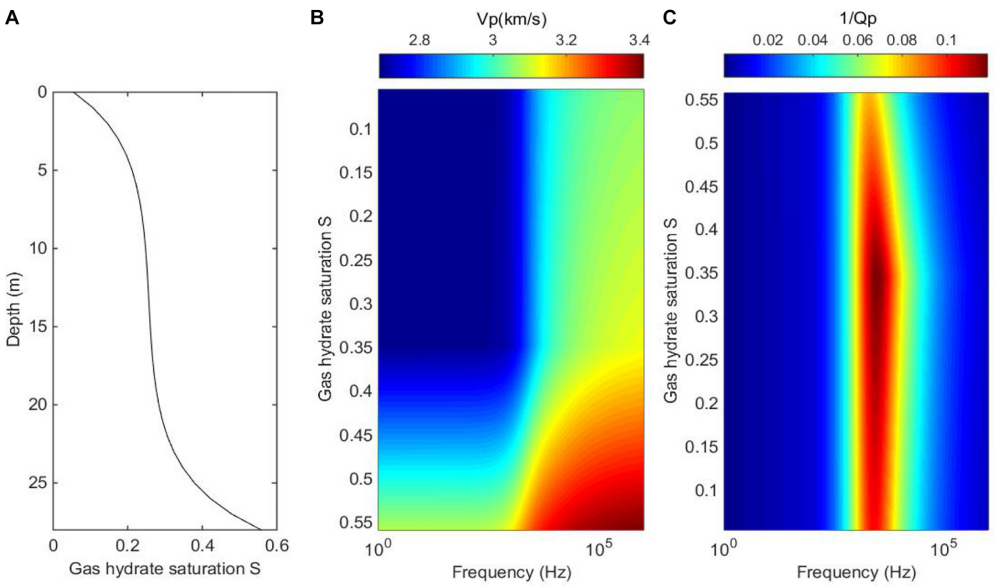

FIGURE 12 | (A) The model of heterogeneous hydrate saturation varying with depth; **(B)** the P-wave velocity Vp dispersion; and **(C)** corresponding P-wave attenuation factor 1/Qp.

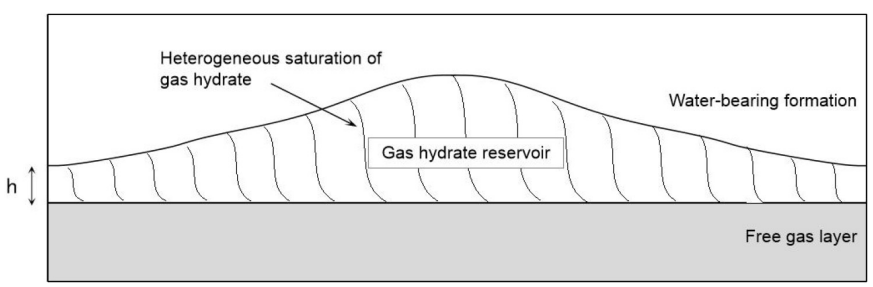

FIGURE 13 | A model of gas hydrate-bearing sediment that the gas hydrate saturation varies vertically and layer thickness varies laterally.

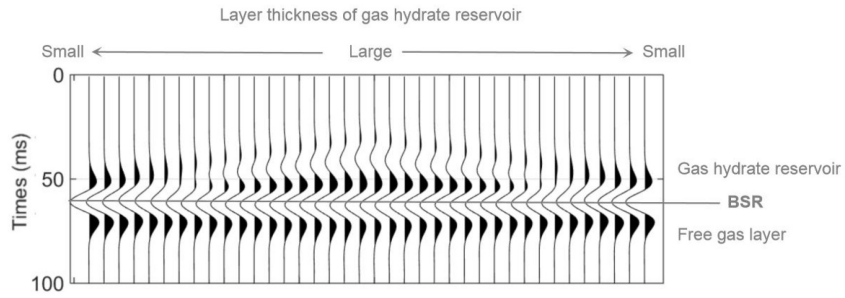

FIGURE 14 | The post-stacked seismic responses of the model in **Figure 13**.

Figure 11A shows the post-stacked PP reflections obtained from AVO responses in **Figure 9**. **Figure 11B** shows the post-stacked mode-converted PS reflection obtained from **Figure 10**. For both the PP and PS reflections in **Figure 11**, the difference is very small for the two cases where gas hydrate saturations are 0.2 and 0.35, respectively. However, by comparing gas hydrate saturations of 0.35 and 0.5, the differences between the stacked reflection amplitudes are quite large. This can be interpreted by the analysis on **Figure 4** where the Vp shows little variation with hydrate saturation for the case that the saturation is lower than the critical value 0.35, and represents significant variations for the hydrate saturation higher than the critical value 0.35.

Seismic Responses for a Model With Heterogeneous Gas Hydrate Saturation

Berge et al. (1999) and Dvorkin et al. (1999) showed that when free gas migrates upward to gas hydrate-bearing sediments, it may lead to heterogeneous hydrate saturation in the sediments. Thus, we design a model as shown in **Figure 12A**, where the hydrate saturation gradually decreases from about 0.55 at the bottom interface to the value just above zero at the top of the gas hydrate-bearing layer, which has a layer thickness about 28 m. According to the rock physics model built in this study, the P-wave velocity Vp dispersion and attenuation factor 1/Qp for varied hydrate saturation and frequency are calculated and shown in **Figures 12B,C**.

Based on the model of heterogeneous hydrate saturation in **Figure 12A**, we design a 2D model where the gas hydrate saturation varies vertically and layer thickness of the reservoir varies laterally, as shown in **Figure 13**. The thickness of the gas hydrate-bearing reservoir gradually decreases from 28 to 2.8 m from the center to both sides in the model. We calculate the AVO responses for each model in **Figure 13**, and then obtain the stacked waveforms as shown in **Figure 14**. In the calculation, the dominate frequency of the Ricker wavelet is 40 Hz, and the incidence angle ranges from 0 to 40 degrees. As can be seen in **Figure 14**, larger thickness of the gas hydrate-bearing reservoir corresponds to stronger reflection amplitudes from the BSR, Amplitude and phase of reflections vary with the thickness due to interference.

DISCUSSION AND CONCLUSION

The critical hydrate saturation parameter Sc was introduced into the rock physics model to describe two typical modes of gas hydrate concentration, including the pore filling and the co-existence of pore filling and particle cementation. The rock physics model simulates the dynamic changes in the mode of gas hydrate concentration as the hydrate saturation increases, and considers corresponding variations in porosity and permeability. P-wave velocity dispersion and attenuation caused by the squirt flow of fluid in the gas hydrate-bearing reservoir are calculated. By integrating the rock physics model and the propagator matrix method, seismic AVO responses are calculated to investigate the effects of hydrate saturation on seismic signatures. The conclusions are as the followings:

We observe two trends that the P-wave velocity Vp varies with increasing gas hydrate saturation S. For the pore filling mode ($S < Sc$), the Vp increases slightly with increasing S, while for the co-existence mode of pore filling and particle cementation ($S \geq Sc$), the Vp increases significantly with increasing S for all frequencies. Meanwhile, seismic modeling results show that for both the PP and mode-converted PS responses, reflection waveforms are insensitive to the gas hydrate saturation lower than the critical value, while the reflection waveforms tend to change obviously for the gas hydrate saturation higher than the critical value. These can be interpreted that the hydrate begins to be a part of solid matrix when hydrate saturation is higher than the critical value, and thus shows more impact on elastic modulus of the gas hydrate-bearing sediments.

Synthetic seismograms are calculated for a 2D heterogeneous model where the gas hydrate saturation varies vertically and layer thickness of the hydrate reservoir varies laterally. Modeling results shows that larger thickness of the gas hydrate-bearing reservoir corresponds to stronger reflection amplitudes from the BSR, while reflection amplitude and phase may vary with the thickness due to interference.

DATA AVAILABILITY STATEMENT

The original contributions presented in the study are included in the article/supplementary material, further inquiries can be directed to the corresponding author/s.

AUTHOR CONTRIBUTIONS

ZG and JJ contributed as the major authors of the manuscript. XW did a part of writing and coding works. HC provided some interesting ideas. All authors contributed to the article and approved the submitted version.

FUNDING

The research was supported by the National Natural Science Foundation of China (No. 42074153) and the CNPC Science Research and Technology Development project (No. 2019A-3308).

REFERENCES

Berge, L. I., Jacobsen, K. A., and Solstad, A. (1999). Measured acoustic wave velocities of R11 (CCl3F) hydrate samples with and without sand as a function of hydrate concentration. *J. Geophys. Res. Solid Earth* 104, 15415–15424. doi: 10.1029/1999jb900098

Carcione, J. M. (2001). AVO effects of a hydrocarbon source-rock layer. *Geophysics* 66, 419–427. doi: 10.1190/1.1444933

Dvorkin, J., and Nur, A. (1993). Dynamic poroelasticity: a unified model with the squirt and the Biot mechanisms. *Geophysics* 58, 524–533. doi: 10.1190/1.1443435

Dvorkin, J., Nolen-Hoeksema, R., and Nur, A. (1994). The squirt-flow mechanism: macroscopic description. *Geophysics* 59, 428–438. doi: 10.1190/1.1443605

Dvorkin, J., Prasa, M., Sakai, A., and Lavoie, D. (1999). Elasticity of marine sediments: rock physics modeling. *Geophys. Res. Lett.* 26, 1781–1784. doi: 10.1029/1999gl900332

Ecker, C. (2001). *Seismic Characterization of Methane Hydrate Structures*. Stanford, US: Stanford University.

Ecker, C., Dvorkin, J., and Nur, A. (1998). Sediments with gas hydrates: internal structure from seismic AVO. *Geophysics* 63, 1659–1669. doi: 10.1190/1.1444462

Ecker, C., Dvorkin, J., and Nur, A. (2000). Estimating the amount of gas hydrate and free gas from marine seismic data. *Geophysics* 65, 565–573. doi: 10.1190/1.1444752

Gei, D., and Carcione, J. M. (2003). Acoustic properties of sediments saturated with gas hydrate, free gas and water. *Geophys. Prospect.* 51, 141–157. doi: 10.1046/j.1365-2478.2003.00359.x

Helgerud, M. B., Dvorkin, J., Nur, A., Sakai, A., and Collett, T. (1999). Elastic wave velocity in marine sediments with gas hydrates: effective medium modeling. *Geophys. Res. Lett.* 26, 2021–2024. doi: 10.1029/1999gl900421

Hill, R. (1952). The elastic behavior of crystalline aggregate. *Proc. Phys. Soc. A* 65, 349–354. doi: 10.1088/0370-1298/65/5/307

Krief, M., Garat, J., Stellingwerff, J., and Ventre, J. (1990). A petrophysical interpretation using the velocities of P and S waves (full waveform sonic). *Log Analyst.* 31, 355–369.

Lee, M. W. (2002a). Biot–Gassmann theory for velocities of gas hydrate-bearing sediments. *Geophysics* 67, 1711–1719. doi: 10.1190/1.1527072

Lee, M. W. (2002b). Modified Biot-Gassmann theory for calculating elastic velocities for unconsolidated and consolidated sediments. *Mar. Geophys. Res.* 23, 403–412. doi: 10.1023/b:mari.0000018195.75858.12

Lee, M. W., Hutchinson, D. R., Collett, T. S., and Dillon, W. P. (1996). Seismic velocities for hydrate-bearing sediments using weighted equation. *J. Geophys. Res.* 101, 20347–20358. doi: 10.1029/96jb01886

Marc-André, P. C., Michael R., Roy, D. H., and Stan, E. D. (2007). AVO inversion of BSRs in marine gas hydrate studies. *Geophysics* 72, C31–C43. doi: 10.1190/1.2435604

Muller, T. M., Gurevich, B., and Lebedev, M. (2010). Seismic wave attenuation and dispersion resulting from wave-induced flow in porous rocks - a review. *Geophysics* 75, A147–A164.

Petersen, C. J., Papenberg, C., and Klaeschen, D. (2007). Local seismic quantification of gas hydrates and BSR characterization from multi-frequency OBS data at northern Hydrate Ridge. *Earth Planetary Sci. Lett.* 255, 414–431. doi: 10.1016/j.epsl.2007.01.002

Priest, J. A., Best, A. I., and Clayton, R. I. (2006). Attenuation of seismic waves in methane gas hydrate-bearing sand. *Geophys. J. Int.* 164, 149–159. doi: 10.1111/j.1365-246X.2005.02831.x

Qadrouh, A., Carcione, J. M., Salim, A. M., and Harith, Z. Z. T. (2015). Attenuation effects on the seismic response of a bottom-simulating reflector. *J. Nat. Gas Sci. Eng.* 24, 510–517. doi: 10.1016/j.jngse.2015.04.011

Santos, J. E., Corbero, J. M., Ravazzoli, C., and Hensley, J. (1992). Reflection and transmission coefficients in fluid-saturated porous media. *J. Acoustical Soci. Am.* 91, 1911–1923. doi: 10.1121/1.403702

Song, H. B. (2002). Petrophysical property model of natural gas hydrate sediments and AVA characteristics of seafloor like reflective layers. *J. Geophys.* 45, 546–556.

Sun, W. T., Ba, J., Muller, T. M., Carcione, J. M., and Cao, H. (2014). Compaison of P-wave attenuation models of wave-induced flow. *Geophys. Prospect.* 63, 378–390. doi: 10.1111/1365-2478.12196

Toms, J., Muller, T. M., Ciz, R., and Gurevich, B. (2006). Comparative review of theoretical models for elastic wave attenuation and dispersion in partially saturated rocks. *Soil Dyn. Earthq. Eng.* 26, 548–565. doi: 10.1016/j.soildyn.2006.01.008

White, J. E. (1975). Computed seismic speeds and attenuation in rocks with partial gas saturation. *Geophysics* 40, 224–232. doi: 10.1190/1.1440520

Wood, A. W. (1955). *A Textbook of Sound*. New York: The MacMillan Co.

Yun, T. S., Francisca, F. M., Santamarina, J. C., and Rupple, C. (2005). Compressional and shear wave velocities in uncemented sediment containing gas hydrate. *Geophys. Res. Lett.* 32:L10609.

Zhang, R. W., Li, H. Q., Wen, P. F., and Zhang, B. J. (2016). Analysis of velocity dispersion and attenuation characteristics of marine hydrate deposits. *J. Geophys.* 59, 3417–3427.

Zhang, R. W., Li, H. Q., Zhang, B. J., Huang, H.-D., and Wen, P.-F. (2015). Detection of gas hydrate sediments using prestack seimic AVA inversion. *Appl. Geophys.* 12, 453–464. doi: 10.1007/s11770-015-0503-3

Conflict of Interest: HC was employed by the company BGP Inc.

The remaining authors declare that the research was conducted in the absence of any commercial or financial relationships that could be construed as a potential conflict of interest.

Copyright © 2021 Guo, Wang, Jiao and Chen. This is an open-access article distributed under the terms of the Creative Commons Attribution License (CC BY). The use, distribution or reproduction in other forums is permitted, provided the original author(s) and the copyright owner(s) are credited and that the original publication in this journal is cited, in accordance with accepted academic practice. No use, distribution or reproduction is permitted which does not comply with these terms.

APPENDIX A

In Eq. 13, the propagator matrices A_1 and A_2 of the upper and lower media are shown as follows:

$$A_1 = i\omega \begin{pmatrix} \beta_{P1} & \beta_{S1} & 0 & 0 \\ -\gamma_{P1} & -\gamma_{S1} & 0 & 0 \\ -Z_{P1} & -Z_{S1} & 0 & 0 \\ W_{P1} & W_{S1} & 0 & 0 \end{pmatrix}, \quad (A1)$$

$$A_2 = i\omega \begin{pmatrix} 0 & 0 & \beta_{P2}\exp\left(-i\omega s_{Z_{P2}}h\right) & \beta_{S2}\exp\left(-i\omega s_{Z_{S2}}h\right) \\ 0 & 0 & \gamma_{P2}\exp\left(-i\omega s_{Z_{P2}}h\right) & \gamma_{S2}\exp\left(-i\omega s_{Z_{S2}}h\right) \\ 0 & 0 & -Z_{P2}\exp\left(-i\omega s_{Z_{P2}}h\right) & -Z_{S2}\exp\left(-i\omega s_{Z_{S2}}h\right) \\ 0 & 0 & -W_{P2}\exp\left(-i\omega s_{Z_{P2}}h\right) & -W_{S2}\exp\left(-i\omega s_{Z_{S2}}h\right) \end{pmatrix}, \quad (A2)$$

where i is the imaginary unit; ω is the incidence wave frequency; and $h = \sum_{\alpha=1}^{N} h_\alpha$ is the total thickness of the layer. The variables S_Z, β , γ , W, and Z have two groups of subscripts. The subscripts P and S correspond to the quasi-compressional wave and the quasi-shear wave, respectively.

frontiers in Earth Science

ORIGINAL RESEARCH
published: 31 March 2021
doi: 10.3389/feart.2021.640194

Broadband Q-Factor Imaging for Geofluid Detection in the Gulf of Trieste (Northern Adriatic Sea)

Aldo Vesnaver, Gualtiero Böhm, Martina Busetti, Michela Dal Cin and Fabrizio Zgur*

National Institute of Oceanography and Applied Geophysics–OGS, Trieste, Italy

Seismic surveys allow estimating lithological parameters, as P-wave velocity and anelastic absorption, which can detect the presence of fracture and fluids in the geological formations. Recently, a new method has been proposed for high-resolution imaging of anelastic absorption, which combines a macro-model from seismic tomography with a micro-model obtained by the pre-stack depth migration of a seismic attribute, i.e., the instantaneous frequency. As a result, we can get a broadband image that provides clues about the presence of saturating fluids. When the saturation changes sharply, as for gas reservoirs with an impermeable caprock, the acoustic impedance contrast produces "bright spots" because of the resulting high reflectivity at its top. When the fluid content changes smoothly, the anelastic absorption becomes a good detector, as fluid-filled formations absorb more seismic energy than hard rocks. We apply this method for imaging the anelastic absorption in a regional seismic survey acquired by OGS in the Gulf of Trieste (northern Adriatic Sea, Italy).

Keywords: broadband, Q factor, anelastic, seismic, fluid, Adriatic sea, imaging

OPEN ACCESS

Edited by:
Jing Ba,
Hohai University, China

Reviewed by:
Yongjia Song,
Harbin Institute of Technology, China
Ping Tong,
Nanyang Technological University, Singapore

****Correspondence:***
Aldo Vesnaver
aldo.l.vesnaver@gmail.com

Specialty section:
This article was submitted to Solid Earth Geophysics, a section of the journal Frontiers in Earth Science

Received: *10 December 2020*
Accepted: *02 February 2021*
Published: *31 March 2021*

Citation:
Vesnaver A, Böhm G, Busetti M, Dal Cin M and Zgur F (2021) Broadband Q-Factor Imaging for Geofluid Detection in the Gulf of Trieste (Northern Adriatic Sea). Front. Earth Sci. 9:640194. doi: 10.3389/feart.2021.640194

INTRODUCTION

In the Adriatic Sea, the occurrence of fluids within the sediment and fluid seeps at the sea floor are well known. Source of these fluids have been identified in the buried several kilometer thick Meso-Cenozoic carbonate reservoir, with salty water occurrence (Cimolino et al., 2010), and within the overlying Late Cenozoic terrigenous sedimentary units bearing biogenic gas (e.g., Casero, 2004). Fluids upward migration from several km deep rocks and feeding local seeps have been documented in the central and northern Adriatic (Geletti et al., 2008; Busetti et al., 2013; Donda et al., 2019). Fluid accumulation in the shallow sediments and fluid seeps have been encountered by the high-resolution seismic, often associated to fluid seeps, in the Adriatic basin (e.g., Hovland and Curzi, 1989; Conti et al., 2002), including the Gulf of Trieste (e.g., Gordini et al., 2004; Busetti et al., 2020).

Fluid accumulation in the shallow sediments and fluid seeps are expected to be encountered by the high-resolution seismic profile acquired in the Gulf of Trieste in 2009 by OGS (**Figure 1**). The aim of this paper is characterizing some shallow formations by a broadband Q-factor imaging, as a low Q factor is often associated to rocks saturation and unconsolidated formations. This method merges the macro-model obtained from Q tomography with the micro-model provided by the pre-stack depth migration of the instantaneous frequency. In this way, also tiny local anomalies might be detected, pushing the resolution of seismic data up to its physical limits.

Delineating areas where the fracture density is higher provides relevant hints for geodynamic and geothermal studies. They highlight faulted or stressed formations, whose response to seismic surveys affects two propagation phenomena: anisotropy and anelastic absorption (see, e.g., Shapiro and

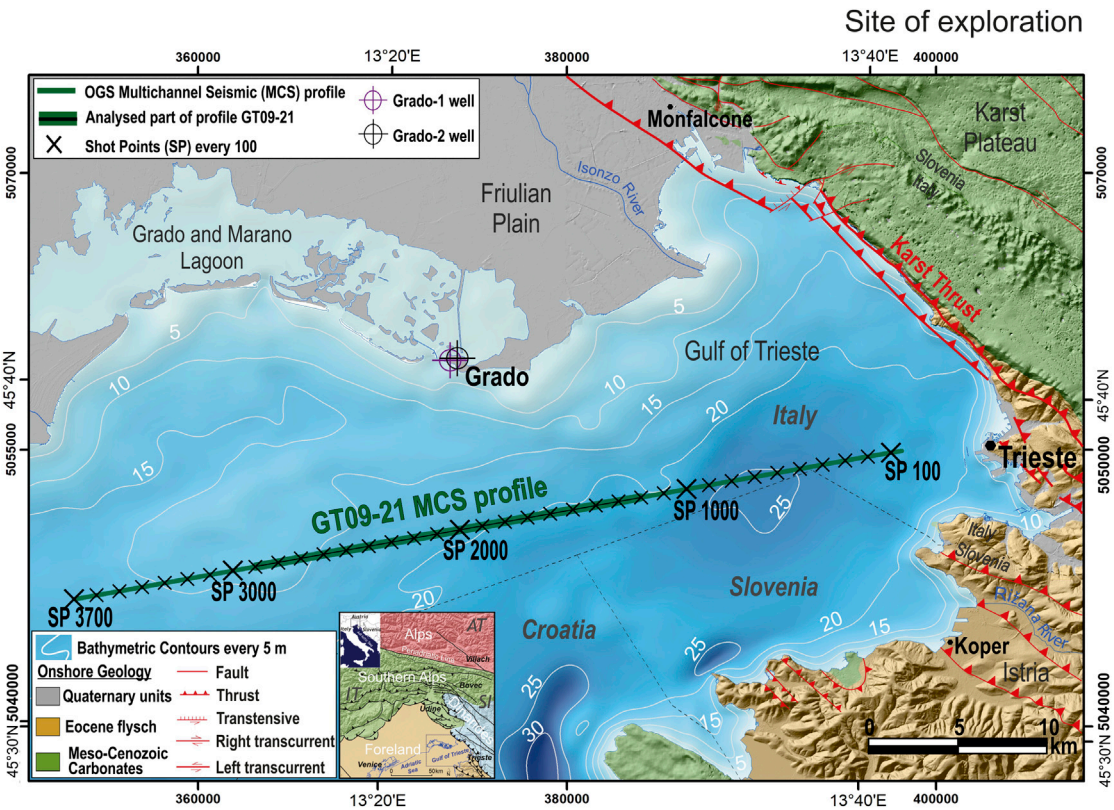

FIGURE 1 | Location map of the seismic profile GT09–21 (green line) with shot points (SP) every 100 (black crosses) acquired by OGS in the Gulf of Trieste (Adriatic Sea). Circles show position of Grado geothermal wells. Bathymetry in depth with cells of 50 m, gridding performed by Zampa (2020) by using grids from Italy and Slovenia (Trobec et al., 2018) and Croatia (EMODnet Digital Bathymetry, 2018). Onshore geology is represented for Friulian Plain and Italian Karst Plateau (Cucchi et al., 2013), Slovenian Karst Plateau (Jurkovšek et al., 2016) and Istria (Placer et al., 2010). Digital Elevation Model compiled for Italy (10 m cells; IRDAT-FVG, 2017), Slovenia (10 m cells; Arso, 2017) and Istria (25 m cells; EU-DEM, 2017). Inset: chains and foreland domains of the region surrounding the Gulf of Trieste. Map compiled by using ArcGis® software by Esri; datum WGS84, projection UTM33.

Hubral 1999; Carcione 2014; Song et al., 2020b, among others). Anisotropy measurement requires very expensive acquisition technologies, as full-azimuth 3D surveys, possibly using ocean-bottom seismometers. Detecting anelastic absorption is more affordable, although it may be anisotropic itself: 2D surveys can provide reasonable estimations at cheaper costs.

The anelastic absorption we observe is actually a composite effect of other causes too, as fluid saturation, pore pressure, random distribution of inhomogeneities and frequency tuning by thin layers, in addition to fractures. Thus, it is not a direct indicator of fluids' presence, unless there is a borehole calibration or geological information that may single out one or part of these possible contributions (Jannsen et al., 1985; Tonn 1991). Trying to distinguish them is still an open challenge and a subject for current research (Wu 1985; Best et al., 1994; Hackert and Parra 2003; Helle et al., 2003; Picotti and Carcione 2006; Mulder and Hak 2009; Cheng and Margrave 2012; Ba et al., 2015; Bai et al., 2017; Agudo et al., 2018; Song et al., 2020a, among others). In this paper, we apply a recent method introduced by Lin et al. (2018) to marine seismic data, producing high-resolution, broadband images of the anelastic absorption contrasts, and the related Q factor. These parameters allow characterizing the geological formations and provide better clues about the fluids' pathways.

GEOLOGICAL SETTING

The Gulf of Trieste is a shallow marine area located in the north-easternmost corner of the Adriatic Sea (**Figure 1**). The geological setting is characterized by several kilometer-thick carbonate units, deposited from Permian to Early Cenozoic (Busetti et al., 2010). During the Cretaceous, the carbonate sedimentation formed the aggradation of about 1 km thick Friuli and Dinaric Carbonate Platform, with the shelf margin located in the western side of the Gulf of Trieste, outcropping along the eastern coast and at the north-west of the Istria peninsula. At the same time, in the western basin area, pelagic carbonate draped the basin floor. The carbonate sedimentation ended with the compressional phase of the Dinaric mountain chain, which caused the development of the Dinaric foredeep, with the eastern tilted carbonate platform. The Dinaric foredeep was filled by the turbiditic sequence of Eocene, produced by the

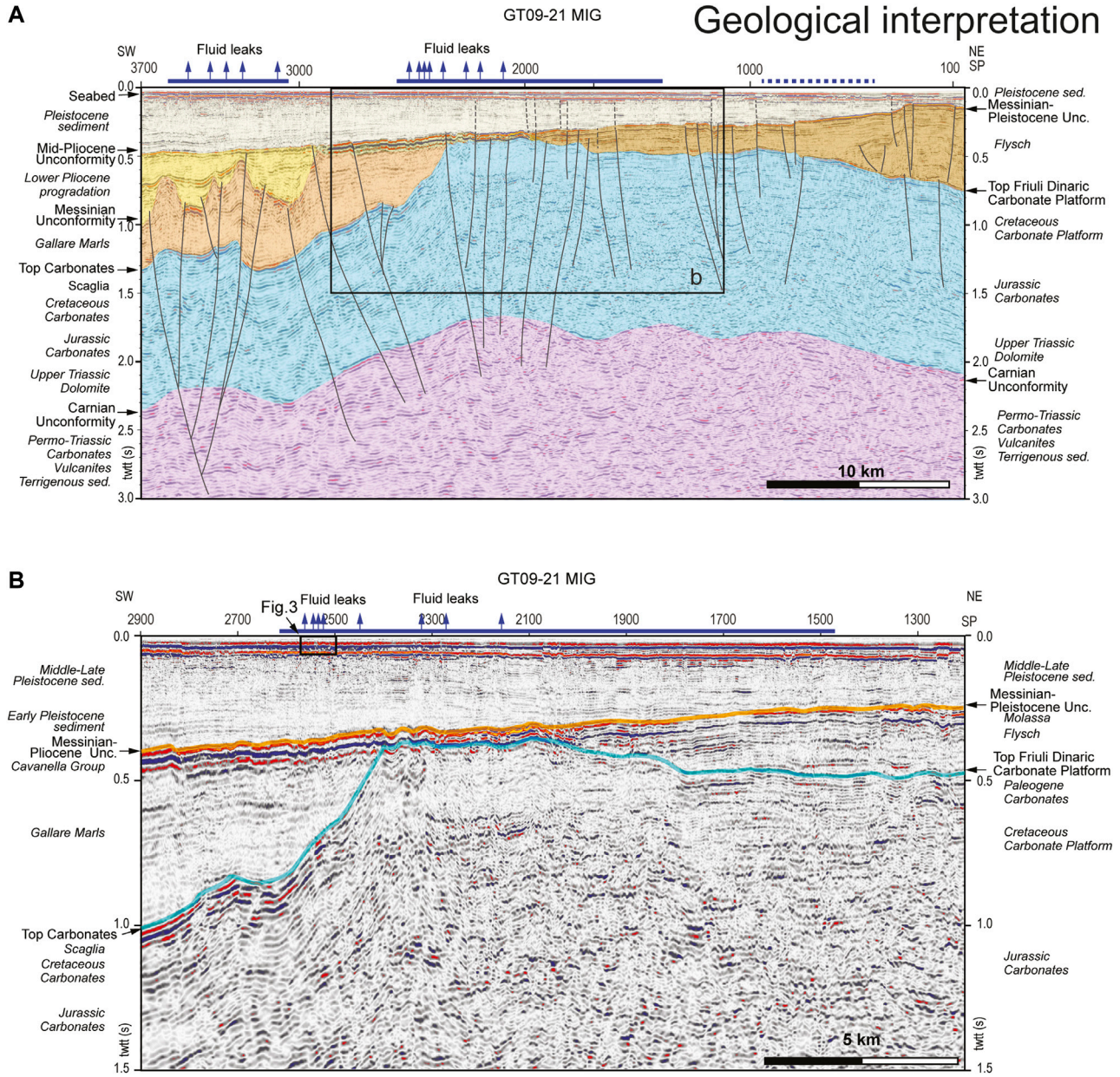

FIGURE 2 | Time-migrated seismic profile GT09–21: **(A)** seismo-stratigraphic interpretation (see **Figure 1** for location); **(B)** section of the seismic profile analyzed in the present work with the picked horizons. Blue lines along the profile indicate evidence of fluids within the sediment, dashed line where the fluids are less evident or discontinuous, and the blue arrows indicate the location of fluid seeps in the water column.

progressive erosion of the rising mountains, outcropping along the eastern and southern coasts of the gulf (**Figure 2**). In the same period, the basin was progressively filled by the Gallare Marls and topped by the Early Miocene Cavanella Group, composed of sand, sandstone and marls. These lithologies were shaped by the main erosional event occurred at the Miocene end, due to the Messinian Salinity Crisis of the Mediterranean Sea (Busetti et al., 2010).

In subaerial conditions, the peripheral Mediterranean lands were deeply incised by canyons several km large and several hundred of meter deep (Busetti et al., 2010). In the Gulf of Trieste this event is well imaged in the seismic profiles by a high-amplitude horizon at the top the Gallare Marls, at the top of the Cavanella Group, and at the top of the turbidites of the Dinaric foredeep. The following Early Pliocene marine ingression reached only the western-most part, providing the filling of the canyons in the Gallare Marls, leaving in subaerial condition the eastern-most part. The diachronous erosional surface was progressively draped eastward by sediments during the Pleistocene (Busetti et al., 2010).

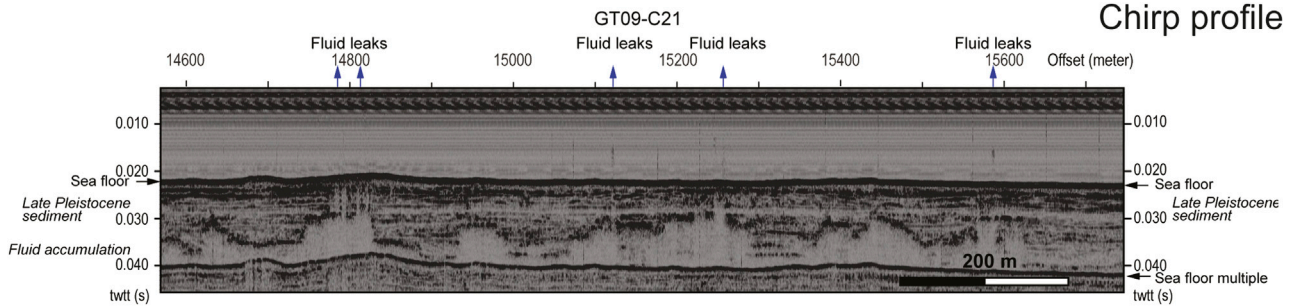

FIGURE 3 | The chirp profile GT09-C21, located along the initial part of the seismic profile (see the small rectangle in **Figure 2B**), imaging fluid accumulation in the Late Pleistocene sediment, evidenced by the blanking effect and by the high amplitude reflectors on the top. Where the fluid migration rises very close to the sea floor, fluid plumes occur in the water column (blue arrows in the section).

The fluids' bearing by the rocks in the gulf have different components: brackish and fresh waters, and hydrocarbon, mainly in the gas phase (Busetti et al., 2013). The Meso-Cenozoic carbonates are characterized by permeability due to tectonic fractures and karstification that provide a confined aquifer for the geothermal reservoir. They are the reservoir of sulfurous-salty-alkaline waters at low enthalpy (about 40°C), considered to be trapped sea water of Miocene age (Petrini et al., 2013). These waters naturally spring on land in the NE coast of the gulf at the Roman Baths of Monfalcone, exploited since ancient times, and in eight submarine thermal springs in the southern offshore close to the Istria coast, with temperature from 22 to 30°C (Žumer, 2004). To exploit their geothermal potential, the Grado-1 and Grado-2 wells were drilled in 2008 and in 2015, respectively. In the Grado-1 well, water was found at 42–45°C in fractured carbonates at depths between 736 and 740 m, and from 1,040 to downhole at 1,108 m depth, while in well bottom at 1,200 m of Grado-2 well the water has 45°C with salinity more than 30‰ (Della Vedova et al., 2008; Cimolino et al., 2010; Piffer et al., 2015).

Gas seepings from the sea floor are quite common in the gulf too. Chemical analyses revealed that gas consists primarily of methane (81–84%), nitrogen (15–18%) and oxygen (0.7–1.3%). C^{14} datation reveals that the methane dates back to Late Pleistocene age, rising from organic rich layers, as peats (Gordini et al., 2012). Gas pockets in the shallow Late Pleistocene deposit as well as plume within the water column are well imaged by chirp data (Gordini et al., 2004; Gordini et al., 2012; Busetti et al., 2020). Fluid accumulations in the Late Pleistocene sediment are evidenced by blanking effects and high-amplitude reflectors on the top, and fluid plumes in the water column (**Figure 3**).

SEISMIC SURVEY PARAMETERS AND BASIC PROCESSING

The data presented in this paper is part of a set of 13 multi-channel seismic profiles acquired in the Gulf of Trieste by the R/V OGS Explora in 2009, for a total length of 281 km. The seismic source is a linear array of eight sleeve guns, with a total volume of 1180 cubic inch, able to guarantee a proper penetration down to a few kilometers' depth through the flysch and limestones hard formations, which were the original target of the survey.

The data was collected by a 96 channel, 1,200 m long digital streamer with a receiver distance of 12.5 m that, together with a shot point interval of 12.5 m, provided a nominal coverage of 48 traces per Common-Mid-Point gather. The offset between the source and the nearest channel was kept at 25 m, long enough to prevent the saturation of the recorder, but still comparable to the depth of the shallowest horizon, that is, the seafloor. Chirp profiles were collected together with the seismic data (**Figure 3**).

A conventional processing sequence (including deconvolution, short period seafloor multiples removal and velocity analysis) was initially adopted to produce a stack section, which was eventually migrated in depth (**Figure 4**). The main horizons identified in the migrated section were used as a reference to assist the picking procedure in the pre-stack domain. These horizons are indicated in the figure by arrows: the sea floor, the base of the Pleistocene sediments and the top of the carbonates.

A minimum-impact processing was applied first, consisting essentially in quality control, editing and geometry assignment. A spherical divergence compensation, based on the stacking velocities used to correct the signals in the CMP domain (**Figure 5**), was then applied to the pre-stack raw data, to preserve as much as possible their spectral characteristics. Indeed, the pre-processing for Q-factor imaging must not include procedures that affect heavily the signal spectrum, as bandpass filtering, Normal Move-Out (NMO) stretching, Automatic Gain Control (AGC), FX-deconvolution and even surface-consistent deconvolution. Instead, common editing (and statics, for land surveys), surface-consistent amplitude compensation or velocity-based spherical divergence recovery are fine, having a minimal impact on the frequency content. As the traveltime picking and waveform analysis are carried out in the pre-stack domain, we have not problems with the NMO stretching. After the basic processing just mentioned, the tomographic inversion of traveltimes provides a velocity model

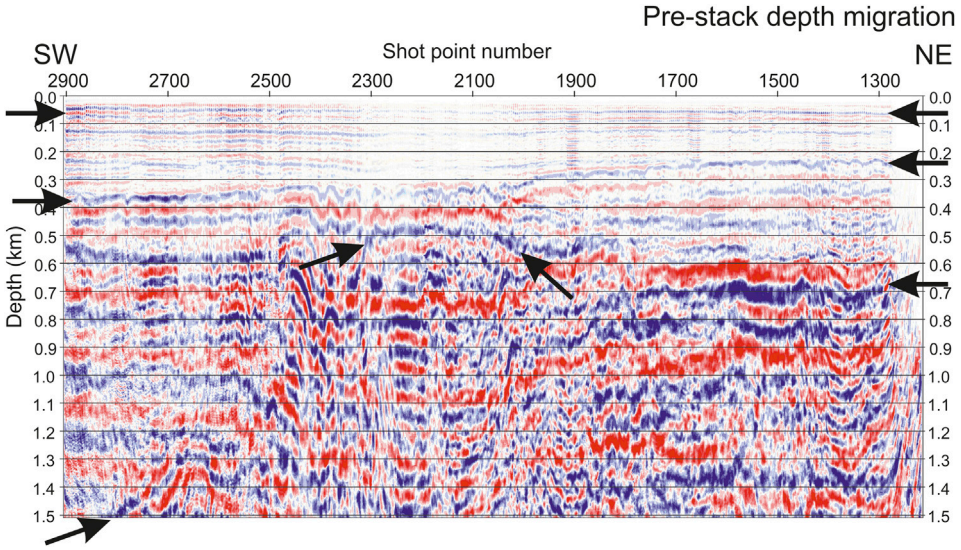

FIGURE 4 | Pre-stack depth migrated section of the central part of the seismic profile GT09–21 in **Figure 2**.

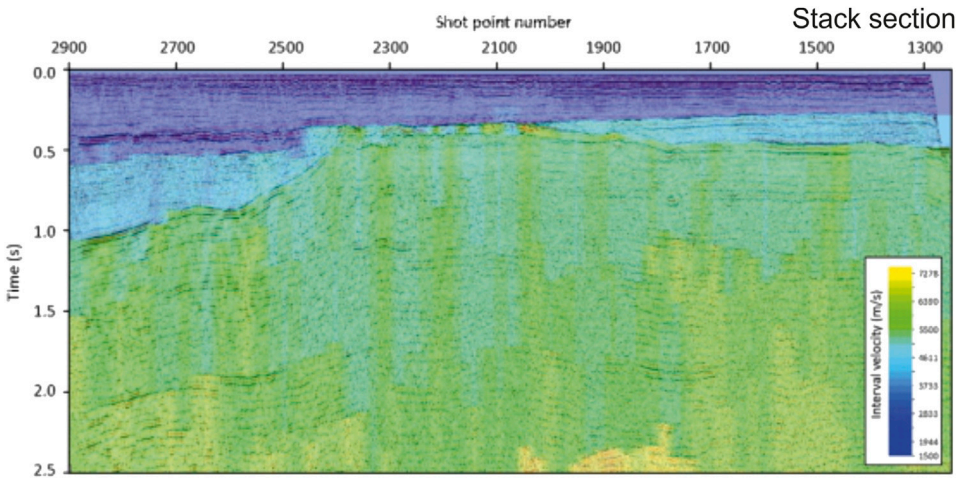

FIGURE 5 | Interval velocities (colored background) derived from stacking velocities, which we used for the spherical divergence correction and the stacked time section (superimposed wiggle plot).

in depth. This model is used both for the pre-stack depth migration of the instantaneous frequency and for computing the Q factor from the anelastic absorption α_0 obtained by the frequency-shift tomography (Quan and Harris, 1997).

Complex Attributes and Anelastic Absorption

In this section, we summarize the mathematical background of broadband imaging for anelastic absorption presented by Vesnaver et al. (2016), Lin et al. (2018), to provide a critical understanding of its later application to the seismic profile.

The complex trace $c(t)$, a function of the arrival time t, is composed of a real part $r(t)$, which is the seismic trace recorded in the field, and of an imaginary part $h(t)$, which is the Hilbert transform H{.} of $r(t)$:

$$c(t) = r(t) + \mathrm{i}\, h(t) = r(t) + \mathrm{iH}\{r(t)\} \tag{1}$$

Representing $c(t)$ as a complex exponential, we get:

$$c(t) = e(t) \exp\left[\mathrm{i}\, \phi(t)\right] \tag{2}$$

where:

$$e(t) = \left[r(t)^2 + h(t)^2\right]^{1/2} = |c(t)| \tag{3}$$

$$\phi(t) = Arg\{c(t)\} \tag{4}$$

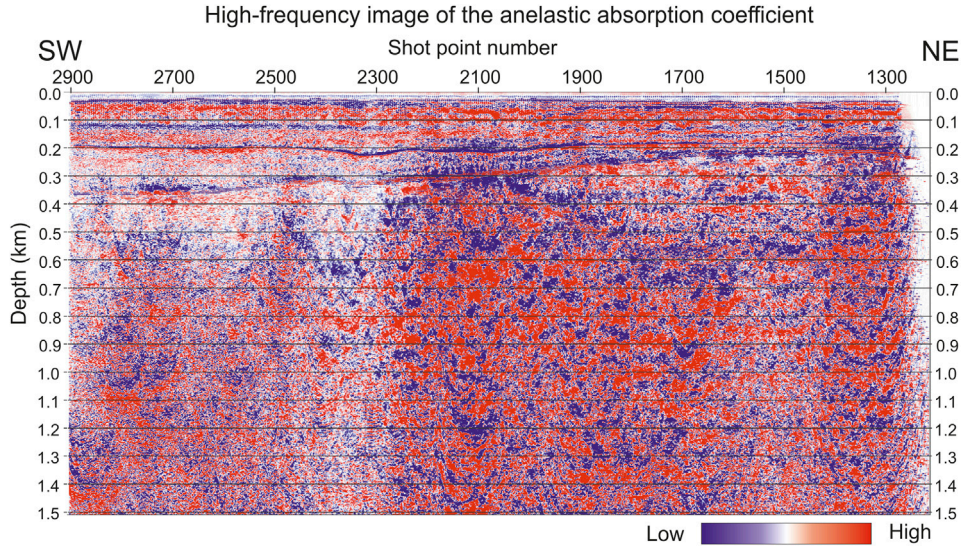

FIGURE 6 | Depth migrated and derived instantaneous frequency of the line GT09–21, i.e., the high-frequency component of the anelastic absorption coefficient.

The names assigned by Taner et al. (1979) to *e(t)* is envelope, and to $\phi(t)$ is instantaneous phase. Dividing the complex trace *c(t)* by its envelope, which is a non-negative real function, we get the normalized complex trace *n(t)*:

$$n(t) = c(t)/e(t) = \exp[\mathrm{i}\,\phi(t)], \quad if: e(t) > 0 \text{ and} \qquad (5)$$
$$n(t) = 0, \qquad if: e(t) = 0$$

Taking the time derivative of **Eq. 5** and substituting (5) in the result, Poggiagliolmi and Vesnaver (2014) obtained a simple expression for the instantaneous frequency $\phi'(t)$, which is the time derivative of the instantaneous phase:

$$\phi'(t) = -\mathrm{i}\, n^*(t)\, n'(t) \qquad (6)$$

where $n^*(t)$ is the complex conjugate of *n(t)*, and $n'(t)$ is its time derivative. According to Ackroyd (1970), Saha (1987), the value of the instantaneous frequency at the envelope extrema t_e equals the centroid of the related waveform amplitude spectrum:

$$\phi'(t_e) = \frac{\int f\, A(f)\, df}{\int A(f)\, df} \qquad (7)$$

where *f* is the frequency and *A(f)* is the amplitude spectrum of the waveform surrounding the extremum point t_e.

This property may be used directly for the Q-factor tomography, as presented by Vesnaver et al. (2020), Bruno and Vesnaver (2020). In our paper, however, we exploit it to compute the high-frequency component of the anelastic absorption, to complement the low frequency part provided by reflection tomography. As the latter one is obtained in the depth domain, the next step is a depth migration of the instantaneous frequency, getting $\Phi(\boldsymbol{x})$, where $\boldsymbol{x}$ is a point in depth. The final expression for the high-frequency component of the anelastic absorption parameter $A_{high}(\boldsymbol{x})$ is:

$$A_{high}(x) = \frac{F}{2}\frac{\partial \boldsymbol{\Phi}(\boldsymbol{x})}{\partial \boldsymbol{z}} \qquad (8)$$

where *F* is a real constant that depends on the seismic source spectrum. **Eq. 8** defines the attribute displayed later in the example in **Figure 6**.

The Hilbert transform is linear, so if the substitute *r(t)* in (A-1) with its opposite *–r(t)*, we get:

$$-r(t) + \mathrm{i}\,\mathrm{H}\{-r(t)\} = -r(t) - \mathrm{i}\,\mathrm{H}\{r(t)\} = -[r(t) + \mathrm{i}\,\mathrm{H}\{r(t)\}]$$
$$= -c(t) \qquad (9)$$

This means that reversing the polarity of the real trace *r(t)*, we reverse also the sign of the related complex trace. One can prove similarly that the same happens for its complex conjugate normalized trace $n^*(t)$ and the derivative $n'(t)$ in **Eq. 6**. Thus, substituting *r(t)* with - *r(t)* in **Eq. 6**, we obtain:

$$-[-n^*(t)]\,[-n'(t)] = -\mathrm{i}\, n^*(t)\, n'(t) = \phi'(t) \qquad (10)$$

i.e., the instantaneous frequency does not change when the polarity of the real trace is reversed. This is not surprising, because the same happens for the trace envelope or its amplitude spectrum. However, this invariance with respect to polarity reversals has a consequence on the anelastic absorption parameter in **Eq. 8**. As the derivative is linear, and the pre-stack depth migration preserves the signal polarity, this invariance applies also to the high-frequency component defined in that formula.

TOMOGRAPHIC IMAGING

The broadband imaging we adopted is a combination of a low-resolution macro-model, including very low frequencies, and a micro-model with higher frequencies. The macro-model is

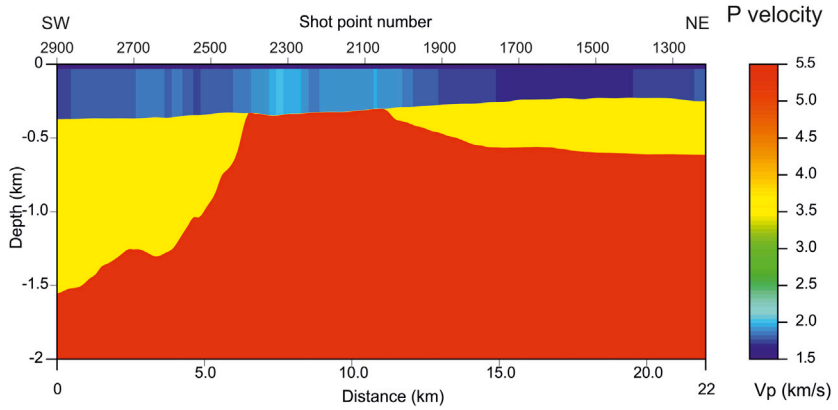

FIGURE 7 | Tomographic estimation of the P velocity by the traveltime inversion of reflected arrivals from a few shallow horizons of the profile GT09–21.

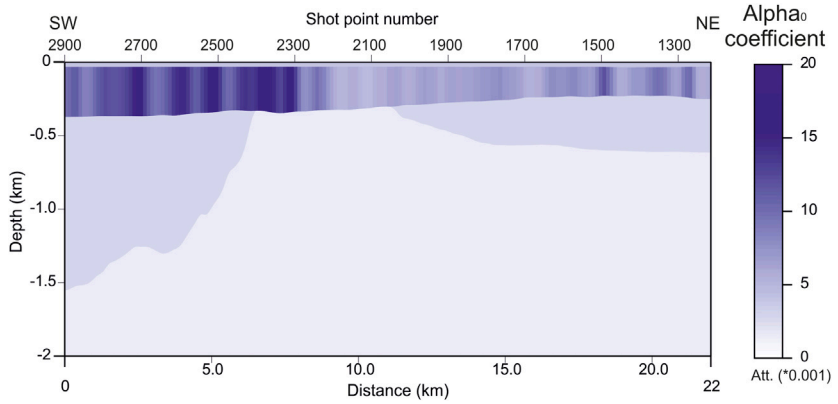

FIGURE 8 | Tomographic estimation of the anelastic absorption coefficient α_0 by the local waveform analysis of reflected arrivals from a few shallow horizons of the profile GT09–21. This is the low-frequency component of the anelastic absorption.

obtained by reflection tomography (see, e.g., Vesnaver et al., 2000; Rossi et al., 2007, 2011) for delineating the reflecting interfaces and the P velocity. The traveltime inversion exploits a minimum-time ray tracing algorithm (Vesnaver, 1996a; Böhm et al., 1999), able to compute the ray paths of direct, reflected, refracted and diving arrivals in irregular grids.

The macro-model for anelastic absorption is estimated by the frequency-shift method by Quan and Harris (1997). The latter method is based on experimental studies of Ward and Toksöz (1971), who found that the anelastic absorption $A_{ray}(f)$ along a given ray path can be expressed as a function of the frequency f as:

$$A_{ray}(f) = \exp\left(-f \int_{ray} \alpha_0 \, dr \right) \tag{11}$$

where α_0 is the anelastic absorption parameter that depends on the lithology of the crossed rocks. In the most general case, absorption depends on frequency too; however, seismic surveys cover a quite limited band, as most propagating energy at significant distances ranges between 8 and 80 Hz, for standard seismic surveys. Within such a band, assuming α_0 to be frequency-independent is an acceptable approximation, used in the frequency-shift method that we adopt in this paper. Based on this assumption, we may write the following approximate equation, linking the P velocity $v(\boldsymbol{x})$ and the anelastic absorption parameter $\alpha_0(\boldsymbol{x})$ to the Q factor Q(x):

$$Q(x) \approx \pi / [v(x)\alpha_0(x)] \tag{12}$$

at any point $\boldsymbol{x}$ in space.

By picking reflected events (and possibly, direct and refracted arrivals too), we build a depth model for P velocity and the major layer interfaces, where the acoustic impedance contrast produces clear seismic signals. Using the waveforms surrounding the picked events, we compute the centroid of their spectrum and, comparing it with that one known of the seismic source, we can reconstruct the anelastic absorption along the ray path of picked arrivals. The obtained model is composed of a few "thick" layers

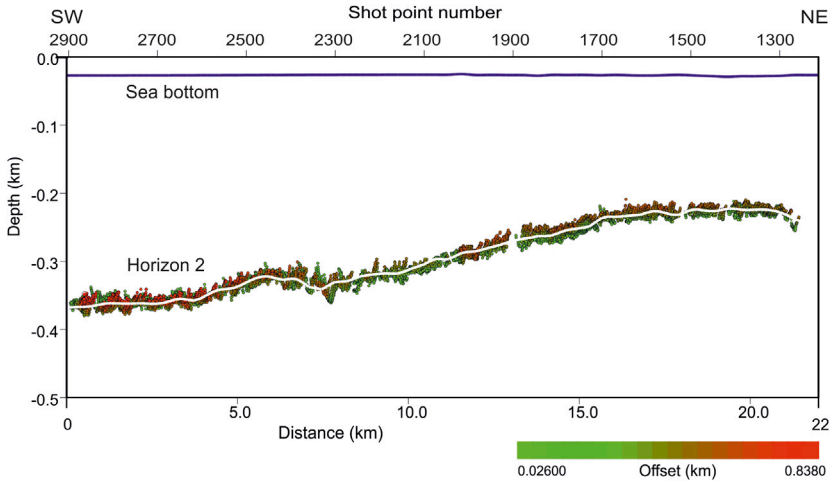

FIGURE 9 | Estimated reflection points in depth for the second picked horizon, corresponding to the base of Pleistocene sediment.

only, so over-simplifying the much more complex actual layering, but getting information about the low spatial frequencies of the Earth model that otherwise is limited if using the seismic traces directly.

Figures 7, **8** show the P velocity and anelastic absorption coefficient α_0, respectively, estimated by inverting the picked traveltimes and the spectral centroids of the related waveforms. For both lithological properties, we notice some lateral variations in the uppermost sedimentary layers, just below the sea floor, i.e., in the Pleistocene sediment, while the underlying Eocene-Miocene terrigenous sediment and the Meso-Cenozoic carbonates is quite homogeneous. The lowest part presents only guessed values, as deeper reflectors could not be picked and inverted reliably. In both tomographic images, the lateral resolution is fair, i.e., about 122 m, as the final number of cells is 180, obtained by 3 staggering steps of basic grids of 60 cells. For more details about this algorithm, we send the reader to Vesnaver and Böhm (2000). Other application examples for traveltime and Q-factor tomography, using the same algorithm adopted in this paper, can be found in Vesnaver et al. (2000), Böhm et al. (2006), Rossi et al. (2007), Rossi et al. (2011), Bruno and Vesnaver (2020).

Two picked and inverted horizons are displayed in **Figures 2**, **4**: the sea floor and the base of Pleistocene sediment. The third one, i.e., the top of carbonates, was estimated by the pre-stack depth migration, because of the lower Signal/Noise ratio along that horizon. Due to the high fold and fair data quality, the reliability of our estimates is satisfying, and can be quantified by a few indicators. **Figure 9** displays the estimated reflection points for the second horizon (the base of Pleistocene sediment). Their dispersion around the resulting interpolant line (superimposed in white) is low: the average absolute difference along the whole profile between estimated and interpolated points is about 5 m. As the average depth of that horizon is 300 m, the mismatch is lower than 2%. Another accuracy indicator is the Root Mean Square (RMS) difference between picked and modeled two-way traveltimes, which is about 1%, i.e., about 3.3 ms, close to the sampling rate. A further check is provided by the colors of the estimated reflection points: red for the far offsets, green for the near ones. When the two colors overlap, this indicates a flatness of the corresponding Common-Image gathers; when they do not do so, a residual velocity update is needed. We notice that almost everywhere along the interface this overlap is good.

Having a good fit between measured and modeled traveltimes is a necessary but not sufficient condition to get a unique, reliable solution, as many other Earth models may fit the experimental data too. This happens when a null space exists in the system of linear equations that is the core of the inversion algorithm we adopted (see, e.g., Van der Sluis and Van der Vorst, 1987). A measure for this uncertainty is the null space energy (Vesnaver,

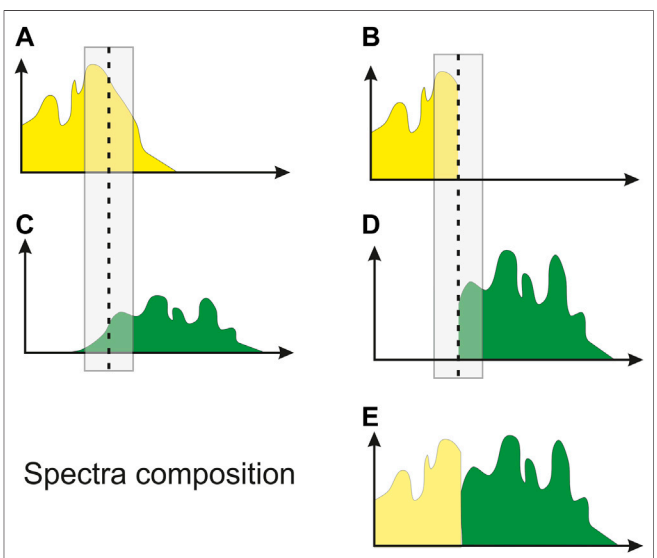

FIGURE 10 | The averages of two partially overlapping spectra **(A, C)** are evaluated in a common window, rescaled to be similar and clipped at the window center **(B, D)** and merged into a single, broader spectrum.

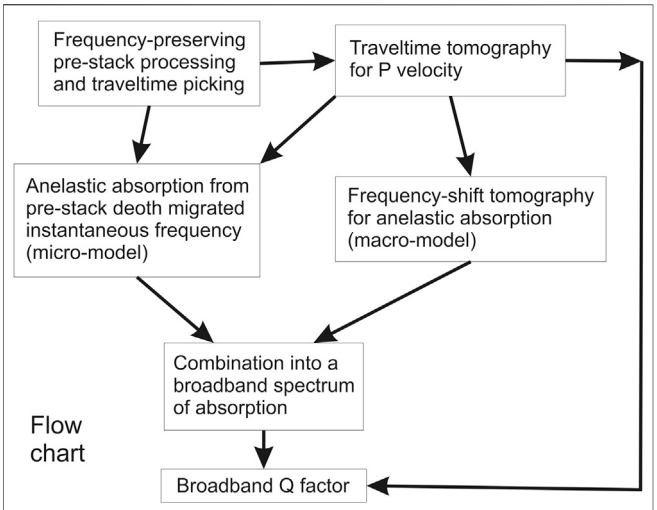

FIGURE 11 | Flow chart for the broadband estimation of anelastic absorption and Q factor.

1994; Vesnaver, 1996b), which is based on the Singular Value Decomposition (SVD) of the matrix composed of the coefficients of the linear equations. In our case, we discarded the eigen-components of the solutions' space whose eigen-values are lower than 1% of the maximum eigen-value. The resulting local energy of the null space is mostly less than 1%: this means that 99% of the solution depends on the input data only, i.e., is only marginally affected by the initial mode choice. Such a good stability is due to the wide extension of cells (366 m) that we chose for the staggered grid inversion.

In the vertical direction, the resolution of the tomographic images in **Figures 7**, **8** is very limited, as the properties are constant between the reflecting interfaces, and we could pick only three major reflecting horizons. We need adding new information that could improve the vertical resolution. Picking further intermediate and deeper horizons is the ideal way, when the signal/noise ratio is good and the reflectivity continuous. This is not our case, so a different fix is required.

BROADBAND IMAGING OF ANELASTIC ABSORPTION

Obtained a macro-model for P velocity and Q factor from reflection tomography, we can get the high-frequency contribution by the instantaneous frequency. This popular seismic attribute, introduced by Taner et al. (1979), can be efficiently computed without any user-defined parameter (Poggiagliolmi and Vesnaver 2014; Vesnaver 2017), i.e., by a data-driven procedure. Ackroyd (1970) proved that the instantaneous frequency is the centroid of the instantaneous spectrum of a waveform. Saha (1987) and Barnes (1991) proved that the instantaneous frequency is exactly the waveform spectral centroid at the maximum (or minimum) of its envelope. One can prove also that this is not true elsewhere (Carcione, personal communication); however, we can assume the instantaneous frequency as a reasonable proxy for the actual centroid, which is reliable only in the vicinity of the most energetic part of the seismic signal. With this *caveat* in mind, we will use the instantaneous frequency for complementing the low-frequency part of the anelastic absorption image obtained from seismic tomography.

The cartoon in **Figure 10** explains an ideal approach for integrating macro- and micro-model. The amplitude spectra of the two components span different ranges that may partially overlap, and each of them may have a different average amplitude. We may choose part of the overlapping area where the signal energy is significant for both, and compute their average value in it. Finally, we can compensate for the amplitude value of the second spectrum by rescaling it with the inverse ratio obtained in the overlapping area, merging it with the first spectrum.

The wider the overlapping area, the better may be relative spectra compensation, because the information from the experimental data becomes more solid from a statistical point of view. However, the overlap window should avoid the noisiest parts of the amplitude spectra, which normally are the high frequencies for the seismic signal. For the tomographic contribution, high frequencies should be avoided too, as mostly due to the Gibbs phenomenon at sharp changes of P velocity or Q factor in the blocky models we adopted. In the low frequency part, the limit is dictated mainly by the lowest values achievable by seismic sources and receivers, which are very rarely lower than a few Hz. The window choice depends so on the data quality and the parametrization of the Earth model, but also on what the interpreter assumes as signal or noise in the seismic data.

Figure 11 shows a block diagram summarizing the broadband imaging work flow. Its basic steps are:

1. Basic pre-stack processing, calculation of the instantaneous frequency and traveltime picking.
2. Traveltime inversion of direct, reflected and refracted arrivals to get a P-velocity macro-model in depth.
3. Frequency-shift tomography, using velocity and ray tracing from Step 2, getting a corresponding macro-model for the anelastic absorption parameter α_0.
4. Using the tomographic velocities from Step 2, perform a pre-stack depth migration of the instantaneous frequency from Step 1 and convert it into a micro-model for the α_0 parameter.
5. Combine micro-model from Step 4 and macro-model from Step 3 into a broadband model, carrying out a relative normalization by exploiting the possible overlapping frequency bands.
6. Convert the depth model for α_0 into a Q-factor model by using **Eq. 2** and the P velocity obtained at Step 2.

Figure 6 is the high-frequency component of the anelastic absorption, obtained as the derivative with respect to depth of the depth-migrated instantaneous frequency, defined by **Eq. 8**. Blue colors correspond to low absorption, while the red ones correspond to high absorption. This attribute provides only relative variations, so the scale is just qualitative without a

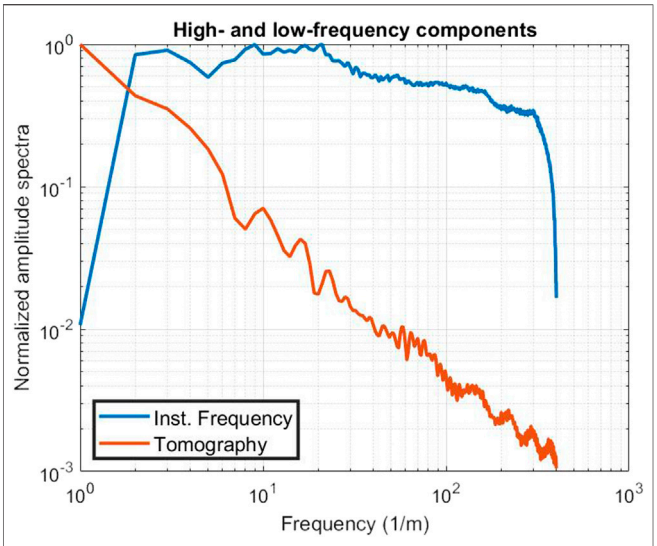

FIGURE 12 | Normalized amplitude spectra of the high- and low-frequency components of the estimated anelastic absorption, in bi-logarithmic scale.

calibration. Since the derivative is boosting the highest frequencies a lot, where the signal is much weaker than the noise, we applied a high-cut filter with a cut-off threshold of 300 Hz, as we do not expect reliable signals beyond that limit. This component highlights well two nearly flat interfaces at a depth of 120 and 190 m, which are weaker in terms of reflectivity (**Figure 4**), but suggest vertical discontinuities of the anelastic absorption. We note also that the horizons at 120 m depth and the sea floor are gradually dimming out when moving from left (SW) to right (NE), so detecting a lateral change of the formations' properties.

Figure 12 shows the normalized amplitude spectra of the low-frequency component of anelastic absorption from tomography and the high-frequency component from the instantaneous frequency; both are averaged over the whole sections. We notice that the high-frequency part (blue line) approximates zero at the zero frequency and is low up to 1 Hz, where it reaches a plateau. This is due, again, to the derivative in its definition – (see **Eq. 8**) – as this process strongly attenuates the lowest frequencies. That part, however, is where the tomographic contribution is stronger. The area where the two components have comparable magnitude is between 4 and 16 Hz, which we selected to try a balance of the two components.

Figure 13 shows the two components and their combination in the frequency band defined by an Ormsby filter with corner frequencies 3,4,16, and 20 Hz. We notice that in the merged section (bottom), improvements are obtained in the depth range from 200 to 700 m in terms of signal continuity and sharpness. Instead, from 0 to 200 m, the part coming from tomography (top) overwhelms that one from the instantaneous frequency (center). This apparent unbalance is probably due to different noise content, which is totally absent in the tomographic component, and definitely present in the other component. Thus, the noise reduces the contribution of the signal in the high-frequency component, underweighting it if a plain energy balance is adopted to equalize the tomographic and instantaneous-frequency components. Similar effects show up when merging the full bandwidth of the two components. For this reason, we adjusted the relative weight by imposing that the highest frequency peak of the two components is nearly equal, and that there are no negative values in the resulting broadband combined absorption estimate. The result is displayed in **Figure 14**. The most striking difference is that there are not "negative" values any more (i.e., red colors), as the ultra-low frequencies, up to 0 Hz, are now included, provided by the tomographic contribution. When compared with the image at the bottom of **Figure 13**, we notice a better definition of shallow reflectors between 0 and 150 m, an improved strength and continuity of the main reflectors picked for tomography, between 200 and 600 m depth, and a decrease of the random scattering in the lowest part. The differences are visible, but not huge: probably, this is due to the extended bandwidth of the shallow signals provided by the instantaneous frequency, and the lack of usable reflectors in the deeper part. The useful signal added by the tomography is so restricted to a frequency band from 0 to 3 Hz.

Figure 14 was obtained by choosing a real positive number for the scaling factor to balance the high- and low-frequency component. This choice is not obvious in general, as a negative factor could be chosen, in principle: the two components might be both added or subtracted. This potential ambiguity is solved by **Figure 13**, where we notice that, in the overlapping frequency band, the polarity of the main reflectors is the same for the two components. Thus, in this particular case, a positive sign for the scaling factor will properly sum in phase the signals from the same interface. Furthermore, comparing **Figure 8** and **Figure 13** (top), we understand that the blue color in **Figure 13** corresponds to layers with a low absorption, as the sea water and the top of carbonates, while the red color characterizes lithologies that may be either fractured or fluid-saturated, or both, so indicating a higher absorption.

We see in **Figure 14** that the shallowest 30 m, composed of sea water and unconsolidated sediments, is colored in light blue, corresponding to a low absorption. Between 40 m and over a gently dipping interface, at 350 m on the left and 210 m on the right, the absorption is higher, between the shot points 2,900 and 2,300. In the central part (shot points 2,200–1800), the absorption decreases quite sharply, while it increases again slightly in the final part, in the NE direction. Below this strong marker, up to a depth of 600 m on the right and up to the top of the carbonates on the left, we see areas of weaker and scattered signals, which have different patterns: more homogeneous on the left, where the Gallare Marls are located; characterized by patchy scatterers of increasing size in the center, where fractured and karstified carbonates are present; and a very peculiar feature on the right, where there is a slight increase in the absorption. In the central part we see that the morpho-structural high, corresponding to the paleo-shelf margin of the carbonate platform (at 350 m depth, between shot points 2,400 and 2,000) is affected by a severe blanking effect of the left flank, which is attenuated on the right side, where weak

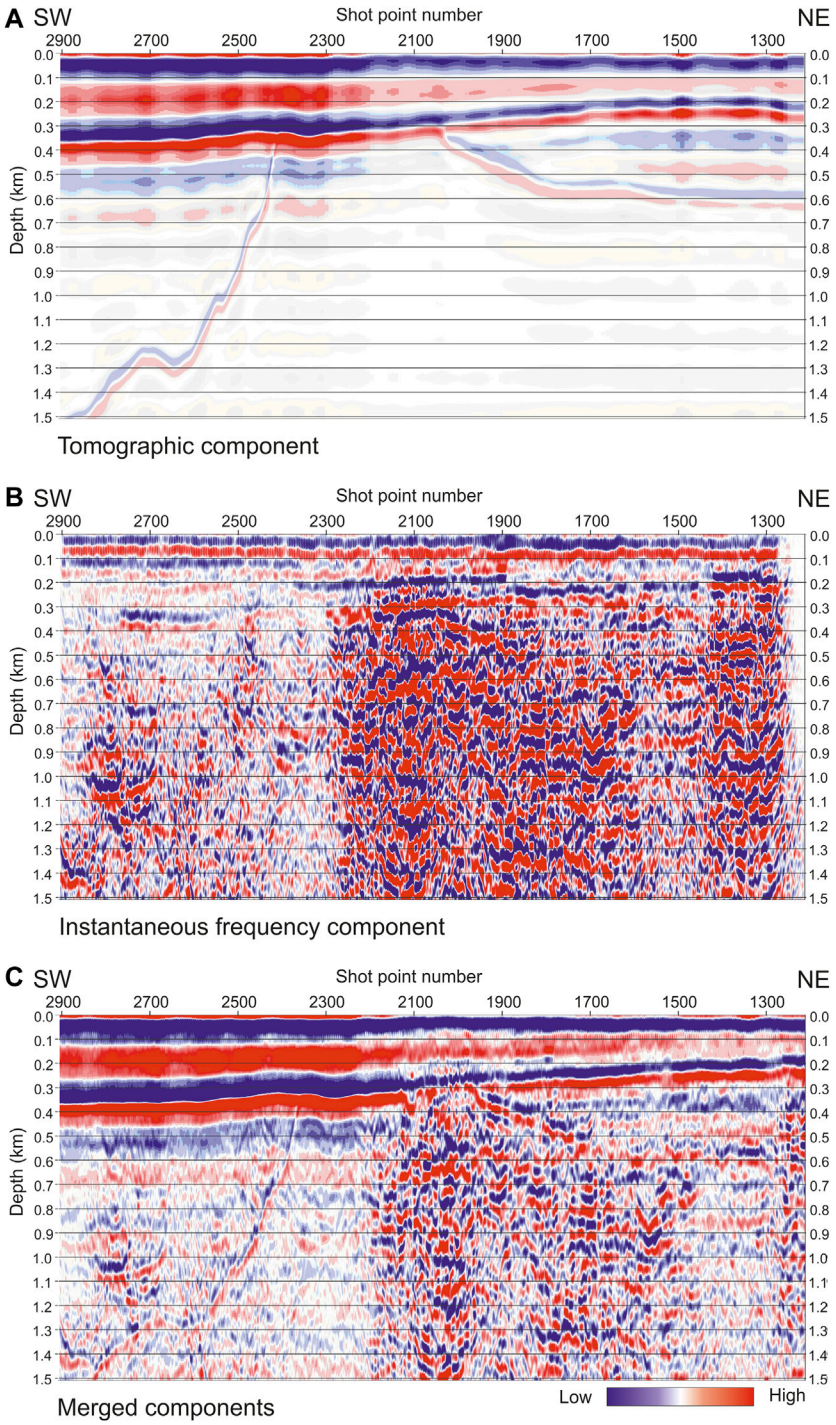

FIGURE 13 | Components of the estimated anelastic absorption from tomography (top) and instantaneous frequency (center) in the frequency band defined by the Ormsby filter with corner frequencies 3,4,16, and 20 Hz, and their combination (bottom), obtained by normalizing and averaging their amplitude spectra.

scattered, high-frequency signals show up. We interpret this difference as a major footprint of the overlying formations, which are highly absorbing on the left, and not so much on the right, or by different sedimentation environment causing progradational layers at the shelf margin, usually characterized by poorly sorted material, on the left, from the stratified inner platform carbonates on the right.

The red arrows on the top of **Figure 14** indicate the locations on the known plume areas, which are located along the profile (**Figure 2**). Most of these plumes, located from shot points 2,600

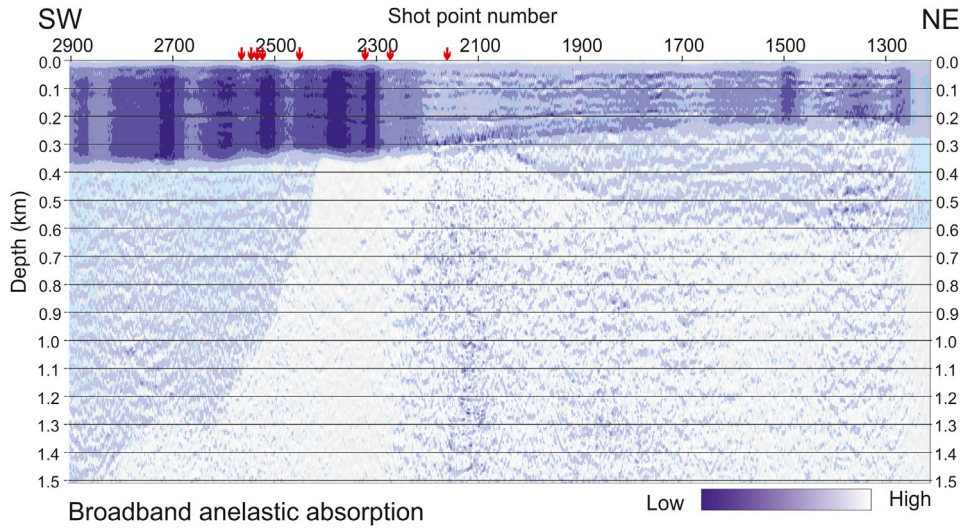

FIGURE 14 | Broadband anelastic absorption, obtained combining the low-pass filtered tomographic component in **Figure 8** with the high-pass filtered from the instantaneous-frequency component (**Figure 6**). The small red arrows on top indicate the proximity of known plume areas.

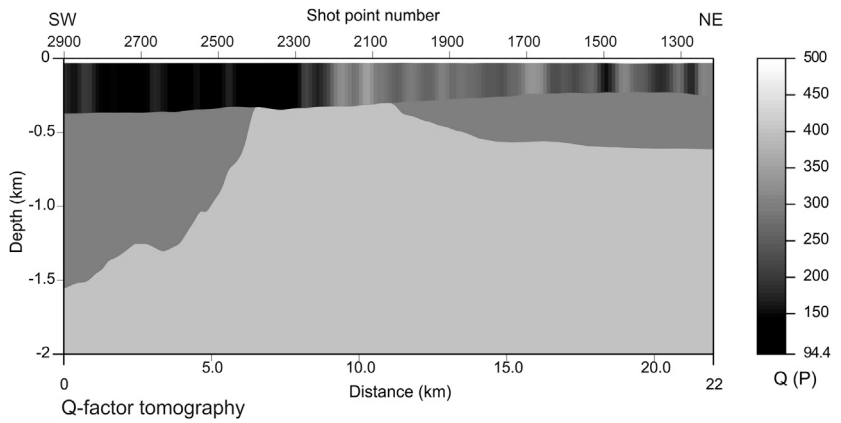

FIGURE 15 | Q factor estimation obtained by P velocity in **Figure 7** and the anelastic absorption coefficient in **Figure 8**. This result is the low-frequency component, based on tomography only.

and 2,180 correlate with the imaged anomalies. The two arrows on the left correspond to highly absorbing sedimentary units, with a lower P velocity (**Figure 7**). This may suggest some gas as saturating fluid. Between shot points 2,000 and 1,600, the velocity is higher and the absorption lower, which might suggest water or brine as possible saturating fluids. These hypotheses need further data collection and analysis.

Converting the anelastic absorption coefficient to the Q factor involves using **Eq. 12**. This is immediate when it comes to the low-frequency component provided by tomography only (**Figure 15**). There are lateral variations in the formations just below the sea floor, up to a depth of 300 m. Between 300 and 600 m, the variations are much lower, except for the central morpho-structural carbonate high. The deeper part is not actually inverted, as mentioned above, because of the lack to strong, continuous reflectors. As for the contributing parameters (displayed in **Figures 7**, **8**), the vertical resolution is poor, because of the difficulty in picking additional horizons. However, a much better result is obtained when using the broadband anelastic absorption coefficient (**Figure 14**) instead, providing food for thought to the interpretation (**Figure 16**). The shallowest part (0–380 m) is almost covered by vertical gray bars on the left up to the shot point 2,200, indicating a low Q factor, while it is populated by a few reflectors in the remaining part. The interfaces between the interpreted horizons are a bit sharper. Remarkable is the signal continuity at 300 m depth, which is strong from the central horst-like structure to the left, while it is fainter toward the right side. The difference between these two parts suggests different petrophysical properties for the underlying lithologies. This clue is strengthened by the

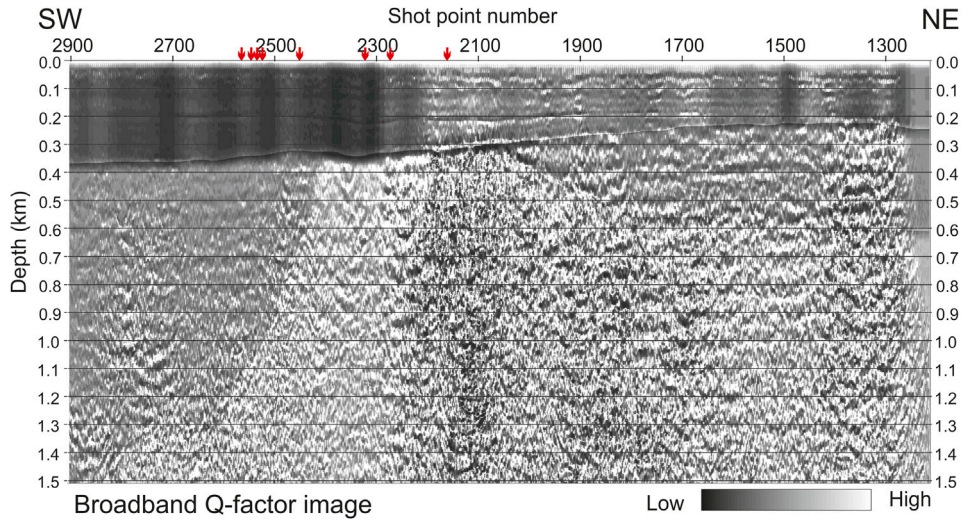

FIGURE 16 | Q factor estimation obtained by P velocity in **Figure 7** and the broadband anelastic absorption coefficient in **Figure 6**. The small red arrows on top indicate the proximity of known plume areas.

different seismic stratigraphy of the two lithologies: on the left, composed of scattered signals with medium frequencies; on the right, characterized by a few low-frequency reflectors. Below the picked horizons, the signal is discontinuous and randomly scattered, in a different way in the three parts (left, center, right) of the carbonates. As mentioned above, these differences may be a footprint of the overlying different formations.

As for **Figure 13** and other similar ones, the color scale is qualitative only, because without a well calibration, the high-frequency component and its percentage contribution to the final broadband estimate (**Figure 16**) depend on acquisition and user-defined processing parameters. Although the latter ones are bounded by physical constraints and geological knowledge about rock properties, at this stage our estimation is only semi-quantitative.

GEOLOGICAL REMARKS

The most evident result of the absorption model within the Pleistocene sediment, with high absorption in the western part, low in the central part, and medium in the eastern part (**Figure 14**), could reflect the occurring of the different phases and components of the fluids present in the study area.

Seismic facies of the Late Pleistocene sediment in the seismic profiles and in the high-resolution chirp data (**Figure 2**) show the occurrence of fluids and fluid seepages at the sea floor, that sample analysis revealed to be mainly methane of biogenic origin (Busetti et al., 2020; Gordini et al., 2004; Gordini et al., 2012). From the correlation between seismic and Chirp data, the main area with gas bearing sediments results in the western part of the analyzed profiles. The western Gulf of Trieste is rich of sites related to gas seepages (Gordini et al., 2003) and some of them are quite close the analyzed profiles. Chirp data permits identifying some plume sites (**Figure 2**), but gas seepages nearby could be significantly more than those ones recognized. These evidences suggest that the high absorption within the Pleistocene sediment in the western part of the profile (**Figure 14**) could reflect the occurrence of gas.

The carbonate units are the confined reservoir of trapped Miocene sea water (Petrini et al., 2013). The sonic log acquired in the Grado-2 well indicates that the Paleogene carbonates, located in the eastern upper few hundred-meter part of the carbonate platform, are characterized by more fractures and stratification than the Cretaceous limestone, being potentially a more efficient reservoir (Piffer et al., 2015). The carbonate reservoir is sealed on the east by the turbiditic units of the Eocene flysch and by the terrigenous Miocene Molasse, while in correspondence of the morpho-structural high, the carbonates are draped by about 100 m of the Miocene Cavanella Group composed of sand, sandstones and marls (Nicolich et al., 2004). The Cavanella Group, occurring in the Friulian Plain, thins southward pinching out in the Gulf of Trieste. Hence, thinning southward, the Cavanella Group loose progressively the capacity to be an efficient seal, and the salty waters may migrate upward, in the Pleistocene sediment. This hypothesis could explain the low absorption zone in correspondence of the Pleistocene sediment lying above the eastern part of the morpho-structural carbonate high. The medium absorption in the eastern part could be related to less evident gas occurrence within the sediment.

DISCUSSION

The broadband imaging method presented in this paper is a heuristic approach, based on a few major approximations. Thus, we should regard it as a semi-quantitative tool, able to highlight local lithology variations, but not providing a precise measurement to be used for direct engineering applications. Within these premises, however, it is a clear advance with respect to current technologies in terms of spatial resolution

for detecting saturated formations and fluid pathways. Using synthetic seismograms (and thus known models), Vesnaver and Lin (2019) showed that this method works nicely also when the acoustic impedance contrast is modest in a hydrocarbon reservoir, so that the oil/water contact cannot be detected by a standard approach. However, if a production technique as fracking is applied, the rock matrix is affected and the Q factor decreases: then, it becomes a good parameter to delineate fracked regions and optimize the production of hydrocarbons or geothermal energy.

Some heuristic methods have been used effectively. A similar approach to our one was introduced for a broadband estimation of the acoustic impedance by Lindseth (1976), Lavergne and Willm (1977) and Becquey et al. (1979), getting successful applications for decades in oil and gas exploration. Other comparable hybrid methods were presented by Mora (1989) for seismic reflectivity and by Tura et al. (1998) for the depth conversion of attributes derived by Amplitude vs. Offset analysis.

We remark that the absorption images highlight the relative contrast of this property among different formations illuminated by the seismic waves, and not absolute values. This applies to both low- and high-frequency components. For the tomographic contribution, the adopted method of Quan and Harris (1997) assumes a few hypotheses, as a white spectrum for the Earth reflectivity, which can be violated in real experiments. Vesnaver et al. (2020) showed that a calibration by well logs can fix such a drawback, but when such information is missing (as in our test case), we must be aware that our results might need to be adjusted by a scaling factor. Another scaling factor is needed to calibrate the high-frequency component, as it is dependent on the frequency band spanned by the seismic source. Thus, the relative weight of high- and low-frequency component may be just guessed, within physical constraints, unless a well calibration is available to consolidate both items.

The improvement in the broadband Q-factor estimation vs. the purely tomographic one is dramatic, but suffers a weakness: the tomographic velocity field is available only at a low-resolution. Ideally, the high-resolution version should be provided a full-waveform inversion, may be even just with an acoustic implementation. We expect significant improvements in this case, which is left to further studies.

The frequency band of seismic signals is limited: in the chase history presented here, it ranges from a few Hz to over 200 Hz (**Figure 12**). The lowest missing frequencies (from 0 to a few Hz) correspond to the averages of velocity and absorption, which are the zero frequency, and to the linear trend of their values. The traveltime inversion estimates the absolute values of P velocities: it is very amenable for injecting "a priori" information in the inversion process, as physical limits for acceptable velocities and a certain smoothness level for their later variations. Furthermore, an increasing trend is expected for both P velocity and Q factor in most cases, due to the increasing lithostatic load as a function of depth. This additional information is a key contribution for filling the low-frequency gap for P velocities and the main interfaces' structure. When it comes to anelastic absorption (or Q factor), this gap is filled properly only if a calibration by well logs is available (see Vesnaver et al., 2020). If this data is missing, as in our case study, we may use only more general constraints: for example, high Q values in the sea water and much lower ones in unconsolidated sea floor sediments. In the latter case, however, the result is semi-quantitative only: as just the relative contrasts are data driven, the absolute values may be biased by the chosen constraints.

CONCLUSION

The broadband estimation of anelastic absorption is an effective tool for characterizing fractures or fluid-saturated formations, or both. We tested this recent method on a marine survey acquired in the Gulf of Trieste (Italy) to validate a few geological hypotheses about fluid occurrence within the sediment and emissions at the sea floor. We hypothesize that the high absorption of the Pleistocene sediment is related to biogenic gas occurrence, while the low absorption zones are reasonably correlated to possible migration of salty water from deep carbonate reservoir to the Miocene-Pleistocene sediment.

DATA AVAILABILITY STATEMENT

The raw data supporting the conclusions of this article will be made available by the authors, without undue reservation.

AUTHOR CONTRIBUTIONS

AV prepared the basic manuscript and developed the algorithm for the broadband imaging. GB carried out the tomographic inversion of P velocity and Q factor, and the related pre-stack depth migration. MDC and MB cared the geological setting and interpreted the seismic data. MB managed the project for the data acquisition and interpretation. FZ acquired the seismic data and completed its basic processing. All authors contributed to the final discussion and the manuscript editing and revision.

FUNDING

Our work was supported by the National Institute of Oceanography and Applied Geophysics – OGS, in the framework of the projects "Geological and tectonic evolution of the Gulf of Trieste (N-Adriatic)", supported by OGS.

ACKNOWLEDGMENTS

We acknowledge our colleagues that contributed to the seismic data acquisition by the vessel OGS-Explora. We acknowledge IHS Markit® and Schlumberger® that provided to OGS the academic Kingdom® and Vista® software licenses.

REFERENCES

Ackroyd, M. H. (1970). Instantaneous spectra and instantaneous frequency. *Proc. IEEE* 58, 141. doi:10.1109/proc.1970.7552

Agudo, Ò. C., da Silva, N. V., Warner, M., Morgan, J., and Morgan, J. (2018). Acoustic full-waveform inversion in an elastic world. *Geophysics* 83, R257–R271. doi:10.1190/geo2017-0063.1

Arso (2017). Ministry of the environment and spatial planning, Slovenian environment agency. Available at: https://gis.arso.gov.si (Accessed April 5, 2017).

Ba, J., Carcione, J. M., and Sun, W. (2015). Seismic attenuation due to heterogeneities of rock fabric and fluid distribution. *Geophys. J. Int.* 202, 1843–1847. doi:10.1093/gji/ggv255

Bai, T., Tsvankin, I., and Wu, X. (2017). Waveform inversion for attenuation estimation in anisotropic media. *Geophysics* 82, WA83–WA93. doi:10.1190/geo2016-0596.1

Barnes, A. E. (1991). Instantaneous frequency and amplitude at the envelope peak of a constant-phase wavelet. *Geophysics* 56, 1058–1060. doi:10.1190/1.1443115

Becquey, M., Lavergne, M., and Willm, C. (1979). Acoustic impedance logs computed from seismic traces. *Geophysics* 44, 1485–1501. doi:10.1190/1.1441020

Best, A. I., McCann, C., and Sothcott, J. (1994). The relationships between the velocities, attenuations and petrophysical properties of reservoir sedimentary rocks1. *Geophys. Prospect.* 42, 151–178. doi:10.1111/j.1365-2478.1994.tb00204.x

Böhm, G., Rossi, G., and Vesnaver, A. (1999). Minimum time ray tracing for 3D irregular grids. *J. Seism. Explor.* 8, 117–131.

Böhm, G., Accaino, F., Rossi, G., and Tinivella, U. (2006). Tomographic joint inversion of first arrivals in a real case from Saudi Arabia. *Geophys. Prospect.* 54, 721–730. doi:10.1111/j.1365-2478.2006.00563.x

Bruno, P. P., and Vesnaver, A. (2020). Groundwater characterization in arid regions using seismic and gravity attributes: Al Jaww Plain, UAE. *Front. Earth Sci.* 8, 575019. doi:10.3389/feart.2020.575019

Busetti, M., Babich, A., and Del Ben, A. (2020). Geophysical evidence of fluids emission in the gulf of Trieste (North Adriatic Sea). *Mem. Descr. Carta Geol. d'Italia* 105, 11–16.

Busetti, M., Volpi, V., Nicolich, R., Barison, E., Romeo, R., Baradello, L., et al. (2010). Dinaric tectonic features in the gulf of Trieste (Northern Adriatic). *Boll. Geof. Teor. Appl.* 51 (2–3), 117–128.

Busetti, M., Zgur, F., Vrabec, M., Facchin, L., Pelos, C., Romeo, R., et al. (2013). "Neotectonic reactivation of Meso-Cenozoic structures in the Gulf of Trieste and its relationship with fluid seepings," in Proceedings of the 32nd gruppo nazionale di geofisica della terra solida (GNGTS) congress, Rome, Italy, November 19–21, 2013 (Trieste, Italy: GNGTS), 29–34.

Carcione, J. M. (2014). *Wave Fields in Real Media. Theory and numerical simulation of wave propagation in anisotropic, anelastic, porous and electromagnetic media*. 3rd Edn. Amsterdam, Netherlands: Elsevier, 690.

Casero, P. (2004). Structural setting of petroleum exploration plays in Italy. Geology of Italy: special volume of the Italian geological society for the international geological congress 32, Florence, Italy, August 20–28, 2004 (Florence, Italy: International Geological Congress), 189–199.

Cheng, P., and Margrave, G. F. (2012). "Q estimation by a match-filter method," in Expanded Abstracts, SEG Annual Meeting, Las Vegas, Nevada, November 4–9, 2012 (Las Vegas, Nevada: SEG), 1–5.

Cimolino, A., Della Vedova, B., Nicolich, R., Barison, E., and Brancatelli, G. (2010). New Evidence of the outer Dinaric deformation front in the Grado area (NE-Italy). *Rend. Fis. Acc. Lincei* 21 (Suppl. 1), 167–179. doi:10.1007/s12210-010-0096-y

Conti, A., Stefanon, A., and Zuppi, G. M. (2002). Gas seeps and rock formation in the northern Adriatic Sea. *Cont. Shelf Res.* 22, 2333–2344. doi:10.1016/s0278-4343(02)00059-6

Cucchi, F., Piano, C., Fanucci, C. F., Pugliese, N., Tunis, G., et al. (2013). *Brevi Note Illustrative della Carta Geologica del Carso Classico Italiano*. Friuli Venezia Giulia: Progetto GEO-CGT, 43. Available at: http://www.regione.fvg.it/rafvg/cms/RAFVG/ambiente-territorio/tutela-ambiente-gestione-risorse-naturali/ (Accessed April 2016).

Della Vedova, B., Castelli, E., Cimolino, A., Vecellio, C., Nicolich, R., and Barison, E. (2008). La valutazione e lo sfruttamento delle acque geotermiche per il riscaldamento degli edifici pubblici. *Rassegna Tecnica Del. Friuli Venezia Giulia* 6, 16–19.

Donda, F., Tinivella, U., Gordini, E., Panieri, G., Volpi, V., and Civile, D. (2019). The origin of gas seeps in the Northern Adriatic Sea. *Italian J. Geosci.* 138 (2), 171.183. doi:10.3301/IJG.2018.34

EMODnet Digital Bathymetry (2018). EMODnet bathymetry consortium. Available at: https://www.emodnet.eu (Accessed September 14, 2018).

EU-DEM (2017). Copernicus land monitoring service. Available at: https://www.eea.europa.eu/data-and-maps/data/copernicus-land-monitoring-service-eu-dem (Accessed December 7, 2017).

Geletti, R., Del Ben, A., Busetti, M., Ramella, R., and Volpi, V. (2008). Gas seeps linked to salt structures in the Central Adriatic Sea. *Basin Res.* 20, 473–487. doi:10.1111/j.1365-2117.2008.00373.x

Gordini, E., Caressa, S., and Marocco, R. (2003). New morpho-sedimentological map of the Trieste Gulf (from punta tagliamento to isonzo mouth). *Atti Del. Museo Friulano di Storia Nat.* 35, 5–29. doi:10.1016/j.quaint.2007.08.044

Gordini, E., Marocco, R., Tunis, G., and Ramella, R. (2004). I depositi cementati del Golfo di Trieste (Adriatico Settentrionale): distribuzione areale, caratteri geomorfologici e indagini acustiche ad alta risoluzione. *Il Quaternario* 17 (2/2), 555–563.

Gordini, E., Falace, A., Kaleb, S., Donda, F., Marocco, R., and Tunis, G. (2012). "Methane-related carbonate cementation of marine sediments and related macroalgal coralligenous assemblages in the northern Adriatic Sea," in *Seafloor geomorphology as benthic habitats*. Editors P. T. Harris and E. K. Baker (Amsterdam, Netherlands: Elsevier), 183–198.

Hackert, C. L., and Parra, J. O. (2003). Estimating scattering attenuation from vugs or karsts. *Geophysics* 68, 1182–1188. doi:10.1190/1.1598111

Helle, H. B., Pham, N. H., and Carcione, J. M. (2003). Velocity and attenuation in partially saturated rocks: poroelastic numerical experiments. *Geophys. Prospect.* 51, 551–566. doi:10.1046/j.1365-2478.2003.00393.x

Hovland, M., and Curzi, P. V. (1989). Gas seepage and assumed mud diapirism in the Italian central Adriatic Sea. *Mar. Pet. Geol.* 6, 161–169. doi:10.1016/0264-8172(89)90019-6

IRDAT-FVG (2017). Infrastruttura Regionale di Dati Ambientali e Territoriali per il Friuli Venezia Giulia. Available at: https://irdat.regione.fvg.it/WebGIS/ (Accessed September 8, 2012).

Jannsen, D., Voss, J., and Theilen, F. (1985). Comparison of methods to determine Q in shallow marine sediments from vertical reflection seismograms*. *Geophys. Prospect.* 33, 479–497. doi:10.1111/j.1365-2478.1985.tb00762.x

Jurkovšek, B., Biolchi, S., Furlani, S., Kolar-Jurkovšek, T., Zini, L., Jež, J., et al. (2016). Geology of the classical Karst region (SW Slovenia–NE Italy). *J. Maps* 12, 352–362. doi:10.1080/17445647.2016.1215941

Lavergne, M., and Willm, C. (1977). Inversion of seismograms and pseudo-velocity logs. *Geophys. Prospect.* 25, 232–250. doi:10.1111/j.1365-2478.1977.tb01165.x

Lin, R., Vesnaver, A., Böhm, G., and Carcione, J. M. (2018). Broad-band viscoacoustic Q-factor imaging by seismic tomography and instantaneous frequency. *Geophys. J. Int.* 214, 672–686. doi:10.1093/gji/ggy168

Lindseth, R. O. (1976). Seislog process uses seismic reflection traces. *Oil Gas J.* 38, 481–488.

Mora, P. (1989). Inversion = migration + tomography. *Geophysics* 54, 1575–1586. doi:10.1190/1.1442625

Mulder, W. A., and Hak, B. (2009). An ambiguity in attenuation scattering imaging. *Geophys. J. Int.* 178, 1614–1624. doi:10.1111/j.1365-246x.2009.04253.x

Nicolich, R., Della Vedova, B., Giustiniani, M., and Fantoni, R. (2004). *Carta del sottosuolo della Pianura Friulana (Map of subsurface of the Friuli Plain)*. LAC-Firenze, Italy. RAFVG–UNITS-DIC, 32.

Petrini, R., Italiano, F., Ponton, M., Slejko, F. F., Aviani, U., and Zini, L. (2013). Geochemistry and isotope geochemistry of the Monfalcone thermal waters (Northern Italy): inference on the deep geothermal reservoir. *Hydrogeol. J.* 21, 1275–1287. doi:10.1007/s10040-013-1007-y

Picotti, S., and Carcione, J. M. (2006). Estimating seismic attenuation (Q) in the presence of random noise. *J. Seism. Explor.* 15, 165–181.

Piffer, G., Rinaldi, M., and Della Vedova, B. (2015). "Well logging for the geothermal reservoir characterization: the Grado geothermal project (Gorizia, Italy)–Part 2," in Proceedings of the geo alp kongress–geologie und hydrogeologie der alpen–geologia e idrogeologia della alpi, Gorizia, Italy, November 5–7, 2015 (Fortezza, Italy: Ordine dei Geologi Regione del

Veneto), 2. Available at: http://www.waterstones-srl.it/wp-content/uploads/2015/11/100x80-A-B.pdf.

Placer, L., Vrabec, M., and Celarc, B. (2010). The bases for understanding of the NW Dinarides and Istria Peninsula tectonics. *Geologija* 53, 55–86. doi:10.5474/geologija.2010.005

Poggiagliolmi, E., and Vesnaver, A. (2014). Instantaneous phase and frequency derived without user-defined parameters. *Geophys. J. Int.* 199, 1544–1553. doi:10.1093/gji/ggu352

Quan, Y., and Harris, J. M. (1997). Seismic attenuation tomography using the frequency shift method. *Geophysics* 62, 895–905. doi:10.1190/1.1444197

Rossi, G., Gei, D., Böhm, G., Madrussani, G., and Carcione, J. M. (2007). Attenuation tomography: an application to gas-hydrate and free-gas detection. *Geophys. Prospect.* 55, 655–669. doi:10.1111/j.1365-2478.2007.00646.x

Rossi, G., Chadwick, R. A., and Williams, G. A. (2011). "Traveltime and attenuation tomography of CO_2 plume at Sleipner," in Expanded abstracts, EAGE annual meeting, Vienna, Austria, May 23–26 2011 (EAGE), A039.

Saha, J. G. (1987). "Relationship between Fourier and instantaneous frequency," in Expanded abstracts, SEG annual meeting, (SEG), 591–594.

Shapiro, S., and Hubral, P. (1999). *Elastic waves in random media*. Berlin, Germany: Springer, 191.

Song, Y., Hu, H., and Han, B. (2020a). Seismic attenuation and dispersion in a cracked porous medium: an effective medium model based on poroelastic linear slip conditions. *Mech. Mater.* 140, 103229. doi:10.1016/j.mechmat.2019.103229

Song, Y., Rudnicki, J. W., Hu, H., and Han, B. (2020b). Dynamics anisotropy in a porous solid with aligned slit fractures. *J. Mech. Phys. Solids* 137, 103865. doi:10.1016/j.jmps.2020.103865

Taner, M. T., Koehler, F., and Sheriff, R. E. (1979). Complex seismic trace analysis. *Geophysics* 44, 1041–1063. doi:10.1190/1.1440994

Tonn, R. (1991). The determination of the seismic quality factor Q from vsp data: a comparison of different computational Methods1. *Geophys. Prospect.* 39, 1–27. doi:10.1111/j.1365-2478.1991.tb00298.x

Trobec, A., Busetti, M., Zgur, F., Baradello, L., Babich, A., Cova, A., et al. (2018). Thickness of marine holocene sediment in the Gulf of Trieste (Northern Adriatic Sea). *Earth Syst. Sci. Data* 10, 1077–1092. doi:10.5194/essd-10-1077-2018

Tura, A., Hanitzsch, C., and Calandra, H. (1998). 3-D AVO migration/inversion of field data. *Lead. Edge* 17, 1578. doi:10.1190/1.1437898

Van der Sluis, A., and Van der Vorst, H. A. (1987). "Numerical solution of large, sparse linear algebraic systems arising from tomographic problems," in *Seismic tomography with applications in global seismology and exploration geophysics*. Editor G. Nolet (Dordrecht: Reidel), 49–83.

Vesnaver, A. (1994). Towards the uniqueness of tomographic inversion solutions. *J. Seism. Explor.* 3, 323–334.

Vesnaver, A. (2017). Instantaneous frequency and phase without unwrapping. *Geophysics* 82, F1–F7. doi:10.1190/geo2016-0185.1

Vesnaver, A. (1996a). The contribution of reflected, refracted and transmitted waves to seismic tomography: a tutorial. *First Break* 14, 159–168. doi:10.3997/1365-2397.1996010

Vesnaver, A. L. (1996b). Ray tracing based on Fermat's principle in irregular grids1. *Geophys. Prospect.* 44, 741–760. doi:10.1111/j.1365-2478.1996.tb00172.x

Vesnaver, A., and Böhm, G. (2000). Staggered or adapted grids for seismic tomography?. *Lead. Edge* 19, 944–950. doi:10.1190/1.1438762

Vesnaver, A., Böhm, G., Madrussani, G., Rossi, G., and Granser, H. (2000). Depth imaging and velocity calibration by 3D adaptive tomography*. *First Break* 18, 303–312. doi:10.1046/j.1365-2397.2000.00093.x

Vesnaver, A., Lin, R., and Böhm, G. (2016). Merging macro- and micro-models for a broadband estimation of the Q factor. *Soc. Explor. Geophys.*, 3613–3617. doi:10.1190/segam2016-13859201.1

Vesnaver, A., Böhm, G., Cance, P., Dal Cin, M., and Gei, D. (2020). Windowless Q-factor tomography by the instantaneous frequency. *Geophys. Prospect.* 68, 2611–2636. doi:10.1111/1365-2478.13020

Vesnaver, A., and Lin, R. (2019). Broadband Q-factor tomography for reservoir monitoring. *J. Appl. Geophys.* 165, 1–15. doi:10.1016/j.jappgeo.2019.04.004

Ward, R. W., and Toksöz, M. N. (1971). Causes of regional variation of magnitude. *Bull. Seismol. Soc. Am.* 61, 649–670.

Wu, R.-S. (1985). Multiple scattering and energy transfer of seismic waves–separation of scattering effect from intrinsic attenuation–I. Theoretical modelling. *Geophys. J. Int.* 82, 57–80. doi:10.1111/j.1365-246x.1985.tb05128.x

Zampa, L. S. (2020). Technical Report 05/2020OGS. New bathymetric maps of the north east Adriatic Sea. Available at: https://www2.eecs.berkeley.edu/Pubs/TechRpts/ (Accessed October 5, 2020).

Žumer, J. (2004). Odkritje podmorskih termalnih izvirov. *Geografski Obzornik* 51, 11–17.

Conflict of Interest: The authors declare that the research was conducted in the absence of any commercial or financial relationships that could be construed as a potential conflict of interest.

Copyright © 2021 Vesnaver, Böhm, Busetti, Dal Cin and Zgur. This is an open-access article distributed under the terms of the Creative Commons Attribution License (CC BY). The use, distribution or reproduction in other forums is permitted, provided the original author(s) and the copyright owner(s) are credited and that the original publication in this journal is cited, in accordance with accepted academic practice. No use, distribution or reproduction is permitted which does not comply with these terms.

frontiers in Earth Science

ORIGINAL RESEARCH
published: 01 April 2021
doi: 10.3389/feart.2021.641637

Numerical Investigation of the Effect of Heterogeneous Pore Structures on Elastic Properties of Tight Gas Sandstones

Zhiqi Guo[1], Xiaoying Qin[1], Yiming Zhang[2], Cong Niu[2], Di Wang[2] and Yun Ling[2]*

[1] College of Geo-Exploration Science and Technology, Jilin University, Changchun, China, [2] CNOOC Research Institute Co., Ltd., Beijing, China

Strong heterogeneity of pore microstructures leads to complicated velocity-porosity relationships in tight sandstone that cannot be well explained by conventional empirical formulas. To better understand the effect of complex pore structures on elastic properties of tight gas sandstone, we compared three rock physics models. In the first model, we used a single aspect ratio value to quantify varied pore geometry in the tight sands. In the second model, complex pore space was equivalent to the combination of high-aspect-ratio round pores (stiff pores) and low-aspect-ratio compliant microcracks (soft pores). In the third multiple pore-aspect-ratio model, pore spaces are represented using a set of pores with varied values of aspect ratio following statistical normal distribution. Modeling results showed that complex velocity-porosity relationships could be interpreted by the variations in pore aspect ratio in the first model, by the fraction of soft pores in the second model, and by the mean value and variance in the third statistical model. For a given mean value in the third model, higher variance of the multiple pore-aspect-ratio indicated stronger heterogeneity of pore spaces. Further studies on rock physical inversion showed that, compared with the first single pore-aspect-ratio model, the second dual-pore model gave better prediction in shear wave velocity by regarding the soft pore fraction as a fitting parameter. This finding revealed that the dual-pore model could be a more realistic representation of tight sandstone. The third statistical model showed comparable precision in the prediction of shear wave velocity compared with the dual-pore model; however, uncertainty existed for simultaneously determining mean value and variance of pore aspect ratio. On the basis of the dual-pore model, we evaluated the elastic modulus of dry frames of the tight sandstone using logging data in a borehole. Compared with empirical formulas, such as the Krief methods, the method in this paper provided a more rigorous way to determine elastic properties of dry frames for the tight sandstone. Comparisons of rock physical modeling methods offer a better understanding of the microstructures controlling the elastic behaviors of tight gas sandstone.

Keywords: tight gas sandstone, rock physics, pore structure, dry frame, elastic properties

OPEN ACCESS

Edited by:
Jing Ba,
Hohai University, China

Reviewed by:
Hemin Yuan,
China University of Geosciences, China
Xiao He,
Institute of Acoustics, Chinese Academy of Sciences, China

****Correspondence:***
Zhiqi Guo
zhiqiguo@aliyun.com

Specialty section:
This article was submitted to Solid Earth Geophysics, a section of the journal Frontiers in Earth Science

Received: *14 December 2020*
Accepted: *15 March 2021*
Published: *01 April 2021*

Citation:
Guo Z, Qin X, Zhang Y, Niu C, Wang D and Ling Y (2021) Numerical Investigation of the Effect of Heterogeneous Pore Structures on Elastic Properties of Tight Gas Sandstones. Front. Earth Sci. 9:641637. doi: 10.3389/feart.2021.641637

INTRODUCTION

Tight sandstone of low porosity and low permeability usually represent complex pore structures, which significantly impacts elastic properties of the tight sandstone. Complicated elastic behaviors of the tight sandstone with heterogeneous pore structures cannot be properly described by traditional rock physical methods that rely on empirical relations. Thus, it is necessary to investigate elastic properties related to heterogeneity using rock physical methods that incorporate pore structures.

The effect of microcracks on the rock elastic properties has been studied by Stuart and David (1977) in their theoretical rock physics models. After that, numerous works have been dedicated to the connection between elastic properties and microstructures in the tight sandstone reservoirs. According to study by Tutuncu et al. (1994), the existence of microcracks with low aspect ratio leads to the phenomenon that the P- and S-wave velocities *Vp* and *Vs* are sensitive to pressure changes. The presence of low-aspect-ratio pores or microcracks can explain the complex relationship between velocity and porosity in tight sandstone gas reservoirs (Smith et al., 2009; Vernik and Kachanov, 2010). Ruiz and Cheng (2010) introduced two sets of pores with different aspect ratios in the rock physical modeling, and applied the model to the prediction of elastic modulus of a tight sandstone.

Yin et al. (2017) conducted experimental measurements and rock physical modeling to investigate the effect of pressure and fluid on elastic moduli of the tight sandstone, and found that microcracks in tight sandstone dominate the changes in elastic properties of the rock. Yan et al. (2011) employed the Mori–Tanaka model (Mori and Tanaka, 1973) to analyze experimental measurements on the dry frame of sandstone of low porosity. Deng et al. (2015) explored the influence of pore structures on velocity dispersion of tight sandstone, and found that the existence of microcracks is related to the heterogeneity of the rock skeleton and the fluid distribution. Ba et al. (2017) established a double dual-pore model for the anelasticity of P-wave propagation to analyze the effect of dissipation mechanisms caused by the heterogeneity of fabric and fluid distribution. Wang (2017) proposed a rock physics model for the prediction of gas-bearing sandstone properties based on the measurements and analysis on data for tight sandstone samples. Wang et al. (2020) incorporated the Bayes discriminant and deterministic rock physics modeling method to implement joint probabilistic fluid discrimination of tight sandstone reservoirs.

In this study, we built three rock physics models for the description of elastic properties associated with heterogeneous pore structures in tight gas sandstone. Using the three built models, we then predicted shear wave velocity and inverted corresponding parameters of pore structure to evaluate and compare the applicability of the models. Finally, we used the built model to estimate elastic modulus of the rock skeleton of tight gas sandstone.

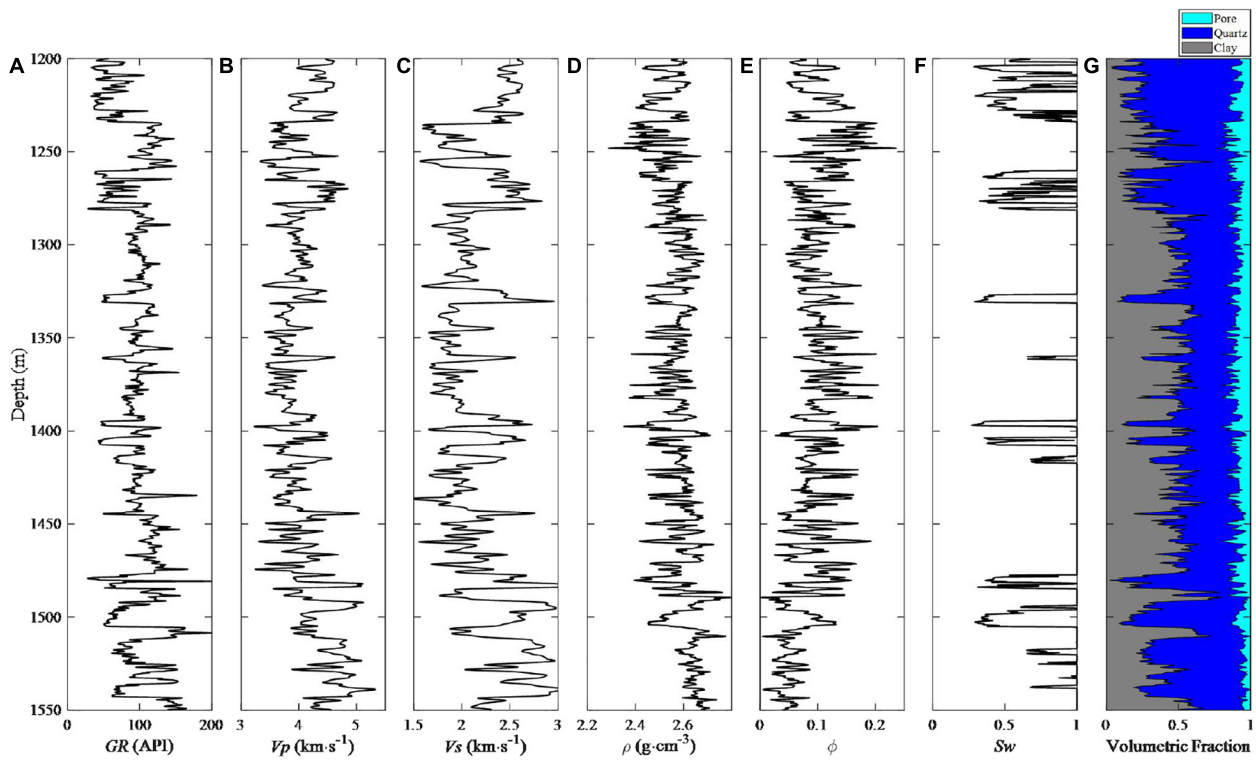

FIGURE 1 | Logging data of the tight gas sandstone reservoirs in the Ordos Basin, China. **(A)** Gamma Ray. **(B)** P-wave velocity *Vp*. **(C)** S-wave velocity *Vs*. **(D)** Density ρ. **(E)** Porosity ϕ. **(F)** Water saturation *Sw*. **(G)** Volume fraction of compositions.

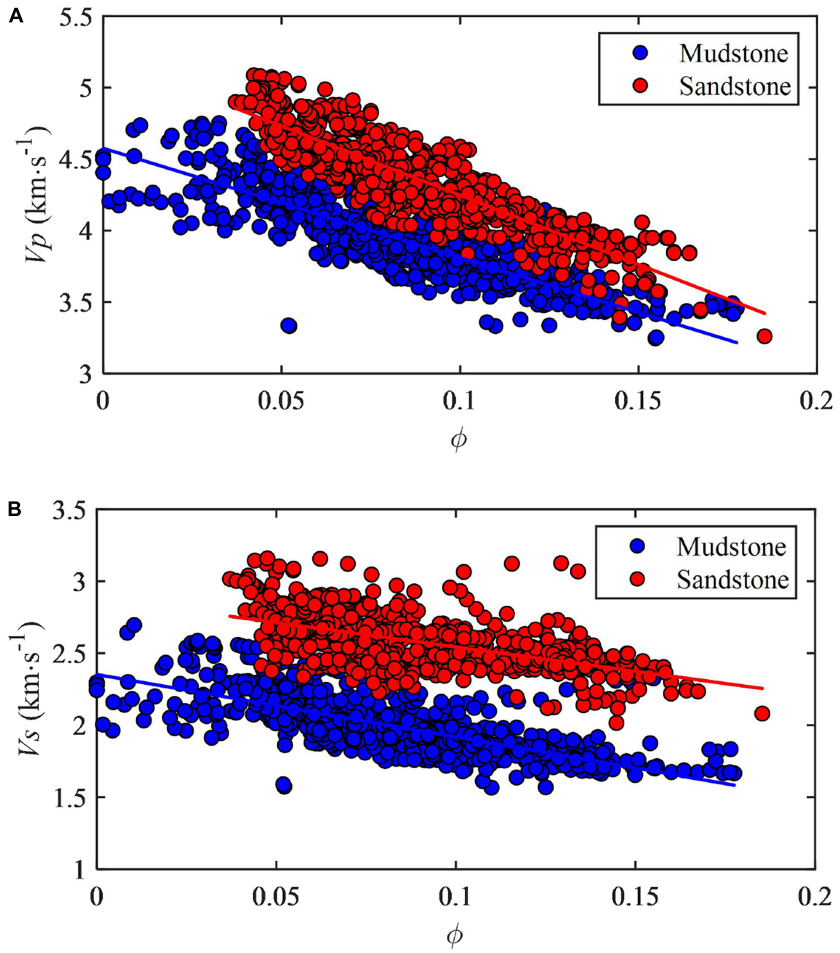

FIGURE 2 | Cross plot of **(A)** P-wave velocity *Vp* versus ϕ and **(B)** S-wave velocity *Vs* versus ϕ.

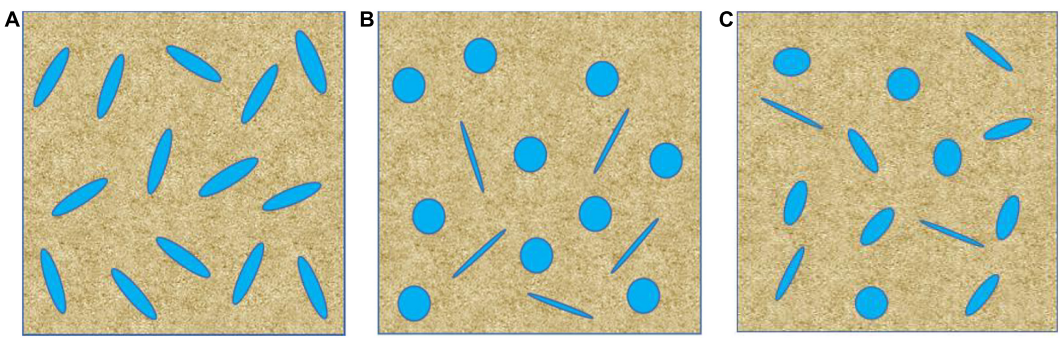

FIGURE 3 | Schematics of rock physics models for tight sandstone: **(A)** single pore-aspect-ratio model, **(B)** dual-pore model, and **(C)** multiple pore-aspect-ratio model.

WELL DATA OF TIGHT GAS SANDSTONE RESERVOIR

Figure 1 shows the logging data from the tight gas sandstone reservoir in the Ordos Basin, China. The strata consist of the interbed of sandstone and mudstone. The tight sandstone corresponds relatively local low value of GR. Compared with the mudstone, the sandstone has relatively higher P-wave and S-wave velocities around 4.5 km/s and 2.5 km/s, and a relatively lower density of approximately 2.5 g cm^{-3}. Porosity generally is below 15% for the sandstone. As illustrated by the logging data of water saturation, the sandstone has a gas saturation usually higher than

40%. Data of the mineralogical volume show variations in the fraction of quartz and clay in the formation.

Using the logging data in **Figures 1**, **2** show the variations in P-wave velocity *Vp* and S-wave velocity *Vs* versus porosity ϕ for sandstone and mudstone in the strata. Although velocities generally decrease with increasing porosity, the data points represent certain degree of scatting distributions, which indicates that porosity is not the only factor that affected the elastic properties of the tight sandstone. According to the discussion given by Smith et al. (2009) and Ruiz and Cheng (2010), both the volume of pore space (porosity) and the distribution or geometry of the pore (such as aspect ratio) have an impact on the elastic modulus of the tight sandstone. Thus, it is necessary to establish rock physical models that consider complex pore structures to quantitatively predict elastic behaviors for tight sandstone reservoirs.

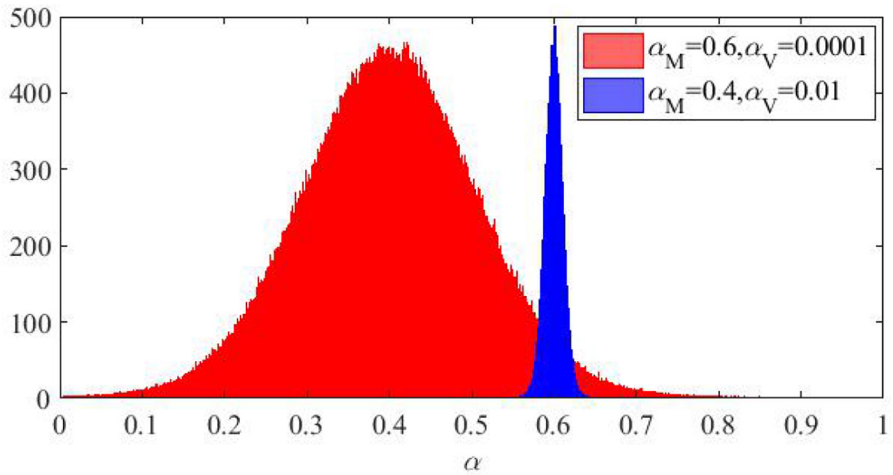

FIGURE 4 | Histogram of normal distributions of pore aspect ratio quantified by α_M and α_V.

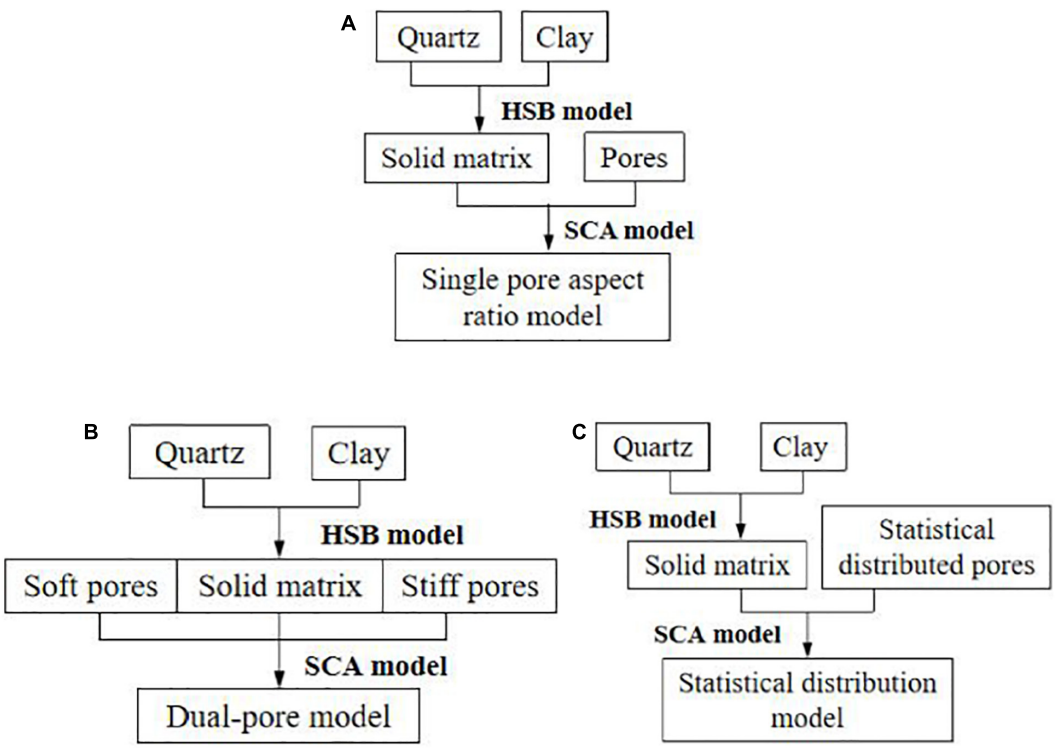

FIGURE 5 | Workflow for the construction of rock physics models corresponding to **Figure 3**: **(A)** single pore-aspect-ratio model, **(B)** dual-pore model, and **(C)** multiple pore-aspect-ratio model.

TABLE 1 | Elastic properties of constituents used in the rock physical model.

	Bulk modulus (GPa)	Shear modulus (GPa)	Density (g cm^{-3})
Quartz	37	44	2.65
Clay	21	7	2.6
Water	2.5	–	1
Gas	0.063	–	0.11

ROCK PHYSICS MODEL

Theory

As illustrated by the schematic diagrams in **Figure 3**, we compare three methods for modeling heterogeneous pore structures of tight sandstone. **Figure 3A** shows the single pore-aspect-ratio model, where all pores have the same geometry represented by the pore aspect ratio. **Figure 3B** shows the dual-pore model, where the total porosity ϕ_{Total} is equivalent to the combination of two parts, including the stiff pores with a porosity ϕ_{Stiff} and soft pores with a porosity ϕ_{Soft}, that is, $\phi_{Total} = \phi_{Stiff} + \phi_{Soft}$. The stiff pores are set to be spherical and have an aspect ratio $\alpha_{Stiff} = 1$, whereas the soft pores are assumed to have an aspect ratio $\alpha_{Soft} = 0.01$. We use the fraction of soft pores in the total pore space, that is, $f_{Soft} = \phi_{Soft} / \phi_{Total}$, to represent heterogeneous distribution of the pore space in the dual-pore model.

Figure 3C illustrates that the value of the pore aspect ratio is assumed to have the normal distribution. In this model, heterogeneous distributions of pore space are controlled by the mean value α_M of the pore aspect ratio and corresponding variance α_V. Accordingly, **Figure 4** shows two cases of normal distribution of pore aspect ratio, where α_M and α_V are 0.4 and 0.01 for the first scenario, and 0.6 and 0.0001 for the second. A higher value of α_M means that the pores tend to be round and a higher α_V implies that the pore geometry has a wide range of shapes.

The rock physical methods for the three cases in **Figure 3** are illustrated in **Figure 5**. In all the three models, we use the average of the Hashin–Shtrikman bounds (HSB) (Hashin and Shtrikman, 1963) to obtain elastic properties of solid matrix, and then apply the self-consistent approximation (SCA) method (Berryman, 1995; Mavko et al., 2009) to add pores with different geometries and distributions as discussed above. Elastic properties of minerals and fluids used in the rock physical model are given in **Table 1**.

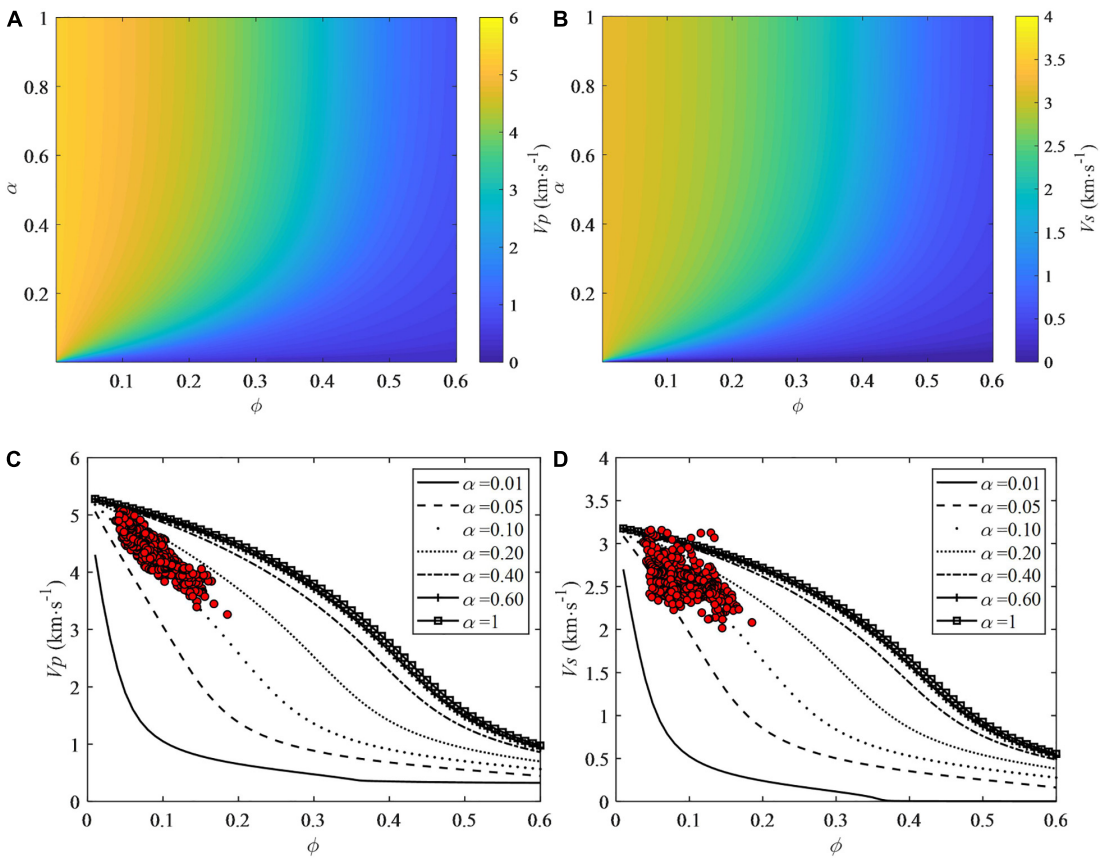

FIGURE 6 | (A) P-wave velocity *Vp* and **(B)** S-wave velocity *Vs* varying with pore aspect ratio α and porosity ϕ for the single pore-aspect-ratio model of the tight sandstone. **(C)** P-wave velocity *Vp* and **(D)** S-wave velocity *Vs* varying with porosity ϕ for a series of pore aspect ratio α for the single pore-aspect-ratio model with logging data from the target zone overlapped.

For the construction of the rock physical models in **Figure 5**, the SCA theory for multi-phase media is as follows:

$$\sum_{j=1}^{n} f_j(K_j - K_{SC}^*)P^{*j} = 0 \quad (1)$$

$$\sum_{j=1}^{n} f_j(\mu_j - \mu_{SC}^*)Q^{*j} = 0 \quad (2)$$

where $_j$ is the j-th material, f_j is its volume fraction, $_{K_j}$ and $_{\mu_j}$ represent the bulk modulus and shear modulus of the j-th component, $_{K_{SC}^*}$ and $_{\mu_{SC}^*}$ represent the calculated equivalent bulk modulus and shear modulus, and $_{P^{*i}}$ and $_{Q^{*i}}$ are geometric factors of the inclusion added to the background medium.

The bulk module of the fluid mixture consisting of gas and water is calculated by the Wood (1955) theory, as follows:

$$K_f = \left[S_w/K_w + S_g/K_g\right]^{-1} \quad (3)$$

where $_{K_w}$ and $_{K_g}$ are bulk modulus of water and gas, respectively, $_{S_w}$ and $_{S_g}$ are water and gas saturation, respectively.

The density of the fluid mixture is as follows:

$$\rho_f = S_w\rho_w + S_g\rho_g \quad (4)$$

where $_{\rho_w}$ and $_{\rho_g}$ are the densities of water and gas, respectively.

Rock Physical Modeling

Figures 6A,B show the *Vp* and *Vs* varying with pore aspect ratio α and porosity ϕ for the single pore-aspect-ratio model of the tight sandstone. It can be observed that *Vp* and *Vs* decrease rapidly with increasing porosity, especially for lower-valued pore aspect ratio α, because the presence of elongated pores can dramatically reduce the elastic modulus of rocks.

Accordingly, **Figures 6C,D** illustrate calculated *Vp* and *Vs* varying with porosity ϕ for a set of pore aspect ratio α that has a value ranging from 0.05 to 0.2. Corresponding logging data from the target zone are overlapped. The relationship between *Vs* and ϕ is more scattered compared with the relationship between *Vp* and ϕ.

In **Figures 7A,B**, the presence of small amount of soft pores can dramatically reduce velocities of the tight sandstone. Accordingly, **Figures 7C,D** indicates that the parameter f_{Soft} ranges from 0.05 to 0.2 for the *Vp* data and from 0.05 to 0.4 for the *Vs* data for the interpretation of the velocity-porosity relationships.

Similarly, **Figures 8A,B** show velocities that change for varied mean value α_M and variance α_V of pore aspect ratio in the multiple pore-aspect-ratio model. A higher value of α_M corresponds to the presence of more spherical pores and thus results in higher modulus and velocities. The value of α_V denotes the spread range of the pore aspect ratio, and

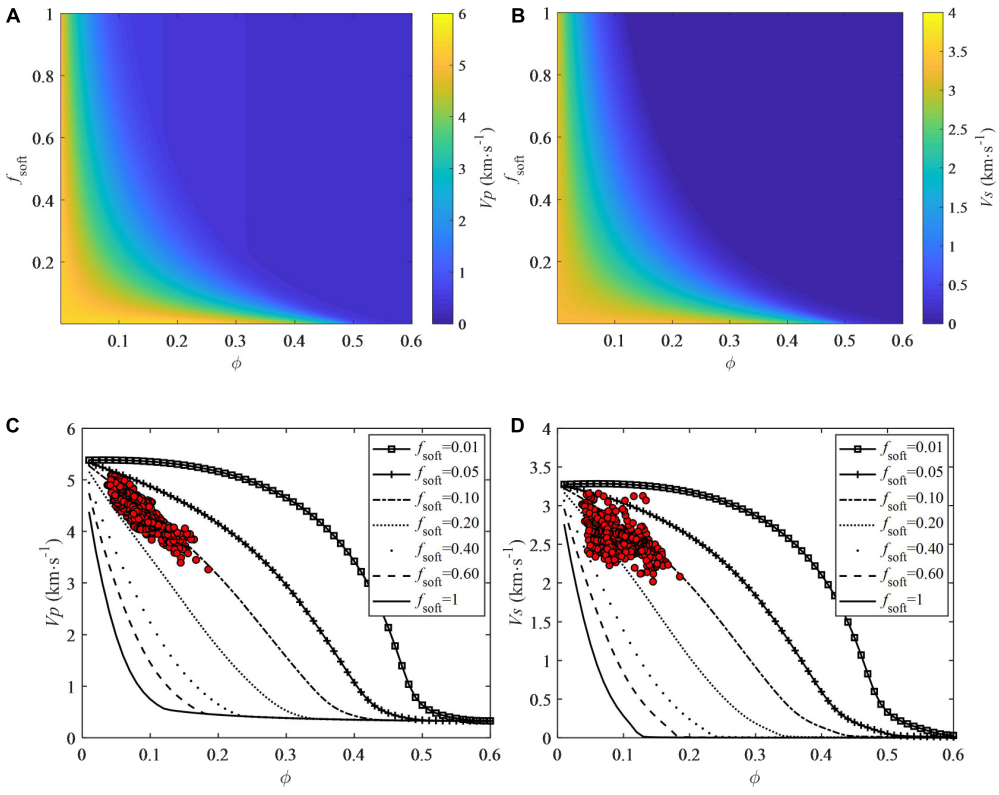

FIGURE 7 | (A) P-wave velocity *Vp* and **(B)** S-wave velocity *Vs* varying with the proportion of soft pore f_{soft} and porosity ϕ for the dual-pore model of the tight sandstone. **(C)** P-wave velocity *Vp* and **(D)** S-wave velocity *Vs* varying with porosity ϕ for a series of parameter f_{soft} for the dual-pore model with logging data from the target zone overlapped.

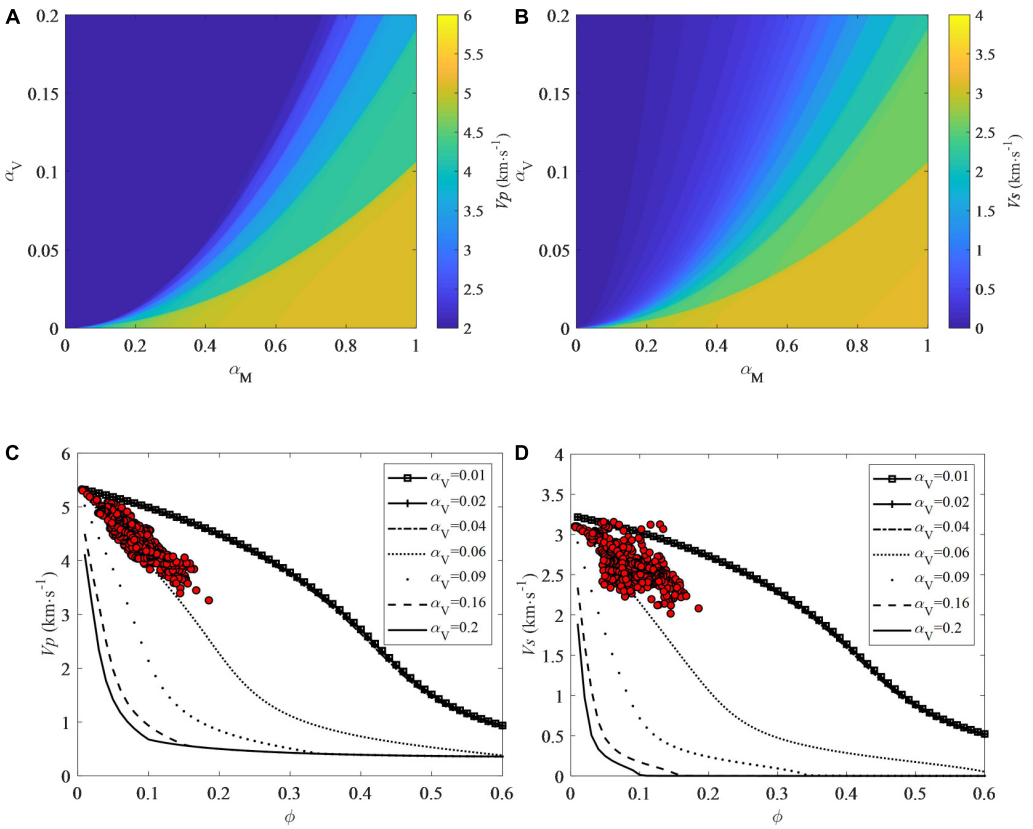

FIGURE 8 | (A) P-wave velocity *Vp* and **(B)** S-wave velocity *Vs* varying with mean value α_M and variance α_V of pore aspect ratio for the normal distribution model of the tight sandstone. **(C)** P-wave velocity *Vp* and **(D)** S-wave velocity *Vs* varying with porosity ϕ for a series of values of α_V with the assumption α_M = 0.75 in the normal distribution model with logging data from the target zone overlapped.

a higher α_V means more heterogeneity of pore geometry distribution. For a specific value of α_M, the increase in α_V reduces velocities.

In **Figures 8C,D**, we assume α_M = 0.75 in the tight sandstone. We find that α_V should vary from 0.01 and 0.06 to interpret the velocity-porosity relationships of the overlapped logging data.

Figures 6–8 show rock physical modeling using the constructed models in **Figure 5**, where the procedures for calculation are described in details. The purpose of the rock physical modeling is to illustrate how the porosity and pore geometry parameters influence the *Vp* and *Vs*. As shown in **Figures 6–8**, it means that the model can interpret the data if the overlapped data fall into the ranges covered by the calculated curves. Then, it is feasible to conduct rock physical inversion to estimate pore geometry parameter as shown in **Figure 9**.

Vs PREDICTION USING THE BUILT ROCK PHYSICS MODELS

On the basis of the constructed rock physics models shown in **Figure 5**, we predict S-wave velocity *Vs*, when the information of porosity, mineral compositions, and fluid saturation is known as illustrated in **Figure 1**.

According to the method by Guo and Li (2015), we find the best fit parameters, including pore aspect ratio α, the proportion of soft pores f_{soft}, and the variance of pore aspect ratio α_V in the three models by adjusting the values of them to minimize the absolute difference between the P-wave velocities *Vp* measured in the well and those calculated by the rock physics models in **Figure 5**. The S-wave velocities *Vs* calculated by the estimated α, f_{soft} and α_V are regarded as the predicted values.

Figures 9A–C show the prediction results from the three rock physics models, where all of the prediction results provide reasonable estimates of *Vs*. The correlation coefficients between the predicted and measured *Vs* are 0.9077, 0.9375, and 0.9277, respectively. As illustrated in **Figure 9B**, the inversion based on the dual-pore model generates the best result for the *Vs* prediction. Theoretically, the multiple pore-aspect-ratio model in **Figure 5C** may work better, as there always exists a certain normal distribution of the multiple pore-aspect-ratio in the model to fit the true scenario. However, it may takes too many parameters to determine, which is unlikely to realize. Comparatively, the dual-pore model shows the advantage to obtain a relatively fine and stable result without solving too many parameters.

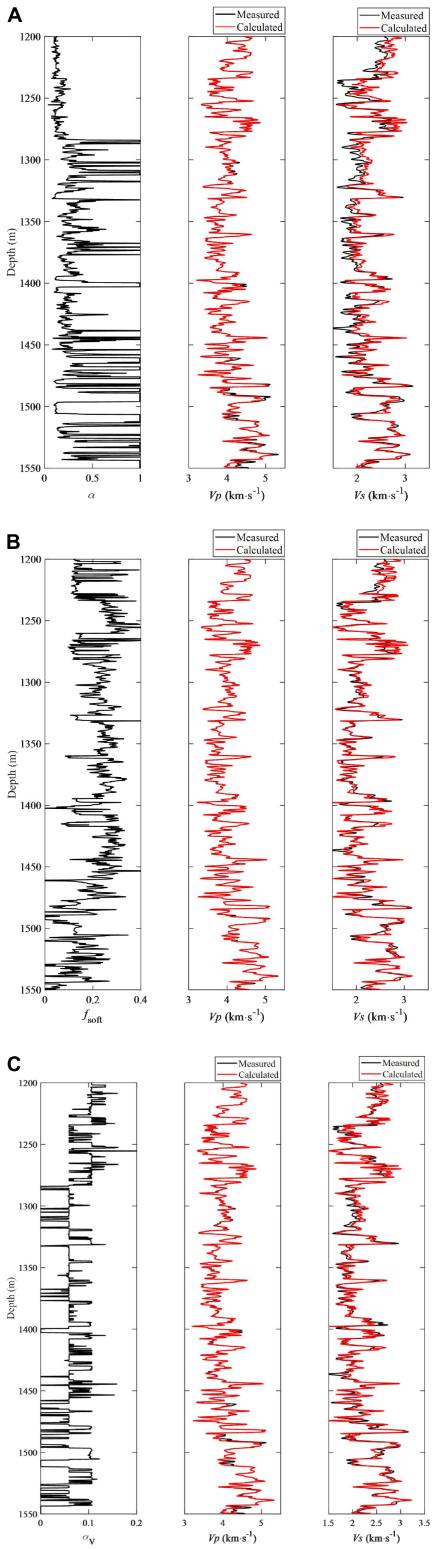

FIGURE 9 | (A) Inverted pore aspect ratio, estimated *Vp* and *Vs* by the single pore-aspect-ratio model. **(B)** Inverted proportion of soft pores, estimated *Vp* and *Vs* by the dual-pore model. **(C)** Inverted variance of pore aspect ratio, estimated *Vp* and *Vs* by the multiple pore-aspect-ratio. Black curves are the measured logging data while and red curves show the predicted results.

ELASTIC MODULUS OF DRY FRAME OF TIGHT SANDSTONE

Calculation of Elastic Modulus for Dry Frame

The elastic modulus of rock skeleton that are determined by minerals, porosity, and pore structures are the key input parameters for various rock physical theories, including the Gassmann fluid substitution theory (Gassmann, 1951), the Biot theory (Biot, 1955) and the BISQ theory (Dvorkin and Nur, 1993; Dvorkin et al., 1994).

Although the elastic modulus of the rock skeleton can be obtained through laboratory measurements of specimens, it is difficult to estimate these properties for *in situ* underground formations. Empirical formulas usually are used to estimate elastic modulus of the dry frame.

Based on the experimental data from Raymer et al. (1980); Krief et al. (1990) proposed the nonlinear empirical relationships between the rock skeleton modulus and porosity, as shown by the followings:

$$K_{\mathrm{dry}} = K_0(1-\phi)^{m/(1-\phi)} \tag{5}$$

$$\mu_{\mathrm{dry}} = \mu_0(1-\phi)^{m/(1-\phi)} \tag{6}$$

where K_0 and μ_0 are the bulk and shear modulus of the solid matrix, respectively, and φ is porosity. Empirical parameter m generally ranges from 0 to 10, which is related to porosity, pressure, temperature, clay content, and other lithology factors (Han et al., 1986).

Because these empirical relationships between elastic modulus of rock skeleton and porosity were established based on data from specific study areas, it may limit the application of the methods to other field data which represent different lithology or microstructures.

In this work, based on the inverted results of pore structures using the dual-pore model shown in **Figure 9B**, we can calculate the elastic modulus of rock skeleton in a manner that represents more physical meaning. We conduct rock physical modeling to calculate the elastic modulus of rock skeleton by using the inverted values of pore structure parameter f_{soft}, and by setting the bulk and shear modulus of the pore fillings to 0. The calculation results are shown in **Figure 10**.

Data points in **Figure 11** show the elastic modulus of skeleton predicted by the method presented discussed above. Curves in **Figure 11** are the elastic modulus estimated by the Krief empirical formulas in Eqs 5 and 6. Due to the presence of complex pore structure in tight sandstone, the relationship between the modulus of the skeleton and porosity are scattering and thus cannot be well described by adjusting the empirical parameter m in the Krief theory.

Comparatively, the methods presented in this study have considered the influence of minerals, porosity, and pore structures in the calculation of the elastic modulus of dry frame, which show more physical meaning compared to the Krief empirical relations.

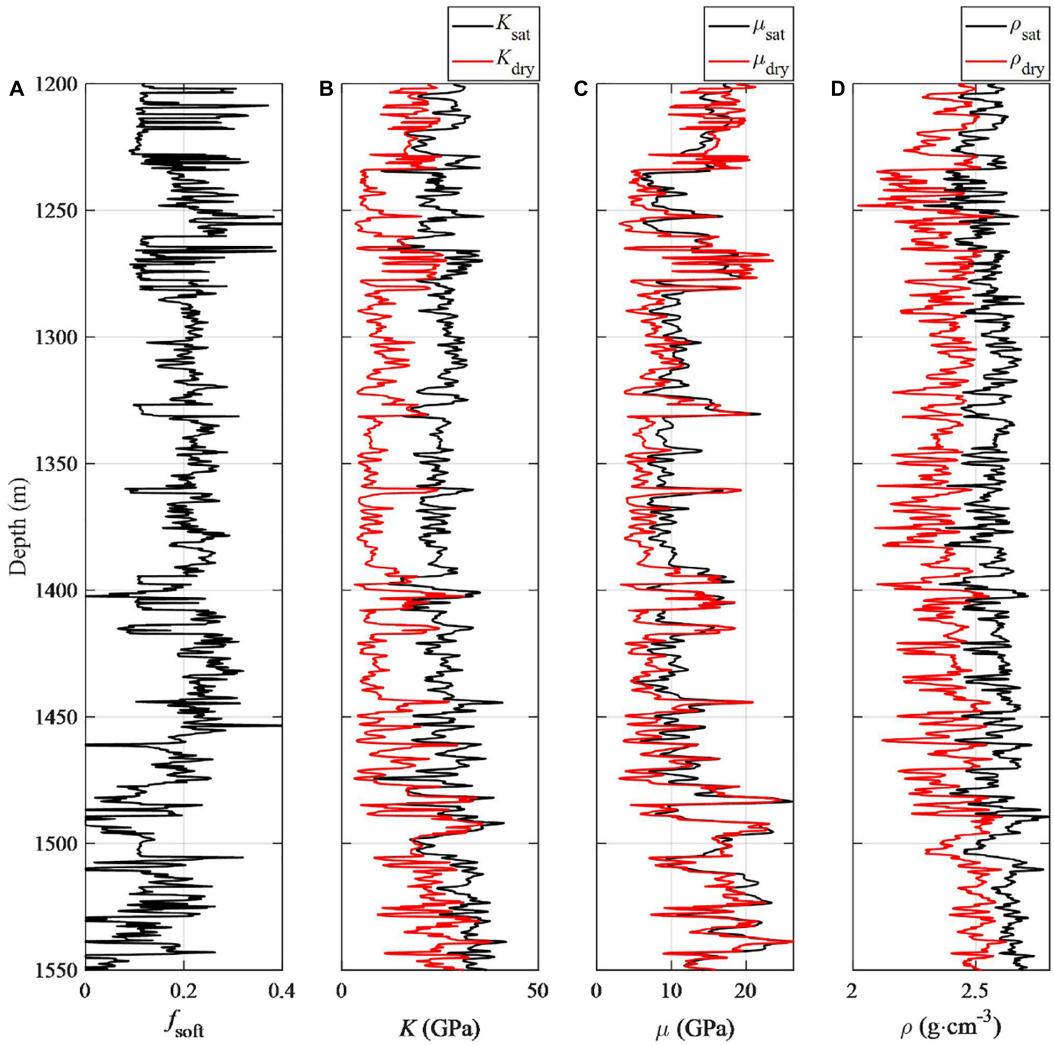

FIGURE 10 | (A) Inverted soft pore fraction f_{soft} as given by **Figure 9**; **(B)** bulk modulus and **(C)** shear modulus of rock skeleton, and **(D)** density. Red curves show the calculated values while the black curves denote measured logging data.

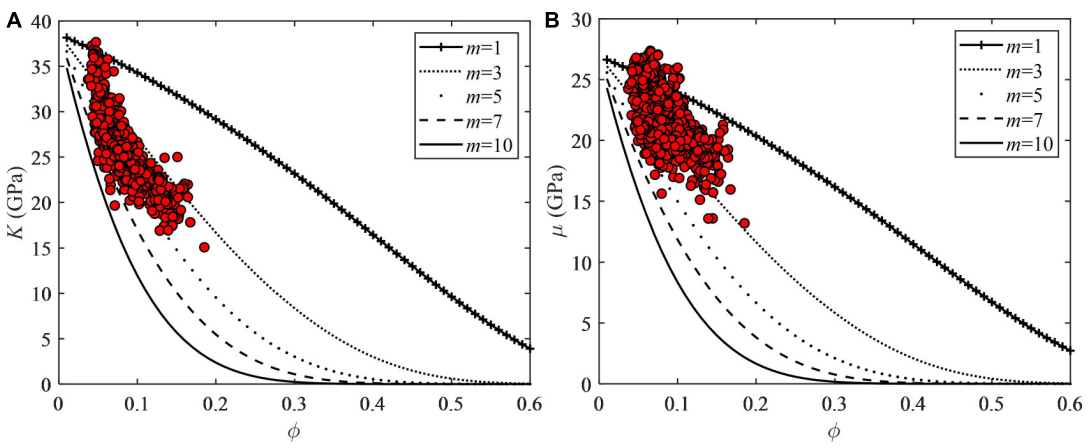

FIGURE 11 | Crossplot of **(A)** rock skeleton bulk modulus K versus porosity ϕ and **(B)** rock skeleton shear modulus μ versus porosity ϕ. Data points indicate elastic modulus calculated by the dual-pore model and curves show the elastic properties modeled by the Krief's empirical relationship.

Analysis on Elastic Properties of Dry Frame

Figure 12A is the crossplot of the Poisson's ratio versus porosity of the fluid-saturated tight sandstone from the logging data in **Figure 1**. In **Figure 12A**, the Poisson's ratio of tight sandstone is mainly between 0.2 and 0.3 when the porosity is less than 0.1. Porosity that is greater than 0.1 corresponds to higher gas saturation and relatively lower Poisson's ratio. **Figure 12B** is the crossplot of the Poisson's ratio versus porosity of the rock skeleton of the same sandstone, with calculated elastic modulus of the rock skeleton shown in **Figure 10**. In **Figure 12B**, it is found that the Poisson's ratio of the rock skeleton of the sandstone decreases with increasing porosity.

For further analysis, **Figures 12C,D** are the crossplot of the Poisson's ratio versus the micro-crack porosity ϕ_{soft} ($\phi_{soft} = \phi f_{soft}$) of the fluid-saturated rock and the rock skeleton of the tight sandstone, respectively. **Figure 12D** shows that the micro-crack porosity has a linear relationship with the Poisson's ratio of the rock skeleton. The decrease in the Poisson's ratio of the dry frame corresponds to an increase in the fraction of micro-cracks. It reveals that the Poisson's ratio of the rock skeleton is sensitive to the heterogeneity of pore spaces.

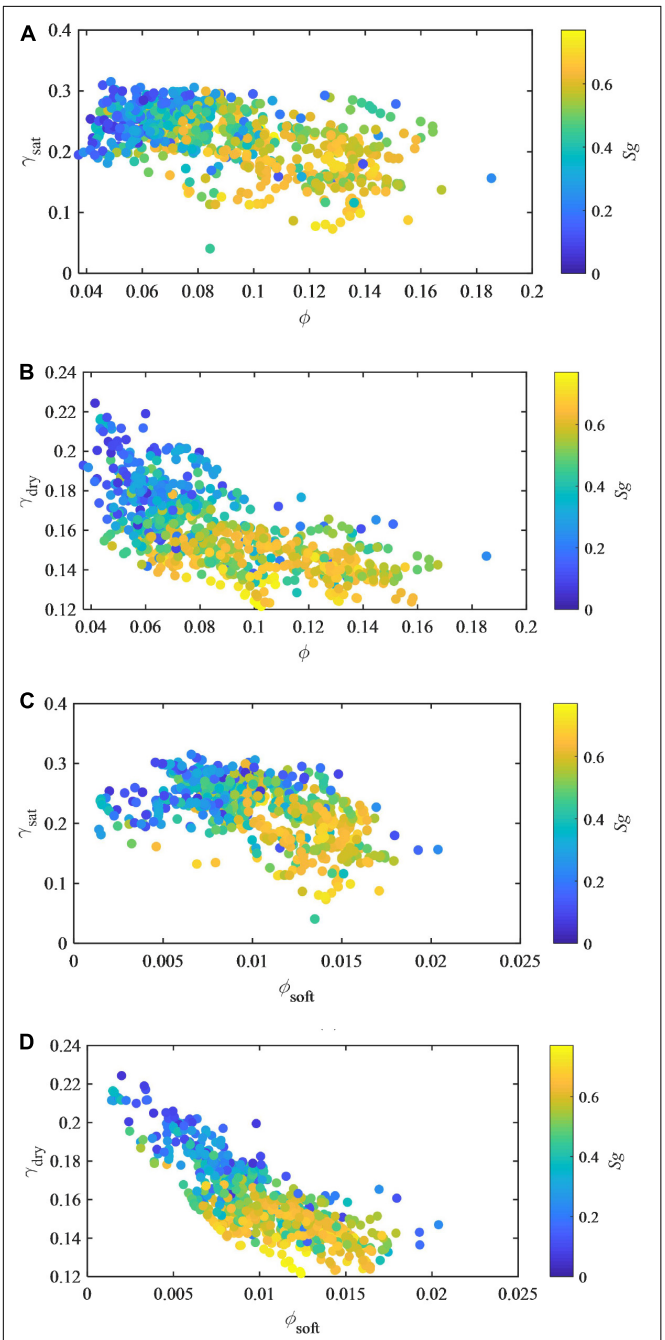

FIGURE 12 | Crossplot of **(A)** the Poisson's ratio versus porosity of fluid-saturated tight sandstone; **(B)** the Poisson's ratio versus porosity of dry frame of tight sandstone; **(C)** the Poisson's ratio versus soft porosity of fluid-saturated tight sandstone; **(D)** the Poisson's ratio versus soft porosity of tight sandstone rock skeleton. Gas saturation S_g is color-coded for all the crossplots.

DISCUSSION AND CONCLUSION

For the tight gas sandstone with low porosity and permeability, porosity is not the only factor that affects elastic behaviors of the sandstone. Heterogeneity of pore spaces should be considered in rock physical modeling to reasonably predict elastic modulus.

We established three rock physics model to describe the complex pore structure of tight gas sandstone reservoirs. In the single pore-aspect-ratio model, all pores are assumed to have the same pore aspect ratio. In the dual-pore model, the pore space is equivalent to a combination of stiff and soft pores. In the multiple pore-aspect-ratio model, the aspect ratio mean value and variance are used to represent statistical normal distribution of pores with varied aspect ratio.

Results for pore structure inversion and S-wave velocity prediction show that the dual-pore model works well and behaves as a more appropriate representation of the tight gas sandstone compared to the other model built in this study. The inverted parameter of soft pore fraction f_{Soft} can explain the heterogeneity of pore structure of the tight sandstone. Increasing fraction of soft pores can dramatically decrease elastic modulus of the tight sandstone.

We applied the dual-pore rock physics model to estimate elastic modulus of rock skeleton. Compared to conventional empirical formulas, such as the Krief methods, the methods presented in this study considered the influence of minerals, porosity and pore structures in the calculation of the elastic modulus of dry frame of tight sandstone, which show more physical meaning and is more appropriate for the dry frame representing heterogeneous pore structures.

As to the applicability of the built rock physics models, it is not sure whether these models are valid for the tight sandstone from different areas. However, the rock physics models that are constructed using effective medium theories generally work well than those empirical models. The reason is that the former ones follow certain kinds of physical laws by incorporating parameters

with specific physical meaning (for example, aspect ratio of pores). If the geological scenario agrees with the assumptions of the effective medium theories, the built model will work well and generate good results. The application results show that the models in this study are suitable for the tight sandstone of the research area. However, it may be that not all the tight sands are the same. So, the applicability of the built rock physics models should be carefully checked when applied to other fields.

DATA AVAILABILITY STATEMENT

The original contributions presented in the study are included in the article/supplementary material, further inquiries can be directed to the corresponding author/s.

AUTHOR CONTRIBUTIONS

ZG contributed as the major author of the manuscript. XQ did a part of writing and coding works. YZ, CN, DW, and YL provided some interesting ideas. YZ provided the suggestions. CN and DW gave analysis on results. YL collected the data. All authors contributed to the article and approved the submitted version.

FUNDING

This research was supported by the China National Offshore Oil Corporation (CNOOC) research project (No. YXKY-2019-ZY-04) and the National Natural Science Foundation of China (No. 42074153).

REFERENCES

Ba, J., Xu, W., Fu, L. Y., Carcione, J. M., and Zhang, L. (2017). Rock anelasticity due to patchy saturation and fabric heterogeneity: a double double-porosity model of wave propagation. *J. Geophys. Res. Solid Earth* 122, 1949–1976. doi: 10.1002/2016JB013882

Berryman, J. G. (1995). "Mixture theories for rock properties," in *Rock Physics and Phase Relations - a Handbook of Physical Constants*, ed. T. J. Ahrens (Washington, DC: American Geophysical Union).

Biot, M. A. (1955). Theory of propagation of elastic waves in a fluid-saturated porous solid. I. Low frequency range. II. Higher frequency range. *J. Acoust. Soc. Am.* 28, 168–191. doi: 10.1121/1.1908239

Deng, J. X., Zhou, H., Wang, H., Zhao, G., and Wang, S. X. (2015). The influence of pore structure in reservoir sandstone on dispersion properties of elastic waves. *Chin. J. Geophys. Chin. Edition* 58, 3389–3400. doi: 10.6038/cjg20150931

Dvorkin, J., Nolen-Hoeksema, R. C., and Nur, A. (1994). The squirt-flow mechanism: macroscopic description. *Geophysics* 59, 428–438. doi: 10.1190/1.1443605

Dvorkin, J., and Nur, A. (1993). Dynamic poroelasticity: a unified model with the squirt and the Biot mechanisms. *Geophysics* 58, 524–533. doi: 10.1190/1.1443435

Gassmann, F. (1951). Uber die elastizitat poroser medien. *Vier. Der Nat. Gesellschaft Zurich* 96, 1–23.

Guo, Z. Q., and Li, X. Y. (2015). Rock physics model-based prediction of shear wave velocity in the Barnett Shale formation. *J. Geophys. Eng.* 12, 527–534.

Han, D. U., Nur, A., and Morgan, D. (1986). Effects of porosity and clay content on wave velocities in sandstones. *Geophysics* 51, 2093–2107. doi: 10.1190/1.1442062

Hashin, Z., and Shtrikman, S. (1963). A variational approach to the theory of the elastic behaviour of multiphase materials. *J. Mech. Phys. Solids* 11, 127–140. doi: 10.1016/0022-5096(63)90060-7

Krief, M., Garat, J., Stellingwerff, J., and Ventre, J. (1990). A rock physical interpretation using the velocities of P and S waves (full-waveform sonic). *Log Anal.* 31, 355–369.

Mavko, G., Mukerji, T., and Dovrkin, J. (2009). *The Rock Physics Handbook*, 2nd Edn. New York, NY: Cambridge University Press.

Mori, T., and Tanaka, K. (1973). Average stress in matrix and average elastic energy of materials with misfitting inclusions. *Acta Metallurgica* 21, 571–574. doi: 10.1016/0001-6160(73)90064-3

Raymer, L. L., Hunt, E. R., and Gardner, J. S. (1980). "An improved sonic transit time-to-porosity transform," in *Paper presented at the SPWLA 21st Annual Logging Symposium*, (Lafayette, LA), doi: 10.1029/2003JB002639

Ruiz, F., and Cheng, A. (2010). A rock physics model for tight gas sand. *Lead. Edge* 29, 1484–1489. doi: 10.1190/1.3525364

Smith, T. M., Sayers, C. M., and Sondergeld, C. H. (2009). Rock properties in low-porosity//low-permeability sandstones. *Lead. Edge* 28, 48–59. doi: 10.1190/1.3064146

Stuart, C., and David, B. (1977). Inversion of P-wave velocity anisotropy. *Geophys. J. Int.* 49, 123–132. doi: 10.1111/j.1365-246X.1977.tb03704.x

Tutuncu, A. N., Podio, A. L., and Sharma, M. M. (1994). An experimental investigation of factors influencing compressional- and shear-wave velocities and attenuations in tight gas sandstones. *Geophysics* 59, 77–86. doi: 10.1190/1.1443536

Vernik, L., and Kachanov, M. (2010). Modeling elastic properties of siliciclastic rocks. *Geophysics* 75:E171. doi: 10.1190/1.3494031

Wang, D. X. (2017). A study on the rock physics model of gas reservoir in tight sandstone. *Chin. J. Geophys.* 60, 64–83. doi: 10.1002/cjg2.30028

Wang, P., Li, J., Chen, X., and Wang, B. (2020). Joint probabilistic fluid discrimination of tight sandstone reservoirs based on Bayes discriminant and deterministic rock physics modeling. *J. Pet. Eng.* 191:107218. doi: 10.1016/j.petrol.2020.107218

Yan, X. F., Yao, F. C., Cao, H., Ba, J., Hu, L. L., and Yang, Z. F. (2011). Analyzing the mid-low porosity sandstone dry frame in central Sichuan based on effective medium theory. *Appl. Geophys.* 18, 163–170. doi: 10.1007/s11770-011-0293-1

Yin, H., Zhao, J., Tand, G., Zhao, L., Ma, X., and Wang, S. (2017). Pressure and fluid effect on frequency-dependent elastic moduli in fully saturated tight sandstone. *J. Geophys. Res. Solid Earth* 122, 8925–8942. doi: 10.1002/2017JB014244

Conflict of Interest: YZ, CN, DW, and YL were employed by the company CNOOC and declare that this study received funding from CNOOC.

The remaining authors declare that the research was conducted in the absence of any commercial or financial relationships that could be construed as a potential conflict of interest.

Copyright © 2021 Guo, Qin, Zhang, Niu, Wang and Ling. This is an open-access article distributed under the terms of the Creative Commons Attribution License (CC BY). The use, distribution or reproduction in other forums is permitted, provided the original author(s) and the copyright owner(s) are credited and that the original publication in this journal is cited, in accordance with accepted academic practice. No use, distribution or reproduction is permitted which does not comply with these terms.

frontiers in Earth Science

ORIGINAL RESEARCH
published: 08 April 2021
doi: 10.3389/feart.2021.626903

Roughness Effects of Crack Surfaces on the Elastic Moduli of Cracked Rocks

Bo-Ye Fu[1,3]*, *Li-Yun Fu*[2,4]*, *Tongcheng Han*[2,4] and *Chenghao Cao*[5]

[1]Key Laboratory of Earth and Planetary Physics, Institute of Geology and Geophysics, Chinese Academy of Sciences, Beijing, China, [2]Key Laboratory of Deep Oil and Gas, China University of Petroleum (East China), Qingdao, China, [3]Institutions of Earth Science, Chinese Academy of Sciences, Beijing, China, [4]Laboratory for Marine Mineral Resources, Qingdao National Laboratory for Marine Science and Technology, Qingdao, China, [5]School of Transportation Engineering, Nanjing Tech University, Nanjing, China

Crack surfaces are usually rough on various scales, and are sensitive to loading stresses and hence significantly affecting the mechanical properties of cracked rocks. We design a number of dry- and fluid-saturated numerical cracked samples to investigate the roughness influence of crack surfaces on the elastic stiffness. The fracture surface roughness is characterized by non-uniform fracture radii. We calculate the elastic moduli of cracked samples by finite-element simulation. Comparisons with the theoretical predictions by Gassmann and C&S (Ciz and Shapiro) (Ciz and Shapiro, Geophysics, 2007, 72(6), A75–A79) substitution equations demonstrate that the rough crack surfaces for both dry- and fluid-saturated samples can induce a stress concentration around the crack that reduces the elastic moduli and decreases the stiffness of rocks. For the fluid/solid-saturated cracks under the normal (shear) loading stresses, because the stress-concentration can induce shear (normal) strains around fracture, shear (bulk) modulus of the filling material will have contributions to the effective bulk (shear) modulus of rocks. The extra contribution, however, makes the Gassmann equation and C&S equation invalid.

Keywords: effective medium, cracked rock, crack surface, elastic modulus, rock physics model

OPEN ACCESS

Edited by:
Sung Keun Lee,
Seoul National University, South Korea

Reviewed by:
Yongjia Song,
Harbin Institute of Technology, China
Luanxiao Zhao,
Tongji University, China

***Correspondence:**
Bo-Ye Fu
fuboye@mail.iggcas.ac.cn
Li-Yun Fu
lfu@upc.edu.cn

Specialty section:
This article was submitted to Earth and Planetary Materials, a section of the journal Frontiers in Earth Science

Received: *11 November 2020*
Accepted: *18 February 2021*
Published: *08 April 2021*

Citation:
Fu B-Y, Fu L-Y, Han T and Cao C (2021) Roughness Effects of Crack Surfaces on the Elastic Moduli of Cracked Rocks. Front. Earth Sci. 9:626903. doi: 10.3389/feart.2021.626903

INTRODUCTION

The characterization of fracture geometry is essential for a wide range of applications, such as geothermal production, hydrocarbon exploration, nuclear waste disposal, and CO_2 storage (Pruess, 2006; Hyman et al., 2015). The medium stiffness can be an effective tool for characterizing their surface geometry because of the sensitivity of medium stiffness to the fracture surface geometry, (e.g. Liu, 2005; Sevostianov and Kachanov, 2008; Gao and Gibson, 2012), which has been a strong interest of researchers.

Techniques aiming to detect fracture networks and surfaces in formations have attracted many attentions, (e.g. Kawahara, 1992; Sevostianov and Kachanov, 2008; Guo et al., 2018a). Fracture networks and surface geometry will influence the effective elastic moduli of rocks, which, in turn, can be used to detect the fracture networks and surface geometry features, (e.g. Zimmerman et al., 1986; Kachanov, 1993; Sevostianov and Kachanov, 2008). Researches on these issues can be traced back to around 1970s. Toksöz et al. (1976) take pores and flaws in porous rocks as oblate spheroids with varying aspect ratios, which tend to be closed under differential pressures, and the change of fracture density will influence the stiffness of rocks. Cheng and Toksöz. (1979) conduct a comprehensive

investigation of stress-induced velocity variations using fractures with varying aspect ratios, and confirm that the deformation of fractures significantly influences elastic wave velocities. Then, more researchers have focused on the influence of fractures on the rock stiffness properties, (e.g. Zimmerman et al., 1986; Zimmerman, 1991; Shapiro, 2003; David and Zimmerman, 2012; Fu and Fu, 2017, Fu and Fu, 2018). According to these studies, in conclusion, the open or closure of fractures will influence the fractured rock stiffness. The tectonic stress controls the closure or open of the fractures, and therefore changes the stiffness of the fractured rocks (Shapiro, 2003; Grechka and Kachanov, 2006; David and Zimmermann, 2012; Fu and Fu, 2018; Zong et al., 2020). However, many investigations are based on phenomenological models, relating the fracture geometry influence to its stiffness by empirical equations. The parameters of the empirical equations are obtained by fitting experimental measurements, which do not really explain the influencing mechanism of the fracture geometry on the rock effective elastic moduli.

To approach the elastic properties of fractured rocks more theoretically, the compliance of ellipsoidal fractures becomes a major issue, (e.g. Eshelby, 1957; Budiansky and O'connell, 1976; Kachanov, 1980; Sevostianov and Kachanov, 2002a). Hudson (1981); Hudson. (1988) takes fractures as circular inclusions in an elastic host medium and formulates the fracture influence on the elastic properties. Kawahara et al., (e.g. Kawahara, 1992; Kawahara and Yamashita, 1992; Kawahara, 2011) further regard fractures as first-order perturbations on the host medium and propose a model of frequency-dependent elastic moduli for aligned slit fractured sample based on the Foldy approximation (Foldy, 1945). This method has been extended to poroelastic media (Galvin and Gurevich, 2007; Galvin and Gurevich, 2009; Song et al., 2017a; Song et al., 2017b; Fu et al., 2020), focusing on the fracture lengths influence on the elastic moduli. Guo et al. (2018d) and Song et al. (2019); Song et al. (2020c) further study the fracture thicknesses influence on the frequency-dependent elastic moduli for fluid-saturated fractured rocks. Recently, Song et al. (2020a), Song et al. (2020b) have further researched the frequency-dependent elastic moduli for fluid-saturated fractured rocks with rectangular cracks and compressible fluid. However, these researches focus on the analytical solutions with the assumption of aligned fractures of the same scale.

Because fractures are distributed randomly with complex networks and rough surface, numerical simulations have been widely used to calculate effective elastic moduli, for example, finite-difference method (FDM) simulation for the variation of effective elastic moduli vs. fracture density (Saenger and Shapiro, 2002; Saenger et al., 2004), and the scattering effect of fractures (Vlastos et al., 2003; Vlastos et al., 2006; Vlastos et al., 2007). Recently, poroelastic finite-element method (FEM) simulation has been used to investigate the frequency-dependent elastic properties of porous rocks with intersecting fractures (Rubino et al., 2008; Rubino et al., 2016), and has indicated that the attenuation of *P*- and *S*-waves becomes dominant in the presence of fluid diffusion in the connected fractures, (e.g. Quintal et al., 2014; Rubino et al., 2015). Zhu and Shao. (2017) have done a complete review of the models describing the fractured rock effective moduli. However, all the researches studying the fractured rock effective elastic moduli above assume the fractures are penny-shaped or slit, with smooth surface.

The fracture surfaces in real rocks are rough, (e.g., Sevostianov and Kachanov, 2002b; Zong et al., 2017, Zong et al., 2020). The surface roughness significantly affects the fracture stiffness. Although the fracture surfaces are complex for natural rocks, their characteristics can be described by random functions, (e.g. Brown and Scholz, 1985; Gao and Gibson, 2012). Greenwood and Williamson. (1966) investigate the normal contact deformation problem of a rough surface and a flat surface based on the Hertzian contact theory, by assuming the Gaussian and exponential distribution of the asperity heights. Walsh and Grosenbaugh. (1979) apply the assumptions and methods of Greenwood and Williamson (1966) to study the effective compressibility of the two contacted rough surfaces and conclude that the effective stiffness is linearly proportional with the pressure. After that, more attentions are paid to the elastic mechanisms of rough fracture surfaces, (e.g. Johnson et al., 1972; Brown and Scholz, 1985; Priest and Taylor, 2000). A comprehensive review on these researches is made by Johnson (1985). The fracture compliance has been calculated for several types of irregularities, (e.g. Gao and Gibson, 2012; Sevostianov and Kachanov, 2012). However, these researches are limited to a single fracture with rough surface. For real rocks, the fractures are existent in rocks as fracture cluster, (e.g. Saenger and Shapiro, 2002; Saenger et al., 2004). However, there are no detailed researches about the fracture cluster with rough surface influence on the effective elastic properties of the fractured rocks.

In this paper, we study the dependency of fractured rock effective elastic moduli on the fracture surface roughness. We design seven fractured numerical samples. Each sample contains a series of fractures with the same perturbation of the square of the radius of the fracture. Different samples have fractures with different perturbation of the square of the radius. The square of fracture radius is controlled by the normal distribution function (Brown and Scholz, 1985; Adler and Thovert, 1999). To focus on the perturbation of the square of fracture radius influence on the fractured medium, we maintain the expectance of the square of the fracture radius and the aspect ratios of the fractures as constants, and vary the standard square of the fracture radius deviation to change the roughness of the fracture. We use the perturbation of square of fracture radius to represent the fracture surface roughness. The FEM simulation is used to compute the effective elastic moduli of each sample. We also assume the orientation and distribution of fractures are uniform to eliminate their effects. The calculated elastic moduli can be correlated to different levels of surface roughness. Comparisons with the Gassmann and C&S substitution equations predictions are conducted to evaluate the influence of the fracture surfaces roughness.

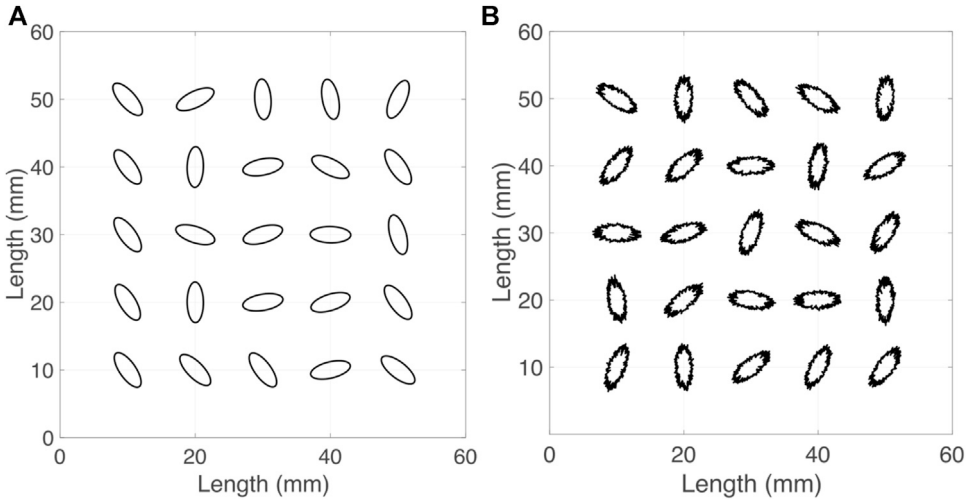

FIGURE 1 | The cracked rock models. **(A)** The crack with the standard deviation of R^2 as 0 mm^2 **(B)** The crack with the standard deviation of R^2 as 2.1 mm^2.

METHODOLOGY

The rough fracture surfaces can be generated by random functions, (e.g. Gangi, 1978; Sevostianov and Kachanov, 2008; Fu et al., 2020). On the other hand, the ellipses are widely used to characterize the fractures, (e.g. Eshelby, 1957; Cheng, 1978; Hudson, 1981; Kachanov, 1992; Guo et al., 2018a). In this work, fractures are considered as ellipses with the square of radii controlled by random functions, (e.g., Eshelby, 1957; Budiansky and O'connell, 1976; Sevostianov and Kachanov, 2012), as formed by **Eq. 1**,

$$\frac{x^2}{a^2}+\frac{y^2}{b^2}=R^2, \tag{1}$$

where x and y are the coordinates of the point in 2D surface. $a = 1$, $b = 0.4$. The aspect ratio ($\alpha = bR/aR = b/a$) of the fracture is 0.4. In this research, we focus on the influence of the perturbation of square of factures radius (R^2) on the effective elastic moduli of the sample. We maintain the mean area of the fractures in the sample as a constant value, and vary R^2 using the normal distribution function with the expectation of R^2 as 9 mm^2. Seven numerical samples, containing fractures with standard R^2 deviation (perturbation of R^2) ranging from 0 to 2.1 mm^2, are generated. The side length L of each sample is fixed at 60 mm. The area of each fracture is a constant as $\pi ab < R^2 >$, equaling 11.304 mm^2, where $< >$ represents the expectation value. Twenty-five fractures are inserted in each sample. The total fracture area for each sample is 282.600 mm^2. We assume there are no other pores in the host medium, and the porosity of the sample is the ratio between the total fracture area and the sample area, determined to be 7.85%. We consider the orientations of fractures are distributed uniformly. The uniform distribution of the centers of fractures are also assumed, so the rock samples are macroscopically isotropic. The samples with different perturbation of R^2 are shown in **Figures 1A,B**.

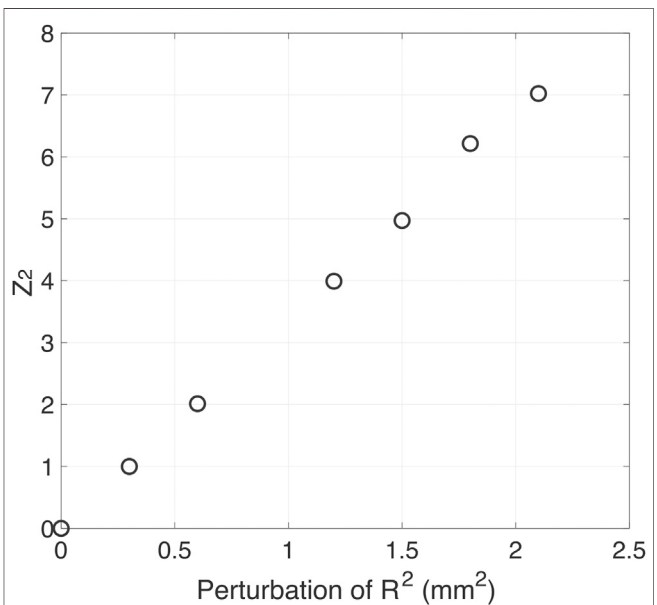

FIGURE 2 | The relation between perturbation of R^2 and Z_2.

For the fractures with rough surfaces, among the parameters describing fracture surface roughness, (e.g. Joint Roughness Coefficient (JRC), Z_2, and fractal dimension), Z_2 is one of the most widely used statistical parameters in surface roughness analysis, and is shown to correlate well with JRC. The equation calculating Z_2 is given by (Barton et al., 1985)

$$Z_2=\frac{1}{n}\sum_n\left[\frac{1}{L}\sum\frac{(z_{i-1}-z_i)^2}{x_{i-1}-x_i}\right]^{1/2}, \tag{2}$$

where n is the number of surface profiles, L is the profile length, and x_i is the coordinate of the surface profile in the point i. z_i is the

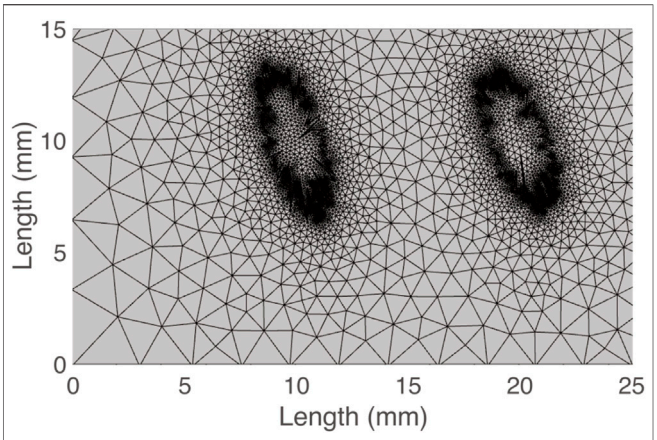

FIGURE 3 | The mesh around the fracture.

height of fracture surface at point *i*. If the value of x_{i-1}-x_i is a constant, as *C*. **Eq. 2** can be simplified as

$$Z_2 = \frac{1}{n}\sum_n \left[\frac{1}{L}\sum \frac{(z_{i-1}-z_i)^2}{C}\right]^{1/2.} \tag{3}$$

In this research, we use the radius in point *i*, R_i, replacing z_i, and **Eq. 3** can be rewritten as

$$Z_2 = \frac{1}{n}\sum_n \left[\frac{1}{LC}\sum (R_{i-1}-R_i)^2\right]^{1/2.} \tag{4}$$

Therefore, it can be obtained that

$$Z_2 = \sqrt{\frac{1}{LC}}\,\frac{1}{n}\sum_n \left[\sum (R_{i-1}-R_i)^2\right]^{1/2} \propto \frac{1}{n}\sum_n \left[\sum (R_{i-1}-R_i)^2\right]^{1/2.} \tag{5}$$

According to Zhao et al. (2019), surface with higher value of Z_2 is rougher. We have calculated the relation between Z_2 and perturbation of R^2 as shown in **Figure 2**. There is a positive linear relation between the perturbation of R^2 and Z_2. Therefore, the perturbation of R^2 can represent the roughness of the fracture surface.

To compute the effective elastic moduli of the fractured samples, we load the static homogeneous stresses on the samples, and solve the static elastic equation at each node by FEM simulation (Saxena and Mavko, 2014), with the static elastic equations as

$$\sigma_{ij,j} = 0. \tag{6}$$

and the stress σ_{ij} is expressed as

$$\sigma_{ij} = \left(K - \frac{2}{3}\mu\right)e\delta_{ij} + 2\mu e_{ij}, \tag{7}$$

where e_{ij} is the strain tensor, given by

$$e_{ij} = \frac{1}{2}\left(u_{i,j} + u_{j,i}\right). \tag{8}$$

and

$$e = e_{kk}, \tag{9}$$

where u_i is the displacement of each node of the sample, *K* and μ are the bulk and shear moduli of each node in the sample, respectively. The elastic moduli of fractures are different from those of the host medium. The elastic moduli of the host medium are the same for the all samples. Combining equations from **Eqs. 6–9**, we can calculate the stress σ_{ij} and strain e_{ij} in each node of the samples, by FEM simulation. Through the stress distribution, we can observe the stress concentration directly.

All the FEM numerical simulations are conducted using commercial software (COMSOL 5.5), which can mesh the fractures automatically, and satisfy the stable condition. This kind of commercial software has been used widely (Li et al., 2009). To maintain the accuracy of the simulation, the smallest scale of the mesh is 0.05 mm, as shown in **Figure 3**. It should be noted that, although the 3-D simulation is more suitable for modeling real rocks, according to Rubino et al. (2008); Rubino et al. (2015); Rubino et al. (2016), and Saxena and Mavko (2014), the accuracy of 2-D numerical simulation is acceptable to extract the effects of fracture surface roughness on effective elastic moduli. In this research, we conduct numerical simulation on 2-D model.

To compute the effective bulk moduli of isotropic samples, we load a homogenous confining pressure *P*, as presented in **Figure 4A**. By solving **Eqs. 6–9**, the strain e_{ij} and *e* at each node are obtained, and the effective bulk modulus K_e of each sample is

$$K_e = \frac{P}{< e >}. \tag{10}$$

Similarly, we obtain the effective shear modulus μ_e from the shear tests, by loading the homogenous pure shear stress τ_{12}, as shown in **Figure 4B**. The effective shear modulus μ_e is expressed as

$$\mu_e = \frac{\tau_{12}}{2 < e_{12} >}. \tag{11}$$

The fractures are important channels and spaces for water/kerogen diffusion and enrichment. Especially for the rocks with low porosity and permeability, (e.g., Gale et al., 2014; Guo et al., 2018c), fractures are usually saturated with water or kerogen. It is important to study the fracture surface roughness influence on fluid/solid substitution process of fractured samples. The elastic moduli of dry sample are computed by FEM simulation, and then, we calculate the elastic moduli of the water- and kerogen-saturated samples by FEM simulation, Gassmann equation and C&S (Ciz and Shapiro) equation (e.g., Gassmann, 1951; Ciz and Shapiro, 2007), respectively.

Gassmann equation (Gassmann, 1951) is expressed as

$$K_{sat}^{w} = K_{dry} + \alpha^2 M, \tag{12}$$

$$\mu_{sat}^{w} = \mu_{dry}, \tag{13}$$

where $K_{sat}{}^{w}$ and $\mu_{sat}{}^{w}$ are the bulk and shear moduli of the water-saturated sample, respectively. K_{dry} and μ_{dry} are the bulk and shear moduli of the dry sample calculated by FEM, respectively, in this research. The pore space modulus *M* is given as

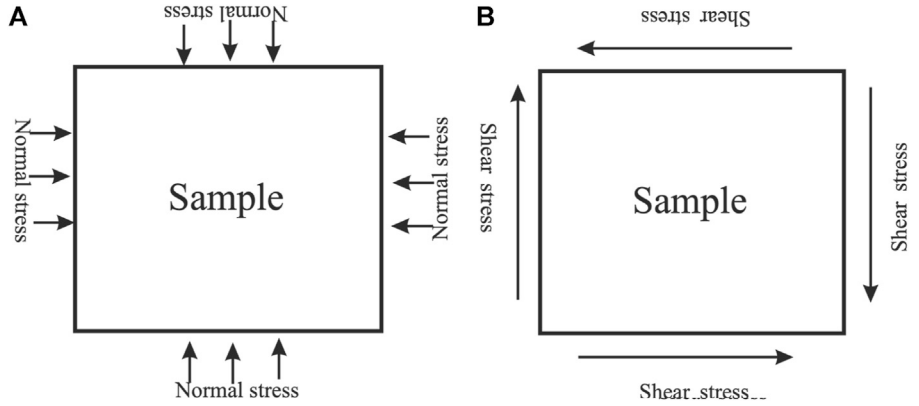

FIGURE 4 | The test models, **(A)** The confining pressure test, **(B)** the pure shear stress test.

$$M = \left[\frac{(\alpha-\phi)}{K_B} + \frac{\phi}{K_f}\right]^{-1}, \tag{14}$$

where $\alpha = 1\text{-}K_{dry}/K_B$ is the Biot-Willis coefficient (Biot and Willis, 1957). K_B is the bulk modulus of the host medium. K_f is the bulk modulus of water.

The C&S equation (Ciz and Shapiro, 2007) is summarized as

$$\left(K_{sat}^{k}\right)^{-1} = K_{dry}^{-1} - \frac{\left(K_{dry}^{-1} - K_B^{-1}\right)^2}{\phi\left(K_k^{-1} - K_B^{-1}\right) + \left(K_{dry}^{-1} - K_B^{-1}\right)}, \tag{15}$$

$$\left(\mu_{sat}^{k}\right)^{-1} = \mu_{dry}^{-1} - \frac{\left(\mu_{dry}^{-1} - \mu_B^{-1}\right)^2}{\phi\left(\mu_k^{-1} - \mu_B^{-1}\right) + \left(\mu_{dry}^{-1} - \mu_B^{-1}\right)}, \tag{16}$$

where ${K_{sat}}^k$ and ${\mu_{sat}}^k$ are the bulk and shear moduli of the kerogen saturated medium. K_k and μ_k are the bulk and shear moduli of kerogen. μ_B is the shear modulus of the host medium. Because Gassmann equation and C&S equation are valid to predict the effective elastic moduli of homogenous saturated rocks, comparison between the FEM simulation results and the Gassmann equation/C&S equation results will verify whether the two equations are valid, and whether the samples are homogenous. The difference between FEM simulation results and the Gassmann equation/C&S equation results indicates the changing of the heterogeneity of the sample, (e.g. Brown and Korringa, 1975; Saxena and Mavko, 2014). The differences should be increasing with the increase of the heterogeneity of the samples.

According to Saxena and Mavko. (2014), both Gassmann equation and C&S equations are set up based on reciprocal theory. These two kinds of equations assume samples are homogenous (Mavko and Mukerji, 2013). When confining pressure is loaded on samples, there are only elastic energy and normal strain induced by the normal stress of the sample, and only the bulk modulus of the inclusion has contributions to the effective bulk modulus. It is the same for the effective shear modulus.

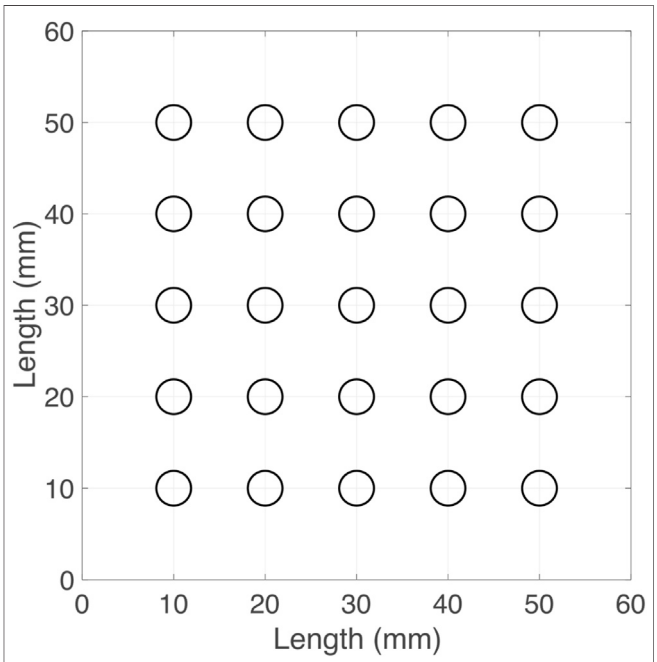

FIGURE 5 | The model for the test.

However, as verified by Saxena and Mavko. (2014), when the sample is heterogenous (the heterogeneity is induced by the distribution or geometry of the inclusion), if the normal stress is loaded on the sample, it will induce shear stress around the inclusions, and shear strain will be generated. Therefore, the shear modulus of the inclusions will have contribution to the effective bulk modulus. It is also the same for the effective shear modulus. All the explanations above mean the distribution or geometry of the inclusion maybe will make the Gassmann equation and C&S equation invalid (Mavko and Mukerji, 2013).

TABLE 1 | The simulation and substitution equation results of the test sample.

Sample type	Bulk modulus (GPa)			Shear modulus (GPa)			
	Substitution equation	Numerical result	Relative error	Substitution equation	Numerical result	Relative error	
Dry	–	23.66	–	–	16.81	–	
Water-saturated (gassmann)	24.74	24.36	1.5%	16.81	16.81	0.0%	
Kerogen-saturated (C&S)	25.01	25.11	0.4%	18.47	18.47	0.0%	

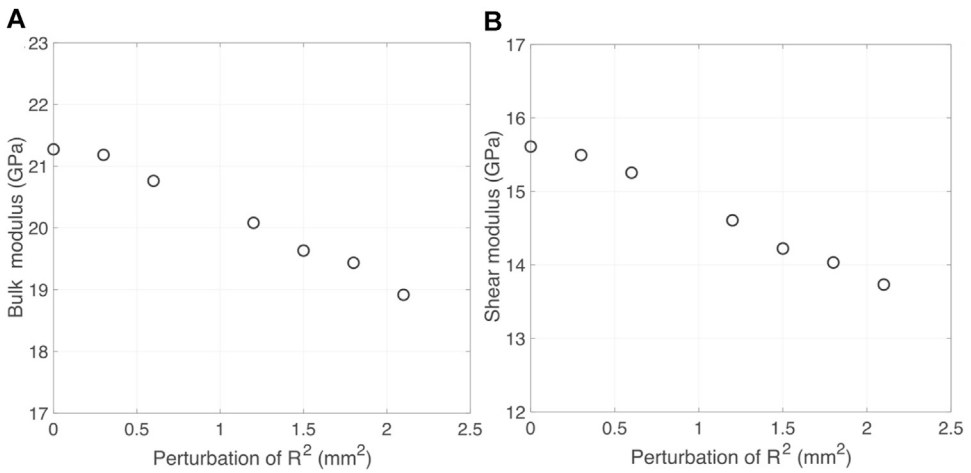

FIGURE 6 | (A) the variation of bulk modulus of dry samples vs. the perturbation of R^2, **(B)** the variation of shear modulus of dry samples vs. the perturbation of R^2.

RESULTS

The effective elastic moduli K_e and μ_e are obtained by FEM simulation. The host medium bulk modulus K_B = 29.78 GPa, the host medium shear modulus μ_B = 22.30 GPa. For the dry numerical samples, the elastic moduli of filling material are zero. In the first stage, effective elastic moduli of dry samples are computed. Then, the water- and kerogen-saturated sample are considered. The bulk modulus of water K_f is 2.25 GPa, and the shear modulus is zero. The bulk modulus of kerogen K_k is 2.9 GPa, and shear modulus of kerogen μ_k is 2.70 GPa (Mavko et al., 2009). Before doing the calculation, we do verify that all the numerical samples maintain the isotropic assumption, first. We conduct the numerical tests as shown in Appendix A. According to the results in Appendix A, the macroscopic isotropic assumption of each sample is maintained. In addition, we should also test the consistency between FEM simulation and Gassmann equation/C&S equation for homogenous and isotropic medium. The numerical test sample is presented in **Figure 5**. To maintain homogeneity and isotropy of the sample, all fractures are perfect circles, with radius as 1.895 mm to maintain the fracture area as 11.304 mm^2. The total porosity of the test sample is the same as the numerical samples in the study as 7.85%.

We use FEM simulation to calculate the elastic moduli of dry sample, first. Then, we use FEM simulation, Gassmann equation and C&S equation to calculate the elastic moduli of water- and kerogen-saturated samples, respectively. The results are given by **Table 1**. The numerical error between the substitution equations and numerical results are less than 0.4% for the elastic moduli of kerogen-saturated sample, and the shear modulus of water-saturated sample. The numerical error between Gassmann equation and numerical result is 1.5% for the bulk modulus of water-saturated sample. The error in the bulk modulus might be induced by the interaction between fractures (Guo et al., 2018a). Both Gassmann and C&S equations are valid for homogenous and isotropic and homogenous medium. When we compare the difference between the FEM simulation results and substitution equation, if the differences between the numerical and substitution equation results are larger than the numerical errors, it should be induced by the fracture surface roughness.

Elastic Moduli of Dry Cracked Sample

In this section, we calculate the elastic moduli of dry numerical samples. Through FEM simulation, we obtain the variation of bulk and shear moduli of dry samples. As presented in **Figures 6A,B**, both bulk and shear moduli of the dry samples are decreasing sharply with the increase of the perturbation of R^2. Because porosity is a constant, and there are no fluid or solid filling the fractures, the decrease of the bulk and shear moduli are resulting solely from the increase of the perturbation of R^2. The sample with higher fracture surface roughness has lower stiffness.

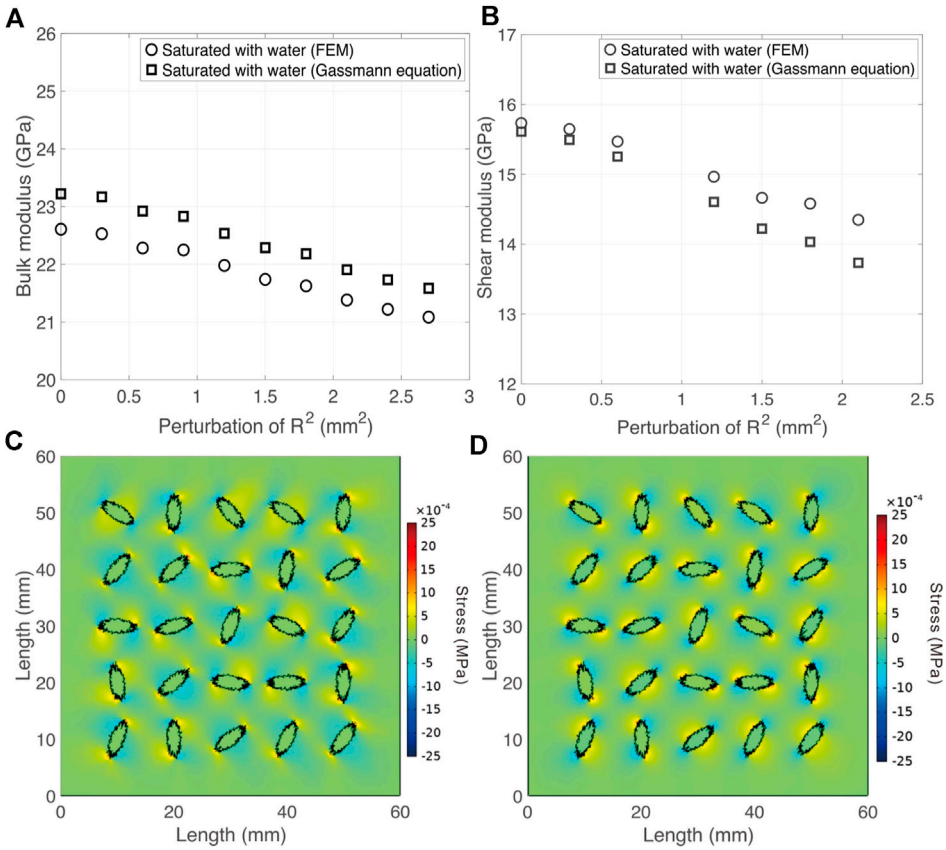

FIGURE 7 | (A) the variation of bulk moduli of water-saturated samples vs. perturbation of R^2, **(B)** the variation of shear moduli of water-saturated samples vs. perturbation of R^2, **(C)** the distribution of shear stress when the sample loaded by normal stress, **(D)** the distribution of normal stress when the sample loaded by shear stress.

Elastic Moduli of Samples Saturated With Water

We further calculate the bulk and shear moduli of water-saturated sample by FEM and Gassmann equation based on the elastic moduli of dry numerical sample calculated in the last subsection, respectively. **Figures 7A,B** show the bulk and shear moduli variations vs. perturbation of R^2 of the water-saturated samples for both Gassmann equation predictions and FEM results. The comparisons between the results of FEM simulation (circle) and the Gassmann equation (square) show that the bulk moduli calculated by FEM simulation are less than those from Gassmann equation with a constant value. This kind of difference may be caused by the interaction between the fractures, which is as also observed by Zhao et al. (2016); Guo et al. (2018a); Guo et al. (2018b); Cao et al. (2019); Cao et al. (2020); Zhao et al. (2020) have also used the stress amplification and stress shielding to explain the influence of the interaction. Because the relative difference between the two kinds of bulk moduli are at about 1.5%, similar to the numerical error, we do not focus on the bulk modulus variation of water-saturated sample. We mainly focus on the shear modulus. The difference in shear modulus is obvious, and is larger than numerical error. The shear moduli obtained from FEM simulation are higher than the value of Gassmann equation (**Figure 7B**). As shown in **Figure 7D**, the rough fracture surfaces will induce normal stress around the fractures, when shear stress is loaded. Because the saturated fluid has bulk modulus, and the normal stress around fractures will interact with the fluid, the bulk modulus of the filling fluid will increase the effective shear modulus. However, for Gassmann equation, as shown in **Eq. 13**, the effective shear modulus is only related to the shear modulus of dry samples. Therefore, the effective shear moduli of water-saturated samples obtained by Gassmann equation are less than the values of FEM simulation. As plotted in **Figure 7B**, with the increase of the perturbation of R^2, the differences of shear moduli between Gassmann equation and FEM simulation are increasing. This indicates the contribution of the bulk modulus of the filling fluid to the shear modulus is increasing. In this study, the porosity of each sample is maintained as a constant, and the orientations of the fractures are also uniformly randomly distributed (the probability of different orientations are the same). Only the fracture surface roughness can generate this difference. The fracture with rougher surface will cause more normal stress around the fractures. The contribution of the bulk modulus of the filling fluid will also be increased.

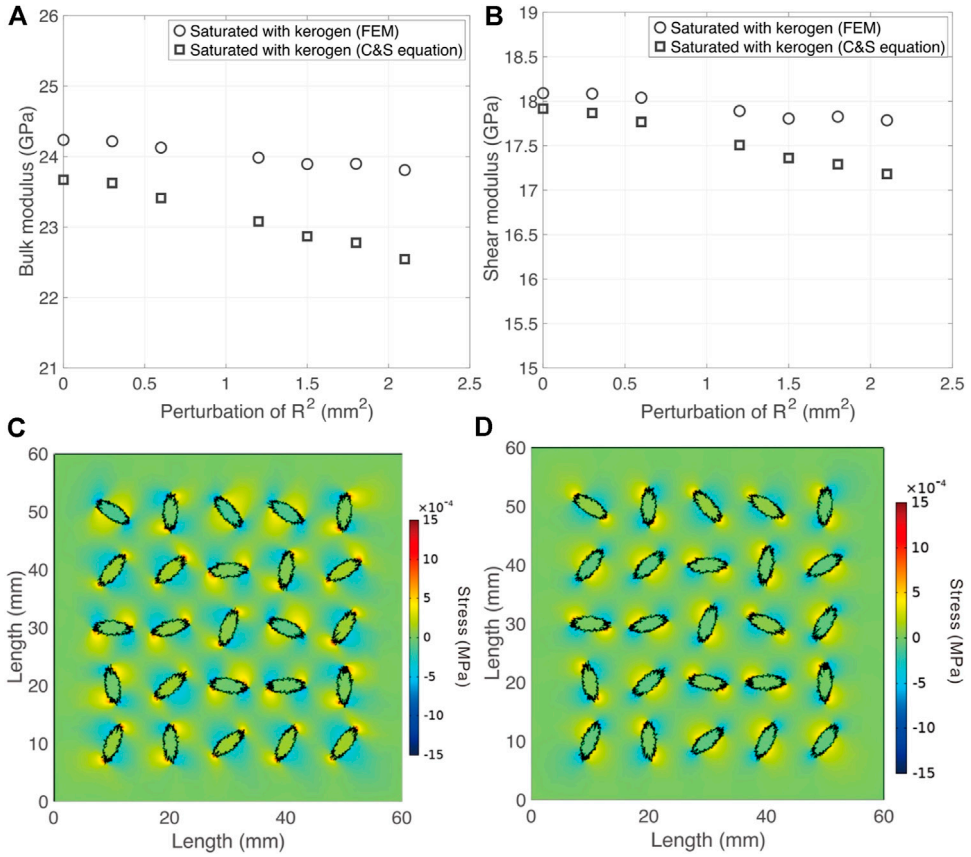

FIGURE 8 | (A) The variation of bulk moduli of kerogen-saturated samples vs. the perturbation of R^2, **(B)** the variation of shear moduli of kerogen-saturated samples vs. the perturbation of R^2, **(C)** the distribution of shear stress when the sample loaded by normal stress, **(D)** the distribution of normal stress when the sample loaded by shear stress.

Gassmann equation is valid for homogenous medium (Saxena and Mavko, 2014). However, the difference between the numerical simulation and Gassmann equation results and the stress distribution in **Figures 7A–D** verify that the ellipsoidal fractures with rough surfaces will induce the local stress heterogeneity and strain heterogeneity of the sample. The local stress heterogeneity and strain heterogeneity will lead to the failure of the Gassmann equation (Mavko and Mukerji, 2013; Saxena and Mavko, 2014).

Elastic Moduli of Samples Saturated With Kerogen

We continue to analyze the two sets of kerogens-saturated results predicted by FEM simulation and C&S equation (Ciz and Shapiro, 2007) in this subsection, respectively. In **Figures 8A,B**, both bulk and shear moduli are decreasing with the increasing perturbation of R^2. The results of FEM simulation are higher than the results of C&S equation. C&S equation is only valid for homogenous sample. According to **Eq. 15**, the effective bulk modulus is only influenced by the bulk moduli of the host medium and the filling solid. However, for the fractured sample in this research, as shown in **Figure 8C**, there are shear stresses around the fractures, when the normal stress is loaded. The shear stress will interact with the inclusions, and the shear modulus of the inclusion will have contributions to the effective bulk modulus of the sample. Therefore, the effective bulk modulus calculated by FEM simulation is higher than the result of C&S equation. To analyze the variation of shear modulus as plotted in **Figure 8B**, we also calculate the normal stress around the fractures. According to the normal stress distribution in **Figure 8D**, the bulk modulus of kerogen will also increase the effective shear modulus, and generate higher shear modulus, as calculated by the FEM simulation. Additionally, compared with the elastic moduli calculated by C&S equation, the variation of the elastic moduli calculated by FEM simulation are more stable. One reason for this phenomenon is that, although the perturbation of R^2 will decrease the stiffness of dry samples, when we load normal (or shear) stress around the fractures, the fractures with rougher surfaces will induce more shear (or normal) stress around the fractures, and the shear (or bulk) modulus of the filling solid will also have contribution to the effective elastic moduli. C&S equation does not calculate the contribution of the shear (bulk) modulus of the inclusions. Therefore, the effective elastic moduli calculated by the FEM simulation is higher than that obtained by C&S equation, and the FEM simulated elastic moduli are more stable.

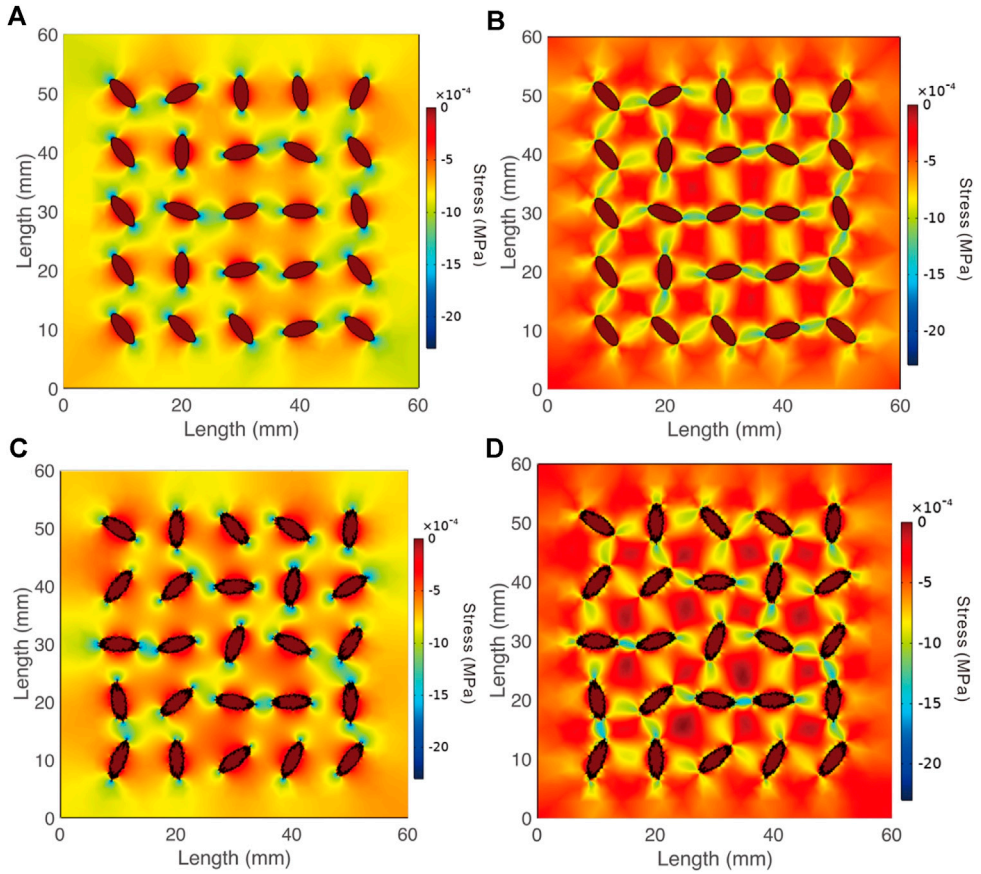

FIGURE 9 | The stress distribution of cracked rock models, **(A)** normal stress distribution of the crack rock model with deviation as 0, **(B)** shear stress distribution of the crack rock model with deviation as 0, **(C)** normal stress distribution of the crack rock model with deviation as 2.1 mm^2, **(D)** shear stress distribution of the crack rock model with deviation as 2.1 mm^2.

As verified by Saxena and Mavko. (2014), only when samples are homogeneous and isotropic, C&S equation is valid (**Eqs. 15, 16**). According to the results in **Figures 8C,D**, because of the stress concentration around the fractures induced by the rough fracture surface (Kubair and Bhanu-Chandar, 2008), the strain distributions of saturated samples are heterogenous, and the C&S equation is invalid.

DISCUSSIONS

From the simulation results of dry numerical samples, we have observed linear decrease of elastic moduli of dry samples vs. the perturbation of R^2 of the fractures, as presented in **Figures 6A,B**. When samples are saturated with water and kerogen, because of the stress concentration caused by the rough fracture surfaces, the shear and bulk moduli of the inclusions will have contributions to the effective bulk and shear moduli, respectively. The fracture with rougher surface will generate higher stress concentration, and the shear and bulk moduli of the inclusions will have more contributions to the effective bulk and shear moduli, which will decrease the reducing speed of the elastic moduli.

In this study, we have also calculated the stress distribution of the dry samples with different fracture surface roughness, as shown in **Figures 9A–D**. **Figures 9A,B** show normal and shear stress distribution for the dry rock sample with the fracture radius standard deviation as 0 mm, for confining pressure and shear stress loaded tests respectively. Because there is no fluid or solid in the sample, the elastic moduli of fractures are zero, and the stress inside the fracture is low. Because the fracture surface is smooth, the stresses concentration around the fracture is low. The stress distribution heterogeneity is also low, and the elastic moduli is higher, as shown in **Figures 6A,B**. With the increase in the perturbation of R^2, the stress concentration around fractures become larger, as shown in **Figures 9C,D** (standard R^2 deviation is 2.1 mm^2). As a result, the heterogeneity of the stress distribution of the sample is increasing, and the elastic moduli become lower (**Figures 6A,B**). In this research, we have maintained the porosity unchanged, and the orientations of fractures are uniform. The increase of the stress concentration is induced by the increase of fracture surface roughness (perturbation of R^2). It also can be known that the stress concentration induces the decrease of elastic moduli of dry samples.

According to the analysis above, fracture surface roughness controls the stress concentration around the fracture surface and the heterogeneity of the stress. The higher perturbation of R^2 of fracture will induce higher stress concentration. The stress will concentrate around the peak of the fractures with large ratio between its length and its thickness (Kubair and Bhanu-Chandar, 2008). When the perturbation of R^2 (roughness) of the fracture is higher, it will generate more peaks with larger ratio, as well as higher stress concentration. Stress concentration will induce strain concentration around the fracture, and increase the strain in local region. When the loaded stress is the same, (e.g. Kubair and Bhanu-Chandar, 2008; Fu and Fu, 2018), the total strain will increase, because of the strain concentration. Therefore, the sample, with larger stress concentration, will be softer, and the elastic moduli will decrease.

According to the results in **Figures 7**, **8**, the elastic moduli variation of saturated samples predicted by Gassmann and C&S equations are more drastic. According to Gassmann equation and C&S equation, the effective bulk moduli of samples saturated with fluid or solid are only related to the bulk moduli of the inclusions and host medium, and the effective shear moduli are only related to the shear moduli of the inclusions and host medium. However, because of the surface roughness of the ellipsoidal fractures, when stress is loaded on the sample, there is stress concentration around the fractures, the shear and bulk moduli of the filling medium will also have contributions to the effective bulk and shear moduli, respectively. The fractures with higher perturbation of R^2 will induce higher stress concentration, and the filling medium will have more contribution to the effective bulk and shear moduli. As a result, the elastic moduli obtained by FEM simulation is larger than that predicted by Gassmann equation and C&S equation, and the variation of the elastic moduli obtained by FEM are the more stable.

It should be noted that, the bulk moduli of the water-saturated samples obtained by FEM simulation is less than that obtained by Gassmann equation with a constant value. The difference may be caused by the interaction between fractures. This kind of difference are also observed in previous studies, (e.g. Guo et al., 2018a; Guo et al., 2018b; Cao et al., 2019; Cao et al., 2020).

According to the works of Zhao et al. (2016); Zhao et al. (2020), the interaction of the cracks (stress amplification) will induce the inconsistency between the substitution equations and numerical simulation in the elastic moduli of the sample. Comparing the stress distribution as shown in **Figures 9A–D**, the crack interaction is stronger for the cracks with rougher surface. The difference between the substitution equation results and the numerical simulation is also increasing with the crack surface roughness as shown in **Figure 7B** and **Figures 8A,B**. Therefore, there the difference between the substitution equation results and the numerical simulation is also induced by the interaction between the interaction between the cracks, and the rougher crack surface will induce higher interaction.

In this research, we study the substitution process in the limitation of linear elastic problem, and we do not consider the fracture surface slipping and the intersection between factures, when stress is loaded. Although fracture surface slipping and the intersection between factures will change fracture stiffness a lot, it is a kind of nonlinear elastic/hypoplasticity problem (Jiang and Liu, 2008; Khidas and Jia, 2010; Jia et al., 2011). Generally speaking, both fracture surface slipping and the intersection between factures can increase the facture porosity and change the connection of the fractures (Shapiro 2003; Guo et al., 2018c), and they will change the structure and decrease the stiffness of the dry sample. In this research, we focus on the influence of fracture surface roughness on the substitution process, and we should maintain the fracture porosity and the stiffness of the dry sample as a constant during the stress loaded. Therefore, the fracture surface slipping, and the intersection influence are out of the region of this research. However, it should be noted that because the fracture surface slipping and the intersection between factures will change the stiffness of the dry sample and connection of the fracture during the stress loading process, it will also influence the substitution process. In addition, to focus on the fracture surface roughness influence, we assume all fractures are isolated to each other. However, for the for fractures in the natural world, it is possible that the fractures are intersecting to each other. When fractures are intersecting to each other, the interaction between the fractures will increase, and the stiffness of both dry and saturated samples will decrease. All the problem about the slip of fracture surface and fracture intersection will be researched in the future.

CONCLUSIONS

In this paper, we have studied the dependency of fractured sample elastic moduli on the fracture surface roughness. We design seven fractured numerical samples. Each sample contains twenty-five fractures with the same surface roughness. Different samples have different fracture surface roughness. The square of fracture radius is controlled by the normal distribution law. The FEM simulation is used to compute the effective elastic moduli of each sample. The resulting elastic moduli can be correlated to different levels of fracture surface roughness. Comparisons between the FEM simulation and theoretical predictions by the Gassmann and C&S substitution equations demonstrate that the fracture surface roughness could induce stress concentration, and thus reduce the elastic moduli of samples. For the sample with fractures orientated radomy uniformly, the factures with higher rough surface will induce more stress concentration around the fractures, and the interaction between fractures will increase, making the Gassmann and C&S equation invalid.

DATA AVAILABILITY STATEMENT

The original contributions presented in the study are included in the article/Supplementary Material, further inquiries can be directed to the corresponding authors.

AUTHOR CONTRIBUTIONS

L-YF and B-YF conceive this research. B-YF writes the manuscript and prepares the figures. L-YF and TH reviews and supervises the manuscript. The co-authors CC are involved in the discussion of the manuscript. All authors finally approve the manuscript and thus agree to be accountable for this work.

ACKNOWLEDGMENTS

The authors would like to thank the sponsors of the Strategic Priority Research Program of the Chinese Academy of Sciences, Grant No. XDA14010303, National Natural Science Foundation of China (Grant No.41821002) for the financial support. In this research, all the data are numerical simulation result, and there are no experiment data.

REFERENCES

Adler, P. M., and Thovert, J. F. (1999). *Fractures and fracture networks*. Berlin, Germany: Springer Science and Business Media, Vol. 15.

Barton, N., Bandis, S., and Bakhtar, K. (1985). Strength, deformation and conductivity coupling of rock joints. *Int. J. Rock Mech. Mining Sci. Geomechanics Abstr.*, 22 (3), 121–140. doi:10.1016/0148-9062(85)93227-9

Biot, M. A., and Willis, D. G. (1957). The elastic coefficients of the theory of consolidation. *J. Appl. Mech.* 24, 594–601.

Brown, R. J. S., and Korringa, J. (1975). On the dependence of the elastic properties of a porous rock on the compressibility of the pore fluid. *Geophysics* 40 (4), 608–616. doi:10.1190/1.1440551

Brown, S. R., and Scholz, C. H. (1985). Closure of random elastic surfaces in contact. *J. Geophys. Res.* 90 (B7), 5531–5545. doi:10.1029/jb090ib07p05531

Budiansky, B., and O'connell, R. J. (1976). Elastic moduli of a cracked solid. *Int. J. Solids Struct.* 12 (2), 81–97. doi:10.1016/0020-7683(76)90044-5

Cao, C., Fu, L.-Y., Ba, J., and Zhang, Y. (2019). Frequency- and incident-angle-dependent P-wave properties influenced by dynamic stress interactions in fractured porous media. *Geophysics* 84 (5), MR173–MR184. doi:10.1190/geo2018-0103.1

Cao, C., Chen, F., Fu, L. Y., Ba, J., and Han, T. (2020). Effect of stress interactions on anisotropic P-SV-wave dispersion and attenuation for closely spaced cracks in saturated porous media. *Geophys. Prospect.* 68 (8), 2536–2556. doi:10.1111/1365-2478.13007

Cheng, C. H. A. (1978). Seismic velocities in porous rocks: direct and inverse problems. Doctoral dissertation. Cambridge, United States: Massachusetts Institute of Technology.

Cheng, C. H., and Toksöz, M. N. (1979). Inversion of seismic velocities for the pore aspect ratio spectrum of a rock. *J. Geophys. Res.* 84 (B13), 7533–7543. doi:10.1029/jb084ib13p07533

Ciz, R., and Shapiro, S. A. (2007). Generalization of Gassmann equations for porous media saturated with a solid material. *Geophysics* 72 (6), A75–A79. doi:10.1190/1.2772400

David, E. C., and Zimmerman, R. W. (2012). Pore structure model for elastic wave velocities in fluid-saturated sandstones. *J. Geophys. Res. Solid Earth* 117 (B7), 185–201. doi:10.1029/2012jb009195

Eshelby, J. D. (1957). The determination of the elastic field of an ellipsoidal inclusion, and related problems. *Proc. R. Soc. Lond. Ser. A. Math. Phys. Sci.* 241 (1226), 376–396. doi:10.1098/rspa.1957.0133

Foldy, L. L. (1945). The multiple scattering of waves. I. General theory of isotropic scattering by randomly distributed scatterers. *Phys. Rev.* 67 (3-4), 107. doi:10.1103/physrev.67.107

Fu, B. Y., and Fu, L. Y. (2017). Poro-acoustoelastic constants based on Padé approximation. *The J. Acoust. Soc. Am.* 142 (5), 2890–2904. doi:10.1121/1.5009459

Fu, B. Y., and Fu, L. Y. (2018). Poro-acoustoelasticity with compliant pores for fluid-saturated rocks. *Geophysics* 83 (3), WC1–WC14. doi:10.1190/geo2017-0423.1

Fu, B. Y., Fu, L. Y., Guo, J., Galvin, R. J., and Gurevich, B. (2020). Semi-analytical solution to the problem of frequency dependent anisotropy of porous media with an aligned set of slit cracks. *Int. J. Eng. Sci.* 147, 103209. doi:10.1016/j.ijengsci.2019.103209

Gale, J. F. W., Laubach, S. E., Olson, J. E., Eichhuble, P., and Fall, A. (2014). Natural Fractures in shale: a review and new observations. *Bulletin* 98 (11), 2165–2216. doi:10.1306/08121413151

Galvin, R. J., and Gurevich, B. (2007). Scattering of a longitudinal wave by a circular crack in a fluid-saturated porous medium. *Int. J. Solids Struct.* 44 (22-23), 7389–7398. doi:10.1016/j.ijsolstr.2007.04.011

Galvin, R. J., and Gurevich, B. (2009). Effective properties of a poroelastic medium containing a distribution of aligned cracks. *J. Geophys. Res.* 114 (B7), B07305. doi:10.1029/2008jb006032

Gangi, A. F. (1978). Variation of whole and fractured porous rock permeability with confining pressure. *Int. J. Rock Mech. Mining Sci. Geomech. Abstr.* 15 (5), 249–257. doi:10.1016/0148-9062(78)90957-9

Gao, K., and Gibson, R. L. (2012). Pressure-dependent seismic velocities based on effective compliance theory and an asperity deformation model. *Geophysics* 77 (6), D229–D243. doi:10.1190/geo2012-0041.1

Gassmann, F. (1951). Uber die elastizitat poroser medien. *Vier. Der Natur. Gesellschaft in Zurich* 96, 1–23.

Grechka, V., and Kachanov, M. (2006). Effective elasticity of cracked rocks. *A snapshot work Prog. Geophys.* 71 (6), 0016–8033. doi:10.1190/1.2360212

Greenwood, J. A., and Williamson, J. P. (1966). Contact of nominally flat surfaces. *Proc. R. Soc. Lond. Ser. A. Math. Phys. Sci.* 295 (1442), 300–319. doi:10.1098/rspa.1966.0242

Guo, J., Germán Rubino, J., Barbosa, N. D., Glubokovskikh, S., and Gurevich, B. (2018a). Seismic dispersion and attenuation in saturated porous rocks with aligned fractures of finite thickness: theory and numerical simulations—Part 1: P-wave perpendicular to the fracture plane. *Geophysics* 83 (1), WA49–WA62. doi:10.1190/geo2017-0065.1

Guo, J., Germán Rubino, J., Barbosa, N. D., Glubokovskikh, S., and Gurevich, B. (2018b). Seismic dispersion and attenuation in saturated porous rocks with aligned fractures of finite thickness: theory and numerical simulations—Part 2: frequency-dependent anisotropy. *Geophysics* 83 (1), WA63–WA71. doi:10.1190/geo2017-0066.1

Guo, J., Rubino, J. G., Glubokovskikh, S., and Gurevich, B. (2018c). Dynamic seismic signatures of saturated porous rocks containing two orthogonal sets of fractures: theory versus numerical simulations. *Geophys. J. Int.* 213 (2), 1244–1262. doi:10.1093/gji/ggy040

Guo, J., Shuai, D., Wei, J., Ding, P., and Gurevich, B. (2018d). P-wave dispersion and attenuation due to scattering by aligned fluid saturated fractures with finite thickness: theory and experiment. *Geophys. J. Int.* 215 (3), 2114–2133. doi:10.1093/gji/ggy406

Hudson, J. A. (1981). Wave speeds and attenuation of elastic waves in material containing cracks. *Geophys. J. Int.* 64 (1), 133–150. doi:10.1111/j.1365-246x.1981.tb02662.x

Hudson, J. A. (1988). Seismic wave propagation through material containing partially saturated cracks. *Geophys. J. Int.* 92 (1), 33–37. doi:10.1111/j.1365-246x.1988.tb01118.x

Hyman, J. D., Karra, S., Makedonska, N., Gable, C. W., Painter, S. L., and Viswanathan, H. S. (2015). dfnWorks: a discrete fracture network framework for modeling subsurface flow and transport. *Comput. Geosci.* 84, 10–19. doi:10.1016/j.cageo.2015.08.001

Jia, X., Brunet, T., and Laurent, J. (2011). Elastic weakening of a dense granular pack by acoustic fluidization: slipping, compaction, and aging. *Phys. Rev. E* 84 (2), 020301. doi:10.1103/physreve.84.020301

Jiang, Y., and Liu, M. (2008). Incremental stress-strain relation from granular elasticity: comparison to experiments. *Phys. Rev. E* 77 (2), 021306. doi:10.1103/physreve.77.021306

Johnson, K. L. (1985). *Contact mechanics*. Cambridge, United Kingdom: Cambridge University Press.

Johnson, K. L., Greenwood, J. A., and Poon, S. Y. (1972). A simple theory of asperity contact in elastohydro-dynamic lubrication. *Wear* 19 (1), 91–108. doi:10.1016/0043-1648(72)90445-0

Kachanov, M. (1980). Continuum model of medium with cracks. *J. Engrg. Mech. Div.* 106 (5), 1039–1051. doi:10.1061/jmcea3.0002642

Kachanov, M. (1992). Effective elastic properties of cracked solids: critical review of some basic concepts. *Appl. Mech. Rev.* 45 (8), 304–335. doi:10.1115/1.3119761

Kachanov, M. (1993). Elastic solids with many cracks and related problems. *Adv. Appl. Mech.* 30, 259–445. doi:10.1016/S0065-2156(08)70176-5

Kawahara, J. (1992). Scattering of P, SV waves by random distribution of aligned open cracks. *J. Phys. Earth* 40 (3), 517–524. doi:10.4294/jpe1952.40.517

Kawahara, J. (2011). Scattering attenuation of elastic waves due to low-contrast inclusions. *Wave Motion* 48 (3), 290–300. doi:10.1016/j.wavemoti.2010.11.004

Kawahara, J., and Yamashita, T. (1992). Scattering of elastic waves by a fracture zone containing randomly distributed cracks. *Pure Appl. Geophys.* 139 (1), 121–144. doi:10.1007/bf00876828

Khidas, Y., and Jia, X. (2010). Anisotropic nonlinear elasticity in a spherical-bead pack: influence of the fabric anisotropy. *Phys. Rev. E* 81 (2), 021303. doi:10.1103/physreve.81.021303

Kubair, D. V., and Bhanu-Chandar, B. (2008). Stress concentration factor due to a circular hole in functionally graded panels under uniaxial tension. *Int. J. Mech. Sci.* 50 (4), 732–742. doi:10.1016/j.ijmecsci.2007.11.009

Li, Q., Ito, K., Wu, Z., Lowry, C. S., and Loheide II, S. P., II (2009). COMSOL Multiphysics: a novel approach to ground water modeling. *Groundwater* 47 (4), 480–487. doi:10.1111/j.1745-6584.2009.00584.x

Liu, E. (2005). Effects of fracture aperture and roughness on hydraulic and mechanical properties of rocks: implication of seismic characterization of fractured reservoirs. *J. Geophys. Eng.* 2 (1), 38–47. doi:10.1088/1742-2132/2/1/006

Mavko, G., Mukerji, T., and Dvorkin, J. (2009). *The rock physics handbook: tools for seismic analysis of porous media*. England: Cambridge University Press.

Mavko, G., and Mukerji, T. (2013). Estimating Brown-Korringa constants for fluid substitution in multimineralic rocks. *Geophysics* 78 (3), L27–L35. doi:10.1190/geo2012-0056.1

Priest, M., and Taylor, C. M. (2000). Automobile engine tribology—approaching the surface. *Wear* 241 (2), 193–203. doi:10.1016/s0043-1648(00)00375-6

Pruess, K. (2006). Enhanced geothermal systems (EGS) using CO2 as working fluid-A novel approach for generating renewable energy with simultaneous sequestration of carbon. *Geothermics* 35 (4), 351–367. doi:10.1016/j.geothermics.2006.08.002

Quintal, B., Jänicke, R., Rubino, J. G., Steeb, H., and Holliger, K. (2014). Sensitivity of S-wave attenuation to the connectivity of fractures in fluid-saturated rocks. *Geophysics* 79 (5), WB15–WB24. doi:10.1190/geo2013-0409.1

Rubino, J. G., Ravazzoli, C. L., and Santos, J. E. (2008). Equivalent viscoelastic solids for heterogeneous fluid-saturated porous rocks. *Geophysics* 74 (1), N1–N13. doi:10.1190/1.3008544

Rubino, J. G., Caspari, E., Milani, M., Holliger, K., Müller, T. M., and Holliger, K. (2015). "Seismic anisotropy in fractured low-permeability formations: the effects of hydraulic connectivity," in SEG Technical Program Expanded Abstracts 2015; New Orleans, Louisiana, October 8–23, 2015 (Tulsa, Oklahoma: Society of Exploration Geophysicists), 3219–3223.

Rubino, J. G., Caspari, E., Müller, T. M., Milani, M., Barbosa, N. D., and Holliger, K. (2016). Numerical upscaling in 2-D heterogeneous poroelastic rocks: anisotropic attenuation and dispersion of seismic waves. *J. Geophys. Res. Solid Earth* 121 (9), 6698–6721. doi:10.1002/2016jb013165

Saenger, E. H., Krüger, O. S., and Shapiro, S. A. (2004). Effective elastic properties of randomly fractured soils: 3D numerical experiments. *Geophys. Prospect.* 52 (3), 183–195. doi:10.1111/j.1365-2478.2004.00407.x

Saenger, E. H., and Shapiro, S. A. (2002). Effective velocities in fractured media: a numerical study using the rotated staggered finite-difference grid. *Geophys. Prospect.* 50 (2), 183–194. doi:10.1046/j.1365-2478.2002.00309.x

Saxena, N., and Mavko, G. (2014). Exact equations for fluid and solid substitution. *Geophysics* 79 (3), L21–L32. doi:10.1190/geo2013-0187.1

Sevostianov, I., and Kachanov, M. (2002a). Explicit cross-property correlations for anisotropic two-phase composite materials. *J. Mech. Phys. Sol.* 50 (2), 253–282. doi:10.1016/s0022-5096(01)00051-5

Sevostianov, I., and Kachanov, M. (2002b). On elastic compliances of irregularly shaped cracks. *Int. J. Fract.* 114 (3), 245–257. doi:10.1023/a:1015534127172

Sevostianov, I., and Kachanov, M. (2008). Normal and tangential compliances of interface of rough surfaces with contacts of elliptic shape. *Int. J. Solids Struct.* 45 (9), 2723–2736. doi:10.1016/j.ijsolstr.2007.12.024

Sevostianov, I., and Kachanov, M. (2012). Is the concept of "average shape" legitimate, for a mixture of inclusions of diverse shapes?. *Int. J. Sol. Struct.* 49 (23-24), 3242–3254. doi:10.1016/j.ijsolstr.2012.06.018

Shapiro, S. A. (2003). Elastic piezosensitivity of porous and fractured rocks. *Geophysics* 68 (2), 482–486. doi:10.1190/1.1567215

Song, Y., Hu, H., and Rudnicki, J. W. (2017a). Dynamic stress intensity factor (Mode I) of a permeable penny-shaped crack in a fluid-saturated poroelastic solid. *Int. J. Solids Struct.* 110-111, 127–136. doi:10.1016/j.ijsolstr.2017.01.034

Song, Y., Hu, H., and Rudnicki, J. W. (2017b). Normal compression wave scattering by a permeable crack in a fluid-saturated poroelastic solid. *Acta Mech. Sin.* 33 (2), 356–367. doi:10.1007/s10409-016-0633-8

Song, Y., Hu, H., and Han, B. (2019). Elastic wave scattering by a fluid-saturated circular crack and effective properties of a solid with a sparse distribution of aligned cracks. *J. Acoust. Soc. Am.* 146 (1), 470–485. doi:10.1121/1.5116917

Song, Y., Hu, H., and Han, B. (2020a). Effective properties of a porous medium with aligned cracks containing compressible fluid. *Geophys. J. Int.* 221 (1), 60–76. doi:10.1093/gji/ggz576

Song, Y., Hu, H., and Han, B. (2020b). P-wave attenuation and dispersion in a fluid-saturated rock with aligned rectangular cracks. *Mech. Mater.* 147, 103409. doi:10.1016/j.mechmat.2020.103409

Song, Y., Rudnicki, J. W., Hu, H., and Han, B. (2020c). Dynamics anisotropy in a porous solid with aligned slit fractures. *J. Mech. Phys. Sol.* 137, 103865. doi:10.1016/j.jmps.2020.103865

Toksöz, M. N., Cheng, C. H., and Timur, A. (1976). Velocities of seismic waves in porous rocks. *Geophysics* 41 (4), 621–645. doi:10.1190/1.1440639

Vlastos, S., Liu, E., Main, I. G., and Li, X.-Y. (2003). Numerical simulation of wave propagation in media with discrete distributions of fractures: effects of fracture sizes and spatial distributions. *Geophys. J. Int.* 152 (3), 649–668. doi:10.1046/j.1365-246x.2003.01876.x

Vlastos, S., Liu, E., Main, I. G., Schoenberg, M., Narteau, C., Li, X. Y., et al. (2006). Dual simulations of fluid flow and seismic wave propagation in a fractured network: effects of pore pressure on seismic signature. *Geophys. J. Int.* 166 (2), 825–838. doi:10.1111/j.1365-246x.2006.03060.x

Vlastos, S., Liu, E., Main, I. G., and Narteau, C. (2007). Numerical simulation of wave propagation in 2-D fractured media: scattering attenuation at different stages of the growth of a fracture population. *Geophys. J. Int.* 171 (2), 865–880. doi:10.1111/j.1365-246x.2007.03582.x

Walsh, J. B., and Grosenbaugh, M. A. (1979). A new model for analyzing the effect of fractures on compressibility. *J. Geophys. Res.* 84 (B7), 3532–3536. doi:10.1029/jb084ib07p03532

Zhao, L., Yao, Q., Han, D.-h., Yan, F., and Nasser, M. (2016). Characterizing the effect of elastic interactions on the effective elastic properties of porous, cracked rocks. *Geophys. Prospecting* 64 (1), 157–169. doi:10.1111/1365-2478.12243

Zhao, Z., Dou, Z., Xu, H., and Liu, Z. (2019). Shear behavior of Beishan granite fractures after thermal treatment. *Eng. Fract. Mech.* 213, 223–240. doi:10.1016/j.engfracmech.2019.04.012

Zhao, L., Cao, C., Yao, Q., Wang, Y., Li, H., Yuan, H., et al. (2020). Gassmann consistency for different inclusion-based effective medium theories: implications for elastic interactions and poroelasticity. *J. Geophys. Res. Solid Earth* 125 (3), e2019JB018328. doi:10.1029/2019jb018328

Zhu, Q., and Shao, J. (2017). Micromechanics of rock damage: advances in the quasi-brittle field. *J. Rock Mech. Geotech. Eng.* 9 (1), 29–40. doi:10.1016/j.jrmge.2016.11.003

Zimmerman, R. W. (1991). Elastic moduli of a solid containing spherical inclusions. *Mech. Mater.* 12 (1), 17–24. doi:10.1016/0167-6636(91)90049-6

Zimmerman, R. W., Somerton, W. H., and King, M. S. (1986). Compressibility of porous rocks. *J. Geophys. Res.* 91 (B12), 12765–12777. doi:10.1029/jb091ib12p12765

Zong, J., Stewart, R. R., Dyaur, N., and Myers, M. T. (2017). Elastic properties of rock salt: laboratory measurements and Gulf of Mexico well-log analysis. *Geophysics* 82 (5), D303–D317. doi:10.1190/geo2016-0527.1

Zong, J., Stewart, R. R., and Dyaur, N. (2020). Attenuation of rock salt: ultrasonic lab analysis of Gulf of Mexico coastal samples. *J. Geophys. Res. Solid Earth* 125 (7), e2019JB019025. doi:10.1029/2019jb019025

Conflict of Interest: The authors declare that the research was conducted in the absence of any commercial or financial relationships that could be construed as a potential conflict of interest.

Copyright © 2021 Fu, Fu, Han and Cao. This is an open-access article distributed under the terms of the Creative Commons Attribution License (CC BY). The use, distribution or reproduction in other forums is permitted, provided the original author(s) and the copyright owner(s) are credited and that the original publication in this journal is cited, in accordance with accepted academic practice. No use, distribution or reproduction is permitted which does not comply with these terms.

APPENDIX A. THE VERIFICATION OF THE ISOTROPY OF THE SAMPLE

In this research, we make the orientations of the fractures are unform, assuming the samples are isotropic. To verify the correction of this assumption, we conduct the numerical test as shown in **Figure A-1**.

We load normal stress P in the two boundaries of the sample, for the dry rocks, and the other boundaries are made to be fixed, and we calculate the strain e_{xx} and e_{yy} for the test in **Figures A-1A, 1B** respectively, and the elastic moduli in the two tests are given by

$$C_{11} = \frac{P}{e_{xx}}. \tag{A-1}$$

and

$$C_{22} = \frac{P}{e_{yy}}, \tag{A-2}$$

where C_{11} and C_{22} are the elastic moduli of the samples in the two directions as shown in **Figures A-1A, 1B**. Then we calculate the relative error between C_{11} and C_{22} by **Eq. A3** as

$$e = \frac{|C_{11} - C_{22}|}{C_{11}}. \tag{A-3}$$

The variation of the relative error vs. perturbation of R^2 is shown in **Figure A-2**. According to the results in **Figure A-2**, the relative errors are all less than 5%. Therefore, the samples can be regarded as isotropic.

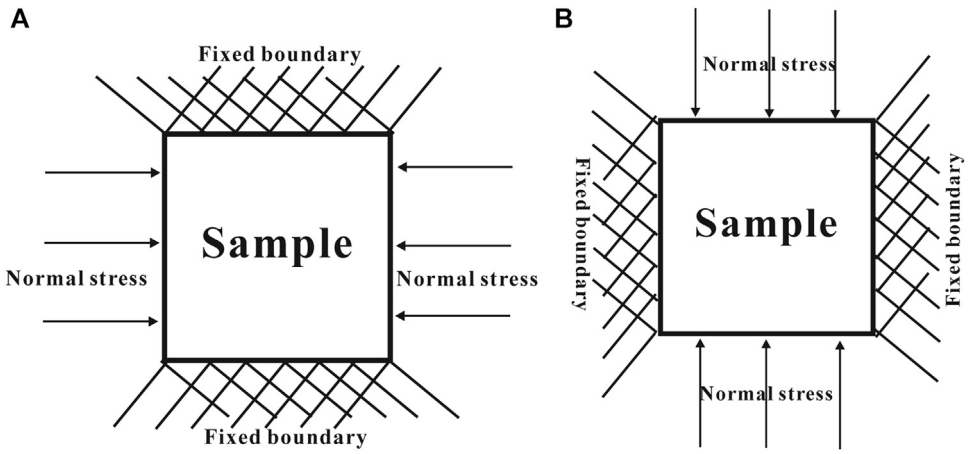

FIGURE A-1 | The test model to verify the isotropy of the sample.

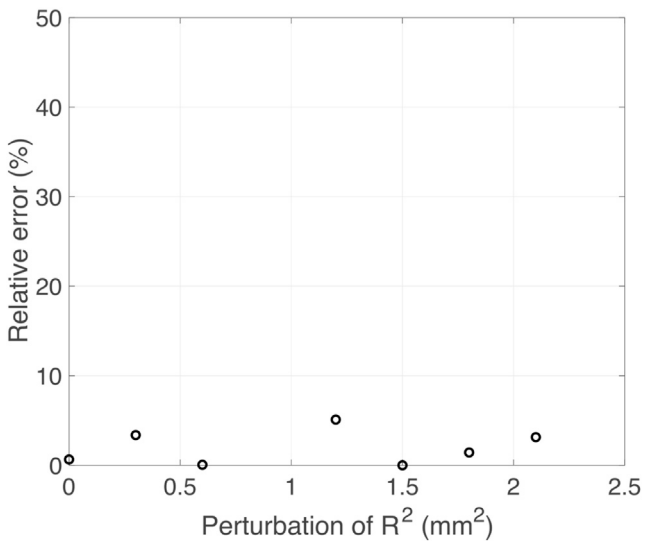

FIGURE A-2 | The Relative error between C_{11} and C_{22}.

frontiers in Earth Science

ORIGINAL RESEARCH
published: 15 April 2021
doi: 10.3389/feart.2021.641177

Attenuation of Seismic Waves in Partially Saturated Berea Sandstone as a Function of Frequency and Confining Pressure

Nicola Tisato[1,2], Claudio Madonna[3] and Erik H. Saenger[4,5,6]*

[1] Jackson School of Geosciences, The University of Texas at Austin, Austin, TX, United States, [2] Department of Civil Engineering, University of Toronto, Toronto, ON, Canada, [3] Structural Geology and Tectonics Group, Department of Earth Sciences, Geological Institute, ETH Zurich, Zurich, Switzerland, [4] Hochschule Bochum, Fachbereich Bau- und Umweltingenieurwesen, Bochum, Germany, [5] Fraunhofer IEG, Bochum, Germany, [6] Ruhr-Universität Bochum, Fakultät für Geowissenschaften, Bochum, Germany

Frequency-dependent attenuation (1/Q) should be used as a seismic attribute to improve the accuracy of seismic methods and imaging of the subsurface. In rocks, 1/Q is highly sensitive to the presence of saturating fluids. Thus, 1/Q could be crucial to monitor volcanic and hydrothermal domains and to explore hydrocarbon and water reservoirs. The experimental determination of seismic and teleseismic attenuation (i.e., for frequencies < 100 Hz) is challenging, and as a consequence, 1/Q is still uncertain for a broad range of lithologies and experimental conditions. Moreover, the physics of elastic energy absorption (i.e., 1/Q) is often poorly constrained and understood. Here, we provide a series of measurements of seismic wave attenuation and dynamic Young's modulus for dry and partially saturated Berea sandstone in the 1–100 Hz bandwidth and for confining pressure ranging between 0 and 20 MPa. We present systematic relationships between the frequency-dependent 1/Q and the liquid saturation, and the confining pressure. Data in the seismic bandwidth are compared to phenomenological models, ultrasonic elastic properties and theoretical models for wave-induced-fluid-flow (i.e., squirt-flow and patchy-saturation). The analysis suggests that the observed frequency-dependent attenuation is caused by wave-induced-fluid-flow but also that the physics behind this attenuation mechanism is not yet fully determined. We also show, that as predicted by wave-induced-fluid-flow theories, attenuation is strongly dependent on confining pressure. Our results can help to interpret data for near-surface geophysics to improve the imaging of the subsurface.

Keywords: Attenuation of seismic waves, dispersion of seismic waves, near-surface geophysics, sedimentary rocks, confining pressure, saturation

OPEN ACCESS

Edited by:
Chong Xu,
National Institute of Natural Hazards, Ministry of Emergency Management, China

Reviewed by:
Jianyong Xie,
Chengdu University of Technology, China
Hanjun Yin,
Hebei GEO University, China

****Correspondence:***
Nicola Tisato
nicola.tisato@jsg.utexas.edu

Specialty section:
This article was submitted to Solid Earth Geophysics, a section of the journal Frontiers in Earth Science

Received: *13 December 2020*
Accepted: *15 March 2021*
Published: *15 April 2021*

Citation:
Tisato N, Madonna C and Saenger EH (2021) Attenuation of Seismic Waves in Partially Saturated Berea Sandstone as a Function of Frequency and Confining Pressure. Front. Earth Sci. 9:641177. doi: 10.3389/feart.2021.641177

INTRODUCTION

Frequency-dependent attenuation of seismic waves ($1/Q$) should be considered in geophysical processing to improve exploration geophysics (e.g., De Siena et al., 2014). In particular, $1/Q$ could provide insights about the physical-chemical state of the Earth's interior including the nature of saturating phases (Chapman et al., 2006; McCarthy et al., 2011; Thakur and Rajput, 2011;

Spencer, 2013; Tisato and Quintal, 2013; Amalokwu et al., 2014; Mikhaltsevitch et al., 2014a,b; Pimienta et al., 2015a,b; Tisato et al., 2015). Geo-materials attenuate seismic waves as a consequence of different mechanisms. For example, in the seismic bandwidth saturated rocks mostly attenuate waves as a consequence of wave-induced-fluid-flow (WIFF) and wave-induced-gas-exsolution-dissolution (WIGED) (e.g., White, 1975; Dutta and Odé, 1979; Mavko and Jizba, 1991; Müller et al., 2010; Tisato et al., 2015). While dry rocks typically exhibit $1/Q < 0.02$, saturated rocks may exhibit frequency-dependent attenuation as high as ∼0.1 (e.g., Winkler and Nur, 1982; Peselnick and Liu, 1987; Yin et al., 1992; Batzle et al., 2006; Barton, 2007; Adam et al., 2009; Tisato and Madonna, 2012; Madonna and Tisato, 2013; Tisato and Quintal, 2014; Pimienta et al., 2015a,b; Tisato et al., 2015; Chapman et al., 2016). For instance, Tisato and Madonna (2012) and Yin et al. (1992) report that in dry and partially saturated Berea sandstone attenuation at ∼100 Hz is ∼0.01 and ∼0.04, respectively.

Wave-induced-fluid-flow can occur at macro-, meso-, or micro- scale depending on the wavelength to the fluid-flow-distance ratio (Mavko et al., 2009). WIFF at the meso- and micro-scale are also known as patchy-saturation and squirt-flow, respectively, and they have been modeled by several authors (e.g., Dvorkin and Nur, 1993; Gurevich and Lopatnikov, 1995; Pride et al., 2004; Jakobsen and Chapman, 2009; Gurevich et al., 2010; Müller et al., 2010; Quintal et al., 2011; Papageorgiou and Chapman, 2015).

Laboratory studies offer the opportunity to understand the physics of attenuation mechanisms and to validate theories (e.g., Tisato and Quintal, 2013). However, the few lithologies and physical conditions investigated to date are insufficient to achieve such a goal, and some studies report measurements which are not yet fully understood (e.g., Tisato and Madonna, 2012).

The present contribution reports a series of seismic wave attenuation measurements in extensional mode (Green et al., 1967, 1974a,b) as a function of frequency and confining pressure for two partially saturated Berea sandstone specimens. Samples were saturated with water, glycerin, and air. Saturation levels were chosen to mimic different saturation conditions as proxies of subsurface reservoir conditions. Moreover, an additional sample is used to estimate pressure-dependent ultrasonic wave velocities for dry Berea sandstone.

We employ phenomenological models to fit the dataset confirming the relation of causality between modulus dispersion and attenuation in our measurements (i.e., Kramers-Kronig relation). Further, squirt-flow and patchy-saturation models and ultrasonic wave speed measurements indicate that WIFF can cause the observed frequency-dependent seismic wave attenuation.

MATERIALS AND METHODS

Samples and Measurements

We present measurements of physical properties for three Berea sandstone samples named: BS2, BS3, and BS5s. The three cylindrical samples were acquired from Cleveland Quarries[1] and had dimensions (length x diameter) of 250 x 75.1 mm, 250 x 75.1 mm, and 59 x 25.6 mm, respectively. The samples' length and diameter were measured with an uncertainty of ± 0.025 mm using a 0.01 mm division caliper. Sample BS3 has hydraulic permeability of $\sim 10^{-12}$ m^2, while BS2 and BS5s, which originated from the same block, have hydraulic permeability of $\sim 0.75 \times 10^{-12}$ m^2. Permeability values were provided by Cleveland Quarries. Berea sandstone contains bedding planes controlling elastic properties anisotropy (Lo et al., 1986; Sayers et al., 1990). The axes of our cylindrical samples were perpendicular to such bedding planes.

For samples BS2 and BS3, we measured the frequency-dependent Young's modulus (E) and seismic wave attenuation, i.e., $1/Q_E$ that here we call $1/Q$ for the sake of simplicity. Measurements were performed at room temperature (∼20° C) in the bandwidth 1– 100 Hz and at confining pressures (P_c) ranging 0 - 20 MPa. Samples were oven-dried at 105° C for more than 24 h, then let cool at room temperature and humidity for several hours, jacketed for testing, and finally loaded inside the testing apparatus. Data are presented for dry and partially saturated samples. Under the aforementioned conditions, we also measured the ultrasonic longitudinal wave speeds of sample BS3. Such measurements were performed at a frequency (f) of ∼100 kHz.

Sample BS5s was smaller than BS2 and BS3, and used to estimate the longitudinal and transverse ultrasonic (f∼1 MHz) velocities of dry samples. The density (ρ) of the dry samples is 2110 ± 31 kg/m^3, and it was obtained from the sample volume and weight, which was measured with a 0.1 g resolution scale. Porosity (Φ) of sample BS5s is 0.205, and it was estimated using a helium pycnometer (AccuPyc 1330, Micromeritics). We use such a porosity value as a proxy for the porosity of BS2 and BS3.

We saturated the samples with air, water, and a water-glycerin mixture. The latter is called GWmix and contains 55 and 45 volume % of glycerin and distilled water, respectively. In general, the subscript W and GW refer to water and GWmix, respectively. GWmix viscosity ($\eta_{GW} = 11 \pm 0.25$ mPa s) and density ($\rho_{GW} = 1.12 \pm 0.02$ g/cm^3) were measured with a falling ball viscometer, a 0.1 mg precision scale and a 0.1 ml precision vial, respectively. The bulk modulus of GWmix ($K_{GW} = 2.4 \pm 0.1$ GPa) was estimated by analyzing the pressure-volume curve obtained with a high-pressure syringe pump (ISCO 260D). Sample BS2 was saturated with air and water, while BS3 was saturated with air and GWmix.

While inside the pressure vessel, water or GWmix (i.e., liquid) was pumped into the sample through the sample bottom-end-face, letting air flow through the sample top-end-face. Saturation was calculated according to the quantity of injected liquid and the porosity of the sample. The injected liquid was drained from a graduated burette, and any excess liquid flowing through the top end-faces was collected on a second graduated burette. Thus, the volume of injected liquid was estimated as the difference between the liquid levels in the two graduated burettes. Some of the injected fluid was used to fill

[1]https://www.bereasandstonecores.com

the hydraulic circuit and was not considered in the saturating fluid volume. In particular, before recording the initial volume of fluid in the burettes, we prefilled the injection circuit except for the bottom sample holder to avoid sample imbibition. We also estimated the internal volumes of the sample holders and draining circuit with an accuracy of +/−1 ml representing less than 0.5% of BS2 or BS3 pore space volume. Once the wanted saturation was reached, the sample was isolated from the hydraulic circuit by closing the inlet and outlet valve. All the experiments were performed with fluid pressure equal to room pressure (∼0.1 MPa), and P_c represents a proxy for effective stress (σ').

Each saturated sample effective density (ρr) was estimated considering the rock porosity, saturation, and fluid density. **Table 1** reports a summary of the characteristics of each sample and the conducted tests.

Low-Frequency Testing

Attenuation and complex Young's modulus in the bandwidth 1 – 100 Hz are obtained employing the sub-resonance method (McKavanagh and Stacey, 1974). Attenuation is:

$$\frac{1}{Q} = \tan\varphi, \tag{1}$$

where φ is the phase shift between the stress (σ) imposed by the seismic wave and the strain (ε) measured across the whole sample. Q is the quality factor. The σ to ε ratio equals the complex Young's

TABLE 1 | Properties of samples and measurements performed.

	Properties				Measurements			Saturated with		
Sample	**Length [mm]**	**Diameter [mm]**	**Φ**	**κ x 10^{12} [m^2]**	**$1/Q_E$ at 1-100 Hz**	**V_p at MHz**	**V_s at MHz**	**Air**	**Water**	**GWmix**
BS2	250	75.1	20.5 ± 0.5	0.75	X			X	X	
BS3	250	75.1	20.5 ± 0.5	1	X	X		X		X
BS5s	59.03	25.64	20.5 ± 0.5	0.75		X	X	X		

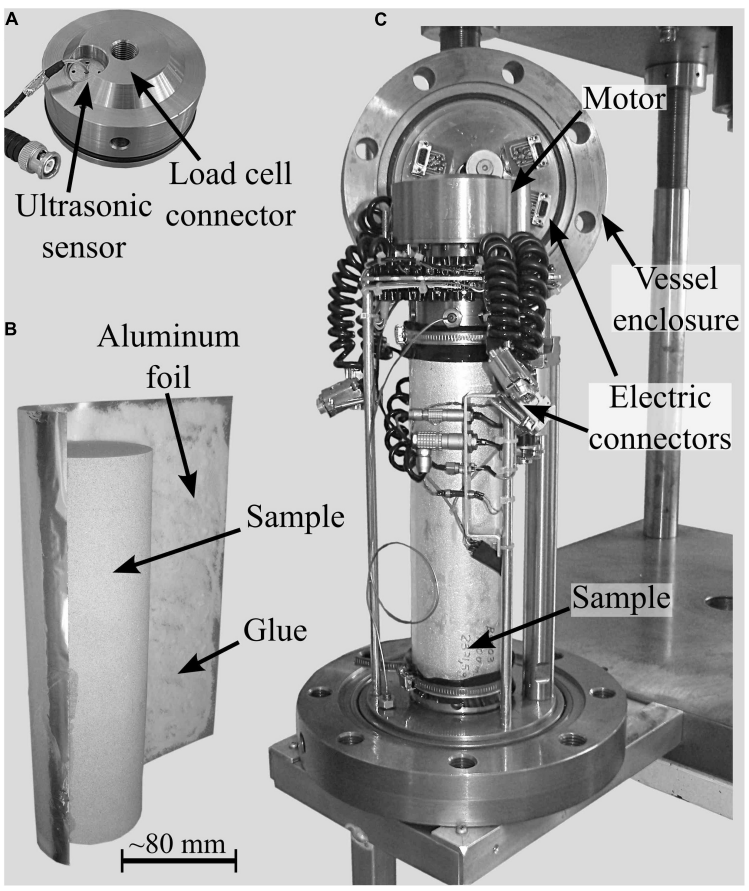

FIGURE 1 | The Burlini attenuation vessel (BBAV). **(A)** Top-sample holder. **(B)** Detail about the application of the aluminum foil on the sample. We employed "tesa spray glue extra strong." **(C)** Measuring column of the BBAV that during testing is mounted inside the pressure vessel (here not shown).

modulus (E_z), so that $1/Q$ is also:

$$\frac{1}{Q} = \frac{Im(E_Z)}{Re\,(E_Z)}, \quad (2)$$

The real part of E_z [i.e., $Re(E_z)$] or simply E_{SF} is given by:

$$E_{SF} = \frac{\sigma_{pp}}{\varepsilon_{pp}}\cos\varphi, \quad (3)$$

where *SF* stands for "seismic-frequencies," σ_{pp} and ε_{pp} are the peak-to-peak values of the σ and ε, respectively (Lakes, 2009). ε_{pp} was kept around $1.2x10^{-6}$, which is similar to the strain caused by the propagation of a seismic wave (Karato and Spetzler, 1990).

The extensional seismic wave attenuation ($1/Q$) and complex Young's modulus (E_Z) of sample BS2 and BS3 were measured using the Burlini attenuation vessel (BBAV) (**Figure 1**; Tisato and Madonna, 2012). We calculated i) the stress from the load-cell measurement (i.e., force) and the sample cross-section area, and ii) the strain from the displacement sensor measurement (i.e., sample shortening) and sample length. Force and shortening time series are fit with sinusoidal functions. Amplitude and phase of the fitting functions yield the parameters to calculate $1/Q$ and E_{SF}. The fitting functions are assumed to represent the true values. We calculate two standard deviations between the true values and the measurements to estimate the 95% confidence bounds on both the amplitude and the phase of the signals. Such uncertainties and those related to the sample cross area and length provide a proxy for accuracy on Young's modulus and attenuation. Precision (i.e., repeatability) is estimated by calculating the standard deviation of five measurements performed at each frequency. Accuracy and precision are summed to provide uncertainty on the measurements that are provided as error bars in **Figures 2–8**.

The curved face of the samples was covered with an aluminum foil, which was glued onto the rock, and a jacket made of Fluorinated Ethylene Propylene (FEP) shrink-tubing. These two layers do not affect the stiffness of the sample, isolate the sample from the confining medium (i.e., silicon oil) and avoid that the curved face of the sample acts as a free-flow boundary by limiting the saturating fluid to escape radially while the sample is dynamically stressed (Gardner, 1962; Dunn, 1986) (see **Supplementary Material**). In addition, the specimen end-faces were machined on a grinder to obtain a parallelism tolerance of ∼40 μm to meet the required experimental accuracy (Paffenholz and Burkhardt, 1989).

A uniaxial press, which is driven by a servo-electric uniaxial actuator, hosts the BBAV and applies the vertical stress on the sample (σ_1). During testing, the stress field applied to the specimen was: $\sigma_1 = P_c + 2.8$ MPa and $\sigma_2 = \sigma_3 = P_c$. The vertical stress ($\sigma_1$) was intentionally kept 2.8 MPa higher than the confining pressure to ensure good coupling between the horizontal interfaces of the sample assembly.

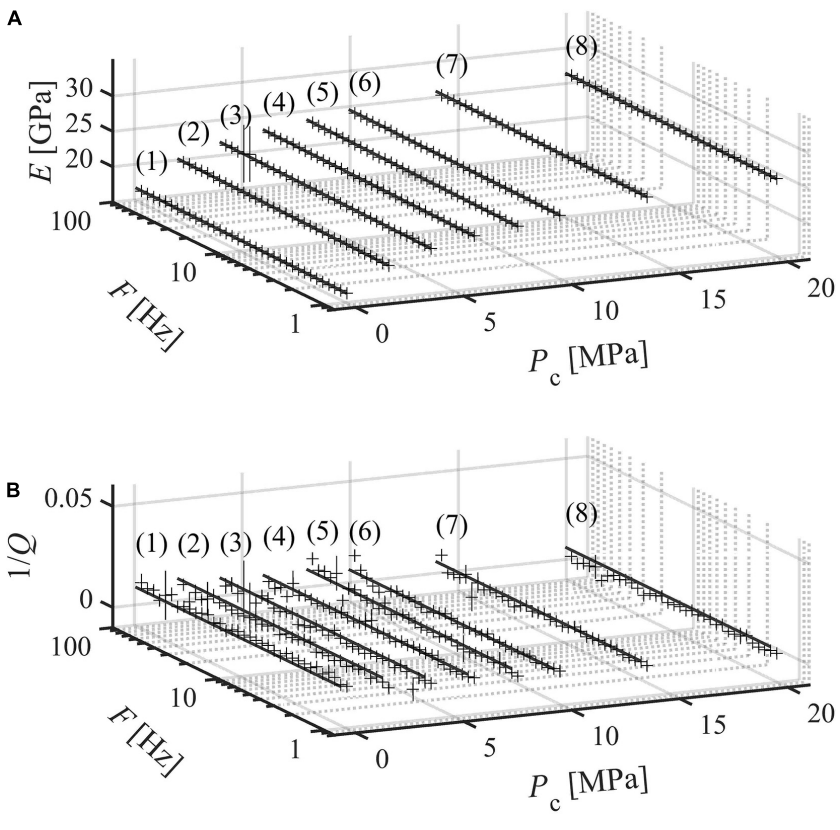

FIGURE 2 | Measurements for *case i* (BS3 dry). **(A)** Dynamic Young's modulus and **(B)** attenuation in the bandwidth 1–100 Hz. Vertical bars indicate the sum of measurement uncertainty and repeatability. Results are interpolated with the nearly constant *Q* model (NCM) (Liu et al., 1976).

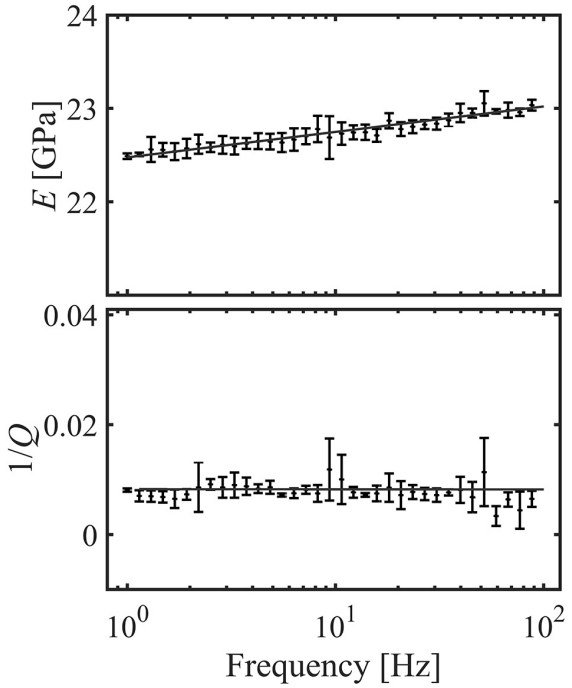

FIGURE 3 | Close up of **Figure 2** curves 4A and 4B (P_c = 6 MPa). Fits (solid lines) are performed by means of the nearly constant *Q* model (NCM) (Liu et al., 1976).

The low-frequency seismic wave was generated as a sinusoidal variation (σ) of the vertical stress. A piezoelectric motor, which is controlled by a high voltage amplifier, generates such a sinusoidal variation of σ_1 that is necessary to estimate the complex Young's modulus and attenuation. σ and ε are estimated for the measurements performed using a load cell and a cantilever, respectively. Calibration and additional details about the BBAV apparatus are reported in Tisato and Madonna (2012).

Ultrasonic Testing

Longitudinal (V_P) and transverse (V_S) ultrasonic velocities were obtained using the pulse transmission method (Birch, 1960). V_P of BS3 was measured during low-frequency testing inside the BBAV, and the stress field applied to the specimen was: $\sigma_1 = P_c + 2.8$ MPa and $\sigma_2 = \sigma_3 = P_c$. Uncertainties were estimated combining: (i) the uncertainty on picking the first arrival, (ii) the uncertainty on the delay introduced by the apparatus (26.1 ± 2 μs), (iii) the uncertainty on the sample length (1 mm), and (iv) the variability between two consecutive sets of measurements. The two sets of measurements were respectively collected for consecutive increasing and then decreasing P_c. For each confining pressure, the velocity was computed as the average between such two measurements. For each seismogram, the first arrival uncertainty was assessed by picking a minimum (t_{min}) and a maximum (t_{max}) time value to the first arrival. Such values were always around the wavelet onset, and they typically differ of ∼1 μs. The first arrival and its uncertainty were then calculated as $\frac{t_{min} + t_{max}}{2}$ and $\frac{t_{min} - t_{max}}{2}$, respectively.

On the other hand, V_P and V_S of BS5s were measured employing another pressure vessel named Geneva-Rig in which the stress field applied to the specimen was hydrostatic, i.e., $\sigma_1 = \sigma_2 = \sigma_3 = P_c$ (Zappone et al., 2000; Kästner et al., 2020). We calculated uncertainties combining: (i) the uncertainty on picking the P- and S-wave arrivals, (ii) the uncertainties on the delay introduced by the apparatus (∼1.06 ± 0.4 μs and ∼10.5 ± 0.8 μs for P and S-waves, respectively) and (iii) the uncertainty on the sample length. Two tests were conducted at increasing and decreasing confining pressures between 1 and 40 MPa. The results, i.e., velocities vs confining pressure, were fit with empirical relations that are described by the following equation:

$$V_{P,S} = A + B\,P_C + C\,e^{D\,P_C}, \tag{4}$$

where *A*, *B*, *C*, and *D* are the best-fit parameters estimated through least square minimization (Eberhart-Phillips et al., 1989). Ultrasonic shear (μ_{HF}) and bulk (K_{HF}) moduli were estimated as:

$$\mu_{HF} = {V_S}^2\,\rho_r, \tag{5}$$

$$K_{HF} = {V_P}^2\,\rho_r - \frac{4}{3}\mu_{HF} \tag{6}$$

where *HF* stands for "high-frequency" and ρ_r is the effective sample density. For dry conditions, we refer to the ultrasonic bulk and shear modulus as: $K_{HF(Sa\,=\,1)}$ and $\mu_{HF(Sa\,=\,1)}$, respectively; where S_a is the gas (air) saturation. Then, ultrasonic Young's modulus (E_{HF}) was estimated as:

$$E_{HF} = \frac{9K_{HF}\,\mu_{HF}}{3K_{HF} + \mu_{HF}} \tag{7}$$

(Mavko et al., 2009).

Phenomenological Models

Modulus dispersion and attenuation are linked through the Kramers-Kronig relation or causality (Lakes, 2009). Experimental data have been previously verified through the Kramers-Kronig relation (e.g., Mikhaltsevitch et al., 2016). Here, to verify that our results honor causality, we use two phenomenological models that obey the Kramers-Kronig relation. For frequency-independent measurements, we utilize the nearly constant *Q* model (NCM) (Liu et al., 1976). For frequency-dependent measurements, we use the sum of the NCM and the standard linear solid model (SLS) (Carcione, 2007) (see **Supplementary Material**). We assume that the sum of attenuation is an appropriate operation as Johnston et al. (1979) and Tisato and Quintal (2013) show that the frame-related attenuation and the fluid-related attenuation are independent and can be summed to obtain the total attenuation of the saturated sample. In particular, we assume that the frame related attenuation is constant, regardless of the saturation level, and the fluid-related attenuation is a function of saturation and can be represented by the SLS rheology. Such fitting is possible as wave-induced fluid flow mechanisms and SLS produce a low-frequency asymptote that scale as $Q^{-1} \propto f$ (Mueller et al., 2010).

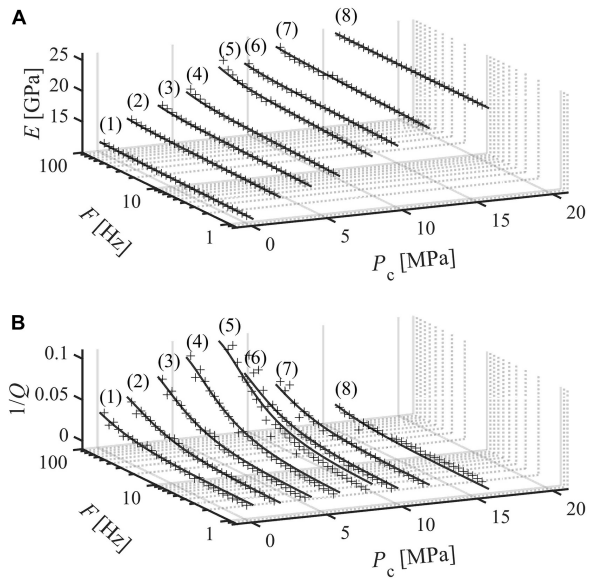

FIGURE 4 | Measurements for *case ii* (BS2 S_W = 60%). **(A)** Young's modulus and **(B)** attenuation in the bandwidth 1–100 Hz. Vertical bars indicate the sum of measurement uncertainty and repeatability. Results are interpolated with the nearly constant *Q* model (NCM) and the standard linear solid model (SLS) (Liu et al., 1976; Carcione, 2007).

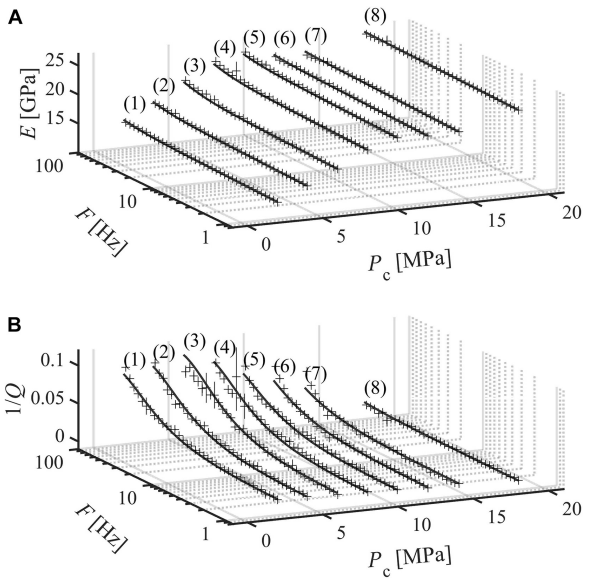

FIGURE 6 | Measurements for *case iv* (BS3 S_{GW} = 80.2%). **(A)** Young's modulus and **(B)** attenuation in the bandwidth 1–100 Hz. Vertical bars indicate the sum of measurement uncertainty and repeatability. Results are interpolated with the nearly constant *Q* model (NCM) and the standard linear solid model (SLS) (Liu et al., 1976; Carcione, 2007).

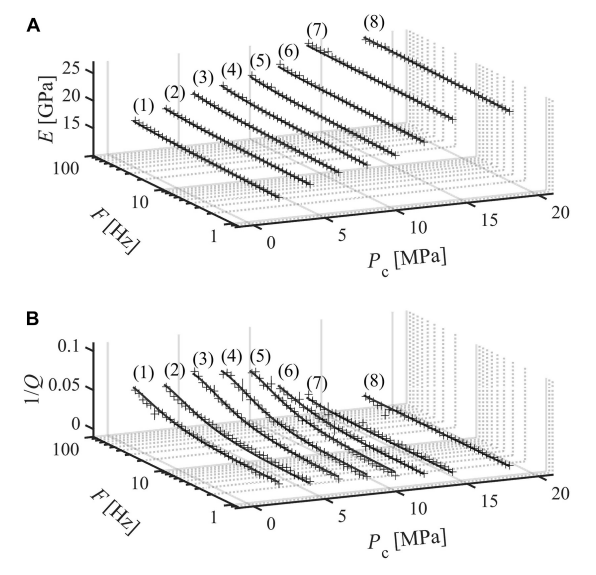

FIGURE 5 | Measurements for *case iii* (BS3 S_{GW} = 53.5%). **(A)** Young's modulus and **(B)** attenuation in the bandwidth 1–100 Hz. Vertical bars indicate the sum of measurement uncertainty and repeatability. Results are interpolated with the nearly constant *Q* model (NCM) and the standard linear solid model (SLS) (Liu et al., 1976; Carcione, 2007).

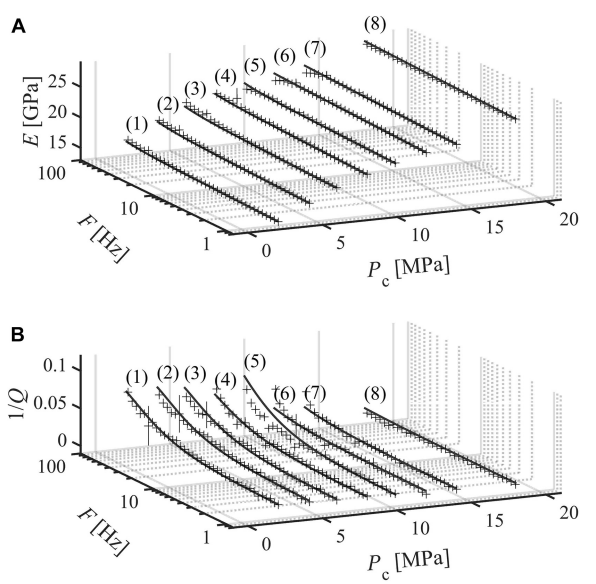

FIGURE 7 | Measurements for *case v* (BS3 S_{GW} = 86.4%). **(A)** Young's modulus and **(B)** attenuation in the bandwidth 1–100 Hz. Results are interpolated with the nearly constant *Q* model (NCM) and the standard linear solid model (SLS) (Liu et al., 1976; Carcione, 2007).

Wave-Induced-Fluid-Flow Modeling

The characteristic frequency for patchy-saturation is:

$$f_{patchy} \approx \frac{\kappa K_s}{\pi L^2 \eta_f}, \tag{8}$$

where κ is the rock permeability, K_s is the bulk modulus of the saturated rock, L is the characteristic size of the patches (White, 1975). For the present experiments, we can assume $\kappa = 10^{-12}$ m^2, L ranging between 1 and 10 cm, η_f ranging between η_W and η_{GW} and K_s ranging between 10 and 20 GPa. The selected range of K_s

agrees with the literature, and the ultrasonic measurements will later confirm it. According to this parameter space, f_{patchy} ranges between ∼28 Hz and ∼63 kHz.

Jones (1986) provides a formula for the squirt-flow characteristic frequency, which is:

$$f_{squirt} \approx \alpha^3 \frac{K_g}{\eta_f}, \tag{9}$$

where α is the characteristic crack aspect ratio for the rock, and K_g is the bulk modulus of the rock frame. For the present experiments, we assume α ranging between 10^{-4} and 10^{-3} (Zimmerman, 1991), η_f ranging between η_W and η_{GW} and K_g = 37 GPa, as Berea sandstone is mainly composed of quartz. According to this parameter space, f_{squirt} ranges between ∼3 Hz and 37 kHz.

The two wave-induced-fluid-flow mechanisms operate in the bandwidth of investigation (i.e., 1–100 Hz); therefore, both are considered as potential attenuation mechanisms in our experiments. We also rule out the possibility that the observed frequency-dependent attenuation is caused by global flow as the characteristic frequency of such attenuation mechanism ranges above 30 kHz, which is well above the upper limit of the investigated bandwidth (Biot, 1956).

To further investigate the occurrence of wave-induced-fluid-flow we compared ultrasonic and low-frequency elastic properties to effective medium theories: namely Biot-Gassmann-Hill (Johnson, 2001) and Gassmann fluid substitution (Gassmann, 1951), respectively; And, we also compared the phenomenological model fittings with analytical solutions for squirt-flow and patchy-saturation (White, 1975; Dutta and Odé, 1979; Gurevich et al., 2010).

Analytical Solution for Squirt-Flow

We use the model proposed by Gurevich et al. (2010) to estimate complex frequency-dependent Young's modulus due to squirt-flow. Such a model deals with fully saturated rocks while our samples are partially saturated. Thus, we assume that squirt-flow operates only in the liquid saturated portion of the sample and that the dry portion of the sample presents negligible attenuation. Under this assumption, we approximate the imaginary part of the sample Young's modulus by multiplying the imaginary part of the calculated Young's modulus and the saturation. Attenuation is then computed as the ratio between the imaginary and the real part of Young's modulus. The procedure and the equations that are used to model squirt-flow are reported in the **Supplementary Material**.

The model requires the knowledge of: (i) Bulk and shear modulus of the dry rock; (ii) Bulk and shear modulus of the mineral making up the rock (K_g and μ_g); (iii) Crack porosity (Φ_c); and (iv) Mean crack aspect ratio (α). For the saturating fluid, the required properties are: (i) Density (ρ_w or ρ_{GW}); (ii) Viscosity (η_w or η_{GW}); and (iii) Bulk modulus (K_w or K_{GW}). In addition, the model needs the effective pressure at which the cracks can be considered closed (P_h) and the related rock bulk modulus (K_h).

Analytical Solution for Patchy-Saturation

Complex Young's modulus and attenuation related to patchy-saturation are calculated according to the model proposed by White (1975) and Dutta and Odé (1979). To model patchy saturation, we use the Matlab code "patchw" provided by Mavko et al. (2009), and that can be downloaded at https://pangea.stanford.edu/departments/geophysics/dropbox/SRB/public/data/RPHtools.htm.

The model assumes that the rock is saturated with two fluid phases, i.e., liquid and gas. In addition to the petrophysical parameters that are listed in the previous paragraph, and with the exception of Φ_c, α, P_h, and K_h, the model requires (i) Rock porosity (Φ); (ii) Hydraulic permeability (κ); (iii) Gas density (ρ_a); (iv) Gas viscosity (η_a); (v) Gas bulk modulus (K_a); and (vi) The radius representing the average size of the liquid patches that are surrounded by air (r_p).

LABORATORY RESULTS

Here, we report the measurements for seven different cases. For the sake of simplicity, we present all the measurements for case *i* to *v* but not for case *vi* and *vii*. Nevertheless, results from all the cases are available for download and used later for the modeling and discussion:

i. Sample BS3 when dry (equilibrated with room humidity);
ii. Sample BS2 saturated with 60% water (S_W = 60%);
iii. Sample BS3 saturated with 53.5 ± 1.6% GWmix (S_{GW} = 53.5%);
iv. Sample BS3 saturated with 80.2 ± 2.3% GWmix (S_{GW} = 80.2%);
v. Sample BS3 saturated with 86.4 ± 2.5% GWmix (S_{GW} = 86.4%);
vi. Sample BS3 saturated with 35.6 ± 1.1% GWmix (S_{GW} = 35.6%);
vii. Sample BS3 saturated with 71.6 ± 2.1% GWmix (S_{GW} = 71.6%).

The portion of pore volume that was not saturated with water or GWmix was saturated with air. Thus, we express air saturation as:

$$S_a = 1 - (S_{GW} \vee S_W). \tag{10}$$

Where ∨ means or.

We present Young's modulus and attenuation values for *case i* through *v*. For each *case* we report curves for eight different confining pressures ranging between 0 and 20 MPa. Each curve consists of 30 to 36 measurements taken at frequencies between 1 and 100 Hz. Therefore, we present ∼1440 measurements of Young's modulus and attenuation. Each attenuation measurement is calculated as the average of five measurements acquired at the same frequency. The standard deviation of the five repetitions is used to estimate precision that is shown as half-height of the error bar.

For dry Berea sandstone (*case i)*, attenuation is frequency-independent, and around 0.01, and Young's modulus increases

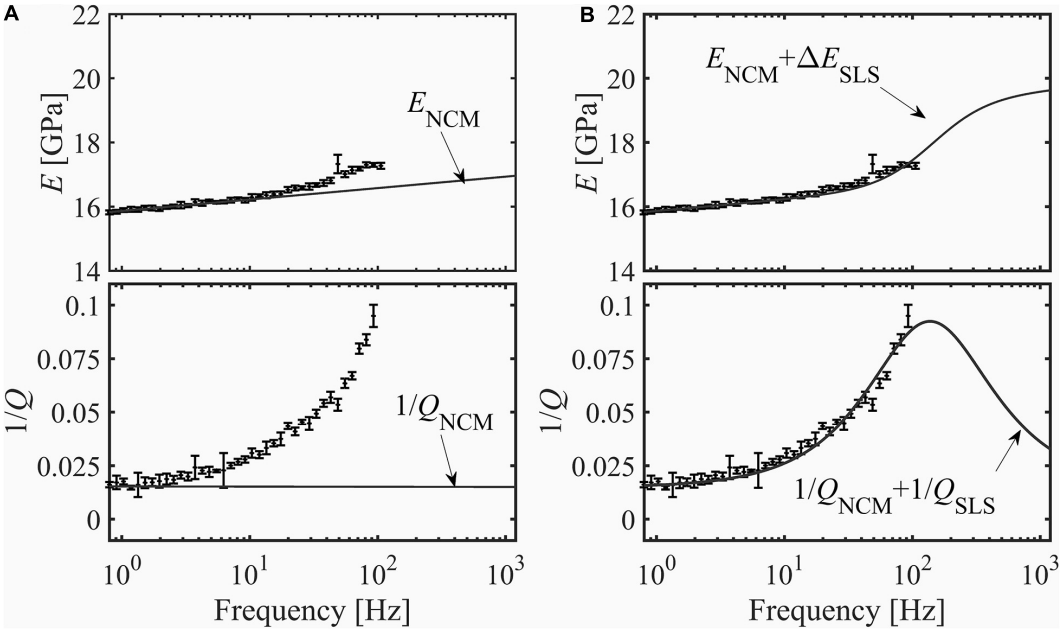

FIGURE 8 | Close up of **Figure 7** curves 4A and 4B. **(A)** First step of the fitting procedure. The linear increase of *E* and the frequency independent part of 1/*Q* are interpolated with the nearly constant *Q* model (NCM) (Liu et al., 1976). **(B)** Second step of the fitting procedure. The residuals between the NCM fitting and the measurements are interpolated with the standard linear solid model (SLS) (Carcione, 2007). Finally, NCM and SLS fittings are summed.

logarithmically with frequency (**Figure 2**). Data are in agreement with the NCM model (**Figure 3**).

For each test of *case i*, we averaged Young's modulus and the attenuation over the frequency bandwidth. As a general trend, we observe that as confining pressure increases, the averaged *E* increases from ∼17 to ∼26 GPa, and 1/*Q* decreases from ∼0.01 to ∼0.005.

Besides, measurements performed on partially saturated samples (*case ii*, *iii*, *iv,* and *v*) show two distinct regimes:

a. At confining pressures above 14 MPa, attenuation is frequency-independent with values similar to those measured in *case I* (i.e., at dry conditions). Moreover, Young's modulus increases logarithmically with frequency, which is in agreement with the NCM model;
b. At confining pressures below 14 MPa, attenuation and Young's modulus are frequency-dependent (**Figures 4–7**) and can fit the sum of the NCM and SLS model (**Figure 8**).

SLS fitting provides an estimate for corner frequency (f_c), i.e., the frequency at which attenuation is maximum. Such corner frequencies range between 114 and 579 Hz (**Table 2**). For example, for *case ii* (S_W = 60%) and confining pressure 8 MPa, 1/*Q* increases from ∼0.01 to ∼0.08 as frequency increases from 1 to 100 Hz (**Figure 4** curve 5). Similarly, measurements conducted on the samples saturated with GWmix (*case iii*, *iv* and *v*) are frequency-dependent, and 1/*Q* varies with confining pressure. For *case iii* (S_{GW} = 53.5%), 1/*Q* values are statistically lower than those measured for *case iv* and *v* (S_{GW} = 80.2% and 86.4%, see **Figures 6–8**), suggesting that the higher the saturation - in the considered range - the higher the attenuation. For each curve in **Figures 4A**, **5A**, **6A**, **7A** and each curve in **Figures 4B**, **5B**, **6B**, **7B** we calculate:

a. the mean value of Young's modulus ($\hat{E}$);
b. the maximum values of attenuation [$Max(1/Q)$];
c. the minimum values of attenuation [$Min(1/Q)$].

Such values are reported in **Figure 9**, highlighting how $\hat{E}$ increases with confining pressure and how dispersion and attenuation decrease for confining pressures > 12 MPa.

Longitudinal (V_p) and transverse (V_s) ultrasonic velocities of dry BS5s increase with confining pressure (0 - 40 MPa) from 2426 to 3752 m/s and from 1880 to 2429 m/s, respectively. Curves that show velocities as a function of confining pressure are fit according to Eq. 4, yielding the following two equations:

$$V_P\left(\frac{m}{s}\right) = 3601 + 4.2\,P_C\,(MPa) - 1192\,e^{-0.16\,P_C\,(MPa)}, \tag{11}$$

$$V_S\left(\frac{m}{s}\right) = 2413 + 0.86\,P_C\,(MPa) - 533\,e^{-0.08\,P_C\,(MPa)}, \tag{12}$$

V_p was also measured for sample BS3. **Figure 10** shows velocities curves as a function of confining pressure for different cases. Saturated BS3 exhibits higher V_p than those measured for dry BS3. For example, for *case v* (S_{GW} = 86.4%) and *vi* (S_{GW} = 35.6%), and confining pressure comprised between 2 and 25 MPa, V_p ranges between 3328 and 3822 m/s and between 3073 and 3652 m/s, respectively. These results agree well with the literature (e.g, Christensen and Wang, 1985; Winkler, 1985; Prasad and Manghnani, 1997).

TABLE 2 | Summary of low-frequency Young's modulus and attenuation measurements.

	Case	Figure	curve	P_c [MPa]	a [GPa]	E_0 [GPa]	Q_{NCM}	t_0 [ms]	t_d [ms]	f_c [Hz]
Dry (BS3)	i	2	1	0	0.214	16.3	112	–	–	–
			2	2	0.318	19.6	91	–	–	–
			3	4	0.288	21.3	109	–	–	–
			4	6	0.273	22.5	121	–	–	–
			5	8	0.300	23.2	114	–	–	–
			6	10	0.230	24.1	154	–	–	–
			7	14	0.220	25.4	170	–	–	–
			8	20	0.236	26.0	162	–	–	–
S_W = 60% (BS2)	ii	4	1	0	0.171	11.1	95	3.34	3.09	311
			2	2	0.200	14.1	104	5.91	5.40	177
			3	4	0.287	15.3	79	5.93	5.19	180
			4	6	0.350	16.6	70	7.28	6.20	149
			5	8	0.573	19.2	50	8.07	6.76	135
			6	10	0.370	20.5	81	5.43	4.80	196
			7	12	0.422	22.8	80	4.09	3.72	256
			8	16	0.001	25.0	> 1000	–	–	–
S_{GW} = 53.5% (BS3)	iii	5	1	2	0.368	14.6	58	7.07	6.60	146
			2	4	0.278	16.3	87	7.88	7.31	132
			3	6	0.423	18.0	63	9.02	8.27	116
			4	8	0.417	18.8	66	9.15	8.38	114
			5	10	0.425	20.0	69	7.94	7.31	131
			6	12	0.266	21.9	121	5.62	5.32	183
			7	14	0.235	25.5	160	–	–	–
			8	18	0.255	25.9	149	–	–	–
S_{GW} = 80.2% (BS3)	iv	6	1	2	0.318	13.6	63	7.15	6.18	150
			2	4	0.356	15.9	66	7.72	6.60	140
			3	6	0.413	18.2	65	8.68	7.29	126
			4	8	0.384	20.9	80	7.75	6.62	140
			5	10	0.396	22.5	83	6.16	5.43	173
			6	12	0.367	22.3	89	3.89	3.41	274
			7	14	0.400	22.4	83	–	–	–
			8	18	0.284	25.1	130	–	–	–
S_{GW} = 86.4% (BS3)	v	7	1	2	0.299	14.3	70	6.00	5.30	177
			2	4	0.366	16.8	68	6.05	5.34	176
			3	6	0.362	18.8	77	5.83	5.17	182
			4	8	0.368	20.5	82	4.86	4.39	216
			5	10	0.328	21.7	96	3.95	3.28	278
			6	12	0.397	23.1	86	1.79	1.66	579
			7	14	0.372	23.9	94	–	–	–
			8	18	0.346	27.0	113	–	–	–

*Parameters a and E_0 are the fitting parameters for the nearly constant Q model (NCM) (see **Supplementary Material**). Parameter Q_{NCM} is the quality factor value obtained from the NCM fitting. Parameters t_0 and t_1 are the fitting parameters for the standard linear solid model (SLS) (see **Supplementary Material**). Parameter f_c is the corner frequency at which the SLS model gives maximum attenuation.*

MODELING AND DISCUSSION

Frequency-independent attenuation is observed for dry samples and samples confined at $P_c \geq 14$ MPa, and it could be caused by grain-to-grain friction (Walsh, 1966). Measurements show that as confining pressure increases, elastic moduli increase, and $1/Q$ decrease (**Table 2**). Similar results for ultrasonic waves were presented, for instance, by Molyneux and Schmitt (1999), Prasad and Manghnani (1997), and Toksöz et al. (1979). Elastic moduli increase as confining pressure closes cracks increasing grain-to-grain traction (Zimmerman, 1991). A decreasing $1/Q$ might be explained by pressure-dependent crack closure and grain-to-grain traction increment (Molyneux and Schmitt, 1999). The contact between two grains occurs only on a limited area throughout the contact of several asperities populating the grains' surfaces (Archard, 1953). Hulikal et al. (2015) suggest that each single asperity contact rheology could be modeled by a standard linear solid exhibiting a specific relaxation time (i.e., corner frequency). Relaxation time is a function of the asperity state and the petrophysical properties of the material. A large number of asperity contacts,

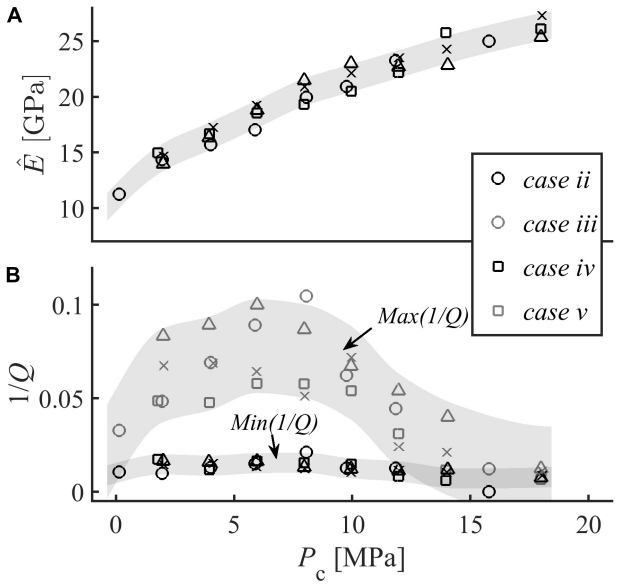

FIGURE 9 | (A) Mean values of Young's modulus ($\hat{E}$) measured in the bandwidth 1–100 Hz for *case ii, iii, iv, and v*. **(B)** Minimum [*Min*(1/*Q*)] and maximum [*Max*(1/*Q*)] values of attenuation in the bandwidth 1–100 Hz measured for *case ii, iii, iv, and v*.

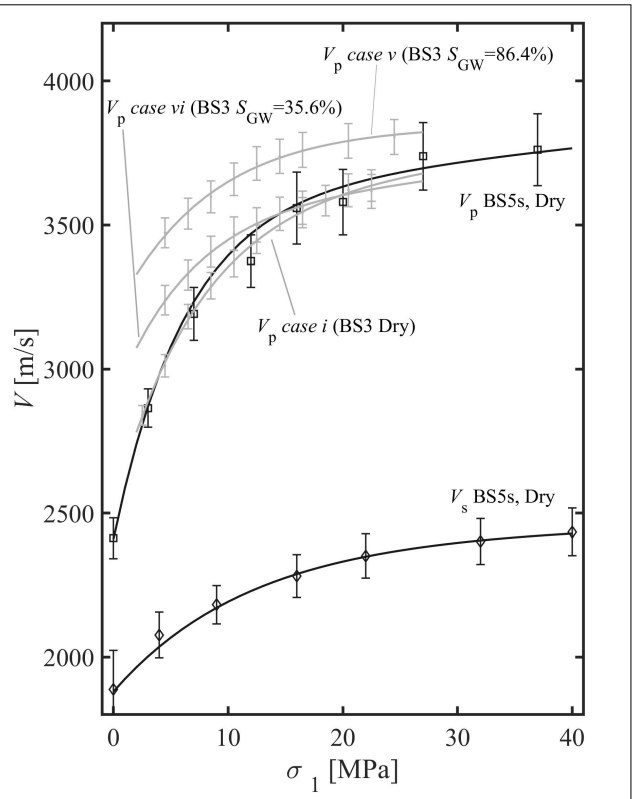

FIGURE 10 | Longitudinal (V_p) and transverse (V_s) wave speeds measured for samples BS5s and BS3 as a function of vertical stress (σ_1). Ultrasonic wave speeds were measured for all the *cases* except *case ii*. However, for the sake of visualization, we show only a few cases. Error bars are calculated based on manual-picking uncertainty, sample length uncertainty and apparatus calibration.

making up the whole population of grain-to-grain contacts of a rock sample, will eventually exhibit a broad spectrum of corner frequencies. The superposition of all the corner frequencies would eventually produce a macroscopic rheology that might be described by a nearly constant attenuation model (Liu et al., 1976). We hypothesize that a decrease in attenuation, as P_c increases, could be the result of contact stiffening and increase of the grain contacts areas (Archard, 1957). In fact, contact stiffening would change the strain partitioning between contacts and solid grains, hindering the overall viscous behavior due to contact deformation (Johnston et al., 1979).

Attenuation measurements are frequency-dependent for partially saturated Berea sandstone and confining pressure < 14 MPa. Measurements agree with the sum of the nearly constant Q model (NCM) and the standard solid model (SLS), confirming that attenuation and Young's modulus obey the Kramers-Kronig relation (Lakes, 2009; **Figures 4–7**). As already suggested by Kuteynikova et al. (2014) and Tisato and Quintal (2013, 2014) in partially saturated Berea sandstone attenuation can result from the sum of frequency-independent and frequency-dependent mechanisms. Here, we assume that also in saturated samples, friction causes the frequency-independent attenuation, while patchy-saturation and/or squirt-flow cause the frequency-dependent attenuation (White, 1975; Dutta and Odé, 1979; Mavko and Jizba, 1991)(White, 1975; Dutta and Odé, 1979; Mavko and Jizba, 1991). In the next paragraphs, we will test such a hypothesis by employing some theoretical models to fit the observations. The petrophysical parameters employed in the modeling are listed in **Table 3**.

Evidences for Patchy-Saturation

Patchy-saturation characteristic frequency f_{patchy} sets the limit between the flow or "relaxed" limit and no-flow or "unrelaxed" limit. The two limits are valid for $f << f_{patchy}$ and $f >> f_{patchy}$, respectively. As already mentioned in par. 2.5, in our case patchy-saturation might operate at frequencies between 28 Hz and 63 kHz. Thus, ultrasonic measurements (E_{HF}), which have been collected at $f >$ 100 kHz, represent a good proxy for the "unrelaxed" limit.

The unrelaxed Young's modulus (E_U) can be calculated as:

$$E_U = \frac{9K_U\mu_{HF}}{3K_U + \mu_{HF}} \tag{13}$$

where K_U is the unrelaxed bulk modulus calculated according to the Biot-Gassmann-Hill limit (Johnson, 2001):

$$K_U = \frac{1}{\frac{1-S_a}{K_1+\frac{4}{3}\mu_{HF}} + \frac{S_a}{K_2+\frac{4}{3}\mu_{HF}}} - \frac{4}{3}\mu_{HF}, \tag{14}$$

TABLE 3 | Petrophysical parameters employed for modeling.

	Case ii, BS2			Case iii, BS3			Case v, BS3			Unit	Description	*Squirt flow*	*Patchy saturation*
	Water			**GWmix**			**GWmix**				**saturating liquid**		
SW or SGW		*60*			*53.5*			*86.4*		*%*	liquid saturation		
Curve #	**1**	**2**	**3**	**4**	**5**	**6**	**7**	**8**	**9**		**Figure 12 and 13 curve**		
Pc	2	8	12	2	8	12	2	8	12	MPa	confining pressure		
Kdry	5.0	9.9	11.4	5.0	9.9	11.4	5.0	9.9	11.4	GPa	dry rock bulk modulus	X	X
μ*dry*	8.1	9.7	10.5	8.1	9.7	10.5	8.1	9.7	10.5	GPa	dry rock shear modulus	X	X
Kg					37					GPa	quartz bulk modulus	X	X
μg					44					GPa	quartz shear modulus	X	X
ρ*r*					2110					kg/m3	density of dry rock	X	X
ρ*W*		1000								kg/m3	density of water	X	X
η*W*		0.001								Pa s	viscosity of water	X	X
KW		2.2								GPa	bulk modulus of water	X	X
ρ*GW*						1121				[kg/m3]	density of GWmix	X	X
η*GW*						0.011				Pa s	viscosity of GWmix	X	X
KGW						2.4				GPa	bulk modulus of GWmix	X	X
Φc	0.3, 1.47	0.09, 0.47	0.05, 0.34	0.3, 1.47	0.09, 0.47	0.05, 0.34	0.3, 1.47	0.09, 0.47	0.05, 0.34	%	crack porosity	X	
α	0.49	0.41	0.37	0.49	0.41	0.37	0.49	0.41	0.37	x10-3	crack aspect ratio	X	
Ph					20, 100					MPa	closed cracks conf. P	X	
Kh					12.55, 16.51					GPa	rock bulk modulus at *Ph*	X	
Φ					0.205						porosity		X
κ		0.75				1				x10-12 [m2]	hydraulic permeability		X
ρ*a*					1.25					kg/m3	density of air		X
η*a*					0.02					mPa s	viscosity of air		X
Ka					0.15					MPa	bulk modulus of air		X
rp					0.003, 0.03					m	patchy radii		X

where K_1 or K_2 (i.e., $K_{1 \vee 2}$) are:

$$K_{1 \vee 2} = \frac{K_g + \left(\Phi \frac{K_g}{K_{f \vee a}} - \Phi - 1\right) K_{dry}}{1 - \Phi - \frac{K_{dry}}{K_g} + \Phi \frac{K_g}{K_{f \vee a}}}, \quad (15)$$

where K_f is the liquid bulk modulus, K_a is the air bulk modulus, $K_{dry}$is the dry bulk modulus measured at ultrasonic frequencies, i.e., $K_{HF\,(S_a = 1)}$.

At low frequencies, we observe the left flanks of attenuation peaks whose corner frequencies are typically above 100 Hz. Thus, E_{SF} at $f < 100$ Hz represents a good proxy for the "relaxed" limit. We calculate Young's modulus for the "relaxed" limit (E_{LF}) by averaging E_{SF} measurements at frequencies < 10 Hz.

The relaxed Young's modulus (E_R) is then calculated as:

$$E_R = \frac{9 K_R \mu_R}{3K_R + \mu_R}, \quad (16)$$

(Mavko et al., 2009), where $K_R$is the relaxed bulk modulus for a specific fluid saturation (i.e., $K_{R\,(S_a < 1)}$) and can be estimated by means of the Gassmann fluid substitution:

$$K_{R\,(S_a < 1)} = K_{dry} + \frac{(1 - K_{dry}/K_g)^2}{\Phi/K_f + (1 - \Phi)/K_g - K_{dry}/K_g{}^2}, \quad (17)$$

(Gassmann, 1951). Because we have no direct measurements of bulk modulus at low frequencies and dispersion is negligible at seismic frequency, in Eq. 17 we use K_{dry}. Dry Young's modulus calculated from $K_{HF}$and μ_{HF} agree very well with low frequency dry Young's modulus indicating negligible dispersion. In Eq. 17 K_f is the effective fluid bulk modulus that can be estimated as:

$$\frac{1}{K_f} = \frac{(1 - S_a)}{K_l} + \frac{S_a}{K_a}, \quad (18)$$

where K_a and K_l are the bulk moduli of the gas and the liquid, respectively (Reuss, 1929). The liquid can be either water or GWmix.

According to Gassmann (1951) shear modulus is not affected by saturation, therefore we assume that the relaxed shear modulus μ_R is:

$$\mu_R = \mu_{SF} = \mu_{HF}, \quad (19)$$

E_{HF} and E_{LF} at different saturations and confining pressures (i.e., 2, 6, 10, and 14 MPa) are then compared to E_U and E_R (**Figure 11**). E_{LF} and E_{HF} follow the two theoretical limits and the dispersion - i.e., the vertical distance between E_{LF} and E_{HF} decreases with increasing confining pressure, similarly, to the dispersion between E_R and E_U, suggesting again that the wave-induced-fluid-flow mechanism is more active at low confining pressures.

Both theoretical limits do not predict the decrease in Young's modulus between dry and saturated conditions. Such a behavior is common in sandstones and, according to the literature, in rocks like Berea sandstone, it could be related to the softening of the cement or the swelling of the clay minerals at grain boundaries (Cadoret, 1993).

Evidences for Squirt Flow

Squirt-flow could also explain the observed frequency-dependent attenuation curves (Mavko and Jizba, 1991; Gurevich et al., 2010). Here we show that the observed corner frequencies are compatible with squirt-flow theory and typical values of crack aspect ratios for Berea sandstone. We estimate the range for crack aspect ratio by means of Eq. 9 and by substituting f_{squirt} with f_c. This, provides a crack aspect ratio α' ranging between $\sim 1.4 \text{x} 10^{-4}$ and $\sim 4.5 \text{x} 10^{-4}$, which is in agreement with the literature (Zimmerman, 1991).

On the other hand, ultrasonic measurements suggest that crack closure occurs at confining pressure ~40 MPa, where ultrasonic velocities vs. confining pressure curves tend to flatten (**Figure 10**). Walsh (1965) indicates that elliptical cross-section cracks under plane-stress conditions close at confining pressure P_{cc}:

$$\frac{1}{P_{cc}} = \frac{2}{E_g}\left(\alpha + \frac{1}{\alpha}\right) \quad (20)$$

by substituting P_{cc} with 40 MPa and E_g with 95 GPa (i.e., quartz Young's modulus), we obtain a value of crack aspect ratio α'' of $\sim 8 \text{x} 10^{-4}$.

The fact that α' and α'', which are independently estimated, are similar suggests that our samples bear cracks whose geometry could have generated squirt-flow in a bandwidth close to 100 Hz.

Squirt-Flow vs. Patchy-Saturation Modeling

Squirt flow and Patchy saturation have been calculated for the conditions of *case ii, iii,* and *v* and confining pressures of 2, 8 and 12 MPa, i.e., we generated nine attenuation and dispersion curves (**Figure 12**). Precisely, **Figures 12A,B** show the comparison between the modeling results and the best fitting curves from the phenomenological models.

Patchy saturation was calculated for an interval of patchy radii comprised between 3 and 30 mm. Squirt flow was calculated for an interval of P_h comprised between 20 and 100 MPa. Such values were chosen to span an order of magnitude and according to the sample dimensions and the increase of ultrasonic wave speed as a function of confining pressure. As a consequence, in **Figure 12**, the modeling results appear as shaded areas where the two attenuation mechanisms operate.

From the comparison, we observe that patchy saturation accurately describes attenuation in 3 cases - **Figure 12**, curves 4, 7 and 9 - and slightly underestimates the measurements in one case – **Figure 12**, curve 8. However, in 5 cases, patchy saturation strongly underestimates the measurements presenting corner frequencies much higher than those observed in the laboratory. Similarly, squirt flow accurately describes attenuation in 3 cases - **Figure 12**, curves 7, 8, and 9. However, in 6 cases, squirt flow strongly underestimates the measurements presenting corner frequencies much higher than those observed in the laboratory. Although the modeled Young's moduli overestimated the measurements of 1 to 4 GPa, the modeled increase of Young's modulus with confining pressure is similar to the experimental results

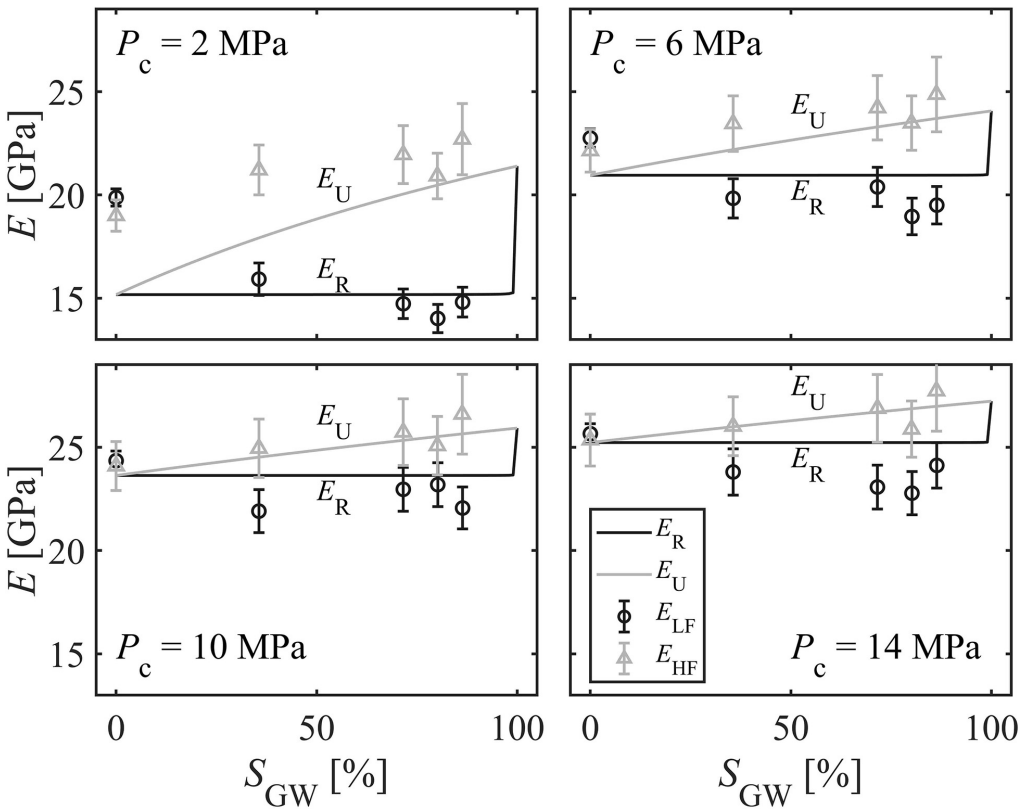

FIGURE 11 | Young's modulus measured at low frequencies (1–10 Hz, E_{LF}) and at ultrasonic frequencies (0.1 MHz, E_{HF}) compared to the Biot-Gassmann-Hill limit (E_U) and the Gassmann fluid substitution (E_R) (Gassmann, 1951; Johnson, 2001). The former represents a proxy for patchy-saturation model (Mavko et al., 2009).

(**Figure 12**), suggesting a nearly constant offset between the measurements and the models.

From the present analysis, it is difficult to assess whether patchy saturation or squirt flow is more appropriate to describe the observed frequency-dependent attenuation. In particular, the largest discrepancies between modeling and experimental data occur at 8 MPa confining pressure suggesting that both the models do not accurately capture the evolution of the petrophysical parameters with confining pressure.

The models are less accurate in describing the water-saturated case than the GWmix saturated cases. In particular, they largely overestimate the corner frequencies of *case ii* but less those of *case iii and v*. For instance, although *case ii* and *iii* have similar saturation and probably patchy sizes, the models describe better *case iii*. This might suggest that the characteristic frequency of patchy-saturation and squirt-flow might not be a simple inverse relation with viscosity. The fluid flow of low-viscosity fluids in porous media might be turbulent, increasing the dragging forces and limiting the fluid flow (Reynolds, 1883). Such a process would result in reduced mobility (Batzle et al., 2006). Thus, we speculate that under certain conditions, wave-induced-fluid-flow might not be laminar as assumed in squirt-flow and patchy-saturation models manifesting as a nonlinear relation between corner frequencies and petrophysical parameters.

Final Remarks and Future Work

Models for both patchy-saturation and squirt-flow predict that attenuation fades as confining pressure increases. Such behavior is also present in our experimental data. Nevertheless, during experiments, the sample was deformed of a fixed strain amount. Thus, as confining pressure increases and cracks close, the strain must redistribute differently within the sample. At low confining pressures, a change in vertical stress mainly causes the splitting of vertical cracks and the closure of horizontal cracks. In contrast, at higher confining pressure, cracks tend to be closed, and a change of vertical stress causes shear strain along inclined faults (Jaeger et al., 2007). In the former case, crack deformation creates the local overpressures needed to generate the wave-induced-fluid-flow at the microscopic scale (i.e., squirt-flow). Nevertheless, we assume that overpressures generated in cracks also control the mesoscopic overpressure leading to patchy-saturation. The disappearance of frequency-dependent attenuation for $P_c \geq 14$ MPa could be related to the closure of the cracks and the strain distribution variation affecting both the attenuation mechanisms analyzed.

The modeling that we present here should be furthered in future work. Petrophysical parameters could be estimated more precisely following the literature, and different models could be employed. For example, we could follow de Paula et al. (2012) to better estimate squirt-flow parameters, Buckingham

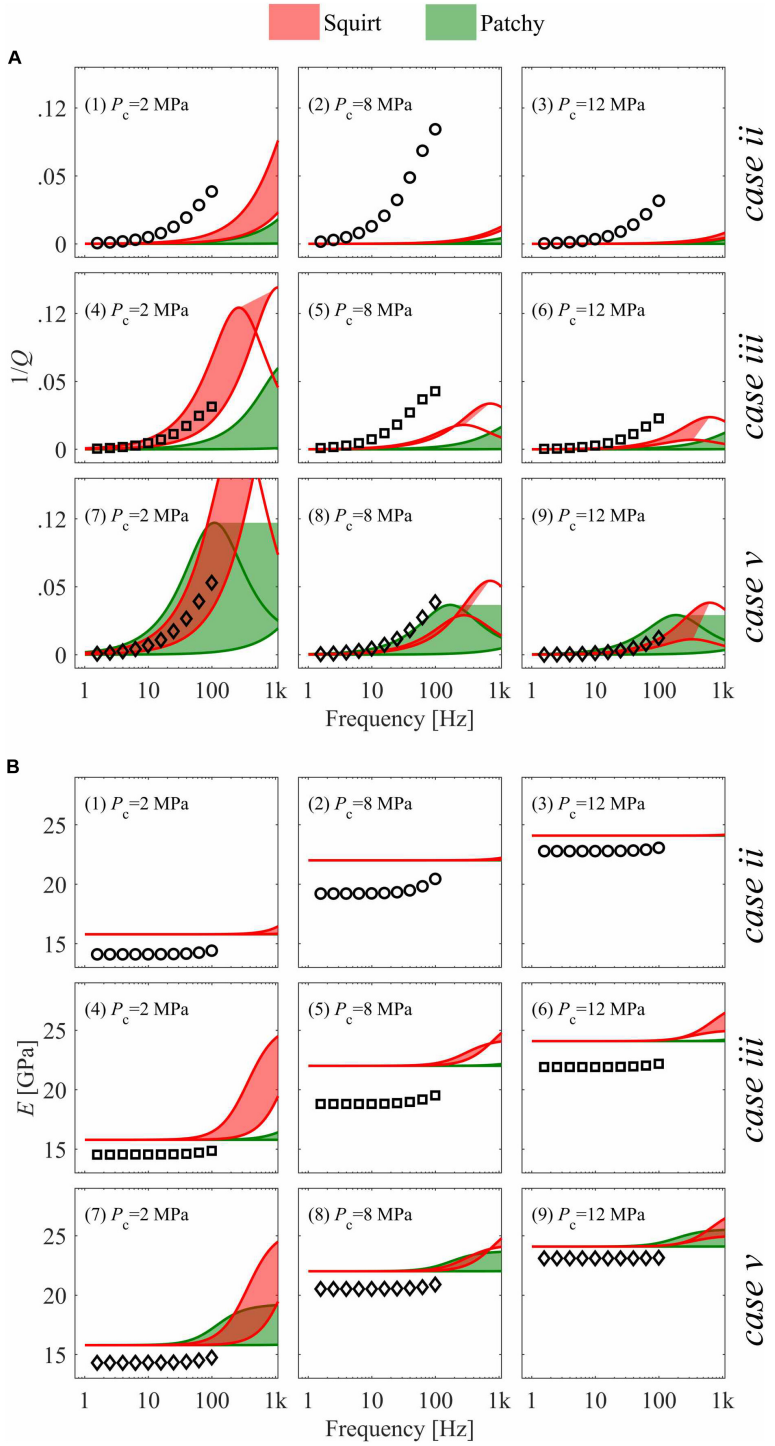

FIGURE 12 | Comparison between (i) measured attenuation (**A** - symbols) and Young's modulus (**B** - symbols), and (ii) calculated attenuation and Young's modulus for squirt-flow (red) and patchy-saturation (green) models. Squirt-flow is modeled for a minimum and a maximum value of P_h, 20 and 100 MPa, respectively. Patchy saturation is modeled for a minimum and maximum value of r_p of 0.003 and 0.03 m, respectively.

(1999) to verify the hypothesis that frequency-independent attenuation in dry samples is related to grain friction, and use Vogelaar et al. (2010) to model the patchy saturation. Since the observed attenuation might result from the combination of squirt flow and patchy saturation, we could model our data using the double double-porosity model proposed by

Ba et al. (2017). Besides, we could test analog materials whose physical properties could be thoroughly controlled (e.g., Xie et al., 2019). Nevertheless, results and modeling presented here suggest that in near-surface sedimentary terrains, where the effective stress is low - e.g., < 20 MPa - and partial saturation is likely to be present, attenuation and dispersion might strongly affect the propagation of seismic waves like suggested by field observations (e.g., Abercrombie, 1997).

CONCLUSION

We have measured low-frequency seismic wave attenuation and Young's modulus, and ultrasonic wave speeds for three dry and partially saturated Berea sandstone samples. Measurements have been conducted at confining pressure between 0 and 40 MPa, and frequency ranges 1–100 Hz, and 0.1–1 MHz. Seismic wave attenuation in samples partially saturated and confined with pressures below 14 MPa are frequency-dependent and as high as 0.08. On the other hand, the dry sample and samples confined above 14 MPa exhibit negligible and frequency independent attenuation.

Low-frequency attenuation and dispersion curves obey to the Kramers-Kronig relation. Low frequency and ultrasonic Young's moduli are compatible with effective-medium theories that are calculated for relaxed and unrelaxed conditions. This suggests that the observed frequency-dependent attenuation is caused by a wave-induced-fluid-flow type of mechanism and that attenuation could be significant in the near-surface ($<\sim$1 km) where effective stress is low and partial saturation might be present. Nevertheless, it is not yet clear whether the observed frequency-dependent attenuation is the result of squirt-flow or patchy-saturation as analytical modeling provides similar results for these two attenuation mechanisms. Such and other aspects, like the role of non-laminar fluid-flow in controlling attenuation, are not yet clear and demand further investigation.

DATA AVAILABILITY STATEMENT

The full datasets including data not shown in figures can be found here: https://zenodo.org/record/4517286#.YCCtDXlMGUk.

AUTHOR CONTRIBUTIONS

NT conceived and performed the experiments, analyzed and modeled the results, wrote the manuscript, and prepared the figures and tables. CM assisted in preparing and performing the experiments. ES provided funding and supervised the study. All authors contributed to the article, edited the manuscript, and approved the submitted version.

FUNDING

This project has been partially funded by the Swiss Innovation Promotion Agency (KTI) project nr. 22701.

ACKNOWLEDGMENTS

We want to thank Boris Gurevich, Luca Duranti, Beatriz Quintal, and Jean-Pierre Burg for providing insightful feedback. We also want to thank the editors Jing Ba and CX, and two reviewers whose comments improved the article. Robert Hofmann and Reto Seifert solved many technical issues.

SUPPLEMENTARY MATERIAL

The Supplementary Material for this article can be found online at: https://www.frontiersin.org/articles/10.3389/feart.2021.641177/full#supplementary-material

REFERENCES

Abercrombie, R. E. (1997). Near-surface attenuation and site effects from comparison of surface and deep borehole recordings. *Bull. Seismol. Soc. Am.* 87, 731–744.

Adam, L., Batzle, M., Lewallen, K. T., and van Wijk, K. (2009). Seismic wave attenuation in carbonates. *J. Geophys. Res.* 114:B06208. doi: 10.1029/2008JB005890

Amalokwu, K., Best, A. I., Sothcott, J., Chapman, M., Minshull, T., and Li, X.-Y. (2014). Water saturation effects on elastic wave attenuation in porous rocks with aligned fractures. *Geophys. J. Int.* 197, 943–947. doi: 10.1093/gji/ggu076

Archard, J. F. (1953). Contact and rubbing of flat surfaces. *J. Appl. Phys.* 24:981. doi: 10.1063/1.1721448

Archard, J. F. (1957). Elastic deformation and the laws of friction. *Proc. R. Soc. A Math. Phys. Eng. Sci.* 243, 190–205. doi: 10.1098/rspa.1957.0214

Ba, J., Xu, W., Fu, L.-Y., Carcione, J. M., and Zhang, L. (2017). Rock anelasticity due to patchy saturation and fabric heterogeneity: a double double-porosity model of wave propagation: double double-porosity wave modeling. *J. Geophys. Res. Solid Earth* 122, 1949–1976. doi: 10.1002/2016JB013882

Barton, N. (2007). *Rock Quality, Seismic Velocity, Attenuation and Anisotropy*. London: Taylor & Francis.

Batzle, M. L., Han, D.-H., and Hofmann, R. (2006). Fluid mobility and frequency-dependent seismic velocity — direct measurements. *Geophysics* 71, N1–N9. doi: 10.1190/1.2159053

Biot, M. A. (1956). Theory of propagation of elastic waves in a fluid-saturated porous solid. I. Low-frequency range. *J. Acoust. Soc. Am.* 28:168. doi: 10.1121/1.1908239

Birch, F. (1960). The velocity of compressional waves in rocks to 10 kilobars: 1. *J. Geophys. Res.* 65, 1083–1102. doi: 10.1029/JZ065i004p01083

Buckingham, M. J. (1999). Theory of compressional and transverse wave propagation in consolidated porous media. *J. Acoust. Soc. Am.* 106, 575–581. doi: 10.1121/1.427026

Cadoret, T. (1993). *Effet de la Saturation Eau-gaz Sur les Proprietes Acoustiques Des Roches*. Ph.D. thesis, Université Paris Diderot–Paris 7, Paris. Available online at: http://www.theses.fr/1993PA077130 (accessed December 12, 2020).

Carcione, J. M. (2007). *Wave Fields in Real Media: Wave Propagation in Anisotropic, Anelastic, Porous and Electromagnetic Media*, 2nd Edn. Amsterdam: Elsevier. rev.extended.

Chapman, M., Liu, E., and Li, X.-Y. (2006). The influence of fluid-sensitive dispersion and attenuation on AVO analysis. *Geophys. J. Int.* 167, 89–105. doi: 10.1111/j.1365-246X.2006.02919.x

Chapman, S., Tisato, N., Quintal, B., and Holliger, K. (2016). Seismic attenuation in partially saturated Berea sandstone submitted to a range of confining pressures: seismic attenuation in berea sandstone. *J. Geophys. Res. Solid Earth* 121, 1664–1676. doi: 10.1002/2015JB012575

Christensen, N. I., and Wang, H. F. (1985). The Influence of pore pressure and confining pressure on dynamic elastic properties of Berea sandstone. *Geophysics* 50, 207–213. doi: 10.1190/1.1441910

de Paula, O. B., Pervukhina, M., Makarynska, D., and Gurevich, B. (2012). Modeling squirt dispersion and attenuation in fluid-saturated rocks using pressure dependency of dry ultrasonic velocities. *Geophysics* 77, WA157–WA168. doi: 10.1190/geo2011-0253.1

De Siena, L., Thomas, C., Waite, G. P., Moran, S. C., and Klemme, S. (2014). Attenuation and scattering tomography of the deep plumbing system of Mount St. Helens. *J. Geophys. Res. Solid Earth* 119, 8223–8238. doi: 10.1002/2014JB011372

Dunn, K.-J. (1986). Acoustic attenuation in fluid-saturated porous cylinders at low frequencies. *J. Acoust. Soc. Am.* 79:1709. doi: 10.1121/1.393232

Dutta, N. C., and Odé, H. (1979). Attenuation and dispersion of compressional waves in fluid-filled porous rocks with partial gas saturation (White model)—Part II: results. *Geophysics* 44, 1789–1805. doi: 10.1190/1.1440939

Dvorkin, J., and Nur, A. (1993). Dynamic poroelasticity: a unified model with the squirt and the Biot mechanisms. *Geophysics* 58, 524–533. doi: 10.1190/1.1443435

Eberhart-Phillips, D., Han, D.-H., and Zoback, M. D. (1989). Empirical relationships among seismic velocity, effective pressure, porosity, and clay content in sandstone. *Geophysics* 54, 82–89. doi: 10.1190/1.1442580

Gardner, G. H. F. (1962). Extensional waves in fluid-saturated porous cylinders. *J. Acoust. Soc. Am.* 34, 36–40. doi: 10.1121/1.1909010

Gassmann, F. (1951). Elastic waves through a packing of spheres. *Geophysics* 16, 673–685. doi: 10.1190/1.1437718

Green, A. E., Laws, N., and Naghdi, P. M. (1967). A linear theory of straight elastic rods. *Arch. Ration. Mech. Anal.* 25, 285–298. doi: 10.1007/BF00250931

Green, A. E., Naghdi, P. M., and Wenner, M. L. (1974a). On the theory of rods. I. Derivations from the three-dimensional equations. *Proc. R. Soc. A Math. Phys. Eng. Sci.* 337, 451–483. doi: 10.1098/rspa.1974.0061

Green, A. E., Naghdi, P. M., and Wenner, M. L. (1974b). On the theory of rods. II. Developments by direct approach. *Proc. R. Soc. A Math. Phys. Eng. Sci.* 337, 485–507. doi: 10.1098/rspa.1974.0062

Gurevich, B., and Lopatnikov, S. L. (1995). Velocity and attenuation of elastic waves in finely layered porous rocks. *Geophys. J. Int.* 121, 933–947. doi: 10.1111/j.1365-246X.1995.tb06449.x

Gurevich, B., Makarynska, D., de Paula, O. B., and Pervukhina, M. (2010). A simple model for squirt-flow dispersion and attenuation in fluid-saturated granular rocks. *Geophysics* 75, N109–N120. doi: 10.1190/1.3509782

Hulikal, S., Bhattacharya, K., and Lapusta, N. (2015). Collective behavior of viscoelastic asperities as a model for static and kinetic friction. *J. Mech. Phys. Solids* 76, 144–161. doi: 10.1016/j.jmps.2014.10.008

Jaeger, J. C., Cook, N. G. W., and Zimmerman, R. W. (2007). *Fundamentals of Rock Mechanics*, 4th Edn. Malden, MA: Blackwell Pub.

Jakobsen, M., and Chapman, M. (2009). Unified theory of global flow and squirt flow in cracked porous media. *Geophysics* 74, WA65–WA76. doi: 10.1190/1.3078404

Johnson, D. L. (2001). Theory of frequency dependent acoustics in patchy-saturated porous media. *J. Acoust. Soc. Am.* 110, 682–694. doi: 10.1121/1.1381021

Johnston, D. H., Toksöz, M. N., and Timur, A. (1979). Attenuation of seismic waves in dry and saturated rocks: II. Mechanisms. *Geophysics* 44, 691–711. doi: 10.1190/1.1440970

Jones, T. D. (1986). Pore fluids and frequency-dependent wave propagation in rocks. *Geophysics* 51, 1939–1953. doi: 10.1190/1.1442050

Karato, S., and Spetzler, H. A. (1990). Defect microdynamics in minerals and solid-state mechanisms of seismic wave attenuation and velocity dispersion in the mantle. *Rev. Geophys.* 28:399. doi: 10.1029/RG028i004p00399

Kästner, F., Pierdominici, S., Elger, J., Zappone, A., Kück, J., and Berndt, C. (2020). Correlation of core and downhole seismic velocities in high-pressure metamorphic rocks: a case study for the COSC-1 borehole, Sweden. *Solid Earth* 11, 607–626. doi: 10.5194/se-11-607-2020

Kuteynikova, M., Tisato, N., Jänicke, R., and Quintal, B. (2014). Numerical modeling and laboratory measurements of seismic attenuation in partially saturated rock. *Geophysics* 79, L13–L20. doi: 10.1190/geo2013-0020.1

Lakes, R. S. (2009). *Viscoelastic Materials*. Cambridge: Cambridge University Press.

Liu, H.-P., Anderson, D. L., and Kanamori, H. (1976). Velocity dispersion due to anelasticity; implications for seismology and mantle composition. *Geophys. J. Int.* 47, 41–58. doi: 10.1111/j.1365-246X.1976.tb01261.x

Lo, T., Coyner, K. B., and Toksöz, M. N. (1986). Experimental determination of elastic anisotropy of Berea sandstone, Chicopee shale, and Chelmsford granite. *Geophysics* 51, 164–171. doi: 10.1190/1.1442029

Madonna, C., and Tisato, N. (2013). A new seismic wave attenuation module to experimentally measure low-frequency attenuation in extensional mode: a seismic wave attenuation module to measure low-frequency attenuation. *Geophys. Prospect.* 61, 302–314. doi: 10.1111/1365-2478.12015

Mavko, G., and Jizba, D. (1991). Estimating grain-scale fluid effects on velocity dispersion in rocks. *Geophysics* 56, 1940–1949. doi: 10.1190/1.1443005

Mavko, G., Mukerji, T., and Dvorkin, J. (2009). *The Rock Physics Handbook: Tools for Seismic Analysis of Porous Media*, 2nd Edn. Cambridge: Cambridge University Press.

McCarthy, C., Takei, Y., and Hiraga, T. (2011). Experimental study of attenuation and dispersion over a broad frequency range: 2. The universal scaling of polycrystalline materials. *J. Geophys. Res.* 116:B09207. doi: 10.1029/2011JB008384

McKavanagh, B., and Stacey, F. D. (1974). Mechanical hysteresis in rocks at low strain amplitudes and seismic frequencies. *Phys. Earth Planet. Inter.* 8, 246–250. doi: 10.1016/0031-9201(74)90091-0

Mikhaltsevitch, V., Lebedev, M., and Gurevich, B. (2014a). A laboratory study of low-frequency wave dispersion and attenuation in water-saturated sandstones. *Lead. Edge* 33, 616–622. doi: 10.1190/tle33060616.1

Mikhaltsevitch, V., Lebedev, M., and Gurevich, B. (2014b). A laboratory study of the elastic and anelastic properties of the sandstone flooded with supercritical CO2 at seismic frequencies. *Energy Proc.* 63, 4289–4296. doi: 10.1016/j.egypro.2014.11.464

Mikhaltsevitch, V., Lebedev, M., and Gurevich, B. (2016). Validation of the laboratory measurements at seismic frequencies using the Kramers-Kronig relationship. *Geophys. Res. Lett.* 43, 4986–4991. doi: 10.1002/2016GL069269

Molyneux, J. B., and Schmitt, D. R. (1999). First-break timing: arrival onset times by direct correlation. *Geophysics* 64, 1492–1501. doi: 10.1190/1.1444653

Mueller, S., Llewellin, E. W., and Mader, H. M. (2010). The rheology of suspensions of solid particles. *Proc. R. Soc. A Math. Phys. Eng. Sci.* 466, 1201–1228. doi: 10.1098/rspa.2009.0445

Müller, T. M., Gurevich, B., and Lebedev, M. (2010). Seismic wave attenuation and dispersion resulting from wave-induced flow in porous rocks — a review. *Geophysics* 75, 75A147–75A164. doi: 10.1190/1.3463417

Paffenholz, J., and Burkhardt, H. (1989). Absorption and modulus measurements in the seismic frequency and strain range on partially saturated sedimentary rocks. *J. Geophys. Res.* 94:9493. doi: 10.1029/JB094iB07p09493

Papageorgiou, G., and Chapman, M. (2015). Multifluid squirt flow and hysteresis effects on the bulk modulus–water saturation relationship. *Geophys. J. Int.* 203, 814–817. doi: 10.1093/gji/ggv333

Peselnick, L., and Liu, H.-P. (1987). 2. Laboratory measurement of internal friction in rocks and minerals at seismic frequencies. *Methods Exp. Phys.* 24, 31–56. doi: 10.1016/S0076-695X(08)60583-9

Pimienta, L., Fortin, J., and Guéguen, Y. (2015a). Bulk modulus dispersion and attenuation in sandstones. *Geophysics* 80, D111–D127. doi: 10.1190/geo2014-0335.1

Pimienta, L., Fortin, J., and Guéguen, Y. (2015b). Experimental study of Young's modulus dispersion and attenuation in fully saturated sandstones. *Geophysics* 80, L57–L72. doi: 10.1190/geo2014-0532.1

Prasad, M., and Manghnani, M. H. (1997). Effects of pore and differential pressure on compressional wave velocity and quality factor in Berea and Michigan sandstones. *Geophysics* 62, 1163–1176. doi: 10.1190/1.1444217

Pride, S. R., Berryman, J. G., and Harris, J. M. (2004). Seismic attenuation due to wave-induced flow: wave-induced flow losses. *J. Geophys. Res. Solid Earth* 109:B01201. doi: 10.1029/2003JB002639

Quintal, B., Steeb, H., Frehner, M., and Schmalholz, S. M. (2011). Quasi-static finite element modeling of seismic attenuation and dispersion due to wave-induced fluid flow in poroelastic media. *J. Geophys. Res.* 116:B01201. doi: 10.1029/2010JB007475

Reuss, A. (1929). Berechnung der fließgrenze von mischkristallen auf grund der plastizitätsbedingung für einkristalle. *Z. Angew. Math. Mech.* 9, 49–58. doi: 10.1002/zamm.19290090104

Reynolds, O. (1883). An experimental investigation of the circumstances which determine whether the motion of water shall be direct or sinuous, and of the law of resistance in parallel channels. *Philos. Trans. R. Soc. Lond.* 174, 935–982. doi: 10.1098/rstl.1883.0029

Sayers, C. M., Van Munster, J. G., and King, M. S. (1990). Stress-induced ultrasonic anisotrophy in Berea sandstone. *Int. J. Rock Mech. Min. Sci. Geomech. Abstr.* 27, 429–436. doi: 10.1016/0148-9062(90)92715-Q

Spencer, J. W. (2013). Viscoelasticity of ells river bitumen sand and 4D monitoring of thermal enhanced oil recovery processes. *Geophysics* 78, D419–D428. doi: 10.1190/geo2012-0535.1

Thakur, N. K., and Rajput, S. (2011). *Exploration of Gas Hydrates: Geophysical Techniques*. Heidelberg: Springer.

Tisato, N., and Madonna, C. (2012). Attenuation at low seismic frequencies in partially saturated rocks: measurements and description of a new apparatus. *J. Appl. Geophys.* 86, 44–53. doi: 10.1016/j.jappgeo.2012.07.008

Tisato, N., and Quintal, B. (2013). Measurements of seismic attenuation and transient fluid pressure in partially saturated Berea sandstone: evidence of fluid flow on the mesoscopic scale. *Geophys. J. Int.* 195, 342–351. doi: 10.1093/gji/ggt259

Tisato, N., and Quintal, B. (2014). Laboratory measurements of seismic attenuation in sandstone: strain versus fluid saturation effects. *Geophysics* 79, WB9–WB14. doi: 10.1190/geo2013-0419.1

Tisato, N., Quintal, B., Chapman, S., Podladchikov, Y., and Burg, J.-P. (2015). Bubbles attenuate elastic waves at seismic frequencies: first experimental evidence. *Geophys. Res. Lett.* 42, 3880–3887. doi: 10.1002/2015GL063538

Toksöz, M. N., Johnston, D. H., and Timur, A. (1979). Attenuation of seismic waves in dry and saturated rocks: I. Laboratory measurements. *Geophysics* 44, 681–690. doi: 10.1190/1.1440969

Vogelaar, B., Smeulders, D., and Harris, J. (2010). Exact expression for the effective acoustics of patchy-saturated rocks. *Geophysics* 75, N87–N96. doi: 10.1190/1.3463430

Walsh, J. B. (1965). The effect of cracks on the compressibility of rock. *J. Geophys. Res.* 70, 381–389. doi: 10.1029/JZ070i002p00381

Walsh, J. B. (1966). Seismic wave attenuation in rock due to friction. *J. Geophys. Res.* 71, 2591–2599. doi: 10.1029/JZ071i010p02591

White, J. E. (1975). Computed seismic speeds and attenuation in rocks with partial gas saturation. *Geophysics* 40, 224–232. doi: 10.1190/1.1440520

Winkler, K. W. (1985). Dispersion analysis of velocity and attenuation in Berea sandstone. *J. Geophys. Res.* 90:6793. doi: 10.1029/JB090iB08p06793

Winkler, K. W., and Nur, A. (1982). Seismic attenuation: effects of pore fluids and frictional-sliding. *Geophysics* 47, 1–15. doi: 10.1190/1.1441276

Xie, J., Cao, J., Schmitt, D. R., Di, B., Xiao, L., Wang, X., et al. (2019). Effects of kerogen content on elastic properties-based on artificial organic-rich shale (AORS). *J. Geophys. Res. Solid Earth* 124, 12660–12678. doi: 10.1029/2019JB017595

Yin, C.-S., Batzle, M. L., and Smith, B. J. (1992). Effects of partial liquid/gas saturation on extensional wave attenuation in Berea sandstone. *Geophys. Res. Lett.* 19, 1399–1402. doi: 10.1029/92GL01159

Zappone, A., Fernàndez, M., Garcìa-Dueñas, V., and Burlini, L. (2000). Laboratory measurements of seismic P-wave velocities on rocks from the Betic chain (southern Iberian Peninsula). *Tectonophysics* 317, 259–272. doi: 10.1016/S0040-1951(99)00319-4

Zimmerman, R. W. (1991). *Compressibility of Sandstones*. Amsterdam: Elsevier.

Conflict of Interest: The authors declare that the research was conducted in the absence of any commercial or financial relationships that could be construed as a potential conflict of interest.

Copyright © 2021 Tisato, Madonna and Saenger. This is an open-access article distributed under the terms of the Creative Commons Attribution License (CC BY). The use, distribution or reproduction in other forums is permitted, provided the original author(s) and the copyright owner(s) are credited and that the original publication in this journal is cited, in accordance with accepted academic practice. No use, distribution or reproduction is permitted which does not comply with these terms.

frontiers in Earth Science

ORIGINAL RESEARCH
published: 21 April 2021
doi: 10.3389/feart.2021.645532

Fracture Shape and Orientation Contributions to P-Wave Velocity and Anisotropy of Alpine Fault Mylonites

Jirapat Charoensawan[1], Ludmila Adam[1], Michael Ofman[2], Virginia Toy[3], Jonathan Simpson[4], Xin Zhong[5] and Bernhard Schuck[6†]*

[1] School of Environment, The University of Auckland, Auckland, New Zealand, [2] Department of Geology, University of Otago, Dunedin, New Zealand, [3] Institut für Geowissenschaften, Johannes Gutenberg-Universität Mainz, Mainz, Germany, [4] Department of Physics, The University of Auckland, Auckland, New Zealand, [5] Institute of Geological Sciences, Freie Universität Berlin, Berlin, Germany, [6] Helmholtz Centre Potsdam, GFZ German Research Centre for Geosciences, Section 4.2: Geomechanics and Scientific Drilling, Potsdam, Germany

P-wave anisotropy is significant in the mylonitic Alpine Fault shear zone. Mineral- and texture-induced anisotropy are dominant in these rocks but further complicated by the presence of fractures. Electron back-scattered diffraction and synchrotron X-ray microtomography (micro-CT) data are acquired on exhumed schist, protomylonite, mylonite, and ultramylonite samples to quantify mineral phases, crystal preferred orientations, microfractures, and porosity. The samples are composed of quartz, plagioclase, mica and accessory garnet, and contain 3–5% porosity. Based on the micro-CT data, the representative pore shape has an aspect ratio of 5:2:1. Two numerical models are compared to calculate the velocity of fractured rocks: a 2D wave propagation model, and a differential effective medium model (3D). The results from both models have comparable pore-free fast and slow velocities of 6.5 and 5.5 km/s, respectively. Introducing 5% fractures with 5:2:1 aspect ratio, oriented with the longest axes parallel to foliation decreases these velocities to 6.3 and 5.0 km/s, respectively. Adding both randomly oriented and foliation-parallel fractures hinders the anisotropy increase with fracture volume. The anisotropy becomes independent of porosity when 80% of fractures are randomly oriented. Modeled anisotropy in 2D and 3D are different for similar fracture aspect ratios, being 30 and 15%, respectively. This discrepancy is the result of the underlying assumptions and limitations. Our numerical results explain the effects that fracture orientations and shapes have on previously published field- and laboratory-based studies. Through this numerical study, we show how mica-dominated, pore-free P-wave anisotropy compares to that of fracture volume, shape and orientation for protolith and shear zone rocks of the Alpine Fault.

Keywords: P-wave velocity, anisotropy, Alpine Fault, fracture, electron backscattered diffraction, numerical modeling, synchrotron X-ray microtomography

OPEN ACCESS

Edited by:
Pascal Audet, University of Ottawa, Canada

Reviewed by:
Sarah Brownlee, Wayne State University, United States
Thomas Leydier, Université de Montpellier, France

****Correspondence:***
Jirapat Charoensawan
jcha673@aucklanduni.ac.nz

†Present address:
Bernhard Schuck, Institut für Geowissenschaften, Johannes Gutenberg-Universität Mainz, Mainz, Germany

Specialty section:
This article was submitted to Solid Earth Geophysics, a section of the journal Frontiers in Earth Science

Received: *23 December 2020*
Accepted: *22 March 2021*
Published: *21 April 2021*

Citation:
Charoensawan J, Adam L, Ofman M, Toy V, Simpson J, Zhong X and Schuck B (2021) Fracture Shape and Orientation Contributions to P-Wave Velocity and Anisotropy of Alpine Fault Mylonites. Front. Earth Sci. 9:645532. doi: 10.3389/feart.2021.645532

1. INTRODUCTION

The Alpine Fault is located along the West Coast of the South Island, New Zealand. It marks the transpressional plate boundary between the Australian and the Pacific Plates (**Figure 1**). The fault hosts many earthquakes a year, but a large earthquake ($M_w > 7.0$) occurs every <300 years on average with the last one occurring in 1717 AD (Sutherland et al., 2007; Howarth et al., 2018). The

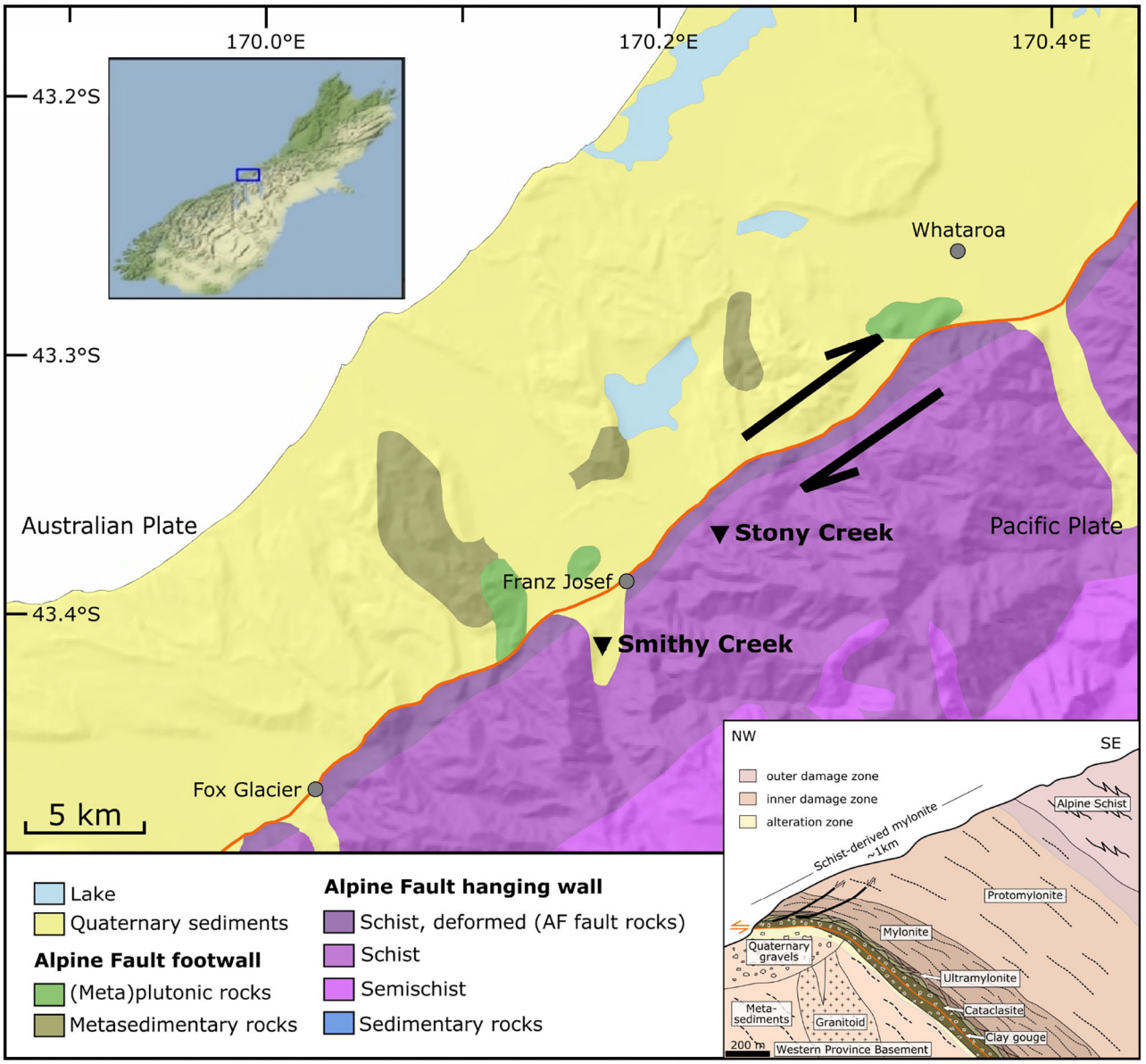

FIGURE 1 | Simplified geological map of the study area and cross-section showing typical shallow-depth sequence of the Alpine Fault rocks (Norris and Cooper, 2007; Schuck et al., 2020). Alpine Fault trace shown in orange; Stony Creek and Smithy Creek are indicated by black triangles. Map is based on the geological map of New Zealand's South Island (Edbrooke et al., 2015) and the digital elevation model of Columbus et al. (2011).

majority of the rocks on the Pacific Plate (hanging wall) are schist and fault rocks. Rocks sheared during the collision of the two plates form a series of fault rocks close to the principal slip zone consisting of fault gouge, cataclasite, and variable grades of mylonites which vary according to fault-perpendicular distance. Mylonites do not outcrop in the footwall, but the hanging wall mylonite zone is approximately 1 km thick (Norris and Cooper, 1997). The mylonites are derived from the Alpine Schist and developed foliation parallel and sub-parallel to the fault plane (Toy et al., 2008). In general, the mylonites and schist are composed of quartz, plagioclase, biotite, muscovite, and accessory minerals such as chlorite, garnet, and calcite (Grapes and Watanabe, 1994; Little et al., 2002; Toy et al., 2015; Boulton et al., 2017).

Field passive and active source seismic data has been used to investigate the Alpine Fault geometry and rock physical properties. Such data show a low-velocity zone in the hanging wall that lies parallel to the Alpine Fault (Smith et al., 1995; Stern et al., 2001, 2007; Feenstra et al., 2016; Lay et al., 2016). Within the first 10 km depth, the P-wave velocity of the low-velocity zone is 5.5–6.0 km/s compared to the velocity outside the zone of 6.0–6.5 km/s. This low-velocity zone is commonly interpreted

to be due to the presence of fluid-filled microfractures, but experimental and model data needed to validate such a claim are rare (Allen et al., 2017; Adam et al., 2020). The fault damage zone has been investigated using fault guided (trapped) seismic wave observation and modeling (Eccles et al., 2015; Kelly et al., 2017). However, these field studies that aim to characterize the fault geometry and physical properties do not account for seismic anisotropy. It is well-known that assuming isotropic seismic velocity models for anisotropic rocks will result in erroneous modeling and interpretations (Chapman and Pratt, 1992; Godfrey et al., 2002; Tsvankin et al., 2010). It is therefore critical to quantify how the physical properties of Alpine Fault rocks influence elastic wave anisotropy.

Previous studies using seismic data (Savage et al., 2007; Karalliyadda and Savage, 2013), core measurements (Okaya et al., 1995; Godfrey et al., 2000; Christensen and Okaya, 2007; Allen et al., 2017; Simpson et al., 2019; Adam et al., 2020; Jeppson and Tobin, 2020) and numerical modeling (Godfrey et al., 2002; Dempsey et al., 2011; Adam et al., 2020; Simpson et al., 2020) demonstrate that the rock in the vicinity of the Alpine Fault is strongly anisotropic. The anisotropy is attributed to many factors such as mineral crystallographic preferred orientation (CPO), grain shape preferred orientation (SPO), foliation and fractures. The Alpine Fault rocks contain significant (>15 vol%) mica with preferred orientation (Dempsey et al., 2011; Adam et al., 2020). Dempsey et al. (2011) has shown how the volume of aligned mica influences P-wave anisotropy in mylonite from the Alpine Fault. Moreover, grain size insensitive creep-accommodated ductile shear resulted in a CPO of quartz and plagioclase as well as their SPO (Toy et al., 2008). Velocity measurements under confining pressure also show directionally, non-uniform changes in P-wave velocities with depth which implies that aligned fractures are present (Adam et al., 2020; Simpson et al., 2020).

Fractures herein are described as flat-shaped pores. Fractures can form within the rock as intergranular spaces between flat-shaped grains in sedimentary rocks (Loucks et al., 2009), or can form as a secondary structures when the rocks are exposed to differential stress (e.g., Pischiutta et al., 2015). In many tectonic scenarios, fractures can develop as an aligned set. These aligned fractures affect the seismic anisotropy of rocks. The fractures can induce seismic anisotropy in an isotropic host rock, or further enhance pre-existing anisotropy (Kern et al., 2008; Novitsky et al., 2018). The degree of fracture-induced seismic anisotropy enhancement depends on many factors such as fracture volume (porosity), orientation, and shape (Hong-Bing et al., 2013; Vasin et al., 2013). These factors should be incorporated into seismic velocity modeling.

Adam et al. (2020) showed that open grain boundaries and microfractures can enhance the seismic wave anisotropy at all depths of the seismogenic zone in the Alpine Fault. Simpson et al. (2020) predict the P-wave anisotropy of shallow Alpine Fault rocks. However, those studies did not systematically consider the effect of mica CPO and shape/orientation of fractures on seismic anisotropy.

Here we quantify fracture shape, mineral phase, and crystal orientations from synchrotron X-ray microtomography data and electron back-scattered diffraction (EBSD) data. Based on these measurements, we model P-wave speeds and anisotropy for a range of Alpine Fault rocks. The effect of fractures on Alpine Fault rocks is modeled using two numerical methods: a wave propagation and a differential effective medium modeling approach. The methods differ in being dynamic and static respectively, as well as in the way that fractures are in 2D and 3D. Our study compares the models and their limitations for the inclusion of mica CPO and distribution, and fractures to predict seismic wave anisotropy.

2. MATERIALS AND METHODS

2.1. Electron Back-Scattered Diffraction (EBSD)

Rock samples were collected from Central Alpine Fault outcrops which span shear zone mylonites and schist. The schist sample was collected at Smithy Creek and is part of the Alpine Schist tectonostratigraphic unit (Cooper and Palin, 2018). The protomylonite, mylonite and ultramylonite samples are from Stony Creek (**Figure 1**). Thin sections of 35 μm thickness are prepared for all samples and subjected to fine SYTON polish to be examined using EBSD. Thin sections for the samples are created for two angles to foliation: 90^o (perpendicular to foliation) and 30^o. No pores or fractures are visible in the specimens under optical microscope or in microphotographs.

EBSD experiments are performed to produce a phase map containing mineralogical and crystallographic orientation data. EBSD data were acquired on 2 by 2 mm areas on the thin sections using a Zeiss Sigma VP FE-SEM fitted with an Oxford Instruments HKL INCA Premium Synergy Inte30 grated ED/BSD system, located at the Otago Microscopy and Nano-Imaging (OMNI). The SEM is operated with an accelerating voltage of 30 keV, an aperture size of 300 μm, and a working distance of approximately 30 mm. The EBSD data were acquired at a 2 μm step size then used to quantify mineral phase composition and crystallographic preferred orientation (CPO).

The EBSD data were processed to reduce noise and fill any data gaps using the MTEX toolbox (Mainprice et al., 2015). First, grain boundaries were reconstructed by grouping same-phase mineral data with less than 10^o misorientation angle. Then, all isolated 1-pixel grains were deleted to eliminate wild pixels (i.e., noise). Grain boundaries were reconstructed again using the same criteria as the previous step. Grains with less than 30% indexed fraction were removed. The indexed fraction is a ratio between the area of the indexed pixel in the grain to the whole grain area. Grains smaller than 10 pixels were also removed. Lastly, in-grain pixels were smoothed and filled based on their surrounding pixels using a spline filter.

Fine-grained phyllosilicate minerals, dominant in mylonite rocks, are mostly unable to be indexed by EBSD and appear in the maps as non-indexed phase (Prior and Mariani, 2009; Dempsey et al., 2011; Adam et al., 2020). To improve indexing of mica, we performed EBSD on an additional cut to the samples at 30^o from foliation with the hope to gain surface area on the mica to improve indexing. Unfortunately, we had about the same volume of non-indexed phase as for the 90^o cut to foliation. Toy et al.

(2008) and Dempsey et al. (2011) show the smallest phases in the Alpine Fault mylonites are dominantly mica. We therefore assign the non-indexed phases to mica. Moreover, based on photomicrographs and synchrotron micro-CT imaging, mica within Alpine Fault mylonite (Toy et al., 2008; Adam et al., 2020) is parallel and subparallel to foliation. We therefore, assume that most non-indexed phases (i.e., mica) are parallel to foliation and account for the sub-parallel mica in terms of randomly oriented mica. Microfractures and open grain boundaries would also show as non-indexed phases, however, these are mostly not resolved in the EBSD imaging. It is important to understand that the EBSD data does not have information regarding pores or fractures of these rocks. Since all non-indexed pixels are substituted with mica in our models, the effect of microfractures is later included separately in the finite difference and the wave propagation models.

It is clear that not all micas are perfectly parallel to foliation. To determine the mica orientation, we use the P-wave high pressure data from Adam et al. (2020) where most of the fractures are assumed to be closed with a 0.5% modeled porosity to estimate the volumetric contribution of parallel and randomly oriented mica basal plane orientation. We compare MTEX models of fast and slow P-wave velocities based on the combinations of perfectly and randomly aligned fractures volume to the laboratory data (**Supplementary Figure 4**). We show that model and experimental data match for a 80:20 volume of parallel:random fractures. We therefore, use this volumetric distribution of mica for all of our models.

2.2. Synchrotron X-Ray Micro-Tomography (Micro-CT)

Micro-CT is a non-destructive method used to investigate the 3D internal structure of an object. The shape of rock microfractures can be extracted and these can statistically be analyzed and converted into mathematical shapes. We use such information to model fracture effects on seismic anisotropy with the wave propagation and differential effective medium models.

Micro-CT data used in this study was collected using beamline 20XU at SPring-8, Japan on a 3 mm height and 1 mm diameter cylinder. The sample was mounted on a rotary stage. X-ray beam of 20 keV energy was shone through the sample onto the scintillator which converts X-ray to visible light. The image was then captured by the CMOS camera detector. The process was repeated over 180^o rotation with 0.1^o step size. The sample cross-sections were reconstructed using a convolution back-projection method, producing a stack of gray-scale which then re-scaled to 8-bit gray-scale images. The data resolution is 0.524 μm.

The micro-CT data were processed using the Avizo software. The gray-scale micro-CT images were cropped into an approximately 250-micron cube. The data were smoothed with a first-degree median filter to reduce noise and artifacts. The filter replaces the CT number in a voxel with the median of the 27 neighboring voxels (voxels within a 1-voxel radius of the center voxel). All pores which are smaller than 8 voxels were also removed, and a hole-filling algorithm was used. After that, pore segmentation was performed using a threshold method based on the CT number. Lastly, 3D pores were reconstructed, and the pore dimension and volume fraction were measured. EBSD and micro-CT data were used to model wave speeds in pore-free and fractured mylonites and schist. These data were combined to compare two modeling approaches: wave propagation and GassDEM modeling.

2.3. Wave Propagation Modeling (EWAVE)

Wave propagation modeling is performed using EWAVE Matlab code (Zhong and Frehner, 2018). The code simulates wave propagation through the EBSD data using an explicit finite-difference time-marching model. The model discretizes the input EBSD data into cells and an elastic stiffness tensor (**Table 1**) is assigned to each cell based on mineralogy and crystallographic orientation. A Ricker wavelet is digitally propagated across the sample by solving a momentum balance equation and Hooke's law. The wave travel time is recorded and the wave velocity is calculated from the width of the EBSD data and the travel time. The fast and slow velocities are determined by propagating waves parallel and perpendicular to rock foliation, respectively. A detailed explanation is provided in Zhong and Frehner (2018). A time snapshot of wave propagation through a medium is shown in **Figure 2**. The buffer length and wavelength used in this study are 300 and 100 μm, respectively. P-wave anisotropy is calculated as a ratio between the difference between fast and slow velocity, and the average of the two velocities.

Two types of modeling are performed: (1) a porosity-free EBSD model and (2) the same model but with added fractures defined by specific aspect ratios. EWAVE models EBSD data and could include imaged natural fractures (non-indexed phases) as it propagates a wave through the model (Zhong and Frehner, 2018). However, for our mylonitic rocks, natural fractures were not imaged via EBSD so are not immediately accounted for. We include pore information by extracting natural 3D fracture shapes from micro-CT data. This fracture set is statistically and mathematically simplified into 2D fractures which are deterministically included into the model. These pores are added randomly to the EBSD model at specific aspect ratios parallel to foliation.

2.4. Differential Effective Medium Modeling (MTEX and GassDEM)

A different approach to model the pore-free rock elasticity is by applying the Hill effective medium model implemented in the Matlab MTEX toolbox (Mainprice et al., 2015). The calculation uses the mineral volume fraction and CPO from the EBSD data, together with the single-crystal stiffness tensor of each mineral (**Table 1**) to predict the whole rock effective stiffness tensor from which wave speeds with direction can be estimated.

To model the effect of pores and fluids on the wave velocities, the pore-free effective stiffness tensor output from MTEX is set as a background rock for GassDEM (Gassmann and DEM) modeling (Kim et al., 2019; Simpson et al., 2020). GassDEM modeling adds fixed aspect ratio inclusions (3D fractures in this case) into the background medium. The process is iterative with additions of small volumes of pores until the target sample porosity is reached (Bruggeman, 1935). Gassmann's equation

TABLE 1 | Elasticity (in GPa) and density (in kg/m^3) of mineral phases present in our samples.

	Quartz	Plag.	Musc.	Biotite	Chlorite	Garnet	Air	Water
Density	2646	2653	2844	3215	2800	3570	1	1000
c_{11}	86.6	87.1	184.3	186	183.30	295.63	1.3 E-04	2.2
c_{22}	86.6	174.9	178.4	186	183.30	295.63	1.3 E-04	2.2
c_{33}	106.1	166.1	59.1	54	96.80	295.63	1.3 E-04	2.2
c_{44}	57.8	22.9	16.0	58	11.50	91.04	2 E-09	2 E-09
c_{55}	57.8	29	17.6	58	11.50	91.04	2 E-09	2 E-09
c_{66}	39.95	35	72.4	76.8	57.20	91.04	2 E-09	2 E-09
c_{12}	6.7	43.9	48.3	32.4	68.90	113.55	1.3 E-04	2.2
c_{13}	12.6	35.4	23.8	11.6	39.68	113.55	1.3 E-04	2.2
c_{14}	-17.8	6.1	0	0	0	0	0	0
c_{15}	0	-0.4	-2.0	0	0	0	0	0
c_{16}	0	-0.6	0	0	0	0	0	0
c_{23}	12.6	18	21.7	11.6	39.68	113.55	1.3 E-04	2.2
c_{24}	17.8	-5.9	0	0	0	0	0	0
c_{25}	0	-2.9	3.9	0	0	0	0	0
c_{26}	0	-6.5	0	0	0	0	0	0
c_{34}	0	-2.9	0	0	0	0	0	0
c_{35}	0	4.6	1.2	0	0	0	0	0
c_{36}	0	-10.7	0	0	0	0	0	0
c_{45}	0	-1.3	0	0	0	0	0	0
c_{46}	0	-5.2	0.5	0	0	0	0	0
c_{56}	-17.8	0.8	0	0	0	0	0	0

These mineral stiffness tensors are used in the EWAVE and MTEX modeling.
References: Quartz (Heyliger et al., 2003; Naus-Thijssen et al., 2010); plagioclase (Brown et al., 2016); muscovite (Bass, 1995); biotite and chlorite (Alexandrov and Ryzhova, 1961); garnet (Chen et al., 1999). Air and water are assumed to have non-zero (1 Pa) shear modulus to satisfy the GassDEM model requirements.

allows the effect of fluids on the elasticity of the rock to be modeled (Gassmann, 1951; Smith et al., 2003).

We study the effect of fractures on P-wave velocity and anisotropy in two ways: (1) fractures are aligned to foliation and porosity volume is varied and (2) the porosity volume is constant, but the contribution of the fracture orientation is changed for different combinations of aligned and randomly oriented fractures.

3. RESULTS

3.1. Electron Back-Scattered Diffraction (EBSD)

EBSD data show that the shear-zone Alpine Fault rocks are composed of quartz, plagioclase, garnet and a considerable amount of non-indexed phase (**Figure 3**, **Table 2**), assumed to be biotite mica as the phyllosilicate minerals in the Alpine Fault mylonites are predominantly biotite (Toy et al., 2015). There is no significant mineralogical difference between the 90^o and 30^o sections nor an improvement of imaging the micas. 80% of the non-indexed mica is assumed to align with foliation and 20% of the non-indexed mica is assumed to be randomly oriented (see section 1.3 in **Supplementary Material**).

3.2. Synchrotron X-Ray Micro-Tomography (Micro-CT)

Micro-CT data of ultramylonite, mylonite, and protomylonite samples are analyzed to quantify porosity and pore aspect ratio. After pore segmentation is performed (**Figure 4**), the number of pore voxels is divided by the total number of voxels to calculate porosity. The calculated porosity of ultramylonite, mylonite, and protomylonite are 3.36, 2.08, and 4.88%, respectively. A 5% porosity will be used in the following velocity modeling as it covers all the calculated porosity from the micro-CT data. Pore aspect ratio is measured as a ratio of three orthogonal pore axis lengths (e.g., X:Y:Z where $X \geq Y \geq Z$). The three numbers represent the longest axis, the second-longest and the shortest axial length, respectively (**Figure 5**). Two axial ratios are extracted from the segmented pores: elongation and flatness (**Figure 6**). Elongation is a ratio between the second-longest and the longest axial length (i.e., Y/X) and flatness is a ratio between the shortest to the second-longest axial length (i.e., Z/Y).

The elongation and flatness histogram plots of all three rocks are similar. Elongation plots are right-skewed with mode around 0.16 with the mean and median range from 0.36 to 0.40 and 0.32 to 0.38, respectively. The flatness for the ultramylonite and the protomylonite are almost symmetric with 0.48 mean and median. For the mylonite however, the flatness plot is slightly left-skewed. The mean and median of the mylonite flatness are 0.54 and 0.56, respectively. Pores with small elongation and flatness would represent low aspect ratio fractures, which are thin, long and narrow. Pores with elongation and flatness close to 1 represent close-to-spherical pores. Based on the histogram analysis, the average pore aspect ratio determined from the mean flatness and elongation is 5:2:1. This fracture shape is defined as

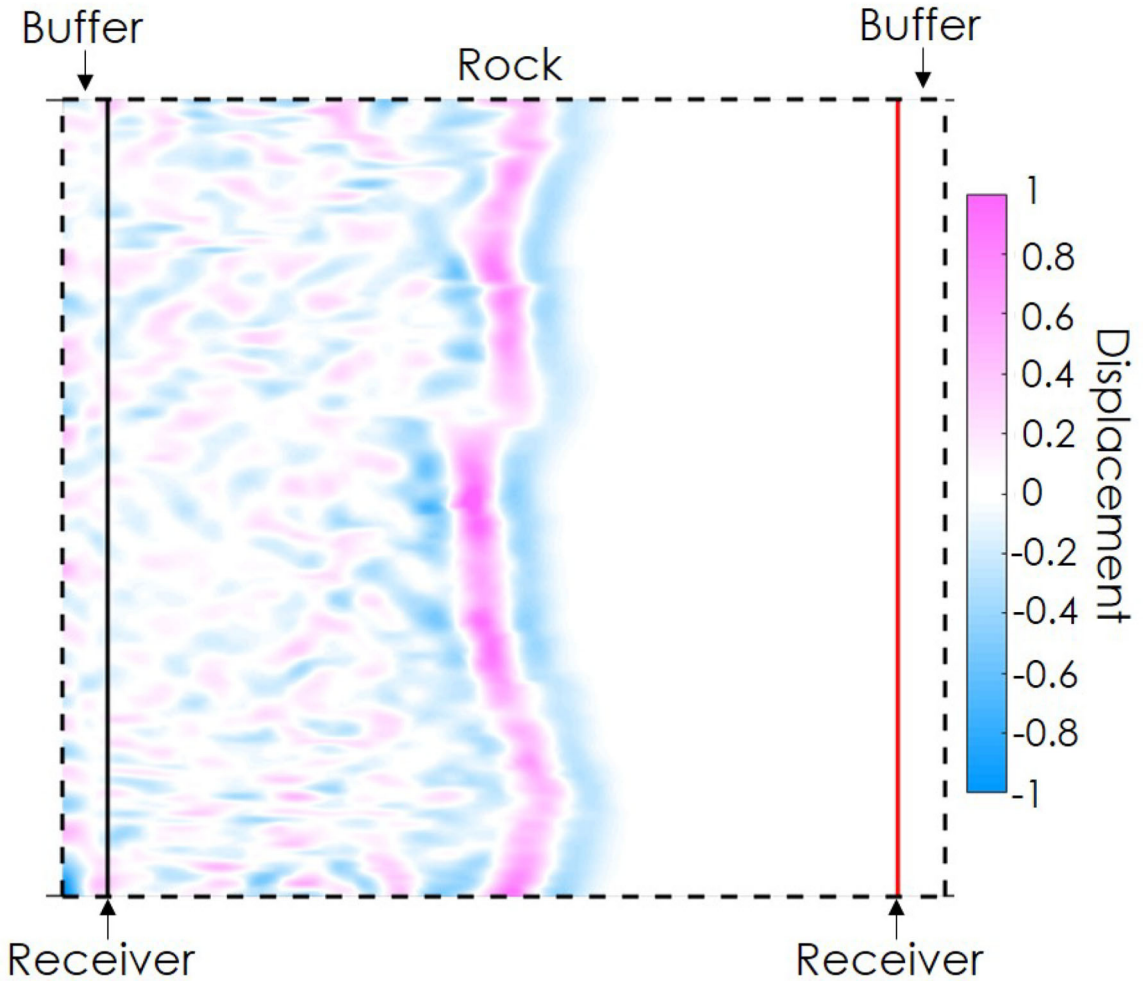

FIGURE 2 | EWAVE model component: EBSD data ("Rock") is placed between two buffers. A Ricker wave (pink and blue) is propagated from left to right of the model. Two receivers (left: black line, right: red line) are used to record the wave signal and calculate wave travel times. Displacement is dimensionless and does not affect the velocity.

a flat-shaped pore (fracture) and used for the following P-wave velocity modeling.

3.3. Wave Propagation Modeling (EWAVE)

Fast and slow P-wave velocities are modeled using the EWAVE code. Fracture porosity is added randomly as a 2D projection of the extracted micro-CT fractures of aspect ratio 5:2:1 (**Figure 7**). Fractures are added with their long-axis parallel to foliation as rectangles of aspect ratio 5:1. For this study, fractures are added by randomly replacing pixels in the EBSD data with air/water. The influence of fracture porosity volume is studied by adding fractures in 1% increments up to a total porosity of 5%. In this modeling, pores are dry (filled with air). For such low porosity, modeling air- or water-filled fractures results in a velocity difference of less than 2% of the air-filled fracture model. The pore-free fast velocities are similar for all rocks at 6.5 km/s, while the slow velocities range from 5.5 to 6.0 km/s depending on the lithology (**Figure 8A**). As porosity is added to the model, both fast and slow velocities decrease linearly. The fast velocities decrease slightly to 6.3 km/s at 5% porosity. The slow velocities however, decrease rapidly to 4.5 km/s. The P-wave anisotropy is also calculated (**Figure 8C**), ranging from 10 to 15% and increasing linearly to 30–35% for a 5 % fracture porosity.

3.4. Differential Effective Medium Modeling (MTEX and GassDEM)

The fast and slow velocities estimated with MTEX have similar values to the EWAVE modeling at approximately 6.5 and 5.5–6.0 km/s, respectively. Foliation-parallel ellipsoidal fractures of aspect ratio 5:2:1 are added to the model for porosity volume from 0.1 to 5% at 0.1% increments. The fast velocities decrease from 6.5 to 6.3 km/s at 5% porosity (**Figure 8B**), while the slow velocities decrease from 5.5 to 5 km/s. The pore-free P-wave anisotropy ranges from 10 to 15% and increases to 15–20% for a 5% porosity. Although EWAVE and GassDEM/MTEX use the same fracture volume and orientation, slow velocities -

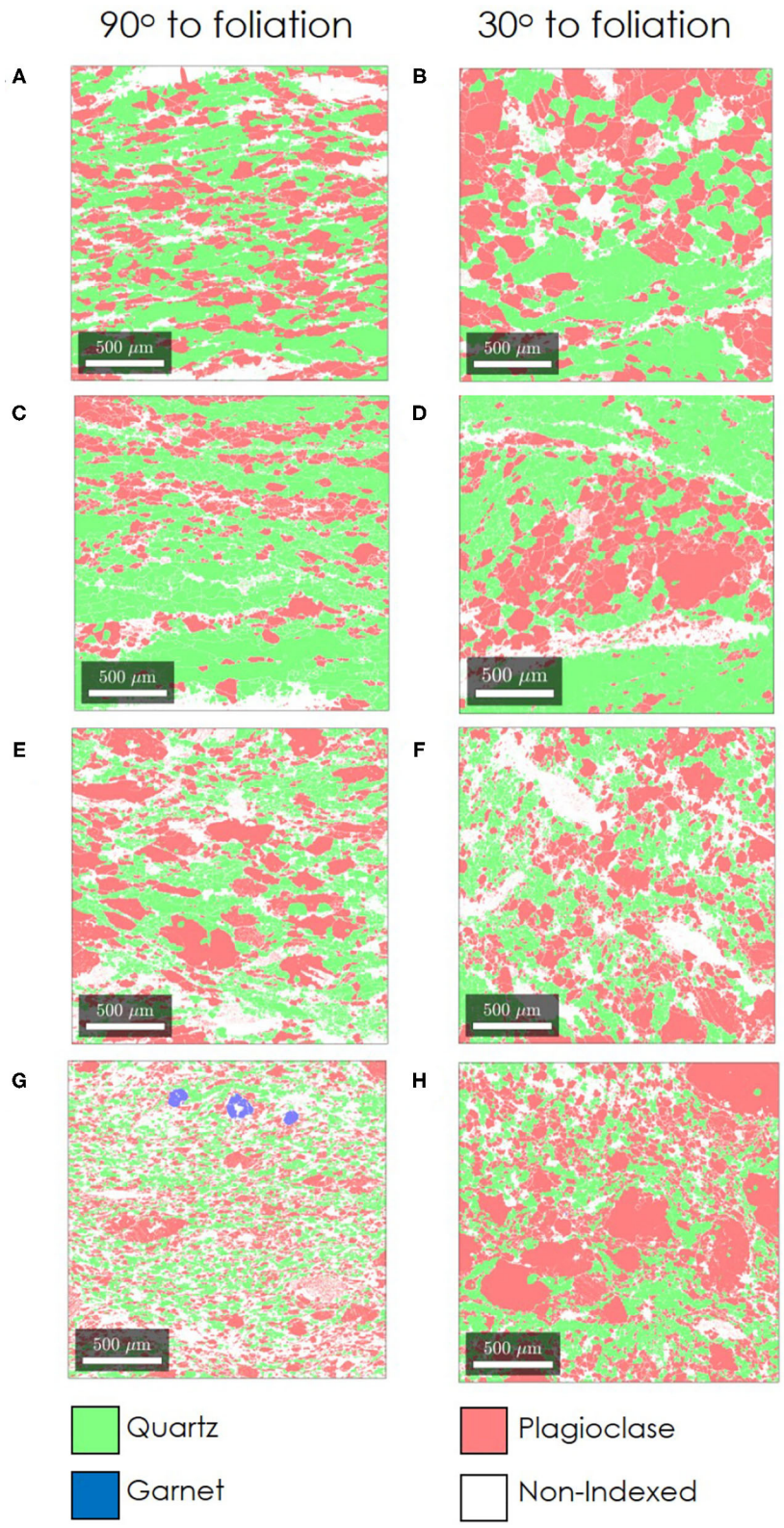

FIGURE 3 | Processed EBSD data of mineral phases distribution of **(A,B)** schist, **(C,D)** protomylonite, **(E,F)** mylonite, and **(G,H)** ultramylonite cut 90° and 30° to foliation, respectively.

and thus P-wave anisotropy—greatly differ between the models. The P-wave velocity and anisotropy results for the section cut at 30^o from foliation and water-filled samples are presented in the **Supplementary Material**.

The previous models assumed that all fractures are the same size and align with foliation. Fractures in real rocks however, vary in size and orient in different directions. For this, we use the modified GassDEM code (Simpson et al., 2020) to model how different combinations of foliation, parallel and randomly oriented fractures, as well as fracture size, affect P-wave velocities.

TABLE 2 | Mineral composition (vol.%) and mineral density (kg/m^3).

Sample	Lithology	Quartz	Plagioclase	Mica	Garnet	Density
S-90	Schist	41.83	35.69	22.46	0.02	2777
S-30	Schist	39.94	40.97	19.08	0.01	2758
P-90	Protomylonite	55.95	23.93	20.12	0.00	2762
P-30	Protomylonite	47.40	33.40	19.20	0.00	2758
M-90	Mylonite	30.85	36.66	32.49	0.00	2833
M-30	Mylonite	29.94	36.25	33.80	0.01	2841
U-90	Ultramylonite	31.27	39.26	28.53	0.94	2820
U-30	Ultramylonite	27.70	51.21	21.08	0.01	2770

-90 refers to thin section cut perpendicular to foliation, and -30 30^o degree to foliation.

Two fracture aspect ratios are used: a 5:2:1 aspect ratio which used in this study, and a 50:50:1 ratio as a representative of flat fractures. Eleven fracture orientation combinations are modeled from 0% aligned (random) fractures, to 100% aligned fractures, with combinations of these. Because all rocks show similar velocity and anisotropy trends, only the protomylonite data are used in this model. The P-wave velocities and anisotropy of all fracture models are calculated as a function of propagation angle to foliation. At 90^o the P-wave propagates parallel to foliation, and at 180^o perpendicular to it.

For the flat-shaped pore of 5:2:1 aspect ratio (**Figure 9A**), the fracture alignment can increase and decrease the fast and slow P-wave velocity, respectively, by approximately 0.4 km/s. Velocity changes become more prominent for the flatter aspect ratio fractures (50:50:1) resulting in overall slower velocities for all azimuthal directions compared to fractures of 5:2:1 aspect ratio (**Figure 9B**). The aligned fractures with a 50:50:1 aspect ratio increase the fast velocity by 3 km/s and decrease the slow velocity by 1.5 km/s. Fracture porosity has more influence on the P-wave anisotropy as more fractures are aligned (**Figures 9C,D**). However, when fracture alignment drops below 30% the anisotropy decreases with porosity instead.

The modeled velocity using spherical pores (black dashed lines) is presented for comparison (**Figure 9**). The spherical pore model yields a similar fast velocity to the model including 30% aligned fractures of 5:2:1 aspect ratio. The slow velocity of the 100% randomly oriented fracture model coincides only with the model that only contains spherical pores. For the 50:50:1 models,

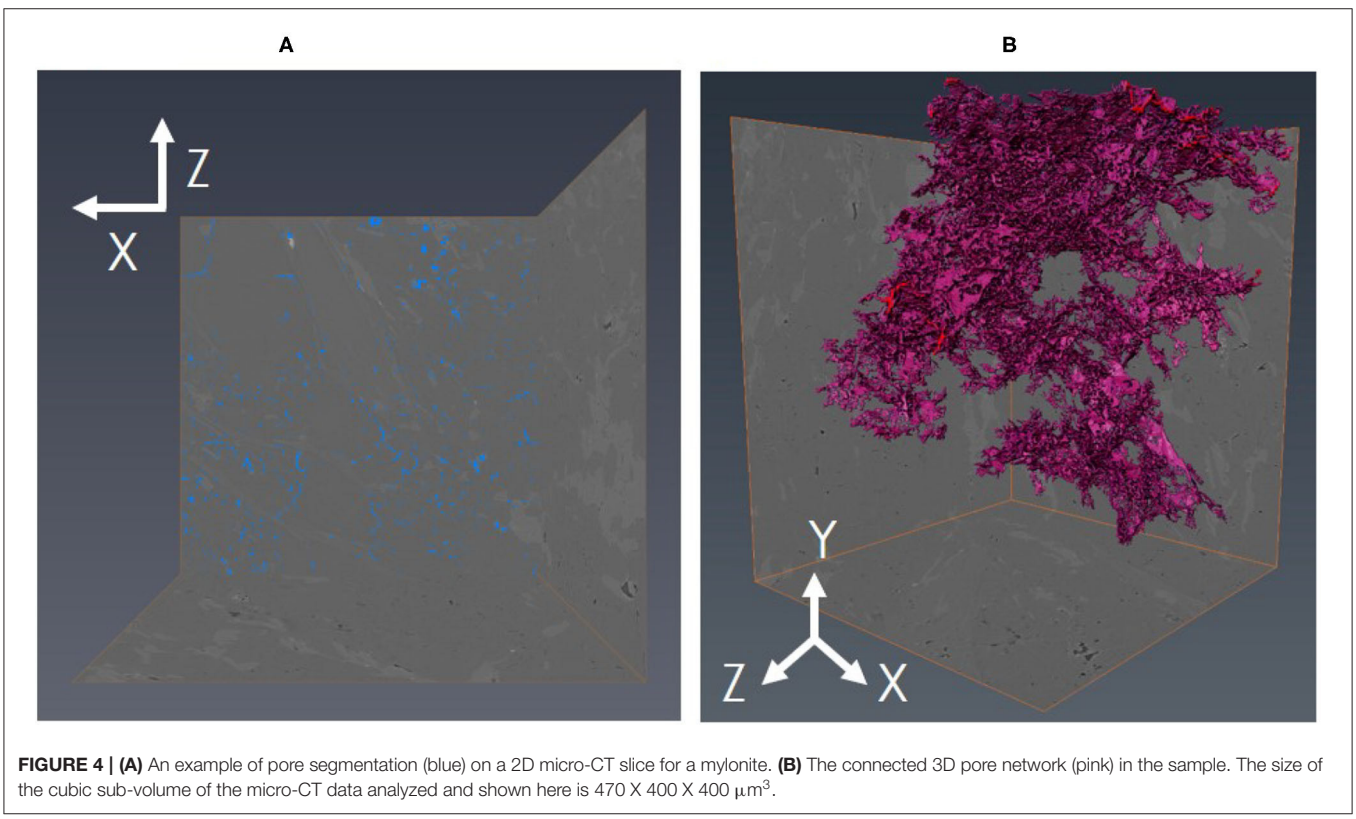

FIGURE 4 | (A) An example of pore segmentation (blue) on a 2D micro-CT slice for a mylonite. **(B)** The connected 3D pore network (pink) in the sample. The size of the cubic sub-volume of the micro-CT data analyzed and shown here is 470 X 400 X 400 μm^3.

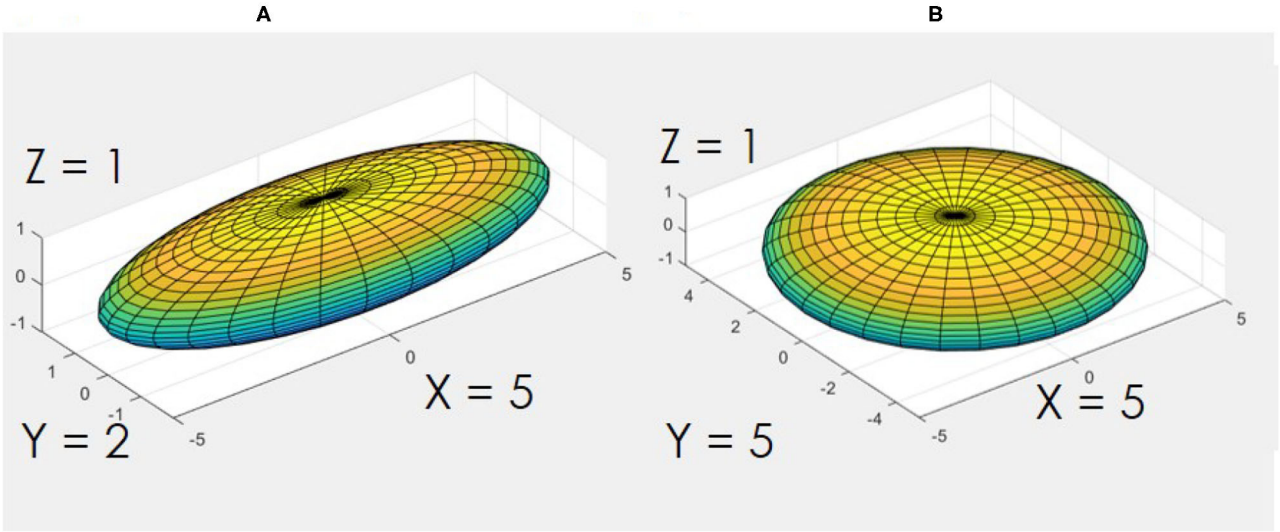

FIGURE 5 | Ellipsoid examples representing fractures of **(A)** 5:2:1 and **(B)** 5:5:1 aspect ratio.

the fast velocity from the spherical pore model is comparable to the perfectly aligned 50:50:1 pore aspect ratio model. However, the 50:50:1 pore model's slow velocity is significantly lower than that of the spherical pore model. The anisotropy of the spherical pore model remains almost constant and equal to the pore-free anisotropy because spherical pores reduce P-wave velocity equally, regardless of direction as opposed to fractures. If only 10–20% of the fractures align with foliation, then the P-wave anisotropy is equal to that of a rock with the same porosity but made up of spherical pores. This is observed for fractures of both aspect ratios investigated here.

4. DISCUSSION

4.1. P-Wave Velocity: EWAVE vs. MTEX-DEM

Pore-free rock P-wave velocities and anisotropy were calculated using the wave propagation model (EWAVE) and the Hill average effective medium model (MTEX), for samples cut perpendicular to foliation. The pore-free EWAVE and Hill average MTEX modeled velocities (velocities at 0% porosity in **Figure 8A**) are consistent between both methods, which is similar to observations by Zhong et al. (2014). As mentioned above, the non-indexed phases by EBSD are assumed to be mica. Based on Toy et al. (2008) and Dempsey et al. (2011), we also assume that most mica basal planes are parallel to foliation (80:20 parallel:random to foliation). Nonetheless, future studies should perform analyses capable of quantifying mica CPO on these mylonites to conclude on the true extent of the influence of mineralogy on the Alpine Fault rock anisotropy.

EWAVE and MTEX-GassDEM models are used to calculate the fractured rock P-wave velocity. A key difference between the model is that the GassDEM models a 3D pore, while the EWAVE model uses either natural rock fractures (e.g., extracted from micro-imaging techniques) or simplified 2D fractures, as done in this study. The simplified 2D fracture shape misses one dimension of the aspect ratio. For example, fractures with a 5:2:1 and 5:5:1 ratio would be simplified to a 5:1 2D ratio.

Individually these two types of 3D fractures (5:2:1 and 5:5:1) result in different GassDEM wave velocities, which also differ even more from the EWAVE modeled velocities using a 5:1 2D pore shape (**Figure 10**). The effect of pore aspect ratio on the fast velocities is insignificant. However, the 5:1 aspect ratio slow velocity deviates from the 5:2:1 and 5:5:1 aspect ratio trends by 12% and 5.3% at 5% porosity, respectively. As a result, the 5:1 ratio yields almost double the anisotropy of the 5:2:1 ratio.

A discrepancy between the elastic modeling using 2D and 3D data and their relationship has been previously reported (e.g., Saxena and Mavko, 2016; Hooghvorst et al., 2020). Because the 2D EWAVE model assumes a plane wave perpendicular to the EBSD model (Zhong and Frehner, 2018), the pore or fracture length perpendicular to the EBSD 2D model is thus assumed to be infinitely long. This is in contrast with the finite shape of the fracture used in the 3D GassDEM model. In this study, a simplified 2D pore shape is determined by reducing the 3D aspect ratio X:Y:1 to X:1. Having an infinitely long Y-axis in such a way contradicts this pore dimension reduction assumption and such infinite fractures exaggerate the effect of pores on the P-wave velocity. This explains why the modeled slow velocities from the 2D EWAVE model are always lower than those of the 3D GassDEM model. A key conclusion is that both the 2D and 3D pore aspect ratios strongly affect the modeled P-wave velocity and anisotropy. While both EWAVE and GassDEM models provide similar velocity predictions for pore-free rocks, a well-constrained pore shape in 3D is needed to accurately model P-wave velocity and anisotropy in a porous medium.

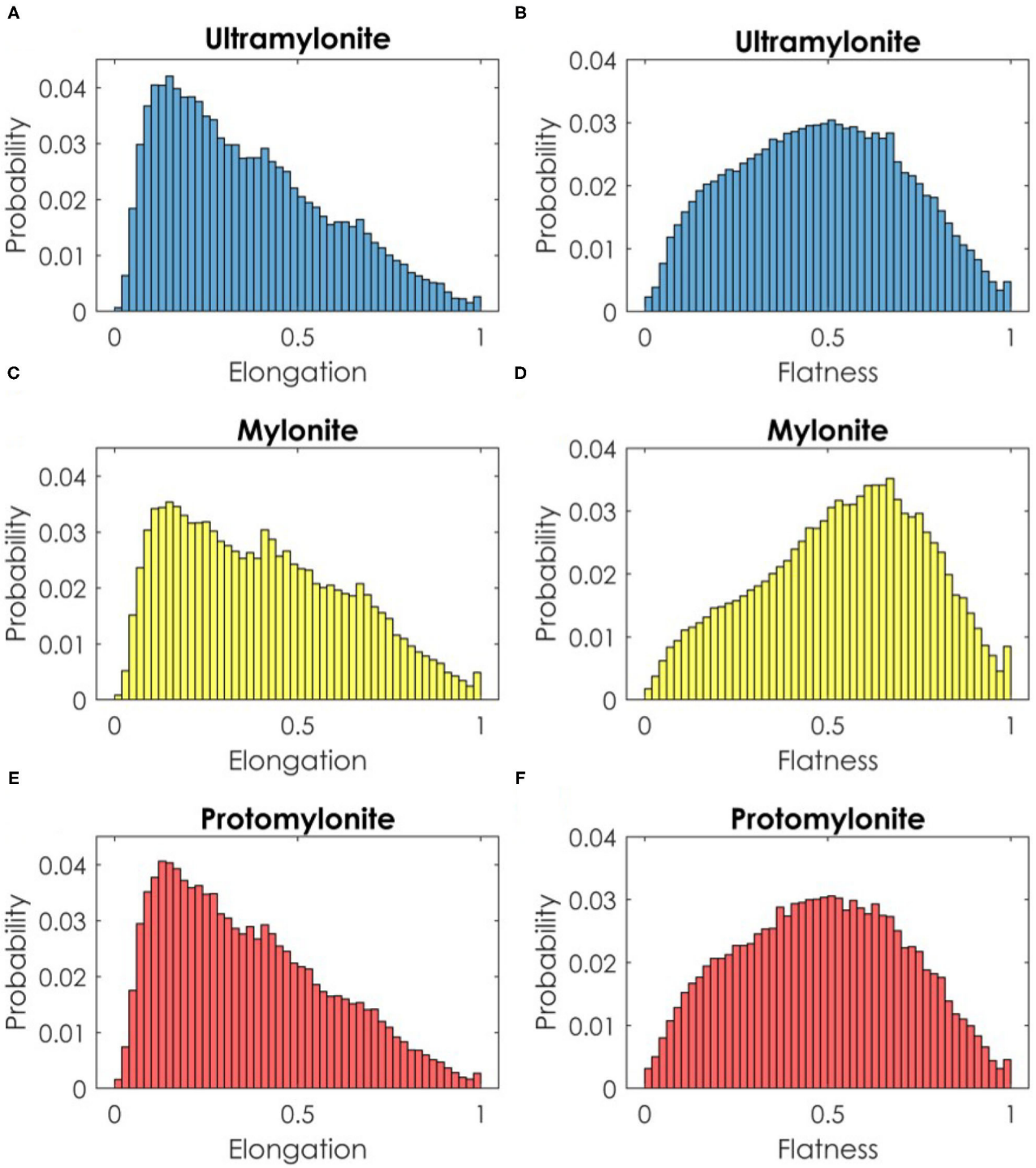

FIGURE 6 | Histograms of pore elongation and flatness in **(A,B)** ultramylonite, **(C,D)** mylonite, and **(E,F)** protomylonite.

4.2. Pore Aspect Ratio Assumption

This study makes three assumptions regarding the pore aspect ratio used in EWAVE and GassDEM velocity modeling. First, all pores in a rock are assumed to have the same shape based on the average aspect ratio extracted from the micro-CT data. The average aspect ratio used in our models (5:2:1) is different from that of other works. For example, Vasin et al. (2013) uses a pore aspect ratio of 100:100:1 and 50:50:1 to model shale

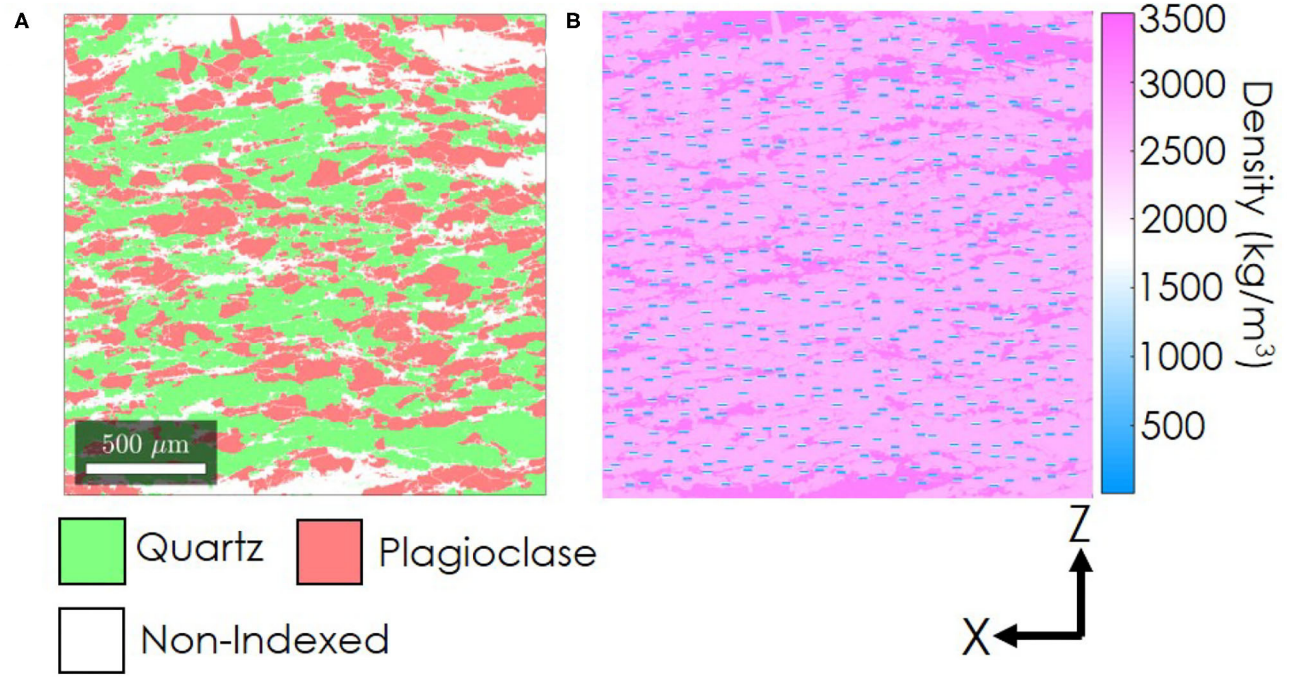

FIGURE 7 | (A) Schist EBSD data cut perpendicular to foliation and **(B)** the EWAVE model of the schist data with 5% fractures included. The color represents the phase density. The air-filled fractures are shown in blue.

elasticity. Microfractures in shales also form parallel to layering, in particular, between clay platelets. The pore aspect ratio used in GassDEM modeling is referred to as an effective pore aspect ratio (e.g., Hong-Bing et al., 2013). It is the aspect ratio that best predicts the elasticity from experimental/field measurements at a fixed given porosity. Given that rocks contain various pore shapes and orientations, assuming one aspect ratio is idealistic and would not match all the real pore shapes in a rock.

Figure 4 shows that a pore network is composed of several connected pores of different shapes, sizes and orientations. The pore aspect ratio used in this work (5:2:1) represents the average pore shape of the whole rock, not individual pores which have a wide range of shapes (**Figure 6**). Finding a representative pore aspect ratio is challenging, but predicting pore shapes and volumes from laboratory data (Adam et al., 2020; Simpson et al., 2020) can be aided by modeling constrained micro-CT analysis for variable shapes and volumes of pores.

Second, we assumed that all lithologies of the shear zone and metamorphic Alpine Fault rocks in this study have the same pore shape. This assumption results in the same velocity relationship with porosity for all lithologies. **Figure 6** shows that a similar dominant pore shape is estimated from the micro-CT data for all rocks. However, the pore shape distributions are different, pointing at the fact that the shape of individual pores could be different. In particular, the mylonite has flatness and elongation distributions that slightly differ from the protomylonite and ultramylonite.

Third, while modeling aligned fractures, we assumed that all pores have their longest axis aligned parallel to the rock foliation. Although this is the dominant direction for many microfractures, it is not realistic because not all pores align in the same direction in real rocks. A previous study on serpentinite (Kim et al., 2019) shows that a fracture effect on P-wave velocity is directionally dependent on fracture alignment. In our study, the fracture effect on velocity reduction is minimized when fractures align with wave propagation direction, and maximized when fractures align normal to the propagation direction. This results in the slow velocity being more susceptible to a change on fracture porosity than the fast velocity.

4.3. Velocity Comparison With Previous Studies

The pore-free modeled velocities of this study are compared to previous Alpine Fault EBSD-based velocity modeling works. The fast and slow pore-free velocities from this study (6.4 km/s, 5.5–5.9 km/s) are slightly higher than the velocities (6.2 km/s, 5.5 km/s) reported by Dempsey et al. (2011) but lower than the velocities (6.8–7.0 km/s, 5.7 km/s) reported by Adam et al. (2020). We suspect two possible causes for this discrepancy: mica volume and orientation. The rock samples Dempsey et al. (2011) analyzed contain 15-20 vol.% mica and their mica orientation is extracted from the EBSD data. Adam et al. (2020) worked with samples with a mica content of 35–40 vol.% and the orientation is assumed to align parallel to the rock foliation. In our study however, the samples contain 20–30 vol.% mica and

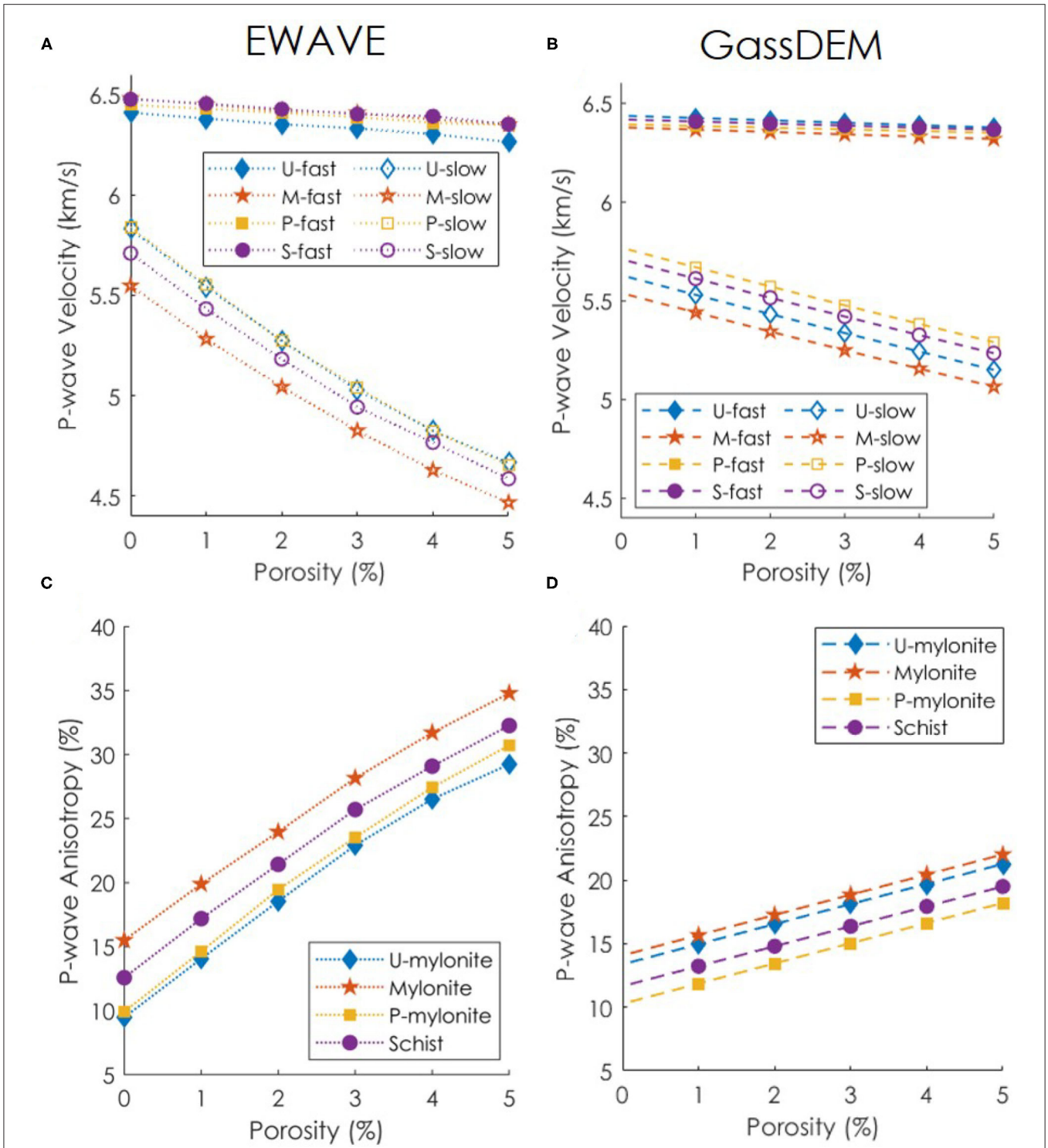

FIGURE 8 | Modeled P-wave velocity and anisotropy with **(A,C)** EWAVE model (5:1 fracture aspect ratio) and **(B,D)** GassDEM model (5:2:1 fracture aspect ratio). U, M, P, S refer to ultramylonite, mylonite, protomylonite and schist, respectively. -fast and -slow refer to fast and slow velocity.

only 80% of micas are assumed to align with foliation. This shows that understanding and quantifying volumes and orientations of mica-dominated rocks are critical to the estimation of seismic wave anisotropy.

We now compare our modeled velocity with the velocity measurements of Alpine Fault rock samples reported in previous studies (Okaya et al., 1995; Allen et al., 2017; Simpson et al., 2019; Adam et al., 2020). The velocities were measured

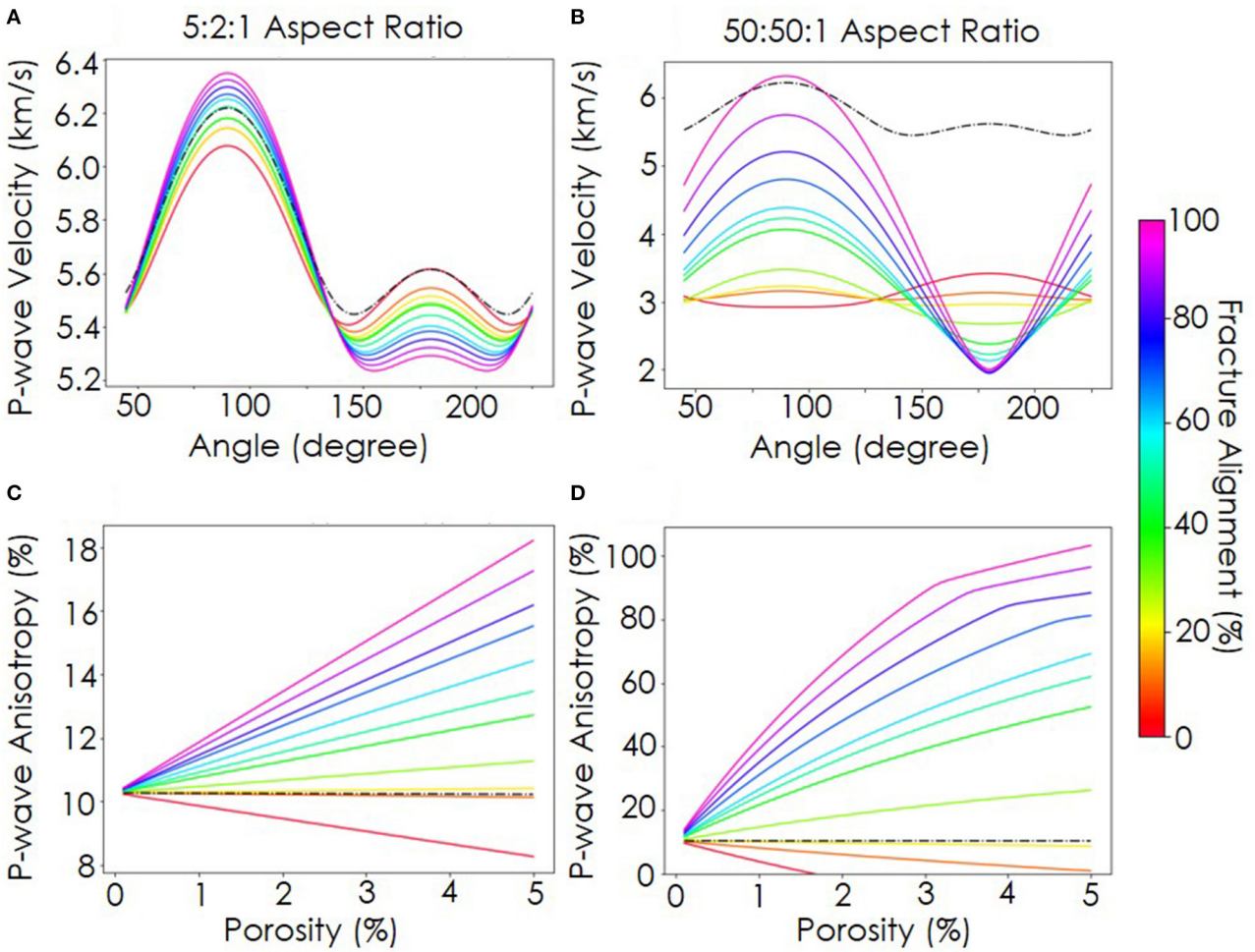

FIGURE 9 | P-wave velocity and anisotropy with angles of propagation to foliation for a 5% porosity protomylonite from GassDEM modeling. Two aspect ratios are compared: **(A,C)** 5:2:1 and **(B,D)** 50:50:1. The color represents fracture alignment to foliation, from all fractures being randomly oriented (0%) to perfectly aligned fractures to foliation (100%), and combinations of these. The black dashed lines are results for a rock with 100% spherical pores (1:1:1 aspect ratio) for reference.

under high confining pressure, thus assumed to be pore-free. The reported experimental fast and slow velocities range between 6.2–6.7 and 5.0–5.7 km/s, respectively. The velocities from this study fall within these ranges. Okaya et al. (1995) reports an increase in P-wave anisotropy toward the Alpine Fault plane. They interpret this increase in anisotropy as a result of increasing mica alignment due to metamorphism. Although we were unable to image mica orientations, we note that a 12% difference in mica volume fraction with 80% of micas being aligned with foliation can result in almost 5% increase in P-wave anisotropy (**Figure 8D**, **Table 2**). We further show that even small volumes of microfractures can significantly affect anisotropy. Adam et al. (2020) show that such fractures can remain open at 4 km depths at the Alpine Fault.

Field seismic data show that the rock in the vicinity of the Alpine Fault has a fast velocity of 6.2-6.5 km/s and a slow velocity of 5.6–5.7 km/s (Godfrey et al., 2002; Stern et al., 2007), which agrees with the velocities in this study. Additionally, the fluid-interpreted low velocity zone of 5.5 km/s velocity is also reported (Stern and McBride, 1998; Stern et al., 2007). Our porosity and fracture orientation models (**Figure 9**) predict the field velocities in the following sense: the fracture aspect ratio is 5:2:1 and 80% of fractures align with foliation while the rest are randomly oriented. It is important to recall that GassDEM models are non-unique, and different combinations of porosity, pore aspect ratio and orientation can result in identical velocity predictions.

5. CONCLUSION

In this study, P-wave elastic wave speeds in Alpine Fault rocks are modeled with and without microfractures. The four lithologies represent the protolith and the shear zone of the Alpine Fault:

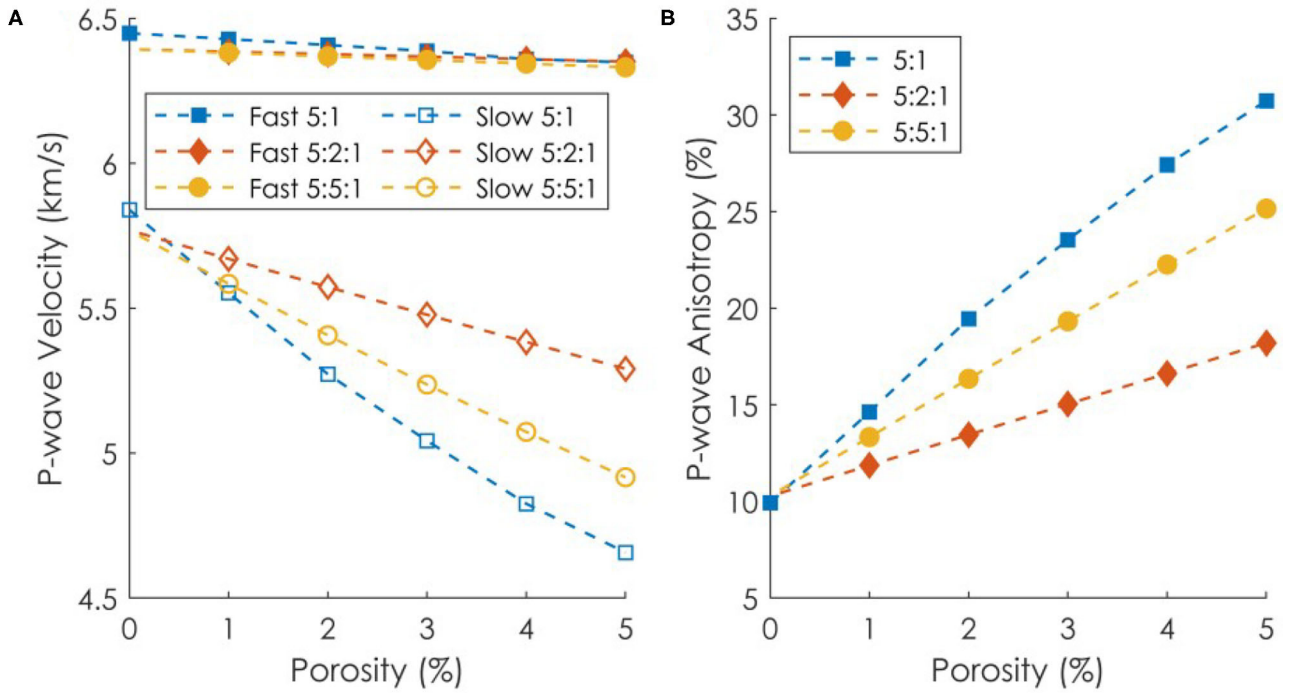

FIGURE 10 | Comparison between **(A)** modeled P-wave velocities and **(B)** P-wave anisotropy of the three rock models with three different pore aspect ratios: 5:1 (2D), 5:2:1 (3D), and 5:5:1 (3D).

schist, protomylonite, mylonite and ultramylonite. Although samples were cut at 30^o and 90^o angles to foliation, the tiny mica minerals were not indexed in the EBSD analysis for both orientations. Through numerical modeling and laboratory data, the orientation of the micas is assumed to be 80% aligned to foliation and 20% random. Because all lithologies have similar mica volumes, the pore-free wave velocities and anisotropies are similar among the samples. However, we were not able to quantify mica CPO because of limitations of EBSD imaging of such small crystals. Therefore, it remains inconclusive whether variable mica CPO between the Alpine Fault lithology can have any significant influence on P-wave anisotropy.

The effect of fractures on the P-wave anisotropy of fault zone mylonite is the most important result of our study. Three sets of micro-CT data of protomylonite, mylonite and ultramylonite are analyzed to quantitatively extract porosity and pore shape information with a resulting average pore aspect ratio of 5:2:1 across all lithologies. Pore-free wave velocities are similarly predicted by EWAVE and MTEX. However, significant differences arise in the slow P-wave velocity prediction (i.e., anisotropy) when fractures are included as 2D rectangles (EWAVE) or 3D ellipsoids (GassDEM). The type of method used to model fractures can double the P-wave anisotropy in these rocks for a constant porosity. It is thus critical to understand how each numerical model approaches microfractures and to constrain shapes and volumes of such fractures with quantitative microstructural analysis.

DATA AVAILABILITY STATEMENT

The original contributions presented in the study are included in the article/**Supplementary Material**, further inquiries can be directed to the corresponding author/s.

AUTHOR CONTRIBUTIONS

JC prepared the thin sections, acquired EBSD data and performed the numerical models for this manuscript. LA developed the idea, co-wrote the manuscript and advised JC. VT and MO helped with the design and acquisition of the EBDS data and thin section preparation and revised the manuscript. BS and VT provided the micro-CT data. JS provided a modified GassDEM code and helped via discussions on numerical modeling. XZ provided advice on the EWAVE code and ways to modify it to include fractures.

FUNDING

We thank the Royal Society of New Zealand, Marsden Contract #14-UOA-028. The Avizo software and workstation employed were supported by Nvidia Corporation who donated the Titan X Pascal GPU, the Royal Society of New Zealand Rutherford Discovery Fellowship (RDF) 16-UOO-1602 and a subcontract to GNS Science (GNS-MBIE00056). Synchrotron and electron

microscopic data acquisition was supported by RDF 16-UOO-1602, and SPring8 Proposals No. 2017B1378 and 2018A1506.

ACKNOWLEDGMENTS

We would like to thank Marianne Negrini for helping with the EBSD experiments. We also thank Andres Arcila-Rivera and Brent Pooley for helping with the sample preparation. Analyzing of the micro-CT data was assisted by Francesco Cappuccio.

SUPPLEMENTARY MATERIAL

The Supplementary Material for this article can be found online at: https://www.frontiersin.org/articles/10.3389/feart.2021.645532/full#supplementary-material

REFERENCES

Adam, L., Frehner, M., Sauer, K., Toy, V., and Guerin-Marthe, S. (2020). Seismic anisotropy and its impact on imaging the Alpine Fault: an experimental and modeling perspective. *J. Geophys. Res.* 125:e2019JB019029. doi: 10.1029/2019JB019029

Alexandrov, K. S., and Ryzhova, T. V. (1961). Elastic properties of rock-forming minerals. II. Layered silicates. *Izv. Acad. Sci. USSR Geophys.Ser.* 12, 165–1168.

Allen, M. J., Tatham, D., Faulkner, D. R., Mariani, E., and Boulton, C. (2017). Permeability and seismic velocity and their anisotropy across the Alpine Fault, New Zealand: an insight from laboratory measurements on core from the Deep Fault Drilling Project phase 1 (DFDP-1). *J. Geophys. Res. Solid Earth* 122, 6160–6179. doi: 10.1002/2017JB014355

Bass, J. D. (1995). Elasticity of minerals, glasses, and melts. *Miner. Phys. Crystallogr.* 23, 45–63. doi: 10.1029/RF002p0045

Boulton, C., Menzies, C. D., Toy, V. G., Townend, J., and Sutherland, R. (2017). Geochemical and microstructural evidence for interseismic changes in fault zone permeability and strength, Alpine Fault, New Zealand. *Geochem. Geophys. Geosyst.* 18, 238–265. doi: 10.1002/2016GC006588

Brown, J. M., Angel, R. J., and Ross, N. L. (2016). Elasticity of plagioclase feldspars. *J. Geophys. Res. Solid Earth* 121, 663–675. doi: 10.1002/2015JB012736

Bruggeman, D. (1935). Berechnung verschiedener konstanten von heterogenen substanzen: 1. dielektrizitatskonstanten und leitfahigkeiten der mischkorper aus isotropen substanzen. *Ann. Phys.* 24, 636–679. doi: 10.1002/andp.19354160705

Chapman, C. H., and Pratt, R. G. (1992). Traveltime tomography in anisotropic media—I. Theory. *Geophys. J. Int.* 109, 1–19. doi: 10.1111/j.1365-246X.1992.tb00075.x

Chen, G., Cooke, J. A., Gwanmesia, G. D., and Liebermann, R. C. (1999). Elastic wave velocities of $Mg_3Al_2Si_3O_12$-pyrope garnet to 10 GPa. *Am. Mineral.* 84, 384–388. doi: 10.2138/am-1999-0322

Christensen, N., and Okaya, D. (2007). *Compressional and Shear Wave Velocities in South Island, New Zealand Rocks and Their Application to the Interpretation of Seismological Models of the New Zealand Crust*. Washington, DC: American Geophysical Union Geophysical Monograph Series, 123–155.

Columbus, J., Sirguey, P., and Tenzer, R. (2011). A free, fully assessed 15-m dem for New Zealand. *Surv. Q.* 66, 16–19.

Cooper, A., and Palin, J. (2018). Two-sided accretion and polyphase metamorphism in the Haast Schist belt, New Zealand: constraints from detrital zircon geochronology. *GSA Bull.* 130, 1501–1518. doi: 10.1130/B31826.1

Dempsey, E. D., Prior, D. J., Mariani, E., Toy, V. G., and Tatham, D. J. (2011). Mica-controlled anisotropy within mid-to-upper crustal mylonites: an EBSD study of mica fabrics in the Alpine Fault Zone, New Zealand. *Geol. Soc. Lond. Spec. Publ.* 360, 33–47. doi: 10.1144/SP360.3

Eccles, J. D., Gulley, A. K., Malin, P. E., Boese, C. M., Townend, J., and Sutherland, R. (2015). Fault zone guided wave generation on the locked, late interseismic Alpine Fault, New Zealand. *Geophys. Res. Lett.* 42, 5736–5743. doi: 10.1002/2015GL064208

Edbrooke, S. W., Heron, D. W., Forsyth, P. J., and Jongens, R. (2015). Geological map of New Zealand 1: 1,000,000, GNS Science Geological Map 2, 2 print maps. Lower Hut: GNS Science."

Feenstra, J., Thurber, C., Townend, J., Roecker, S., Bannister, S., Boese, C., et al. (2016). Microseismicity and P-wave tomography of the central Alpine Fault, New Zealand. *N. Z. J. Geol. Geophys.* 59, 483–495. doi: 10.1080/00288306.2016.1182561

Gassmann, F. (1951). Uber die elastizitat poroser medien. *Vierteljahrssch. Naturforsch. Gesellsch. Zurich* 96, 1–23.

Godfrey, N. J., Christensen, N. I., and Okaya, D. A. (2000). Anisotropy of schists: contribution of crustal anisotropy to active source seismic experiments and shear wave splitting observations. *J. Geophys. Res. Solid Earth* 105, 27991–28007. doi: 10.1029/2000JB900286

Godfrey, N. J., Christensen, N. I., and Okaya, D. A. (2002). The effect of crustal anisotropy on reflector depth and velocity determination from wide-angle seismic data: a synthetic example based on South Island, New Zealand. *Tectonophysics* 355, 145–161. doi: 10.1016/S0040-1951(02)00138-5

Grapes, R., and Watanabe, T. (1994). Mineral composition variation in Alpine Schist, Southern Alps, New Zealand: implications for recrystallization and exhumation. *Island Arc* 3, 163–181.

Heyliger, P., Ledbetter, H., and Kim, S. (2003). Elastic constants of natural quartz. *J. Acoust. Soc. Am.* 114, 644–650. doi: 10.1121/1.1593063

Hong-Bing, L., Jia-Jia, Z., and Feng-Chang, Y. (2013). Inversion of effective pore aspect ratios for porous rocks and its applications. *Chinese J. Geophys.* 56, 43–51. doi: 10.1002/cjg2.20004

Hooghvorst, J. J., Harrold, T. W. D., Nikolinakou, M. A., Fernandez, O., and Marcuello, A. (2020). Comparison of stresses in 3D vs. 2D geomechanical modelling of salt structures in the Tarfaya Basin, West African coast. *Petrol. Geosci.* 26, 36–49. doi: 10.1144/petgeo2018-095

Howarth, J. D., Cochran, U. A., Langridge, R. M., Clark, K., Fitzsimons, S. J., Berryman, K., et al. (2018). Past large earthquakes on the Alpine Fault: paleoseismological progress and future directions. *N. Z. J. Geol. Geophys.* 61, 309–328. doi: 10.1080/00288306.2018.1464658

Jeppson, T. N., and Tobin, H. J. (2020). Elastic properties and seismic anisotropy across the Alpine Fault, new zealand. *Geochem. Geophys. Geosyst.* 21:e2020GC009073. doi: 10.1029/2020GC009073

Karalliyadda, S. C., and Savage, M. K. (2013). Seismic anisotropy and lithospheric deformation of the plate-boundary zone in South Island, New Zealand: inferences from local S-wave splitting. *Geophys. J. Int.* 193, 507–530. doi: 10.1093/gji/ggt022

Kelly, C. M., Faulkner, D. R., and Rietbrock, A. (2017). Seismically invisible fault zones : laboratory insights into imaging faults in anisotropic rocks. *Geophys. Res. Lett.* 44, 8205–8212. doi: 10.1002/2017GL073726

Kern, H., Ivankina, T. I., Nikitin, A. N., Lokajíček, T., and Pros, Z. (2008). The effect of oriented microcracks and crystallographic and shape preferred orientation on bulk elastic anisotropy of a foliated biotite gneiss from Outokumpu. *Tectonophysics* 457, 143–149. doi: 10.1016/j.tecto.2008.06.015

Kim, Y., Kim, E., and Mainprice, D. (2019). GassDem: a MATLAB program for modeling the anisotropic seismic properties of porous medium using differential effective medium theory and Gassmann's poroelastic relationship. *Comput. Geosci.* 126, 131–141. doi: 10.1016/j.cageo.2019.02.008

Lay, V., Buske, S., Lukács, A., Gorman, A. R., Bannister, S., and Schmitt, D. R. (2016). Advanced seismic imaging techniques characterize the Alpine Fault at Whataroa (New Zealand). *J. Geophys. Res. Solid Earth* 121, 8792–8812. doi: 10.1002/2016JB013534

Little, T. A., Holcombe, R. J., and Ilg, B. R. (2002). Kinematics of oblique collision and ramping inferred from microstructures and strain in middle crustal rocks, central Southern Alps, New Zealand. *J. Struct. Geol.* 24, 219–239. doi: 10.1016/S0191-8141(01)00060-8

Loucks, R. G., Reed, R. M., Ruppel, S. C., and Jarvie, D. M. (2009). Morphology, genesis, and distribution of nanometer-scale pores in siliceous

mudstones of the Mississippian Barnett Shale. *J. Sediment. Res.* 79, 848–861. doi: 10.2110/jsr.2009.092

Mainprice, D., Bachmann, F., Hielscher, R., Schaeben, H., and Lloyd, G. E. (2015). Calculating anisotropic piezoelectric properties from texture data using the MTEX open source package. *Geol. Soc. Lond. Spec. Publ.* 409, 223–249. doi: 10.1144/SP409.2

Naus-Thijssen, F. M. J., Johnson, S. E., and Koons, P. O. (2010). Numerical modeling of crenulation cleavage development: a polymineralic approach. *J. Struct. Geol.* 32, 330–341. doi: 10.1016/j.jsg.2010.01.004

Norris, R. J., and Cooper, A. F. (1997). Erosional control on the structural evolution of a transpressional thrust complex on the Alpine fault, New Zealand. *J. Struct. Geol.* 19, 1323–1342. doi: 10.1016/S0191-8141(97)00036-9

Norris, R. J., and Cooper, A. F. (2007). *The Alpine Fault, New Zealand: Surface Geology and Field Relationships*. American Geophysical Union (AGU), 157–175.

Novitsky, C. G., Holbrook, W. S., Carr, B. J., Pasquet, S., Okaya, D., and Flinchum, B. A. (2018). Mapping inherited fractures in the critical zone using seismic anisotropy from circular surveys. *Geophys. Res. Lett.* 45, 3126–3135. doi: 10.1002/2017GL075976

Okaya, D., Christensen, N., Stanley, D., Stern, T., and Group, S. I. G. T. S. W. (1995). Crustal anisotropy in the vicinity of the Alpine Fault Zone, South Island, New Zealand. *N. Z. J. Geol. Geophys.* 38, 579–583.

Pischiutta, M., Savage, M. K., Holt, R. A., and Salvini, F. (2015). Fracture-related wavefield polarization and seismic anisotropy across the Greendale Fault. *J. Geophys. Res. Solid Earth* 120, 7048–7067. doi: 10.1002/2014JB011560

Prior, D., and Mariani, E. (2009). *EBSD in the Earth Sciences: Applications, Common Practice, and Challenges*. Electron Backscatter Diffraction in Materials ScienceElectron Backscatter Diffraction in Materials Science. Boston, MA: Springer, 345–360.

Savage, M. K., Duclos, M., and Marson-Pidgeon, K. (2007). *Seismic Anisotropy in South Island, New Zealand*. A Continental Plate Boundary: Tectonics at South Island, New Zealand. Washington, DC: American Geophysical Union, 95–114.

Saxena, N., and Mavko, G. (2016). Estimating elastic moduli of rocks from thin sections: digital rock study of 3D properties from 2D images. *Comput. Geosci.* 88, 9–21. doi: 10.1016/j.cageo.2015.12.008

Schuck, B., Schleicher, A. M., Janssen, C., Toy, V. G., and Dresen, G. (2020). Fault zone architecture of a large plate-bounding strike-slip fault: a case study from the Alpine Fault, New Zealand. *Solid Earth* 11, 95–124. doi: 10.5194/se-11-95-2020

Simpson, J., Adam, L., van Wijk, K., and Charoensawan, J. (2020). Constraining microfractures in foliated Alpine Fault rocks with laser ultrasonics. *Geophys. Res. Lett.* 47:e2020GL087378. doi: 10.1029/2020GL087378

Simpson, J., van Wijk, K., Adam, L., and Smith, C. (2019). Laser ultrasonic measurements to estimate the elastic properties of rock samples under *in situ* conditions. *Rev. Sci. Instrum.* 90:114503. doi: 10.1063/1.5120078

Smith, E. G. C., Stern, T., and O'Brien, B. (1995). A seismic velocity profile across the central South Island, New Zealand, from explosion data. *N. Z. J. Geol. Geophys.* 38, 565–570. doi: 10.1080/00288306.1995.9514684

Smith, T. M., Sondergeld, C. H., and Rai, C. S. (2003). Gassmann fluid substitutions: a tutorial. *Geophysics* 68, 430–440. doi: 10.1190/1.1567211

Stern, T., Kleffmann, S., Okaya, D., Scherwath, M., and Bannister, S. (2001). Low seismic-wave speeds and enhanced fluid pressure beneath the Southern Alps of New Zealand. *Geology* 29, 679–682. doi: 10.1130/0091-7613(2001)029<0679:LSWSAE>2.0.CO;2

Stern, T., Okaya, D., Kleffmann, S., Scherwath, M., Henrys, S., and Davey, F. (2007). *Geophysical Exploration and Dynamics of the Alpine Fault Zone*. A Continental Plate Boundary: Tectonics at South Island, New Zealand. Washington, DC: American Geophysical Union, 207–233.

Stern, T. A. and McBride, J. H. (1998). Seismic exploration of continental strike-slip zones. *Tectonophysics* 286, 63–78.

Sutherland, R., Eberhart-Phillips, D., Harris, R. A., Stern, T., Beavan, J., Ellis, S., et al. (2007). *Do Great Earthquakes Occur on the Alpine Fault in Central South Island, New Zealand?* A Continental Plate Boundary: Tectonics at South Island, New Zealand. Washington, DC: American Geophysical Union, 235–251.

Toy, V. G., Boulton, C. J., Sutherland, R., Townend, J., Norris, R. J., Little, T. A., et al. (2015). Fault rock lithologies and architecture of the central Alpine fault, New Zealand, revealed by DFDP-1 drilling. *Lithosphere* 7, 155–173. doi: 10.1130/L395.1

Toy, V. G., Prior, D. J., and Norris, R. J. (2008). Quartz fabrics in the Alpine Fault mylonites: Influence of pre-existing preferred orientations on fabric development during progressive uplift. *J. Struct. Geol.* 30, 602–621. doi: 10.1016/j.jsg.2008.01.001

Tsvankin, I., Gaiser, J., Grechka, V., Van Der Baan, M., and Thomsen, L. (2010). Seismic anisotropy in exploration and reservoir characterization: an overview. *Geophysics* 75, 75A15–75A29. doi: 10.1190/1.3481775

Vasin, R. N., Wenk, H., Kanitpanyacharoen, W., Matthies, S., and Wirth, R. (2013). Elastic anisotropy modeling of Kimmeridge shale. *J. Geophys. Res. Solid Earth* 118, 3931–3956. doi: 10.1002/jgrb.50259

Zhong, X., and Frehner, M. (2018). E-Wave software: EBSD-based dynamic wave propagation model for studying seismic anisotropy. *Comput. Geosci.* 118, 100–108. doi: 10.1016/j.cageo.2018.05.015

Zhong, X., Frehner, M., Kunze, K., and Zappone, A. (2014). A novel EBSD-based finite-element wave propagation model for investigating seismic anisotropy: application to Finero peridotite, ivrea-verbano zone, Northern Italy. *Geophys. Res. Lett* 41, 7105–7114. doi: 10.1002/2014GL060490

Conflict of Interest: The authors declare that the research was conducted in the absence of any commercial or financial relationships that could be construed as a potential conflict of interest.

Copyright © 2021 Charoensawan, Adam, Ofman, Toy, Simpson, Zhong and Schuck. This is an open-access article distributed under the terms of the Creative Commons Attribution License (CC BY). The use, distribution or reproduction in other forums is permitted, provided the original author(s) and the copyright owner(s) are credited and that the original publication in this journal is cited, in accordance with accepted academic practice. No use, distribution or reproduction is permitted which does not comply with these terms.

frontiers in Earth Science

METHODS
published: 22 April 2021
doi: 10.3389/feart.2021.641705

Anisotropic Rock Model-Guided Post-Stack Attribute Analysis With Pore Type and Production Data for a Carbonate Gas Reservoir

Xuri Huang[1,2]*, *Yungui Xu*[2], *Haoyuan Li*[2], *Zhiwen Zhang*[2] *and Wei Xu*[3]

[1] State Key Laboratory of Oil and Gas Reservoir Geology and Exploitation, Southwest Petroleum University, Chengdu, China, [2] School of Geosciences and Technology, Southwest Petroleum University, Chengdu, China, [3] Petro-China Southwest Exploration and Production Research Institute, Chengdu, China

The Moxi area in the Sichuan Basin is dominated by carbonate gas reservoirs, where gas productivity is most strongly influenced by their pore types. Fractured caves are the most favorable pore structure type for reservoir productivity, followed by cave and vuggy pore structures, and interparticle pore structures are the least productive. The spatial discrimination of these three pore types is important for cost-effective development. However, the pore type identification remains difficult owing to poor-quality azimuthal seismic data. A practical approach is to understand the seismic signatures of the different pore types and the related productivities from the post-stack data. In this work, seismic forward modeling is conducted using a constructed theoretical model of Hudson's anisotropic representation, and the pre-stack and post-stack anisotropy signatures are analyzed for different pore types. The rock model is further calibrated using log data, and forward modeling is performed based on the calibrated logs. We propose a new attribute of these signatures: namely, the ratio of the absolute peak and the absolute trough immediately below the peak, which is applied to the three-dimensional seismic data in the Moxi area. In contrast with other conventional attributes, this ratio effectively correlates with pore type, which allows the pore types in wells to be differentiated. This attribute also reasonably correlates with open flow gas rate of the well. The results demonstrate that this attribute from the post-stack data is a promising indicator of pore type and gas productivity and can also be readily mapped spatially for the selection of new drilling locations.

Keywords: anisotropy, rock model, gas productivity, pore type, fractures, caves

OPEN ACCESS

Edited by:
Jing Ba,
Hohai University, China

Reviewed by:
Aldo Vesnaver,
National Institute of Oceanography and Applied Geophysics, Italy
Qiang Guo,
China Jiliang University, China
Zhenwei Guo,
Central South University, China
Sanyi Yuan,
China University of Petroleum, China

***Correspondence:**
Xuri Huang
xrhuang@sunrisepst.com

Specialty section:
This article was submitted to Solid Earth Geophysics, a section of the journal Frontiers in Earth Science

Received: *14 December 2020*
Accepted: *22 March 2021*
Published: *22 April 2021*

Citation:
Huang X, Xu Y, Li H, Zhang Z and Xu W (2021) Anisotropic Rock Model-Guided Post-Stack Attribute Analysis With Pore Type and Production Data for a Carbonate Gas Reservoir. Front. Earth Sci. 9:641705. doi: 10.3389/feart.2021.641705

BACKGROUND

A giant Precambrian gas field called the Moxi–Gaoshiti gas field was recently discovered and put into production in the Sichuan Basin (Liao et al., 2011). Recent studies have shown that the gas field is a structural and stratigraphic reservoir (Li Z. et al., 2014; Xu et al., 2019). The lithology is Sinian carbonate with small amounts of shale and silica. The reservoir thickness ranges from 0 to 200 m with erosion breccia, arenite dolomite, silty dolomite, and straticulate dolomite. Shale and silicalite normally serve as the caprock or sealing formation. The pore system is mainly composed of small caves, vuggy pores, interparticle pores, and fractured caves. The pores include interparticle

dissolution pores, interparticle pores, intercrystalline dissolution pores, and intercrystalline pores, all of which can develop owing to dolomization and dissolution processes. The pore system in the Dengying group is dominated by dissolution processes, and caves and vuggy pores have developed in response to weathering and dissolution processes. Most of the vuggy pores and caves exhibit elongated "string bean" patterns including bedding features and the path alignment of fractures and dissolution. The fracture geometry is mainly disk-shaped, ellipsoidal, or irregular. The most commonly developed fractures in the reservoir include structural fractures, dissolution fractures, and stylolite lines. Structural fractures are commonly filled with dolomite, asphalt, and quartz. Mid- to high-angle fractures dominate the upper Deng-4 zone, whereas low- to mid-angle fractures dominate the lower Deng-4 zone (Li Y. et al., 2014). Fracture systems with vuggy pores/caves provide a good reservoir pore system (Shirmohamadi et al., 2017; Abdlmutalib et al., 2019), but these features tend to cause a high degree of seismic anisotropy, and current seismic data at present lack high-quality azimuthal information. This poses a challenge to interpret the anisotropy and identify the reservoir pore types and fluid producibilities using the seismic data. In this work, we focus on the Moxi area of the giant gas field, which is a development area with eight gas-producing wells with geological characteristics as described above. Anisotropic modeling is performed based on a theoretical model and log data to guide the extraction of post-stack seismic attributes (Payne et al., 2010; Shiri and Falahat, 2020). Vuggy pores and fractured caves are found to be the pore types that typically yield a high initial gas rate. A newly extracted attribute is applied to correlate with the initial open flow gas rate, which can serve as a productivity indicator and allow the initial open flow gas rate to be spatially mapped as a guide for future drilling.

SEISMIC RESPONSES BASED ON ANISOTROPIC MODELS

The pores in the Moxi area are classified into three types based on the aforementioned geological processes: (1) fractured-vuggy pores/caves, (2) vuggy pores/caves, and (3) interparticle pores (**Figure 1**) (Sain et al., 2008; Kittridge, 2015). The production data show that the pore type strongly impacts gas productivity. Fractured-vuggy pore/cave type structures are generally associated with the highest production levels, whereas interparticle pore structures are associated with the lowest productivity. The three pore types cannot be identified from the seismic data using traditional approaches. The seismic anisotropy can be a critical factor for signal characteristic analysis because fractures are often mixed with caves and vuggy pores. Anisotropic models are therefore required to represent this geology type for a better understanding of the post-stack seismic signatures. The Hudson model (Hudson, 1980, 1986) has been used to characterize anisotropy using a "coin-shaped" pore based on geology. However, this assumed shape generates uncertainties because some particularly long fractures may be present. Nevertheless, the intensity of long fractures is relatively low in this area, thus the model is still applicable (Simon and Philip, 2010; Peng and Xiao, 2017). The related anisotropic parameters are determined to model their corresponding post-stack seismic signatures.

ROCK MODEL REVIEW AND PROCEDURE

In this work, we use the Hudson model for anisotropic modeling. The linear Wyllie average formula is used to obtain the elastic moduli of the rock matrix and fluid. The Hudson model is used to insert the cracks and then perform the fluid replacement. The procedure includes the following steps (**Figure 2**).

Elastic Parameters of the Rock Matrix

The elastic parameters of the rock matrix are required for the Hudson model. In this work, the velocities of the rock matrix minerals are linearly combined according to their percentages to obtain the matrix background velocity (Hill, 1952; Wyllie et al., 1956):

$$\frac{1}{V_m} = \sum_{i=1}^{m} \frac{C_{min\_i}}{V_{min\_i}}, \tag{1}$$

where V_m is the P-wave velocity (Vp) or S-wave velocity (Vs) of the matrix rock, C_{min_i} is the volume fraction of the i^{th} mineral, and V_{min_i} is the P-wave or S-wave velocity of the i^{th} mineral.

The Lamé constants (λ and μ) of the matrix can be calculated using Vp and Vs obtained using the above formula and converted into an elastic constant matrix:

$$\lambda = \rho\left(V_p{}^2 - 2V_s{}^2\right) \tag{2}$$

$$\mu = V_s{}^2\rho \tag{3}$$

$$c_{11}^0 = \lambda + 2\mu \tag{4}$$

$$c_{12}^0 = \lambda \tag{5}$$

$$c_{44}^0 = \lambda., \tag{6}$$

where c_{ij} is the Voigt expression of the sixth-order matrix of c_{ijkl}. Assuming that the rock matrix is an isotropic medium, as discussed in section Rock Skeleton Model, the complete sixth-order expression of the rock matrix (c_0) is as follows:

$$c_0 = \begin{bmatrix} c_{11}^0 & c_{12}^0 & c_{12}^0 & 0 & 0 & 0 \\ c_{12}^0 & c_{11}^0 & c_{12}^0 & 0 & 0 & 0 \\ c_{12}^0 & c_{12}^0 & c_{11}^0 & 0 & 0 & 0 \\ 0 & 0 & 0 & c_{44}^0 & 0 & 0 \\ 0 & 0 & 0 & 0 & c_{44}^0 & 0 \\ 0 & 0 & 0 & 0 & 0 & c_{44}^0 \end{bmatrix}. \tag{7}$$

Rock Skeleton Model

Based on the constant matrix as above in which the matrix lithology or mineral properties can be determined from lab or log data, the Hudson model is used to introduce the effects of cracks into the matrix parameters, which is expressed as:

$$c_{ij}{}^{dry} = c_{ij}^0 + c_{ij}^1 + c_{ij}^2, \tag{8}$$

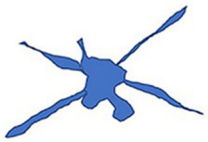

Fractured-cave/vug — Strong anisotropy, the highest yield

Caves and vugs — Medium anisotropy and high yield when the caves are connected

Interparticle pore — Weak anisotropy and large scale may have good yield

FIGURE 1 | Schematic diagram of the three investigated pore types.

where c_{ij}^0 is the isotropic background modulus obtained in the previous step, c_{ij}^1 is the first-order fracture influence factor, and c_{ij}^2 is the second-order fracture influence factor that reflects the interaction between fractures. According to the model of Hudson (1980, 1981), we obtain the following.

$$c_{11}^1 = -\frac{\lambda^2}{\mu}\varepsilon U_3 \tag{9}$$

$$c_{13}^1 = -\frac{\lambda(\lambda+2\mu)}{\mu}\varepsilon U_3 \tag{10}$$

$$c_{33}^1 = -\frac{(\lambda+2\mu)^2}{\mu}\varepsilon U_3 \tag{11}$$

$$c_{44}^1 = -\mu\varepsilon U_1 \tag{12}$$

$$c_{66}^1 = 0 \tag{13}$$

$$c_{11}^2 = \frac{q}{15}\frac{\lambda^2}{(\lambda+2\mu)}(\varepsilon U_3)^2 \tag{14}$$

$$c_{13}^2 = \frac{q}{15}\lambda(\varepsilon U_3)^2 \tag{15}$$

$$c_{33}^2 = \frac{q}{15}(\lambda+2\mu)(\varepsilon U_3)^2 \tag{16}$$

$$c_{44}^2 = \frac{2}{15}\frac{\mu(3\lambda+8\mu)}{\lambda+2\mu}(\varepsilon U_1)^2 \tag{17}$$

$$c_{66}^2 = 0, \tag{18}$$

where

$$\varepsilon = \frac{N}{V}a^3 = \frac{3\phi}{4\pi\alpha} = \text{crack density} \tag{19}$$

$$q = 15\frac{\lambda^2}{\mu^2} + 28\frac{\lambda}{\mu} + 28. \tag{20}$$

Here, a is the crack aspect ratio.

U_1 and U_3 represent the functions reflecting the conditions imposed on the crack surface such as dry or fluid-filled (Hudson, 1980, 1981). For a dry rock,

$$U_1 = \frac{16(\lambda+2\mu)}{3(3\lambda+4\mu)},\ U_3 = \frac{4(\lambda+2\mu)}{3(\lambda+\mu)}. \tag{21}$$

Pores are not filled with fluid in this step.

Hydrodynamic Effect

After the rock skeleton model is built, the Brown–Korringa formula is used to calculate the fluid effect in the rock skeleton as follows (Gassmann, 1951; Brown and Korringa, 1975).

$${S_{ijkl}}^m = \frac{1}{{C_{ijkl}}^m} \tag{22}$$

$$S_{ijkl}^{dry} - S_{ijkl}^{eff} = \frac{\left(S_{ij\alpha\alpha}^{dry} - S_{ij\alpha\alpha}^0\right)\left(S_{kl\alpha\alpha}^{dry} - S_{kl\alpha\alpha}^0\right)}{\left(S_{\alpha\alpha\beta\beta}^{dry} - S_{\alpha\alpha\beta\beta}^0\right) + (\beta_{fl} - \beta_0)\phi} \tag{23}$$

$$\beta_{fl} = \frac{1}{K_f} = \frac{1}{\left(c_{11}^f + \frac{2}{3}c_{44}^f\right)} \tag{24}$$

$$\beta_0 = S_{\alpha\alpha\beta\beta}^0 = \frac{1}{K_0} = \frac{1}{\left(c_{11}^0 + \frac{2}{3}c_{44}^0\right)} \tag{25}$$

$${C_{ijkl}}^{eff} = \frac{1}{{S_{ijkl}}^{eff}}, \tag{26}$$

where the superscript m in ${C_{ijkl}}^m$ represents either dry rock or fluid, and the fluid elastic parameters can be calculated by repeating the first step using the linear combination formula.

Anisotropic Parameter

Thomsen (1986) proposed the following notation for a weakly anisotropic transversely isotropic (TI) medium. His parameters use *Vp* and *Vs* propagating along the symmetry axis of the TI medium, in addition to three other constants as follows:

$$\alpha = \sqrt{\frac{{c_{33}}^{eff}}{\rho}} \tag{27}$$

$$\beta = \sqrt{\frac{{c_{44}}^{eff}}{\rho}} \tag{28}$$

$$\varepsilon = \frac{{c_{11}}^{eff} - {c_{33}}^{eff}}{2{c_{33}}^{eff}} \tag{29}$$

$$\gamma = \frac{{c_{66}}^{eff} - {c_{44}}^{eff}}{2{c_{44}}^{eff}} \tag{30}$$

$$\delta = \frac{\left({c_{13}}^{eff} + {c_{44}}^{eff}\right)^2 - \left({c_{33}}^{eff} - {c_{44}}^{eff}\right)^2}{2{c_{33}}^{eff}\left({c_{33}}^{eff} - {c_{44}}^{eff}\right)} \tag{31}$$

TABLE 1 | Qualitative model parameters.

Layer	Characteristic	Qualitative model parameters	Rock model results
Shale layer (thickness = 150 m)		Porosity: 0.1, Shale content: 80%, with given *Vp, Vs*	*vp* = 4086.8 m/s, Density = 2.57 g/cm^3, *Vs* = 2120.1 m/s
Upper layer (thickness = 100 m)		Porosity: 0.1, Shale content: 5%, with given *Vp*, *Vs*	*vp* = 6547.9 m/s, Density = 2.77 g/cm^3, *Vs* = 3999.4 m/s
Mid-layer	Strong anisotropy (thickness = 150 m)	Porosity 0.1, Shale 20%, Gas 100%,Water 0%, Crack aspect ratio 0.3	*vp* = 4487 m/s, Density = 2.56 g/cm^3, *Vs* = 3215 m/s, δ = 0.53, ε = 0.4108, γ = 0.1101
	Mid-anisotropy (thickness = 150 m)	Porosity 0.08, Shale content 15%, Gas 50%, Water 50%, Crack aspect ratio 0.5	*vp* = 5620.6 m/s, Density = 2.65 g/cm^3, *Vs* = 3520.6 m/s, δ = 0.13, ε = 0.1291, γ = 0.0478
	Weak anisotropy (thickness = 150 m)	porosity 0.06, Shale content 10%, Gas 0%, Water 100%, Crack aspect ratio 0.7	*vp* = 6167.9 m/s, Density = 2.74 g/cm^3, *Vs* = 3760.2 m/s, δ = 0.0555, ε = 0.059, γ = 0.0248
Low layer (thickness = 150 m)		Porosity: 0.1, Shale content: 5%, with given *Vp*, *Vs*	*vp* = 6547.9 m/s, Density = 2.77 g/cm^3, *Vs* = 3999.4 m/s

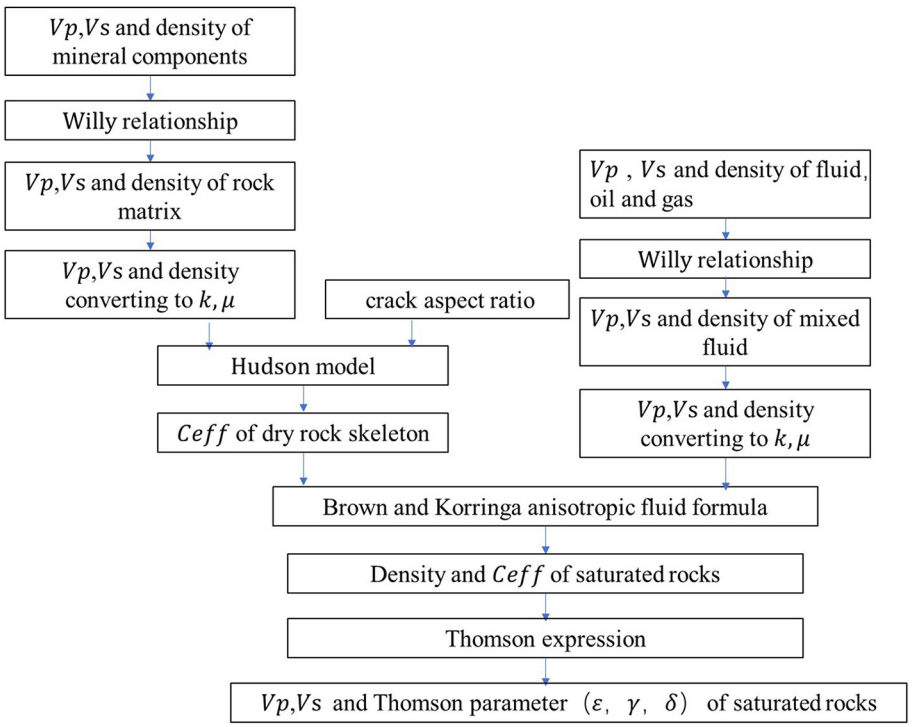

FIGURE 2 | Model building process.

where

$$\varepsilon = \frac{V_P(90^\circ) - V_P(0^\circ)}{V_P(0^\circ)} = \text{Compressional wave anisotropy} \quad (32)$$

$$\gamma = \frac{V_{SH}(90^\circ) - V_{SH}(0^\circ)}{V_{SH}(0^\circ)} = \text{Shear wave anisotropy.} \quad (33)$$

According to these parameters, the three-phase velocity can be conveniently approximated as:

$$V_{SV}(\theta) \approx \beta\left[1+\frac{\alpha^2}{\beta^2}(\varepsilon-\delta)\sin^2\theta\cos^2\theta\right] \quad (34)$$

$$V_{SH}(\theta) \approx \beta\left(1+\gamma\sin^2\theta\right) \quad (35)$$

$$V_P(\theta) \approx \alpha\left(1+\delta\cos^2\theta\sin^2\theta+\varepsilon\,\theta\right). \quad (36)$$

QUALITATIVE MODEL

In the Moxi area, the sealing caprock is a shale with a thickness of ∼150 m. Below this reservoir is a tight dolomite with an approximate thickness of 100 m. A reservoir with various pore types of ∼150 m thickness occurs immediately below the tight dolomite, followed by another 150 m of tight reservoir. Three models are therefore designed with four layers: the top layer is a 150-m-thick shale to represent the caprock; the second layer (upper reservoir) is designed as a 100-m-thick tight carbonate rock; the third layer (middle reservoir) is designed to represent the 150-m-thick reservoir; and the bottom or fourth layer is a

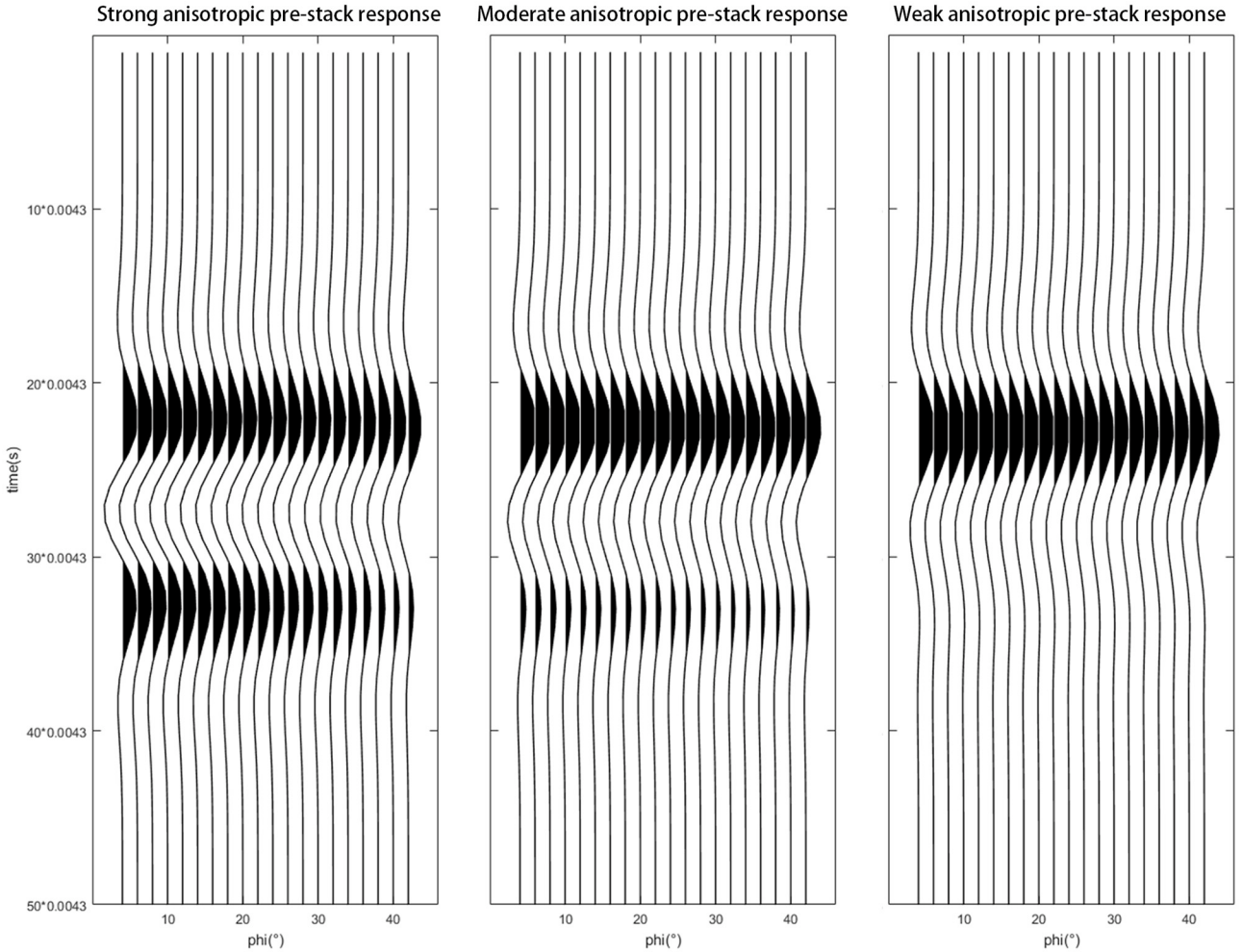

FIGURE 3 | Qualitative model pre-stack response.

150-m-thick tight carbonate. The three models are assigned for the reservoir zone with strong anisotropy for fractured caves, moderate anisotropy for vuggy pores/caves, and weak anisotropy for interparticle pores.

The aspect ratio of the intergranular pores of minerals mainly depends on the mineral petrophysical properties (Pellerin et al., 2015; Henriques et al., 2018; Wang and Zhang, 2019; Falahat and Farrokhnia, 2020). Carbonate rocks dominate the study area with a small amount of siliceous rocks and mudstones. The aspect ratio of the intergranular pores is therefore ∼0.8. The intergranular pores tend to be flat under the effect of the overburden pressure, and the aspect ratio is relatively reduced. The interparticle pore aspect ratio of the formation medium is therefore set to 0.7.

Core and imaging log analyses revealed that the target layer mainly developed caves elongated by underground tectonic movement and dissolution. Most of these caves are distributed in layers or along cracks and fractures. The two-dimensional form is an irregular polygon, and the three-dimensional form is a flat ellipsoid and strip. The cave aspect ratio is set to 0.5.

Most of the fracture openings are not wider than 0.3 mm in areas far from the fault (Xu et al., 2019), with fracture lengths on the order of meters. The aspect ratio of the cracks is therefore substantially smaller than that of the pores and caves. The fractures that connect the caves, which can be on the cm-scale, are more elongated than the caves. We estimate an equivalent pore aspect ratio of 0.3 because the fractures may connect several caves.

The background information of the work area is used to obtain reasonable input for the theoretical model of these three models. The Hudson input parameters for the theoretical model are tuned by matching the typical zone average acoustic properties. The lithological parameters of each layer of each model are given in **Table 1**. The Hudson modeling process is used to obtain the velocity and Thomsen anisotropy parameters of each layer of the three models (**Table 1**) using the designed model parameters.

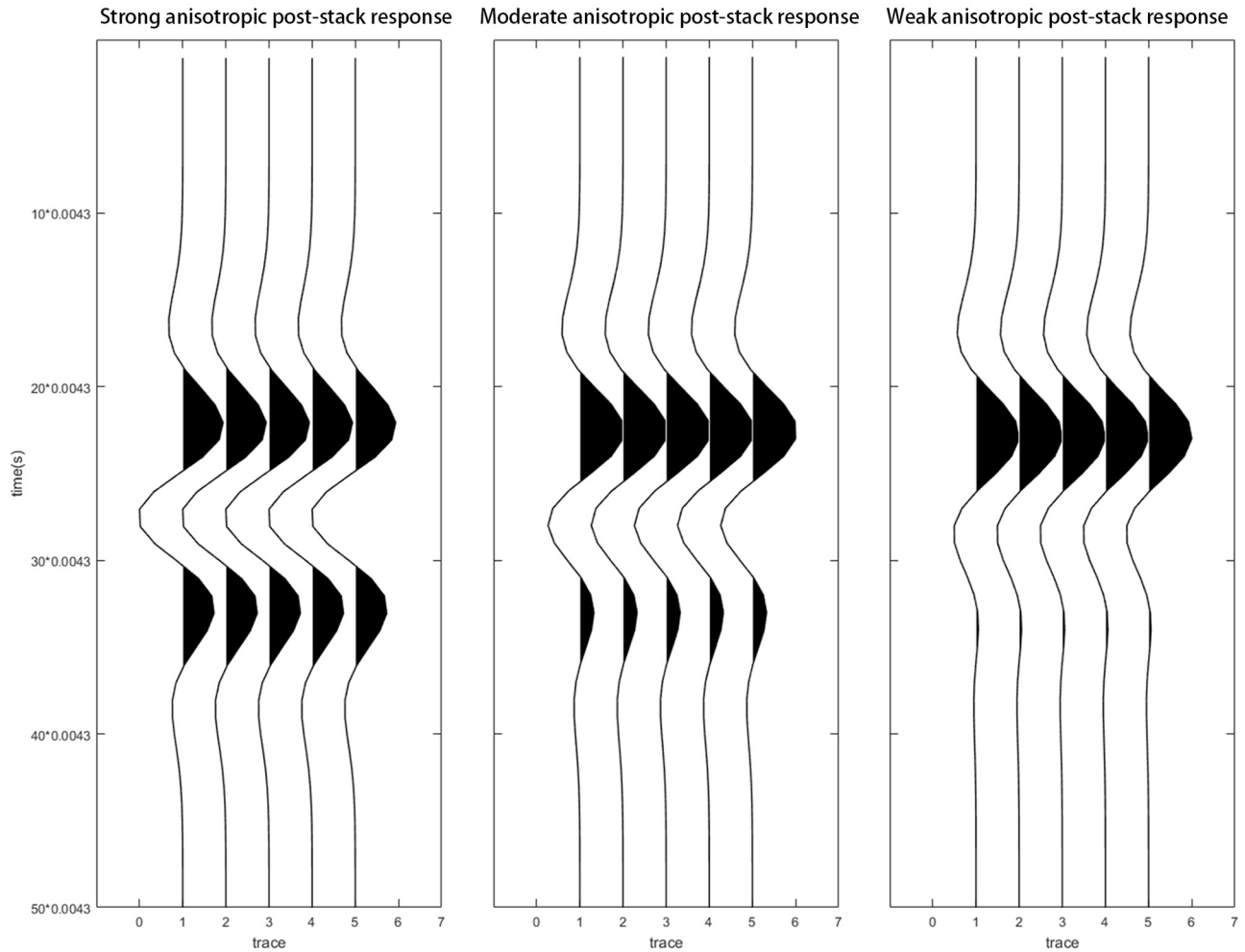

FIGURE 4 | Qualitative model post-stack response.

Table 1 shows that the anisotropic parameters (e.g., δ, ε, γ) follow the designed trend. The models, therefore, represent the three types of pore systems. However, it is quite challenging to understand the anisotropic properties under the geological settings because of the poor azimuthal quality of the seismic data in the study area (Yuan et al., 2020).

TABLE 2 | Open flow gas rate of wells with different pore structures.

Well	Pore type	Gas open flow rate (10^4 m^3/day)
MX22	Fractured-cave/vug	217.58
MX108	Fractured-cave/vug	62.5
MX52	Caves and vugs	/
MX105	Caves and vugs	45.51
MX111	Caves and vugs	58.62
MX103	Interparticle pore	33.95

SEISMIC MODELING

The pre-stack angle gathers are forward modeled based on the designed models (Pang and Stovas, 2020; Yuan et al., 2020) and then further stacked to simulate the post-stack data (Zoeppritz and Erdbebenwellen, 1919). Most of the caves and vuggy pores are compressed as oriented coin shapes owing to the deepness of the reservoir. With the *Vp*, *Vs*, and Thomsen anisotropy parameters obtained from the rock physics model, the Rüger equation (Rüger, 1997, 1998) is used to obtain the reflection coefficient of each interface at different incident angles (0°-40°).

$$R_p^{VTI}(\theta) = \frac{1}{2}\frac{\Delta Z}{\overline{Z}} + \frac{1}{2}\left[\frac{\Delta V_{p0}}{\overline{V_{p0}}} - \left(\frac{2\overline{V_{s0}}}{\overline{V_{p0}}}\right)^2 \frac{\Delta G}{\overline{G}} + \Delta\sigma\right]\sin\theta^2 + \frac{1}{2}\left(\frac{\Delta V_{p0}}{\overline{V_{p0}}} + \Delta\varepsilon\right)\sin\theta^2\tan\theta^2, \quad (37)$$

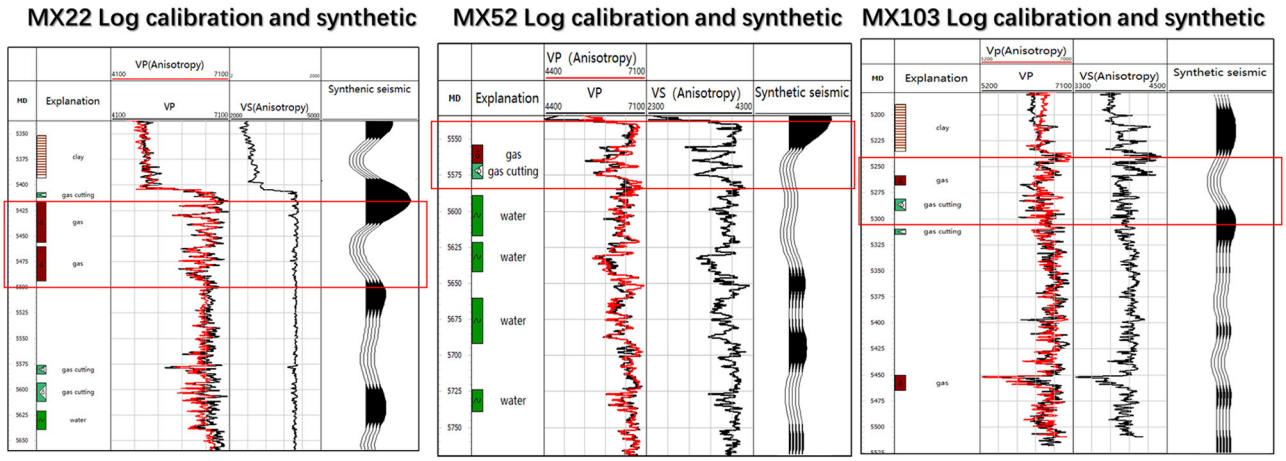

FIGURE 5 | Log calibration and synthetic seismic data.

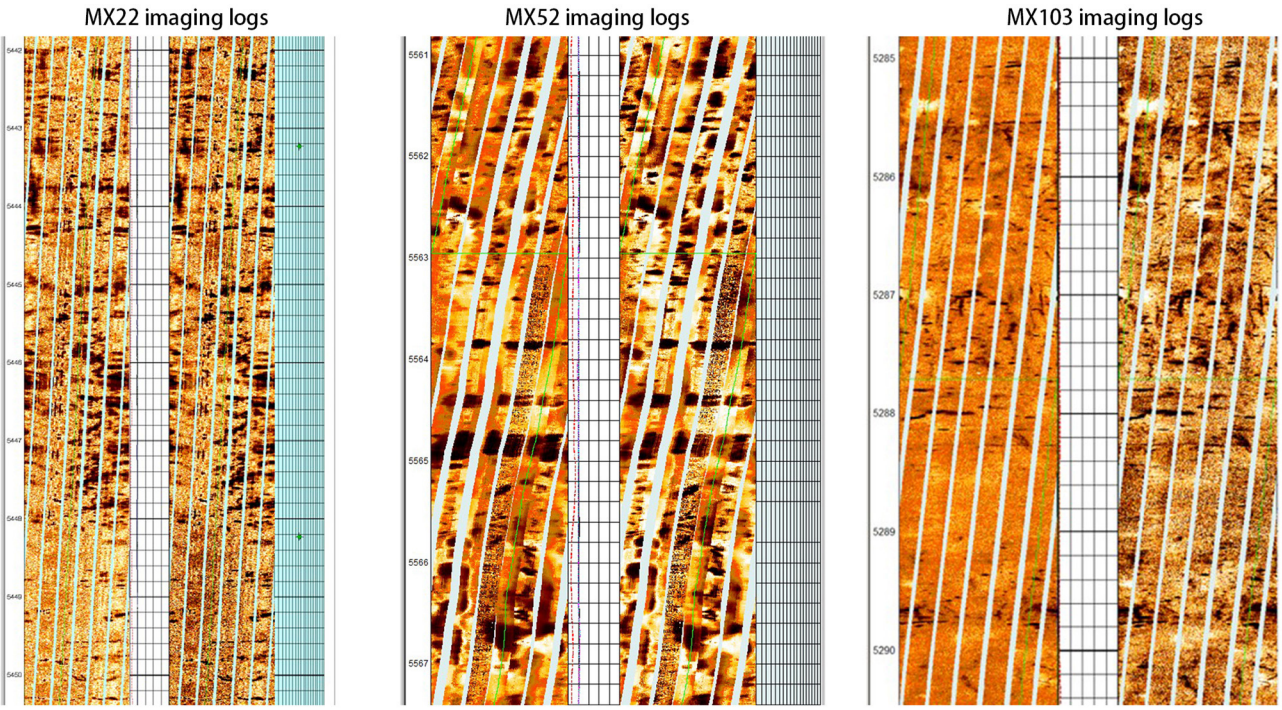

FIGURE 6 | Imaging logs.

where θ represents the incident angle, $Z = \rho V_{p0}$ is the vertical compressional wave impedance, and $G = \rho {V_{s0}}^2$ is the vertical shear modulus. The "—" and "Δ" symbols represent the "average of" and "difference between" the upper and lower layer parameters, respectively.

The seismic data have a dominant frequency around 30–40 Hz. A zero-phase wavelet with a 30-Hz frequency is therefore designed for the modeling. The convolution for each angle is applied and the pre-stack angle gathers are then stacked to form a single trace. **Figure 3** illustrates the pre-stack angle gathers. **Figure 4** shows the full stack traces that have been duplicated five times. The pre-stack gathers show that the strong anisotropic model has strong reflectors on the top and bottom of the reservoir. The mid-anisotropic model shows a strong top reflector, but a relatively weaker bottom reflector. The weak anisotropic model shows the weakest lower reflector. The full stack traces have a similar

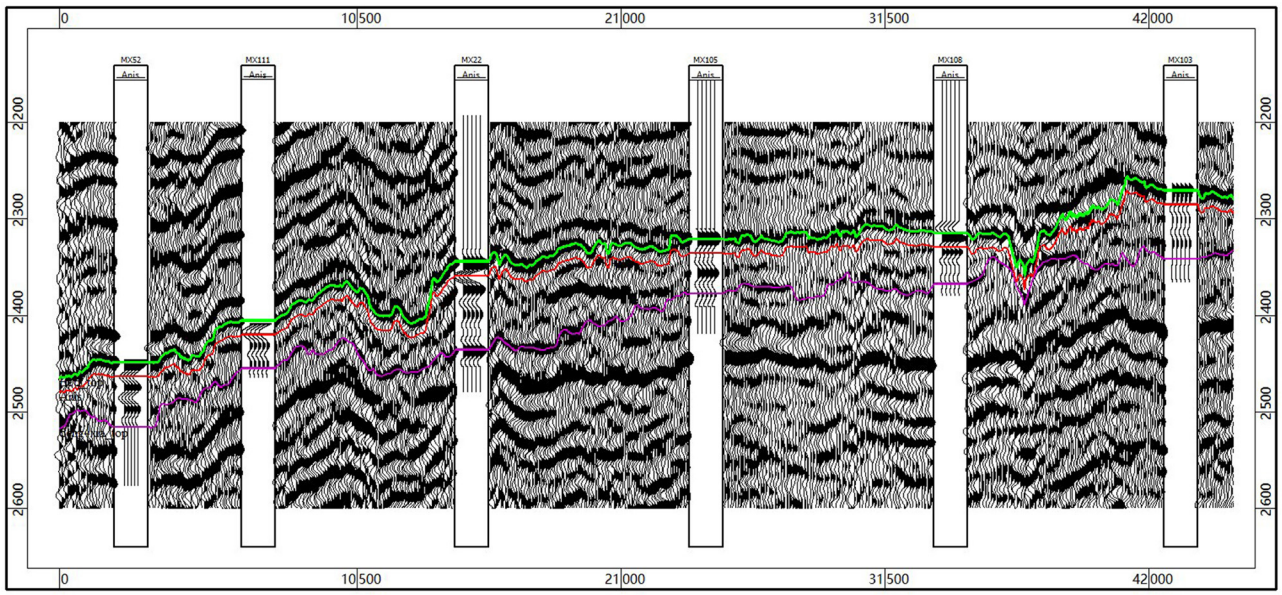

FIGURE 7 | Cross-well seismic section.

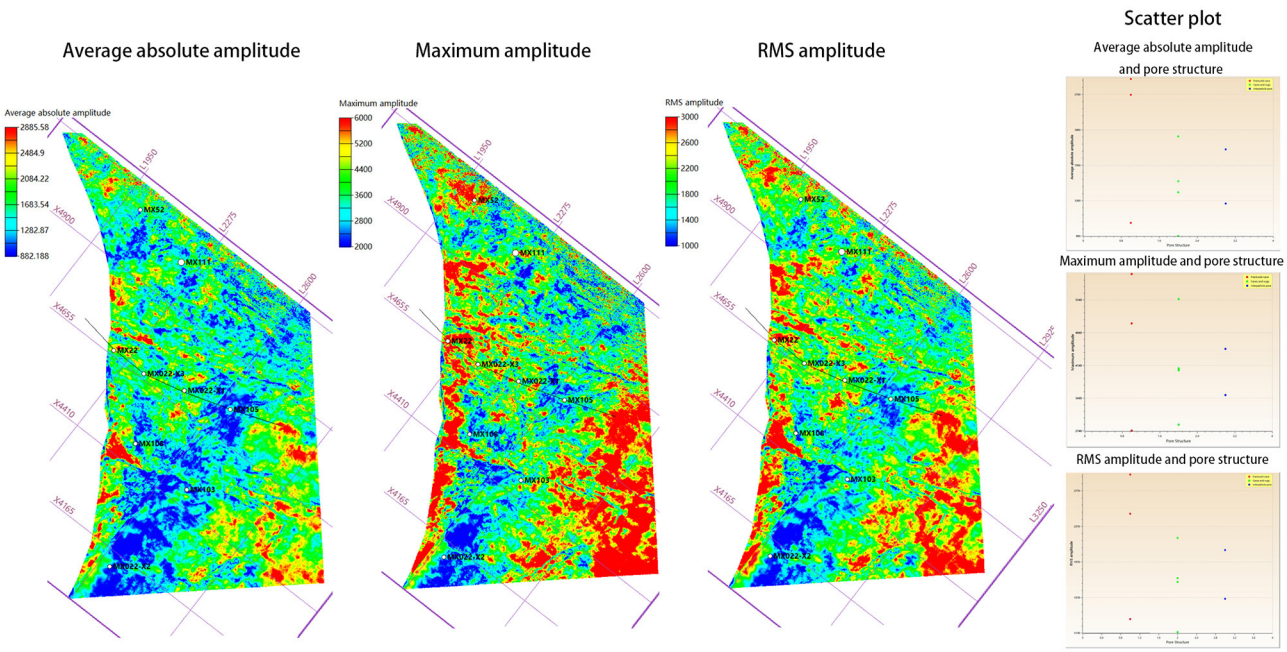

FIGURE 8 | Conventional seismic attribute (average absolute amplitude, RMS amplitude, and maximum amplitude) profiles and their relationship with the pore structures.

signature to that of the pre-stack. All of the results show a certain degree of asymmetry between the peak and trough amplitudes, which indicates that these characteristics have the potential to detect pore types but must be verified using local log data.

LOG CALIBRATION

Data from five wells in the study area are used to verify the observed theoretical model results. The resistivity scan image log is first used to determine the formation pore type (**Table 2**).

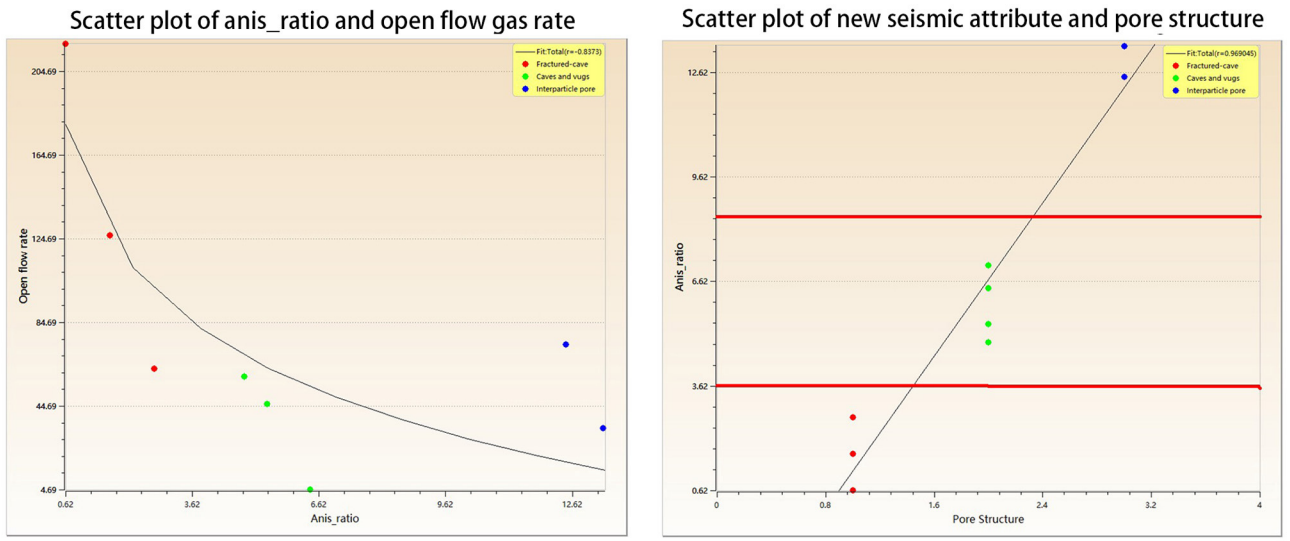

FIGURE 9 | Correlation plot of the anisotropy ratio (anis_ratio) and pore structure and open flow gas rate.

Certain model input parameters, including porosity, shale content, gas saturation, and water saturation, are obtained from the interpretation of the log data, and the others are obtained from the common mineral physical parameters. According to the pore type determined by the resistivity scan image log data, the aspect ratio setting of each confirmed pore type is similar to that of the theoretical model setting.

Figure 5 compares the log (black) and synthetic log (red) results from the Hudson model. The synthetic seismograms are formed based on the log data, using the same process as in the theoretical model.

As shown in **Figure 5**, the log and geology indicate that the red block zone in well MX22 is dominated by a fractured vuggy pore/cave type structure, the red block zone in well MX52 is dominated by a vuggy or cave type pore structure, and the well MX103 zone marked by a red line is dominated by an interparticle pore type. These findings are also verified from the image logs (**Figure 6**), and the anisotropic parameters (δ, ε, and γ) also match the logs after tuning the pore type geometry parameters, such as aspect ratio, according to the image log estimation.

The synthetic seismic data from the well MX22 log shows a strong peak and trough, consistent with the theoretical model for the fractured vuggy pores/cave zone. The well MX52 log shows relatively strong peaks and troughs for the vuggy pore and cave zones, whereas the well MX103 log has weak reflection energy. A cross-well seismic line with synthetic seismograms in the wells is shown in **Figure 7**. The synthetic seismic matches well with the observed seismic, which implies that the pore types are detectable from the latter. From the cross-well seismic line, it can be seen that the observed seismic data also show a clear pattern that is visible in the theoretical model and well-synthetic data.

SEISMIC ATTRIBUTE RELATIONSHIP WITH PORE TYPES AND OPEN FLOW GAS RATE

The theoretical model and log synthetic modeling highlight the possibility to extract the post-stack seismic signature for pore types, which can be used to semiquantitatively predict gas rates. A promising pore type identification strategy involves the correlation of certain attributes with pore types (Chen et al., 2005). The fractured vuggy pore and cave type pore structure is generally associated with the highest gas rates because the fractures can serve as connective channels to vuggy pores and caves. The vuggy pore/cave type pore structure is associated with moderate gas rates because it has relatively high pore sizes. The interparticle pore type structure can connect adjacent caves, but the connectivity is weaker. The interparticle pore type is normally associated with the lowest productivity because of its low pore space and weak pore connectivity. In the study area, the top horizon is identified from the peak amplitude. To spatially map the productivity, the attributes are extracted from the seismic horizon and correlated with pore type number and open flow gas rate. Twenty-four attributes are extracted from the seismic data using the conventional attribute analysis. **Figure 8** shows the correlations between the average absolute amplitude, maximum amplitude, and root mean square (RMS) amplitude with pore type. All other attributes show a similar poor correlation. Traditional attributes are considered to mainly capture values related to the amplitude, phase, and frequency. However, although certain shape information can be obtained, the anisotropic setting and geology are not strictly considered in our case and the traditional attributes cannot be used to differentiate the pore types.

To classify the patterns observed in the theoretical and log synthetic models, the top horizon, which reflects the boundary between the caprock shale and carbonate, is moved 15 ms

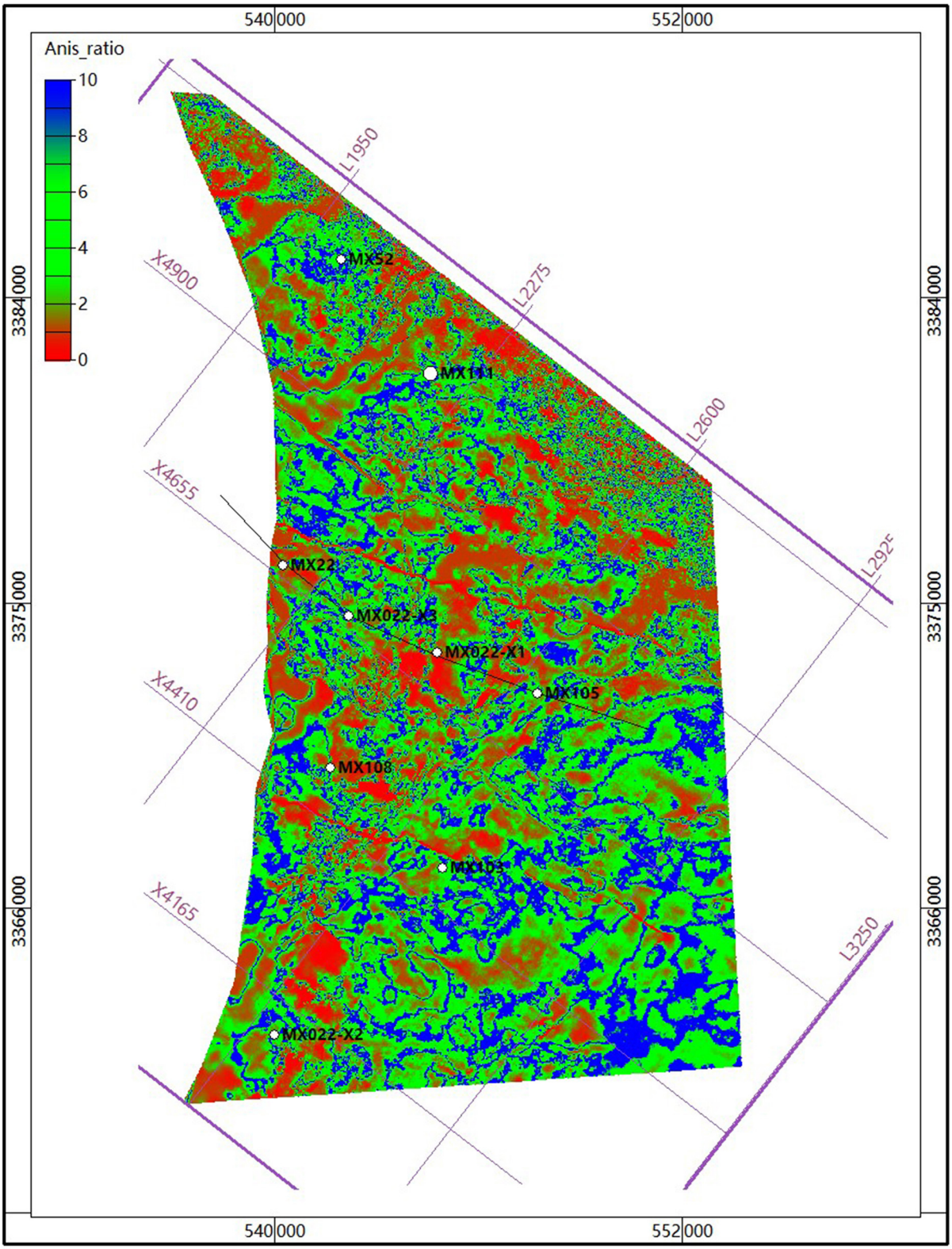

FIGURE 10 | New seismic attribute extracted in the study area.

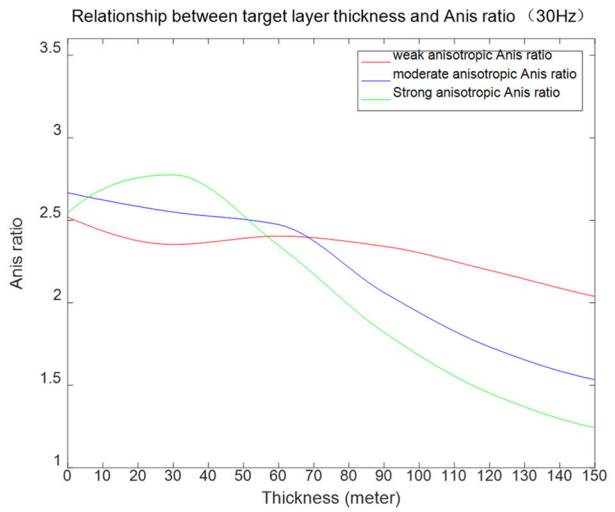

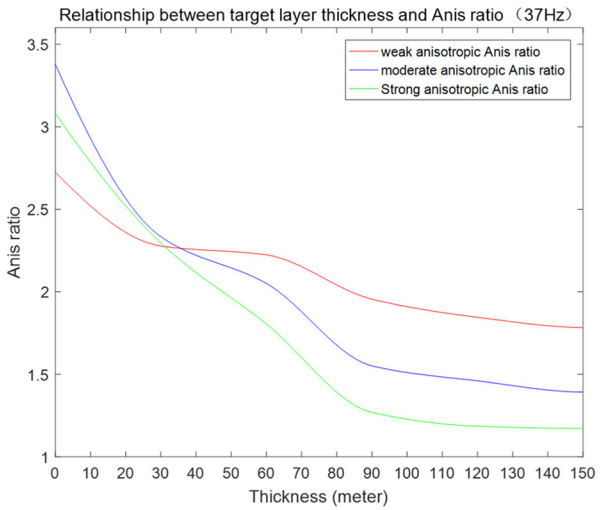

FIGURE 11 | Reflection coefficient of the qualitative model.

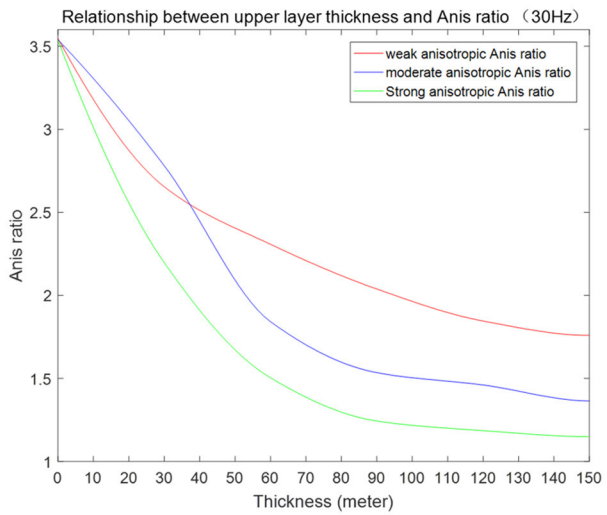

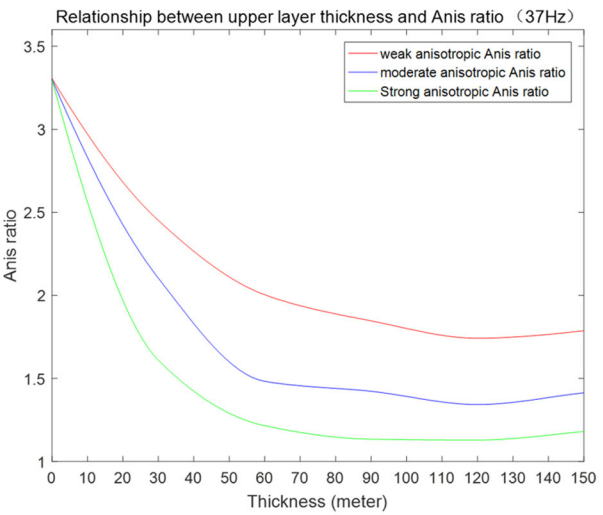

FIGURE 12 | Adjusted model seismic response.

downward and then snapped to the trough minimum. To obtain a single attribute for representing the pore type map, the peak and trough amplitudes are extracted along the top and closest lower horizons, respectively. The procedure for the new attribute is as follows:

(1) Select the amplitude peak as the top horizon and snap to the maximum value (AMPmax).
(2) Move the horizon to the closest trough and snap to the minimum value (AMPmin).
(3) Calculate the asymmetry ratio of the peak and trough:

$$Anis_{ratio} = \frac{|AMPmax|}{|AMPmin|}. \quad (38)$$

The attribute defines a certain degree of waveform asymmetry in the major porous zone with different anisotropies as described in the previous sections. As we discussed in "Discussion" section, even if the wavelet phase is changed, the relationship still holds under this geological setting. However, the magnitude is changed. The results indicate that the new attribute can differentiate between pore types by correlating with pore type number and exhibits a good correlation with the open flow gas rate. **Figure 9** shows the correlation between the new attribute with the three pore types and with open flow rate.

We define this ratio as the "anisotropic attribute," even though the high value corresponds to low anisotropy (i.e., strong anisotropy corresponds to a low value). The attribute can be mapped along the horizon, as shown in **Figure 10**.

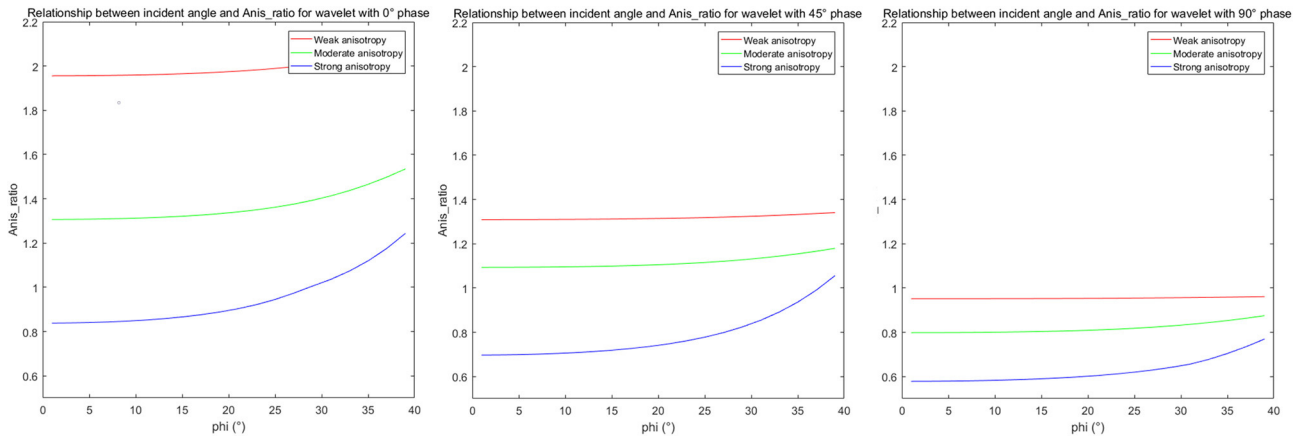

FIGURE 13 | Wavelet phase impact on anis_ratio.

The maps for pore type and gas rate are the same but with different scales because of their linear correlations with the anisotropic attribute. Red or yellow areas in **Figure 10** indicate the best zones for fractured vuggy pore/cave type pore structures, which are expected to represent the best gas open flow rates.

CONCLUSIONS

We developed and tested a theoretical model for guided seismic attribute analysis based on a Precambrian dolomite reservoir and obtained the following conclusions:

(1) The Hudson model can be used to characterize the anisotropic properties of the Precambrian carbonate fractured vuggy pores or caves. However, log calibration is important to obtain more representative model parameters.
(2) The theoretical model and log seismic forward modeling show that under the specific geological setting, the strong anisotropic zone corresponds to a strong peak and trough with lower asymmetry, whereas the weak anisotropic zone has a relatively lower trough with more asymmetry. The phase of wavelet does affect the magnitude of the attribute. Its relationship with pore types is still similar (see **Figure 13** and section "Discussion"). Therefore, we recommend to be aware with the wavelet phase if this attribute is applied.
(3) The newly proposed ratio of absolute peak and trough amplitude can be used to better differentiate pore types compared with the conventional attributes. This attribute can also be related to open flow gas rates. The ratio can be used identify the anisotropic properties possibly because the degree of anisotropy leads to different asymmetric wave shapes and amplitude strengths. However, we recommend performing a similar procedure as described here to validate the attribute effectiveness if applying this attribute in similar reservoirs.

DISCUSSION

The results of anisotropy-guided post-stack attribute analysis indicate an attribute that can be used to differentiate pore types and correlates well with the open flow gas rate. Although the model and log calibration support this application, the mechanism remains poorly understood and requires further discussion.

The amplitude is affected by many factors; thus, this phenomenon must be validated in a range of geological settings. The seismic frequency in this case ranges from 30 to 40 Hz with a central frequency around 37 Hz. The fractured or vuggy reservoir thickness varies from 0 to 150 m. **Figure 11** shows that the relationship between this attribute and the three pore types holds for 30 Hz above 60 m and for 37 Hz with thicknesses above 30 m. Furthermore, the top tight carbonate zone thickness also varies from 0 to 150 m. **Figure 12** illustrates the relationship between the new attribute and pore type for the tight zone variation. When the wavelet frequency in the tight zone is ∼30 Hz, the weak and moderate anisotropies can be reversed below 40 m, which may introduce uncertainties. However, for a wavelet with a frequency of 37 Hz, all of the thicknesses show a similar relationship. The reservoirs in the Moxi area are relatively thick, above 50 m for the porous zone, particularly in the bank inset reef area. Interpretations determined from this approach may, therefore, need to be reevaluated for thin reservoirs. Also, the wavelet phase may not be zero phase. **Figure 13** is a comparison of 0, 45, and 90° wavelets (mirror for 180, 135, and 90°). Due to that, we picked the top strong reflector in the interpretation (trough picking for 180° wavelet), and we could see that the relationships between the new attribute and pore types still hold. However, the magnitudes are changed. By rescaling the color bar, the spatial patterns are still the similar. Based on these modeling, we believe that the geological setting is thus a critical aspect of determining whether or not the post-stack signature relationship can be applied to differentiate pore types and gas productivity. Our recommendation is that the procedure detailed herein should be applied to obtain a reasonable interpretation, instead of directly applying this new attribute.

DATA AVAILABILITY STATEMENT

The data analyzed in this study is subject to the following licenses/restrictions: The data were owned by company, but results for publication can be shared. Requests to access these datasets should be directed to xrhuang@sunrisepst.com.

AUTHOR CONTRIBUTIONS

XH designed the procedure and new attribute and wrote the manuscript. YX developed the rock model and reviewed the manuscript. HL performed the log calibration and edited the manuscript. ZZ performed the attribute analysis. WX performed the seismic interpretation. All authors contributed to the article and approved the submitted version.

FUNDING

This research was funded by the China Natural Science Foundation (41874167), China Natural Science Foundation (u20b2016), and the Petro-China Southwest Exploration and Production Research Institute Project.

ACKNOWLEDGMENTS

The authors thank the Petro-China Southwest Exploration and Production Research Institute for permission to publish this work and financial support. The authors also thank the China Natural Science Foundation (41874167, u20b2016) for supporting this work. The authors are grateful to all those who supported this work and helped to improve this manuscript, particularly Allyson Gajraj of SunRise PetroSolutions Tech., Inc. They also thank Esther Posner, PhD, from Liwen Bianji, Edanz Editing China (www.liwenbianji.cn/ac), for editing the English text of a draft of this manuscript.

SUPPLEMENTARY MATERIAL

The Supplementary Material for this article can be found online at: https://www.frontiersin.org/articles/10.3389/feart.2021.641705/full#supplementary-material

REFERENCES

Abdlmutalib, A., Abdullatif, O., Abdelkarim, A., and Yousif, I. (2019). Factors influencing acoustic properties of carbonate rocks: examples from middle Jurassic carbonates, Central Saudi Arabia. *J. African Earth Sci.* 150, 767–782. doi: 10.1016/j.jafrearsci.2018.10.005

Brown, R., and Korringa, J. (1975). On the dependence of the elastic properties of a porous rock on the compressibility of the pore fluid. *Geophysics* 40, 608–616. doi: 10.1190/1.1440551

Chen, Z., Dai, Y., and Lang, Z. (2005). Reservoir permeability model and production characteristics of fractured carbonate reservoir. *Petrol. Explor.* 3, 101–105.

Falahat, R., and Farrokhnia, F. (2020). Rock physics modelling of the carbonate reservoirs: a log-based algorithm to determine the pore aspect ratio. *J. Appl. Geophys.* 173. doi: 10.1016/j.jappgeo.2019.103930. [Epub ahead of print].

Gassmann, F. (1951). Elastic waves through a packing of spheres. *Geophysics* 16, 673–685. doi: 10.1190/1.1437718

Henriques, J. P., de Figueiredo, J. J. S., Santos, L. K., Macedo, D. L., Coutinho, I., da Silva, C. B., et al. (2018). Experimental verification of effective anisotropic crack theories in variable crack aspect ratio medium. *Geophys. Prospect.* 166, 141–156. doi: 10.1111/1365-2478.12544

Hill, R. (1952). The elastic behavior of crystalline aggregate. *Proc. Phys. Soc. London A* 65, 349–354. doi: 10.1088/0370-1298/65/5/307

Hudson, J. A. (1980). Overall properties of a cracked solid. *Proc. Camb. Philol. Soc.* 88, 371–384. doi: 10.1017/S0305004100057674

Hudson, J. A. (1981). Wave speeds and attenuation of elastic waves in material containing cracks. *Geophys. J. R. Astronomical Soc.* 64, 133–150. doi: 10.1111/j.1365-246X.1981.tb02662.x

Hudson, J. A. (1986). A higher order approximation to the wave propagation constants for a cracked solid. *Geophys. J. R. Astronomical Soc.* 87, 265–274. doi: 10.1111/j.1365-246X.1986.tb04556.x

Kittridge, M. G. (2015). Investigating the influence of mineralogy and pore shape on the velocity of carbonate rocks: insights from extant global data sets. *Interpretation* 3, SA15–SA31. doi: 10.1190/INT-2014-0054.1

Li, Y., Wu, F., Liu, D., Peng, Y., Chen, S., Deng, X., et al. (2014). Distribution rule and exploration prospect of the Longwangmiao Fm reservoirs in the Leshan-Longnüsi Paleouplift: Sichuan Basin. *Natural Gas Industry* 34, 61–66. doi: 10.1016/j.ngib.2014.10.009

Li, Z., Jiang, H., Wang, Z., Wang, T., Lu, W., and Lü, Z. (2014). Control of tectonic movement on hydrocarbon accumulation in the Sinian strata: Sichuan Basin. *Natural Gas Industry* 34, 23–30.

Liao, Q., Hu, H., Lin, J., Liu, Z., and Mu, X. (2011). Petroleum exploration prospect of the Jurassic tight reservoirs in central Sichuan Basin. *Oil Gas Geol.* 32, 815–822,838.

Pang, S., and Stovas, A. (2020). Frequency-dependent PP and PS reflection coefficients in fractured media. *Geophys. Prospect.* 68, 926–940. doi: 10.1111/1365-2478.12880

Payne, S., Wild, P., and Lubbe, R. (2010). "An integrated solution to rock physics modelling in fractured carbonate reservoirs," *SEG Technical Program Expanded Abstracts 2010*, (Denver, CO). doi: 10.1190/1.3513596

Pellerin, M., Fournier, F., Leonide, P., Borgomano, J., and Hairabian, A. (2015). "Deciphering pore-type signatures from acoustic data in carbonates: equivalent pore aspect ratio approach," in *14th International Congress of the Brazilian Geophysical Society & EXPOGEF*, (Rio De Janeiro). doi: 10.1190/sbgf2015-167

Peng, D., and Xiao, F. (2017). "An estimation method of hole-vug-fracture parameters and its sensitivity to elastic properties for carbonate reservoirs based on anisotropic rock physics models," *SEG 2017 Workshop: Carbonate Reservoir E&P Workshop*, (Chengdu). doi: 10.1190/carbonate2017-28

Rüger, A. (1997). P-wave reflection coefficients for transversely isotropic media with vertical and horizontal axis of symmetry. *Geophysics* 62, 713–722. doi: 10.1190/1.1444181

Rüger, A. (1998). Variation of P-wave reflectivity with offset and azimuth in anisotropic media. *Geophysics* 63, 935–947 doi: 10.1190/1.1444405

Sain, R., Chen, G., Payne, A. M., Xu, S., and Sultan, A. A. (2008). "Carbonate rock physics: geophysical and petrophysical pore types of carbonate rocks from an offshore carbonate field," in *2008 SEG Technical Program Expanded*, (Las Vegas, NV) doi: 10.1190/1.3059226

Shiri, S., and Falahat, R. (2020). Rock physics modeling and 4D seismic feasibility study in one of the Iranian carbonate reservoirs. *J. Appl. Geophys.* 172. doi: 10.1016/j.jappgeo.2019.103855

Shirmohamadi, M., Kadkhodaie, A., Rahimpour-Bonab, H., and Faraji, M. A. (2017). Seismic velocity deviation log: an effective method for evaluating spatial distribution of reservoir pore types. *J. Appl. Geophys.* 139, 223–238. doi: 10.1016/j.jappgeo.2017.03.001

Simon, S. P., Philip, W. and Rudi, L. (2010). *An Integrated Solution to Rock Physics Modelling in Fractured Carbonate Reservoirs.* SEG Technical Program Expanded Abstracts 2010.

Thomsen, L. (1986). Weak elastic anisotropy. *Geophysics* 51, 1954–1966. doi: 10.1190/1.1442051

Wang, H., and Zhang, J. (2019). The effect of various lengths of pores and throats on the formation resistivity factor. *J. Appl. Geophys.* 162, 35–46. doi: 10.1016/j.jappgeo.2019.01.005

Wyllie, M. R. J., Gregory, A. R., and Gardner, L. W. (1956). Elastic wave velocities in heterogeneous and porous media. *Geophysics* 21, 41–70. doi: 10.1190/1.1438217

Xu, K., Dai, J., Feng, J., and Ren, Q. (2019). The control effect of faults on fracture distribution in Moxi-Gaoshiti block. *J. Southwest Petrol. Univ.* 41, 10–22.

Yuan, S., Wang, J., Liu, T., Xie, T., and Wang, S. (2020). 6D phase-difference attributes for wide-azimuth seismic data interpretation. *Geophysics* 85, IM37–IM49. doi: 10.1190/geo2019-0431.1

Zoeppritz, K., and Erdbebenwellen, V. I. I. I. B. (1919). On the reflection and propagation of seismic wave. *Gottinger Nachrichten* 1, 66–84.

Conflict of Interest: WX was employed by the company PetroChina.

The remaining authors declare that the research was conducted in the absence of any commercial or financial relationships that could be construed as a potential conflict of interest.

Copyright © 2021 Huang, Xu, Li, Zhang and Xu. This is an open-access article distributed under the terms of the Creative Commons Attribution License (CC BY). The use, distribution or reproduction in other forums is permitted, provided the original author(s) and the copyright owner(s) are credited and that the original publication in this journal is cited, in accordance with accepted academic practice. No use, distribution or reproduction is permitted which does not comply with these terms.

frontiers in Earth Science

ORIGINAL RESEARCH
published: 22 April 2021
doi: 10.3389/feart.2021.633930

Rock Physical Model and AVO Patterns for the Mud-Rich Source Rock

Songhe Yu[1,2], *Zhaoyun Zong*[1,2]* *and Xingyao Yin*[1,2]

[1] School of Geosciences, China University of Petroleum (East China), Qingdao, China, [2] Laboratory for Marine Mineral Resources, Qingdao National Laboratory for Marine Science and Technology, Qingdao, China

Rock physical model and amplitude variation with offset (AVO) patterns considering the content of organic matter and the composition of minerals have a wider significance for guiding the identification and prediction of the mud-rich source rock. A rock physical model is proposed for describing the elastic properties of kerogen in different maturity stages. The proposed rock physical model builds an intrinsic connection between the elastic properties and physical parameters of the mud-rich source rock, thereby providing a theoretical basis for a seismic inversion and a seismic forward modeling. To overcome the limitations of laboratory measurement, a combination-four-parameter regression (CFPR) method is further proposed to estimate the continuous total organic carbon (TOC) values for the verification and analysis of the rock physical model. The modeling results reveal that the P-wave velocity and P-wave impedance will decrease with an increase in TOC, and the Poisson ratio and Poisson impedance will increase as the mud content increases, which are consistent with the conclusions of the cross plot using the actual well data. Based on the proposed rock physical model, the seismic responses of the mud-rich source rock are further modeled. The synthetic seismic records are consistent with the well-side seismic records, the top reflection of the mud-rich source rock behaves as a stronger negative event dimming with an incident angle corresponding to a class IV AVO pattern, and the bottom reflection exhibits a class I AVO anomaly. In addition, a two-layer model is constructed to analyze an effect of the TOC content and mud content on the AVO characteristics. The results indicate that increasing the TOC content and mud content will significantly increase the interceptions and slightly change the gradients of the P-P reflection coefficients. These results help to guide the identification and evaluation of the mud-rich source rock.

Keywords: rock physical model, AVO pattern, mud-rich source rock, TOC, mud content

OPEN ACCESS

Edited by:
Jing Ba,
Hohai University, China

Reviewed by:
Chenghao Cao,
Nanjing Tech University, China
Ding Wang,
Shaoxing University, China

***Correspondence:**
Zhaoyun Zong
zhaoyunzong@yahoo.com

Specialty section:
This article was submitted to Solid Earth Geophysics, a section of the journal Frontiers in Earth Science

Received: *26 November 2020*
Accepted: *18 March 2021*
Published: *22 April 2021*

Citation:
Yu S, Zong Z and Yin X (2021) Rock Physical Model and AVO Patterns for the Mud-Rich Source Rock. Front. Earth Sci. 9:633930. doi: 10.3389/feart.2021.633930

INTRODUCTION

Given the importance of the spatial distribution of source rocks and the abundance of organic matter in source rocks on the prospect of petroleum plays, a plenty of methods are discussed to predict and determine source rocks by using the seismic data in the literature. Løseth et al. (2011) described and explained the seismic section characteristics of source rocks based on the relationship between the total organic carbon (TOC) content and acoustic impedance, and the spatial distribution of source rocks could be identified by the seismic data only.

Carcione (2001) analyzed the amplitude variation with offset (AVO) effects caused by kerogen in source rocks, and verified the ability and applicability of determining the TOC content in the source rock layers by using an AVO technique. del Monte et al. (2018) compared the conventional methods including seismic impedance inversion, AVO technique, and seismic attribute analysis for detecting source rocks. From this study, seismic inversion could predict a lateral variation of source rocks, and the AVO response of source rocks was a strong class IV anomaly. In particular, the AVO and seismic attribute analysis did not need the well-information, and could be used to investigate source rocks in undrilled basins. Kiswaka and Felix (2020) utilized a combination analysis of amplitude versus angle/offset (AVA)/AVO to determine the distribution of the organic carbon-rich deposits in the deeper basin areas, and the AVO class IV elements could be as an indicator of an organic carbon-rich layer. Besides, those methods were also well-discussed in the literature to guide the identification and evaluation of source rocks (Ogiesoba and Hammes, 2014; Badics et al., 2015; Ding et al., 2015; Lee et al., 2020). Therefore, revealing and characterizing the interaction between the seismic responses and the rock physical properties of source rocks is critical.

The rock physical model sets a fundamental basis for analyzing the elastic properties and seismic attributes caused by kerogen of source rocks and shales. Organic-rich shales behave as a transversely isotropic material due to a specific distribution of organic matter in the rock (Vernik and Nur, 1992). Vernik and Landis (1996) and Vernik and Liu (1997) described the velocity anisotropy due to kerogen of source rocks and shales using the Backus averaging method (Backus, 1962). The seismic-velocity attenuation caused by the conversion of kerogen to oil was interpreted by Carcione (2000, 2001) using the Backus averaging and Kuster–Toksöz model, and the AVO effects of source rocks were further analyzed. Carcione et al. (2011) and Carcione and Avseth (2015) further characterized the effects of the kerogen content on the seismic velocity by the Backus averaging and the Krief/Gassmann models. The elastic anisotropy and AVO responses caused by kerogen of the organic shales were also described by Sayers (2013a,b) based on the developed rock physical model. However, it is still challenging to investigate the elastic properties and AVO responses of the mud-rich source rock, especially the effects of the TOC content and mud content. Therefore, an appropriate rock physical model of the mud-rich source rock is developed, and its AVO characteristics are analyzed in this study.

Generally, the mud-rich source rock is mainly formed in deep water and stable water, and consists of clay minerals, quartz particles, and organic matter (Pichevin et al., 2004; Jiang and Zha, 2005; Aplin and Macquaker, 2011; Ma et al., 2016), and it does not display the same strong anisotropy as shales. Therefore, we simplify the mud-rich source rock as a homogeneous and an isotropic rock. The elastic characteristics of the mud-rich source rock are not only sensitive to the kerogen content and mineral compositions, but also depending on the maturity of kerogen (Avseth and Carcione, 2015; Carcione and Avseth, 2015; Zhao L. et al., 2016). The effects of the maturity on the elastic properties of source rocks and shales were also well-investigated (Guo et al., 2013; Zargari et al., 2013; Zhao L. et al., 2016; Hansen et al., 2019). In particular, Zhao L. et al. (2016) summarized that kerogen played a load-bearing role in the immature and mature stages, and the overmatured kerogen could be treated as a filling inclusion instead of the load-bearing matrix. To highlight the effects of the kerogen content and to weaken the impact of the thermal maturity, we use the self-consistent approximate (SCA) theory (Berryman, 1980, 1995) to handle the effects of kerogen in the immature and mature stages, and utilize the solid substitution equation (Ciz and Shapiro, 2007) to model the overmatured kerogen based on the assumptions of Zhao L. et al. (2016).

While verifying the accuracy and validity of the proposed rock physical model, well logs can be used in the absence of the laboratory data, which can provide more abundant and continuous rock stratum information under real geological conditions than the laboratory data (Xu and White, 1995; Xu et al., 2020; Yin et al., 2020). Moreover, the TOC logs are also required in the application and analysis of actual well logs. However, the accurate TOC values measured through laboratory geochemical analyses are almost discontinuous and insufficient because of the limitations of experimental samples (Fertl and Chilingar, 1988; Khoshnoodkia et al., 2011; Kenomore et al., 2017; Zhao et al., 2017). Therefore, many researchers estimated the TOC content curves using conventional well logs, including the formation-density logs, gamma-ray logs, sonic logs, and resistivity logs (Schmoker, 1979, 1981; Fertl and Chilingar, 1988; Zhao et al., 2016; Alshakhs and Rezaee, 2017). The common methods for calculating the continuous TOC curves involve traditional linear fit methods (Schmoker, 1981; Schmoker and Hester, 1983; Fertl and Chilingar, 1988), the $\Delta \log R$ model and its modifications (Passey et al., 1990; Kenomore et al., 2017; Rahmani et al., 2019), multiparameter regression and multivariate statistical methods (Mendelzon and Toksoz, 1985; Zhu and Jin, 2003; Tan et al., 2015), and artificial neural network methods (Khoshnoodkia et al., 2011; Tan et al., 2015; Shi et al., 2016; Mahmoud et al., 2017, 2020).

In the case of the mud-rich source rock, the thermal maturation is mainly immature or mature. The background values of the TOC content are close to zero. The rock formation is normally compacted, and most of the non-source rocks are sandstones or igneous rocks (Cui et al., 2019). Therefore, the $\Delta \log R$ model is suitable to predict the continuous TOC curves in the mud-rich source rock (Passey et al., 1990; Cui et al., 2019). To eliminate the uncertainty of the artificially selected baselines and avoid the difficulties caused by the unknown maturity in using the $\Delta \log R$ model, Zhu and Jin (2003) proposed a three-parameter regression method by considering a strong relation between organic matter and bulk density. On the basis of the kerogen characteristics, including a high-gamma value, high-sonic transit time, high resistivity, and low density, we also propose a combination-four-parameter regression (CFPR) method to improve the accuracy of the TOC estimation in the mud-rich source rock based on the $\Delta \log R$ model and Zhu's revision (Fertl and Rieke, 1980; Fertl and Chilingar, 1988; Khoshnoodkia et al., 2011).

In this study, to interpret how the rock physical parameters change the elastic properties and thereby affecting the seismic

responses of the mud-rich source rock, a rock physical model is initially presented in detail, and kerogen of different maturity stages is modeled. Furthermore, a CFPR method is further introduced and used to estimate the TOC curves. In addition, the elastic responses of the TOC content and mud content are illustrated by using a numerical modeling and the crossplot of the actual well data. Based on the proposed rock physical model, the seismic responses and AVO patterns of the mud-rich source rock are introduced. The synthetic seismic records are compared with the well-side seismic records to verify the validity and reliability of a forward modeling process. Besides, a two-layer model is constructed to further analyze the effects of the TOC content and mud content on the AVO responses of the mud-rich source rock. Finally, we end with discussions and conclusions.

ROCK PHYSICAL MODEL FOR THE MUD-RICH SOURCE ROCK

Modeling Methodology

Different from the published methods for a rock physics modeling (Vernik and Landis, 1996; Vernik and Liu, 1997; Carcione, 2000; Vernik and Milovac, 2011; Sayers, 2013a,b; Carcione and Avseth, 2015; Zhao L. et al., 2016; Ba et al., 2017; Tan et al., 2020; Pang et al., 2021), a rock physical model is proposed in this study by focusing on the effects of the kerogen content and kerogen maturity of the mud-rich source rock. The main processes and modeling methods used in the rock physical model are illustrated in **Figure 1**.

First, the Voigt-Reuss-Hill average is used to estimate the effective moduli of a mineral mixture, which is assumed to be a homogeneous and an isotropic medium consisting of clay particles, quartz particles, and other solid grains. The elastic moduli of the mineral mixture are (Hill, 1952; Mavko et al., 2009),

$$M_{mixture} = \left[\sum_{i=1}^{N} f_i M_i + \left(\sum_{i=1}^{N} f_i / M_i\right)^{-1}\right]/2, \tag{1}$$

where $M_{mixture}$ represents the equivalent modulus of a mineral mixture, including $K_{mixture}$ and $\mu_{mixture}$. M_i and f_i are the elastic moduli and volume fractions of the ith component, respectively. N is the sum of total types of solid mineral components.

It is clearly known that the thermal maturation of kerogen strongly affects the effective elastic properties of the mud-rich source rock (Modica and Lapierre, 2012; Guo et al., 2013; Zargari et al., 2013; Zhao L. et al., 2016). **Figure 1** displays that the immature and mature kerogen appear as solid inclusions and play a load-bearing role. During the thermal maturation, the mature kerogen decomposes into hydrocarbon, and organic pores are gradually formed in solid kerogen. Overmatured kerogen and generated hydrocarbons constitute a solid–liquid mixture, which is regarded as filling inclusions instead of the load-bearing matrix. Considering different elastic properties and occurrence forms of kerogen, the appropriate effective medium theories are used in different maturity stages. More specifically, the effects of kerogen are described by using the SCA theory in the immature and mature stages, and the elastic moduli of the rock matrix are (Berryman, 1980, 1995),

$$\begin{aligned} \sum_{i=1}^{N} f_i \left(K_i - K_{mixuture}\right) \beta^{*i} &= 0 \\ \sum_{i=1}^{N} f_i \left(\mu_i - \mu_{mixture}\right) \xi^{*i} &= 0, \end{aligned} \tag{2}$$

where $K_{mixture}$ and $\mu_{mixture}$ are the equivalent bulk and shear moduli of mineral mixtures, respectively. K_i and μ_i are the bulk and shear moduli of the ith material, respectively. f_i is the volume fraction of the ith inclusion component. N is the sum of total types of solid mineral components. The factors β^{*i} and ξ^{*i} represent the geometry parameters and are the functions of the aspect ratios and the equivalent moduli of inclusions and background medium (Berryman, 1995; Mavko et al., 2009).

The solid substitution equations are then used to model the effect of overmatured kerogen, the equations for the isotropic case are (Ciz and Shapiro, 2007),

$$\begin{aligned} K_{sat}^{*-1} &= K_{dry}^{-1} - \frac{\left(K_{dry}^{-1} - K_{gr}^{-1}\right)^2}{\phi(K_{in}^{-1} - K_{\phi}^{-1}) + (K_{dry}^{-1} - K_{gr}^{-1})} \\ \mu_{sat}^{*-1} &= \mu_{dry}^{-1} - \frac{\left(\mu_{dry}^{-1} - \mu_{gr}^{-1}\right)^2}{\phi(\mu_{in}^{-1} - \mu_{\phi}^{-1}) + (\mu_{dry}^{-1} - \mu_{gr}^{-1})}, \end{aligned} \tag{3}$$

where K_{sat}^{*} and μ_{sat}^{*} represent the bulk and shear moduli of the rock saturated with an inclusion-filling material, respectively. K_{dry} and μ_{dry} are the bulk and shear moduli of the inorganic matrix, respectively. K_{gr} and μ_{gr} denote the bulk and shear moduli of a solid grain material of matrix frame, respectively. K_{ϕ} and μ_{ϕ} are the bulk and shear moduli of the inclusion pore space, respectively. K_{in} and μ_{in} are the bulk and shear moduli of the pores filled by a mixed material of hydrocarbons and kerogen, respectively.

The effective elastic properties of clay-sand rocks are calculated by Xu and White (1995), which assumed that the matrix pores involved clay pores and sand pores. For the mud-rich source rock, the matrix pores also can be divided into ductile pores (related to the clay minerals) and rigid pores (related to the sand minerals) by referring to the Xu–White model (Xu and White, 1995),

$$\phi_{ductile} = V_{clay}\phi_{matrix}, \phi_{rigid} = \phi_{matrix} - \phi_{ductile} \tag{4}$$

where V_{clay} is the volume fraction of the clay mineral normalized by the total volume fraction of an inorganic matrix.

Assuming the Poisson's ratio of the dry rock skeleton as constant, Keys and Xu (2002) simplified the dry rock approximation based on the Kuster–Toksöz and differential effective medium (DEM) theories used in the Xu–White model, and derived two direct and efficient formulations to calculate the elastic moduli of a dry rock skeleton,

$$\begin{aligned} K_{dry} &= K_m(1-\phi)^p \\ \mu_{dry} &= \mu_m(1-\phi)^q, \end{aligned} \tag{5}$$

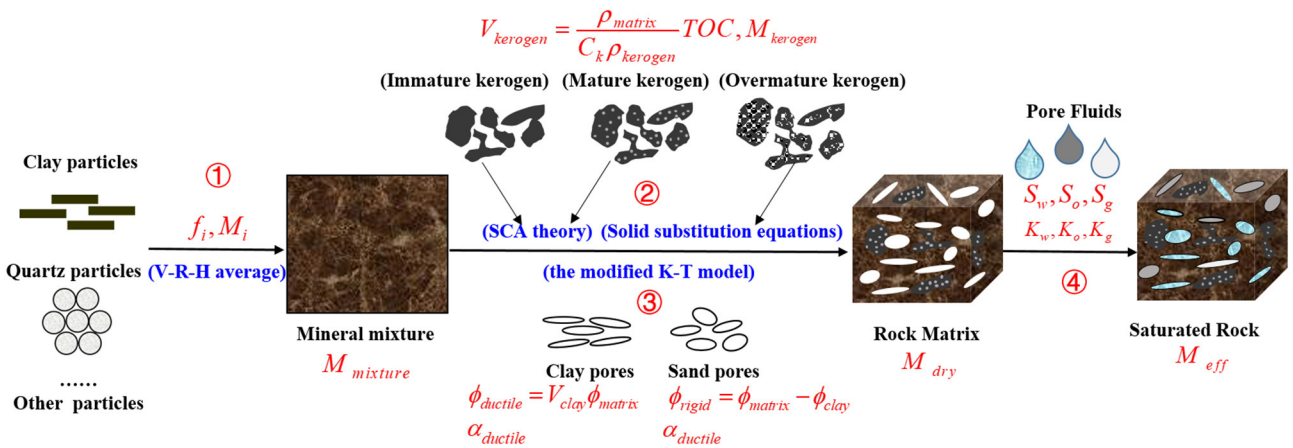

FIGURE 1 | Schematic diagram of rock physical modeling in the mud-rich source rock.

where K_{dry} and μ_{dry} are the bulk and shear moduli of a dry rock skeleton, respectively. K_m and μ_m are the matrix bulk and shear moduli, respectively. p and q are the geometric factors depending on the shapes of the pore inclusions. ϕ is the rock porosity.

In view of that the pore-filling materials depend on the kerogen type and maturity (Tissot et al., 1974, 1987; Espitalié et al., 1977), the effective moduli of the saturated rock are (Gassmann, 1951; Mavko et al., 2009),

$$K_s = K_d + \alpha^2 K_f \left[\phi + (\alpha - \phi) K_f / K_m\right]^{-1}, \mu_s = \mu_d, \quad (6)$$

where $\alpha = 1 - K_d/K_m$, K_s,K_d, K_f, and K_m are the bulk moduli of the saturated rock, dry rock frame, pore-filling material, and rock matrix, respectively. μ_s andμ_d are the shear moduli of the saturated rock and dry rock frame, respectively.

Estimation of the TOC Content

Continuous TOC content curves are necessary for the verification and application of the proposed rock physical model, especially for the analysis of actual well logs. The TOC value is an important factor (weight percent) for evaluating the abundance of organic matter in source rocks and can be transformed to the kerogen volumetric content (Vernik and Nur, 1992; Vernik and Landis, 1996; Carcione, 2000; Vernik and Milovac, 2011; Carcione and Avseth, 2015; Vernik, 2016),

$$V_{kerogen} = \frac{\rho_{matrix}}{C_k \rho_{kerogen}} TOC, \quad (7)$$

where ρ_{matrix} and $\rho_{kerogen}$ are the density of the dry rock matrix and solid kerogen, respectively. C_k is the carbon concentration of the solid organic matter and depends on the kerogen maturity ranging from 0.7 to 0.85 (Vernik and Milovac, 2011; Carcione and Avseth, 2015; Vernik, 2016).

The accurate TOC values measured by using a rock pyrolysis analysis (Rock-Eval) are almost discontinuous and insufficient (Fertl and Chilingar, 1988; Khoshnoodkia et al., 2011; Kenomore et al., 2017; Zhao et al., 2017). Therefore, it is of great significance and demand to estimate the continuous curves of the TOC content using the common well logs. The $\Delta \log R$ method proposed by Passey et al. (1990) is one of the most common methods to determine the continuous TOC curves. The TOC value is calculated by using the $\Delta \log R$ method by a logarithmic separation between the sonic and resistivity values and depending on the maturity (Passey et al., 2010),

$$TOC = \left(\log(R_t/R_0) - 0.02 \times (\Delta t - \Delta t_0)\right) \times 10^{(2.297 - 0.1688 \times LOM)}, \quad (8)$$

where R_t is the resistivity log value (ohm). Δt is the sonic log value (μs/ft). R_0 and Δt_0 are the baseline value of the resistivity logs and sonic logs coincided in a non-source rock, respectively. LOM represents the level of organic maturity, such as vitrinite reflectance, R_0.

However, there are many uncertainties and difficulties caused by artificially selecting baselines and lacking of the maturity formation in using the $\Delta \log R$ method. To avoid the shortcomings of the $\Delta \log R$ method, Zhu and Jin (2003) proposed a three-parameter regression method by modifying the $\Delta \log R$ model and considering a strong correlation of organic matter and bulk density. The modified TOC calculation equation is,

$$TOC = (a \times \log R_t + b \times \Delta t + c)/\rho, \quad (9)$$

where a, b, and c are the coefficients to be estimated by the regression analysis using the measured TOC values and well logs.

By modifying the $\Delta \log R$ model and Zhu's revision, a CFPR method is further proposed based on the characteristics of organic matter, which involve a high-gamma value, high-sonic transit time, high resistivity, and low density (Fertl and Rieke, 1980; Fertl and Chilingar, 1988; Khoshnoodkia et al., 2011), the estimating equation of TOC value is,

$$TOC = a \times (\log R_t/\rho) + b \times (\Delta t/\rho) + c \times (GR/\rho) + d \times (1/\rho) + e, \quad (10)$$

where GR is the gamma-ray value (API) of the source rock. ρ is the rock density value ing/cm^3. a, b, c, d, and e are the coefficients to be determined by the multiple regression analysis.

The same four parameters (R_t, Δt, GR, and ρ) can also be used to linearly calculate the TOC curves (Fertl and Chilingar, 1988; Alshakhs and Rezaee, 2017), defined as a simple-four-parameter regression (SFPR) method, the calculation equation is

$$TOC = a \times R_t + b \times dt + c \times GR + d \times (1/\rho) + e. \quad (11)$$

Different from the SFPR method, the CFPR method utilizes the four combination parameters, which are $\log R_t/\rho$, $\Delta t/\rho$, GR/ρ, and $1/\rho$, to predict the TOC values. Because organic matter exhibits a high-gamma value, a high-sonic transit time, high resistivity, and low-density characteristics, the combination parameters $\log R_t/\rho$, $\Delta t/\rho$, and GR/ρ have stronger positive correlations and are more sensitive to the TOC values than the simple parameters R_t, Δt, GR, and ρ. In addition, the combination parameter $\log R_t/\rho$ can also avoid the large-scale changes of R_t logs.

The $\Delta \log R$ method, the Zhu's method, the SFPR method, and the CFPR method are utilized for the actual well L1 including 47 measured TOC samples from the Zhu I depression in the South of China, and the results are illustrated in **Figure 2**. The estimated TOC values from the SFPR and CFPR methods are more accurate and reasonable than those from the $\Delta \log R$ method and Zhu's method. Because the TOC curves calculated by four parameters can bring more wiggles and have higher matching rates than those of two or three used parameters. The fitting goodness (denoted as R^2) of the CFPR method is 89.5%, which is 23.2% higher than that of the SFPR method, 35.2% higher than that of Zhu's method, and 102.6% higher than that of the $\Delta \log R$ method. Moreover, the root mean square error (RMSE) of the estimated results using the CFPR method is 20.24%, which is 38.0% less than that of the SFPR method, 44.3% less than that of Zhu's method, and 56.6% less than that of the $\Delta \log R$ method. The satisfactory R^2 and RMSE indicate that the CFPR method can reliably and accurately predict the TOC content curves of the mud-rich source rock.

Figure 3 displays the regression residual analysis of the CFPR method. The residuals are mainly distributed in the interval [-0.3, 0.3], and the residual distribution is consistent with the normal distribution, which also verifies the effectivity and reliability of the CFPR method.

Numerical Modeling

Compared with the laboratory data, well logs can provide a large amount of continuous rock formation information taken under real geological conditions and can also be used to verify the validity and applicability of the proposed rock physical model in the absence of the laboratory data (Xu and White, 1995; Xu et al., 2020; Yin et al., 2020). **Figure 4** illustrates that the actual well L2 is used to verify the proposed rock physical model of the mud-rich source rock. The P-wave velocity and S-wave velocity estimated by using the proposed rock physical model are consistent with the measured well log values, and the fitting goodness of the calculated S-wave velocity is 90.08%. **Figure 5** displays the errors of the calculated P-wave velocity and S-wave velocity. The relative errors of S-wave velocity are <10% and demonstrate a normal distribution, which demonstrates that the proposed rock physical model can reliably and effectively characterize the elastic properties of the mud-rich source rock.

Clay minerals and kerogen are the most abundant compositions in the mud-rich source rock. The rock will become ductile due to the clay minerals, and the compressional elasticity and density of rock will decrease by the existence of kerogen. Therefore, the TOC content and mud content can be regarded as two dominant factors of affecting the elastic responses of the mud-rich source rock. Using the proposed rock physical model, the elastic responses of the mud content and TOC content are quantified and illustrated in **Figures 6**, **7**. For simplicity, the mud-rich source rock is considered to be composed of kerogen, clay, and quartz. The aspect ratios of ductile pores and rigid pores are supposed to be 0.015 and 0.22, respectively. The matrix pores are filled by water.

Figure 6 indicates that the P-wave velocity (V_p), S-wave velocity (V_S), and P-wave impedance (I_p) decrease with an increase of the mud content, and the density, the ratio of P-wave velocity and S-wave velocity (V_p/V_s), Poisson's ratio, and Poisson impedance increase as the mud content increases. As the mud content grows from 10 to 100%, the relative decrements of V_p are 25.2 and 23.0% when TOC is set to 0 and 3.0%, respectively. And the same relative decrements of V_S are 28.7 and 26.6%, and of I_p are 16.7 and 15.0%, respectively. The decrement magnitude of I_p is lower than that of V_p or V_S because of the high bulk density of clay minerals. Moreover, a varying TOC content will slightly change the decrement magnitudes of the elastic parameters.

Figures 6D–F prove that V_p/V_s, Poisson's ratio and Poisson impedance all have positive correlations with the mud content. As the mud content grows from 10 to 100%, the relative increments of V_p/V_s are 5.0 and 4.9% when TOC is set to 0 and 3.0%, respectively. The same relative increments of Poisson's ratio are 7.7 and 26.6%, and of Poisson impedance are 19.9 and 19.1% when TOC is set to 0 and 3.0%, respectively. The decrement magnitude of the Poisson impedance is higher than those of V_p/V_s and Poisson ratio because the bulk density increases with the mud content. In conclusion, increasing the mud content will make V_p, V_S, and I_p to decrease, and cause V_p/V_s, Poisson ratio, and Poisson impedance to increase in the mud-rich source rock.

In **Figure 7**, all elastic parameters decrease with increasing the TOC content. From no organic matter up to 5.0% TOC content, the relative decrements of V_p are 10.0 and 8.1% when the mud content is 50 and 90%, respectively. And the same relative decrements of V_S are 9.3 and 7.5%, respectively, and they are equivalent to the relative decrements of V_p. The same relative decrements of I_p are 15.3 and 14.1%, respectively, which are larger than those of V_p and V_s. However, the change magnitudes of V_p/V_s and Poisson's ratio caused by the TOC content are lower than 1.0%, which demonstrates that TOC will slightly affect V_p/V_s and Poisson's ratio. In summary, V_p, V_S, and I_p of the mud-rich source rock will significantly decrease with an increase of the TOC content, and in particular, $I_p$is more sensitive to

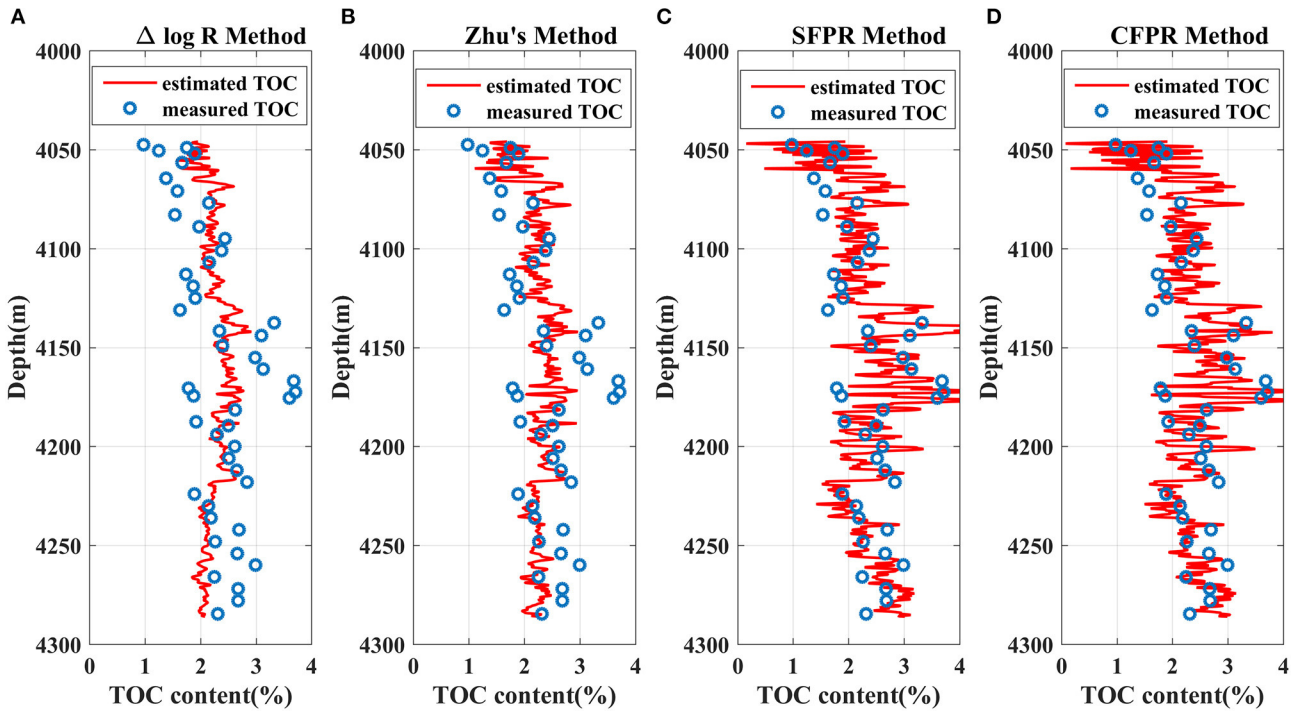

FIGURE 2 | A comparison of estimated TOC using different methods of the mud-rich source rock. **(A)** The Δ method, **(B)** the Zhu's method, **(C)** the SFPR method, **(D)** the CFPR method. The red lines represent estimated TOC values, and the blue scatters represent measured TOC values.

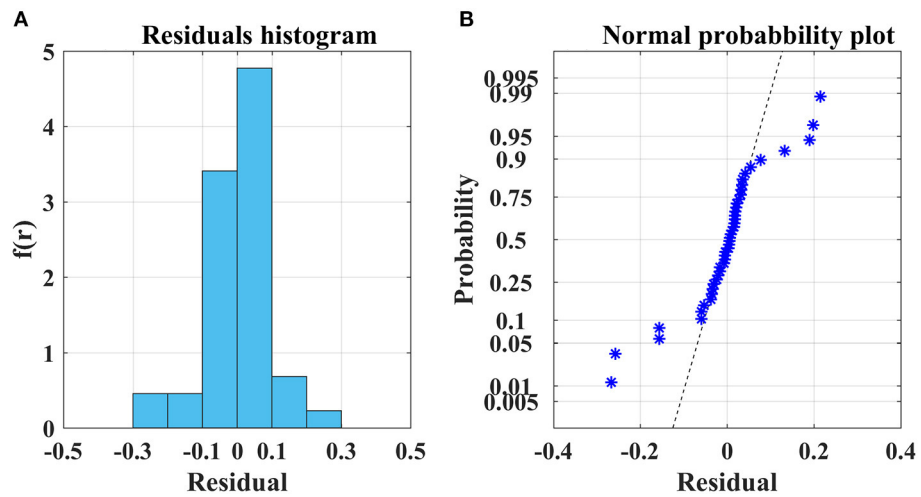

FIGURE 3 | Residuals analysis of estimated TOC from the CFPR method. **(A)** Residuals distribution histogram, **(B)** Residuals probability graph.

the TOC content because of the low elastic moduli and density of kerogen.

Application in Real Data

Figures 8, **9** display that the real data of the actual wells from the Zhu I depression in the South of China are utilized to verify the relation between the elastic parameters and the TOC content and mud content simulated by the proposed rock physical model. **Figure 8** illustrates that the crossplot of the elastic parameters for the mud content, the combinations of elastic parameters including V_p/V_s with V_p, Poisson's ratio with V_p, and Poisson impedance with V_p, can well-distinguish the mud content. The indicating abilities of V_p/V_s, Poisson's ratio, and Poisson impedance for the mud content are equivalent. More specifically, the mud content is in positive correlation with V_p/V_s, Poisson's ratio, and Poisson impedance, and negatively

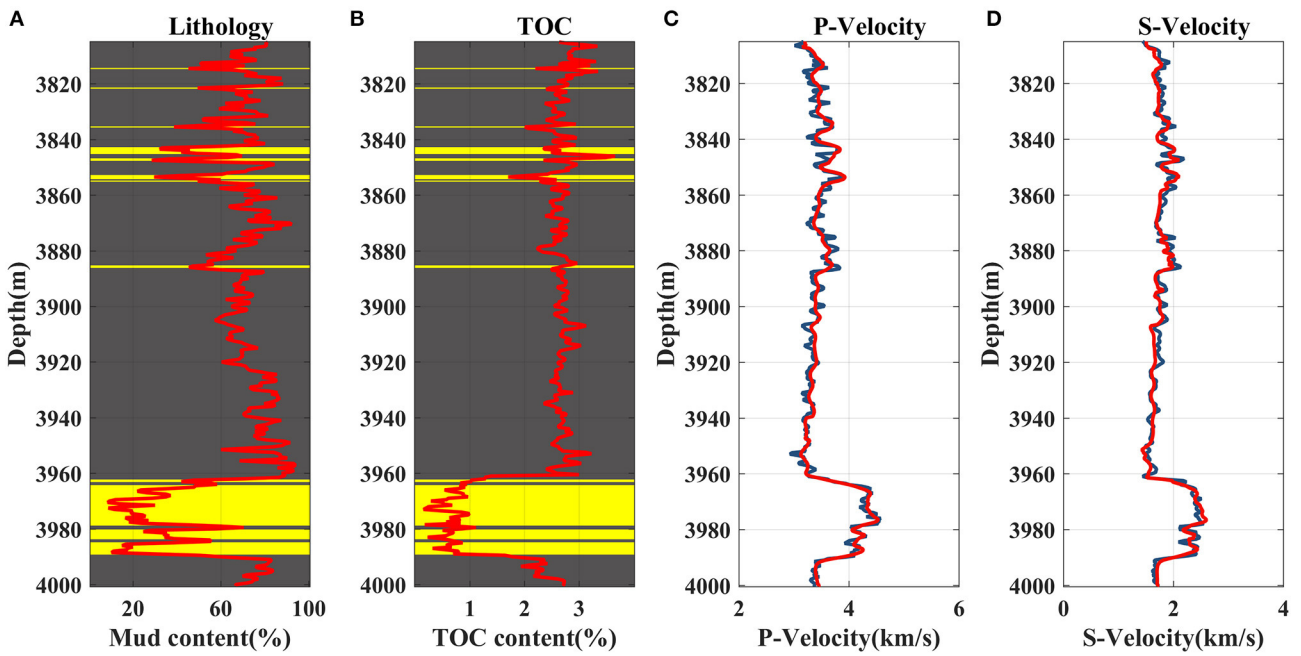

FIGURE 4 | The comparison of the estimated (in red) and the actual (in blue) P-wave and S-wave velocity of the actual well L2. **(A)** Lithology information (the mud-rich source rock in gray and sandstones in yellow) and mud content, **(B)** Lithology information and TOC content, **(C)** P-wave velocity, **(D)** S-wave velocity.

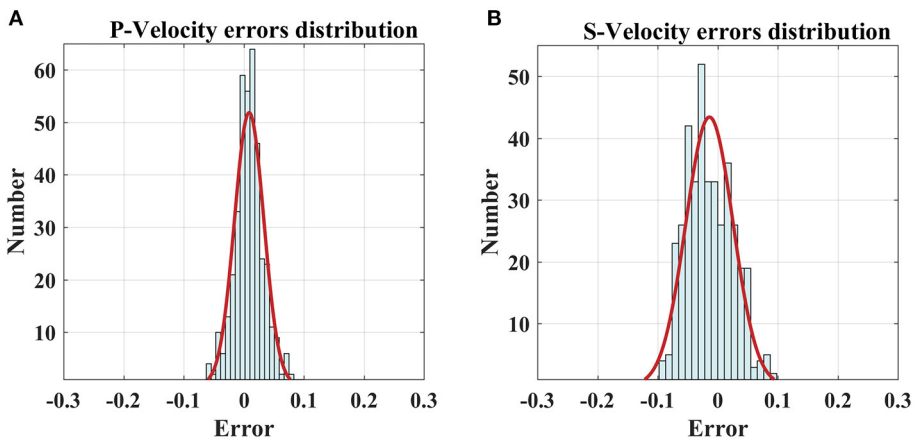

FIGURE 5 | Errors between the estimated P-wave/S-wave velocity and measured values. **(A)** The errors distribution of P-wave velocity, **(B)** the errors distribution of S-wave velocity.

related to V_p. **Figure 9** indicates that the combinations involving V_p with density, V_s with density, and $I_p$with density have better indicating abilities to the TOC content, and V_p, V_s, and I_p exhibit significantly low values at high TOC content.

The actual well data used in the crossplots are also utilized to test the sensitivities of different elastic parameters to the mud content and TOC content. Sensitivities to the mud content and TOC content can also be understood as the indicating abilities of elastic parameters to the mudstone and high-quality source rock. In the mud-rich source rock, we assume the mudstone with the TOC content higher than 1.5% as the high-quality source rock. The sensitivity coefficient of each elastic parameter is defined as the ratio of the difference in the mean values and the standard deviation (SD) of the parameter value at the mudstone (or high-quality source rock), is (Yin et al., 2015; Zong et al., 2015),

$$S^* = \left| \frac{P^*_{mean} - P^0_{mean}}{P^*_{std}} \right|, \tag{12}$$

where S^* is the sensitivity coefficient of the elastic parameter for the mudstone or high-quality source rock. P^*_{mean} and P^0_{mean} are

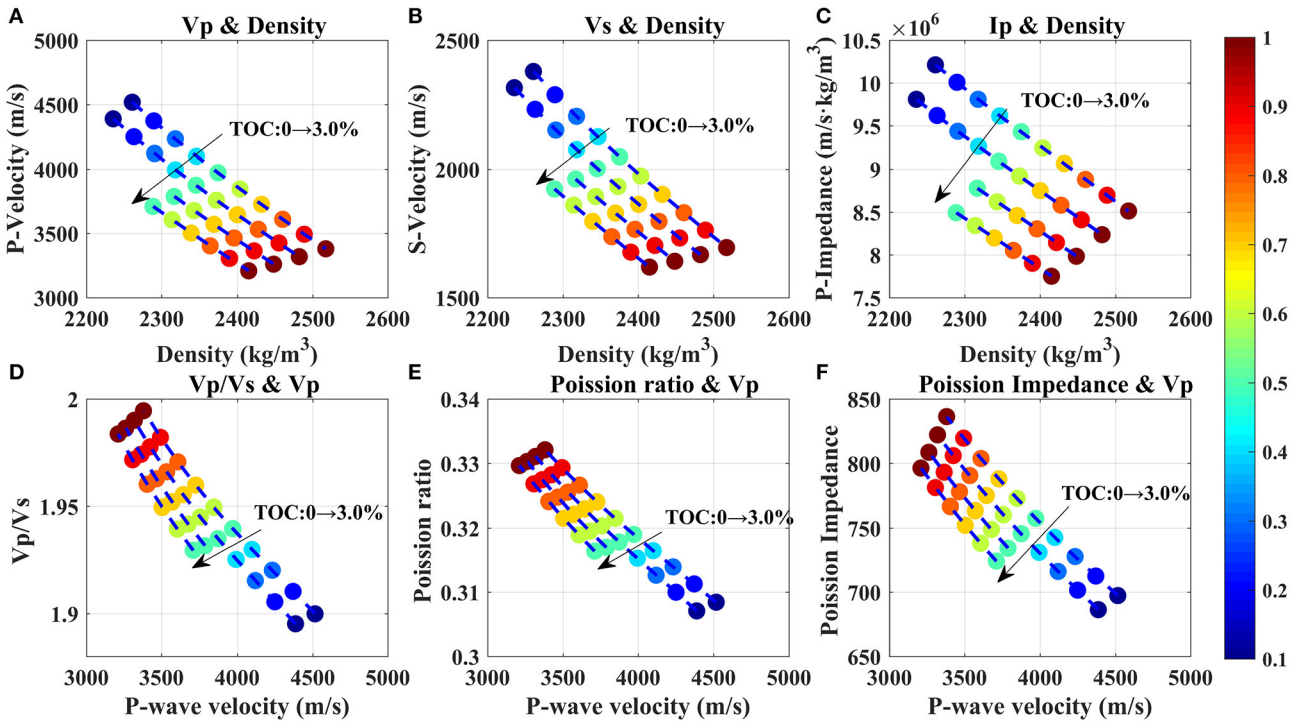

FIGURE 6 | Crossplot of elastic parameters versus mud content at different TOC values based on the rock physical model of the mud-rich source rock. **(A)** V_p and ρ, **(B)** V_s and ρ, **(C)** I_p and ρ, **(D)** V_p/V_s and V_p, **(E)** Poisson's ratio and V_p, **(F)** Poisson impedance and V_p. The color bar on the right represents the mud content.

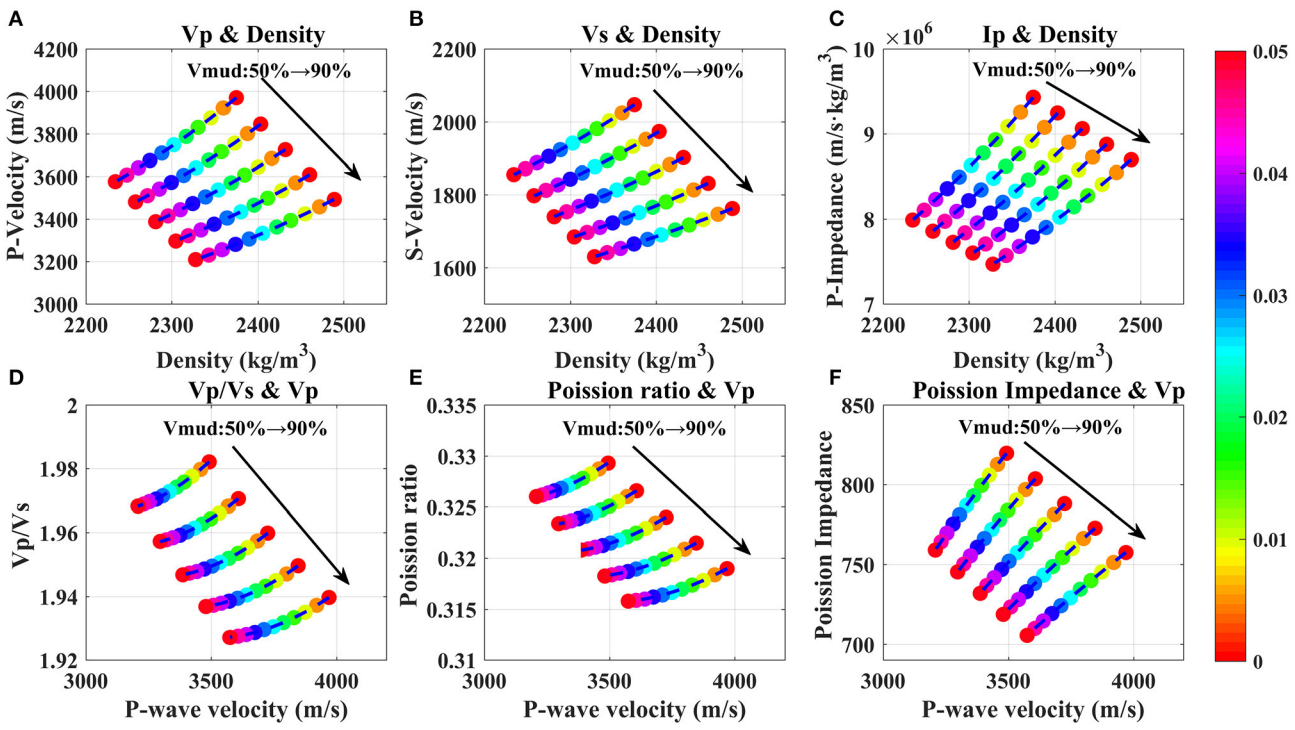

FIGURE 7 | Crossplot of elastic parameters versus TOC content at different mud content based on the rock physical model of the mud-rich source rock. **(A)** V_p and ρ, **(B)** V_s and ρ, **(C)** I_p and ρ, **(D)** V_p/V_s and V_p, **(E)** Poisson's ratio and V_p, **(F)** Poisson impedance and V_p. The color bar on the right represents the TOC content.

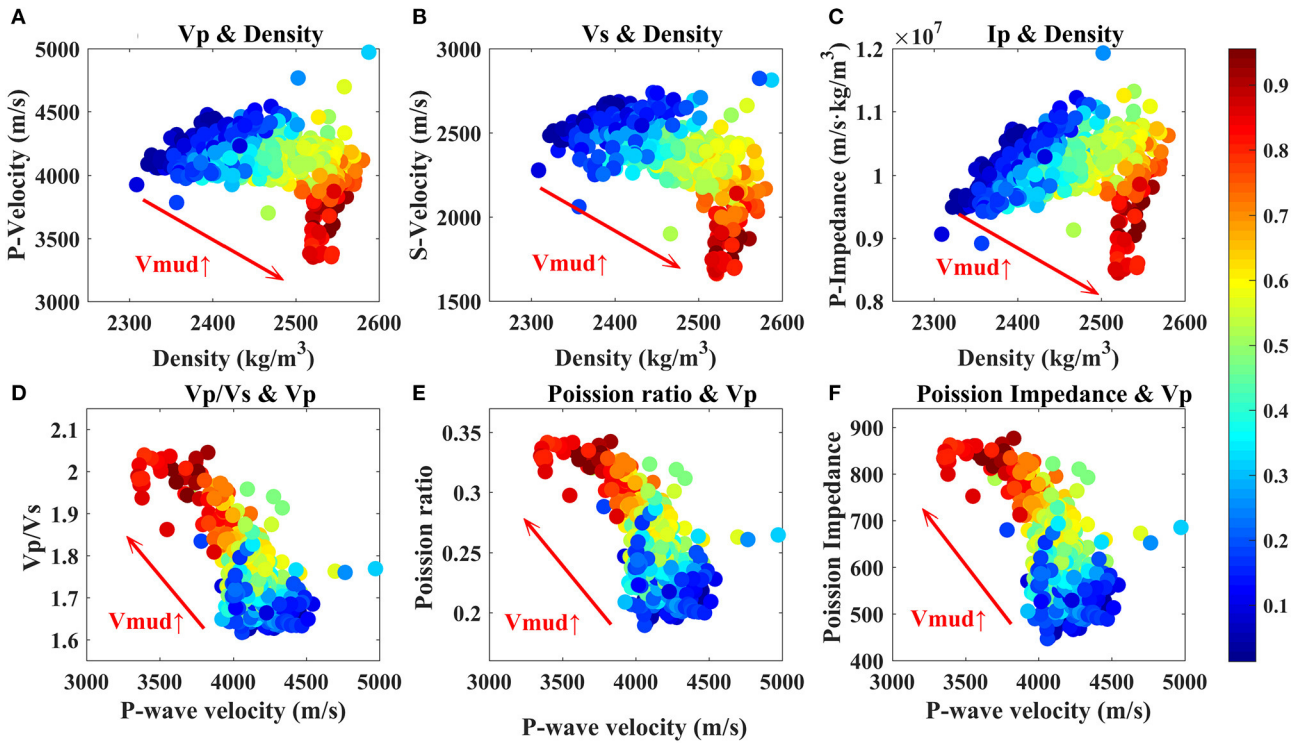

FIGURE 8 | Crossplot of elastic parameters versus mud content using actual well L2 data. **(A)** V_p and ρ, **(B)** V_s and ρ, **(C)** I_p and ρ, **(D)** V_p/V_s and V_p, **(E)** Poisson's ratio and V_p, **(F)** Poisson impedance and V_p. The color bar on the right represents the mud content.

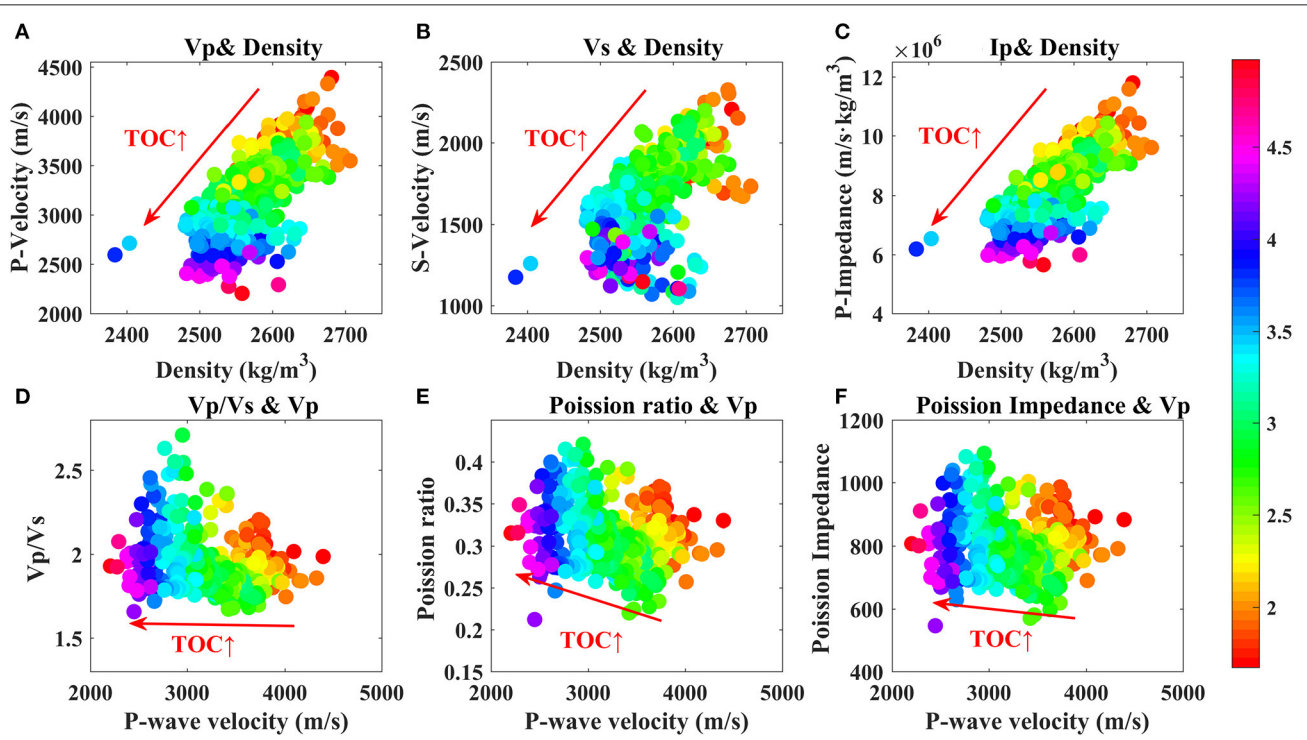

FIGURE 9 | Crossplot of elastic parameters versus TOC content using actual well L2 data. **(A)** V_p and ρ, **(B)** V_s and ρ, **(C)** I_p and ρ, **(D)** V_p/V_s and V_p, **(E)** Poisson's ratio and V_p, **(F)** Poisson impedance and V_p. The color bar on the right represents the TOC content.

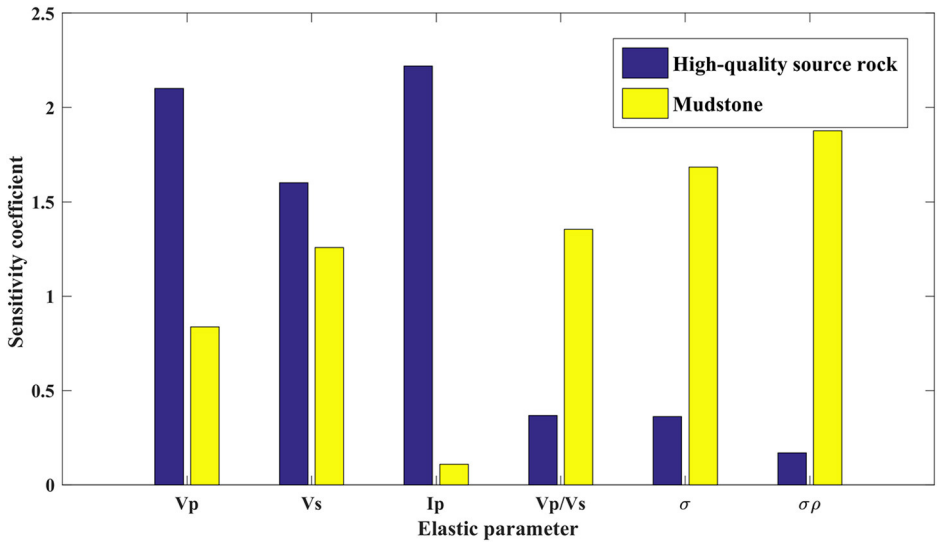

FIGURE 10 | Sensitivity coefficients of different elastic parameters to the mudstone (in yellow) and the high-quality source rock (in blue).

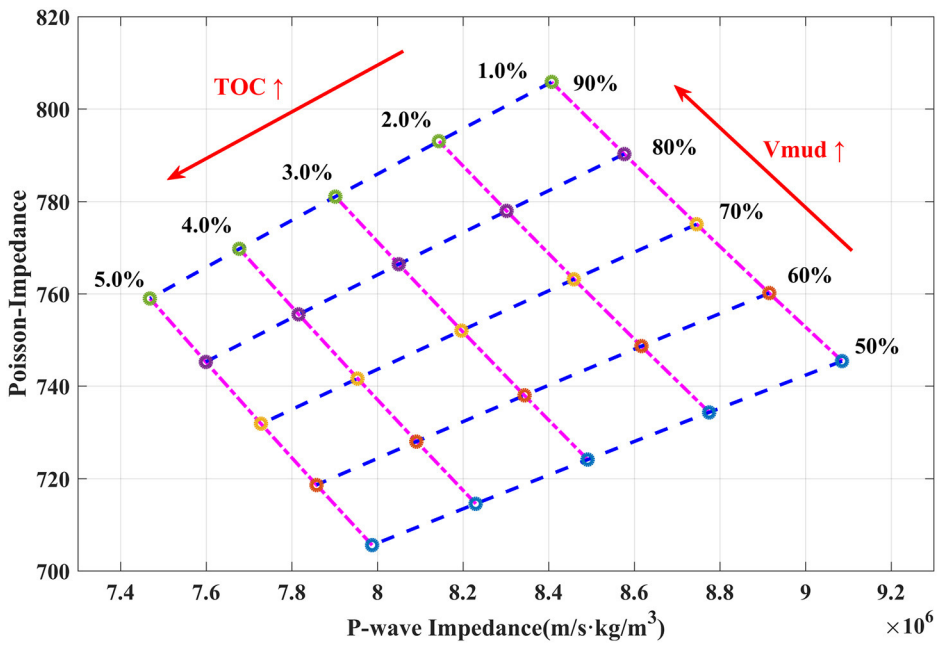

FIGURE 11 | Diagram of the P-wave impedance versus Poisson impedance of varying TOC content and mud content based on the rock physical model of the mud-rich source rock.

the mean values of the elastic parameters at the mudstone (or high-quality source rock) and sandstone (or non-high-quality source rock), respectively. P^*_{std} is the SD of the elastic parameter at the mudstone (or high-quality source rock).

Figure 10 displays the sensitivity coefficients for discriminating the high-quality source rock and mudstone of different elastic parameters, including V_P, V_S, I_P, V_P/V_S, Poisson's ratio (denotes as σ), and Poisson impedance (denotes as $\sigma\rho$), respectively. V_P and I_P have better sensitivities to the high-quality source rock, and the Poisson's ratio and Poisson impedance are more sensitive to the mudstone. Therefore, the Poisson's ratio and Poisson impedance can be considered as indicators for discriminating the mudstone, and then V_P and I_P are used to identify the high-quality source rock from the distribution of the mudstone.

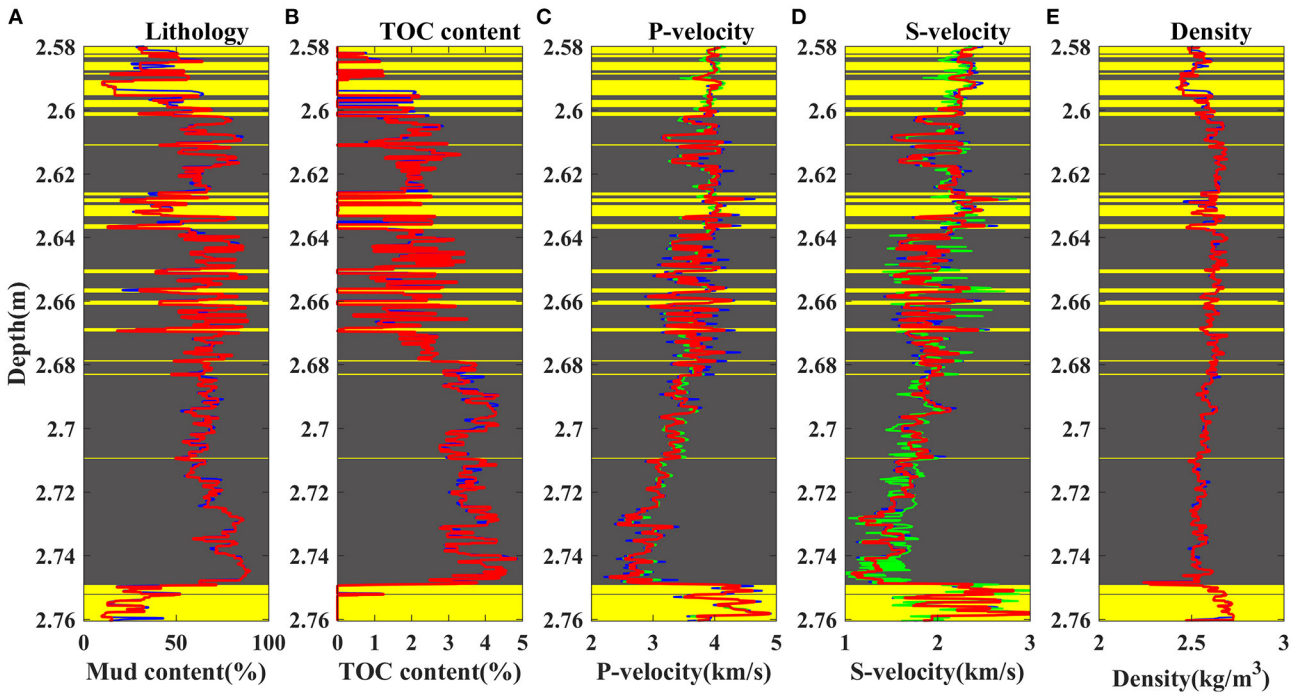

FIGURE 12 | The lithology information (the mud-rich source rock in gray and sandstones in yellow), actual physical properties (blue curves), and estimated elastic properties (green curves) of actual well L3. **(A)** Mud content, **(B)** TOC content, **(C)** P-wave velocity, **(D)** S-wave velocity **(E)** Density.

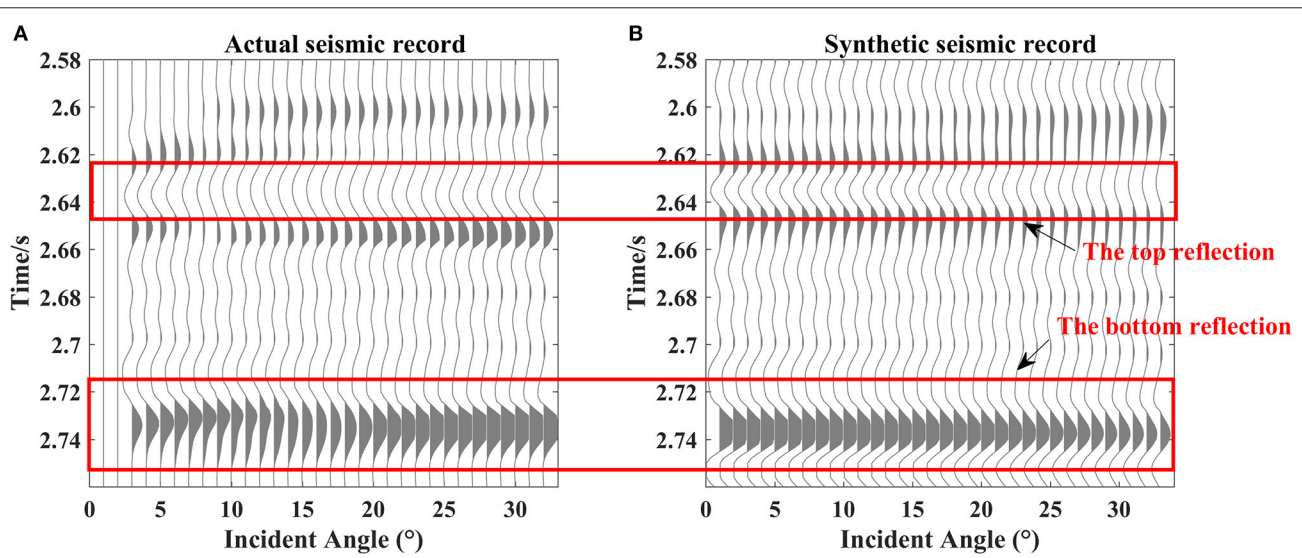

FIGURE 13 | (A,B) A comparison of actual seismic records and synthetic seismic records.

Discussion

Using the proposed rock physical model, the impact of the TOC content and mud content on the Poisson impedance and P-impedance of the mud-rich source rock are illustrated in **Figure 11**. As the mud content increases, the P-wave impedance generally decreases, and the Poisson impedance significantly increases, which is due to a high Poisson's ratio and the density of clay minerals in the mud-rich source rock. In contrast, the TOC content trends to make both the P-wave impedance and Poisson impedance decrease, which is caused by the very low modulus and density of kerogen in the mud-rich source rock.

Figure 11 demonstrates that the TOC content and mud content have a synergic effect on a decrease of the P-impedance, which will bring difficulties to determine the mud-rich source

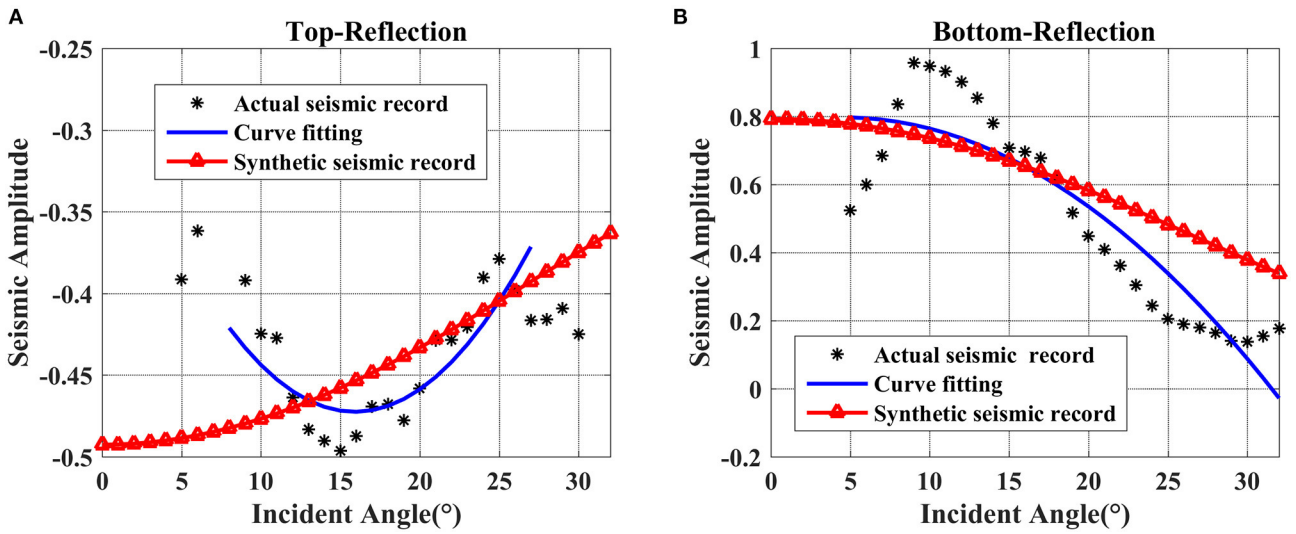

FIGURE 14 | AVO characteristics analysis of the top and bottom reflection events picked from the well-side seismic records and synthetic seismic records. **(A)** Top reflection, **(B)** bottom reflection.

rock based on the interpretation of the P-wave impedance alone. However, the TOC content and mud content have a competing effect on an increase of the Poisson impedance. Moreover, the Poisson impedance is more sensitive to the mud content than the TOC content. Therefore, the Poisson impedance can be considered as an indicator to identify the spatial distribution of the mudstone. And then, the P-impedance can be further used to distinguish the mud-rich source rock from the determined mudstone. In addition, the P-impedance also can be used to evaluate the TOC content and discriminate the high-quality source rock. These results can help to interpret the seismic inversion results and guide the identification and evaluation of the mud-rich source rock.

AVO PATTERNS FOR THE MUD-RICH SOURCE ROCK

In this section, the seismic responses of the mud-rich source rock are analyzed by using the proposed rock physical model to interpret the effects of the TOC content and mud content on the AVO characteristics.

The elastic parameters of the actual well L3 are calculated by using the proposed rock physical model. When the TOC content is higher than 1.0%, the mudstone is defined as the mud-rich source rock. From **Figures 12A,B**, the mud content and TOC content logs indicate that the mud-rich source rock has a thickness up to 300–400 m, and mainly consists of thick mudstones with less amount of thin sandstones. **Figures 12C,D** demonstrate that the calculated P-wave velocity and S-wave velocity (represented by green curves) are in good agreement with the measured well logs (represented by blue curves), which verifies the accuracy of the proposed rock physical model and thereby implies the feasibility and reliability of the seismic forward modeling. Moreover, the variations of P-wave velocity and S-wave velocity with depth give that the mud-rich source rock has significantly low velocity compared with sandstones. **Figure 12E** indicates the density of the mud-rich source rock is higher than the shallow sandstones and lower than the base sandstones due to the increasing formation compaction.

The well-seismic-calibration process is divided into two main steps. The first one is blocking well logs, and is aimed to match the frequencies of the well logs and seismic data. The well log is stratified and blocked based on the minimum-stratification-thickness principle and minimum-velocity-difference principle (Zhou et al., 2015). In this study, the minimum-stratification-thickness is set at twice the seismic sampling interval, and the minimum-velocity-difference is set to 30 m/s for the actual well L3. The second main stage is the conventional well-seismic-calibration process.

The Aki–Richards approximation of the exact Zoeppritz equation is used to calculate the P-wave reflection coefficients for the AVO modeling (Aki and Richards, 1980),

$$R_{PP}(\theta) = \frac{1}{2}(1 - 4\frac{V_S^2}{V_P^2}\sin^2\theta)\frac{\Delta\rho}{\rho} + \frac{\sec^2\theta}{2}\frac{\Delta V_P}{V_P} - 4\frac{V_S^2}{V_P^2}\sin^2\theta\frac{\Delta V_S}{V_S}, \quad (13)$$

where V_P, V_S, and ρ are the average values of P-wave velocity, S-wave velocity and density on both sides of the reflection interface, respectively. ΔV_P, ΔV_S, and $\Delta\rho$ are the difference of P-wave velocity, S-wave velocity, and density on both sides of the reflection interface, respectively. θ is an incident angle.

Figure 13 displays the synthetic seismic records that are consistent with the actual seismic records (on the side of well L3), which verifies the accuracy and effectivity of a seismic forward modeling. Both synthetic and well-side seismic records have four obvious strong reflection events, which sequentially match

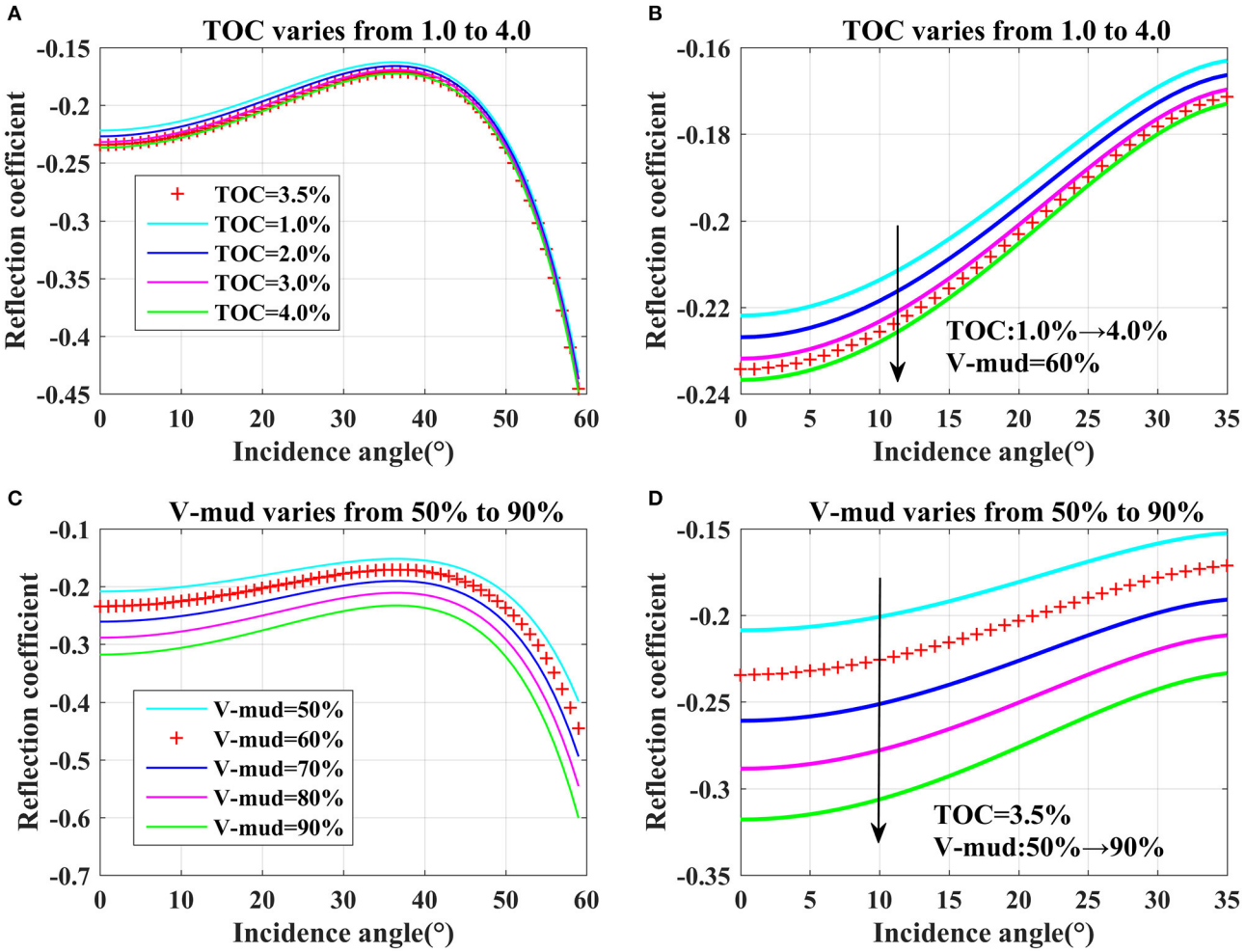

FIGURE 15 | The PP-reflection coefficients vary with incident angle (denoted as θ) for different TOC content and mud content. **(A)** TOC content increases from 1.0 to 4.0%, θ is 0–60°, **(B)** TOC content increase from 1.0 to 4.0%, θ is 0–35°, **(C)** mud content increase from 50 to 90 %, θ is 0–60°, **(D)** mud content increases from 50% to 90%, θ is 0–35°. (Red crosses represent the PP-reflection coefficients calculated by the average elastic properties of the actual well L3.).

the top and bottom reflections of the upper and lower mud-rich source rock in the well L3, due to an obvious impedance contrast of the mud-rich source rock with respect to the background sandstones.

The top and bottom reflection events of the lower mud-rich source rock are picked to analyze the AVO characteristics of the mud-rich source rock. **Figure 13** displays that the top reflection of the mud-rich source rock has a strong negative reflection event dimming with an incident angle. **Figure 14A** indicates that the P-P reflection coefficient curves of the top reflection behave as negative interceptions and positive gradients, which demonstrate the class IV AVO pattern. This is mainly because the mud-rich source rock has lower P-wave impedance and higher Poisson's ratio than the upper sandstone (Ostrander, 1984; Avseth et al., 2010). The similar behaviors were also described in the previous researches on source rocks and organic-rich shales (Carcione, 2001; Sayers, 2013a; Ogiesoba and Hammes, 2014; del Monte et al., 2018; Kiswaka and Felix, 2020). Conversely, **Figures 13**, **14B** display that the bottom reflection of the mud-rich source rock present a strong positive reflection event and the P-P reflection coefficient curves exhibit positive interceptions and negative gradients, which are consistent with the class I AVO characteristics. This is because the base sandstone have higher P-wave impedance and lower Poisson's ratio than the upper mud-rich source rock (Ostrander, 1984; Avseth et al., 2010). Moreover, **Figure 14** displays that the AVO characteristics of the P-P reflection coefficient curves picked from the synthetic seismic records are in agreement with the fitting curves of the well-side seismic records, which also confirms the reliability of AVO modeling.

Furthermore, the average physical properties of the mud-rich source rock and background sandstone in the well L3 are selected to construct a two-layer model for analyzing the effects of the TOC content and mud content on the AVO characteristics. The upper layer is set to the sandstone with no kerogen, and the lower layer consists of the mud-rich source rock with a varying

TOC content and mud content. **Figures 15A,B** display that the P-P reflection coefficients for the TOC content increase from 1.0 to 4.0%. In agreement with the conclusions of Carcione (2001), the P-P reflection coefficients remain negative, and the absolute values of the reflection coefficients gradually decrease within 40°, and then sharply increase in the range of 40–60°. **Figure 15B** highlights the variation of P-P reflection coefficients between 0° and 35°. As the TOC content increases, the interceptions of the P-P reflection coefficients decrease and the absolute values of the interceptions increase. This is because of an increase of the TOC content, which will make the elastic impedance of the mud-rich source rock to decrease and the impedance difference between the mud-rich source rock and sandstone to increase. As the TOC content increases from 1.0 to 4.0%, the interceptions of P-P reflection coefficients change from −0.221 to −0.237, and the relative change rate is 6.7%. When TOC is 4.0%, the P-P reflection coefficients vary from −0.237 to −0.173 as an incident angle changes from 0° to 35°, and the relative change rate is 27.0%. In conclusion, the TOC content has a significant effect on the P-P reflection coefficients because the presence of kerogen will largely weaken the elastic impedance of the mud-rich source rock.

Similarly, **Figures 15C,D** display that the P-P reflection coefficients change as the mud content increases from 50 to 90%, and their variation characteristics are similar to those of increasing the TOC content. As the mud content increases from 50.0 to 90.0%, the P-P reflection coefficients decrease from −0.209 to −0.318, and the relative change rate is 52.4%. When the mud content is 90.0%, the P-P reflection coefficients increase from −0.318 to 0.236 with an incident angle changing from 0° to 35°, and the relative change rate is 25.8%. The effects of the mud content are more significant than the TOC content on the AVO responses, which is due to a larger variation of the mud content than the TOC content in the mud-rich source rock.

In conclusion, the AVO responses of the top reflections of the mud-rich source rock are consistent with the class IV AVO patterns, and the bottom reflections display a class I AVO anomaly. Moreover, the AVO characteristics can be strongly affected by the TOC content and mud content, and the TOC content and mud content will significantly decrease the interception and slightly change the gradient of the P-P reflection coefficients. In particular, the effects of the mud content are stronger than the TOC content.

CONCLUSIONS

In this study, we initially develop a rock physical model to reveal an inherent mechanism of the mud-rich source rock by focusing on the effects of the TOC content and mud content on the elastic properties and seismic responses. The rock physical modeling results and the crossplots of the actual well logs reveal that the TOC content and mud content have a synergic effect on a decrease of the P-wave impedance, and have an opposite impact on an increase of the Poisson impedance. In particular, the Poisson impedance is more sensitive to the mud content, and the P-wave impedance is more sensitive to the TOC content, which can help to interpret the seismic inversion results and guide the identification and evaluation of the mud-rich source rock. In addition, a CFPR method is also presented to acquire the continuous TOC curves for the application and analysis of the proposed rock physical model.

The seismic responses of the mud-rich source rock are later analyzed by using a seismic forward modeling. The synthetic seismic records and the well-side seismic records exhibit the same characteristics. Specifically, the top reflections of the mud-rich source rock behave as stronger negative events and their amplitudes decrease with an incident angle corresponding to a class IV AVO pattern, and the bottom reflections present class I AVO anomalies.

The AVO characteristics are a function of the TOC content and mud content, which is interpreted by using a two-layer model. Both the TOC content and mud content will significantly increase the interceptions and slightly change the gradients of the P-P reflection coefficients. Moreover, the effects of the mud content on the AVO responses are greater than those of the TOC content on the AVO responses due to a larger variation of the mud content in comparison to the TOC content in the mud-rich source rock.

In the conclusion, we concern that the mud-rich source rock has the same elastic properties and seismic responses as the mudstone. To avoid the confusion about the mudstone, the spatial distribution of mudstones can first be identified, and then the TOC content is estimated to further discriminate the mud-rich source rock from the determined mudstone. Besides, the interference of the mudstone to the mud-rich source rock will be solved by decoupling the elastic responses of the mud content and TOC content in the future studies.

DATA AVAILABILITY STATEMENT

The data analyzed in this study is subject to the following licenses/restrictions: National confidential data. Requests to access these datasets should be directed to zhaoyunzong@yahoo.com.

AUTHOR CONTRIBUTIONS

ZZ and XY provided the ideas and experimental data of this paper, constructive comments for the paper, and reviewed and revised the manuscript. SY proposed the rock physical model of the mud-rich source rock, realized the numerical modeling and analysis of the rock physical model, completed the seismic forward modeling and AVO pattern analysis, and organized the content of article. All authors contributed to the article and approved the submitted version.

FUNDING

We would like to acknowledge the sponsorship of National Natural Science Foundation of China (41974119 and 42030103) and Science Foundation from Innovation and Technology Support Program for Young Scientists in Colleges of Shandong province and Ministry of Science and Technology of China.

REFERENCES

Aki, K., and Richards, P. G. (1980). *Quantitative Seismology: Theory and Methods*. San Francisco, CA: W.H. Freeman.

Alshakhs, M., and Rezaee, M. R. (2017). A new method to estimate total organic carbon (TOC) content, an example from goldwyer shale formation, the canning basin. *Open Petrol. Eng. J.* 10, 118–133. doi: 10.2174/1874834101710010118

Aplin, A. C., and Macquaker, J. H. S. (2011). Mudstone diversity: origin and implications for source, seal, and reservoir properties in petroleum systems. *AAPG Bull.* 95, 2031–2059. doi: 10.1306/03281110162

Avseth, P., and Carcione, J. M. (2015). Rock-physics analysis of clay-rich source rocks on the Norwegian Shelf. *Lead. Edge* 34, 1340–1348. doi: 10.1190/tle34111340.1

Avseth, P., Mukerji, T., and Mavko, G. (2010). *Quantitative Seismic Interpretation: Applying Rock Physics Tools to Reduce Interpretation Risk*. Cambridge, MA: Cambridge University Press.

Ba, J., Xu, W., Fu, L., Carcione, J. M., and Zhang, L. (2017). Rock anelasticity due to patchy saturation and fabric heterogeneity: a double double-porosity model of wave propagation. *J. Geophys. Res.* 122, 1949–1976. doi: 10.1002/2016JB013882

Backus, G. (1962). Long-wave elastic anisotropy produced by horizontal layering. *J. Geophys. Res.* 67, 4427–4440. doi: 10.1029/JZ067i011p04427

Badics, B., Avu, A., and Mackie, S. (2015). Assessing source rock distribution in heather and draupne formations of the Norwegian North Sea: a workflow using organic geochemical, petrophysical, and seismic character. *Interpretation* 3, SV45–SV68. doi: 10.1190/INT-2014-0242.1

Berryman, J. G. (1980). Long-wavelength propagation in composite elastic media II. Ellipsoidal inclusions. *J. Acoust. Soc. Am.* 68, 1820–1831. doi: 10.1121/1.385172

Berryman, J. G. (1995). Mixture theories for rock properties. *Rock Phys. Phase Relat.* 3, 205–228. doi: 10.1029/RF003p0205

Carcione, J. M. (2000). A model for seismic velocity and attenuation in petroleum source rocks. *Geophysics* 65, 1080–1092. doi: 10.1190/1.1444801

Carcione, J. M. (2001). AVO effects of a hydrocarbon source-rock layer. *Geophysics* 66, 419–427. doi: 10.1190/1.1444933

Carcione, J. M., and Avseth, P. (2015). Rock-physics templates for clay-rich source rocks. *Geophysics* 80, D481–D500. doi: 10.1190/geo2014-0510.1

Carcione, J. M., Helle, H. B. and Avseth, P. (2011). Source-rock seismic-velocity models: Gassmann versus Backus. *Geophysics.* 76: N37–N45. doi: 10.1190/geo2010-0258.1

Ciz, R., and Shapiro, S. A. (2007). Generalization of Gassmann equations for porous media saturated with a solid material. *Geophysics* 72, A75–A79. doi: 10.1190/1.2772400

Cui, J., Zhu, R., Li, S., Qi, Y., Shi, X., and Mao, Z. (2019). Development patterns of source rocks in the depression lake basin and its influence on oil accumulation: case study of the Chang 7 member of the Triassic Yanchang Formation, Ordos Basin, China. *J. Natural Gas Geosci.* 4, 191–204. doi: 10.1016/j.jnggs.2019.08.002

del Monte, A. A., Antonielli, E., De Tomasi, V., Luchetti, G., Paparozzi, E., and Gambacorta, G. (2018). Methods for source rock identification on seismic data: an example from the Tanezzuft Formation (Tunisia). *Mar. Petrol. Geol.* 91, 108–124. doi: 10.1016/j.marpetgeo.2017.12.015

Ding, J., Xiaozhi, C., Xiudi, J., Bin, W., and Jinmiao, Z. (2015). *Application of AVF Inversion on Shale Gas Reservoir TOC Prediction, 2015 SEG Annual Meeting*. New Orleans, LA: Society of Exploration Geophysicists.

Espitalié, J., Madec, M., Tissot, B., Mennig, J., and Leplat, P. (1977). "Source rock characterization method for petroleum exploration," in *Offshore Technology Conference* (Houston, TX: OnePetro). doi: 10.4043/2935-MS

Fertl, W. H., and Chilingar, G. V. (1988). Total organic carbon content determined from well logs. *SPE Form. Eval.* 3, 407–419. doi: 10.2118/15612-PA

Fertl, W. H., and Rieke, H. H. (1980). Gamma ray spectral evaluation techniques identify fractured shale reservoirs and source-rock characteristics. *J. Petrol. Technol.* 32, 2053–2062. doi: 10.2118/8454-PA

Gassmann, F. (1951). Elastic waves through a packing of spheres. *Geophysics* 16, 673–685. doi: 10.1190/1.1437718

Guo, Z., Li, X., Ren, Y., Chapman, M., and Shen, Y. (2013). "A rock physics workflow for the modeling of the effect of kerogen content and maturity level in shales," in *SEG Technical Program Expanded Abstracts 2013* (Houston, TX: Society of Exploration Geophysicists), 2948–2952. doi: 10.1190/segam2013-0458.1

Hansen, J. A., Mondol, N. H., and Fawad, M. (2019). Organic content and maturation effects on elastic properties of source rock shales in the Central North Sea. *Interpretation* 7, T477–T497. doi: 10.1190/INT-2018-0105.1

Hill, R. (1952). The elastic behaviour of a crystalline aggregate. *Proc. Phys. Soci.* 65:349. doi: 10.1088/0370-1298/65/5/307

Jiang, Y., and Zha, M. (2005). *Oil and Gas Geology and Exploration*. Beijing: Petroleum Industry Press, 78–95.

Kenomore, M., Hassan, M., Dhakal, H., and Shah, A. (2017). Total organic carbon evaluation of the Bowland Shale Formation in the Upper Bowland of the Widmerpool Gulf. *J. Petrol. Sci. Eng.* 150, 137–145. doi: 10.1016/j.petrol.2016.11.040

Keys, R. G., and Xu, S. (2002). An approximation for the Xu-White velocity model. *Geophysics* 67, 1406–1414. doi: 10.1190/1.1512786

Khoshnoodkia, M., Mohseni, H., Rahmani, O., and Mohammadi, A. (2011). TOC determination of Gadvan Formation in South Pars Gas field, using artificial intelligent systems and geochemical data. *J. Petrol. Sci. Eng.* 78, 119–130. doi: 10.1016/j.petrol.2011.05.010

Kiswaka, E. B., and Felix, M. (2020). Norwegian Sea area Permo-Triassic organic-carbon-rich deposits from seismic. *Mar. Petrol. Geol.* 119:104463. doi: 10.1016/j.marpetgeo.2020.104463

Lee, J., Lim, U. Y., and Lumley, D. (2020). "Improved TOC and lithology prediction for Wolfcamp shales using AVO attribute analysis," *Unconventional Resources Technology Conference. Unconventional Resources Technology Conference (URTeC)* (Denver, CO). doi: 10.15530/urtec-2020-1028

Løseth, H., Wensaas, L., Gading, M., Duffaut, K. and Springer, M. (2011). Can hydrocarbon source rocks be identified on seismic data? *Geology.* 39, 1167–1170. doi: 10.1130/G32328.1

Ma, Y., Fan, M., Lu, Y., Guo, X., Hu, H., Chen, L., et al. (2016). Geochemistry and sedimentology of the Lower Silurian Longmaxi mudstone in southwestern China: Implications for depositional controls on organic matter accumulation. *Mar. Petrol. Geol.* 75, 291–309. doi: 10.1016/j.marpetgeo.2016.04.024

Mahmoud, A. A., Elkatatny, S., Ali, A., Abdulraheem, A., and Abouelresh, M. (2020). "Estimation of the total organic carbon using functional neural networks and support vector Machine," in *International Petroleum Technology Conference* (Dhahran: OnePetro). doi: 10.2523/IPTC-19659-MS

Mahmoud, A. A., Elkatatny, S., Mahmoud, M., Abouelresh, M., Abdulraheem, A., and Ali, A. (2017). Determination of the total organic carbon (TOC) based on conventional well logs using artificial neural network. *Int. J. Coal Geol.* 179, 72–80. doi: 10.1016/j.coal.2017.05.012

Mavko, G., Mukerji, T., and Dvorkin, J. (2009). *The Rock Physics Handbook: Tools for Seismic Analysis of Porous Media*. Cambridge, MA: Cambridge University press. doi: 10.1017/CBO9780511626753

Mendelzon, J. D., and Toksoz, M. N. (1985). "Source rock characterization using multivariate analysis of log data," in *SPWLA 26th Annual Logging Symposium* (Dallas, TX: Society of Petrophysicists and Well-Log Analysts).

Modica, C. J., and Lapierre, S. G. (2012). Estimation of kerogen porosity in source rocks as a function of thermal transformation: example from the Mowry Shale in the Powder River Basin of Wyoming. *AAPG Bull.* 96, 87–108. doi: 10.1306/04111110201

Ogiesoba, O., and Hammes, U. (2014). Seismic-attribute identification of brittle and TOC-rich zones within the Eagle Ford Shale, Dimmit County, South Texas. *J. Petrol. Explor. Product. Technol.* 4, 133–151. doi: 10.1007/s13202-014-0106-1

Ostrander, W. J. (1984). Plane-wave reflection coefficients for gas sands at nonnormal angles of incidence. *Geophysics* 49, 1637–1648. doi: 10.1190/1.1441571

Pang, M., Ba, J., Carcione, J. M., Zhang, L., Ma, R., and Wei, Y. (2021). Seismic identification of tight-oil reservoirs by using 3D rock-physics templates. *J. Petrol. Sci. Eng.* 201:108476. doi: 10.1016/j.petrol.2021.108476

Passey, Q., Moretti, F., Kulla, J., Creaney, S., and Stroud, J. (1990). Practical model for organic richness from porosity and resistivity logs. *AAPG Bull.* 74, 1777–1794. doi: 10.1306/0C9B25C9-1710-11D7-8645000102C1865D

Passey, Q. R., Bohacs, K., Esch, W. L., Klimentidis, R., and Sinha, S. (2010). "From oil-prone source rock to gas-producing shale reservoir - geologic and petrophysical characterization of unconventional shale gas reservoirs," in

International Oil and Gas Conference and Exhibition in China (Beijing: Society of Petroleum Engineers). doi: 10.2118/131350-MS

Pichevin, L., Bertrand, P., Boussafir, M., and Disnar, J. R. (2004). Organic matter accumulation and preservation controls in a deep sea modern environment: an example from Namibian slope sediments. *Organic Geochem.* 35, 543–559. doi: 10.1016/j.orggeochem.2004.01.018

Rahmani, O., Khoshnoodkia, M., Kadkhodaie, A., Beiranvand Pour, A., and Tsegab, H. (2019). Geochemical analysis for determining total organic carbon content based on ΔLogR technique in the south pars field. *Minerals* 9:735. doi: 10.3390/min9120735

Sayers, C. M. (2013a). The effect of kerogen on the AVO response of organic-rich shales. *Lead. Edge* 32, 1514–1519. doi: 10.1190/tle32121514.1

Sayers, C. M. (2013b). The effect of kerogen on the elastic anisotropy of organic-rich shales. *Geophysics* 78, D65–D74. doi: 10.1190/geo2012-0309.1

Schmoker, J. W. (1979). Determination of organic content of appalachian devonian shales from formation-density logs. *AAPG Bull.* 63, 1504–1537. doi: 10.1306/2F9185D1-16CE-11D7-8645000102C1865D

Schmoker, J. W. (1981). Determination of organic-matter content of appalachian devonian shales from gamma-ray logs. *AAPG Bull.* 65, 1285–1298. doi: 10.1306/03B5949A-16D1-11D7-8645000102C1865D

Schmoker, J. W., and Hester, T. C. (1983). Organic carbon in Bakken formation, United States portion of Williston basin. *AAPG Bull.* 67, 2165–2174. doi: 10.1306/AD460931-16F7-11D7-8645000102C1865D

Shi, X., Wang, J., Liu, G., Yang, L., Ge, X., and Jiang, S. (2016). Application of extreme learning machine and neural networks in total organic carbon content prediction in organic shale with wire line logs. *J. Natural Gas Sci. Eng.* 33, 687–702. doi: 10.1016/j.jngse.2016.05.060

Tan, M., Song, X., Yang, X., and Wu, Q. (2015). Support-vector-regression machine technology for total organic carbon content prediction from wireline logs in organic shale: a comparative study. *J. Natural Gas Sci. Eng.* 26, 792–802. doi: 10.1016/j.jngse.2015.07.008

Tan, W., Ba, J., Müller, T., Fang, G., and Zhao, H. (2020). Rock physics model of tight oil siltstone for seismic prediction of brittleness. *Geophys. Prospect.* 68, 1554–1574. doi: 10.1111/1365-2478.12938

Tissot, B., Durand, B., Espitalié, J., and Combaz, A. (1974). Influence of nature and diagenesis of organic matter in formation of petroleum1. *AAPG Bull.* 58, 499–506. doi: 10.1306/83D91425-16C7-11D7-8645000102C1865D

Tissot, B. P., Pelet, R., and Ungerer, P. H. (1987). Thermal history of sedimentary basins, maturation indices, and kinetics of oil and gas generation. *AAPG Bull.* 71, 1445–1466. doi: 10.1306/703C80E7-1707-11D7-8645000102C1865D

Vernik, L. (2016). *Seismic Petrophysics in Quantitative Interpretation*. Tulsa: Society of Exploration Geophysicists. doi: 10.1190/1.9781560803256

Vernik, L., and Landis, C. (1996). Elastic anisotropy of source rocks: implications for hydrocarbon generation and primary migration. *AAPG Bull.* 80, 531–544. doi: 10.1306/64ED8836-1724-11D7-8645000102C1865D

Vernik, L., and Liu, X. (1997). Velocity anisotropy in shales: a petrophysical study. *Geophysics* 62, 521–532. doi: 10.1190/1.1444162

Vernik, L., and Milovac, J. (2011). Rock physics of organic shales. *Lead. Edge* 30, 318–323. doi: 10.1190/1.3567263

Vernik, L., and Nur, A. (1992). Ultrasonic velocity and anisotropy of hydrocarbon source rocks. *Geophysics* 57, 727–735. doi: 10.1190/1.1443286

Xu, M., Yin, X., Zong, Z., and Li, H. (2020). Rock-physics model of volcanic rocks, an example from Junggar Basin of China. *J. Petrol. Sci. Eng.* 195:107003. doi: 10.1016/j.petrol.2020.107003

Xu, S., and White, R. E. (1995). A new velocity model for clay-sand mixtures1. *Geophys. Prospect.* 43, 91–118. doi: 10.1111/j.1365-2478.1995.tb00126.x

Yin, L., Yin, X., Zong, Z., Chen, B., and Chen, Z. (2020). A new rock physics model method for shale on the theory of micro-nanopores. *Chin. J. Geophys.* 63, 1642–1653. doi: 10.3997/2214-4609.202010308

Yin, X., Zong, Z., and Wu, G. (2015). Research on seismic fluid identification driven by rock physics. *Sci. China Earth Sci.* 58, 159–171. doi: 10.1007/s11430-014-4992-3

Zargari, S., Prasad, M., Mba, K. C., and Mattson, E. D. (2013). Organic maturity, elastic properties, and textural characteristics of self resourcing reservoirs. *Geophysics* 78, D223–D235. doi: 10.1190/geo2012-0431.1

Zhao, L., Qin, X., Han, D. H., Geng, J., Yang, Z., and Cao, H. (2016). Rock-physics modeling for the elastic properties of organic shale at different maturity stages. *Geophysics* 81, D527–D541. doi: 10.1190/geo2015-0713.1

Zhao, P., Ma, H., Rasouli, V., Liu, W., Cai, J., and Huang, Z. (2017). An improved model for estimating the TOC in shale formations. *Mar. Petrol. Geol.* 83, 174–183. doi: 10.1016/j.marpetgeo.2017.03.018

Zhao, P., Mao, Z., Huang, Z., and Zhang, C. (2016). A new method for estimating total organic carbon content from well logs. *AAPG Bull.* 100, 1311–1327. doi: 10.1306/02221615104

Zhou, J., Yin, X., and Cao, D. (2015). Research on fine layering method of acoustic log data in the process of scale matching between acoustic log data and seismic data. *Comput. Tech. Geophys. Geochem. Explor.* 37, 242–248.

Zhu, G., and Jin, Q. (2003). Using logging information to evaluate the geochemical characteristics of source rocks. *Geosci. Front.* 10, 494–494.

Zong, Z., Yin, X., and Wu, G. (2015). Geofluid discrimination incorporating poroelasticity and seismic reflection inversion. *Surv. Geophys.* 36, 659–681. doi: 10.1007/s10712-015-9330-6

Conflict of Interest: The authors declare that the research was conducted in the absence of any commercial or financial relationships that could be construed as a potential conflict of interest.

Copyright © 2021 Yu, Zong and Yin. This is an open-access article distributed under the terms of the Creative Commons Attribution License (CC BY). The use, distribution or reproduction in other forums is permitted, provided the original author(s) and the copyright owner(s) are credited and that the original publication in this journal is cited, in accordance with accepted academic practice. No use, distribution or reproduction is permitted which does not comply with these terms.

frontiers in Earth Science

ORIGINAL RESEARCH
published: 26 April 2021
doi: 10.3389/feart.2021.641815

How Nanopores Influence Dry-Frame V_P Pressure Sensitivity

Rohit Raj[1], Priyank Jaiswal[1], Yulun Wang[1], G. Michael Grammer[1] and Ralf J. Weger[2]*

[1]Boone Pickens School of Geology, Oklahoma State University, Stillwater, OK, United States, [2]Comparative Sedimentology Laboratory (CSL)–Center for Carbonate Research, Rosenstiel School of Marine and Atmospheric Science, Department of Marine Geosciences, University of Miami, Miami, FL, United States

This paper investigates how nanopore size distribution influences dry-frame P-wave velocity (V_P) pressure sensitivity. The study uses a set of twenty-three samples belonging to a single vertical core from the Mississippian-age Meramec formation of the mid-continent US. Individual samples had their facies interpreted, composition estimated, He-gas porosity (Φ_{He}) determined, and P-wave and S-wave transit times systematically measured for dry core-plugs in a 5–40 MPa loading and unloading cycle. Data from the unloading cycle were linearized in the log scale, and the slope of the best fitting line was considered as a representative of the dry-frame V_P pressure sensitivity. A series of photomicrographs from each sample were analyzed using image processing methods to obtain the shape and size of the individual pores, which were mostly in the nanopore (10^{-6}–10^{-9} m) scale. At the outset, the pore-shape distribution plots were used to identify and discard samples with excessive cracks and complex pores. When the remaining samples were compared, it was found that within the same facies and pore-shape distribution subgroups V_P pressure sensitivity increased as the dominant pore-size became smaller. This was largely independent of Φ_{He} and composition. The paper postulates that at the nanopore scale in the Meramec formation, pores are mostly isolated, and an increase in the confining pressure increased the bulk moduli of the fluids in the isolated pores, which in turn increased the V_P pressure sensitivity. The study proposes incorporating this effect quantitatively through a dual-fluid model where the part of the fluid in unconnected pores is considered compressible while the remaining is considered incompressible. Results start to explain the universal observation of why the presence of microporosity quintessentially enhances V_P pressure sensitivity.

Keywords: digital image analysis (DIA), nanopores, Pwave velocity (VP), dynamic modulus, pore architecture

OPEN ACCESS

Edited by:
Beatriz Quintal,
University of Lausanne, Switzerland

Reviewed by:
Kyle Spikes,
University of Texas at Austin, United States
Ken Ikeda,
The University of Texas at Austin, United States

****Correspondence:***
Priyank Jaiswal
priyank.jaiswal@okstate.edu

Specialty section:
This article was submitted to Solid Earth Geophysics, a section of the journal Frontiers in Earth Science

Received: *15 December 2020*
Accepted: *03 February 2021*
Published: *26 April 2021*

Citation:
Raj R, Jaiswal P, Wang Y, Grammer GM and Weger RJ (2021) How Nanopores Influence Dry-Frame V_P Pressure Sensitivity. Front. Earth Sci. 9:641815. doi: 10.3389/feart.2021.641815

INTRODUCTION

Rocks resist bulk deformation against pressure. This property, known as the bulk modulus (K), is a measure of the volume change with respect to a change in the confining pressure. In a porous material, the change of K is not linear with pressure (Robin, 1973; Hart and Wang, 1995; Zhang et al., 2019). Why and how K changes with loading can provide critical insights into the drainage and injection behavior of reservoir rocks, which in turn is necessary for production and sequestration (Angerer et al., 2002; Vanorio et al., 2011; Vanorio, 2015). Volumetric strain can be measured directly in axial loading experiments yielding what is referred to as the "static" modulus. However, measuring small strains in static loading can be difficult and the experiments are often destructive. A

common practice is to instead measure the P-wave (V_P) and S-wave (V_s) velocities at ultrasonic frequencies over loading and unloading cycles and, using standard relationships, obtain what is referred to as the "dynamic" modulus (Nur and Simmons, 1969; Martínez-Martínez et al., 2012; Asef and Najibi, 2013). For elastic material such as steel, the static and dynamic moduli are essentially the same. For dry porous rocks, however, one reason of the difference between the two is due to a difference in how rock responds to rate and magnitude of loading (Mashinsky, 2003; Fjær et al., 2013; Fjær, 2019). For example, the strain rate induced by axial loading (typically, 10^{-6} s^{-1}) is much lower than that induced by ultrasonic frequencies (typically, 10^{-1} s^{-1}) (Fjær et al., 2013; Fjær, 2019) while the strain amplitude in axial loading is higher, e.g., 10^{-2} to 10^{-1} vs. 10^{-7} to 10^{-6} (Batzle et al., 2006; Fjær, 2019; Muqtadir et al., 2020). Likewise, parts of the rock that accommodate that static stress, e.g., compliant features such as a crack (Han et al., 2016), are different than the parts that contribute to the elastic stress propagation, e.g., grain contacts. Other experimental conditions such as dispersion and drainage can also set dynamic and static moduli apart. Regardless, the goal of geomechanical measurements is not as much to reconcile the two kinds of moduli as to use them for understanding different aspects of the rock and gain predictability of its behavior. This paper focuses on understanding how the pore-size distribution affects the rate at which V_P changes with confining pressure, hereafter referred to as pressure sensitivity.

Static measurements provide stress-strain relationships that can be used for investigating fatigue, relaxation, creep, and rupture. Dynamic measurements provide elastic velocities that can be in turn related to the rock texture and fluid dynamics. Several elastic and elastoplastic models that formulate moduli and velocity in terms of measurable properties such as bulk porosity (Φ) and composition can be explored to explain both static and dynamic modulus and gain insights into the mechanistic nature of the rock (Mavko et al., 2020). However, challenges remain. Why stress-strain relationships in static experiments with simple Hookean porous rocks are often more non-linear than what is expected from their moduli and texture, remains debated (Morgenstern and Phukan, 1969; Biot, 1973; Darling et al., 2004). Similarly, while velocities at a given pressure can be modeled under a set of mechanistic assumptions, being able to explain the entire hysteresis with the same mechanistic model has been rarely done. In dynamic measurements, empirical relationships most commonly emerge between V_P pressure sensitivity, and pore topology (Eberhart-Phillips et al., 1989; Prasad and Manghnani, 1997; Kirstetter and MacBeth, 2001; David and Zimmerman, 2012). Static experiments also indicate that the nature of the stress-strain curve can be strongly influenced by the pore topology (Fredrich et al., 1993; Davis et al., 2017). To date, however, for explaining both the dynamic and static results the emphasis has been on using the bulk value of porosity rather than the pore architecture, distribution, or connectivity.

In general, both moduli and velocity of a porous material have several dependencies. Closed-form expressions that view rock as a continuous medium with an even distribution of regular pores can explain the role of key causations such as the composition (grains and fluids) and Φ. Cracks, grain boundaries, and geometrical irregularities are difficult to include in a continuum and are therefore often treated as boundary conditions or an end member problem (Pyrak-Nolte et al., 1990; Liu et al., 2000; Pyrak-Nolte and Morris, 2000). Interestingly, when it comes to the V_P pressure sensitivity, end members might outweigh the contribution of composition and Φ. Assuming that the grains remain intact, it is commonly accepted that increase in V_P due to loading is mainly due to the closure of cracks and grain boundaries (Darot and Reuschlé, 2000; Freund, 1992; Prasad and Manghnani, 1997) or change in grain arrangement (Kitamura et al., 2010). In this context, the role of microporosity (pores smaller than what Optical Light Microscopy can discern; ~30 μm; Baechle et al., 2008) seems to be critical. Despite constituting only a small fraction of Φ their presence is known to strongly influence V_P pressure sensitivity (de Oliveira et al., 2016; Wang et al., 2015) and possibly both strain rate and amplitude during loading. Microporosity makes the rock behave differently at low and high pressure naturally prompting researchers to conceive dual-porosity models, e.g., Ba et al. (2008), to explain the rock behavior across the entire range of confining pressure. Why and how the presence of pores that are smaller than a certain dimension should affect static or dynamic moduli differently than the rest of the porosity remains unclear.

Unlike that of composition and Φ, understanding the effect of pore shape and size on static or dynamic moduli is not straightforward. Pore aspect ratio (major (l) over minor (w) axis), their orientation, and complexity (perimeter (P_e) over area (A_r)) are theoretically expected to explain how stress accumulates and the material is strained (Zimmerman et al., 1986). Although, their experimental confirmation is widely available (Weger et al., 2009; Weibo et al., 2020), the extent of their exclusivity remains unclear. For example, compressibility might not always be tied to geometry, i.e., the set of compliant features have a large intersection with the set of features that have a high aspect ratio, but they are not identical. The role of the size distribution probably remains even less explored. With a set of synthetic carbonate samples, Wang et al. (2015) have shown how size affects velocity, which may be a function of the dominant wavelength. In the meso-to-micro range (4 mm–1 μm), Weger et al. (2009) found that ultrasonic V_P increased as the pores became larger and less complex. On the other hand, in the micro-to-nano range (62.5 μm–1 nm), Raj et al. (2019) discovered the opposite; they noted that the ultrasonic V_P increased as the dominant pore size decreased. A key difference between the two experiments was that Weger et al. (2009) samples were saturated while Raj et al. (2019) samples were dry. Another difference was that while Weger et al. (2009) compared samples of vastly different pore architectures, Raj et al. (2019) first classified their sample facies-wise and then composition-wise, ensuring that samples of similar pore architecture are compared. Regardless, both studies showed that, at least in the

carbonate rocks, the pore-size distribution might play an equally important role in determining the V_P as does Φ.

Almost all existing studies on V_P pressure sensitivity have used rocks with pore-size dominantly in the meso- or larger scale. This paper extends the line of inquiry started by Raj et al. (2019) and fills the knowledge gap of examining how nanopores affect dry-frame V_P pressure sensitivity. Raj et al. (2019) demonstrated the effect of pore-size distribution on V_P with samples from the Mississippian age mixed carbonate-siliciclastic reservoir rocks from the mid-continent, United States, commonly known as the "Miss Lime" formation. This paper uses samples from the distal equivalent of Miss Lime, known as the Meramec formation. The dataset in this paper comprises X-ray diffraction (XRD)-based composition, Φ_{He} from helium injection porosimetry, ultrasonic velocities of ~1.5-inch dry core plugs over 5–40 MPa loading and unloading cycle, and pore-size distribution from Digital Image Analysis (DIA) of Scanning Electron Microscopy (SEM) photomicrographs of twenty-three samples. Although the results are presented in the context of dynamic modulus, the idea can be extended to understand static measurements as well.

STUDY AREA

The study area, which is in present-day Oklahoma, was situated 10°–15° south of the paleo equator in the Mississippian epoch (359–323 Ma) (Lane and De Keyser, 1980; Blakey, 2013; Mazzullo et al., 2011). The Mississippian epoch was a transitional period moving from a greenhouse to an icehouse environmental condition that resulted in an overall regressive coastline (Buggisch et al., 2008; Haq and Schutter, 2008). This led to the development of an extensive east-west trending carbonate shelf on a shallow tropical epeiric sea over Devonian-age Woodford shale (Gutschick and Sandberg, 1983). The architecture of this shelf was dominated by both tectonism and higher-order eustatic sea-level changes resulting in high-frequency transgressive-regressive shallowing upward cycles (Childress and Grammer, 2015; Mazzullo et al., 2011; Watney et al., 2001). The shelf development ceased in the late Mississippian due to uplift and erosion associated with Gondwana and Euramerica collision. The Mississippian strata record a transition in composition from the shallow-water Miss Lime carbonates in the north (Watney et al., 2001) to deep-water mixed carbonate-siliciclastic sediments in the Anadarko and Ardmore basin in the south (Price et al., 2017). Currently, from north to south, several laterally and vertically varying proximal and distal facies comprising various permutations of limestones, chert, and silicified limestone with depositional and diagenetic pore systems are found with a gradation in grain size and mineral chemistry depending on their distance from the shoreline.

The Mississippian-age reservoirs are mainly sourced by the underlying Devonian-age Woodford shale and ultimately capped by the overlying Pennsylvanian-age transgressive shale. The core used in this study lies in the Meramec formation of the Sooner Trend Anadarko Canadian and Kingfisher (STACK) play in the Anadarko Basin. At the core location (**Figure 1**), the Meramec formation is located above the Devonian-age Woodford (Shale) formation and is overlain by Pennsylvanian-age shale units. Compositionally, the Meramec formation is a mixed carbonate-siliciclastic system with Φ in the range of 1–6% and permeability in the range of 0.1–10 mD (Almasoodi et al., 2020). The main reason why the Meramec formation is gaining popularity with the operators is its overpressured nature and low water content that resulting in high initial production (IP) rate (Chopra et al., 2018). The sustained production, such as in the other tight reservoirs, however, requires a detailed understanding of the pore architecture and connectivity.

DATASET

The core used for this study is located in Canadian County, Oklahoma, and contained ~152.5 m (500 ft) thick Meramec formation. First, the Meramec facies were interpreted. Then, within the access restrictions, 23 core plugs with 1.5-inch (3.8 cm) diameter and ~2 in (5.1 cm) length were extracted ensuring that the key facies were adequately sampled. A small (~0.5 cm) portion from one end was sawed and separated for XRD and SEM photomicrography, and the remainder of the core plug was used for ultrasonic transit-time measurement under loading and unloading conditions and Φ_{He} measurement using helium gas porosimetry.

Facies

In the core, the start and end of the Meramec formation was identified using color change from the bounding Devonian and the Pennsylvanian shales (LeBlanc, 2014; Vanden Berg and Grammer, 2016). Within the Meramec Formation, the facies interpretation was based on differences in texture, composition, sedimentary structures, trace fossils (MacEachern et al., 2009) and color (Geological Society of America, 1995). Three facies, hereafter referred to as A, B, and C, were dominant in the core (**Figure 2**). Facies A (**Figure 2A**) was laminated siltstone and had millimeter thick black dark brown mud rich and gray calcite-rich layering. It had scattered trace fossils with a variable abundance of brachiopods and crinoids. Facies B (**Figure 2B**) was a massive-bedded packstone-grainstone. It was grayish with a dominant massive-bedded structure and had abundant skeletal trace fossil fragments of brachiopods, crinoids, and peloids. Facies C (**Figure 2C**) was a hummocky cross-stratified and planar-laminated packstone-grainstone. It was darker than Facies B and was abundant in skeletal trace fossil fragments of brachiopods, crinoids, and peloids.

Photomicrographs

For DIA, a small portion from the 0.5 cm disk was cut and polished using a JEOL IB-19500 CP argon-ion mill machine. The ion-milled samples were kept in a vacuum for 2 h and sputter-coated with gold/palladium coating using a Balzers MED 010 machine for 20 s. The photomicrographs were captured with FEI Quanta 600F field emission SEM (**Figure 3A**). The photomicrographs were then analyzed in grayscale using the Leica's Application Suite (LAS). Typically, pores and organic

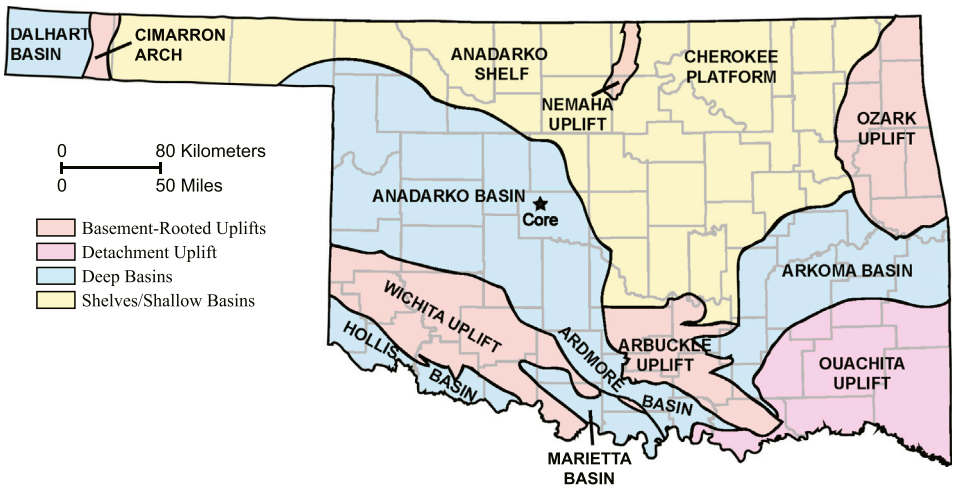

FIGURE 1 | Base Map. Major geological features and county lines within the state boundary of Oklahoma are labeled (after Northcutt and Campbell, 1996). Solid star is the core location in Canadian County.

matters appear as darker features whereas grains appear as lighter features in SEM photomicrographs. At core location, it is unlikely to contain organic matter (Miller et al., 2019). So, whenever possible, as a rule of thumb, the darker features were interpreted as "pores" while the lighter features were considered as "grains" (**Figure 3B**). Occasionally, when the distinction of boundary between pores and grains was not obvious, coherency filters were used to make the parts of the image clearer. All photomicrographs were analyzed individually, and every step of DIA was carefully monitored to avoid imaging and interpretational artifacts.

The software measured P_e, A_r, l and w of an individual pore in terms of pixels (inset; **Figure 3B**). All pixels along the periphery of a pore contributed to P_e, and all pixels lying within and on the pore-periphery contributed to A_r. The l and w of the pore were the length and width of a rectangle that tightly enclosed the pore. The spatial orientation of the rectangle was not relevant to the analysis in this paper. After counting the pixels, the software assigned a metric length or size to individual features using the magnification set by the user. In this application, 1.5 nm was heuristically set as the limit of resolution of the SEM photomicrographs, and features below this size were not interpreted. Finally, for every sample, a database with the architectural parameters of all the pores interpreted in its photomicrographs was created.

Ultrasonic V_P

Transit times corresponding to P- and two independent orthogonally polarized S-waves were recorded for all core plugs in dry conditions using New England Research Autolab 1000. Saturated-rock measurements were not attempted because of the difficulties in ensuring that samples achieve a complete saturation. Each plug was inserted in a rubber sleeve before setting it between a transducer-receiver assembly. The entire assembly was then put inside a pressure chamber filled with mineral oil. The central frequency of the transducer generated wave signals was 1 MHz for both P- and S-waves. The confining pressure within the pressure chamber was systematically and gradually increased from 5 MPa to 40 MPa (loading) and then decreased to 5 MPa (unloading). Assuming a hydrostatic gradient of 3.102 kPa/ft (10.18 kPa/m), this pressure range was intended to mimic a burial depth from ~1612 ft to ~12,895 ft which encompassed the reservoir depth in the core of 10400–10900 ft (~3170–3322 m). Transit times were recorded at 5, 10, 15, 20, 30, and 40 MPa in both segments (**Figure 4A**). Measurements at 30 MPa best corresponds to the reservoir conditions which, assuming a hydrostatic gradient, varied from 32.27 MPa to 33.81 MPa. First arrivals in the waveforms were picked manually and converted to velocities using the known sample dimension and instrument-related parameters (**Figure 4B**). The average uncertainty due to first arrival time picking of P-wave and S-waves were less than 1.25% and 2%, respectively. Only unloading cycle measurements are used in this paper following the common practice in the art where it is assumed that the loading cycle has permanently closed stress cracks that originated from the core first being exposed to the atmospheric conditions.

He-gas Porosity

Φ_{He} measurement was done using a helium gas injection technique on all core plugs using an AccuPyc II 1340 Pycnometer. The pycnometer uses helium-gas displacement to measure solid phase volume. The instrument has a sample chamber and a precision chamber. The core plug was put first in a compartment of known volume, which was then placed in the sample chamber and sealed. Helium filled the sample chamber and equilibrated. The gas was then allowed to flow into the precision chamber and equilibrate. The pressure-drop as a result of discharge of helium-gas into the empty precision chamber from the sample chamber provides the solid phase volume. Before using the pycnometer, the bulk volume of the core plugs was estimated by measuring diameter and length with a vernier caliper. Φ_{He} is the ratio of the difference between the bulk and

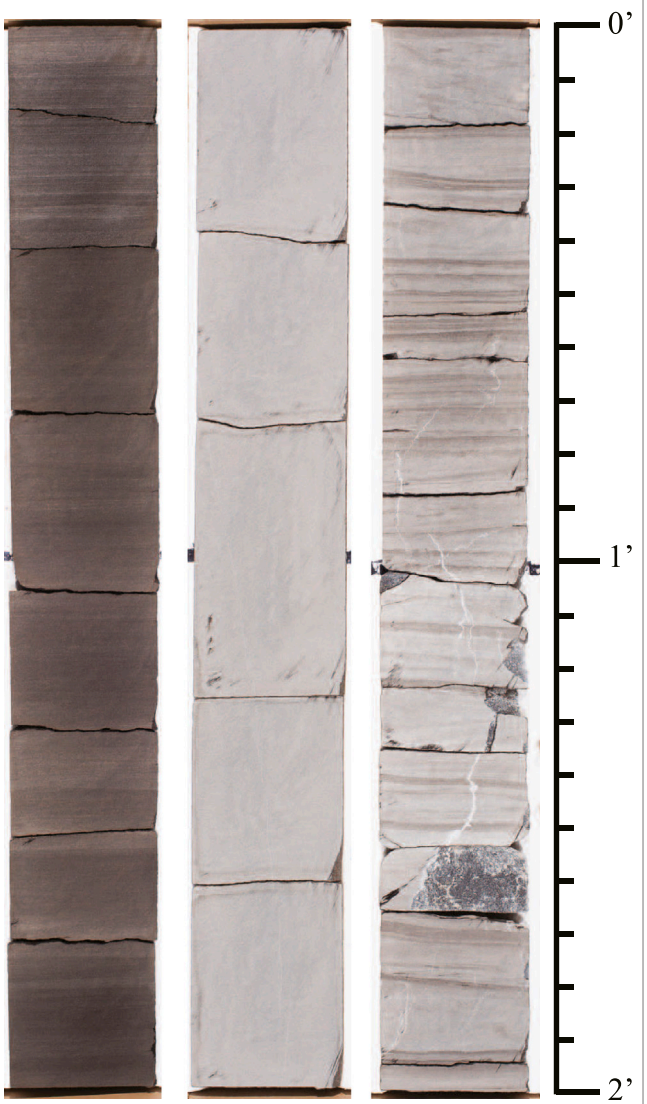

FIGURE 2 | Facies. **(A) A**: mudstone to siltstone with scattered sedimentary features such as lamination, burrowing and bioturbations, **(B) B**: massive bedded packstone to grainstone, and **(C) C**: hummocky cross-stratified-planar laminated packstone to grainstone. Transitions From **(A)** to **(C)**, facies represent a change from distal to proximal shelf depositional environment.

the solid phase volume and the bulk volume. Data are mentioned in **Tables 1–3**.

Composition

Mineralogy was quantified using XRD. First, the samples were powdered in SPEX ball mill. Powdered samples were then analyzed in Rigaku MiniFlex Diffraction instrument. A quartz sample was used to calibrate the machine before analyzing any sample. Mineralogy was identified using standard Powder Diffraction File and quantified using Rietveld refinement scheme in RIQAS software. Data are tabulated in **Tables 1–3**.

DATA ANALYSIS

We had eleven samples in facies A, and six each in B and C, respectively. We fitted the unloading cycle of the P-wave with the following linear trend (**Supplementary Figures S3–S6**):

$$V_P(P_C) = s + r_P \log_{10}(P_C) \quad (1)$$

where s and r_P are the intercept (measurement at 5 MPa) and gradient, respectively, and P_C is confining pressure. For the purpose of this paper, r_P represents the V_P pressure sensitivity. **Equation 1** could be fit to data from all samples with sufficiently high correlation ($R^2 > 0.95$).

Contoured two-dimensional (2D) histograms were used to analyze the pore shape and size distribution for every sample. Two sets of plots were generated. The first set was along the lines of **Figure 3C**, which is a crossplots between $\log_{10}A_r$/$\log_{10}P_e$ and $\log_{10}$(l/w), binned to best preserve the continuity of the distribution. A bin size of 20 was found to be optimal for this kind of plot. Visualizing data in this manner provided an overview of the pore-shape distribution without much regard to their size. Displaying the pore architectural parameters along the lines of **Figure 3C** was necessary to identify samples with excessive cracks and complex pores. Because these features strongly affect V_P pressure sensitivity, it was necessary to discard such samples for this paper to avoid bias. Samples discarded using **Figure 3C** as a guide are shown in **Supplementary Figure S2**. This reduced the number of samples for further analysis to five in Facies A (**Figure 5**), five in Facies B (**Figure 6**), and four in Facies C (**Figure 7**). The second set of plots were along the lines of **Figure 3D**, which is a crossplots between $\log_{10}A_r$ and $\log_{10}P_e$ of the individual pores, binned to best preserve the continuity of the distribution, e.g., Raj et al. (2019). Visualizing data in this manner provided an overview of the pore-size distribution without much regards to the shape. A bin size of 15 was found to be optimal for this kind of plot.

Raj et al. (2019) classified their samples first based on facies and then their composition. In this paper we use the pore-shape distribution instead of composition as the second criterion for two reasons. First, samples in this paper were not as compositionally diverse as Raj et al. (2019), and second, a peer study, Baechle et al. (2008), found that pore-shape rather than the composition may have a stronger influence on V_P pressure sensitivity. Within each facies, broad pore-shape subgroups were identified and within each subgroup, samples were arranged in increasing order of r_P.

In Facies A two pore-shape groups, G_{AI} and G_{AII}, were interpreted (**Figure 5**). Group G_{AI} (**Figures 5A.1, 5A.2**) dominantly have pores with an aspect ratio ~1.7 and a subset that extends into the complex and elongated domain with a pore aspect ratio of as much as up to 10. Group G_{AII} (**Figures**

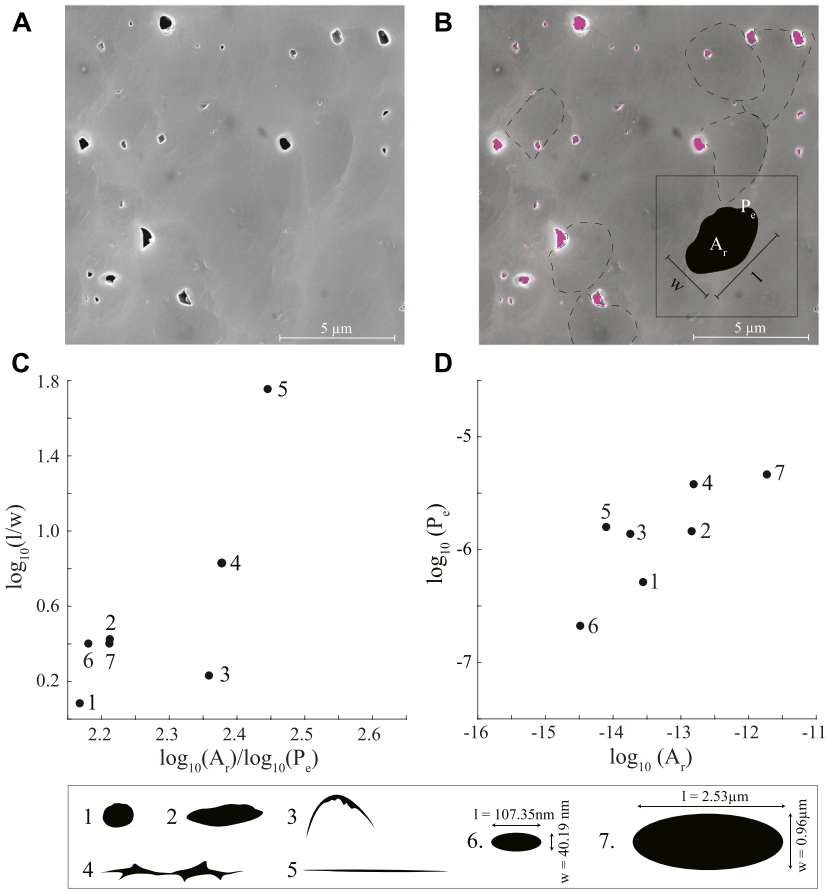

FIGURE 3 | Digital Image Analysis (DIA). **(A)** Representative SEM photomicrograph, **(B)** same as **(A)** showing pores identified by DIA in solid color and grain boundaries in dashed line. Inset shows the cartoon of a pore and its architectural parameters, length [l], width [w], area [A_r] and perimeter [P_e], that are measured by DIA, **(C)** $\log_{10}(A_r)/\log_{10}(P_e)$ vs. $\log_{10}$ (l/w), and **(D)** $\log_{10}(A_r)$ vs. $\log_{10}(P_e)$ crossplots for pores of different shapes and sizes numbered 1–7 shown in the lowest panel. Note that shapes are better resolved in **(C)** while sizes are better resolved in **(D)**.

5C.1–C.3) dominantly have pores with an aspect ratio between ~1.6 and an overall tendency of the pores to remain concentrated around this geometrical shape. The pore-size distribution plots for Group G_{AI} (**Figures 5B.1, 5B.2**) show a decrease in the dominant pore size depicted by a shift in the warmest color as r_P increases from 96.3 to 100.9. Changes in the pore-size distribution plots for Group G_{AII} are more subtle. From **Figure 5D.1** to **Figure 5D.2**, as r_P increase from 62.0 to 107.9, the dominant size does not change as much, e.g., the dominant pore size maintains its location, but the pore population includes more pores that are smaller than the smallest pore in **Figure 5D.1**. Likewise, From **Figure 5D.2** to **Figure 5D.3**, as r_P increase from 107.9 to 114.7, the overall distribution does not change but the dominant pore size becomes more pronounced.

In Facies B two pore-shape groups, G_{BI} and G_{BII}, are interpreted (**Figure 6**). Group G_{BI} (**Figures 6A.1, 6A.2**) dominantly have pores with an aspect ratio between ~1.8 and ~2.5 and a subset that extends into the complex and elongated domain with a pore aspect ratio of as much as up to 16. Group G_{BII} (**Figures 6C.1–C.3**) dominantly have pores with an aspect ratio between ~1.7 and ~2.3 and an overall tendency of the pores to remain concentrated around this geometrical shape with a pore aspect ratio below 10. The pore-size distribution plots for Group G_{BI} (**Figures 6B.1, 6B.2**) show an overall decrease in the dominant pore size without much change in the pore-size distribution as r_P increases from 159.4 to 236.6. Changes in the dominant pore-size distribution for Group G_{BII} are more obvious although the overall pore-size distribution itself does not change much. From **Figure 6D.1** to **Figure 6D.2**, as r_P increase from 87.4 to 187.5, the dominant pore size shift toward smaller size and becomes more pronounced. Likewise, from **Figure 6D.2** to **Figure 6D.3**, as r_P increase from 187.5 to 200.0, the dominant pore size shifts toward the smaller size.

In Facies C as well, two pore-shape groups, G_{CI} and G_{CII}, are interpreted (**Figure 7**). Group G_{CI} (**Figures 7A.1, 7A.2**) dominantly have pores with an aspect ratio ~1.4 and an overall tendency of the pores to remain concentrated around this geometrical shape with an aspect ratio below 6.5. Group G_{CII} (**Figures 7C.1, 7C.2**) dominantly have pores with aspect ratio ~1.9 and an overall tendency of the pores to remain concentrated around this geometrical shape with pore aspect ratio below 10.

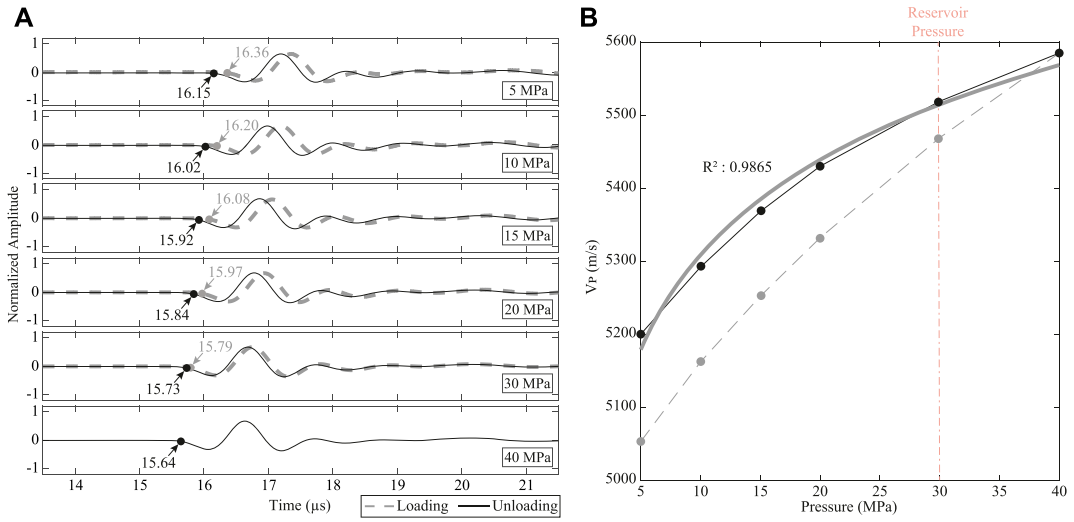

FIGURE 4 | P-wave velocity (V_P) estimation. **(A)** Representative ultrasonic waveforms for loading (dashed gray) and unloading (solid black) segments. The corresponding gray and black dots are the interpreted P-wave first arrival times, which are then converted to V_P based on known sample length and instrument calibration constants. Confining pressures for individual waveforms are mentioned. **(B)** V_P pressure sensitivity for loading (dashed gray) and unloading (solid black) segments. The thick gray line represents a function of the form $V_P(P_C) = s + r_P \log_{10}(P_C)$ that is fit to the unloading cycle. For unloading segment of **(A)**, a high correlation coefficient ($R^2 = 0.9865$) is obtained. The process is repeated for P-, S1- and S2-waves for all 23 samples (**Supplementary Figures S3–S14**). A high value of r_p implies a higher-pressure sensitivity.

TABLE 1 | Facies A sample properties.

Group	Panel	Depth (ft)	Porosity (%)	Quartz (%)	Carbonate (%)	Clay (%)	Others (%)	r_P	r_{S1}	r_{S2}
G_{AI}	**A.1 and B.1**	10450.20	3.70	48.5	3.4	30.5	17.6	96.3	41.9	41.5
	A.2 and B.2	10670.30	3.70	47.1	12.0	22.9	18.0	100.9	36.1	28.4
G_{AII}	**C.1 and D.1**	10826.30	1.25	47.6	20.7	18.2	13.5	62.0	115.5	76.6
	C.2 and D.2	10630.15	3.28	48.0	16.9	17.3	17.8	107.9	25.3	31.2
	C.3 and D.3	10532.00	3.83	54.9	19.7	12.1	13.3	114.7	28.1	30.6

TABLE 2 | Facies B sample properties.

Group	Panel	Depth (ft)	Porosity (%)	Quartz (%)	Carbonate (%)	Clay (%)	Others (%)	r_P	r_{S1}	r_{S2}
G_{BI}	**A.1 and B.1**	10640.25	2.07	26.6	57.5	6.4	9.5	159.4	69.0	69.3
	A.2 and **B.2**	10639.90	2.41	30.7	53.4	5.7	10.2	236.6	84.4	84.5
G_{BII}	**C.1 and D.1**	10694.15	1.11	31.7	54.8	4.2	9.3	87.7	28.3	34.6
	C.2 and D.2	10696.00	2.09	34.7	55.3	3.2	6.8	187.5	76.6	74.7
	C.3 and D.3	10650.15	4.16	52.4	27.1	7.1	13.4	200.0	114.5	124.0

TABLE 3 | Facies C sample properties.

Group	Panel	Depth (ft)	Porosity (%)	Quartz (%)	Carbonate (%)	Clay (%)	Others (%)	r_P	r_{S1}	r_{S2}
G_{CI}	**A.1 and B.1**	10580.90	2.66	47.0	38.0	4.6	10.4	112.4	44.0	49.0
	A.2 and B.2	10700.15	2.96	37.3	47.5	3.8	11.4	243.4	85.0	122.9
G_{CII}	**C.1 and D.1**	10490.15	2.80	47.8	33.3	6.6	12.3	55.9	25.9	21.0
	C.2 and D.2	10600.85	2.31	45.4	30.2	10.5	13.9	73.9	25.8	49.3

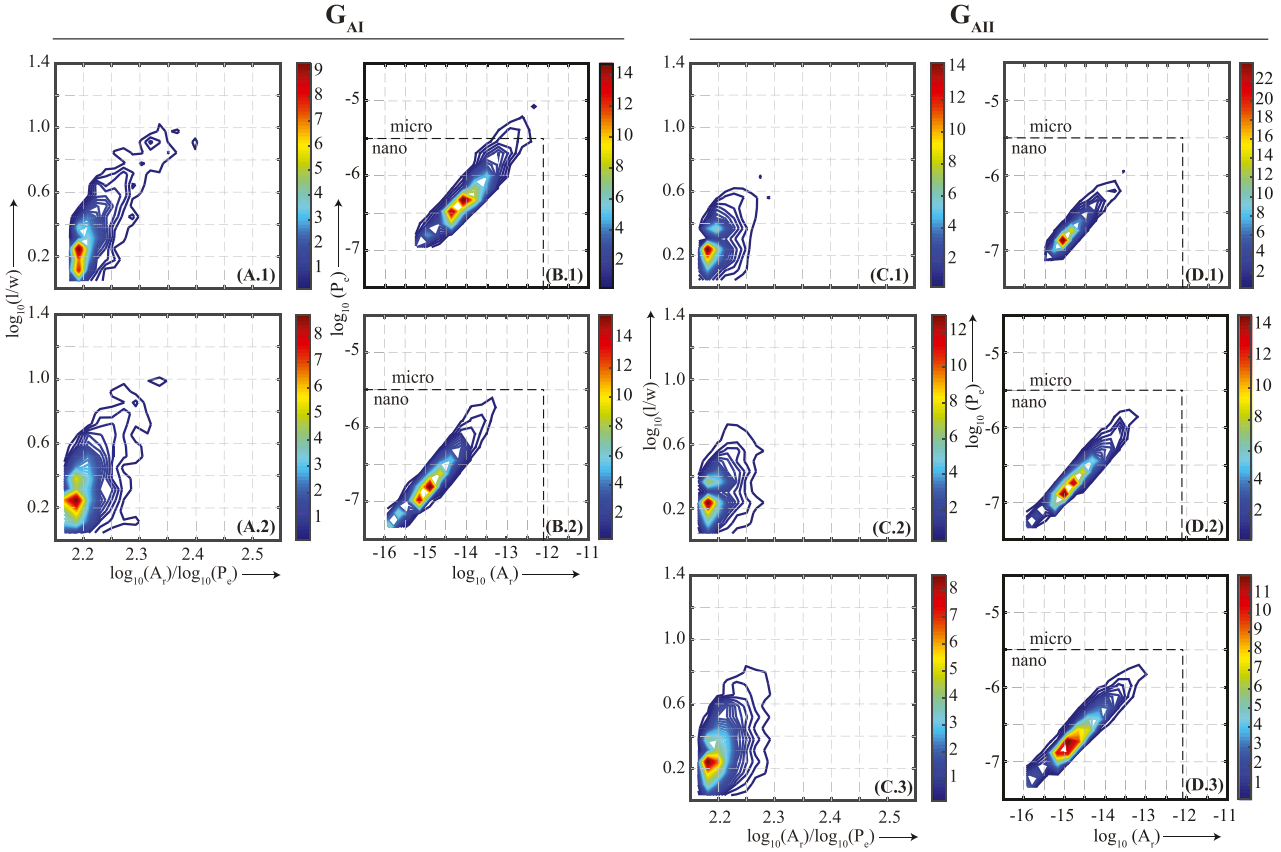

FIGURE 5 | Facies **A**. Contoured histograms of pore l, w, A_r, and P_e are binned and plotted along the lines of **Figure 3C** to visualize pore-shape (**A.1-2** and **C.1–3**) and **Figure 3D** to visualize pore-size (**B.1-2** and **D.1–3**) distributions. Based on the pore-shape distribution, samples are classified into two groups, G_{AI} (**A.1-2** and **B.1–2**) and G_{AII} (**C.1-3** and **D.1–3**). In **(A)–(D)**, warm color indicates higher pore population. In (**B.1–2**) and (**D.1–3**), a dashed line separates micro- (1–62.5 μm) and nano- (1 nm-1 μm) pores. Sample depth, porosity, composition and gradients for P- (r_P), S1- (r_{S1}) and S2- (r_{S2}) waves are mentioned in the **Table 1**. The figure indicates that within the same pore-shape distribution, r_P increases as the dominant pore-size decreases.

The pore-size distribution plots for Group G_{CI} (**Figures 7B.1, 7B.2**) show a decrease in the dominant pore size as r_P increase from 112.4 to 243.4. Likewise, changes in the dominant pore-size distribution for Group G_{CII} are also more obvious. From **Figure 7D.1** to **Figure 7D.2**, as r_P increase from 55.9 to 73.9, the dominant pore size shift toward smaller size and becomes more pronounced. In Facies C, the effect of dominant pore size is more pronounced for both the groups.

Thus, at the core of this paper was examining how pore-size distribution affects V_P pressure sensitivity in samples that have a similar pore-shape distribution. Overall, **Figures 5–7**, suggest within the same pore-shape distribution the V_P pressure sensitivity increased as the dominant pore size decreased regardless of composition and Φ_{He}.

DISCUSSION

Photomicrograph Attributes

Of all measurements performed for this paper, using DIA to quantify the pore-size distribution was the most challenging. When pores are fully connected, Φ_{He} and pore-size distribution down to nano-scale can be realized through porosimetry or pulse decay methods (Anovitz and Cole, 2015). Regardless of the connectivity, when pores are large (micro- and greater), micro-computerized-tomography scanning can provide a sense of its architecture (Dong and Blunt, 2009). Imaging becomes increasingly more difficult as pores get smaller and isolated. For nanopores, such as the subject of this paper, direct visualization can only be obtained through SEM in 2D or Focused Ion Beam SEM in 3D. However, because of the small sample size (1–2 mm) representativeness of the pore size and distribution plots, e.g., **Figures 5–7**, is always in question. Determining what fraction of the imaged pores are connected and if so to what extent and whether they behave similarly outside the sample under investigation is interpretive but due to the intensity of the data collection process, inferences have to be made on a limited number of samples. Emerging studies (Dvorkin et al., 2011; Dvorkin and Derzhi, 2012; Andrä et al., 2013; Karimpouli and Tahmasebi, 2016; Berg et al., 2017) have shown that even with limited sampling, an interpreter's

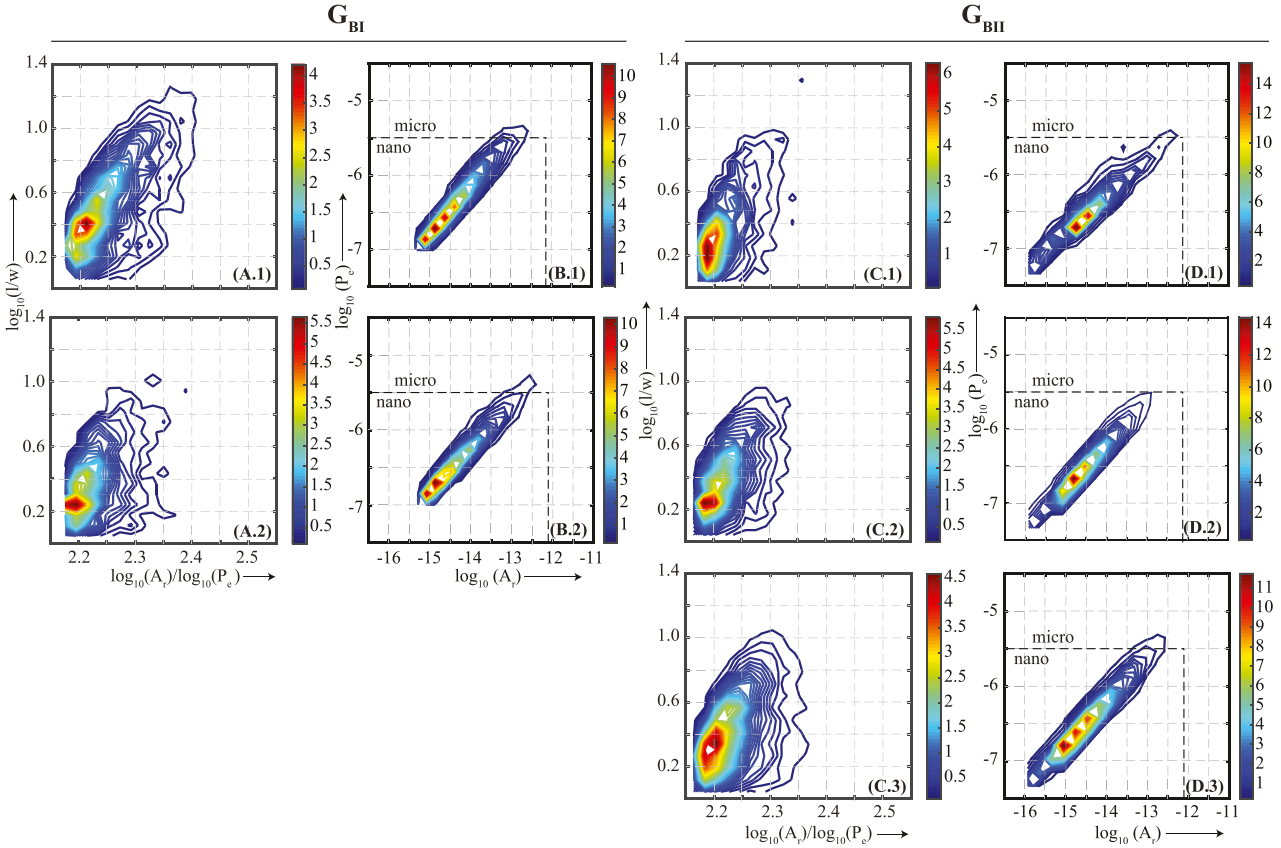

FIGURE 6 | Facies **B**. Symbols and labels are the same as in **Figure 5**. Sample depth, porosity, composition and gradients for P- (r_P), S1- (r_{S1}) and S2- (r_{S2}) waves are mentioned in the **Table 2**. The figure indicates that within the same pore-shape distribution, r_P increases as the dominant pore-size decreases.

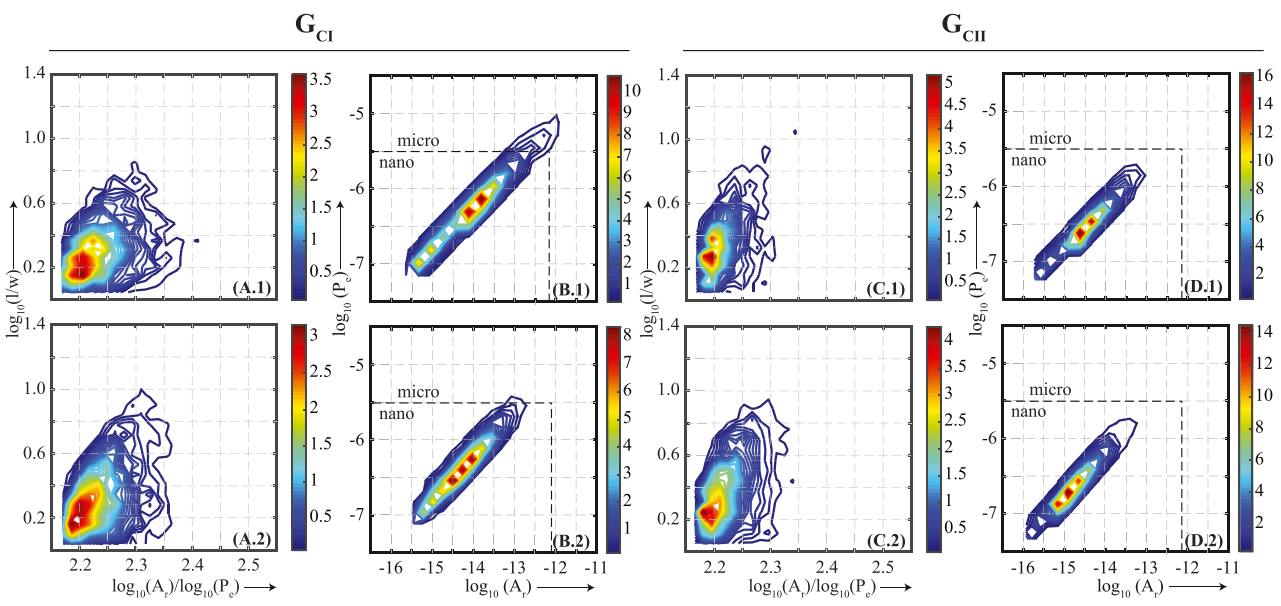

FIGURE 7 | Facies C. Symbols and labels are the same as in **Figure 5**. Sample depth, porosity, composition and gradients for P- (r_P), S1- (r_{S1}) and S2- (r_{S2}) waves are mentioned in the **Table 3**. The figure indicates that within the same pore-shape distribution, r_P increases as the dominant pore-size decreases.

experience and judgement can allow extracting dependable results from DIA.

Nanopores and V_P

Neither Raj et al. (2019) nor their peer provided a reason as to why the dominant pore-size should affect V_P, although Raj et al. (2019) did observe that the nanopore size (10^{-9}–10^{-6} m) is in the range of strain amplitude caused by P-wave at ultrasonic frequency. Using a set of synthetic carbonate samples, Wang et al. (2015) have previously suggested that it is the dominant wavelength of the propagating wave that decides how pore-size influences the wave velocity. Results in this paper provide opportunities to explore an additional factor. Along with the P-wave arrival times, the authors measured two orthogonal S-wave arrival times under the same confining pressures. Using an equation similar to **Equation 1**, V_S pressure sensitivity was also computed and the corresponding gradients, r_{S1} and r_{S2}, are mentioned in **Tables 1–3**. Fitting of V_S data is shown in **Supplementary Figures S7–S14**. **Figures 5–7** and **Tables 1–3** show that unlike their V_P counterparts, V_S pressure sensitivity does not have any obvious correspondence to the dominant pore size. Because S- and P-wave frequencies in the experiment were same, one could argue that if pressure sensitivity is only a pore-size compounded with wavelength phenomenon, V_S pressure sensitivity should have reflected the same trend as V_P pressure sensitivity. Because S-waves are largely transparent to fluids, the V_P pressure sensitivity may therefore be due to pore fluids. The reader is reminded that the experiment being conducted in dry conditions imply that pores are air-filled.

Size Effects

For discussion, consider pores as void spaces devoid of any inherent physical property. Consequently, its compressibility is essentially the aggregate compressibility of the mineral grains surrounding it in addition to how tightly the grains fit into each other. In a scenario where grains fit seamlessly around the pore, the distortion of the grains under static or harmonic pressure changes is manifested as the distortion of the pore itself, which in turn stimulates the trapped pore fluid. For an isolated pore at constant temperature, how the bulk modulus of trapped fluid changes can be understood to the first order of approximation using the ideal gas equation as follows:

$$PV = nRT \tag{2}$$

$$dP.V + P.dV = 0 \tag{3}$$

$$-V\left(\frac{dP}{dV}\right) = P \tag{4}$$

where -V(dP/dV) is the same as K. According to **Eqs 2–4**, K remains proportional to the pore pressure, which, in turn, is the same as the confining pressure under isothermal conditions. Thus, in principle, the bulk modulus of fluids trapped in an isolated pore will increase with an increase in confining pressure. The effect should be more pronounced in compliant pores. A stiff pore may not display the same phenomenon. Regardless, this explains one way through which V_P can increase in presence of isolated pores. However, it does not explain why V_P sensitivity will increase with decreasing pore size unless one assumes that the smaller the pore, the more likely it is to occur in isolation. In the Meramec formation, this is like. Processes such as cementation, carbonate pressure dissolution, and clay diagenesis that remain active throughout the burial history can create isolated pores that are independent of the pore network created during sedimentation or even fractures from subsequent tectonics. In the Mississippian-age rocks of the study area, such processes have been widely recorded (Vanden Berg and Grammer, 2016; Vanden Berg et al., 2018; Bode et al., 2019).

Two factors might together be contributing to the observed increase in V_P pressure sensitivity with decreasing pore size. The primary factor might not directly be the size itself. The smaller pore size in the Meramec formation might imply a greater probability of the pore remaining isolated. **Figures 3A,B**, suggest presence of both intercrystalline and intracrystalline isolated pores in the Meramec formation. It is understood that a number of interpreted pores in **Figures 3A,B** maybe connected in the third dimension. Regardless, stress from static loading can localize along the grain boundaries and can readily strain the isolated intercrystalline pores increasing the bulk moduli of the trapped fluids. Likewise, the intracrystalline isolated pores in soft grains such as that of clay and organic matter, can also get strained from static loading. Wave propagation through a "stiffer" fluid would manifests as high V_P. The second factor might be the investigation tool itself, which creates particle displacements in the nanopore range (10^{-6}–10^{-8} m; O'Sullivan et al., 2016; Nourifard and Lebedev, 2019). When ultrasonic waves traverse a pore larger than the strain amplitude, different parts of the pore would get distorted at different instances. On the other hand, smaller pores are expected to be compressed (or dilated) in their entirety at the same instance. Thus, a nanopore dominated system such as the Meramec formation might just be best displaying the effect of the fluid bulk-moduli increase due to static loading on V_P. Because the strain amplitude remains comparable across a wide range of seismic frequencies (Hz–MHz), the effect of isolated pores on V_P in the Meramec formation might be observable in logs and surface seismic.

Dual-Fluid Model

Independent research exploring fluid behavior in nanopores also exists which is worth reviewing. Gor et al. (2015) and Dobrzanski et al. (2018) have argued that the thermodynamic behavior of fluids trapped in nanopores may be different than the same fluids in the bulk. Like in this paper, they have found that the bulk modulus of the fluid increases as the pore size decreases. However, the experimental confirmation of the theoretical development in these initiatives was done using tools and techniques that are similar to this study. Thus, it may not be unfair to say that whether fluid thermodynamics at the nanoscale is fundamentally different or it manifests differently due to the investigation tool (seismic), could remain an open-ended question.

If indeed V_P sensitivity is due to fluids in unconnected pores, the next obvious question is how to include the fluid effect in numerical models. In unstressed rocks, the fluid-solid and fluid-fluid particle interactions during elastic wave propagation can be accounted for through two end-member frameworks: a) Biot's, where pores vibrate but do not distort (Biot, 1956a; Biot, 1956b); and b) squirt flow, where pores undergo harmonic deformation

(Dvorkin et al., 1994; Dvorkin et al., 1995). Both end-members assume complete pore connectivity. As long as pore connectivity is maintained, Biot's equation can also be adjusted for pre-stressed conditions (Gutierrez and Lewis, 2002). Fluids in unconnected pores are not accounted for directly. In Biot's framework, unconnected pores are part of the solid matrix, e.g., like a separate grain. In other popular models such as differential effective medium, self-consistent, and Kuster-Toksöz, pores are treated as inclusions with specific geometries within a background matrix (Mavko et al., 2020). Models for unconnected pores consider pore shapes to remain unchanged and the pore-fluids to remain immobile during the elastic wave propagation.

To include V_P pressure sensitivity in numerical models, the paper proposes the use of a dual-fluid model where a part of the porosity, e.g., the microporosity, may be seen as isolated containers filled with compressible fluids vs. the rest of the rock that is filled with incompressible fluid. The idea build along the lines of dual-porosity (Pride and Berryman, 2003a; Pride and Berryman, 2003b) and dual stiffness (Liu et al., 2009; Zhao and Liu, 2012) models, but does not require partitioning the pore topology or strain explicitly. In the proposed model, the pore fluid would be separated into a compressible and an incompressible part. The K of the compressible part would remain proportional to the confining pressure while K of the incompressible part would remain unchanged. The proposed model can be implemented within existing frameworks such as Biot's and differential effective medium to explain the behavior of the same rock at different confining pressure and might provide a graceful way of accounting for microporosity whose presence is known to quintessentially enhance V_P pressure sensitivity in both static and dynamic experiments.

CONCLUSIONS

Using a set of 23 samples belonging to a vertical core from the Mississippian-age mixed carbonate-siliciclastic Meramec formation, this study found that the dry-frame V_P pressure sensitivity can depend on pore shape and size distribution. In the study, these distributions were obtained by first measuring P_e, A_r, l, and w of the individual pores through DIA of SEM photomicrographs and then displaying them as 2D histograms of A_r/P_e–l/w and A_r-P_e crossplots. The parameter representing V_P pressure sensitivity was obtained by first measuring the P-wave transit times at ultrasonic frequencies under a 5–40 MPa loading and unloading cycle and then fitting a line to the data from the unloading cycle linearized in the log scale. In samples within the same facies that had a similar pore-shape distribution, V_P increased more rapidly with confining pressure as the dominant pore-size, which was in the nanopore range, decreased. The phenomenon was largely independent of composition and Φ_{He} and only applicable to samples that did not have excessive amounts of cracks and complex pores. The observation is explained by postulating that the pores were mostly isolated at the nanopore scale and an increase in confining stress increased the bulk moduli of the trapped fluids, which in turn increased the V_P. The paper concludes that, in the Meramec formation, a) the likelihood of pores becoming isolated became higher as their size decreases, b) V_P pressure sensitivity was a function of fluid (air) behavior in isolated pores, and c) the effect was prominent because a nanopore dominated system ($<10^{-6}$ μm) was being investigated by frequencies that had comparable strain amplitudes. The study proposes incorporating this effect numerically through a dual-fluid model where fluids in the isolated pores are considered compressible while the remaining are considered incompressible. Results start to explain the common observation of why presence of microporosity quintessentially increases V_P pressure sensitivity.

DATA AVAILABILITY STATEMENT

Core belongs to Devon Energy Corporation. For access permissions as of 12/2020, contact: Aubrey Humbolt (Aubrey.Humbolt@dvn.com). DIA data and sonic waveforms can be obtained with permission from the authors.

AUTHOR CONTRIBUTIONS

This study is a part of RR's PhD dissertation. PJ mentored RR in conceptualizing the paper, analyzing the data and presenting the results. YW interpreted facies. GMG oversaw the sample preparation for SEM. RW oversaw He-gas porosity and ultrasonic velocity measurements.

FUNDING

Data and funding for the lead student author was provided by Devon Energy Corporation, Oklahoma City, OK, United States.

ACKNOWLEDGMENTS

Winton Cornell (retired), the University of Tulsa, helped with XRD. SEM imagery was generated at Oklahoma State University Microscopy Laboratory. This is Boone Pickens School of Geology contribution number 2021-120.

SUPPLEMENTARY MATERIAL

The Supplementary Material for this article can be found online at: https://www.frontiersin.org/articles/10.3389/feart.2021.641815/full#supplementary-material.

REFERENCES

Almasoodi, M., Vaidya, R., and Reza, Z. (2020). Drawdown-management and fracture-spacing optimization in the Meramec formation: numerical-and economics-based approach. *SPE Reserv. Eval. Eng.* 23 (4), 1251–1264. doi:10.2118/201245-pa

Andrä, H., Combaret, N., Dvorkin, J., Glatt, E., Han, J., Kabel, M., et al. (2013). Digital rock physics benchmarks-part II: computing effective properties. *Comput. Geosci.* 50, 33–43. doi:10.1016/j.cageo.2012.09.008

Angerer, E., Crampin, S., Li, X.-Y., and Davis, T. L. (2002). Processing, modelling and predicting time-lapse effects of overpressured fluid-injection in a fractured reservoir. *Geophys. J. Int.* 149 (2), 267–280. doi:10.1046/j.1365-246x.2002.01607.x

Anovitz, L. M., and Cole, D. R. (2015). Characterization and analysis of porosity and pore structures. *Rev. Mineral. Geochem.* 80 (1), 61–164. doi:10.2138/rmg.2015.80.04

Asef, M. R., and Najibi, A. R. (2013). The effect of confining pressure on elastic wave velocities and dynamic to static Young's modulus ratio. *Geophysics* 78 (3), D135–D142. doi:10.1190/geo2012-0279.1

Ba, J., Cao, H., Yao, F., Nie, J., and Yang, H. (2008). Double-porosity rock model and squirt flow in the laboratory frequency band. *Appl. Geophys.* 5 (4), 261–276. doi:10.1007/s11770-008-0036-0

Baechle, G. T., Colpaert, A., Eberli, G. P., and Weger, R. J. (2008). Effects of microporosity on sonic velocity in carbonate rocks. *Leading Edge* 27 (8), 1012–1018. doi:10.1190/1.2967554

Batzle, M. L., Han, D.-H., and Hofmann, R. (2006). Fluid mobility and frequency-dependent seismic velocity - direct measurements. *Geophysics* 71 (1), N1–N9. doi:10.1190/1.2159053

Berg, C. F., Lopez, O., and Berland, H. (2017). Industrial applications of digital rock technology. *J. Pet. Sci. Eng.* 157, 131–147. doi:10.1016/j.petrol.2017.06.074

Biot, M. A. (1973). Nonlinear and semilinear rheology of porous solids. *J. Geophys. Res.* 78 (23), 4924–4937. doi:10.1029/jb078i023p04924

Biot, M. A. (1956a). Theory of propagation of elastic waves in a fluid-saturated porous solid. I. Low-Frequency range. *J. Acoust. Soc. america* 28 (2), 168–178. doi:10.1121/1.1908239

Biot, M. A. (1956b). Theory of propagation of elastic waves in a fluid-saturated porous solid. II. Higher frequency range. *J. Acoust. Soc. america* 28 (2), 179–191. doi:10.1121/1.1908241

Blakey, R. C. (2013). *Paleogeography and geologic evolution of North America*. Phoenix, AZ: Colorado Plateau Geosystems, Inc.

Bode, I. Y., Zhang, C., Vanden Berg, B., and Grammer, G. M. (2019). Multiscale imaging and nuclear magnetic resonance pore characterization in unconventional carbonate mudrocks of the southern midcontinent (USA): Mississippi Lime play. *SEPM (Soc. Sediment. Geolo.)* 18 (2), 196–219. doi:10.2110/sepmsp.112.11

Buggisch, W., Joachimski, M. M., Sevastopulo, G., and Morrow, J. R. (2008). Mississippian δ13Ccarb and conodont apatite δ18O records—their relation to the Late Palaeozoic Glaciation. *Palaeogeogr. Palaeoclimatol. Palaeoecol.* 268 (3-4), 273–292. doi:10.1016/j.palaeo.2008.03.043

Childress, M., and Grammer, G. M. (2015). High resolution sequence stratigraphic architecture of a Mid-Continent Mississippian outcrop in Southwest Missouri. Available at: https://hdl.handle.net/11244/33395.

Chopra, S., Sharma, R. K., and Keay, J. (2018). SCOOP and STACK inversion case studies. *SEG Tech. Program Expanded Abstr. Soc. Explor. Geophys.* 2018, 3392–3396. doi:10.1190/segam2018-2997345.1

Darling, T., TenCate, J., Brown, D., Clausen, B., and Vogel, S. (2004). Neutron diffraction study of the contribution of grain contacts to nonlinear stress-strain behavior. *Geophys. Res. Lett.* 31, L16604. doi:10.1029/2004gl020463

Darot, M., and Reuschlé, T. (2000). Effect of pore and confining pressures on VPin thermally pre-cracked granites. *Geophys. Res. Lett.* 27 (7), 1057–1060. doi:10.1029/1999gl008414

David, E., and Zimmerman, R. W. (2012). Pore structure model for elastic wave velocities in fluid-saturated sandstones. *J. Geophys. Res. Solid Earth* 117 (B7), B07210. doi:10.1029/2012jb009195

Davis, T., Healy, D., Bubeck, A., and Walker, R. (2017). Stress concentrations around voids in three dimensions: the roots of failure. *J. Struct. Geol.* 102, 193–207. doi:10.1016/j.jsg.2017.07.013

de Oliveira, G. L. P., Ceia, M. A. R., Missagia, R. M., Archilha, N. L., Figueiredo, L., Santos, V. H., et al. (2016). Pore volume compressibilities of sandstones and carbonates from Helium porosimeter measurements. *J. Pet. Sci. Eng.* 137, 185–201. doi:10.1016/j.petrol.2015.11.022

Dobrzanski, C. D., Maximov, M. A., and Gor, G. Y. (2018). Effect of pore geometry on the compressibility of a confined simple fluid. *J. Chem. Phys.* 148 (5), 054503. doi:10.1063/1.5008490

Dong, H., and Blunt, M. J. (2009). Pore-network extraction from micro-computerized-tomography images. *Phys. Rev. E Stat. Nonlin Soft Matter Phys.* 80 (3), 036307. doi:10.1103/PhysRevE.80.036307

Dvorkin, J., Derzhi, N., Diaz, E., and Fang, Q. (2011). Relevance of computational rock physics. *Geophysics* 76 (5), E141–E153. doi:10.1190/geo2010-0352.1

Dvorkin, J., and Derzhi, N. (2012). Rules of upscaling for rock physics transforms: composites of randomly and independently drawn elements. *Geophysics* 77 (3), WA129–WA139. doi:10.1190/geo2011-0268.1

Dvorkin, J., Mavko, G., and Nur, A. (1995). Squirt flow in fully saturated rocks. *Geophysics* 60 (1), 97–107. doi:10.1190/1.1443767

Dvorkin, J., Nolen-Hoeksema, R., and Nur, A. (1994). The squirt-flow mechanism: macroscopic description. *Geophysics* 59 (3), 428–438. doi:10.1190/1.1443605

Eberhart-Phillips, D., Han, D.-H., and Zoback, M. (1989). Empirical relationships among seismic velocity, effective pressure, porosity, and clay content in sandstone. *Geophysics* 54 (1), 82–89. doi:10.1190/1.1442580

Fjær, E. (2019). Relations between static and dynamic moduli of sedimentary rocks. *Geophys. Prospect.* 67 (1), 128–139. doi:10.1111/1365-2478.12711

Fjær, E., Stroisz, A. M., and Holt, R. M. (2013). Elastic dispersion derived from a combination of static and dynamic measurements. *Rock Mech. Rock Eng.* 46 (3), 611–618. doi:10.1007/s00603-013-0385-8

Fredrich, J. T., Greaves, K. H., and Martin, J. W. (1993). "Pore geometry and transport properties of Fontainebleau sandstone," in Proceedings international journal of rock mechanics and mining sciences & geomechanics abstracts1993, Great Britain, December 1993; (Elsevier), 691–697.

Freund, D. (1992). Ultrasonic compressional and shear velocities in dry clastic rocks as a function of porosity, clay content, and confining pressure. *Geophys. J. Int.* 108 (1), 125–135. doi:10.1111/j.1365-246x.1992.tb00843.x

Geological Society of America (1995). Rock Color Chart with Genuine Munsell Color Chips 8, 8.

Gor, G. Y., Siderius, D. W., Rasmussen, C. J., Krekelberg, W. P., Shen, V. K., and Bernstein, N. (2015). Relation between pore size and the compressibility of a confined fluid. *J. Chem. Phys.* 143 (19), 194506. doi:10.1063/1.4935430

Gutierrez, M. S., and Lewis, R. W. (2002). Coupling of fluid flow and deformation in underground formations. *J. Eng. Mech.* 128 (7), 779–787. doi:10.1061/(asce)0733-9399(2002)128:7(779)

Gutschick, R. C., and Sandberg, C. A. (1983). "Mississippian continental margins of the conterminous United States," in *The Shelfbreak: Critical Interface on Continental Margins*. Editor D Jean Stanley and G. T. Moore. (Tulsa, Oklahoma: Society of Economic Paleontologists and Mineralogists).

Han, T., Gurevich, B., Pervukhina, M., Clennell, M. B., and Zhang, J. (2016). Linking the pressure dependency of elastic and electrical properties of porous rocks by a dual porosity model. *Geophys. J. Int.* 205 (1), 378–388. doi:10.1093/gji/ggw019

Haq, B. U., and Schutter, S. R. (2008). A chronology of Paleozoic sea-level changes. *Science* 322 (5898), 64–68. doi:10.1126/science.1161648

Hart, D. J., and Wang, H. F. (1995). Laboratory measurements of a complete set of poroelastic moduli for Berea sandstone and Indiana limestone. *J. Geophys. Res.* 100 (B9), 17741–17751. doi:10.1029/95jb01242

Karimpouli, S., and Tahmasebi, P. (2016). Conditional reconstruction: an alternative strategy in digital rock physics. *Geophysics* 81 (4), D465–D477. doi:10.1190/geo2015-0260.1

Kirstetter, O., and MacBeth, C. (2001). Compliance-based interpretation of dry frame pressure sensitivity in shallow marine sandstone. *SEG Tech. Program Expanded Abstr. 2001 Soc. Exploration Geophys.* 2001, 2132–2135. doi:10.1190/1.1816572

Kitamura, K., Takahashi, M., Mizoguchi, K., Masuda, K., Ito, H., and Song, S. R. (2010). Effects of pressure on pore characteristics and permeability of porous rocks as estimated from seismic wave velocities in cores from TCDP Hole-A. *Geophys. J. Int.* 182 (3), 1148–1160. doi:10.1111/j.1365-246x.2010.04694.x

Lane, H. R., and De Keyser, T. (1980). "Paleogeography of the late Early Mississippian (Tournaisian 3) in the central and southwestern United States," in *Paleozoic Paleogeography of the West-Central United States*. Editors T. D. Fouch and E. R. Magathan (Denver, Colorado: Rocky Mountain Symposium 1: Rocky Mountain Section SEPM), 149–162.

LeBlanc, S. L. (2014). *High resolution sequence stratigraphy and reservoir characterization of the "Mississippian Limestone" in north-central Oklahoma*. Oklahoma: Oklahoma State University, ProQuest Dissertations Publishing.

Liu, E., Hudson, J. A., and Pointer, T. (2000). Equivalent medium representation of fractured rock. *J. Geophys. Res.* 105 (B2), 2981–3000. doi:10.1029/1999jb900306

Liu, H.-H., Rutqvist, J., and Berryman, J. G. (2009). On the relationship between stress and elastic strain for porous and fractured rock. *Int. J. Rock Mech. Mining Sci.* 46 (2), 289–296. doi:10.1016/j.ijrmms.2008.04.005

MacEachern, J. A., Bann, K. L., Gingras, M. K., and Pemberton, S. G. (2009). *Applied Ichnology, Short Course Notes 52: SEPM*. Tulsa: OklahomaSociety for Sedimentary Geology), 380.

Martínez-Martínez, J., Benavente, D., and García-del-Cura, M. A. (2012). Comparison of the static and dynamic elastic modulus in carbonate rocks. *Bull. Eng. Geol. Environ.* 71 (2), 263–268. doi:10.1007/s10064-011-0399-y

Mashinsky, E. (2003). Differences between static and dynamic elastic moduli of rocks. *Phys. Causes Russ. Geology. Geophys.* 44 (9), 953–959.

Mavko, G., Mukerji, T., and Dvorkin, J. (2020). *The rock physics handbook*. 2nd Edn. Cambridge, England: Cambridge University Press.

Mazzullo, S. J., Wilhite, B. W., and Boardman, D. R., II (2011). Lithostratigraphic architecture of the Mississippian reeds spring formation (middle Osagean) in southwest Missouri, northwest Arkansas, and northeast Oklahoma: outcrop analog of subsurface petroleum reservoirs. *Shale Shaker*. 61 (5), 254–269.

Miller, J. C., Pranter, M. J., and Cullen, A. B. (2019). *Regional stratigraphy and organic richness of the Mississippian Meramec and associated strata*. Central Oklahoma: Anadarko Basin.

Morgenstern, N. R., and Tamuly Phukan, A. L. (1969). Non-linear stress-strain relations for a homogeneous sandstone. *Int. J. Rock Mech. Mining Sci. Geomech. Abstr.* 6, 127–142. doi:10.1016/0148-9062(69)90031-x

Muqtadir, A., Al-Dughaimi, S., and Dvorkin, J. (2020). Deformation of granular aggregates: static and dynamic bulk moduli. *J. Geophys. Res. Solid Earth* 125 (1), e2019JB018604. doi:10.1029/2019jb018604

Northcutt, R. A., and Campbell, J. A. (1996). "Geologic provinces of Oklahoma," in *Basement Tectonics 12.*Proceedings of the International Conferences on Basement Tectonics. Editors J. P. Hogan and M. C. Gilbert (Berlin, Germany: Springer, Dordrecht), vol 6.

Nourifard, N., and Lebedev, M. (2019). Research note: the effect of strain amplitude produced by ultrasonic waves on its velocity. *Geophys. Prospecting* 67 (4), 715–722. doi:10.1111/1365-2478.12674

Nur, A., and Simmons, G. (1969). The effect of saturation on velocity in low porosity rocks. *Earth Planet. Sci. Lett.* 7 (2), 183–193. doi:10.1016/0012-821x(69)90035-1

O'Sullivan, C., O'Donovan, J., Ibraim, E., Hamlin, S., Muir Wood, D., and Marketos, G. (2016). *Micromechanics of seismic wave propagation in granular materials*. Berlin, Germany: Springer.

Prasad, M., and Manghnani, M. H. (1997). Effects of pore and differential pressure on compressional wave velocity and quality factor in Berea and Michigan sandstones. *Geophysics* 62 (4), 1163–1176. doi:10.1190/1.1444217

Price, B., Haustveit, K., and Lamb, A. (2017). "Influence of stratigraphy on barriers to fracture growth and completion optimization in the Meramec stack play, Anadarko basin, Oklahoma," in Proceedings unconventional resources technology conference, 24-26 July 2017; Austin, Texas Editors T. Blasingame, S. Maxwell, and D. Valleau. (Austin, Texas: Society of Exploration Geophysicists, American Association of Petroleum), 3453–3460.

Pride, S. R., and Berryman, J. G. (2003a). Linear dynamics of double-porosity dual-permeability materials. I. Governing equations and acoustic attenuation. *Phys. Rev. E Stat. Nonlin Soft Matter Phys.* 68 (3), 036603. doi:10.1103/PhysRevE.68.036603

Pride, S. R., and Berryman, J. G. (2003b). Linear dynamics of double-porosity dual-permeability materials. II. Fluid transport equations. *Phys. Rev. E Stat. Nonlin Soft Matter Phys.* 68 (3), 036604. doi:10.1103/PhysRevE.68.036604

Pyrak-Nolte, L., and Morris, J. (2000). Single fractures under normal stress: the relation between fracture specific stiffness and fluid flow. *Int. J. Rock Mech. Mining Sci.* 37 (1-2), 245–262. doi:10.1016/s1365-1609(99)00104-5

Pyrak-Nolte, L. J., Myer, L. R, and Cook, N. G. W (1990). Transmission of seismic waves across single natural fractures. *J. Geophys. Res.* 95 (B6), 8617–8638. doi:10.1029/JB095iB06p08617

Raj, R., Jaiswal, P., Vanden Berg, B., and Grammer, G. M. (2019). Pore size and ultrasonic velocity: lessons from Miss Lime reservoirs. *SEPM (Society for Sedimentary Geology)* 18 (2), 183–195. doi:10.2110/sepmsp.112.04

Robin, P. Y. F. (1973). Note on effective pressure. *J. Geophys. Res.* 78 (14), 2434–2437. doi:10.1029/jb078i014p02434

Vanden Berg, B., and Grammer, G. M. (2016). 2-D pore architecture characterization of a carbonate mudrock reservoir: insights from the mid-continent "Mississippi Lime"," in *Imaging Unconventional Reservoir Pore Systems*. Editor T. Olson (Oklahoma: American Association of Petroleum Geologists), 185–231. doi:10.1306/13592022M1123698

Vanden Berg, B., Nussbaumer, C., Noack, A., Thornton, J., Weger, R. J., Eberli, G. P., et al. (2018). A comparison of the relationship between measured acoustic response and porosity in carbonates across different geologic periods, depositional basins, and with variable mineral composition. *Interpretation* 6 (2), T245–T256. doi:10.1190/int-2017-0108.1

Vanorio, T., Nur, A., and Ebert, Y. (2011). Rock physics analysis and time-lapse rock imaging of geochemical effects due to the injection of CO2 into reservoir rocks. *Geophysics* 76 (5), O23–O33. doi:10.1190/geo2010-0390.1

Vanorio, T. (2015). Recent advances in time-lapse, laboratory rock physics for the characterization and monitoring of fluid-rock interactions. *Geophysics* 80 (2), WA49–WA59. doi:10.1190/geo2014-0202.1

Wang, Z., Wang, R., Wang, F., Qiu, H., and Li, T. (2015). Experiment study of pore structure effects on velocities in synthetic carbonate rocks. *Geophysics* 80 (3), D207–D219. doi:10.1190/geo2014-0366.1

Watney, W. L., Guy, W. J., and Byrnes, A. P. (2001). Characterization of the Mississippian chat in south-central Kansas. *AAPG Bull.* 85 (1), 85–113. doi:10.1306/8626C767-173B-11D7-8645000102C1865D

Weger, R. J., Eberli, G. P., Baechle, G. T., Massaferro, J. L., and Sun, Y. F. (2009). Quantification of pore structure and its effect on sonic velocity and permeability in carbonates. *Bulletin* 93 (10), 1297–1317. doi:10.1306/05270909001

Weibo, S., Zihan, Q., Yanan, H., and Cheng, H. (2020). Estimating pore volume compressibility by spheroidal pore modeling of digital rocks. *Pet. Explor. Develop.* 47 (3), 603–612. doi:10.1016/s1876-3804(20)60077-5

Zhang, L., Ba, J., Fu, L., Carcione, J. M., and Cao, C. (2019). Estimation of pore microstructure by using the static and dynamic moduli. *Int. J. Rock Mech. Mining Sci.* 113, 24–30. doi:10.1016/j.ijrmms.2018.11.005

Zhao, Y., and Liu, H. H. (2012). An elastic stress-strain relationship for porous rock under anisotropic stress conditions. *Rock Mech. Rock Eng.* 45 (3), 389–399. doi:10.1007/s00603-011-0193-y

Zimmerman, R. W., Somerton, W. H., and King, M. S. (1986). Compressibility of porous rocks. *J. Geophys. Res.* 91 (B12), 12765–12777. doi:10.1029/jb091ib12p12765

Conflict of Interest: The authors declare that this study received funding from Devon Energy Corporation. The funder was not involved in the study design, collection, analysis, interpretation of data, the writing of this article or the decision to submit it for publication.

Copyright © 2021 Raj, Jaiswal, Wang, Grammer and Weger. This is an open-access article distributed under the terms of the Creative Commons Attribution License (CC BY). The use, distribution or reproduction in other forums is permitted, provided the original author(s) and the copyright owner(s) are credited and that the original publication in this journal is cited, in accordance with accepted academic practice. No use, distribution or reproduction is permitted which does not comply with these terms.

frontiers in Earth Science

ORIGINAL RESEARCH
published: 29 April 2021
doi: 10.3389/feart.2021.640424

Wave Properties of Gas-Hydrate Bearing Sediments Based on Poroelasticity

Wei Wang[1], Jing Ba[1], José M. Carcione[1,2], Xu Liu[3] and Lin Zhang[1]*

[1] School of Earth Sciences and Engineering, Hohai University, Nanjing, China, [2] Istituto Nazionale di Oceanografa e di Geofsica Sperimentale, Sgonico, Italy, [3] College of Petroleum Engineering & Geosciences, King Fahd University of Petroleum and Minerals, Dhahran, Saudi Arabia

Natural gas hydrates have the properties of ice with a microporous structure and its concentration in sediments highly affects the wave velocity and attenuation. Previous studies have performed investigations based on the measurements of laboratory data, sonic-log data, and field data, whereas the variation trend of wave dissipation with increasing hydrate concentration at different frequencies is still unclear. We consider two different models to study this problem, both based on the Biot-Rayleigh double-porosity theory. In the first model, hydrate is part of the pore infill, unbonded from the grains, and brine saturates the remaining pore space. In the second model, hydrate forms a second skeleton and cements the grains. We obtain the P-wave velocity dispersion and attenuation as a function of the inclusion radius, porosity, and hydrate content. The analysis shows that the predictions of both models agree with the experimental data. At sonic log frequencies, the second model predicts much more attenuation, due to wave-induced local fluid flow (mesoscopic loss), and the behavior is such that below a given hydrate concentration the dissipation increases and then decreases beyond that concentration.

Keywords: Biot-Rayleigh double-porosity theory, rock-physical model, effective medium theory, velocity dispersion, attenuation, gas hydrate

OPEN ACCESS

Edited by:
Jack Petrovich Dvorkin,
Stanford University, United States

Reviewed by:
Nicola Tisato,
University of Texas at Austin, United States
David Iacopini,
University of Naples Federico II, Italy

***Correspondence:**
Jing Ba
jba@hhu.edu.cn

Specialty section:
This article was submitted to Solid Earth Geophysics, a section of the journal Frontiers in Earth Science

Received: *11 December 2020*
Accepted: *06 April 2021*
Published: *29 April 2021*

Citation:
Wang W, Ba J, Carcione JM, Liu X and Zhang L (2021) Wave Properties of Gas-Hydrate Bearing Sediments Based on Poroelasticity. Front. Earth Sci. 9:640424. doi: 10.3389/feart.2021.640424

INTRODUCTION

The concentration of natural gas hydrate in sediments affects their acoustic properties (Guerin and Goldberg, 2002). In particular, the wave velocity highly increases, even with small concentrations (Chand and Minshull, 2003; Dvorkin et al., 2003; Chand et al., 2004; Guerin and Goldberg, 2005; Lee and Waite, 2008). This property is used to determine the distribution of hydrate in sediments (Tinivella and Carcione, 2001). Moreover, the P-wave quality factor obtained, by attenuation tomography, for instance, can also be used to monitor the presence of gas hydrate (Carcione et al., 2012). Samples from marine sediments or from permafrost regions show that hydrates are microporous (Kuhs et al., 2004). It has been observed that seismic attenuation decreases due to a stiffening effect when the hydrate concentration increases (Dvorkin et al., 2003; Rossi et al., 2007; Gei and Carcione, 2003). Vertical-seismic-profile data in Nankai areas showed no significant attenuation (Matsushima, 2006). However, the sonic log data in the Mallik area show that attenuation increases linearly with hydrate saturation (Guerin and Goldberg, 2002; Chand and Minshull, 2004).

Actually, attenuation depends not only on hydrate concentration, but also on other reservoir properties, such as microstructure (Ecker et al., 2000; Priest et al., 2009). **Figure 1** shows different cases (Ecker et al., 1998, 2000; Waite et al., 2009; Zhan and Matsushima, 2018): (1) hydrate grows freely in the pores away from the grains (pore-filling hydrate); (2) hydrate forms a second skeleton (load-bearing hydrate); (3) hydrate cements the grains (contact-cementing hydrate); (4) hydrate evenly deposited on the grain surface (envelope-cementing hydrate). Gas hydrate can be part of the pore infill or rock skeleton (Liu et al., 2018; Lin et al., 2019). Dvorkin and Nur (1993) proposed the BISQ model to effectively combine the global Biot-flow mechanism with the local squirt-flow mechanism. This model can be used to describe seismic attenuation in combination with frozen porous-media theories (Leclaire et al., 1994; Guerin and Goldberg, 2005). The effective-medium theory has been implemented by Helgerud et al. (1999) and Dvorkin et al. (1999). Carcione and Tinivella (2000) presented a Biot-type theory with two solids and one fluid, where hydrate forms an additional skeleton and water is the pore fluid. The concentration of gas hydrate and saturation of free gas has been estimated from seismic velocity and attenuation based on this theory (Carcione and Gei, 2004; Carcione et al., 2005). Lee (2002a,b) extended the classical Biot–Gassmann theory to predict the S-wave velocity. Chand et al. (2006) use the self-consistent approximation, differential effective medium theory and consider the Biot and squirt-flow attenuation mechanisms to estimate the hydrate concentration in the Mallik area. An effective-medium model, considering different microstructures, has been considered in Liu et al. (2017) and Qu et al. (2016) use a model based on penny-shaped and infinite cracks. Sell et al. (2016) combine tomography and 3D modeling to simulate the acoustic properties with digital rock physics, whereas Sell et al. (2018) show that there is an interfacial water film between hydrate and grains through 3D micro-tomography, and a new conceptual squirt-flow model is proposed. Tuan et al. (2019) uses a homogenization theory for multiphase composites to predict wave velocities that agree with laboratory and sonic-log data.

Based on the effective-grain model (Leurer, 1997), Best et al. (2013) apply the squirt-flow mechanism to explain the observed attenuation, and Marín-Moreno et al. (2017) consider squirt-flow mechanisms and gas-bubble damping factors, showing that there are different behaviors of the attenuation as a function of frequency above and below a given hydrate saturation (6%) (Sahoo et al., 2019).

In this work, the Biot-Rayleigh theory of wave propagation in double-porosity media is used here to describe the gas-hydrate distribution in the sediment and study wave dispersion and attenuation (Ba et al., 2011). The model predictions are then compared with laboratory data (Priest et al., 2005, 2009) and sonic-logging data (Zhan and Matsushima, 2018).

ROCK-PHYSICS MODELS

As shown in **Figure 2**, solid hydrate can be part of the pore infill (Model 1, **Figure 2A**) or constitute a skeleton and cement the grains (Model 2, **Figures 2B,C**). The skeleton or frame properties are obtained with the effective-medium theory according to Ecker et al. (2000), and the wet-rock P-wave properties with the Biot-Rayleigh theory. **Figures 3**, **4** show the modeling workflow and the description of the two models, respectively. Hydrate is abundant in the seafloor and permafrost (e.g., Marín-Moreno et al., 2017), for instance, in Qilian region (China) (Qu et al., 2016), the Mount Elbert in Alaska (Pan et al., 2019), and in the Eastern Nankai Trough offshore Japan (Konno et al., 2015). These cases showed the characteristics of Model 1. Lei et al. (2018) and Chen et al. (2020) observed the distribution characteristics of Model 2 by CT imaging.

Model 1: Hydrate as Pore Infill

At low concentrations, hydrate can be assumed as pore infill (Lee et al., 2010), such that a fluid is formation water and the other is a mixture of solid hydrate and free gas (hydrate/gas shortly), with

$$K_f^{(1)} = K_w, \tag{1}$$

$$\rho_f^{(1)} = \rho_w, \tag{2}$$

where K_w and ρ_w are the water bulk modulus and density, respectively, and

$$K_f^{(2)} = \left(\frac{c_h}{K_h} + \frac{c_g}{K_g}\right)^{-1}, \tag{3}$$

$$\rho_f^{(2)} = c_h\rho_h + c_g\rho_g, \tag{4}$$

where K_h and K_g are the bulk moduli of gas hydrate and free gas, respectively, and c_h and c_g are the respective volume ratios (c_h+$c_g = 1$). ρ_h and ρ_g are the densities of gas hydrate and free gas, respectively. The saturation of free gas is

$$S_g = \frac{c_g S_h}{c_h}, \tag{5}$$

with $S_h + S_g + S_w = 1$.

The bulk and shear moduli of the m-phase mineral mixture without hydrate (moduli of the mineral mixture, referred to as mineral moduli) are obtained with Hill's average:

$$\begin{cases} K_s = \frac{1}{2}\left[\sum_{i=1}^{m} f_i K_i + \left(\sum_{i=1}^{m} \frac{f_i}{K_i}\right)^{-1}\right] \\ G_s = \frac{1}{2}\left[\sum_{i=1}^{m} f_i G_i + \left(\sum_{i=1}^{m} \frac{f_i}{G_i}\right)^{-1}\right] \end{cases}, \tag{6}$$

Where f_i is the volumetric fraction of the i-th component and K_i and G_i are the respective bulk and shear moduli.

The dry-rock moduli can be obtained by combining Eqs 1–6 and the modified Hashin–Shtrikman theory given in **Supplementary Appendix A**. By substituting a plane-wave solution into the Biot-Rayleigh equations (see **Supplementary Appendix B**) of Ba et al. (2011, 2012), we obtain

$$\begin{vmatrix} a_{11}k^2 + b_{11} & a_{12}k^2 + b_{12} & a_{13}k^2 + b_{13} \\ a_{21}k^2 + b_{21} & a_{22}k^2 + b_{22} & a_{23}k^2 + b_{23} \\ a_{31}k^2 + b_{31} & a_{32}k^2 + b_{32} & a_{33}k^2 + b_{33} \end{vmatrix} = 0, \tag{7}$$

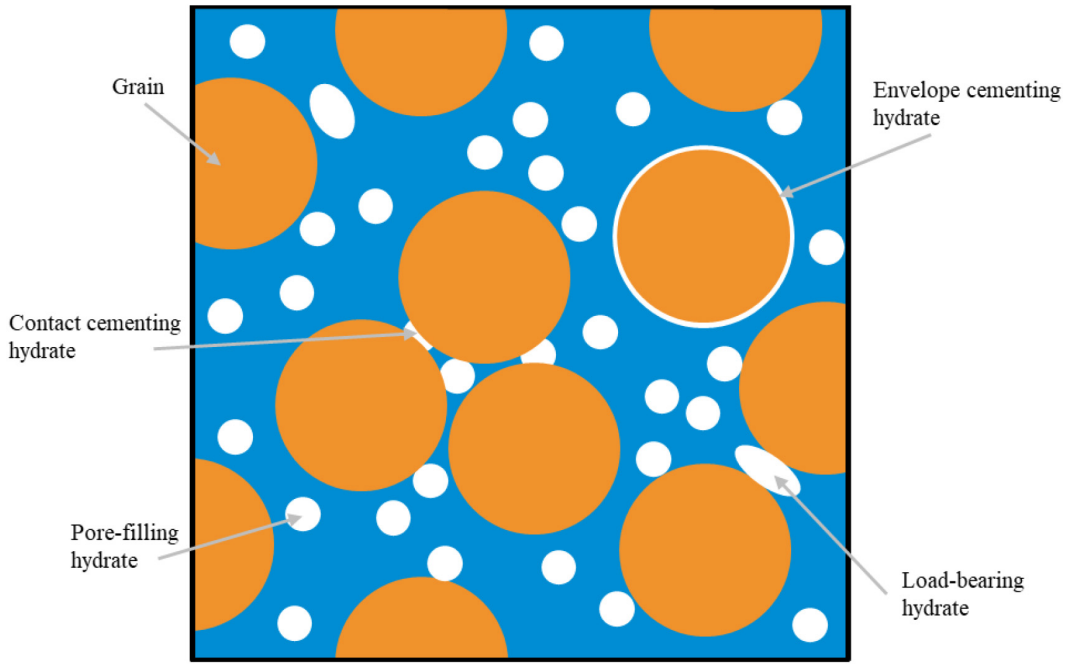

FIGURE 1 | Microstructure in gas hydrate-bearing sediments. The white, orange, and blue colors indicate the hydrate, grain, and pore fluid.

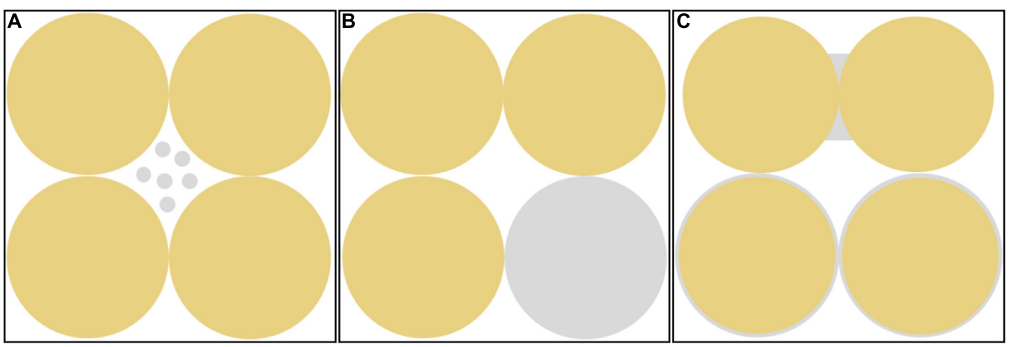

FIGURE 2 | Different distributions of hydrate in the sediment. **(A)** Pore-filling hydrate; **(B)** load-bearing hydrate; **(C)** contact-cementing and envelope-cementing hydrate.

where ω is the angular frequency, k is the complex P-wave wave number,

$$a_{11} = A + 2N + \mathrm{i}\left(Q_2\phi_1 - Q_1\phi_2\right)x_1,\ \ b_{11} = -\rho_{11}\omega^2 + \mathrm{i}\omega\left(b_1 + b_2\right),$$

$$a_{12} = Q_1 + \mathrm{i}\left(Q_2\phi_1 - Q_1\phi_2\right)x_1, \quad b_{12} = -\rho_{12}\omega^2 - \mathrm{i}\omega b_1,$$

$$a_{13} = Q_2 + \mathrm{i}\left(Q_2\phi_1 - Q_1\phi_2\right)x_3, \quad b_{13} = -\rho_{13}\omega^2 - \mathrm{i}\omega b_2,$$

$$a_{21} = Q_1 - \mathrm{i}R_1\phi_2 x_1, \quad b_{21} = -\rho_{12}\omega^2 - \mathrm{i}\omega b_1,$$

$$a_{22} = R_1 - \mathrm{i}R_1\phi_2 x_2,\ \ b_{22} = -\rho_{22}\omega^2 + \mathrm{i}\omega b_1,$$

$$a_{23} = \mathrm{i}R_1\phi_2 x_3, \quad b_{23} = 0,$$

$$a_{31} = Q_2 + \mathrm{i}R_2\phi_1 x_1, \quad b_{31} = -\rho_{13}\omega^2 - \mathrm{i}\omega b_2,$$

$$a_{32} = \mathrm{i}R_2\phi_1 x_2, \quad b_{32} = 0,$$

$$a_{33} = R_2 + \mathrm{i}R_2\phi_1 x_3, \quad b_{33} = -\rho_{33}\omega^2 + \mathrm{i}\omega b_2,$$

where $x_1 = \mathrm{i}\left(\phi_2 Q_1 - \phi_1 Q_2\right)/Z, \quad x_2 = \mathrm{i}\phi_2 R_1/Z, \quad x_3 = -\mathrm{i}\phi_1 R_2/Z,$

$$Z = \frac{\mathrm{i}\omega\eta\phi_1^2\phi_2\phi_{20}R_0^2}{3\kappa_{10}} - \frac{\rho_f\omega^2 R_0^2\phi_1^2\phi_2\phi_{20}}{3\phi_{10}} - \left(\phi_2^2 R_1 + \phi_1^2 R_2\right).$$

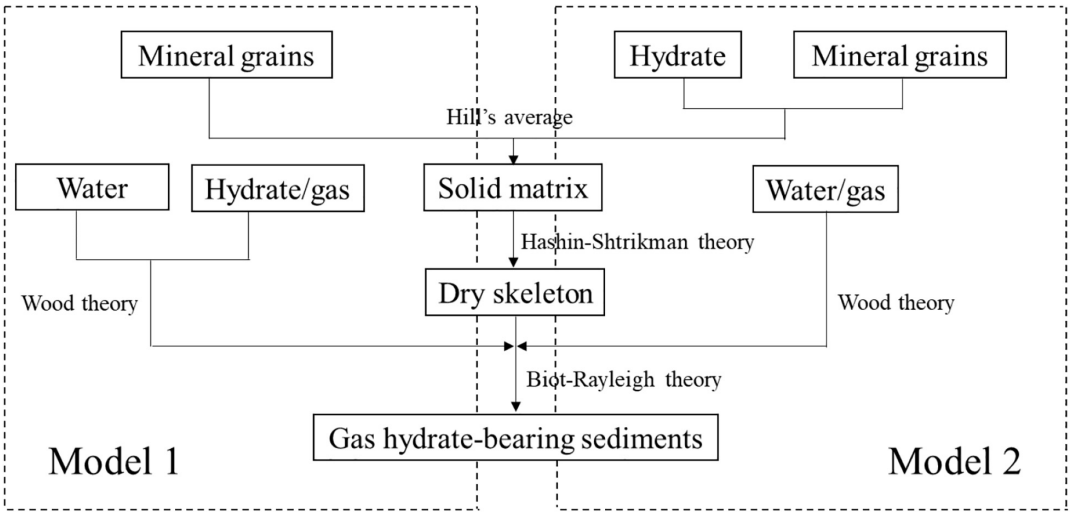

FIGURE 3 | Modeling workflow methods for the two models.

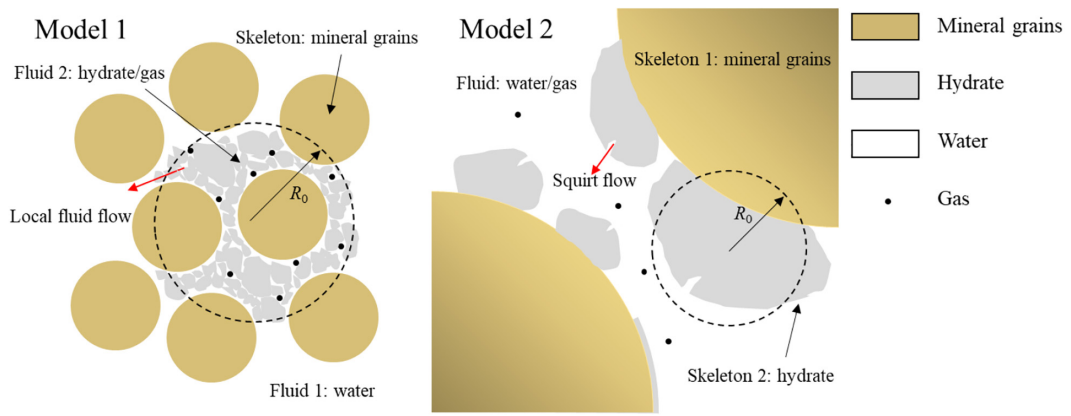

FIGURE 4 | The two models used in the workflow with the definition of the inclusion radius.

where ϕ_1 and ϕ_2 are the porosities of the water- and hydrate-saturated pores, respectively, ϕ_{10} and ϕ_{20} are the local porosities in the two regions, ρ_f, η_1 and κ_1 are the density, viscosity and permeability of the host phase fluid, respectively. b_1 and b_2 are Biot dissipation coefficients, ρ_{11}, ρ_{12}, ρ_{13}, ρ_{22}, and ρ_{33} are density coefficients, and A, Q_1, Q_2, R_1, and R_2 are stiffnesses (see **Supplementary Appendix C**).

The mixture of hydrate/gas forms a spherical inclusion of radius of R_0. It is related to the scale of hydrate as a solid component or a hydrate (fluid type)-saturated porous solid, which are embedded in the host rock frame. The phase velocity and quality factor are (Carcione, 2014).

$$V_p = [Re(v^{-1})]^{-1}, \quad Q = \frac{Re(v)}{2Im(v)}. \tag{8}$$

The volume ratios of formation water and hydrate/gas mixture are υ_1 and υ_2, respectively. According to the Biot-Rayleigh theory of patchy-saturated rocks with one solid phase and two fluid phases (Ba et al., 2012; Sun et al., 2015), $\phi_1=\phi_{10}\upsilon_1$, $\phi_2=\phi_{20}\upsilon_2$, and $\phi_{10}=\phi_{20}=\phi$. The volume ratio of mixture of hydrate/gas mixture is

$$\upsilon_2=S_h+S_g \tag{9}$$

Examples

The properties of the components the of hydrate-bearing sediment are given in **Table 1**, and other properties are shown in **Table 2** (Best et al., 2013). The free gas properties in **Table 1** are given in Ecker et al. (2000), and the free gas ratio is set as $c_g = 0.02$.

The energy losses caused by local fluid flow depends on the inclusion radius of the mixture of hydrate/gas in the pores. Four radii are selected to illustrate the physics. **Figure 5** shows the P-wave phase velocity (**Figure 5A**) and dissipation factor (**Figure 5B**) as a function of frequency for different inclusion radii. Two peaks occur, corresponding to the local and global flow mechanisms. The first moves towards the low frequencies with increasing radius. The radius mainly controls the location

TABLE 1 | Properties of the sediment constituents.

	Bulk modulus (GPa)	Shear modulus (GPa)	Density (g m^{-3})
Quartz	36.5	45	2650
Hydrate	7.9	3.3	910
Formation water	2.17	0	1006
Free gas	0.1	0	235

TABLE 2 | Other input properties.

	Value		Value
Effective pressure	500 kPa	Grain coordination number	8.5
Water viscosity	0.001 Pa s	Bulk permeability (Model 1)	100×10^{-15} m^2
Critical porosity	0.38	Bulk permeability (Model 2)	10×10^{-15} m^2

of the peak and has no significant effect on the global flow dispersion/attenuation, which occurs at high frequencies.

Porosity is an important reservoir property that affects the dry-rock moduli. The porosity of core samples in gas hydrate-bearing sediments of the Nankai Trough ranges between 35 and 43% (Zhan and Matsushima, 2018), while the porosity in Qilian Mountain permafrost is much smaller, with values between 1 and 5% (Lin et al., 2019). **Figure 6** shows the P-wave phase velocity (**Figure 6A**) and dissipation factor (**Figure 6B**) as a function of frequency for different porosities. Velocity decreases and the local and global-flow attenuations increase with increasing porosity. At 10% porosity, these loss mechanisms start to be evident and at higher porosities the two peaks split, with the global-flow one more affected.

Figure 7 shows the P-wave phase velocity (**Figure 7A**) and dissipation factor (**Figure 7B**) as a function of frequency for different hydrate concentrations. Model 1 is assumed for hydrate content less than 40%. Velocity increases with hydrate concentration. The local- and global flow peak amplitude increase with concentration. The locations of peaks are hardly affected. Basically, **Figure 7B** shows that attenuation depends on hydrate content and frequency.

Model 2: Hydrate as an Additional Skeleton

In this case, the pore fluid is a mixture of water and free gas, such that the effective bulk modulus is

$$K_f = (S_w/K_w + S_g/K_g)^{-1}, \tag{10}$$

where $S_g + S_w = 1$.

The density of the pore fluid is

$$\rho_f = \rho_w S_w + \rho_g S_g. \tag{11}$$

The porosity, after the gas-hydrate deposition can be obtained as (Helgerud et al., 1999; Ecker et al., 2000)

$$\phi_r = \phi(1 - S_h), \tag{12}$$

and the volume percentage of hydrate in the solid matrix is

$$f_h = \frac{\phi S_h}{1 - \phi_r}. \tag{13}$$

According to Eq. 6, the mineral moduli considering the presence of hydrate are

$$\begin{cases} K_s = \frac{1}{2}\left\{f_h K_h + (1-f_h)K_n + \left[\frac{f_h}{K_h} + \frac{1-f_h}{K_n}\right]^{-1}\right\} \\ G_s = \frac{1}{2}\left\{f_h G_h + (1-f_h)G_n + \left[\frac{f_h}{G_h} + \frac{1-f_h}{G_n}\right]^{-1}\right\} \end{cases}, \tag{14}$$

where K_n and G_n are the bulk modulus and shear modulus of the mineral mixtures without hydrate, respectively.

Clay is a solid component in the theory of Ba et al. (2016), i.e., and the host skeleton is composed of grains and intergranular pores, forming two solids and one fluid (water/gas). The clay squirt-flow mechanism induced by acoustic waves is discussed in that paper. Compared with hydrate as a pure solid, the hydrate micropores and intergranular pores are connected to favor squirt flow. Here, gas hydrate is modeled as clay, and it is considered to also cause wave-induced fluid flow and dissipation (Best et al., 2013; Marín-Moreno et al., 2017; Sahoo et al., 2019). X-ray CT analysis has observed the contact and cementation of gas hydrate and mineral grains in the core samples, supporting the setup of skeleton type model (Lei et al., 2018).

The dry-rock moduli are also determined with the modified Hashin–Shtrikman theory given in **Supplementary Appendix A** and the wave propagation by Eq. 7, redefining the variables and properties as in **Supplementary Appendix C** (Ba et al., 2011; Sun et al., 2015). ϕ_{10} and ϕ_{20} are the local porosities of the main skeleton and inclusions, and ϕ_1 and ϕ_2 are the absolute porosities of the main skeleton and inclusions, respectively. The hydrate skeleton forms a spherical inclusion with a radius of R_0.

The volume ratio of the inclusion phase is υ_2, and that of main skeleton is υ_1, with $\upsilon_1 + \upsilon_2 = 1$. The inclusion porosity is set $\phi_{20} = 0.05\%$. $\phi_1 = \phi_{10}\upsilon_1$ and $\phi_2 = \phi_{20}\upsilon_2$, with

$$\upsilon_2 = \phi S_h. \tag{15}$$

The porosity of the main skeleton is

$$\phi_1 = \phi_r = \phi(1 - S_h), \tag{16}$$

and the total porosity is $\bar{\phi} = \phi_1 + \phi_2$.

Examples

The inclusion radius of hydrate, which contains micropores, also affects the squirt flow. We choose the same four inclusion radii for the comparison with Model 1. **Figure 8** shows the P-wave phase velocity (**Figure 8A**) and dissipation factor (**Figure 8b**) as a function of frequency for different inclusion radii. If the radius increases, the local fluid-flow attenuation peak moves to the low frequencies. The global fluid-flow peak, occurring at high frequencies, is much weaker, almost negligible.

Figure 9 shows the P-wave phase velocity (**Figure 9A**) and dissipation factor (**Figure 9B**) as a function of frequency for

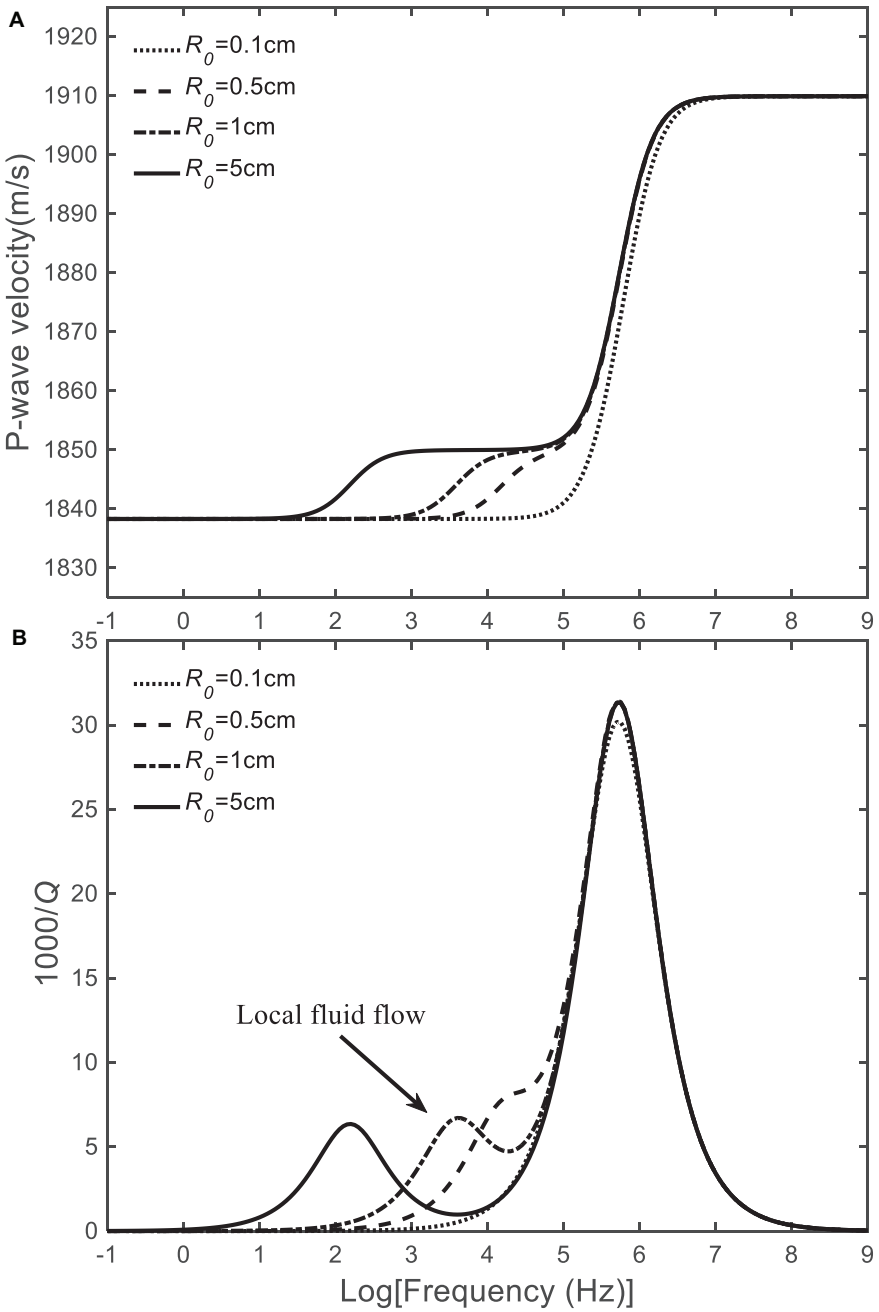

FIGURE 5 | Model 1. P-wave velocity **(A)** and dissipation factor **(B)** as a function of frequency for different inclusion radii of hydrate/gas. The hydrate concentration is 20%, and the porosity is 40%.

different porosities. As in Model 1, increasing porosity implies decreasing P-wave velocity and increasing local-flow attenuation. Beyond 40%, two attenuation peaks can be observed, with the weaker one at high frequencies being the global-flow one.

Figure 10 shows the P-wave phase velocity (**Figure 9A**) and dissipation factor (**Figure 9B**) as a function of frequency for different hydrate concentrations. The P-wave velocity increases with the concentration and the local-flow peak dissipation has a maximum value at 30% and then decreases, while the global-flow peak is weak. The first peak is mainly located at seismic frequencies.

COMPARISON WITH REAL DATA

Laboratory Data

We have used the experimental data from Priest et al. (2005, 2009) and Best et al. (2013), who performed the resonance-column

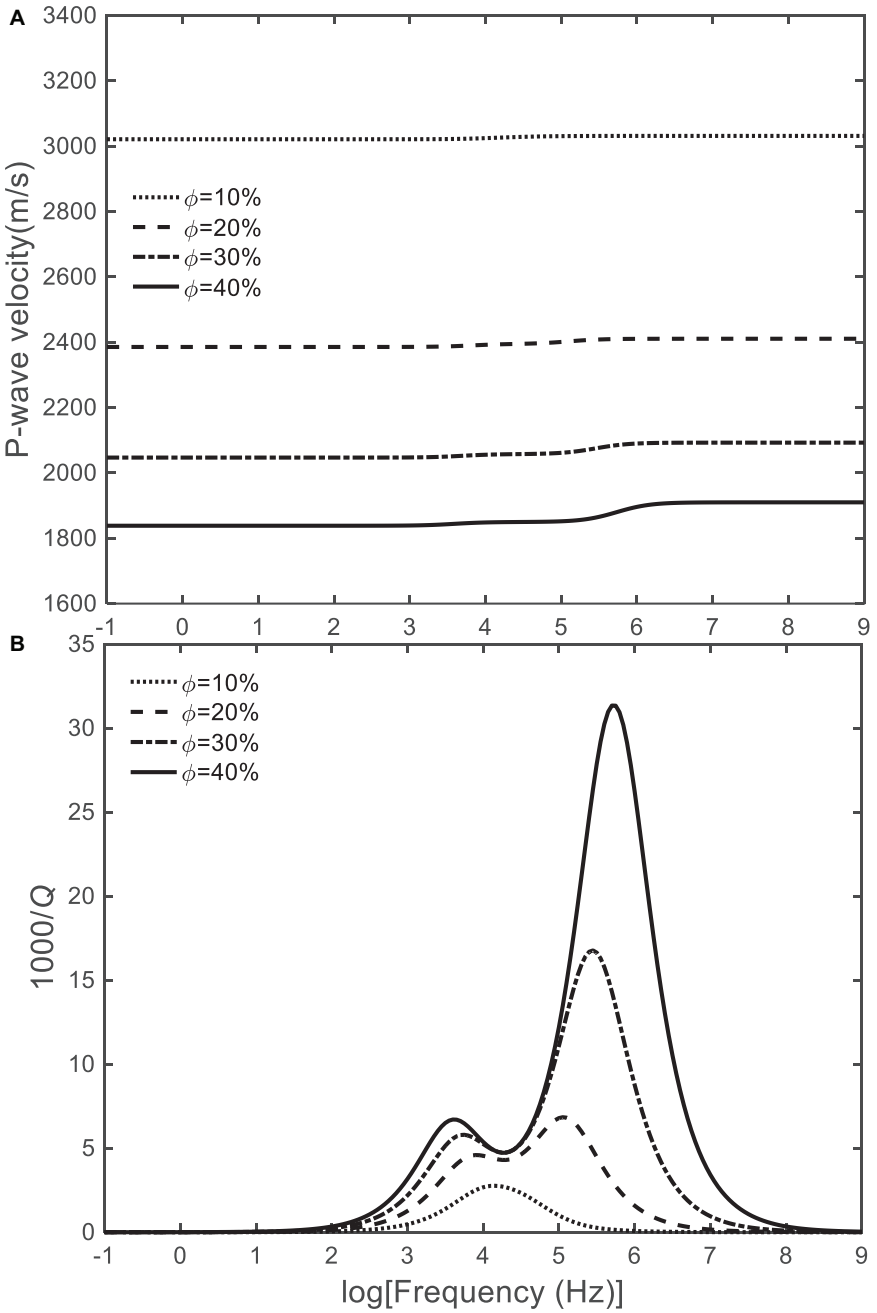

FIGURE 6 | Model 1. P-wave velocity **(A)** and dissipation factor **(B)** as a function of frequency for different rock porosities. The inclusion radius is 1 cm, and hydrate concentration is 20%.

experiments on synthetic hydrates, to further analyze the two models. Two methods, termed "excess water" and "excess gas," are implement to generate solid hydrate (Priest et al., 2009). P-wave velocity and attenuation at an effective pressure of 500 kPa were measured in sand samples (Priest et al., 2005; Priest et al., 2009; Best et al., 2013). The moduli, permeability, and critical porosity are given in **Tables 1**, **2**. In section "Laboratory Data," we choose the same grain coordination number $n = 4$ as Best et al. (2013), to compare the theoretical curves proposed by those authors.

Excess-Water Method

The continuously injected water reacts with a certain amount of methane gas to form small quantities of hydrates, which are not in contact with the grains. In this case, we have the assumption of Model 1 (Best et al., 2013; Tuan et al., 2019), with hydrate concentrations less than 40% (Priest et al., 2009; Zhao et al., 2015). **Figures 11**, **12** compare the theoretical and experimental P-wave velocities and dissipation factors as a function of hydrate concentration around 200 Hz, respectively. Porosities are 40

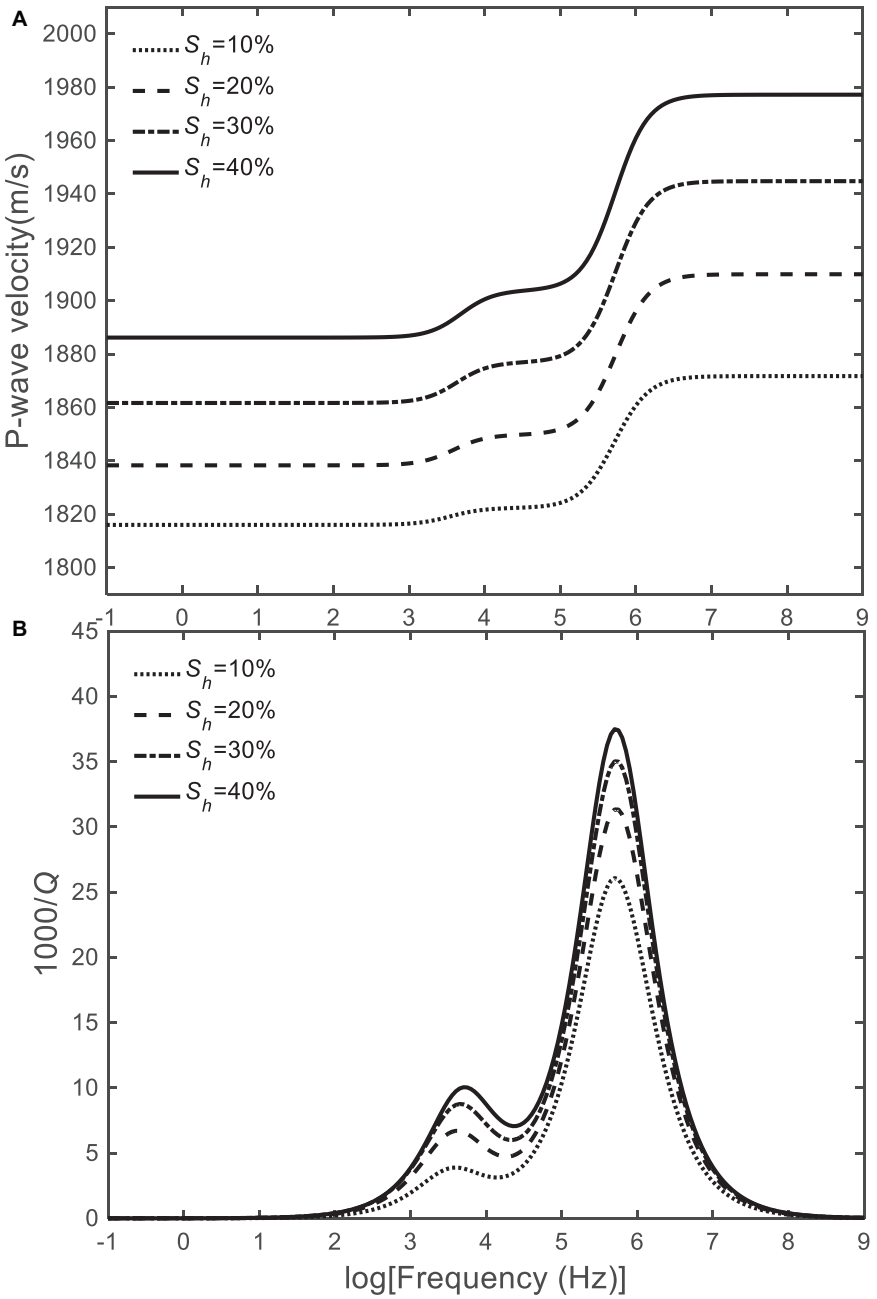

FIGURE 7 | Model 1. P-wave velocity **(A)** and dissipation factor **(B)** as a function of frequency for different hydrate contents. The inclusion radius is 1 cm and the porosity is 40%.

and 42%, respectively. The inclusion radius is 0.8 and 4 cm, respectively, based on fitting. We assume a small free-gas volume ratio (0.002), considering that the free gas does not fully react with water during the experiment. As the hydrate content increases, it gradually cements the mineral grains and we have Model 2. Chen et al. (2020) applied microtomography (CT) to analyze the evolution of hydrate pore habit during hydrate formation. Therefore, at low concentrations, the P-wave velocity increases slowly with hydrate content (Ecker et al., 1998).

Both the pore-filling model and cementing model proposed by Priest et al. (2009) are based on effective-medium theories, because Gassmann equation cannot describe the characteristics of rocks with a double-porosity structure. Therefore, Model 1 can better describe the P-wave velocity, as shown in **Figure 11**. As the hydrate content exceeds 30%, Model 1 does not fit the P-wave velocity and the assumptions of Model 2 hold. Best et al. (2013) used the effective-medium theory and the correspondence principle to model attenuation (poro-filling curve shown in

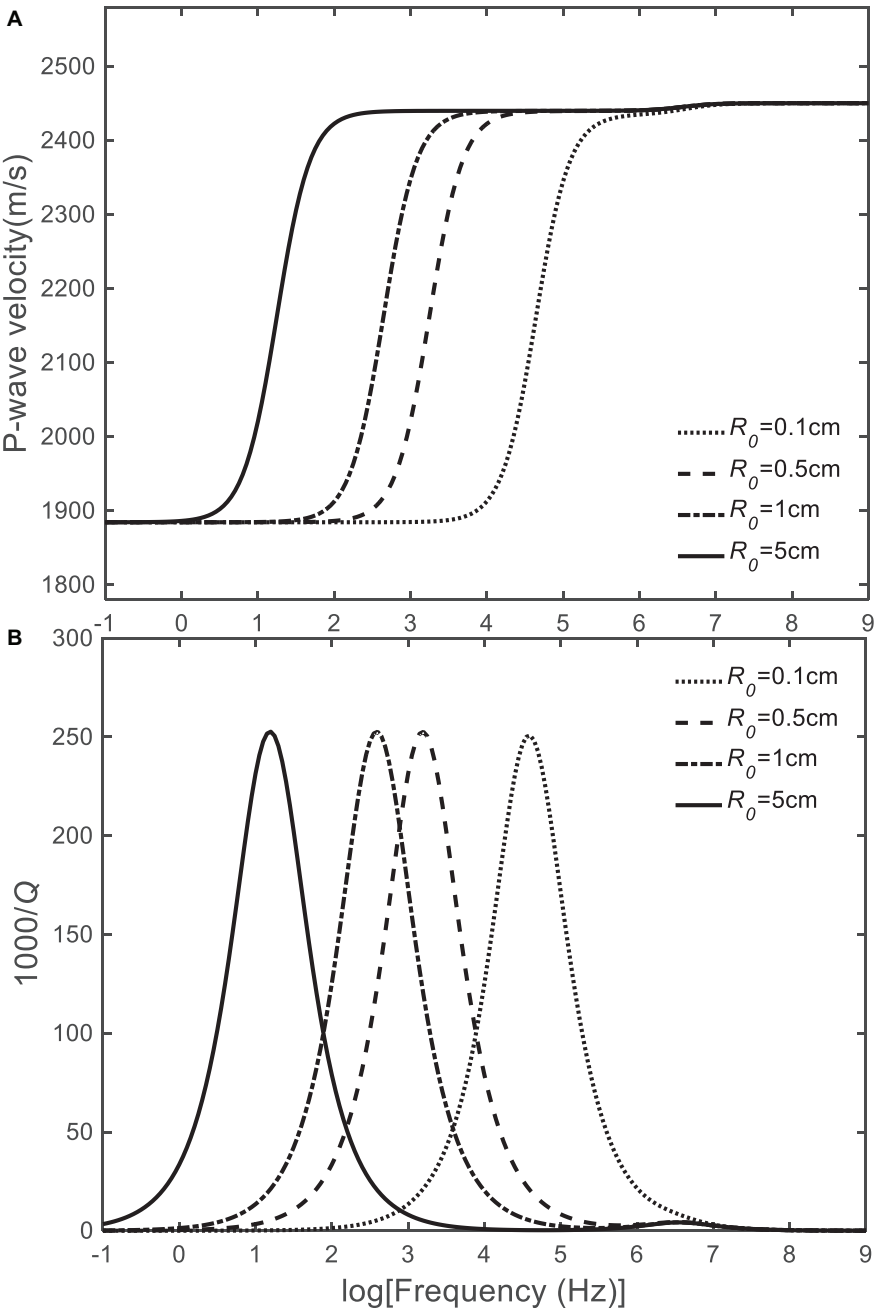

FIGURE 8 | Model 2. P-wave velocity **(A)** and dissipation factor **(B)** as a function of frequency for different inclusion radii of hydrate/gas. The hydrate concentration is 20% and the porosity is 40%.

Figure 12). Their prediction results are lower than the measured attenuation values, while Model 1 provides a relatively good fit. The key parameter is the size of the hydrate-inclusion radius.

Excess-Gas Method

A high amount of methane gas is injected to react with water, and then gas hydrate is formed at the grain contacts or at the surface of the grains. Thus, we have the conditions of Model 2 (Best et al., 2013; Tuan et al., 2019). **Figures 13**, **14** compare the theoretical and experimental P-wave velocities and dissipation factors as a function of hydrate concentration around 200 Hz, respectively (the porosities are 42%). The hydrate inclusion radius are 2 and 0.2 cm, respectively, and as in section "Excess-Water Method," the free-gas volume ratio is 0.002.

The hydrate cementing the grains significantly increases the dry-rock moduli and the P-wave velocity. Although the P-wave velocity of the cementing model proposed by Priest et al. (2009) does not fit the experimental data (**Figure 13**), it follows the trend

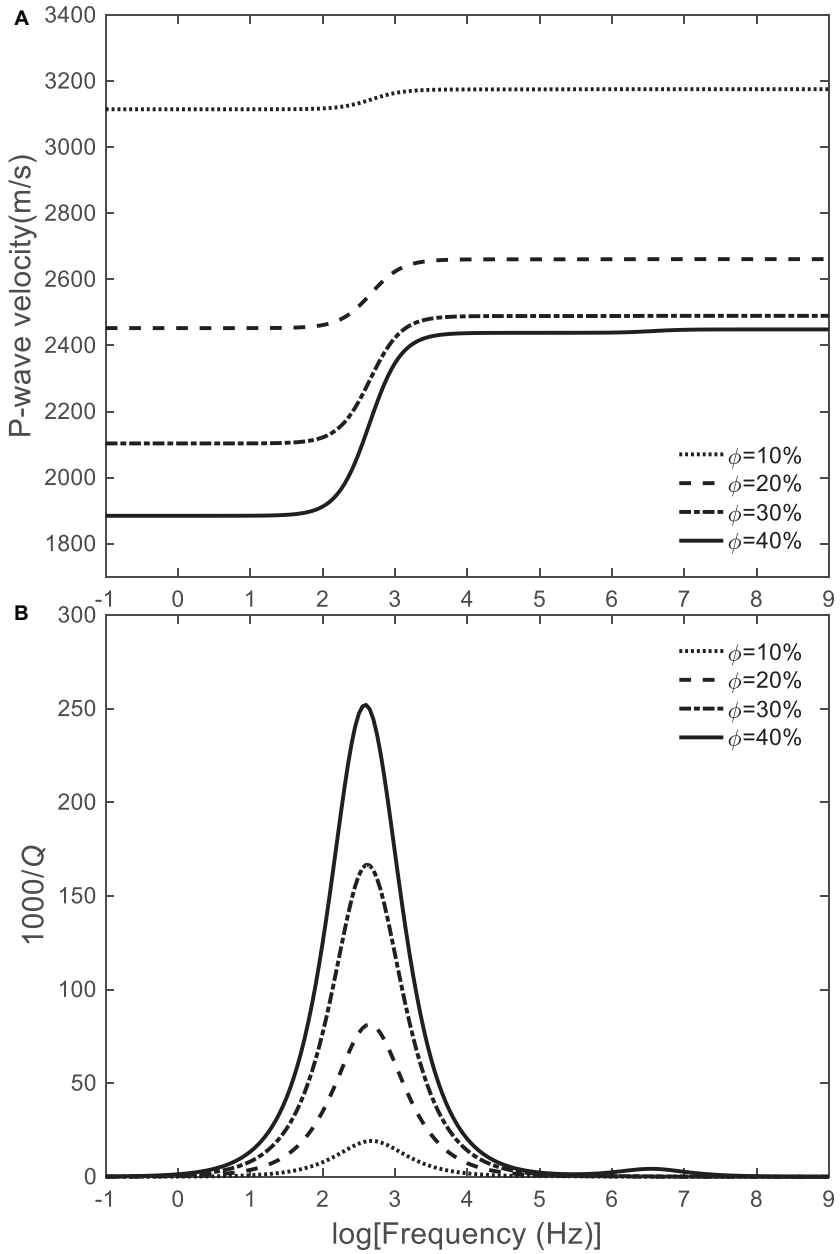

FIGURE 9 | Model 2. P-wave velocity **(A)** and dissipation factor **(B)** as a function of frequency for different rock porosities. The inclusion radius is 1 cm, and hydrate concentration is 20%.

at low hydrate content. The results from Model 2 show that the P-wave velocity increases sharply at low hydrate saturations. It is evident that Model 2 better describes the P-wave velocity data. In **Figure 14**, the load-bearing curve proposed by Best et al. (2013) agrees with the data when the hydrate content is lower than 10%, but the match of the attenuation peak of attenuation is not good. Instead, Model 2, shows a better agreement.

Sonic-Logging Data

In the hydrate-bearing sediments, estimations of hydrate concentration based on a single model may not be appropriate, because of the different spatial distributions of the hydrate. For instance, Liu et al. (2020) confirmed the coexistence of different gas-hydrate distributions from seismic velocity.

We have used the sonic-log data obtained by Zhan and Matsushima (2018) in Nankai Trough of Japan for the analysis, data required by the two models. In their work, the sonic-log (magnetic monopoles) frequency is 14 kHz, the average porosity is 40%, the grain coordination number is 8.5, the seawater viscosity is 0.0018 Pa s, and the effective pressure is about 500 kPa. The hydrate inclusion radius is 0.18 cm. **Figure 15** shows the results. The sonic-log data in **Figure 15A** shows that

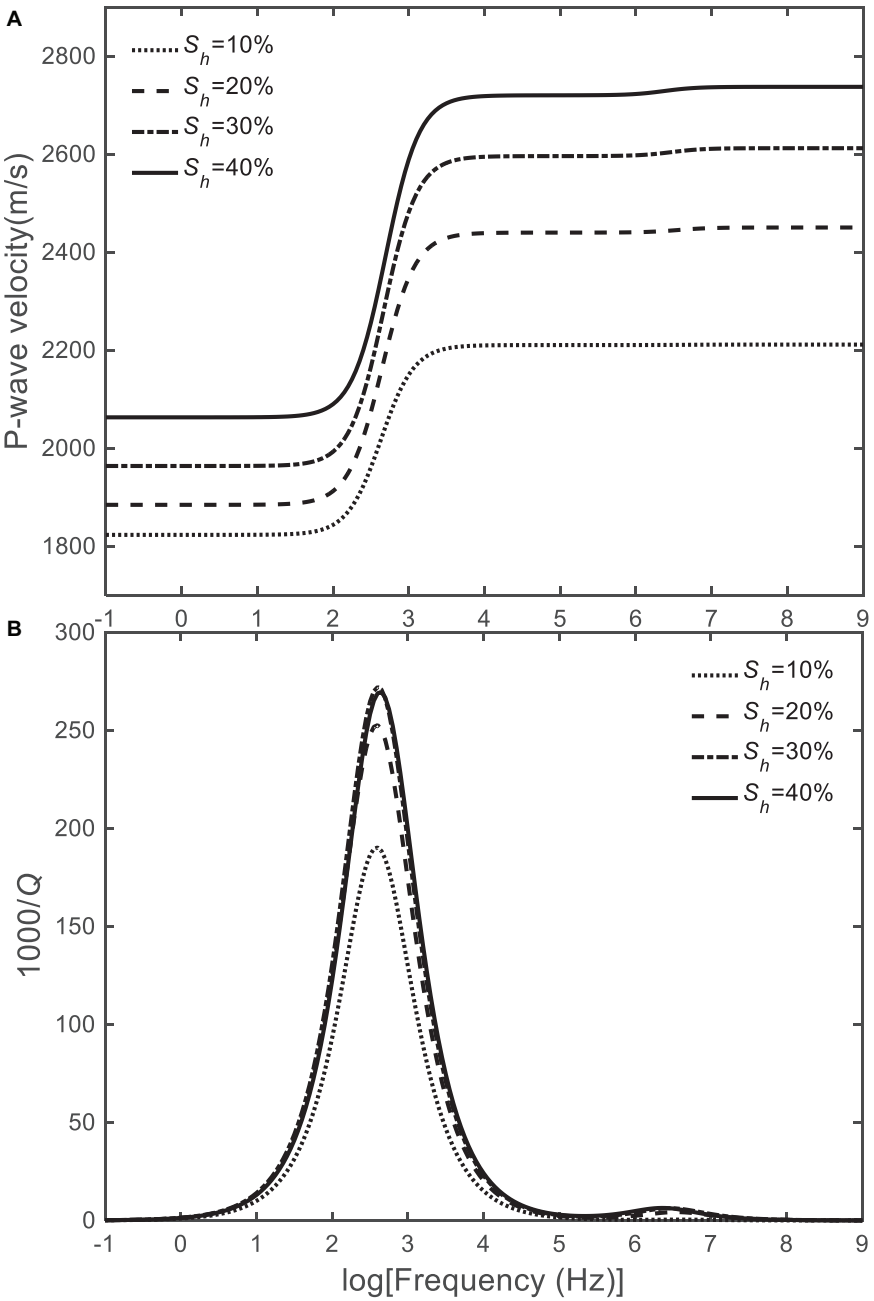

FIGURE 10 | Model 2. P-wave velocity **(A)** and dissipation factor **(B)** as a function of frequency for different hydrate contents. The inclusion radius is 1 cm and the porosity is 40%.

the P-wave velocity gradually increases with hydrate content, showing a linear relation. Zhan and Matsushima (2018) used the Marín-Moreno and Guerin models to predict P-wave velocity and attenuation, respectively. When the hydrate saturation is higher than 20%, the Guerin model is consistent with the P-wave velocity of sonic-logging data. The Marín-Moreno model considers 20% pore-filling hydrate and 80% contact cementing hydrate, giving a better prediction. Without considering the diverse hydrate morphologies, the Models 1 and 2 are applied to predict the velocities in the lower and higher bounds, respectively. **Figure 15B**, shows that the experimental dissipation factor is distributed on a wide range, which may be related to different geometrical distributions of the hydrate. Model 1 predicts low values, while those of Model 2 are more consistent with the data. The attenuation of P-wave increases first and then decreases with hydrate saturation increasing. Rossi et al. (2007) estimated a lower dissipation factor when hydrate is present at lower frequencies than those involved in **Figure 15B**. The increasing

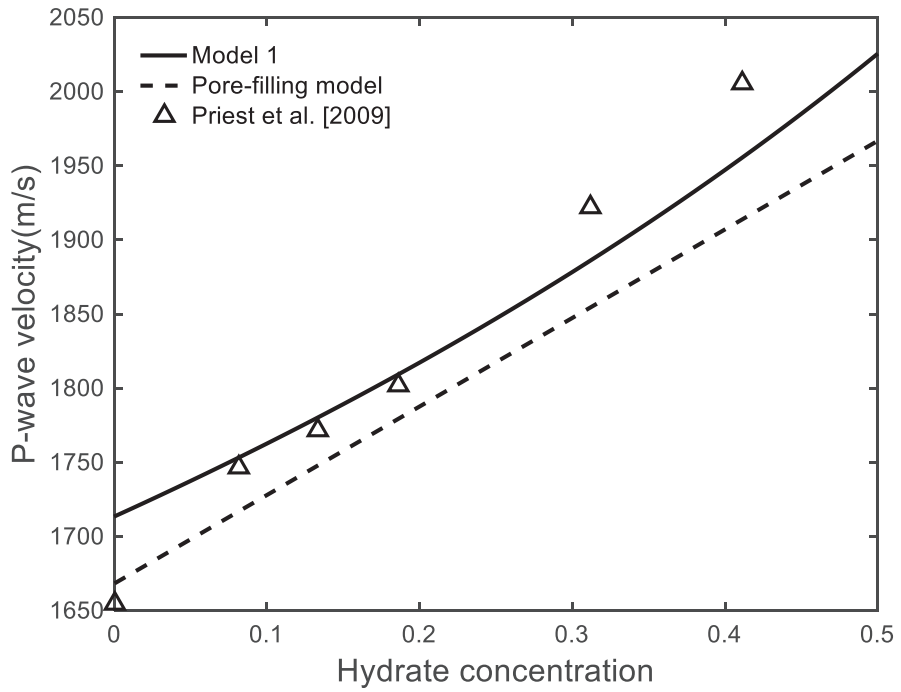

FIGURE 11 | Model 1. P-wave velocity as a function of hydrate concentration. The frequency is around 200 Hz. The pore-filling model curve and the experimental data (triangles) are taken from Priest et al. (2009).

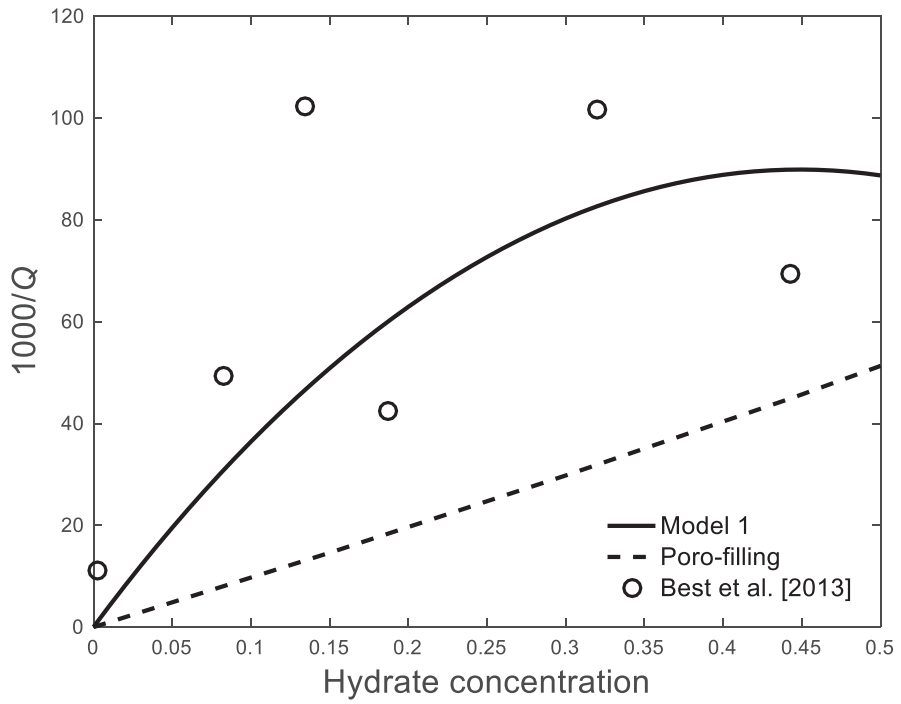

FIGURE 12 | Model 1. Dissipation factor as a function of hydrate concentration. The frequency is around 200 Hz. The pore-filling model and the experimental data (circles) are taken from Best et al. (2013).

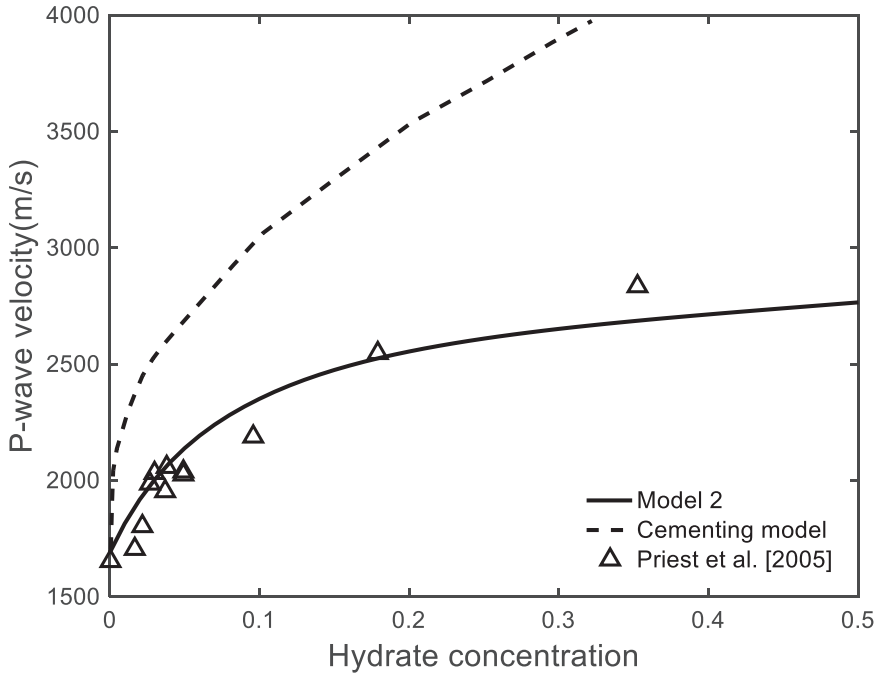

FIGURE 13 | Model 2. P-wave velocity as a function of hydrate concentration. The frequency is around 200 Hz. The cementing-model curve and experimental data (triangles) are taken from Priest et al. (2005).

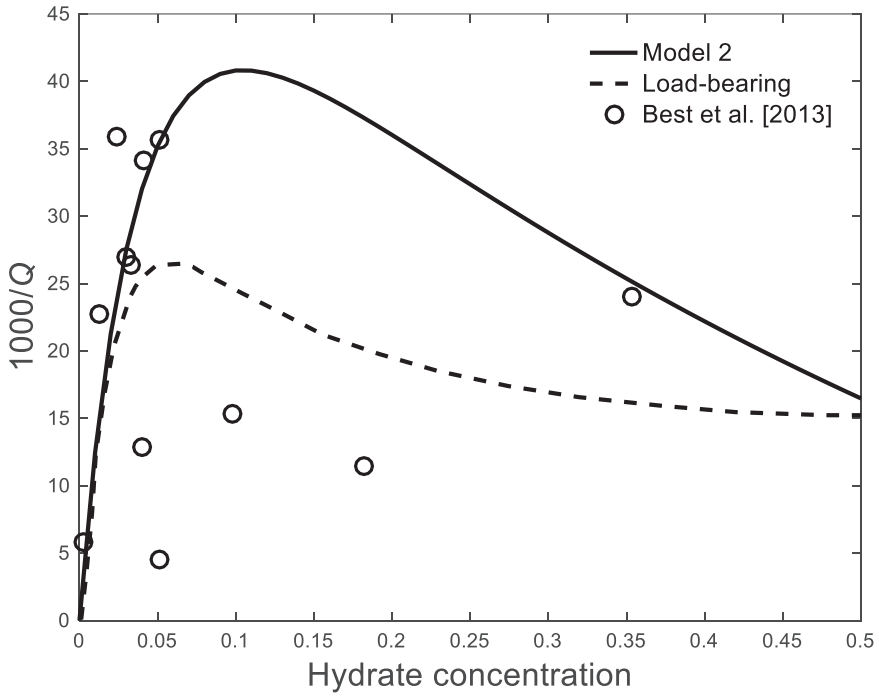

FIGURE 14 | Model 2. Dissipation factor as a function of hydrate concentration. The frequency is around 200 Hz. The load-bearing model curve and experimental data (circles) are taken from Best et al. (2013).

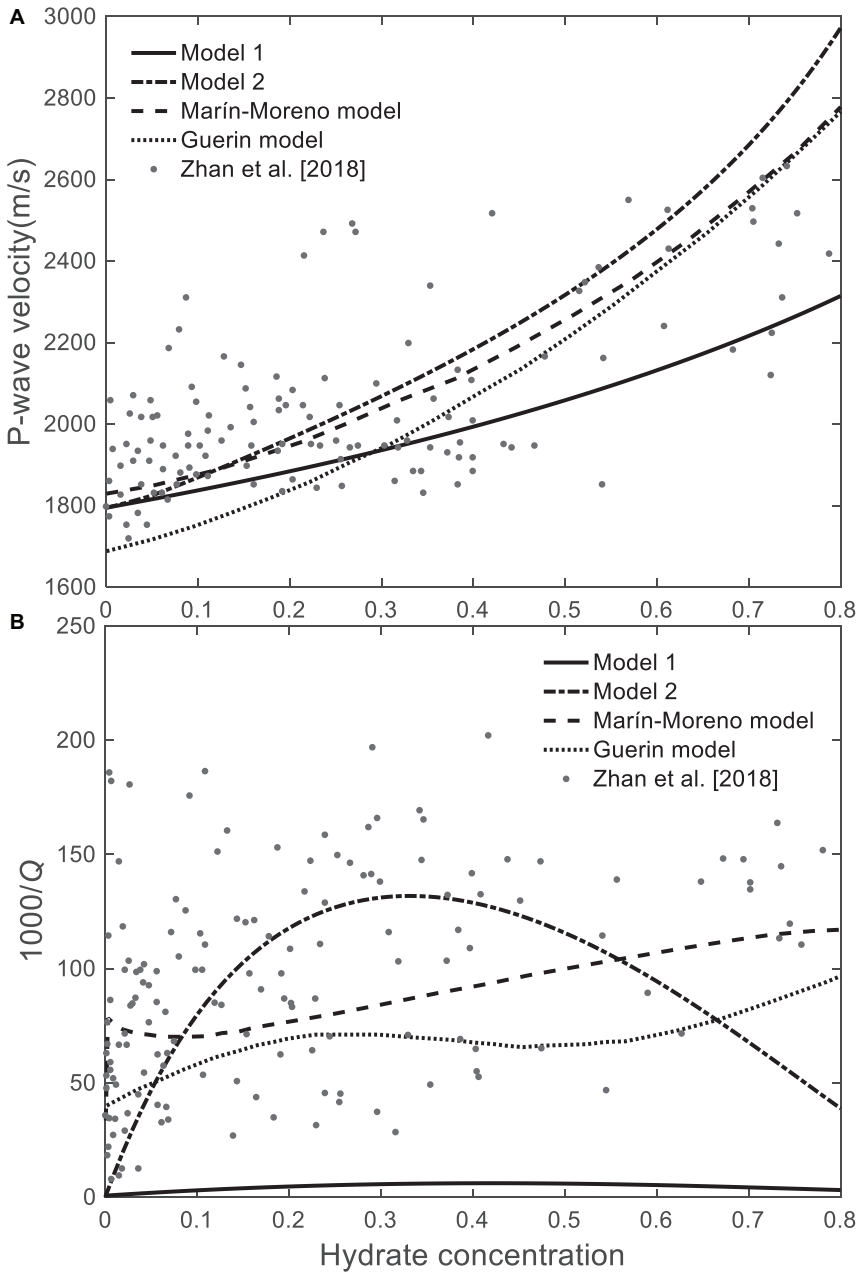

FIGURE 15 | Model comparison with those of the other authors. **(A)** P-wave velocity and **(B)** dissipation factor.

attenuation at low concentrations can be due to a local-flow mechanism or to scattering loss, since the data corresponds to sonic frequencies.

CONCLUSION

We propose two models to calculate the wave velocity and attenuation of gas-hydrate bearing sediments, based on the Biot-Rayleigh double-porosity theory and two different distributions of the hydrate in the porous medium. The difference is that in one case hydrate is part of the pore infill and in the other constitutes an additional (load-bearing) skeleton. The local inclusion radius of the Biot-Rayleigh theory is related to the hydrate/gas mixture in the first model and to the hydrate frame in the second. The models predict two relaxation peaks, namely the local-flow one (mesoscopic loss) and the classical global flow one, also predicted by the Biot theory. As expected, P-wave velocity decreases and attenuation increases with porosity. The local-flow relaxation (attenuation) peak moves to the low frequencies with increasing inclusion radius. More hydrate content has the effect to increase the attenuation at low values, reach a maximum loss and then decrease it. Modeling results are compared with data obtained from the excess-water and excess-gas experiments,

which generally reproduce the conditions of the first and second models, respectively. The predictions describe quite satisfactory the measured data in both cases. Moreover, comparisons with log data show a good agreement, in particular the second model (hydrate forming a frame). The models can be useful to estimate gas-hydrate content from seismic data.

DATA AVAILABILITY STATEMENT

The original contributions presented in the study are included in the article/**Supplementary Material**, and further inquiries can be directed to the corresponding author/s.

AUTHOR CONTRIBUTIONS

WW: modeling and writing. JB: modeling and writing and verification. JC: translation and suggestion. XL: suggestion. LZ: communication and guidance. All authors contributed to the article and approved the submitted version.

FUNDING

The authors were grateful to the support of the Jiangsu Innovation and Entrepreneurship Plan, the research funds from SINOPEC Key Laboratory of Geophysics, Jiangsu Province Science Fund for Distinguished Young Scholars (BK20200021), and National Natural Science Foundation of China (41974123).

SUPPLEMENTARY MATERIAL

The Supplementary Material for this article can be found online at: https://www.frontiersin.org/articles/10.3389/feart.2021.640424/full#supplementary-material

REFERENCES

Ba, J., Carcione, J. M., Cao, H., Du, Q. Z., Yuan, Z. Y., and Lu, M. H. (2012). Velocity dispersion and attenuation of P waves in partially-saturated rocks: wave propagation equations in double-porosity medium. *Chinese J. Geophys. (in Chinese)* 55, 219–231.

Ba, J., Carcione, J. M., and Nie, J. X. (2011). Biot-Rayleigh theory of wave propagation in double-porosity media. *J. Geophys. Res. Solid Earth* 116:B06202.

Ba, J., Zhao, J., Carcione, J. M., and Huang, X. X. (2016). Compressional wave dispersion due to rock matrix stiffening by clay squirt flow. *Geophys. Res. Lett.* 43, 6186–6195. doi: 10.1002/2016gl069312

Best, A. I., Priest, J. A., Clayton, C. R. I., and Rees, E. V. L. (2013). The effect of methane hydrate morphology and water saturation on seismic wave attenuation in sand under shallow sub-seafloor conditions. *Earth Planetary Sci. Lett.* 368, 78–87. doi: 10.1016/j.epsl.2013.02.033

Carcione, J. M. (2014). *Wave Fields in Real Media. Theory and Numerical Simulation of Wave Propagation in Anisotropic, Anelastic, Porous and Electromagnetic Media*, 3rd Edn. Amsterdam: Elsevier.

Carcione, J. M., and Gei, D. (2004). Gas-hydrate concentration estimated from P- and S-wave velocities at the Mallik 2L-38 research well, Mackenzie Delta. Canada. *J. Appl. Geophys.* 56, 73–78. doi: 10.1016/j.jappgeo.2004.04.001

Carcione, J. M., Gei, D., Rossi, G., and Madrussani, G. (2005). Estimation of gas-hydrate concentration and free-gas saturation at the Norwegian-Svalbard continental margin. *Geophys. Prospect.* 53, 803–810. doi: 10.1111/j.1365-2478.2005.00502.x

Carcione, J. M., Gei, D., Rossi, G., and Tinivella, U. (2012). *Wave Theory, Simulation, and Determination of Gas-hydrate Content in Sediments*. Tulsa, OK: Society of Exploration Geophysicists.

Carcione, J. M., and Tinivella, U. (2000). Bottom-simulating reflectors: seismic velocities and AVO effects. *Geophysics* 65, 54–67. doi: 10.1190/1.1444725

Chand, S., and Minshull, T. A. (2003). Seismic constraints on the effects of gas hydrate on sediment physical properties and fluid flow: a review. *Geofluids* 3, 275–289. doi: 10.1046/j.1468-8123.2003.00067.x

Chand, S., and Minshull, T. A. (2004). The effect of hydrate content on seismic attenuation: a case study for Mallik 2L-38 well data, Mackenzie delta. Canada. *Geophys. Res. Lett.* 31:L14609.

Chand, S., Minshull, T. A., Gei, D., and Carcione, J. M. (2004). Elastic velocity models for gas-hydrate-bearing sediments—a comparison. *Geophys. J. Int.* 159, 573–590. doi: 10.1111/j.1365-246x.2004.02387.x

Chand, S., Minshull, T. A., Priest, J. A., Best, A. I., Clayton, C. R. I., and Waite, W. F. (2006). An effective medium inversion algorithm for gas hydrate quantification and its application to laboratory and borehole measurements of gas hydrate-bearing sediments. *Geophys. J. Int.* 166, 543–552. doi: 10.1111/j.1365-246x.2006.03038.x

Chen, X. Y., Espinoza, D. N., Luo, J. S., Tisato, N., and Flemings, P. B. (2020). Pore-scale evidence of ion exclusion during methane hydrate growth and evolution of hydrate pore-habit in sandy sediments. *Mar. Petroleum Geol.* 117:104340. doi: 10.1016/j.marpetgeo.2020.104340

Dvorkin, J., and Nur, A. M. (1993). Dynamic poroelasticity: a unified model with the squirt and the Biot mechanisms. *Geophysics* 58, 524–533. doi: 10.1190/1.1443435

Dvorkin, J., Nur, A. M., Uden, R., and Taner, T. (2003). Round table—rock physics of a gas hydrate reservoir. *Leading Edge* 22, 842–847. doi: 10.1190/1.1614153

Dvorkin, J., Prasad, M., Sakai, A., and Lavoie, D. (1999). Elasticity of marine sediments: rock physics modeling. *Geophys. Res. Lett.* 26, 1781–1784. doi: 10.1029/1999gl900332

Ecker, C., Dvorkin, J., and Nur, A. M. (1998). Sediments with gas hydrates: internal structure from seismic AVO. *Geophysics* 63, 1659–1669. doi: 10.1190/1.1444462

Ecker, C., Dvorkin, J., and Nur, A. M. (2000). Estimating the amount of gas hydrate and free gas from marine seismic data. *Geophysics* 65, 565–573. doi: 10.1190/1.1444752

Gei, D., and Carcione, J. M. (2003). Acoustic properties of sediments saturated with gas hydrate, free gas and water. *Geophys. Prospect.* 51, 141–158. doi: 10.1046/j.1365-2478.2003.00359.x

Guerin, G., and Goldberg, D. (2002). Sonic waveform attenuation in gas hydrate-bearing sediments from the Mallik 2L-38 research well, Mackenzie Delta, Canada, Mackenzie Delta, Canada. *J. Geophys. Res. Solid Earth* 107:2088.

Guerin, G., and Goldberg, D. (2005). Modeling of acoustic wave dissipation in gas hydrate-bearing sediments. *Geochem. Geophys. Geosystems* 6:Q07010.

Helgerud, M. B., Dvorkin, J., Nur, A., Sakai, A., and Collett, T. (1999). Elastic-wave velocity in marine sediments with gas hydrates: effective medium modeling. *Geophys. Res. Lett.* 26, 2021–2024. doi: 10.1029/1999gl900421

Konno, Y., Jin, Y., Yoneda, J., Kida, M., Egawa, K., Ito, T., et al. (2015). Effect of methane hydrate morphology on compressional wave velocity of sandy sediments: analysis of pressure cores obtained in the Eastern Nankai Trough. *Mar. Petroleum Geol.* 66, 425–433. doi: 10.1016/j.marpetgeo.2015.02.021

Kuhs, W. F., Genov, G., Goreshnik, E., Zeller, A., Techmer, K. S., and Bohrmann, G. (2004). The impact of porous microstructures of gas hydrates on their macroscopic properties. *Int. J. Offshore Polar Eng.* 14, 305–309.

Leclaire, P., Cohen-Tenoudji, F., and Aguirre-Puente, J. (1994). Extension of Biot's theory of wave propagation to frozen porous media. *J. Acoustical Soc. Am.* 96, 3753–3768.

Lee, J. Y., Francisca, F. M., Santamarina, J. C., and Ruppel, C. (2010). Parametric study of the physical properties of hydrate-bearing sand, silt, and clay sediments: 2. Small-strain mechanical properties. *J. Geophys. Res. Solid Earth* 115:B11105.

Lee, M. W. (2002a). Biot–Gassmann theory for velocities of gas hydrate-bearing sediments. *Geophysics* 67, 1711–1719. doi: 10.1190/1.1527072

Lee, M. W. (2002b). Modified biot-gassmann theory for calculating elastic velocities for unconsolidated and consolidated sediments. *Mar. Geophys. Res.* 23, 403–412. doi: 10.1023/b:mari.0000018195.75858.12

Lee, M. W., and Waite, W. F. (2008). Estimating pore-space gas hydrate saturations from well log acoustic data. *Geochem. Geophys. Geosystems* 9:Q07008.

Lei, L., Seol, Y., Choi, J. H., and Jarvis, K. (2018). Pore-Scale visualization of methane hydrate-bearing sediments with micro-CT. *Geophys. Res. Lett.* 104, 451–467.

Leurer, K. C. (1997). Attenuation in fine-grained marine sediments: extension of the Biot-Stoll model by the "effective grain model" (EGM). *Geophysics* 62, 1465–1479. doi: 10.1190/1.1444250

Lin, Z. Z., Dong, H. M., Pan, H., Sun, J. M., Fang, H., and Wang, X. J. (2019). Study on the equivalence between gas hydrate digital rocks and hydrate rock physical models. *J. Petroleum Sci. Eng.* 181:UNS106241.

Liu, J., Liu, J. P., Cheng, F., Wang, J., and Liu, X. X. (2017). Rock-physics models of hydrate-bearing sediments in permafrost, Qilian Mountains, China. *Appl. Geophys.* 14, 31–39. doi: 10.1007/s11770-017-0608-y

Liu, X. X., Yin, X. Y., and Luan, X. W. (2018). Seismic rock physical modelling for gas hydrate-bearing sediments. *Sci. China-Earth Sci.* 61, 1261–1278. doi: 10.1007/s11430-017-9214-2

Liu, Z. C., Ning, F. L., Hu, G. W., Liu, L. L., Liu, C. L., Peng, L., et al. (2020). Characterization of seismic wave velocity and attenuation and interpretation of tetrahydrofuran hydrate-bearing sand using resonant column testing. *Mar. Petroleum Geol.* 122:104620. doi: 10.1016/j.marpetgeo.2020.104620

Marín-Moreno, H., Sahoo, S. K., and Best, A. I. (2017). Theoretical modeling insights into elastic wave attenuation mechanisms in marine sediments with pore-filling methane hydrate. *J. Geophys. Res. Solid Earth* 122, 1835–1847.

Matsushima, J. (2006). Seismic wave attenuation in methane hydrate-bearing sediments: vertical seismic profiling data from the Nankai Trough exploratory well, offshore Tokai, central Japan. *J. Geophys. Res. Solid Earth* 111:B10101.

Pan, H. J., Li, H. B., Chen, J. Y., Zhang, Y., Liu, X. B., Cai, S. J., et al. (2019). Evaluation of gas hydrate resources using hydrate morphology-dependent rock physics templates. *J. Petroleum Sci. Eng.* 182:106268. doi: 10.1016/j.petrol.2019.106268

Priest, J. A., Best, A. I., and Clayton, C. R. I. (2005). A laboratory investigation into the seismic velocities of methane gas hydrate-bearing sand. *J. Geophys. Res. Solid Earth* 110:B04102.

Priest, J. A., Rees, E. V. L., and Clayton, C. R. I. (2009). Influence of gas hydrate morphology on the seismic velocities of sands. *J. Geophys. Res. Solid Earth* 114:B11205.

Qu, L., Zou, C. C., Lu, Z. Q., Yu, C. Q., Li, N., Zhu, J. C., et al. (2016). Elastic-wave velocity characterization of gas hydrate-bearing fractured reservoirs in a permafrost area of the Qilian Mountain, Northwest China. *Mar. Petroleum Geol.* 88, 1047–1058. doi: 10.1016/j.marpetgeo.2016.08.017

Rossi, G., Gei, D., Bohm, G., and Madrussani, G. (2007). Attenuation tomography: an application to gas-hydrate and free-gas detection. *Geophys. Prospect.* 55, 655–669. doi: 10.1111/j.1365-2478.2007.00646.x

Sahoo, S. K., North, L. J., Marín-Moreno, H., Minshull, T. A., and Best, A. I. (2019). Laboratory observations of frequency-dependent ultrasonic P-wave velocity and attenuation during methane hydrate formation in Berea sandstone. *Geophys. J. Int.* 219, 713–723. doi: 10.1093/gji/ggz311

Sell, K., Quintal, B., Kersten, M., and Saenger, E. H. (2018). Squirt flow due to interfacial water films in hydrate bearing sediments. *Solid Earth* 9, 699–711. doi: 10.5194/se-9-699-2018

Sell, K., Saenger, E. H., Falenty, A., Chaouachi, M., Haberthur, D., Enzmann, F., et al. (2016). On the path to the digital rock physics of gas hydrate-bearing sediments - processing of in situ synchrotron-tomography data. *Solid Earth* 7, 1243–1258. doi: 10.5194/se-7-1243-2016

Sun, W. T., Ba, J., Muller, T. M., Carcione, J. M., and Cao, H. (2015). Comparison of P-wave attenuation models of wave-induced flow. *Geophys. Prospect.* 63, 378–390. doi: 10.1111/1365-2478.12196

Tinivella, U., and Carcione, J. M. (2001). Estimation of gas-hydrate concentration and free-gas saturation from log and seismic data. *Leading Edge* 20, 200–203. doi: 10.1190/1.1438914

Tuan, N. S., Tang, A. M., To, Q. D., and Vu, M. N. (2019). A model to predict the elastic properties of gas hydrate-bearing sediments. *J. Appl. Geophys.* 169, 154–164. doi: 10.1016/j.jappgeo.2019.05.003

Waite, W. F., Santamarina, J. C., Cortes, D. D., Dugan, B., Espinoza, D. N., Germaine, J., et al. (2009). Physical properties of hydrate-bearing sediments. *Rev. Geophys.* 47:RG4003.

Zhan, L. S., and Matsushima, J. (2018). Frequency-dependent P-wave attenuation in hydrate-bearing sediments: a rock physics study at Nankai Trough, Japan. *Geophys. J. Int.* 214, 1961–1985. doi: 10.1093/gji/ggy229

Zhao, J. F., Yang, L., Liu, Y., and Song, Y. C. (2015). Microstructural characteristics of natural gas hydrates hosted in various sand sediments. *Phys. Chem. Chem. Phys.* 17, 22632–22641. doi: 10.1039/c5cp03698d

Conflict of Interest: The authors declare that the research was conducted in the absence of any commercial or financial relationships that could be construed as a potential conflict of interest.

Copyright © 2021 Wang, Ba, Carcione, Liu and Zhang. This is an open-access article distributed under the terms of the Creative Commons Attribution License (CC BY). The use, distribution or reproduction in other forums is permitted, provided the original author(s) and the copyright owner(s) are credited and that the original publication in this journal is cited, in accordance with accepted academic practice. No use, distribution or reproduction is permitted which does not comply with these terms.

frontiers in Earth Science

ORIGINAL RESEARCH
published: 29 April 2021
doi: 10.3389/feart.2021.641651

Rock Physical Modeling and Seismic Dispersion Attribute Inversion for the Characterization of a Tight Gas Sandstone Reservoir

Han Jin[1], Cai Liu[1], Zhiqi Guo[1], Yiming Zhang[2], Cong Niu[2], Di Wang[2] and Yun Ling[2]*

[1] College of Geo-Exploration Science and Technology, Jilin University, Changchun, China, [2] CNOOC Research Institute Co., Ltd., Beijing, China

Gas identification using seismic data is challenging for tight gas reservoirs with low porosity and permeability due to the complicated poroelastic behaviors of tight sandstone. In this study, the Chapman theory was used to simulate the dispersion and attenuation caused by the squirt flow of fluids in the complex pore spaces, which are assumed to consist of high aspect-ratio pores (stiff pores) and low aspect-ratio microcracks (soft pores). The rock physics modeling revealed that as the gas saturation varies, P-wave velocity dispersion and attenuation occurs at seismic frequencies, and it tends to move to high frequencies as the gas saturation increases. The velocity dispersion of the tight gas sandstone causes a frequency-dependent contrast in the P-wave impedance between the tight sandstone and the overlying mudstone, which consequently leads to frequency-dependent incidence reflection coefficients across the interface. In the synthetic seismic AVO modeling conducted by integrating the rock physics model and the propagator matrix method, the variations in the amplitudes and phases of the PP reflections can be observed for various gas saturations. The tests of the frequency-dependent AVO inversion of these synthetic data revealed that the magnitude of the inverted P-wave dispersion attribute can be used to indicate gas saturation in tight sandstone reservoirs. The applications of the frequency-dependent AVO inversion to the field pre-stacked seismic data revealed that the obtained P-wave dispersion attribute is positively correlated with the gas production from the pay zone at the well locations. Thus, the methods of the rock physics modeling and the frequency-dependent AVO inversion conducted in this study have good potential for the evaluation of the gas saturation in tight gas sandstone reservoirs.

Keywords: tight gas sandstone, rock physics, seismic responses, dispersion attribute, gas saturation

OPEN ACCESS

Edited by:
Jing Ba,
Hohai University, China

Reviewed by:
Zhiwei Wang,
China University of Petroleum (Huadong), China
Fei Gong,
China University of Petroleum, China

****Correspondence:***
Zhiqi Guo
zhiqiguo@aliyun.com

Specialty section:
This article was submitted to Solid Earth Geophysics, a section of the journal Frontiers in Earth Science

Received: *14 December 2020*
Accepted: *01 March 2021*
Published: *29 April 2021*

Citation:
Jin H, Liu C, Guo Z, Zhang Y, Niu C, Wang D and Ling Y (2021) Rock Physical Modeling and Seismic Dispersion Attribute Inversion for the Characterization of a Tight Gas Sandstone Reservoir. Front. Earth Sci. 9:641651. doi: 10.3389/feart.2021.641651

INTRODUCTION

Tight gas sandstone is generally characterized by a strong heterogeneity, low effective porosity, and extremely low permeability. It is challenging to predict the complicated poroelastic behaviors of tight gas sandstone due to the presence of a complex pore and crack system. Correspondingly, the seismic responses from tight gas sandstone are complex because of the dispersion and attenuation caused by the squirt flow of fluids in the complex pore spaces when the seismic waves pass through the tight sandstone. Thus, in order to evaluate the fluid properties of tight sandstone, it is essential to construct valid rock physics models for the investigation

of seismic dispersion and attenuation and to develop effective techniques for estimating gas saturation using such poroelastic properties.

For rock physics modeling for a poroelastic medium, Biot (1956a,b) established a macroscopic pore elasticity model in order to consider global fluid-flow in a fluid saturated medium. White (1975) proposed a model that considers the dispersion and attenuation that occurs at the seismic frequencies associated with the patchy saturation of two fluid phases. Dvorkin and Nur (1993) developed the Biot/Squirt (BISQ) model by combining the global Biot flow and the local squirt-flow mechanism. Chapman et al. (2002) and Chapman (2003, 2009) proposed the theory of multiscale fractures for an effective medium containing microscopic pores and cracks and with mesoscopic fractures. Ba et al. (2012) investigated the Biot-Rayleigh theory for modeling tight gas sandstone using a double-pore model. Ba et al. (2016) researched compressional wave dispersion due to rock matrix stiffening by clay squirt flow. Ba et al. (2017) investigated the wave propagating in an anelastic rock with patchy-saturation and fabric heterogeneity.

For the investigation of the seismic responses associated with fluid flow, the frequency-dependent amplitude variation with offset (AVO) method was proposed. Chapman et al. (2005, 2006) analyzed the frequency dependency of the AVO signatures associated with the dispersion and attenuation caused by the presence of fluids. Wilson et al. (2009) and Wilson (2010) extended the conventional AVO approximation to frequency dependency and derived the P-wave dispersion attribute as an indicator for reservoir fluid characterization, in which the spectral decomposition technique was used in the implement of the dispersion attribute inversion. Wu (2010) improved the accuracy of the time-frequency analysis in the inversion in the application of field data. Zhang et al. (2014) extended the AVO Shuey approximation and introduced the concepts of a frequency-dependent intercept and gradient into the AVO inversion. Li (2013) investigated numerical and physical modeling as well as field data for the frequency-dependent AVO in order to enable the quantitative estimation of gas saturation. Wu et al. (2014) also illustrated another field case study of the frequency-dependent AVO by improving the procedure of inversion. Chen et al. (2015) quantitatively calculated the gas saturation based on the dispersion inversion using stacked seismic data. Wang et al. (2019) investigated the problem of reflection and transmission of plane elastic waves at an interface between two double-porosity media.

In this study, we developed a rock physics model for a tight gas sandstone reservoir based on the Chapman theory that considers the squirt flow of fluids in complex pore spaces. Then we used our model to investigate the influence of gas saturation on P-wave velocity dispersion and attenuation. The frequency-dependent AVO modeling and inversion were tested and analyzed for various gas saturations using synthetic data. Finally, the frequency-dependent AVO inversion was applied to field data for a tight gas sandstone reservoir, and the P-wave dispersion attributes were inverted and calibrated in order to determine the gas saturation in the tight sandstone reservoir.

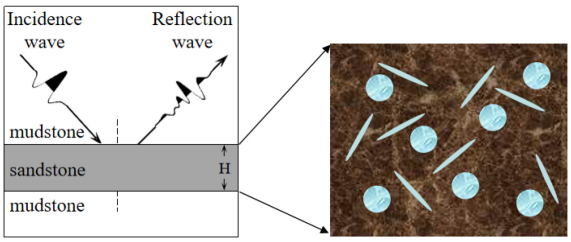

FIGURE 1 | Schematics of the microstructural distributions of stiff and soft pores in tight sandstone.

MATERIALS AND METHODS

Rock Physics Model of Tight Sandstone

For tight gas sandstone reservoirs, their complex pore structures result in complicated elastic properties and seismic responses associated with fluids. Smith et al. (2009) and Ruiz and Cheng (2010) investigated a rock model including soft and stiff pores, which divided the complex pores into stiff pores and soft pores. They studied the influence of the distributions of stiff and soft pores on the elastic properties of tight sandstone. Their results indicated that the dual-porosity model can well predict the elastic behaviors of tight sandstone. However, this model could not describe inelasticity associated with fluids. Chapman (2003) proposed the theory of multiscale pores and fractures and studied the dispersion and attenuation related to the squirt flow of fluids in complex pore spaces in gas sandstone reservoirs. Thus, we used the concept of stiff and soft pores in Chapman's theory to describe pore structures of tight gas sandstone reservoirs. A schematic diagram of the complex pore spaces consisting of stiff and soft pores is shown in **Figure 1**.

In Chapman's theory (Chapman, 2003), the expression for the anisotropic stiffness matrix of an equivalent medium is

$$C_{ijkl} = C^0_{ijkl} - \phi_p C^1_{ijkl} - \varepsilon_c C^2_{ijkl} - \varepsilon_f C^3_{ijkl} \tag{1}$$

where $C^0{}_{ijkl}$ *is* the stiffness of the isotropic background; $C^1{}_{ijkl}$, $C^2{}_{ijkl}$, and $C^3{}_{ijkl}$ are the disturbances caused by the pores, microcracks, and fractures, respectively; φ_p *is* the porosity; ε_c is the crack density; and ε_f is the fracture density.

According to geological understanding of the tight sandstone reservoir in this study area, mesoscale fractures are not developed, and the pore space is dominated by micro pores and cracks. Thus, in Eq. 1, we maintain the terms of the micro pores and cracks, while we drop the term of the mesoscale fractures. So, Eq. 1 becomes

$$C_{ijkl} = C^0_{ijkl} - \varphi_p C^1_{ijkl} - \varepsilon_c C^2_{ijkl} \tag{2}$$

According to Chapman et al. (2002), the relaxation time τ plays an important role in determining the frequency bandwidth of the seismic dispersion and attenuation:

$$\tau = \frac{4\eta a^3 (1-\nu)}{9k_S\mu} \tag{3}$$

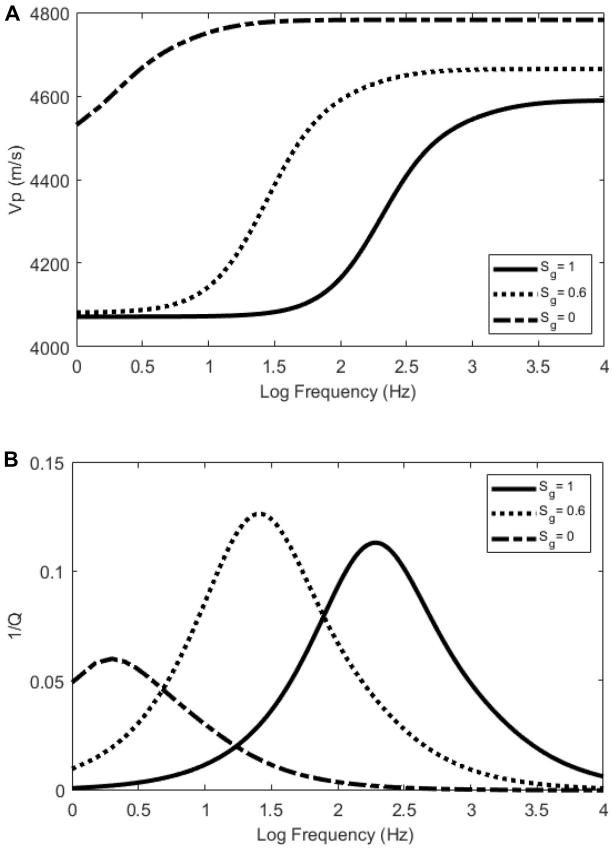

FIGURE 2 | (A) Dispersion of *Vp;* and **(B)** attenuation factor 1/*Q* for various gas saturations Sg.

where μ is the shear modulus; and v is the Poisson ratio of the solid matrix. a is the crack radius; r is the aspect ratio; η is the fluid viscosity; ς is the grain size; and k is the permeability.

The frequency-dependent P-wave velocity $V_p(\omega)$ and the attenuation factor $1/Q(\omega)$ can be calculated from $C_{3333}(\omega)$ in Eq. 2 and the density ρ_s of the fluid-saturated sandstone. The equations are as follows:

$$V_p(\omega) = \sqrt{\frac{C_{3333}(\omega)}{\rho_s}} \tag{4}$$

$$\frac{1}{Q(\omega)} = \frac{Im\left(C_{3333}(\omega)\right)}{Re\left(C_{3333}(\omega)\right)} \tag{5}$$

where Re and Im indicate the real part and imaginary part of a complex modulus, respectively.

Physical Parameters of a Mixed Fluid

The viscosity of the mixed fluid in Eq. 1 has an impact on the frequency band of the dispersion and attenuation. For a mixture of water and gas, the viscosity has the following form (Davide and Carcione, 2003):

$$\eta = \eta_g \left(\frac{\eta_w}{\eta_g}\right)^{1-S_g} \tag{6}$$

TABLE 1 | Properties of tight gas sandstone.

Property	Symbol	Value	Unit
P velocity	V_p	4,500	m/s
S velocity	V_s	2,500	m/s
Sandstone density	ρ	2,460	kg/m^3
Water velocity	V_w	1,710	m/s
Gas velocity	V_g	620	m/s
Water density	ρ_w	1,000	kg/m^3
Gas velocity	ρ_g	65	kg/m^3
Water viscosity	η_w	2×10^{-5}	Pa·s
Gas viscosity	η_g	3×10^{-3}	Pa·s
Porosity	φ_p	0.1	
Crack density	ε_c	0.1	
Permeability	K	0.1	mD
Aspect ratio	r	2×10^{-4}	
Crack/pore radius	a	2×10^{-4}	m
Grain size	ζ	2×10^{-4}	m
Poisson ratio	σ	0.25	
Shear modulus	μ	21	GPa

where η_g is the viscosity of the gas; η_w is the viscosity of water; and S_g is the gas saturation.

Under different gas saturations, the density of the fluid mixture and that of the fluid saturated sandstone are as follows:

$$\rho_f = S_g \rho_g + \left(1 - S_g\right) \rho_w \tag{7}$$

$$\rho_s = \varphi \rho_f + (1 - \varphi)\, \rho_m. \tag{8}$$

where ρ_f is the density of the fluid mixture; ρ_g is the density of the gas; ρ_w is the density of water; ρ_s is the density of the saturated rock; ρ_m is the density of the solid matrix; and φ is the porosity.

The bulk module K_f and the velocity V_f of the fluid mixture are calculated using Wood's equations (Wood, 1995):

$$K_f = \frac{1}{\frac{S_g}{K_g} + \frac{1-S_g}{K_w}} \tag{9}$$

$$V_f = \sqrt{\frac{K_f}{\rho_f}} \tag{10}$$

In these equations, K_g and K_w are the bulk modulus of gas and water, respectively.

The Method for the Modeling of the Frequency-Dependent AVO

Based on the rock physics model, the propagator matrix theory was used to calculate the seismic responses of the tight sandstone gas reservoir.

The reflection and transmission coefficient vectors $r=[R_{PP}, R_{PS}, T_{PP}, T_{PS}]$ in the case of the P-wave incidence are solved using the following equation (Carcione, 2001):

$$r = -\left[A_1 - \left(\prod_{\alpha=1}^{N} B_\alpha\right) A_2\right]^{-1} i_p \tag{11}$$

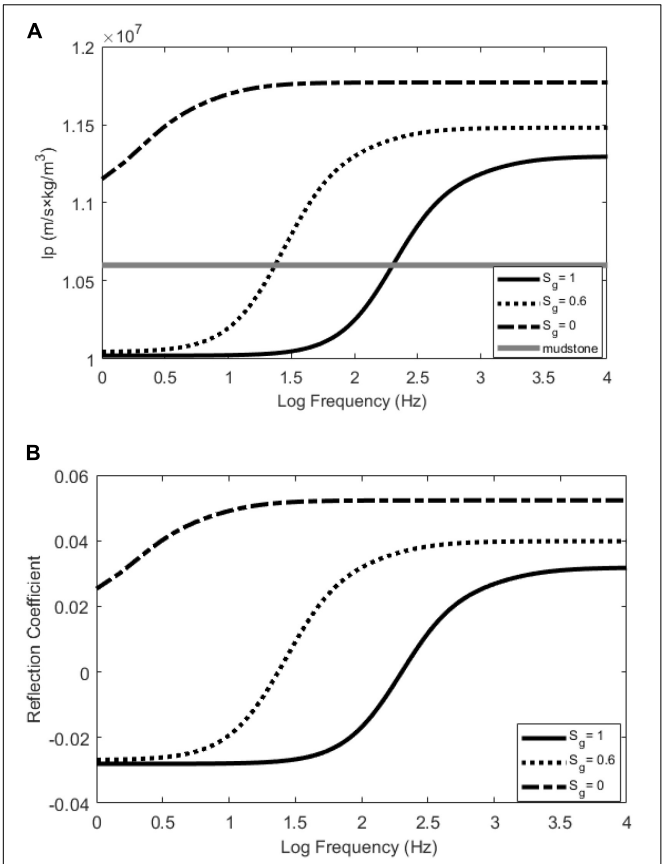

FIGURE 3 | (A) Frequency-dependent P-wave impedance *Ip;* and **(B)** frequency-dependent reflection coefficient of the normal incidence at the interface between the mudstone and the tight gas sandstone.

where the matrices A_1 and A_2 are the propagation matrices related to the elastic moduli of the upper and lower media, respectively. $B_\alpha = T(0)T^{-1}(h_\alpha)(\alpha=1,\ldots,N)$ is the propagation matrix of the middle layer, which has an N-layer structure. h_α is the thickness of each individual layer. i_p is the P-wave incident vector related to the elastic properties of the incidence medium.

The reflection coefficient R_{pp} at each frequency can be calculated using the propagator matrix theory. We use R_f to denote R_{pp} in the following. By multiplying the frequency reflection coefficient R_f by the spectrum of the seismic wavelet W_f, we can calculate the amplitude spectrum U_f of the reflected wave.

$$U_f = W_f \times R_f \tag{12}$$

After the inverse Fourier transform of U_f, the reflection waveform U_t in the time domain can be calculated as

$$U_t = \frac{1}{2\pi}\int_{-\infty}^{\infty} U_f \exp\left(-i2\pi f t\right) df \tag{13}$$

where f is the angular frequency; i is the unit of the imaginary number; and t is time.

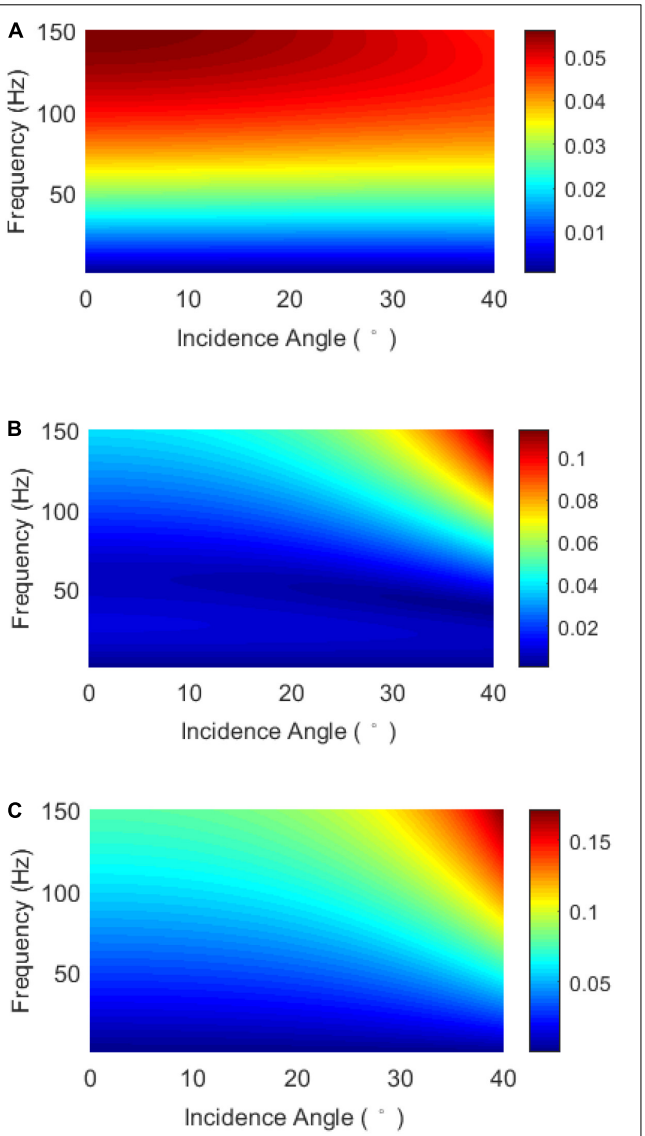

FIGURE 4 | Frequency-dependent reflection coefficients of the PP waves for gas saturations of **(A)** 1, **(B)** 0.6, and **(C)** 0.

The Frequency-Dependent AVO Theory

Based on the AVO approximate formula given by Shuey (1985); Chapman et al. (2006) deduced the frequency-dependent AVO formula shown as

$$R_{PP}(\theta, f) = R_{PP}(\theta, f_0) + D_P(f - f_0) + D_G(f - f_0)\sin^2\theta \tag{14}$$

where D_P represents the derivatives of the seismic wave velocities with frequency; and D_G is the frequency-dependent AVO gradient.

$$D_P = \frac{\partial}{\partial f}\left(\frac{\Delta V_P(f)}{2V_P(f)}\right), \text{ and } D_G = \frac{\partial G(f)}{\partial f} \tag{15}$$

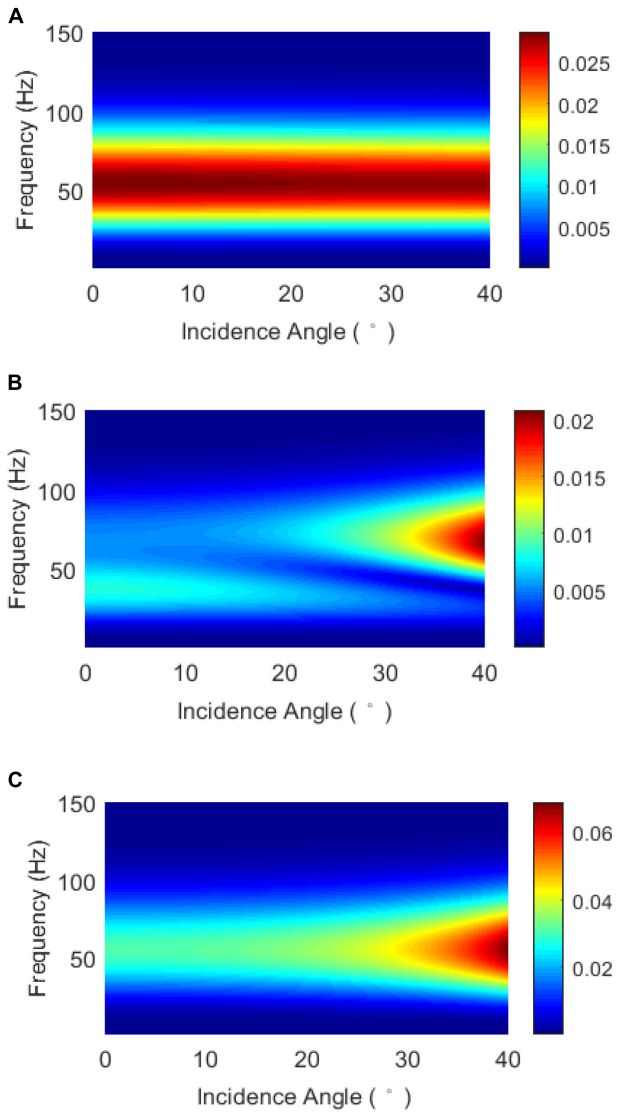

FIGURE 5 | Amplitude spectra of the PP reflection waves for gas saturations of **(A)** 1, **(B)** 0.6, and **(C)** 0.

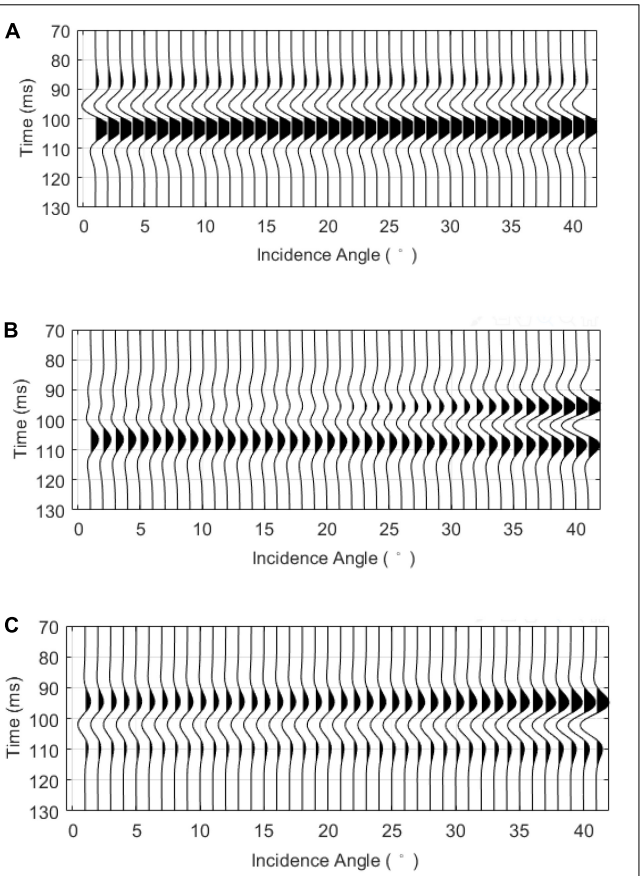

FIGURE 6 | AVO response model for gas saturations of **(A)** 1, **(B)** 0.6, and **(C)** 0.

Equations 14, 15 form the basis of the frequency-dependent AVO inversion. More details for the implementation of the inversion are displayed in **Appendix A**.

MODELING AND INVERSION USING SYNTHETIC DATA

Dispersion and Attenuation in Tight Sandstone

Based on the rock physics model discussed above, **Figure 2** shows the calculated velocity dispersion and attenuation of a tight gas sandstone reservoir for different gas saturations. The properties used in the rock physics model are presented in **Table 1**. As can be seen from **Figure 2A**, the P-wave velocity Vp in the seismic frequency bandwidth decreases as the gas saturation Sg increases from 0 to 0.6 to 1. Moreover, the range of the frequency at which the velocity dispersion occurs moves to a higher frequency. Accordingly, as illustrated in **Figure 2B**, the attenuation peak also moves to a higher frequency as Sg increases. According to Eqs. 3, 6, Sg affects the viscosity coefficient of the fluid mixture, and thus, it changes the relaxation time parameter τ, which controls the frequency range of the velocity dispersion and attenuation. Therefore, variations in the gas saturation have a significant impact on the dispersion and attenuation of the tight gas sandstone reservoirs.

Seismic Modeling and Dispersion Attribute Inversion in the Theoretical Models

In the theoretical model shown in **Figure 1**, the velocity dispersion and attenuation of the tight gas sandstone are calculated using results shown in **Figure 2**. Given a density of 2,460 kg/m^3 for tight sandstone, the corresponding P-wave impedance can be calculated for various gas saturations as shown in **Figure 3A**. Also, we assume that the surrounding mudstone is elastic and has a P-wave velocity of 4,000 m/s, a shear wave velocity of 2,350 m/s, and a density of 2,650 kg/m^3. Thus, the

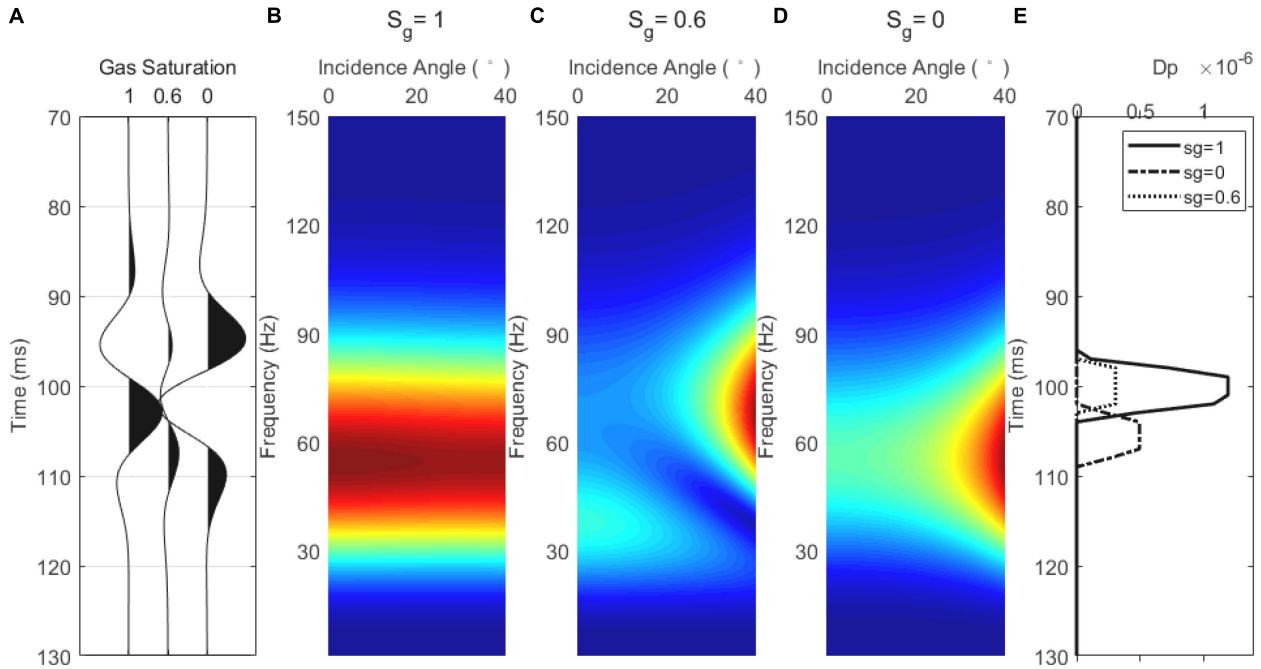

FIGURE 7 | (A) Stacked seismic responses for three gas saturations of 1, 0.6, and 0; **(B)** spectrum of the PP reflection for a gas saturation of 1; **(C)** spectrum of the PP reflection for a gas saturation of 0.6; **(D)** spectrum of the PP reflection for a gas saturation of 0; **(E)** inverted Dp for the three gas saturation cases.

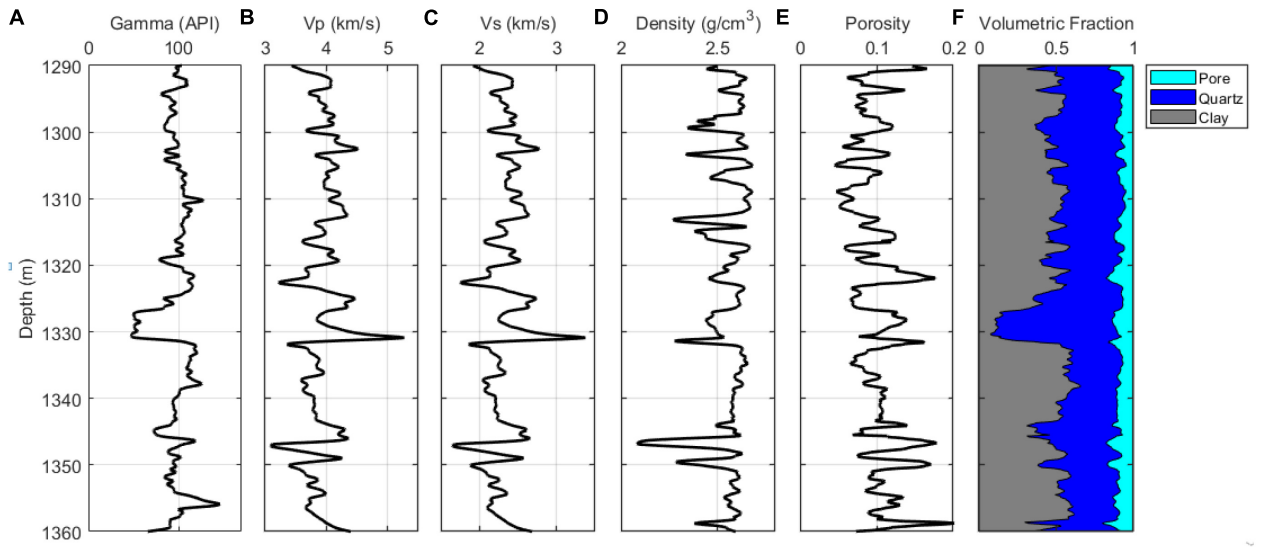

FIGURE 8 | Logging data for the tight sandstone reservoir. **(A)** Gamma; **(B)** Vp; **(C)** Vs; **(D)** density; **(E)** porosity; and **(F)** volumetric fraction of minerals.

frequency-independent P-wave impedance of the mudstone is shown by the gray line in **Figure 3A**.

The two intersecting points in **Figure 3A** show the frequencies where the P-wave impedance Ip of the shale equals that of the tight sandstone with a gas saturation of 0.6 and 1, respectively. Accordingly, **Figure 3B** shows that normal-incidence reflection coefficients are 0 at the two frequencies, and will change from negative to positive for increasing frequencies across the two frequencies.

In the following, the frequency-dependent seismic responses of the tight sandstone gas reservoir are calculated using the propagator matrix method. We assume that the thickness of the tight sandstone layer is 5 m. **Figure 4** shows the absolute values of the complex frequency-dependent PP wave reflection coefficients for gas saturations of 1, 0.6, and 0, with incidence angles ranging

from 0° to 40°. For an incident Ricker wavelet of 45 Hz, the amplitude spectra of the reflected PP waves can be obtained by multiplying the spectrum of the incident Ricker wavelet by the frequency-dependent reflection coefficients. The results are shown in **Figure 5**. Furthermore, the reflected waveforms can be calculated by conducting an inverse Fourier transform of the reflected spectra. The results are shown in **Figure 6**. For the various gas saturations, there were significant differences in the PP wave frequency-dependent reflection coefficients, the spectrum, and the waveforms.

As can be seen from the AVO waveforms in **Figure 6**, the phase of the waveform for complete gas saturation is opposite to that for complete water saturation, and the variations in the reflection amplitude with incidence angle are different. When the gas saturation is 0.6, the polarity reversal can be observed as the incidence angle increases.

Figure 7A shows the stacked seismic responses for various gas saturations obtained from AVO gathers in **Figure 6**. **Figures 7B–D** show the frequency spectrum of the AVO reflections corresponding to gas saturations of 1, 0.6, and 0, respectively. **Figure 7E** shows the P-wave dispersion attribute D_P calculated using the frequency-dependent AVO inversion method. As can be seen, the case of high gas saturation corresponds to the value of the high D_P attribute. Due to the change in reflection phase

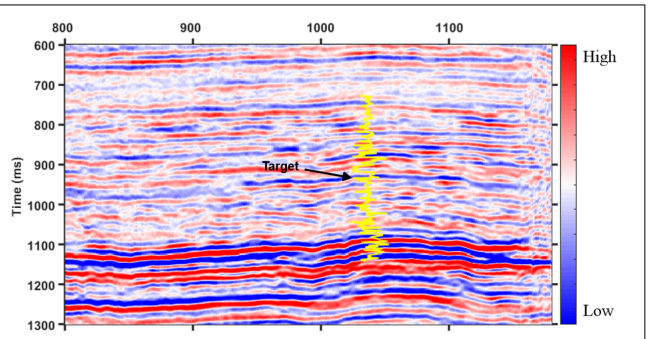

FIGURE 9 | Post-stacked seismic profile across well A.

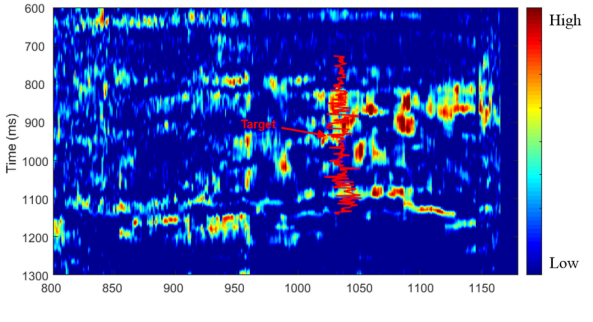

FIGURE 11 | Profile of the dispersion attribute Dp calculated using the frequency-dependent AVO inversion method.

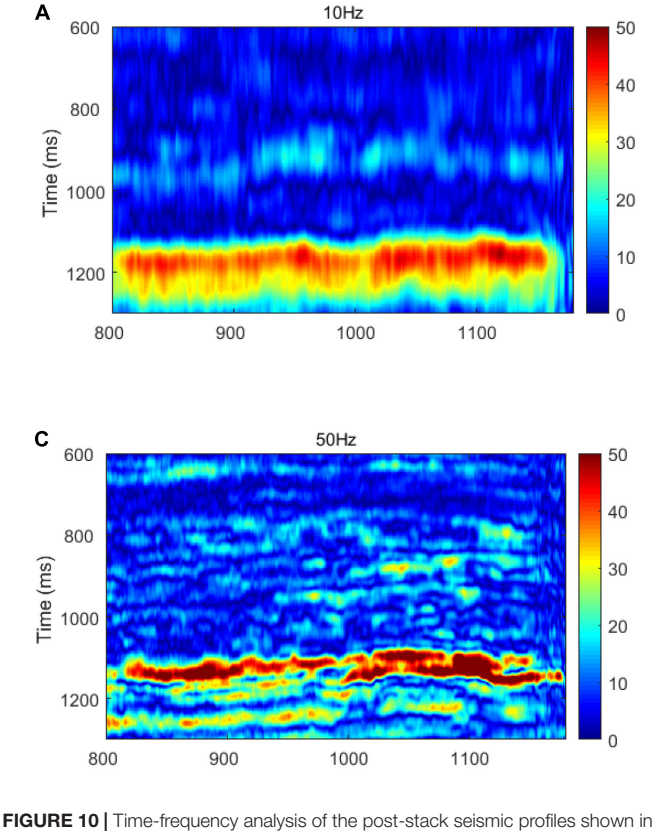

FIGURE 10 | Time-frequency analysis of the post-stack seismic profiles shown in **Figure 9**. **(A)** 10 Hz; **(B)** 30 Hz; **(C)** 50 Hz; and **(D)** 70 Hz.

for the case of the gas saturation of 0.6, there is a time shift for the inverted D_P attribute compared to the cases of complete gas saturation and complete water saturation. Thus, the calculation results using synthetic data of the theoretical model verify the feasibility of identifying gas-bearing tight sandstone reservoirs using the P-wave velocity dispersion attribute.

REAL DATA APPLICAIONS

Logging and Seismic Data

Figure 8 shows the logging data for the tight sandstone gas reservoir in the study area. The target layer is tight sandstone with a thickness of about 5.5 m below a depth of about 1,325 m. The target layer has a lower gamma ray value and relative higher P- and S-wave velocities than the surrounding mudstone. It has a density about 2.5 g/cm^3 and a porosity of about 0.12. The quartz content of the tight sandstone is greater than 85%.

Figure 9 shows the post-stacked seismic profile across the well. The yellow curve shows the gamma ray values from the well, and the target layer can be recognized by its low gamma value of around 920 ms.

Inversion of P-Wave Dispersion Attribute Dp

Figure 10 shows the results of the time-frequency analysis of the post-stacked seismic data in **Figure 9**. The time-frequency analysis profiles correspond to frequencies of 10, 30, 50, and 70 Hz. As shown in **Figure 10**, the variations in the strength reflected from the target layer at different frequencies form the basis for the inversion of the P-wave dispersion attributes.

Based on the frequency-dependent AVO inversion theory, the dispersion attribute profile of Dp is calculated and shown in **Figure 11**. The red curve in **Figure 11** is the logging gamma ray value. Strong P-wave velocity dispersion can be observed at the position of the target layer around 920 ms, as pointed out by an arrow.

However, in **Figure 11**, a high value of the Dp attribute can be observed just above the target zone. A reasonable interpretation on this may be the interbedded structure consisting of thin layers of mudstone and sandstone over the position of the target zone. Such interbedded layers that can be observed on logging data in **Figure 8** mean that seismic events represent more phases (peaks and troughs) as shown in **Figure 9**. Strong reflection energy reveals the presence of interference between reflected waves.

The frequency-dependent attributes of seismic reflections are affected by both the interference caused by stacked thin layers, and by the dispersion and attenuation related to fluid flow. Thus, when we intend to identify reservoir fluids using frequency-dependent attributes, it is necessary to notice this uncertainty.

When comparing **Figures 9**, **11**, it is meaningful that the inverted Dp attribute reveals the location of the pay zone which has high gas saturation. Such a pay zone cannot be predicted on the post-stacked seismic profile, where the seismic events show fewer obvious variations laterally.

Figure 12 shows a horizontal slice of the RMS amplitude of the seismic reflection from the target zone. **Figure 13** is the corresponding slice of P-wave velocity dispersion attribute Dp. The values of the dispersion attribute Dp for wells A, B, and C in the study area range from high to low. The development of the reservoir shows that the productivities of the three wells are consistent with the inverted Dp attributes, which verifies the feasibility of identifying gas-bearing tight sandstone reservoirs based on frequency-dependent AVO inversion.

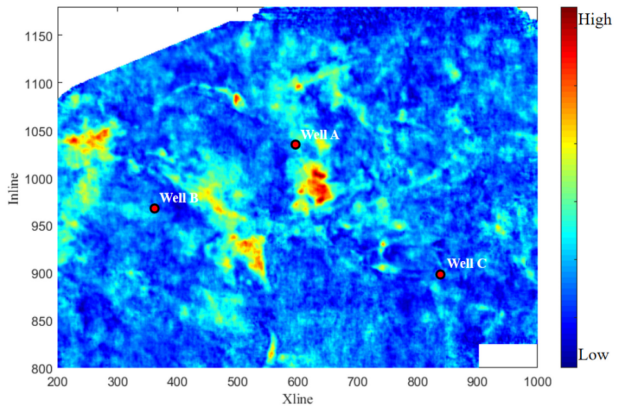

FIGURE 12 | Horizontal slice of the RMS amplitudes of the seismic reflection area.

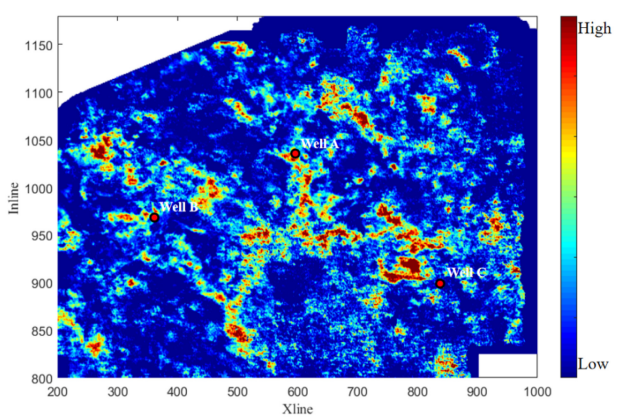

FIGURE 13 | Horizontal slice of the P-wave velocity dispersion attribute Dp.

DISCUSSION AND CONCLUSION

We conducted rock physics modeling of tight gas sandstone by employing the Chapman theory to simulate the dispersion and attenuation caused by the squirt flow of fluids in complex pore spaces. The frequency dependence of the AVO signatures and the inversion of the P-wave dispersion attribute were investigated in different theoretical models with various gas saturations in tight gas sandstone. The field data applications of the frequency-dependent AVO inversion indicate that the estimated P-wave dispersion attribute can be used as a reliable indicator of gas identification in tight gas sandstone reservoirs.

In the constructed rock physics model, the complex pore space is equivalent to a combination of high aspect-ratio pores (stiff pores) and low aspect-ratio microcracks (soft pores). The velocity dispersion and attenuation were simulated by the squirt flow of fluids in the complex pore spaces, which is affected by the gas saturation and the viscosity of the fluid mixtures of gas and brine. The rock physics modeling revealed that as the gas saturation increases, the P-wave velocity generally decreases. P-wave velocity dispersion and attenuation occurs at seismic frequencies, and it tends to move toward higher frequencies as the gas saturation increases.

According to the rock physics modeling results, P-wave velocity dispersion in tight sandstone results in the frequency-dependence of the contrast in the elastic impedance at the interface between the tight sandstone and the overlying mudstone, and therefore, it leads to frequency-dependent reflection coefficients. The synthetic model based on the propagator matrix method revealed that the reflection coefficient varies significantly with frequency, and the variations in the amplitudes and phases of the PP reflections can be observed for various gas saturations.

The tests of the frequency-dependent AVO inversion using synthetic data revealed that the magnitude of the P-wave dispersion attribute is an effective indicator of gas saturation in the tight sandstone. Finally, the frequency-dependent AVO inversion was applied to pre-stacked field seismic data. The results indicate that the inverted P-wave dispersion attribute is well correlated with the production of the pay zone for the evaluation wells. Thus, the methods investigated in this study have good potential for the evaluation of gas saturation in tight gas sandstone reservoirs.

DATA AVAILABILITY STATEMENT

The original contributions presented in the study are included in the article/supplementary material, further inquiries can be directed to the corresponding author.

AUTHOR CONTRIBUTIONS

ZG contributed as the corresponding author of the manuscript. HJ did a part of writing and coding works. CL, YZ, CN, DW, and YL provided some interesting ideas. All authors contributed to the article and approved the submitted version.

FUNDING

This research was supported by the China National Offshore Oil Corporation (CNOOC) research project (No. YXKY-2019-ZY-04) and the National Natural Science Foundation of China (No. 42074153).

REFERENCES

Ba, J., Carcione, J. M., Cao, H., Du, Q. Z., Yuan, Z. Y., and Lu, M. H. (2012). Vertical wave dispersion and attenuation in unsaturated rock: wave propagation equation of dual pore medium. *Chin. J. Geophys.* 55, 219–231. doi: 10.6038/j.issn.0001-5733.2012.01.021

Ba, J., Xu, W., Fu, L., Carcione, J. M., and Zhang, L. (2017). Rock anelasticity due to patchy-saturation and fabric heterogeneity: a double double-porosity model of wave propagation. *J. Geophys. Res. Solid Earth* 122, 1949–1976. doi: 10.1002/2016JB013882

Ba, J., Zhao, J., Carcione, J. M., and Huang, X. (2016). Compressional wave dispersion due to rock matrix stiffening by clay squirt flow. *Geophys. Res. Lett.* 43, 6186–6195.

Biot, M. A. (1956a). Theory of propagation of elastic waves in a fluid-saturated porous solid. I. Low frequency range. *J. Acoust. Soc. Am.* 138, 168–178. doi: 10.1121/1.1908239

Biot, M. A. (1956b). Theory of propagation of elastic waves in a fluid-saturated porous solid. II. Higher frequency range. *J. Acoust. Soc. Am.* 138, 179–191. doi: 10.1121/1.1908241

Carcione, J. M. (2001). AVO effects of a hydrocarbon source-rock layer. *Geophysics* 66, 419–427. doi: 10.1190/1.1444933

Chapman, M. (2003). Frequency-dependent anisotropy due to meso-scale fractures in the presence of equant porosity. *Geophys. Prospect.* 51, 369–379. doi: 10.1046/j.1365-2478.2003.00384.x

Chapman, M. (2009). Modeling the effect of multiple sets of mesoscale fractures in porous rock on frequency-dependent anisotropy. *Geophysics* 74, 97–103. doi: 10.1190/1.3204779

Chapman, M., Liu, E., and Li, X. Y. (2005). The influence of abnormally high reservoir attenuation on the AVO signature. *Lead. Edge* 24, 1120–1125. doi: 10.1190/1.2135103

Chapman, M., Liu, E., and Li, X. Y. (2006). The influence of fluid-sensitive dispersion and attenuation on AVO analysis. *Geophys. J. Int.* 167, 89–105. doi: 10.1111/j.1365-246X.2006.02919.x

Chapman, M., Sergei, V., and Zatsepin, S. C. (2002). Derivation of a microstructural poroelastic model. *Geophys. J. Int.* 151, 427–451. doi: 10.1046/j.1365-246X.2002.01769.x

Chen, S. Q., Chapman, M., and Wu, X. Y. (2015). The application of quantitative gas saturation estimation based on the seismic wave dispersion inversion. *J. Appl. Geophys.* 20, 81–95. doi: 10.1016/j.jappgeo.2015.07.001

Davide, G., and Carcione, J. M. (2003). Acoustic properties of sediments saturated withgas hydrate, free gas and water. *Geophys. Prospect.* 51, 141–157. doi: 10.1046/j.1365-2478.2003.00359.x

Dvorkin, J., and Nur, A. (1993). Dynamic poroelasticity: a unified model with the squirt and the Biot mechanisms. *Geophysics* 58, 524–533. doi: 10.1190/1.1443435

Li, X. Y. (2013). "Quantitative estimation of gas saturation by frequency dependent AVO: numerical, physical modelling and field studies," in *Proceedings of the 6th International Petroleum Technology Conference*, (Beijing).

Ruiz, F., and Cheng, A. (2010). A rock physics model for tight gas sand. *Lead. Edge* 29, 1484–1489. doi: 10.1190/1.3525364

Shuey, R. T. (1985). Simplification of the zoeppritz equations. *Geophysics* 50, 609–614. doi: 10.1190/1.1441936

Smith, T. M., Sayers, C. M., and Sondergeld, C. H. (2009). Rock properties in low-porosity//low-permeability sandstones. *Lead. Edge.* 28, 48–59. doi: 10.1190/1.3064146

Wang, E., Carcione, J. M., Ba, J., and Liu, Y. (2019). Reflection and transmission of plane elastic waves at an interface between two double-porosity media: effect of local fluid flow. *Surv. Geophys.* 41, 283–322.

White, J. E. (1975). Computed seismic speeds and attenuation in rocks with partial gas saturation. *Geophysics* 40, 224–232. doi: 10.1190/1.1440520

Wilson, A. (2010). *Theory and Methods of Frequency-Dependent AVO Inversion*. Edinburgh: The University of Edinburgh.

Wilson, A., Chapman, M., and Li, X. Y. (2009). "Frequency-dependent AVO Inversion," in *79th annual SEG meeting Expanded Abstracts*, Vol. 28, (Tulsa, OK: Society of Exploration Geophysicists), 341–345.

Wood, A. W. (1995). *A Textbook of Sound*. New York, NY: The MacMillan Co, 360.

Wu, X. Y. (2010). *Frequency Dependent AVO Inversion Using Spectral Decomposition Techniques*. Beijing: China University of Geosciences.

Wu, X. Y., Chapman, M., Li, X. Y., and Boston, P. (2014). Quantitative gas saturation estimation by frequency-dependent amplitude-versus-offset analysis. *Geophys. Prospect.* 62, 1224–1237. doi: 10.2307/1933611

Zhang, Z., Yin, X. Y., and Hao, Q. Y. (2014). Frequency variable fluid identification based on AVO inversion. *Chin. J. Geophys.* 12, 4171–4184. doi: 10.6038/cjg20141228

Conflict of Interest: YZ, CN, DW, and YL were employed by the company CNOOC and declare that this study received funding from CNOOC. The funder had the following involvement with the study: YZ provided some new ideas and suggestions, CN and DW gave analysis on results, and YL collected the data.

The remaining authors declare that the research was conducted in the absence of any commercial or financial relationships that could be construed as a potential conflict of interest.

Copyright © 2021 Jin, Liu, Guo, Zhang, Niu, Wang and Ling. This is an open-access article distributed under the terms of the Creative Commons Attribution License (CC BY). The use, distribution or reproduction in other forums is permitted, provided the original author(s) and the copyright owner(s) are credited and that the original publication in this journal is cited, in accordance with accepted academic practice. No use, distribution or reproduction is permitted which does not comply with these terms.

APPENDIX A

The Frequency-Dependent AVO Theory

Shuey (1985) gave an approximate formula for the PP reflection coefficient for isotropic media:

$$R_{PP}(\theta) \approx \frac{1}{2}\left(\frac{\Delta V_P}{V_P} + \frac{\Delta \rho}{\rho}\right) + G\sin^2\theta \tag{A1}$$

where θ is the incident angle. V_p and ρ are the mean values of the P-wave velocity and density across the interface, respectively. ΔV_p and $\Delta\rho$ are the differences in the P-wave velocity and density across the interface, respectively. G is the AVO gradient.

Based on Eq. A1, Chapman et al. (2006) concluded that the dispersion of the P-wave velocity caused the frequency dependency of the reflection coefficient. Thus, Eq. A1 can be rewritten as

$$R_{PP}(\theta, f) \approx \frac{\Delta V_P}{2V_P}(f) + \frac{\Delta \rho}{2\rho} + G(f)\sin^2\theta \tag{A2}$$

Using the Taylor series expansion method, we obtained the frequency-dependent R_{PP} for a reference frequency:

$$R_{PP}(\theta, f) \approx \frac{\Delta V_P}{2V_P}(f_0) + (f - f_0)\frac{\partial}{\partial f}\left(\frac{\Delta V_P(f)}{2\bar{V}_P(f)}\right) + \frac{\Delta \rho}{2\rho} + G(f_0)\sin^2\theta + (f - f_0)\frac{\partial G(f)}{\partial f}\sin^2\theta \tag{A3}$$

Thus,

$$R_{PP}(\theta, f) = R_{PP}(\theta, f_0) + D_P(f - f_0) + D_G(f - f_0)\sin^2\theta \tag{A4}$$

where D_P represents the derivatives of the seismic wave velocities with frequency; and D_G is the frequency-dependent AVO gradient.

$$D_P = \frac{\partial}{\partial f}\left(\frac{\Delta V_P(f)}{2V_P(f)}\right), \text{ and } D_G = \frac{\partial G(f)}{\partial f} \tag{A5}$$

In the application of the frequency-dependent AVO method to real data, the time-frequency spectra S(t,θ,f) of the pre-stacked gathers contains the information for the incidence wavelet spectrum, so it is necessary to eliminate the effect of the incidence wavelet.

$$M(t, \theta, f) = S(t, \theta, f)\, w(f, \theta) \tag{A6}$$

$$w(f, \theta) = \frac{\max\left(A_{f=ref}(\theta)\right)}{\max\left(A_f(\theta)\right)} \tag{A7}$$

where $_{\max(A_{f=ref}(\theta))}$ is the maximum value of the amplitude spectrum in the selected time window used for the calculation.

According to Eq. A4,

$$\Delta M(t, \theta, f) = (f - f_0)\left(D_P + D_G\sin^2\theta\right) \tag{A8}$$

where $_{\Delta M(t,\theta,f)=M(t,\theta,f)-M(t,\theta,f_0)}$.

Eq. A8 can be rewritten in the form of a matrix:

$$\begin{bmatrix} \Delta M(t, \theta_1, f_1) \\ \vdots \\ \Delta M(t, \theta_n, f_m) \end{bmatrix} = \begin{bmatrix} f_1 - f_0 & (f_1 - f_0)\sin^2(t, \theta_1) \\ \vdots & \vdots \\ f_m - f_0 & (f_m - f_0)\sin^2(t, \theta_n) \end{bmatrix} \times \begin{bmatrix} D_P \\ D_G \end{bmatrix} \tag{A9}$$

where the D_P and D_G values of inversion parameters can be obtained by solving the over-determined equation.

frontiers in Earth Science

ORIGINAL RESEARCH
published: 04 May 2021
doi: 10.3389/feart.2021.649984

Fluid Discrimination in Ultra-Deep Reservoirs Based on a Double Double-Porosity Theory

Xinyang Zhou[1], Jing Ba[1], Juan E. Santos[2,3], José M. Carcione[1,4], Li-Yun Fu[5] and Mengqiang Pang[1]*

[1] School of Earth Sciences and Engineering, Hohai University, Nanjing, China, [2] Laboratorio de Geofísica Numérica, Instituto del Gas y del Petróleo, Facultad de Ingeniería, Universidad de Buenos Aires, Buenos Aires, Argentina, [3] Department of Mathematics, Purdue University, West Lafayette, IN, United States, [4] National Institute of Oceanography and Applied Geophysics, Trieste, Italy, [5] Key Laboratory of Deep Oil and Gas, China University of Petroleum, Qingdao, China

We develop a methodology, based on rock-physics templates, to effectively identify reservoir fluids in ultra-deep reservoirs, where the poroelasticity model is based on the double double-porosity theory. P-wave attenuation, the ratio of the first Lamé constant to mass density (λ/ρ) and Poisson ratio are used to build the templates at the ultrasonic and seismic frequency bands to quantitatively predict the total and crack (soft) porosities and oil saturation. Attenuation on these frequency bands is estimated with the spectral-ratio and frequency-shift methods. We apply the methodology to fault-controlled karst reservoirs in the Tarim Basin (China), which contain ultra-deep hydrocarbon resources with a diverse pore-crack system, low porosity/permeability and complex oil-water spatial distributions. The results are consistent with well-log data and actual oil recovery. Crack porosity can be used as an indicator to find regions with high oil saturation, since high values implies a good pore connectivity.

Keywords: double double-porosity theory, fault-controlled karst reservoirs, fluid detection, ultra-deep reservoirs, 3D rock-physics template

OPEN ACCESS

Edited by:
Pier Paolo Bruno,
University of Naples Federico II, Italy

Reviewed by:
Per Avseth,
Norwegian University of Science and Technology, Norway
Ken Ikeda,
The University of Texas at Austin, United States

***Correspondence:**
Jing Ba
jingba@188.com

Specialty section:
This article was submitted to Solid Earth Geophysics, a section of the journal Frontiers in Earth Science

Received: *06 January 2021*
Accepted: *06 April 2021*
Published: *04 May 2021*

Citation:
Zhou X, Ba J, Santos JE, Carcione JM, Fu L-Y and Pang M (2021) Fluid Discrimination in Ultra-Deep Reservoirs Based on a Double Double-Porosity Theory. Front. Earth Sci. 9:649984. doi: 10.3389/feart.2021.649984

INTRODUCTION

With the depletion of relatively shallow conventional reservoirs, ultra-deep resources will become an important target for oil and gas exploration. Carbonate reservoirs are typical examples (e.g., Zou et al., 2014), which, due to their burial depth and high degree of diagenesis, their pay zone is located in areas with secondary pores or cracks (or rift caves and karst caves) (Pang, 2010). The tectonic action, abnormal high pressure, the presence of fractures and thermal fluid activity favor the development of this secondary pore space. Fracture-cavern carbonate reservoirs are among the most important types (Tian et al., 2017; Li et al., 2019). A "fault-controlled karst reservoir" is a large-scale fracture-cavern carbonate reservoir formed by a series of geological processes including the dissolution of atmospheric fresh water or hydrothermal fluid that flows along faults and associated complex fracture system under unexposed conditions (Lan et al., 2015).

The fabric of carbonate rocks has at least two dissimilar porosities, leading to a heterogeneous distribution of immiscible fluids or patchy saturation (Ba et al., 2017). Early models consider a single porosity, such as that of White (1975), who assumed patchy saturation with spherical gas inclusions, and a generalization to non-spherical patches by Johnson (2001). Then,

Pride et al. (2004) studied attenuation caused by patchy saturation based on a double-porosity theory, while Dvorkin and Nur (1993) combined the Biot and squirt flow mechanisms into a set of poroelasticity equations, explicitly considering attenuation due to global flow at cracks or grain contacts. The model has been applied to predict wave velocity and attenuation (Dvorkin et al., 1994, 1995). Deng et al. (2015) extended the squirt-flow model and Tang (2011) analyzed the effect of fractures on the elastic waves. Ba et al. (2011) introduced the Biot-Rayleigh theory to model wave propagation in double-porosity media with a single saturating fluid, and Ba et al. (2017) extended this model to the case of two fluids, i.e., a double double-porosity medium model (DDP).

Rock-physics templates (RPT) relate the reservoir and seismic properties (Odegaard and Avseth, 2004; Carcione and Avseth, 2015). For instance, Chi and Han (2009) interpreted the lithology and obtained fluid content by using RPTs and logging data, and RPTs were used to compute reservoir porosity and oil/gas saturation by Michel (2010). Picotti et al. (2018) analyzed the effects of different fluid saturations, porosities, and permeabilities on seismic waves, and introduced an attenuation RPT for sandstone reservoirs. Pang et al. (2020) estimated the microfracture porosity in carbonate reservoirs by using these attenuation templates. Tran et al. (2020) predicted organic matter content of source rocks using RPTs.

Building a RPT implies to choose the proper properties sensitive to lithology or fluid type and saturation (Batzle et al., 2001; Dillon et al., 2003; Qiao and An, 2007). Goodway et al. (1997) proposed to identify and detect reservoir fluids by using the Lamé constants. Hedlin (2000) proposed the pore modulus as a fluid recognition factor through experiments to distinguish shale, calcite, gas sand, oil sand, and wet sand. The Gassmann fluid term and its product with mass density were used as a fluid discriminator by Russell et al. (2003, 2006), and Quakenbush et al. (2006) used Poisson's ratio for the same purpose. Quintal (2012) suggested that frequency-dependent attenuation due to wave-induced fluid flow is a potential index of saturation, and Xue et al. (2017) used a combination of the normal crack compliance of the saturated and dry rocks as a fluid factor.

We choose P-wave attenuation, Poisson's ratio and the ratio of the first Lamé constant to mass density (λ/ρ) to build the templates at ultrasonic and seismic frequencies, based on the DDP theory, and associate the total and crack porosities and oil saturation to the seismic properties. The theory considers the effects of fabric heterogeneity and heterogeneous distribution of immiscible fluids. Ultrasonic, well-log and seismic data are used to calibrate the templates. Then, these are applied to quantitatively predict the rock properties and oil saturation.

ROCK-PHYSICS MODEL

Overview of the Work Area

The area is located at the Tarim Basin, China, and the reservoir section is constituted by the upper members of the Yijianfang to Yingshan formation (Ordovician), formed during the Caledonian-Hercynian period. It is a marine fault-controlled karst reservoir (Li et al., 2019). The multi-stage fault activity has a controlling effect on the accumulation and distribution of oil and gas in the reservoir. Fractures and fluid transformation

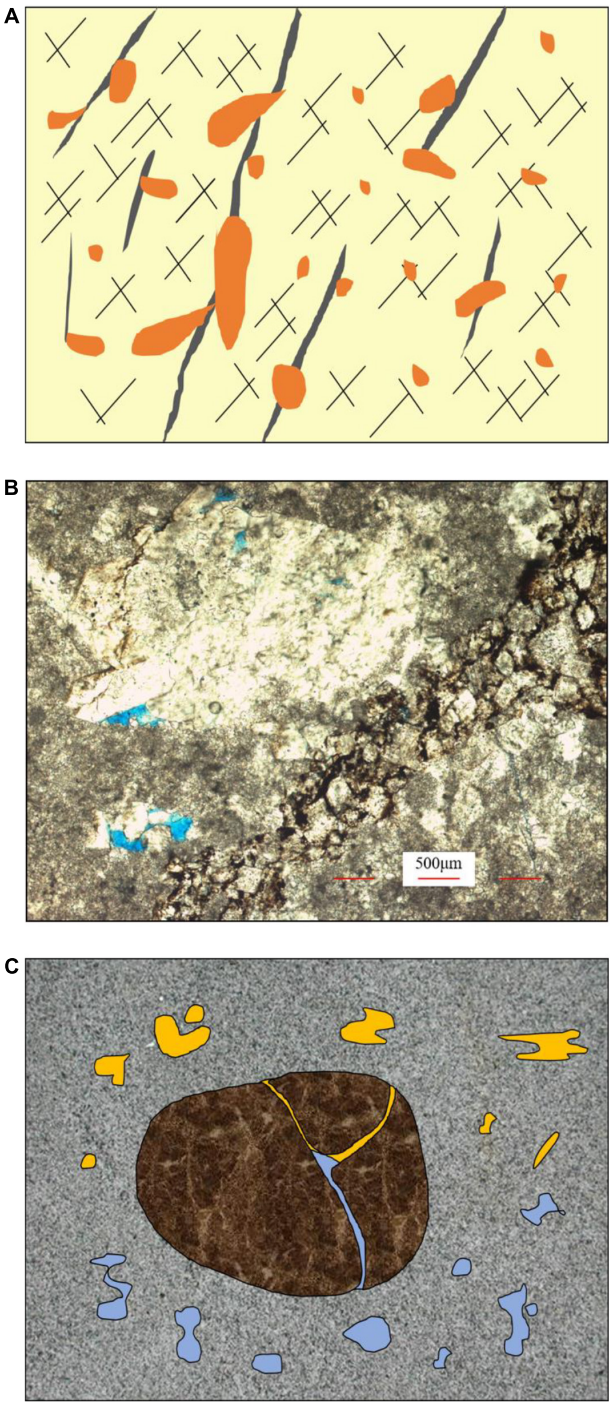

FIGURE 1 | (A) Schematic of a fault-controlled karst reservoir (orange represents caverns and vugs, while black refers to cracks); **(B)** thin section of a carbonate sample; **(C)** schematic of a double-porosity structure with patchy saturation of fluids (two skeletons and two fluids; orange represents oil and blue is water).

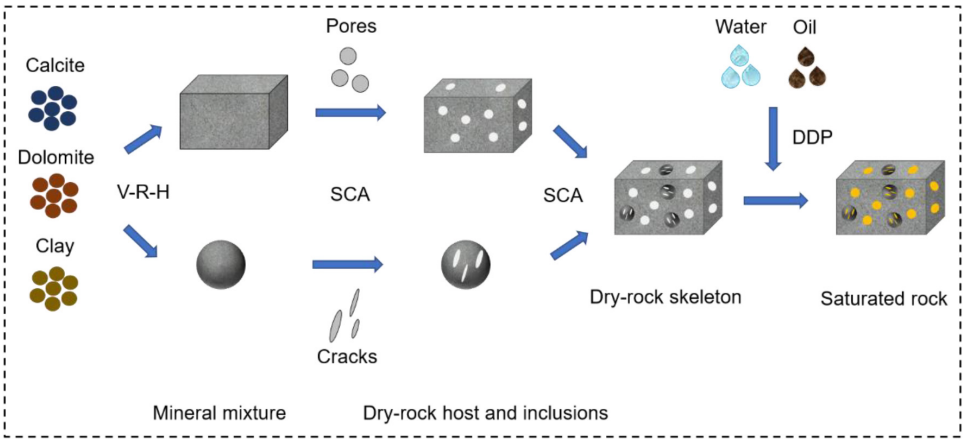

FIGURE 2 | Flowchart of the rock-physics modeling.

have formed a diverse reservoir system including dissolved pores, inter-crystalline pores and cracks, which make the structure quite complex (Lan et al., 2015). The reservoir along the fault zone is oil-bearing and unevenly enriched. It is characterized by an ultra-deep burial (>7 km), high temperature (>150°C) and high pressure (>160 MPa). **Figure 1A** shows a diagram of the reservoir, where the orange color represents caverns and vugs, and the black lines represent cracks.

Figure 1B shows a thin section of a rock sample collected at a depth of 7443 m. The lithology is limestone, with a dolomite content of 6% and a calcite content of 94%. Dissolution of pores and multiple cracks of various diameters are observed and the surface porosity is extremely low (less than 1%).

Rock-Physics Modeling Flowchart

The reservoir characteristics are simplified with a double-porosity structure with cracks and pores and saturation with two immiscible fluides, oil and water (**Figure 1C**). **Figure 2** shows the flowchart of the modeling methodology, which can be summarized as follows.

(1) The minerals are mainly calcite and a small amount of dolomite and clay. The Voigt-Reuss-Hill (VRH) equation (see **Supplementary Appendix Eq. A1**) is used to calculate the elastic moduli of the mineral mixture (Voigt, 1910; Reuss, 1929; Hill, 1952). The bulk and shear moduli of calcite, dolomite, and clay are 63.7 and 31.7, 76.4 and 49.7, and 21 and 7 GPa, respectively (Mavko et al., 2009).

(2) The pores and cracks are assumed spherical and oblate in shape (Shapiro, 2003), with aspect ratios of 1 and 0.00035 (generally in range of 10^{-5}∼10^{-4}, according to Tan et al., 2020 and Pimienta et al., 2015), respectively. The connectivity of these two kinds of pores affects P-wave attenuation and dispersion, as well as the elastic parameters (Agersborg et al., 2008). In this model, the two pore systems are connected and the composite medium is isotropic. Based on the self-consistent approximation (SCA) (Berryman, 1980, 1992, 1998), the pores and cracks are treated as inclusions and mixed with the minerals to obtain two partial dry-rock elastic moduli and then mixed again with the SCA model to obtain the dry-rock

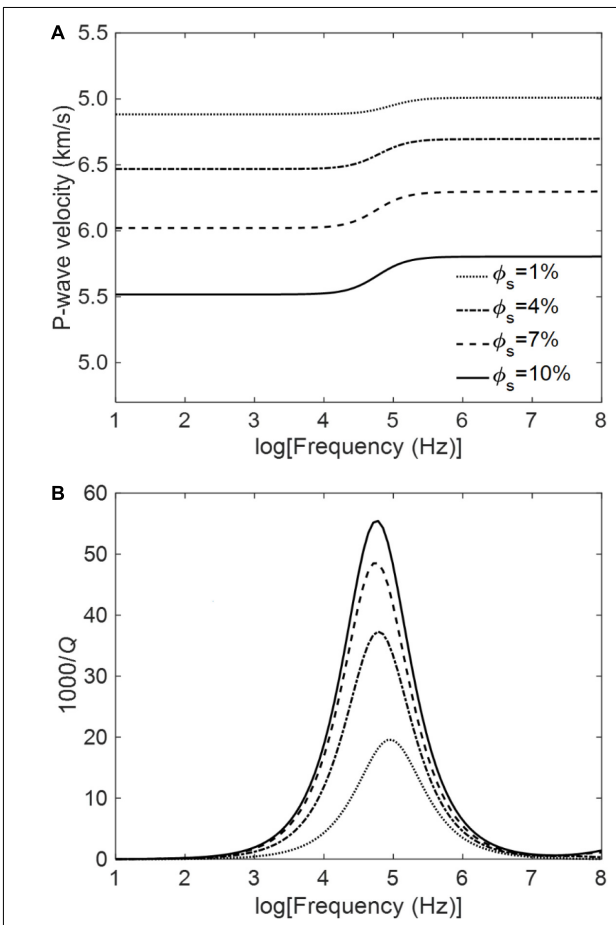

FIGURE 3 | P-wave velocity **(A)** and attenuation **(B)** as a function of frequency for varying stiff porosity.

elastic moduli. At this point, the frame (or skeleton) is a double-porosity structure. The relevant equations are given in **Supplementary Appendix Eq. A2**.

(3) The volume content of the host medium v_1 and the volume content of inclusion v_2 satisfy $v_1+v_2=1$. The total porosity $\phi = \phi_{10} \cdot v_1 + \phi_{20} \cdot v_2$, where ϕ_{10} is the porosity of the host medium and ϕ_{20} is the porosity of the inclusions, and the crack porosity is $\phi_c = \phi_{20} \cdot v_2$. ϕ_{20} is 0.006 (in range of 0.005∼0.1, by considering that a larger cracked grain is modeled as a cylinder of axial length around 100 μm, containing a transverse crack with an average effective aperture of several microns, according to Pride et al., 2004; Pang et al., 2020, and Ba et al., 2017). The stiff porosity is $\phi_s = \phi - \phi_c$.

The equations proposed by Batzle and Wang (1992) are used to estimate the bulk moduli, densities, and viscosity of the fluids at 180°C and 80 MPa. The bulk modulus, density, and viscosity of oil and water in the oil-water mixture are 0.79 and 2.2 GPa, 0.70 and 0.93 g/cm3, and 0.002289 and 0.000647 Pa s, respectively. Then, fluid substitution is performed by using the DDP theory to obtain the acoustic properties. The main skeleton is composed of two components, namely, a host one with dissolved pores and an inclusion one with cracks, and each of them is patchy saturated. Each component can be considered as a secondary double-porosity structure, i.e., two pore phases saturated with different fluids (there are four types of pores globally). By performing a plane-wave analysis (see **Supplementary Appendix Eq. A5**), we obtain the P-wave velocity and attenuation.

3D RPTs

P-Wave Phase Velocity and Attenuation

The stiff porosity, crack porosity, and oil saturation are basic factors related to oil production in reservoirs. First, we study the effects of these properties on P-wave velocity and attenuation in the frequency range of $10^1 \sim 10^8$ Hz. Attenuation is represented by the dissipation factor, defined as $1000/Q$, where Q is the quality factor. Oil saturation is 100%, stiff porosity is 6%, crack porosity

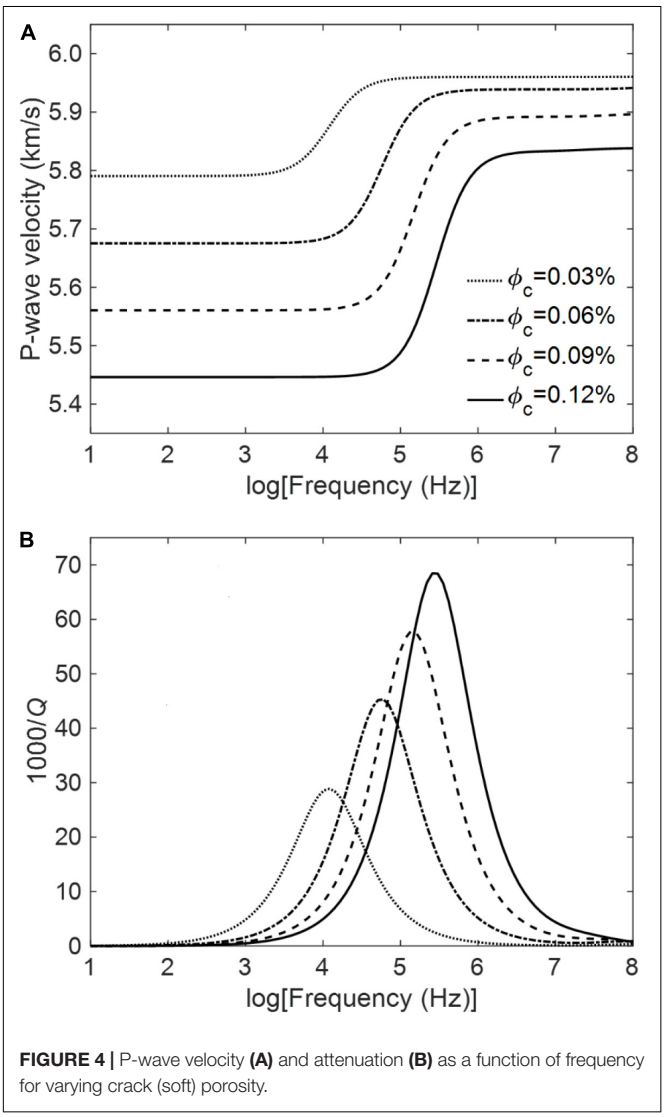

FIGURE 4 | P-wave velocity **(A)** and attenuation **(B)** as a function of frequency for varying crack (soft) porosity.

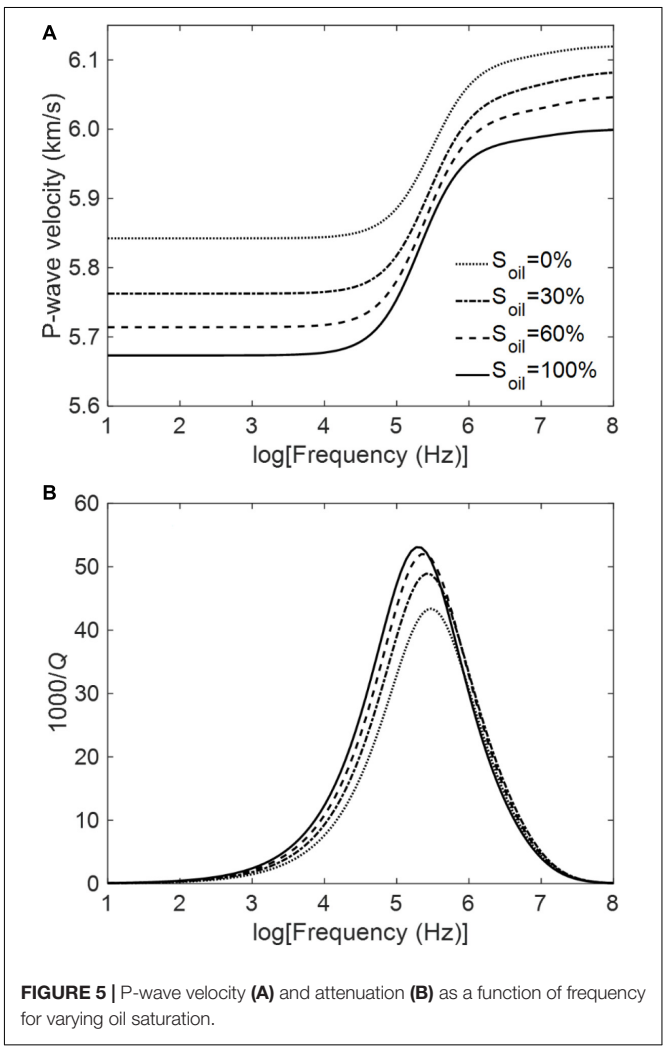

FIGURE 5 | P-wave velocity **(A)** and attenuation **(B)** as a function of frequency for varying oil saturation.

is 0.06%. In the analysis, we vary one property and set the others constant. The fluid patch radius of the host medium is 50 μm, the inclusion radius is 50 μm (at pore/grain scale), and the fluid patch radius in the inclusion is 5 μm.

Figures 3A,B show the effect of the stiff porosity on the P-wave phase velocity and dissipation factor, respectively, where it can be seen that velocity dispersion and attenuation increase with increasing porosity and the relaxation peaks move slightly to the low frequencies. **Figure 4** shows that increasing crack porosity, the velocity dispersion becomes stronger, attenuation increases and the peaks move to the high frequencies, while **Figure 5** indicates that dispersion and attenuation increase with increasing oil saturation, and the peaks move to the low frequencies.

Fluid Identification Factors

Poisson's ratio and λ/ρ are used to identify the fluids (Goodway et al., 1997; Quakenbush et al., 2006). **Figures 6**, **7** show the effects of stiff porosity, crack porosity, and oil saturation at 1 MHz, respectively. As can be seen, increasing stiff porosity and oil saturation, λ/ρ gradually decreases, while increasing crack porosity has the opposite effect. On the other hand (**Figure 7**),

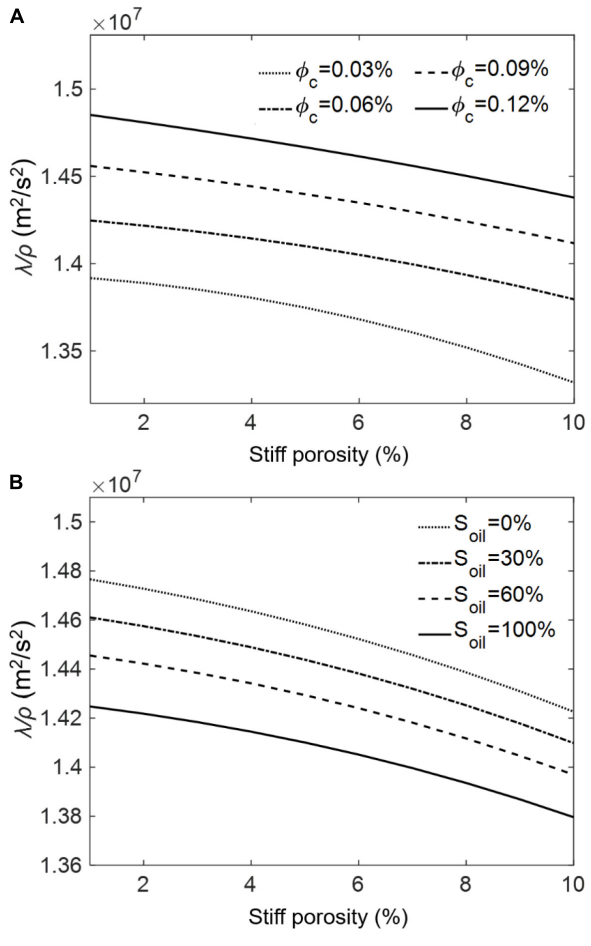

FIGURE 6 | λ/ρ at 1 MHz as a function of stiff porosity for different crack (soft) porosities **(A)** and oil saturations **(B)**.

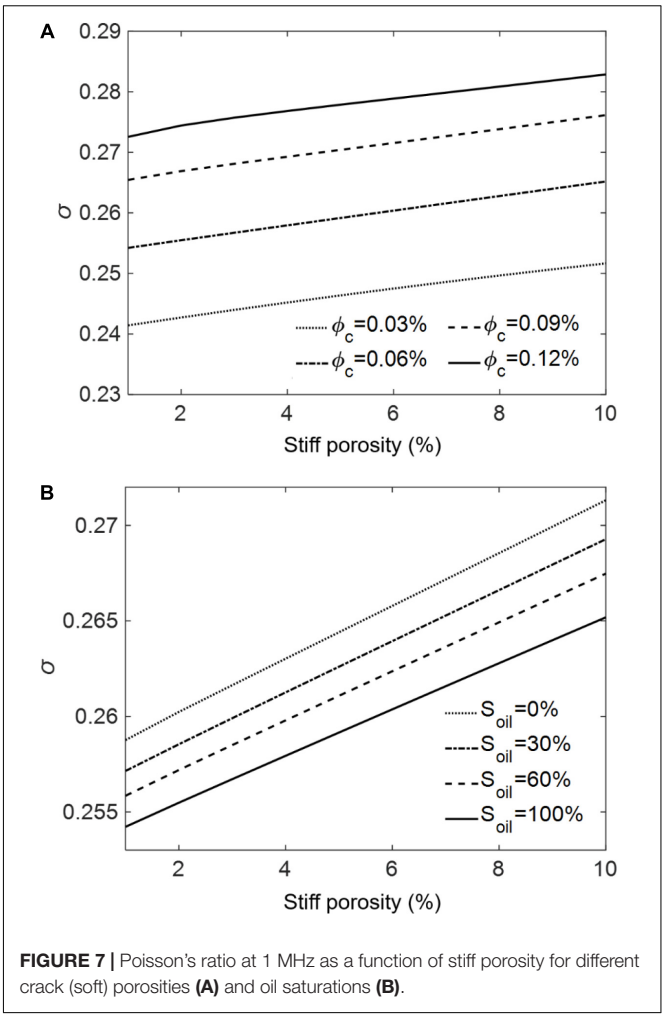

FIGURE 7 | Poisson's ratio at 1 MHz as a function of stiff porosity for different crack (soft) porosities **(A)** and oil saturations **(B)**.

Poisson's ratio increases with increasing stiff and crack porosities and decreases with increasing saturation.

Rock-Physics Templates

Total and crack porosities and oil saturation are set as variables to build a 3D RPT at 1 MHz, which is displayed in **Figure 8A**, where the parameters are the same as in section "P-Wave Phase Velocity and Attenuation." The blue and red line refers to water and oil saturations, respectively, and the behavior of the template agrees with the previous results. On the other hand, **Figure 8B** shows the 3D RPT at 35 Hz, where the radii of the inclusion, fluid patch in the host medium and fluid patch in the inclusion are 50, 50, and 5 mm, respectively. The characteristics of the seismic template are identical to those of the ultrasonic template.

CALIBRATION OF THE RPTs

Ultrasonic Band

Ultrasonic experiments were performed on five water- and oil-saturated samples at 1 MHz, a pore pressure of 70 MPa and 140°C, whose properties are given in **Table 1**. The carbonate

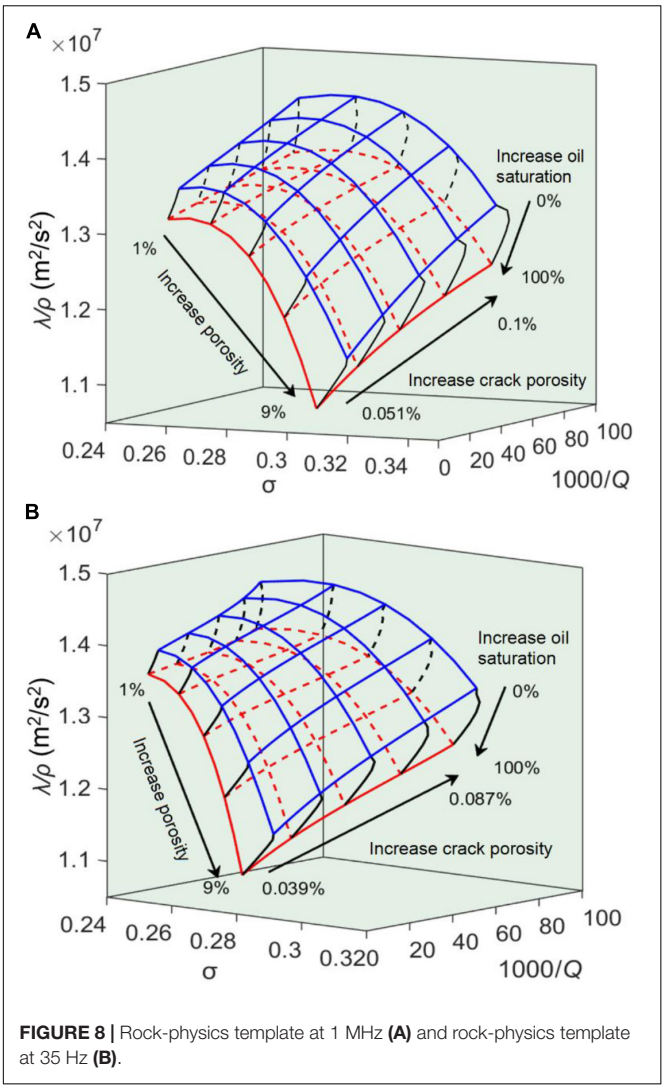

FIGURE 8 | Rock-physics template at 1 MHz **(A)** and rock-physics template at 35 Hz **(B)**.

TABLE 1 | Properties of the limestone samples.

Sample	A	B	C	D	E
Porosity (%)	1.37	1.12	1.63	0.71	2.50
Dry-rock density (g/cm^3)	2.67	2.63	2.65	2.67	2.66
Permeability (mD)	0.068	0.051	0.006	1.559	0.023

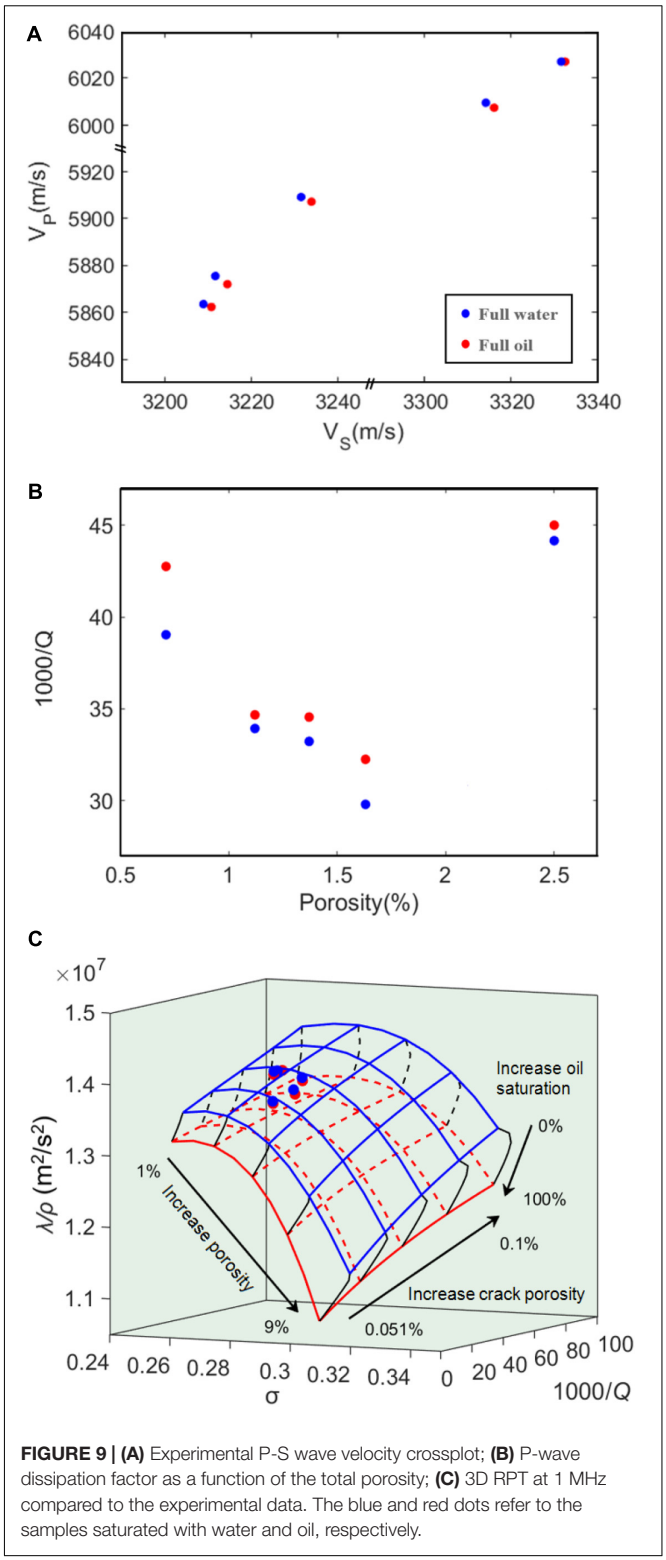

FIGURE 9 | (A) Experimental P-S wave velocity crossplot; **(B)** P-wave dissipation factor as a function of the total porosity; **(C)** 3D RPT at 1 MHz compared to the experimental data. The blue and red dots refer to the samples saturated with water and oil, respectively.

samples used in the ultrasonic measurements are mainly made of limestone, and parts of cracks are filled with asphalt, calcite, and pyrite. Moreover, there are micro-cracks and a relative amount of dissolved pore cavities. In the experiments, the sample is fully saturated, jacketed, and put into a container according to the experimental setup of Guo et al. (2018a). The first arrivals are picked to obtain the wave velocities. **Figure 9A,B** show the velocities and the attenuation factor estimated with the spectral-ratio method (Toksöz et al., 1979; Guo and Fu, 2006; see **Supplementary Appendix Eq. A3**).

Figure 9A shows that P-wave velocity at full water saturation is higher than that at full oil saturation, while the S-wave velocity exhibits the opposite behavior. **Figure 9B** indicates that the oil-saturated samples have a stronger P-wave attenuation. As shown in the template of **Figure 9C**, the experimental data of these five samples are used for the calibration at ultrasonic frequencies,

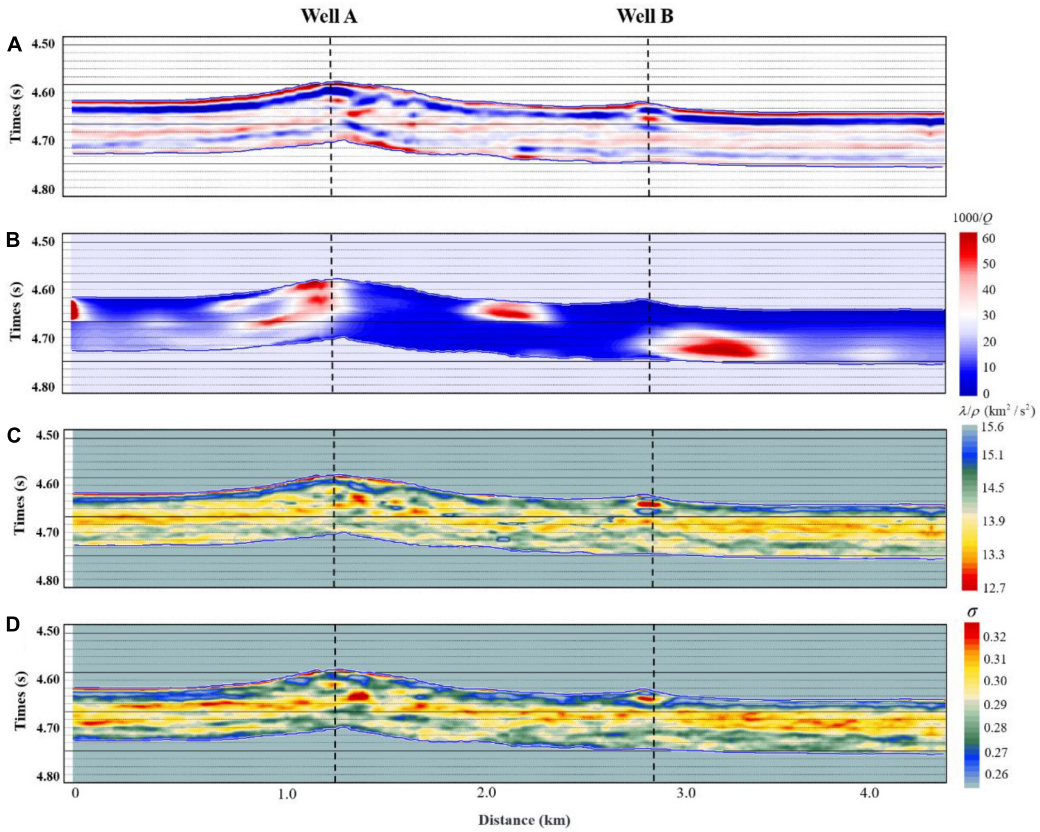

FIGURE 10 | 2D profiles of the post-stack seismic data **(A)**, dissipation factor (1000/Q) **(B)**, λ/ρ **(C)**, and Poisson's ratio **(D)** of the target layer.

where the blue and red circles refer to the water- and oil-saturated samples, respectively. The average error between the predicted total porosities (based on ultrasonic wave attributes) and the measured porosities under oil saturation is 0.00344. The template shows good agreement with the experimental measurements.

Seismic Band

Based on well-log and seismic data, the RPT is calibrated at 35 Hz. The seismic quality factor is estimated with the improved frequency-shift method (Pang et al., 2019, 2020), as shown in **Supplementary Appendix Eq. A4**. **Figures 10A,B** show the post-stack seismic data and attenuation (the dissipation factor 1000/*Q*) profiles of the target layer, respectively, where the red and blue colors indicate high and low attenuation (**Figure 10B**). The results show that the rocks at the two wells exhibit significant attenuation. On the other hand, Poisson's ratio and λ/ρ are obtained from AVO inversion (Guo et al., 2018b; Luo et al., 2020a,b). The pre-stack angle gather data contains useful information about the amplitude change with angle. The three-parameter inversion method of pre-stack seismic data, based on the AVO theory, can directly estimate P-wave impedance, S-wave impedance and density, and from these the Poisson's ratio and λ/ρ are obtained. **Figures 10C,D** show 2D profiles of λ/ρ and Poisson's ratio obtained with pre-stack seismic inversion. We can see that Poisson's ratio is low in regions with a high λ/ρ.

Attenuation, Poisson's ratio and λ/ρ at well A were used to calibrate the RPT at seismic frequencies (see **Figure 11**) and the log porosity of well A is assumed. Comparing the seismic inversion data with the RPT, we can observe that the seismic data

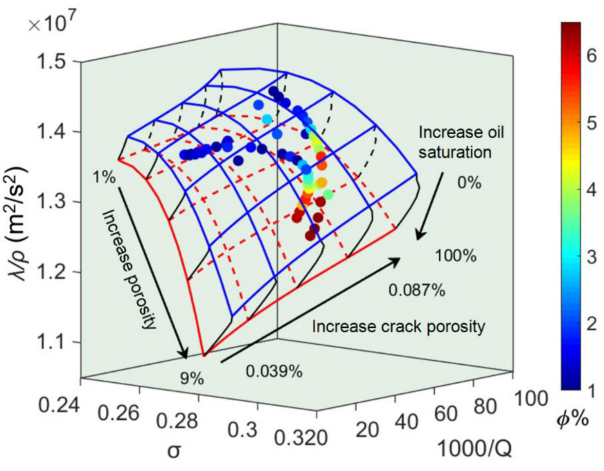

FIGURE 11 | 3D RPT at 35 Hz and seismic data (dots). The color bar indicates total porosity.

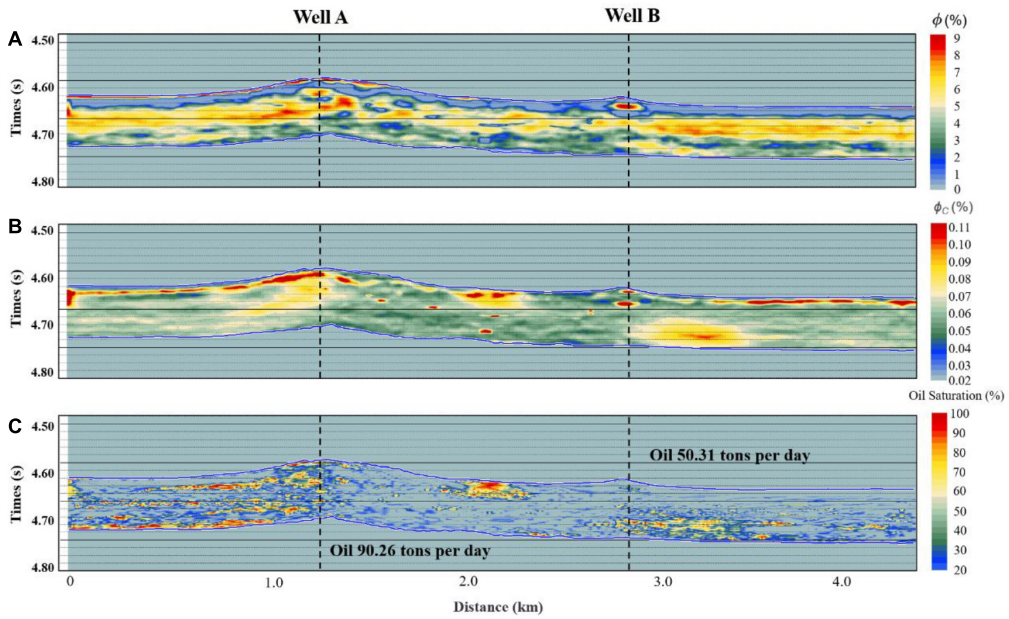

FIGURE 12 | Vertical section of total porosity **(A)**, crack porosity **(B)**, and oil saturation **(C)** of the target layer. The oil production of both wells are shown.

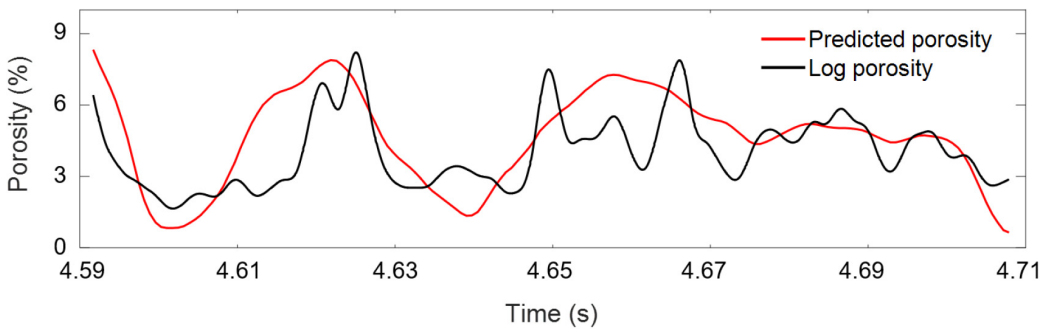

FIGURE 13 | Comparison between the predicted total porosity and log porosity of well A.

with porosity is consistent with the template. According to the color bar of **Figure 11**, the porosity of the seismic data is low (less than 7%), which agrees with the characteristics of the ultra-deep reservoirs. Attenuation, Poisson's ratio, and λ/ρ can be obtained from seismic data, and a quantitative prediction of total porosity, crack porosity, and oil saturation can be achieved by overlapping the data on the template.

PREDICTION OF THE RESERVOIR PROPERTIES

The calibrated RPTs are applied to estimate the reservoir properties. **Figure 12** shows the reservoir total and crack porosities, and oil saturation on a 2D survey line crossing wells A and B. In **Figure 12A**, total porosity is generally less than 10% and areas around the wells exhibit higher porosity. As shown in **Figure 13**, the predicted results of well A are consistent with the porosity log profile. The average error between the predicted porosities (based on seismic wave attributes) and the measured porosities of well A is 0.0125. By combining **Figures 12B,C**, high crack porosity enables good connectivity and better oil storage capacity. In **Figure 12**, we also can see that the upper part of well B has a pore-crack system with low oil saturation, while the lower part has high oil saturation, indicating that the reservoir is not homogeneous. Comparative analysis shows that the predicted results are consistent with the reported oil production of well A (90.26 tons/day) and well B (50.31 tons/day). The prediction results of well A are used to analyze the correlation between crack porosity and oil saturation. The correlation coefficient is 0.6296 between fracture porosity and oil saturation.

Figure 14 gives horizontal sections of total and crack porosities and oil saturation, showing that well A exhibits higher porosity and oil saturation than well B, while the difference in crack porosity is small. The storage space of fault-controlled karst reservoirs is formed by the dissolution of water or

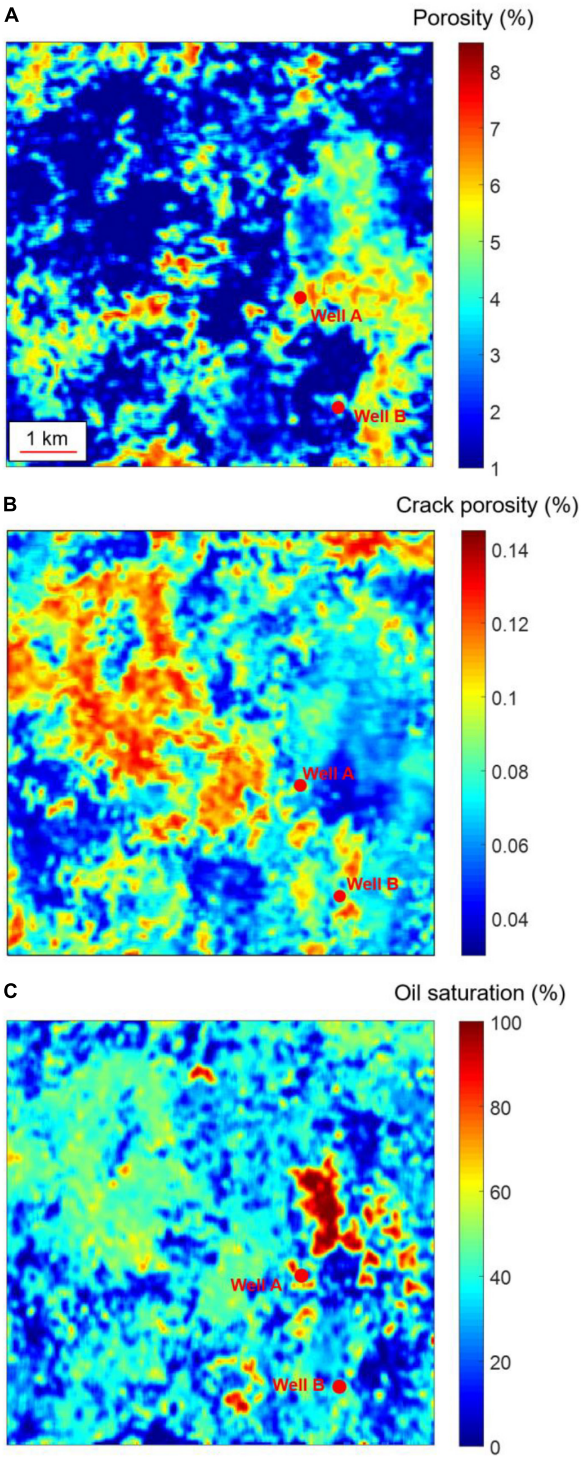

FIGURE 14 | Horizontal section of total porosity **(A)**, crack porosity**(B)**, and oil saturation **(C)** of the target layer.

hydrothermal fluid along the fault and the distribution of the fluid is extremely uneven. Combining **Figures 14A,B**, the distributions of total and crack porosities are complementary and the oil saturation distribution in **Figure 14C** is irregular. These are typical characteristics of fault-controlled karst reservoirs.

It can be seen in **Figures 12**, **14** that fault-controlled karst reservoirs do not have a defined oil-water interface, but a patchy fluid saturation due to dissimilar crack-pore characteristics. Crack porosity can be used as an indicator to find regions with high oil saturation. Stiff pores mainly store oil and soft pores act as flow channels and also play an important storage role. These findings are consistent with the actual characteristics of the reservoirs, indicating that the proposed method can be successfully applied.

CONCLUSION

We have implemented a double double-porosity theory to build RPT in order to estimate the properties of deep carbonate reservoirs. The dry-rock moduli were obtained with a combination of the VRH equation and the self-consistent model. The templates axes involve attenuation, Poisson's ratio and the ratio Lamé constant to density. Ultrasonic experiments were performed on rock samples of the study area and used to calibrate the templates, as well as information from well logs. Then, we have predicted total porosity, crack porosity and oil saturation of the carbonate reservoirs. According to the results, the reservoir has low porosity with developed cracks, which is consistent with the local geological features. Moreover, the results are basically consistent with the actual oil production in the area.

DATA AVAILABILITY STATEMENT

The original contributions presented in the study are included in the article/**Supplementary Material**, and further inquiries can be directed to the corresponding author/s.

AUTHOR CONTRIBUTIONS

XZ: ideas and writing. JB: theories and applications. JS and JC: revising. L-YF: suggestions and revising. MP: modeling. All authors contributed to the article and approved the submitted version.

FUNDING

The authors were grateful to the support of National Natural Science Foundation of China (Grant No. 41821002), the Jiangsu Innovation and Entrepreneurship Plan, Jiangsu Province Science Fund for Distinguished Young Scholars (BK20200021), National Natural Science Foundation of China (41974123), the National Science and Technology Major Project of China (2017ZX05069-002), and the research funds from SINOPEC Key Laboratory of Geophysics.

SUPPLEMENTARY MATERIAL

The Supplementary Material for this article can be found online at: https://www.frontiersin.org/articles/10.3389/feart.2021.649984/full#supplementary-material

REFERENCES

Agersborg, R., Johansen, T. A., Jakobsen, M., Sothcott, J., and Best, A. I. (2008). Effects of fluids and dual-pore systems on pressure-dependent velocities and attenuations in carbonates. *Geophysics* 73, N35–N47.

Ba, J., Carcione, J. M., and Nie, J. X. (2011). Biot-Rayleigh theory of wave propagation in double-porosity media. *J. Geophys. Res. Solid Earth* 116: B06202.

Ba, J., Xu, W. H., Fu, L. Y., Carcione, J. M., and Zhang, L. (2017). Rock anelasticity due to patchy-saturation and fabric heterogeneity: a double-double porosity model of wave propagation. *J. Geophys. Res. Solid Earth* 122, 1949–1976.

Batzle, M., and Wang, Z. J. (1992). Seismic properties of pore fluids. *Geophysics* 57, 1396–1408. doi: 10.1190/1.1443207

Batzle, M., Han, D., and Hofmann, R. (2001). Optimal hydrocarbon indicators. *Paper Presented at the 71st Ann. Internat. Mtg., Soc. Explor, Geophys*, Tulsa, OK. 1697–1700.

Berryman, J. G. (1980). Long wavelength propagation in composite elastic media II. ellipsoidal inclusions. *Acoustical Soc. Am. J.* 68, 1820–1831. doi: 10.1121/1.385172

Berryman, J. G. (1992). Single-scattering approximations for coefficients in Biot's equations of poroelasticity. *Acoustical Soc. Am. J.* 91, 551–571. doi: 10.1121/1.402518

Berryman, J. G. (1998). Long-wavelength propagation in composite elastic media I. spherical inclusions. *J. Acoustical Soc. Am.* 68, 1809–1819. doi: 10.1121/1.385171

Carcione, J. M. (2014). *Wave Fields in Real Media, Theory and Numerical Simulation of Wave Propagation in anisotropic, Anelastic, Porous and Electromagnetic Media*, 3rd Edn. Amsterdam: Elsevier.

Carcione, J. M., and Avseth, P. (2015). Rock-physics templates for clay-rich source rocks. *Geophysics* 80, D481–D500.

Chi, X. G., and Han, D. H. (2009). Lithology and fluid differentiation using a rock physics template. *Lead. Edge* 28, 60–65. doi: 10.1190/1.3064147

Deng, J. X., Zhou, H., Wang, H., Zhou, G., and Wang, S. X. (2015). The influence of pore structure in reservoir sandstone on dispersion properties of elastic waves. *Chinese J. Geophys. (in Chinese)* 58, 3389–3400.

Dillon, L., Schwedersky, G., Guilherme, V., Velloso, R., and Numes, C. (2003). A multiscale DHI elastic attributes evaluation. *Leading Edge* 22, 1024–1029. doi: 10.1190/1.1623644

Dvorkin, J., Mavko, G., and Nur, A. (1995). Squirt flow in fully saturated rocks. *Geophysics* 60, 97–107. doi: 10.1190/1.1443767

Dvorkin, J., Nolen-Hoeksema, R., and Nur, A. (1994). The Squirt-flow t mechanism: macroscopic description. *Geophysics* 59, 428–438. doi: 10.1190/1.1443605

Dvorkin, J., and Nur, A. (1993). Dynamic poroelasticity: a unified model with the squirt and the biot mechanisms. *Geophysics* 58, 524–533. doi: 10.1190/1.1443435

Goodway, W., Chen, T., and Downton, J. (1997). Improved AVO fluid detection and lithology discrimination using Lame petrophysical parameters from P and S inversion. *Paper Presented at 67th Annual International Mtg Social. Explor. Geophysics*, Dallas: 183–186.

Guo, J. X., Shuai, D., Wei, J. X., Ding, P. B., and Gurevich, B. (2018a). P-wave dispersion and attenuation due to scattering by aligned fluid saturated fractures with finite thickness: theory and experiment. *Geophys. J. Int.* 215, 2114–2133. doi: 10.1093/gji/ggy406

Guo, Q., Zhang, H. B., Han, F. L., and Shang, Z. P. (2018b). Prestack seismic inversion based on anisotropic Markov random field. *IEEE Trans. Geosci. Remote Sens.* 56, 1069–1079. doi: 10.1109/tgrs.2017.2758800

Guo, M. Q., and Fu, L. Y. (2006). Stress associated coda attenuation from ultrasonic waveform measurements. *Geophys. Res. Lett.* 34:L09307.

Hedlin, K. (2000). Pore space modulus and extraction using AVO. *Paper presented at 70th Ann. Internat. Mtg., Soc. Explor. Geophys*, Calgary: 170–173.

Hill, R. (1952). The elastic behaviour of a crystalline aggregate. *Proc. Phys. Soc.* 65, 349–354. doi: 10.1088/0370-1298/65/5/307

Johnson, D. L. (2001). Theory of frequency dependent acoustics in patchy-saturated porous media. *J. Acoustical Soc. Am.* 110, 682–694. doi: 10.1121/1.1381021

Lan, X. D., Lü, X. X., Zhu, Y. M., and Yu, H. F. (2015). The geometry and origin of strike-slip faults cutting the Tazhong low rise megaanticline (central uplift, Tarim Basin, China) and their control on hydrocarbon distribution in carbonate reservoirs. *J. Nat. Gas Sci. Eng.* 22, 633–645. doi: 10.1016/j.jngse.2014.12.030

Li, Y. Q., Sun, J. F., Wei, H. H., and Song, S. H. (2019). Architectural features of fault-controlled karst reservoirs in the Tahe oilfield. *J. Petroleum Sci. Eng.* 181:106208. doi: 10.1016/j.petrol.2019.106208

Luo, C., Ba, J., Carcione, J. M., Huang, G. T., and Guo, Q. (2020a). Joint PP and PS pre-stack AVA inversion for VTI medium based on the exact Graebner equation. *J. Petroleum Sci. Eng.* 194:107416. doi: 10.1016/j.petrol.2020.107416

Luo, C., Ba, J., Carcione, J. M., Huang, G. T., and Guo, Q. (2020b). Joint PP and PS pre-stack seismic inversion for stratified models based on the propagator matrix forward engine. *Surveys Geophys.* 41, 987–1028. doi: 10.1007/s10712-020-09605-5

Mavko, G., Mukerji, T., and Dvorkin, J. (2009). *The Rock Physics Handbook: Tools for Seismic Analysis of Porous Media*. Cambridge: Cambridge University Press.

Michel, K. (2010). Rock physics driven inversion: the importance of workflow. *First Break* 28, 68–81.

Odegaard, E., and Avseth, P. A. (2004). Well log and seismic data analysis using rock physics templates. *First Break* 22, 37–43.

Pang, M. Q., Ba, J., Carcione, J. M., Picotti, S., Zhou, J., and Jiang, R. (2019). Estimation of porosity and fluid saturation in carbonates from rock-physics templates based on seismic Q. *Geophysics* 84, M25–M36.

Pang, M. Q., Ba, J., Fu, L. Y., Carcione, J. M., Markus, U. I., and Zhang, L. (2020). Estimation of microfracture porosity in deep carbonate reservoirs based on 3D rock-physics templates. *Interpretation* 8, 1–10. doi: 10.1190/geo2020-0550.1

Pang, X. Q. (2010). Key challenges and research methods of petroleum exploration in the deep of superimposed basins in western China. *Oil Gas Geol.* 31, 517–534.

Picotti, S., Carcione, J. M., and Ba, J. (2018). Rock-physics templates for seismic Q. *Geophysics* 84, MR13–MR23.

Pimienta, L., Fortin, J., and Guéguen, Y. (2015). Bulk modulus dispersion and attenuation in sandstones. *Geophysics* 80, D111–D127.

Pride, S. R., Berryman, J. G., and Harris, J. M. (2004). Seismic attenuation due to wave induced flow. *J. Geophys. Res.* 109:B01201.

Qiao, Y. D., and An, H. W. (2007). Study of petrophysical parameter sensitivity from well log data. *Appl. Geophys.* 4, 28–287.

Quakenbush, M., Shang, B., and Tuttle, C. (2006). Poisson impedance. *Leading Edge* 25, 128–138. doi: 10.1190/1.2172301

Quintal, B. (2012). Frequency-dependent attenuation as a potential indicator of oil saturation. *J. Appl. Geophys.* 82, 119–128. doi: 10.1016/j.jappgeo.2012.03.001

Reuss, A. (1929). Calculation of the flow limits of mixed crystals on the basis of the plasticity of monocrystals. *Zeitschrift fur Angewandte Mathenatik* 9, 49–58.

Russell, B. H., Gray, D., Hampson, D. P., and Lines, L. (2006). Linearized AVO and poroelasticity. *CREWES Res. Report* 18, 1–25.

Russell, B. H., Hedlin, K., Hilterman, F. J., and Lines, L. R. (2003). Fluid-property discrimination with AVO: a Biot-Gassmann perspective. *Geophysics* 68, 29–39. doi: 10.1190/1.1543192

Shapiro, S. A. (2003). Elastic piezosensitivity of porous and fractured rocks. *Geophysics* 68, 482–486. doi: 10.1190/1.1567215

Tan, W. H., Ba, J., Müller, T., Fang, G., and Zhao, H. B. (2020). Rock physics model of tight oil siltstone for seismic prediction of brittleness. *Geophys. Prospect.* 68, 1554–1574. doi: 10.1111/1365-2478.12938

Tang, X. M. (2011). A unified theory for elastic wave propagation through porous media containing cracks-An extension of Biot's poroelastic wave theory. *Sci. China Earth Sci.* 54, 1441–1452. doi: 10.1007/s11430-011-4245-7

Tian, F., Lu, X. B., Zheng, S. Q., Zhang, H. F., Rong, Y. S., Yang, D. B., et al. (2017). Structure and Filling Characters of Paleokarst Reservoirs in Northern Tarim Basin, Revealed by Outcrop, Core and Borehole Images. *Open Geosci.* 9, 266–280.

Toksöz, M. N., Johnston, D. H., and Timur, A. (1979). Attenuation of seismic waves in dry and saturated rocks: I, Laboratory measurements. *Geophysics* 44, 681–690. doi: 10.1190/1.1440969

Tran, M., Mukerji, T., and Hosford Scheirer, A. (2020). Lithofacies-dependent rock physics templates of an unconventional shale reservoir on the North Slope, Alaska. *Interpretation* 8, 1–49. doi: 10.1190/int-2019-0156.1

Voigt, W. (1910). Lehrbuch der Kirstallphysik. *Teubner Leipzig* 1928:739.

White, J. E. (1975). Computed seismic speeds and attenuation in rocks with partial gas saturation. *Geophysics* 40, 224–232. doi: 10.1190/1.1440520

Xue, J., Gu, H., and Cai, C. (2017). Model-based amplitude versus offset and azimuth inversion for estimating fracture parameters and fluid content. *Geophysics* 82, M1–M17.

Zou, C. N., Hou, L. H., Hu, S. Y., Zhu, R. K., Liu, S. B., Yang, Z., et al. (2014). Prospect of ultra-deep petroleum onshore China. *Energy Explorat. Exploit.* 32, 19–40. doi: 10.1260/0144-5987.32.1.19

Conflict of Interest: The authors declare that the research was conducted in the absence of any commercial or financial relationships that could be construed as a potential conflict of interest.

Copyright © 2021 Zhou, Ba, Santos, Carcione, Fu and Pang. This is an open-access article distributed under the terms of the Creative Commons Attribution License (CC BY). The use, distribution or reproduction in other forums is permitted, provided the original author(s) and the copyright owner(s) are credited and that the original publication in this journal is cited, in accordance with accepted academic practice. No use, distribution or reproduction is permitted which does not comply with these terms.

frontiers in Earth Science

ORIGINAL RESEARCH
published: 12 May 2021
doi: 10.3389/feart.2021.652344

Experimental Study on Petrophysical Properties as a Tool to Identify Pore Fluids in Tight-Rock Reservoirs

Rupeng Ma[1,2], *Jing Ba*[1]*, *José Carcione*[3], *Maxim Lebedev*[2] *and Changsheng Wang*[4]

[1] School of Earth Sciences and Engineering, Hohai University, Nanjing, China, [2] WA School of Mines: Minerals, Energy and Chemical Engineering, Curtin University, Perth, WA, Australia, [3] Department of Geophysics, Istituto Nazionale di Oceanografia e di Geofisica Sperimentale (OGS), Trieste, Italy, [4] Exploration and Development Research Institute of Changqing Oilfield, PetroChina, Xi'an, China

The petrophysical properties can be proper indicators to identify oil and gas reservoirs, since the pore fluids have significant effects on the wave response. We have performed ultrasonic measurements on two sets of tight siltstones and dolomites at partial saturation. P- and S-wave velocities are obtained by the pulse transmission technique, while attenuation is calculated using the centroid-frequency shift and spectral-ratio methods. The fluid sensitivities of different properties (i.e., P- and S-wave velocities, impedances and attenuation, Poisson's ratio, density, and their combinations) are quantitatively analyzed by considering the data distribution, based on the crossplot technique. The result shows that the properties (P- to S-wave velocity and attenuation ratios, Poisson's ratio, and first to second Lamé constant ratio) with high fluid-sensitivity indicators successfully distinguish gas from oil and water, unlike oil from water. Moreover, siltstones and dolomites can be identified on the basis of data distribution areas. Ultrasonic rock-physics templates of the P- to S-wave velocity ratio vs. the product of first Lamé constant with density obtained with a poroelastic model, considering the structural heterogeneity and patchy saturation, are used to predict the saturation and porosity, which are in good agreement with the experimental data at different porosity ranges.

Keywords: tight rocks, experimental observation, petrophysical properties, fluid sensitivity, rock physics template, attenuation

OPEN ACCESS

Edited by:
Pinbo Ding,
China University of Petroleum, China

Reviewed by:
Lingyun Kong,
University of North Dakota, United States
Junxin Guo,
Southern University of Science and Technology, China
Zhiqi Guo,
Jilin University, China

***Correspondence:**
Jing Ba
jba@hhu.edu.cn;
jingba@188.com

Specialty section:
This article was submitted to Solid Earth Geophysics, a section of the journal Frontiers in Earth Science

Received: *12 January 2021*
Accepted: *19 April 2021*
Published: *12 May 2021*

Citation:
Ma R, Ba J, Carcione J, Lebedev M and Wang C (2021) Experimental Study on Petrophysical Properties as a Tool to Identify Pore Fluids in Tight-Rock Reservoirs. Front. Earth Sci. 9:652344. doi: 10.3389/feart.2021.652344

INTRODUCTION

The rock-physics properties are affected by the reservoir characteristics (i.e., lithology, porosity, permeability, and pattern) and the presence of pore fluids. Understanding the corresponding variations is essential for seismic exploration. Although these variations have been extensively investigated for intermediate- to high-porosity fluid-saturated rocks, the effects of partial saturation on low-porosity tight rocks are not well-understood and a fluid-sensitivity analysis can be useful to interpret the porosity-based saturation logs and related seismic data.

A set of fluid-sensitive identification factors (rock-physics properties and their combinations) have been proposed to identify pore fluids (e.g., Fatti et al., 1994; Smith and Sutherland, 1996; Goodway, 2001; Dillon et al., 2003; Qiao and An, 2007; Qi et al., 2017; Zeng et al., 2017). For example, Ostrander (1984) and Carcione and Cavallini (2002) showed that Poisson's ratio of gas-saturated rocks is lower than those of brine- and oil-saturated ones. Zhou and Hilterman (2010) used three seismic attributes to predict pore fluid and lithology and showed that their sensitivities are not significantly affected by the scale factors. Moreover, Pei et al. (2010) proposed a new fluid

identification factor, which is more effective than the amplitude versus offset (AVO) attributes in low-porosity reservoirs. However, these methods are incomplete due to the lack of statistical analysis of data distribution, and most of the methods have been applied to detect gas reservoirs.

The problem is that a single physical property is insufficient to predict the reservoir features and fluid content, especially for the tight rocks. A set of properties should be used, because P and S waves respond differently to variations in fluid saturation. Previous studies show that P- and S-wave velocity and attenuation ratios (and Q_P^{-1}/Q_S^{-1}) are more sensitive to partial gas–water saturation (Murphy, 1982; Winkler and Nur, 1982; Klimentos, 1995; Chichinina et al., 2009; Qi et al., 2017). For example, Murphy (1982) showed that P-wave attenuation is more robust than S-wave attenuation in partially saturated Massillon sandstone, but the difference is small at full water saturation. Winkler and Nur (1982) found that the ratio of P- to S-wave attenuation is more sensitive to gas saturation than the P- to S-wave velocity ratio, showing that $Q_P^{-1}/Q_S^{-1} \leq 1$ for water-saturated rocks and $Q_P^{-1}/Q_S^{-1} > 1$ for gas-saturated rocks. These relations can be useful, but they have been applied to intermediate- and high-porosity rocks. Only a few studies deal with tight-rock reservoirs (e.g., Pei et al., 2010; Xue et al., 2013; Han et al., 2017; Qi et al., 2017; Pang et al., 2019). They mainly distinguish gas from liquid-saturated rocks for sandstone and shale reservoirs. However, the relations were hardly analyzed for tight siltstone and dolomite reservoirs.

The challenge is to propose a suitable theoretical model that can predict the elastic properties and wave response characteristics in partially saturated rocks. Seismic wave velocity dispersion and attenuation are considered to be caused by the wave-induced fluid flow mechanism (Mavko and Nur, 1979; Murphy, 1982; Winkler and Nur, 1982; Müller et al., 2010). Different poroelastic models have been developed to predict the velocity and attenuation observed in the laboratory and in the field data (Biot, 1956; White, 1975; Pride et al., 2004; Gurevich et al., 2010; Ba et al., 2017; Guo and Gurevich, 2020). Based on these models, rock-physics templates (RPTs) can be used to estimate porosity and saturation (Liu et al., 2015; Pang et al., 2019, 2020). Studies showed that RPTs, built with acoustic impedance and P- to S-wave velocity ratio, serve as tools for lithology and fluid identification (Chi and Han, 2009; Datta Gupta et al., 2012; Ba et al., 2013). RPTs based on seismic attenuation also describe the effect of partial saturation, porosity, and permeability (Dvorkin and Mavko, 2006; Picotti et al., 2018). The Gassmann's equation is mainly used to conduct fluid substitution in generating RPTs and obtain the elastic modulus of the saturated rock, but neglecting the effect of patchy saturation. The tight-rock reservoirs usually have complex structures and highly variable saturation due to the complex rock patterns, and we used a double double-porosity (DDP) model, considering the structural heterogeneity and the uneven patchy saturation, for fluid substitution in the RPTs.

The rock-physics properties and ultrasonic waveforms can be obtained at different fluid-saturated conditions from the laboratory measurements. In this study, we performed ultrasonic measurements on tight siltstones and dolomites, where the P- and S-wave velocities and attenuation are obtained at *in situ* confining pressure. These properties and their combinations are then evaluated by means of fluid-sensitive indicators (FSIs) and crossplots are shown to validate their effectiveness. Finally, RPTs are built by using the DDP model of Ba et al. (2017) to match the experimental data.

EXPERIMENTS

Two sets of tight rocks are collected from the reservoirs. One set of 12 siltstones are collected from the oil reservoirs of the Qingshankou Formation, Northeast China, whereas another set of 13 dolomites are collected from Ordovician and Cambrian Formations, West China. The porosities and permeabilities of siltstones range from 2.88 to 13.97% and 0.0045 to 0.39 mD and those of dolomites from 4.99 to 16.87% and 0.075 to 162.753 mD, respectively. The corresponding parameters are listed in **Tables 1**, **2**, sorted from smallest to largest based on porosity. The low permeability in siltstones is due to the high clay content and fine texture, while the highly variable permeability in dolomites indicates the presence of fractures. More details on the rock properties can be found in the study by Ba et al. (2019).

The systematic ultrasonic measurements have been performed on the two sets of rocks at different saturations and *in situ* confining pressure. Siltstones were measured at a confining pressure of 50 MPa and a pore pressure of 25 MPa, whereas dolomites at 80 and 10 MPa, respectively. The adopted saturation method is described in the studies by Ba et al. (2017) and Ma and Ba (2020). The partially gas–water and oil–water saturation tests were performed on the dolomites, but we conducted these tests only in five siltstones, and we set full saturation in others (gas, water, and oil, respectively). The waveforms of P and S

TABLE 1 | Rock properties for tight siltstones.

Samples	Lithology	Porosity (%)	Permeability (mD)	Dry density (g/cm^3)	Clay volume content (%)
A	Muddy siltstone	2.88	0.0045	2.61	2.8
B	Muddy siltstone	4.6	0.38	2.56	8.2
C	Siltstone	5.2	0.019	2.58	1.9
D	Silty mudstone	5.56	0.011	2.53	12.5
E	Siltstone	5.6	0.017	2.52	2.4
F	Siltstone	5.79	0.035	2.41	3.9
G	Siltstone	5.8	0.02	2.55	3.0
H	Siltstone	6.45	0.097	2.38	5.5
I	Siltstone	10.87	0.39	2.29	5.5
J	Muddy siltstone	12.75	0.17	2.3	4.4
K	Siltstone	13.09	0.08	2.28	5.5
L	Siltstone	13.97	0.084	2.26	5.5

waves were recorded by the pulse transmission technique, and the corresponding velocities were calculated on the basis of the arrival time of the first high-amplitude signals. P- and S-wave attenuation were estimated by using one wave period with the centroid-frequency shift and spectral-ratio methods (Toksöz et al., 1979; Quan and Harris, 1997). The detailed measuring procedures and error analysis are given in the study by Ma and Ba (2020).

FLUID-SENSITIVE INDICATOR AND PETROPHYSICAL PROPERTIES

To quantitatively evaluate the sensitivity when the rocks are saturated with different fluids, an indicator (I) has been introduced by Pei et al. (2010) and Guo et al. (2015):

$$\mathrm{I} = \left| \frac{\overline{X_i} - \overline{X_\mathrm{w}}}{\overline{X_\mathrm{w}}} \right|, \tag{1}$$

where $\overline{X_i}$ and $\overline{X_\mathrm{w}}$ are the average values of measured data at gas/oil and water saturations, respectively. A high I indicates that the property is more sensitive to the change of pore fluid. However, I values of different rocks can be similar and the data distribution pattern must be considered. A coefficient of dispersion (CD), which reflects the distribution range, is given by the following equation:

$$\mathrm{CD} = \mathrm{SD}_i / \overline{X_i}, \tag{2}$$

$$\mathrm{SD}_i = \sqrt{\sum\nolimits_{i=1}^{n} \left(X_i - \overline{X_i}\right)^2 / n}, \tag{3}$$

where SD_i denotes the standard deviation for the gas/oil-saturated rocks and n is the number of samples. For rocks with partial saturation, $\overline{X_i}$ and SD_i are the average and standard deviations, respectively. A small CD indicates that the data distribution is focused around the average value. Thus, the FSI is defined as follows:

$$\mathrm{FSI} = \mathrm{I}/\mathrm{CD}. \tag{4}$$

The larger the FSI value, the higher the fluid detection capability.

Both the pore fluid and the characteristics of the rock frame affect the bulk modulus, while the fluid has almost no effect on the shear modulus. P- and S-wave velocities (V_P, V_S), attenuations (Q_P^{-1}, Q_S^{-1}), and density (ρ) are obtained from the laboratory measurements. Other properties can be obtained from these properties described above, such as $V_\mathrm{P}/V_\mathrm{S}$, impedances Z_p and Z_s, Poisson's ratio ν, Young's modulus E, first and second Lamé constants λ, μ, $\lambda\rho$, λ/μ, and $Q_\mathrm{P}^{-1}/Q_\mathrm{S}^{-1}$. These 14 properties, except μ, are used for the fluid-sensitivity analysis.

TABLE 2 | Rock properties for carbonates.

Samples	Lithology	Porosity (%)	Permeability (mD)	Dry density (g/cm^3)
DO1	Dolomite	4.99	1.34	2.67
DO2	Clean dolomite	5.10	0.091	2.69
DO3	Clean dolomite	5.34	0.458	2.66
DO4	Clean dolomite	5.47	0.174	2.67
DO5	Dolomite	6.08	0.130	2.65
DO6	Dolomite	6.93	0.601	2.64
DO7	Dolomite	10.37	1.430	2.52
DO8	Dolomite	11.63	0.661	2.45
DO9	Dolomite	11.73	0.138	2.51
DO10	Dolomite	11.75	0.075	2.45
DO11	Dolomite	11.63	0.661	2.45
DO12	Clean dolomite	12.08	162.753	2.41
DO13	Dolomite	16.87	3.31	2.32

TABLE 3 | Fluid-sensitivity indicators for tight rocks.

Property	Siltstones (gas)			Siltstones (oil)			Dolomites (gas)			Dolomites (oil)		
	I	CD	FSI	I	CD	FSI	I	CD	FSI	I	CD	FSI
V_P	0.030	0.090	0.333	0.004	0.079	0.051	0.028	0.086	0.329	0.005	0.080	0.06
V_S	0.010	0.073	0.143	0.002	0.075	0.027	0.010	0.071	0.148	0.002	0.072	0.031
P	0.023	0.087	0.258	0.006	0.078	0.081	0.034	0.087	0.386	0.007	0.074	0.094
$V_\mathrm{P}/V_\mathrm{S}$	0.041	0.020	2.063	0.006	0.009	0.683	0.070	0.018	2.150	0.014	0.012	0.650
Z_P	0.050	0.166	0.300	0.010	0.146	0.068	0.059	0.170	0.349	0.012	0.151	0.078
Z_S	0.012	0.150	0.080	0.004	0.144	0.029	0.023	0.155	0.146	0.005	0.144	0.032
ν	0.086	0.048	1.790	0.012	0.018	0.664	0.104	0.054	1.904	0.019	0.028	0.662
E	0.091	0.257	0.354	0.015	0.221	0.070	0.102	0.263	0.389	0.020	0.234	0.086
λ	0.172	0.304	0.566	0.028	0.231	0.120	0.200	0.317	0.629	0.040	0.258	0.154
$\lambda\rho$	0.183	0.371	0.493	0.032	0.294	0.108	0.220	0.395	0.556	0.045	0.326	0.137
λ/μ	0.187	0.105	1.785	0.030	0.044	0.670	0.201	0.111	1.806	0.040	0.064	0.625
Q_P^{-1}	0.154	0.614	0.250	0.155	0.432	0.359	0.038	0.740	0.051	0.017	0.982	0.017
Q_S^{-1}	0.078	0.559	0.139	0.069	0.601	0.116	0.074	0.593	0.125	0.218	1.157	0.188
$Q_\mathrm{P}^{-1}/Q_\mathrm{S}^{-1}$	0.500	0.960	0.521	0.429	1.074	0.399	0.085	0.811	0.105	0.297	0.852	0.348

RESULTS

The I, CD, and FSI values of the above-mentioned properties are reported in **Table 3**. **Figure 1** shows the indicators for siltstones, where it can be seen that I corresponding to Q_P^{-1}/Q_S^{-1} is the most sensitive and those of λ, $\lambda\rho$, λ/μ, and attenuation are high (**Figure 1A**). This is due to the fact that attenuation is more sensitive to the changes in fluid properties and saturation. The FSI values of V_P/V_S, ν, and λ/μ are the highest when their CD values are the lowest (**Figures 1B,C**), i.e., the most sensitive to fluid-type variations. Since P and S waves respond differently to the variations of rock and fluid properties, the S-wave properties

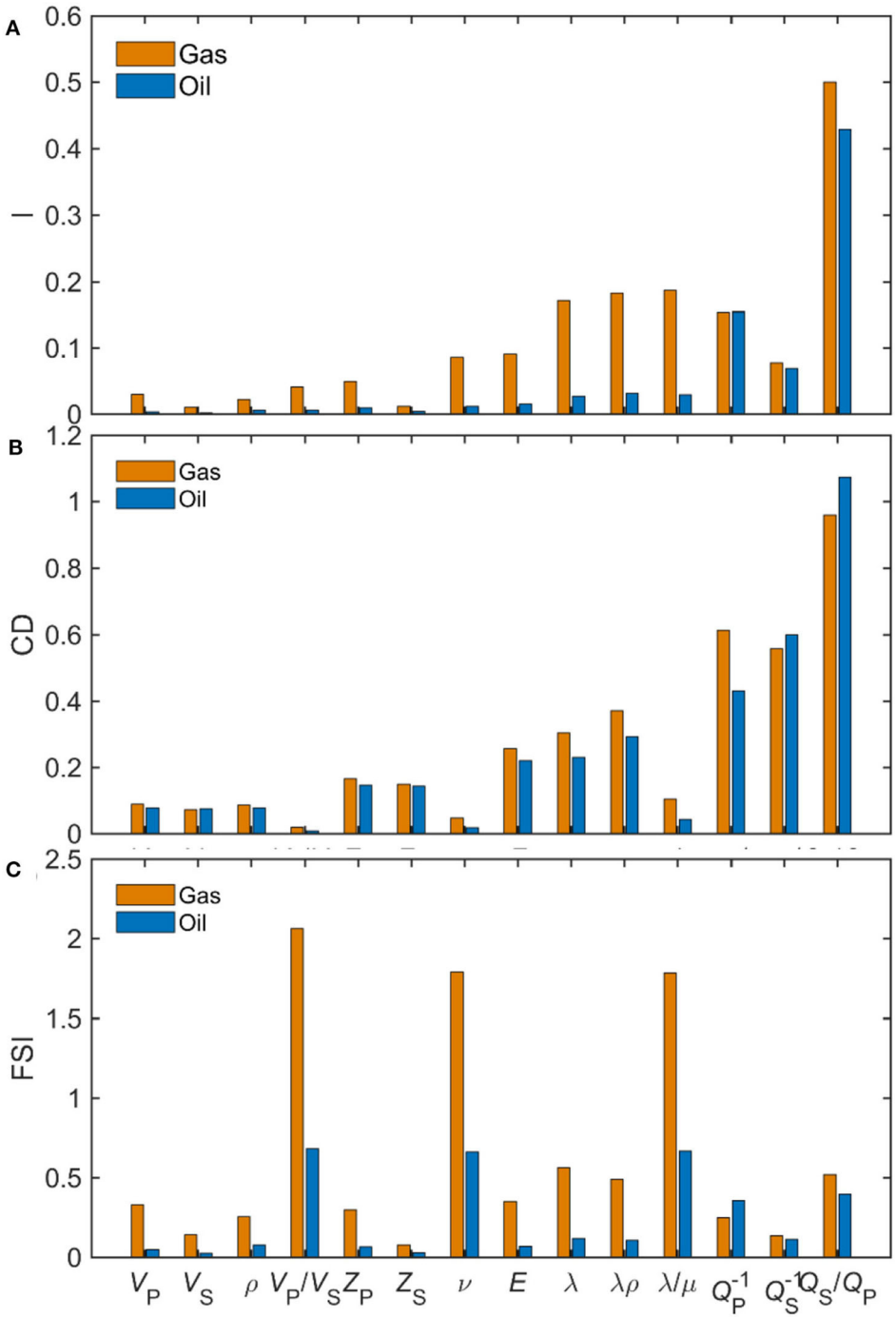

FIGURE 1 | (A) I, **(B)** CD, and **(C)** FSI for siltstones at full saturation. The brown and blue rectangles denote the values of fluid sensitivity to distinguish gas from water and oil from water, respectively.

can be used as normalization quantities with which we compared P-wave properties, to remove in part the effect of rock frame. Moreover, they can better distinguish gas from water than oil from water. Although the I values of Q_P^{-1}/Q_S^{-1} are the highest, the data distribution is scattered due to the complex fluid distribution, resulting in low FSI values. **Figure 2** shows the I, CD, and FSI values for the dolomites, which are similar to those of siltstones.

The crossplot technique is used to verify the fluid identification capability of the properties with the high indicators I and FSI. **Figures 3A,B** shows the crossplots between λ vs. $\lambda\rho$ in siltstones and dolomites, respectively, indicating

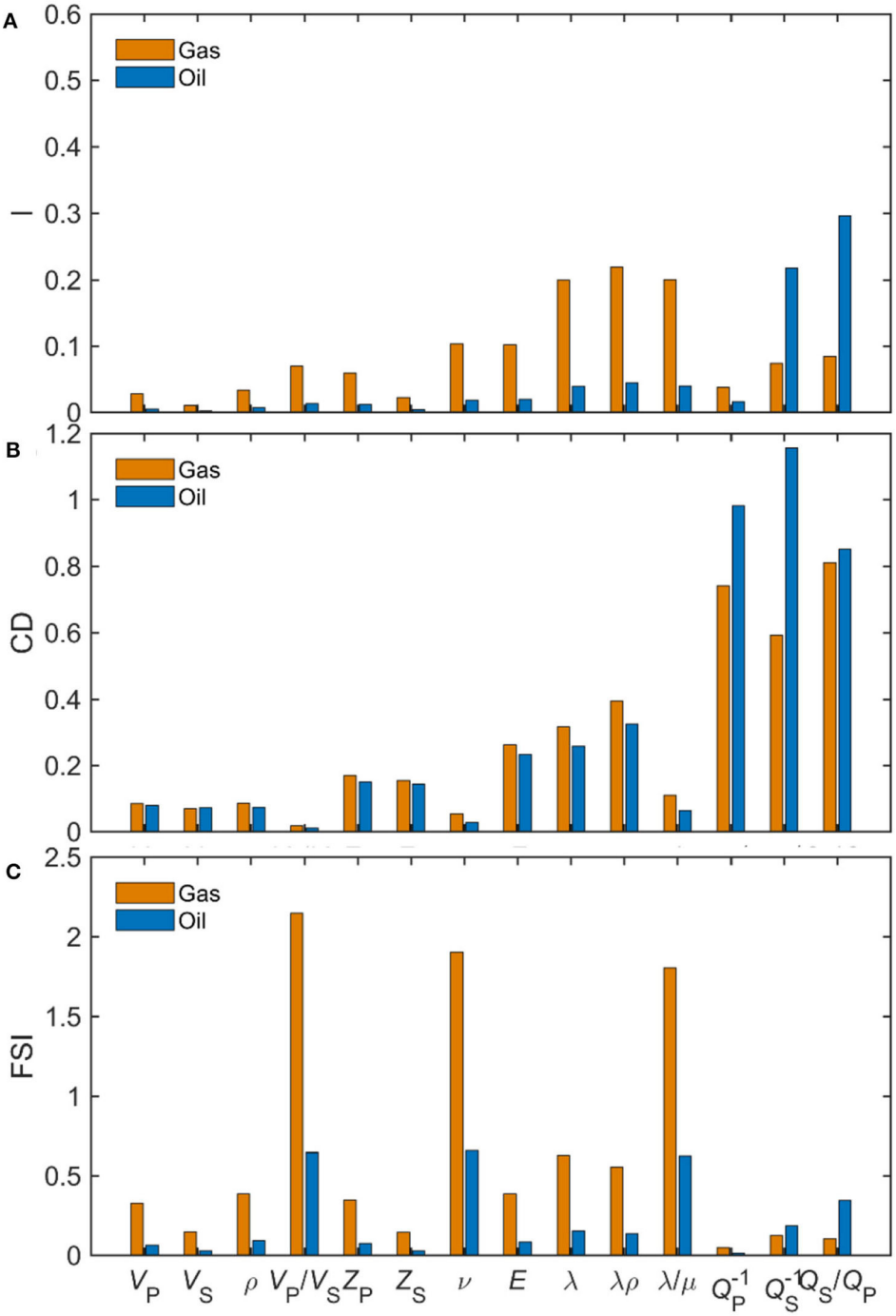

FIGURE 2 | (A) I, **(B)** CD, and **(C)** FSI for dolomites (see **Figure 1** for the explanations).

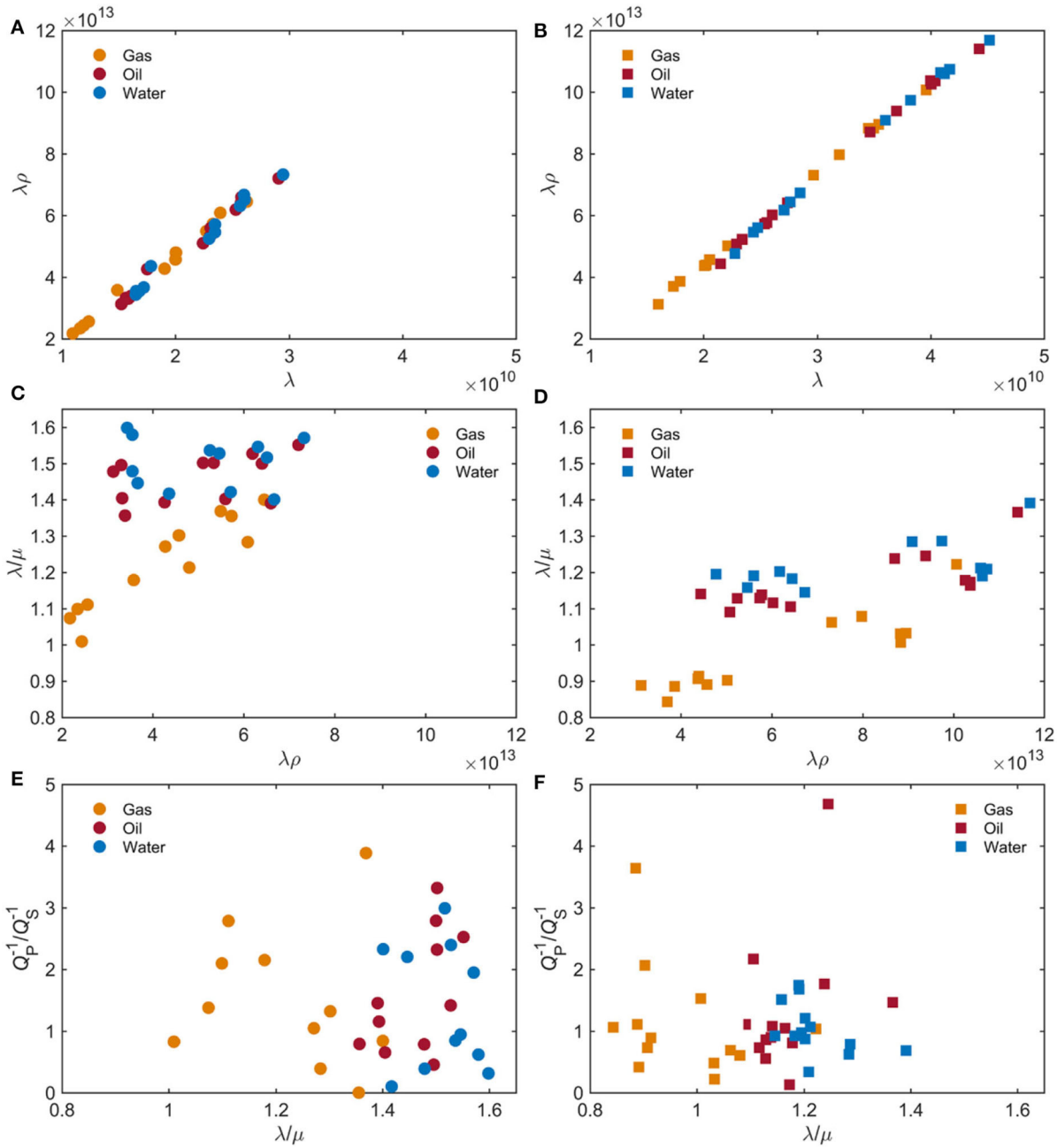

FIGURE 3 | Crossplots of $\lambda\rho$ –λ, λ/μ –$\lambda\rho$, and Q_P^{-1}/Q_S^{-1}–λ/μ for siltstones **(A,C,E)** and dolomites **(B,D,F)**. The brown, red, and blue points denote the data at full gas, oil, and water saturation, respectively. The units of λ and $\lambda\rho$ are kg/m^3 × (m/s)^2 and (kg/m^3 × m/s)^2, respectively.

that the fluid discrimination is difficult. **Figures 3C,D**, which displays crossplots of $\lambda\rho$ vs. λ/μ, shows that the gas-saturated samples can be identified from those saturated with water and oil, but the water and oil cannot be distinguished. In fact, λ/μ has smaller values and significant variations with gas saturation, from 1 to 1.4 for siltstones and ∼from 0.8 to 1.1 for dolomites. **Figures 3E,F** shows the similar trends of λ/μ and Q_P^{-1}/Q_S^{-1}as **Figures 3C,D**, but the data points are widely distributed and have poor convergence. **Figure 4** shows the crossplots of ν, λ/μ, Q_P^{-1}/Q_S^{-1}, and V_P/V_S with high FSI values. There is a linear relation between ν, λ/μ, and V_P/V_S (**Figures 4A–D**), indicating that these properties have a similar variation trend when the pore fluid changes. Gas saturation can be identified from water saturation, while the data for full oil and water saturation are mixed. **Figures 4E,F** indicates that the crossplots of V_P/V_S and Q_P^{-1}/Q_S^{-1} discriminate between gas and water or oil. The properties with high FSI values show a better fluid identification capability than those with high I values, showing that the data

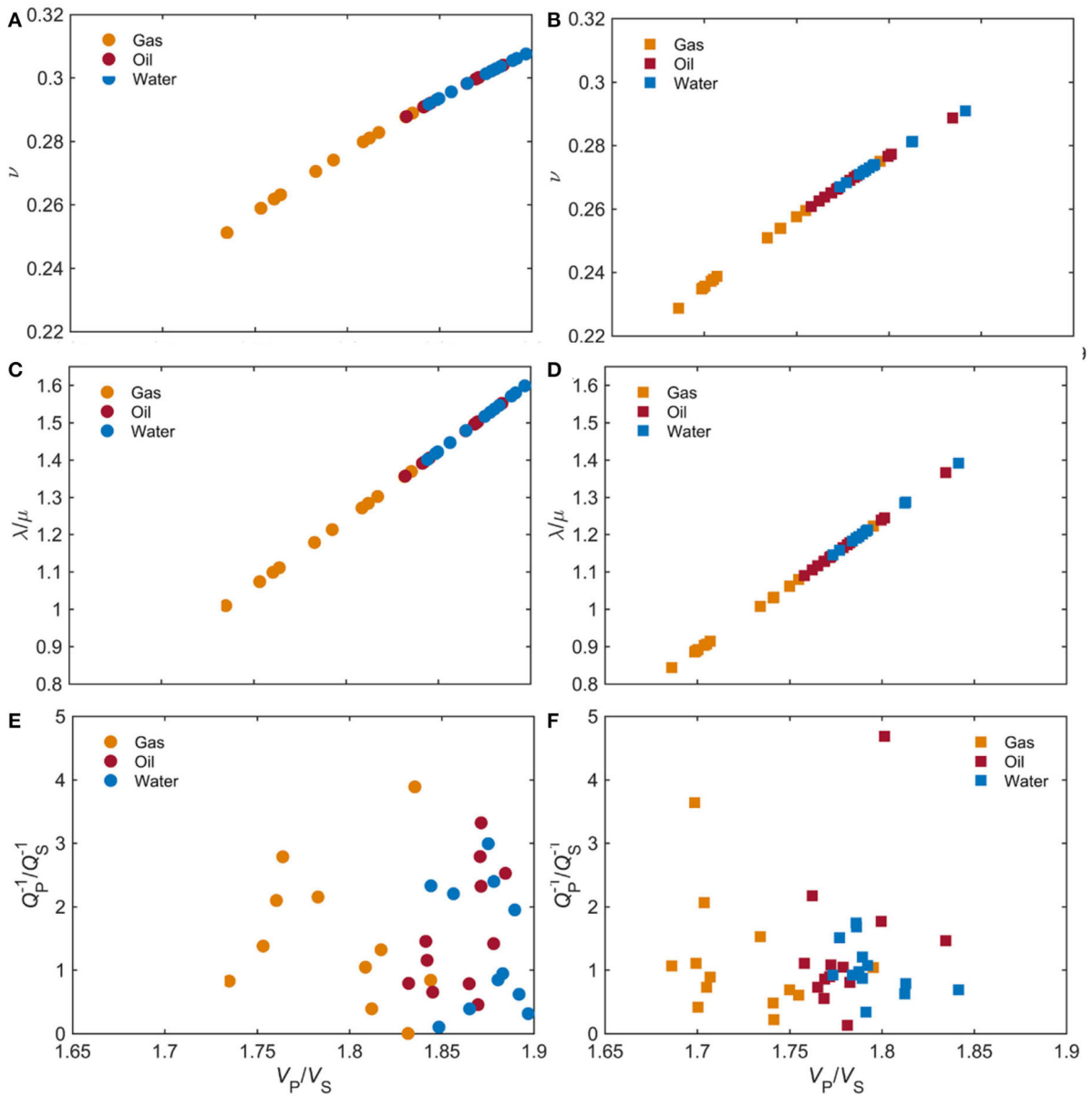

FIGURE 4 | Crossplots of ν –V_P/V_S, λ/μ –V_P/V_S, and Q_P^{-1}/Q_S^{-1}–V_P/V_S for siltstones **(A,C,E)** and dolomites **(B,D,F)** (see **Figure 3** for the explanations).

distribution characteristic is important when quantifying the fluid sensitivity.

Next, we studied the fluid sensitivity in partially saturated rocks (gas–water or oil–water). **Figure 5** shows that V_P/V_S, ν, and λ/μ are high, in agreement with the full saturation case. Since these properties have a similar variation trend, we only obtained the crossplots of V_P/V_S and λ/μ, and are shown in **Figures 6A,B**. They decrease with increasing gas saturation and distinguish between partial and full saturation. However, the data cannot reflect the petrophysical property variation with the variations in reservoir property (i.e., porosity). The $\lambda\rho$ and Q_P^{-1}/Q_S^{-1} are used, which have been verified at full saturation. **Figures 6C,D** shows that V_P/V_S vs. $\lambda\rho$ decreases with gas saturation, while Q_P^{-1}/Q_S^{-1} increases (**Figures 6E,F**). Similar results have been obtained in the studies by Murphy (1982) and Winkler and Nur (1982). **Figure 7** shows the crossplots for partially oil–water saturated rocks. These properties have smaller variations with oil saturation than in the case of gas, and it is difficult to distinguish oil from water. However, the data of siltstones and dolomites have different distribution areas, which can be well-discriminated using the crossplots.

The RPTs are the useful tools in petroleum exploration, relating reservoir, fluid, and petrophysical properties. In this study, we used the DDP model developed by Ba et al. (2017) (see

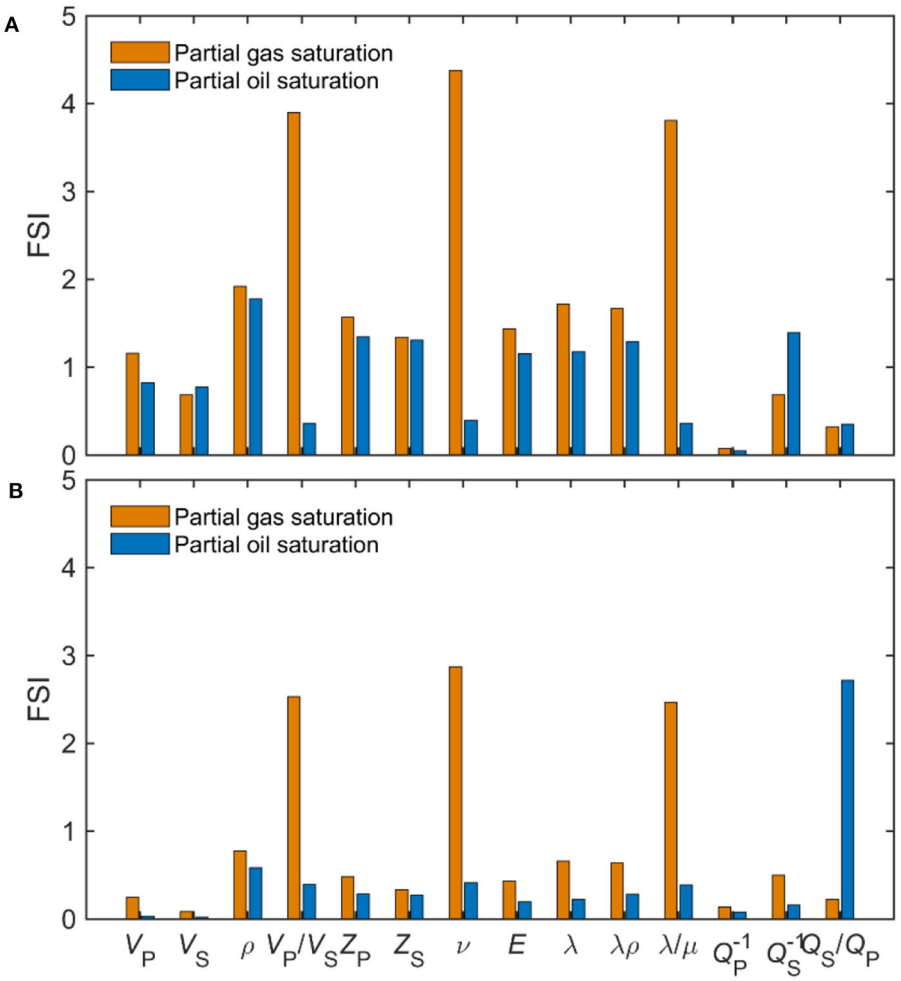

FIGURE 5 | FSI for siltstones **(A)** and dolomites **(B)** at partial saturation.

Appendix A), which considers the fabric structure heterogeneity and uneven patchy saturation to build the templates at ultrasonic frequencies. Siltstones mainly consist of feldspar, quartz, and clay, and we considered clay with intragranular pores as the inclusion with a mean radius of 40 μm embedded in the host medium. Porosity and saturation are set as independent variables. The grain bulk and shear moduli are set to 39 and 31 GPa, respectively, estimated by the average Voigt–Reuss–Hill equation (Hill, 1952; Picotti et al., 2018), while the grain density is 2.6 g/cm^3. The dry-frame and inclusions moduli vs. porosity are calculated by the differential effective medium model (Mavko et al., 2009). The fluid properties at the experimental conditions are obtained by the equations from Batzle and Wang (1992), which are reported in the study by Ba et al. (2019), and the permeability is given by the Kozeny–Carman relation (e.g., Mavko et al., 2009). **Figure 8** shows the template at 1 MHz, compared with the measured data of V_P/V_S and $\lambda\rho$. The black and red curves denote the isolines of constant saturation and porosity, respectively. The figure shows that the predicted porosities (red lines) agree with the sample porosities. For samples I–L with relatively high porosities (10.87–13.97%), the data agree well with the predicted saturation (black lines) at high gas saturations, but the predictions underestimate the data at low gas saturation. The data corresponding to sample H do not match the gas saturation, which may be due to the fact that frame properties of this sample (6.45% porosity) have a significant difference from those of samples I–L.

The dolomites contain cracks and intergranular pores. Soft cracks are inclusions and have a mean radius of 80 μm. The density, bulk modulus, and shear modulus of the mineral grains are 2.7 g/cm^3, 78 and 52 GPa, respectively. **Figure 9A** shows the ultrasonic template compared with the experimental data, from which it can be noted that the porosities and saturation of samples DO2–6 (4.99–6.93%) agree with the template predictions. However, samples DO7–13 with a porosity ranging from 10.37 to 16.87% are outside the template even if the predicted porosities match the data. The data between samples DO1–6 and DO7–13 are dissimilar, and the reason may be the different frame properties at relatively high porosities compared with the low porosity case. Then, we recalculated the template

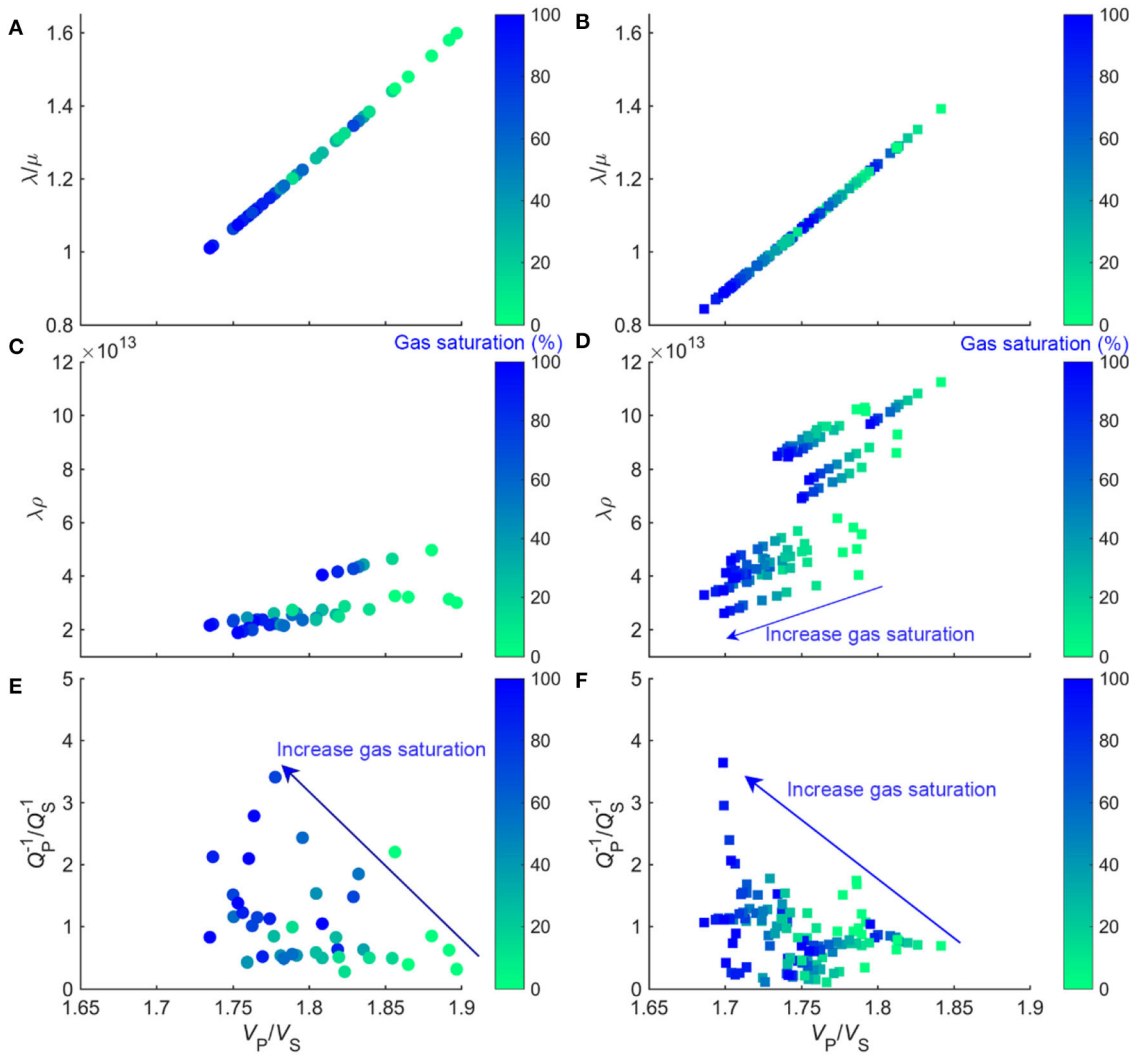

FIGURE 6 | Crossplots of λ/μ –V_P/V_S, $\lambda\rho$ –V_P/V_S, and Q_P^{-1}/Q_S^{-1}–V_P/V_S for siltstones **(A,C,E)** and dolomites **(B,D,F)** at partial gas–water saturation. The color from green to blue denotes gas saturation increasing from 0 to 100%.

by changing the bulk and shear moduli of the mineral grains to 55 and 50 GPa, respectively (**Appendix B**). The results show that the porosities and saturations of samples DO7–13 agree with the template in **Figure 9B**. Some data points are outliers owing to the complex pore structures and fluid distribution. Nevertheless, the present template describes the general trends of porosity and saturation.

Other models (e.g., White, 1975; Pride et al., 2004; Gurevich et al., 2010; Müller et al., 2010) can also be used to build RPTs, but most of them only consider the fabric (pattern) or fluid heterogeneity. Our model considers the effect of the two heterogeneities. Based on the templates of V_P/V_S and $\lambda\rho$ combined with the experimental data, gas can be identified from oil and water at the ultrasonic frequency band. However, the templates of Q_P^{-1}/Q_S^{-1} and V_P/V_S cannot be built because S-wave attenuation is not predicted by the model. Moreover, we have to consider an upscaling of attenuation to lower (seismic) frequencies. In practical applications, the seismic template can be obtained by combining the laboratory, sonic, and seismic data (e.g., Pang et al., 2019, 2020).

CONCLUSION

We have studied the fluid sensitivity of petrophysical properties based on the experimental data by calculating fluid indicators and using crossplots. The FSI considering the data distribution in quantifying the sensitivity is better than the I indicator. The crossplots of ν, λ/μ, Q_P^{-1}/Q_S^{-1}, and V_P/V_S discriminate well between gas and liquids (i.e., water and oil). The siltstone and dolomite data can be identified based on the data distribution areas. As a prediction tool, a DDP theory has been used to build RPTs between V_P/V_S and $\lambda\rho$ and to obtain gas saturation and porosity from the ultrasonic data. Moreover, the frame properties of dolomites may greatly

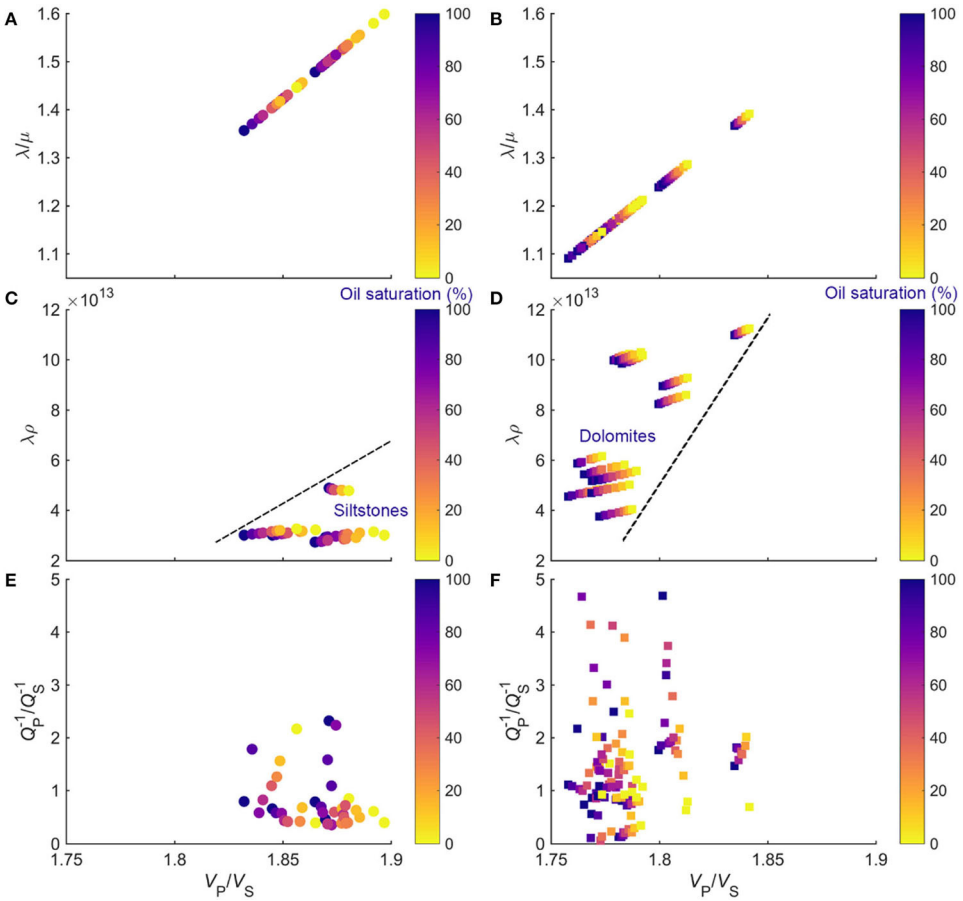

FIGURE 7 | Crossplots of λ/μ –V_P/V_S, $\lambda\rho$ –V_P/V_S, and Q_P^{-1}/Q_S^{-1}–V_P/V_S for siltstones **(A,C,E)** and dolomites **(B,D,F)** at partial oil–water saturation. The color from yellow to purple denotes oil saturation increasing from 0 to 100%.

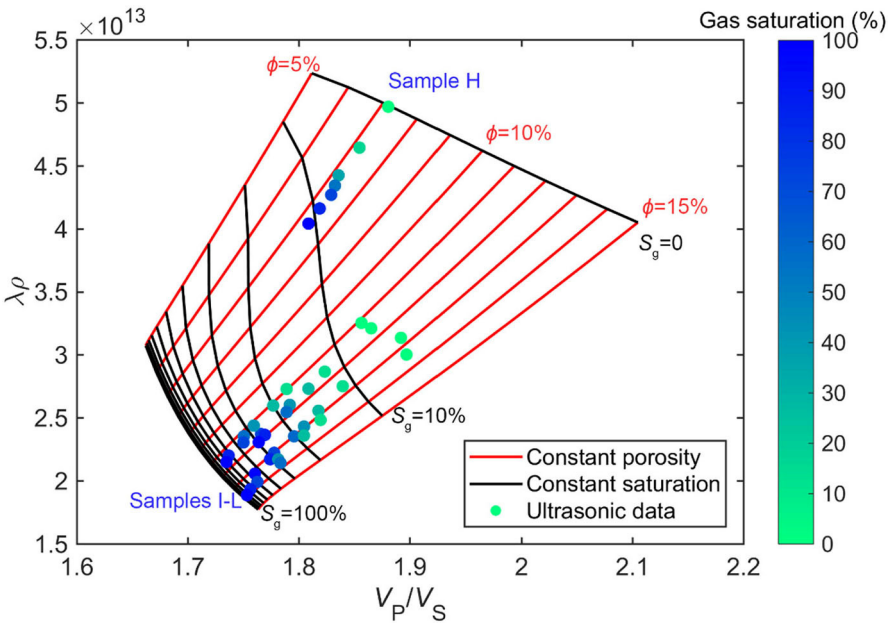

FIGURE 8 | Comparisons between the ultrasonic template and measured data for siltstones.

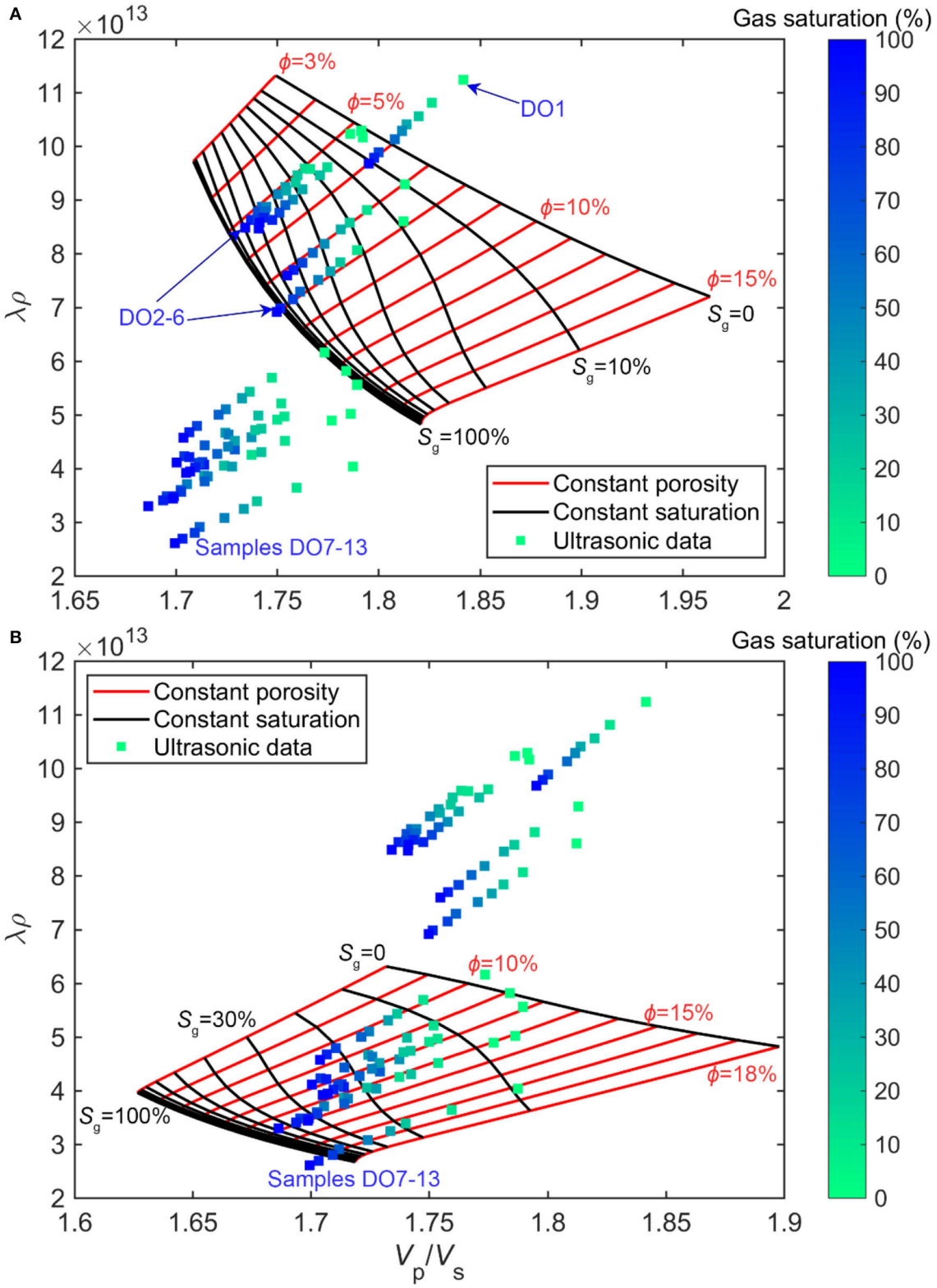

FIGURE 9 | Comparisons between the ultrasonic template and measured data for dolomites. **(A)** Template for samples DO1–6 with low porosities (4.99–6.93%). **(B)** Template for samples DO7–13 with relatively high porosities (10.37–16.87%).

vary at relatively high porosities compared with the low porosity case.

DATA AVAILABILITY STATEMENT

The original contributions presented in the study are included in the article/**Supplementary Material**. Further inquiries can be directed to the corresponding author.

AUTHOR CONTRIBUTIONS

JB conceived and designed the experiments. RM analyzed the experimental data. RM and JB wrote the manuscript. JB, JC, ML, and CW provided critical revisions of the manuscript. All authors contributed to the article and approved the submitted version.

FUNDING

This work was supported by the Jiangsu Province Science Fund for Distinguished Young Scholars (BK20200021), the National Science and Technology Major Project of China (2017ZX05069-002), the research funds from SINOPEC Key Laboratory of Geophysics, the Jiangsu Innovation and Entrepreneurship Plan, the National Natural Science Foundation of China (41974123, 41704109), and the Fundamental Research Funds for the Central Universities, and the China Scholarship Council (201906710129).

SUPPLEMENTARY MATERIAL

The Supplementary Material for this article can be found online at: https://www.frontiersin.org/articles/10.3389/feart.2021.652344/full#supplementary-material

REFERENCES

Ba, J., Cao, H., Carcione, J. M., Tang, G., Yan, X.-F., Sun, W., et al. (2013). Multiscale rock-physics templates for gas detection in carbonate reservoirs. *J. Appl. Geophys.* 93, 77–82. doi: 10.1016/j.jappgeo.2013.03.011

Ba, J., Ma, R., Carcione, J. M., and Picotti, S. (2019). Ultrasonic wave attenuation dependence on saturation in tight oil siltstones. *J. Petrol Sci. Eng.* 179, 1114–1122. doi: 10.1016/j.petrol.2019.04.099

Ba, J., Xu, W., Fu, L.-Y., Carcione, J. M., and Zhang, L. (2017). Rock anelasticity due to patchy saturation and fabric heterogeneity: a double double-porosity model of wave propagation. *J. Geophys. Res. Solid Earth* 122, 1949–1976. doi: 10.1002/2016JB013882

Batzle, M., and Wang, Z. (1992). Seismic properties of pore fluids. *Geophysics* 57, 1396–1408. doi: 10.1190/1.1443207

Biot, M. A. (1956). Theory of propagation of elastic waves in a fluid-saturated porous solid. II. Higher frequency range. *J. Acoust. Soc. Am.* 28, 179–191. doi: 10.1121/1.1908241

Carcione, J. M., and Cavallini, F. (2002). Poisson's ratio at high pore pressure. *Geophys. Prospect.* 50, 97–106. doi: 10.1046/j.1365-2478.2002.00299.x

Chi, X., and Han, D. (2009). Lithology and fluid differentiation using a rock physics template. *Lead. Edge* 28, 60–65. doi: 10.1190/1.3064147

Chichinina, T., Obolentseva, I., Gik, L., Bobrov, B., and Ronquillo-Jarillo, G. (2009). Attenuation anisotropy in the linear-slip model: interpretation of physical modeling data. *Geophysics* 74, WB165–WB176. doi: 10.1190/1.3173806

Datta Gupta, S., Chatterjee, R., and Farooqui, M. Y. (2012). Rock physics template (RPT) analysis of well logs and seismic data for lithology and fluid classification in Cambay Basin. *Int. J. Earth Sci.* 101, 1407–1426. doi: 10.1007/s00531-011-0736-1

Dillon, L., Schwedersky, G., Vásquez, G., Velloso, R., and Nunes, C. (2003). A multiscale DHI elastic attributes evaluation. *Lead. Edge* 22, 1024–1029. doi: 10.1190/1.1623644

Dvorkin, J. P., and Mavko, G. (2006). Modeling attenuation in reservoir and nonreservoir rock. *Lead. Edge* 25, 194–197. doi: 10.1190/1.2172312

Fatti, J. L., Smith, G. C., Vail, P. J., Strauss, P. J., and Levitt, P. R. (1994). Detection of gas in sandstone reservoirs using AVO analysis: a 3-D seismic case history using the Geostack technique. *Geophysics* 59, 1362–1376. doi: 10.1190/1.1443695

Goodway, B. (2001). AVO and lamé constants for rock parameterization and fluid detection. *CSEG Rec.* 6, 39–60.

Guo, J., and Gurevich, B. (2020). Frequency-dependent P wave anisotropy due to wave-induced fluid flow and elastic scattering in a fluid-saturated porous medium with aligned fractures. *J. Geophys. Res. Solid Earth* 125:e2020JB020320. doi: 10.1029/2020JB020320

Guo, Y., Ma, H., Ba, J., Yu, H., and Long, C. (2015). Impact of data distribution on fluid sensitivity analysis: a quantitative investigation. *J. Appl. Geophys.* 119, 1–15. doi: 10.1016/j.jappgeo.2015.05.003

Gurevich, B., Makarynska, D., de Paula, O. B., and Pervukhina, M. (2010). A simple model for squirt-flow dispersion and attenuation in fluid-saturated granular rocks. *Geophysics* 75, N109–N120. doi: 10.1190/1.3509782

Han, X., Wu, E., Guo, J., Xu, D., Sun, Z., Luo, X., et al. (2017). Fluid factor index for fluid saturation estimation. *J. Nat. Gas Sci. Eng.* 39, 72–81. doi: 10.1016/j.jngse.2017.01.026

Hill, R. (1952). The elastic behaviour of a crystalline aggregate. *Proc. Phys. Soc. A* 65, 349–354. doi: 10.1088/0370-1298/65/5/307

Klimentos, T. (1995). Attenuation of P- and S-waves as a method of distinguishing gas and condensate from oil and water. *Geophysics* 60, 447–458. doi: 10.1190/1.1443782

Liu, Q., Yin, X., and Li, C. (2015). Fluid discrimination based on rock physics templates. *J. Geophys. Eng.* 12, 830–838. doi: 10.1088/1742-2132/12/5/830

Ma, R., and Ba, J. (2020). Coda and intrinsic attenuations from ultrasonic measurements in tight siltstones. *J. Geophys. Res. Solid Earth* 125:e2019JB018825. doi: 10.1029/2019JB018825

Mavko, G., Mukerji, T., and Dvorkin, J. (2009). *The Rock Physics Handbook: Tools for Seismic Analysis of Porous Media, 2nd Edn*. Cambridge; New York, NY: Cambridge University Press.

Mavko, G. M., and Nur, A. (1979). Wave attenuation in partially saturated rocks. *Geophysics* 44, 161–178. doi: 10.1190/1.1440958

Müller, T. M., Gurevich, B., and Lebedev, M. (2010). Seismic wave attenuation and dispersion resulting from wave-induced flow in porous rocks — a review. *Geophysics* 75, 75A147–75A164. doi: 10.1190/1.3463417

Murphy, W. F. (1982). Effects of partial water saturation on attenuation in Massilon sandstone and Vycor porous glass. *J. Acoust. Soc. Am.* 71, 1458–1468. doi: 10.1121/1.387843

Ostrander, W. J. (1984). Plane-wave reflection coefficients for gas sands at nonnormal angles of incidence. *Geophysics* 49, 1637–1648. doi: 10.1190/1.1441571

Pang, M., Ba, J., Carcione, J. M., Picotti, S., Zhou, J., and Jiang, R. (2019). Estimation of porosity and fluid saturation in carbonates from rock-physics templates based on seismic *Q*. *Geophys.* 84, M25–M36. doi: 10.1190/geo2019-0031.1

Pang, M., Ba, J., Fu, L.-Y., Carcione, J. M., Markus, U. I., and Zhang, L. (2020). Estimation of microfracture porosity in deep carbonate reservoirs based on 3D rock-physics templates. *Interpretation* 8, SP43–SP52. doi: 10.1190/INT-2019-0258.1

Pei, F.-G., Zou, C.-C., He, T., Shi, G., Qiu, G.-G., and Ren, K.-Y. (2010). Fluid sensitivity study of elastic parameters in low-medium porosity and permeability reservoir rocks. *Appl. Geophys.* 7, 1–9. doi: 10.1007/s11770-010-0005-2

Picotti, S., Carcione, J. M., and Ba, J. (2018). Rock-physics templates based on seismic Q. *Geophysics* 84, MR13–MR23. doi: 10.1190/geo2018-0017.1

Pride, S. R., Berryman, J. G., and Harris, J. M. (2004). Seismic attenuation due to wave-induced flow. *J. Geophys. Res. Solid Earth* 109:B01201. doi: 10.1029/2003JB002639

Qi, Q., Müller, T. M., and Pervukhina, M. (2017). Sonic QP/QS ratio as diagnostic tool for shale gas saturation. *Geophysics* 82, MR97–MR103. doi: 10.1190/geo2016-0499.1

Qiao, Y., and An, H. (2007). Study of petrophysical parameter sensitivity from well log data. *Appl. Geophys.* 4, 282–287. doi: 10.1007/s11770-007-0038-3

Quan, Y., and Harris, J. M. (1997). Seismic attenuation tomography using the frequency shift method. *Geophysics* 62, 895–905. doi: 10.1190/1.1444197

Smith, G. C., and Sutherland, R. A. (1996). The fluid factor as an AVO indicator. *Geophysics* 61, 1425–1428. doi: 10.1190/1.1444067

Toksöz, M. N., Johnston, D. H., and Timur, A. (1979). Attenuation of seismic waves in dry and saturated rocks: I. Laboratory measurements. *Geophysics* 44, 681–690. doi: 10.1190/1.1440969

White, J. E. (1975). Computed seismic speeds and attenuation in rocks with partial gas saturation. *Geophysics* 40, 224–232. doi: 10.1190/1.1440520

Winkler, K. W., and Nur, A. (1982). Seismic attenuation: effects of pore fluids and frictional-sliding. *Geophysics* 47, 1–15. doi: 10.1190/1.1441276

Xue, Y., Cao, J., Wang, D., Tian, R., and Shu, Y. (2013). Detection of gas and water using HHT by analyzing P- and S-wave attenuation in tight sandstone gas reservoirs. *J. Appl. Geophys.* 98, 134–143. doi: 10.1016/j.jappgeo.2013.08.023

Zeng, Q., Guo, Y., Jiang, R., Ba, J., Ma, H., and Liu, J. (2017). Fluid sensitivity of rock physics parameters in reservoirs: quantitative analysis. *J. Seism. Explor.* 26, 125–140.

Zhou, Z., and Hilterman, F. J. (2010). A comparison between methods that discriminate fluid content in unconsolidated sandstone reservoirs. *Geophysics* 75, B47–B58. doi: 10.1190/1.3253153

Conflict of Interest: CW was employed by the company Petrochina.

The remaining authors declare that the research was conducted in the absence of any commercial or financial relationships that could be construed as a potential conflict of interest.

Copyright © 2021 Ma, Ba, Carcione, Lebedev and Wang. This is an open-access article distributed under the terms of the Creative Commons Attribution License (CC BY). The use, distribution or reproduction in other forums is permitted, provided the original author(s) and the copyright owner(s) are credited and that the original publication in this journal is cited, in accordance with accepted academic practice. No use, distribution or reproduction is permitted which does not comply with these terms.

frontiers in Earth Science

ORIGINAL RESEARCH
published: 13 May 2021
doi: 10.3389/feart.2021.643372

Effect of Stress Interactions on Effective Elasticity and Fracture Parameters in the Damage Zones

Chenghao Cao[1], *Li-Yun Fu*[2]*, *Bo-Ye Fu*[3] *and Qiang Guo*[4]

[1] College of Transportation Science & Engineering, Nanjing Tech University, Nanjing, China, [2] Key Laboratory of Deep Oil and Gas, China University of Petroleum (East China), Shandong, China, [3] Institute of Geology and Geophysics, Chinese Academy of Sciences (CAS), Beijing, China, [4] College of Information Engineering, China Jiliang University, Hangzhou, China

Elastic interactions between fractures will greatly affect the effective elasticity, which, in turn, will reshape the effective fracture parameters. The disturbance will be more complex in the fault zone due to the complicated fracture distributions. This problem is addressed by the comparison of two types of solutions: one containing the stress interaction while the other one excluding the stress interaction. The gap between the two solutions allows the quantitative estimation of stress interactions on elasticity. Furthermore, based on the orthorhombic assumption for fracture clustering in the damage zone, the effect of stress interaction on the equivalent fracture parameter is estimated. We first characterize the fracture parameters in the fault damage zone considering more realistic distributions of fractures. Then, a series of numerical simulations are conducted to study the effective parameters of the fractured model. Finally, assuming the orthorhombic system of the fracture clustering, we invert the crack density and validate the accuracy of the inversion through the incidence angle seismic velocities. Our numerical results suggest that the size of fractures will determine the dominant type of stress interactions, and thus significantly reshape the effective properties of the models regardless of the spatial distribution of the fracture. Furthermore, the stress interactions tend to underestimate the fracture density for models containing long fractures but generate a relatively satisfactory inverted fracture density for short fractures.

Keywords: stress interaction, fracture clustering, damage zone, inversion, modeling

OPEN ACCESS

Edited by:
Pascal Audet,
University of Ottawa, Canada

Reviewed by:
Ke Gao,
Southern University of Science and Technology, China
Junxin Guo,
Southern University of Science and Technology, China

***Correspondence:**
Li-Yun Fu
lfu@upc.edu.cn

Specialty section:
This article was submitted to Solid Earth Geophysics, a section of the journal Frontiers in Earth Science

Received: *18 December 2020*
Accepted: *21 April 2021*
Published: *13 May 2021*

Citation:
Cao C, Fu L-Y, Fu B-Y and Guo Q (2021) Effect of Stress Interactions on Effective Elasticity and Fracture Parameters in the Damage Zones. Front. Earth Sci. 9:643372. doi: 10.3389/feart.2021.643372

INTRODUCTION

In general, local stress distribution generated by a single crack hardly influences their neighbors for a sparse concentration for cracks, which, however, would be significant as the crack density exceeds the dilute limit (Zhao et al., 2015; Cao et al., 2020a). That is, for a small fracture density, the resultant effective compliance tensor depends linearly on the crack density but non-linearly for a high concentration for cracks, implying a non-negligible effect of stress interactions.

Actually, there are two types of stress interactions, namely shielding and amplification, with opposite signs (Cao et al., 2019). Stress shielding considerably stiffens rocks while stress amplification appreciably reduces the effective elasticity (Zhao et al., 2015). Furthermore, the shielding and amplification effect dominate for stacked cracks and co-planar cracks, respectively (Grechka and Kachanov, 2006b). The effect of stress interactions has been described by both numerical simulations and analytical expressions of the effective elasticity for the fractured media in a series of publications (Kachanov, 1993; Hopkins, 2000; Lapin et al., 2018; Cao et al., 2020a).

Many effective analytical medium theories have been developed for the fractured media, including the self-consistent theory (SC), differential effective medium (DEM) theory, and T-matrix solution (Jakobsen, 2012), and a comprehensive review of these theories can be found in Mavko et al. (2009). These methods could be used to characterize the mechanical properties of an effective sample considering the stress interactions. Besides the analytical solutions, a series of numerical solutions have also been developed for characterizing the fractured media (Masson and Pride, 2007). Using the finite-element (FE) solution, Wenzlau et al. (2010) obtain five independent elastic moduli in a heterogeneous layered medium. Similarly, Quintal et al. (2011) propose a computationally efficient method to solve Biot's quasi-static equations of consolidation. Furthermore, based on the solution, Quintal et al. (2012) also obtain S-wave attenuation for a medium containing periodically distributed circular inclusions. Due to the tectonic movement, the underground medium often behaves like a triclinic medium with the highest degree of anisotropy, which, however, is hard to describe using the aforementioned numerical methods. Therefore, a novelty numerical method, developed by Rubino et al. (2016), is used to solve the problem by generating complex-valued, frequency-dependent equivalent stiffness tensors, the advantage of which lies in the quantification of six elastic tensors for the two-dimensional (2D) case. However, neither the analytical nor the numerical solutions could explicitly identify the dominant type of stress interactions. Cao et al. (2020a) proposed a workflow to address the problem through the gaps between the analytical results without stress interactions and the numerical one with stress interactions, making the quantification of stress interaction possible.

The non-interaction approximation (NIA) or the linear slip (LS) theory treats the compliance tensors of the fractured rock as a sum of the compliance tensors of the host matrix plus individual fractures, which works well for a low concentration for cracks, and thus provides a benchmark for a quantitative estimation of stress interactions. However, when applied to fractured solids, NIA has a larger-than-expected range of applicability in the cases of dilute limit as well as the high fracture densities (Grechka and Kachanov, 2006b). The reason lies in that, the opposite effects of shielding and amplification largely cancel one another in the medium with the fractures distributed randomly (Lapin et al., 2018), thus making the result similar to that of the NIA solution.

Strictly speaking, only the equivalence between the normal fracture compliance and the shear fracture compliance could ensure the orthorhombic symmetry of the fractured medium (Schoenberg and Sayers, 1995). However, Kachanov (1993) believes that, in the NIA approximation, effective elasticity for the cracked model could also be orthorhombic. Based on this, Grechka (2007) extends the case to the transversely isotropic with a host with a vertical symmetry axis (VTI), which also satisfies the aforementioned orthorhombic assumption. Therefore, it is possible to retrieve some key parameters related to the fractured information based on seismic recordings such as fracture density (Barbosa et al., 2018).

In the damage zone, fractures often exhibit spatial variation in the petro-physical properties, such as characteristics of the fracture length distribution (Lei and Gao, 2018) and the spatial distribution for the fractures inside (Harris et al., 2003). In recent years, there have been some attempts at describing the fracture length distribution based on the power law. Hunziker et al. (2018) adopted the power law to describe the fracture length distribution for the systematic exploration of the attenuation sensitivity to the properties characterizing the fracture network. Lei and Gao (2018) also characterize the stress variability in geological media based on the assumed synthetic fracture networks following power law length scaling. On the other hand, the fracture also exhibits in some forms of spatial distribution (Odling et al., 2005). The aspect ratio (Ξ), proposed by Jakobsen et al. (2003), is used to characterize the fracture spatial distribution, which, however, is more complex in nature.

For example, the fracture clustering in the damage zone, often distributed in a complex pattern and, hence, characterizing realistic spatial distributions of fractures quantitatively, is necessary for an accurate interpretation of seismic measurements. Savage and Brodsky (2011) investigate the development of fracture spatial distributions as a function of displacement to determine whether damage around small and large faults is governed by the same process. Harris et al. (2003) also capture the characteristics of the damage zone using distance from the fault surface. Although the fracture clustering in the damage zone is a rather common scenario in nature, description of the effects of stress interaction on the elasticity and effective fracture parameters of the damage zone remains largely unexplored, partly due to the limitations of the analytical models as well as the high computational cost because of the complex fracture distribution.

In this study, the authors address this problem by the following procedures. First, we develop a numerical model for the fracture clustering in the 2D fault damage zone. This model includes the statistical parameters of the fault damage zones observed in outcrop, followed by the investigation of effective elasticity as well as anisotropic parameters of the models. Finally, assuming the damage zone possesses the orthorhombic symmetry in the NIA, the fracture parameters for two sets of orthogonal fractures are inverted, based on which we could obtain the incidence angle dependency of the seismic wave.

GENERATION OF FRACTURE CLUSTERING IN THE FAULT DAMAGE ZONE

For modeling the fracture clustering in the fault damage zones, the characteristics of the fracture system must be quantified in advance, including fracture length distribution, spatial distribution, and orientation distributions. Therefore, in the following section, detailed information about these characteristics, and how they are systematically incorporated into numerical models, is introduced.

Rules for the Fracture Length

The power law for fracture length distribution (Bonnet et al., 2001) is often used to characterize the natural fracture system. The stochastic distribution m for the fracture length l (Hunziker

et al., 2018) is expressed as:

$$m\left(I,l\right)=d_cL^2\left(a-0.1\right)\frac{I^{-a}}{I_{\min}^{-a+1}}\;I\in\left[I_{\min},I_{\max}\right],\qquad(1)$$

where L is the scale of the modeling domain while $I_{\min}$ and $I_{\max}$ are the minimum and maximum fracture lengths, respectively. Furthermore, the maximum fracture length ($I_{\max}$) is only one-third of the square length ($L/3 = 0.33$ m), because having fractures greater than half the sample size would mechanically weaken the sample. In this study, the size L of the sample was fixed at 1.0 m. Throughout the study, the aperture of the fracture is set to be 3 mm. The exponent a is the power law length exponent, which affects the relative probability of long and short fractures. A smaller a prefers the long fractures at the expense of the short fractures. Here, we would like to set two values for the length exponent, $a = 1.5$ and 3, which covers two scenarios, one dominated by long fractures and the other by short fractures, respectively.

The parameter *dc* is the fracture density term, defined as the number of fracture centers per unit area. However, throughout the study, the fracture density, *e*, (Equation 1) is used as defined by Guo et al. (2018), which is quite different from that defined by de Dreuzy et al. (2001). As for *dc*, we set it as a function of the fracture number as follows:

$$d_c=0.03n/L^2,\qquad(2)$$

where n is the fracture number inside the 2D sample, with four different values (50, 100, 150, and 200) in our study. The constant 0.03 is an optimized parameter. For keeping the units unchanged, the factor L^2 is imposed into equation 1 as the denominator.

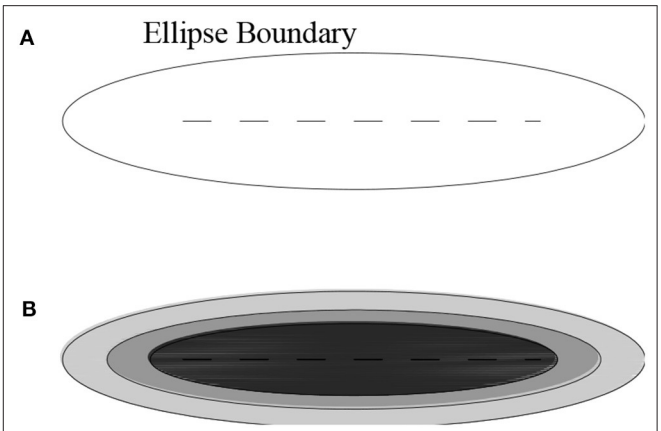

FIGURE 1 | (A) The ellipsoid area, defined by the aspect ratio (Ξ), encompasses all fractures surrounding the major faults. **(B)** Concentric ellipsoidal shells around the major fault in **(A)**. Each shell contains equal fractures, and thus, the resultant fracture density decreases gradually toward the outside. The darker area means a greater fracture density.

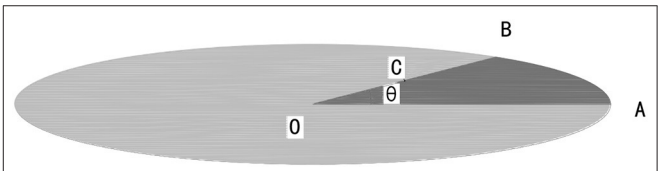

FIGURE 2 | Location of the fracture center, C. The azimuthal angle θ as well as the radius OB could be defined according to the random black area swept out by a radius of this ellipse. Point C is chosen along OB using a normalized function (Equations 3, 4).

Rules for Fracture Spatial Distribution

In addition to the aforementioned length distribution, particular focus is also given to characteristics of fracture spatial distribution, one of the most challenging tasks that remain to be unexplored.

For fracture clustering, the fracture density often decays away from the main fault. Moreover, for any fracture, except the fracture with the smallest length, there is a chance that a smaller fracture will be clustered about it. That is, each fracture is placed depending on the location of the long fracture.

To construct such a kind of fractured model, an ellipsoidal volume with the aspect ratio Ξ is generated. This ellipsoid is supposed to include all centers of the clustering fractures (**Figure 1A**). Then, the volume is divided into a series of concentric ellipsoidal shells (**Figure 1B**), which cuts the vertical principal axis into equal parts. The fractures are sorted by size scale and further divided equally into concentric shells. The centers of the largest fracture are located inside the smallest ellipsoidal shell. The successive clusters of fractures with decreasing scales are then located in successive shells, which are of increasing volume (Harris et al., 2003).

Based on the extended ellipse around the major fault, a random proportion of the area (black area in **Figure 2**) swept by a radius of this ellipsoidal volume is used to define an azimuthal angle θ and the radius OB (**Figure 2**). Compared with the adoption of the random angle, the use of the swept area (black zone in **Figure 1**) would produce a bias toward the major axis of the ellipse, which is more representative of the natural fault zone.

For the location of the fracture center C, the authors would like to introduce the normalized function, *t(r)*, as the function of normalized distance, *r*, along with the radius OB, with $r = 1$ being the shell boundary and $r = 0$ being the shell center. The normalized function has the form given in equation 3:

$$t\left(r\right)=\begin{cases}1 & 0\le r\le p\\ \frac{1}{2}\left[1+\cos\left(\pi\frac{r-p}{1-p}\right)\right] & p\le r\le 1\end{cases},\qquad(3)$$

$$l_{OC}=l_{OB}\times t\left(r\right).\qquad(4)$$

where the value $p = 0.15$, which is used throughout this study, resembles a pyramid-like displacement profile, making the fractures distributed more evenly over the major fault.

For a better description of the generation of the numerical model, a workflow chart to describe the generation procedure is presented in **Figure 3**.

Rules for Fracture Orientation

According to Harris et al. (2003), fractures inside both the Moab and Ninety Fathom fault damage zones are generally oriented

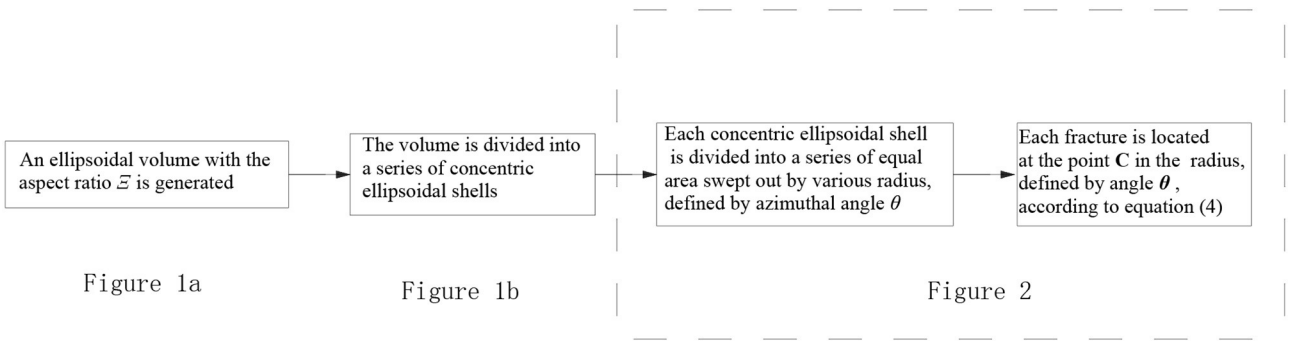

FIGURE 3 | A work flow chart to describe the generation procedure for the fracture set in the damage zone.

TABLE 1 | The boundary conditions for the three models (**Figure 4**).

Figure 4A	Figure 4B	Figure 4C
T: $u_3 = -\Delta u$ B: $u_2 = 0$ $L\&R$: $u_2 = 0$	T: $u_2 = -\Delta u$ R: $u_2 = 0$ $L\&R$: $u_3 = 0$	T: $u_2 = \Delta u$ B: $u_2 = -\Delta u$ $L\&R$: Free boundary

Where L, R, B, and T are the left, right, bottom, and top boundaries of the domain, respectively.

sub-parallel to the major fault. Therefore, in the following models presented here, the strike of the fractures is set according to the Gaussian distribution law, each with a standard deviation of 10°.

A smaller Ξ results in a locally dense fracture clustering, thus leading to more fracture intersections, which, however, would bias the realistic fracture densities. Therefore, in this study, none of the fractures inside the models have intersections with each other.

NUMERICAL METHODOLOGY

Methodology of the Numerical Simulation

Due to tectonic movement, the rock mass often shows a certain degree of deformation, resulting in the triclinic crystal models with the highest degree of anisotropy, which could characterize a homogeneous distribution of cracks.

In order to study the elastic properties of this complex medium, three numerical simulations with various boundary conditions are conducted here (Rubino et al., 2016) to obtain the elasticity matrix of the model. Detailed information about the process is given in **Table 1** and as follows: (1) a fixed displacement is imposed on the upper boundary while keeping the vertical displacement to the other boundaries zero (**Figure 4A**); (2) the displacement is applied on the lateral side while keeping the displacement vertical to the other boundaries zero (**Figure 4B**); (3) a simple shear test is conducted (**Figure 4C**). The displacements Δu are all static rather than oscillatory.

In this work, for each test (**Figure 4**) with specified boundary conditions, the stress–strain relation (Equation D-2) is solved based on the finite-element method (FEM). Detailed information on the process can be found in **Appendix D**.

A cost function based on the three sets of stress–strain relations could be used to determine the equivalent stiffness tensors (six unknowns) by using the least square method. Details describing the process can be found in the publication reported by Rubino et al. (2016).

Two-Dimensional NIA Solution

According to the NIA theory, the effective elastic compliance tensor **S** of a cracked medium is determined by two additive components: the compliance tensor of the background medium ($\mathbf{S}_b$) and that of the cracks ($\mathbf{\Delta S}$).

$$\mathbf{S}_{NIA} = \mathbf{S}_b + \Delta\mathbf{S}, \tag{5}$$

where the crack compliance tensor $\mathbf{\Delta S}$ represents the accumulative contributions of the fractures to the effective compliance tensors, which is a function of the Eshelby (1957) tensors:

$$\Delta\mathbf{S} = \phi\left[(\mathbf{S}_i - \mathbf{S}_b)^{-1} + \mathbf{c_b} : \left(\mathbf{J} - \mathbf{S}_{E\text{shelby}}\right)\right]^{-1}, \tag{6}$$

where φ represents the crack porosity, $\mathbf{J}$ is the fourth-order symmetric identity tensor, $\mathbf{S}_i$ are the compliance tensors of the individual fractures, and $\mathbf{S}_b$corresponds to the tensors of host matrix surrounding the fractures, respectively; the components $\mathbf{S}_{Eshelby}$ represents the Eshelby tensor (Eshelby, 1957; Guo et al., 2019).

For the 2D case, the ellipsoidal fracture inside the volume could be treated as an infinite cylinder ($a_3 \rightarrow \infty$); therefore, we have the Eshelby tensors in **Appendix B** (Masson and Pride, 2014). Therefore, the input parameters include the tensors of the host matrix $\mathbf{S}_b$, semiaxis of the fractures, fracture orientations, Poisson ratio, and so on.

In order to get the compliant tensors, a series of parameters are input in advance, including the host matrix $\mathbf{S}_b$; all fracture apertures are assumed to be 3 mm; and the fracture length and the fracture number for two orthogonal fractures are selected by using ant colony algorithms.

The NIA, considering no stress interactions, works well-under the dilute assumption of crack densities. Moreover, according to

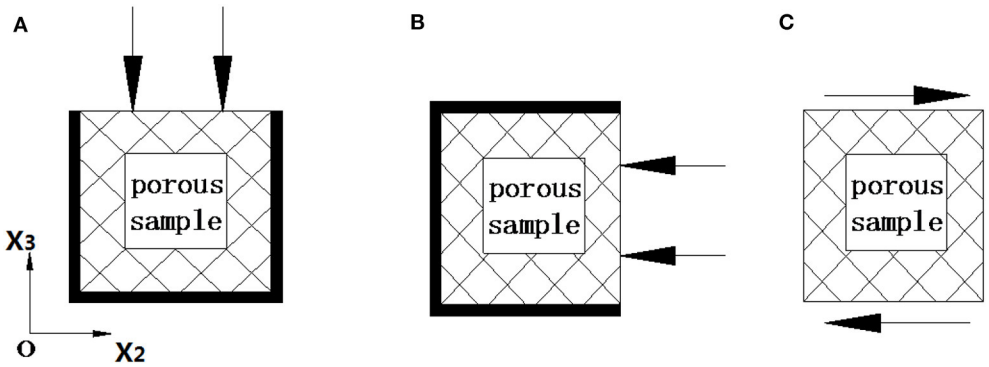

FIGURE 4 | (A–C) Schematic illustration of the three tests adopted to get the corresponding stress–strain relations. The thick bold line represents a zero solid displacement vertical to the edge (Cao et al., 2019). The arrow shows the direction of displacement at the boundary.

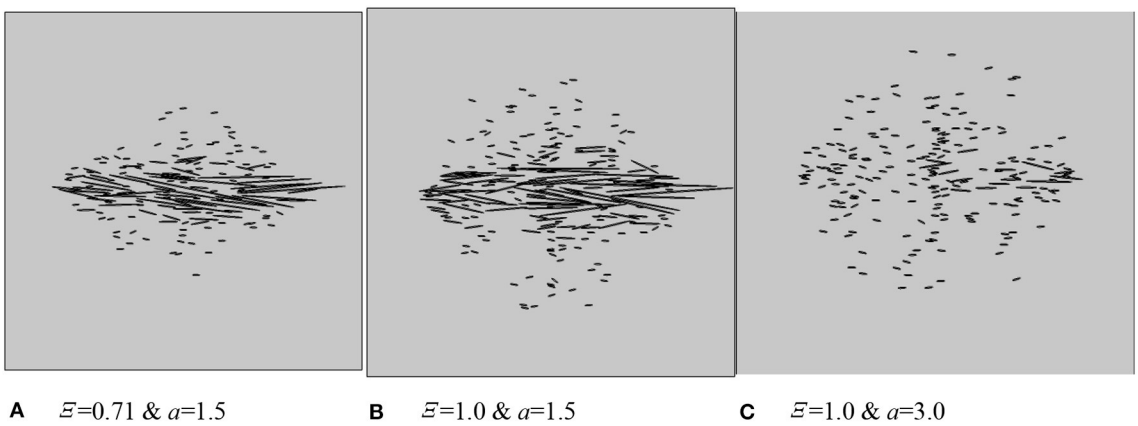

FIGURE 5 | Three different fractured models with various length distributions **(A)** and spatial distributions (Ξ). The relating characteristic exponent *a* and the aspect ratio Ξ are given at the bottom of each plot. **(A)** $\Xi = 0.71$ & $a = 1.5$; **(B)** $\Xi = 1.0$ & $a = 1.5$; **(C)** $\Xi = 1.0$ & $a = 3.0$.

equation (6), there is no parameter describing the fracture spatial distribution or fracture size distribution; therefore, it could not provide detailed information about fracture clustering.

Evaluation of the Stress Interactions

According to Hudson's theory (Hudson et al., 1996), the effective stiffness tensors of the medium are composed of three parts:

$$\underbrace{C}_{C^{NUM}} = \underbrace{C_b + \Delta C}_{S_{NIA}^{-1}} + \Delta\Delta C, \tag{7}$$

where the summation of the first and second terms corresponds to the inverse matrix of $\mathbf{S}_{\mathrm{NIA}}$ (equation 6), while the third term $\Delta\Delta\mathbf{C}$ is the result of the stress interaction between different fractures. C equals the C^{NUM} (Equation D-2), which could be obtained through the numerical simulation directly. Therefore, a comparison between the S_{NIA}^{-1} and C^{NUM}, allows for the quantification of the effect of stress interactions.

NUMERICAL RESULTS

In this part, a series of fractured models are introduced, with various spatial and length distributions. The corresponding elasticity and anisotropic parameters, affected by the stress interactions, are then studied using the FEM, respectively. Finally, assuming the orthotropy of the fracture clustering, we get the two sets of inverted fracture parameters[3].

Fracture Parameter Setup

For a better illustration of the considered fracture networks, we vary the fracture density (*e*), fracture size distribution (*a* in equation 1), and aspect ratio (Ξ in **Figure 1A**) of the fracture clustering. For each parameter combination, 20 stochastic fracture networks are generated. Three typical examples are presented in **Figure 5**.

For each of the fracture densities (**Table 2**), a series of numerical models with a given fracture density is presented, with the fracture centers located in different areas for each model (**Figure 5**).

We choose the hypothetical dry sample with isotropic background medium, which has the following parameters: $\lambda = 7.83$ GPa; $\mu = 19.74$ GPa (Guo et al., 2019). Moreover, the filling material is the gas whose Young's modulus is 0.066 GPa and the Poisson ratio $\upsilon = 0$. Additionally, the definition of the fracture density in the 2D sample is introduced as follows:

$$e = \frac{nr^2}{A}, \tag{8}$$

where n defines the total fracture number inside the 2D sample, r is the major radius of the elliptical 2D fracture, and A is the area of the sample (Guo et al., 2018). Detailed information about the fracture densities for different cases is listed in **Table 2**.

Effective Elasticity Affected by Stress Interactions

To gain insight into the dominant stress interactions in the fracture clustering, the elastic NIA modulus (Equations B-1, B-2), which neglects stress interactions, is used to compare with the numerical results considering the stress interaction, the gap between them allows for a quantitative description of the dominant stress interactions.

For C_{33}, opposite signs of the gaps between the NIA and the numerical results can be obtained for both long fractures ($a = 1.5$ in **Figure 6A**) and short fractures ($a = 3.0$ in **Figure 6B**), implying different dominant stress interactions determined by the fracture size. For instance, a smaller C_{33} produced by NIA compared with the numerical one implies a dominant amplification effect, as given in **Figure 6A**, while a greater C_{33} obtained from NIA suggests a weakly dominant shielding effect for case b (**Figure 6B**; Cao et al., 2020b). Similar rules could also be applied to the shear modulus C_{44} in **Figure 7**.

Moreover, modulus discrepancies between different models with various aspect ratios (Ξ) of the bounding ellipsoid are quite different for C_{33}. In **Figure 6A**, the discrepancies for C_{33} with different Ξ are negligible for long fractures but more significant for short fractures ($a = 3.0$ in **Figure 6B**). Conversely, C_{44} with various Ξ is greater for long fractures but almost negligible for short fractures.

This can be explained by the effect of the fracture interactions. For long fractures, it is believed that a smaller aspect ratio (Ξ) leads to a smaller distance between the fracture surfaces, which thus leads to a greater shielding effect, especially for the models containing long fractures. However, for the fracture clustering in this study, most of the long fractures concentrate at the core part, and therefore, Ξ variation contributes little to the distance between the close fracture, and thus, the additional shielding effect due to the increment in Ξ is comparably negligible. For short fracture, due to the cancellation of stress interactions (Kachanov, 1993), the net effect of stress interaction is small, and therefore, the additional stress interaction caused by a small variation in Ξ will lead to a more significant change in C_{33}. On the other side, for the shear test (**Figure 4C**), the shear stress distribution is quite different from the compressive stress in the compressive test (**Figures 4A,B**; Cao et al., 2020a); it is more than a function of the distance between the ajacent fracture surface; further exploration is expected in the future.

TABLE 2 | Fracture densities for eight cases with various values of *a*.

	Case 1–2	Case 3–4	Case 5–6	Case 7–8
a = 1.5	0.1056	0.1806	0.2938	0.3815
a = 3.0	0.0083	0.0144	0.0258	0.0341

Anisotropic Properties

Besides the effective stiffness tensors (C_{44} and C_{33}), the anisotropic properties of the fractured samples (**Figure 5**) could be described by ε and δ. For orthorhombic media, the velocity

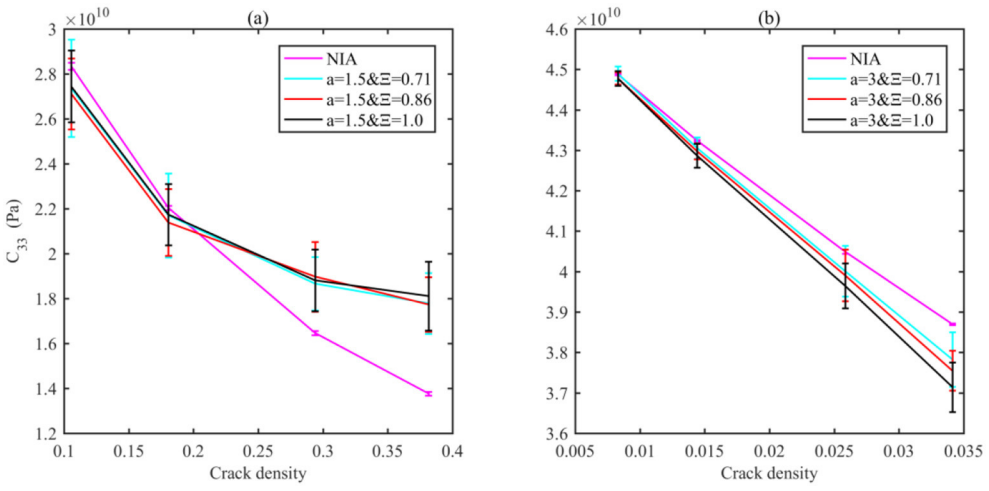

FIGURE 6 | C_{33} as the functions of fracture densities for different models determined by *a* and Ξ, using the NIA solution and the numerical method. The lengths of bars are the standard deviations for 20 different realizations by changing the crack locations with the same crack density.

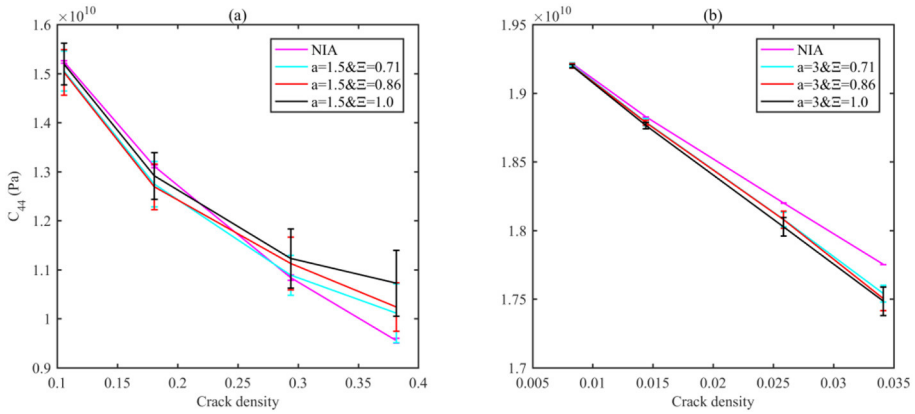

FIGURE 7 | C_{44} as the functions of fracture densities for different models determined by a and Ξ, using the NIA solution and the numerical method. The numerical result bars are in line with those in **Figures 5**, **6**.

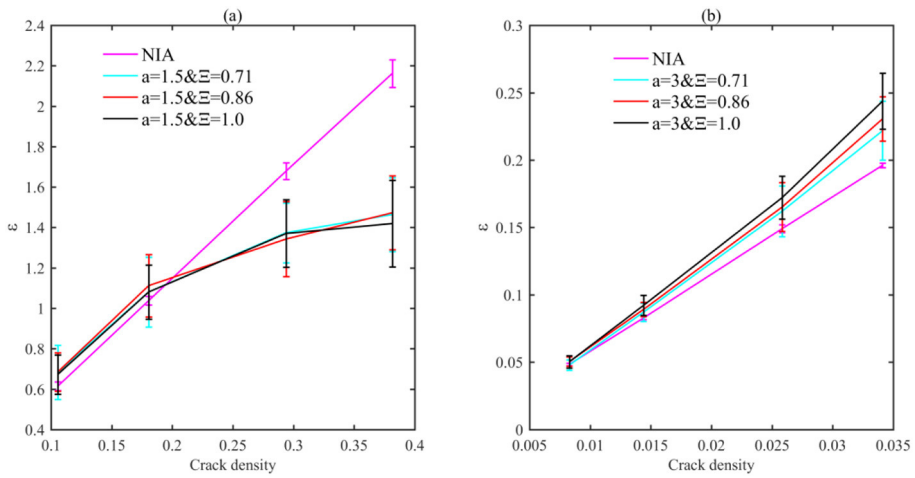

FIGURE 8 | Anisotropic parameters ε, as the function of fracture density, are presented for various rock samples. The bar centers correspond to the averaged values of the numerical ε; the bar sizes define their standard deviations. In the legend, Ξ is the aspect ratio for the ellipse boundary of the fracture clustering, while $a = 1.5$ **(A)** and 3 **(B)** correspond to long and short fractures, respectively. The numerical result bars are in line with those in **Figure 6**.

anisotropic parameters in the 2D can be computed according to equations C-1, C-2.

For the models with long fractures ($a = 1.5$ in **Figure 8A**), the shielding effect corresponds to a larger C_{33}. Meanwhile, since the fractures are almost parallel with the X-axis, variation in C_{22} due to the stress interaction is negligible. Therefore, the stress interaction minimizes the contrast between C_{22} and C_{33}, corresponding to a decreasing ε, according to equation C-1.

However, for ε in the models with short fractures ($a = 3$ in **Figure 8B**), similar discrepancies could be observed, but in a reverse pattern, that is, the numerical result is greater than the NIA result. This is understandable since the dominant amplification effect leads to a smaller C_{33} (**Figure 6B**).

According to the definition of δ by Woodruff et al. (2015), δ means the difference between the short-offset velocity and the vertical velocity. For the model containing long fractures, the vertical velocity, mainly determined by the shielding effect, leads to a hardening effect that compensates for the shrinking elasticity due to the individual fracture, corresponding to a smaller gap between the short-offset velocity and vertical velocity, which, in turn, leads to a smaller δ in **Figure 9A**. Furthermore, a greater Ξ means a less dense fracture clustering, and thus a weaker shielding effect, corresponding to a greater δ in **Figure 9B**.

In contrast to the model with long fractures, δ for the model containing short fractures is greater compared with the NIA solution (**Figure 9B**), due to the dominant amplification effect.

INVERSION FOR FRACTURE PARAMETERS

Actually, a model containing multiple sets of vertical dry fractures in an isotropic background matrix behaves more like orthotropic media, suggesting that the accumulative contribution of variously oriented fractures to the effective elastic properties is equivalent

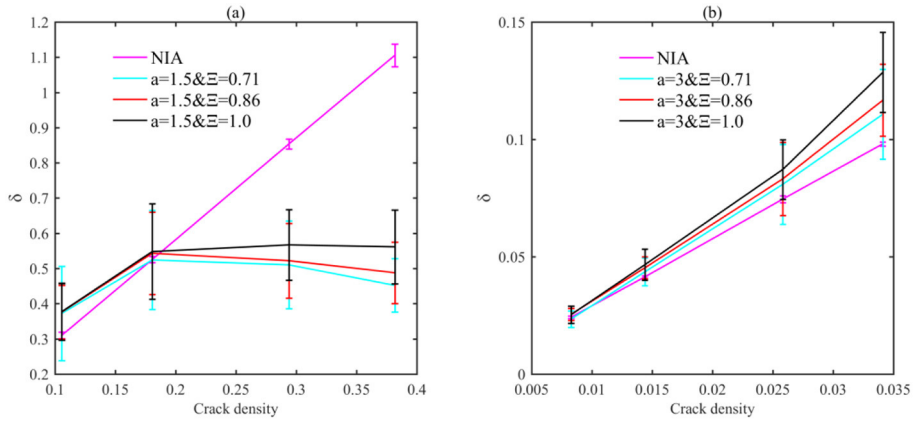

FIGURE 9 | Anisotropic parameters δ, as the function of fracture density, are presented for various rock samples. The centers of the bars correspond to the averaged numerical anisotropic parameter. The numerical result bars are in line with those in **Figure 6**. In the legend, Ξ is the aspect ratio for the ellipse boundary of the fracture clustering, while $a = 1.5$ **(A)** and 3 **(B)** correspond to the long and short fractures, respectively.

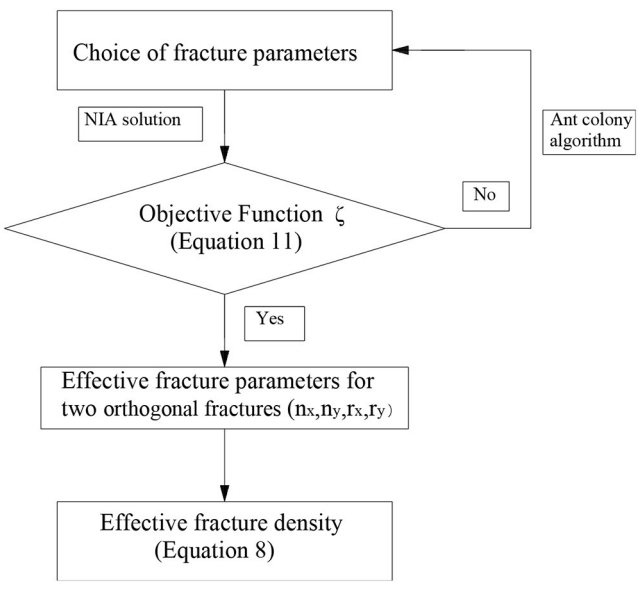

FIGURE 10 | A workflow chart to describe the inversion procedure.

to that of only two principal fracture sets (Lapin et al., 2018). However, previous publications focused on the application of the approximation in the randomly located models where the net stress interaction is negligible (Grechka and Kachanov, 2006a, Grechka and Kachanov, 2006b; Lapin et al., 2018). As for the damage zone with significant stress interaction, the effects of two types of stress interactions on the effective fracture densities for the two orthogonal sets have not been fully explored yet. We first evaluate the incidence angle dependence of the seismic velocity, so as to check the accuracy of the inverted result. Then, the fracture densities, e_x and e_y, associated with these two principle fracture sets are inverted from the effective elasticity.

Inversion Methodology

The problem of characterizing multiple fractures has been studied extensively by Grechka and Tsvankin (2003) and Grechka (2007). Using 2D NIA, the authors of the previous publications observed that the accumulative effect of variously oriented fractures on the effective elasticity approaches that of just two orthogonal sets of fractures. Thus, we prefer to employ the NIA solution (**Appendix B**) to invert the equivalent orthogonal fracture parameters for two orthogonal fractures.

$$\mathbf{S}=\mathrm{S}\left(\tilde{\boldsymbol{m}}\right), \tag{9}$$

where the unknown vector $\tilde{m}$ for fracture characterization contains four parameters:

$$\tilde{\boldsymbol{m}} = \{n_x, n_y, r_x, r_y\}, \tag{10}$$

where n is the fracture number while r is the radius of the fracture; the subscripts x and y refer to the principal axes of a 2D Cartesian coordinate system. In accordance with equation 8, e_x and e_y for the two orthogonal fracture sets can be predicted based on the assumed orthorhombic effective elasticity.

Based on the stiffness tensors c_{ij}^{num} through the numerical solution (**Figures 6**, **7**), we adopt the 2D NIA to compute $S_{ij}^{inversion}$ for a trial vector $\tilde{m}$. Using the ant colony algorithm, we could get the expected fracture parameters, which could minimize the discrepancies (Equation 11) between the trial result and the numerical result. Based on the unknowns in the vector $\tilde{m}$., the fracture density could be deduced according to equation 6. Detailed information about the inversion procedure is displayed in **Figure 10**.

$$\zeta = \min_{(\tilde{\boldsymbol{m}})} \left\{ \sum abs\left(c_{ij}^{num} - c_{ij}^{inversion}\left(\tilde{\boldsymbol{m}}\right)\right) / c_{ij}^{num} \right\} \tag{11}$$

Besides, in NIA, the fracture densities for two sets of orthorhombic fractures could also be obtained directly like

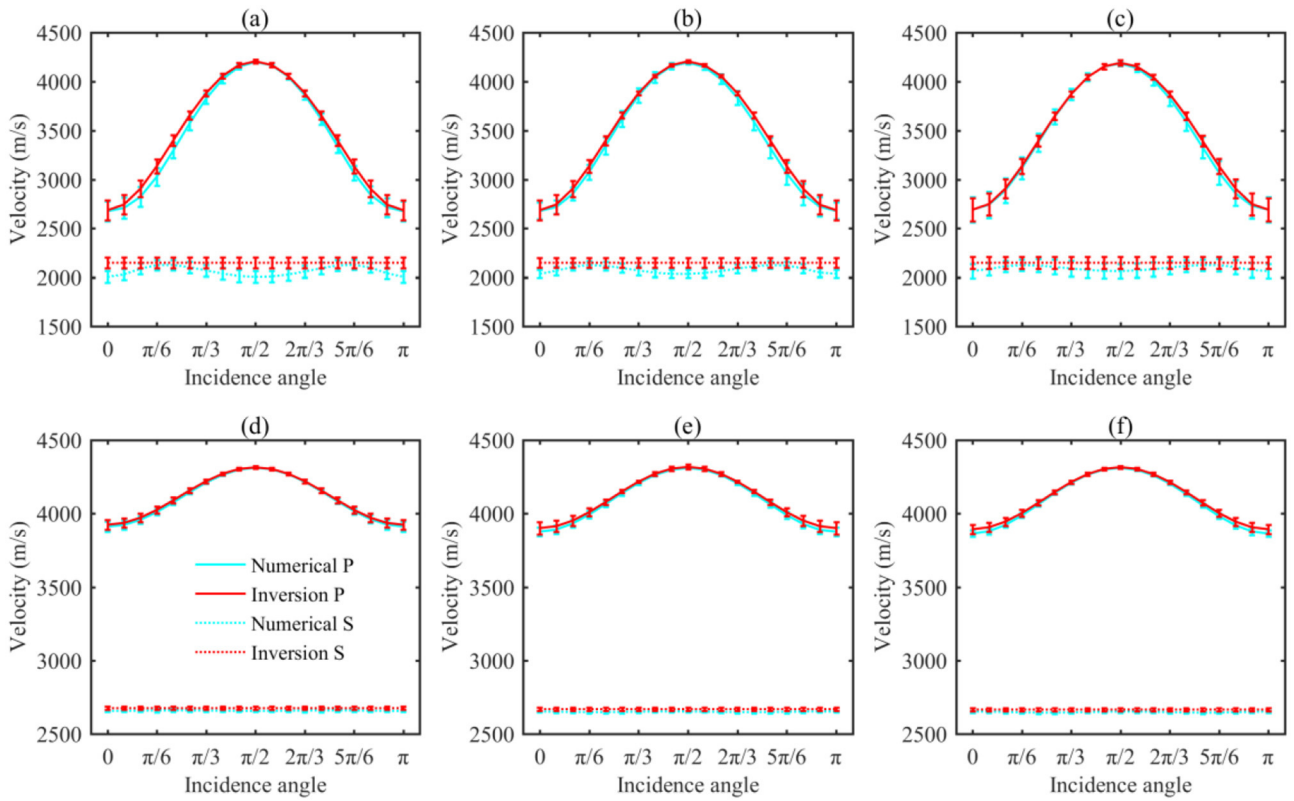

FIGURE 11 | P-wave (solid lines) and SV-wave (dashed lines) velocities as functions of different incidence angles for six kinds of models. **(A)** $a = 1.5$, $\Xi = 0.71$; **(B)** $a = 1.5$, $\Xi = 0.86$; **(C)** $a = 1.5$, $\Xi = 1$; **(D)** $a = 3$, $\Xi = 0.71$; **(E)** $a = 3$, $\Xi = 0.86$; **(F)** $a = 3$, $\Xi = 1$. The blue line denotes the results obtained from the numerical simulations, which is based on the real fracture parameters, while the red line represents the results obtained from NIA, but using the inverted fracture parameters.

the eigenvalues of the second-order fracture–density tensor estimated in equation 9.

$$\alpha = \sum_{(l)}^{L} e^{(l)} \mathbf{n}^{(l)} \mathbf{n}^{(l)}. \tag{12}$$

The difference between the two types of fracture densities lies in that, both densities fit well with each other under the dilute fracture density assumption. However, at high fracture densities, the two densities will be quite different due to the stress interactions, which also allow for a quantitative description of the stress interaction on the inverted fracture densities.

Incidence Angle Dependence of the Inverted Seismic Velocity

So far, the inversion methodology based on the orthorhombic assumption for fracture clustering has been displayed. In the following, by employing the inverted fracture parameters (Equation 8), the comparability of the inverted result through the incidence angle dependence of the seismic wave is to be checked.

The inverted P- and SV-wave velocities, as functions of the inverted parameters for the two equivalent sets of fractures (blue solid/dashed lines in **Figure 11**), fit well with the numerical seismic velocities based on the real fracture parameters (Equation A1–A4), suggesting that the inverted parameters obtained are reasonable and that, as expected, the accuracy of the orthorhombic approximation is acceptable.

However, some minor gaps in the magnitude of the SV-wave anisotropy exist, especially for the case with long fractures (**Figure 11A**). These are expected for the following reasons: for long fractures ($a = 1.5$, **Figures 11A–C**), the medium is the one with the triclinic system, and thus, the nonzero C_{24} and C_{34} (Equation 5), due to the stress interactions, lead to greater SV-wave fluctuations.

Effect of Stress Interactions on the Inverted Fracture Densities

Considering the good agreement between the numerical velocities and the inverted data (**Figure 11**), the authors would like to further explore the effect of stress interactions on the inverted fracture parameters.

For long fractures ($a = 1.5$ in **Figure 12A**), the inverted e_y is gradually biased toward the smaller values, especially at the high fracture densities, where the relative error reaches nearly 50%. A similar bias that was observed by Grechka and Kachanov (2006b) corresponds to the hardening effect of the shielding effect. On the other side, for short fractures ($a = 3$ in **Figure 12B**), the greater slope of the inverted fracture density e_y (solid lines)

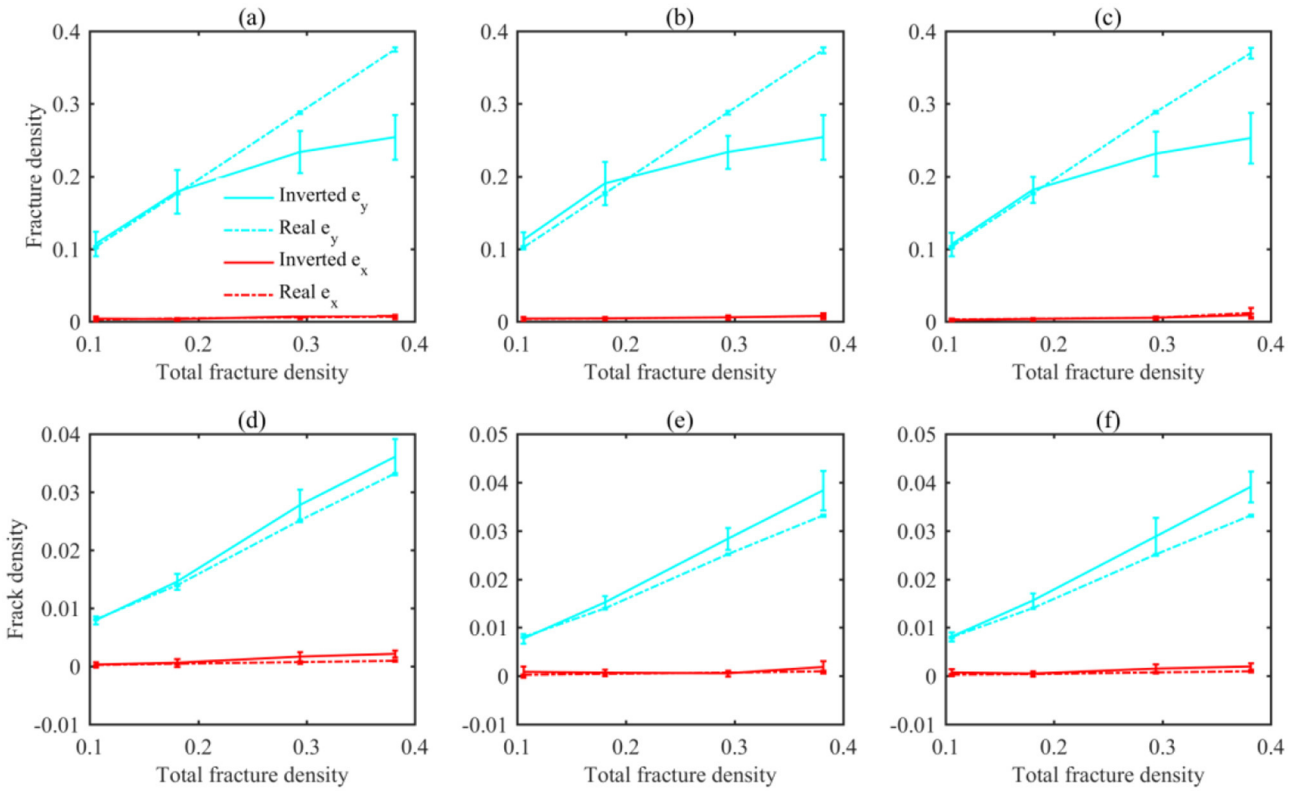

FIGURE 12 | Principal fracture densities e_x and e_y for different models. **(A)** $a = 1.5$, $\Xi = 0.71$; **(B)** $a = 1.5$, $\Xi = 0.86$; **(C)** $a = 1.5$, $\Xi = 1$; **(D)** $a = 3$, $\Xi = 0.71$; **(E)** $a = 3$, $\Xi = 0.86$; **(F)** $a = 3$, $\Xi = 1$. The solid line corresponds to the inverted result. The numerical result bars are in line with those in **Figure 6**. The dashed line corresponds to e_x and e_y predicted as eigenvalues of the density tensor illustrated by **Equation 10**.

suggests a slightly dominant amplification effect of fracture interactions, whose relative error is about 10%, which is much smaller compared with that of the long fracture.

Moreover, for both long (**Figures 12A–C**) and short fractures (**Figures 12D–F**), similar gaps between the blue solid and blue dashed lines for the models with various Ξ suggest that aspect ratio (Ξ) contributes little to inverted fracture densities.

On the other hand, for the wave propagates along with the fracture surface, the effect of stress interaction is negligible; therefore, the inverted fracture density e_x has an overall agreement with the NIA ones generally.

Actually, the inverted fracture densities based on NIA share the same size, which, however, bias the real models with various length scales and spatial distributions. Furthermore, due to the limitation of the NIA solution, the inverted result could not provide information about the spatial distribution of fractures.

DISCUSSIONS

According to many previous publications about the T-matrix method (Jakobsen, 2012, Jakobsen and Chapman, 2009), the aspect ratio (Ξ) characterizing the spatial distribution of fractures (Jakobsen et al., 2003, Zhao et al., 2015) represents the conditional probability of finding another inclusion given the position of a known inclusion. However, the definition of such a parameter limits its application in describing fracture clustering. In the present work, the aspect ratio is used to characterize the boundary of the fracture clustering. Such a definition change for the aspect ratio (Ξ) allows for the description of the properties for the fracture clustering.

According to Lapin et al. (2018), for the NIA, the effective elastic properties of an isotropic matrix with fractures distributed in certain spatial patterns always possess the orthorhombic symmetry, regardless of the orientations of the fractures without the same symmetry. However, due to the effect of stress interactions, the model behaves like a triclinic medium rather than an orthorhombic one. Thus, the nonzero moduli C_{24} and C_{34}, due to the stress interaction, contribute more to the SV-wave anisotropy, leading to more obvious SV-wave velocity fluctuation (such as the SV-wave velocity in **Figure 11A**).

Both the fracture size and the aspect ratio of the fracture cluster contribute to the effective elasticity. However, an agreement between C_{33} for the models with various aspect ratios suggests that the contribution of aspect ratio to the stress interaction is negligible, partly due to the fact that variation in the

aspect ratio influences the distance between the short fractures distributed at the outer part of the damage zone more when compared to the long fractures at the core part.

It should be noted that all the fractures inside the cluster have no intersection with each other, which, however, is counterintuitive to reality. Nonetheless, according to the conclusion of Grechka and Kachanov (2006b), the fracture intersections impose negligible influence on the effective tensors. Therefore, the conclusion presented in this study still holds acceptable accuracy for the fractured clustering in the field.

Garboczi and Berryman (2001) believe that the error of the numerical simulation may come from statistical variation due to the inhomogeneous distribution of fractures. For the inhomogeneous distribution with a given concentration of cracks, there are multiple spatial arrangements for the cracks, which may have somewhat different elastic moduli. The error size due to inhomogeneous distribution could be assessed by computing the elastic parameters for various realizations of the same system. Therefore, all numerical results as well as the inverted parameters are determined based on the 20 different realizations by changing the crack locations with the same crack density, which could guarantee the accuracy of the conclusions in this study.

Throughout the article, the fracture aperture is set to be 3 mm. However, the aperture varies a lot in the field, which would also contribute to the effect of stress interactions. According to current knowledge, the aperture will also affect both types of stress interactions; further development in this aspect is expected in the future.

CONCLUSION

Aiming at the damage zone in the fault, numerical models based on the characteristics of the fracture clustering were built, based on which the authors analyzed the effective elastic tensors of the fracturing clusters and estimated the fracture parameters based on the orthorhombic assumption.

Long parallel fractures tend to generate a strong shielding effect, which, therefore, contribute more to the C_{33} and C_{44}, and a smaller ε. Conversely, the weakly dominant amplification effect induced by the short fractures leads to smaller C_{33} and C_{44}, and a greater ε. Moreover, the effect of the boundary aspect ratio (Ξ) on the stress interaction for fracture clustering is almost negligible for long fractures ($a = 1.5$) but relatively more significant for the short fractures ($a = 3$), where a greater Ξ corresponds to a greater amplification effect.

The inverted fracture density is also strongly influenced by the stress interaction. Amplification tends to weakly overestimate the fracture density while the shielding effect underestimates the fracture density. Furthermore, the incidence angle dependency for the P-wave velocity in fracture clustering is similar to that for the medium containing two orthogonal or principal fracture sets; however, the similarity is somewhat less satisfactory for the SV-wave velocity.

DATA AVAILABILITY STATEMENT

The raw data supporting the conclusions of this article will be made available by the authors, without undue reservation.

AUTHOR CONTRIBUTIONS

L-YF and CC conceived the research. CC wrote the manuscript and prepares the figures. L-YF reviewed and supervised the manuscript. B-YF and QG are involved in the modeling and inversion programme, respectively. All authors finally approve the manuscript and thus agree to be accountable for this work.

FUNDING

The Strategic Priority Research Program of the Chinese Academy of Sciences (Grant No. XDA14010303).

SUPPLEMENTARY MATERIAL

The Supplementary Material for this article can be found online at: https://www.frontiersin.org/articles/10.3389/feart.2021.643372/full#supplementary-material

REFERENCES

Barbosa, N. D., Rubino, J. G., Caspari, E., and Holliger, K. (2018). Impact of fracture clustering on the seismic signatures of porous rocks containing aligned fracturesFracture clustering effects on WIFF. *Geophysics* 83:A65–A68. doi: 10.1190/geo2017-0799.1

Bonnet, E., Bour, O., Odling, N. E., Davy, P., Main, I., Cowie, P., et al. (2001). Scaling of fracture systems in geological data. *Rev. Geophys.* 39, 347–383. doi: 10.1029/1999RG000074

Cao, C., Chen, F., Fu, L.-Y., Ba, J., and Han, T. (2020a). Effect of stress interactions on anisotropic P-SV-wave dispersion and attenuation for closely spaced cracks in saturated porous media. *Geophys. Prospect.* 68, 2536–2556. doi: 10.1111/1365-2478.13007

Cao, C., Fu, L.-Y., Ba, J., and Zhang, Y. (2019). Frequency- and incident-angle-dependent P-wave properties influenced by dynamic stress interactions in fractured porous media. *Geophysics.* 84, 1–12. doi: 10.1111/1365-2478.12446

Cao, C., Fu, L.-Y., and Fu, B.-Y. (2020b). An elastic numerical method based on the 3D complex medium. *Chin. J. Geophys.* 63, 2836–2845. doi: 10.6038/cjg2020N0035

de Dreuzy, J.-R., Davy, P., and Bour, O. (2001). Hydraulic properties of two-dimensional random fracture networks following a power law length distribution: 1. Effective connectivity. *Water Res. Res.* 37, 2065–2078. doi: 10.1029/2001WR900011

Eshelby, J. D. (1957). The Determination of the elastic field of an ellipsoidal inclusion, and related problems. *Proc. R. Soc. Lond.* 241, 376–396. doi: 10.1098/rspa.1957.0133

Garboczi, E. J., and Berryman, J. G. (2001). Elastic moduli of a material containing composite inclusions: effective medium theory and finite element computations. *Mech. Mater.* 33, 455–470. doi: 10.1016/S0167-6636(01)00067-9

Grechka, V. (2007). Multiple cracks in VTI rocks: effective properties and fracture characterization. *Geophysics* 72, D81–D91. doi: 10.1190/1.2751500

Grechka, V., and Kachanov, M. (2006a). Effective elasticity of fractured rocks: a snapshot of the work in progress. *Geophysics* 71, W45–W58. doi: 10.1190/1.2360212

Grechka, V., and Kachanov, M. (2006b). Effective elasticity of rocks with closely spaced and intersecting cracks. *Geophysics* 71, D85–D91. doi: 10.1190/1.2197489

Grechka, V., and Tsvankin, I. (2003). Feasibility of seismic characterization of multiple fracture sets. *Geophysics* 68, 1399–1407. doi: 10.1190/1.1598133

Guo, J., Han, T., Fu, L., Xu, D., and Fang, X. (2019). Effective elastic properties of rocks with transversely isotropic background permeated by aligned penny-shaped cracks. *J. Geophys. Res. Solid Earth* 124, 400–424. doi: 10.1029/2018JB016412

Guo, J., Rubino, J. G., Barbosa, N. D., Glubokovskikh, S., and Gurevich, B. (2018). Seismic dispersion and attenuation in saturated porous rocks with aligned fractures of finite thickness: theory and numerical simulations — part 1: P-wave perpendicular to the fracture plane. *Geophysics* 83, WA49–WA62. doi: 10.1190/geo2017-0065.1

Harris, S., McAllister, E., Knipe, R., and Odling, N. E. (2003). Predicting the three-dimensional population characteristics of fault zones: a study using stochastic models. *J. Struct. Geol.* 25, 1281–1299. doi: 10.1016/S0191-8141(02)00158-X

Hopkins, D. L. (2000). The implications of joint deformation in analyzing the properties and behavior of fractured rock masses, underground excavations, and faults. *Int. J. Rock Mech. Min. Sci.* 37, 175–202. doi: 10.1016/S1365-1609(99)00100-8

Hudson, J. A., Liu, E., and Crampin S. (1996). The mechanical properties of materials with interconnected cracks and pores. *Geophys. J. Int.* 124,105–112. doi: 10.1111/j.1365-246X.1996.tb06355.x

Hunziker, J., Favino, M., Caspari, E., Quintal, B., Rubino, J. G., Krause, R., et al. (2018). Seismic attenuation and stiffness modulus dispersion in porous rocks containing stochastic fracture networks. *J. Geophys. Res. Solid Earth* 123, 125–143. doi: 10.1002/2017JB014566

Jakobsen, M. (2012). T-matrix approach to seismic forward modelling in the acoustic approximation. *Stud. Geophys. Et Geodaet.* 56, 1–20. doi: 10.1007/s11200-010-9081-2

Jakobsen, M., and Chapman, M. (2009). Unified theory of global flow and squirt flow in cracked porous media. *Geophysics* 74, WA65–WA76. doi: 10.1190/1.3078404

Jakobsen, M., Hudson, J. A., and Johansen, T. A. (2003). T-matrix approach to shale acoustics *Geophys. J. Int.* 154, 533–558. doi: 10.1046/j.1365-246X.2003.01977.x

Kachanov, M. (1993). Elastic solids with many cracks and related problems. *Adv. Appl. Mech.* 30, 259–445. doi: 10.1016/S0065-2156(08)70176-5

Lapin, R., Kuzkin, V., and Kachanov, M. (2018). On the anisotropy of cracked solids. *Int. J. Eng. Sci.* 124, 16–23. doi: 10.1016/j.ijengsci.2017.11.023

Lei, Q., and Gao, K. (2018). Correlation between fracture network properties and stress variability in geological media. *Geophys. Res. Lett.* 45, 3994–4006. doi: 10.1002/2018GL077548

Masson, Y. J., and Pride, S. R. (2007). Poroelastic finite difference modeling of seismic attenuation and dispersion due to mesoscopic-scale heterogeneity. *J. Geophys. Res. Atmosph.* 112, 1642–1642. doi: 10.1029/2006JB004592

Masson, Y. J., and Pride, S. R. (2014). On the correlation between material structure and seismic attenuation anisotropy in porous media. *J. Geophys. Res. Solid Earth* 119, 2848–2870. doi: 10.1002/2013JB010798

Mavko, G., Mukerji, T., and Dvorkin, J. (2009). *The Rock Physics Handbook, 2nd Edn*. Cambridge: Cambridge University Press.

Odling, N., Harris, S., Vaszi, A., and Knipe, R. (2005). Properties of fault damage zones in siliclastic rocks: a modelling approach. *Geolog. Soc. Lond.* 249, 43–59. doi: 10.1144/GSL.SP.2005.249.01.04

Quintal, B., Steeb, H., Frehner, M., and Schmalholz, S. (2011). Quasi-static finite element modeling of seismic attenuation and dispersion due to wave-induced fluid flow in poroelastic media. *J. Geophys. Res.* 116:B01201. doi: 10.1029/2010JB007475

Quintal, B., Steeb, H., Frehner, M., Schmalholz, S. M., and Saenger, E. H. (2012). Pore fluid effects on S-wave attenuation caused by wave-induced fluid flow. *Geophysics* 77, L13–L23. doi: 10.1190/geo2011-0233.1

Rubino, J. G., Caspari, E., Müller, T. M., Milani, M., Barbosa, N. D., and Holliger, K. (2016). Numerical upscaling in 2-D heterogeneous poroelastic rocks: Anisotropic attenuation and dispersion of seismic waves. *J. Geophys. Res. Solid Earth* 121, 6698–6721. doi: 10.1002/2016JB013165

Savage, H., and Brodsky, E. (2011). Collateral damage: Evolution with displacement of fracture distribution and secondary fault strands in fault damage zones. *J. Geophys. Res.* 116:B03405. doi: 10.1029/2010JB007665

Schoenberg, M., and Sayers, C. (1995). Seismic anisotropy of fracture rock. *Geophysics* 60, 204–211. doi: 10.1190/1.1443748

Wenzlau, F., Altmann, J. B., and Müller, T. M. (2010). Anisotropic dispersion and attenuation due to wave-induced fluid flow: Quasi-static finite element modeling in poroelastic solids. *J. Geophys. Res.* 115:B07204. doi: 10.1029/2009JB006644

Woodruff, W. F., Revil, A., Prasad, M., and Torres-Verdín, C. (2015). Measurements of elastic and electrical properties of an unconventional organic shale under differential loading. *Geophysics* 80, D363–D383. doi: 10.1190/geo2014-0535.1

Zhao, L., Yao, Q., Han, D. H., Yan, F., and Nasser, M. (2015). Characterizing the effect of elastic interactions on the effective elastic properties of porous, cracked rocks. *Geophys. Prospect.* 64, 157–169. doi: 10.1111/1365-2478.12243

Conflict of Interest: The authors declare that the research was conducted in the absence of any commercial or financial relationships that could be construed as a potential conflict of interest.

Copyright © 2021 Cao, Fu, Fu and Guo. This is an open-access article distributed under the terms of the Creative Commons Attribution License (CC BY). The use, distribution or reproduction in other forums is permitted, provided the original author(s) and the copyright owner(s) are credited and that the original publication in this journal is cited, in accordance with accepted academic practice. No use, distribution or reproduction is permitted which does not comply with these terms.

frontiers in Earth Science

ORIGINAL RESEARCH
published: 29 June 2021
doi: 10.3389/feart.2021.646372

Estimation of the Pore Microstructure of Tight-Gas Sandstone Reservoirs with Seismic Data

Wei Cheng[1], *Jing Ba*[1]*, *José M. Carcione*[1,2], *Mengqiang Pang*[1] *and Chunfang Wu*[1]

[1]School of Earth Sciences and Engineering, Hohai University, Nanjing, China, [2]National Institute of Oceanography and Applied Geophysics–OGS, Trieste, Italy

Tight-sandstone reservoirs have a complex pore structure with microcracks and intergranular pores, which have a significant impact on the seismic properties. We have performed ultrasonic measurements at different confining pressures for 15 tight-gas sandstone samples of the Xujiahe formation in Western Sichuan Basin, and have available well-log and seismic data of this area. The aim of this work is to estimate the porosity and crack properties for variable pressure conditions. The EIAS (equivalent inclusion-average stress) model is adopted to compute the high- and low-frequency bulk and shear moduli as a function of crack aspect ratio and (soft) and (stiff) porosities. Then, we use the EIAS-Zener anelastic model to obtain the wave properties as a function of frequency, and compare results with those of the constant Q (Kjartansson) one for verification of the robustness of the approach. The corresponding P-wave impedance, density and phase velocity ratio (V_P/V_S) are computed in order to built 3D rock-physics templates (RPTs) at the ultrasonic, well-log and seismic frequency bands. The methodology is applied to a survey line crossing two wells, which together with the laboratory experiments, provide calibration suitable data. The estimated stiff porosity and crack porosity and density are consistent with the available data and actual production records, indicating that 3D RPTs provide a useful interpretation tool in seismic exploration and prospect evaluation.

Keywords: tight-gas sandstone, rock-physics templates, porosity, crack porosity, EIAS-Zener model, attenuation

OPEN ACCESS

Edited by:
Xin Li,
China National Offshore Oil Corporation, China

Reviewed by:
Luca De Siena,
Johannes Gutenberg University Mainz, Germany
David Iacopini,
University of Naples Federico II, Italy
Tingting Gu,
Purdue University, United States

****Correspondence:***
Jing Ba
jingba@188.com

Specialty section:
This article was submitted to Solid Earth Geophysics, a section of the journal Frontiers in Earth Science

Received: *26 December 2020*
Accepted: *07 June 2021*
Published: *29 June 2021*

Citation:
Cheng W, Ba J, Carcione JM, Pang M and Wu C (2021) Estimation of the Pore Microstructure of Tight-Gas Sandstone Reservoirs with Seismic Data. Front. Earth Sci. 9:646372. doi: 10.3389/feart.2021.646372

INTRODUCTION

Unconventional gas resources offer significant gas production growth potential. Tight-gas sandstones represent an important part of the unconventional production and abundant reserves are yet to be developed (Khlaifat et al., 2011). There are tight-gas sandstone reservoirs almost in all oil and gas bearing areas with significant gas reserves (Zhu et al., 2008). These reservoirs have sandstones with low porosity, permeability and gas saturation and abundant microcracks (Guan and Niu, 1995, Anjos et al., 2003; Cheng et al., 2019; Guo et al., 2018). An effective reservoir characterization is the key to their successful exploration (Storker et al., 2013; Liu et al., 2019). The reservoir contains a large number of natural fractures, which provide main seepage channels and effective storage space, and favor single-well productivity (Harmelen and Weijermars, 2018; Xiao et al., 2019). Therefore, an accurate identification of the pore properties is essential.

In this case, rock physics is required to relate the wave properties to the composition and microstructure of these rocks, which have been affected by complex diagenetic and sedimentary processes during their formation (Vernik and Kachanov, 2010; Zhang et al., 2019; Dvorkin et al.,

2020). Walsh (1965) developed some of the first techniques to study the effects of cracks and confining pressure on the dry-rock moduli. Thomsen (1995) considered aligned circular cracks and analyzed the effects of the associated anisotropy on the elastic properties, and Smith et al. (2009) quantified how microcracks affect the wave velocities in tight-gas sandstone reservoirs. Tang (2011) proposed an elastic-wave model to describe the effects of pores and cracks by extending the Biot and BISQ theories. Double-porosity models that consider two phases with different compressibilities are relatively new and useful approaches to model wave propagation in heterogeneous media (Pride et al., 2004; Ba et al., 2016; Ba et al., 2017; Fu et al., 2018).

To model the relation between pore geometry and elasticity attributes, we used the EIAS (equivalent inclusion-average stress) model (Endres and Knight, 1997), which is consistent with Gassmann equation at low frequencies and with the Hashin-Shtrikman bounds when applied to two-phase systems. Moreover, we used the EIAS-Zener model that generalizes the EIAS model to the full frequency range, by incorporating the Zener (standard linear solid) model (Cheng et al., 2020). The crack porosity, average crack aspect ratio and quality factors and phase velocities were obtained as a function of frequency by fitting experimental data at the unrelaxed and relaxed states.

RPTs establish a link between the reservoir properties (e.g., porosity, fluid saturation, clay content, etc) and the elastic properties, such as velocity, density, impedance, and wet-rock stiffness moduli (Carcione and Avseth, 2015; Hao et al., 2016; Li et al., 2019; Tan et al., 2020). Pang et al. (2019) used the P-wave quality factor and impedance to build RPTs, and shown that the estimated porosity and saturation are consistent with actual gas production results and well-log data. Gegenhuber and Pupos (2015) used RPTs based on V_P/V_S and acoustic impedance applied to carbonate samples.

We used V_P/V_S, impedance and density to build 3D RPTs, based on the EIAS model and the Zener frequency kernels, to characterize the relation between elastic properties and reservoir attributes, i.e., equant porosity and crack porosity and aspect ratio (Carcione, 2014). The templates were calibrated with ultrasonic, log and seismic data. Thereafter, a quantitative interpretation of those attributes can be performed by superposing the seismic-inversion data on the templates.

LABORATORY EXPERIMENTS

The Study Area

The reservoir in the Xujiahe formation of the western Sichuan Basin (China) belongs to the braided river delta sedimentary system. The main mineral components are quartz, feldspar, rock debris, mica, and heavy minerals. The size of the mineral particles is mainly medium to fine, most sandstones are sorted well, and the crushed particles are medium to poorly rounded. These sandstone reservoirs, of low porosity and permeability, have a high crack density and a heterogeneous distribution of pore fluids, due to long-term diagenesis.

TABLE 1 | Tight-gas sandstones properties.

Sample	Total porosity	Permeability (mD)	Mineral density (g cm^{-3})
TSA1	0.0243	<0.001	2.695
TSA2	0.0303	<0.001	2.687
TSA3	0.0346	0.005	2.694
TSA4	0.0388	<0.001	2.670
TSA5	0.0419	<0.001	2.676
TSA6	0.0439	0.004	2.691
TSA7	0.0626	0.046	2.672
TSA8	0.0633	0.047	2.665
TSA9	0.0757	0.0225	2.679
TSA10	0.0855	0.082	2.670
TSA11	0.0865	0.028	2.668
TSA12	0.0897	0.140	2.662
TSA13	0.1326	1.21	2.659
TSA14	0.1335	1.320	2.653
TSA15	0.1391	1.370	2.660

Rock Specimens and Data

Fifteen samples were collected at approximately 2 km depth. They have low porosity and permeability, and are mainly composed of quartz, feldspar and rare clay. Moreover, there are calcite and quartz cementation in intergranular pores, and cracks. The ultrasonic experiments measurements (samples TSA1-TSA15) follow the experimental set-up of Guo et al. (2009), which is composed of a high pressure vessel and several units to control the temperature and the confining and pore pressures, and perform acoustic wave testing. The acquisition rate for ultrasonic waveforms (1 MHz) is 50 M/s and the time resolution is 0.02 μs.

The tests were performed at zero pore pressure and 22°C, whereas the confining pressure increases from 1 to 35 MPa (1, 5, 10, 15, 20, 25, 30 and 35 MPa). The differential pressure (P_d) is defined here as the difference between the confining and pore pressures. Ultrasonic compressional and shear-wave velocities (V_P and V_S) at full-gas (nitrogen) were obtained by picking the first arrivals of waveforms with 1 MHz dominant frequency. These samples have low porosity and permeability, with a maximum of 13.91% and 1.37 mD, respectively. The properties are given in **Table 1**. **Figure 1** shows a crossplot of V_P and V_S for varying differential pressure. As can be seen, the velocities increase with pressure, as expected. The correlation of a linear fitting between V_P and V_S is excellent, the R-square is 0.956, and the slope of V_P vs. V_S is 1.6.

Figure 2 shows ultrasonic velocities as a function of differential pressure at full gas saturation. Velocities are non-linear at low differential pressure, becoming almost linear above 25 MPa, because cracks with lower aspect ratio close first and when the differential pressure exceeds approximately 25 MPa, the stiffer pores are also affected. The velocities increase faster for samples TSA4, TSA5 and TSA8, that can be due to a higher crack density, resulting in a higher sensitivity to pressure. Similar results have been observed previously by Yin et al. (2017), David et al. (2013), Pervukhina et al., 2010, Deng et al. (2015), Sun and Goldberg (1997) with different types of sandstones.

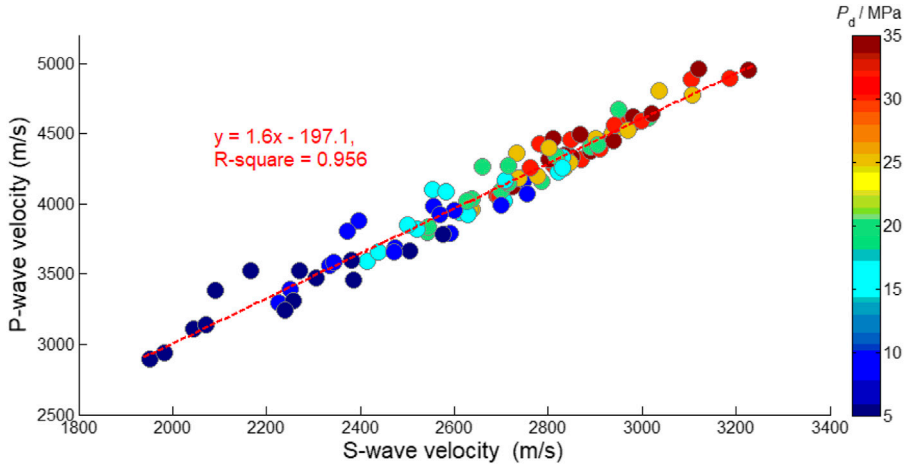

FIGURE 1 | Crossplot of V_P and V_S for varying differential pressures for 15 tight-gas sandstone samples at full gas saturation. The color bar indicates differential pressure.

Determination of the Experimental Crack Porosity

Cracks with lower aspect ratio close first when the differential pressure increases, leading to higher velocities and decreasing crack density. We use sample TSA13 as an example to estimate crack porosity and the pressure dependency of the total, stiff (equant) and crack porosity (**Figure 3**) (The former is the sum of the last two porosities). The total porosity as a function of pressure is obtained by measurement, whereas the stiff porosity by a linear extrapolation of the high-pressure trend determined between 30 and 35 MPa. The similar method was used by Yin et al. (2017) and Pervukhina et al., 2010. The crack porosity is estimated by subtracting the stiff one from the total porosity. **Figure 4** shows the crack porosity as a function of the differential pressure. When the differential pressure is less than 25 MPa, the crack porosity decreases rapidly and non-linearly. As the pressure increases, the crack porosity exhibits linear characteristics until it approaches zero at high differential pressures.

ROCK-PHYSICS MODEL

The EIAS Model

The microscopic pore structure is important because it affects the rock skeleton properties and the fluid distribution. The EIAS model can effectively address the relation between pore geometry and the elastic attributes, and it is consistent with the Hashin-Shtrikman bounds for two-phase systems (Endres and Knight 1997; Cheng et al., 2020). Assuming a background medium containing spherical pores and cracks, the resulting expressions for the effective high-frequency elastic moduli of the saturated rock are

$$K_{HF}^{\mathrm{sat}} = K_0 + \frac{\phi\left(K_f - K_0\right)\overline{\gamma}}{1-\phi\left(1-\overline{\gamma}\right)}, \tag{1}$$

$$G_{HF}^{\mathrm{sat}} = \frac{G_0\left(1-\phi\right)}{1-\phi\left(1-\overline{\chi}\right)}, \tag{2}$$

where ϕ denotes the rock total porosity, K_0 and G_0 are the bulk and shear moduli of the mineral mixture, respectively, K_f is the fluid bulk modulus and

$$\overline{\gamma} = (1-c)P_1 + cP_2, \overline{\chi} = (1-c)Q_1 + cQ_2, \tag{3}$$

$$P_1 = \frac{K_0 + 4G_0/3}{K_f + 4G_0/3}, P_2 = \frac{K_0}{K_f + \pi a\beta_m}, \tag{4}$$

$$Q_1 = 1 + G_0/\zeta, Q_2 = \frac{1}{5}\left[1 + \frac{8G_0}{\pi a\left(G_0 + 2\beta_m\right)} + 2\cdot\frac{K_f + 2G_0/3}{K_f + \pi a\beta_m}\right], \tag{5}$$

β_m and ζ are intermediate variables, which can be expressed as

$$\beta_m = G_0\cdot\frac{3K_0 + G_0}{3K_0 + 4G_0}, \zeta = \frac{G_0}{6}\cdot\frac{9K_0 + 8G_0}{K_0 + 2G_0}, \tag{6}$$

(Berryman 1995; Mavko et al., 2009; Carcione et al., 2020; Sun et al., 2020), where a is the crack aspect ratio, c is the soft-pore (crack) fraction and 1 - c is the stiff-pore fraction; the crack density is $\rho_c = 3\phi c/4\pi a$. The coefficients P_1 and Q_1 correspond to spherical pores and P_2 and Q_2 are approximations for penny-shaped cracks.

The effective low-frequency moduli (when complete fluid-pressure communication occurs) are

$$K_{LF}^{\mathrm{sat}} = K_0 + \frac{\phi K_0\left(K_f - K_0\right)\overline{\gamma}_0}{\left(1-\phi\right)\left(K_0 - K_f\right) + \left[K_f + \phi\left(K_0 - K_f\right)\right]\overline{\gamma}_0}, \tag{7}$$

$$G_{LF}^{\mathrm{sat}} = \frac{G_0\left(1-\phi\right)}{1-\phi\left(1-\overline{\chi}_0\right)}, \tag{8}$$

where

$$\overline{\gamma}_0 = (1-c)P_{01} + cP_{02}, \overline{\chi}_0 = (1-c)Q_{01} + cQ_{02}, \tag{9}$$

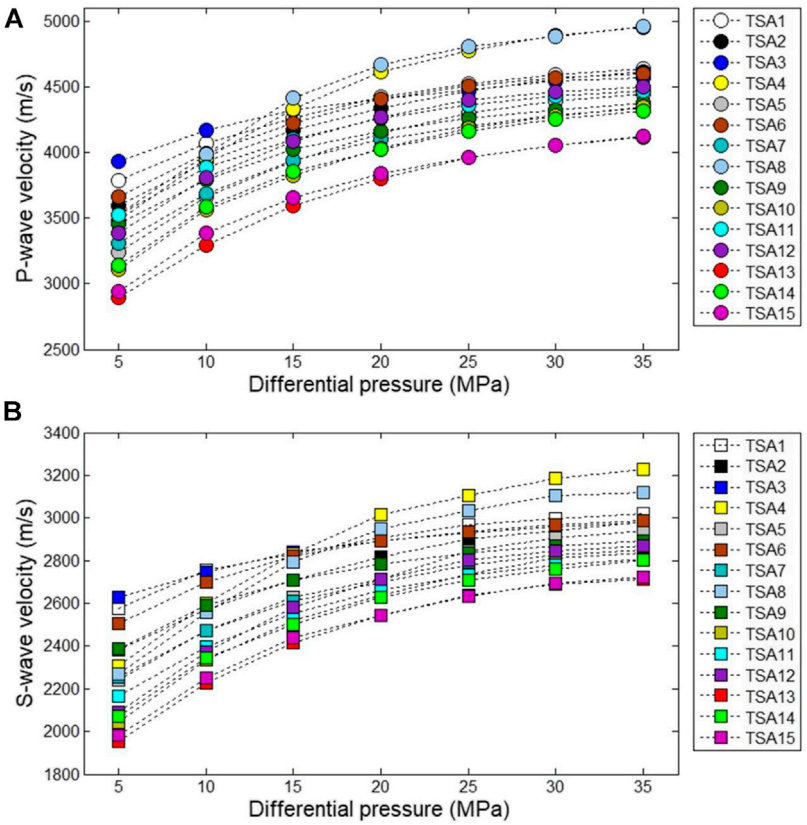

FIGURE 2 | Ultrasonic velocities as a function of differential pressure at full-gas saturation, **(A)** P wave; **(B)** S wave.

$$P_{01} = 1 + \frac{3K_0}{4G_0}, P_{02} = \frac{K_0}{\pi a \beta_m}, \tag{10}$$

$$Q_{01} = Q_1, Q_{02} = \frac{1}{5}\left[1 + \frac{4G_0}{\pi a} \cdot \frac{G_0 + 8\beta_m}{3\beta_m (G_0 + 2\beta_m)}\right], \tag{11}$$

and

$$P_{0n} = P_n\left(K_f = 0\right), (n = 1, 2), Q_{0n} = Q_n\left(K_f = 0\right), (n = 1, 2), \tag{12}$$

The detailed derivation of these equations can be found in Endres and Knight (1997). The model considers the interactions between cracks and has no restrictions on the crack density. In order to generalize the model to all frequencies, we combine the EIAS model with the Zener (standard linear solid) and Kjartansson kernels, to describe the physics with two very dissimilar approaches and check the robustness of the methodology.

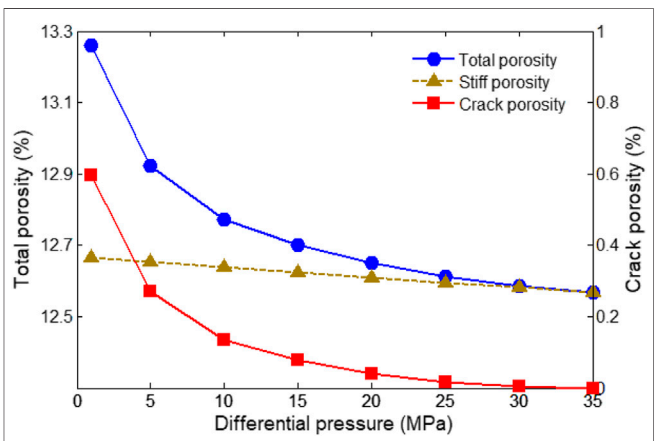

FIGURE 3 | Pressure dependency of the total, stiff and crack porosity of sample TSA13.

EIAS-Zener Model

The Zener mechanical model can be used to described the frequency dependence of dispersion and attenuation (e.g., Carcione et al., 2012; Carcione 2014). This model satisfies the Kramers-Kronig relations (Carcione et al., 2018). The minimum quality factors of the bulk and shear relaxation peaks are given by

$$Q_{0K} = \frac{2\sqrt{K_{HF}^{sat} K_{LF}^{sat}}}{K_{HF}^{sat} - K_{LF}^{sat}} \text{ and } Q_{0G} = \frac{2\sqrt{G_{HF}^{sat} G_{LF}^{sat}}}{G_{HF}^{sat} - G_{LF}^{sat}}, \tag{13}$$

respectively, whereas the bulk and shear complex moduli are

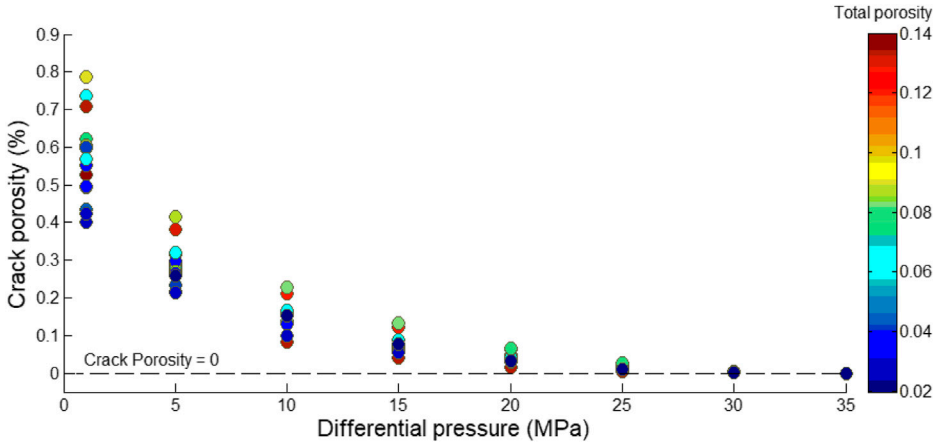

FIGURE 4 | Crossplot of crack porosity and differential pressure at full gas saturation. The color bar indicates total porosity.

$$K(f) = \frac{Q_{0K} + i(f/f_0)\left(\sqrt{1+Q_{0K}^2}+1\right)}{Q_{0K} + i(f/f_0)\left(\sqrt{1+Q_{0K}^2}-1\right)} \cdot K_{LF}^{\text{sat}}, \tag{14}$$

$$G(f) = \frac{Q_{0G} + i(f/f_0)\left(\sqrt{1+Q_{0G}^2}+1\right)}{Q_{0G} + i(f/f_0)\left(\sqrt{1+Q_{0G}^2}-1\right)} \cdot G_{LF}^{\text{sat}}, \tag{15}$$

where $i = \sqrt{-1}$, f_0 is the frequency of the relaxation peak, such that for $f \to \infty$, $K \to K_{HF}^{\text{sat}}$ and for $f \to 0$, $K \to K_{LF}^{\text{sat}}$.

The phase velocity and quality factor of the body waves are

$$V = \left[\text{Re}\left\{\frac{1}{v}\right\}\right]^{-1}, \tag{16}$$

and

$$Q = \frac{\text{Re}\{v^2\}}{\text{Im}\{v^2\}}, \tag{17}$$

respectively, where v denotes v_P or v_S, being the frequency-dependent complex P- and S-wave velocities

$$v_P = \sqrt{\frac{K + 4G/3}{\rho}} \text{ and } v_S = \sqrt{\frac{G}{\rho}}, \tag{18}$$

(Carcione, 2014), respectively, where ρ is the mass density.

EIAS-Kjartansson Model

Kjartansson (1979) presented a constant-Q model specified by the phase velocity at a reference frequency f_1 and the value of Q. To combine this model with the EIAS model, we consider $f_1 = 50$ Hz, which is the average frequency of the event corresponding to the target layer, i.e., $\omega_1 = 2\pi f_1 = 100\pi$ rad/s. The phase velocity at low frequencies is

$$V_P^{LF} = \sqrt{(K_{LF}^{\text{sat}} + 4/3G_{LF}^{\text{sat}})/\rho}, \tag{19}$$

For $f_2 = 1$ MHz (the ultrasonic experimental frequency), $\omega_2 = 2\pi f_2 = 2 \times 10^6 \pi$ rad/s, and the phase velocity is

$$V_P^{HF} = \sqrt{(K_{LF}^{\text{sat}} + 4/3G_{LF}^{\text{sat}})/\rho}, \tag{20}$$

The phase velocity as a function of frequency is (Carcione, 2014, Eq. 2.214),

$$V_P(\omega) = V_P^{LF}\left|\frac{\omega}{\omega_1}\right|^{\gamma},$$

as an approximation for Q>>1. We obtain after some calculations,

$$\gamma = \log(V_P^{HF}/V_P^{LF})/\log(\omega_2/\omega_1), \tag{21}$$

Defining,

$$M_1 = K_{LF}^{\text{sat}} + \frac{4}{3}G_{LF}^{\text{sat}} \tag{22}$$

the complex modulus is (Carcione, 2014, Eq. 2.212)

$$M(\omega) = M_1\left(\frac{i\omega}{\omega_1}\right)^{2\gamma}, \tag{23}$$

Therefore, the complex velocity and quality factor are

$$V_P(\omega) = \sqrt{M(\omega)/\rho}, \tag{24}$$

$$Q_P(\omega) = \frac{\text{Re}(M)}{\text{Im}(M)}, \tag{25}$$

respectively.

Example

The previous models are used to relate the crack properties (aspect ratio and porosity) and the frequency-dependent elastic moduli, phase velocities and quality factors. The purpose of using two dissimilar models is to verify the robustness of the approach, i.e., if the two models give similar results, we can rely on the methodology. Let us consider sample TSA13 (porosity is 13.26%). We assume that the mineral bulk and shear modulus are 39 and 36 GPa, respectively (Mavko et al., 2009), the fluid properties are obtained from Batzle and Wang

(1992). We consider a Zener kernel with f_0 = 10 KHz and the parameters of the constant-Q kernel assumed in the previous section. **Figure 5** shows the phase velocities and dissipation factors as a function of frequency, where it is clear both kernels honor the velocity dispersion between the seismic and laboratory frequency bands. Therefore, they can be used to build multi-scale 3D RPTs in the ultrasonic, logging and seismic frequency bands.

Thereafter, we assume a crack porosity of 0.2% and crack aspect ratios of 0.001, 0.0014, 0.0018, 0.0022, 0.0026. Velocities and dissipation factors as a function of frequency are shown in **Figures 6A,B**. When the crack porosity is a constant and the crack aspect ratio increases, the rock becomes stiffer and the P-wave velocity increases, but attenuation decreases. If we take a crack aspect ratio of 0.002 and crack porosities of 0.2, 0.3, 0.4, 0.5, 0.6%, the results are shown in **Figures 6C,D**, where the trend opposite to the previous one.

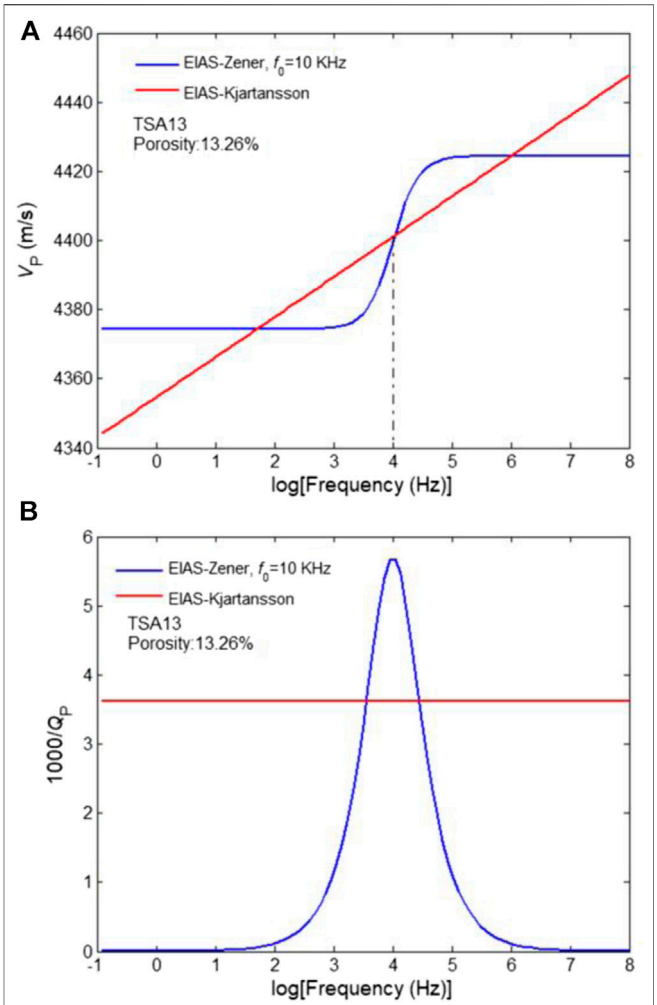

FIGURE 5 | Phase velocity **(A)** and dissipation factor **(B)** as a function of frequency (sample TSA13).

MULTI-SCALE 3D RPTS

Building the RPTs

By setting the crack aspect ratio, crack porosity and total porosity as variables, the corresponding P-wave impedance, density and V_P/V_S value are calculated by using the EIAS-Zener model. Then, we build the 3D RPTs at ultrasonic (1 MHz) well-log (10 kHz) and seismic (50 Hz) frequencies, and the seismic template is used to estimate the microstructure of the sandstone reservoirs. Similar templates have been used by Pang et al. (2020a) to estimate the microfracture porosity of deep carbonate reservoirs. **Figures 7A,B** show the 3D RPTs at ultrasonic and seismic frequencies, respectively (the well-log template is similar to the seismic one).

As the stiff porosity increases, the P-wave impedance and mass density decrease, but the variation in V_P/V_S is small. With the increase of crack porosity, the P-wave impedance decreases and V_P/V_S increases, but the density hardly changes. As the crack aspect ratio increases, the P-wave impedance increases, V_P/V_S decreases. This behavior is similar at all frequencies.

Calibration at Ultrasonic Frequencies

The templates are calibrated with the crack porosity obtained in Section *Determination of the Experimental Crack Porosity*. **Figure 8** superposes the data to the template. The porosity (2.43–13.91%) of samples is basically consistent with the corresponding values in the templates, and the agreement is also good for the crack porosity. What's more, the average error between the predicted porosities (based on ultrasonic wave attributes) and the measured one is 0.00455. In addition, as this increases, the P-wave impedance decreases.

Calibration at Well-Log and Seismic Frequencies

Figure 9 shows the calibration of the 3D RPTs at log and seismic frequencies, where the data is extracted from well B. The template at seismic frequencies is calibrated with inversion results (P-wave impedance, density and V_P/V_S) of pre-stack seismic data that has been verified, whole the porosity is taken from the logs. Similar methods have been used by Pang et al. (2020b). The velocities and density at seismic frequency band are extracted from the seismic traces around the borehole by using a three-term inversion method (Aki and Richards, 1980). We use the partial-stack method to obtain the seismic data based on pre-stack angle gathers, which improves the signal-noize ratio and suppresses random noises. In addition, the velocities and porosity at sonic-log frequency band are extracted from the well-log data by using the velocity-time semblance method, which avoids picking arrival times and can accurately determine the phase velocities for different modes (Wang et al., 2020), and the density is obtained from density logging. **Figure 9** shows that the porosity is basically consistent with the corresponding values in the templates. **Figure 10** shows a crossplot of V_P and V_S of well B, where the velocities increase with decreasing porosity, as expected. The

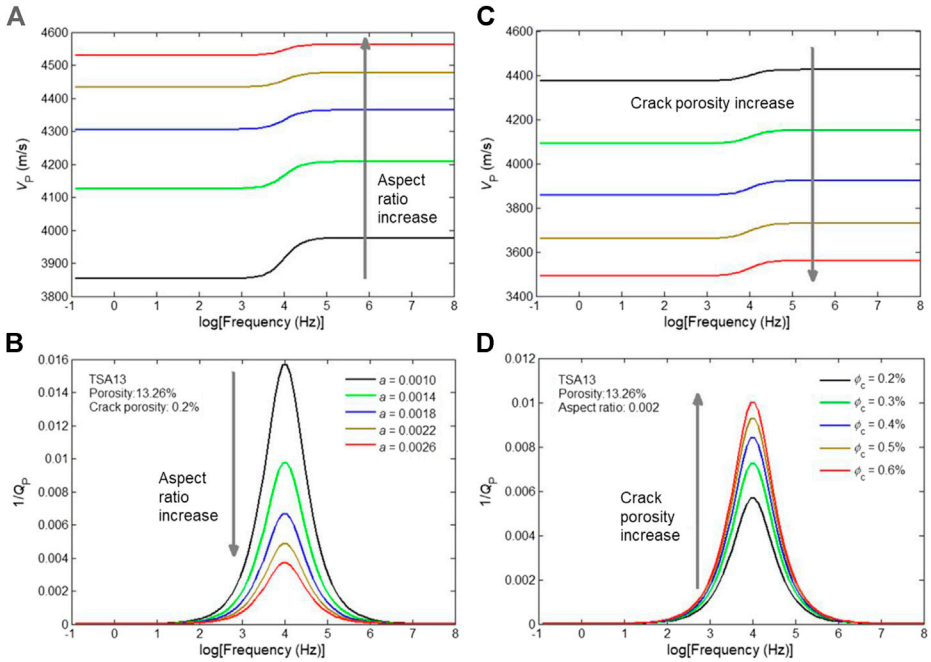

FIGURE 6 | Effects of crack aspect ratio and crack porosity on P-wave dispersion and attenuation at seismic frequencies.

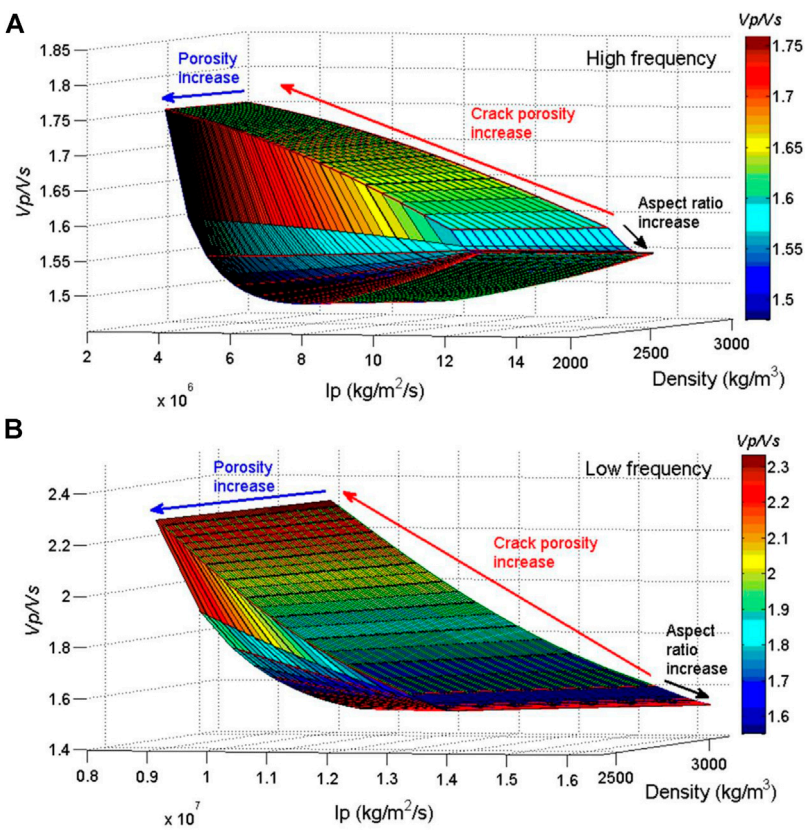

FIGURE 7 | 3D RPTs at ultrasonic **(A)** and seismic **(B)** frequencies.

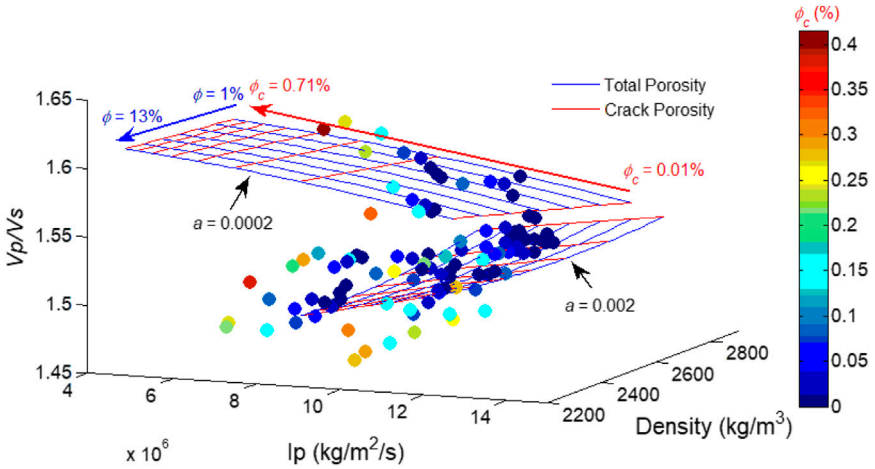

FIGURE 8 | 3D RPT at ultrasonic frequencies with the superposed experimental data (symbols). The color bar is crack porosity.

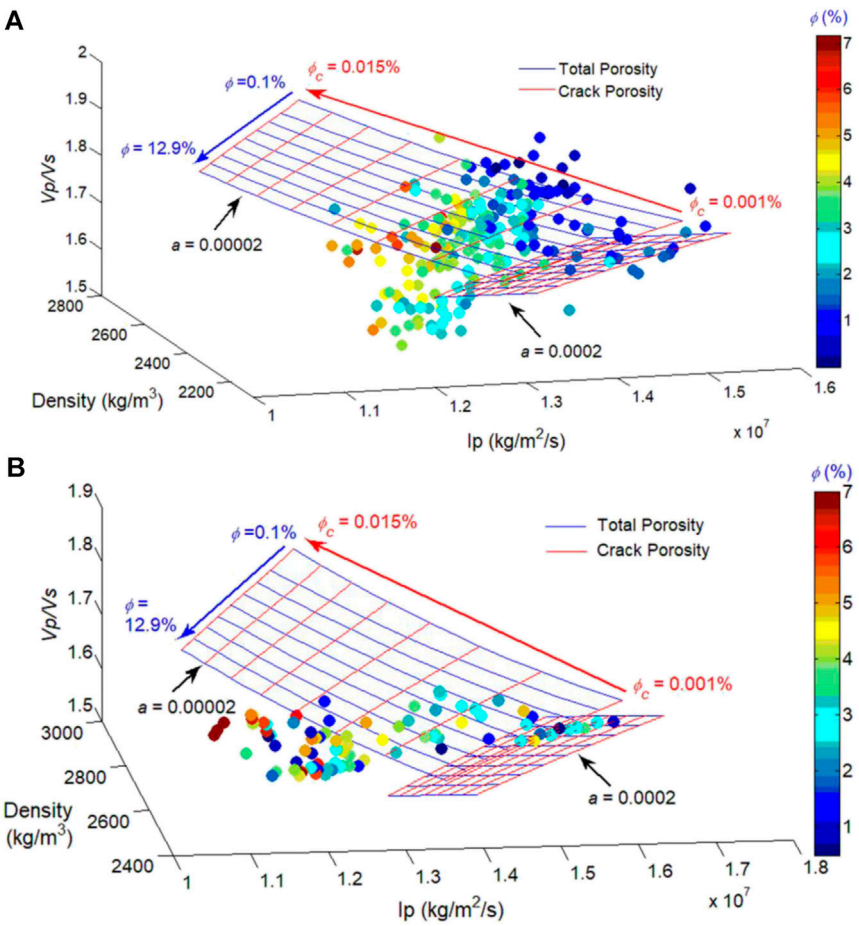

FIGURE 9 | 3D RPTs at the well-log **(A)** and seismic **(B)** frequency bands, with the superposed experimental data (symbols). The color bar is porosity.

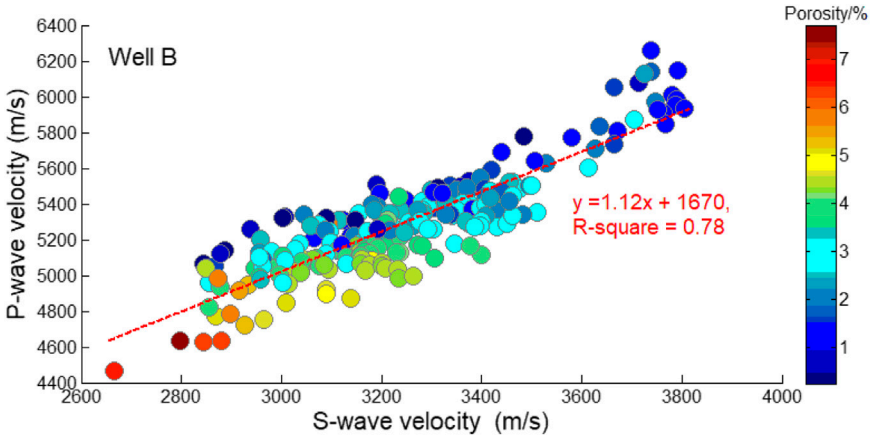

FIGURE 10 | Crossplot of V_P and V_S of well B. The color bar indicates porosity.

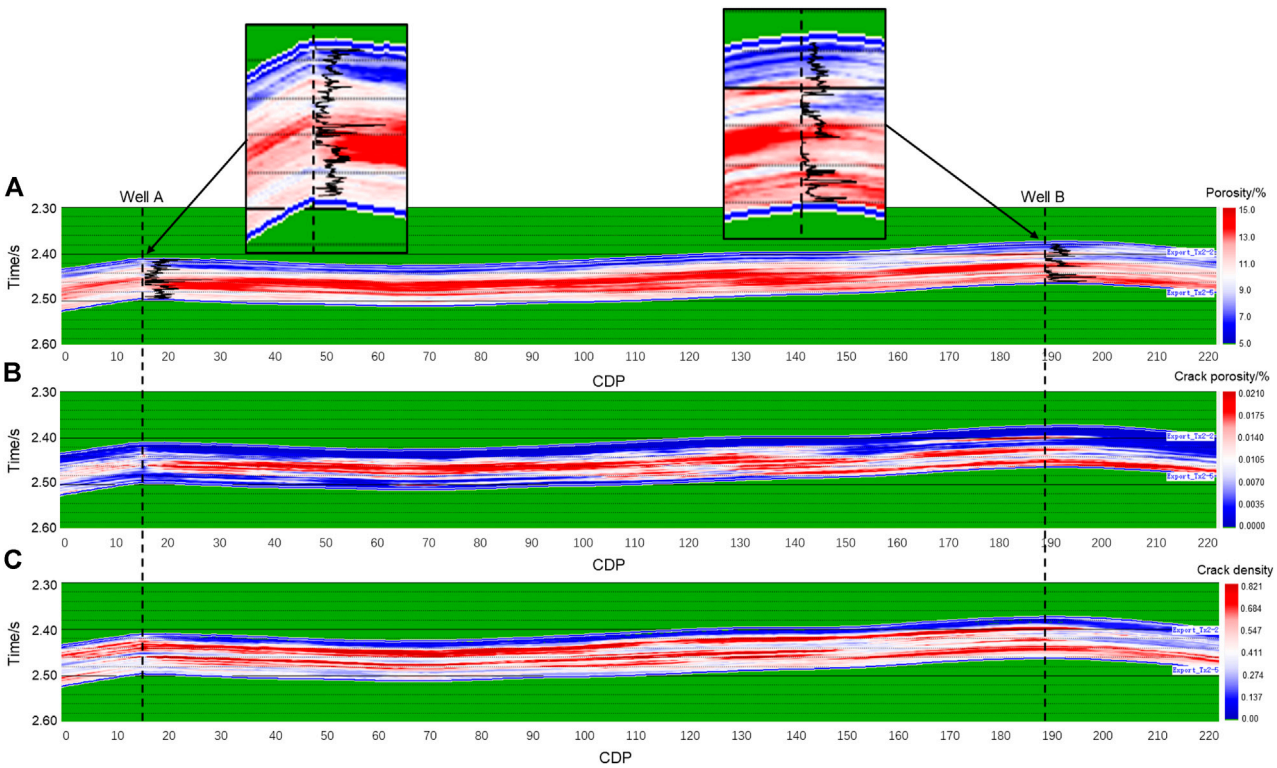

FIGURE 11 | Vertical sections of the estimated porosity **(A)**, crack porosity **(B)** and crack density **(C)**.

correlation of a linear fitting between V_P and V_S is excellent, and the slope of V_P vs. V_S is 1.12.

The P-wave impedance, density and V_P/V_S decreases with increasing porosity, and the latter decreases with increasing crack aspect ratio. The porosity is low (less than 7%), which is consistent with the geological characteristics of the reservoirs.

ESTIMATION OF THE MICROSTRUCTURE FROM SEISMIC DATA

The predictions of reservoir stiff porosity and crack porosity and density are performed on a 2D seismic line crossing wells A and B. P-wave impedance, density and V_P/V_S are overlapped onto the 3D RPTs, and the microstructural properties are estimated.

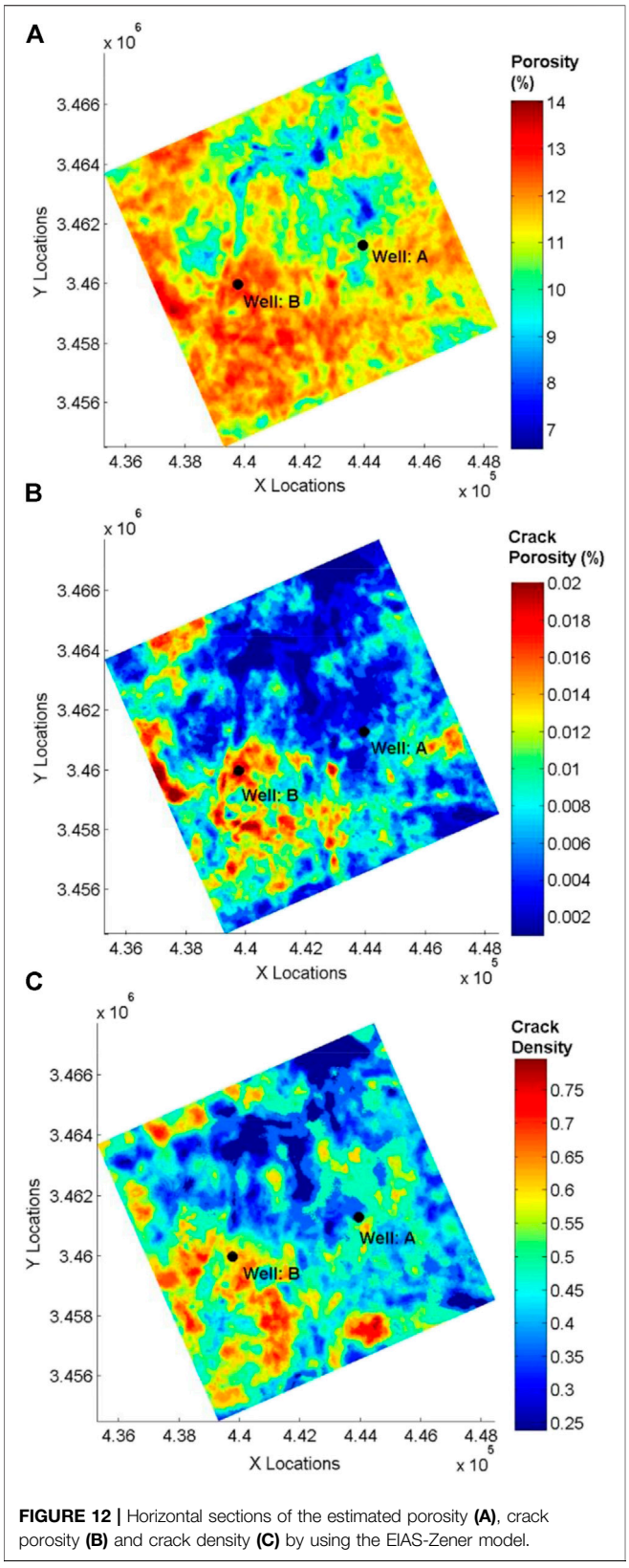

FIGURE 12 | Horizontal sections of the estimated porosity **(A)**, crack porosity **(B)** and crack density **(C)** by using the EIAS-Zener model.

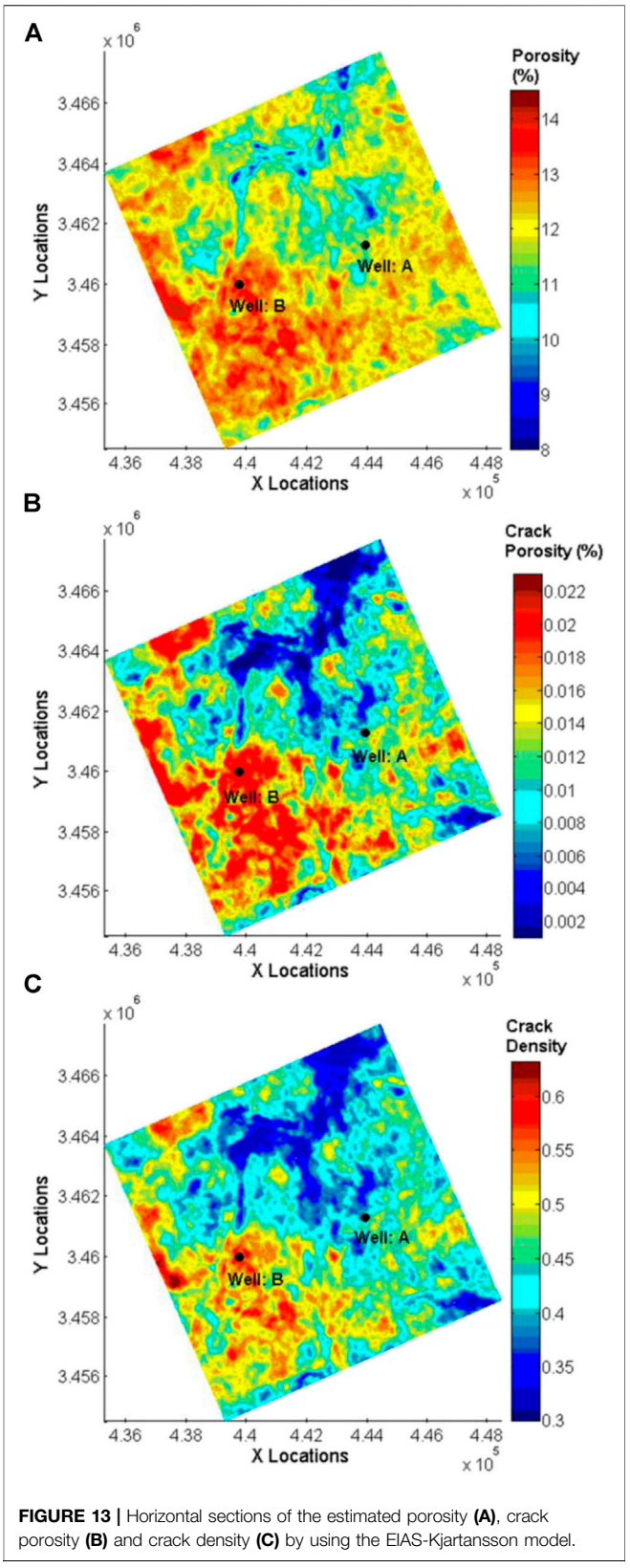

FIGURE 13 | Horizontal sections of the estimated porosity **(A)**, crack porosity **(B)** and crack density **(C)** by using the EIAS-Kjartansson model.

Figure 11A shows the porosity from well log A and B are superposed, showing a good agreement. By taking well B as an example, the average error between the predicted porosities (based on seismic wave attributes) and the measured porosities is 0.00923, which is higher than the one at ultrasonic frequency, because the resolution of the seismic data is low. **Figures 11B,C** show the crack porosity and density, respectively. It shows that well B has a higher crack porosity and density. The horizontal sections are created from target layer (depth 4,787 m) of the study area in the Xujiahe formation of the western Sichuan Basin (China). **Figures 12**, **13** show horizontal section of those attributes, which are simulated by using EIAS-Zener and EIAS-Kjartansson models, respectively. The results show that the two models give similar results, thus indicating that the methodology is working. The total porosity and crack porosity and density effectively serve to identify high-quality reservoirs. Well B is located in an area with high porosity and crack content, where the target layer has a good pore connectivity, storage capability, and natural gas accumulation conditions. The gas production report of well B indicates 5148929 m^3 per day, while well A yields 57559 m^3 per day. The results agree with the actual production of the two wells. Therefore, the methodology is reliable, and is expected to provide an important basis for further rock-physics studies and field applications of seismic exploration.

CONCLUSION

Rock-physics templates constitute an easy-to-use "tool-box" for pore microstructure properties interpretation from seismic data. We have implemented the EIAS-Zener model to describe the crack properties and elastic moduli of tight-gas sandstone reservoirs as a function of frequency from the seismic to the ultrasonic bands. Since P-wave impedance, mass density and V_P/V_S are sensitive to the pore and crack properties, we built the templates to estimate these attributes from seismic data. First, we calibrate the templates with ultrasonic, well-log and seismic data. Then, we estimate the total porosity and crack porosity and density from inversion of seismic data. The results indicate that these estimated attributes are consistent with the actual gas production reports. Thus, these templates can effectively be used to estimate the microstructure characteristics of tight-gas sandstone reservoirs based on seismic data.

DATA AVAILABILITY STATEMENT

The raw data supporting the conclusions of this article will be made available by the authors, without undue reservation.

AUTHOR CONTRIBUTIONS

WC: Methodology, writing original manuscript JB: Funding support, data and discussion, writing original manuscript, supervision JC: Model building, revising manuscript MP: Seismic data analysis CW: Ultrasonic experimental data analysis.

FUNDING

The authors are grateful to the support of the Jiangsu Innovation and Entrepreneurship Plan, Jiangsu Province Science Fund for Distinguished Young Scholars (BK20200021), National Natural Science Foundation of China (41974123), China Postdoctoral Science Foundation (2021M690863), Fundamental Research Funds for the Central Universities (B210202112) and the research funds from SINOPEC Key Laboratory of Geophysics.

REFERENCES

Aki, K., and Richards, P. G. (1980). *Quantitative Seismology, Theory and Methods*. San Francisco: W.H. Freeman and Company.

Anjos, S. M. C., De Ros, L. F., and Silva, C. M. A. (2003). Chlorite Authigenesis and Porosity Preservation in the Upper Cretaceous marine Sandstones of the Santos Basin, Offshore Eastern Brazil. *Int. Assoc. Sedimentologists* 34, 289–316. doi:10.1002/9781444304336.ch13

Ba, J., Xu, W., Fu, L.-Y., Carcione, J. M., and Zhang, L. (2017). Rock Anelasticity Due to Patchy Saturation and Fabric Heterogeneity: A Double Double-Porosity Model of Wave Propagation. *J. Geophys. Res. Solid Earth* 122 (3), 1949–1976. doi:10.1002/2016JB013882

Ba, J., Zhao, J., Carcione, J. M., and Huang, X. (2016). Compressional Wave Dispersion Due to Rock Matrix Stiffening by clay Squirt Flow. *Geophys. Res. Lett.* 43, 6186–6195. doi:10.1002/2016GL069312

Batzle, M., and Wang, Z. (1992). Seismic Properties of Pore Fluids. *Geophysics* 57 (11), 1396–1408. doi:10.1190/1.1443207

Berryman, J. G. (1995). *Mixture Theories for Rock Propertie. A Handbook of Physical Constants*. Washington, D C: American Geophysical Union, 205–228. doi:10.1029/RF003p0205

Carcione, J. M., and Avseth, P. (2015). Rock-physics Templates for clay-rich Source Rocks. *Geophysics* 80 (5), D481–D500. doi:10.1190/geo2014-0510.1

Carcione, J. M., Cavallini, F., Ba, J., Cheng, W., and Qadrouh, A. (2018). On the Kramers-Kronig Relations. *Rheologica Acta* 58 (1-2), 21–28. Available at: https://link.springer.com/article/10.1007%2Fs00397–018-1119–3. doi:10.1007/s00397-018-1119-3

Carcione, J. M., Farina, B., Poletto, F., Qadrouh, A. N., and Cheng, W. (2020). Seismic Attenuation in Partially Molten Rocks. *Phys. Earth Planet. Interiors* 309, 106568. doi:10.1016/j.pepi.2020.106568

Carcione, J. M., Gei, D., Picotti, S., and Michelini, A. (2012). Cross-hole Electromagnetic and Seismic Modeling for CO2 Detection and Monitoring in a saline Aquifer. *J. Pet. Sci. Eng.* 100, 162–172. doi:10.1016/j.petrol.2012.03.018

Carcione, J. M. (2014). *Wave Fields in Real Media. Theory and Numerical Simulation of Wave Propagation in Anisotropic, Anelastic, Porous and Electromagnetic media*. Third edition. Elsevier extended and revised.

Cheng, W., Ba, J., Fu, L.-Y., and Lebedev, M. (2019). Wave-velocity Dispersion and Rock Microstructure. *J. Pet. Sci. Eng.* 183, 106466. doi:10.1016/j.petrol.2019.106466

Cheng, W., Carcione, J. M., Qadrouh, A. N., Alajmi, M., and Ba, J. (2020). Rock Anelasticity, Pore Geometry and the Biot-Gardner Effect. *Rock Mech. Rock Eng.* 53, 3969–3981. doi:10.1007/s00603-020-02155-7

David, E. C., Fortin, J., Schubnel, A., Guéguen, Y., and Zimmerman, R. W. (2013). Laboratory Measurements of Low- and High-Frequency Elastic Moduli in Fontainebleau sandstone. *Geophysics* 78 (5), D369–D379. doi:10.1190/geo2013-0070.1

Deng, J., Zhou, H., Wang, H., Zhao, J., and Wang, S. (2015). The Influence of Pore Structure in Reservoir sandstone on Dispersion Properties of Elastic Waves. *Chin. J. Geophysics-Chinese* 58 (9), 3389–3400. doi:10.6038/cjg20150931

Dvorkin, J., Walls, J., and Davalos, G. (2020). Velocity-Porosity-Mineralogy Model for Unconventional Shale and its Applications to Digital Rock Physics. *Front. Earth Sci.* 8. doi:10.3389/feart.2020.613716

Endres, A. L., and Knight, R. J. (1997). Incorporating Pore Geometry and Fluid Pressure Communication into Modeling the Elastic Behavior of Porous Rocks. *Geophysics* 62 (1), 106–117. doi:10.1190/1.1444110

Fu, B.-Y., Guo, J., Fu, L.-Y., Glubokovskikh, S., Galvin, R. J., and Gurevich, B. (2018). Seismic Dispersion and Attenuation in Saturated Porous Rock with Aligned Slit Cracks. *J. Geophys. Res. Solid Earth* 123, 6890–6910. doi:10.1029/2018JB015918

Gegenhuber, N., and Pupos, J. (2015). Rock Physics Template from Laboratory Data for Carbonates. *J. Appl. Geophys.* 114, 12–18. doi:10.1016/j.jappgeo.2015.01.005

Guan, D. S., and Niu, J. Y. (1995). *Unconventional Oil and Gas Geology in China*. Beijing: Petroleum Industry Press, 60–85.

Guo, M.-Q., Fu, L.-Y., and Ba, J. (2009). Comparison of Stress-Associated Coda Attenuation and Intrinsic Attenuation from Ultrasonic Measurements. *Geophys. J. Int.* 178, 447–456. doi:10.1111/j.1365-246X.2009.04159.x

Guo, M. Q., Ba, J., Ma, R. P., Chen, T. S., Zhang, L., Pang, M. Q., et al. (2018). P-wave Velocity Dispersion and Attenuation in Fluid-Saturated Tight Sandstones: Characteristics Analysis Based on a Double Double-Porosity Structure Model Description. *Chin. J. Geophys.* 61 (3), 1053–1068. doi:10.6038/cji2018L0678

Hao, Z., Ba, J., Zhang, L., Zeng, Q., JiangLiu, R. J., Qian, W., et al. (2016). Rock Physics Inversion Workflow on Reservoir Parameters: A Case Study of Seismic Hydrocarbon Detection in Large-Area Tight Dolomite Reservoirs. *J. Seismic Exploration* 25, 561–588.

Harmelen, A. V., and Weijermars, R. (2018). Complex Analytical Solutions for Flow in Hydraulically Fractured Hydrocarbon Reservoirs with and without Natural Fractures. *Appl. Math. Model.* 56, 137–157. doi:10.1016/j.apm.2017.11.027

Khlaifat, A., Qutob, H., and Barakat, N. (2011). *Tight Gas Sands Development Is Critical to Future World Energy Resources*. Society of Petroleum Engineers, 1–12. doi:10.2118/142049-MS

Kjartansson, E. (1979). ConstantQ-wave Propagation and Attenuation. *J. Geophys. Res.* 84, 4737–4748. doi:10.1029/jb084ib09p04737

Li, H. B., Zhang, J. J., Cai, S. J., and Pan, H. J. (2019). 3D Rock Physics Template for Reservoir with Complex Pore Structure. *Chin. J. Geophys. (in Chinese)* 62, 2711–2723. doi:10.6038/cjg2019K0672

Liu, L., Tang, D., Wo, Y., Liu, L., and Sun, W. (2019). Favorable Area Prediction of Tight sandstone: A Case Study of the He8 Formation in the Kangning Area, Eastern Ordos Basin, China. *J. Pet. Sci. Eng.* 175, 430–443. doi:10.1016/j.petrol.2018.12.069

Mavko, G., Mukerji, T., and Dvorkin, J. (2009). *The Rock Physics Handbook*. Cambridge Univ. Press. doi:10.1017/cbo9780511626753

Pang, M., Ba, J., Carcione, J. M., Picotti, S., Zhou, J., and Jiang, R. (2019). Estimation of Porosity and Fluid Saturation in Carbonates from Rock-Physics Templates Based on Seismic Q. *Geophysics* 84 (6), M25–M36. doi:10.1190/geo2019-0031.1

Pang, M., Ba, J., Carcione, J., Vesnaver, A., Ma, R., and Chen, T. (2020b). Analysis of Attenuation Rock-Physics Template of Tight Sandstones: Reservoir Microcrack Prediction. *Chin. J. Geophys.* 63, 4205–4219.

Pang, M., Ba, J., Fu, L. Y., Carcione, J. M., Markus, U., and Zhang, L. (2020a). Estimation of Microfracture Porosity in Deep Carbonate Reservoirs Based on 3d Rock-Physics Templates. *Interpretation* 8 (4), 1–41. doi:10.1190/int-2019-0258.1

Pervukhina, M., Gurevich, B., Dewhurst, D. N., and Siggins, A. F. (2010). Applicability of Velocity-Stress Relationships Based on the Dual Porosity Concept to Isotropic Porous Rocks. *Geophys. J. Int.* 181, 1473–1479. doi:10.1111/j.1365-246X.2010.04535.x

Pride, S. R., Berryman, J. G., and Harris, J. M. (2004). Seismic Attenuation Due to Wave-Induced Flow. *J. Geophys. Res.* 109 (B1). doi:10.1029/2003jb002639

Smith, T. M., Sayers, C. M., and Sondergeld, C. H. (2009). Rock Properties in Low-Porosity/low-Permeability Sandstones. *The Leading Edge* 28 (1), 48–59. doi:10.1190/1.3064146

Stroker, T. M., Harris, N. B., Crawford Elliott, W., and Marion Wampler, J. (2013). Diagenesis of a Tight Gas Sand Reservoir: Upper Cretaceous Mesaverde Group, Piceance Basin, Colorado. *Mar. Pet. Geology.* 40, 48–68. doi:10.1016/j.marpetgeo.2012.08.003

Sun, Y., Carcione, J. M., and Gurevich, B. (2020). Squirt-flow Seismic Dispersion Models: A Comparison. *Geophys. J. Internat.* 222, 2068–2082. doi:10.1093/gji/ggaa274

Sun, Y. F., and Goldberg, D. (1997). Estimation of Aspect-Ratio Changes with Pressure from Seismic Velocities. *Geol. Soc. Lond. Spec. Publications* 122, 131–139. doi:10.1144/GSL.SP.1997.122.01.10

Tan, W., Ba, J., Müller, T., Fang, G., and Zhao, H. (2020). Rock Physics Model of Tight Oil Siltstone for Seismic Prediction of Brittleness. *Geophys. Prospecting* 68 (5), 1554–1574. doi:10.1111/1365-2478.12938

Tang, X. M. (2011). A Unified Theory for Elastic Wave Propagation through Porous media Containing Cracks—An Extension of Biot's Poroelastic Wave Theory. *Sci. China Earth Sci. (In Chinese)* 41 (6), 784–795.

Thomsen, L. (1995). Elastic Anisotropy Due to Aligned Cracks in Porous Rock1. *Geophys. Prospect* 43, 805–829. doi:10.1111/j.1365-2478.1995.tb00282.x

Vernik, L., and Kachanov, M. (2010). Modeling Elastic Properties of Siliciclastic Rocks. *Geophysics* 75 (6), E171–E182. doi:10.1190/1.3494031

Walsh, J. B. (1965). The Effect of Cracks on the Compressibility of Rock. *J. Geophys. Res.* 70, 381–389. doi:10.1029/JZ070i002p00381

Wang, H., Toksöz, M. N., and Fehler, M. C. (2020). *Borehole Acoustic Logging – Theory and Methods*. Petroleum Engineering. doi:10.1007/978-3-030-51423-5

Xiao, Z., Ding, W., Liu, J., Tian, M., Yin, S., Zhou, X., et al. (2019). A Fracture Identification Method for Low-Permeability sandstone Based on R/S Analysis and the Finite Difference Method: A Case Study from the Chang 6 Reservoir in Huaqing Oilfield, Ordos Basin. *J. Pet. Sci. Eng.* 174, 1169–1178. doi:10.1016/j.petrol.2018.12.017

Yin, H., Zhao, J., Tang, G., Zhao, L., Ma, X., and Wang, S. (2017). Pressure and Fluid Effect on Frequency-dependent Elastic Moduli in Fully Saturated Tight sandstone. *J. Geophys. Res. Solid Earth* 122, 8925–8942. doi:10.1002/2017JB014244

Zhang, L., Ba, J., Fu, L., Carcione, J. M., and Cao, C. (2019). Estimation of Pore Microstructure by Using the Static and Dynamic Moduli. *Int. J. Rock Mech. Mining Sci.* 113, 24–30. doi:10.1016/j.ijrmms.2018.11.005

Zhu, R., Zou, C., Zhang, N., Wang, X., Cheng, R., Liu, L., et al. (2008). Diagenetic Fluids Evolution and Genetic Mechanism of Tight sandstone Gas Reservoirs in Upper Triassic Xujiahe Formation in Sichuan Basin, China. *Sci. China Ser. D-earth Sci.* 51 (9), 1340–1353. doi:10.1007/s11430-008-0102-8

Conflict of Interest: The authors declare that the research was conducted in the absence of any commercial or financial relationships that could be construed as a potential conflict of interest.

Copyright © 2021 Cheng, Ba, Carcione, Pang and Wu. This is an open-access article distributed under the terms of the Creative Commons Attribution License (CC BY). The use, distribution or reproduction in other forums is permitted, provided the original author(s) and the copyright owner(s) are credited and that the original publication in this journal is cited, in accordance with accepted academic practice. No use, distribution or reproduction is permitted which does not comply with these terms.

frontiers in Earth Science

ORIGINAL RESEARCH
published: 29 June 2021
doi: 10.3389/feart.2021.673753

Digital Rock Physics: A Geological Driven Workflow for the Segmentation of Anisotropic Ruhr Sandstone

Martin Balcewicz[1,2], Mirko Siegert[1,2], Marcel Gurris[1], Matthias Ruf[3], David Krach[3], Holger Steeb[3,4] and Erik H. Saenger[1,2,5]*

[1]Reservoir Engineering and Rock Physics, Bochum University of Applied Sciences, Bochum, Germany, [2]Institut für Geologie, Mineralogie und Geophysik, Ruhr-Universität Bochum, Bochum, Germany, [3]Institute of Applied Mechanics (CE), University of Stuttgart, Stuttgart, Germany, [4]Stuttgart Centre for Simulation Technology, University of Stuttgart, Stuttgart, Germany, [5]Fraunhofer-Einrichtung für Energieinfrastrukturen und Geothermie IEG, Bochum, Germany

Over the last 3 decades, Digital Rock Physics (DRP) has become a complementary part of the characterization of reservoir rocks due to the non-destructive testing character of this technique. The use of high-resolution X-ray Computed Tomography (XRCT) has become widely accepted to create a digital twin of the material under investigation. Compared to other imaging techniques, XRCT technology allows a location-dependent resolution of the individual material particles in volume. However, there are still challenges in assigning physical properties to a particular voxel within the digital twin, due to standard histogram analysis or sub-resolution features in the rock. For this reason, high-resolution image-based data from XRCT, transmitted-light microscope, Scanning Electron Microscope (SEM) as well as geological input properties like geological diagenesis, mineralogical composition, sample's microfabrics, and estimated sample's porosity are combined to obtain an optimal spatial segmented image of the studied Ruhr sandstone. Based on a homogeneity test, which corresponds to the evaluation of the gray-scale image histogram, the preferred scan sample sizes in terms of permeability, thermal, and effective elastic rock properties are determined. In addition, these numerically derived property predictions are compared with laboratory measurements to obtain possible upper limits for sample size, segmentation accuracy, and a geometrically calibrated digital twin of the Ruhr sandstone. The comparison corresponding gray-scale image histograms as a function of sample sizes with the corresponding advanced numerical simulations provides a unique workflow for reservoir characterization of the Ruhr sandstone.

Keywords: digital rock physics, anisotropy, multi-phase segmentation, digital twin, pore network, tight sandstone, high-resolution x-ray computed tomography

OPEN ACCESS

Edited by:
Pascal Audet, University of Ottawa, Canada

Reviewed by:
Steffen Berg, Shell, Netherlands
Arne Jacob, Johannes Gutenberg University Mainz, Germany

****Correspondence:***
Martin Balcewicz
martin.balcewicz@hs-bochum.de

Specialty section:
This article was submitted to Solid Earth Geophysics, a section of the journal Frontiers in Earth Science

Received: *28 February 2021*
Accepted: *04 June 2021*
Published: *29 June 2021*

Citation:
Balcewicz M, Siegert M, Gurris M, Ruf M, Krach D, Steeb H and Saenger EH (2021) Digital Rock Physics: A Geological Driven Workflow for the Segmentation of Anisotropic Ruhr Sandstone. Front. Earth Sci. 9:673753. doi: 10.3389/feart.2021.673753

1 INTRODUCTION

Digital Rock Physics (DRP) and its use of non-destructive methods to determine permeability or effective elastic rock properties have become a complementary part in reservoir characterization over the past 3 decades (e.g., Blunt and King, 1991; Iassonov et al., 2009; Andrä et al., 2013a; Andrä et al., 2013b). Whether in estimating the total reservoir volume, potential reservoir production rates, or interpreting seismic lines above reservoirs, DRP contributes in all major subfields (e.g., Fan et al., 2010; Aljamaan et al., 2017). To cover the increasing demand for energy supply (e.g., Scheer et al.,

2013; Araújo, 2014) and to achieve the climate targets that have been set (e.g., Rogelj et al., 2016), currently non-fossil reservoirs are studied, such as in geothermal energy projects (e.g., Fridleifsson et al., 2008; Goldstein et al., 2011). For this purpose, the determination of the thermal conductivity, as well as the heat capacity, is becoming increasingly important in DRP. In the course of future regional explorations of the geothermal potentials in North Rhine-Westfalia, western Germany (e.g., Knutzen, 2017; Lippert et al., 2019; Kruszewski et al., 2020; Weiß, 2020; Balcewicz et al., 2021a; Jüstel, 2021; Lippert et al., 2021), results from DRP will become more important for this region. The Ruhr sandstone is to be the start of a comprehensive DRP investigation of the Upper Carboniferous Ruhr cyclothem, which occupies a predominant part in the Rhine-Ruhr metropolitan region, featuring the largest European district heating network (AGFW, 2009). One of the essential questions to be answered in the coming years is: Which geological horizons are suitable for geothermal projects? DRP will be used to further investigate the specific rock properties of the Ruhr sandstone, which so far can only be answered with great effort using classical laboratory methods.

Although high-resolution X-Ray Computed Tomography (XRCT) technology has opened up many possibilities through the visualization of the third spatial plane, it is not a stand-alone tool for material characterization (e.g., Holzer and Cantoni, 2012). This is especially true for fine-pored phases in carbonates or grain and phase boundaries in general (e.g., Saenger et al., 2016b). Nevertheless, in order to use the three-dimensional information provided by XRCT, it is necessary to utilize additional sources of information. An already established source of information is laboratory measurements that can provide rock properties such as permeability or porosity at ambient or elevated pressure and temperature conditions (e.g., Ahrens et al., 2018; Schepp and Renner, 2021). However, such laboratory measurements are resource and cost intensive, which is why the application of DRP is particularly interesting for small sample quantities. Nevertheless, basic laboratory measurements are helpful for appropriate XRCT interpretation, but they are not sufficient. Recent studies have already shown that by using additional imaging techniques (e.g., transmitted light microscope or Scanning Electron Microscope, SEM), features unrecognized by the XRCT can be visualized and implemented into the digital rock model (e.g., Saxena et al., 2017; Karimpouli et al., 2019). However, an additional source of information should always be the rock's provenance. Especially in geological formations, diagenesis as well as the current geological setting is of crucial importance and can lead to internal changes in the rock at all scales. This study, therefore, focuses specifically on geologic features of the Ruhr sandstone formed during the diagenesis and the possibility of incorporating corresponding observations from thin sections into the segmentation process. In the context of the sandstone's microstructure, this study takes a special role compared to similar studies of the Berea sandstone or the Fontainebleau sandstone (e.g., Bourbie and Zinszner, 1985; Churcher et al., 1991; Øren and Bakke, 2003), since eight individual phases were assigned to the digital twin of the Ruhr sandstone, showing indications of pressure dependencies, microporosities, and phase transformations. However, the workflow presented in this study implies more than just the assignment of gray-scale intensities within the XRCT volume. Rather, it is a process that begins before the actual segmentation and ends with assigning physical mineral properties to the corresponding segmented phases, which properties may have to be adjusted due to the prevailing microstructure. The incorporation of geologically based information for geophysical interpretations is already well established in areas of image processing, such as seismic reflection image interpretation, large-scale velocity modeling, or time reverse imaging interpretations (e.g., Ritzmann et al., 2007; Finger and Saenger, 2020). In DRP, a comparable geological interpretation of gray-scale images is not well established, yet. Despite this, the combination of all information sources is indispensable to perform an appropriate rock characterization-especially when it comes to the interpretation of reduced image information such as the gray-scale images of a XRCT volume. To obtain meaningful results, a Representative Elementary Volume (REV) must be used for the respective numerical studies (Bear and Braester, 1972; Ostoja-Starzewski, 1999). A studied rock sample may show different grain sizes (from < 0.1 to > 60 mm) due to geologically induced processes. Increasing grain sizes must be compensated with an increasing sample size in order to meet representative sample criteria. However, increased sample sizes can lead to difficulties when using a XRCT [see Lambert–Beer's Law e.g., in Buzug (2011)]. Nevertheless, optimal spatial gray-scale images must be extensively processed before advanced numerical simulation results can be provided. This processing requires detailed knowledge of the material in order to assign physical mineral properties to the appropriate gray-scale intensities. Regarding the Ruhr sandstone, the basis for the correct assignment of the gray-scale intensities to the corresponding phases is geological property information such as phase and pore fractions, phase transitions, or the microstructures of the Ruhr sandstone. The technical assignment of gray-scale intensities to the corresponding phases, called segmentation, is a fast-developing aspect of DRP. Numerous mathematical approaches have already been used, such as gray-scale-filtering, gray-scale histogram processing, watershed algorithms, or the use of neural networks (e.g., Nehler, 2018; Karimpouli et al., 2019). The strengths of automated segmentation methods that are less prone to operator bias are increasingly being developed and applied (e.g., Schlüter et al., 2014; Khan et al., 2016). Nevertheless, advanced machine learning segmentation algorithms such as k-means clustering, fuzzy C-means clustering, or artificial neural networks need to be trained with a sufficient database (e.g., Chauhan et al., 2016; Alqahtani et al., 2021), which is not ensured in the present study of the Ruhr sandstone. At this stage of the study, no novel segmentation workflow can be presented that can reasonably prove itself against other segmentation methods. Rather, a possible segmentation approach is presented how a corresponding training dataset for possible unsupervized machine learning segmentation methods could look like. Due to the complex microstructure of the Ruhr sandstone, this training dataset requires extensive manual

processing, which is presented in this manuscript based on gray-scale thresholding. The presented method is highly susceptible to operator bias, but also allows manual assignment of gray-scale intensities in the complex microfabrics of the present Ruhr sandstone. Sensitivity studies have shown that even small segmentation inaccuracies due to operator bias can lead to significant errors in numerical characterization approaches, such as permeability measurements (e.g, Leu et al., 2014). For this reason, geologic verifications were implemented along the segmentation process to minimize the extent of inaccuracies. Numerous DRP studies focus on the distinction between pore space and solid phase, which is sufficient for numerical permeability approaches. However, in this study, a raw XRCT volume is used for one specific segmentation and then provided for modeling permeability, thermal, and effective elastic rock properties. Thus, the limitations will be discussed in more detail, which XRCT resolution (e.g., Saxena et al., 2018; Guan et al., 2019; Feng et al., 2020), segmentation accuracy (e.g., Leu et al., 2014; Garfi et al., 2020) or numerical application (e.g., Andrä et al., 2013b) is sufficient for the Ruhr sandstone.

Deriving permeability, thermal, or effective elastic rock properties from a digital twin require a five-step workflow: 1) Preparation of an XRCT volume, 2) tomographic reconstruction, 3) assessment and handling of the X-Ray artifacts 4) segmentation of pore and grain phases, respectively, and 5) solving equations due to the demanded properties. However, these strictly separated processes are increasingly becoming blurred by cross-process procedures, such as the process of reconstruction and segmentation (e.g., Yoon et al., 2010; Storath et al., 2015). This study will demonstrate that the derivation of a digital Ruhr sandstone twin cannot be reduced to just one of these five steps, but that the presented workflow is a cross-disciplinary method to produce reasonable numerical results for the complex microstructure of the Ruhr sandstone. Finally, the geological optimized digital twin can assist in minimizing the uncertainty of predicted rock properties at the mesoscopic and macroscopic scale in a non-destructive manner.

In the following, the geological formation of the Ruhr sandstone is presented first. Then, the Ruhr sandstone's microfabrics and basic laboratory methods are described. Finally, after presenting the laboratory and numerical results, we discuss the workflow as a tool for deriving the digital twin of the Ruhr sandstone.

2 MATERIALS AND METHODS

2.1 Geological Setting and Microfabrics Analysis of Ruhr Sandstone

The studied Ruhr sandstone from the Oberste quarry in Dortmund, Germany, is assigned to Namur B (Kaisberg) and Wesphalian A formation of the Upper Carboniferous. It is part of the Upper Carboniferous Ruhr cyclothem, which consists of clay-, silt-, mud-, sandstones and interbedded coal seams. These sedimentary deposits were chemically and mechanically compacted, folded, and faulted during the Hercynian orogeny. Therefore, paleo high burial depths of up to 6,000 m can be assigned to the Ruhr sandstone, which is located in a complex geologic setting in the Rhine-Ruhr metropolitan area (Drozdzewski, 1993; Karg et al., 2005).

The preparation of the studied thin sections was provided by the preparation facility of the Institute of Geology, Mineralogy, and Geophysics, at the Ruhr-Universität Bochum. Due to temporal tool limitations the thickness of the thin sections is 38 µm. This results in abnormal interference colors for the studied minerals (**Figure 1A**). The thin sections were digitized using the Keyence digital microscope, VHX-2000D, combined with a VH-Z100UR lens. The SEM images are open access and were acquired by the Ruhr-Universität Bochum using the high-resolution thermal-assisted field emission SEM Gemini2 Merlin HR-FESEM from ZEISS (Balcewicz et al., 2021c).

Typically, Ruhr sandstone consists mainly of quartz ca. 70 ± 5 %, feldspar ca. 10 ± 2 %, and clay and feldspar alterations ca. 15 ± 2 %, and minor constituents of iron oxides ($< 5 \pm 2$ %) (e.g., Kneuper, 1957; Rosenfeld, 1967; Duda and Renner, 2013; Stöckhert, 2015). The studied specimen consists mainly of quartz 70 ± 5 %, minor amount of feldspar phases like albite or orthoclase $< 5 \pm 2$ %, and 20 ± 2 % of feldspar altered phases like muskovite, sericite, kaolinite, as well as some illite, chlorite, and ankerite. Additionally, accessory minerals like zircon, tourmaline and pyrite are determined in the Ruhr sandstone (cf. Kneuper, 1957; Scherp, 1963; Rosenfeld, 1967). Furthermore, some grain conglomerates and a small amount of carbonates can be observed, which are most likely part of the feldspar altered matrix. The quartz grains show the largest shape with no systematic deviation from isometry or significant shape preferred orientation, and have a diameter of about 400 ± 200 µm. The clay-rich and sericite-rich matrix will be referred to as the sericitic phase in further discussions.

Quartz grains indicate both types of grain boundaries, high angle and low angle grain boundaries. Some grains show undulous extinction, other low angle boundaries have already transformed into quartz subgrains (**Figure 1A**). All intermediate steps of the transformation can be observed in the studied specimens. In addition, trans- and intragranular fluid inclusion trails can be observed in quartz (**Figure 1A**). Some high angle grain boundaries show sutured or concavo-convex grain boundaries. Further SEM analysis shows partially broken quartz grains in size between 10 and 100 µm (**Figure 1B**). The sericitic phase was pushed close to the quartz phase boundaries during diagenesis in the course of coalification, folding, overburdening, and alteration, indicating low porosity due to its cementing effect (e.g., Kneuper, 1957). In addition, the SEM images showed two types of pore spaces. On the one hand, free pore spaces corresponding to open cavities in the sandstone were found. On the other hand, pore spaces occupied by rock fragments such as debris or Quartzites could be identified (**Figures 1B,C**). The source of these fragments is mainly the host material. In the following, the pore spaces are referred to as clean pore (open cavities) and soiled pore (occupied by rock fragments). It is important to note that ankerite and bicarbonate solutions from mudstone deposits migrated into the Ruhr sandstone. Paleoenvironmental influences and precipitation of ankerite favored sericitization of the feldspars. This cementation

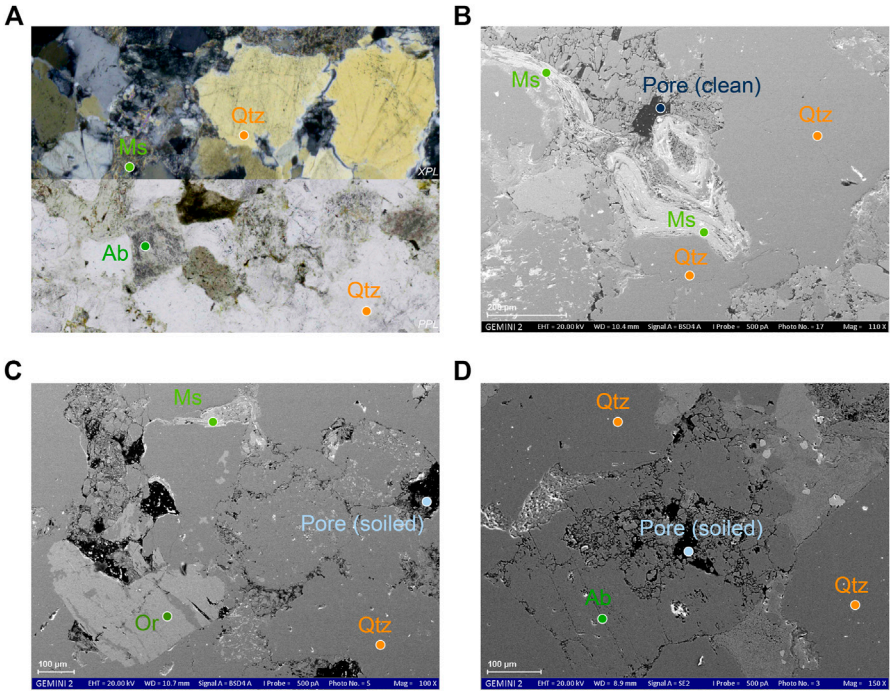

FIGURE 1 | (A) Thin section of Ruhr sandstone shown in the upper half in crossed polars (XPL) and in the lower half in plane light (PPL). SEM images of Ruhr sandstone showing **(B)** broken quartz grains, **(C)** soiled pore space, and resulting **(D)** microporosities due to the sericitization process in feldspars. The abbreviations of the rock-forming minerals like Qtz (quartz), Ms (muskovite), Ab (albite), and Or (orthoclase) are used according to Kretz (1983).

by silica occurred at all depths and resulted in a quartzitic grain-to-grain structure observed in the microstructure analysis, which was found to be clearly temperature and depth dependent (e.g., Scherp, 1963; Hesemann, 2013).

2.2 Laboratory Measurements: Petrophysical Characterization of Samples

Cored samples were drilled from a Ruhr sandstone cube with an edge length of 0.15 m. At the time of drilling, the orientation of the cube specimen in the field was not known. Nevertheless, macroscopic anisotropy was suspected, so the cube was cored in three direction x, y, and z. A total of 24 samples with a diameter of 20 mm and a mean length of 80 mm were extracted by diamond core drilling. Additionally, a cylindrical core sample with a diameter of 5 mm and a length of about 10 mm was extracted from x direction of the initial Ruhr sandstone cube for a high-resolution XRCT image. All samples were sawed perpendicular to the sample axis and their faces were ground square to the maximum possible length. All steps of the preparation were performed with water as the cooling medium. Basic petrophysical properties were determined on identically prepared samples at ambient conditions.

Bulk density ρ_{geo} was derived by the geometrical volume of the cylindrical samples and their dry masses. The grain density ρ_{grain} was determined by pycnometer measurements from rock powder according to the German standard (Normenausschuss Bauwesen (NABau), 2011). The total porosity results from the ratio between bulk density and grain density according to $\phi_{tot} = 1 - (\rho_{geo}/\rho_{grain})$. The connected porosity was determined from the mass difference of dry and distilled water saturated samples (see Duda and Renner, 2013).

The ultrasonic P-and S-wave velocities, v_P and v_S, were picked by hand on dry samples based on the first arrival times of the detected wavefront. Therefore, an ultrasonic device consisting of a waveform generator, two identical broadband ultrasonic sensors and a digital storage oscilloscope was used. The two identical broadband ultrasonic sensors were placed on the two ground head surfaces, resulting in measurements parallel to the drilling direction. P-and S-wave velocities were calculated by dividing the sample length by the determined arrival times less the internal device run time.

Thermal conductivity λ_{dry}, thermal effusivity e_{dry} and specific heat capacity c_{dry} was determined with a thermal conductivity scanner from C-therm using a modified transient surface source (MTPS) at ambient conditions. The samples were installed in the direction of drilling, i.e., the bottom surfaces of the samples were treated with a thermal paste and then placed on the MTPS. Within the MTPS, a helical heating element is surrounded by a guard ring that supports one-dimensional heat transfer into the sample. The small amount of heat supplied results in a temperature rise at the interface between the sensor and the sample, which induces a change in the voltage drop of the sensing element. The rate of rise of the sensor voltage, which is factory calibrated to temperature, is used to determine the thermal properties of the sample. The precision and accuracy are

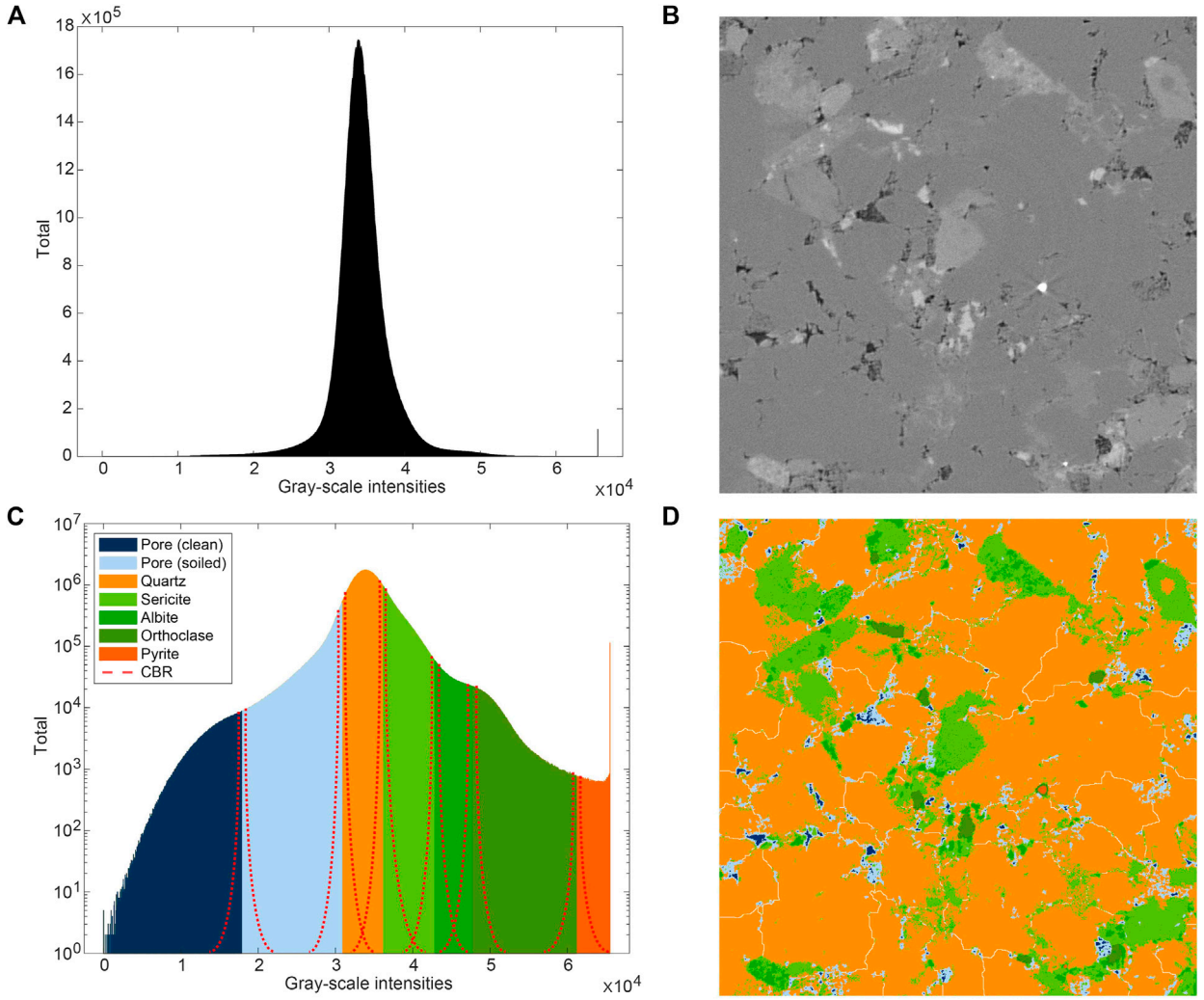

FIGURE 2 | (A) Gray-scale intensities after a subsequent 2 × 2 × 2 binning operation resulting from the XRCT volume and a corresponding slice in **(B)** with an edge length of 800 pixel. **(C)** Segmented gray-scale intensities color-coded with corresponding segmented phases. Note that the color-coded boundaries reflect the selected gray-scale intensity, but should not be interpreted as strict boundaries between two phases. Rather, the phase boundaries show overlapping characteristics that were adjusted by morphological post-processing operations (Sheppard et al., 2004; Jones et al., 2007). These critical areas between two phases are indicated by the critical boundary regions (CBR). **(D)** Segmented result with corresponding gray-scale intensities **(C)** of slice **(B)**. Additionally, high angle quartz grain boundaries are implemented by the watershed-algorithm in a white color. The figures were created with Avizo (2019) and Matlab (2020).

specified by C-therm and correspond to better than 1% and better than 5% respectively.

2.3 Imaging and Processing of Ruhr Sandstone

The scan of the sample was performed in a self-built, modular µXRCT system employing an open micro-focus tube *FineTec FORE 180.01C TT* with a tungsten transmission target from Finetec Technologies GmbH, Germany in combination with a *Shad-o-Box 6K HS* detector with a CsI scintillator option from Teledyne DALSA Inc., Waterloo, Ontario, Canada. Latter provides a resolution of 2,940 × 2,304 pixel with a pixel size of 49.5 µm (see Ruf and Steeb, 2020). The geometric magnification for the scan was set to 24.78 which leads to the highest achievable spatial resolution of about 50 linepairs/mm of the system for 10% Modulation Transfer Function (MTF) (cf. Rossmann, 1969). The corresponding voxel size results in 2 µm. The X-ray tube voltage was set to 80 kVp and the tube flux to 120 µA. The resulting X-ray spectrum was additionally modified by the usage of a 0.5 mm thick Aluminium-filter. In total 1,800 projections angles were used with an exposure time of 3,000 ms each. The reconstruction was performed with the filtered back projection method using the software Octopus Reconstruction (Version 8.9.4–64 bit), Vlassenbroeck et al. (2007). The resulting data set consists of 2,940 × 2,940 × 2,141 voxel and shows a physical volume of 5.88 × 5.88 × 4.28 mm^3. Consequently, the sample was scanned over the entire diameter of 5 mm and allows

basically the definition and extraction of an appropriate REV. The XRCT dataset and associated metadata of the scan settings are open access (Ruf et al., 2021). The corresponding gray-scale intensities of the μXRCT volume and one characteristic 2D slice are shown in **Figures 2A,B**.

The voxel size v_{size} of the tomogram is the result of the employed geometric magnification M and the given pixel size p_{size} of the detector, $v_{size} = p_{size}/M$ holds. The maximum spatial resolution of the system is about 50 linepairs/mm at 10% of the MTF (cf. Ruf and Steeb, 2020). This corresponds to a resolvable feature size of about 10 μm. Therefore, most features should be preserved and no significant information loss should occur if the data set is sub-sampled to a uniform voxel edge length of 4 μm. With this motivation, a subsequent $2 \times 2 \times 2$ binning of the raw tomogram data was performed to reduce the data set size. Before this, a $1{,}600^3$ voxel subvolume was extracted from the center of the original XRCT volume which corresponds to x = (650, 2,249), y = (750, 2,349), and z = (0, 1,599). Thus, the final voxel size after the performed binning of the 800^3 voxel subvolume is 4 μm. This allows easier data handling and due to the limitation of the numeric simulation schemes, with respect to the maximum number of possible degrees of freedom, to cover a larger field of view. In addition, the $1{,}600^3$ voxel subvolume was reduced again by a factor of $4 \times 4 \times 4$, taking into account the loss of information. Thus, the 400^3 subvolume's voxel size is 8 μm. Both binned subvolumes are published open access (Balcewicz et al., 2021b). Considering the number of largest grains per edge length of the initial $1{,}600^3$ voxel subvolume, a REV of the Ruhr sandstone can be assumed (Saxena et al., 2019). A detailed REV analysis should follow the approach of Ostoja-Starzewski (1999), which is beyond the scope of this study.

TABLE 1 | Matrix properties determined by laboratory measurements on Ruhr sandstone samples from the Oberste quarry in Dortmund. All measurements were conducted at ambient conditions. The abbreviations RSST and e.g., X indicate the rock sample Ruhr sandstone and the drilled direction from the parent cube, respectively.

Sample	L	ρ_{geo}	ρ_{grain}	ϕ_{tot}	ϕ_{con}
	(m)	(kg m^{-3})	(kg m^{-3})	(%)	(%)
RSST-X-01	0.086	2,498 ± 13	2,670 ± 1	6.4 ± 1.9	3.0 ± 0.4
RSST-X-02	0.086	2,499 ± 13	2,671 ± 1	6.4 ± 1.9	4.5 ± 0.6
RSST-X-03	0.087	2,499 ± 13	2,669 ± 1	6.4 ± 1.9	5.0 ± 0.7
RSST-X-04	0.086	2,505 ± 13	2,679 ± 1	6.5 ± 1.9	5.1 ± 0.7
RSST-X-05	0.087	2,506 ± 13	2,721 ± 1	7.9 ± 1.8	4.9 ± 0.7
RSST-X-06	0.087	2,508 ± 13	2,705 ± 1	7.3 ± 1.8	6.3 ± 0.9
RSST-X-07	0.086	2,505 ± 13	2,687 ± 1	6.8 ± 1.9	5.3 ± 0.8
RSST-X-08	0.094	2,503 ± 13	2,673 ± 1	6.4 ± 1.9	4.9 ± 0.7
RSST-X-09	0.092	2,495 ± 13	2,675 ± 1	6.7 ± 1.9	5.2 ± 0.7
RSST-X-10	0.094	2,490 ± 13	2,681 ± 1	7.1 ± 1.9	5.8 ± 0.8
RSST-Y-01	0.093	2,498 ± 13	2,674 ± 1	6.6 ± 1.9	6.1 ± 0.9
RSST-Y-02	0.093	2,496 ± 13	2,678 ± 1	6.8 ± 1.9	4.9 ± 0.7
RSST-Y-03	0.093	2,502 ± 13	2,671 ± 1	6.3 ± 1.9	5.6 ± 0.8
RSST-Y-04	0.094	2,501 ± 13	2,681 ± 1	6.7 ± 1.9	5.4 ± 0.8
RSST-Y-05	0.094	2,495 ± 13	2,676 ± 1	6.8 ± 1.9	5.6 ± 0.8
RSST-Y-06	0.094	2,493 ± 13	2,677 ± 1	6.9 ± 1.9	5.1 ± 0.7
RSST-Z-01	0.093	2,505 ± 13	2,667 ± 1	6.1 ± 1.9	3.9 ± 0.5
RSST-Z-02	0.089	2,509 ± 13	2,685 ± 1	6.5 ± 1.9	5.2 ± 0.7
RSST-Z-03	0.091	2,500 ± 13	2,684 ± 1	6.8 ± 1.9	5.1 ± 0.7
RSST-Z-04	0.092	2,506 ± 13	2,568 ± 1	6.1 ± 1.9	4.6 ± 0.7
RSST-Z-05	0.093	2,506 ± 13	2,689 ± 1	6.8 ± 1.9	6.4 ± 0.9
RSST-Z-06	0.092	2,507 ± 13	2,686 ± 1	6.7 ± 1.9	5.5 ± 0.8
RSST-Z-07	0.092	2,505 ± 13	2,678 ± 1	6.5 ± 1.9	5.2 ± 0.7
RSST-Z-08	0.088	2,508 ± 13	2,657 ± 1	5.6 ± 1.9	5.0 ± 0.7

l: sample length; ρ_{geo}: bulk density; ρ_{grain}: grain density; ϕ_{tot}: total porosity; ϕ_{con}: connected porosity. Quoted uncertainties reflect accuracy of the measurements.

2.4 Initial Ruhr Sandstone Segmentation

Based on the microfabrics analysis, eight phases were segmented in the respective 800^3 and 400^3 voxel subvolumes: 1) clean pore, 2) soiled pore, 3) quartz, 4) sericitic phase, 5) albite, 6) orthoclase, 7) pyrite, and 8) quartz high angle phase boundaries. All segmentation was done in Avizo (2019) with basic installed modules. Both segmented subvolumes are open access (Balcewicz et al., 2021b). All applied segmentation processes are based on simplified gray-scale thresholding methods which are probably the simplest way to binarize an image. Nevertheless, some adjustments were made to avoid known problems such as overlapping phase boundaries (e.g., Sheppard et al., 2004). The applied segmentation can thus basically be assigned to the supervised multistage approaches (e.g., Sezgin and Taşaltın, 2000; Wu and Amin, 2003). Starting with a global threshold value that roughly divides the Ruhr sandstone into the individual phases, followed by a local threshold to incorporate additional information such as geological input parameters into the segmentation. In the course of adaptive methods, morphological post-processing operators such as "remove small holes" or logical difference operators were used (**Table 3**).

After the initial gray-scale thresholding, a geologic review was performed before further steps could be applied. During the geological review, the segmented image was compared and evaluated with thin section images, SEM images, and porosity measurements. The geological verification may result in some modifications to the segmented image, such as fitting the pore space or elimination of incorrectly assigned phases due to X-ray artifacts. The geological verification was based on qualitative and quantitative evaluation criteria such as adjacent mineral phases or calculation of pore space (**Table 1**; c.f. **Table 3**). This process of adjusting the initial segmentation results was repeated until the geologic input parameters, such as phase or porosity fractions, approximately matched the binarized phases.

After all individually segmented phases passed the geologic verification, a location-dependent model of the digital Ruhr sandstone twin was generated. This includes the merging of seven individually segmented phases into a single binary object. Afterwards, a watershed algorithm was applied to the segmented volume according to Beucher and Meyer (1992) to automatically assign unassigned voxels to the appropriate phases. The watershed algorithm is based on the idea of a gray-scale image interpreted as a topographic relief, provided that the pixel values are considered as altitudes. Based on this idea, the watershed algorithm calculates the catchment basin located between two maxima. These catchment basins define the image partitions. This results into a simplified digital twin of the Ruhrsandstone.

In a final step, the quartz grain boundaries were added to the Ruhr sandstone model. For this purpose, the quartz phase was isolated from the rest of the location-dependent digital twin and processed individually. The "separate objects" module was used

to implement grain boundaries. This module is a high-level combination of watershed, distance transform, and numerical reconstruction algorithms which computes the watershed lines of a binary image. The selected properties are 3D interpretation, voxels with a least one common vertex are considered connected, marker extent is set to seven, output type is set to line, and a repeatable algorithm method for a conservative chosen method. Followed by an erosion module to set the quartz boundaries to a maximum size of one voxel. Finally, all segmented phases were merged resulting into the digital twin of the Ruhr sandstone (**Figure 2D**).

2.5 Modelling Permeability, Thermal, and Effective Elastic Rock Properties

Smoothed Particle Hydrodynamics (SPH) is a fully-Lagrangian mesh-free collocation method, which has proven feasible for the calculation of flows through porous materials. In SPH the continuous weakly compressible Navier–Stokes equations are transformed in discrete summation of short-range interaction forces.

For the calculation of the permeabilities the 400^3 voxel subvolume was used which corresponds to a number of about $16 \cdot 10^6$ degrees of freedom (DOF) after subtracting non-essential solid fractions. For the simulation, the HOOSPH code was used in which the specific SPH-particle-particle interactions are implemented and that is based on HOOMD-blue (Anderson et al., 2008; Glaser et al., 2015). This is a rather computationally expensive method but has shown to be highly suitable for effective permeability computations of porous rocks in the Darcy and weak inertia regime as well as with onset of more pronounced inertia effects (Sivanesapillai et al., 2014; Osorno et al., 2020).

In order to determine the effective thermal conductivity, the steady-state heat conduction equation is solved using the finite volume method (Siegert et al., 2021). To limit the numerical error, the interfacial conductivity is modelled with two different averaging approaches, namely the harmonic mean (HM) and the arithmetic mean (AM). Each phase of the numerical model is assigned a fixed thermal conductivity to determine the effective thermal conductivity of the entire sample, these are: $\lambda_{air} = 0.026\ W\,(mK)^{-1}$, $\lambda_{sericitic} = \lambda_{muscovite} = 2.28\ W\,(mK)^{-1}$, $\lambda_{albite} = 2.14\ W\,(mK)^{-1}$, $\lambda_{orthoclase} = 2.31\ W\,(mK)^{-1}$, and $\lambda_{pyrite} = 19.21\ W\,(mK)^{-1}$ (e.g., Clauser and Huenges, 2013). Considering the observed reduced physical properties of quartz in Saenger et al. (2016a), the original literature value of the thermal conductivity of quartz was reduced by 27.75%, resulting in $\lambda_{quartz} = 5.56\ W\,(mK)^{-1}$.

Effective elastic P- and S-wave velocity were derived by using the rotated staggered finite difference grid technique (Saenger and Bohlen, 2004). This numerical scheme allows modeling of seismic waves in complex viscoelastic and anisotropic media with strong contrast interfaces of arbitrary shape. All calculations were performed with second-order spatial finite-difference operators and with a second-order time update. The method was successfully compared with other approaches (see in Andrä et al., 2013b; Saxena et al., 2019). The segmented phases (A) clean pore, (B) soiled pore, (C) quartz, (D) sercitic phase, (E) albite, (F) orthoclase, and (G) pyrite were assigned with the corresponding elastic moduli c_{11}, c_{44}, and $\rho_{solid-phase}$: (A,B) 0.0 and 0.0 GPa, (C) 68.0 GPa, 33.5 GPa, and 2,648 kgm^{-3}, (D) 184.3 GPa, 16.0 GPa, and 2,844 kgm^{-3}, (E) 74.0 GPa, 17.3 GPa, and 2619 kgm^{-3}, (F) 67.0 GPa, 14.3 GPa, and 2,575 kgm^{-3}, (G) 361.0 GPa, 105.2 GPa, and 5,016 kgm^{-3}, respectively (Bass, 1995; Saenger et al., 2016a). Additionally, for the $800^3_{watershed}$ and $400^3_{watershed}$ subvolumes the quartz grain boundaries were assigned with half the elastic moduli of the host mineral, i.e., $c_{11,\,watershed} = 0.5 \times c_{11,\,qtz}$ and $c_{44,watershed} = 0.5 \times c_{44,\,qtz}$. This factor was determined within the numerical studies as a result of a first calibration approach.

3 RESULTS

3.1 Laboratory Characterizations

Twenty-four samples were obtained from one Ruhr sandstone cube with an edge length of 0.15 m. Samples were drilled parallel to the three directions *x*, *y*, and *z*. All ten samples drilled in the *x* direction showed macroscopic indications of weathering, which decreased gradually from top to bottom. Except for this, no large fractures were observed in the Ruhr sandstone. The mean grain densities of the samples retrieved from *x*, *y*, and *z* direction are 2,676 ± 1, 2,632 ± 1, and 2,647 ± 1 kgm^{-3}, respectively (**Table 1**). Considering the measurement uncertainty and standard deviation, all studied samples showed comparable densities.

Mean total and connected porosity results show slightly higher total and connected porosities for samples drilled in *x* direction. The derived mean total porosities are 6.58 ± 1.87, 5.13 ± 1.90, and 5.37 ± 1.88% in *x*, *y*, and *z* direction, respectively (**Table 1**). Maximum and minimum derived total porosities show results of 7.89 and 6.07%, respectively. Connected porosity results show a similar trend, revealing 5.53 ± 0.78, 5.45 ± 0.77, and 5.10 ± 0.72% for samples taken from *x*, *y*, and *z* direction, respectively. However, a maximum connected porosity was determined in sample RSST-Z-05 with 6.42%. Corresponding minimum result was determined for sample RSST-X-01 sampled from *x* direction.

Ultrasound P- and S-wave velocities of dry Ruhr sandstone range between 4,667 and 2,303 ms^{-1}, respectively (**Table 2**). P-wave velocities measured in *x* direction appear to be up to 300 ms^{-1} lower than corresponding measurements in *y* and *z* direction. P-wave velocities measured in *y* direction show the highest values of about 4,667 ms^{-1}. Equivalent measurements in *z* direction show a small variation from P-wave velocities determined in *y* direction. The mean P-wave velocities for *x*, *y*, and *z* directions are 4,363, 4,644, and 4,542 ms^{-1}, respectively. Similar to the P-wave velocities, determined S-wave velocities in *x* direction appeared to be the lowest among all measurements. Mean S-wave velocities for *x*, *y*, and *z* direction are 2,368, 2,507, and 2,558 ms^{-1}, respectively.

Thermal conductivity results show similar values for samples oriented in *y* and *z* direction. The derived maximum and minimum thermal conductivity for samples oriented in *y* and *z* direction are 3.64 and 4.03 W $(mK)^{-1}$, respectively. Mean thermal conductivity results for samples oriented in y or *z* direction are 3.96 and 3.87 W $(mK)^{-1}$ (**Table 2**). Compared to this, samples oriented in *x* direction show a lower thermal conductivity on average. Here,

TABLE 2 | Ultrasound velocities, thermal conductivity, thermal effusivity, and specific heat capacity derived by laboratory measurements for Ruhr sandstone from Oberste quarry in Dortmund. All measurements were conducted at ambient conditions. The abbreviations RSST and e.g., X indicate the rock sample Ruhr sandstone and the drilled direction from the parent cube, respectively.

Sample	$v_{P,dry}$	$v_{S,dry}$	$\lambda_{dry,bottom}$	$e_{dry,bottom}$	$c_{dry,bottom}$
	(m s^{-1})	(m s^{-1})	[W $(mK)^{-1}$]	[$Ws^{-1/2}(m^2K)^{-1}$]	[J $(kgK)^{-1}$]
RSST-X-01	4,372 ± 20	2,418 ± 150	–	–	–
RSST-X-02	4,335 ± 30	2,303 ± 160	–	–	–
RSST-X-03	4,382 ± 20	2,391 ± 170	–	–	–
RSST-X-04	4,350 ± 20	2,367 ± 160	–	–	–
RSST-X-05	4,355 ± 30	2,347 ± 140	–	–	–
RSST-X-06	4,300 ± 20	2,318 ± 180	3.32 ± 0.17	2,601 ± 130	812 ± 41
RSST-X-07	4,387 ± 20	2,359 ± 150	3.61 ± 0.18	2,742 ± 137	831 ± 42
RSST-X-08	4,399 ± 40	2,361 ± 160	3.47 ± 0.17	2,674 ± 134	823 ± 41
RSST-X-09	4,361 ± 20	2,318 ± 160	3.32 ± 0.17	2,601 ± 130	816 ± 41
RSST-X-10	4,386 ± 20	2,498 ± 170	3.48 ± 0.17	2,678 ± 134	827 ± 41
RSST-Y-01	4,627 ± 30	2,556 ± 150	3.99 ± 0.20	2,919 ± 146	854 ± 43
RSST-Y-02	4,667 ± 20	2,411 ± 160	3.96 ± 0.20	2,908 ± 145	853 ± 43
RSST-Y-03	4,635 ± 20	2,563 ± 180	3.93 ± 0.20	2,890 ± 144	849 ± 42
RSST-Y-04	4,614 ± 20	2,548 ± 220	3.92 ± 0.20	2,886 ± 144	849 ± 42
RSST-Y-05	4,666 ± 30	2,558 ± 280	3.92 ± 0.20	2,886 ± 144	850 ± 43
RSST-Y-06	4,653 ± 20	2,407 ± 290	4.00 ± 0.20	2,924 ± 146	856 ± 43
RSST-Z-01	4,635 ± 14	2,549 ± 140	4.04 ± 0.20	2,941 ± 147	853 ± 43
RSST-Z-02	4,505 ± 20	2,482 ± 170	3.88 ± 0.19	2,867 ± 143	844 ± 42
RSST-Z-03	4,506 ± 10	2,845 ± 110	3.94 ± 0.20	2,896 ± 145	850 ± 43
RSST-Z-04	4,527 ± 20	2,514 ± 160	3.94 ± 0.20	2,895 ± 145	847 ± 42
RSST-Z-05	4,474 ± 30	2,553 ± 170	3.95 ± 0.20	2,899 ± 145	848 ± 42
RSST-Z-06	4,598 ± 40	2,524 ± 140	3.86 ± 0.19	2,861 ± 143	843 ± 42
RSST-Z-07	4,589 ± 20	2,530 ± 200	3.75 ± 0.19	2,807 ± 140	837 ± 42
RSST-Z-08	4,505 ± 20	2,466 ± 160	3.64 ± 0.18	2,755 ± 138	830 ± 42

$v_{P,dry}$, $v_{S,dry}$: P- and S-wave velocity of dry samples; $\lambda_{dry,bottom}$: thermal conductivity of dry samples; $e_{dry,bottom}$: thermal effusivity dry samples; $c_{dry,bottom}$: specific heat capacity for dry Ruhr sandstone samples. Quoted uncertainties reflect accuracy of the measurements.

the mean thermal conductivity is 3.44 W $(mK)^{-1}$. The mean measured thermal effusivity for samples in x direction is 2,659 $Ws^{-1/2}(m^2K)^{-1}$ with a minimum and maximum thermal effusivity of 2,601 and 2,678 $Ws^{-1/2}(m^2K)^{-1}$, respectively. Samples oriented in y and z direction show a mean thermal effusivity of 2,902 and 2,865 $Ws^{-1/2}(m^2K)^{-1}$, respectively. The maximum thermal effusivity was measured for sample RSST-Z-01 with a result of 2,941 $Ws^{-1/2}(m^2K)^{-1}$. Average derived thermal heat capacities were measured for the same amount of samples as thermal conductivity and thermal effusivity. The mean thermal heat capacities for samples taken from x, y, and z direction are 822, 852, and 844 J $(kg\ K)^{-1}$, respectively (**Table 2**).

3.2 Digital Rock Physics Results

The presented segmentation resulted in the corresponding fractions for both 800^3 voxel subvolume phases (A–G) and 400^3 voxel subvolume phases (see **Table 3**; A'–G'): (A) clean pore phase 0.38%, (B) soiled pore phase 6.11%, (C) quartz 72.71%, (D) sericitic phase 16.71%, (E) albite 1.38%, (F) orthoclase 1.48%, and (G) pyrite 0.05%. The implemented high angle quartz grain boundary fractions are 1.16 and 1.58% for both subvolumes 800^3 and 400^3 voxel, respectively. The total porosity showed 6.50 and 8.51% for 800^3 and 400^3 voxel subvolumes, respectively. For connected porosity further distinctions can be made like the considered connectivity between measured voxels. For example, considering that at least one common vertex should be analyzed for the segmented pore voxels, the connected porosity for the 800^3 voxel subvolume is 4.65 percent. In case of the 400^3 voxel subvolume, the connected porosity is 6.59% (**Table 4**). Considering the mentioned porosities, this results in a higher total and connected porosity for the 400^3 voxel subvolume by 2.01 and 1.94%, respectively. All segmented label analysis was derived by Avizo (2019) modules [e.g., volume fraction, axis connectivity, and label analysis; see in Thermo Fisher Scientific (2018)].

Numerical permeability was calculated using the SPH method for the 400^3 voxel subvolume with a total and connected porosity of 8.51 and 6.59%, respectively. Using a body force **b** as the driving force, all components of the intrinsic permeability tensor can be determined as follows

$$\boldsymbol{k}^I = \begin{bmatrix} 5.9710 & 0.00376 & 0.00519 \\ 0.00343 & 5.5045 & 0.00478 \\ 0.00294 & 0.00537 & 5.4968 \end{bmatrix} \cdot 10^{-12}\,\mathrm{m}^2. \quad (1)$$

The entries that do not lie on the main diagonal can be computed using the entries in the velocity vector perpendicular to the direction of the driving force. In this case, however, these are in the small single-digit per mille range relative to the main diagonal. Thus, a consideration of k^I_{11}, k^I_{22}, and k^I_{33} is sufficient

TABLE 3 | Phase segmentation matrix with applied settings and derived phase quantities for the subvolumes of Ruhr sandstone 800^3 and 400^3 voxel.

Phase	Phase Index	Interactive Threshold	Remove small Spots/holes	Logical difference Operator	Amount* (%)
Pore (clean)	A	0–17,873	–	–	0.39
	A′	0–13,540	–	–	0.49
Pore (soiled)	B	0–30,872	10 px/ –	*B* – *A*	6.11
	B′	0–33,580	2 px/ –	*B*' – *A*'	8.02
Quartz	C	30,872–36,112	10010 px	*C* – *B*	72.71
	C′	33,581–39,962	510 px	*C*' – *B*'	69.78
Sericite	D	0–42,787	–	*D* – (*A* + *B* + *C*)	16.71
	D′	0–51,995	–	*D*' – (*A*' + *B*' + *C*')	18.57
Albite	E	42,788–47,662	– /100 px	*E* – *F*	1.38
	E′	51,996–58,709	– /10 px	–	0.20
Orthoclase	F	47,663–61,202	– /100 px	–	1.48
	F′	59,710–65,528	–	–	0.54
Pyrite	G	61,203–65,535	–	–	0.05
	G′	65,529–65,535	–	–	0.08

The phase indices A–G and A′–G′ correspond to the respective 800^3 and 400^3 voxel subvolumes; Interactive threshold indicates the selected gray-value intensities for the given phase; Logical difference operator illustrates the applied equations within Avizo (2019).

**The derived quantities also include the proportions of high angle quartz grain boundaries, which are assigned to the 800^3 and 400^3 voxel subvolumes with 1.16 and 1.58%, respectively.*

TABLE 4 | Derived porosity measurements considering three cases of segmented pore voxels obtained for the 800^3 and 400^3 voxel subvolume, respectively.

Subvolume size	Total porosity	Connected porosity		
		I	II	III
(Voxels)	(%)	(%)	(%)	(%)
800^3	6.50	2.68	4.56	4.65
400^3	8.51	4.52	6.49	6.59

I: voxels with a common face are considered connected; II: voxels with at least one common edge are considered connected; III: voxels with at least one common vertex are considered connected.

to make a statement about anisotropy of the investigated subvolume.

The segmented 800^3 and 400^3 voxel subvolumes were further subdivided into: 1) $\text{subvolume}_{\text{watershed}}$, corresponding to the segmented digital twin with high angle quartz grain boundaries and 2) $\text{subvolume}_{\text{solid}}$, without watershed segmented quartz grain boundaries. This results in a total of 24 simulations for the thermal conductivity. Results based on the AM-approach for the $800^3_{\text{watershed}}$ voxel subvolume in *x*, *y*, and *z* direction are 4.049, 4.121, and 4.123 W $(\text{mK})^{-1}$, respectively. Corresponding results for

TABLE 5 | Correlation between laboratory and numerical derived results.

Sample Direction	Source	$v_{P,dry}$ (m s^{-1})	$v_{S,dry}$ (m s^{-1})	λ_{dry} [W $(\text{mK})^{-1}$]	*k* (m^2)
X	Laboratory	4,367 ± 24	2,371 ± 164	3.44 ± 0.17	–
	$800^3_{\text{watershed}}$	4,713	3,194	3.721	–
	800^3_{solid}	4,735	3,210	3.922	–
	$400^3_{\text{watershed}}$	4,591	–	3.512	5.971×10^{-12}
	400^3_{solid}	4,620	–	3.713	5.971×10^{-12}
Y	Laboratory	4,644 ± 23	2,507 ± 213	3.95 ± 0.20	–
	$800^3_{\text{watershed}}$	–	–	3.696	–
	800^3_{solid}	4,865	3,240	4.068	–
	$400^3_{\text{watershed}}$	4,729	–	3.541	5.5045×10^{-12}
	400^3_{solid}	–	–	3.879	5.5045×10^{-12}
Z	Laboratory	4,542 ± 22	2,558 ± 156	3.87 ± 0.19	–
	$800^3_{\text{watershed}}$	–	–	3.706	–
	800^3_{solid}	4,845	3,259	4.068	–
	$400^3_{\text{watershed}}$	4,740	–	3.546	5.4968×10^{-12}
	400^3_{solid}	–	–	3.880	5.4968×10^{-12}

$v_{P,dry}$, $v_{S,dry}$: P- and S-wave velocity of dry samples; λ_{dry}: thermal conductivity of dry samples; k: numerical derived permeability. Analysis of the total and connected porosity showed 6.50 and 4.65%, as well as 8.51 and 6.59% respectively for the respective 800^3 and 400^3 voxel subvolumes. Quoted uncertainties reflect accuracy of the measurements.

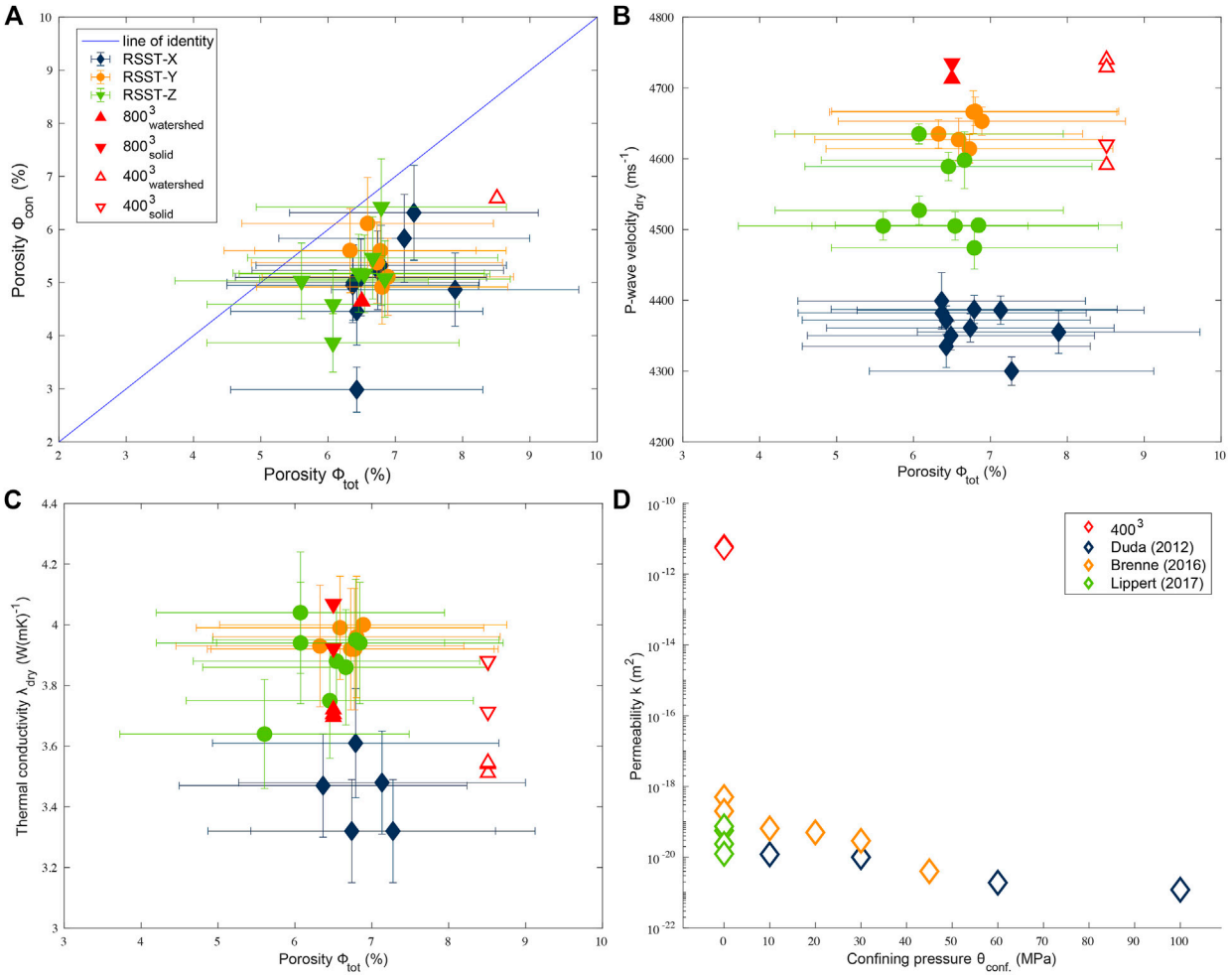

FIGURE 3 | Correlation between **(A)** connected and total porosity, **(B)** P-wave velocity and total porosity, **(C)** thermal conductivity and total porosity, and between **(D)** permeability and confining pressure [see permeability measurements in Duda (2012), Brenne (2016), Lippert (2017)]. Filling and coloring of markers indicate sample and sample direction, respectively. Measurement uncertainties are indicated by error bars. Where error bars do not exceed marker size, uncertainties appear to be small. The blue line in panel **(A)** indicates identity, i.e., connected porosity corresponds exactly to total porosity. Filled and unfilled red triangles indicate different numerical approaches for 800^3 and 400^3 voxel subvolumes, respectively. Measurements in panel **(A–C)** were conducted at ambient conditions. Laboratory measurements in panel **(D)** have not been determined in the scope of this study and can be looked up for detailed information in Duda (2012), Brenne (2016), Lippert (2017). The abbreviations RSST and e.g., X indicate the rock sample Ruhr sandstone and the drilled direction from the parent cube, respectively.

800^3_{solid} show 4.139, 4.246, and 4.247 W $(mK)^{-1}$ for *x*, *y*, and *z* directions, respectively. Lower results are derived for the simulations based on the HM-approach. Here, the results of the $800^3_{watershed}$ voxel subvolume are 3.721, 3.696, and 3.706 W $(mK)^{-1}$ for the *x*, *y*, and *z* directions. The corresponding results for the 800^3_{solid} voxel subvolume show higher values than for $800^3_{watershed}$ and read as 3.922, 4.068, and 4.068 W $(mK)^{-1}$ for *x*, *y*, and *z* directions, respectively.

Derived thermal conductivity results for the corresponding $400^3_{watershed}$ and 400^3_{solid} show comparable tendencies for the individual measurements. Simulations based on the AM-approach vary in the range of 3.902 and 4.115 W $(mK)^{-1}$ for $400^3_{watershed}$ and 400^3_{solid}. Results of the HM-approach vary in the range of 3.512 and 3.880 for the corresponding $400^3_{watershed}$ and 400^3_{solid} subsamples. This results in total lower values for 400^3 voxel subvolumes than for 800^3 voxel subvolumes and generally lower values for segmented digital twins with high angle quartz grain boundaries than for those without (cf. **Table 5** and **Figure 3**).

Effective P-and S-wave velocities were modelled for 800^3 and 400^3 voxel subvolumes of the Ruhr sandstone. Similar to thermal conductivity models, the segmented subvolumes were subdivided into $subvolume_{watershed}$ and $subvolume_{solid}$. Derived P- and S-wave velocities for the 800^3_{solid} voxel subvolume were modelled without the segmented high angle quartz grain boundaries and result in 4,735, 4,845, and 4,865 ms^{-1} for *x*, *y*, *z* directions, respectively. Determined S-wave velocities read as 3,210, 3,259, and 3,240 ms^{-1} for the corresponding $subvolume_{solid}$ in *x*, *y*, and *z* directions,

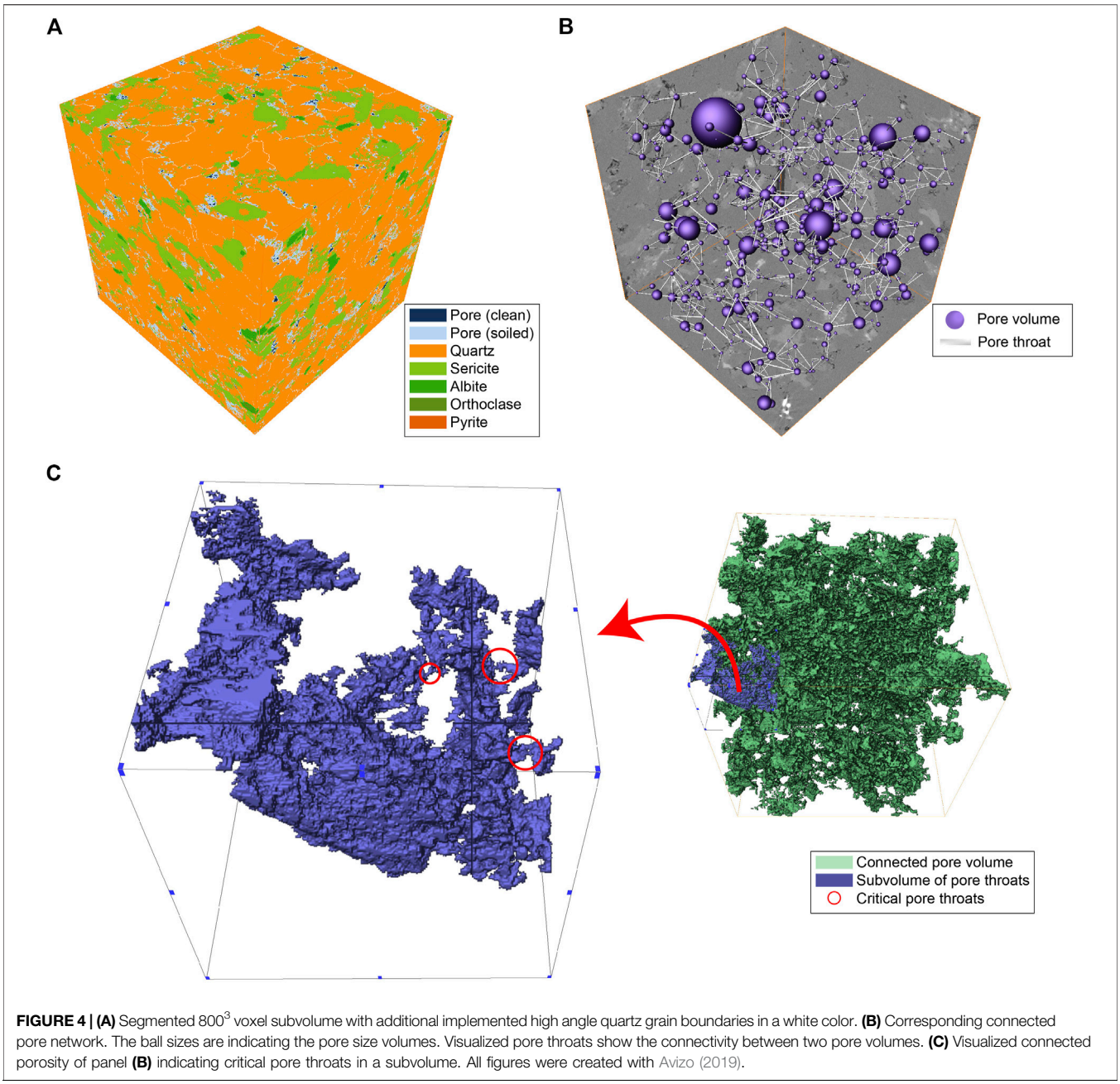

FIGURE 4 | (A) Segmented 800^3 voxel subvolume with additional implemented high angle quartz grain boundaries in a white color. **(B)** Corresponding connected pore network. The ball sizes are indicating the pore size volumes. Visualized pore throats show the connectivity between two pore volumes. **(C)** Visualized connected porosity of panel **(B)** indicating critical pore throats in a subvolume. All figures were created with Avizo (2019).

respectively. Modeled P- and S-wave velocity in x direction with segmented quartz grain boundaries $800^3_{watershed}$ result in 4,713 and 3,194 ms^{-1}, respectively.

Computed P-wave velocity results for $400^3_{watershed}$ show 4,591, 4,740, and 4,729 ms^{-1} for the three directions. The 400^3_{solid} P-wave velocity in x direction is 4,620 ms^{-1}. Additionally, the P-wave velocity was determined for the 400^3 voxel subvolume with assigned quartz grain boundaries of either 10% of quartz moduli or equal to pore moduli. Corresponding results are 4,540 and 4,500 ms^{-1} for 10% of quartz moduli and equal to pore moduli, respectively.

4 DISCUSSION

To develop a digital Ruhr sandstone twin a three-step interdisciplinary geological driven workflow is proposed, starting with the 1) pre-segmentation process, followed by the 2) assignment of gray-scale intensities to the resolved phases, and finally a 3) numerical characterization approach of the digital Ruhr sandstone twin in terms of permeability, thermal conductivity, and effective elastic wave propagation (**Figure 4**). In the pre-segmentation process, geological properties serve as input, such as Ruhr sandstone's diagenesis, or mineralogical

composition. Additionally, the raw XRCT data set must be technically evaluated based on the gray-scale histogram, existing X-ray artifacts, and the agreement with a REV. The gray-scale assignment to the corresponding mineralogical phases presented in this study is based on the simple gray-scale thresholding method, which allows a maximum of individual manipulation to ensure a first approximation of a meaningful segmented Ruhr sandstone model. The manipulation of the assigned phases is contrasted with four geological verification steps, which are intended to ensure a meaningful result during the segmentation process (**Figure 4**). The first geological verification is the number of expected phases based on the mineralogical composition and the accepted, high-quality XRCT image. The second geological review is during the individual phase segmentation based on visual evaluation of wrongly assigned voxels and the inspection of segmented phase fractions. The latter criterion results from the geological input properties. After individual phase segmentation, all phases are merged into a location-dependent model of the digital twin, which is supported technically by watershed algorithms and assisted by the third geological verification based on the geological property input. The last geological driven verification is the additional implementation of features, which cannot be resolved by the XRCT but might show a significant impact on further numerical characterizations. For Ruhr sandstone, this applies to high angle quartz grain boundaries.

4.1 The Pre-Segmentation Process: Evaluating the Reconstructed Gray-Scale Intensities

The reconstructed gray-scale intensities result from the materials' mass attenuation coefficients which, in case of this study, can be defined as the phase attenuation coefficient μ_{mineral} divided by the phase density ρ_{mineral}. This leads to the fact that minerals with similar attenuation coefficients are located very close to each other in the gray-scale histogram. Comparable observations are made when fine structures cannot be resolved by the XRCT (e.g., micritic phases in carbonates, see in Saenger et al., 2016b). At perfect conditions, each gray-scale intensity peak represents a single phase. However, in XRCT-based characterizations, image noise and artifacts are always present and should somehow not be included in the segmentation interpretation (e.g., ring artefacts or beam hardening; Münch et al., 2009; Hsieh, 2009). For this reason, numerous image denoizing algorithms are evaluated in the literature (e.g., linear and nonlinear filtering methods; Mery, 2015). However, first applications of a 3D-based nonlocal-mean filter have shown that individual voxels associated with the sericitic phases became filtered. One common answer could be the achieved technical resolution of the used acquisition system, which could not sufficiently reproduce the grain contacts. Another explanation could be the tight grain-to-grain boundaries observed in the Ruhr sandstone's microstructure due to the diagenesis. As a result, no distinct edges appear in the XRCT volume, making the edge-preserving smoothing by the nonlocal-mean filter give false results. This is especially true for those voxels whose size roughly corresponds to the resolution of the subvolume to be segmented. Due to the already applied binning procedure, we decided not to extract any further gray-scale intensities from the respective subvolumes and thus not to apply any of the established filtering methods (e.g., Schlüter et al., 2014; Saxena et al., 2018). However, the X-ray artifacts within the subvolumes could be handled and reduced to a minimum by the subsequent morphological post-processing operations during the segmentation process. Nevertheless, we would like to point out that the application of linear or nonlinear filtering methods during reconstruction or in the course of segmentation handles these artifacts much better than manual processing of the voxels.

The applied binning procedure increased the contrast of the 400^3 voxel subvolume compared to the 800^3 voxel subvolume at the sacrifice of imaged small particles in the XRCT volume. This results in a higher total and connected porosity for the 400^3 than for the 800^3 voxel subvolume (cf. **Table 4** and **Figure 3A**). Results of the modeled thermal conductivity as well as the effective elastic wave propagation show that the chosen coarsening of the data set is not in disadvantage for the mentioned physical investigations. This suggests that both the $2 \times 2 \times 2$ and $4 \times 4 \times 4$ binned data sets are basically sufficient in terms of the resolution provided for thermal conductivity and effective elastic wave propagation simulations. This statement does not apply if the permeability is determined numerically. The resolved pore throats show that the binning procedure resulted in incorrect permeability simulations (cf. **Figures 3D**, **5C**, **Supplementary Material S1**). At this state of the study, it is not possible to say whether the original data set (Ruf et al., 2021) has the necessary spatial resolution to provide sufficient resolution in the segmented rock model. We therefore advise a critical evaluation of the physical quantities to be studied and the resolution offered by the segmented data set, especially for small resolved features like micro porosities.

4.2 The Segmentation Process: Evaluating the Mineralogical Segmentation Based on Reconstructed Gray-Scale Intensities

Primarily, the applied segmentation workflow is based on the observed mineral structure in the examined thin sections. Minor differences may occur within the studied microstructures of the Ruhr sandstone due to local geologically influenced processes (cf. Kneuper, 1957). Subsequently, the reconstructed XRCT volume must be compared to the given microfabrics and the observations of the available reconstructed gray-scale histogram. The gray-scale histogram already gives a good indication of which phases could be resolved by the XRCT (see **Figure 2A**).

The presented workflow is based on a repeated application of gray-scale thresholding. In this approach, the minima and maxima of the gray-scale intensities of a phase are segmented, resulting in strict boundaries between the two phases. However, studies have shown that, e.g., in terms of noise in the gray-scale histogram due to multiple phase attenuation coefficients, this is not necessarily correct (e.g., Ketcham and Carlson, 2001; Sheppard et al., 2004; Jones et al., 2007; Wildenschild and Sheppard, 2013). Therefore, critical boundary regions arise

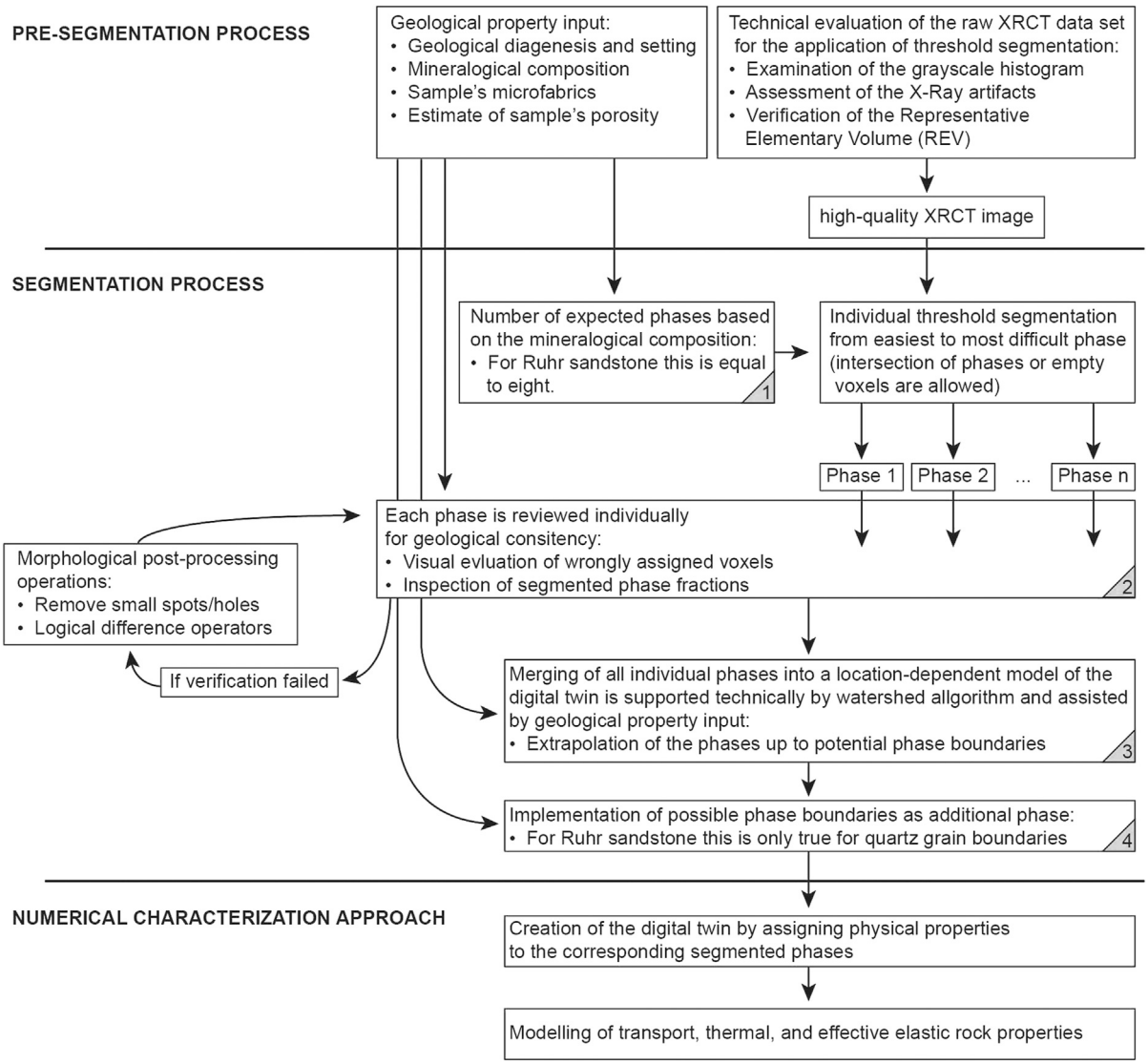

FIGURE 5 | Schematic representation of the geologically driven workflow. It should be noted that geological input parameters such as geological diagenesis, mineral composition, existing microstructure, or estimated sample porosity are repeatedly consulted in the segmentation process in order to obtain meaningful results. The so-called geological verification thus takes place a total of four times during the threshold segmentation.

during the segmentation of the individual phases (**Figure 2C**). Critical boundary regions close to two peaks can be approximated by a watershed algorithm. However, the main idea of the presented segmentation workflow is to reduce critical boundary regions between two peaks to minimize possible watershed errors, i.e., exact numerical assignment of gray-scale intensities, which, however, is not geologically meaningful. Furthermore, the presented segmentation method allows control over the segmentation process, which in our opinion is not necessarily the case with e.g., watershed-based segmentations. Jones et al. (2007) presented a method for minimizing critical boundary regions by the use of intensity–gradient histograms. The extent to which the described segmentation also provides meaningful results for the example of the Ruhr sandstone must be further analyzed. First segmentation attempts using the intensity-gradient-histogram did not yield satisfactory results. The reason for this could be that the described phase contrasts of the Ruhr sandstone's minerals, i.e., the mean of total observed phase attenuation coefficients, is much lower than the phase contrasts between the scaffold of a bone and air in the gray-scale histograms of the examined biomaterials. Based on the presented segmentation idea, only those phases can be assigned which phase attenuation coefficients is sufficient to be detected by the given XRCT. Furthermore, these distinguishable phases must be large enough to exceed the occurring signal-to-noise ratio (SNR). The presented segmentation workflow has shown that

phases that have very similar gray-scale intensities (e.g., both feldspar phases) can be separated clearly from each other, by manipulating false-assigned gray-scale intensities. The presented manipulation does not only imply the separation of phase contrasts at possible grain boundaries, but also assigns gray-scale intensities within grain boundaries to the correct phases - without a necessarily application of watershed algorithms. Due to the subsequent correction of mismatched gray-scale intensities, we expect a clear quality improvement of the segmented images compared to the simple threshold based phase separation e.g., multi-thresholding segmentation. Nevertheless, the segmentation workflow does not work entirely without watershed algorithms. Primarily, it is used to assign individual unassigned voxels to the appropriate ambient phase in the final process of segmentation. This step is mandatory to ensure that the resulting segmentation model does not contain any unassigned voxels that may have been created during processing. Although the critical boundary regions were previously reduced to a minimum, we cannot exclude the possibility of voxels being incorrectly assigned at this point due to the automation of the watershed algorithm. However, with regard to the corresponding model sizes of 400^3 and 800^3 voxel subvolumes, these incorrectly assigned voxels are assumed to be neglected.

A much more critical process of segmentation occurs during the implementation of grain boundaries (i.e., high angle quartz grain boundaries). Madonna et al. (2012) already presented a possible implementation of unresolved features within a XRCT image, almost ten years ago. We have adopted the described process by Madonna et al. (2012), which is based on watershed algorithms and assumed pressure-dependent quartz contact zones (Saenger et al., 2016a). However, numerical P- and S-wave velocity modelling results indicated further pressure-dependent features. These numerical results are in a good agreement with the observed quartz microfabrics (e.g., low angle quartz grain boundaries). Based on the geological setting, we assume at least a third pressure-dependent phase - namely the sericitic phase.

The used threshold segmentation can be applied to a single XRCT dataset with fairly inexpensive effort. This differs from the approach used for advanced machine learning algorithms, which require a critical amount of training data to produce satisfactory initial results. Consequently, the presented segmentation workflow should present a possible approach how future neural network based segmentation methods can be trained. The obvious advantages of unsupervised segmentation methods are the expected consistency, repeatability, and comparability of the segmented results (e.g., Chauhan et al., 2016; Alqahtani et al., 2021). These arguments gain importance especially when a segmented model of the digital twin is already accepted. However, these arguments can only apply to a limited extent when it comes to the first approximations to create a new verified 3D binary. This is where geological verification comes in for DRP. The steps presented in this study are intended to illustrate that operator bias can be well estimated by microfabric analyses (phase fractions or phase transformations) or by simple laboratory experiments (e.g., determination of porosity) and does not have to be characterized as arbitrariness of the operator. Finally, with respect to the results from the microfabric analysis or laboratory measurements, it can be considered that the raw XRCT data set has been reasonably segmented. In the future, these initial observations need to be applied to a larger data set and verified with appropriate methods. Here, the application of neural network based segmentation methods can make a major contribution to future Ruhr sandstone segmentations.

4.3 The Capabilities of the Geological Driven Workflow

Diagenesis reconstructions have shown that the Ruhr sandstone was covered at depths of up to 6,000 m (Karg et al., 2005). Assuming a normal gradient, this results in a pressure of about 150 MPa, which was applied to the Ruhr sandstone. Karg et al. (2005) also reconstructed possible temperatures of above 120°C that must have acted on the Ruhr sandstone. These P-T conditions fit both the presented microfabrics and the generally accepted highly complex geologic setting (e.g., Balcewicz et al., 2021a, and references therein). Saenger et al. (2016a) have already shown that pressure-dependent indicators of a Berea sandstone sample at 20 MPa confining pressure cannot be resolved in the XRCT. This resulted in pressure-dependent grain contact zones. The presented microfrabric analyses also show highly stressed quartz grains. Implemented high angle quartz grain boundaries decrease the results for the effective elastic wave propagation as well as for the numerically derived thermal conductivity approach. These results fit to the insulating character of thin segmented phases assigned with elastic moduli properties of air. To be specific regarding thermal conductivity results, comparing the two averaging methods, it also becomes clear that the HM-approch reflects the insulating character of the contact phase much more strongly than the AM-approach. The reason for this is the low resolution of the contact phase. In such a case, the AM-approach cannot fully capture the isolating effect. However, additional low angle quartz grain boundaries, subgrains, fluid inclusion trails, and sutured grain boundaries could be identified for quartz grains compared to the observations in Saenger et al. (2016a). For this reason, we conclude that it is mandatory to assign reduced elastic properties to the digital rock twin in order to achieve meaningful agreements with laboratory results. This results in reduced elastic properties for the quartz phase by ca. 30% (cf. Bass, 1995; Saenger et al., 2016a). It must be pointed out that the degree of reduction derived in Saenger et al. (2016a) is not necessarily correct for the Ruhr sandstone (**Figure 3B**). An explicit numerical calibration of the elastic quantities must follow this study of geometrical calibration to answer open questions. The purpose of this study is to demonstrate that the geologically driven workflow potentially opens up the possibilities to answer subsequent questions. A corresponding numerical calibration should therefore also be investigated for all further segmented phases. Due to the geological diagenesis of the Ruhr sandstone and the resulting segmentation possibilities we want to inspire other research

groups to focus on the soiled pore phase and the sericitic phase for future studies.

SEM images (**Figures 1B–D**) have shown that the pore space in the Ruhr sandstone occurs in at least two different types. The process of segmentation can be approximated as a function of the applied time vs. the location-dependent accuracy of the segmented phases. For this reason, only two pore space observations were segmented: 1) clean pore and 2) soiled pore phase. While the explanation of the clean pore space and further handling for numerical purpose is obvious, more extensive aspects have to be considered for the soiled pore space. Particles located in this soiled pore space can have different influence on the rock properties. Mineral fragments from the Ruhr sandstone are likely to be present within the soiled pore space. However, these particles may seal off the connected porosity during permeability measurements, which would effectively result in lower permeabilities being measured in the laboratory. This observation should be taken into account, especially when evaluating numerical permeability results with comparable microfabrics. Besides sealing the connected porosity, the mineral particles can also influence hydrochemical reactions. Tran et al. (2020) studied mine waters in the Rhine-Ruhr metropolitan area and the influence on the local rheological units (e.g., Ruhr sandstone). First results showed that mine waters were weakly acidic to neutral, resulting in significant water-rock interaction correlations. Transport or hydrochemical induced clogging indicate that numerical permeability results tend to be too high compared to laboratory measurements (**Figure 3D**). In this respect, we recommend explicit investigations of particle transport or mineral scaling in the Ruhr sandstone based on XRCT and other imaging techniques (e.g, Weinhardt et al., 2021). Until then, the segmented soiled pore phase provides an opportunity for other research groups to adapt their numerical approaches to the observed Ruhr sandstone's microfabric and incorporate possible reduced permeabilities.

Another phase that was segmented due to the workflow, but needs to be studied in more detail as part of a numerical calibration, is the sericitic phase. The segmented sericite phase consists of a mixture of different mineral phases. Basically, this is due to the feasibility of XRCT resolution of microporosities and extremely fine-grained mineral phases (e.g., pore diameter $<$ 1 µm and mean grain size $<$ 5 µm). In addition, however, the sericitic phase also exhibits distinct paragenetic sequences that can be attributed to the metasedimentary background of the Ruhr sandstone. Blatt (1967) has already pointed out the importance of provenance studies on recycled sediments and that identical mineral phases may occur at different shapes and with different properties. Thus, considering the described Ruhr sandstone's diagenesis of Kneuper (1957) and Scherp (1963) and the large number of phases combined in the segmented sericitic phase, the digital rock twin can only be described as an approximation of the real Ruhr sandstone. SEM images show enclosed fine pore spaces by the sericitic phase and quartzitic-sericitic grain-to-grain structures which show further possible pressure-dependent zones (**Figures 1B,C**). Due to simplifications, we have assumed for the elastic properties of the sericitic phase the most represented mineral, i.e., muscovite. This means that observed phases such as kaolinite, illite, or chlorite are not considered for the numerical approaches. Therefore, we have reasonable concerns to suspect that the numerical results of the thermal conductivities as well as P- and S-wave velocities are too high for the digital rock twin. Reduced elastic properties and thermal conductivities could be a solution to the discrepancy between laboratory and numerical results - which, however, we consider to be the wrong approach for this phase. Instead, the individual phases must be segmented in an additional process (based on thin section, SEM or XRCT) and then implemented as high-resolution subvolumes into the digital rock twin. Karimpouli et al. (2019) has already shown that a similar method can be used to implement pore spaces in a XRCT volume which resolution is insufficient for small features (e.g., XRCT volumes from medical tomography scanners).

4.4 The Numerical Characterization Approach: Verification of Observed Anisotropy

During preparation, macroscopic indications of weathering were observed assuming macroscopic anistropy. Laboratory results show a weak anistropy for samples drilled in x direction. This is especially true for derived P- and S-wave velocities (cf. **Figure 3B** and **Table 2**). Similar observations were made for laboratory derived thermal conductivity results. Samples taken from x direction tend to show lower thermal conductivity results than samples from y and z direction, respectively (**Figure 3C**). However, this observation cannot be made for the comparison between total and connected porosities (**Figure 3A**). Advanced numerical approaches to determine permeability, thermal conductivity, and P- and S-wave velocity were applied for a cylindrical core sample parallel to laboratory determined sample results in x direction. Due to the cylindrical shape of the scanned sample, true y and z directions could not be reconstructed for the digital rock twin. The numerical results have shown a fairly good agreement with the results obtained in the laboratory, considering the XRCT resolution as well as the assignment of the elastic moduli to the segmented phases. In addition, weak anisotropies were determined independently from the respective numerical approaches.

The thermal conductivities in y and z direction show almost identical results, while the thermal conductivity in x direction seems to be lower. In the case of implemented high angle quartz grain boundaries, this effect seems to be suppressed for the thermal conductivity results. The numerically derived P- and S-wave velocity results do also show weak but clear anisotropy for x direction. Modeled P- and S-wave velocity show up to 100 ms^{-1} lower results for x direction of the 800^3 voxel subvolume and up to 200 ms^{-1} lower results for x direction of the 400^3 voxel subvolume compared to y and z directions, respectively. These observations are in good agreement with the mean velocity differences determined in the laboratory of approx. 300 ms^{-1}, which are smaller for the x direction than for the y and z directions. Löer et al. (2018) have demonstrated the degree of anisotropy using installed seismic

arrays in the Parkfield area. This verified anisotropy, which could be determined from surface wave measurements, is in the range of about 100 ms^{-1}. Thus, because of the explicit alignment of our samples with respect to the assumed anisotropy, we can demonstrate a comparable degree of anisotropy. The influence of an anisotropy of about 300 ms^{-1} is shown by the interpretation of a velocity model in a geothermal field in Los Humeros (Mexico). The combination of a geological subsurface model and a geophysical velocity model shows a good agreement between both interpretations, which provide either a resolution of tens of meters or hundreds of meters per second, respectively (Löer et al., 2020).

Due to the observed macroscopic anisotropy of the samples, further investigations were considered. Thus, it was initially assumed that the anisotropy occurring in the color of the rock samples was caused by the intrusion of the pyrites. A comparison of the modeled P-wave velocities, in which all phases except the pyrites were assigned to quartz, did not provide clear evidence for this hypothesis. In a second set of tests, all phases were set equal to quartz except for the sericitic phase, which was shown to be the result of alteration of the feldspars. This comparison of the modeled P-wave velocities also did not confirm any anisotropy due to the solid phases. In a final numerical run, all phases were assigned equal to quartz moduli except for the two pore phases, i.e., clean and soiled pore. The result for this analysis reads as 4,484, 4,615, and 4,626 ms^{-1} for x, y, and z directions, respectively.

The applied SPH based permeability solver confirms the observed anisotropy in the x direction. Nevertheless, the comparison between the numerical and laboratory derived results reveals that not all physical quantities can be derived with the same degree of sophistication using the identical segmented model. In particular, the resolution of micro porosities and the associated pore throats make, for example, the segmented 400^3 voxel subvolume an inappropriate choice for such permeability simulations. However, the same segmented data set gives reasonable results for both numerical thermal conductivity and effective elastic wave propagation results. From this, we conclude that valuable numerical thermal conductivity or effective elastic wave propagation results can be expected from segmented volumes after binning processes as described in this study. We consider this observation to be equivalent to the lower resolution in XRCT images. Whereas numerical permeability approaches at this reduced resolution can no longer provide reasonable results. This implies high resolutions in microtomography processing are necessary to visualize critical volume zones in the pore throats for very low porosity rocks like Ruhr sandstone (see supplementary materials).

Thus, we summarize that the main anisotropy is due to the Ruhr sandstone's pore network (**Figure 5**). This result indicates that the apparent seismic anisotropy at the field-scale (Löer et al., 2018) can not only stem from fault systems but from the pore network, too. Future studies may analyze the implications regarding fluid flow directions in reservoirs.

5 CONCLUSION

Based on the example of the Ruhr sandstone, we presented a simple segmentation approach that takes into account geological properties such as mineralogy, microfabrics, and basic laboratory measurements like total and connected porosity. To create the digital twin of the Ruhr sandstone sample we have prepared a cylindrical core sample with a diameter of 5 mm and a length of about 10 mm to provide an appropriate REV. The created XRCT volume resulted in a 800^3 voxel subvolume with a voxel size of 4 μm. Due to the limitation of the numeric simulation schemes a second 400^3 voxel subvolume with a voxel size of 8 μm was prepared. The geological driven workflow was applied on both subvolumes, primarily based on gray-scale threshold segmentation. By the additional use of e.g., logical difference operators or watershed segmentation, a digital Ruhr sandstone twin with eight phases could be acquired. The presented segmentation workflow is intended to serve as a first approach to train future neural network-based segmentation approaches with sufficiently accurate segmentation phases.

The laboratory results indicate a transversely isotropic medium whose properties vary only with the x direction studied, but not with the y or z directions studied. After comparing the laboratory measurements with the numerical results, a weak anisotropy was confirmed by the numerical approaches, i.e., modeling permeability, thermal, and effective elastic rock properties. Further investigations suggest that the observed anisotropy is due to the existing pore network in the Ruhr sandstone. Moreover, we present the complex microstructure of the Ruhr sandstone with its altered and clay-rich matrix on the basis of thin section and SEM images. On the one hand, the assigned properties are intended to reflect the investigated rock properties, such as low porosity, and on the other hand, they are intended to provide suggestions for matching the numerical results more closely to the laboratory measurements. We encourage other research groups to take advantage of our segmented datasets and use the elaborated phases to address open questions, such as how to assign elastic moduli for pressure- and temperature-dependent phases or how to simulate the effect of clogging or hydrochemical reactions during flow modeling.

DATA AVAILABILITY STATEMENT

The datasets presented in this study can be found in online repositories. The names of the repository/repositories and accession number(s) can be found in the article/ **Supplementary Material**.

AUTHOR CONTRIBUTIONS

Seven authors have contributed to this paper. MB was the lead author and carried out laboratory measurements, sample characterization, segmentation, and analytical calculations. MS helped with numerically derived thermal conductivity. MG was

involved in interpreting numerical derived results. MR provided high-resolution XRCT images. DK was involved in numerical permeability calculations and their interpretations. HS provided helpful background knowledge and laboratory as well as numerical resources. ES was involved in effective elastic wave propagation simulations, provided helpful background knowledge, and was involved in the data interpretation. All authors contributed to writing the manuscript.

FUNDING

MB and ES acknowledge generous funding by the Federal Ministry of Education and Research and geomecon GmbH for the project 3D-RuhrMarie ("FHprofUnt2016"; Project No. 13FH279PX6). MR and HS acknowledge funding from the German Science Foundation (DFG) through Project No. STE 969/13-1. HS thanks the DFG for supporting this work under Grant No. SFB 1313 (Project No. 327154368). The authors declare that this study received funding from geomecon GmbH. The funder was not involved in the study design, collection, analysis, interpretation of data, the writing of this article or the decision to submit it for publication.

ACKNOWLEDGMENTS

We thank all students and researchers involved in the laboratory measurements, in particular Mandy Duda. We especially thank Claudia Finger for fruitful discussions and helpful comments on an earlier draft of the manuscript. Furthermore, we would like to thank the editor Pascal Audet and the two reviewers Steffen Berg and Arne Jacob for their comments and discussions on the manuscript.

SUPPLEMENTARY MATERIAL

The Supplementary Material for this article can be found online at: https://www.frontiersin.org/articles/10.3389/feart.2021.673753/full#supplementary-material

REFERENCES

AGFW (2009). Arbeitsgemeinschaft für Wärme und Heizkraftwirtschaft: Technisches Handbuch Fernwärme *Technik und Normung* (Frankfurt am Main: AGFW-Projektges. für Rationalisierung, Information und Standardisierung).

Ahrens, B., Duda, M., and Renner, J. (2018). Relations between Hydraulic Properties and Ultrasonic Velocities during Brittle Failure of a Low-Porosity sandstone in Laboratory Experiments. *Geophys. J. Int.* 212, 627–645. doi:10.1093/gji/ggx419

Aljamaan, H., Ross, C. M., and Kovscek, A. R. (2017). "Multiscale Imaging of Gas Adsorption in Shales," in SPE Unconventional Resources Conference. Society of Petroleum Engineers, 1–26. doi:10.2118/185054-MS

Alqahtani, N. J., Chung, T., Wang, Y. D., Armstrong, R. T., Swietojanski, P., and Mostaghimi, P. (2021). Flow-Based Characterization of Digital Rock Images Using Deep Learning. *SPE J.* 1–12. doi:10.2118/205376-PA

Avizo (2019). Version 2019.1 (Waltham, Massachusetts: Thermo Fisher Scientific and Zuse Institute Berlin).

Anderson, J. A., Lorenz, C. D., and Travesset, A. (2008). General Purpose Molecular Dynamics Simulations Fully Implemented on Graphics Processing Units. *J. Comput. Phys.* 227, 5342–5359. doi:10.1016/j.jcp.2008.01.047

Andrä, H., Combaret, N., Dvorkin, J., Glatt, E., Han, J., Kabel, M., et al. (2013a). Digital Rock Physics Benchmarks-Part I: Imaging and Segmentation. *Comput. Geosciences* 50, 25–32. doi:10.1016/j.cageo.2012.09.005

Andrä, H., Combaret, N., Dvorkin, J., Glatt, E., Han, J., Kabel, M., et al. (2013b). Digital Rock Physics Benchmarks-Part II: Computing Effective Properties. *Comput. Geosciences* 50, 33–43. doi:10.1016/j.cageo.2012.09.008

Araújo, K. (2014). The Emerging Field of Energy Transitions: Progress, Challenges, and Opportunities. *Energ. Res. Soc. Sci.* 1, 112–121. doi:10.1016/j.erss.2014.03.002

Balcewicz, M., Ahrens, B., Lippert, K., and Saenger, E. H. (2021a). Characterization of Discontinuities in Potential Reservoir Rocks for Geothermal Applications in the Rhine-Ruhr Metropolitan Area (Germany). *Solid Earth* 12, 35–58. doi:10.5194/se-12-35-2021

Balcewicz, M., Ruf, M., Steeb, H., and Saenger, E. H. (2021b). *Digital Rock Physics: A Geological Driven Workflow for the Segmentation of Anisotropic Ruhr Sandstone: Segmented Subvolumes*. [Dataset] DaRUS. doi:10.18419/darus-1435

Balcewicz, M., Ruf, M., Steeb, H., and Saenger, E. H. (2021c). *Digital Rock Physics: A Geological Driven Workflow for the Segmentation of Anisotropic Ruhr Sandstone: SEM Images*. [Dataset] DaRUS. doi:10.18419/darus-1812

Bass, J. D. (1995). "Elasticity of Minerals, Glasses, and Melts," in *Mineral Physics & Crystallography: A Handbook of Physical Constants*, 2 Washington, DC: Wiley Online Library, 45–63. doi:10.1029/RF002p0045

Bear, J., and Braester, C.IAHR (1972). "On the Flow of Two Immscible Fluids in Fractured Porous Media," in *Fundamentals of Transport Phenomena in Porous Media*. *Of* Developments In Soil Science (Elsevier), Vol. 2, 177–202. doi:10.1016/S0166-2481(08)70538-5

Beucher, S., and Meyer, F. (1992). "The Morphological Approach to Segmentation: The Watershed Transformation," *Mathematical Morphology in Image Processing*. Editor E. Dougherty (Boca Raton: Taylor & Francis Inc), 1, 433–481.

Blunt, M., and King, P. (1991). Relative Permeabilities from Two- and Three-Dimensional Pore-Scale Network Modelling. *Transport Porous Med.* 6, 407–433. doi:10.1007/bf00136349

Bourbie, T., and Zinszner, B. (1985). Hydraulic and Acoustic Properties as a Function of Porosity in Fontainebleau Sandstone. *J. Geophys. Res.* 90, 11524–11532. doi:10.1029/JB090iB13p11524

Brenne, S. (2016). Hydraulic Fracturing and Flow Experiments on Anisotropic and Pre-fractured Rocks. Ph.D. Thesis Bochum: Ruhr Universität Bochum.

Buzug, T. M. (2011). *Computed Tomography – from Photon Statistics to Modern Cone-Beam CT*. Berlin, Heidelberg: Springer. doi:10.1007/978-3-540-39408-2

Chauhan, S., Rühaak, W., Khan, F., Enzmann, F., Mielke, P., Kersten, M., et al. (2016). Processing of Rock Core Microtomography Images: Using Seven Different Machine Learning Algorithms. *Comput. Geosciences* 86, 120–128. doi:10.1016/j.cageo.2015.10.013

Churcher, P. L., French, P. R., Shaw, J. C., and Schramm, L. L. (1991). "Rock Properties of Berea Sandstone, Baker Dolomite, and Indiana Limestone," in SPE International Conference on Oilfield Chemistry. All Days, 431–449. doi:10.2118/21044-MS

Clauser, C., and Huenges, E. (2013). "Thermal Conductivity of Rocks and Minerals," in *AGU Reference Shelf*. Washington D.C. American Geophysical Union, 105–126. doi:10.1029/rf003p0105

Drozdzewski, G. (1993). The Ruhr Coal basin (Germany): Structural Evolution of an Autochthonous Foreland basin. *Int. J. Coal Geology* 23, 231–250. doi:10.1016/0166-5162(93)90050-k

Duda, M. (2012). An Integrated Experimental Study on Elastic and Inelastic Properties of Sandstones and the Role of Transient Pore Pressure. Ph.D. Thesis, Ruhr Universität Bochum.

Duda, M., and Renner, J. (2013). The Weakening Effect of Water on the Brittle Failure Strength of sandstone. *Geophys. J. Int.* 192, 1091–1108. doi:10.1093/gji/ggs090

Fan, L., Thompson, J. W., and Robinson, J. R. (2010). "Understanding Gas Production Mechanism and Effectiveness of Well Stimulation in the

Haynesville Shale through Reservoir Simulation," in Canadian Unconventional Resources and International Petroleum Conference. Society of Petroleum Engineers, 1–15. doi:10.2118/136696-MS

Feng, X., Zeng, J., Zhan, H., Hu, Q., Ma, Z., and Feng, S. (2020). Resolution Effect on Image-Based Conventional and Tight sandstone Pore Space Reconstructions: Origins and Strategies. *J. Hydrol.* 586, 124856. doi:10.1016/j.jhydrol.2020.124856

Finger, C., and Saenger, E. H. (2020). Sensitivity Maps for Time-Reverse Imaging: an Accuracy Study for the Los Humeros Geothermal Field (Mexico). *Geophys. J. Int.* 222, 231–246. doi:10.1093/gji/ggaa160

Fridleifsson, I. B., Bertani, R., Huenges, E., Lund, J. W., Ragnarsson, A., and Rybach, L. (2008). "The Possible Role and Contribution of Geothermal Energy to the Mitigation of Climate Change.," in *IPCC Scoping Meeting on Renewable Energy Sources, Proc. Luebeck, Germany (Citeseer)* 20, 59–80. doi:10.500.11850/13474

Garfi, G., John, C. M., Berg, S., and Krevor, S. (2020). The Sensitivity of Estimates of Multiphase Fluid and Solid Properties of Porous Rocks to Image Processing. *Transp Porous Med.* 131, 985–1005. doi:10.1007/s11242-019-01374-z

Glaser, J., Nguyen, T. D., Anderson, J. A., Lui, P., Spiga, F., Millan, J. A., et al. (2015). Strong Scaling of General-Purpose Molecular Dynamics Simulations on GPUs. *Comput. Phys. Commun.* 192, 97–107. doi:10.1016/j.cpc.2015.02.028

Goldstein, B., Hiriart, G., Tester, J., Bertani, B., Bromley, R., Gutierrez-Negrin, L., et al. (2011). "Great Expectations for Geothermal Energy to 2100," in Proceedings 36th Workshop on Geothermal Reservoir Engineering, 1–8.

Guan, K. M., Nazarova, M., Guo, B., Tchelepi, H., Kovscek, A. R., and Creux, P. (2019). Effects of Image Resolution on sandstone Porosity and Permeability as Obtained from X-ray Microscopy. *Transp Porous Med.* 127, 233–245. doi:10.1007/s11242-018-1189-9

Harvey Blatt, H. (1967). Provenance Determinations and Recycling of Sediments. *Sepm Jsr* Vol. 37, 1031–1044. doi:10.1306/74D71825-2B21-11D7-8648000102C1865D

Hesemann, J. (2013). *Die Ergebnisse der Bohrung Münsterland 1*. Krefeld: Springer-Verlag.

Holzer, L., and Cantoni, M. (2012). "Review of FIB-Tomography," in *Nanofabrication Using Focused Ion and Electron Beams: Principles and Applications*. New York: Oxford University Press, 410–435.

Hsieh, J. (2009). *Computed Tomography: Principles, Design, Artifacts, and Recent Advances*. second edn. Bellingham, Washington USA: SPIE press.

Iassonov, P., Gebrenegus, T., and Tuller, M. (2009). Segmentation of X-ray Computed Tomography Images of Porous Materials: A Crucial Step for Characterization and Quantitative Analysis of Pore Structures. *Water Resour. Res.* 45. doi:10.1029/2009WR008087

Jones, A., Arns, C., Sheppard, A., Hutmacher, D., Milthorpe, B., and Knackstedt, M. (2007). Assessment of Bone Ingrowth into Porous Biomaterials Using MICRO-CT. *Biomaterials* 28, 2491–2504. doi:10.1016/j.biomaterials.2007.01.046

Jüstel, A. (2021). Increasing the Knowledge Base for Deep Geothermal Energy Exploration in the Aachen-Weisweiler Area, Germany, through 3D Probabilistic Modeling with GemPy and Quantitative Data Analysis. Master's thesis Aachen: RWTH Aachen.

Karg, H., Carter, A., Brix, M. R., and Littke, R. (2005). Late- and post-Variscan Cooling and Exhumation History of the Northern Rhenish Massif and the Southern Ruhr Basin: New Constraints from Fission-Track Analysis. *Int. J. Earth Sci. (Geol Rundsch)* 94, 180–192. doi:10.1007/s00531-005-0467-2

Karimpouli, S., Faraji, A., Balcewicz, M., and Saenger, E. H. (2020). Computing Heterogeneous Core Sample Velocity Using Digital Rock Physics: A Multiscale Approach. *Comput. Geosciences* 135, 104378. doi:10.1016/j.cageo.2019.104378

Ketcham, R. A., and Carlson, W. D. (2001). Acquisition, Optimization and Interpretation of X-ray Computed Tomographic Imagery: Applications to the Geosciences. *Comput. Geosciences* 27, 381–400. doi:10.1016/s0098-3004(00)00116-3

Khan, F., Enzmann, F., and Kersten, M. (2016). Multi-phase Classification by a Least-Squares Support Vector Machine Approach in Tomography Images of Geological Samples. *Solid Earth* 7, 481–492. doi:10.5194/se-7-481-2016

Kneuper, G. (1957). Zur Petrographie der Sandsteine des flözführenden Ruhrkarbons. Mitt. Westfäl. Berggewerkschaftskasse *(Kukuk-festschrift)* 12, 47–57.

Knutzen, L. K. (2017). Geothermal and Spatial Coupled Site Selection for the Connection of Deep Geothermal Plants to Existing District Heating Networks on the Example of the Ruhr Metropolitan Region. Ph.D. Thesis Bochum: Ruhr-Universität Bochum.

Kretz, R. (1983). Symbols for Rock-Forming Minerals. *Am. Mineral.* 68, 277–279.

Kruszewski, M., Montegrossi, G., Backers, T., and Saenger, E. (2020). "The *In-Situ* Stress State of the Rhine-Ruhr Region and its Implications for the Geothermal Energy Utilization," in EGU General Assembly Conference Abstracts, 4246.

Leu, L., Berg, S., Enzmann, F., Armstrong, R. T., and Kersten, M. (2014). Fast X-ray Micro-tomography of Multiphase Flow in berea sandstone: A Sensitivity Study on Image Processing. *Transp Porous Med.* 105, 451–469. doi:10.1007/s11242-014-0378-4

Lippert, K., Nehler, M., Balcewicz, M., Bracke, R., and Immenhauser, A. (2021). "Assessment of the Reservoir Potential of Devonian Carbonates in the Rhine-Ruhr Area, Germany," in World Geothermal Congress 2020+1 (World Geothermal Congress 2020 Reykjavik), 11141.

Lippert, K., Nehler, M., Balcewicz, M., Bracke, R., and Immenhauser, A. (2019). "Facies-Related Evaluation of the Geothermal Reservoir Potential of Devonian Carbonates in North Rhine-Westphalia, Germany," in 81st EAGE Conference and Exhibition 2019, 1–5. European Association of Geoscientists & Engineers.

Lippert, K. (2017). The Effect of Cyclic thermal Loading on the Permeability of the Upper Carboniferous Strata in the Ruhr Area. Master's thesis Aachen: RWTH Aachen.

Löer, K., Riahi, N., and Saenger, E. H. (2018). Three-component Ambient Noise Beamforming in the Parkfield Area. *Geophys. J. Int.* 213, 1478–1491. doi:10.1093/gji/ggy058

Löer, K., Toledo, T., Norini, G., Zhang, X., Curtis, A., and Saenger, E. H. (2020). Imaging the Deep Structures of Los Humeros Geothermal Field, Mexico, Using Three-Component Seismic Noise Beamforming. *B. Seismol. Soc. Am.* 91, 3269–3277. doi:10.1785/0220200022

Madonna, C., Almqvist, B. S. G., and Saenger, E. H. (2012). Digital Rock Physics: Numerical Prediction of Pressure-dependent Ultrasonic Velocities Using Micro-CT Imaging. *Geophys. J. Int.* 189, 1475–1482. doi:10.1111/j.1365-246X.2012.05437.x

Matlab (2020). Version 9.8.0*(R2020a)*. Natick, Massachusetts: The MathWorks Inc.

Mery, D. (2015). *Computer Vision for X-Ray Testing*. Switzerland: Springer International Publishing: Springer. doi:10.1007/978-3-319-20747-6

Münch, B., Trtik, P., Marone, F., and Stampanoni, M. (2009). Stripe and Ring Artifact Removal with Combined Wavelet-Fourier Filtering. *Opt. Express* 17, 8567–8591. doi:10.1364/OE.17.008567

Nehler, M. (2018). Evaluation of Porositiy and Permeability Estimates for Rock Samples Based on X-ray Micro-tomography. Ph.D. Thesis Bochum: Ruhr-universität Bochum.

Normenausschuss Bauwesen (NABau) (2011). *Determination of Density of Solid Particles – Capillary Pyknometer, Wide Mouth Pycnometer, Gas Pycnometer*. Berlin: Beuth).

Øren, P.-E., and Bakke, S. (2003). Reconstruction of berea sandstone and Pore-Scale Modelling of Wettability Effects. *J. Pet. Sci. Eng.* 39, 177–199. doi:10.1016/s0920-4105(03)00062-7

Osorno, M., Schirwon, M., Kijanski, N., Sivanesapillai, R., Steeb, H., and Göddeke, D. (2020). A Cross-Platform, High-Performance SPH Toolkit for Image-Based Flow Simulations on the Pore Scale of Porous Media. *Comput. Phys. Commun* 267, 108059. doi:10.1016/j.cpc.2021.108059

Ostoja-Starzewski, M. (1999). Scale Effects in Materials with Random Distributions of needles and Cracks. *Mech. Mater.* 31, 883–893. doi:10.1016/S0167-6636(99)00039-3

Ritzmann, O., Maercklin, N., Inge Faleide, J., Bungum, H., Mooney, W. D., and Detweiler, S. T. (2007). A Three-Dimensional Geophysical Model of the Crust in the Barents Sea Region: Model Construction and Basement Characterization. *Geophys. J. Int.* 170, 417–435. doi:10.1111/j.1365-246X.2007.03337.x

Rogelj, J., Den Elzen, M., Höhne, N., Fransen, T., Fekete, H., Winkler, H., et al. (2016). Paris Agreement Climate Proposals Need a Boost to Keep Warming Well below 2 °C. *Nature* 534, 631–639. doi:10.1038/nature18307

Rosenfeld, U. (1967). Zur Stratigraphie der Kaisberg-Schichten (oberes Namur) im Ruhr-Karbon. *Geol. Rundsch* 56, 494–520. doi:10.1007/bf01848739

Rossmann, K. (1969). Point Spread-Function, Line Spread-Function, and Modulation Transfer Function. *Radiology* 93, 257–272. doi:10.1148/93.2.257

Ruf, M., Balcewicz, M., Saenger, E. H., and Steeb, H. (2021). *Digital Rock Physics: A Geological Driven Workflow for the Segmentation of Anisotropic Ruhr Sandstone: Micro-XRCT Data Set*. [Dataset] DaRUS. doi:10.18419/darus-1152

Ruf, M., and Steeb, H. (2020). An Open, Modular, and Flexible Micro X-ray Computed Tomography System for Research. *Rev. Scientific Instr.* 91, 113102. doi:10.1063/5.0019541

Saenger, E. H., and Bohlen, T. (2004). Finite-difference Modeling of Viscoelastic and Anisotropic Wave Propagation Using the Rotated Staggered Grid. *Geophysics* 69, 583–591. doi:10.1190/1.1707078

Saenger, E. H., Lebedev, M., Uribe, D., Osorno, M., Vialle, S., Duda, M., et al. (2016a). Analysis of High-Resolution X-ray Computed Tomography Images of Bentheim sandstone under Elevated Confining Pressures. *Geophys. Prospecting* 64, 848–859. doi:10.1111/1365-2478.12400

Saenger, E. H., Vialle, S., Lebedev, M., Uribe, D., Osorno, M., Duda, M., et al. (2016b). Digital Carbonate Rock Physics. *Solid Earth* 7, 1185–1197. doi:10.5194/se-7-1185-2016

Saxena, N., Hofmann, R., Alpak, F. O., Dietderich, J., Hunter, S., and Day-Stirrat, R. J. (2017). Effect of Image Segmentation & Voxel Size on Micro-CT Computed Effective Transport & Elastic Properties. *Mar. Pet. Geology* 86, 972–990. doi:10.1016/j.marpetgeo.2017.07.004

Saxena, N., Hofmann, R., Hows, A., Saenger, E. H., Duranti, L., Stefani, J., et al. (2019). Rock Compressibility from Microcomputed Tomography Images: Controls on Digital Rock Simulations. *Geophysics* 84, WA127–WA139. doi:10.1190/GEO2018-0499.1

Saxena, N., Hows, A., Hofmann, R., O. Alpak, F. F., Freeman, J., Hunter, S., et al. (2018). Imaging and Computational Considerations for Image Computed Permeability: Operating Envelope of Digital Rock Physics. *Adv. Water Resour.* 116, 127–144. doi:10.1016/j.advwatres.2018.04.001

Scheer, D., Konrad, W., and Scheel, O. (2013). Public Evaluation of Electricity Technologies and Future Low-Carbon Portfolios in Germany and the USA. *Energ. Sustain. Soc.* 3, 8. doi:10.1186/2192-0567-3-8

Schepp, L. L., and Renner, J. (2021). Evidence for the Heterogeneity of the Pore Structure of Rocks from Comparing the Results of Various Techniques for Measuring Hydraulic Properties. *Transp Porous Med.* 136, 217, 243. doi:10.1007/s11242-020-01508-8

Scherp, A. (1963). Die Petrographie der paläozoischen Sandsteine in der Bohrung Münsterland 1 und ihre Diagenese in Abhängigkeit von der Teufe. *Fortschr. Geol. Rheinl.-Westf.* 11, 251–282.

Schlüter, S., Sheppard, A., Brown, K., and Wildenschild, D. (2014). Image Processing of Multiphase Images Obtained via X-ray Microtomography: a Review. *Water Resour. Res.* 50, 3615–3639. doi:10.1002/2014wr015256

Sezgin, M., and Taşaltín, R. (2000). A New Dichotomization Technique to Multilevel Thresholding Devoted to Inspection Applications. *Pattern Recognition Lett.* 21, 151–161. doi:10.1016/s0167-8655(99)00142-7

Sheppard, A. P., Sok, R. M., and Averdunk, H. (2004). Techniques for Image Enhancement and Segmentation of Tomographic Images of Porous Materials. *Physica A: Stat. Mech. its Appl.* 339, 145–151. doi:10.1016/j.physa.2004.03.057

Siegert, M., Gurris, M., and Saenger, E. H. (2021). Validation Suite for Numerical Solvers Calculating Effective thermal Conductivity in Porous media. *J. Appl. Geophys.* 189, 104323. doi:10.1016/j.jappgeo.2021.104323

Sivanesapillai, R., Steeb, H., and Hartmaier, A. (2014). Transition of Effective Hydraulic Properties from Low to High Reynolds Number Flow in Porous media. *Geophys. Res. Lett.* 41, 4920–4928. doi:10.1002/2014gl060232

Stöckhert, F. (2015). *Fracture Mechanics Applied to Hydraulic Fracturing in Laboratory Experiments*. Ph.D. Thesis, Ruhr-Universität Bochum.

Storath, M., Weinmann, A., Frikel, J., and Unser, M. (2015). Joint Image Reconstruction and Segmentation Using the Potts Model. *Inverse Probl.* 31, 025003. doi:10.1088/0266-5611/31/2/025003

Thermo Fisher Scientific (2018). *Thermo Scientific Avizo Software 9 User's Guide*. Berlin.

Tran, T. Q., Banning, A., Wisotzky, F., and Wohnlich, S. (2020). Mine Water Hydrogeochemistry of Abandoned Coal Mines in the Outcropped Carboniferous Formations, Ruhr Area, Germany. *Environ. Earth Sci.* 79, 1–16. doi:10.1007/s12665-020-8821-z

Vlassenbroeck, J., Dierick, M., Masschaele, B., Cnudde, V., Van Hoorebeke, L., and Jacobs, P. (2007). Software Tools for Quantification of X-ray Microtomography at the UGCT. *Nucl. Instr. Methods Phys. Res. Section A: Acc. Spectrometers, Detectors Associated Equipment* 580, 442–445. doi:10.1016/j.nima.2007.05.073

Weinhardt, F., Class, H., Vahid Dastjerdi, S., Karadimitriou, N., Lee, D., and Steeb, H. (2021). Experimental Methods and Imaging for Enzymatically Induced Calcite Precipitation in a Microfluidic Cell. *Water Res.* 57, e2020WR029361. doi:10.1029/2020WR029361

Weiß, E.-G. (2020). Renewable Geothermal Energy–Latest Developments in Geothermics in North Rhine-Westphalia: New Finds. New Projects. New Research Facilities. *Mining Rep.* 156, 533–540.

Wildenschild, D., and Sheppard, A. P. (2013). X-ray Imaging and Analysis Techniques for Quantifying Pore-Scale Structure and Processes in Subsurface Porous Medium Systems. *Adv. Water Resour.* 51, 217–246. doi:10.1016/j.advwatres.2012.07.018

Wu, S., and Amin, A. (2003). "Automatic Thresholding of gray-level Using Multistage Approach," in Seventh International Conference on Document Analysis and Recognition, 2003. Proceedings. (IEEE), 493–497.

Yoon, S., Pineda, A. R., and Fahrig, R. (2010). Simultaneous Segmentation and Reconstruction: A Level Set Method Approach for Limited View Computed Tomography. *Med. Phys.* 37, 2329–2340. doi:10.1118/1.3397463

Conflict of Interest: The authors declare that this study received funding from geomecon GmbH. The funder was not involved in the study design, collection, analysis, interpretation of data, the writing of this article or the decision to submit it for publication.

Copyright © 2021 Balcewicz, Siegert, Gurris, Ruf, Krach, Steeb and Saenger. This is an open-access article distributed under the terms of the Creative Commons Attribution License (CC BY). The use, distribution or reproduction in other forums is permitted, provided the original author(s) and the copyright owner(s) are credited and that the original publication in this journal is cited, in accordance with accepted academic practice. No use, distribution or reproduction is permitted which does not comply with these terms.

frontiers in Earth Science

ORIGINAL RESEARCH
published: 22 July 2021
doi: 10.3389/feart.2021.665275

On the Determination of Coordination Numbers of Coupled DEM-DFN Model for Modeling Fractured Rocks

Xiaoyi Xu[1,2], *Li-Yun Fu*[3]*, *Ning Liu*[4]* *and Tongcheng Han*[3]

[1]State Key Laboratory of Ore Deposit Geochemistry, Chinese Academy of Sciences, Institute of Geochemistry, Guiyang, China, [2]University of Chinese Academy of Sciences, Beijing, China, [3]Key Laboratory of Deep Oil and Gas, China University of Petroleum (East China), Qingdao, China, [4]College of Mechanical and Electrical Engineering, Beijing University of Chemical Technology, Beijing, China

Natural fractured rocks usually contain background granular media and multi-scale fractures. The coordination number is a crucial factor to characterize the connection of microstructural elements. The determination of coordination numbers for modeling fractured rocks is essential to interpret the distribution of cracks related to micromechanical properties. We have built a consistent workflow of discrete element models (DEMs) coupled with discrete fracture networks (DFNs). This DEM-DFN model could provide a simple formulation for high calculation efficiency to model a more realistic and detailed description of fracture system. A series of numerical experiments are set up, aiming to correlate window radius, particle size, and crack length, which will benefit the window selection for measuring coordination numbers based on the crack characteristics. The coordination number determined in the DEM-DFN modeling can be used to identify crack patterns in the spatial distribution.

Keywords: numerical simulation, crack information inversion, coordination number, measurement window, DEM-DFN model

OPEN ACCESS

Edited by:
Erik H. Saenger,
Bochum University of Applied Sciences, Germany

Reviewed by:
Luis Gago-Duport,
University of Vigo, Spain
Chuen-Fa Ni,
National Central University, Taiwan

***Correspondence:**
Li-Yun Fu
lfu@upc.edu.cn
Ning Liu
nicolaliu@buaa.edu.cn

Specialty section:
This article was submitted to Earth and Planetary Materials, a section of the journal Frontiers in Earth Science

Received: *11 February 2021*
Accepted: *07 July 2021*
Published: *22 July 2021*

Citation:
Xu X, Fu L-Y, Liu N and Han T (2021) On the Determination of Coordination Numbers of Coupled DEM-DFN Model for Modeling Fractured Rocks. Front. Earth Sci. 9:665275. doi: 10.3389/feart.2021.665275

INTRODUCTION

Natural fractured rocks in sedimentary basins generally consist of background granular media and a cluster of multiscale fractures. The former consists of irregular mineral (rock) grains jointed each other, composing the main body of rock masses. The latter refers to the microgeometry configuration of crack surfaces which control the mechanical behavior of rock masses. Continuum- and discrete-based methods have been widely used to model rocks. The former, mainly including finite-difference and finite-element numerical approaches, takes matter to be continuously distributed throughout a body. It provides a reasonable assumption for analyzing the macroscale behavior of rocks, with a high computational efficiency but suffering from strong homogenization. The latter regards rocks as an assembly of microstructural elements that interact with each other by microstructural forces, where equilibrium, kinematics, and constitutive equations are generated for each microstructural element. In the discrete-based model, the coordination number is a crucial factor to characterize the connection of microstructural elements. In this study, we address the determination of coordination numbers for modeling fractured rocks.

Such jointed media as rocks are natural to treat in a more fundamental and numerically intensive manner (Brown, 2008) that can specifically account for individual factors that affect the mechanical behavior of rocks. A discrete element method (DEM) (Cundall, 1971; Cundall, 1988) has the potential to meet this need and is now often used to model rock deformations (Mühlhaus and Vardoulakis, 1987; van Baars, 1996; Donzé et al., 1997; Williams and Rege, 1997; Oda and Iwashita,

2000; Bolton et al., 2004; Shiu et al., 2008; Scholtès and Donzé, 2013). In this method, the rock mass is represented as an assembly of discrete elements. Granular textures, particle-scale kinematics, and force transmission can be correlated at the microlevel (Cowin, 2004), constituting a powerful tool to study the effect of microstructures on the macroscopic properties of rocks. The DEM now appears as an efficient numerical method to handle most of the problems with rock masses, such as material heterogeneities, irregularly geometric characteristics, nonlinear large deformations, and progressive failure through nucleation and propagation of microcracks (Zhao, 2010; Jiang et al., 2017; Liu and Fu, 2020a; Liu et al., 2021). It is worth to mention that Murphy and Fehler (1986) conduct a DEM modeling for hot dry rocks of enhanced geothermal systems and attribute microseismic responses to shear slip along the joints in rocks. In this study, we use the 2D DEM code PFC2D (Itasca, 2014) to implement the coupled DEM-DFN modeling of fractured rocks.

Even a few cracks can significantly impact on the mechanical behavior of rock masses. Current digital imaging techniques can map heterogeneous rock properties in detail, including both microcracks and grain structures at micrometer resolutions. Spatial heterogeneities, aligned configurations, stress orientations, rough fracture surfaces, and material anisotropies strongly affect crack patterns and effective elastic characteristics of fractured rocks. To model such intersecting and multiscale fractures with a high density, we have to resort to discrete-based models (Jing and Hudson, 2002). A discrete fracture network (DFN) has been proposed for this purpose, which allows simulation of very complex fracture networks. The DFN refers to a microgeometry configuration of crack surfaces that explicitly represents the topological relationship between individual fractures or fracture sets. Combined with continuum- and discrete-based approaches, the DFN has been widely used in various engineering analyses with fractured rocks (Brady and Brown, 1993; van Baars, 1996; Jing, 2003; Gale et al., 2007; McClure, 2012; Alghalandis et al., 2017; Liu and Fu, 2020a). Continuum-based approaches coupled with DFN could model fractured rocks with only a sparsely connected DFN, but become difficult for high-density and complex DFNs because of the intrinsic limit of continuum-based methods (Jiang et al., 2017). For more complex DFNs, discrete-based approaches seem more suitable (Jing and Hudson, 2002), especially for fractured rocks with a wide range of mineral compositions and fabric anisotropies. In discrete-based methods coupled with a DFN, the positions of fractures and cracks are predefined by the DFN where the discrete elements crossing the DFNs are replaced by the corresponding joint particles (i.e., DEs), then solving the resulting system as a set of interacting elements according to Newtonian mechanics. Lei et al. (2017) conduct a DFN modeling for the mechanical and hydrological behavior of fractured rocks. Harthong et al. (2012) propose a coupled DEM-DFN model for strength characterization of rock masses.

The DEM connects elements through contact surfaces, with a flexibility to handle the contact complexity of granular materials (Zhao, 2010). Coordination number, defined as the average number of contacts per grain, is one of the important microstructural indexes of jointed media and contributes largely to particle-scale kinematics and microscopic mechanisms. The contact grid structure by coordination number in a granular system reflects the tightness and strength (e.g., Donzé et al., 1997; Scholtès and Donzé, 2013), critical state (Rothenburg and Kruyt, 2004), dynamic strength (Olson Reichhardt et al., 2015; Lemrich et al., 2017), and pore throat connectivity (Andriamihaja et al., 2019) of rocks. Zhang (2015) identifies the spatial distribution of cracks based on the change of coordination numbers in the measurement window, which shows a specific correlation between coordination numbers and crack distributions. This motivates us to estimate the coordination number in the measurement window for predicting the distribution of cracks from a simple two-dimensional (2D) scenario. For this purpose, we conduct a series of numerical experiments by applying the coupled DEM-DFN 2D model to emulate fractured rocks. We assume a homogeneous rock matrix, which is widely used in the available studies (Lei et al., 2017; Liu and Fu, 2020a; Liu and Fu, 2020b; Liu et al., 2021). Also, we keep a simple formulation of the DEM (i.e., spherical particles and linear elastic contact laws) for high calculation efficiency. The DFN is used to realize a more realistic and detailed description of the fracture system. The objective of this work is to optimize the window size with attempts to determine the distribution of coordination numbers, which captures the structural characteristics of cracks. In general, too large or too small windows cannot be able to localize the contact characteristics accurately and efficiently. We aim to correlate window radii, particle sizes, and crack lengths, which will facilitate the window selection for measuring coordination numbers based on the crack characteristics. It provides us an easy way to monitor the variation of coordination numbers to identify crack patterns in the spatial distribution.

After a brief description of the coupled DEM-DFN model, sensitivity analyses for single-crack and double-crack models with different arrangements will be provided to emphasize the effect of window sizes on the response, with the simulated crack information compared to the actual crack information obtained by digital imaging techniques. The resulting scale dependence of coordination numbers on the window sizes helps to quantify the correlation of window radii, particle sizes, and crack lengths for the single-crack and double-crack models. We then apply rock-fracturing and Brazilian splitting experiments with microcracks to validate our numerical scheme.

THEORY OF COUPLED DEM-DFN MODEL

The coupled DEM-DFN model for fractured rocks combines the rock matrix and fracture geometries represented by DEs and DFs, respectively. The DFN is merged into the background DEM in a simple yet efficient way, where the DE links that cross DFs are removed (Curtin and Scher, 1990; Liu and Fu, 2020a; Liu et al., 2021). In this section, we will introduce the coupled DEM-DFN model in detail.

DEM for Intact Rock Modeling

We use the DEM to model intact rock because of its ability of simulating the large deformation of jointed rock masses and expressing the geometric property of rock grains. In the present

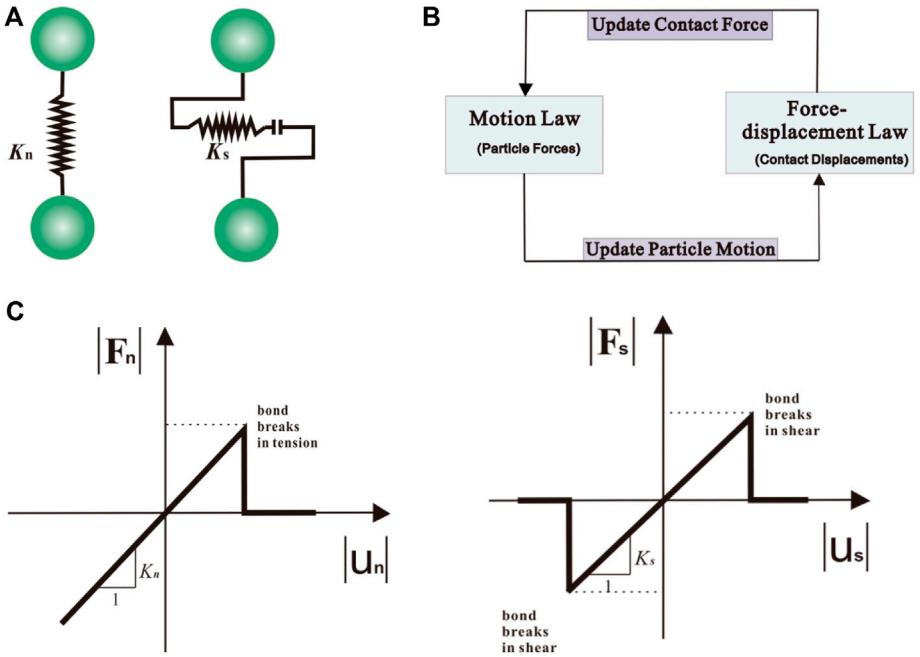

FIGURE 1 | Calculation cycle system **(A)** with normal and shear springs at contact surfaces **(B)** by microscale constitutive law **(C)**.

DEM model, intact rock is represented by a set of bonded spherical particles where elements interact through normal and shear springs at contact surfaces. The density of interaction bonds is controlled by coordination numbers to represent the main aspects of different rock types' behavior (Scholtès and Donzé, 2013). Every unitary force is accumulated for interaction where an explicit central finite difference is introduced to integrate individual motion equations for every element.

In this study, the optimal window of coordination-number measurements for a specific fractured rock is investigated based on the DEM code PFC^{2D} platform (Itasca, 2014) with regular hexagonal packings. The software uses rigid particles with a soft-contact mode, which cannot change their shapes or sizes, but allowing to overlap at contact surfaces. A brief description of the DEM model is given in **Supplementary Appendix A** for its particle-scale kinematics and equilibrium. The DEM algorithm involves two steps. First, interaction forces between DEs are calculated according to the force-displacement law. Second, Newton's law of motion is applied to each DE to update its velocity and position based on the force and moment, which is then time integrated to find its new position. This process is repeated until the simulation is finished. **Figure 1A** demonstrates the calculation cycle system of any DE, connecting with the normal and shear springs (see **Figure 1B**) at contact surfaces. The force-displacement law applied to each contact to update the contacting force using the microscale constitutive law, as shown in **Figure 1C**.

The DEs do not correspond to real mineral grains with distinct angularities and different sizes. The DEM formulation phenomenologically describes the particle-scale contact

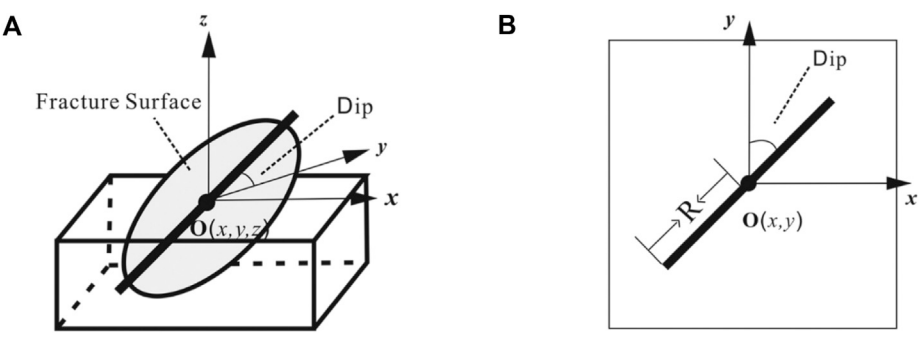

FIGURE 2 | Baecher model for crack characterization. **(A)** 3D Baecher disk. **(B)** 2D simplification.

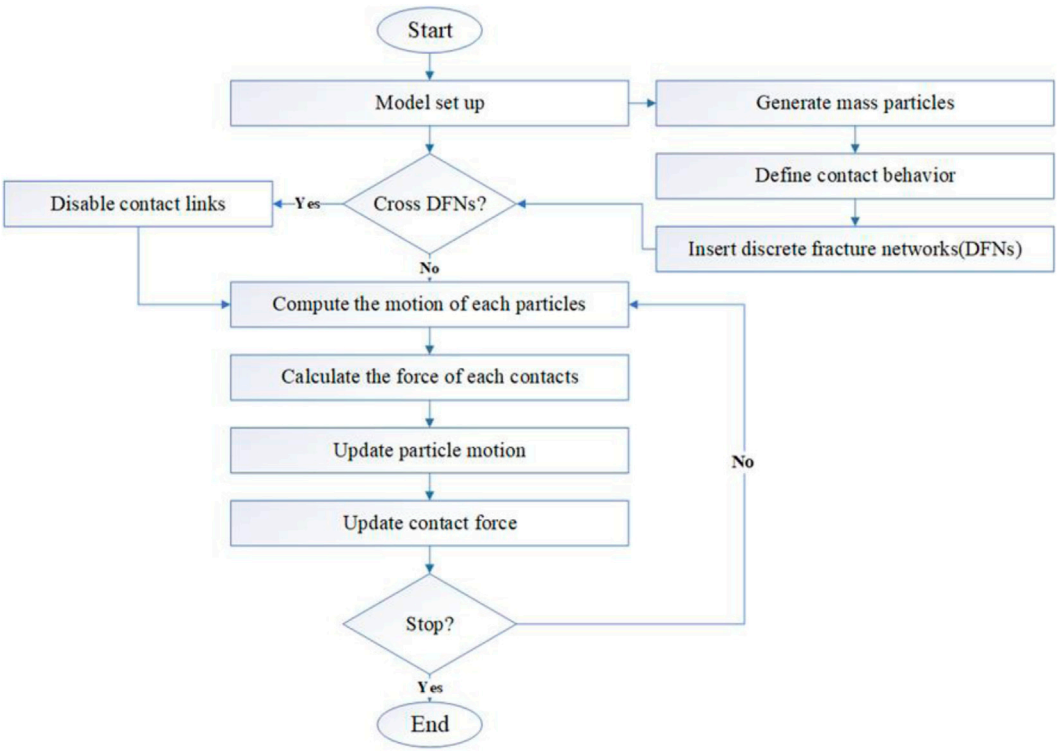

FIGURE 3 | Flowchart for DEM-DFN modeling.

behavior of jointed media by ignoring size-dependent effects for fast computations. The matrix of intact rock is emulated as an elastic, homogeneous, and isotropic medium. Even though this kind of element arrangement is one of the most convenient way to model discontinuum media, it may cause artificial anisotropy (Zhao, 2010). Harthong et al. (2012) generate polydisperse packings to avoid the anisotropic effect linked to regular packings.

DFN for Complex Fracture Modeling

The DFN starts with spatial statistics associated with a fracture network (fracture orientation, size, density etc.) measured by high-resolution SEM (scanning electron microscope) of cores or surface outcrops. These statistics reconstruct the topological relationship between individual fractures or fracture sets and can be used to generate realizations of fracture network with the same spatial properties. Therefore, the resultant DFN is a

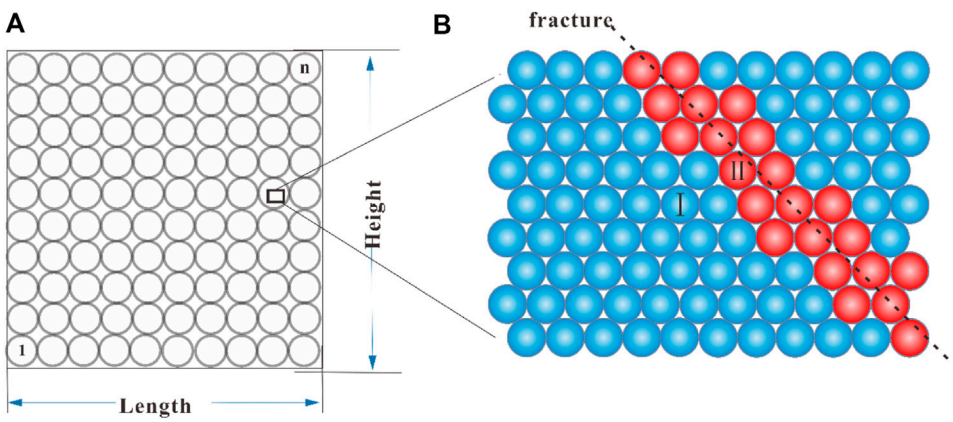

FIGURE 4 | A measurement layout for a sample with Length × Height in size. **(A)** Circular measuring windows. **(B)** Enlarged view of a circular window. Particles with normal contacts are indicated in blue and particles affected by fractures are shown in red.

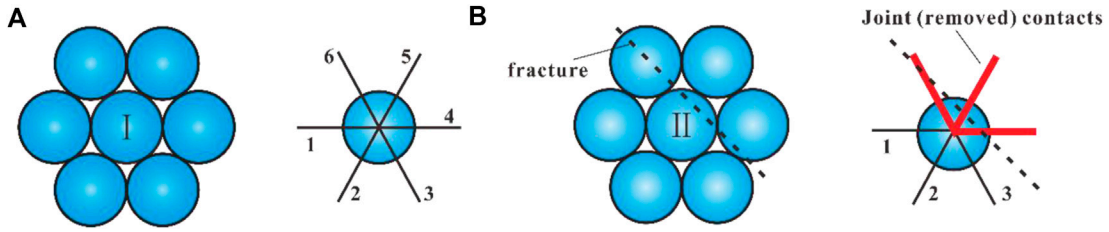

FIGURE 5 | Contact patterns for two different types of DEs away from and near the crack, respectively. **(A)** Normal contacts for Type I. **(B)** Joint (removed) contacts for Type II.

geometry configuration of fracture surfaces that explicitly represents the geometric property of individual fractures.

As shown in **Figure 2**, the DFN geometry is expressed by discrete surface elements, generated usually based on the point process represented by Baecher model (Baecher et al.,1977). For 3D cases, the Baecher model describes a crack as a disk (see **Figure 2A**) with inclination and area. In the 2D plane, the crack can be simplified as a line segment with different lengths and dip angles (see **Figure 2B**). The point process determines the center position of the crack, associated with the attributes of the point, such as crack length, direction, inclination, and other crack properties. It is worth noting that Harthong et al. (2012) do not consider the discontinuity thickness of 2D and 3D models. In this study, we could represent the crack aperture by the relative normal displacement of joint particles on each side of the fracture. We produce single-crack and double-crack models with different lengths and dip angles. We optimize the window size to estimate coordination numbers that capture the structural characteristics of cracks based on a series of numerical experiments.

The obtained DFN can be inserted into the background DEM. The entire calculation process for the coupled DEM-DFN modeling is illustrated in **Figure 3**. First, the coordinates of mass DEs are generate within a specific area, with the contacts between DEs defined properly. Then, the corresponding DFN, created by fracture attributes, is merged into the DEM, where the contact links crossing the DFs are removed (Curtin and Scher, 1990; Liu and Fu, 2020a; Liu et al., 2021). The force and moments acting on each DE are calculated, such that the position of DEs can be updated by a central difference scheme. The updated forces acting on every contact are estimated from the relative displacement of DEs. More details are given in **Supplementary Appendix A**. The resultant DEM-DFN coupling model can be used to simulate fractured rocks.

Coordination Number

Oda (1977) experimentally investigates the coordination number of random assembly of particles, which is defined as the mean number of contacts between a particle and other particles around. Interaction forces between every pair of particles are transferred through their contact surfaces (Cundall, 1988). Therefore, the coordination number is an important parameter to describe the micromechanical behavior of materials. Previous studies have given several typical formulas to compute the coordination number (e.g., Scholtès and Donzé, 2013). Bathurst (1987) defines the average coordination number in the particle aggregation system as M/N, where M and N are the total numbers of contacts and particles, respectively.

Some particles in a particle system are often in the state of no contact or only one contact. Such contacts have no effect on the force transmission in the particle system. These inaction particles should not be considered when analyzing the coordination number of particles in the system. Therefore, Thornton (2000) excludes the inaction particles by defining the average coordination number C_n in the particle system as,

$$C_n = \frac{2M_c - N_1}{N - N_1 - N_0}, C_n \geq 2 \tag{1}$$

where M_c is the number of contact pairs, N is the total number of particles, N_1 is the number of particles with only one contact, and N_0 is the number of suspended particles with no contact. To eliminate suspended particles for the accuracy of measurements, the sample is compacted prior to the start of measurements. In a compact system without suspended particles, the mean coordination number can be calculated as (Itasca, 2014)

$$C_n = \frac{\sum_{i=1}^{N} M_i}{N} \tag{2}$$

where M_i ($i = 1, 2, \cdots, N$) is the contact number of the ith particle.

Measurement Window Generation and Coordination Number Estimation

Mauldon et al. (2001) propose a method of characterizing the crack geometry with circular scanlines and circular windows. Here, we generate a measurement window by specifying a radius at the coordinate center in a similar way. Then, we use a control variable to quantify the relationship between window radii and particle sizes. For a given particle size, we change the window radius and extract crack properties to investigate the effect of window radii. In this way, we can achieve an optimal measurement window.

Aparicio and Cocks (1995) demonstrate that the coordination value of a single particle system under the quasi-static state is 6. That is, when the time step is small enough, the whole movement process under a quasi-static loading is regarded as the static calculation with a constant acceleration and speed. The contact number between each particle and its surrounding particles is approximatively six for a system with the same particle radius according to **Eq. 2**.

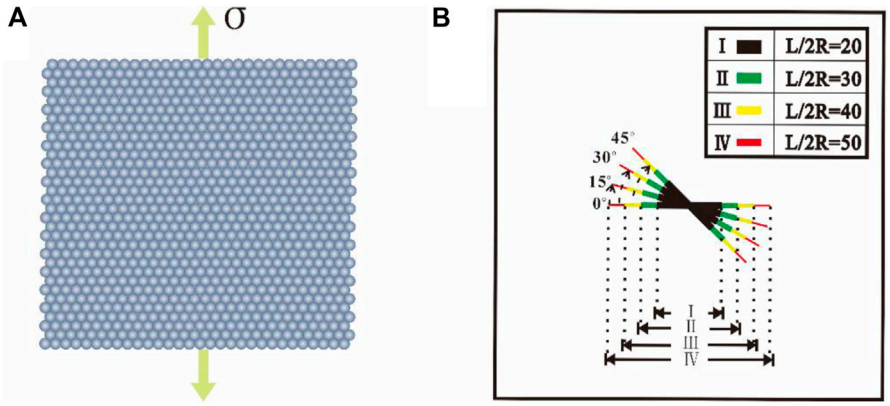

FIGURE 6 | Loading path and single crack diagram. **(A)** Uniaxial tensile test. **(B)** Single-crack design.

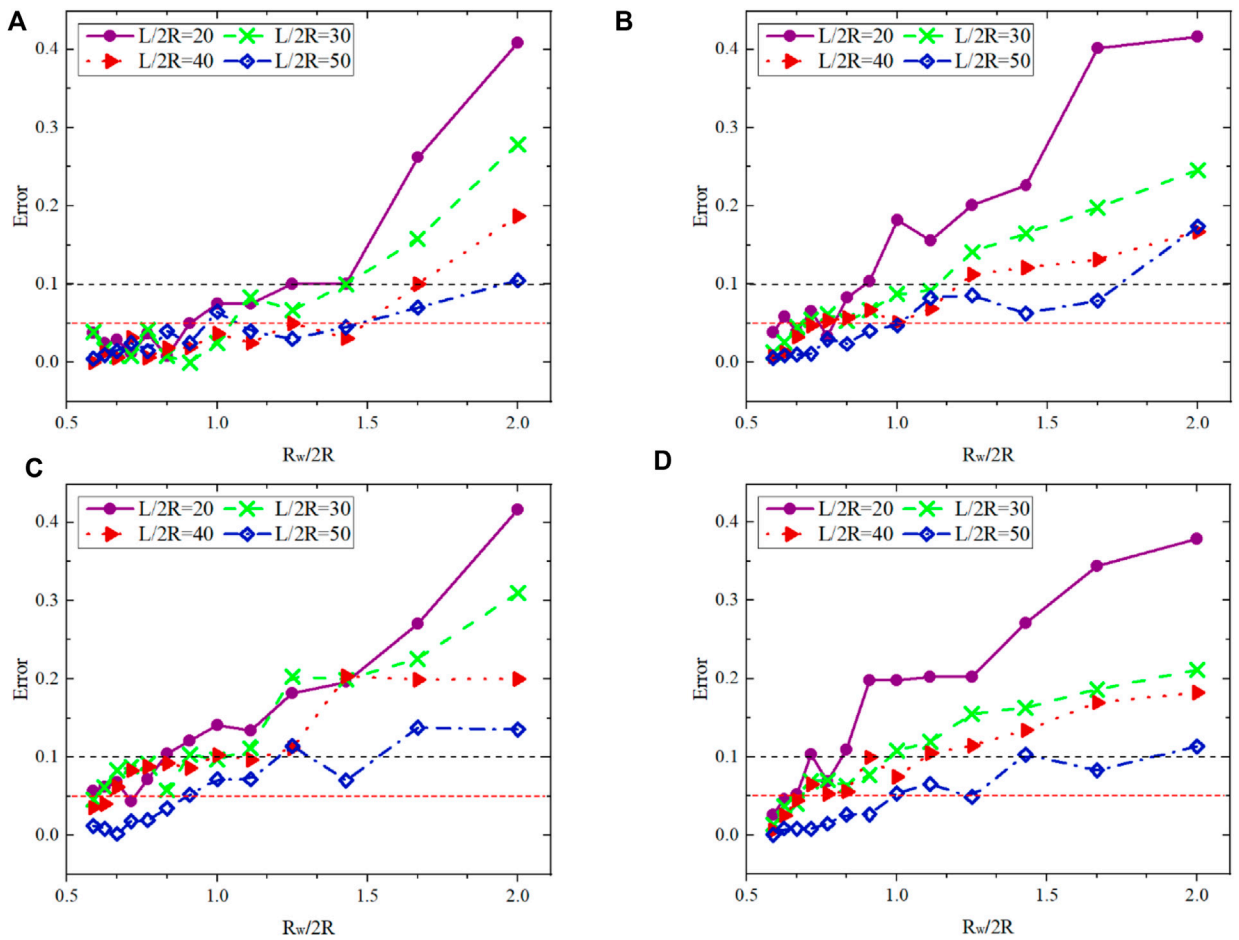

FIGURE 7 | Errors of estimated and realistic crack lengths vs. dimensionless parameter for four different dip angles in the single crack DEM-DFN model. **(A)** 0° single-crack measurement error. **(B)** 15° single-crack measurement error. **(C)** 30° single-crack measurement error. **(D)** 45° single-crack measurement error.

Figure 4A shows a measurement layout covered uniformly with a number of circular measuring windows for a sample (Length × Height in size). We aim to use fewer measuring windows to monitor more particles, achieving the optimal size of measurement windows, as shown in **Figure 4B** for an enlarged view of a circular window.

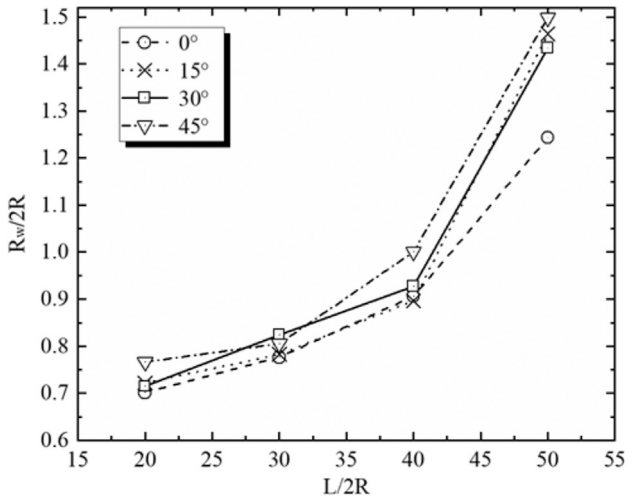

FIGURE 8 | Crossplot of two dimensionless parameters (Rw/2R and L/2R) for the determination of optimal measuring windows in the single-crack DEM-DFN model.

In **Figure 4B**, we see a crack across the DE link of red particles. Two different types of DEs are defined in this measuring window. Type I away from the crack denotes the regular DEs with a normal contact to the surrounding DEs. Type II near the crack represents the DF-DEs with a joint (removed) contact to the surrounding DEs. **Figure 5** shows the contact pattern for these two types of DEs, respectively. We see that these two types of contact patterns have different contact numbers that cause the difference in estimating coordination numbers because the measuring window does not count these joint (removed) contacts. Therefore, we can judge whether there are cracks in the measuring area according to the decrease of coordination numbers. Theoretically, the methodology is suitable for any case where the background medium shares the same or almost the same coordination numbers, even if DEs are in hexagonal, orthogonal, or polydisperse packings with a minimal size ratio that represents different material types, such as rocks (Liu and Fu, 2020b), concrete (Nitka and Tejchman, 2015), or even Martian regolith (Lai and Chen, 2017). In other words, the modeled matrix could be isotropic or anisotropic in 2D or 3D, as long as the measurement window placement is optimized. Specifically,

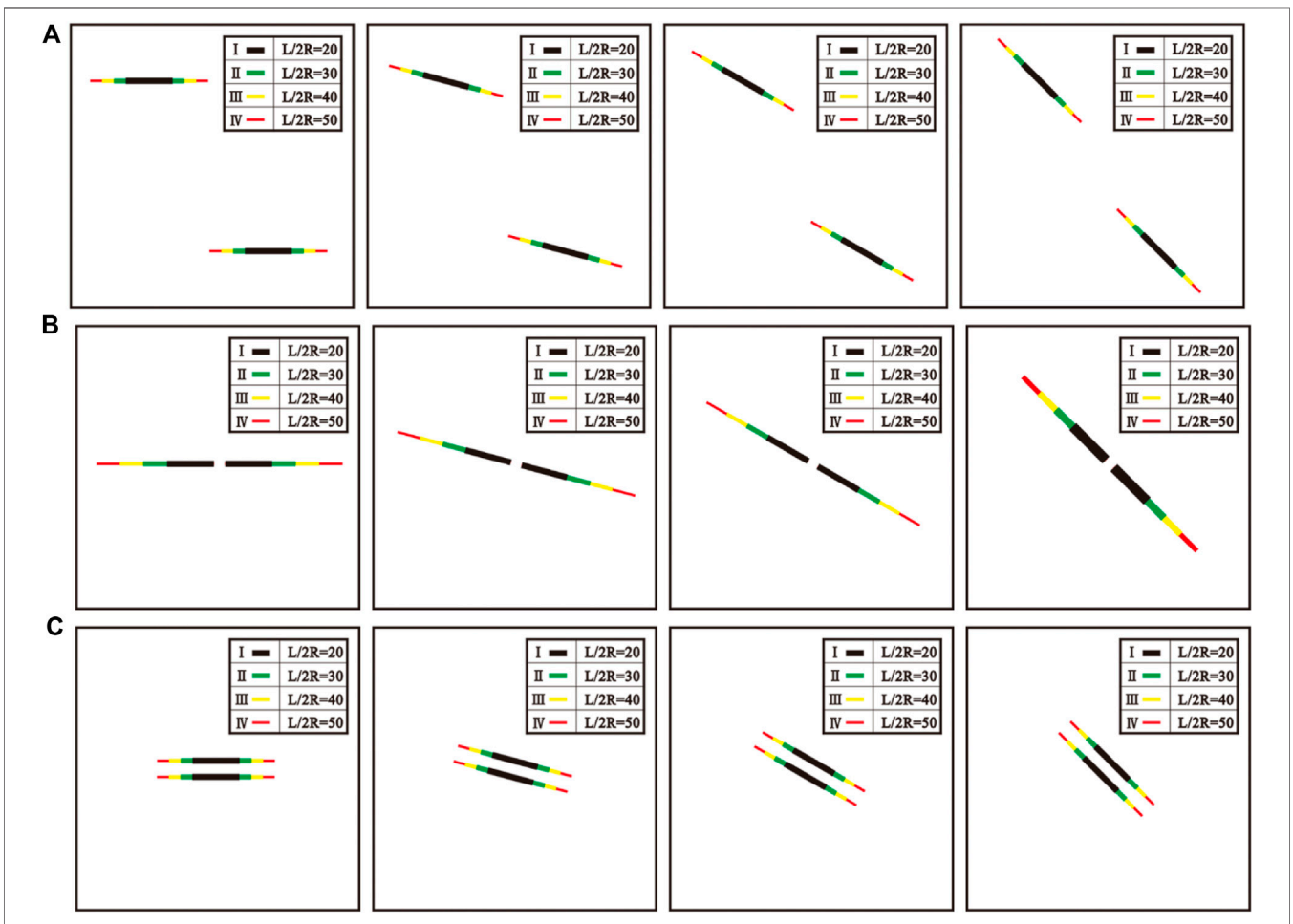

FIGURE 9 | Three types of spatial arrangements of double cracks with different lengths (20, 30,40, and 50 mm) and dip angles (0°, 15°, 30°, and 45°). **(A)** Distant double cracks. **(B)** Collinear double cracks. **(C)** Stacked double cracks.

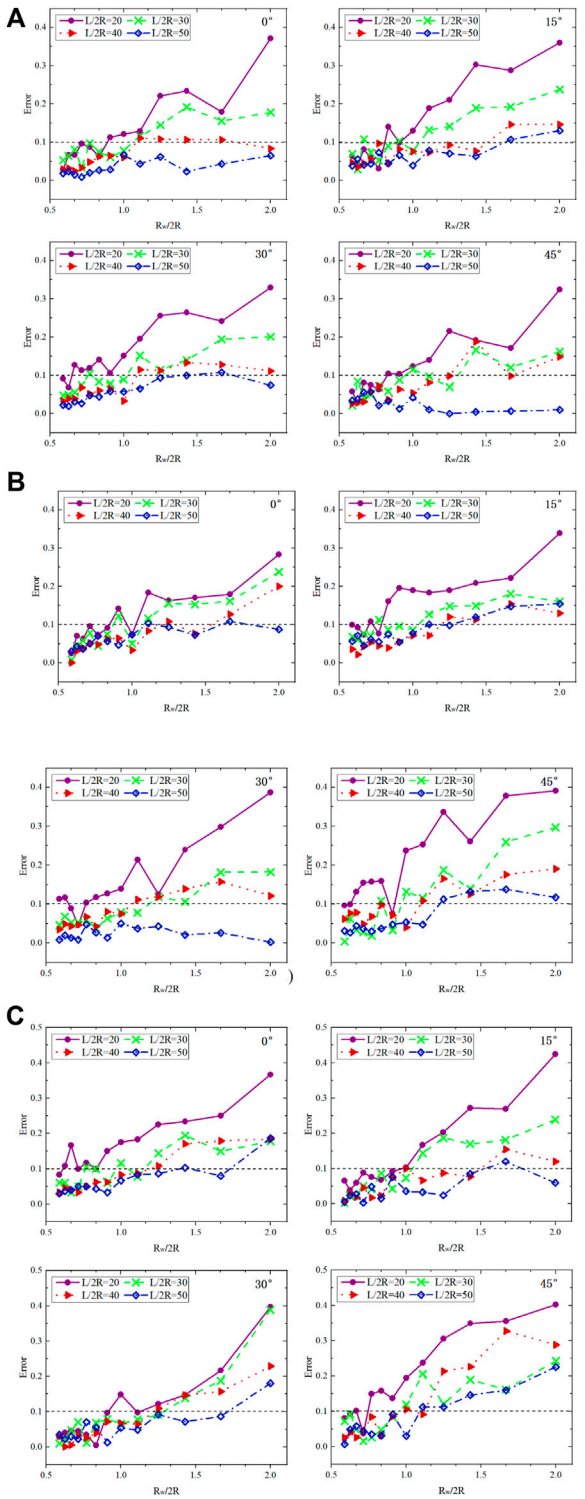

FIGURE 10 | Errors of estimated and realistic crack lengths vs. dimensionless parameter for these three double-crack DEM-DFN models as shown in **Figure 9**. **(A)** Distant double cracks. **(B)** Collinear double cracks. **(C)** Stacked double cracks.

this coordination-number-based crack inversion method is also suitable for the case in that the rock matrix with approximately the same coordination numbers is not isotropic and homogenous media as mentioned in the references (e.g., Liu et al., 2017; Liu and Fu, 2020b).

GUIDELINES FOR OPTIMAL MEASUREMENT WINDOW SELECTION

This section provides clear guidelines for selecting optimal windows in the modeling of fractured media based on the single and double crack DEM-DFN models. We use measuring windows with different radii for a sample to produce groups of coordination data. For each measurement, crack characteristics could be identified by the estimated coordination number image and then extracted using digital image processing techniques. Comparisons between the extracted and the realistic crack properties allow us to select a reasonable measuring window radius.

Single-Crack DEM-DFN Model

We conduct a series of uniaxial tensile tests (see **Figure 6A**) for a sample of L = 10 mm in length using equal-radius (R = 0.5 mm) particles set in a regular hexagonal grid. In the DFN model, we couple a single crack into the DEM model. As shown in **Figure 6B**, the single crack is designed with four different lengths of 20, 30, 40, and 50 mm (denoted by I, II, III, and IV in the figure, respectively) and four different dip angles of 0°, 15°, 30°, and 45°. Noted that, the crack length in the DEM-DFN simulation is generally suggested to be more than ten times the particle radius and less than half the length of the sample (Harthong et al., 2012). It ensures that the pre-existing fractures modeled do not cross the whole sample with enough resolution. We have 16 parameter models in total for uniaxial tensile tests.

For each parameter model, we use 12 different-radius measuring windows to monitor its coordination numbers, respectively. A dimensionless parameter, the size ratio of the measurement window to particles, is introduced to measure the optimization of results. For each simulation, the coordination number is retrieved from the resulting coordination cloud chart and processed by image binarization. **Figure 7** shows the error of estimated and realistic crack lengths vs. dimensionless parameter for four different dip angles, respectively. We see that the different radius measuring windows lead to different deviations in measuring the crack length, implying a metric match between measuring windows and inversion errors for a given crack length. We aim to use fewer measuring windows to monitor more particles. Larger windows cause more significant errors but with fewer computational costs. The errors become quite small for the dimensionless parameter less than 1, with their distribution concentrated around 0.05, as displayed in **Figure 7**.

The simulated data in **Figure 7** are used for first-order differentiation analyses to determine the optimal radius of

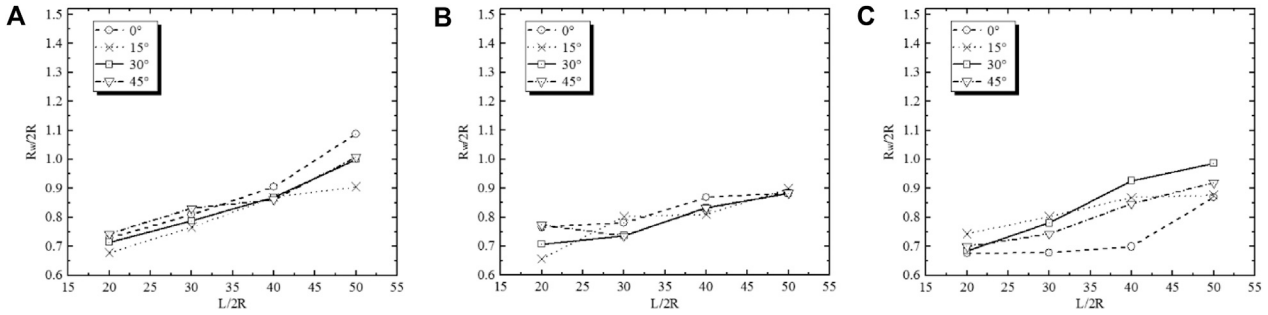

FIGURE 11 | Crossplots of dimensionless parameters (R_w/2R and L/2R) for the determination of optimal measuring windows in these three double-crack DEM-DFN models as shown in **Figure 9**. **(A)** Distant double cracks. **(B)** Collinear double cracks. **(C)** Stacked double cracks.

measuring windows. We take the initial value at the starting point of Rw/2R as the basis for differentiation calculations. The results for different dip angles are shown in **Figure 8**, where two dimensionless parameters are correlated each other. We see that for the regular orthogonal window with the compression direction along the vertical axis, the optimal radius of measuring windows is related to the projection length of a crack in the horizontal direction. Among these cracks with the same length, the 0°crack presents a relatively small radius for the optimization window. The optimal radius is also affected by the size and proportion of cracks. We note that L/2R = 40 corresponds to an inflection point, with the corresponding crack length up to 40% of the sample length. Compared to the model size used in this paper, the crack size for L/2R > 40 is relatively large. We can choose a larger window radius with fewer windows for a rough estimation of coordination numbers that can capture approximately the position of cracks in the sample. This facilitates the estimation of local mechanical properties.

The optimal Rw/2R ranges from 0.7 to 1.5 for given crack lengths. In conclusion, we can select the optimal radius of measuring windows for different-length cracks based on the crossplot of two dimensionless parameters (Rw/2R and L/2R), as shown in **Figure 8**.

Double-Crack DEM-DFN Model

The single-crack numerical experiments addressed previously are extended to a double-crack DEM-DFN model using the same mechanical and testing parameters. Two cracks are coupled into the DEM model by three types of spatial arrangements (Zhao et al., 2016) to characterize different stress interactions, where the distant, collinear, and stacked double cracks represent non interaction, stress amplification, and stress shielding, respectively. **Figure 9** shows different spatial arrangements for double cracks with different lengths and dip angles, with each having 16 parameter models in total for uniaxial tensile tests.

Similarly, for each parameter model, twelve different-radius measuring windows are used to monitor its coordination numbers, respectively. The coordination number for each model is retrieved from the resulting coordination cloud chart, and in turn, is used to estimate the crack length. Errors of the estimated and realistic crack lengths are related to the dimensionless parameter

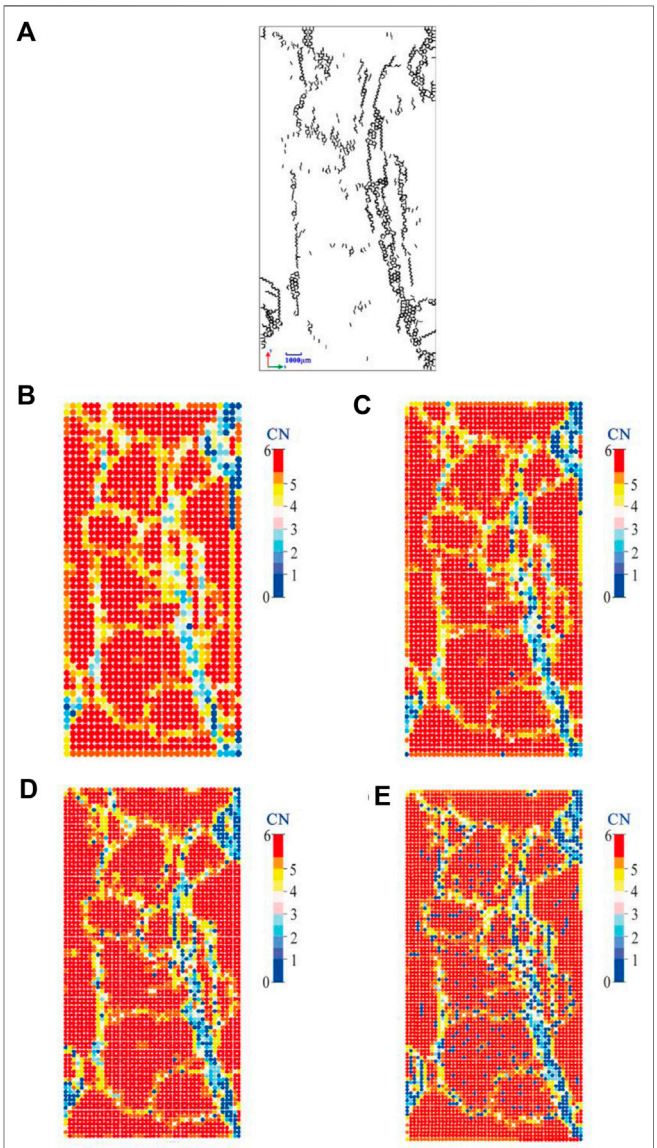

FIGURE 12 | Rock sample with microcracks **(A)** with estimated coordination number (CN) maps for four different-radius measuring windows. **(B)** $\frac{R_w}{2R}$ = 1.5. **(C)** $\frac{R_w}{2R}$ = 1.0. **(D)** $\frac{R_w}{2R}$ = 0.9. **(E)** $\frac{R_w}{2R}$ = 0.8.

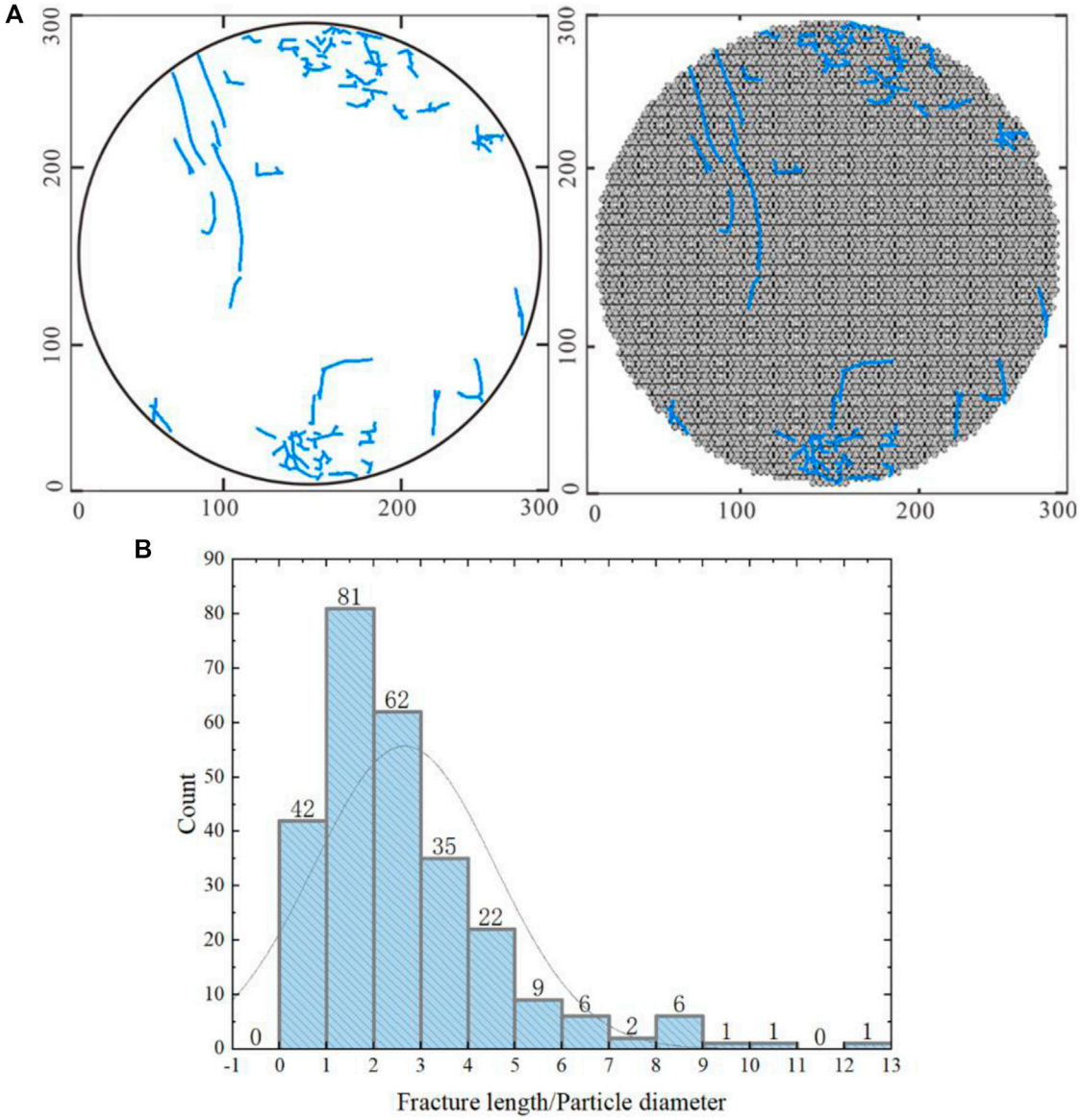

FIGURE 13 | (A) Rock sample with cracks (unit: m). **(B)** Crack length histogram.

(Rw/2R), as shown in **Figure 10** for the three spatial arrangements of double cracks. We see that the deviations of crack lengths by different-radius measuring windows become more complex than those of the single-crack model (see **Figure 7**), though both the models share similar features. Different spatial arrangements of double cracks show a similar trend of error variations. Smaller measuring windows for longer cracks produce smaller measurement errors. However, the interaction between different arrangements of double fractures leads to a worse consistency of error variations than the single-crack model. As shown in Zhao et al. (2016), the double cracks with different spatial arrangements represent different types of stress interactions. Unlike distant double cracks and collinear double cracks, the stacked double cracks show larger errors possibly because of the stress shielding. The change in angles seems to have no obvious effect on the measurement error. The cracks with four different angles share similar trends in error variations. Shorter cracks have a larger measurement error, whereas longer cracks have a smaller measurement error. For the dimensionless parameter less than 1, however, the errors become small with their distribution concentrated around 0–0.1.

The simulated data in **Figure 10** are used for first-order differentiation analysis in terms of the dimensionless parameters Rw/2R and L/2R to determine the optimal radius of measuring windows. The results are shown in **Figure 11** for the three modes of double cracks. We see that unlike **Figure 8** for the single-crack model the optimal window radius for double cracks doesn't change much across different crack lengths and dip angles. Particularly, the effect of dip angles is rather small perhaps because of the

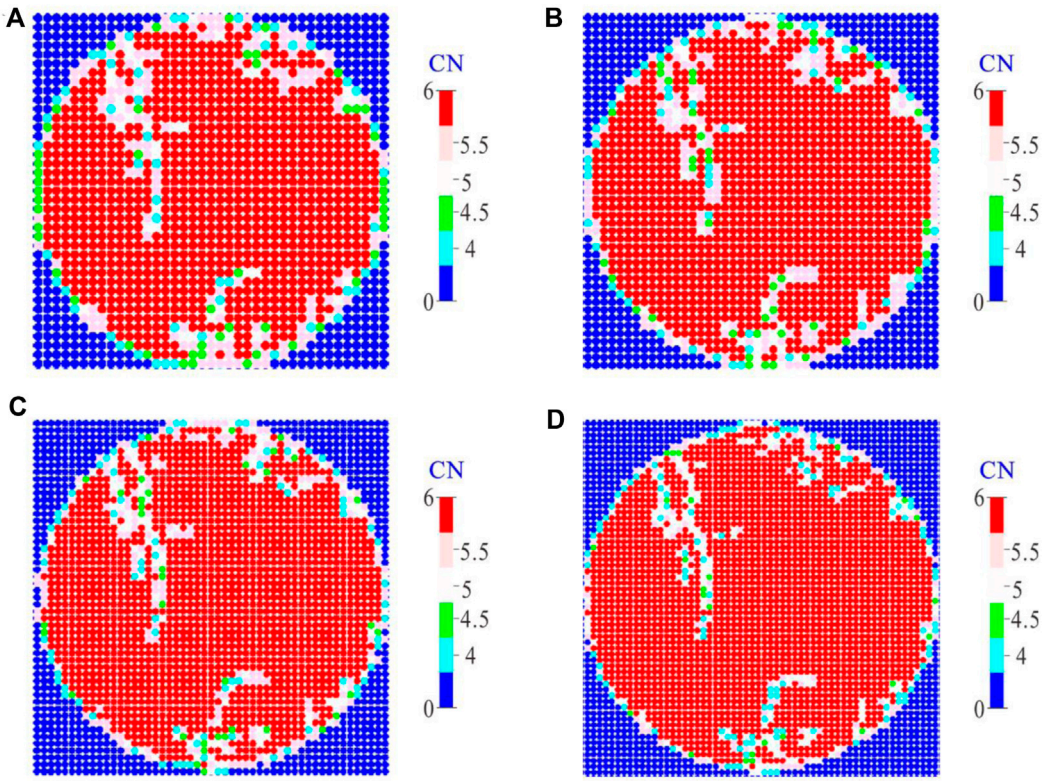

FIGURE 14 | Estimated coordination number (CN) maps for four different-radius measuring windows. **(A)** $\frac{R_w}{2R}$ = 0.9. **(B)** $\frac{R_w}{2R}$ = 0.8. **(C)** $\frac{R_w}{2R}$ = 0.7. **(D)** $\frac{R_w}{2R}$ = 0.6.

interaction between cracks. The measurement error changes slowly with increasing window radii. The optimal Rw/2R ranges from 0.6 to 1.1 for given crack lengths.

METHOD VERIFICATION AND APPLICATION

Direct tension tests are believed to be reliable, but it is difficult to prepare samples and configurate tests (Patel and Martin, 2017). Uniaxial compression and Brazilian split tests have been widely used as a simple and effective way to determine rock tensile strengths (Bieniawski and Hawkes, 1978; ASTM D3967-08, 2008). In this section, we conduct these tests of realistic rock samples to estimate coordination numbers with different-radius measuring windows based on the guidelines in *Guidelines for Optimal Measurement Window Selection*.

Case 1: Uniaxial Compression Test

A rock sample with natural cracks (including crossed fractures) from a real outcrop is imaged by high-resolution SEM techniques. The resulting digital section, as shown in **Figure 12A** is used for uniaxial compression tests. We see groups of complex cracks that distribute over the rock matrix in white. Based on the crossplot (see **Figures 8**, **11**) of dimensionless parameters (Rw/2R and L/2R) for the determination of optimal measuring windows, we select four different-radius measuring windows for tests.

The estimated distribution of coordination numbers is shown in **Figures 12B–E** for different values of Rw/2R, respectively. We see that the most area of sample image can be modeled by normal-contact particles without cracks crossing, leading to the maximum coordination number (in red), whereas the fractured areas by joint particles with cracks crossing cause the decrease of coordination numbers, which becomes more evident for the crossed fracture areas. Compared to **Figure 12A**, we also see that **Figure 12B** at Rw/2R = 1.5 underestimates the effect of cracks because of the distribution of overvalued coordination numbers in the fractured areas, whereas **Figure 12E** at Rw/2R = 0.8 seems to overestimate the effect of cracks because of too many blue particles even in non-crack areas. The optimal measuring window is probably located around Rw/2R = 0.9, as shown in **Figure 12D**.

Case 2: Brazilian Split Test

The Brazilian splitting test is known as the diametrical compressive test or splitting tension test (Bieniawski and Hawkes, 1978), which could be used to calculate the effective elasticity of an object under different loading orientations, with an attempt to minimize the anisotropy caused by cubic specimens (Liu and Fu, 2020a). **Figure 13** shows a real outcrop of Ordovician carbonates in the northwest of the Shuntuoguole low uplift of Tarim Basin. We choose a circle zone as the target to conduct the Brazilian splitting test with a compressive strain rate of 0.015/s. **Figure 13A** shows the extracted fractures from the real

outcrop and the corresponding DEM-DFN model with the length statistics of fracture segments displayed in **Figure 13B**.

Figure 14 shows four groups of coordination-number distributions with different dimensionless parameters with the measurement window (Rw/2R and L/2R). We see that most of the red areas show normal-contact particles without cracks crossing, and the coordination number is approximately 6. In the fractured areas, the coordination number decreases to less than six due to the effect of joint (removed) contacts. Therefore, the inversion result becomes better for smaller dimensionless parameters of Rw/2R, like 0.7, or even 0.6.

CONCLUSION

Coordination number is a crucial microstructural index of jointed rocks. We apply a coupled DEM-DFN model to simulate multi-scale fractured rocks with a high calculation efficiency. The objective is to optimize the size of measurement windows to determine the coordination number distribution that captures the structural characteristics of cracks. The main conclusions can be summarized as follows.

The measurement window is arranged in a regular orthogonal way with its compression direction along the vertical axis. Thus, the optimal window radius can be determined in terms of the projection length of a crack in the horizontal direction. Numerical experiments with various single-crack models show that the optimal radius is affected by the size, dip angle, and proportion of cracks. It can be estimated based on the crossplot of two dimensionless parameters (Rw/2R and L/2R) for different-length cracks. For cracks of the same length, the 0°crack has a relatively small radius for the optimization window. In general, we can choose a larger window radius with fewer windows for the rough estimation of coordination numbers that can capture approximately the position of cracks in the sample.

Unlike single-crack models, double-crack models (distant, collinear, and stacked arrangements) show complex error variations of the estimated and realistic crack lengths against the dimensionless parameter (Rw/2R) because of the interaction (no interaction, stress amplification, and stress shielding) between cracks. Numerical experiments with various double-crack models of different lengths and dip angles are performed to monitor the optimal coordination number for different-radius measuring windows. Although these models share similar error features, the crack interaction increases the deviation of error changes for different-radius measuring windows. Unlike distant double cracks and collinear double cracks, the stacked double cracks show larger errors possibly because of the stress shielding. The change in dip angles has no obvious effect on the measurement error. Shorter cracks have a larger measurement error whereas longer cracks have a smaller measurement error.

Uniaxial compression and Brazilian split tests for a rock sample from a real outcrop with natural cracks are used to validate the inversion of crack properties by the coupled DEM-DFN model through optimizing measurement windows for the estimation of coordination numbers. The estimated distribution of coordination numbers for different values of Rw/2R demonstrates that the optimal measuring window is probably located around Rw/2R = 0.6–0.9. The area without cracks crossing in the image can be modeled by normal contact particles with the maximum coordination number, whereas the area with cracks crossing is modeled by joint particles with less coordination numbers.

This work proposes a coordination-number-based crack inversion method for isotropic homogenous media in 2D. According to the quantitative evaluation and the characteristic comparison, it is reasonable to confirm that the methodology is efficient. Moreover, we may extend the conclusion to any case where the matrix DEs share the same coordination number, regardless of the types of materials, or packings in 2D or 3D. For more complex cases, the measurement window placement needs further optimization. Meanwhile, as we all know, even a few cracks can significantly impact the mechanical behavior of rock masses, so this kind of crack inversion method might have the potential for numerical upscaling from the microstructural responses to the macroscopic properties of fractured rocks. We would investigate the issues in the subsequent work.

DATA AVAILABILITY STATEMENT

The raw data supporting the conclusion of this article will be made available by the authors, without undue reservation.

AUTHOR CONTRIBUTIONS

LF, NL, and XX conceive this research. XX writes the manuscript and prepares the figures. LF and NL review and supervise the manuscript. The co-author TH are involved in the discussion of the manuscript. All authors finally approve the manuscript and thus agree to be accountable for this work.

FUNDING

The research is supported by the National Natural Science Foundation of China (Grant Nos. 41821002, 41720104006) and 111 Project "Deep-Superdeep Oil and Gas Geophysical Exploration" (B18055).

SUPPLEMENTARY MATERIAL

The Supplementary Material for this article can be found online at: https://www.frontiersin.org/articles/10.3389/feart.2021.665275/full#supplementary-material

REFERENCES

Alghalandis, Y. F., Elmo, D., and Eberhardt, E. (2017). *Similarity Analysis of Discrete Fracture Networks*. Ithaca, NY: arXiv 1711.05257.

Andriamihaja, S., Padmanabhan, E., Ben-Awuah, J., and Sokkalingam, R. (2019). Static Dissolution-Induced 3D Pore Network Modification and its Impact on Critical Pore Attributes of Carbonate Rocks. *Pet. Exploration Dev.* 46, 374–383. doi:10.1016/s1876-3804(19)60017-0

Aparicio, N. D., and Cocks, A. C. F. (1995). On the Representation of Random Packings of Spheres for Sintering Simulations. *Acta Metall Mater* 43, 3873–3884. doi:10.1016/0956-7151(95)90170-1

ASTM D3967-08 (2008). *Standard Test Method for Splitting Tensile Strength of Intact Rock Core Specimens*. West Conshohocken, PA: ASTM International.

Baecher, G. B., Lanney, N. A., and Einstein, H. H. (1977). "Statistical Description of Rock Properties and Sampling," in *Proceedings of the 18th US Symposium on Rock Mechanics* (New York: American Rock Mechanics Association).

Bathurst, R. J. (1987). "A Study of Stress and Anisotropy in Idealized Granular Assemblies,". Dissertation thesis (Kingston, Canada: Queen's University).

Bieniawski, Z. T., and Hawkes, I. (1978). Determining Rock Mass Deformability: Experience from Case Histories. *Int. J. Rock Mech. Mining Sci. Geomechanics Abstr.* 15, 237–247. doi:10.1016/0148-9062(78)90956-7

Bolton, M. D., Nakata, Y., and Cheng, Y. P. (2004). Crushing and Plastic Deformation of Soils Simulated Using DEM. *Géotechnique* 54, 131–141.

Brady, B. H., and Brown, E. T. (1993). *Rock Mechanics for Underground Mining*. Springer Science & Business Media.

Brown, E. T. (2008). "Estimating the Mechanical Properties of Rock Masses," in proceedings of the Southern Hemisphere International Rock Mechanics Symposium (Perth: Australian Centre for Geomechanics), 3–22. doi:10.36487/acg_repo/808_16

Cowin, S. C. (2004). Anisotropic Poroelasticity: Fabric Tensor Formulation. *Mech. Mater.* 36, 665–677. doi:10.1016/j.mechmat.2003.05.001

Cundall, P. A. (1971). "A Computer Model for Simulating Progressive Largescale Movements in Blocky Rock Systems," in Proceedings of the Symposium of the International Society of Rock Mechanics (France: Society for Rock Mechanics (ISRM)), 2–8.

Cundall, P. A. (1988). Formulation of a Three-Dimensional Distinct Element Model-Part I. A Scheme to Detect and Represent Contacts in a System Composed of many Polyhedral Blocks. *Int. J. Rock Mech. Mining Sci. Geomechanics Abstr.* 25, 107–116. doi:10.1016/0148-9062(88)92293-0

Curtin, W. A., and Scher, H. (1990). Mechanics Modeling Using a Spring Network. *J. Mater. Res.* 5, 554–562. doi:10.1557/jmr.1990.0554

Donzé, F. L., Bouchez, J., and Magnier, S. A. (1997). Modeling fractures in rock blasting. *Int. J. Rock Mech. Min. Sci.* 34 (8), 1153–1163. doi:10.1016/s1365-1609(97)80068-8

Gale, J. F. W., Reed, R. M., and Holder, J. (2007). Natural Fractures in the Barnett Shale and Their Importance for Hydraulic Fracture Treatments. *Bulletin* 91, 603–622. doi:10.1306/11010606061

Harthong, B., Scholtès, L., and Donzé, F.-V. (2012). Strength Characterization of Rock Masses, Using a Coupled DEM-DFN Model. *Geophys. J. Int.* 191, 467–480. doi:10.1111/j.1365-246x.2012.05642.x

Itasca Consulting Group, Inc (2014). PFC2D (Particle Flow Code in 2 Dimension), Version 5.0. Minneapolis: ICG.

Jiang, C., Zhao, G.-F., and Khalili, N. (2017). On Crack Propagation in Brittle Material Using the Distinct Lattice spring Model. *Int. J. Sol. Structures* 118-119, 41–57. doi:10.1016/j.ijsolstr.2017.04.024

Jing, L. (2003). A Review of Techniques, Advances and Outstanding Issues in Numerical Modelling for Rock Mechanics and Rock Engineering. *Int. J. Rock Mech. Mining Sci.* 40, 283–353. doi:10.1016/s1365-1609(03)00013-3

Jing, L., and Hudson, J. A. (2002). Numerical Methods in Rock Mechanics. *Int. J. Rock Mech. Mining Sci.* 39, 409–427. doi:10.1016/s1365-1609(02)00065-5

Lai, Z., and Chen, Q. (2017). Characterization and Discrete Element Simulation of Grading and Shape-dependent Behavior of JSC-1A Martian Regolith Simulant. *Granular Matter* 19, 1–14. doi:10.1007/s10035-017-0754-1

Lei, Q., Latham, J.-P., and Tsang, C.-F. (2017). The Use of Discrete Fracture Networks for Modelling Coupled Geomechanical and Hydrological Behaviour of Fractured Rocks. *Comput. Geotechnics* 85, 151–176. doi:10.1016/j.compgeo.2016.12.024

Lemrich, L., Carmeliet, J., Johnson, P. A., Guyer, R., and Jia, X. P. (2017). Dynamic Induced Softening in Frictional Granular Materials Investigated by Discrete-Element-Method Simulation. *Phys. Rev. E* 96, 1–8. doi:10.1103/physreve.96.062901

Liu, N., and Fu, L.-Y. (2020a). Stress-orientation Effects on the Effective Elastic Anisotropy of Complex Fractured media Using the Lattice spring Models Coupled with Discrete Fracture Networks Model. *Interpretation* 8, SP31–SP42. doi:10.1190/int-2019-0286.1

Liu, N., and Fu, L. -Y. (2020b). Elastic Characteristics of Digital Cores from Longmaxi Shale Using Lattice spring Models. *Commun. Comput. Phys.* 28, 518–538.

Liu, N., Li, M., and Chen, W. (2017). Mechanical Deterioration of Rock Salt at Different Confinement Levels: a Grain-Based Lattice Scheme Assessment. *Comput. Geotechnics* 84, 210–224. doi:10.1016/j.compgeo.2016.12.007

Liu, N., Li, Y.-Y., Fu, L.-Y., Kong, Y., and Li, W.-S. (2021). Integrated LSM-DFN Modeling of Naturally Fractured Reservoirs: Roughness Effect on Elastic Characteristics. *Pure Appl. Geophys.* 178, 1761–1779. doi:10.1007/s00024-021-02728-9

Mauldon, M., Dunne, W. M., and Rohrbaugh, M. B. (2001). Circular Scanlines and Circular Windows: New Tools for Characterizing the Geometry of Fracture Traces. *J. Struct. Geology.* 23, 247–258. doi:10.1016/s0191-8141(00)00094-8

McClure, M. W. (2012). "Modeling and Characterization of Hydraulic Stimulation and Induced Seismicity in Geothermal and Shale Gas Reservoirs,". Dissertation thesis (Stanford University).

Mühlhaus, H. B., and Vardoulakis, I. (1987). The Thickness of Shear Bands in Granular Materials. *Géotechnique* 37, 271–283. doi:10.1680/geot.1987.37.3.271

Murphy, H. D., and Fehler, M. C. (1986). "Hydraulic Fracturing of Jointed Formations," in Proceedings of the SPE international meeting on petroleum engineering (Beijing: Society of Petroleum Engineers Association). doi:10.2118/14088-ms

Nitka, M., and Tejchman, J. (2015). Modelling of Concrete Behaviour in Uniaxial Compression and Tension with DEM. *Granular Matter* 17, 145–164. doi:10.1007/s10035-015-0546-4

Oda, M. (1977). Co-ordination Number and its Relation to Shear Strength of Granular Material. *Soils and Foundations* 17, 29–42. doi:10.3208/sandf1972.17.2_29

Oda, M., and Iwashita, K. (2000). Study on Couple Stress and Shear Band Development in Granular media Based on Numerical Simulation Analyses. *Int. J. Eng. Sci.* 38, 1713–1740. doi:10.1016/s0020-7225(99)00132-9

Olson Reichhardt, C. J., Lopatina, L. M., Jia, X., and Johnson, P. A. (2015). Softening of Stressed Granular Packings with Resonant Sound Waves. *Phys. Rev. E* 92, 8. doi:10.1103/physreve.92.022203

Patel, S., and Martin, C. D. (2017). Evaluation of Tensile Young's Modulus and Poisson's Ratio of a Bi-modular Rock from the Displacement Measurements in a Brazilian Test. *Rock Mech. Rock Eng.* 51, 361–373. doi:10.1007/s00603-017-1345-5

Rothenburg, L., and Kruyt, N. P. (2004). Critical State and Evolution of Coordination Number in Simulated Granular Materials. *Int. J. Sol. Structures* 41, 5763–5774. doi:10.1016/j.ijsolstr.2004.06.001

Scholtès, L., and Donzé, F.-V. (2013). A DEM Model for Soft and Hard Rocks: Role of Grain Interlocking on Strength. *J. Mech. Phys. Sol.* 61, 352–369. doi:10.1016/j.jmps.2012.10.005

Shiu, W., Donze, F.-V., and Daudeville, L. (2008). Compaction Process in concrete during Missile Impact: a DEM Analysis. *Comput. Concrete* 5, 329–342. doi:10.12989/cac.2008.5.4.329

Thornton, C. (2000). Numerical Simulations of Deviatoric Shear Deformation of Granular Media. *Géotechnique* 50, 43–53. doi:10.1680/geot.2000.50.1.43

Van Baars, S. (1996). "Discrete Element Analysis of Granular Materials,". Dissertation thesis. (Delft, Nederland: Delft University of Technology).

Williams, J. R., and Rege, N. (1997). The Development of Circulation Cell Structures in Granular Materials Undergoing Compression. *Powder Tech.* 90, 187–194. doi:10.1016/s0032-5910(96)03201-9

Zhang, Z. H. (2015). "The Numerical Simulation of the Three-axis Test of the Rough Soil of PFC3D Is Simulated,". Master's thesis (Yichang, China: China Three Gorges University).

Zhao, G. F. (2010). "Development of Micro-macro Continuum-Discontinuum Coupled Numerical Method,". Dissertation thesis (Lausanne, Swiss Confederation: École Polytechnique Fédérale de Lausanne).

Zhao, L., Yao, Q., Han, D.-H., Yan, F., and Nasser, M. (2016). Characterizing the Effect of Elastic Interactions on the Effective Elastic Properties of Porous, Cracked Rocks. *Geophys. Prospecting* 64, 157–169. doi:10.1111/1365-2478.12243

Conflict of Interest: The authors declare that the research was conducted in the absence of any commercial or financial relationships that could be construed as a potential conflict of interest.

The handling editor is currently organizing a Research Topic with one of the authors LF.

Copyright © 2021 Xu, Fu, Liu and Han. This is an open-access article distributed under the terms of the Creative Commons Attribution License (CC BY). The use, distribution or reproduction in other forums is permitted, provided the original author(s) and the copyright owner(s) are credited and that the original publication in this journal is cited, in accordance with accepted academic practice. No use, distribution or reproduction is permitted which does not comply with these terms.

frontiers in Earth Science

CORRECTION
published: 06 October 2021
doi: 10.3389/feart.2021.777904

Corrigendum: On the Determination of Coordination Numbers of Coupled DEM-DFN Model for Modeling Fractured Rocks

Xiaoyi Xu[1,2], *Li-Yun Fu*[3]*, *Ning Liu*[4]* *and Tongcheng Han*[3]

[1]State Key Laboratory of Ore Deposit Geochemistry, Chinese Academy of Sciences, Institute of Geochemistry, Guiyang, China, [2]University of Chinese Academy of Sciences, Beijing, China, [3]Key Laboratory of Deep Oil and Gas, China University of Petroleum (East China), Qingdao, China, [4]College of Mechanical and Electrical Engineering, Beijing University of Chemical Technology, Beijing, China

Keywords: numerical simulation, crack information inversion, coordination number, measurement window, DEM-DFN model

OPEN ACCESS

Edited and reviewed by:
Frontiers in Earth Science Editorial Office,
Frontiers Media SA, Switzerland

***Correspondence:**
Li-Yun Fu
lfu@upc.edu.cn
Ning Liu
nicolaliu@buaa.edu.cn

Specialty section:
This article was submitted to Earth and Planetary Materials, a section of the journal Frontiers in Earth Science

Received: *16 September 2021*
Accepted: *16 September 2021*
Published: *06 October 2021*

Citation:
Xu X, Fu L-Y, Liu N and Han T (2021) Corrigendum: On the Determination of Coordination Numbers of Coupled DEM-DFN Model for Modeling Fractured Rocks. Front. Earth Sci. 9:777904. doi: 10.3389/feart.2021.777904

A Corrigendum on

On the Determination of Coordination Numbers of Coupled DEM-DFN Model for Modeling Fractured Rocks

by Xu, X., Fu, L.-Y., Liu, N., and Han, T. (2021). Front. Earth Sci. 9:665275. doi: 10.3389/feart.2021.665275

In the published article, there was an error regarding the affiliations for Xiaoyi Xu. As well as having affiliation 1, they should also have 2 (University of Chinese Academy of Sciences, Beijing, China).

The authors apologize for this error and state that this does not change the scientific conclusions of the article in any way. The original article has been updated.

Publisher's Note: All claims expressed in this article are solely those of the authors and do not necessarily represent those of their affiliated organizations, or those of the publisher, the editors and the reviewers. Any product that may be evaluated in this article, or claim that may be made by its manufacturer, is not guaranteed or endorsed by the publisher.

Copyright © 2021 Xu, Fu, Liu and Han. This is an open-access article distributed under the terms of the Creative Commons Attribution License (CC BY). The use, distribution or reproduction in other forums is permitted, provided the original author(s) and the copyright owner(s) are credited and that the original publication in this journal is cited, in accordance with accepted academic practice. No use, distribution or reproduction is permitted which does not comply with these terms.

Advantages of publishing in Frontiers

OPEN ACCESS
Articles are free to read for greatest visibility and readership

FAST PUBLICATION
Around 90 days from submission to decision

HIGH QUALITY PEER-REVIEW
Rigorous, collaborative, and constructive peer-review

TRANSPARENT PEER-REVIEW
Editors and reviewers acknowledged by name on published articles

Frontiers
Avenue du Tribunal-Fédéral 34
1005 Lausanne | Switzerland

Visit us: www.frontiersin.org
Contact us: frontiersin.org/about/contact

REPRODUCIBILITY OF RESEARCH
Support open data and methods to enhance research reproducibility

DIGITAL PUBLISHING
Articles designed for optimal readership across devices

FOLLOW US
@frontiersin

IMPACT METRICS
Advanced article metrics track visibility across digital media

EXTENSIVE PROMOTION
Marketing and promotion of impactful research

LOOP RESEARCH NETWORK
Our network increases your article's readership